DOT/FAA/AR-07/13

Air Traffic Organization
Operations Planning
Office of Aviation Research
Washington, DC 20591

Turbine Rotor Material Design—Phase II

April 2008

Final Report

This document is available to the U.S. public through the National Technical Information Service (NTIS), Springfield, Virginia 22161.

U.S. Department of Transportation
Federal Aviation Administration

NOTICE

This document is disseminated under the sponsorship of the U.S. Department of Transportation in the interest of information exchange. The United States Government assumes no liability for the contents or use thereof. The United States Government does not endorse products or manufacturers. Trade or manufacturer's names appear herein solely because they are considered essential to the objective of this report. This document does not constitute FAA certification policy. Consult your local FAA aircraft certification office as to its use.

This report is available at the Federal Aviation Administration William J. Hughes Technical Center's Full-Text Technical Reports page: actlibrary.tc.faa.gov in Adobe Acrobat portable document format (PDF).

Technical Report Documentation Page

1. Report No.	2. Government Accession No.	3. Recipient's Catalog No.
DOT/FAA/AR-07/13		

4. Title and Subtitle	5. Report Date
TURBINE ROTOR MATERIAL DESIGN—PHASE II	April 2008
	6. Performing Organization Code

7. Author(s)

R. C. McClung*, Y.-D. Lee*, J. A. Tschopp†, S. K. Srivatsa†, G. R. Leverant*, C. J. Waldhart*, M. A. Jameel††, M. P. Enright*, H. R. Millwater**, D. J. Lehmann†††, L. Huyse*, S. H. K. Fitch***, J. P. Dubke††††

8. Performing Organization Report No.

9. Performing Organization Name and Address

* Southwest Research Institute®
6220 Culebra Road
San Antonio, TX 78238

** University of Texas at San Antonio
6900 North Loop 1604 West
San Antonio, TX 78249

*** Mustard Seed Software
1634 Brandywine Drive
Charlottesville, VA 22901

† GE Aviation
1 Neumann Way
Cincinnati, OH 45215

†† Honeywell
111 South 34th Street
Phoenix, AZ 85072

††† Pratt & Whitney
400 Main Street
East Hartford, CT 06108

†††† Rolls-Royce Corporation
2001 South Tibbs Avenue
Indianapolis, IN 46241

10. Work Unit No. (TRAIS)

11. Contract or Grant No.
99-G-016

12. Sponsoring Agency Name and Address

U.S. Department of Transportation
Federal Aviation Administration
Air Traffic Organization Operations Planning
Office of Aviation Research and Development
Washington, DC 20591

13. Type of Report and Period Covered
Final Report

14. Sponsoring Agency Code
ANE-110

15. Supplementary Notes

The Federal Aviation Administration Airport and Aircraft Safety R&D Division Technical Monitor was Joseph Wilson.

16. Abstract

The Federal Aviation Administration (FAA) is working with the aircraft engine industry to develop an enhanced life management process, based on probabilistic damage tolerance principles, to address the threat of material or manufacturing anomalies in high-energy rotating components, and the process is documented in current and planned versions of FAA Advisory Circular (AC) 33.14. An integrated team of Southwest Research Institute, GE Aviation, Pratt & Whitney, Honeywell, and Rolls-Royce Corporation has developed enhanced predictive tool capability and supplementary material/anomaly behavior characterization and modeling to support and enhance the process and the AC. Sensitivity studies were performed to guide a planned update of the hard alpha (HA) anomaly distributions. A computer code was developed to describe the diffusion of nitrogen or oxygen in titanium (Ti) from an inclusion during melting and heat treatment. The DEFORM™ forging microcode was validated experimentally and used to study cracking of HA anomalies during forging. Ultrasonic inspection methods were evaluated at the billet and forging stages. The influence of elevated oxygen on Ti-17 was evaluated with tensile and fatigue tests. Spin pit and coupon experiments were conducted to study the fatigue behavior of embedded HA. Vacuum fatigue crack growth (FCG) data were generated for three nickel alloys and Ti-6242. Thermomechanical FCG behavior was studied in IN-718. A literature survey was conducted on the stability and significance of surface residual stresses in fatigue. New DARWIN® versions were developed to address anomalies associated with surface damage in three-dimensional (3D) components and different types of inherent anomalies (including large numbers of 3D anomalies and nonnegligible crack formation lives). Enhancements in the probabilistic methods and many other new capabilities were developed to improve the overall efficiency and accuracy of the risk assessment computations in DARWIN. The partnered engine companies verified the accuracy and usability of DARWIN. A three-day DARWIN training workshop was conducted. An infrastructure was developed to support code licensing and distribution for users employing DARWIN.

17. Key Words	18. Distribution Statement
Aircraft gas turbine engines, Disks, Rotors, Low cycle fatigue, Crack growth, Probabilistic damage tolerance, Risk assessment, Forging, Nondestructive evaluation, Titanium hard alpha	This document is available to the U.S. public through the National Technical Information Service (NTIS), Springfield, Virginia 22161.

19. Security Classif. (of this report)	20. Security Classif. (of this page)	21. No. of Pages	22. Price
Unclassified	Unclassified	610	

Form DOT F 1700.7 (8-72) Reproduction of completed page authorized

ACKNOWLEDGEMENTS

Successful completion of this large, multidisciplinary research project would not have been possible without the significant contributions and assistance of many different people. Some are named as authors on this report, and many others deserve special mention.

Special appreciation is extended to the Federal Aviation Administration (FAA) employees and consultants who provided sustained support, encouragement, and guidance throughout the program. Heartfelt thanks goes to Tim Mouzakis of the Engine and Propeller Directorate in the New England Regional Office, Bruce Fenton (now retired) and Joe Wilson of the William J. Hughes Technical Center, and FAA Consultants Jon Bartos and Nick Provenzano.

The entire program was motivated and guided by the Rotor Integrity Sub-Committee (RISC) of the Aerospace Industries Association (AIA), capably led by chairman Bill Knowles of Honeywell.

Direct leadership was provided by the industry Steering Committee comprising representatives from the four partner companies: GE Aviation, Honeywell, Pratt & Whitney (P&W), and Rolls-Royce Corporation (RRC). Current members are chair Darryl Lehmann (P&W), Jon Tschopp (GE Aviation), Ahsan Jameel (Honeywell), and Jon Dubke (RRC). Previous members during the term of this program include Nichola Howard and Gary Mihlbachler (GE Aviation)—both former chairs, Sandeep Muju (Honeywell), and Geoff Ward and Doug Herrmann, both from RRC.

Jon Tschopp (GE Aviation) provided leadership on the hard alpha anomaly distribution task (appendix A), and Masamichi Hongoh (P&W) performed some supporting sensitivity studies.

Tony Giamei (United Technologies Research Center/Belcan) and Ernesto Gutierrez-Miravete (Rensselaer Polytechnic Institute) developed the GROW code and completed code validation testing (appendix B). Masamichi Hongoh (P&W) prepared the GROW code development plan and provided code testing.

Shesh Srivatsa (GE Aviation) led the modeling of hard alpha deformation during forging, including validation of the DEFORM™ microcode (appendix C) and investigation of strain to cause cracking (appendix F). Jon Bartos and Andy Woodfield (both GE Aviation) led the supporting metallography effort, and Mike Keller (GE Aviation) conducted the seeded forging ultrasonic (UT) inspections (appendix E).

John Schirra (P&W) contributed to the validation work on DEFORM for bulk residual stresses.

Andy Woodfield (GE Aviation) led the investigation of elevated oxygen effects on titanium (Ti) alloys (appendix G).

Peter McKeighan (Southwest Research Institute (SwRI)) led the fatigue testing of coupon specimens from the seeded forgings (appendix H).

Lee Perocchi (GE Corporate Research and Development) performed the experimental measurements of the thermal expansion coefficient of hard alpha, and Peter Laz and Kwai Chan

(both SwRI) performed the analytical investigations of potential thermal residual stress effects on fatigue crack formation and growth from synthetic hard alpha seeds (appendix I).

Darryl Lehmann (P&W) provided leadership for the spin tests of titanium disks with hard alpha inclusions (appendix J). Paul Wawrzonek (Test Devices Inc.) conducted the spin tests, Jeff Umbach, Dave Raulerson, and Karl Gruca (P&W) completed UT inspections of the spin disks, and Hongyang Bao (P&W) led the fractographic assessments. Brent Barber (P&W) conducted vacuum crack growth testing of the Ti-6Al-4V spin disk material. Umbach, Raulerson, and Gruca also performed UT inspections of material containing nickel anomalies (appendix L).

Yancy Gill, Dennis Chamblee, Jim Hartman, Sandeep Muju, and Ahsan Jameel (Honeywell) performed and evaluated vacuum fatigue crack growth tests (appendix K), along with Barney Lawless (GE Aviation). Jack Telesman (NASA Glenn Research Center) is thanked for providing U720 specimen material and corresponding air fatigue crack growth data.

Barney Lawless (GE Aviation) conducted the IN-718 thermomechanical fatigue crack growth test program (appendix M), and Bob VanStone (GE Aviation) provided analytical support to the testing.

Yi-Der Lee (SwRI) developed the Flight_Life fracture mechanics module and all corresponding stress-intensity factor solutions (appendix N), with additional guidance from Craig McClung and Graham Chell (both SwRI). SwRI student employees Nairan Normand and Paul Green provided assistance with the generation of FADD-3D reference solutions to support new weight function stress-intensity factor solutions.

Craig McClung (SwRI) performed the literature survey of the stability and significance of residual stresses in fatigue (appendix O).

DARWIN® development (including appendices P, Q, R, S, T, U, and V) during TRMD-II was led first by Harry Millwater (formerly at SwRI) and then by Mike Enright (SwRI), with substantial support from Luc Huyse (SwRI). Chris Waldhart (SwRI) led DARWIN testing and validation activities, and SwRI student employees Hector Flores, Jeff Magnusson, and David Anderson provided assistance with these activities. Jeremy Zoss (SwRI) provided assistance with the implementation of DARWIN testing algorithms. Simeon Fitch (Mustard Seed Software) performed all graphical user interface development for DARWIN.

Harry Millwater and his students provided additional DARWIN support in his current position at the University of Texas at San Antonio (UTSA): student Faiyazmehadi Momin developed a link between finite element software and DARWIN such that additional random variables can be considered, and Wes Osborn developed and verified probabilistic sensitivity equations (appendix T) for implementation into DARWIN. UTSA student Sridhar Guduru developed a PERL language-based Darwin verification program called SCOUT.

Paul Roth (GE Aviation) provided guidance on the reliability analysis of materials with multiple anomalies (appendix P). Michael Gorelik and Dan Greving (both Honeywell) reviewed probabilistic methodologies.

Steve Schrantz (GE Aviation) provided additional DARWIN code development support.

The partner companies provided extensive evaluation and testing of new DARWIN releases throughout the program. Ting-Chieh Chang was the GE Aviation lead, and Darryl Lehmann was the P&W lead. Doug Hermann, Geoff Ward, and Jon Dubke performed validation studies at RRC. Eddie Perez-Ruberte, Kim Kington, Waled Hassan, Harry Kington, Dan Greving, Sandeep Muju, and Ahsan Jameel were DARWIN evaluators at Honeywell.

Mike Enright (SwRI) managed the development and presentation of the DARWIN short course and also managed the DARWIN industrialization activities. SwRI student employee Hector Flores developed an interactive video tutorial of the DARWIN graphical user interface.

Birdie Matthews (SwRI) provided superlative clerical assistance in preparing this large final report, and Patty Soriano and Roxanne Kerr (both SwRI) provided significant clerical support throughout the program. Gerry Leverant is thanked for his careful peer review of the final report.

Gerry Leverant served as the TRMD-II program manager and principal investigator at SwRI from the beginning of the program in March 1999 through his retirement in February 2003, and Craig McClung filled those roles for the remaining months of the program.

TABLE OF CONTENTS

			Page
EXECUTIVE SUMMARY			xix
1.	INTRODUCTION		1-1
	1.1	Background	1-1
	1.2	Organization of Research	1-3
2.	ANOMALY DISTRIBUTIONS		2-1
	2.1	Titanium HA Anomaly Distribution Updates	2-1
	2.2	Definition of Stealth Anomalies	2-2
	2.2.1	GROW Code Development	2-4
	2.2.2	Studies on Stealth Anomaly Region and Triple Melt Processing	2-4
	2.2.3	Conclusions	2-6
3.	EFFECT OF FORGING ON ANOMALY MORPHOLOGY AND BULK RESIDUAL STRESSES		3-1
	3.1	Validation of DEFORM™ Microcode	3-1
	3.1.1	Seed Polishing Procedure	3-1
	3.1.2	Microcode Validation	3-2
	3.1.3	Regression Analysis	3-4
	3.1.4	Validation of the Regression Equations	3-6
	3.1.5	Comparison of Direct and Regression Approaches	3-7
	3.2	Ultrasonic Inspection of Forgings	3-8
	3.2.1	Documentation of Previous Inspections	3-8
	3.2.2	New Inspection Results	3-8
	3.3	Processing Conditions Needed to Crack HA Anomalies	3-10
	3.3.1	Strain-to-Cracking HA	3-11
	3.3.2	Cracking Strain vs Forging Strain	3-12
	3.3.3	Cracking During Billet Conversion and Component Forging	3-13
	3.3.4	Anomaly Orientation	3-14
	3.4	Monitor Development of SFTC Code for Bulk Residual Stress	3-14
4.	CRACK NUCLEATION AND GROWTH DATA AND MONITORING		4-1

4.1 Mechanical Properties of Titanium With Elevated Oxygen 4-1
4.2 Fatigue Testing of Forged Coupons With HA Anomalies 4-3

4.2.1 Material and Procedures 4-4
4.2.2 Results and Analysis 4-4

4.3 Residual Stresses Associated With HA 4-6

4.3.1 Review of Experimental Results From TRMD-I 4-7
4.3.2 Measurement of Thermal Expansion Coefficient 4-7
4.3.3 Analysis of Residual Stresses in and Around HA Defects 4-7
4.3.4 Fracture Strength Modeling 4-8
4.3.5 Fatigue Modeling 4-8

4.4 Spin Pit Tests of Titanium Rotors Containing HA Anomalies 4-9

4.4.1 Pretest Analysis 4-9
4.4.2 Test Setup and Test Plan 4-9
4.4.3 Test Results 4-10

4.5 Vacuum FCG Testing 4-12

4.5.1 Materials and Test Procedures 4-12
4.5.2 Results 4-13

4.6 Nickel Anomaly Fatigue Testing 4-16

4.6.1 Additional UT Inspection of IN-718 Mults 4-17
4.6.2 Ultrasonic Inspection of IN-718 Forgings 4-18

4.7 Thermomechanical Fatigue Crack Growth Testing 4-19
4.8 Enhancement of Flight_Life Module 4-21

4.8.1 Stress-Intensity Factor Solutions 4-21
4.8.2 Other Flight_Life Enhancements 4-25

4.9 Stability and Significance of RSs in Fatigue 4-25

4.9.1 Literature Survey 4-26
4.9.2 Observations and Conclusions 4-27

5. PROBABILISTIC INTEGRATION DESIGN CODE AND DEVELOPMENT 5-1

5.1 Enhancement of DARWIN for Surface Anomalies 5-1

5.1.1 User Specified Surface Damage (1D Analysis) 5-2

5.1.2 Three Dimensional Finite Element-Based Surface Damage (3D Analysis) 5-2

5.2 Enhancement of DARWIN for General Inherent Anomalies 5-3

5.2.1 Probabilistic Approach 5-3
5.2.2 Adaptive Optimal Sampling Methodology 5-3
5.2.3 User-Supplied Crack Formation Module 5-4
5.2.4 Three-Dimensional Anomalies 5-5

5.3 General DARWIN Enhancements 5-5

5.3.1 Probabilistic Methods 5-5
5.3.2 Zone Discretization 5-6
5.3.3 Inspection 5-8
5.3.4 Mission Mixing 5-8
5.3.5 Stress Conversion 5-9
5.3.6 Stress Processing Enhancements 5-9
5.3.7 Data Management Enhancements 5-10
5.3.8 The PC/Linux Versions of DARWIN 5-10
5.3.9 Parallel Processing Capability 5-10
5.3.10 Influence of Finite Element-Based Random Variables 5-11

5.4 Graphical User Interface 5-11

5.4.1 Visualization and Polynomial Fitting of Stress Gradients 5-11
5.4.2 Report Generation 5-12
5.4.3 The GUI-Directed Execution of Risk Assessment Code 5-13
5.4.4 Additional Enhancements 5-13

5.5 DARWIN Electronic Help System 5-15
5.6 The OEM Evaluation of DARWIN 5-16

5.6.1 Quantitative Verification 5-16
5.6.2 Qualitative Evaluation 5-19
5.6.3 The OEM Review Comments 5-19

6. TECHNOLOGY TRANSFER 6-1

6.1 Progress Reports and Review Meetings 6-1
6.2 DARWIN Training Workshops 6-1
6.3 Conference Presentations and Journal Articles 6-2
6.4 Technology Transfer to Other Government Agencies 6-3

7. INDUSTRIALIZATION OF DARWIN SOFTWARE 7-1
7.1 Automated Software Verification 7-1
7.2 Software Revision Management 7-1

7.3 Internet Distribution of DARWIN 7-2

7.3.1 Internet Distribution of Software 7-2
7.3.2 Electronic Distribution of Manuals 7-2
7.3.3 Resources for New Users 7-2

7.4 User Support 7-2

7.4.1 Live User Support 7-3
7.4.2 Video Tutorials 7-3
7.4.3 Automated Bug Tracking Software 7-3

7.5 Software Licensing 7-3

7.5.1 Software License Agreement 7-3
7.5.2 Registered Trademark 7-3
7.5.3 Commercial Licensing Activity 7-4

8. SUMMARY 8-1

9. REFERENCES 9-1

APPENDICES

A—Supporting Studies for Titanium Hard Alpha Anomaly Distribution Updates

B—GROW Code Development, Validation, and Parametric Studies

C—Validation of DEFORM™ Microcode

D—Summary of Engine Company Inspection Results for Seeded and CBS Mults, Pancakes, and Disk Forgings From TRMD Phase I Program

E—Ultrasonic Inspection of Forgings

F—Deformation Strain Needed to Crack Hard Alpha Anomalies

G—Sensitivity of Ti-17 to an Oxygen-Stabilized Hard Alpha

H—Fatigue Testing of Forged Coupons With Embedded Hard Alpha Anomalies

I—Effects of Residual Stresses Caused by Differential Thermal Expansion in and Around Hard Alpha Particles in Titanium Alloys

J—Spin Pit Tests of Titanium Rotors Containing Natural and Seeded HA Anomalies

K—Vacuum Fatigue Crack Growth Testing

L—Inspection of Nickel Anomalies

M—Thermomechanical Fatigue Crack Growth Testing

N—Development of New Weight Function Stress-Intensity Factor Solutions

O—Literature Survey on the Stability and Significance of Residual Stresses During Fatigue

P—Risk Assessment for Large Numbers of Inherent Material Anomalies

Q—Adaptive Optimal Sampling Methodology for Multiple Anomalies

R—Confidence Bounds

S—Importance Sampling Techniques

T—Probabilistic Sensitivities

U—Optimal Sampling for Zones

V—Efficient Conditional Failure Analysis

W—List of Publications and Presentations During “Turbine Rotor Material Design, Phase II” Grant

LIST OF FIGURES

Figure		Page
1-1	The Broad Vision for an Enhanced Rotor Life Management Process Based on Damage Tolerance	1-3
2-1	Classifications of Stealth Anomalies	2-3
2-2	Stealth Region Predicted for Given Temperature Exposure	2-5
2-3	Core Width as a Function of Initial Particle Size and Concentration for a Representative Exposure History	2-5
2-4	Comparison of JETQC Data to Predicted Core Versus Core Plus Diffusion Zone Size Neglecting Pure Beta Phase	2-6
3-1	Typical Ultrasonic Inspection Data for One Seed	3-2
3-2	Typical Analysis and Metallographic Data for One Seed	3-3
3-3	Comparison of Measured Deformed DZ Size With Predictions From the Direct Application of the Microcode	3-3
3-4	Comparison of Measured Deformed HA Size With Predictions From the Direct Application of the Microcode	3-4
3-5	Comparison of Regression Equation Prediction With Microcode Prediction for the Deformation Strain in the DZ	3-5
3-6	Comparison of Regression Equation Prediction With Microcode Prediction for the Deformation Strain in the HA	3-5
3-7	Comparison of Measured Deformed DZ Size With Regression Equation Predictions	3-6
3-8	Comparison of Measured Deformed HA Size With Regression Equation Predictions	3-7
3-9	Hard Alpha Ultrasonic Response in Billets vs Subsequent Forgings	3-10
3-10	Contours of Strain to Cracking as a Function of Strain Rate and Temperature and Temperature and Damage	3-11
3-11	Contours of HA Damage as a Function of Strain Rate and Temperature and Temperature and Macrostrain	3-11
3-12	Representative Damage Contours in SB-1 to SB-3	3-13
3-13	Surface Stresses Predicted Accurately for As-Quenched Condition	3-15

3-14	Surface Stresses Predicted Accurately for Stress-Relieved Condition	3-16
3-15	Subsurface Stresses Predicted Accurately for As-Quenched Condition	3-16
3-16	Internal Stresses Predicted Accurately or Quenched/Rough Machined Condition	3-17
3-17	Prediction of Influence of Cooldown Rates	3-17
3-18	Prediction of Influence of Geometry Effects on Local Cooldown	3-18
4-1	Effect of Oxygen Additions on Tensile Properties (a) Ultimate Tensile Strength, (b) 0.2% Offset Yield Strength, (c) Percent Elongation, and (d) Percent Reduction in Area	4-2
4-2	Effect of Oxygen Additions on Dwell Fatigue Properties: Stress to Give a 2000-Cycle Dwell Fatigue Life	4-2
4-3	Fracture Surfaces of Specimen SB-3-25C (Cluster With DZ)	4-5
4-4	Comparison of Predicted FCG Lifetime and Actual Total Fatigue Test Lifetime for Forged Coupons With HA Anomalies	4-6
4-5	Disk SB-6 Fracture Surface at Inclusion With Scanning Directions Identified	4-11
4-6	Vacuum FCG Results for P&W and Honeywell Ti-6242 Materials at 600°F	4-14
4-7	Vacuum FCG Results for Waspaloy at R = 0.05 and Three Different Temperatures	4-15
4-8	Effect of Environment (Air Versus Vacuum) on Fatigue Crack Growth Rates in Waspaloy at 500°F, R = 0.05	4-15
4-9	Vacuum FCG Results for IN-718 at R = 0 and Four Different Temperatures	4-16
4-10	C-Scan Images for Mults 804085-3X and 804618-5A1	4-18
4-11	C-Scan Images for Mults 804539-5X and 804618-5A	4-19
4-12	Comparison of Experimental Lifetimes With Predictions Based on the Conventional Stress Rainflow Method for IN-718, René 95, and René 88DT Subjected to TMF Histories	4-21
5-1	Three-Dimensional Surface Damage Analysis Capability Linked Directly to a 3D Finite Element	5-2
5-2	Architecture Linking the User-Supplied Crack Formation Module to DARWIN	5-4
5-3	Illustration of Zone Refinement Capability	5-7
5-4	Illustration of the Element Subdivision Technique	5-7

5-5 Illustration of the Onion Skin Capability 5-8

5-6 Visualization and Polynomial Fitting of Bivariant Stress Gradients 5-12

5-7 Illustration of GUI Report Generation Capability 5-13

5-8 Illustration of Crack Growth Visualization Capability 5-14

5-9 The DARWIN Electronic Help System in Web Browser Format 5-15

5-10 Illustration of OEM Verification of DARWIN for Inherent Anomalies 5-17

5-11 Illustration of OEM Verification of Flight_Life Module 5-17

5-12 Illustration of OEM Verification of Induced Anomalies, Comparing DARWIN Life Predictions to Experimental Results (a) Surface Crack, (b) Center Notch, (c) Compact Tension, and (d) Bolthole 5-18

6-1 Agenda for DARWIN Short Course 6-2

LIST OF TABLES

Table		Page
2-1	Summary of HA Distribution Process Studies	2-2
4-1	Summary of Vacuum FCG Test Conditions	4-13
4-2	Production UT Inspection Results for Ni Billet Indications	4-17
4-3	Maximum UT Response for Billet and Pancake Indications	4-19
4-4	Summary of New or Enhanced SIF Solutions Developed During TRMD-II	4-22
5-1	Summary of DARWIN Enhancements Developed Under TRMD-II	5-1
5-2	Summary of 3D Element Types Supported in DARWIN	5-3

LIST OF ACRONYMS

1D	One-dimensional
2D	Two-dimensional
3D	Three-dimensional
AC	Advisory Circular
AE	Acoustic emission
AFRL	Air Force Research Laboratory
AIA	Aerospace Industries Association
A/P	Actual-to-predicted life
API	Application program interface
ASTM	American Society for Testing and Materials
BE	Boundary element
BEM	Boundary element method
C(T)	Compact tension
CBS	Contaminated Billet Study
CC	Corner crack
CDF	Cumulative distribution function
CFA	Conditional failure analysis
CFL	Courant Friedrich-Levy
CFM	Crack Formation Module
COV	Coefficient of variation
CP	Commercially pure
cpm	Cycles per minute
CTE	Coefficient of thermal expansion
CVS	Concurrent Version System
CX	Cold expansion
DAC	Distance amplitude correction
DARWIN	Design Assessment of Reliability With INspection
DR	Deep rolling
DZ	Diffusion zone
EDM	Electro-discharge machining
ETC	Engine Titanium Consortium
FAA	Federal Aviation Administration
FBH	Flat-bottom hole
FCG	Fatigue crack growth
FE	Finite element
FEA	Finite element analysis
FEM	Finite element method
FPI	Fluorescent penetrant inspection
FTI	Fatigue Technology, Inc.
GE-CR&D	GE Corporate Research and Development
GBP	Glass bead peening
GUI	Graphical user interface
HA	Hard alpha
HIP	Hot isostatically pressed

HP	Hewlett Packard
HPT	High-pressure turbine
IS	Importance sampling
IT	Inspection technique
JETQC	Jet Engine Titanium Quality Committee
LCF	Low-cycle fatigue
LPB	Low-plasticity burnishing
LPT	Low-pressure turbine
LSP	Laser shock peening
MA	Moving average
N	Nitrogen
NASA	National Aeronautics and Space Administration
NAVAIR	Naval Air Systems Command
NDE	Nondestructive evaluation
O	Oxygen
OEM	Original equipment manufacturer
P/N	Part number
P&W	Pratt & Whitney
PC	Personal Computer
PD	Potential drop
pdf	Probability density function
PDF	Portable document format
PDS	Probabilistic design system
PM	Powder metallurgy
POD	Probability of detection
POF	Probability of fracture
PWF	Point weight function
R&D	Research and development
RCF	Risk contribution factor
RISC	Rotor Integrity Sub-Committee
rpm	Revolutions per minute
RS	Residual stress
RT	Room temperature
SB	Seeded billet
SC	Surface crack
S/N	Signal-to-noise ratio
SCOUT	SCanning Outfile Utility
SC(T)	Surface crack tension
SEM	Scanning Electron Microscope
SENBH	Single edge notch button head
SFTC	Scientific Forming Technologies Corporation
SIF	Stress-intensity factor
S-N	Stress life
SP	Shot peening
SwRI	Southwest Research Institute
TMF	Thermomechanical fatigue

TRMD	Turbine Rotor Material Design
USAF	United States Air Force
UT	Ultrasonic
UWF	Univariant weight function
VAR	Vacuum arc remelting
WF	Weight function
XML	Extensible Markup Language

EXECUTIVE SUMMARY

The Federal Aviation Administration (FAA) is currently working with the aircraft engine industry to develop an enhanced life management process, based on probabilistic damage tolerance principles, to address the threat of material or manufacturing anomalies in high-energy rotating components. This process for hard alpha (HA) anomalies in titanium (Ti) rotors is documented in FAA Advisory Circular (AC) 33.14-1, and future revisions to AC 33.14 will address other materials and anomaly types. The Turbine Rotor Material Design Program, Phase II (TRMD-II) was a multiyear research program that addressed shortfalls in the data and technology required to support and enhance the AC and its implementation. The integrated TRMD-II team, comprising Southwest Research Institute®, GE Aviation, Pratt & Whitney, Honeywell, and Rolls-Royce Corporation, developed enhanced predictive tool capability and supplementary material/anomaly behavior characterization and modeling. Major TRMD-II accomplishments include the following:

- Sensitivity studies were performed to guide a planned update of the AC 33.14-1 HA anomaly distributions. These studies incorporated TRMD-generated technology as well as new data and insights from original equipment manufacturer (OEM) experience to identify variables with the most significant impact.

- To better understand the evolution of HA anomalies and predict the maximum expected sizes of undetected anomalies, a computer code was developed and calibrated to describe the diffusion of nitrogen or oxygen in titanium from an inclusion during metal forming and heat treatment.

- Detailed nondestructive evaluation (NDE) and metallography were performed on forgings with seeded or natural HA anomalies to validate the DEFORM™ forging microcode. Measurements of core and diffusion zone (DZ) sizes in the forgings compared favorably with microcode predictions. The microcode was also used to characterize the conditions associated with cracking of HA anomalies during forging. Studies of representative forging shapes indicated that ingot-to-billet conversion and component forging would, under common processing conditions, crack all HA anomalies with nitrogen (N) content greater than 4% (the lowest HA N content evaluated).

- Ultrasonic inspections performed on natural and seeded HA anomalies in final forged shapes indicated that multizone methods detected anomalies more effectively than conventional methods, and synthetic and natural HA inclusions were easier to detect in billets than in forgings.

- Tensile and fatigue tests were performed on high-oxygen seeded Ti-17. Results indicated only a small impact of elevated oxygen on tensile and dwell fatigue properties, a slightly higher impact than for Ti-64, but a much smaller impact than for Ti-6242.

- Experiments were conducted to understand the fatigue behavior of embedded HA. Fatigue tests were performed on coupons machined from seeded forgings. The total fatigue life observed was always nearly at least twice as long the calculated fatigue crack

growth (FCG) life, based on the assumptions that crack nucleation life was zero and the initial crack size was equal to the core plus DZ size. Spin pit tests were performed with material from TRMD-I forgings containing natural and synthetic HA anomalies. Analyses using the fracture mechanic module (Flight_Life) in the Design Assessment of Reliability With Inspection (DARWIN®) code indicated that initial crack sizes nearly corresponded to core sizes than DZ sizes. The thermal expansion coefficient of bulk HA with different nitrogen contents was measured, and the results employed to evaluate the potential effects of thermally induced residual stresses on fatigue crack behavior at synthetic HA inclusions.

- Some damage tolerance issues for nickel-based superalloys were briefly explored. Thermomechanical FCG data for IN-718 were generated to evaluate simple stress rain flow analysis methods. Several Waspaloy mults with sonic indications were obtained, inspected, forged, reinspected, and selected for machining into coupon specimens for future fatigue testing. Vacuum FCG data were generated for two nickel alloys (IN-718 and Waspaloy) and a powder metallurgy nickel alloy (Udimet 720), plus one titanium alloy (coarse-grained Ti-6242).

- A survey was conducted of the scientific literature on the stability and significance of surface residual stresses in fatigue, based on a comprehensive bibliography of over 300 citations.

- New DARWIN versions were developed to address anomalies associated with surface damage (4.x and 5.x), as well as different types of inherent anomalies in other materials (6.0). DARWIN 5.x introduced a sophisticated three-dimensional (3D) graphical user interface (GUI) that enables the user to visualize and then slice a fully 3D finite element model at a chosen surface crack location to create a two-dimensional (2D) model for fracture mechanics analysis. New Version 6.0 capabilities address other types of inherent material anomalies, including risk assessment equations for large numbers of anomalies, user-supplied crack formation modules, and 3D modeling of anomalies and associated production inspections.

- Enhancements in probabilistic methods were developed to improve the overall efficiency and accuracy of the risk assessment computations, including enhanced importance sampling, optimal allocation of Monte Carlo samples, probabilistic confidence bounds, probabilistic sensitivities, conditional failure analysis methods, and an adaptive optimal sampling methodology.

- Many other new DARWIN capabilities were developed and implemented, including zone discretization methods; enhanced inspection capabilities; mission mixing; an enhanced ANS2NEU module; a searchable electronic help system; and computational efficiency improvements such as enhanced stress processing, restart capability, a new XML database system, personal computer (PC) and Linux versions, and parallel and batch processing. The GUI was enhanced significantly to support all new features as well as expanded visualization and report generation. Twelve new or enhanced stress-intensity factor (SIF) solutions were developed for the Flight_Life fracture mechanics module,

including a new bivariant weight function SIF formulation and novel strategies to improve computational speed.

- The partner engine companies participated in substantial review efforts to verify the accuracy and usability of DARWIN, including quantitative comparisons with experimental data, field experience, and internal company software; Alpha/Beta version evaluation to identify bugs and needed enhancements; and assessment of practical DARWIN use for design and certification.

- A 3-day DARWIN training workshop was conducted near the end of the program. Over 40 technical papers were presented and/or published at conferences and in archival journals. Royalty-free DARWIN licenses were provided to several other U.S. Government agencies.

- An infrastructure was developed for software configuration management, code licensing and distribution, and support for users employing DARWIN. License fees collected by Southwest Research Institute are exclusively used to enhance DARWIN for the benefit of engine manufacturers and the FAA.

1. INTRODUCTION.

1.1 BACKGROUND.

The traditional design practice for high-energy aircraft gas turbine rotors, the so-called safe-life method, implicitly assumes that all material or manufacturing conditions that may influence the fatigue life of a rotor have been captured in laboratory coupon and full-scale component fatigue testing. In addition, the final design is usually based conservatively on minimum properties. This methodology provides a structured approach for design and life management that ensures high levels of safety. However, industry experience has shown that certain material and manufacturing anomalies can potentially degrade the structural integrity of high-energy rotors. These anomalies generally occur very rarely and, therefore, are not typically present in laboratory test articles. However, on those rare occasions when anomalies are present in manufactured products in service, they represent a significant departure from the assumed nominal conditions, and they can result in incidents such the Sioux City accident in 1989 [1].

As a result of Sioux City, the Federal Aviation Administration (FAA) requested that industry, through the Aerospace Industries Association (AIA) Rotor Integrity Sub-Committee (RISC), review available techniques to determine whether a damage tolerance approach could be introduced to produce a reduction in the rate of uncontained rotor events. The industry working group concluded that additional enhancements to the conventional rotor life management methodology could be developed that explicitly addressed anomalous conditions. During the development of this probabilistic damage tolerance approach, it became apparent to RISC that the capabilities and effectiveness of the emerging technology could be significantly enhanced by further research and development. In early 1995, Southwest Research Institute® (SwRI®), in partnership with four major U.S. engine manufacturers GE Aviation, Honeywell, Pratt & Whitney (P&W), and Rolls-Royce Corporation) and with guidance from RISC, proposed a multiyear research and development (R&D) program and was awarded an FAA grant to address identified shortfalls in technology and data. This program, titled Turbine Rotor Material Design (TRMD), developed enhanced predictive tool capability and supplementary material/anomaly behavior characterization and modeling with a particular focus on hard alpha (HA) anomalies in titanium (Ti) rotors.

One of the key outcomes of that work was a probabilistic damage tolerance computer code called DARWIN® (Design Assessment of Reliability With INspection). DARWIN integrates finite element models and stress analysis results, a new fracture mechanics module for low-cycle fatigue (LCF) called Flight_Life, material anomaly data, probability of anomaly detection, and uncertain inspection schedules with a user-friendly graphical user interface (GUI) to determine the probability of fracture of a rotor disk as a function of operating cycles with and without inspections. Other major accomplishments under the TRMD grant included:

- The generation of fatigue crack growth (FCG) data in vacuum for three titanium rotor alloys [2]

- Experimental and analytical characterization of the constitutive and damage properties of bulk titanium HA [3 and 4]

- Experimental characterization of HA cracking in titanium alloy matrix material under monotonic and cyclic loading [5]

- Development of a forging microcode capable of predicting the fracture and change of location and shape of HA during reduction from ingot to billet and from billet to final forged shape, forging experiments to validate the microcode

- Development of advanced probabilistic methods for risk assessment of components with rare inherent material anomalies [6]

- Validation of DARWIN against industry experience

Further details are available in the comprehensive TRMD Final Report [7]. The DARWIN code developed under this program received an R&D 100 Award from R&D Magazine as one of the 100 most technologically significant new products of the year in 2000.

An incident at Pensacola, Florida, in 1996 called special attention to surface anomalies induced by manufacturing activities. With guidance from the FAA, RISC began to apply and extend the insights and methods developed for inherent material anomalies in titanium rotors to the broader problem of induced surface anomalies in all rotor materials. SwRI, in continuing collaboration with the industry, proposed and was awarded a second FAA grant (Turbine Rotor Material Design—Phase II).

The broad vision for enhanced life management of high-energy rotors shared by the FAA and RISC is summarized in figure 1-1. Here, damage tolerance is implemented as a supplement to the existing safe-life methodologies. The vision embraces both inherent anomalies introduced during production of the rotor materials and induced surface anomalies introduced during manufacturing or maintenance of the rotors themselves. All rotor materials are addressed—titanium alloys, conventional cast and wrought nickel alloys, and advanced nickel alloys employing powder metallurgy technologies. The red check mark adjacent to the titanium HA box in figure 1-1 indicates that the methods and supporting technologies to address that threat have been developed and are now formally defined in FAA Advisory Circular (AC) 33.14-1.

The TRMD grants have closely mirrored the incremental realization of this vision. TRMD-I focused exclusively on titanium HA anomalies, and some TRMD-II activities were dedicated to the completion of those objectives. The primary focus of TRMD-II was to support the development and implementation of probabilistic damage tolerance methods for induced surface anomalies at boltholes. Other TRMD-II activities explored technology issues relevant to new and anticipated FAA and RISC efforts to address inherent material anomalies in a variety of nickel materials.

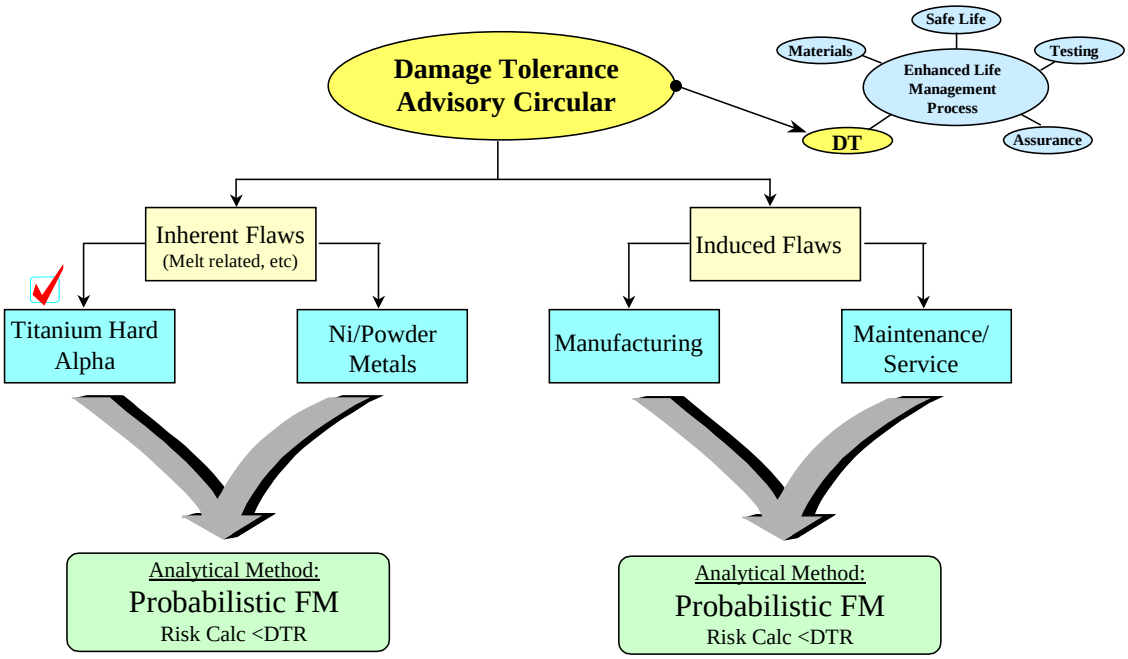

Figure 1-1. The Broad Vision for an Enhanced Rotor Life Management Process Based on Damage Tolerance

1.2 ORGANIZATION OF RESEARCH.

The TRMD-II grant was organized into six major tasks.

Task 1 focused on the supporting technology for the derivation of titanium HA anomaly distributions. Sensitivity studies were performed to support a planned update of the HA anomaly distribution included in AC 33.14, incorporating new TRMD-generated technology (vacuum FCG data, the HA forging microcode, and the spin pit and coupon HA fatigue tests) as well as new data and insights from original equipment manufacturer (OEM) experience to identify the variables with the most significant impact on the resulting distributions. To better understand the evolution and predict the size of HA anomalies, a mathematical model and computer code were also developed and validated to describe the diffusion of nitrogen or oxygen in titanium from an inclusion during metal forming and heat treatment.

Task 2 addressed the effects of forging and heat treatment on HA anomaly morphology and residual stresses (RS). Detailed nondestructive evaluation (NDE) and metallography were performed on the forgings with seeded or natural HA anomalies produced in TRMD-I to validate the HA forging microcode developed in TRMD-I. The HA microcode was also used to assess the influence of nitrogen content, temperature, strain, and strain rate on the orientation, deformation, and cracking of HA anomalies during the forging operation. The relative detectability of HA in billets versus forgings was evaluated. The development of the DEFORM™ forging analysis software to predict bulk RSs was evaluated.

Task 3 generated experimental data and analytical models for various crack nucleation and growth phenomena. Vacuum FCG data were generated at representative temperatures and stress ratios for one titanium rotor alloy (coarse-grained Ti-6242), two nickel rotor alloys (IN-718 and Waspaloy), and a powder metallurgy nickel alloy (Udimet 720). The coefficient of thermal expansion of bulk HA with different nitrogen contents was measured experimentally, and the results were employed in detailed stress, damage, and fracture mechanics analyses to evaluate the potential effects of thermally induced RSs on fatigue crack initiation and growth at HA inclusions. Spin pit tests and coupon fatigue tests were performed with material from the TRMD-I forgings containing natural and synthetic HA anomalies, conducting posttest fractography and metallography, and comparing test lives with Flight_Life analyses. Tensile and fatigue tests were performed on high-oxygen seeded Ti-17 to evaluate the potential impact of elevated oxygen on tensile and dwell fatigue properties. Thermomechanical FCG data for IN-718 were generated with diagnostic stress-temperature histories and used to evaluate simple stress rain flow analysis methods employing isothermal data from the temperature at the maximum stress time point. A robust new weight function (WF) stress-intensity factor (SIF) formulation was developed to accommodate general bivariant stress distributions on the crack plane, and highly accurate new WF SIF solutions were developed for select crack geometries under univariant and bivariant stressing using state-of-the-art, three-dimensional (3D) boundary element analysis to generate the reference solutions.

Task 4 emphasized the further development of the methodologies and software for reliability calculations in a design context. Advanced probabilistic methods were developed to improve the efficiency and accuracy of risk assessment computations. An importance sampling technique and associated confidence bounds were developed that significantly improved the risk computation speed (roughly two orders of magnitude faster than Monte Carlo simulation). A method was developed to assign Monte Carlo samples to zones based on relative risk that dramatically reduces the total number of samples (and associated computation time) required to predict risk for a specified level of accuracy. A sophisticated 3D GUI was developed for DARWIN that enables the user to load and visualize a fully 3D finite element model and stress results, select a surface crack location, slice the 3D model along the principal stress plane at that location, remesh the slice to create a two-dimensional (2D) stress model, build a 2D fracture mechanics model on the cut plane, and extract the necessary input for the 2D fracture mechanics life calculation. New DARWIN versions were developed to implement these and other technology advances in a computer program that can easily be used by engine companies for design and certification purposes. Versions 4.x introduced simple one-dimensional (1D) surface damage capabilities, Versions 5.x introduced full 3D surface damage features, and Version 6.0 introduced generalized capabilities for inherent anomalies. Each DARWIN version was validated against engine company experience.

Task 5 formalized the technology transfer process through meetings, reports, training workshops, publications, and presentations.

Task 6 facilitated technology transfer into industrial production contexts. At the request of the industry and FAA, an infrastructure was developed for formal software configuration management, code licensing and distribution, and user support for engine companies to employ DARWIN for official FAA and company purposes. This infrastructure includes a source code

repository, automated software verification procedures, bug tracking software, user manuals, an on-line help system, and a website.

This document is a comprehensive final report of all the investigations conducted and results obtained under the TRMD-II grant. The main body of the report is a summary of the major activities and the key results from the program. The details of the various investigations and results are contained in a series of appendices.

2. ANOMALY DISTRIBUTIONS.

2.1 TITANIUM HA ANOMALY DISTRIBUTION UPDATES.

Development of anomaly distributions for HA in titanium disk alloys was initiated by RISC in 1991. The Jet Engine Titanium Quality Committee (JETQC) had gathered data between 1990 and 1993 representing HA finds in billet and bar that had been ultrasonically inspected. While the available data were limited, they served as the basis for an extensive analysis performed by RISC to develop HA anomaly distributions that are applicable to Ti-64, Ti-6242, and Ti-17. The final distributions were set based upon calibration to actual field experience and associated assumptions. The analysis process and its results have been summarized elsewhere [8].

Since the development of the original HA distributions, several advancements in technology and available data have made it both possible and desirable to update the original HA anomaly distributions. For example, vacuum FCG data have been generated to characterize more accurately the growth rates of embedded cracks in titanium disk alloys, additional anomaly data from field finds have accumulated, and the DEFORM microcode has been developed to model anomaly deformation and damage during the forging process.

Sensitivity studies were performed on the model elements used to construct the HA distributions in order to determine which elements should be included in a revised derivation process. These studies included (1) variability in crack growth behavior, (2) variability in crack aspect ratio, (3) impact of vacuum crack growth data, (4) DEFORM microcode impact on original billet and forging HA deformation modeling assumptions, (5) possible alloy and melt practice bias, (6) impact of alternate approach to estimating the ingot distribution, (7) impact of effective inclusion size assumption, and (8) the impact of five additional years of JETQC HA data.

Table 2.1 summarizes all of the eight HA distribution studies and the preliminary conclusions on whether a studied effect should be included in the new derivation process for updated HA anomaly distributions. Further details are available in appendix A.

Table 2-1. Summary of HA Distribution Process Studies

No.	Study	Objective	Preliminary Conclusion
1	Crack growth scatter	Quantify the impact of expected material and analytical scatter on component POF predictions.	Negligible impact on POF predictions, but should be considered for technical completeness. INCLUDE
2	Crack aspect ratio	Quantify the impact of crack aspect ratio on component POF predictions.	Negligible impact on POF predictions. DO NOT INCLUDE
3	Titanium vacuum crack growth data	Quantify the impact of vacuum crack growth data on predicted POF for actual components.	Impact not large, but should be considered for technical accuracy and precedence. INCLUDE
4	HA deformation model	Evaluate the impact of the new DEFORM HA microcode on the construction of the HA distribution.	Negligible impact on POF predictions. DO NOT INCLUDE
5	Titanium melt practice	Study the relative differences between titanium melt practices and alloys and their impact on component POF.	Results suggest this is not significant. DO NOT INCLUDE
6	Alternative approach to estimate ingot distribution	Evaluate impact of alternative approaches to estimating the initial ingot distribution shape on correlation to component field experience.	Results suggest this may be significant. INCLUDE
7	Inclusion size, core vs core+ diffusion zone	Study the impact on component POF results due to the assumed initial crack location in the part (surface versus subsurface).	Results suggest this may be significant. POSSIBLY INCLUDE
8	Five additional years of JETQC data	Use 5 years additional JETQC data to study the impact of change in rate of three vacuum arc remelting HA (post-2000) versus vintage from ’90 (1990-1996).	Results suggest this may be significant. INCLUDE

POF = Probability of fracture

2.2 DEFINITION OF STEALTH ANOMALIES.

Historically, a number of rotor disk fracture and cracking events have originated from embedded anomalies, which, although they were substantial in size, were undetected by production

inspections. These anomalies have been called “stealth” anomalies due to their ability to evade inspection detection; i.e., the reflected signal is small relative to the inclusion size. Recent studies into the mechanisms and physics of sonic detection have led to a new understanding of what constitutes a stealth anomaly.

Stealth anomalies basically consist of three types (figure 2-1) in two categories. The first category is comprised of those anomalies whose sonic signal response is minimized. One type (Type A) within this category is due to anomaly orientation unfavorable to the path of the sonic signal. This could be a nearly planar anomaly that is not oriented preferentially with respect to the inspection plane or, as illustrated in figure 2-1, it could be a 3D anomaly (shaded region) with a crack or void (white region) that is not preferentially oriented with respect to the inspection plane. Since it is the crack or void in an anomaly that generally makes it more detectable by ultrasonic (UT) inspections, a crack or void that is not oriented in the plane normal to the inspection can be less detectable. The other type (Type B) within this category is due to sonic signal scattering associated with extreme anomaly surface irregularities. The irregular shape of the anomaly may diffuse a sonic signal and not reflect it back to the sensor for detection.

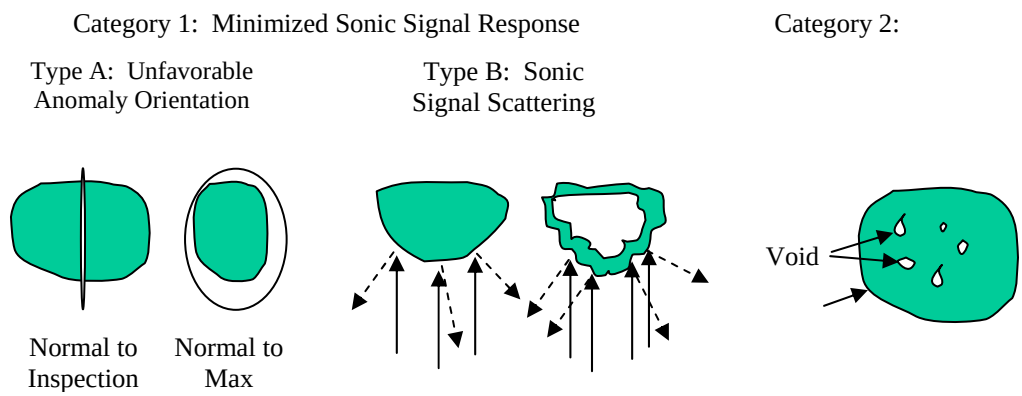

Figure 2-1. Classifications of Stealth Anomalies

The second category of stealth anomaly comprises those types that are ductile and well bonded, making them less likely to have cracking and voiding during ingot and billet conversion. The lack of cracking and voiding, combined with a similarity in elastic modulus and density to the parent alloy, renders them indistinguishable from the parent alloy for sonic detection. These anomalies are frequently created from a smaller material irregularity reacting chemically with the surrounding parent alloy to form a zone of material that is substantially weaker in tensile and fatigue capability than base metal. These areas are known as reaction zones, commonly gamma or gamma prime-depleted zones in nickel alloys, and diffusion zones in titanium alloys. HA nuggets with concentrations of nitrogen or oxygen in titanium characteristically have diffusion zones associated with them. In some instances, the nitrogen nugget can be fully processed out, leaving behind only a residual diffusion zone that is very similar in acoustic response to the parent alloy.

2.2.1 GROW Code Development.

The GROW code, consisting of a set of UNIX scripts and FORTRAN codes, was developed to assist suppliers and users of titanium base alloys in better understanding the dissolution history of nitride and oxide inclusions in molten and solid titanium alloys under various combinations of exposure temperature and time. The code was developed with the intention of allowing users to predict the formation of stealth anomalies, which can go undetected by NDE and may be harmful to fatigue life.

The GROW code takes thermal cycles associated with melting, metal forming, and heat treatment as input. Calculations are based on a finite difference method, using temperature integrated over time to accumulate the growth of the diffusion-affected zone. Concentration profiles are predicted as well as the extent of the various layers surrounding the inclusion. The diffusion process is assumed to follow the standard diffusion equation, which is complicated by the presence of multiple phases, each with its own set of characteristic physical or chemical properties. Since the instantaneous locations of the various phase interfaces depend on the instantaneous value of the nitrogen or oxygen concentration, the mathematical problem becomes nonlinear, and a numerical approach is most appropriate.

The code and user manual are available through the DARWIN website. Detailed information about the GROW code and its calibration and validation is provided in appendix B.

2.2.2 Studies on Stealth Anomaly Region and Triple Melt Processing.

Multiple studies were conducted to assess the formation of stealth anomalies and predictions relative to sizes measured in the JETQC data. A study was carried out to determine the shape of the stealth anomaly region in size and concentration space at fixed temperature and exposure time. The stealth region, as illustrated in figure 2-2, is hyperbolic in shape. The branch at small size and high concentration is bounded, but the branch at large size and low concentration is unbounded (for fixed exposure temperature and time.) At lower temperatures, stealth anomalies are not created, because the original inclusion is preserved due to low diffusivity. At higher temperatures, more dissolution occurs. Whether the stealth anomaly disappears depends on the exact combination of temperature and time selected.

A systematic set of 70 cases was run to determine, for a given temperature history, the residual core width versus initial particle size and nitrogen concentration. As the core width approaches zero (figure 2-3), the anomalies can reach a point where they may not be detectable and are classified as stealth anomalies.

The original JETQC data for the core and the core plus diffusion zone sizes are based on 3 times vacuum arc remelting (3XVAR) billet and bar finds. The data were used to derive the HA relative size distribution in the ingot, which includes the core and the diffusion zone sizes. A Monte Carlo simulation was run with 40 randomly generated core sizes in the ingot to validate the relative core to core plus diffusion zone sizes predictions from the GROW code for a representative 3XVAR process to the JETQC data. The diffusion zone size included the nitrided beta phase and the alpha plus beta phase. If the pure beta phase is neglected, which is less than

1 wt.% of nitrogen at 1400°C, the GROW code prediction compares well with the JETQC data (as shown in figure 2-4), particularly for core sizes greater than 20 mil.

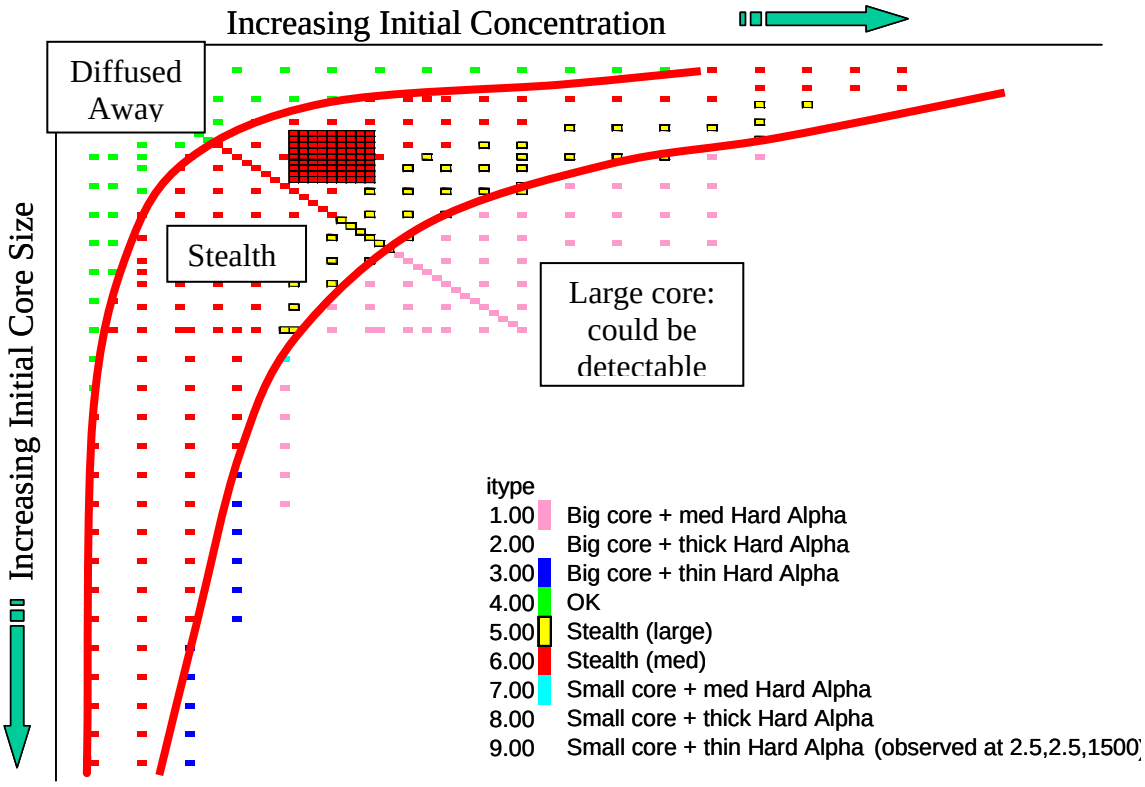

Figure 2-2. Stealth Region Predicted for Given Temperature Exposure

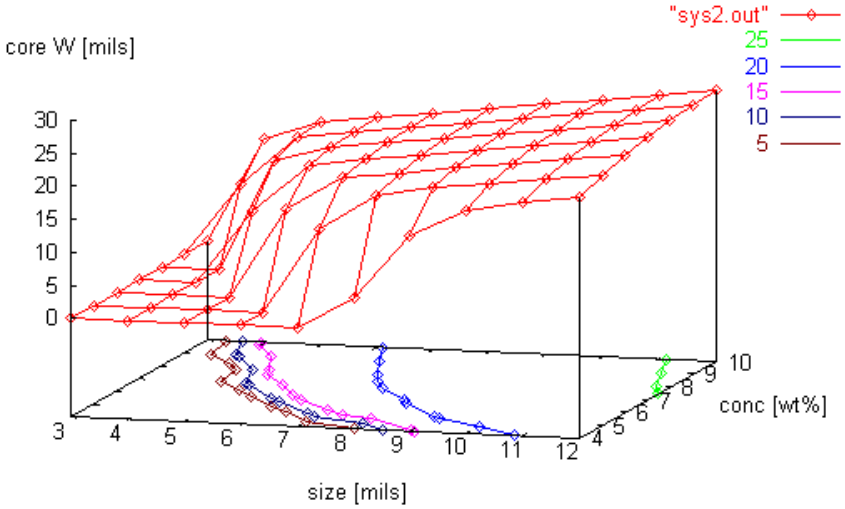

Figure 2-3. Core Width as a Function of Initial Particle Size and Concentration for a Representative Exposure History

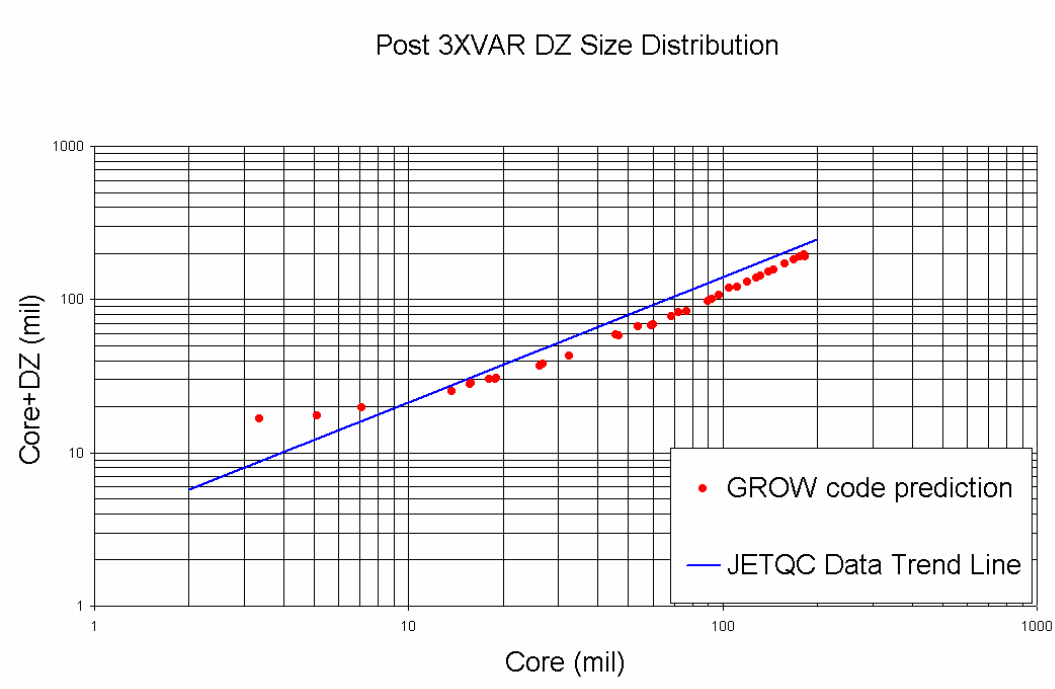

Figure 2-4. Comparison of JETQC Data to Predicted Core Versus Core Plus Diffusion Zone Size Neglecting Pure Beta Phase

2.2.3 Conclusions.

The GROW code development has helped to improve the understanding of the formation of stealth anomalies formed by the diffusion of nitrogen or oxygen inclusions in titanium during the melt processing. The code predicts concentration profiles as a function of the thermal exposure history. The GROW code has been successfully validated to provide acceptable predictions relative to available literature data for a series of dissolution experiments. These validation exercises have indicated a dependence on temperature, likely due to increasing convection with temperature, which can have a second-order effect of increasing the rates of diffusion relative to predictions. Thus, the predictions can be expected to set an upper limit regarding the amount of nitride or oxide remaining for a given anomaly and temperature history.

Parametric studies have demonstrated that the GROW code can provide useful information about the effect of the melting process on the resulting core and the diffusion zone (DZ) sizes. For a given melt process and initial anomaly size distribution, the maximum expected sizes of stealth anomalies can be predicted. This can be useful for material producers to optimize the melt temperature hold time and convection to minimize the number of potential anomalies remaining.

Comparisons of predictions to JETQC data have indicated close agreement between predictions for a random input set and measurements for the core and diffusion zone size relationship. This gives increased confidence in the code predictions as well as in the applicability of the shape of the anomaly distributions originally developed for engine rotor life prediction based on a limited data set of anomaly finds.

3. EFFECT OF FORGING ON ANOMALY MORPHOLOGY AND BULK RESIDUAL STRESSES.

3.1 VALIDATION OF DEFORM MICROCODE.

The HA anomaly distribution developed by RISC [8] was based on certain assumptions regarding the geometrical changes experienced by a HA anomaly when an ingot is converted to a billet and subsequently to an aircraft engine rotating disk forging. To test the validity of these assumptions, a finite element method (FEM) based deformation microcode was developed to predict the change in shape and orientation of HA anomalies during the metal forming processes. The microcode simulates the interaction and deformation among the HA inclusion, nitrogen DZ, and parent material during the forming process, and the degradation of the strength of the HA particle due to fracture using a continuum damage mechanics constitutive model. The information from the microcode could be used to establish the nature of the anomalies that would be interrogated by UT NDE methods during the billet and disk forging inspections and to assess the assumptions made with respect to the flaw size used in fracture mechanics analyses.

In the TRMD-I program, the microcode was developed and tested. This microcode was an add-on to the commercial macrodeformation forging analysis code DEFORM, which was developed by Scientific Forming Technologies Corporation (SFTC). Necessary constitutive property data for the HA and DZ material were determined experimentally. Forging experiments were conducted to generate data for microcode validation. Preliminary validation was performed using data from the constitutive property tests and one forging. The microcode was demonstrated through application to typical Rolls-Royce disk geometries. Further details were provided in the TRMD-I Final Report [7].

In TRMD-II, 28 of the 44 seeds from the TRMD-I forging experiments were cutup for microcode validation. Improved regression equations were developed based on the calculated relationships between anomaly deformation and forging macrostrain. The observed deformation in the forging experiments was compared with predictions based on direct application of the microcode or the regression equations. A detailed report of this activity is available in appendix C. For convenience, a brief summary follows.

3.1.1 Seed Polishing Procedure.

Seeds from pancake forgings of seeded billet (SB) SB-1, SB-3, and SB-4 were located using UT C-scan and time of flight measurements to approximate the depth of the seed from the surface. Once located, wire electro-discharge machining (EDM) was used to remove a cube of material about 0.75″ x 0.75″ x 0.75″ around the seed(s) while maintaining the original orientation from the forging.

After the seeds were removed, high-resolution, 25-MHz UT inspections were made from each side of the cubed blocks (figure 3-1). In addition, a B-scan was taken from the direction in which the seed was to be polished. This is also the direction from which the indication was located in the forging. The depth and location of the seeds in each cube were then reported to the metallography group, which used the information to quickly polish to the seed and to estimate equal distance for the selected number of polish steps (typically ten).

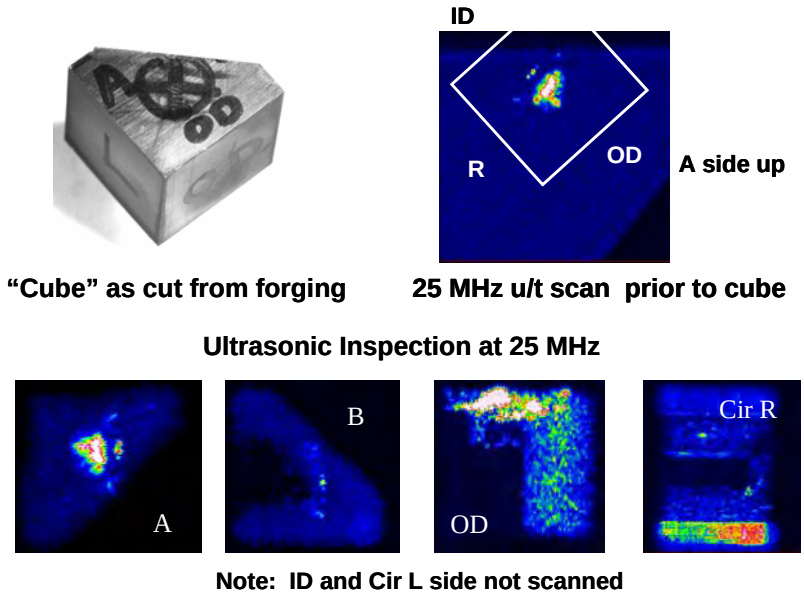

Figure 3-1. Typical Ultrasonic Inspection Data for One Seed

Incremental grinding and polishing of each cube was performed in 40-mil steps until the DZ and core were first revealed or a depth of 200 mil was reached. Thereafter, finish polishing, etching, photography, and microprobe analysis for nitrogen content was performed at 30-mil increments through the seed. The overall dimensions of HA seeds and DZ in axial, radial, and hoop directions were measured from the seed polish images. The measured values were recorded for the largest dimensions of the HA and the DZ in the three directions. Since the microcode cannot predict cracking and voiding, overall seed dimensions were used to validate the predictions, and it was not possible to validate all the details of inclusion damage.

3.1.2 Microcode Validation.

The validation of microcode predictions consisted of comparing the predicted overall deformed shapes of the seed and DZ with the corresponding measured shape, as shown in figure 3-2. Microcode validation was done in two ways: by direct application of the microcode and by application of regression equations derived from the microcode, as described further in sections 3.1.3 and 3.1.4.

Figure 3-3 shows a comparison of measured deformed DZ size with that predicted by the direct application of the microcode for the six seeds in forging SB-1. Figure 3-4 shows a similar comparison for the deformed HA size. Data are in all three directions: hoop, axial, and radial. The agreement between measurements and predictions was good for the radial and axial deformation. The hoop deformation was overpredicted due to the 2D axisymmetric assumption in the analysis.

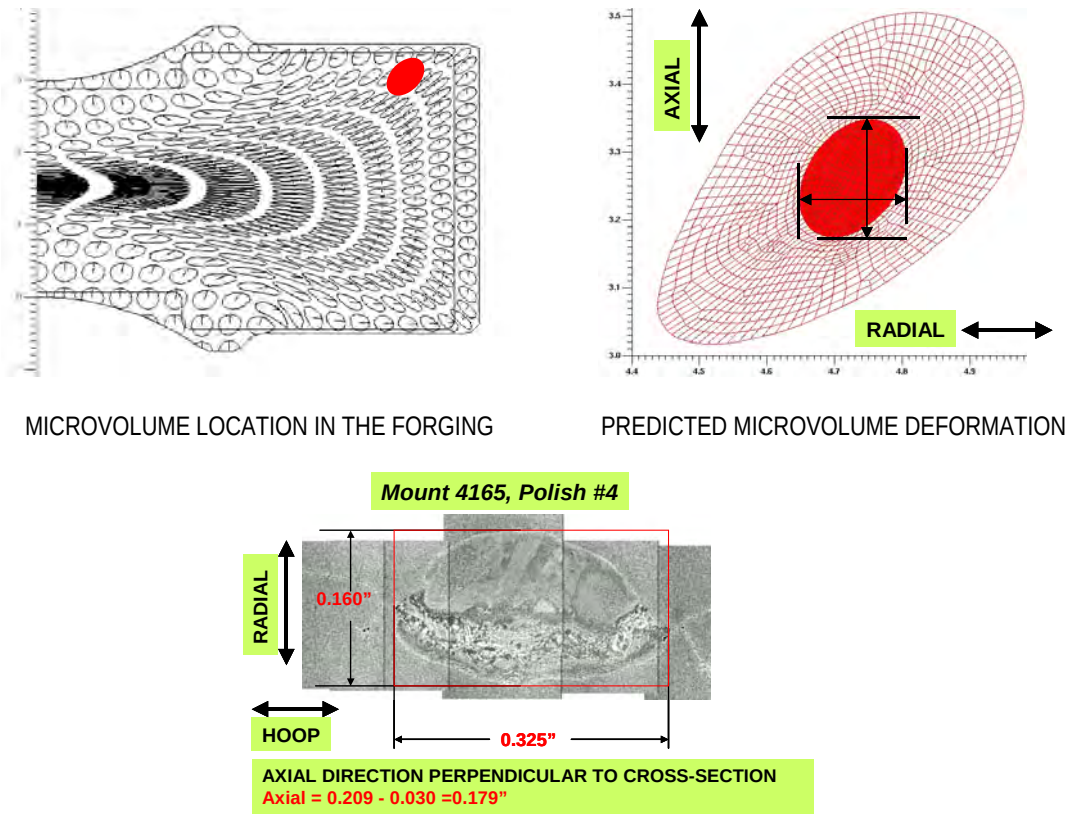

Figure 3-2. Typical Analysis and Metallographic Data for One Seed

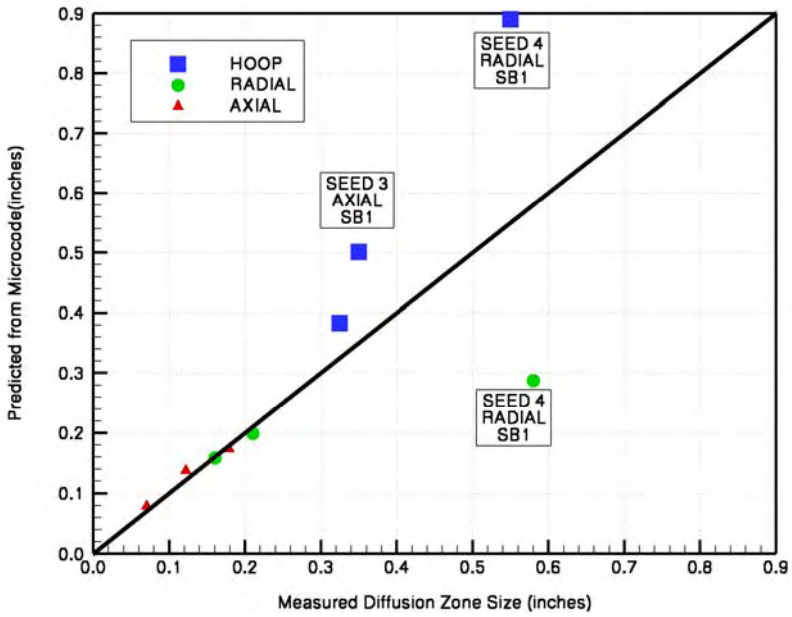

Figure 3-3. Comparison of Measured Deformed DZ Size With Predictions From the Direct Application of the Microcode

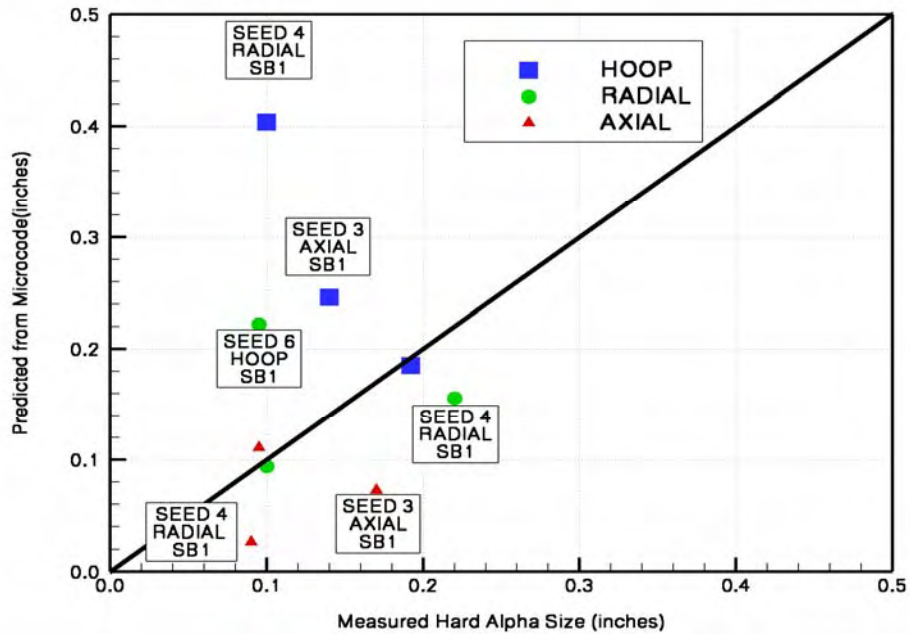

Figure 3-4. Comparison of Measured Deformed HA Size With Predictions From the Direct Application of the Microcode

3.1.3 Regression Analysis.

The deformation microcode is based on a 2D axisymmetric or plane-strain model. To more accurately establish the shape of the HA anomaly and the DZ, regression relationships were generated between the HA and DZ deformation and the forging macrostrain, and then these relationships were used to approximate 3D anomaly deformation in a forging.

Parametric studies were first performed with the microcode to evaluate the relative importance of different variables for anomaly deformation. HA and DZ nitrogen content, forging temperature, strain rate, and macrostrain were found to be the most significant variables; whereas, the aspect ratio of the inclusion, the ratio of DZ size to particle size, and the hydrostatic pressure were found to be relatively insignificant variables.

A new regression analysis was conducted in TRMD-II to obtain the inclusion strain and the DZ strain as a function of the variables investigated, where both the individual variables and their products were included in the regression equations. The resulting regression quality was much higher than in the TRMD-I regressions.

Figures 3-5 and 3-6 show a comparison of the values calculated from the regression equations with the microcode predictions used to generate the regression equations, showing that the regression equations provided an accurate representation of the data generated by the microcode.

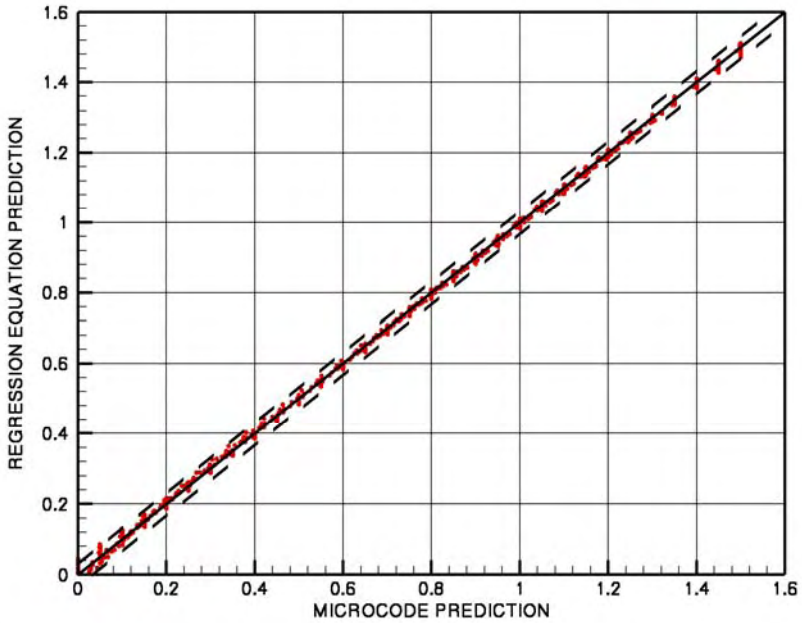

Figure 3-5. Comparison of Regression Equation Prediction With Microcode Prediction for the Deformation Strain in the DZ

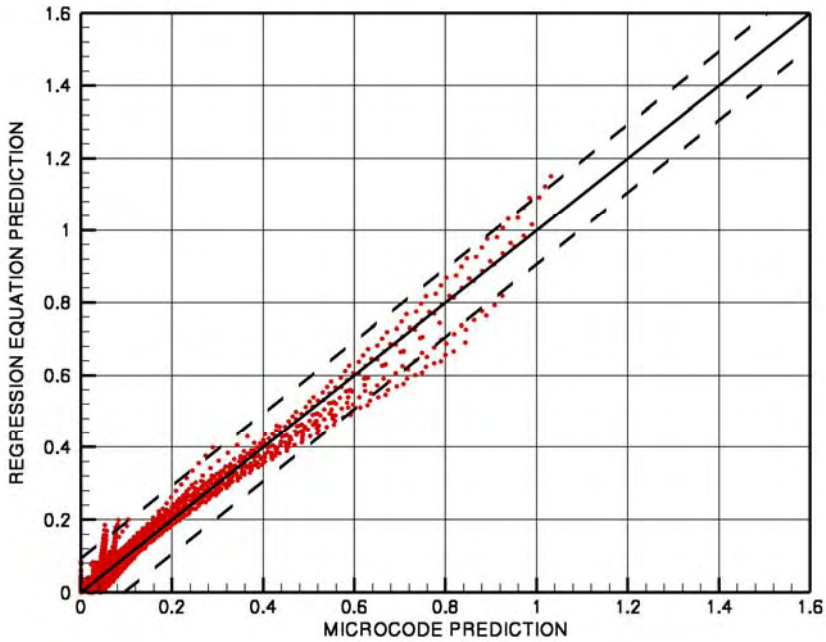

Figure 3-6. Comparison of Regression Equation Prediction With Microcode Prediction for the Deformation Strain in the HA

3.1.4 Validation of the Regression Equations.

The overall dimensions of the HA seeds and the DZ in the axial, radial, and hoop directions were also predicted by application of the regression equations. The regression equations were applied to all the seeds in the synthetically seeded forgings SB-1 to SB-4. Temperature, strain, and strain-rate histories at each of the seed locations were obtained from the model of the forging process using the point-tracking feature in DEFORM. Average values of strain, strain rate, and temperature over the process were used in the regression equations.

Figure 3-7 shows a comparison of the measured deformed DZ size with that predicted by the regression equations, and figure 3-8 shows a similar comparison for the deformed HA size. Data were provided in all three directions (hoop, axial, and radial) from all seeds that were cut up. Overall, the agreement between measurements and predictions was good. The DZ flows smoothly like the base material, but with a higher flow stress, and therefore, the predictions matched the measurements well. The flow of HA is discontinuous (depending on when failure occurs with accumulated damage/strain), and therefore, the agreement between the measurements and predictions for HA was not as good as for the DZ.

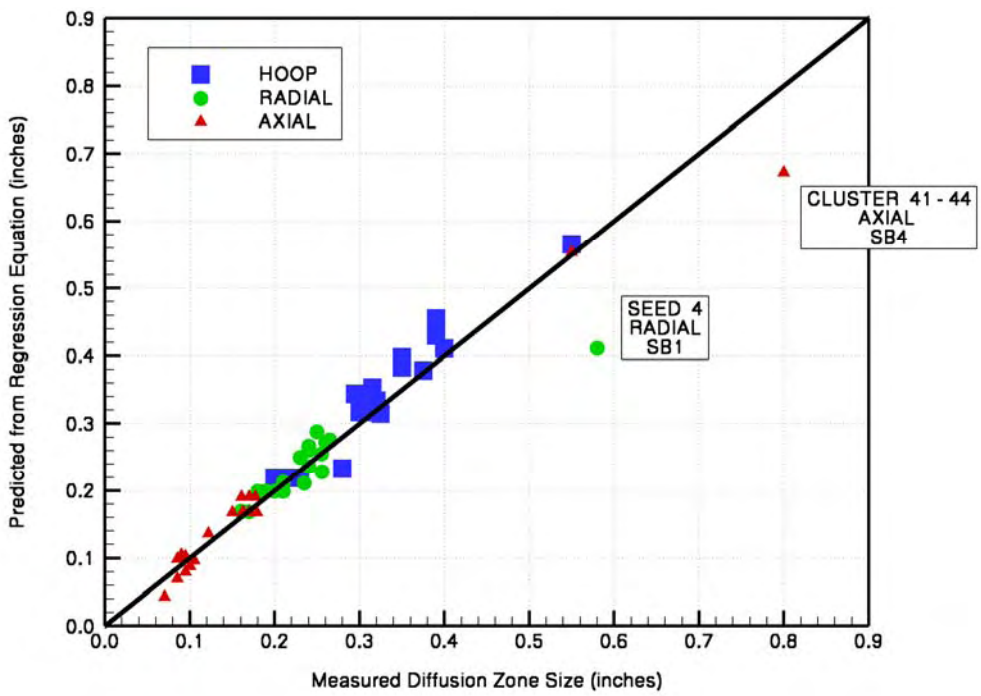

Figure 3-7. Comparison of Measured Deformed DZ Size With Regression Equation Predictions

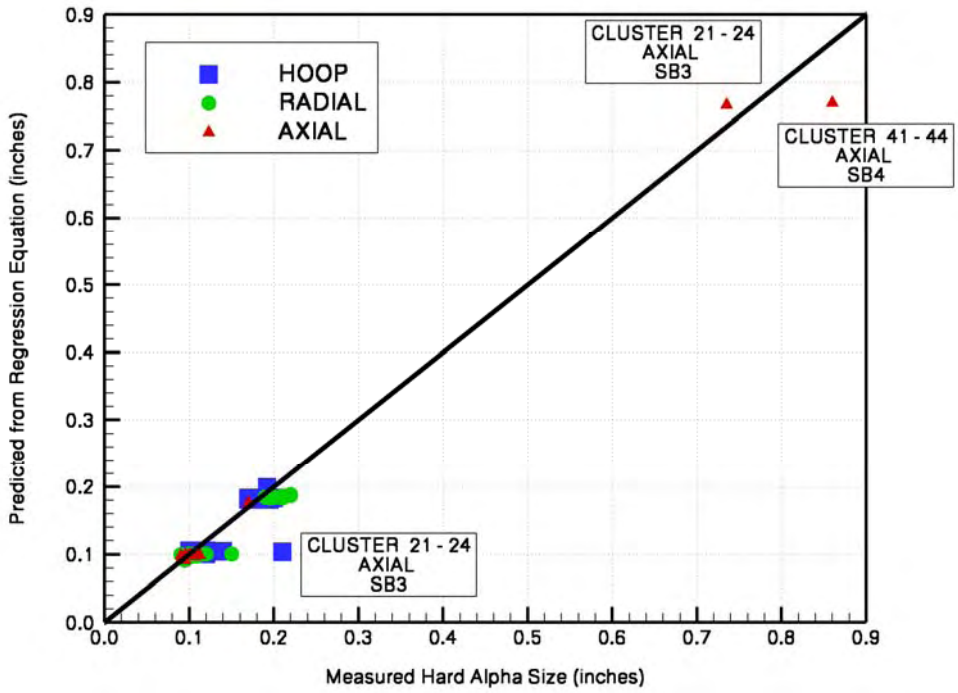

Figure 3-8. Comparison of Measured Deformed HA Size With Regression Equation Predictions

3.1.5 Comparison of Direct and Regression Approaches.

The overall predicted deformed shapes have been compared with measurements without looking at the details of fragmentation and voiding. In some cases, the predictions from a direct application of the microcode were in better agreement with the measurements. In other cases, the regression equations were better.

The microcode treats the seed as being 2D axisymmetric, a ring anomaly over 360 degrees. As a result, the microcode overpredicts hoop deformation and underpredicts radial and axial deformation. The actual deformation is 3D and cannot be accurately predicted by 2D methods.

The regression equations use the individual strain components scaled appropriately. Because the regression equations do not force the anomaly to be a full 360 degrees, they capture the 3D behavior more accurately than the microcode itself. The discontinuity between cracked and noncracked conditions is like a step function and is difficult to fit with regression.

The application of the microcode to each individual seed is more involved, and the use of the regression equations is the preferred way of predicting seed behavior. Overall, the results from the regression equations are satisfactory.

A sensitivity analysis was performed to assess the error bounds in the predictions due to uncertainties in the input variables in the regression equations. The DZ deformation was overpredicted on average by ~3% with a standard deviation of ~10%, and the HA deformation was underpredicted on average by ~5% with a standard deviation of ~8%.

3.2 ULTRASONIC INSPECTION OF FORGINGS.

3.2.1 Documentation of Previous Inspections.

During the TRMD-I program, forging experiments were conducted to evaluate the relative detectability of HA inclusions in billets versus forgings. These forgings included dogbone and backflow parts that were forged at Schlosser Forge Company using hot-die techniques, and pancake and engine disks that were forged at P&W Georgia using isothermal press forging.

The Engine Titanium Consortium (ETC) provided inspection results for the RMI Titanium Co. supplied contaminated billet study (CBS) billets. Initial TRMD-I program plans only called for GE Aviation inspections of the seeded billets, pancakes, and disks, and the CBS pancakes and disks. These inspection results were included in the TRMD-I final report. However, where permitted within the task schedule, Honeywell, P&W Florida, P&W Georgia, and Rolls-Royce Corporation also voluntarily performed additional inspections of the pancake and disk forgings as program enhancements using company funding. The full compilation of inspection results from the different companies includes a combination of production and laboratory inspections, as well as standard UT, multizone, and shear wave inspections.

Since these supplementary inspections were not in the initial program plan and conclusions from ETC had not been received at the time, it was agreed to only include the planned GE Aviation inspections in the TRMD-I final report. After further consideration, the TRMD Steering Committee has agreed to document all of the inspection results under the TRMD Phase II program to preserve these additional results for future reference by the industry team. These results are tabulated in appendix D. Conclusions regarding this data are being deferred to the ETC.

3.2.2 New Inspection Results.

TRMD-II UT NDE efforts examined both conventional and multizone inspection techniques on natural and seeded anomalies in the final forging shapes. Inspection in the billet and intermediate forging shapes was conducted in TRMD-I. The purpose of this study was to examine the effects of material processing on the location in the forging and UT response of synthetic and natural HA anomalies, to compare the inspection sensitivity of conventional and multizone procedures, and to compare the inspection sensitivity in billets versus forgings. A detailed report on this study is provided in appendix E.

3.2.2.1 Procedures.

Forgings identified as SB-# contained synthetic HA seeds that were placed in the billet. SB-1, SB-2, and SB-3 were dogbone forgings about 12 inches in diameter and 4 inches high, whereas, SB-4 was a backflow forging about 12 inches in diameter and 7 inches high at its largest dimension. The dogbone and backflow forgings were inspected from both faces, and each side required two scans corresponding to different regions of thickness.

Forgings B1BW3B and B3W2E were prepared using CBS material obtained from the ETC and had natural HA indications, which were detected and rejected by multizone billet inspection at a

production titanium supplier RMI. Forgings SB-5, SB-6, B1BW3B, and B3W2E were semifinished shapes designed as spin disks, about 12 inches in diameter and 5.5 inches high. These forgings were inspected from two surfaces, the bore face and the bore.

UT inspection took place at the GE Quality Technology Center in Evendale, Ohio. Laboratory equipment and instrumentation meeting all standard production inspection requirements were used for all inspections. GE Aviation conducted three different calibrated inspections on the forgings: Conventional #2 flat-bottom hole (FBH), Conventional #1 FBH, and Multizone #1 FBH.

3.2.2.2 Results.

All synthetic HA seeds were detected in the dogbone and backflow forgings by the Multizone #1 FBH inspection, except for one seed located near the edge of a machined surface. Both conventional inspections detected most of the seeds in these forgings with reasonably high amplitude and signal-to-noise ratio. However, high levels of background noise would have made Conventional #1 FBH impractical as a production inspection technique for the dogbone forgings. The background noise levels in the Conventional #1 FBH scans of the backflow forging were significantly lower than for the dogbone forging, perhaps due to the metallurgical condition resulting from the more severe forging process. The inspection results from the semifinished forgings also supported the general conclusion that the Multizone #1 FBH inspection can more effectively detect HA anomalies than either Conventional #1 or #2 FBH inspections. This advantage in multizone detectability becomes more evident as the reflectivity of the HA anomalies diminishes due to smaller size or lower nitrogen (N) content. The effects of HA composition and DZs on UT detectability were inconclusive.

All of these UT inspection results suggested that both synthetic and natural HA inclusions are easier to detect in the billet than in the forgings. The reported inspection data from dogbone, backflow, pancake, and semifinished forgings are summarized in figure 3-9. Here all the Multizone #1 data from the forgings have been numerically converted to the same calibration (gain) level as the Multizone #2 data from the billet inspections conducted previously. The 45-degree line in figure 3-9 represents equivalent response from the billet and forging inspections. Data falling above the 45-degree line indicate a larger response from the billet inspection, while data below the line indicate the corresponding forging provided a larger UT response.

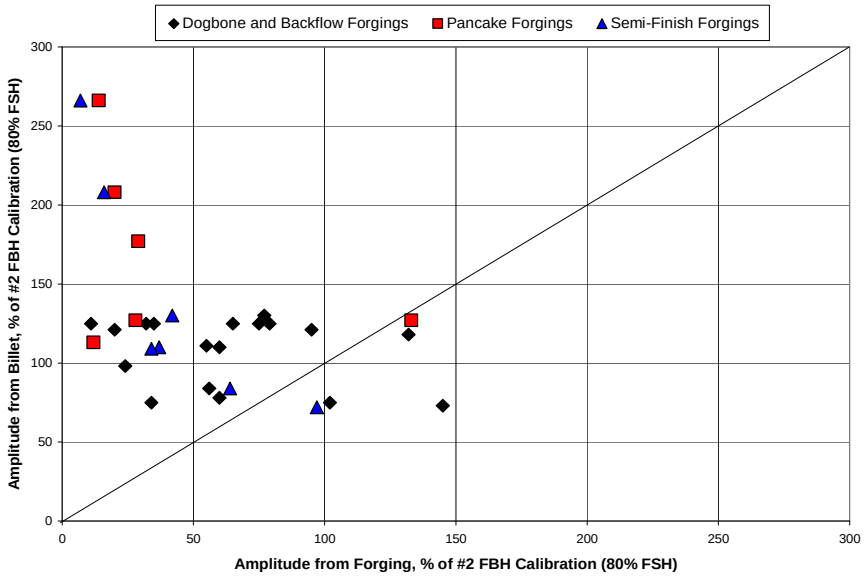

Figure 3-9. Hard Alpha Ultrasonic Response in Billets vs Subsequent Forgings

This detection advantage in billets can be ameliorated somewhat if the forging can be inspected at a higher calibration level (gain level) than the billet. This would appear to be possible in most cases if a Multizone inspection is used on the forging. However, the increase in background noise level associated with increasing conventional inspection sensitivity from a #2 FBH to a #1 FBH will undoubtedly result in some forgings (or parts of forgings) being uninspectable at the high-sensitivity Conventional #1 FBH level. These data tend to corroborate the JETQC production defect information, which indicates more HA anomalies have been ultrasonically detected in billets than in the subsequent forgings.

3.3 PROCESSING CONDITIONS NEEDED TO CRACK HA ANOMALIES.

The DEFORM microcode (see section 3.1) was also used to determine the conditions required to crack HA anomalies. This study was designed to provide insight into the likelihood of existing HA remaining uncracked under typical ingot conversion and component forging conditions, to provide insight into typical orientations of HA in forgings, and potentially, to direct the future development of inspection procedures to enhance detectability of HA anomalies.

The study is comprised of four major activities. The first activity was to determine HA cracking strain and damage (extent of cracking) as a function of nitrogen content and deformation parameters. The second activity was to link these results with DEFORM in order to predict damage (extent of cracking) in representative forging shapes and to validate the predictions by comparisons with observed cracking in the seeded billet studies. The third activity was to use this capability to determine the extent of HA cracking under typical production conditions, including representative ingot to billet conversion and three forging shapes. The fourth activity was to predict the forging flow lines along which melt-related anomalies tend to orient, using the same generic forging shapes. Each of these four activities is described briefly in turn. Further details are provided in appendix F.

3.3.1 Strain-to-Cracking HA.

The objective of the first activity was to determine the relationship between HA nitrogen content and strain-to-cracking in HA. The strain to HA cracking was determined as a function of five variables: HA nitrogen content, DZ nitrogen content, deformation temperature, deformation strain rate, and damage. HA damage was obtained as a function of the first four of these variables plus macrostrain. The results were graphed in contours of two of the five variables and fixed values of the other three variables. Representative graphs are shown in figures 3-10 and 3-11, and more graphs are available in appendix F.

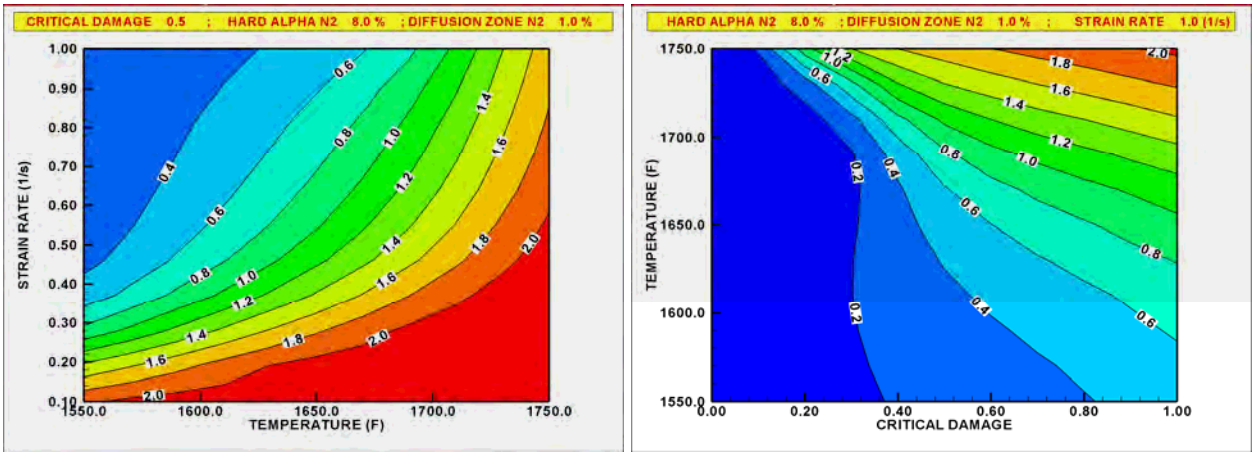

Figure 3-10. Contours of Strain-to-Cracking as a Function of (Left) Strain Rate and Temperature (Right) Temperature and Damage

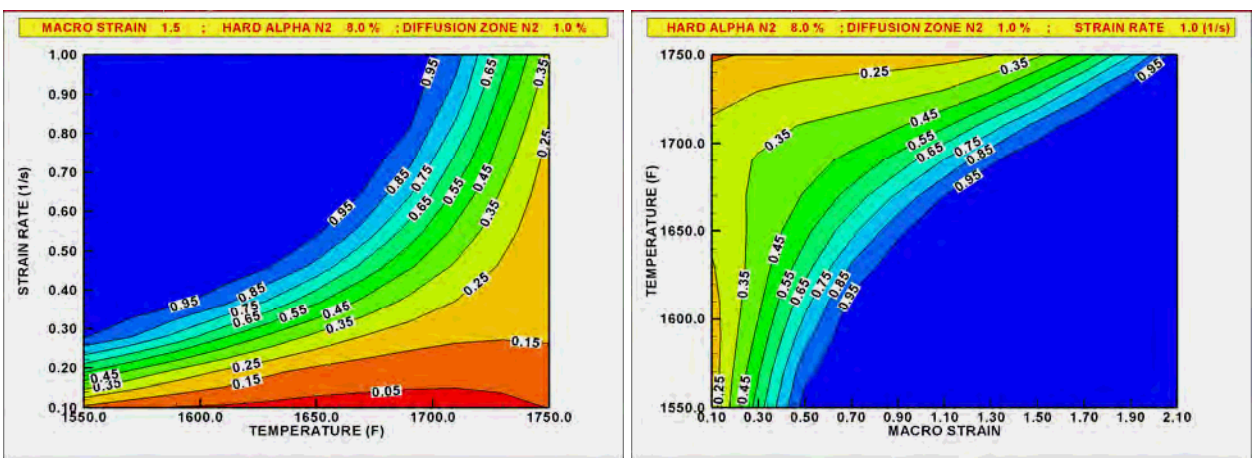

Figure 3-11. Contours of HA Damage as a Function of (Left) Strain Rate and Temperature (Right) Temperature and Macrostrain

The constitutive property data generated experimentally in TRMD-I indicated that HA deforms plastically when the nitrogen content is less than 4 weight %, but fractures when the nitrogen content is 4 weight % or greater. Guided by these experimental observations, constitutive equations were developed [3 and 4] to describe the fracture behavior of HA with nitrogen content >4% and the plastic flow behavior of HA with nitrogen content <4%, which is denoted

as a DZ in this study. These equations were used here to obtain the damage and strain to crack HA. The damage formulation is applied only to HA with >4% N. Calculations were done only up to 8% HA nitrogen content, since there is little difference for higher nitrogen contents.

Note that the microcode does not explicitly predict HA cracking, but instead uses a damage variable to simulate the effects of HA cracking (0 = no cracking; 1 = fully cracked). Therefore, the cracking strain and the extent of cracking were based on the accumulated HA damage.

The flow stress of intact and damaged HA (at 8% HA N2 and 3% DZ N2) and Ti-64 were compared at macrostrains ranging from 0.05 to 2.00 over a range of strain rate and temperature. This was done to show how the relative strengths of HA and Ti-64 change depending on the deformation region (strain, strain rate, and temperature). Results were generated as contour plots of flow stress in temperature strain-rate space for two contrasting values of macrostrain. With increasing macrostrain, HA flow stress was observed to decrease due to increased damage and cracking. Damage and cracking were found to initiate at high strain rate and/or low temperature and spread to lower strain rates and higher temperatures with increasing macrostrain.

Since HA flow stress depends on damage, strain, strain rate, and temperature in a complex way, the strain-to-cracking and damage do not vary monotonically with the deformation parameters. However, the strain to HA cracking was generally found to increase and damage was generally found to decrease with decreasing HA nitrogen content, decreasing DZ nitrogen content, increasing temperature, and decreasing strain rate.

3.3.2 Cracking Strain vs Forging Strain.

The objective of the second activity was to evaluate the strain-to-cracking for HA relative to the strain produced during ingot conversion and during component forging. Contours of strain during the forging of three generic nonproprietary shapes were obtained for one material, Ti-6Al-4V.

A user subroutine was written to process the damage and strain-to-cracking data in DEFORM. The subroutine creates contour plots of the HA damage based on the local forging temperature, strain, and strain rate for given HA and DZ nitrogen contents. The damage values indicate the extent of cracking for the given HA and DZ nitrogen contents. High damage values (approaching 1) indicate severe cracking, whereas low damage values (close to zero) indicate only the onset of cracking. Representative graphs are shown in figure 3-12.

The model was validated using the data from the seeded dogbone and backflow forgings from TRMD-I. A total of 44 seeds were fabricated in TRMD-I, some with and without diffusion zones, and some individual and some clustered. These seeds were inserted into billets SB-1 to S-B4 for subsequent forging, and 28 of the 44 seeds were cut up after forging for detailed investigation of cracking. It was found that the extent of cracking correlated approximately with predicted HA damage.

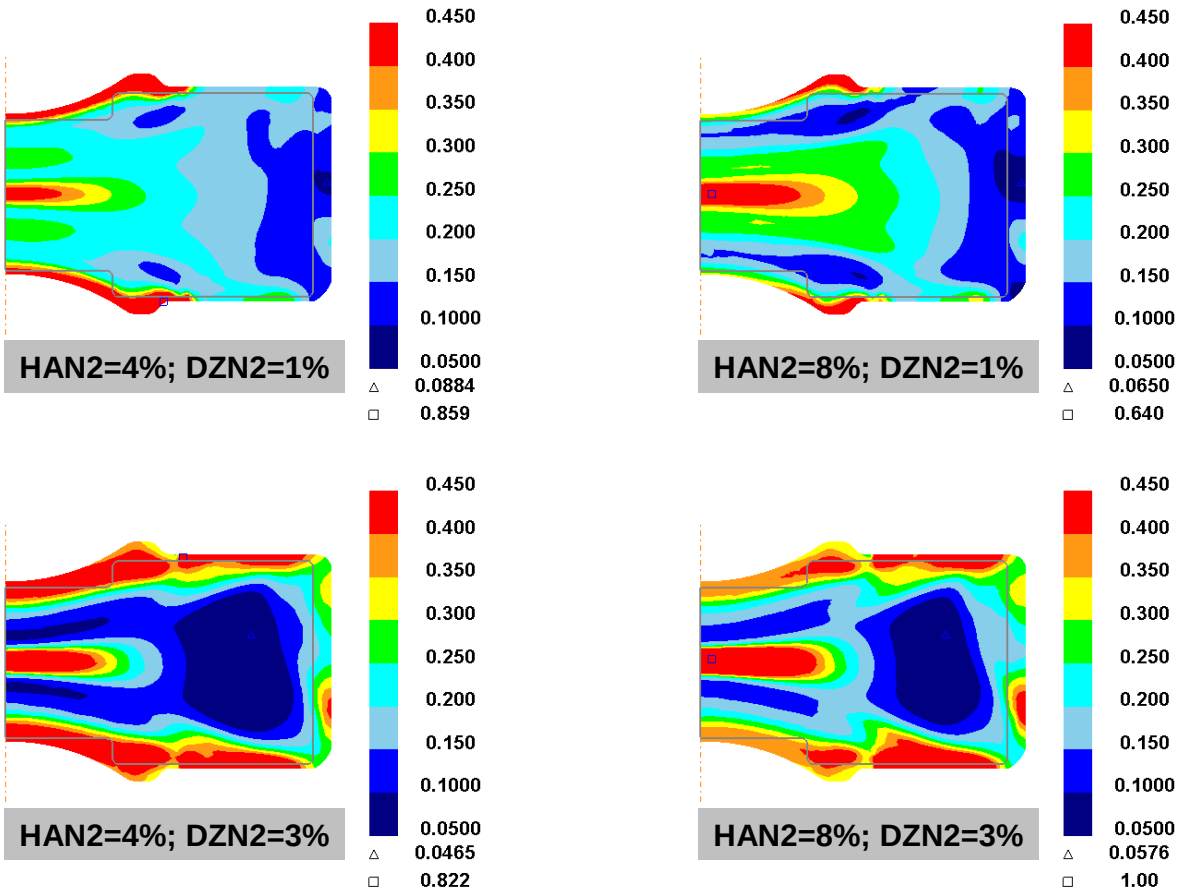

Figure 3-12. Representative Damage Contours in SB-1 to SB-3

3.3.3 Cracking During Billet Conversion and Component Forging.

The objective of the third activity was to determine HA nitrogen content that would not crack during typical production ingot conversion and component forging of Ti-6Al-4V, using generic shapes. A combination of the strain-to-cracking data and the forging macrostrain data was used to make this determination.

Damage was computed for the ingot-to-billet conversion process assuming a 36″ initial diameter and uniform strain set equal to *ln*(square of initial to final diameter ratio). The damage results were tabulated as a function of diameter reduction, HA N2, DZ N2, strain rate, and temperature. The study showed that ingot-to-billet conversion will, under commonly used processing conditions, crack all HA with nitrogen contents greater than 4%, which was the lowest HA nitrogen content evaluated. The extent of cracking will be less if the conversion is carried out at high temperatures (~1750°F) or low strain rates (~0.1/sec). In general, however, typical conversion temperatures and strain rates were observed to result in damage ~1 (i.e., fully cracked HA).

Three generic shapes were used to illustrate the strain-to-cracking capability for component forging. The first shape used was the seeded billet forging (SB-1 to SB-4) from TRMD-I. The

other two shapes were Rolls-Royce forgings that had been modeled in TRMD-I (acoustic emission (AE) 3007 fan disk and AE 2100/3007 Stage 14 compressor disk). Damage, effective strain, effective strain rate, and temperature contour plots were generated. The plots represent different time instants during forging and illustrate the evolution of damage as deformation progresses during forging. Temperatures greater than 1700°F and strain rates less than 0.5/sec were found to cause low rates of HA damage accumulation. Note that these calcuations considered the damage only from the forging process, and damage from the conversion process should be added to assess the total extent of HA cracking.

For nitrogen content less than 4%, the anomaly is treated as a DZ. The DZ results from partially dissolved HA cores during melting or conversion steps. Based on data from the TRMD-I flow stress experiments, the DZ-only anomaly is unlikely to crack after billet conversion and forging; it would only deform along with the base material, but to a lesser extent depending on its nitrogen content. In reality, there is no sharp transition between a DZ and an HA at 4% N. The transition from ductile to brittle behavior occurs over a range of nitrogen contents depending on the deformation conditions (strain, strain rate, and temperature) and the beta to (beta + alpha) transition temperature. More work is needed to characterize the transition zone.

3.3.4 Anomaly Orientation.

The objective of the fourth activity was to determine the orientations of melt-related anomalies during the conversion from ingot-to-billet and during forming from billet-to-component forging. In particular, the important determination was whether melt-related anomalies would likely end up oriented normal to forging surfaces. Forging flow lines along which melt-related anomalies tend to get oriented, along with material deformation patterns, were predicted for the same three generic shapes defined in the previous activity (section 3.3.3).

In some regions of these forgings, the flow lines are normal to forging surfaces. Melt-related anomalies that tend to orient along the flow lines might not be detectable if scanned from the face to which the flow lines are normal. When flow lines are normal to a face, a scan from another face or a shear scan should be used.

3.4 MONITOR DEVELOPMENT OF SFTC CODE FOR BULK RESIDUAL STRESS.

Bulk RSs resulting from the forging and heat treatment of titanium disks may contribute to fatigue initiation and crack growth of material anomalies such as HA inclusions. Tensile RSs may accelerate fatigue crack initiation and growth and subsequently reduce the fatigue life, whereas compressive RSs could retard the crack initiation and growth thus providing longer fatigue life capability. In addition, development of high RSs during quenching from heat treatment can produce quench cracks in the forgings. Scientific Forming Technologies Corporation has developed the DEFORM code to predict RSs resulting from the forging and heat treatment processes. The code development was reviewed to assess its performance relative to the needs of the TRMD program and its compatibility with the forging and heat-treat processes used to manufacture titanium and superalloy disks. The actual code verification studies were performed by P&W under alternate programs, and primarily on superalloy disks, but have been summarized in the TRMD-II program as part of an effort to share lessons learned with the

industry. Experience gained with superalloy disks is directly transferable to titanium disk materials.

In the last decade, use of finite element analyses for predicting RS states induced by processing has significantly increased. This has been driven by three main factors: the drive to reduce the cost of aerospace components, the development of user-friendly analysis routines and robust material models, and improved confidence in the predictions. Confidence in predictions has been gained through a broad range of calibration at various steps in the heat-treat process with respect to the surface stress state (figures 3-13 and 3-14), internal stress state (figures 3-15 and 3-16), influence of heat-treat rates (figure 3-17), and influence of heat-treat shapes (figure 3-18).

A closer review shows very good agreement between predicted and measured surface RSs in both the as-quenched, high RS state (figure 3-13) and stress relieved, reduced level of RS (figure 3-14) state. The same holds true for internal stress states measured in the as-quenched (figure 3-15) and machined condition (figure 3-16). Review of figures 3-17 and 3-18 shows that RS state can be strongly influenced by both component geometry (heat transfer coefficients/thermal behavior) and processing parameters (applied conditions). These are representative examples of several of the validation exercises conducted to develop confidence in the predictive capabilities of the tool and methodologies, provided an adequate knowledge of heat transfer coefficients and an appropriate material is available. It should be noted that this type of stress modeling has been successfully used in conjunction with failure criteria to define the process parameters and part configurations required to prevent quench cracking.

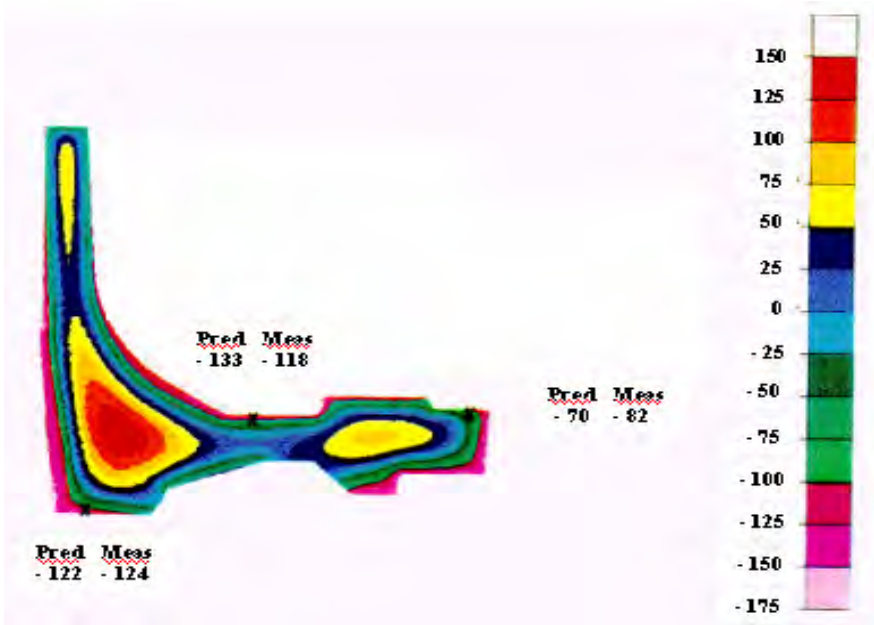

Figure 3-13. Surface Stresses Predicted Accurately for As-Quenched Condition

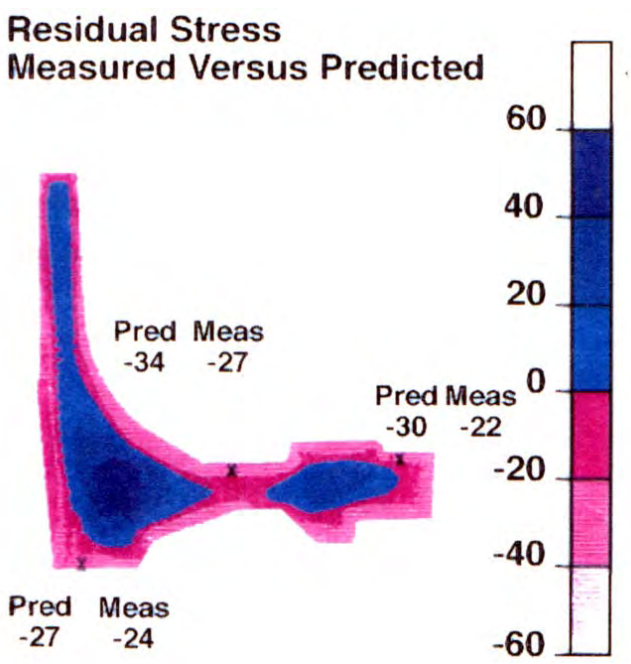

Figure 3-14. Surface Stresses Predicted Accurately for Stress-Relieved Condition

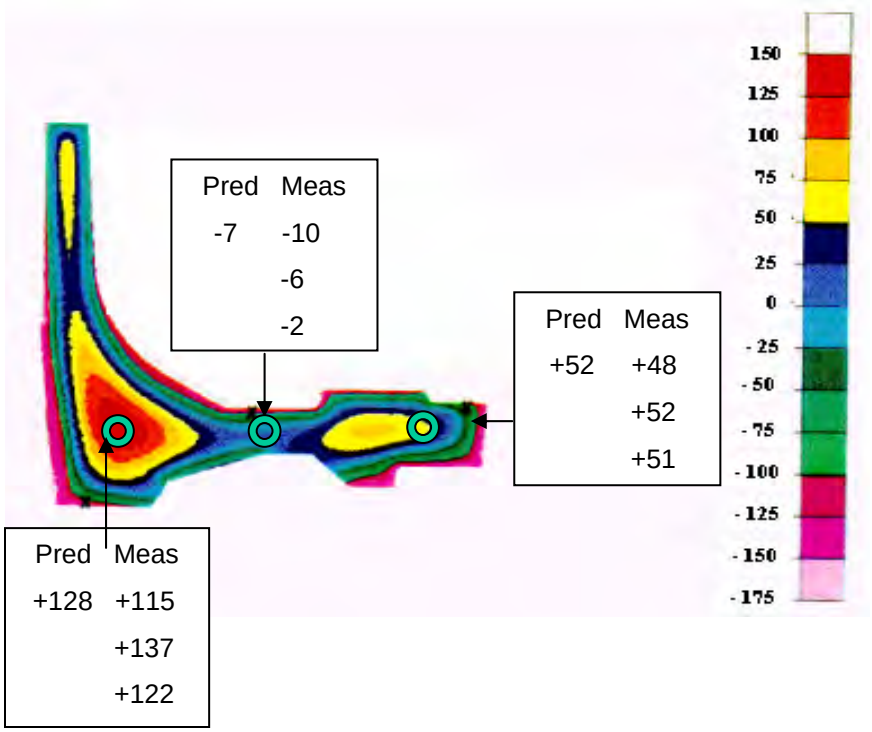

Figure 3-15. Subsurface Stresses Predicted Accurately for As-Quenched Condition

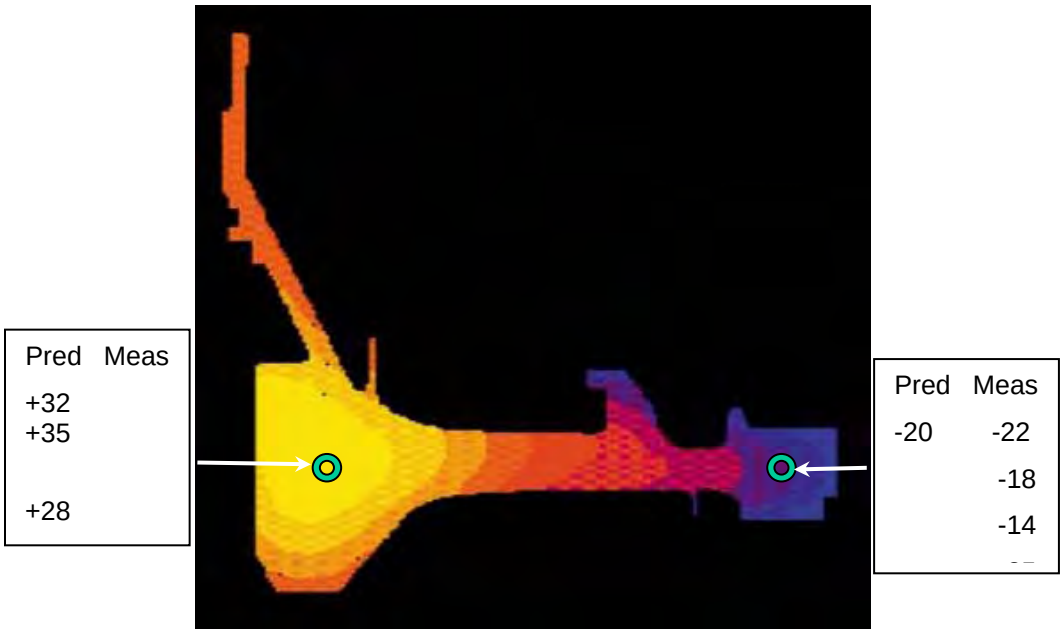

Figure 3-16. Internal Stresses Predicted Accurately or Quenched/Rough Machined Condition

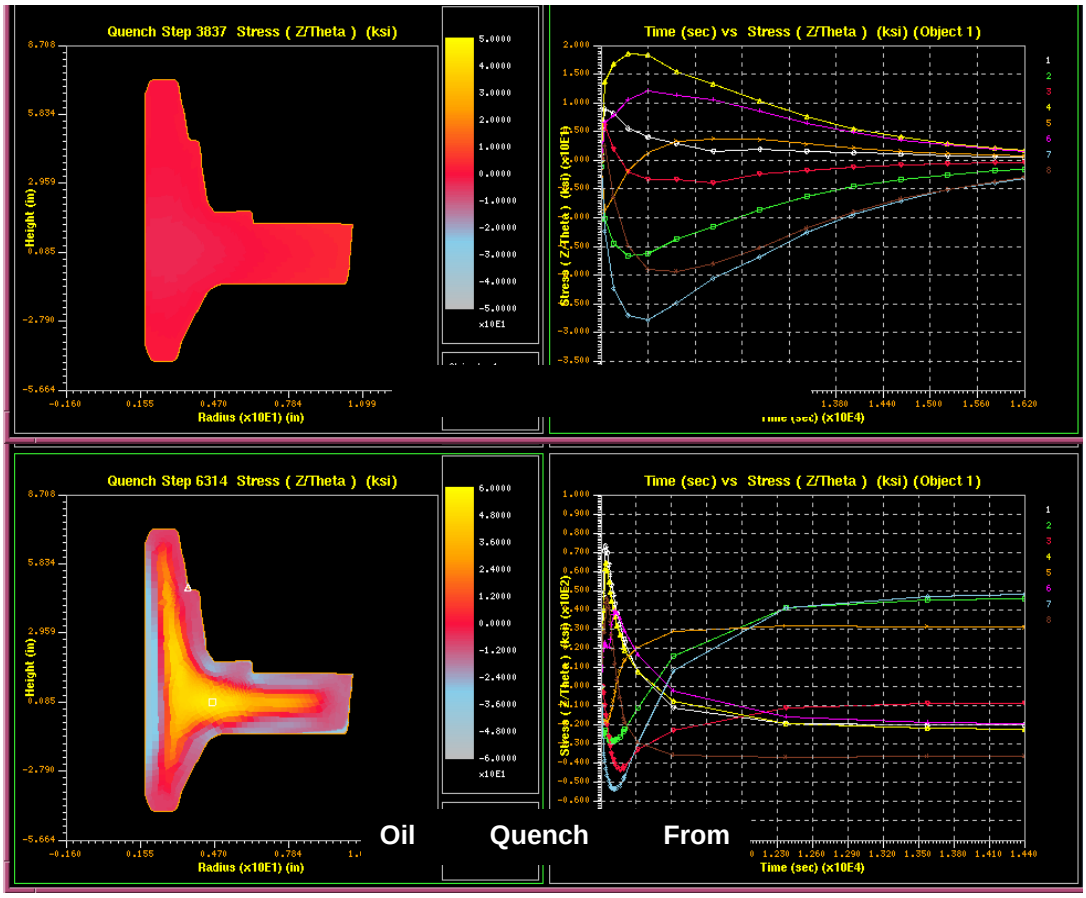

Figure 3-17. Prediction of Influence of Cooldown Rates

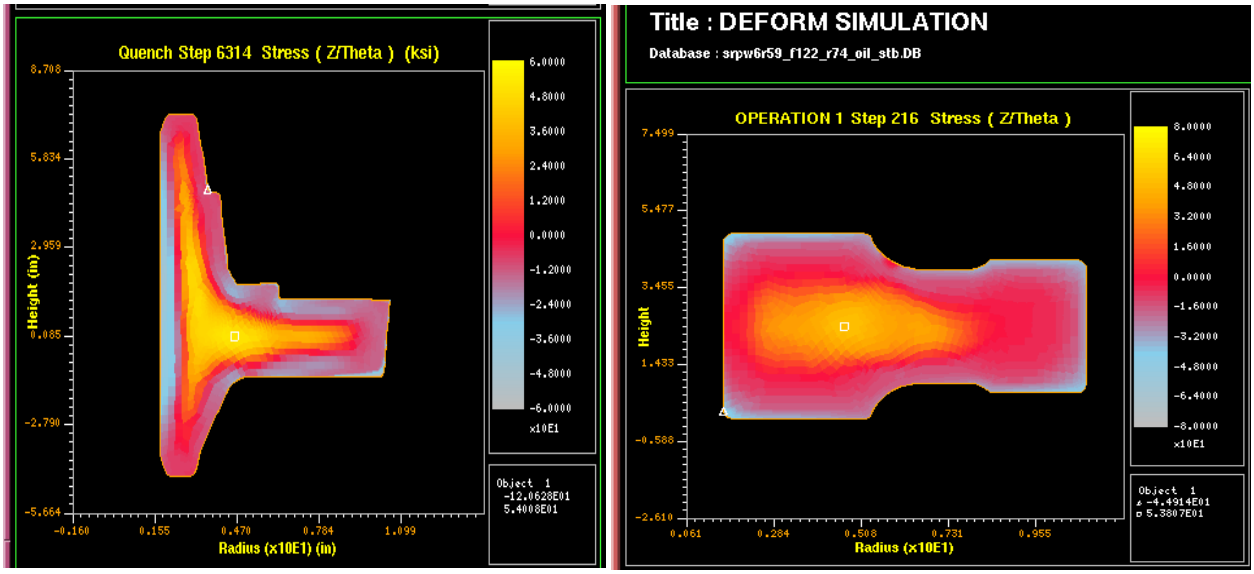

Figure 3-18. Prediction of Influence of Geometry Effects on Local Cooldown

The primary measurement technique in these studies was either through the center hole drill (monitoring strain change while drilling a hole through the center of a rosette strain gage) or plug removal (monitor strain change of a strain gage placed on the surface when the plug is electro-discharge machined from the part). Internal stresses were measured by inserting strain gages into the holes present in the disks when the plugs were removed, EDM a cylinder out of the part, and monitoring strain change. The measured stresses were then compared with analytical predictions for the locations of interest. General agreement across a range of superalloy materials indicates that generalization of analytical RS prediction for aerospace rotor materials is enabled by the development of appropriate material constitutive models. (It should be noted that the analytical predictions of internal RSs required an adjustment using an element removal and redistribution technique.)

One item to take into consideration is that some materials (such as Waspaloy) can exhibit a broad range of microstructural variation dependent upon the specified processing and, as a result, will exhibit a range of RS distributions dependent upon the microstructure of the part and process of interest. One area for future research is the development of the capability to modify constitutive material behavior based on microstructural inputs.

Whereas DEFORM's demonstrated capabilities in the area of forging and heat-treat-induced RS simulation are satisfactory, there are additional opportunities for enhancement. The first is improving the ability to map RS states into alternate finite element analysis codes such as ANSYS for additional analysis. This will enable more robust structural analysis of the influence of disk RSs on structural behavior in areas such as creep, burst, and fatigue life prediction. In addition, the need for coupling of material behavior and processing parameters should be considered so that material effects could be more reliably simulated. Outside the scope of the work conducted and the primary focus for DEFORM development is the process for incorporation of surface effects such as machining- or peening-induced RSs. These play a key

role in disk fatigue behavior and improved methods for the prediction of machining (tool/workpiece interactions) and peening (plastic deformation/bleed off) effects as well as their superposition onto forging/heat-treat processing and integration into subsequent structural analysis should be addressed.

4. CRACK NUCLEATION AND GROWTH DATA AND MODELING.

4.1 MECHANICAL PROPERTIES OF TITANIUM WITH ELEVATED OXYGEN.

A Ti-6242 compressor disk failure from an uncracked, nonvoided, oxygen-rich stabilized HA raised questions about the sensitivity of other titanium alloys such as Ti-64 and Ti-17 to similar anomalies. Internal GE Aviation studies demonstrated that at room temperature, elevated oxygen caused Ti-6242 to lose ductility, whereas dwell LCF tests on base oxygen material containing high-oxygen seeds showed a significant reduction in dwell fatigue life and formation of internal, flat facets at the high-oxygen seed crack initiation sites. The fracture morphology of these bars was similar to that observed in the compressor disk failure. Similar studies on Ti-64 showed no degradation in ductility at low temperature. Based on the Ti-6242 and Ti-64 studies, it was determined that beta processed Ti-17 should be assessed to evaluate whether oxygen impacted low temperature ductility and dwell fatigue properties.

Ti-17 ingots were double VAR melted, converted to 4″ diameter bar, and then extruded to 2″ diameter at 1665°F. One ingot extrusion contained uniformly elevated oxygen (0.5%), one contained high-oxygen (0.5%) seeds, and a third extrusion was base material with normal oxygen levels. Each extrusion was solution heat treated at 1475°F for 4 hours, water quenched, and aged at 1190°F for 8 hours. Tensile and fatigue specimens were machined from the base- and high-oxygen extrusions, and fatigue specimens were machined from the seeded extrusion.

Tensile testing of the base- and high-oxygen alloys was conducted at room temperature, 250°F and 500°F. LCF testing was conducted on both alloys at room temperature and 250°F. LCF tests were conducted at 30 cycles per minute (cpm), and some tests included a 2-minute dwell period. The dwell cycle tests were conducted at different stresses to determine the stress to give a 2000-cycle dwell life. Triplicate 30-cpm LCF tests were then conducted at this stress. After the LCF testing on the base- and high-oxygen specimens was completed, seeded LCF specimens were tested in 30 cpm and 2-minute dwell.

Tensile results are shown in figure 4-1 in terms of the changes in properties with oxygen additions. The high-oxygen material had increased tensile strength of approximately 25 ksi at room temperature and approximately 15 ksi at 500°F. Room temperature plastic elongation for the high-oxygen material was reduced by one half to 5%, but at higher temperatures, plastic elongation in the higher oxygen material was equivalent to, or higher than, the baseline material. The impact of oxygen on both strength and ductility for Ti-17 was intermediate between the effects on Ti-6242 and Ti-64.

The effect of oxygen additions on dwell fatigue behavior is summarized in figure 4-2. At room temperature, the stress for 2000 dwell cycles was 14 ksi higher for high-oxygen Ti-17 material, which was also intermediate between the cold dwell effects on Ti-6242 and Ti-64. At 250°F, there was almost no difference in stress for 2000 dwell cycles between the base- and high-oxygen Ti-17. The 30-cpm LCF lives were longer for oxygen-containing material and were higher at room temperature. The room temperature seeded dwell debit for Ti-17 was ~10× versus ~ 32× for Ti-6242 and an estimated no impact for Ti-64. Crack initiation sites for seeded

Ti-17 bars were relatively rough compared with flat, faceted crack initiations in seeded Ti-6242 bars.

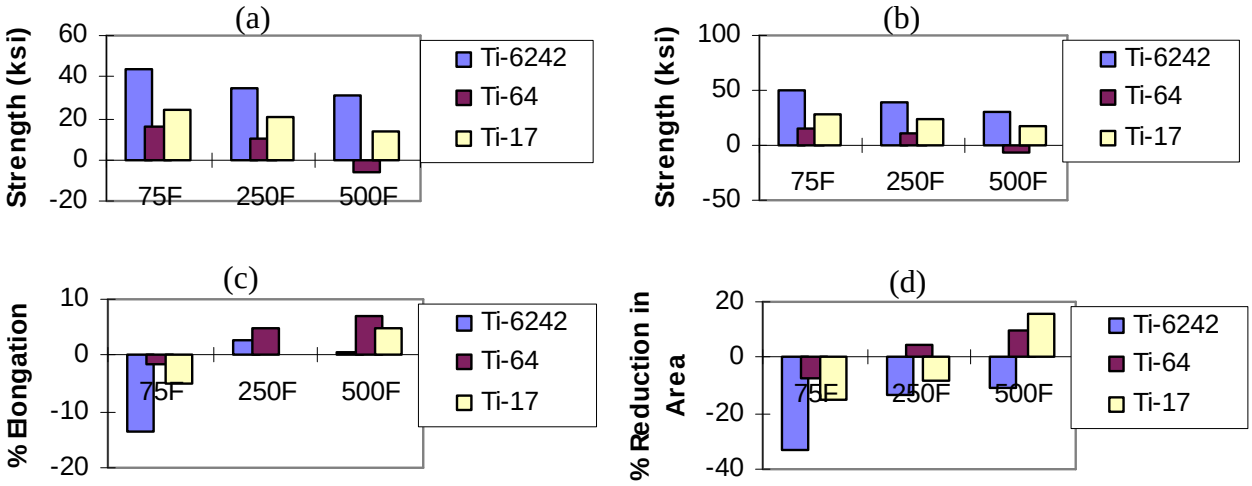

Figure 4-1. Effect of Oxygen Additions on Tensile Properties (a) Ultimate Tensile Strength, (b) 0.2% Offset Yield Strength, (c) Percent Elongation, and (d) Percent Reduction In Area

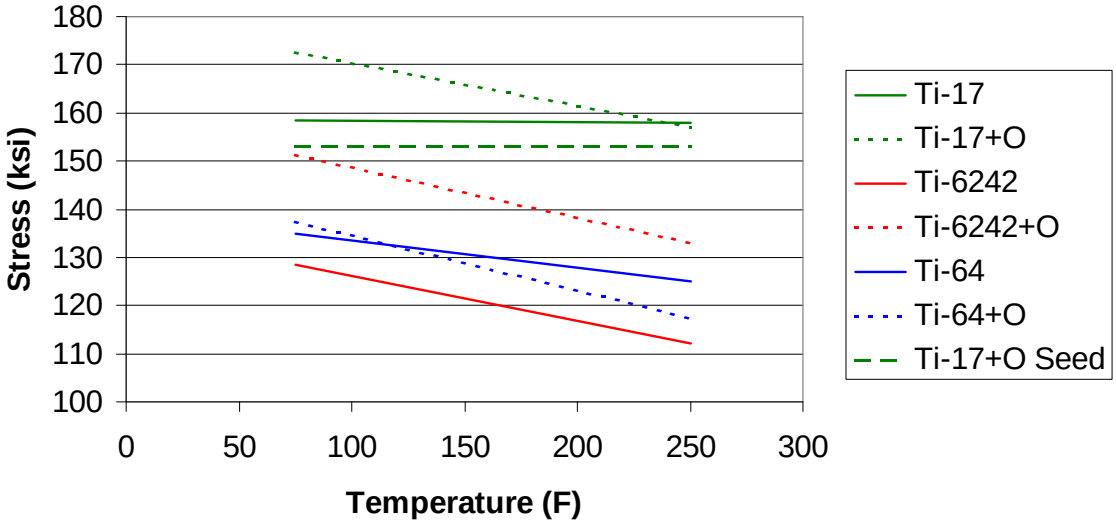

Figure 4-2. Effect of Oxygen Additions on Dwell Fatigue Properties: Stress to Give a 2000-Cycle Dwell Fatigue Life

Based on these tensile and fatigue data, it is believed that Ti-17 is less sensitive to high-oxygen anomalies than Ti-6242. There are several reasons to account for this reduced sensitivity. Increased sensitivity to dwell fatigue is generally associated with higher primary alpha content, higher alpha stabilizer and lower beta stabilizer content, and colony structure in the anomaly and in the surrounding material. In comparison to Ti-6242, Ti-17 generally exhibits lower primary alpha, lower alpha stabilizer, and higher beta stabilizer content. This may also help to explain

the absence of a faceted initiation in the seeded Ti-17 bars. Since a high-oxygen anomaly in Ti-17 is processed closer to its beta transus, there is a reduced probability of colonies in the resulting microstructure, and the surrounding material will have been beta processed and subsequently transformed to a basket weave structure.

Based on these tensile and fatigue data, it is also believed that Ti-17 is more sensitive to oxygen anomalies than Ti-64. There are at least two reasons to account for this increased sensitivity. First, the absolute ductility of high-oxygen Ti-17 at room temperature is significantly lower than high-oxygen Ti-64. During a load-controlled dwell fatigue test in Ti-17 containing a high-oxygen seed, the load will be shed from the weaker base material onto the stronger high-oxygen seed material. Since the high-oxygen seed has a relatively low strain capability, the seed will crack relatively easily, leading to a low fatigue life. In contrast, a Ti-64 high-oxygen seed in Ti-64 has a much greater strain capability than a Ti-17 high-oxygen seed in Ti-17, resulting in a smaller reduction in dwell fatigue life. Furthermore, in the case of Ti-17, there is a larger strength difference between high-oxygen and base material than for Ti-64. The result is that more load will be shed onto the high-oxygen seed in Ti-17, and in conjunction with the lower ductility in Ti-17 high-oxygen material, this will lead to a lower dwell fatigue life.

There is also a significant difference between the processing of Ti-17 and Ti-6242 or Ti-64 that reduces the probability that a high-oxygen anomaly will be present in Ti-17. Ti-17 ingots are homogenized at high temperatures for long periods of time to reduce the level of chromium segregation. Studies have shown that this homogenization treatment results in a large reduction in oxygen content of any high-oxygen anomaly in Ti-17. This type of homogenization treatment is typically not applied to Ti-64 or Ti-6242.

Further details of this study are documented in appendix G.

4.2 FATIGUE TESTING OF FORGED COUPONS WITH HA ANOMALIES.

Hard alpha anomalies are often extensively voided and cracked in the final forged shape. Current life-prediction methodologies assume that an initial fatigue crack size equal to the size of the HA region (high-nitrogen core plus surrounding DZ) is present at the beginning of life. This assumption could be overly conservative, however, for smaller HA anomalies and zones with lower nitrogen content, which are less likely to be extensively cracked and voided after the forging process. Therefore, it is useful to assess the cracking tendencies of the HA anomalies under fatigue loading in order to evaluate the possibility that some nonzero crack nucleation life could be included in the fatigue life-prediction methodology.

An experimental program was conducted in TRMD-I [5 and 9] to characterize the damage evolution occurring at HA anomalies. Mechanical tests were conducted on Ti-6Al-4V specimens containing either synthetic or naturally occurring HA material. Comparisons of observed cracking with predictions based on FCG analysis suggested that a significant number of fatigue cycles could be required to form a dominant, growing fatigue crack in the matrix for both synthetic and natural HA anomalies. However, the small number of tests performed in TRMD-I represent a limited parameter range, and the tests may not be fully representative of hardware under service conditions. For example, actual hardware would have experienced a complete forging operation after anomaly formation, and it is possible that this forging operation would

have either nucleated more severe initial cracks in the HA anomaly or grown cracks into the matrix.

Additional testing was performed in TRMD-II to continue these investigations. The coupon specimens in TRMD-II were extracted from forgings that had been seeded with synthetic HA anomalies prior to forging for the purpose of validating the DEFORM microcode (see section 3.1). A selection of different anomaly compositions was tested, including high-nitrogen core plus DZ, high-nitrogen core only, and low-nitrogen DZ only (also called was-beta). The Flight_Life fracture mechanics computer code was used to predict the fatigue crack growth lifetime of each test, and the analytical and experimental results were compared. A more complete description of this testing and analysis is provided in appendix H.

4.2.1 Material and Procedures.

The seeded forgings from which the specimens were extracted had been produced during TRMD-I. The artificial HA seeds for the forging mults were manufactured by GE Corporate Research and Development (GE-CR&D) Center using a proprietary process and placed into the forging mults. The mults were then forged into one of two different shapes (dogbone and backflow) using hot-die techniques. The synthetic cores had a nominal nitrogen content of 12%, and the DZs were nominally 2% nitrogen.

Maps of the anomalies in the forgings were provided from UT inspections performed by GE Aviation. Five anomalies of different character were selected for testing. Specimen blanks and then specimens were carefully machined from the forgings so that the anomaly of interest would be located in the center of the specimen gage section. Simple flat dogbone test coupons with a rectangular gage section typically 0.5″ thick and 1.0″ wide were used. In addition to these five synthetic anomalies, one additional specimen of similar size and shape remaining from TRMD-I was tested. This specimen contained a small, embedded 6% nitrogen core + DZ anomaly. Fatigue testing was performed in a servohydraulic test machine outfitted with hydraulic grips at a load ratio of $R = 0.1$. Each test was performed at a single constant load amplitude, but different tests were conducted at different load amplitudes. Cyclic frequencies were in the range of 1-10 Hz. Acoustic emission was monitored during fatigue cycling.

4.2.2 Results and Analysis.

The experimental record indicates the total number of fatigue cycles required to cause specimen separation. Some of these cycles were required to nucleate a fatigue crack, and the remaining portion of the cycles was required to propagate the fatigue crack to failure. However, the experimental record provides no explicit information about the numbers of cycles associated with nucleation versus propagation. As noted earlier, the conventional analysis assumption is that the nucleation life is zero and that the total fatigue lifetime is equal to the FCG lifetime.

To evaluate the accuracy of this assumption for the six coupon tests, the FCG life for each specimen was calculated using the Flight_Life FCG analysis module in the DARWIN computer code. FCG properties were based on the Ti-6Al-4V vacuum FCG testing performed in TRMD-I. The initial crack size was selected as the largest ellipse that could be inscribed within the irregularly shaped anomaly on the posttest fractograph (a typical fracture surface for a cluster

specimen is shown in figure 4-3). The dimensions were assigned without differentiating between core and DZ.

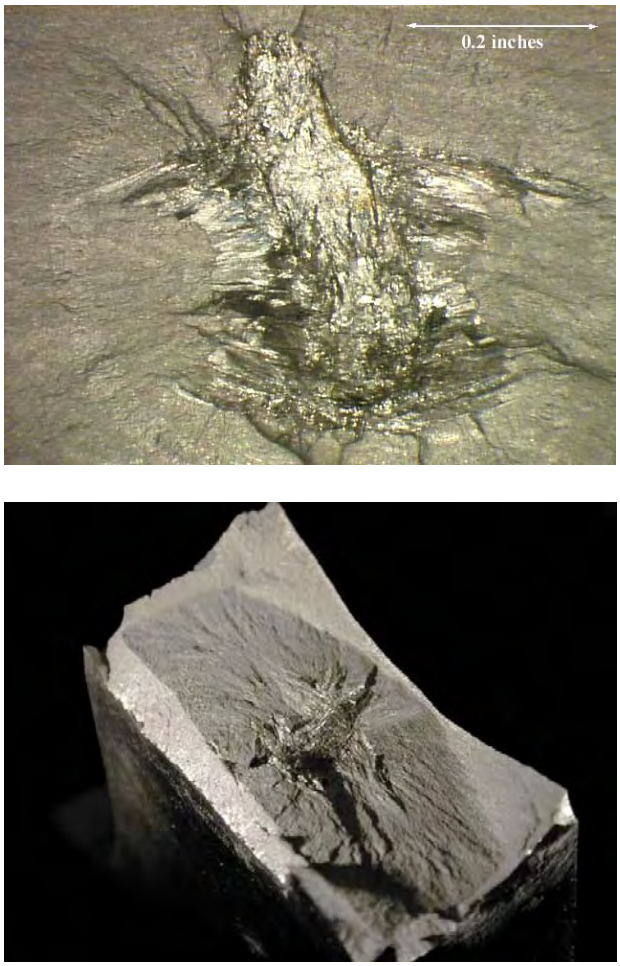

Figure 4-3. Fracture Surfaces of Specimen SB-3-25C (Cluster With DZ)

The actual total experimental fatigue life is compared graphically with the predicted fatigue crack growth life for the six tests in figure 4-4. The actual total fatigue life was significantly larger than the calculated FCG life for all six tests. The actual total life was nearly always at least twice as long as the calculated FCG life, and the average ratio of actual-to-predicted life (A/P) was about 3.5. The difference between the two numbers was greatest for the was-Beta specimen in which the anomaly was completely low-nitrogen DZ material without any high-nitrogen core; in this case, the A/P ratio was 6.9.

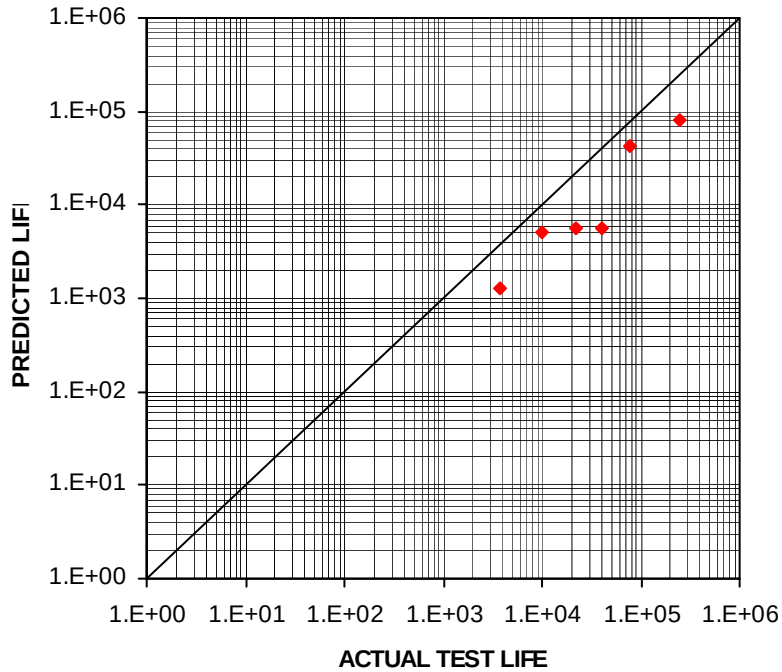

Figure 4-4. Comparison of Predicted FCG Lifetime and Actual Total Fatigue Test Lifetime for Forged Coupons With HA Anomalies

There are several possible explanations for the difference between observed total life and calculated FCG life. First of all, it is possible that some significant number of cycles was required for the crack to form (or nucleate) and begin growing. Second, it is possible that the formation and interaction of multiple cracks on multiple planes caused some retardation of crack growth. Third, it is possible that some RSs may have remained around the HA anomaly that reduced the crack driving force and therefore reduced the FCG rate (see section 4.3), although the applied stresses in these tests may have been great enough to reduce the potential RS effect. Fourth, it is possible that some of the differences can be attributed to the difference between high-nitrogen core material and low-nitrogen DZ material, since the initial crack sizes treated both anomaly compositions as being the same. This line of thinking is generally supported by the long life observed for the DZ-only anomaly.

4.3 RESIDUAL STRESSES ASSOCIATED WITH HA.

Coupon tests on specimens and spin pit testing on forgings containing seeded HA defects were conducted during TRMD-I [7] and TRMD-II (see sections 4.2 and 4.4). The results of the testing indicated that the fracture and fatigue strengths of the embedded HA were higher than anticipated. The presence of RSs caused by differential thermal expansion was postulated as a potential explanation for the observed behavior. A small study was therefore conducted in TRMD-II to estimate the magnitude of these RSs and to determine their potential impact on fracture and fatigue strength: How do the RSs influence the applied stress required to initiate cracking during monotonic loading, and how do the RSs influence the applied stress required to sustain fatigue crack growth in the vicinity of the HA anomaly? A full report of this

investigation is provided in appendix I. For convenience, the experimental and analytical procedures and the key results are summarized below.

4.3.1 Review of Experimental Results From TRMD-I.

Artificial HA anomalies with a cylindrical shape, a core nitrogen content of 5.5% (denoted HA-6N), and a surrounding DZ were manufactured and implanted into Ti-6Al-4V material blocks by GE-CR&D. The blocks were subsequently machined into dogbone specimens with a gage cross section 1 x 0.5 in. The HA defects were of two different sizes and were either surface connected or fully embedded. Static and fatigue tests were conducted with AE and potential drop (PD) monitoring, and the surface defects were closely monitored visually. Further details of the test procedures and results are available elsewhere [5, 7, and 9].

Crack initiation in surface-connected HA cores under monotonic loading was observed in all cases at stresses less than 20 ksi and in many cases less than 10 ksi. In the embedded specimens, significant cracking of the subsurface cores first occurred at applied tensile stresses on the order of 80 to 110 ksi, according to the PD and AE results.

Fatigue tests were performed at $R = S_{min}/S_{max} = 0.1$ at a variety of stress levels. Cracking of the defect and growth in the matrix of the surface HA specimens was observed at maximum stress levels of 40 and 50 ksi. Subsurface specimens exhibited defect cracking but no crack growth into the matrix at 50 ksi. Significant crack growth into the matrix was observed in both of the embedded HA specimens tested at 75 ksi. A fatigue test specimen with a natural HA anomaly from the ETC contaminated billet study sustained over 90,000 cycles at maximum stress levels from 50 to 75 ksi, finally failing after 13,300 cycles at 100 ksi. The embedded HA specimens were all more resistant to fatigue than the surface defect specimens, and life predictions using Flight_Life consistently underpredicted the experimentally observed lives.

4.3.2 Measurement of Thermal Expansion Coefficient.

GE-CR&D fabricated and tested specimens to determine the coefficient of thermal expansion (CTE) of synthetic HA manufactured from pure titanium or Ti-6Al-4V. Specimens with five nitrogen contents (nominally 2%, 4%, 6%, 9%, and 12%) were tested along with two baseline Ti-64 specimens. Measurements of the percent expansion were made using a push rod dilatometer between room temperature and the post-HIP (hot isostatically pressed) temperature of 1650ºF (900ºC). The CTE was determined from the slope of the percent expansion versus temperature plots. The CTE values ranged from 4E-6 to 6E-6/ºF, with generally lower values for higher nitrogen contents.

4.3.3 Analysis of Residual Stresses in and Around HA Defects.

Residual stresses in the HA defect and surrounding matrix can arise from differences in CTE, elastic modulus, and Poisson's ratio between the HA and the Ti-6Al-4V matrix. At the post-HIP temperature of 1650ºF (900ºC), the material is assumed to be RS free. As the material cools to room temperature, the differences between the HA and the matrix introduce RSs. The RS profile was calculated based on a literature solution for thermal expansion differences between cylindrical or spherical inclusions and the surrounding matrix. In all analyses, the embedded HA

was found to be subjected to uniform triaxial compression at room temperature, with estimated stress values ranging from 18-55 ksi depending on nitrogen level. The maximum tensile stress in the matrix occurred at the particle matrix interface, and the magnitude of the stress decreased dramatically as distance from the particle increased. The effect of the particle was practically negligible at a distance of one particle radius away from the interface.

4.3.4 Fracture Strength Modeling.

A fracture model for bulk HA developed by Chan in TRMD-I [3 and 4] was combined with the calculated RS fields to determine the nominal stress required to cause cracking of the HA core. The local pressure (based on the principal stresses) varies as a function of the nominal tensile stress, as the stress state becomes less triaxial under external loading. This loading path can be compared with the Chan fracture criterion to determine the nominal tensile stress when particle cracking occurs. The stress state, and hence the local pressure, is significantly different for surface versus subsurface defects.

This model predicted cracking at about 50 ksi for the surface case and 160 ksi for the subsurface case, compared with the experimentally measured values of 10-20 ksi for surface defects and 80-115 ksi for embedded HA. Therefore, the model correctly explains the substantial difference between surface and subsurface results, although the specific values are predicted incorrectly due to geometrical idealizations in the simple RS model. The analysis implies that the triaxial RSs caused by the thermal expansion differences delay the onset of fracture in the subsurface HA particles during the static load tests.

4.3.5 Fatigue Modeling.

Fatigue modeling focused on the effect of CTE differences on the SIF, K, for cracks spanning the HA defect and attempting to grow into the matrix. The RS effects were estimated by superposition of K values for remote loading and local RSs, where the K due to RS was estimating using a weight function approach.

The compressive RSs in the HA particle were found to result in a negative SIF when the crack is within the particle. When the crack completely spans the particle and even when it has grown into the matrix, the compressive RSs in the HA particle attempt to keep the crack closed and substantially reduce the total K. This reduction in K can impact the onset of fatigue crack growth as well as influence the total fatigue life. However, the total K quickly converges to the applied K value as the crack grows into the matrix.

Comparisons of the calculated K with the crack growth threshold properties as expressed by ΔK_{th} successfully predicted no growth in 50-ksi fatigue tests, although successfully predicting growth in 75-ksi fatigue tests. Similar analyses neglecting RSs would have predicted growth at 50 ksi. A broader parameter study found that the effect of the RSs was greatest for high nitrogen contents and lower applied stresses (especially below 40 to 60 ksi) and lowest for low nitrogen contents and high applied stresses (generally negligible above 100 ksi).

Fatigue life predictions were performed by integrating a simple crack growth equation for Ti-6Al-4V in vacuum from an initial size equal to the defect size to a nominal final size,

choosing a crack closure model to address the changes in effective stress ratio as the crack grows. Including the RSs in the fatigue crack growth model caused an increase in the predicted life ranging from 1.3 to 4, depending on the specific nitrogen level and applied stress level. Note that designs and life predictions made using the traditional analysis methods and neglecting these RSs will be conservative.

4.4 SPIN PIT TESTS OF TITANIUM ROTORS CONTAINING HA ANOMALIES.

Spin pit tests of Ti-6Al-4V disks containing natural and seeded HA inclusions were performed to validate the Flight_Life fracture mechanics code in DARWIN and the assumptions used to develop the HA anomaly distributions in AC 33.14. The spin pit tests were conducted with three disks forged during TRMD-I [7]. Disks B1BW3B and B3W2E contained natural anomalies from the ETC contaminated billet study. Disk SB-6 contained an artificial seed introduced into the billet during TRMD-I. Appendix J summarizes the accomplishments under this spin test program. Highlights of this investigation are provided below.

4.4.1 Pretest Analysis.

DEFORM analyses were performed during TRMD-I to select the candidate forging, to identify the seed placement location for the seeded mults, and to identify which of the mults containing naturally occurring anomalies were acceptable for spin testing. The inclusions were backtracked through the forging process from the desired location in the forged disk to identify where the inclusions needed to be in the mults. To maximize the crack growth from these inclusions, it was desired to have the seeds as close to the corner of the disk bore as possible without intersecting the surface, since this location had the highest predicted stress during the spin testing.

A simple disk forging sonic inspection shape was selected as the configuration for spin testing. Prior to spin testing, ANSYS 2D axisymmetric stress analyses were performed to predict the stresses at the inclusions for multiple candidate forgings. The ANSYS stress analysis results were subsequently input into a stand-alone version of Flight_Life to predict the crack growth life from the inclusions and select the desired test speeds. It was desired to select a speed that would result in approximately 15,000 cycles of crack growth life assuming a 0.2″ crack (the size of the DZ of the seed placed in disk SB-6). The actual size of the natural anomalies in disks B1BW3B and B3W2E was unknown at the start of testing, but it was assumed that they were approximately the same size as the SB-6 seed. In the pretest analysis, it was assumed that there was no incubation and crack growth would initiate at the start of testing.

4.4.2 Test Setup and Test Plan.

The rig hardware was designed and the spin testing was performed at Test Devices, Inc. in Hudson, MA. The spindle and arbor interference fit assembly minimized cost to the program using standard rig hardware already familiar to Test Devices. Since the objective of this testing was to assess the crack growth from internal HA inclusions and surface initiated cracks were not desired, the surfaces of the disks were shot peened to 6A intensity to reduce any concerns regarding premature surface-initiated failure.

Strain gages were installed on disk SB-6 to validate the analytical stress predictions. Strain measurements were recorded during an initial three cycles of testing prior to the LCF cyclic testing. In all cases, the model agreed well with the test measurements.

The initial disk spin test plan called for spinning in 5000-cycle increments with removals from the rig for interim fluorescent penetrant inspection (FPI) and sonic inspections. The sonic inspections were intended to further assist with monitoring the growth of the inclusions. After the completion of the second set of 5,000 spin cycles (10,000 total), the disks would again receive FPI and sonic inspections. If the sonic inspections indicated that the defects were not growing, adjustments to the test speeds would be made prior to continuing testing. During the testing, the disks' vibration amplitude and phase were monitored in an attempt to identify the onset of crack growth and to halt the testing before the cracks grew to rupture and risk damaging the fracture surface.

4.4.3 Test Results.

All three disks completed their initially planned 10,000 cycles of testing without a rupture and without strong conclusive evidence of crack propagation. Since disk SB-6, which was tested first, did not indicate any growth, the speed of the other two disks was increased for their initial 10,000 cycles of testing.

In addition to the normal incidence UT inspections initially planned, angled UT scans were performed at each inspection interval starting at 5000 cycles. The response signal of the angled scans separates as a crack extends out from the core. Signal separation was observed with disks SB-6 and B3W2E at 5,000 and 10,000 cycles, but disk B1BW3B did not indicate any signal separation at 5,000 or 10,000 cycles. FPI inspections of all three disks did not indicate any surface-connected cracks.

While the angled scans did indicate some possible crack growth after 10,000 cycles, the normal incidence inspections were inconclusive at the time, and the Test Devices crack monitoring system had not indicated any crack growth. Specimen testing during TRMD-I had indicated that stresses of 75-100 ksi were required to initiate crack growth from embedded HA inclusions. During the first 10,000 cycles of testing, predicted stresses at the inclusions ranged from 40 to 55 ksi. The speeds were increased to generate stresses of 75 ksi at the locations of the inclusions, and the disks were spun for an additional 7500 cycles.

All three disks containing embedded HA inclusions successfully grew cracks from the inclusions. Disks SB-6 and B3W2E both burst prior to completion of the planned 7500 additional test cycles at increased speeds but tested beyond the initial life predictions. The crack monitoring system did not indicate any crack growth in either of these tests prior to a vibration amplitude spike during the final cycle when the disks burst.

Disk B1BW3B completed, without a burst, 17,500 total cycles of spin testing (10,000 cycles at 18,000 maximum rpm and 7,500 cycles at 24,100 maximum rpm). Inspections at P&W gave mixed results, but were generally consistent with significant crack growth. Multizone and shear scan inspections at GE Aviation also indicated crack growth. Testing of disk B1BW3B was

therefore discontinued, and the disk was cut open for fractography rather than risk damaging the fracture surface with continued testing.

4.4.3.1 Posttest Fractographic Inspections.

Disks SB-6 and B3W2E were shipped to P&W for fractography after bursting in the spin rig. The goals of the fractography were to evaluate the crack growth from the embedded HA inclusions to identify the origin location of the fracture, map the size and shape of the inclusions, and determine the number of striations on the fracture surface. The fractography was performed by visual inspection with the assistance of a Scanning Electron Microscope (SEM). Prior to completing the fractography on the spin disks, two coupon specimens previously fatigue tested in TRMD-I were assessed to provide a baseline reference. Representative fractography of disk SB-6 is shown in figure 4-5. The fatigue fracture initiated from the embedded HA seed. Higher magnification SEM fractography was completed in seven directions surrounding the inclusion. Fracture features were similar to those observed in the seeded coupon specimens except that no striations were observed in disks SB-6 and B3W2E. Some limited striations were identified at a single location on disk B1BW3B.

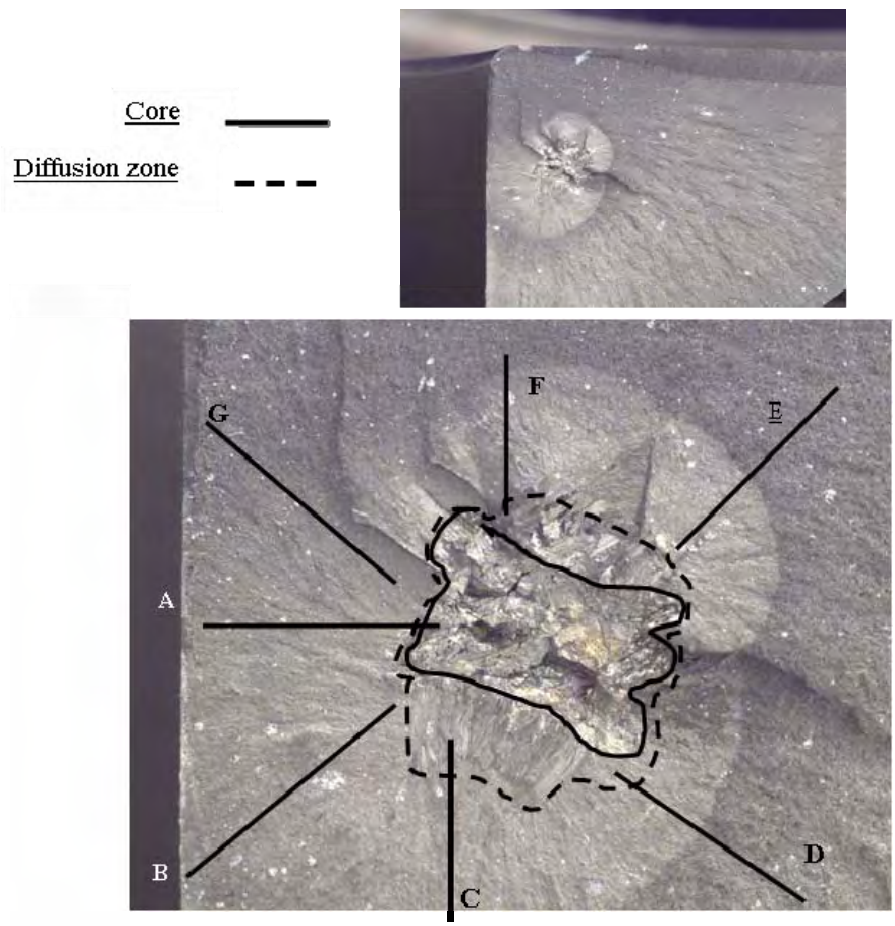

Figure 4-5. Disk SB-6 Fracture Surface at Inclusion With Scanning Directions Identified

4.4.3.2 Flight_Life Comparisons to Test Data.

Results from the fractographic assessments of the three spin disks were used to evaluate the crack growth predictions from Flight_Life. Pretest crack growth predictions were updated to include the measured HA core sizes and locations. No incubation was assumed in the analyses. The analyses assumed the initial crack was circular with a diameter equal to the diameter of the core (for SB-6) or the maximum length of the core in the plane of the crack (for B3W2E and B1BW3B). The crack growth predictions for SB-6 and B3W2E, which had both run to rupture, matched the test results within a few hundred cycles. The predictions for disk B1BW3B exceeded the actual test results by approximately 1000 cycles, still remarkable agreement. Contrary to the assumptions used by RISC to set up the initial HA anomaly size distributions, for both the seeded HA as well as the natural HA, the test experience indicated a closer correlation of initial crack size to the core size than to the total core plus DZ size.

4.4.3.3 Vacuum FCG Specimen Testing of Spin Disk Material.

To verify that the crack growth properties for the TRMD spin test disks were comparable to the assumptions in the analysis, vacuum FCG tests were conducted on specimens machined from the spin disks. The plane of crack growth in the specimens was aligned with the crack growth plane (the axial/radial plane) in the spin disks. The tests were run at room temperature at a stress ratio of $R = 0.1$ for each of the disks. A total of seven tests on three specimens from two disks were completed. The test results were very repeatable and agreed well with data generated at GE Aviation during TRMD-I [7].

4.5 VACUUM FCG TESTING.

Many types of inherent anomalies in both nickel and titanium alloys occur at subsurface locations. Since any fatigue cracks that nucleate at these anomalies are not exposed to the atmosphere, they grow in a vacuum-like environment. Numerous researchers have noted a difference between FCG rates in vacuum and in air. However, the data available in the literature are limited for both titanium and nickel alloys. Moreover, the available data are not sufficient to support a complete lifing system for FCG in turbine engines, and therefore, it is difficult to accurately evaluate the risk associated with crack nucleation at subsurface material anomalies. It is for these reasons that extensive characterization of titanium alloys was conducted in TRMD-I. TRMD-II extended this vacuum FCG testing to nickel alloys that also included a powder metallurgy (PM) nickel alloy. A complete documentation of the test procedures and results is provided in appendix K.

4.5.1 Materials and Test Procedures.

Vacuum FCG tests were performed during TRMD-II on four different rotor grade materials: Ti-6242, Waspaloy, IN-718 and PM U720. The Ti-6242 and Waspaloy were supplied by P&W, the IN-718 was supplied by GE Aviation, and the PM U720 was supplied by National Aeronautics and Space Administration (NASA) Glenn Research Center. Details of the material pedigrees are provided in appendix K.

Tests were conducted for a matrix of temperatures and stress ratios at Honeywell and GE Aviation (GE Aviation performed only a portion of the IN-718 test matrix) following standard test procedures used at those companies to generate production data. Test conditions are summarized in table 4.1.

Table 4-1. Summary of Vacuum FCG Test Conditions

Material	Test Laboratory	Stress Ratios	Temperatures (^{o}F)
Ti-6242	Honeywell	0.05	600
Waspaloy	Honeywell	-0.5, 0.05, 0.5	500, 800, 1200
IN-718	GE Aviation, Honeywell	0, 0.5, 0.7	75, 600, 1000, 1200
PM U720	Honeywell	0.05, 0.5	800

Although the tests were conducted at different sites, similar test procedures were followed. Region II (Paris regime) tests were conducted with small surface crack tension (SC(T)) specimens, also known as Kb bar specimens. Tests in the near-threshold regime were conducted at Honeywell on the same SC(T) geometry and at GE Aviation on a single-edge notch button head specimen. Details of specimen geometries are provided in appendix K.

Crack lengths were monitored using the direct current electric potential drop method, with crack sizes posttest corrected from visual measurements of marked initial and final crack dimensions on the fracture surfaces. SIFs were calculated from established solutions in the literature. Tests were conducted under either constant load or constant ΔK-gradient (increasing or decreasing) at constant R. Vacuum levels were better than 10-7 Torr for all tests. Test frequency was 0.33 Hz (20 cpm) for all tests.

4.5.2 Results.

A complete set of graphical and tabular results is provided in appendix K. For convenience, selected results are provided below.

4.5.2.1 Ti-6242.

Two tests were conducted with the coarse-grained Ti-6242 supplied by P&W. Results are presented in figure 4-6 in comparison with the TRMD-I results for Honeywell's fine-grained Ti-6242.

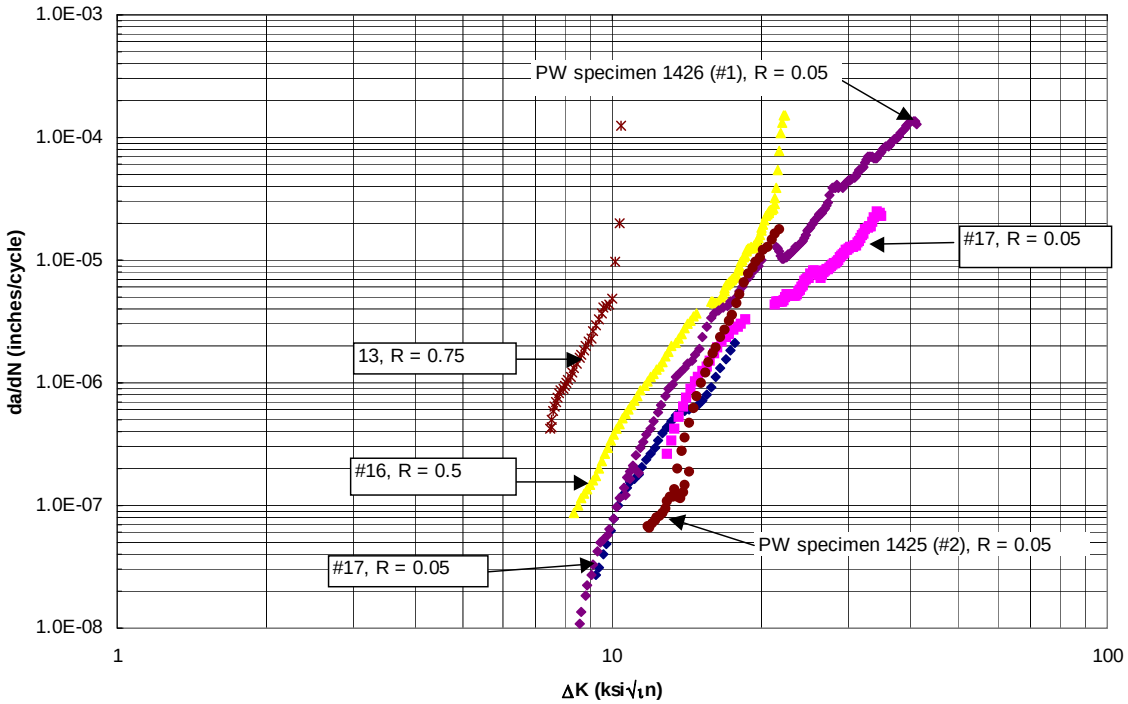

Figure 4-6. Vacuum FCG Results for P&W and Honeywell Ti-6242 Materials at 600°F

4.5.2.2 WASPALOY.

A total of 18 vacuum FCG tests and 1 air FCG test were conducted on Waspaloy. The effects of temperature and stress ratio on crack growth rate are summarized in a series of graphs in Appendix K. Representative results for R = 0.05 at three different temperatures are shown in figure 4-7. Figure 4-8 directly shows the effect of environment—air versus vacuum—at 500°F and R = 0.05.

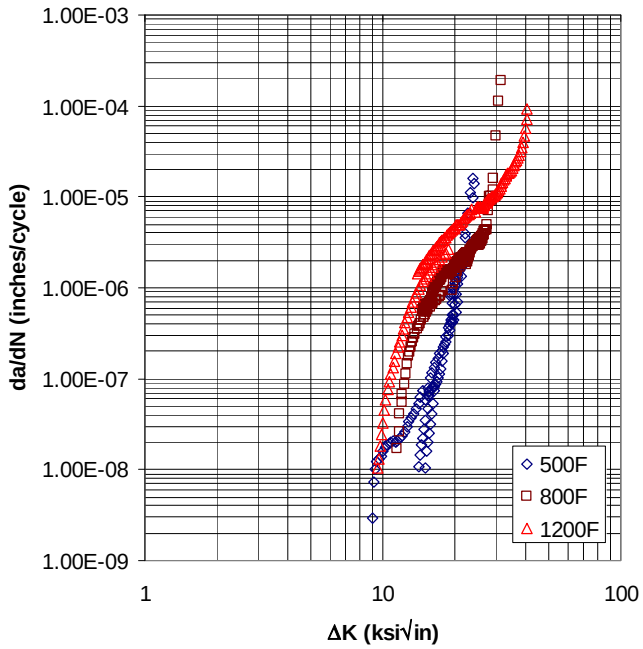

Figure 4-7. Vacuum FCG Results for Waspaloy at R = 0.05 and Three Different Temperatures

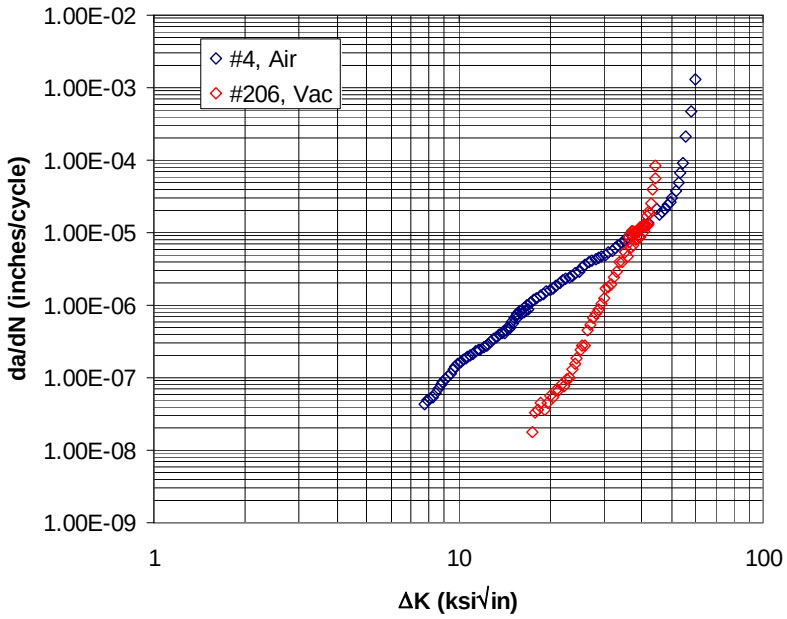

Figure 4-8. Effect of Environment (Air Versus Vacuum) on Fatigue Crack Growth Rates in Waspaloy at 500°F, R = 0.05

4.5.2.3 IN-718.

A total of 13 successful vacuum FCG tests were completed on IN-718. Testing was performed at GE Aviation and Honeywell. Representative results at $R = 0$ for four temperatures are shown in figure 4-9.

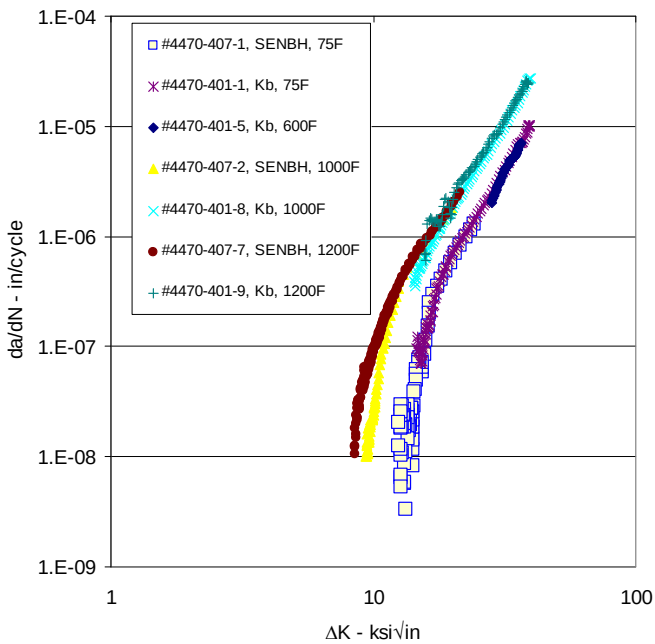

Figure 4-9. Vacuum FCG Results for IN-718 at $R = 0$ and Four Different Temperatures

4.5.2.4 PM U720.

A total of five vacuum fatigue crack growth tests were completed on PM U720. The PM U720 material pedigree and test data are export controlled. Hence, this information is not included in this report. However, the data are available from SwRI after adequate demonstration of export authorization.

4.6 NICKEL ANOMALY FATIGUE TESTING.

The TRMD team has been working with nickel melters to obtain Waspaloy or IN-718 material with sonic indications to support a fatigue test program. The intent of the test program was to investigate the fatigue initiation and propagation of cracks from embedded anomalies in conventional nickel alloys. Existing quality control specifications were complied with to allow for required material cut ups to disposition suspect indications. These requirements, which are necessary for flight safety, limited the availability of suspect material that could be obtained.

In two batches of material, after the required number of cut ups was completed, additional material remained with sonic or surface indications that could be forged and machined into fatigue specimens. The first batch of double melt IN-718 material included eight billet sections (mults) with nine indications from three different heats (table 4-2). Prior to obtaining the

material, DEFORM analyses were performed, which confirmed that these indications were at acceptable depths for machining of fatigue specimens from pancakes to be forged from the mults. The mults were then delivered to P&W for additional UT inspections, forging into pancakes, and machining of test specimens.

Table 4-2. Production UT Inspection Results for Ni Billet Indications

Indication	Heat	Billet Diameter (in.)	Maximum UT Response	Radial Depth (in.)	Length (in.)	Axial Location (in.)
1A	804085	8.0	110% of #2 FBH	3.5	0.520	4.5 to 5
2X	804085	8.0	110% of #2 FBH	2.65	0.320	7.6 to 7.9
2X	804085	8.0	100% of #2 FBH	2.65	0.320	8.1 to 8.4
3A	804085	8.0	110% of #2 FBH	3.9	0.500	3.5 to 4.0
3X	804085	8.0	160% of #2 FBH	2.7	0.700	2 to 2.7
5A	804618	8.07	112% of #2 FBH	3.7	0.275	5
5A	804618	8.07	75% of #2 FBH	3.8	0.230	5
5A	804539	7.874	75% of #2 FBH	2.2	0.205	5
5X	804539	7.874	75% of #2 FBH	1.6	0.216	5

The second batch of IN-718 material was identified near the end of the program and consisted of billets with approximately two or three freckles per cross section. The freckles were identified through surface inspections of the ends of the billets, and it was suspected that the freckles may run the full length of the mults. This material was procured under TRMD-II and will be forged into pancakes in a subsequent program with the FAA.

Both the sonic indications and the freckles will be tested in this subsequent program. No triple melt IN-718 or Waspaloy was obtained during TRMD-II for fatigue testing of anomalies.

4.6.1 Additional UT Inspection of IN-718 Mults.

After receipt of the IN-718 mults with production sonic indications, an additional set of laboratory UT inspections was completed at P&W. These additional inspections would be used as a baseline for comparison in a common environment with subsequent UT inspections of pancakes forged from these mults. C-scan images were recorded for each of the mult inspections at P&W. Figure 4-10 includes representative C-scan images of two of the mults. Along with the maximum responding indications reported from the production inspections, additional smaller indications on some of the mults were identified from the C-scan images. Mult 804085-3X contained five additional indications along with the one high-responding indication as identified in figure 4-10. A full discussion of the P&W UT inspections of the mults is included in appendix L.

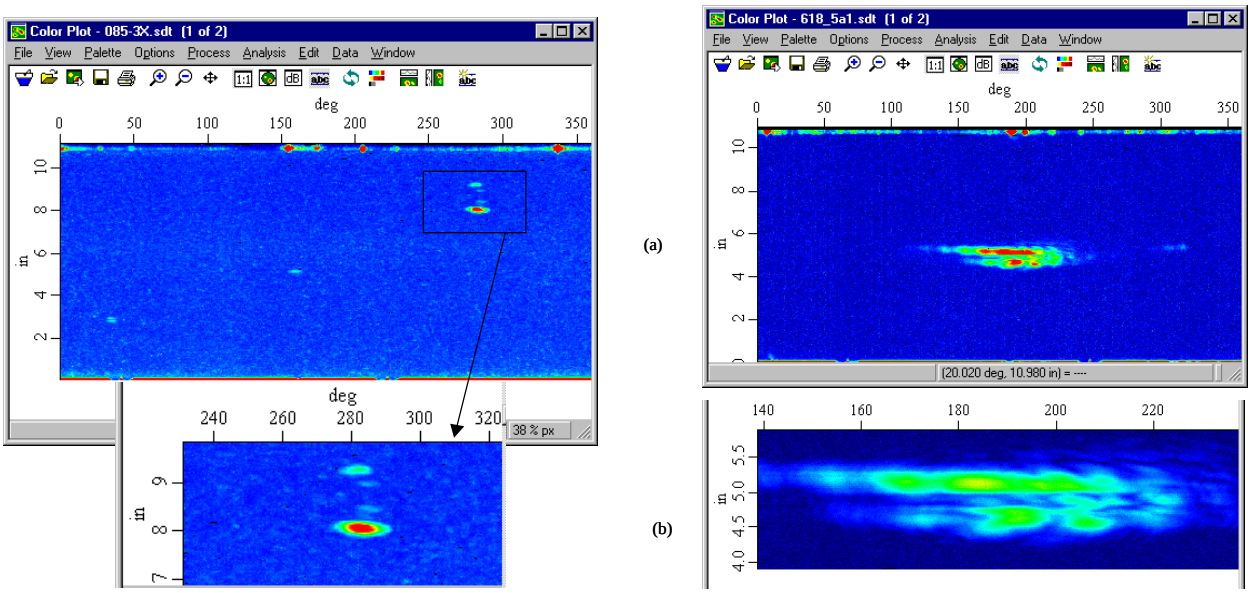

804085-3X 804618-5A1

Figure 4-10. C-Scan Images for Mults 804085-3X and 804618-5A1

4.6.2 Ultrasonic Inspection of IN-718 Forgings.

After the mults were forged to the pancake shape of 16″ diameter and 2.9″ thick, UT inspections were performed to determine the positions of the indications. Indications were seen in only three of the eight pancakes. Several attempts were made to use zoned scanning and angle scanning to try to identify the positions of the previous indications in the other five pancakes. DEFORM analyses were used to help focus the locations in the pancakes to search for the indications. It appears that the indications in those five mults may have been either voids that closed during the forging operation, or, the UT indications in the mults were caused by large grains that were refined during recrystallization at the pancake forging step. Table 4-3 contains a summary of the maximum UT responses for the production and laboratory billet inspections and forging inspections. It is interesting to note that the indications found in the pancakes were not always the highest responding indications in the mults. Indication 804085-3X, shown in figure 4-10, was one of the strongest indications in the mults, yet was not identified in the pancake. A more comprehensive discussion of the forging inspections is included in appendix L.

For the three pancakes with identified indications, blanks with dimensions of approximately 2″ x 3″ (thickness) x 6″ with the indications centered were cut from the pancakes to make round LCF samples with a 0.5″ diameter gage section. Figure 4-11 contains representative C-scan images of two of the pancakes with identified indications in the forging and includes illustrations of the orientation of the blanks machined from the pancakes. The blanks were rescanned and the positions of the indications verified for production of the LCF samples. As the finished specimens are machined, attempts will be made to center the indications within the gage section and, where possible, to keep the anomalies subsurface.

Table 4-3. Maximum UT Response for Billet and Pancake Indications

Indication	Heat	Maximum Production UT Response in Mults	Maximum Laboratory UT Response in Mults	Maximum Laboratory UT Response in Pancakes
1A	804085	110% of #2 FBH	60% of #2 FBH	Not Found
2X	804085	110% of #2 FBH	130% of #2 FBH	Not Found
3A	804085	110% of #2 FBH	90% of #2 FBH	Not Found
3X	804085	160% of #2 FBH	190% of #2 FBH	Not Found
5A	804618	112% of #2 FBH	200% of #2 FBH	125% of #1 FBH*
5A	804618	75% of #2 FBH	40% of #2 FBH	Not Found
5A	804539	75% of #2 FBH	60% of #2 FBH	50% of #1 FBH*
5X	804539	75% of #2 FBH	55% of #2 FBH	100% of #1 FBH*

*C-scan images from pancake UT inspections show larger indications than maximum UT response amplitude.

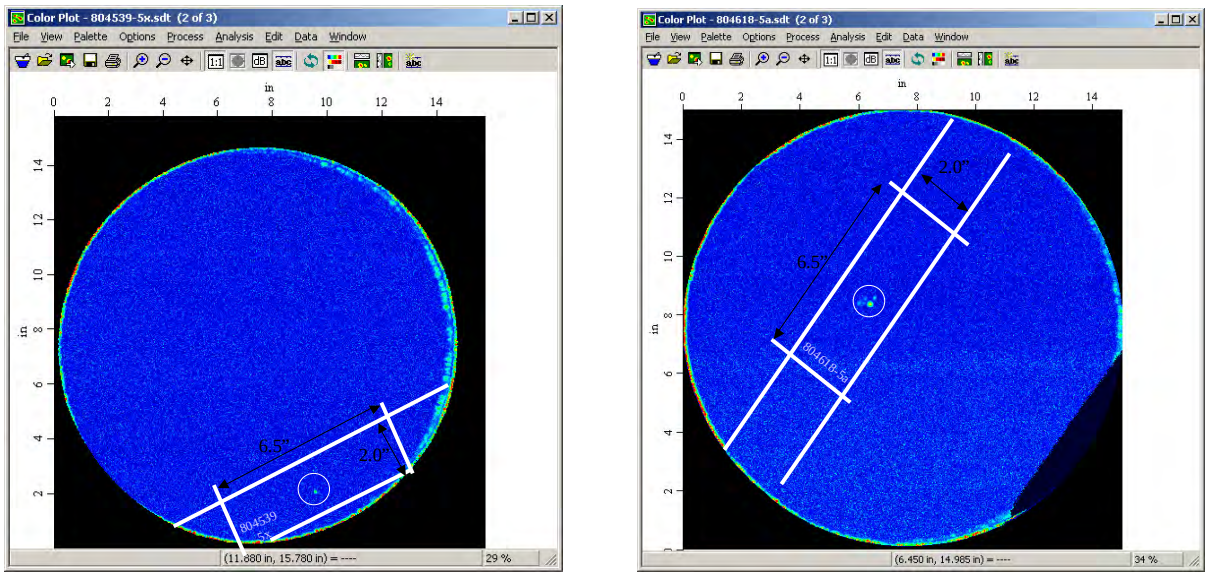

804539-5X 804618-5A

Figure 4-11. C-Scan Images For Mults 804539-5X and 804618-5A

4.7 THERMOMECHANICAL FATIGUE CRACK GROWTH TESTING.

Aircraft turbine engines operate in a complex thermal environment and frequently the stress and thermal cycles are not totally in phase. The so-called stress rain flow method is often used to define cycles for fatigue crack growth analysis. In this method, the major cycle is defined in terms of the maximum stress in the cycle and the temperature at the maximum stress time point. There is often a time point later in the mission with a higher temperature but a lower stress, and this characteristic of the history may be ignored by the stress rain flow method. It is possible, however, that this higher temperature may have some impact on the FCG rate.

To investigate this issue further, the TRMD program team conducted an exploratory study of thermomechanical fatigue (TMF) crack growth. The common high-temperature, nickel-based superalloy IN-718 was chosen for investigation. A simple matrix of isothermal and TMF experiments was designed for the specific purpose of determining if the out-of-phase thermal history had a significant influence on FCG rates, and if the stress rain flow method was an adequate means of characterizing the damage in TMF cycles. All crack growth tests and analyses were performed at GE Aviation. Further details are provided in appendix M.

Crack growth specimens were obtained from two compressor rotor spool production forgings. The grain size was estimated to be ASTM GS 10. Crack growth testing was performed using a Kb bar specimen geometry, with crack length measurement by the direct current electrical potential drop technique.

Four different TMF cycle types were employed. TMF cycles were designed to balance (a) being representative of engine cycles, (b) having significantly different lives than comparable isothermal cycles, (c) slow thermal cycling to avoid excessively high-transient thermal stresses, and (d) test times within program costs. The typical duration of a single TMF cycle (all types) was approximately 210 seconds.

The first cycle in all four TMF types was conducted with a maximum stress of 120 ksi and a temperature of 450°F. In Type I, a second isothermal cycle was conducted at 1100°F with a maximum stress of 60, 80, 100, or 120 ksi. In Type II, the second cycle was a thermal cycle from 450° to 1100°F and back to 450°F, all at zero stress. In Type III, the second cycle was isothermal at 1100°F and involving cycling to a compressive stress of -60 ksi. In Type IV, the first cycle is unloaded only to 60 ksi, the specimen is held at 60 ksi while heated to 1100°F, and then the specimen is unloaded to zero stress at 1100°F. Isothermal tests were performed at 450º, 800º, and 1100ºF. Two experiments were planned for each of the ten test conditions, and 19 of the planned 20 experiments were performed successfully.

The six isothermal FCG tests indicated that FCG rate increases with increasing temperature. The 800ºF crack growth rates were slightly higher than the 450ºF results. The 1100ºF crack growth rates were much higher than those at 450ºF; at low to intermediate ΔK, the 1100ºF crack growth was approximately 10 times faster than the 450ºF results.

The lifetimes of all TMF tests were predicted by the conventional stress rain flow method, and these predictions are compared with the actual test lives in figure 4-12. Also shown on this figure are predictions and test results for additional TMF tests on René 95 and René 88DT conducted independently by GE Aviation (not under TRMD-II). The figure shows that the stress rain flow predictions exhibited a nonconservative bias in the predictions. In other words, TMF cycles produced faster crack growth rates, on average, than were predicted by the stress rain flow method. The bias was less severe for IN-718 than for the René alloys.

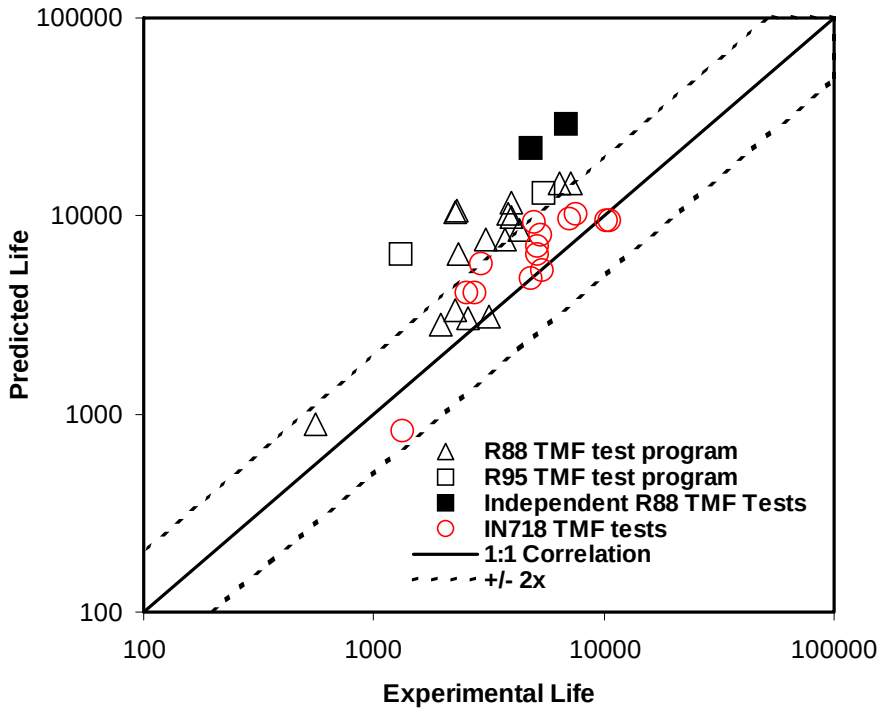

Figure 4-12. Comparison of Experimental Lifetimes With Predictions Based on the Conventional Stress Rain Flow Method for IN-718, René 95, and René 88DT Subjected to TMF Histories

4.8 ENHANCEMENT OF FLIGHT_LIFE MODULE.

The Flight_Life module that performs fracture mechanics analysis in DARWIN was initially developed during TRMD-I and was included in all previous versions of DARWIN developed under TRMD-I. The core analysis capabilities of Flight_Life (crack growth equations, mean stress models, temperature models, crack growth integration schemes, etc.) remained unchanged in TRMD-II. However, the available SIF solutions in Flight_Life were significantly enhanced and expanded in TRMD-II and some other new features were introduced.

4.8.1 Stress-Intensity Factor Solutions.

Table 4-4 summarizes all of the SIF solutions that were either introduced or enhanced during TRMD-II, along with a notation of the DARWIN version in which the new or improved solution first appeared. These new capabilities comprise enhancements in the available geometries, in the handling of arbitrary stress gradients, and in computational speed.

Table 4-4. Summary of New or Enhanced SIF Solutions Developed During TRMD-II

Solution	Description	Type	First DARWIN Version	Comments
SC02	Surface crack in plate	UWF/Poly	4.0	Wider *a/c* and *a/t* limits; replaced by SC17
SC15	Central surface crack at hole (wide plate)	UWF	4.0	Superseded by SC18
SC17	Surface crack in plate	UWF/Poly	5.0, 5.1	Better accuracy, wider *a/c* in 5.1
SC18	Surface crack at offset hole (finite plate)	UWF	5.0, 5.1	Supersedes SC15 (better accuracy in 5.1)
CC01	Corner crack in plate	Bilinear	3.4	Only improved speed
CC05	Corner crack at hole (wide plate)	UWF	4.0	Superseded by CC08
CC08	Corner crack at offset hole (finite plate)	UWF	5.0, 5.1	Supersedes CC05 (better accuracy in 5.1)
CC09	Corner crack in plate	BWF/Poly	5.2	First bivariant solution
CC10	Corner crack at offset hole (finite plate)	BWF	6.0	Second bivariant solution
EC02/03	Embedded crack in plate	UWF/Poly	4.0	Added WF form and increased *a/c* limits
TC11	Through crack at hole (wide plate)	UWF	4.0	Superseded by TC12
TC12	Through crack at offset hole (finite plate)	UWF	5.0	Extends and supersedes TC11

UWF = Univariant weight function
Poly = Polynomial
BWF = Bivariant weight function

4.8.1.1 Available Geometries.

All SIF solutions in TRMD-I were for cracks in simple rectangular cross sections. To address the problem of surface damage at boltholes, new SIF solutions for cracks in the bore of a round hole were required. A first set of crack-at-hole solutions for corner, surface, and through cracks at centered holes in wide plates (sufficiently wide to neglect any finite width effects) were introduced in DARWIN 4.0. A second set of solutions for corner, surface, and through cracks at off-center holes in finite width plates were introduced in DARWIN 5.0, including the effects of a surface crack that is off-centered through the plate thickness. The finite geometry correction scheme was further improved and modified solutions introduced in DARWIN 5.1. These implementations included all of the appropriate geometry transitions (surface to corner and corner to through). All of these new crack-at-hole solutions were based on a univariant weight function method, with most reference solutions generated using advanced 3D boundary element software for fracture mechanics analysis, FADD3D [10]. Further details of the mathematical WF formulation for these crack-at-hole solutions are provided in appendix N.

The crack aspect ratio limits for embedded and surface cracks were increased several times, as noted in the sections below.

4.8.1.2 Arbitrary Stress Gradients.

All of the SIF solutions in TRMD-I were based on sixth-order polynomial representations of a stress gradient varying in 1D only (so-called univariant), except for the CC01 corner-crack-in-a-plate solution (obtained from the NASGRO® fracture mechanics computer software [11]) with linear stress gradients along adjacent edges. However, some stress gradients encountered in practice are not satisfactorily represented by a polynomial expression. Therefore, new WF formulations for the surface crack and embedded crack in a rectangular cross section were derived and implemented in Flight_Life. These formulations directly integrate the so-called WFs with the actual finite element stress values along the crack line in order to calculate the SIF.

The new WF formulation for the elliptical embedded crack in a plate in DARWIN 4.0 was based on the same solution set as the original polynomial solutions, except that the aspect ratio limit of $a/c = 2$ was removed (currently any aspect ratio is permitted, and in the extremes, the SIF value properly approaches the corresponding through crack solution). The $a/c = 2$ limit first introduced in DARWIN 3.3 was itself an increase from the original $a/c = 1$ limit under TRMD-I.

The first implementation of a WF solution for the semielliptical surface crack in a plate (SC02) was based on the reference solutions for the existing NASGRO SC02 solution, which gave slightly different results than the original Flight_Life SC02 polynomial solutions. The NASGRO reference solutions were also supplemented to increase the aspect ratio limit from $a/c = 1.0$ to 2.0 (here a is the maximum crack depth, and $2c$ is the total surface length), and the Flight_Life polynomial solutions were revised for consistency. Due to some lingering concerns about the accuracy and speed of this NASGRO solution, a completely new WF solution was later derived for Flight_Life based on a completely new set of reference solutions generated using FADD3D. This new solution was introduced in DARWIN 5.0 as SC17, and also included a new polynomial

solution that was consistent with the new WF solution for common stress fields. The aspect ratio limit of SC17 was increased from *a/c* = 2.0 to 4.0 in DARWIN 5.1.

These univariant formulations (either WF or polynomial) do not model variations in the crack plane stresses in any direction except for the specified gradient orientation. However, in some applications, the stresses may vary significantly in all directions on the crack plane. The development of efficient SIF solutions that can accurately accommodate this entirely arbitrary stress variation (so-called bivariant solutions) is an extremely challenging task. Previous attempts to solve this problem have all exhibited substantial accuracy and/or speed limitations.

A completely new formulation for bivariant WF SIF solutions with superior speed and accuracy was derived under TRMD-II, and new reference solutions to support this formulation were generated using FADD3D for the quarter-elliptical corner crack in a plate (CC09) and the corner crack at a hole (CC10). Further details of the background, the mathematical formulation, and the resulting solutions are provided in appendix N. This work represents a substantial advance in the state-of-the-art for engineering fracture mechanics analysis.

4.8.1.3 Computational Speed.

Fracture mechanics life analysis can be computationally time-consuming, and the repetitive calculations required for probabilistic analysis can substantially increase the total computational burden. Improvements in SIF accuracy almost inevitably result in further computation expense. Weight function solutions, because they involve numerical integration of the crack plane stresses, are often much slower than polynomial solutions, which have been preintegrated. A large matrix of reference solutions introduces data storage challenges, which can further compromise speed. As geometries become more complex and the number of degrees of freedom increases (e.g, plates with holes, finite width plates, offset holes, and offset cracks), the storage requirements and the associated time penalties can mushroom. Bivariant solutions require 2D numerical integration, which can dramatically increase the required computational time. In the extreme, all of this geometrical and analytical sophistication can be crippling.

Therefore, significant effort was expended during TRMD-II to improve the computational efficiency of existing and new SIF solutions. For example, the original NASGRO CC01 solution was modified for DARWIN 3.4 to increase its speed by about 8 times without changing the results. The original NASGRO SC02 solution was also modified to increase its speed substantially, and the new SC17 solution for the same geometry exhibited a further increase in speed (compared to the improved SC02) of about 5 times. A new storage and preprocessing scheme for large matrices of WF reference solutions was introduced in DARWIN 5.1, and these numerical databases were converted to binary format in DARWIN 5.2 for additional increases in speed.

The dramatic increase in computational burden introduced by bivariant WF solutions was addressed by developing a new dynamic tabular interpolation scheme. In this scheme, rather than calculate new values of the SIF using the full numerical integration on each cycle in which the crack grows to a new size and shape, a small matrix of SIF solutions for *a/c* and *a/t* values in the vicinity of the initial conditions is generated at the beginning of the calculation. The specific

SIF value needed on each cycle during the life calculation is extracted from this table using a rapid and highly accurate interpolation method, and the table is updated on an as-needed basis as the crack grows beyond the geometry limits of the initial table. The total computational burden can be dramatically decreased by this scheme—by several orders of magnitude for some problems. Further details are provided in appendix N.

4.8.2 Other Flight_Life Enhancements.

The Walker interpolation method for stress ratio effects in DARWIN was only available for tabular data formats during TRMD-I. In DARWIN 3.3, this method was extended to all four existing crack growth equations in Flight_Life. The Walker interpolation formulation was more recently modified for improved robustness under a few specific conditions (e.g., interpolation between positive and negative stress ratios when user-supplied data are not available at $R = 0$, and interpolation at stress ratios immediately adjacent to stress ratios at which data were supplied by the user). The new formulation is scheduled for release in a future DARWIN version.

An improved shakedown module was implemented in DARWIN 3.3. The old shakedown module redistributed stresses based on a force balance only, while the new module redistributes stresses based on equilibrium of both forces and moments. Further information about the new method is provided in the DARWIN online help system.

As cracks become large and approach instability conditions, the conventional linear elastic SIF can sometimes slightly underestimate the driving force for fracture, especially when maximum stresses are large, remaining ligaments are small, and the small-scale yielding assumptions of linear fracture mechanics are compromised. A simple correction to the SIF that compensates for this condition is to augment the crack size by one-half of the estimated size of the crack tip cyclic plastic zone, based on conventional (monotonic) tensile properties, and then to recalculate the SIF with this effective crack length. This logic was first added to DARWIN 3.4. The effective crack size is used only for evaluation of crack transitioning (a local instability) or final (global) crack instability.

Enhanced error/warning tracking and handling was first implemented in DARWIN 3.4. These new schemes clearly document unusual conditions, such as negative or zero physical dimensions, a crack larger than its plate, or a crack tip outside of the plate, while avoiding a crash of the code execution.

4.9 STABILITY AND SIGNIFICANCE OF RSs IN FATIGUE.

Some components contain RSs that were established prior to placing the component into service and which remain in place during the service life. These RSs do not cycle as the applied loads cycle, and so they do not directly influence the amplitudes of the in-service cyclic loading. They do influence the mean or maximum value of the load in each cycle and, therefore, they can have a major influence on fatigue.

Residual stresses can arise from many sources. Some RSs are an inherent byproduct of the manufacturing process (e.g., welding). Sometimes additional steps are added to the manufacturing process for the specific purpose of inducing beneficial compressive RS at fatigue

critical locations. Shot peening and related surface treatments such as laser peening, low plasticity burnishing, and deep rolling are common examples of this approach. Cold expansion of holes is also widely employed.

The conventional wisdom is that RS have relatively little influence on fatigue crack nucleation, but potentially a significant influence on FCG. The influence on FCG may be especially pronounced when the fatigue cracks are small and the driving force for FCG is near the grow/no-grow threshold. The effect of RS on stress-life (S-N) behavior is complex. To the extent that the S-N curve is driven by crack nucleation behavior, the effects may be small, but to the extent that the S-N curve is driven by crack growth (including microcracks), RS effects may be large.

However, one of the biggest complications is that the initial RS inherent in, or induced by, the manufacturing process may not remain stable throughout the service life. The RS can relax and redistribute due to a variety of mechanisms. A single applied load that causes yielding in a region of RS (due to the superposition of residual and applied loads of the same sign) will result in changes in the RS upon removal of the applied load. Repeated cyclic loading can cause gradual changes in the RS over time, even if no single fatigue cycle induces local yielding. Exposure to elevated temperatures can also relax RS. Finally, extension of a fatigue crack through an initial RS field can cause significant changes in the RS under some conditions.

4.9.1 Literature Survey.

A broad literature survey has been conducted of the current understandings of significant RS issues for fatigue lifetime, and the full text of the survey is provided in appendix O. The survey focused explicitly on the stability of surface and near-surface RS fields under fatigue conditions, including redistribution and relaxation due to static mechanical load, repeated cyclic loads, thermal exposure, and crack extension. The implications of the initial and evolving RS state for fatigue behavior were addressed, with special attention to FCG. Brief attention was given, where appropriate, to the major approaches to FCG life analysis proposed and practiced in the literature.

The literature survey was based on a comprehensive (but not exhaustive) bibliography assembled over a period of several years and currently containing well over 300 citations.

This literature survey was not a definitive critical review. No attempt was made to evaluate the relative merits of the different explanations and models proposed, and no attempt was made to provide clear answers on important issues, beyond reporting the preponderance of the published opinions.

The scope of the survey was very broad. Primary attention was given to the RS resulting from four major classes of manufacturing operations: peening and related surface treatments, cold expansion of holes, welding, and machining. Special attention was given to aircraft gas turbine engine materials and applications. However, materials and applications related to other products such as aircraft structures, welded steel structures, automotive components, and machinery have also been included, because the technical insights and quantitative models may be relevant to gas turbine engines.

4.9.2 Observations and Conclusions.

A great deal has been observed, measured, modeled, and learned during the past 50 years about the stability of RS. Definitive explanations and models are not yet available for all relaxation phenomena. Nevertheless, a critical reading of the literature leads naturally to a series of general observations and conclusions that should provide a solid foundation for further study, model development, and practical implementation.

First of all, it is clearly important to discern and separate the different relaxation phenomena: thermal effects, static mechanical load effects, cyclic load effects, and crack extension effects. The specific mechanisms are different for each of these effects, and the various effects can superimpose. For example, the first cycle of fatigue loading may induce static relaxation effects, while subsequent load reversals can induce cyclic relaxation effects. A failure to discern and separate these different effects can lead to some confusion. Separation of the different phenomena facilitates simpler and more accurate modeling of each effect, and these simple models can often be superimposed.

The available literature provides insight into the significance of the various relaxation phenomena. For example, thermal relaxation effects do not appear to be extremely large for most practical applications. Some academic studies subjected materials to temperatures greater than their normal operating envelope and observed substantial relaxation, but relaxation at normal operating temperatures tended to be moderate.

Static relaxation effects appear to be relatively easy to identify and characterize based on knowledge of the initial RS field and the applied service loading. In general, compressive loading tends to relax beneficial compressive RS fields in proportion to the magnitude of the applied loading. Tensile loading typically has no effect on compressive RS unless the applied loads are extremely large.

Many of the pronounced cyclic relaxation effects identified in the literature appear to be static effects on the first loading cycle (e.g., compressive loads relaxing compressive peening RS). Once these static effects are set aside, the remaining true cyclic relaxation tends to be gradual and moderate unless the applied fatigue stress amplitudes are large.

The effects of crack extension on tensile RS fields are relatively easy to identify and understand. The effects of crack extension on compressive fields are not so clear and require further study.

No effort was made in this survey to perform a quantitative evaluation of the models proposed to characterize or predict RS stability. However, some general observations are in order. Simple thermal activation models have been developed to treat thermal relaxation effects, but their generality and truly predictive nature have not yet been established. It should not be difficult to formulate a general treatment of static relaxation based on simple mechanics arguments, but this does not appear to have been done yet outside of idealized profiles or finite element models. Empirical models may be useful for focused, well-characterized cyclic relaxation problems. The more general numerical models proposed for cyclic relaxation are encouraging but require some further detailed study to evaluate their practicality. Tractable models have been proposed for

relaxation of tensile RSs due to crack extension, but no well-established theory has yet been laid out for crack extension effects on compressive fields.

The available evidence suggests that, in practical engineering applications, induced RS due to cold expansion, peening, or related manufacturing techniques rarely relax fully to zero. Although some relaxation commonly occurs due to one or more mechanisms, so that final RS fields are rarely the same as the initial fields, some significant fraction of the initial RS often remains at the end of the relevant fatigue exposure. Static effects appear to be the most deleterious, and these should be easily predictable in most cases. Most of the severe degradation of RS reported in the literature appears to be attributable to unrealistically severe thermal or mechanical loading conditions.

Characterizing and employing the correct RS field is essential for accurate life modeling. It is clear that RS effects on S-N lifetimes and FCG lives can be very substantial. A life prediction based on an incorrect assumption about RS may be seriously in error. In view of the uncertainties associated with RS, appropriately conservative assumptions may be in order.

Established methods for modeling FCG in RS fields using WF SIFs and superposition techniques appear to provide satisfactory accuracy in many cases. Special attention must be given to stress ratio effects, and appropriate crack closure methods may be satisfactory for this purpose. Several complicating issues may require further attention, including the multidimensionality of stress fields, nonelliptical crack shapes, and crack face contact.

Finally, it is important to note that the effects of peening and related techniques such as cold expansion, welding, and machining on fatigue behavior are not limited to RS effects, and this is especially true for S-N behavior. The same manufacturing processes that induce RS can also influence the surface quality, microstructure, and material condition, all of which may independently influence fatigue life.

5. PROBABILISTIC INTEGRATION DESIGN CODE AND DEVELOPMENT.

The DARWIN software was originally developed during TRMD-I to predict the risk of fracture associated with rare inherent anomalies in titanium aircraft engine rotors and disks. New capabilities were developed under TRMD-II to address anomalies associated with surface damage, as well as inherent anomalies in other materials that may occur more frequently than the HA anomalies associated with titanium. In addition, a number of new capabilities were developed to improve the efficiency and accuracy of the probabilistic computations. A concise overview of the major DARWIN enhancements developed during TRMD-II is presented in this section and summarized by DARWIN version numbers in table 5-1. Additional details are provided in several appendices referenced where appropriate. Complete details are available in the DARWIN electronic help system (see section 5.5).

Table 5-1. Summary of Darwin Enhancements Developed Under TRMD-II

Version	Description
3.3	Internet distribution of software and manuals
3.4	Inspection transition and Monte Carlo confidence bounds
3.5	Restart, element subdivision, and zone refinement
4.0	1D surface damage, anomaly aspect ratio, and GUI plot export
4.1	Importance sampling confidence bounds, deterministic user-defined initial anomaly size, electronic help system, report generation, and GUI database converter
4.2	Personal Computer and Linux versions and execute analysis code from GUI
5.0	Mission mixing, 3D surface damage, and stress/temp multipliers
5.1	Parallel/batch processing, finite element filtering, execute ANS2NEU from GUI, and support for additional 3D finite elements
5.2	3D bivariant stress visualization, linked shop visit times, and keyword support
6.0	Probabilistic treatment of general inherent anomalies, crack formation module, 3D anomaly modeling, production inspection, and sensitivity analysis

5.1 ENHANCEMENT OF DARWIN FOR SURFACE ANOMALIES.

Recent aircraft engine accident investigations have revealed that uncontained engine failures can be attributed to anomalies that are introduced by abusive machining practices. Industry experience suggests that surface damage can occur in boltholes, and this topic is currently under investigation by the AIA RISC committee. Under the TRMD-II program, DARWIN was enhanced to address anomalies associated with surface damage. In contrast with inherent anomalies that may be present anywhere within a component, surface damage is usually present only on the surfaces of machined features. New capabilities were developed to define zones in terms of physical features (with a focus on cracks occurring at boltholes), and to predict the risk of fracture associated with multiple features.

5.1.1 User-Specified Surface Damage (1D Analysis).

The stress concentrations associated with boltholes can have a significant influence on stress gradients, particularly near the surface of a component. The stress gradient modeling capability developed under TRMD-I for materials with rare inherent anomalies was based on values extracted from 2D finite element models and does not adequately address stress concentrations. A new capability was developed allowing the analyst to enter temperature and 1D stress gradient values via tabular input. A new surface zone editor was also created to allow the analyst to specify the crack geometry and other zone-specific features.

5.1.2 Three-Dimensional Finite Element-Based Surface Damage (3D Analysis).

Three-dimensional FEM are often used to predict the stresses associated with complex geometries such as boltholes. A capability was developed to extract stresses and temperatures from 3D FEM for application to surface damage-based risk assessment. As shown in figure 5-1, DARWIN was enhanced to allow the analyst to visualize a 3D FEM and select the location of a surface damage anomaly. DARWIN identifies the principal stress plane associated with the anomaly and prepares a 2D image of the FEM normal to the principal stress plane. The 2D image can be used to assign zone properties using techniques developed previously for rare inherent anomalies. A number of 3D finite element types are supported by this capability, as indicated in table 5-2.

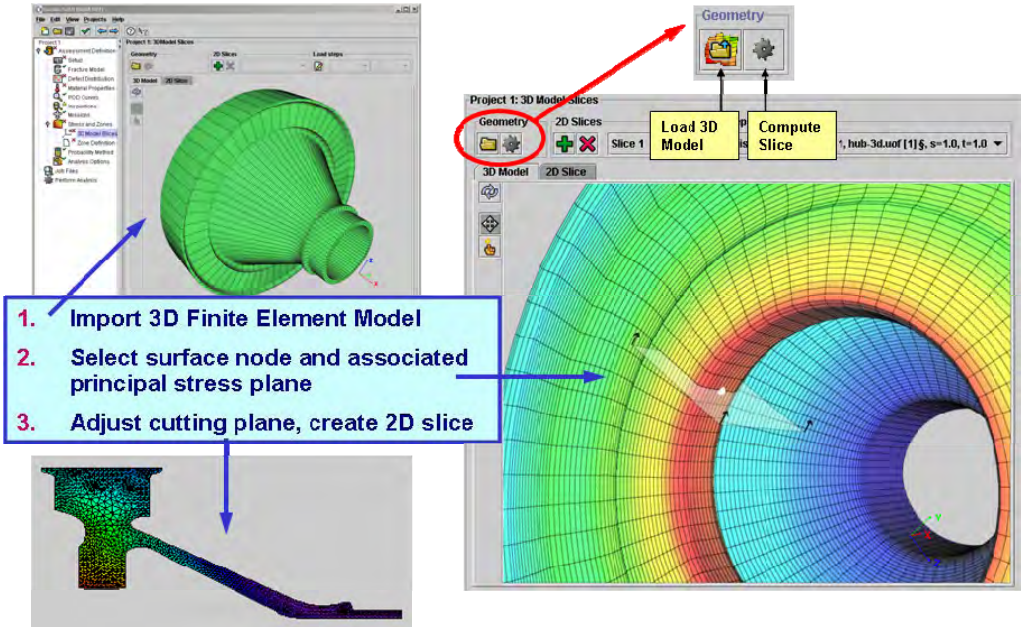

Figure 5-1. Three-Dimensional Surface Damage Analysis Capability Linked Directly to a 3D Finite Element Model

Table 5-2. Summary of 3D Element Types Supported in DARWIN

ANSYS Element	Shape	SIESTA Type
Solid45	Brick	BRI8
	Prism	BRI8
Solid92	Tetrahedron	TETS N10
Solid95	Brick	VANS N20
	Prism	VANS N20
	Tetrahedron	VANS N20
	Pyramid	VANS N20

5.2 ENHANCEMENT OF DARWIN FOR GENERAL INHERENT ANOMALIES.

A number of new concepts were introduced in DARWIN to support risk assessment of materials with multiple anomalies. The risk assessment equations for zones and discs were modified to account for materials with potentially large numbers of anomalies. A crack formation module was developed to allow users to implement and execute OEM-specific crack formation algorithms in conjunction with DARWIN. Additional parameters were introduced to provide 3D modeling of anomalies and associated production inspections.

5.2.1 Probabilistic Approach.

The risk computations in DARWIN were developed for materials with relatively low anomaly occurrence rates, such that a disk has at most one significant anomaly. Since some materials may exhibit higher anomaly frequencies, modifications to the risk computations were implemented to account for multiple (i.e., unlimited) significant anomalies in a disk for both the Monte Carlo and Importance Sampling probabilistic methods (and associated confidence bounds). Details regarding the probabilistic treatment of multiple anomaly materials are presented in appendix P.

5.2.2 Adaptive Optimal Sampling Methodology.

A methodology was developed to improve the computational efficiency of the probabilistic computations associated with general inherent materials. The methodology, described in appendix Q, focuses on variance reduction of sampling-based series system reliability predictions based on optimal allocation of Monte Carlo samples to individual failure modes. It is demonstrated for a simple series system in which it is shown that the variance of the system failure probability is reduced compared to a uniform sampling approach, due to the reduced variances in the failure probabilities associated with the weakest members. The adaptive optimal sampling methodology is also illustrated for a gas turbine engine disk modeled using several methods to estimate the failure probability in each zone prior to optimal sampling. It was shown that the computational accuracy of the method does not appear to depend on the initial failure probability estimate, whereas the computational efficiency is highly dependent on the initial failure probability estimate.

5.2.3 User-Supplied Crack Formation Module.

Rare inherent anomalies in titanium alloys generally exhibit negligible crack formation lives; fatigue cracks nucleated at anomalies can begin growing almost immediately when the component enters service. However, for anomalies in other materials, the crack formation life may be nonnegligible and must be considered in the risk computation to avoid overconservatism. Several OEMs have developed methods to predict anomaly crack formation life, but these methods are proprietary and cannot be shared with other users. A Crack Formation Module (CFM) was therefore introduced in DARWIN to allow users to link OEM-specific crack formation algorithms with DARWIN (figure 5-2). The CFM and associated data are developed and maintained by the individual OEMs. During run time, DARWIN communicates with the CFM to obtain the crack formation life associated with an anomaly with specified temperature and applied stress values.

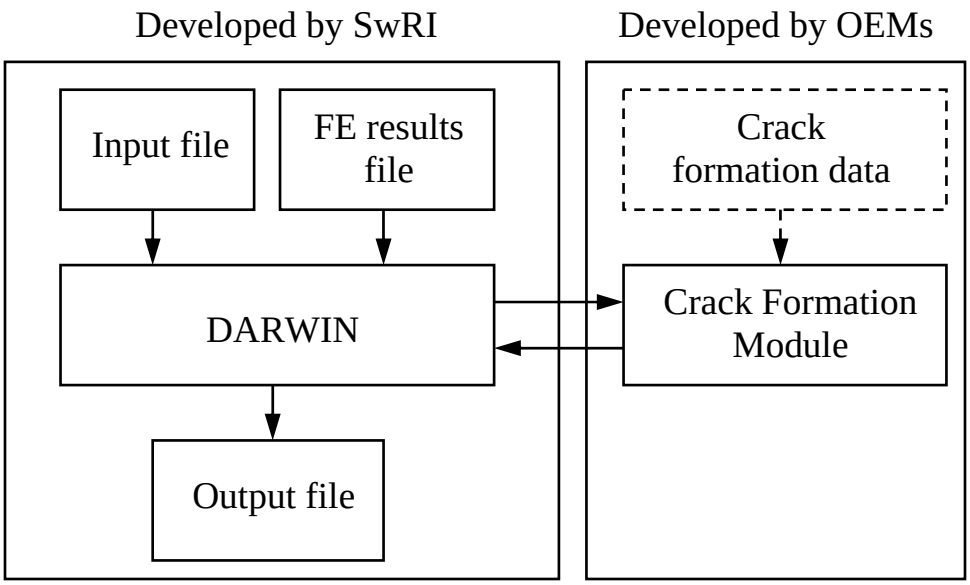

Figure 5-2. Architecture Linking the User-Supplied Crack Formation Module to DARWIN

The CFM is executed as a separate program that receives input from DARWIN. The following data are passed from DARWIN to the CFM: (1) anomaly global coordinates and distance to the nearest free surface of the fracture mechanics plate, (2) anomaly dimension (a, c) in the crack plane, (3) six components of stress at the anomaly location for each load pair, and (4) temperature at the anomaly location for each load pair. The following data are passed from the CFM to DARWIN: crack formation life for entire history and crack dimensions at the end of crack formation life.

Linking two independent computer programs together is a nontrivial task, particularly when multiple platforms and associated operating systems must be supported. One approach is to use a FORTRAN link algorithm, but this often requires the sharing of source code. Another approach is to execute one program from another via a system call, but the computation time associated with this approach can be significant due to the excessive file read/write operations associated with passing information between the programs. As an alternative

approach, an application program interface (API) can be used that allows two programs to share information without the need for ASCII input/output files. A Formation API was developed that links DARWIN with the CFM, allowing the two programs to be compiled separately. During run time, data is passed between DARWIN and the CFM via the Formation API. This approach provides efficient data exchange rates without the requirement to share source code.

5.2.4 Three-Dimensional Anomalies.

The anomaly distribution architecture in previous versions of DARWIN was based on the single degree of freedom distributions for rare anomalies associated with titanium materials (described in AC 33.14-1) and surface damage (currently under development by RISC). To address materials with generalized inherent anomalies, additional parameters were introduced to provide 3D geometry modeling of anomalies using six degrees of freedom (length, two aspect ratios, and three orientation angles). Each of the six degrees of freedom can be modeled as a random variable using several parametric formats (e.g., exceedance curve, lognormal, and deterministic).

The anomaly distributions published in AC 33.14-1 quantify the number of anomalies present following a specific production inspection. A capability was added to DARWIN allowing the user to specify the parameters of the anomaly distribution independent of the production inspection and to specify a probability of detection (PoD) for production inspection for anomaly distributions that do not have a prespecified production inspection.

5.3 GENERAL DARWIN ENHANCEMENTS.

5.3.1 Probabilistic Methods.

A number of probabilistic enhancements were developed to improve the overall efficiency and accuracy of the risk assessment computations, including optimal sampling, importance sampling, and probabilistic confidence bounds. A number of enhancements were also developed to provide the engineer with additional information regarding the influences of design variables on overall risk, such as probabilistic sensitivities and conditional failure analysis.

5.3.1.1 Confidence Bounds.

Confidence bounds for Monte Carlo simulation and importance sampling were introduced in DARWIN versions 3.5 and 4.1, respectively. For a specified number of samples, the importance sampling confidence bounds are narrower than those associated with Monte Carlo simulation, indicating a more accurate solution. These bounds provide an estimate of the accuracy associated with sampling-based probabilistic methods. Further details on the confidence bounds in DARWIN are provided in appendix R.

5.3.1.2 Importance Sampling.

The DARWIN importance sampling method was enhanced to provide improved efficiency and accuracy. A complete description of the DARWIN importance sampling method, including a summary of recent enhancements, is provided in appendix S.

5.3.1.3 Probabilistic Sensitivities.

The probability of fracture is influenced by several random variables that are described in both empirical and parametric terms. Complete analytical expressions were developed that describe the sensitivity of the probability of fracture to changes in various parameters associated with the random variables. Further details are provided in appendix T.

5.3.1.4 Optimum Number of Samples per Zone.

A technique was developed to reduce the variance associated with the probabilistic computations for titanium materials. The technique, described in appendix U, provides an optimal allocation of Monte Carlo samples to individual zones. It is shown that reallocation of samples based on risk contribution factors or an optimal approach can significantly reduce the total number of samples required for a specified accuracy. In addition, a hybrid approach is presented in which optimal sampling is combined with a semiautomated zone refinement procedure. This approach is illustrated for an aircraft rotor disk in which it is shown that zone refinement influences mean disk risk, whereas optimal sampling influences disk risk variance.

5.3.1.5 Conditional Failure Analysis.

When the DARWIN importance sampling method is used, the ranges of random variables associated with failure must be identified to efficiently quantify the influence of inspection. This information can be reviewed using a conditional failure analysis (CFA) approach that provides valuable information to the engineer for improvement of component design, and helps to validate the mathematical models and probabilistic input distributions associated with reliability computations. A CFA technique is presented in appendix V that is based on generation of conditional failure samples obtained during computation of component reliability. It provides a graphical description of the failure region that can be used for failure analysis.

5.3.2 Zone Discretization.

During the TRMD-I program, a zone-based probabilistic approach was developed for risk assessment of rare inherent anomalies that (1) provided a conservative risk result regardless of the number of zones used and (2) converged to a single risk value as the number of zones was increased. The practical implementation of the approach revealed the need for zones smaller than the finite elements defined in 2D FEM and the need to subdivide zones into subzones. These capabilities were developed under TRMD-II.

5.3.2.1 Zone Refinement.

A capability was developed to subdivide zones into two or more subzones (figure 5-3). The size and shape of the subzones are based on the relative values of the stress contours of the original zone, and subzones inherit zone characteristics from the original zone. This capability significantly reduces the human effort associated with zone creation.

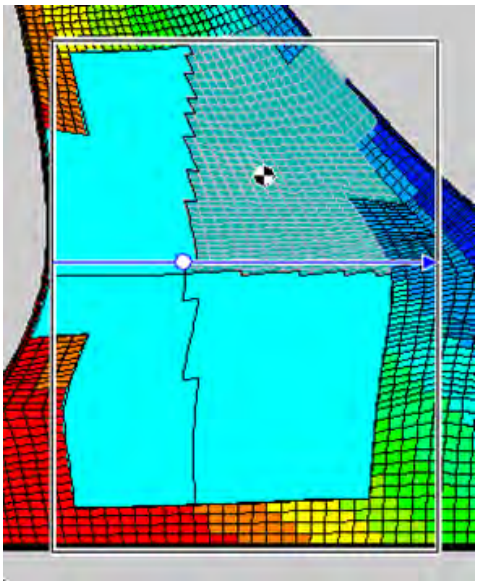

Figure 5-3. Illustration of Zone Refinement Capability

5.3.2.2 Element Refinement.

A zone in DARWIN can be no smaller than a single finite element, but in some cases, the original finite element mesh (developed for purposes of stress analysis) is not sufficiently refined for zoning purposes. Therefore, capabilities were developed to further discretize a finite element mesh. As shown in figure 5-4, the capability can be used to define new elements at specific locations that are smaller than those in the original mesh. In addition, as shown in figure 5-5, the capability can be applied to an entire component to define the near-surface onion skin region for surface zone modeling. This capability reduces the human time that would be required to recreate finite element models to address specific zone modeling issues. The revised finite element mesh is used only for zoning purposes and not for additional stress analysis.

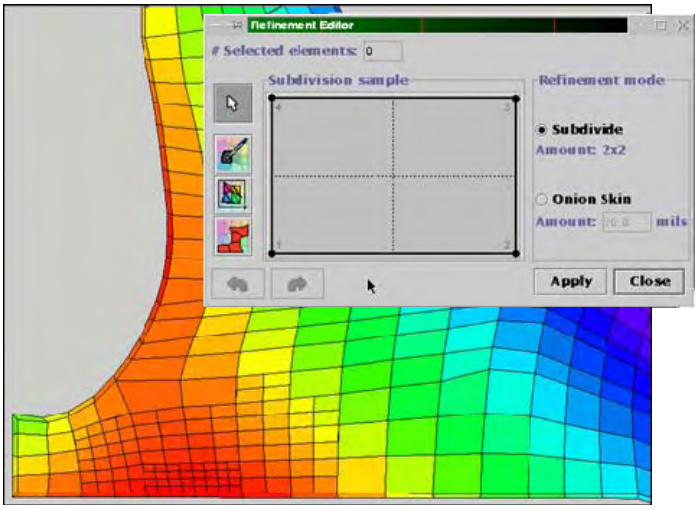

Figure 5-4. Illustration of the Element Subdivision Technique

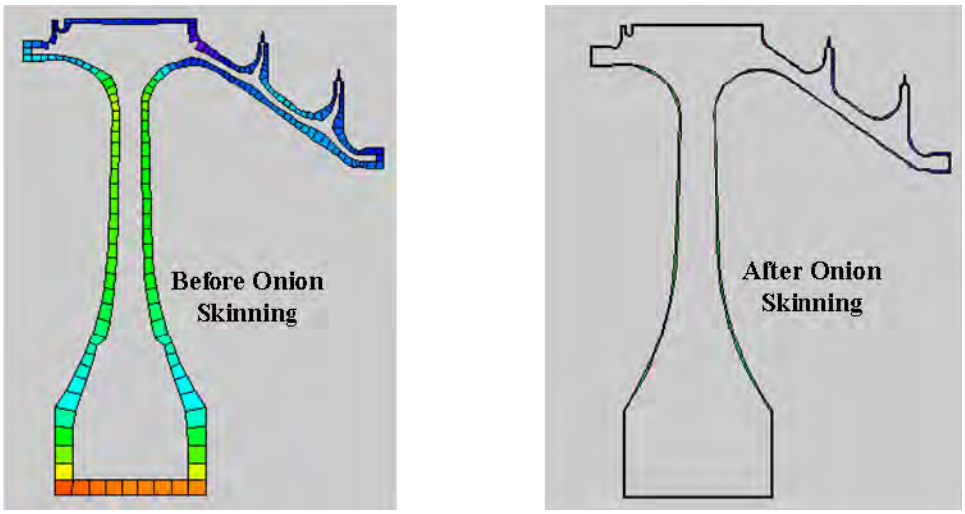

Figure 5-5. Illustration of the Onion Skin Capability

5.3.3 Inspection.

The inspection capabilities developed under the TRMD-I program were enhanced to provide more realistic treatment of shop visit practices in the following areas: inspection following transition of a subsurface to a surface crack and linked shop visit times.

5.3.3.1 Inspection for Transitioned Subsurface Cracks.

A variety of inspection methods may be applied to a component during a shop visit inspection, each with an associated probability of detection. When a crack initiates at the subsurface level, an UT inspection can be used to detect it. However, when a subsurface crack transitions to a surface, it may be more easily detected using a surface inspection method. A capability was developed in DARWIN allowing the analyst to specify different inspection techniques for the pre- and posttransition phases of subsurface crack growth.

5.3.3.2 Linked Shop Visit Time.

In previous versions of DARWIN, shop visit (inspection) times were modeled as independent random variables. This approach did not take into account the potential relationship among inspection times (i.e., the dependency of future inspections on the timing of previous inspections). A new capability was added to allow specification of inspection time in terms of a previous inspection. The capability was implemented in DARWIN for both tabular and normally distributed inspections.

5.3.4 Mission Mixing.

The fracture risk of rotors and disks is highly dependent on the usage history of an engine. During the design stage, a series of predefined missions are sometimes used to establish the design stresses for engine components. A capability was developed in DARWIN to allow

analysts to define multiple missions and to combine them to define the mission mix for risk assessment computations.

5.3.4.1 Stress and Temperature Scaling Factors, and Zone Groups.

Several input formats were required to support OEM requirements for importing stress/temperature data, including (1) finite element data for all missions for the entire disk, (2) data from OEM specific regression tools for specified regions of the disk, and (c) combined scaling factors and finite element data for part or all of a component. A capability was implemented in DARWIN allowing the analyst to apply scaling factors to the stresses and temperatures associated with some or all of the load steps in a mission. Zone groups were also introduced to enable analysts to apply scaling factors to specific regions of a component.

5.3.4.2 Mission Sequencing.

A capability was developed in DARWIN allowing the analyst to specify the number and sequence of missions in a mission mix. For crack growth computations, all of the missions are assembled into a single compound mission.

5.3.5 Stress Conversion.

The ANS2NEU stress conversion program developed under the TRMD-I program was relatively inefficient and was limited to command line use on UNIX systems. It was significantly enhanced during the TRMD-II program, including a new capability to select specific results for use in DARWIN.

5.3.5.1 ANS2NEU Enhancements.

The ANS2NEU program and its companion RDB2UIF program were enhanced to support the personal computer (PC)-based Microsoft® Windows® operating systems. These programs are used to translate ANSYS result files to neutral file format for input to DARWIN and previously were only supported for UNIX-based platforms. An interface was also developed to allow users to execute ANS2NEU directly from the DARWIN GUI.

5.3.5.2 Element Filtering.

The ANS2NEU file translation program was enhanced to provide finite element filtering using element selection/extraction capabilities contained within the SIESTA program. It has the capability to include or exclude elements (and associated stress/temperature results) during translation based on specified ranges of Element ID, Material ID, or Load Case. The DARWIN GUI includes an interface allowing the analyst to specify these ranges.

5.3.6 Stress Processing Enhancements.

A new DARWIN capability was developed to read stress and temperature data directly into memory (rather than perform multiple calls to the ANS2NEU program). By eliminating the time previously required for multiple read/write operations associated with ANS2NEU, the

computation time associated with stress processing was significantly reduced (roughly 80% reduction). Other improvements such as dynamic array allocation also reduced the memory required to execute the DARWIN program.

5.3.7 Data Management Enhancements.

A number of repetitive operations are often required as part of the design process. Since the computation time associated with risk assessment is nontrivial, data management enhancements were developed to reuse results from previous computations where practical. This consisted of a new restart capability coupled with a new Extensible Markup Language (XML) database.

5.3.7.1 Restart.

A restart capability was developed that applies the results of previous computations to a DARWIN analysis to reduce overall computation time. During execution, restart compares the input information for a previous run to the current analysis for each zone. If the zone input data are identical, the zone risk results are extracted from the output database file (*.ddb) of the previous run. This feature was developed for stress processing, deterministic crack growth, and risk assessment computations.

5.3.7.2 XML Database.

The standard ASCII results file format developed under TRMD-I was sufficient for limited read/write operations associated with a single execution of DARWIN. However, this file format is inefficient for restart operations because the entire file must be processed for each retrieved data value. A new XML database system was developed under TRMD-II that provides efficient storage and retrieval of results. It uses a hierarchical format based on a series of address statements in which data values are stored and retrieved directly from memory, eliminating the time-consuming read/write operations associated with the ASCII file format.

5.3.8 The PC/Linux Versions of DARWIN.

The stress processing enhancements described in section 5.3.6 eliminated the need for the use of ANS2NEU in DARWIN. This led to the development of PC and Linux versions of DARWIN. The PC version has been verified on a number of Windows platforms (including 95, 2000, NT 4.0, and XP) and Linux platforms (SUSE 8.0). Fees from commercial DARWIN licenses were used to support the additional verification and code development tools associated with the development of these versions.

5.3.9 Parallel Processing Capability.

A parallel processing capability was developed that allows DARWIN to be executed simultaneously on multiple computers. During execution of the parallel processing feature, the DARWIN input file is reconfigured as a master and multiple slave files. The master input file contains the information for all zones, and the slave files contain information for a subset of zones. The slave files are distributed to multiple computers and executed to predict the risk

associated with individual zones. For disk risk predictions, the master file combines results of the slave files using the restart capability described in section 5.3.7.1.

5.3.10 Influence of Finite Element-Based Random Variables.

The variability associated with applied stress values is currently modeled in DARWIN using a stress scatter factor applied to deterministic finite element stress results. However, a number of random variables can influence the finite element stress results (e.g., applied load, boundary conditions, component geometry, and elastic modulus). The influence of these random variables on the disk probability of fracture was explored using a conditional expectation approach [12 and 13].

A demonstration prototype was developed using the ANSYS probabilistic design system in which a response surface was developed for the probability of fracture in terms of the finite element-based random variables. The mean probability of fracture was computed by applying Monte Carlo sampling to the response surface results. Although the prototype was not implemented in DARWIN, it can be used to quantify the influence of other variables on the probability of fracture for future code planning purposes. Further details are provided in published papers [14 and 15].

5.4 GRAPHICAL USER INTERFACE.

The GUI preprocesses input data for application to the DARWIN risk assessment code and postprocesses the results for display to the analyst. The GUI was enhanced significantly to support the DARWIN enhancements. A number of additional GUI capabilities were developed to improve the interaction with the analyst and to provide hard copy documentation of results. Note that additional enhancements to the DARWIN risk assessment code were required to support many of the capabilities described in this section.

5.4.1 Visualization and Polynomial Fitting of Stress Gradients.

5.4.1.1 Univariant Stress Gradients.

A GUI capability was developed allowing the analyst to specify the number and spacing of points associated with the stress gradient for inherent anomalies. This provides improved accuracy for risk critical zones.

5.4.1.2 Bivariant Stress Gradients.

The bivariant SIF solutions introduced in Flight_Life require the analyst to select a univariant or bivariant solution based on the character of the stress field. Therefore, a new capability was developed to provide visualization of the stress field in 3D space (figure 5-6). This allows the user to decide whether a full bivariant analysis is required to model the crack growth behavior associated with the stress field.

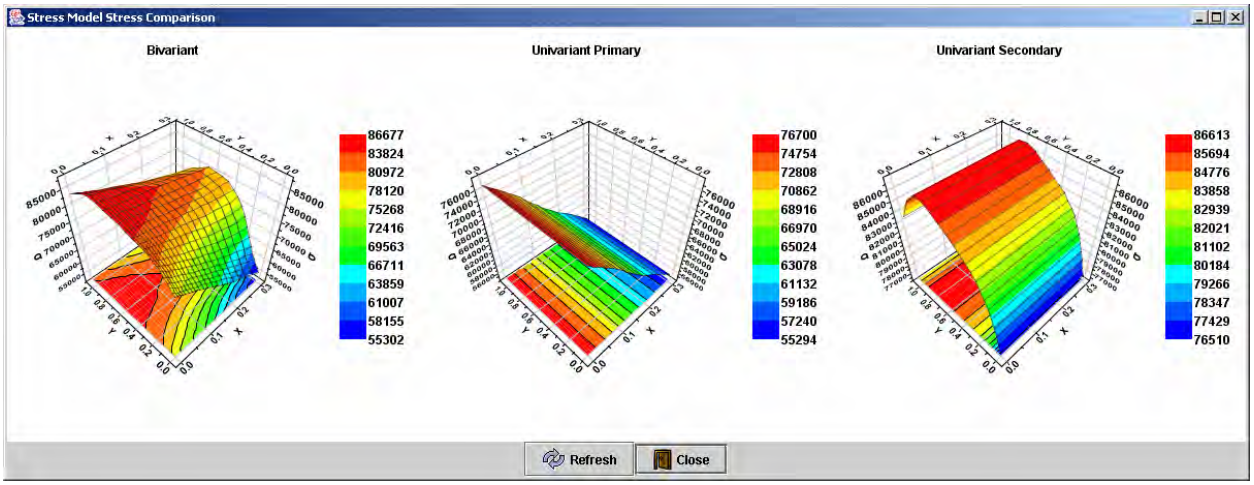

Figure 5-6. Visualization and Polynomial Fitting of Bivariant Stress Gradients

5.4.2 Report Generation.

Following execution of the DARWIN risk assessment code, the complete results are available to the analyst in the form of an ASCII results file or GUI displays. Many of the GUI plots can also be exported for use in word processing programs such as Microsoft® Word® (see section 5.4.4.1). However, these results are not in a condensed format suitable for use in FAA certification reports. A GUI report generation capability was developed to address this need, shown in figure 5-7. In addition, the GUI also provides an analyst report generation option that provides additional plotting options for hard copy reports.

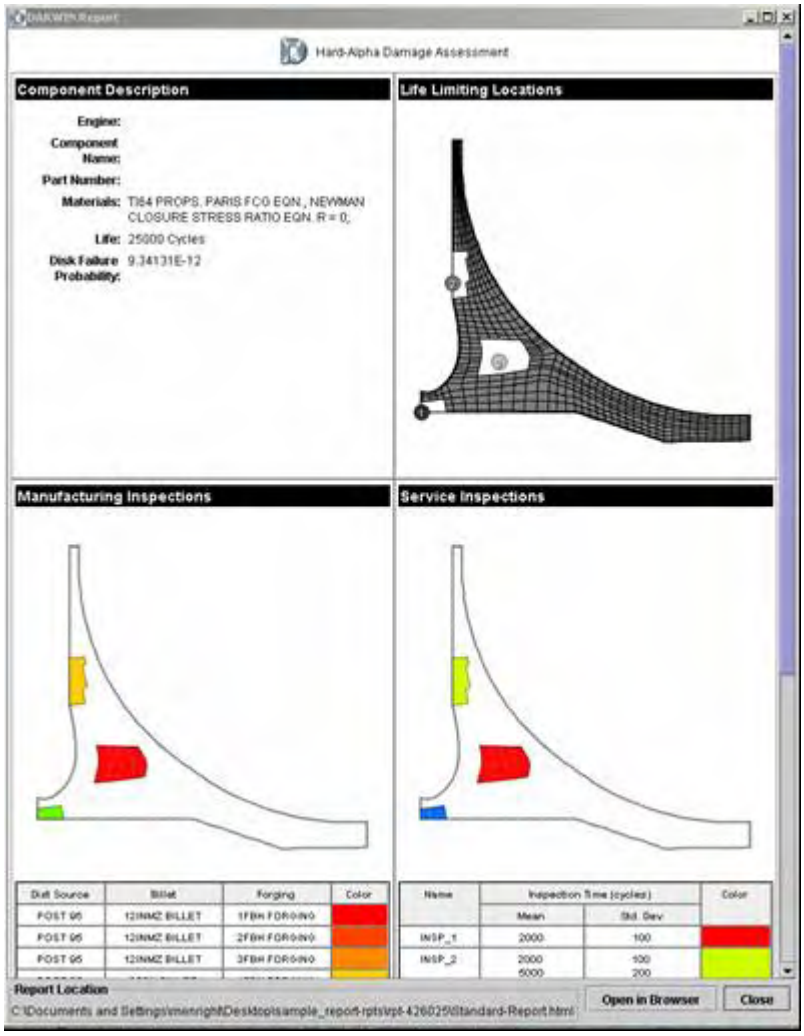

Figure 5-7. Illustration of GUI Report Generation Capability

5.4.3 The GUI-Directed Execution of Risk Assessment Code.

The GUI was enhanced to allow the analyst to execute the DARWIN risk assessment code directly from the GUI. The GUI provides a separate window for display of execution parameters. Upon completion, the GUI loads the results file for display of results.

5.4.4 Additional Enhancements.

5.4.4.1 Plot Export Capability.

A GUI capability was developed to save a plot image to a file (JPEG format). The plot image can be adjusted by the analyst and can be directly imported into word processing software.

5.4.4.2 Input File Preview.

A capability was developed to allow the analyst to preview data files during the assessment definition stage of analysis. This preview capability is provided for a number of input data files, including anomaly distribution, PoD curve, and material properties data.

5.4.4.3 Database Converter.

When developing a commercial software program, backwards compatibility must always be considered to allow analysts to use previously created input/output files in new versions of the code. A database converter was developed that allows the analyst to translate previously created output files for review in new versions of the code. The converter is updated for each major release of DARWIN.

5.4.4.4 Crack Growth Visualization.

In addition to risk predictions, DARWIN also provides complete details regarding the dimensions of the crack over the life of the component. A GUI capability was developed to provide a graphical display of the crack, shown in figure 5-8.

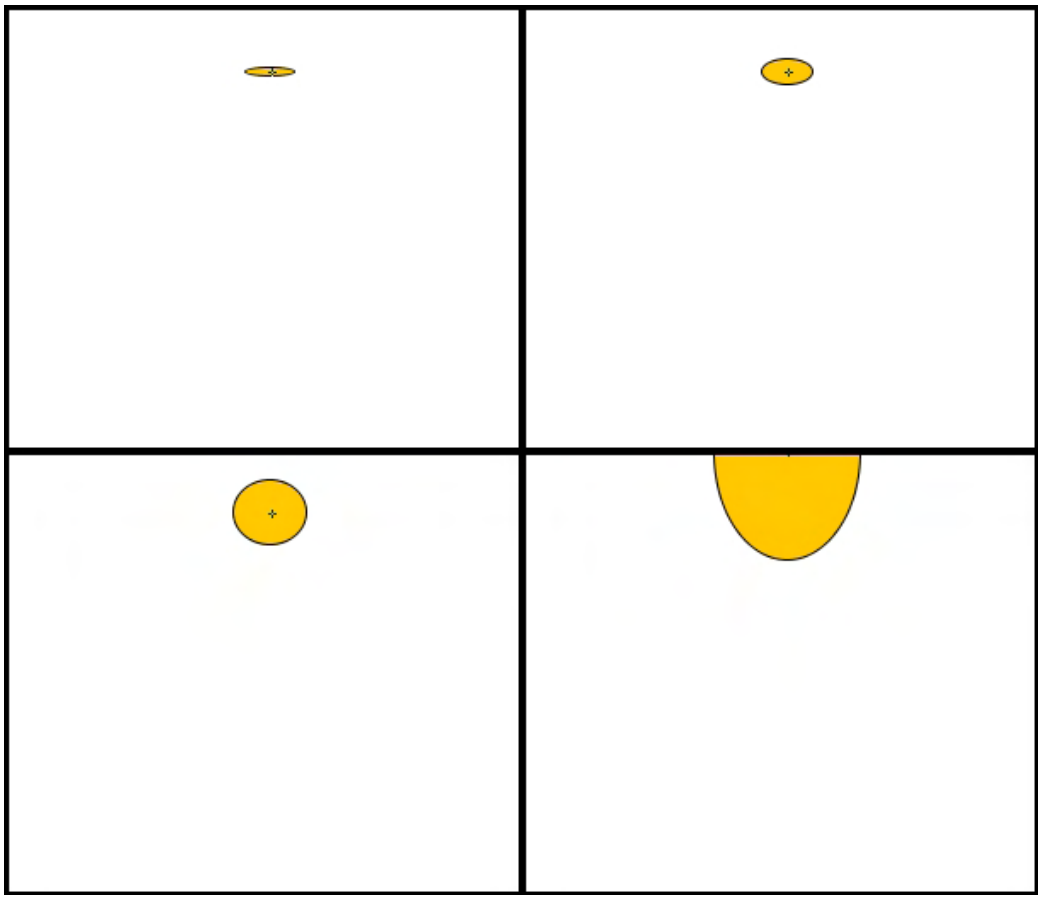

Figure 5-8. Illustration of Crack Growth Visualization Capability

5.4.4.5 Extract Fracture Mechanics Plate Dimensions Directly From FEM.

For inherent anomalies, the GUI provides a feature that allows the user to define the length, width, and orientation of a rectangular plate that is used for fracture mechanics computations. However, for a 3D surface damage assessment, additional parameters are often required to completely describe the fracture mechanics geometry (e.g., location and radius of hole). A new GUI capability was developed that allows the user to define these additional parameters based on geometry values extracted directly from the 3D finite element model. These parameters are displayed in the GUI and can be manually adjusted as necessary by the user.

5.5 DARWIN ELECTRONIC HELP SYSTEM.

An electronic help system was developed to provide assistance to the analyst. As shown in figure 5-9, the DARWIN user's guide and theory manual were combined into a single electronic document available in web browser format. This allows the analyst to consult the help system for questions related to DARWIN theory, verification, and computational procedures. The enhanced help system includes an index and text search capabilities that apply to all sections (including theory and verification sections). These improvements provide improved documentation for support of existing and new DARWIN features.

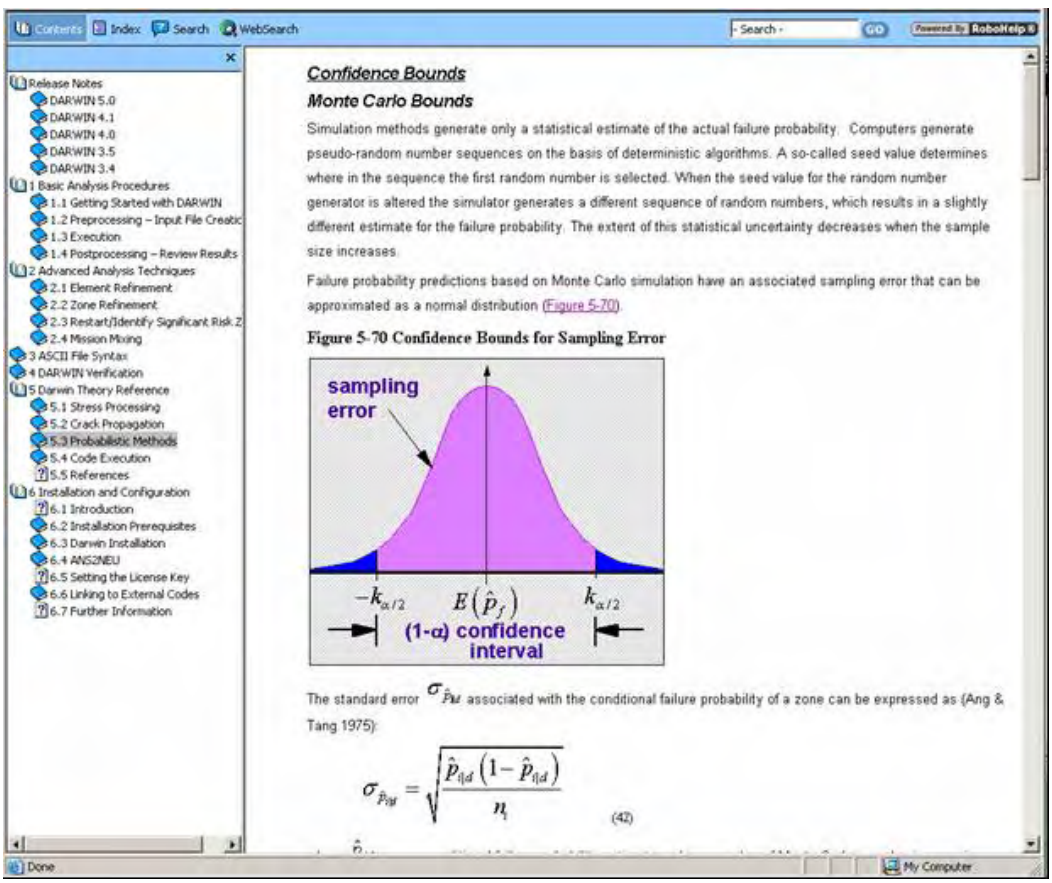

Figure 5-9. The DARWIN Electronic Help System in Web Browser Format

5.6 THE OEM EVALUATION OF DARWIN.

The TRMD Steering Committee was instrumental in the development of the DARWIN computer program. In addition to providing algorithms and design guidance, the partner companies also participated in substantial code review efforts to verify the accuracy and usability of the DARWIN software.

5.6.1 Quantitative Verification.

Throughout the TRMD-II program, DARWIN was evaluated by each of the four TRMD Steering Committee companies. The evaluations consisted of a series of studies focused on comparison of DARWIN predictions to experimental data, field experience, and OEM in-house code results. These studies included an extensive set of test cases that were exercised by multiple users within each of the four OEM companies. The studies were performed using DARWIN versions 3.3-6.0 on several computer platforms, including SUN Microsystem®, Hewlett-Packard (HP), and PC (with a greater emphasis on the PC platform during the final years of the TRMD-II program). OEM evaluation of DARWIN Alpha and Beta versions not only identified a number of bugs that were fixed prior to the production release of the code, but also helped to improve user confidence in the quantitative results.

5.6.1.1 Verification for Inherent Anomalies.

DARWIN verification studies for HA titanium assessed the field experiences of over 50 engine disks of varying levels of maturity. This included various titanium alloys with different disk and hub geometries. The computed probability of fracture predictions representing 2 billion part cycles were combined with representative fleet population and accumulated cycles to predict the number of fractures and finds (HA detection prior to fracture). The probability of fracture predictions were reasonably consistent with earlier results used by the AIA RISC to set the initial HA defect distributions [8].

A number of studies were performed to compare DARWIN probability of fracture predictions to the results of OEM internal codes. The results of one of these studies, focused on the rotating ring disc geometry defined in AC 33.14-1, are shown in figure 5-10. It can be seen that DARWIN results compare very favorably with the risk values computed independently by one manufacturer using their own code and by other OEMs using the DARWIN probabilistic algorithms with their own fracture mechanics modules.

Additional studies assessed the performance of specific algorithms within DARWIN. For example, benchmark testing of the DARWIN rain flow code against an in-house code at P&W has shown agreement between the two codes for test cases with over 6500 load steps. A number of comparisons were made between the Flight_Life fracture mechanics module and various fracture mechanics codes in use by the manufacturers. The selected results shown in figure 5-11 (based on the ring disc geometry defined in AC 33.14-1) illustrate the close agreement between Flight_Life and the results obtained by the OEMs.

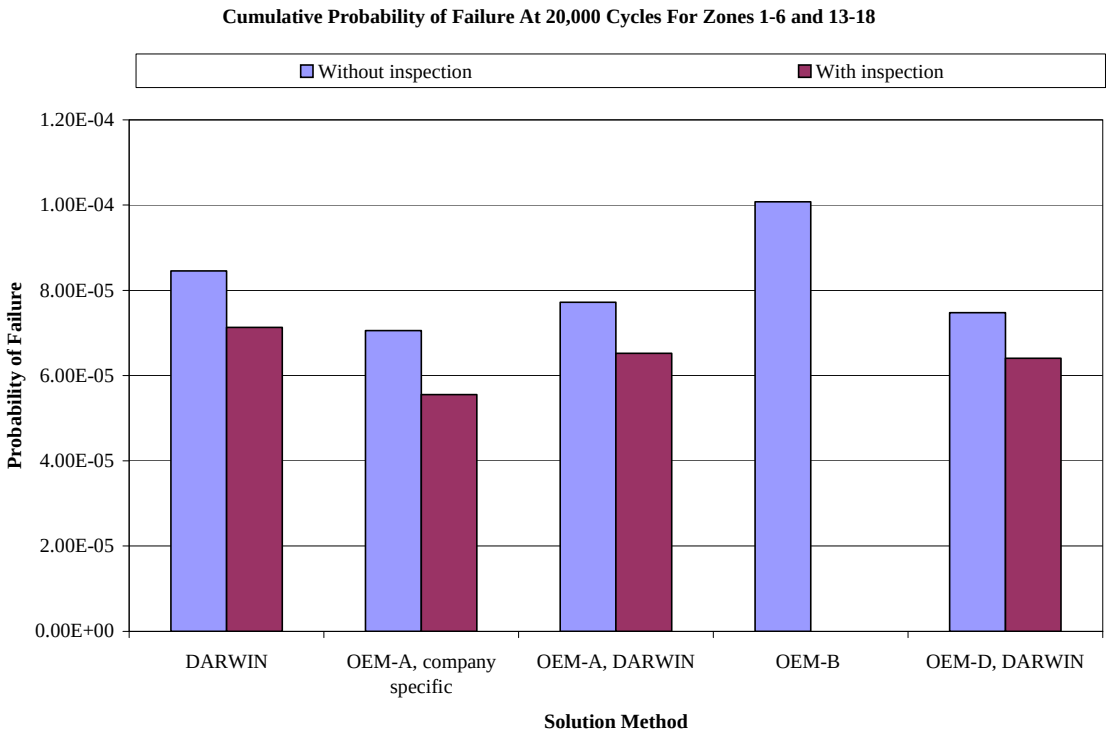

Figure 5-10. Illustration of OEM Verification of DARWIN for Inherent Anomalies

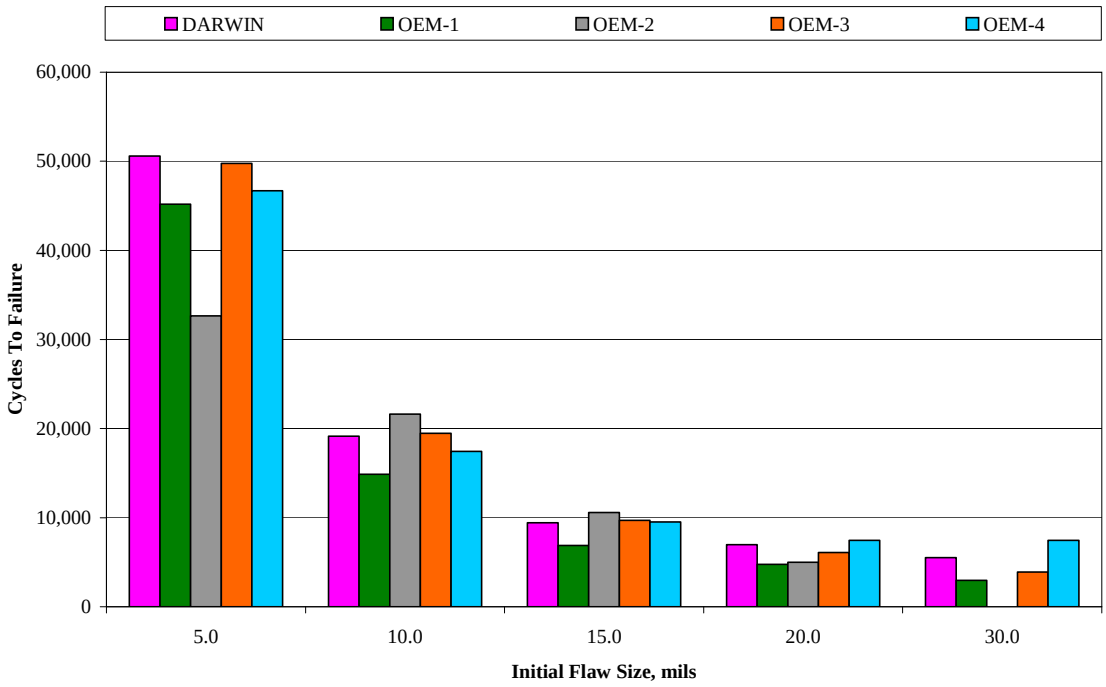

Figure 5-11. Illustration of OEM Verification of Flight_Life Module

5.6.1.2 Verification for Induced Anomalies.

Pratt & Whitney conducted an extensive study comparing DARWIN 5.0/5.2 crack growth life predictions to experimental fatigue test results for surface crack, center notch (through thickness edge crack), compact tension, and bolthole test specimens. Verification of the surface crack specimen was performed for nickel and titanium alloys, and nickel alloys were used for all other specimen types. As shown in figure 5-12, values predicted by DARWIN are in close agreement with the experimental results for both the uniformly stressed surface crack specimens (figure 5-12(a)) and the center notch specimens (figure 5-12(b)). For all specimen types, the results are within the 2.5 times scatter bands for most of the tests considered.

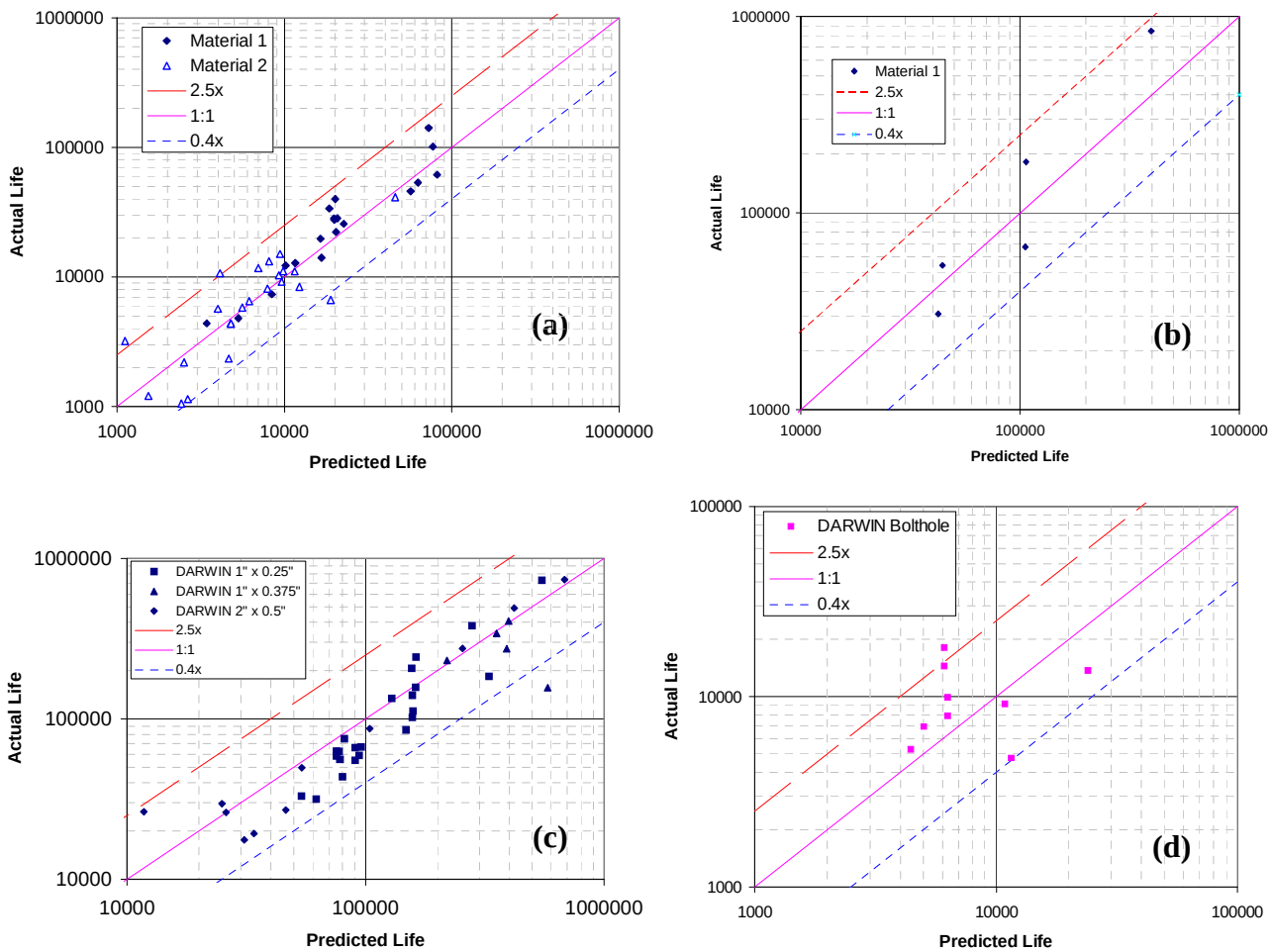

Figure 5-12. Illustration of OEM Verification of Induced Anomalies, Comparing DARWIN Life Predictions to Experimental Results (a) Surface Crack, (b) Center Notch, (c) Compact Tension, and (d) Bolthole

5.6.2 Qualitative Evaluation.

The TRMD Steering Committee performed a series of evaluations to assess the practical use of DARWIN in a design environment. In collaboration with the FAA and the AIA RISC, the Steering Committee identified a number of key enhancements to improve the use of DARWIN as a design and certification tool. Examples include the Standard Report that simplifies the certification process (requested by the FAA, designed by the Steering Committee), the Analyst Report that provides a complete hardcopy summary of results (requested by the Steering Committee), and the linked in-service inspection capability that allows the analyst to specify an inspection in terms of a previous inspection (requested by the Steering Committee). Many additional DARWIN features were improved based on the guidance from the Steering Committee.

5.6.3 The OEM Review Comments.

Over the course of the TRMD-I and TRMD-II programs, the OEMs provided general feedback regarding their experiences with the DARWIN code. The response was very positive, with several of the OEMs electing to license DARWIN for certification of new engine rotors and disks. Some OEMs use the deterministic fracture mechanics capability in DARWIN to supplement (or replace) their internal fracture codes.

OEM feedback has centered primarily on the efficiency, accuracy, and ease of use associated with DARWIN. The OEMs provided a number of positive comments related to the efficiency of DARWIN, focusing on the reduction of human time and computer time required to perform a certification assessment compared to internal codes. For example, one manufacturer reported that the human time required to complete an assessment was reduced from 40 hours to 8 hours when DARWIN was used instead of an internal code. Several OEMs have reported significant computer speed improvements (for a specified accuracy) associated with use of DARWIN advanced probabilistic methods (i.e., importance sampling and life approximation function) compared to the standard Monte Carlo simulation approach. Recent DARWIN enhancements such as zone/element refinement and finite element filtering were noted as substantial human/computational efficiency improvements.

The OEMs also provided a number of positive comments related to the overall ease of use of DARWIN. Several manufacturers mentioned that the GUI was very easy to understand and that new users could quickly learn to use it with minimal training. The OEMs also mentioned that the DARWIN electronic help system was well-documented and provided substantial assistance to both new and experienced users of the code. In addition, the extension of DARWIN to the PC facilitated the use of DARWIN by a wider group of engineers.

6. TECHNOLOGY TRANSFER.

6.1 PROGRESS REPORTS AND REVIEW MEETINGS.

Regular communication with the FAA and the gas turbine engine industry facilitated effective oversight of the research program as well as timely transfer of important new results. Written reports included brief monthly progress reports and substantially longer periodic interim progress reports, which were issued to coincide with program review meetings. These 1-day program review meetings with the FAA were typically held two or three times per year, with frequency and specific schedules directed by the FAA. The program Steering Committee conducted a 1- or 2-day working meeting in conjunction with each program review meeting, and occasionally conducted independent working meetings of 1- or 2-day duration. A representative (usually the Chairman) of the Steering Committee presented a short status report on program activities at each meeting of the RISC (generally held three times per year). Once per year, the SwRI program manager or one of the SwRI co-principal investigators attended the RISC meeting and made the TRMD presentation. The Steering Committee often held a working meeting in conjunction with this particular RISC meeting.

6.2 DARWIN TRAINING WORKSHOPS.

Workshops were conducted to train DARWIN users and FAA staff on the theory and functionality of the DARWIN software. A major workshop was conducted at SwRI on May 3-5, 2005. The scope of this workshop included DARWIN capabilities for titanium HA, surface damage, and generalized inherent anomalies. The first day was an executive overview and software demonstration with 34 people in attendance, including 6 FAA staff as well as representatives from the United States Air Force (USAF), NASA, Transport Canada, Central Institute of Aviation Motors (Russia), and 11 gas turbine engine companies. The second and third days of the workshop were devoted to hands-on DARWIN training, with 26 in attendance for some or all of the training. A course outline is provided in figure 6-1.

Other training workshops with more limited scope were conducted on an as-needed basis throughout the program. One engine company licensing DARWIN sent an engineer to SwRI for a full week of training, while another engine company licensee arranged 1 day of training at their facility for about 30 employees. Two members of the SwRI DARWIN team conducted 3 days of training for about 15 engineers at the Defence Science and Technology Organisation facility in Melbourne, Australia. They also presented 1 day of DARWIN training for about 15 Naval Air Systems Command (NAVAIR) and USAF personnel as part of a 3-day short course on “Probabilistic Analysis and Design for High Performance Computing” at Patuxent River, Maryland. The presentation costs and any travel expenses for these workshops were funded by sources other than the FAA. Some Steering Committee members also provided internal training workshops for employees of their company.

Tuesday, May 3

Time	*Subject*
7:45 - 8:15	Registration
8:15 - 8:30	Welcome
8:30 - 8:45	FAA Opening Remarks
8:45 - 9:00	Introduction & Training Agenda
9:00 - 9:45	RISC Overview
9:45 - 10:00	Break
10:00 - 10:45	Probabilistic Damage Tolerance Analysis Process
10:45 - 11:15	TRMD Overview
11:15 - 12:00	DARWIN Overview
12:00 - 1:00	Lunch
1:00 - 3:00	Use of DARWIN for Titanium Inherent Anomalies
3:00 - 3:15	Break
3:15 - 4:00	Use of DARWIN for General Inherent Anomalies
4:00 - 5:00	Use of DARWIN for Surface Damage

Wednesday, May 4

Time	*Subject*
8:00 - 9:45	Titanium Inherent Anomalies: Hands-On Example Problem
9:45 - 10:00	Break
10:00 - 11:45	Titanium Inherent Anomalies: Hands-On Example Problem (cont'd)
11:45 - 12:45	Lunch
12:45 - 1:45	Stress Processing: Options and Exercises
1:45 - 2:45	Zone Creation: Options and Exercises
2:45 - 3:00	Break
3:00 - 4:00	Fracture Mechanics: Options and Exercises
4:00 - 5:00	Efficient Risk Assessment: Options and Exercises

Thursday, May 5

Time	*Subject*
8:00 - 10:00	Surface Damage: 1D Hands-On Example Problem
10:00 - 10:15	Break
10:15 - 12:00	Surface Damage: 3D Hands-On Example Problem
12:00 - 1:00	Lunch
1:00 - 2:00	Data Preparation Exercises
2:00 - 3:00	General Inherent Anomalies Exercises
3:00 - 3:15	Break
3:15 - 4:15	Zone Refinement Exercises
4:15 - 5:00	Parallel & Batch Processing Exercises

Figure 6-1. Agenda for Darwin Short Course (May 3-5, 2005)

6.3 CONFERENCE PRESENTATIONS AND JOURNAL ARTICLES.

Important results from this research program were disseminated to a much broader audience in the gas turbine engine community or the international technical community in disciplines such as fracture mechanics or reliability through presentations at conferences and symposia or publications in archival technical journals. A complete listing of these presentations and publications is provided in appendix W.

6.4 TECHNOLOGY TRANSFER TO OTHER GOVERNMENT AGENCIES.

Royalty-free DARWIN licenses have been provided to engineers at the NASA Glenn Research Center (Cleveland, Ohio), Air Force Research Laboratory (Dayton, Ohio), Naval Air Warfare Center Aircraft Division (Patuxent River, Maryland), and Army Aviation and Missile Research, Development, and Engineering Center (Redstone Arsenal, Alabama).

DARWIN was installed on the SGI Origin system at the Aeronautical Systems Center, Major Shared Resource Center, at Wright-Patterson AFB, Ohio, and a computational science facility created as part of the Department of Defense High Performance Computing Modernization Program. The SGI Origin system has a large number of central processing units that can be simultaneously exercised using the parallel processing feature in DARWIN.

SwRI collaborates with NASA through a Space Act Agreement on the development and distribution of the NASGRO analysis software for fracture mechanics and fatigue crack growth. NASGRO shares some functionality with the Flight_Life fracture mechanics module in DARWIN, and in fact, some of the early Flight_Life SIF solutions were taken from NASGRO. Many of the new Flight_Life capabilities developed under this grant, including all of the new WF SIF solutions, have now been inserted into recent versions of NASGRO. NASGRO is used extensively by NASA and NASA contractors as well as the European Space Agency, the FAA (especially by FAA designated engineering representatives for damage tolerance analysis), and many aerospace companies. Industrial NASGRO users in the aircraft, rotorcraft, and gas turbine engine businesses include 13 major companies comprising the NASGRO Consortium (Airbus, Boeing, Bombardier, Embraer, Hamilton Sundstrand, Honeywell, Israel Aircraft Industries, Lockheed Martin, Mitsubishi Heavy Industries, Northrop Grumman, Siemens Power Generation, Sikorsky, and Volvo Aero) and many other licensees.

The DARWIN code was used as a demonstration platform in SwRI research programs funded by the Air Force Research Laboratory (AFRL) and the Defense Advanced Research Projects Agency [16, 17, and 18]. Additional features not included in the FAA/production version of DARWIN were added to investigate other technical issues. These enhancements included an interface with simulated engine sensor data for rotational speed (and an algorithm to convert speed into local stress values for select features), simple and advanced crack formation models, integration of crack formation and growth to calculate total life, a spectrum editing algorithm to remove small cycles with negligible contributions to damage, and simulations of continuous crack sensor monitoring. The enhancements were used to study issues such as variability in mission profiles and mission histories, onboard engine monitoring for cracks, improved total fatigue life prediction for cracks in steep stress gradients, and physically informed characterization of fatigue life variability. The larger goals of this research, all in a military context, included the feasibility of prognosis systems to improve reliability and forecast readiness, as well as the potential for engine rotor life extension.

7. INDUSTRIALIZATION OF DARWIN SOFTWARE.

At the request of industry and the FAA, an infrastructure was developed to support the formal use of DARWIN by engine companies for official FAA and company purposes. This industrialization activity addresses formal software configuration management, code licensing and distribution, and user support. The supporting infrastructure includes a source code repository, automated software verification procedures, bug-tracking software, user manuals, an online help system, and a website.

7.1 AUTOMATED SOFTWARE VERIFICATION.

An automated verification procedure was developed to confirm that the DARWIN risk assessment code performs as intended following a major code change. The procedure is used to compare the results of a number of verification output files immediately before and after a change is implemented in the Fortran source code. A comparison results file is created that highlights values that do not fall within specified tolerance values. These highlighted values are used to identify and fix bugs that occasionally occur during the code development stage.

The automated verification procedure consists of a (platform specific) script file and a text extraction program called SCOUT (SCanning Outfile Utility). The script file extracts the DARWIN source code, verification examples, and previous verification results from the concurrent version system (CVS) repository (described below). The script file compiles the DARWIN code and then executes it for each of the verification examples. SCOUT extracts the data from the DARWIN output files, compares it to the previous verification results, and identifies any results that do not fall within specified tolerance values. This process is repeated for all supported computer platforms (SUN, SGI, HP, LiNuX, and PC).

7.2 SOFTWARE REVISION MANAGEMENT.

The development of commercial software requires the interaction of many engineers that serve in a variety of roles (e.g., programmer, reviewer, and end-user). As the software is continuously enhanced, a number of different versions may exist that are in various stages of development. A revision management system is necessary to keep track of the changes to each version.

A revision management system called CVS was identified and implemented for DARWIN to address the issues associated with multiple programmers and versions. CVS provides a directory structure similar to an electronic file manager that serves as a repository for source code. It provides a framework that allows multiple programmers to access and share source code, and it records all changes to the code. CVS can also support multiple versions of the code using a technique called branching. CVS requires a relatively small amount of memory because it stores only the original source code and line-by-line changes to the source code.

CVS has the capability to store most file types including ASCII text, word processing documents, and binary files (e.g., executable programs). It is used to store a variety of information associated with the DARWIN software, including verification example problems and results, programmer's documentation, and user manual documents, among others.

7.3 INTERNET DISTRIBUTION OF DARWIN.

An Internet website (www.darwin.swri.org) was developed for electronic distribution of DARWIN. It serves as a repository for the software and manuals and provides resources for attracting new users, as described below.

7.3.1 Internet Distribution of Software.

In the past, commercial software was often distributed exclusively in electronic media format (i.e., magnetic tape, and CD-ROM). This practice was relatively expensive due to the costs associated with creation and shipment of the media. In addition, this approach required the redistribution of the media to address any changes to the software (including minor bug fixes).

To address these issues (and others), an Internet site was created for the distribution of the DARWIN software (Internet address: www.darwin.swri.org). This site provides the DARWIN executable program for all releasable versions (Alpha, Beta, and Production) of the code on all supported computer platforms (SUN, SGI, HP, Linux, and PC). Internet distribution provides users with instant access to DARWIN following a bug fix or other code change, without the expense associated with the creation and shipping of electronic media. Internet distribution of the software and manuals is password-protected, secure, and restricted to authorized users from the TRMD Steering Committee, AIA RISC, and DARWIN Licensees.

7.3.2 Electronic Distribution of Manuals.

Distribution of the DARWIN user manual is also provided by the DARWIN website. The manual is distributed on the website as Adobe® Acrobat® PDF (portable document format) files. It is also distributed with DARWIN software as an electronic help system that can be accessed directly from the DARWIN GUI.

7.3.3 Resources for New Users.

The DARWIN website also provides valuable information to potential new users. The site provides background information about DARWIN and the TRMD project, including downloadable PDF copies of all the public presentations, published papers, and major reports generated under TRMD-I and -II. In addition, a capability is provided to allow potential new users to download an evaluation version of the code and manuals for a time-limited trial period. Over the period of the TRMD-II program, over 200 evaluation copies were provided to potential new users from government, private industry, and universities.

7.4 USER SUPPORT.

New users often have questions regarding the use and limitations of the computer code. Experienced users occasionally report software bugs that need to be fixed. An infrastructure was developed to address these issues, as described below.

User support to the Steering Committee and RISC members for Alpha and Beta (preproduction) versions of DARWIN and for TRMD-II uses of production versions was funded by the TRMD-II

program. User support to licensees for commercial use of production versions of DARWIN was funded by licensing fees (see section 7.5).

7.4.1 Live User Support.

A help desk was created providing live support to users via telephone, e-mail, and Internet. This allows users to report bugs and to obtain the status on bug resolution, and it also provides general assistance to all licensed users.

7.4.2 Video Tutorials.

An online tutorial was developed as a training aid for new users. The tutorial consists of a Microsoft® PowerPoint® presentation with embedded video sessions that describe the primary menus of the DARWIN GUI. The tutorial is available to the general public via the DARWIN website.

7.4.3 Automated Bug Tracking Software.

A bug tracking system was implemented to ensure efficient tracking and resolution of reported software bugs. The system consists of the Bugzilla® automated bug tracking system, developed by the Mozilla Foundation. Bugzilla was adapted to address the primary software categories associated with DARWIN. Additional features were added to improve the efficiency of bug tracking, including a capability to automatically send bug reports directly to code developers via e-mail. It serves as a repository for all bugs, including placeholders for desired enhancement and new features.

7.5 SOFTWARE LICENSING.

Technology transfer of DARWIN to engine companies and other organizations for official use in both production and research settings is accomplished through a formal commercial licensing process. License fees collected by SwRI are exclusively used to enhance the DARWIN code and to provide user support for the benefit of engine manufacturers, other licensees, and the FAA.

7.5.1 Software License Agreement.

A software license agreement was created that provides a detailed description of the terms, conditions, and options associated with DARWIN. It serves as a legal document for the commercial distribution and use of the DARWIN software.

7.5.2 Registered Trademark.

A number of trademark applications were filed to ensure that the DARWIN acronym could be used in commercial trade to describe the software developed under the TRMD program and to prevent the use of this designation by unauthorized persons. The following U.S. registered

trademarks were approved by the United States Patent and Trademark Office, and in addition, the same trademarks are European registered trademarks were approved by the Office for Harmonization in the Internal Market, European Union:

- D (logo) DARWIN® and DARWIN®

7.5.3 Commercial Licensing Activity.

At this writing, a total of eight commercial licenses have been issued, including six gas turbine engine companies and two foreign government laboratories. The engine companies are based in three different countries, for a total of five countries among the eight existing licenses. The engine company licenses include both single seat and site (company-wide) licenses. Several of the engine companies obtained their first DARWIN license shortly after licensing activity commenced and have renewed their license each year. Three of the eight total licenses were initiated within the last year of the TRMD-II program. Other prospective licenses are in negotiation at this writing.

In accordance with the terms of the FAA grant agreement, agencies of the U.S. Government are entitled to receive a royalty-free license for DARWIN upon request. Licensing to these agencies is described further in section 6.4.

8. SUMMARY.

The TRMD-II program was built on the results and the strong working relationships generated under the previous TRMD-I program. Major accomplishments of the TRMD-II program include the following:

- Sensitivity studies were performed to support a planned update by RISC of the HA anomaly distributions included in AC 33.14-1. These studies incorporated new TRMD-generated technology (vacuum FCG data, the HA forging microcode, and the spin pit and coupon HA fatigue tests) as well as new data and insights from OEM experience to identify the variables with the most significant impact on the resulting distributions. The issues and factors identified as being of sufficient significance to be potentially included in future updates include scatter in crack growth life, vacuum crack growth data, an alternative approach to estimate the ingot distribution, five additional years of JETQC data, and the definition of inclusion size (core versus DZ).

- To better understand the evolution and predict the size of HA anomalies, a mathematical model and computer code were developed to describe the diffusion of nitrogen or oxygen in titanium from an inclusion during metal forming and heat treatment. The code was calibrated with available literature data. For a given melt process and initial anomaly size distribution, the code can be used to predict the maximum expected sizes of undetected (stealth) anomalies.

- Detailed NDE and metallography were performed on the forgings with seeded or natural HA anomalies produced in TRMD-I to validate the DEFORM forging microcode developed in TRMD-I. Detailed experimental measurements of core and DZ sizes in the forgings were compared with predictions from the direct application of the microcode as well as predictions from a new set of regression equations generated with the microcode. Overall, the agreement between measurements and predictions was good.

- The HA microcode was used to characterize the nitrogen contents, temperatures, strain rates, and orientations associated with cracking of HA anomalies during the forging operation. The strain required to cause HA cracking was generally found to increase, and damage was found to decrease, with decreasing HA and DZ nitrogen content, increasing temperature, and decreasing strain rate. Studies of three representative forging shapes indicated that ingot-to-billet conversion and component forging would, under commonly used processing conditions, crack all HA with nitrogen contents greater than 4%, which was the lowest HA nitrogen content evaluated.

- A series of UT inspections were performed using both conventional and multizone inspection techniques on natural and seeded HA anomalies in final forged shapes, for comparison with inspections on billet and intermediate forged shapes conducted previously in TRMD-I. Based on the inspections conducted, the Multizone #1 FBH inspection was found to detect anomalies more effectively than either Conventional #1 or #2 FBH inspections, and both synthetic and natural HA inclusions were easier to detect in the billet than in the forgings.

- The development of the DEFORM forging analysis software to predict bulk RSs was evaluated. Comparisons between predicted and experimentally measured RSs performed outside the TRMD-II program indicated generally good agreement for several different conditions.

- Tensile and fatigue tests were performed on high-oxygen seeded Ti-17. Results indicated only a small impact of elevated oxygen on tensile and dwell fatigue properties, a slightly higher impact than for Ti-64, but a much smaller impact than for Ti-6242.

- Fatigue tests with embedded HA defects were performed on coupon specimens machined from selected seeded forgings in the microcode validation study. The DARWIN Flight_Life module was used to predict the FCG lifetime of each test, based on the assumptions that crack nucleation life was zero and the initial crack size was equal to the core plus DZ size. The actual total fatigue life observed was nearly always at least twice as long the calculated FCG life.

- The coefficient of thermal expansion of bulk HA with different nitrogen contents was measured experimentally. These results were employed in detailed stress, damage, and fracture mechanics analyses to evaluate the potential effects of thermally induced RSs on fatigue crack initiation and growth at synthetic HA inclusions. These RSs appear to be significant for embedded defects at higher nitrogen contents and lower applied stresses, but not significant at lower nitrogen contents and higher applied stresses.

- Spin pit tests were performed with material from the TRMD-I forgings containing embedded natural and synthetic HA anomalies. Posttest fractography and metallography were performed, and the spin disks were also nondestructively inspected periodically during the test. NDE results were provided to the ETC. Test lives were compared with Flight_Life analyses, indicating that initial flaw sizes more nearly corresponded to core sizes than DZ sizes.

- Vacuum FCG data were generated at representative temperatures and stress ratios for one titanium rotor alloy (coarse-grained Ti-6242), two nickel rotor alloys (IN-718 and Waspaloy), and a powder metallurgy nickel alloy (Udimet 720).

- Several mults of Waspaloy with sonic indications were obtained from a nickel melter. The mults were inspected ultrasonically, forged, and then reinspected. Some of the original indications could not be located again following forging. Some remaining indications were selected for machining into coupon specimens for future fatigue testing.

- Thermomechanical FCG data for IN-718 were generated with simple diagnostic stress-temperature histories. Simple stress rain flow analysis methods employing isothermal data from the temperature at the maximum stress time point were shown to exhibit a slightly nonconservative bias.

- Twelve different new or enhanced SIF solutions were developed for the Flight_Life fracture mechanics analysis module. A robust new WF SIF formulation was developed to accommodate general bivariant stress distributions on the crack plane. Highly accurate

new WF SIF solutions were developed for select crack geometries under univariant and bivariant stressing using state-of-the-art 3D boundary element analysis to generate the reference solutions. Novel strategies were developed to increase the computational speed of select SIF solutions. Other Flight_Life improvements included an enhanced Walker interpolation scheme, an improved shakedown module, and first-order plastic corrections to the SIF for instability analysis.

- A broad survey was conducted of the scientific and technical literature on the stability and significance of surface and near-surface RSs in fatigue, based on a comprehensive bibliography containing over 300 citations. Primary attention was given to the RSs resulting from peening and related surface treatments, cold expansion of holes, welding, and machining, with special attention to gas turbine engine materials and applications. Relaxation and redistribution of RSs due to thermal exposure, static mechanical loading, cyclic mechanical loading, and crack extension were addressed in the survey.

- New DARWIN versions were developed to address anomalies associated with surface damage (Versions 4.x and 5.x), as well as different types of inherent anomalies in other materials (Version 6.0).

- New surface damage capabilities in DARWIN initially focused on bolthole configurations. Versions 4.x allowed the user to enter temperature and 1D stress gradient values via tabular input. Versions 5.x introduced a sophisticated 3D GUI that enables the user to load and visualize a fully 3D finite element model and stress results, select a surface crack location, slice the 3D model along the principal stress plane at that location, remesh the slice to create a two-dimensional (2D) stress model, build a 2D fracture mechanics model on the cut plane, and extract the necessary input for the 2D fracture mechanics life calculation.

- A number of new capabilities were introduced in DARWIN 6.0 to support risk assessment of materials with other types of inherent material anomalies. The risk assessment equations for zones and components were modified to account for materials with potentially large numbers of anomalies. A crack formation module was developed to allow users to implement and execute company-specific crack formation modules in DARWIN. Additional parameters were introduced to support 3D modeling of anomalies and associated production inspections. An adaptive optimal sampling methodology was developed to improve computational efficiency for materials with general inherent anomalies.

- A number of enhancements in the probabilistic methods were developed to improve the overall efficiency and accuracy of the risk assessment computations, including enhanced importance sampling that can calculate reliability two orders of magnitude faster than Monte Carlo simulation without loss of accuracy, optimal allocation of Monte Carlo samples to individual zones based on relative risk to dramatically reduce the total number of samples required, probabilistic confidence bounds, computation of probabilistic sensitivities, and conditional failure analysis methods. Some of these enhancements have already been implemented in DARWIN, and others will be implemented in future releases.

- Additional zone discretization methods were developed to improve the efficiency of solution convergence. Capabilities were implemented in DARWIN to automatically subdivide zones into two or more subzones, to subdivide individual finite elements into smaller elements, and to generate a uniform onion skin of surface elements.

- The inspection capabilities in DARWIN were enhanced to provide more realistic treatment of shop visit practices, including inspection following transition of a subsurface to a surface crack, and linked shop visit times.

- A capability was developed in DARWIN to allow users to define multiple missions and to combine them to define the mission mix for risk assessment computations. Supporting features include stress and temperature scaling factors, zone groups, and mission sequencing.

- The ANS2NEU module used to convert ANSYS results files to DARWIN input format was significantly enhanced to support PC-based Windows operating systems, to permit ANS2NEU execution directly from the DARWIN GUI, and to provide finite element filtering based on element type, material, or load case.

- A number of different enhancements were implemented to improve computational efficiency. Stress processing enhancements significantly reduced analysis time and memory requirements. A restart capability was developed that applies the results of previous computations to a DARWIN analysis to reduce overall computation time. A new XML database system was developed to provide improved efficiency for storage and retrieval of results. PC and Linux versions of DARWIN were developed. A parallel processing capability was developed that allows DARWIN to be executed simultaneously on multiple computers, and a batch processing capability was developed that permits execution of multiple DARWIN files in batch mode directly from the GUI.

- The DARWIN GUI was enhanced significantly to support all of the enhancements cited previously. In addition, new capabilities were implemented for visualization and polynomial fitting of univariant and bivariant stress gradients, generation of standard or custom reports of DARWIN results, execution of the risk assessment code directly from the DARWIN GUI, plot export, input file preview, database conversion, crack growth visualization, and extraction of dimensions directly from finite element models.

- An electronic help system was developed to provide assistance to the DARWIN user. The DARWIN user's guide and theory manual were combined into a single electronic document available in web browser format, including an index and text search capabilities.

- The partner gas turbine engine companies participated in substantial code review efforts to verify the accuracy and usability of the DARWIN software. Studies included quantitative comparisons of DARWIN and Flight_Life predictions to experimental data, field experience, and internal company software results. Company evaluation of Alpha and Beta versions not only identified bugs that were fixed prior to production releases of the code, but also helped to improve user confidence in the quantitative results. Qualitative evaluations assessed the practical use of DARWIN in a design environment and identified key enhancements to improve the use of DARWIN for both design and certification. The partner companies provided regular feedback on accuracy, efficiency, and ease of use.

- Technology transfer was accomplished through a variety of mechanisms, including regular progress reports and review meetings focused on FAA needs and regular presentations at RISC meetings. A 3-day DARWIN training workshop was conducted for 34 people (government and industry) near the end of the program, and other training workshops with more limited scope were conducted on an as-needed basis throughout the program. To date, a total of 23 technical papers resulting from TRMD-II research were presented at conferences and published in conference proceedings, an additional 13 papers were presented at conferences or workshops without formally published proceedings, and 8 papers were published in archival journals. Royalty-free DARWIN licenses were provided to engineers at NASA, AFRL, NAVAIR, and the Army, and DARWIN was installed on a Department of Defense (DoD) high-performance (parallel) computer system. DARWIN and DARWIN capabilities were employed in significant research projects for NASA, AFRL, and the Defense Advanced Research Projects Agency.

- An infrastructure was developed for formal software configuration management, code licensing and distribution, and user support. This infrastructure includes a source code repository with revision management system; automated software verification procedures; a website for Internet distribution of software, manuals, published papers, and information for prospective users; live user support; video tutorials; and bug-tracking software. The code is currently licensed by six different engine manufacturers and two foreign government laboratories. License fees collected by SwRI are exclusively used to enhance the DARWIN code for the benefit of engine manufacturers and the FAA.

9. REFERENCES.

1. "Aircraft Accident Report: United Airlines Flight 232, McDonnell Douglas DC-10-10, Sioux Gateway Airport, Sioux City, Iowa, July 19, 1989," National Transportation Safety Board, NTSB/AAR-90/06, 1990.

2. McClung, R.C., Lawless, B.H., Gorelik, M., Date, C., Gill, Y., and Piascik, R.S., "Fatigue Crack Growth of Titanium Rotor Alloys in Vacuum and Air," *Fatigue Behavior of Titanium Alloys*, TMS, 1999, pp. 211-218.

3. Chan, K.S., Perocchi, L., and Leverant, G.R., "Constitutive Properties of Hard Alpha Titanium," *Metallurgical and Materials Transactions A*, Vol. 31A, 2000, pp. 3029-3040.

4. Chan, K.S., "Constitutive Relations for Inelastic Deformation and Damage Accumulation in Hard Alpha Titanium," *ASME Transactions, Journal of Engineering Materials and Technology*, Vol. 123, 2001, pp. 281-286.

5. McKeighan, P.C., Perocchi, L.C., Nicholls, A.E., and McClung, R.C., "Characterizing the Cracking Behavior of Hard Alpha Defects in Rotor Grade Ti-6-4 Alloy," *Fatigue Behavior of Titanium Alloys*, TMS, 1999, pp. 349-356.

6. Wu, Y.-T., Enright, M.P., and Millwater, H.R., "Probabilistic Methods for Design Assessment of Reliability with Inspection," *AIAA Journal*, Vol. 40, 2002, pp. 937-946.

7. Leverant, G.R., McClung, R.C., Wu, Y.-T., Millwater, H.R., Riha, D.S., Enright, M.P., Chell, G.G., Chan, K.S., McKeighan, P.C., Gorelik, M., Fischer, C., Lehmann, D., Green, K., Bartos, J., Howard, N., and Srivatsa S., "Turbine Rotor Material Design," FAA report DOT/FAA/AR-00/64, December 2000.

8. Sub-Team to the Aerospace Industries Association Rotor Integrity Sub-Committee, "The Development of Anomaly Distributions for Aircraft Engine Titanium Disk Alloys," *Proc. 38th AIAA/ASME/ASCE/AHS/ASC Structures, Structural Dynamics, and Materials Conference*, 1997, pp. 2543-2553.

9. McKeighan, P.C., Nicholls, A.E., Perocchi, L.C., and McClung, R.C., "Sensing Crack Nucleation and Growth in Hard Alpha Defects Embedded in Ti-6Al-4V Alloy," *Nontraditional Methods of Sensing Stress, Strain and Damage in Materials and Structures: Second Volume, ASTM STP 1323*, G.F. Lucas, P.C. McKeighan, and J.S. Ransom, eds., American Society for Testing and Materials, West Conshohocken, PA, 2001.

10. Li, S., Mear, M.E., and Xiao, L., "Symmetric Weak-Form Integral Equation Method for Three Dimensional Fracture Analysis," *Computer Methods in Applied Mechanics and Engineering*, Vol. 151, 1998, pp. 435-539.

11. *NASGRO Reference Manual*, Version 4.1, NASA Johnson Space Center and Southwest Research Institute, 2003.

12. Ayyub, B.M. and Chia, C.-Y., "Generalized Conditional Expectation for Structural Reliability Assessment," *Structural Safety*, Vol. 11, 1992, pp. 131-146.

13. Melchers, R.E., *Structural Reliability Analysis and Prediction*, John Wiley & Sons, 2001.

14. Momin, F.N., Millwater, H.R., Osborn, R.W., and Enright, M.P., "Application of a Conditional Expectation Response Surface Approach to Probabilistic Fatigue," *Proc. 9th ASCE Specialty Conference on Probabilistic Mechanics and Structural Reliability*, ASCE Paper PMC2004-204, Albuquerque, New Mexico, 2004.

15. Momin, F.N., Millwater, H.R., Osborn, R.W., and Enright, M.P., "Applications of the Generalized Conditional Expectation Method for Enhancing a Probabilistic Fatigue Design Code," Paper AIAA-2005-2146, *Proc. 46th AIAA/ASME/ASCE/AHS/ASC Structures, Structural Dynamics, and Materials Conference, Non-Deterministic Approaches Forum*, Austin, Texas, 2005.

16. McClung, R.C., Enright, M.P., Millwater, H.R., Leverant, G.R., and Hudak, S.J., Jr., "A Software Framework for Probabilistic Fatigue Life Assessment of Gas Turbine Engine Rotors," *Journal of ASTM International*, Vol. 1, Paper JAI11563, 2004. Also published in *Probabilistic Aspects of Life Prediction, ASTM STP 1450*, W.S. Johnson and B.M. Hillberry, eds., ASTM International, West Conshohocken, PA, 2004, pp. 199-215.

17. Hudak, S.J., Enright, M.P., McClung, R.C., Francis, W.L., and Millwater, H.R., "A Probabilistic Analysis of the Benefits of In-Service Fatigue Damage Monitoring for Turbine Engine Prognosis," Paper AIAA-2004-1953, *Proc. 45th AIAA/ASME/ASCE/ AHS/ASC Structures, Structural Dynamics, and Materials Conference*, Palm Springs, California, 2004.

18. Enright, M.P., Hudak, S.J., Jr., McClung, R.C., and Millwater, H.R., "Probabilistic-Based System for Prognosis of Fatigue in Aircraft Engine Components," AIAA Paper 2003-8014, *Proc. 44th AIAA/ASME/ASCE/AHS/ASC Structures, Structural Dynamics, and Materials Conference*, Norfolk, Virginia, 2003.

APPENDIX A—SUPPORTING STUDIES FOR TITANIUM HARD ALPHA ANOMALY DISTRIBUTION UPDATES

A.1 INTRODUCTION.

Development of anomaly distributions for hard alpha (HA) in titanium disk alloys was initiated by the Rotor Integrity Sub-Committee (RISC) of the Aerospace Industries Association in 1991. The Jet Engine Titanium Quality Committee (JETQC) had gathered data between 1990 and 1993 representing HA finds in billet and bar that had been ultrasonically inspected. While the available data were limited, they served as the basis for an extensive analysis performed by RISC to develop HA anomaly distributions that are applicable to Ti-64, Ti-6242, and Ti-17. The final distributions were set based upon calibration to actual field experience and associated assumptions. The analysis process and its results have been summarized elsewhere [A-1].

Leveraging experience acquired over the past several years deriving HA anomaly distributions and ultrasonic probability of detection (PoD) curves, GE Aviation, teamed with the RISC and members of the Turbine Rotor Material Design Phase II (TRMD-II) Steering Committee, led an effort to formulate revised HA distributions to be incorporated into a future revision of Advisory Circular (AC) 33.14-1 on damage tolerance for titanium rotor components.

The HA distribution update work scope was based on a plan accepted by RISC at their October 2001 meeting. A subteam comprising members from GE, Pratt & Whitney, Honeywell, and Southwest Research Institute® (SwRI®) implemented the plan. The update was broken into two phases. The first phase involved sensitivity studies on model elements used to construct the HA distribution(s). These studies included (1) variability in crack growth behavior, (2) variability in crack aspect ratio, (3) impact of vacuum crack growth data, (4) DEFORM™ microcode impact on original billet and forging HA deformation modeling assumptions, (5) possible alloy and melt practice bias, (6) impact of alternate approach to estimating the ingot distribution, (7) impact of effective inclusion size assumption, and (8) the impact of five additional years of JETQC HA data.

This first phase was performed as part of the TRMD-II program. In the second phase, which was not part of TRMD-II, RISC will make a final decision on which revised model elements will be incorporated into the updated HA anomaly distributions and/or lifing practice based on the results of these sensitivity studies. At this writing, this second phase effort has been put on hold temporarily so that RISC can finish work on other pressing technical issues. Once complete, work on the HA distribution will resume. The second phase is expected to be performed and funded by the RISC membership. This report includes only the results of the first phase.

To perform the sensitivity studies in an efficient manner, GE constructed Design Assessment of Reliability With INspection (DARWIN®) probabilistic fracture mechanics (FM) models for eight key titanium components that were predicted to have the most influence in the GE calibration studies for revising the HA distribution(s). These components included four fan disks and four compressor spools. The following text provides a summary of the completed studies.

A.2 VARIABILITY IN CRACK GROWTH BEHAVIOR.

The goal of this study was to quantify the impact of expected material and analytical scatter on predicted component probability of fracture (POF). The scatter was treated as scatter in life due to variability in both material properties and analytical techniques, not scatter in the material data alone. Predicted-to-observed scatter values for material specimen and feature tests were fit to a lognormal distribution, which was then used to calculate a coefficient of variation (COV) for use in the study. A COV of 0.2582 was used for life scatter in this study. Component POF predictions were made with and without life scatter. The results of this study showed a negligible impact of life scatter on the total POF, no greater than 5%. While variability in crack growth behavior appears to have a negligible impact on POF, it is recommended that it be considered in the HA distribution update for technical completeness.

A.3 VARIABILITY IN CRACK ASPECT RATIO.

The goal of this study was to quantify the impact of varying crack aspect ratio on predicted component POF. The current assumption for HA assessments in the Federal Aviation Administration (FAA) AC 33.14-1 is a 1:1 (*c:a*) ratio, which is a circular crack. Aspect ratios (*c:a*) of 1:1, 2:1, and 3:1 were evaluated. Because the initial crack aspect ratio could not be varied in DARWIN at the time, the fracture mechanics calculations were performed outside of DARWIN in GE's in-house FM code. Since this is a labor-intensive process, only one component (comprising of about 40 zones) was evaluated. However, similar studies performed previously at GE gave similar results to what was shown by this study. Predictions were baselined against a 1:1 crack aspect ratio. As in the life scatter study, the results of this study showed a negligible impact of crack aspect ratio on POF, on the order of 1%. Since the impact of crack aspect ratio appears to be negligible, it is not suggested that it be considered in the HA distribution update.

A.4 VACUUM CRACK GROWTH DATA.

The goal of this study was to quantify the impact of vacuum crack growth data on predicted component POF. The current assumption for HA assessments in AC 33.14-1 is air data for both surface and subsurface crack growth calculations. While it has been known that a vacuum environment can slow crack growth behavior, particularly at low K values, the assumption of air data for subsurface crack growth predictions was made because little vacuum crack data on titanium alloys existed previously. As part of TRMD-1, vacuum data were generated on three titanium alloys: Ti-6Al-4V, Ti-6242, and Ti-17. SwRI prepared generic Paris curves with thresholds, using the new vacuum data and United States Air Force Damage Tolerance Handbook air data, for use in this study (the generic curves are documented in attachment A-1 to this appendix). Component predictions were made assuming air data for surface and subsurface calculations as the baseline (AC 33.14-1), or assuming air properties for surface and vacuum properties for subsurface calculations. The results of this study showed POF decreased approximately 25% to 50% for the air + vacuum predictions without inspection and approximately 15% to 35% with inspection. It is suspected that the reduction may be greater when the vacuum data are fit to GE's standard sigmoidal *da/dN* model due to the more gradual transition in that model from threshold to the Paris regime. While the impact of using vacuum

data for subsurface FM calculations is not large, for technical accuracy and to establish proper precedence for other alloys, where the impact may be larger, it is recommended that vacuum crack growth data be added to the revised POF prediction practice and considered in the HA distribution update.

A.5 DEFORM MICROCODE.

The goal of this study was to evaluate the impact of the new DEFORM HA microcode (see appendix C) on the construction of the HA distribution and component POF calculations. The 1996 distributions (currently in AC 33.14-1) were based on the following HA deformation modeling assumptions:

- Ingot-to-billet deformation. A simple linear model was constructed relating the HA elongation to the amount of elongation in the billet or bar, as shown in figure A-1. The regression relationship was found to be

$$L_{HA_b} = D_{HA_i} \times \left(\frac{D_i^2}{D_b^2} \right)^{0.364}$$

  Where L_{HA_b} is the length of the HA anomaly in the billet, D_{HA_i} the diameter of the HA in the ingot, and D_i and D_b the diameters of the ingot and billet, respectively. The model was constructed using the available three-dimensional (3D) characterization data, founded on the assumption that the HA is spherical in the ingot, illustrated in figure A-2.

- Billet-to-forging deformation. It was assumed that the area normal to the stress field in the forging/part was equivalent to the axial/radial area in the billet. This assumption was based on limited available forging data.

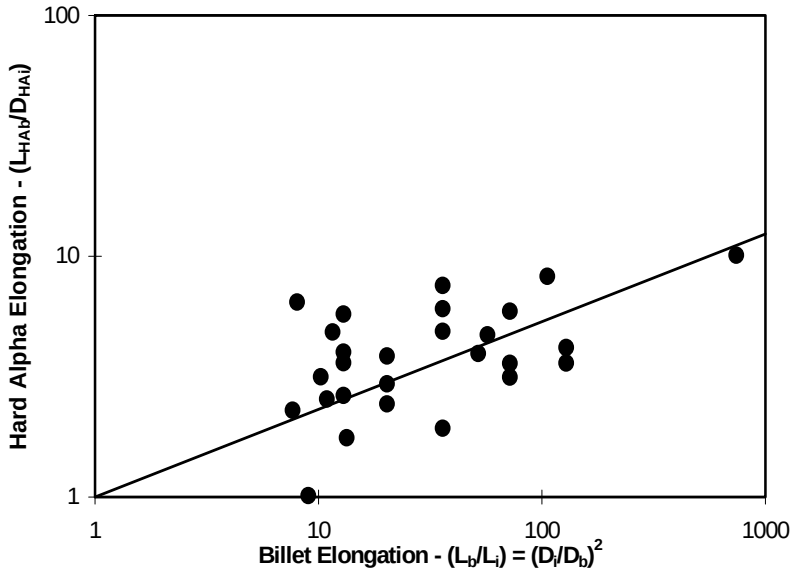

Figure A-1. Empirical Correlation Observed Between HA Elongation and Billet Elongation, Based on Original Assumptions

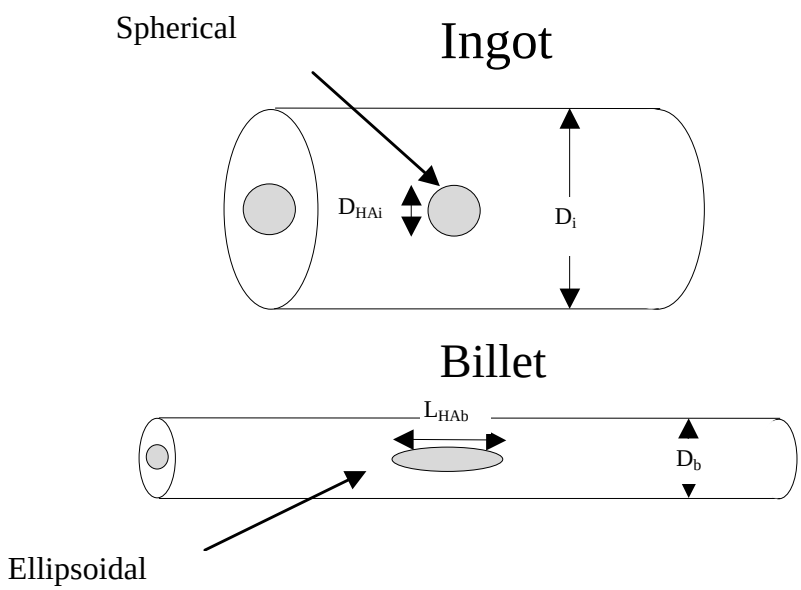

Figure A-2. Idealization of HA Anomaly Morphology in Ingot and Billet Forms

In this study, the original assumptions for billet and forging HA deformation were replaced with the regression model derived by Srivatsa from the DEFORM HA microcode (see appendix C).

- Ingot-to-billet deformation study. In this assessment, the assumption that HA is spherical in the ingot was maintained. The strain in the billet/bar was assumed to be uniform and was calculated as the average strain [Strain = ln $(D_{ingot}^2/D_{billet}^2)$], and HA deformation was predicted using the Srivatsa regression model. This uniform strain assumption is clearly a simplification of what actually takes place in the billet, but it was judged that adding complexity to the strain calculations would not be practical for production analyses. Figure A-3 shows the predicted-to-observed HA deformation for several points taken from the JETQC database. Based on the given assumptions, the study results showed little difference in correlation to the observed data compared to the original deformation model.

- Billet-to-forging deformation study. This study was performed on five GE titanium fan and compressor components. For this assessment, the simple 1996 billet-to-forging assumption that area normal to the principal stress in the forging/part is the same as the area in the axial radial plane in the billet was replaced with the Srivatsa regression model. Forging radial and hoop macrostrain strains were taken from the forging process model results, and axial strain was determined by using the incompressible criterion $e_X + e_Y + e_Z = 0$, where e = ln (final length/initial length). The nitrogen contents assumed for this study were 6.2% for the core and 1.2% for the diffusion zone. These are typical values from the JETQC 3D characterization data. Forging strain rate was assumed to be 0.138 per second (strain rate = die velocity/billet height). Forging average temperature was assumed to be 1720°F. Each part was subdivided into three zones: bore, web, and rim. The average strain was calculated in each zone and used to predict HA deformation in that zone. The baseline distribution was modified using the deformation results, creating a new distribution for each of the three zones. Component POF was then calculated for each part and compared to the baseline analysis with the original 1996 assumption. This entire process is summarized in figure A-4.

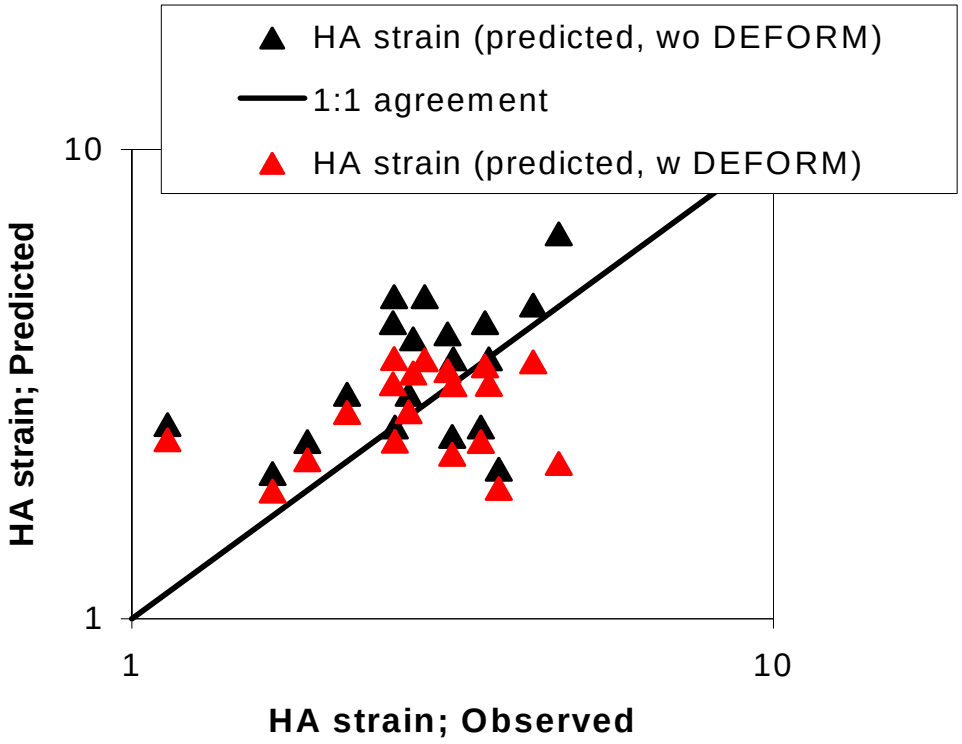

Figure A-3. Comparison of Predicted Versus Observed HA Strain for New (Based on DEFORM Microcode Regression Equations) and old Deformation Models

Results of these studies showed a negligible impact on calculated POF for the five components in the study, as indicated in figure A-5.

Therefore, based on these two studies, it appears that the new HA deformation microcode does not provide significant differences in calculated results, and so the added complexity of using the new deformation model in the HA distribution update is not recommended.

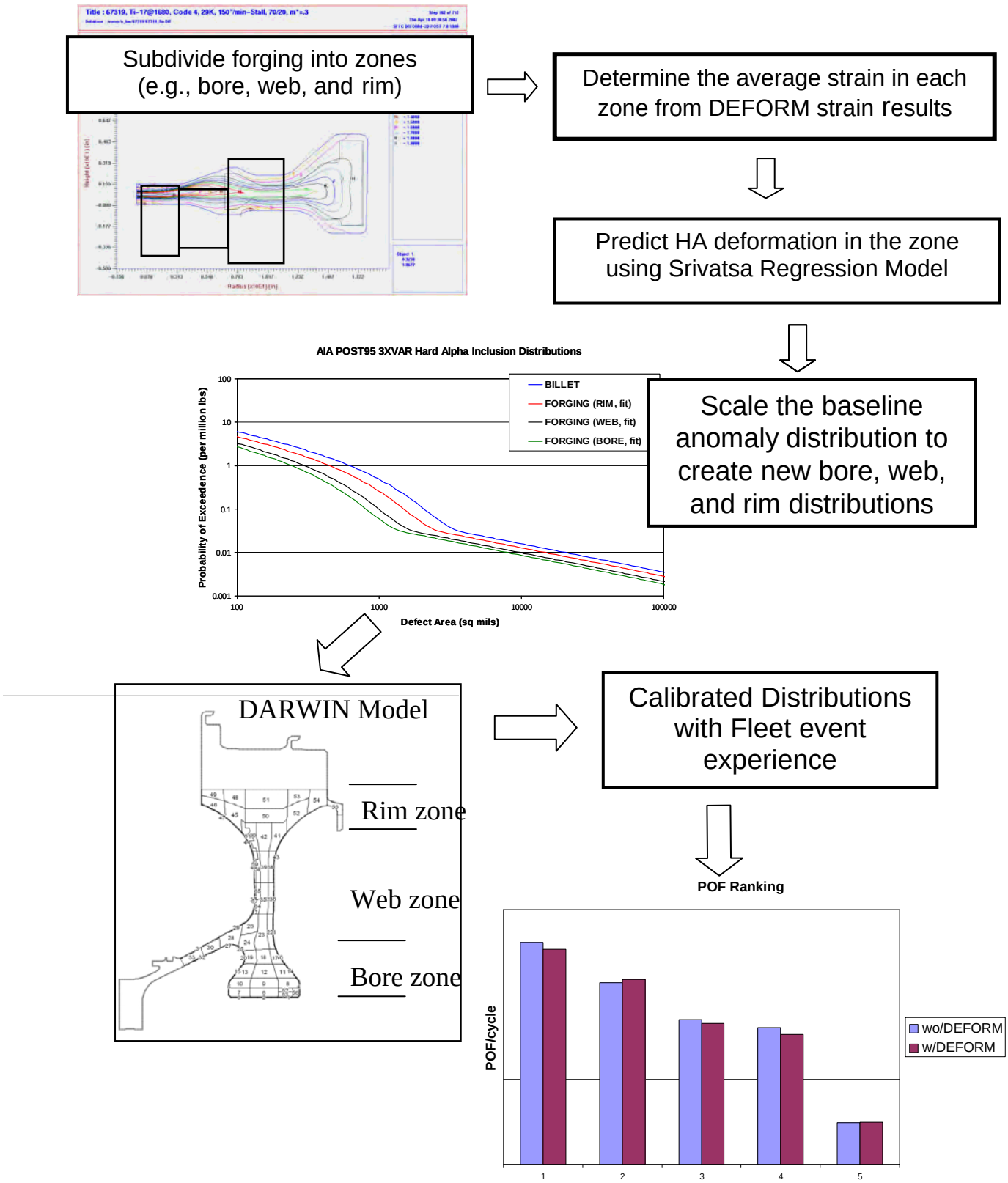

Figure A-4. Summary of Analysis Process to Calculate Component POF Using Information From DEFORM Microcode

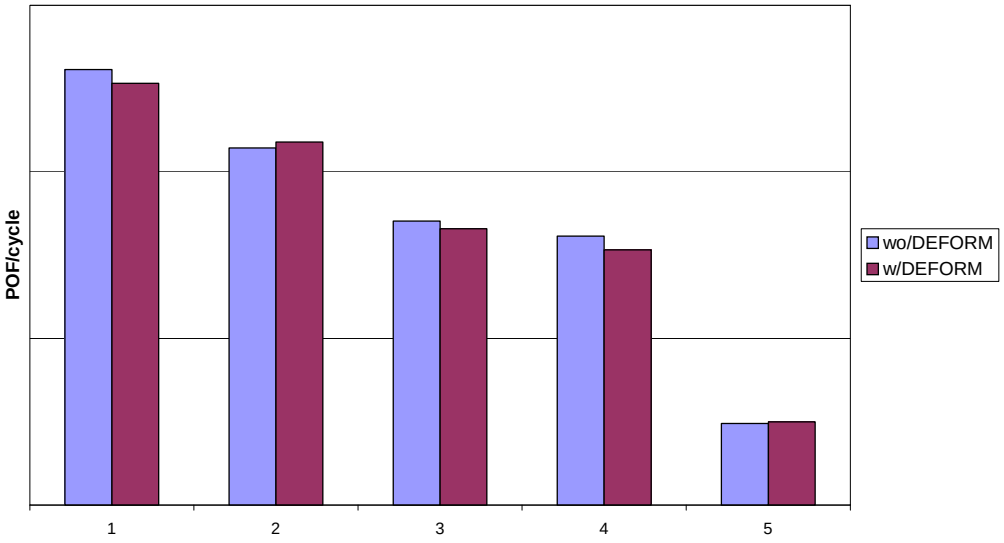

Figure A-5. Comparison of POF Values for Five Representative Components Based on the New (DEFORM) and old Deformation Models

A.6 ALLOY AND MELT PRACTICE BIAS.

The purpose of this study was to quantify the difference in HA frequency between different melt practices and alloy types. JETQC HA data from January 1997 to December 2001 were used in this study to perform the following comparisons:

- 3 times vacuum arc remelting (3xVAR) versus HM+VAR
- Ti-64 versus Ti–6242

A.6.1 THREE TIMES VACUUM ARC REMELTING VERSUS HM+VAR.

In accordance with a March 2003 agreement, a 5-year moving average (MA) was used to estimate the HA rate. The 5-year MA of the find rates from the JETQC data gives a rate of 0.33 HA/M lb for hearth melt (HM)+VAR and 0.25 HA/M lb for 3xVAR (triple melt), as shown in figure A-6. While this HM+VAR rate appears higher than 3xVAR, it should be noted that HM+VAR billet is typically inspected with a more sensitive multizone ultrasonic (UT) process, and 3xVAR is typically inspected with a less sensitive Conventional #3 flat bottom hole (FBH) UT inspection. Therefore, since 3xVAR and HM+VAR are generally inspected to different sensitivities, the inspection bias was removed analytically to put the two rates on equal footing. To remove the inspection bias, the absolute frequency of the ingot distribution for 3xVAR and HM+VAR was estimated using the same technical approach as used in the 1996 HA distribution construction to predict billet and bar finds. The absolute frequencies were determined by selecting a frequency that would predict observed number of JETQC billet and bar finds for each melt practice. The following three assumptions were made in calibrating the ingot distributions: (1) HM+VAR is only inspected with multizone, (2) 3xVAR is only inspected with #3 FBH, and (3) the shape of the distribution is same as the 1996 calibrated ingot distribution. The results of

the study found the HM+VAR ingot distribution to be at about half of the frequency of the 3xVAR, as shown in figure A-7.

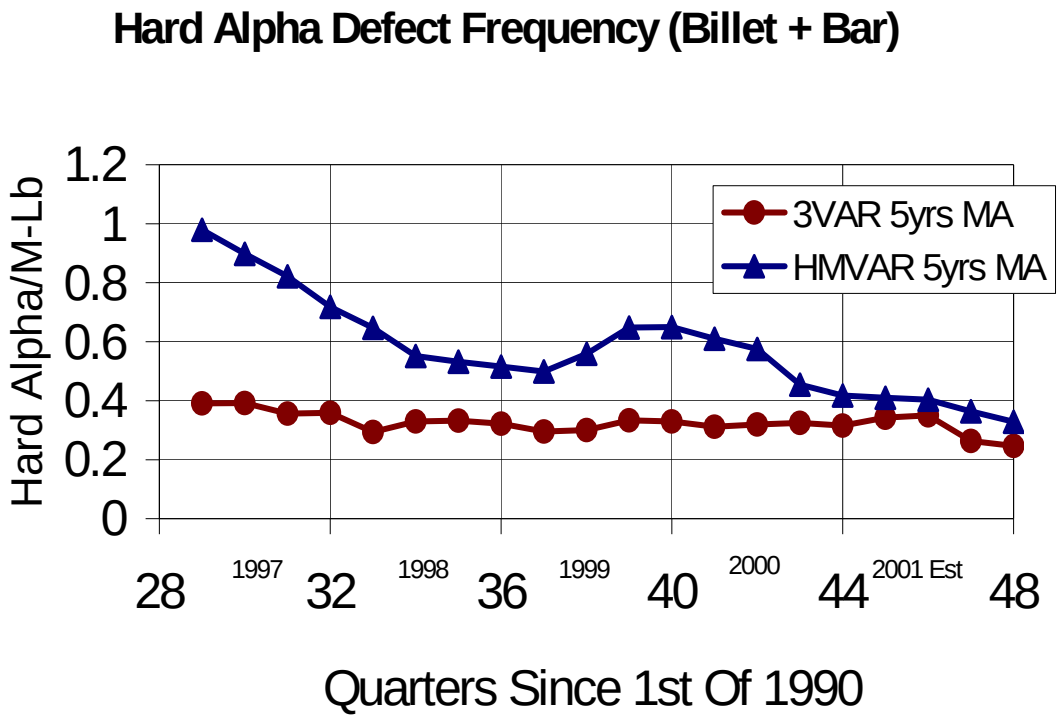

Figure A-6. Comparison of 5-Year MA Find Rates for HA in 3xVAR and HM+VAR

A.6.2 TI-64 VERSUS TI-6242.

Comparing JETQC 1990 to 2001 HA find rates for Ti-64 and Ti-6242 delivers a mixed message. Taking the data at face value suggests for 3xVAR, an average HA rate of 0.56 HA/M lb (10 HA in 18 M lb) for Ti-6242 and 0.33 HA/M lb (31 HA in 93 M lb) for Ti-64. For HM+VAR the HA rates are 2.0/M lb (3 HA in 1.5 M lb) for Ti-6242 and 0.22/M lb (6 HA in 27 M lb) for Ti-64. However, while the raw numbers show apparent differences, simple statistical tests show no statistically significant differences in mean HA rates for the two alloys. This result is apparently influenced by the varying sample sizes and small total numbers of HA finds.

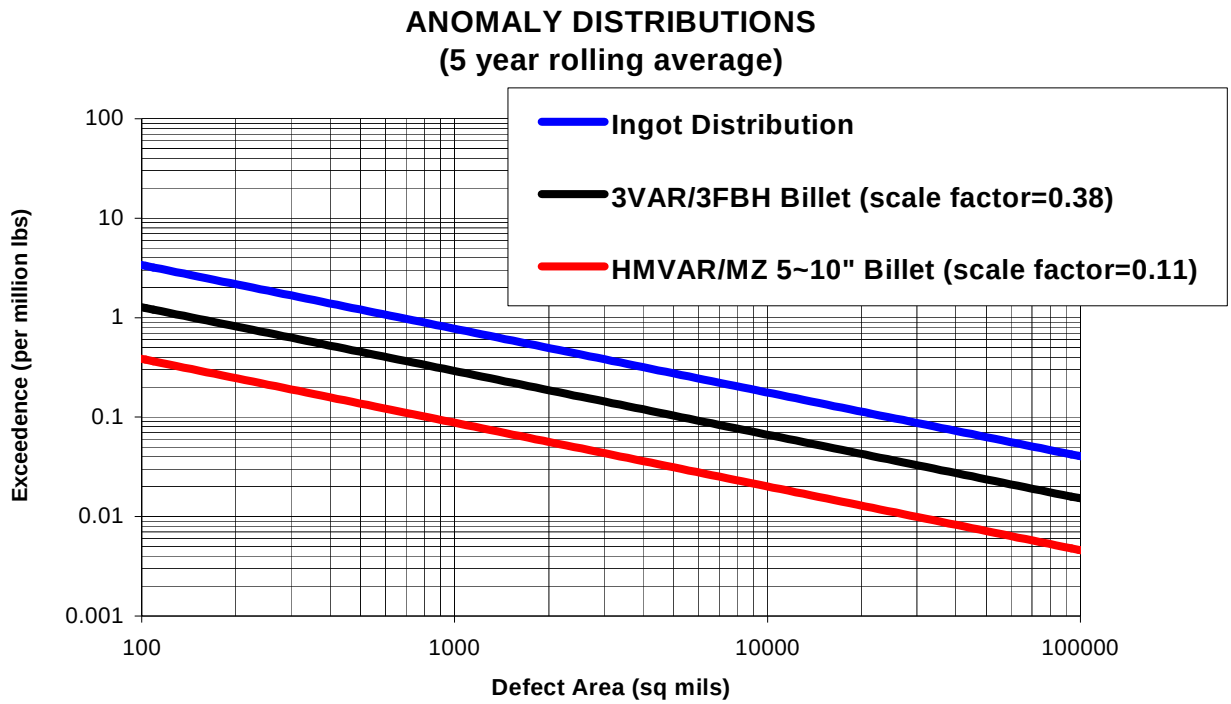

Figure A-7. Comparison of HA Anomaly Frequencies for 3xVAR and HM+VAR After Analytically Correcting for Differences in Inspection Sensitivity

Based on the results discussed in A.6.1 and A.6.2, it is the recommended that the current approach of using one distribution set for all titanium alloys, regardless of melt practice or alloy type, be maintained.

A.7 ALTERNATE INGOT DISTRIBUTION APPROACH.

The goal of this study was to evaluate alternate means for constructing an ingot distribution required as input in the HA distribution construction model. In the 1996 HA distribution development, the ingot distribution shape was estimated by screening the bar and billet finds back through the respective PoD curves, reversing the ingot-to-billet or bar deformation (ellipsoid to a sphere), and combing billet and bar finds into one ingot distribution [A-1]. This approach leads to an initial ingot distribution shape biased by the shape of the PoD curve. However, there is no technical reason that the shape of the ingot distribution should be dictated by PoD. Using these distributions, the resulting cumulative failure distribution for a typical part tends to be age-related. A later study of available component failure data (due to HA) from an FAA report [A-2] revealed that the cumulative failure distribution tended to be random, not age-related.

GE has proposed an alternate approach for estimating the ingot distribution shape to address this apparent disconnect. The alternate approach for estimating the ingot distribution shape involves essentially back-predicting the initial shape from the random failure distribution using a typical component and making a few simplifying assumptions. Studies conducted by GE showed that

by using this alternate approach, an initial ingot distribution could be estimated that would not require the modifications to the PoD curves that were required in the 1996 process. Furthermore, these studies showed that a more robust correlation to field component HA find data were achieved using distributions formulated with this alternate ingot distribution approach, as shown in figure A-8. A comparison of the old and new anomaly distribution shapes is given in figure A-9. It is recommended that this alternate ingot distribution approach be adopted for the HA distribution update.

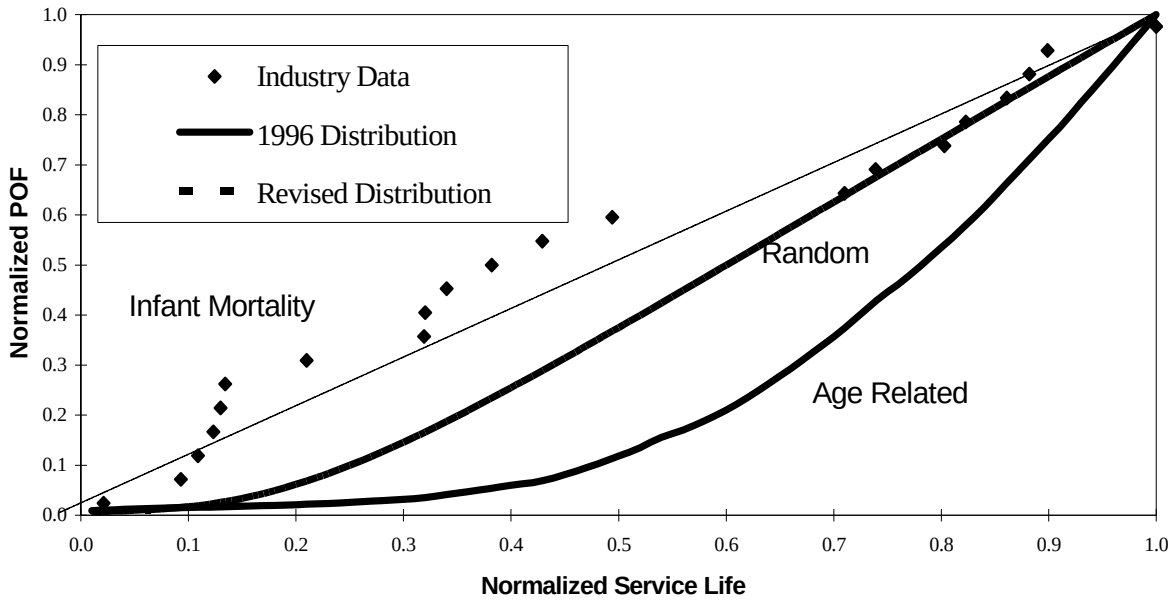

Figure A-8. Comparison of Predicted and Observed Cumulative Failure Distribution Shapes

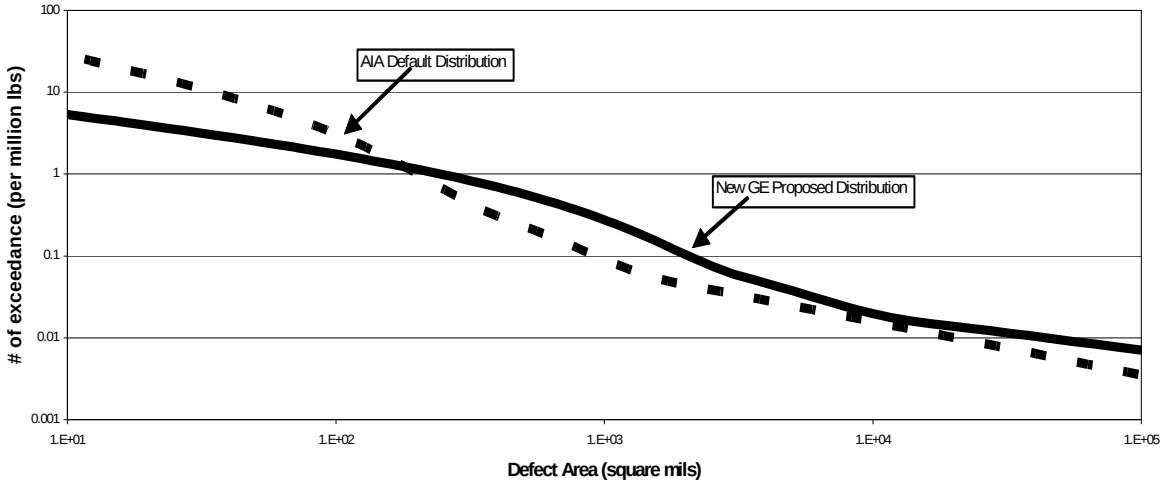

Figure A-9. Comparison of Current Default Anomaly Distribution and Proposed New Distribution Shape for Representative Conditions

A.8 EFFECTIVE INCLUSION SIZE ASSUMPTION.

Results from TRMD synthetic HA specimen and spin pit testing have suggested there is a difference in the effective crack size, depending on whether the HA anomaly is surface connected or subsurface. The assumption in the original anomaly distribution derivation was that the effective initial crack size was equal to the size of the HA core plus the surrounding diffusion zone. However, it now appears that a crack growing from a subsurface HA correlates better to crack growth analysis when the initial flaw size is assumed to be the HA core size.

The objective of this study was to determine the impact on component POF assuming that the effective crack size for surface-connected HA is based on core plus diffusion zone, but that the effective initial crack size for subsurface HA size is based on core size only. The approach taken was to use the current distribution for surface zones (20-mil onion skin) and use a HA distribution representative of core size only for subsurface zones. The core size distribution was estimated by scaling down the current HA distribution, which represents core plus diffusion zone, by the ratio of the average core size to the average core plus diffusion zone from the JETQC 3D characterization data. This ratio was determined to be 0.39. The two distributions are shown in figure A-10.

The results of this study showed an impact on POF ranging from 20% to 50%, with no change in the relative order of the part POF values. On its own, this effect may not be significant enough to be included in HA distribution update. However, initial studies of the interaction of this effect with other recommended changes to the HA update suggested that reducing the subsurface HA size to core only may be significant. Further analytical study and review of field hardware events is necessary to determine if changing the subsurface effective HA size to core only is a reasonable assumption. This work scope will be part of the second-phase activities and is expected to be performed and funded by the RISC membership.

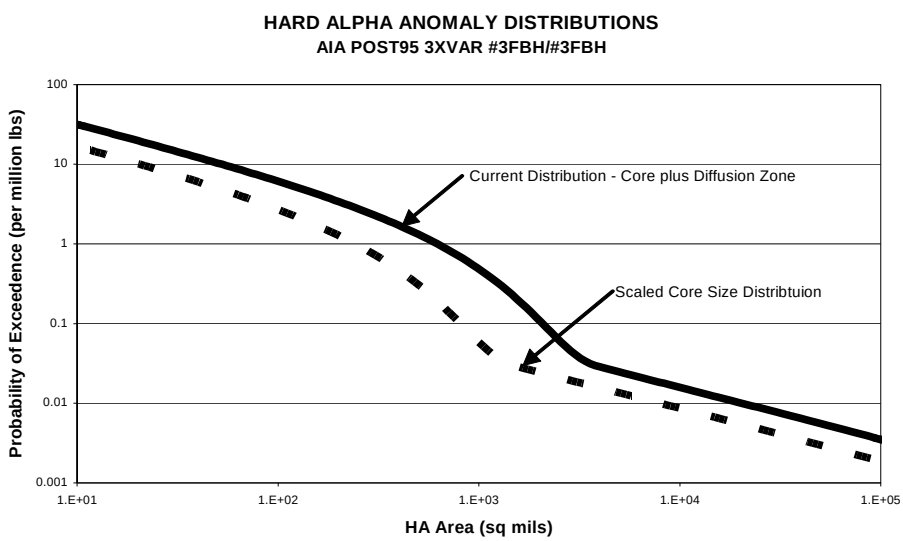

Figure A-10. Representative HA Distribution Based on Core Plus Diffusion Zone and Scaled Distribution for Core Only

A.9 FIVE ADDITIONAL YEARS OF JETQC HA DATA.

The objective of this study was to determine the change in 3xVAR HA rate using the 5 additional years (1997-2001) of JETQC data not available when the original distributions were derived. According to a March 2003 agreement, a 5-year MA was used to estimate the HA rate. Current 1996 HA distributions were defined by reducing the frequency of the calibrated 1990 HA distribution by the ratio of 1993-1995 HA rate to 1990-1993 HA rate:

- 1990-1993 HA Rate = 0.60 HA/Mil Lb (Preliminary Distribution)
- 1993-1995 HA Rate = 0.33 HA/Mil Lb (Current Distributions)

These rates yielded a reduction ratio of 0.55 (0.33/0.60). The 3xVAR HA rate over the last 5 years of data (1997-2001) is 0.25 HA/M lb. This yields a reduction ratio of 0.42 from the 1990-1993 to the 1997-2001 time periods. It is recommended that this average reduction of HA frequency be included in the HA distribution update.

A.10 SUMMARY.

Table A-1 summarizes all of the eight HA distribution studies and provides preliminary conclusions on whether a studied effect should be included in the new derivation process for updated HA anomaly distributions.

Table A-1. Summary of HA Distribution Process Studies

No.	Study	Objective	Preliminary Conclusion
1	Crack growth scatter	Quantify the impact of expected material and analytical scatter on component POF predictions.	Negligible impact on POF predictions, but should be considered for technical completeness. INCLUDE.
2	Crack aspect ratio	Quantify the impact of crack aspect ratio on component POF predictions.	Negligible impact on POF predictions. DO NOT INCLUDE.
3	Titanium vacuum crack growth data	Quantify the impact of vacuum crack growth data on predicted POF for actual components.	Impact not large, but should be considered for technical accuracy and precedence. INCLUDE.
4	HA deformation model	Evaluate the impact of the new DEFORM HA microcode on the construction of the HA distribution.	Negligible impact on POF predictions. DO NOT INCLUDE.
5	Titanium melt practice	Study the relative differences between titanium melt practices and alloys and their impact on component POF.	Results suggest this is not significant. DO NOT INCLUDE.

Table A-1. Summary of HA Distribution Process Studies (Continued)

No.	Study	Objective	Preliminary Conclusion
6	Alternative approach to estimate ingot distribution	Evaluate impact of alternative approaches to estimating the initial ingot distribution shape on correlation to component field experience.	Results suggest this may be significant. INCLUDE.
7	Inclusion size, core versus core+DZ	Study the impact on component POF results due to the assumed initial crack location in the part (surface versus subsurface).	Results suggest this may be significant. POSSIBLY INCLUDE.
8	Five additional years of JETQC data	Use 5 years additional JETQC data to study the impact of change in rate of 3xVAR HA (post-2000) versus vintage from '90 (1990-1996).	Results suggest this may be significant. INCLUDE.

Although all of the planned studies have been completed, the sentiment among the RISC membership was that the impact of combinations of the proposed enhancements and the data supporting the incorporation of the enhancements both needed to be revisited and further evaluated by RISC prior to a final decision on the new HA distribution model. Due to the increase in work scope and the need to give appropriate attention to the important task of distribution revision, RISC decided to postpone further work on the effort until other current business was completed. While this will delay the development and introduction of revised HA distributions, all of the work scope planned for the TRMD-II program has been completed. All of the remaining work will be covered by the RISC membership.

A.11 REFERENCES.

A-1. "The Development of Anomaly Distributions for Aircraft Engine Titanium Disk Alloys," *Proc. 38th AIAA/ASME/ASCE/AHS/ASC Structures, Structural Dynamics, and Materials Conference*, 1997, pp. 2543-2553.

A-2. "Titanium Rotating Components Review Team Report," Federal Aviation Administration, December 14, 1990.

ATTACHMENT A-1. GENERIC TABULAR FATIGUE CRACK GROWTH PROPERTIES FOR TI-64 and TI-6242

The TRMD Steering Committee requested that SwRI prepare a generic set of FCG curves for Ti-64 and Ti-6242 in both air and vacuum that could be used by engine companies in performing sensitivity studies against their own experience or other comparative research investigations. Based on guidance from the team and analysis of the available data by SwRI, a generic set of curves has been developed. In some cases, air curves were required for conditions (temperatures and/or stress ratios) at which public domain experimental data were not available. In these cases, curves were constructed from available experimental data at other temperatures and stress ratios based on established temperature interpolation schemes or stress ratio models. Threshold values for air data were assigned based on information supplied to SwRI by the engine companies and on literature results for similar materials. As a result, the air curves cannot always be traced directly to specific experimental data, but instead they represent a general set of curves that are intended and suitable for comparative research purposes. The vacuum curves are all based directly on experimental data generated in the TRMD-I program. In some cases, properties were modified from values first published in the TRMD-I Final Report, based on a more careful review of all the available data.

The curves are summarized in tabular and graphical form in the following pages. The “C” and “m” values in the tables are the coefficient and exponent, respectively, in a conventional Paris equation describing the highest linear regime of the data.

Ti-6-4 Tabular Summary

	C	9.69E-10	4.52E-09	6.28E-09	
T=75	m	3.11	2.82	2.82	
air		**DK (R=0)**	**DK (R=0.5)**	**DK (R=0.75)**	**da/dN**
		3.98	2.87	2.29	1.00E-09
		3.99	2.88	2.30	6.56E-08
		4.00	2.89	2.38	7.19E-08
		4.31	2.90	2.58	9.08E-08
		80.44	73.06	65.00	8.07E-04

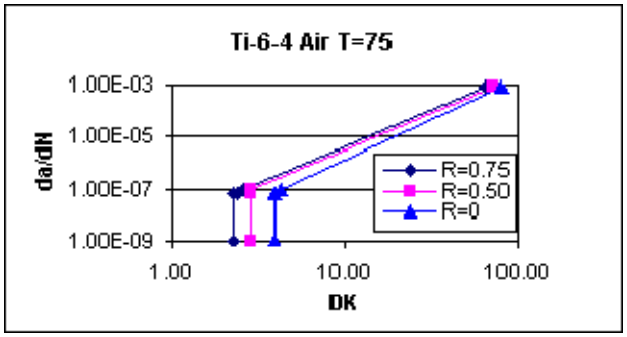

T=400	C	5.88E-10	1.36E-08	1.73E-08	
air	m	3.22	2.30	2.30	
		DK (R=0)	**DK (R=0.5)**	**DK (R=0.75)**	**da/dN**
		3.99	2.87	2.28	1.00E-09
		4.00	2.88	2.29	5.14E-08
		5.18	2.89	2.30	1.18E-07
		5.67	2.90	2.61	1.58E-07
		56.37	72.18	65.00	2.60E-04

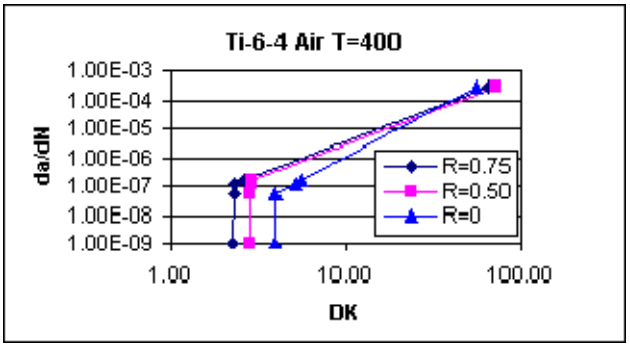

T=75	**DK (R=0)**	**DK (R=0.5)**	**DK (R=0.75)**	**da/dN**
vacuum	8.51	7.17	4.79	1.00E-09
	8.52	7.18	4.80	1.30E-08
	8.53	7.19	5.05	2.00E-08
	8.54	7.25	5.40	3.52E-08
	8.55	7.26	5.52	4.00E-08
	9.99	7.45	7.36	2.12E-07
	14.01	9.45	9.78	1.10E-06
	21.63	14.80	14.07	9.04E-06
	23.16	16.65	14.90	1.26E-05
	27.30	22.12	19.77	2.80E-05
	80.44	73.09	65.00	8.07E-04

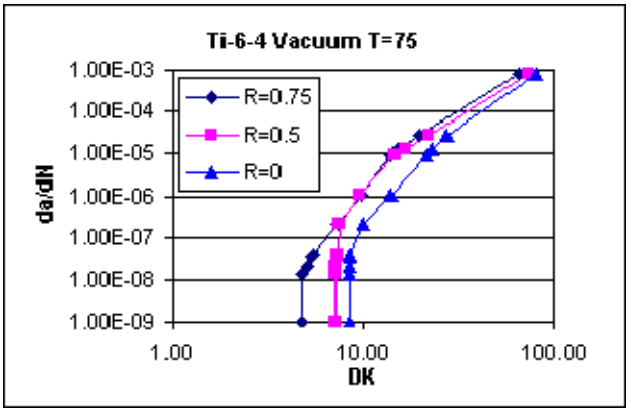

T=400	**DK (R=0)**	**DK (R=0.5)**	**DK (R=0.75)**	**da/dN**
vacuum	11.22	7.31	4.80	1.00E-09
	11.23	7.32	4.81	1.30E-08
	11.24	7.33	5.51	6.00E-08
	11.25	7.46	5.60	7.20E-08
	11.26	7.72	5.95	1.00E-07
	12.96	9.20	8.19	5.50E-07
	13.50	10.22	8.97	9.00E-07
	21.67	15.47	12.90	6.28E-06
	23.49	16.60	14.90	8.75E-06
	44.80	52.36	47.13	1.24E-04
	65.00	88.05	79.34	4.11E-04

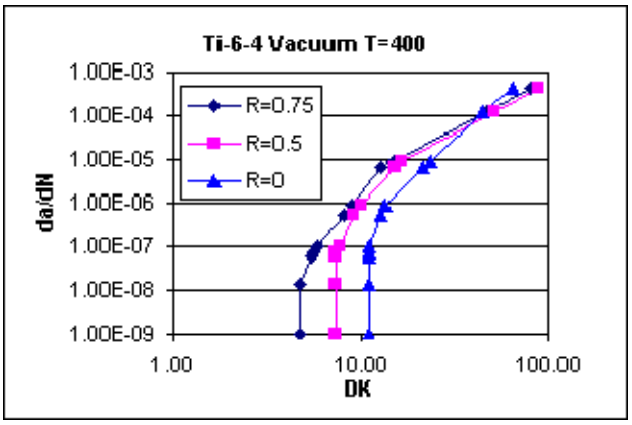

Ti-6-2-4-2 Tabular Summary

T=80 air

C	5.01E-10	3.54E-10	1.49E-09
m	3.31505	3.7689	3.5028

DK (R=0.05)	DK (R=0.5)	DK (R=0.75)	da/dN
3.47	2.49	1.98	1.00E-09
3.48	2.50	1.99	1.12E-08
3.49	2.79	2.00	1.69E-08
3.50	3.30	2.40	3.19E-08
105.14	65.80	60.00	2.52E-03

T=600 air

C	1.37E-09	1.10E-08	1.66E-08
m	2.98	2.63	2.52

DK (R=0.05)	DK (R=0.5)	DK (R=0.75)	da/dN
3.99	2.87	1.98	1E-09
4.00	2.88	1.99	8.53E-08
4.15	2.89	2.00	9.52E-08
5.15	2.90	2.58	1.81E-07
74.63	60.00	60.93	0.000522

T=1000 air

C	1.03E-08	2.30E-07	3.98E-07
m	2.37823	1.61554	1.9981

DK (R=0.05)	DK (R=0.5)	DK (R=0.75)	da/dN
3.99	2.88	1.97	1E-09
4.00	2.89	1.98	2.78E-07
7.61	2.90	1.99	1.28E-06
8.32	3.31	2.00	1.59E-06
103.14	134.60	40.00	0.000632

T=80 vacuum

C	1.80E-13	5.29E-13	1.17E-14
m	5.55E+00	6.01E+00	7.87E+00

DK (R=0.05)	DK (R=0.5)	DK (R=0.75)	da/dN
8.89	4.99	5.67	1.00E-09
8.90	5.00	5.68	1.00E-08
10.00	7.00	7.17	6.33E-08
203.73	112.87	60.00	1.15E+00

T=600 vacuum

C	1.25E-11	5.78E-13	2.34E-14
m	4.09E+00	5.76E+00	8.39E+00

DK (R=0.05)	DK (R=0.5)	DK (R=0.75)	da/dN
8.55	5.44	4.68	1.00E-09
8.56	5.45	4.69	1.00E-08
11.00	9.17	6.70	2.00E-07
415.84	123.91	40.00	6.44E-01

T=1000 vacuum

C	2.35E-11	3.45E-13	1.86E-11
m	4.42E+00	7.04E+00	7.04E+00

DK (R=0.05)	DK (R=0.5)	DK (R=0.75)	da/dN
4.92	4.30	2.44	1.00E-09
4.93	4.31	2.45	1.00E-08
6.80	5.97	3.39	1.00E-07
336.40	70.33	40.00	3.48E+00

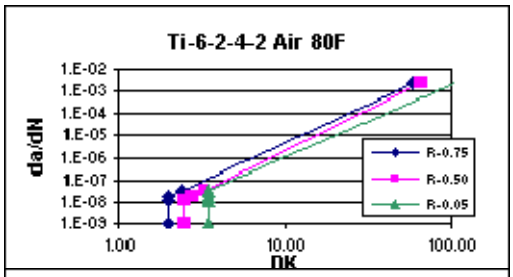

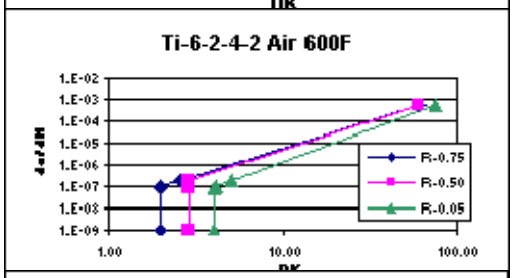

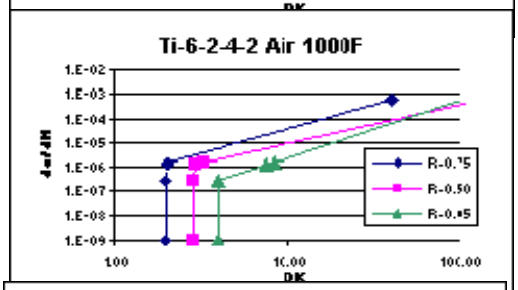

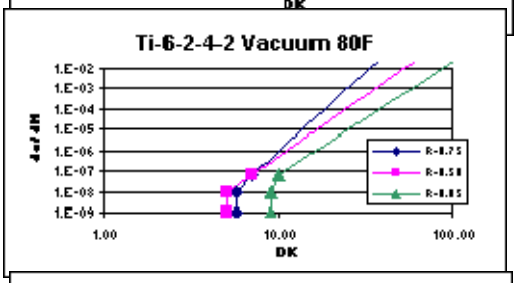

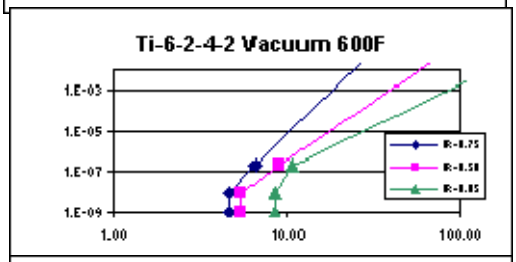

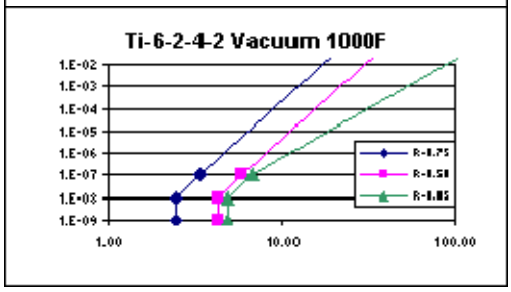

APPENDIX B—GROW CODE DEVELOPMENT, VALIDATION, AND PARAMETRIC STUDIES

B.1 GROW CODE DEVELOPMENT.

The GROW code, consisting of a set of UNIX® scripts and FORTRAN codes, has been developed to assist suppliers and users of titanium (Ti) base alloys. The objective is to better understand the dissolution history of nitride and oxide inclusions in molten and solid titanium alloys under various combinations of exposure temperature and time. While much of the discussion in this section is focused on nitrogen inclusions, the concepts are similar for oxygen diffusion, and both nitrogen and oxygen capability has been included in the GROW code. The code was developed with the intention of allowing users to predict the formation of stealth anomalies, which can go undetected by nondestructive evaluation (NDE) and may be harmful to fatigue life. The GROW code has been delivered to Southwest Research Institute® (SwRI®) and made available through the Design Assessment of Reliability With INspection (DARWIN®) web site. The code was primarily developed and tested on SUN Microsystem® workstations; however, portability to Hewlett-Packard (HP) computers was kept in mind with updates to the run scripts. Earlier versions were successfully tested on both SUN workstations at Pratt & Whitney and HP computers on the SwRI network.

The code is capable of simulating isothermal as well as time varying temperature histories. It takes thermal cycles associated with melting/metal forming and heat treatment as input. The calculations are based on a finite difference method, using temperature integrated over time to accumulate the growth of the diffusion-affected zone. Concentration profiles are predicted as well as the extent of the various layers surrounding the inclusion. To provide capability for users to deal with a distribution of defects, the code allows the users to create lognormal or Weibull distributions or a random case with a known mean for inclusion size or inclusion composition. Further, a bivariate normal distribution can be generated automatically for any number of inclusions.

The diffusion process is assumed to follow the standard diffusion equation, which is complicated by the presence of multiple phases, each with its own set of characteristic physical/chemical properties (figure B-1). For instance, after some time at 1200°C, a delta-TiN inclusion will be surrounded by layers of alpha-Ti and beta-Ti. Since Ti melts at 1670°C, the same inclusion at 2000°C immersed in liquid Ti will be covered by layers of solid alpha and solid beta.

Since the instantaneous locations of the various phase interfaces depend on the instantaneous value of the nitrogen (N) concentration, the mathematical problem becomes nonlinear and a numerical approach is most appropriate. The mathematical model of the multiphase diffusion problem then becomes

$$dc/dt = \text{div}(\text{ grad } a^*) \tag{B-1}$$

where

$$da^* = (D/b)\, da \tag{B-2}$$

and

$$a = b\,c \tag{B-3}$$

with

a = nitrogen activity
a^* = Kirchoff-transformed [B-1] nitrogen activity
b = nitrogen activity coefficient
c = nitrogen concentration
D = nitrogen diffusion coefficient
t = time
div (grad a^*) = d^2 a^*/dx^2 (for 1-dimensional systems)

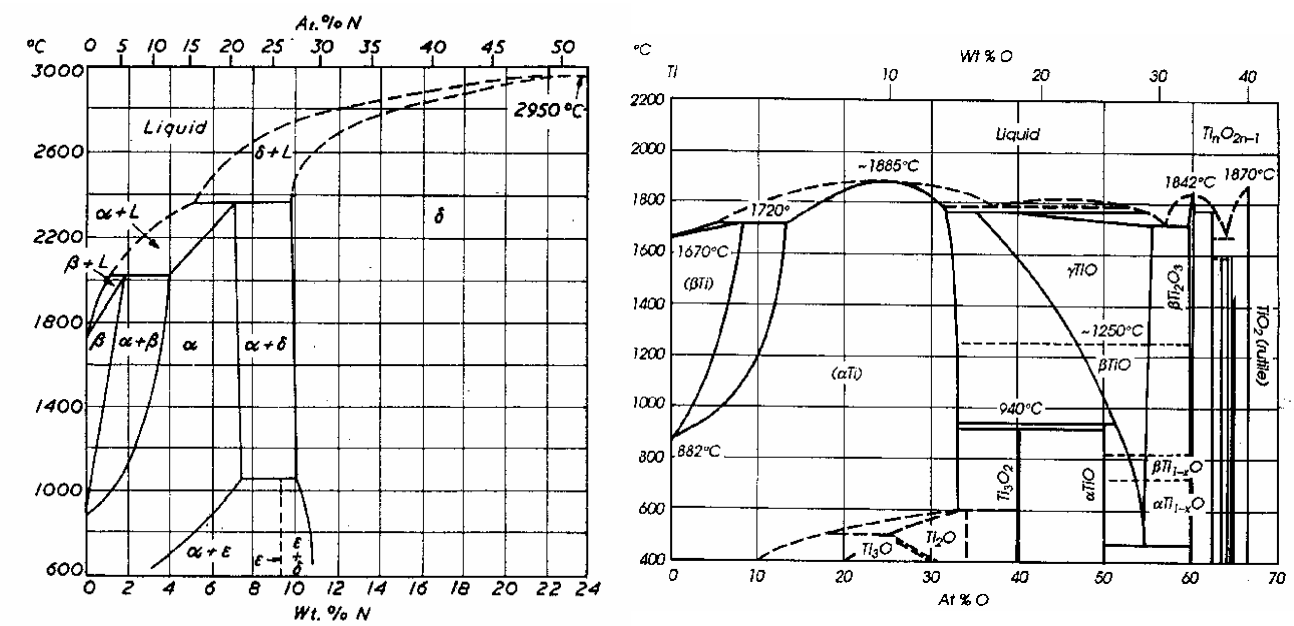

Figure B-1. Ti-N and Ti-O Equilibrium Phase Diagrams

This formulation has the advantage of easily allowing incorporation of the various different properties. A schematic representation of the resulting concentration profile obtained around a delta-TiN inclusion after a few minutes at 2000°C is shown in figure B-2. The associated Kirchoff activity-concentration relationship is shown in figure B-3, and the relationship between the Kirchoff-transformed activity and the activity is shown in figure B-4.

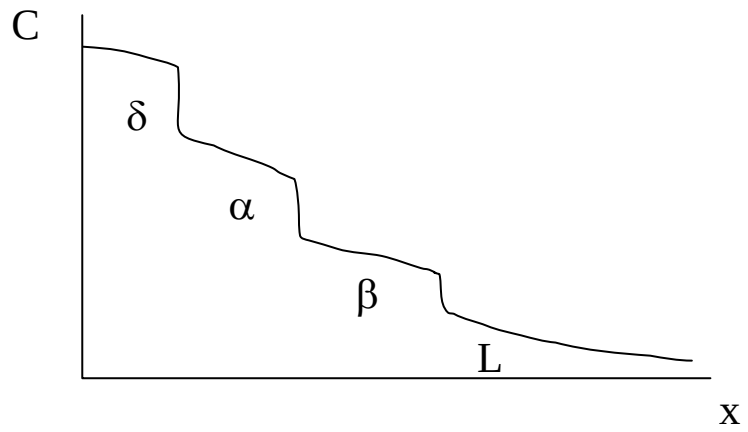

Figure B-2. Schematic Concentration Profile Around a Delta-TiN Inclusion in Liquid Ti at 2000°C

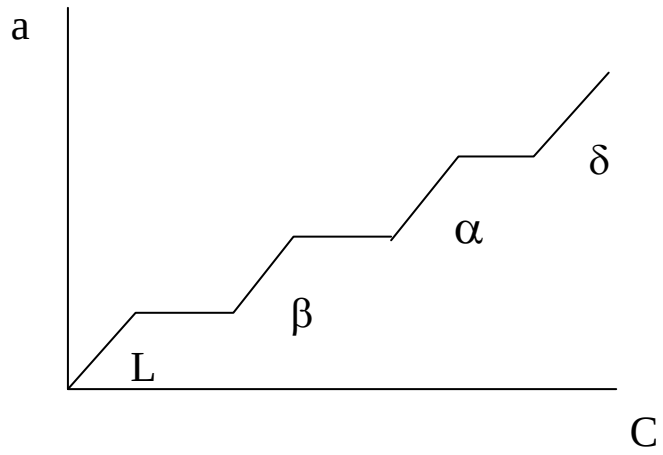

Figure B-3. Activity Versus Concentration Relationship Corresponding to Figure B-2

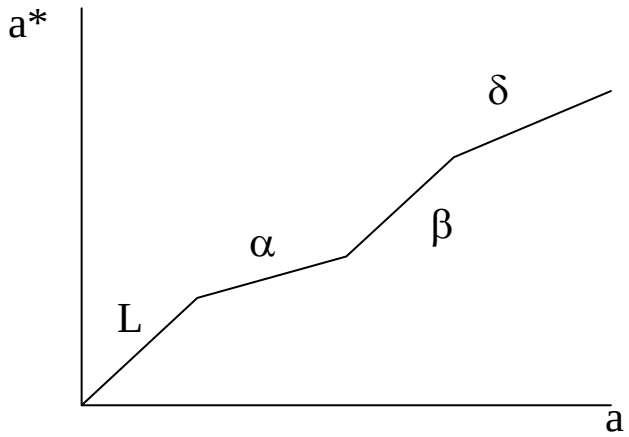

Figure B-4. Kirchoff-Activity Versus Activity Corresponding to Figure B-2

Numerical computation of the evolving concentration profile is performed by means of the finite volume method and an explicit scheme. This method has good numerical stability characteristics subject to the Courant-Friedrich-Levy (CFL) condition [B-2], and it can produce highly accurate results when sufficiently fine meshes are used. The CFL condition states that the time step in a time-dependent computer simulation must be less than the time for some significant action to occur. In industrial scale processing, contaminated sponges as large as 0.25″ in diameter can be found. An intelligent, adaptable meshing strategy is required to efficiently solve diffusion problems for a wide range of anomaly sizes. A coarse mesh would violate mass balance at the boundary, and a very fine mesh would waste computational time. An optimum meshing capability for large anomaly sizes up to 0.25″ diameter was applied.

The method proceeds as follows:

1. The region of interest (inclusion and surroundings) is subdivided into a finite collection of contiguous finite volumes. Computational nodes are located at the center of each volume.

2. The diffusion equation is then discretized by integrating it over the span of a finite volume and using an Euler forward difference formula for the time derivative. The resulting algebraic expression is used to compute subsequent values of nitrogen concentration from given initial values for each node in the mesh.

3. The activity at each node is determined from the given nitrogen activity to nitrogen concentration relationship.

4. The Kirchoff activity is determined from the given Kirchoff-transformed nitrogen activity to nitrogen activity relationship.

5. The process is repeated from (2) above until the desired end time is reached.

Initial calibration of the one-dimensional version of the code was completed with a hard alpha plate with 250-micron thickness and 12%wt. N subjected to 1200°, 1600°, and 2020°C isothermal conditions. The required physical property data were taken from public domain materials handbooks. The mesh spacing was chosen equal to 10 microns. The code calculated the sizes of the delta, alpha, and beta layers as functions of time, as well as changes in the nitrogen concentration profiles. After 12 minutes at 2020°C, it was shown that the delta layer had disappeared, while the alpha layer was receding and the beta layer was still growing. The maximum computed dissolution rate of the delta phase was about 2.5 microns, which was in good agreement with experimental results [B-3].

Figure B-5 shows the computed concentration profiles at 1-hour intervals for a 3-hour-long anneal at 1200°C. The multiple layer structure is clearly seen.

Figure B-6 shows the calculated sizes of the delta and alpha layers. The 3-hour-long hold at this temperature is not only insufficient to dissolve the delta phase but also leads to significant growth of the alpha layer attached to it.

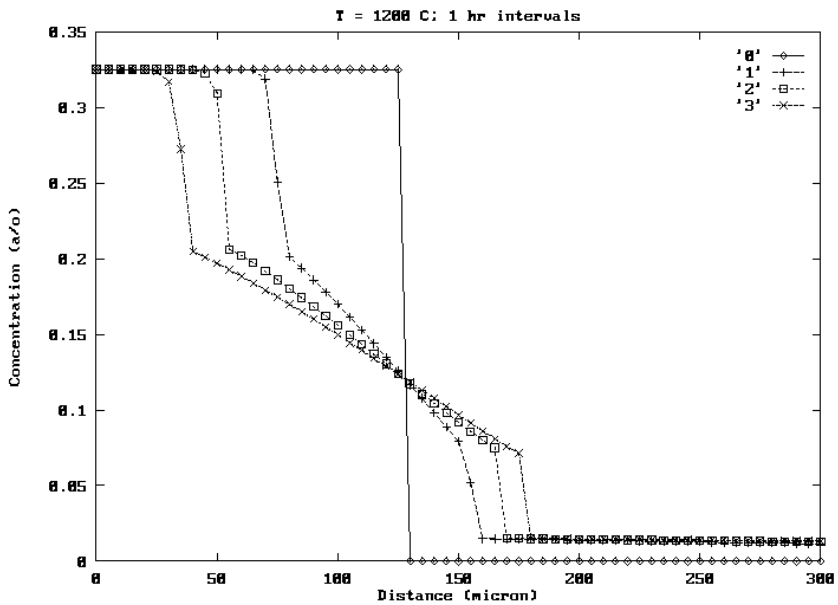

Figure B-5. Computed Concentration Profiles (Isothermal Anneal at 1200°C for 3 Hours)

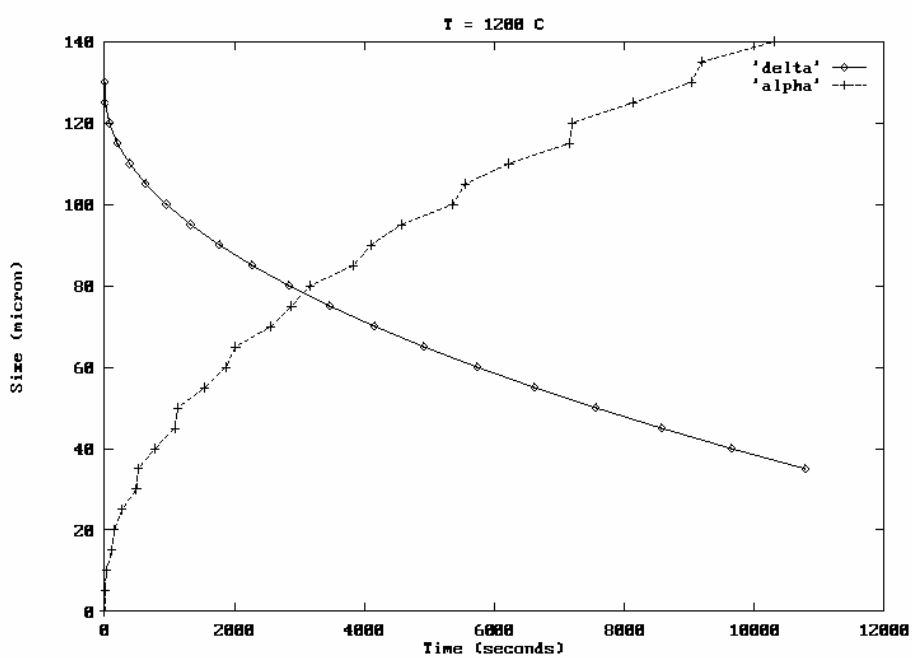

Figure B-6. Calculated Sizes of the Delta and Alpha Layers for Figure B-5

Figure B-7 shows the computed concentration profiles at 5-minute intervals for a 0.5-hour-long hold at 1600°C. Because of the higher temperature involved, both the delta and alpha phases have disappeared at the end of the process.

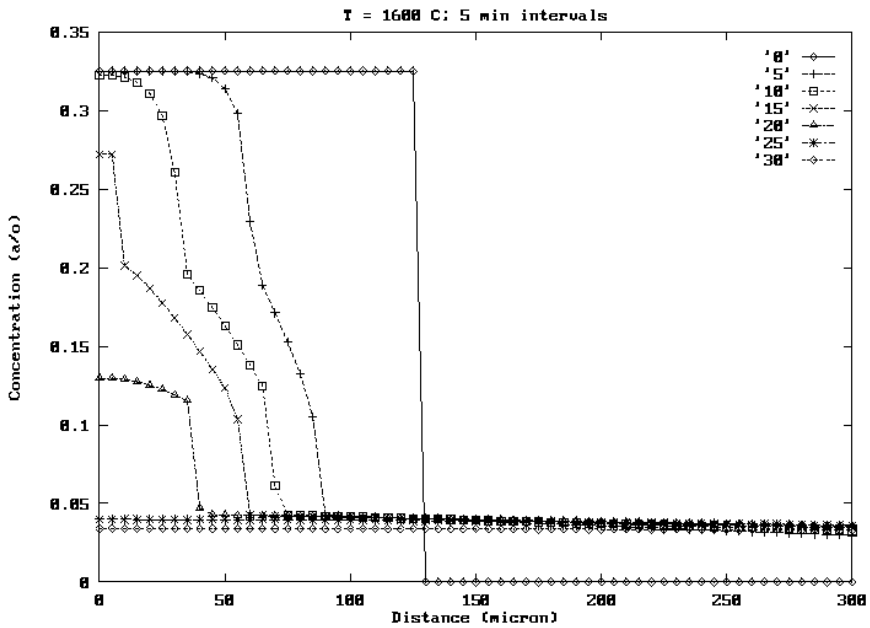

Figure B-7. Computed Concentration Profiles (Isothermal Anneal at 1600°C for 0.5 Hour)

Figure B-8 shows the calculated sizes of the delta and alpha layers. The noise in the computed size of alpha is due to the relatively coarse mesh employed in the calculation.

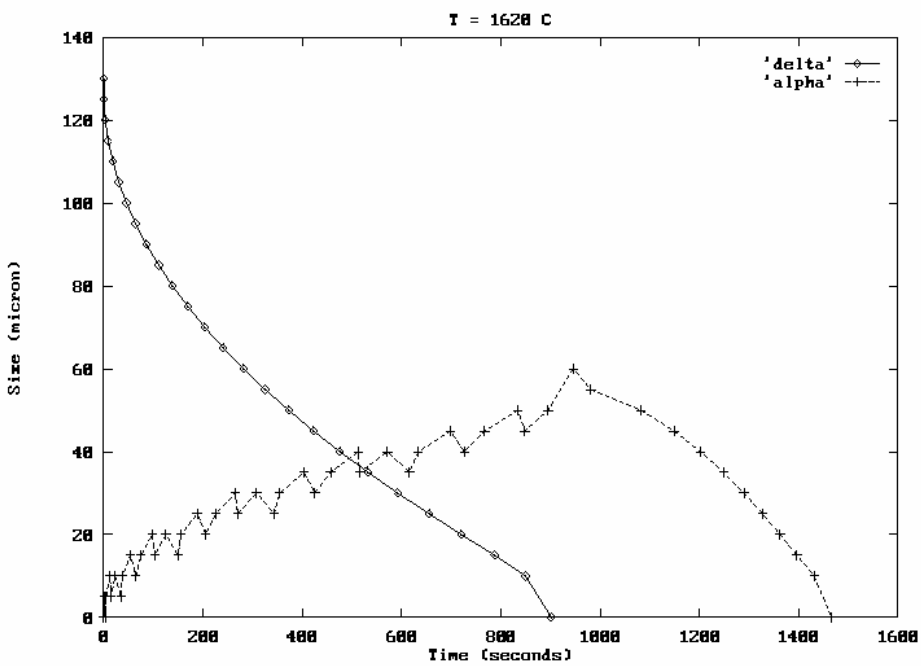

Figure B-8. Calculated Sizes of the Delta and Alpha Layers for Figure B-7

Figure B-9 shows the computed concentration profiles at 2-minute intervals for a 12-minute-long hold at 2020°C. Delta, alpha, beta, and liquid phases are observed. Figure B-10 shows the calculated sizes of the delta, alpha, and beta layers.

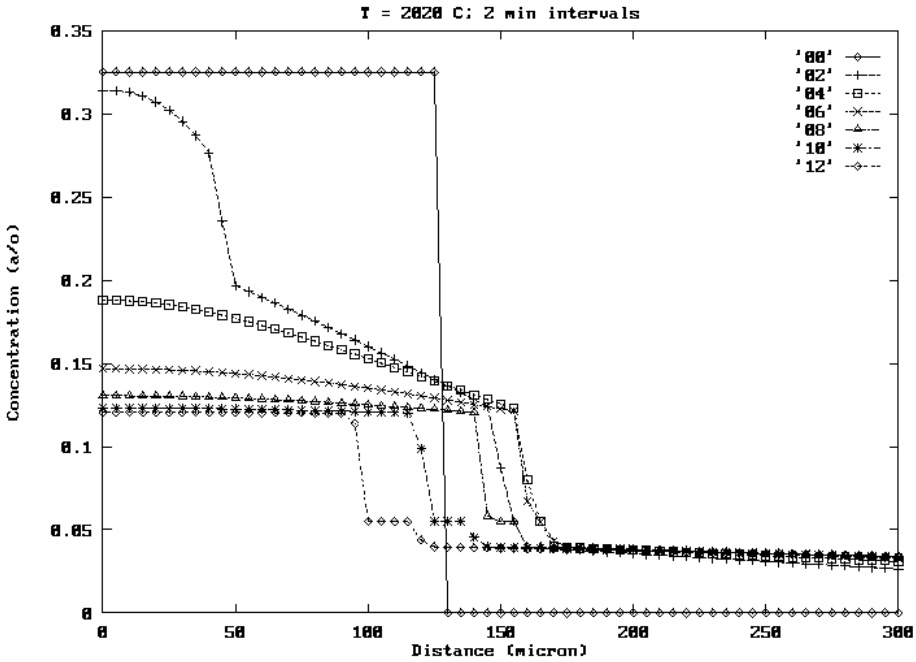

Figure B-9. Computed Concentration Profiles (Isothermal Hold at 2020°C for 12 Minutes)

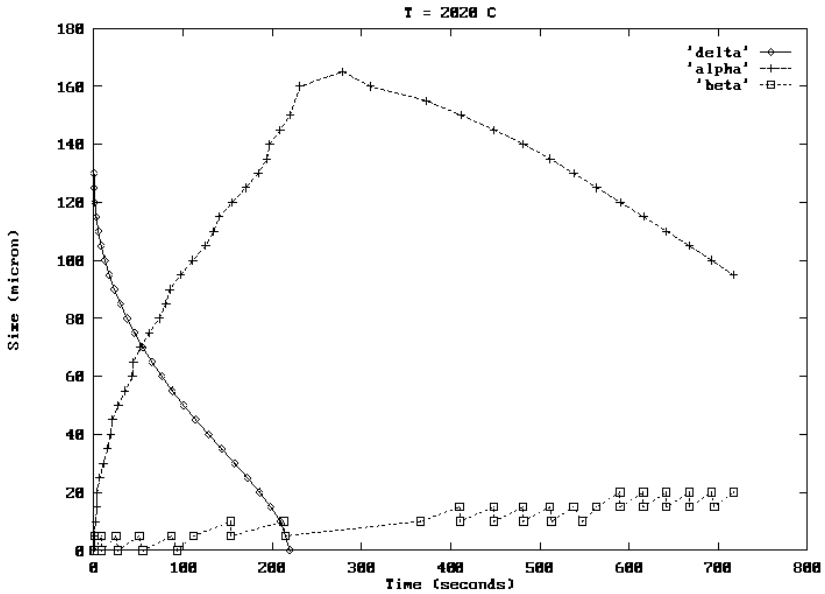

Figure B-10. Calculated Sizes of the Delta, Alpha, and Beta Layers

The nonisothermal capability was demonstrated by specifying the temperature-time history. The code calculated nitrogen concentration profiles at each of the characteristic points in the temperature-time history. The computed evolution of the delta and alpha phases was clearly more complex than in the isothermal cases. The nonisothermal treatment is described by the temperature-time history shown in figure B-11.

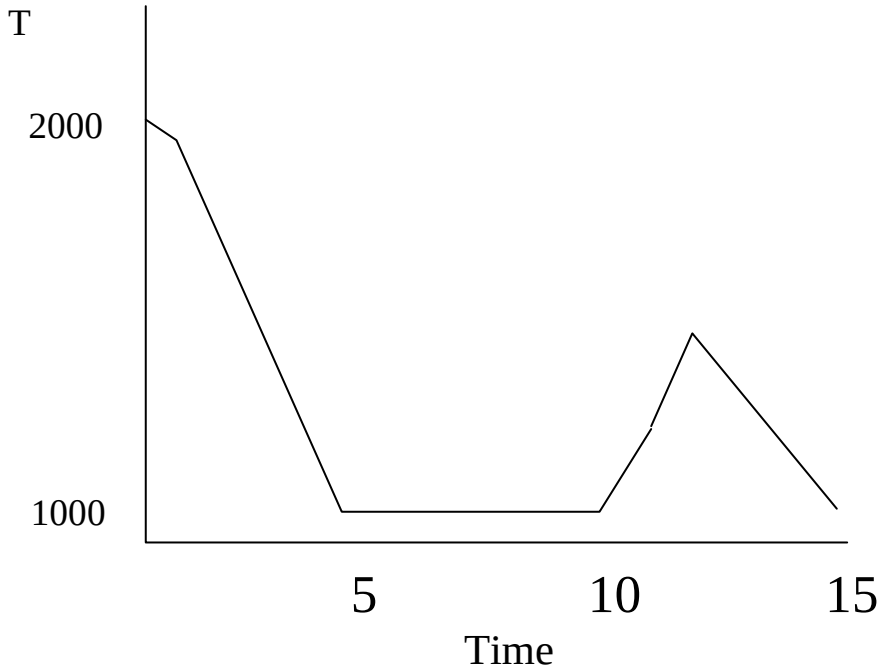

Figure B-11. Nonisothermal Temperature-Time History

Figure B-12 shows the calculated concentration profiles at each of the characteristic points in the temperature-time history. As expected, the profiles shift quickly at high temperatures but rather more slowly at the lower temperatures. Figure B-13 shows the computed sizes of the delta and alpha phases.

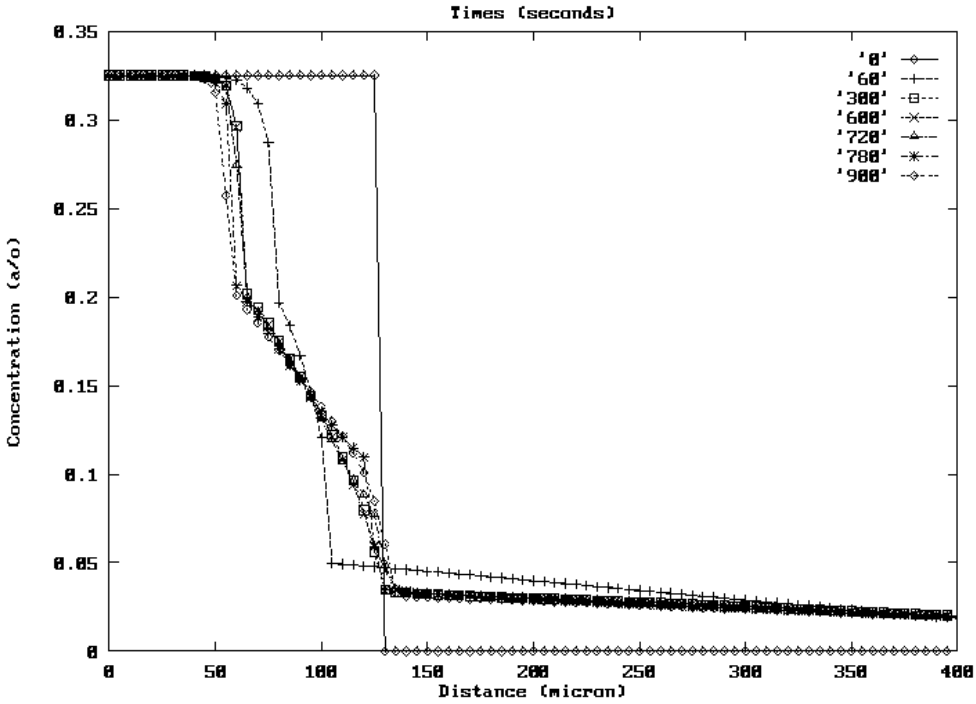

Figure B-12. Computed Concentration Profiles for Figure B-11

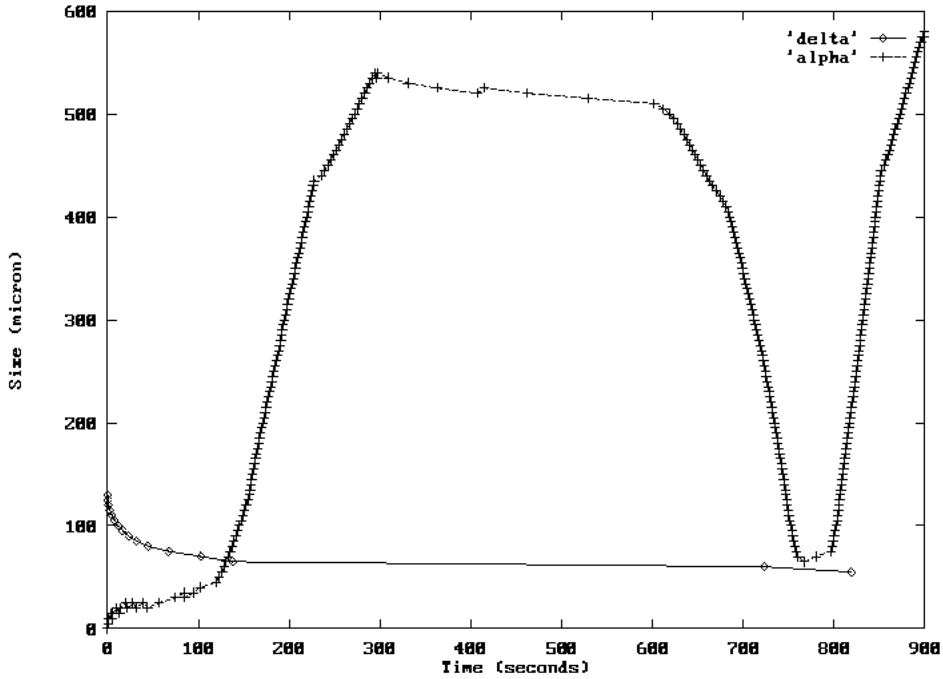

Figure B-13. Calculated Sizes of the Delta and Alpha Layers

B.2 GROW CODE VALIDATION.

The GROW code has been validated against published rates of dissolution of nitrides in several titanium-based alloys for simplified controlled experiments. The values used for the diffusivity in the liquid, alpha, beta, and delta phases were updated in the code, where possible, based on the studies. Activity values for N in Ti were added without assuming an ideal solution. The computed rates of dissolution were of the correct order of magnitude, but still low versus literature values.

Initial validation of the GROW code was attempted based on TiN in Ti-6242 dissolution experiments by Bewlay and Gigliotti [B-4]. In the insertion experiment, a TiN rod was inserted into molten (1725°C) Ti-6242 while partially levitated by the induction coil. The TiN rod was held for up to 30 minutes. The dissolution rate was measured in terms of an interface recession rate for Ti-6242 at the temperature of 1725°C. Immersion experiments were conducted by placing TiN sponge over Ti-6242 bar and then melting both.

The GROW code was run for the TiN rod insertion condition. The calculated nitrogen concentration profile and the sizes of alpha and alpha + beta phases were compared with the microprobe scan results of the dissolution experiments (figure B-14). Results (figure B-15) showed reasonable agreement in the nitrogen concentration profile and the TiN rod recession rate. However, the calculations of the diffusion size (figure B-16) were 2 to 4 times off; over predicting the alpha phase, 76 μm versus 30 μm, and under predicting the alpha + beta phase, 127 μm versus 620 μm. However, a large scatter is common in the dissolution experiments due to the turbulence effect. Also, it was suspected that the TiN dissolution in pure titanium may have been different from the dissolution in Ti-6242, and this could have been a source of discrepancy. Initially, the GROW code was only capable of handling the nitrogen or oxygen diffusion problem in pure titanium. To address these concerns, additional research was conducted to acquire more detailed experimental diffusion data.

A couple of available papers in the open literature were identified, which discussed titanium nitride dissolution in liquid titanium. The references deal with different alloys of interest and give interface recession rates at specific temperatures. A careful review of the literature indicated that the cold hearth melting technique, which was used, exhibits significant convection. This would have the effect of replenishing the boundary layer outside of the nitride or oxide particle with fresh liquid. This could be simulated by using semi-infinite diffusivity in the liquid, or by observing the computed rates at short times, before the boundary layer becomes thick enough to significantly slow the rate of dissolution. The latter method was chosen as an initial attempt.

Three simulations were run for 300 sec at 1650°, 1750° and 1850°C to validate code predictions against experimental results from Buttrill and Shamblen [B-5]. The dissolution process is shown in figures B-17 and B-18. The first 6 seconds were chosen to be representative of enough time for the process to stabilize, but short enough so as to mimic dissolution into fresh liquid. The dissolution rate was computed as microns/min by taking the decrease in thickness of the delta phase (from the centerline) over 6 seconds and multiplying by 10. The match against commercially pure (CP) Ti is shown in table B-1.

- Bewlay and Gigliotti
  - δTiN rod and Ti-6242 interface recession rate provided the dissolution rate of 2.2 ± 0.5 μm/s
  - Microprobe scans provided measurements on the interdiffusion layers

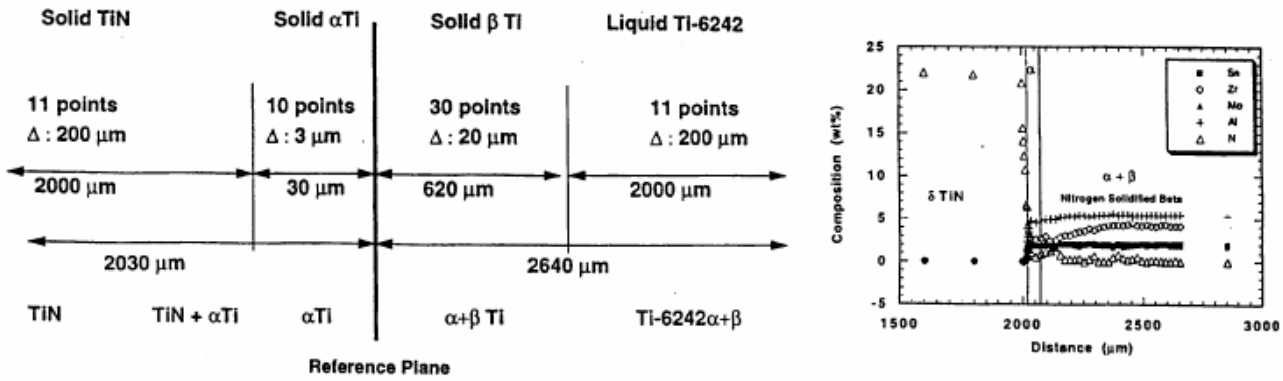

Figure B-14. Ti-6242 Dissolution Experiments

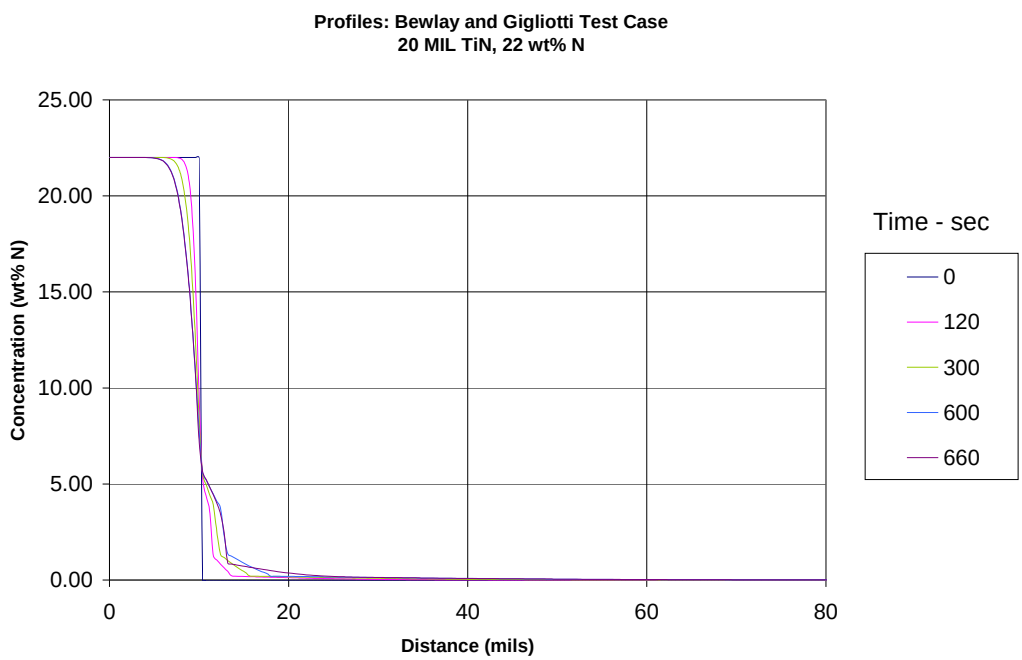

Figure B-15. Nitrogen Concentration Profile

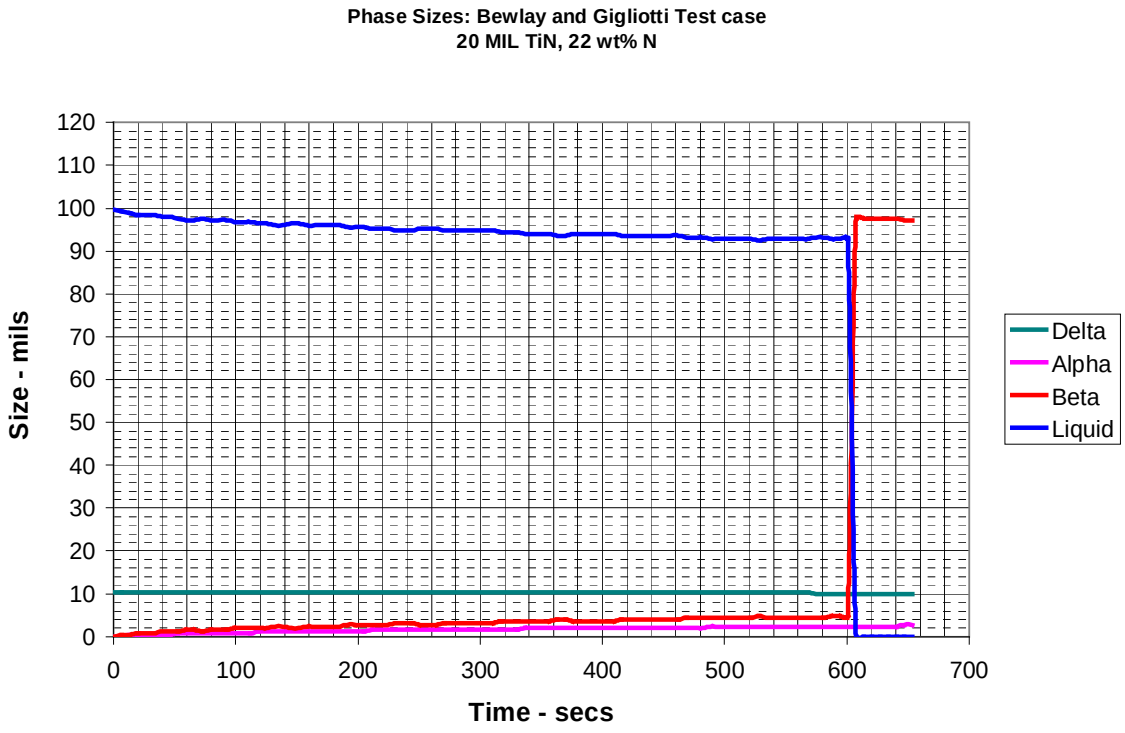

Figure B-16. Diffusion Zone Size

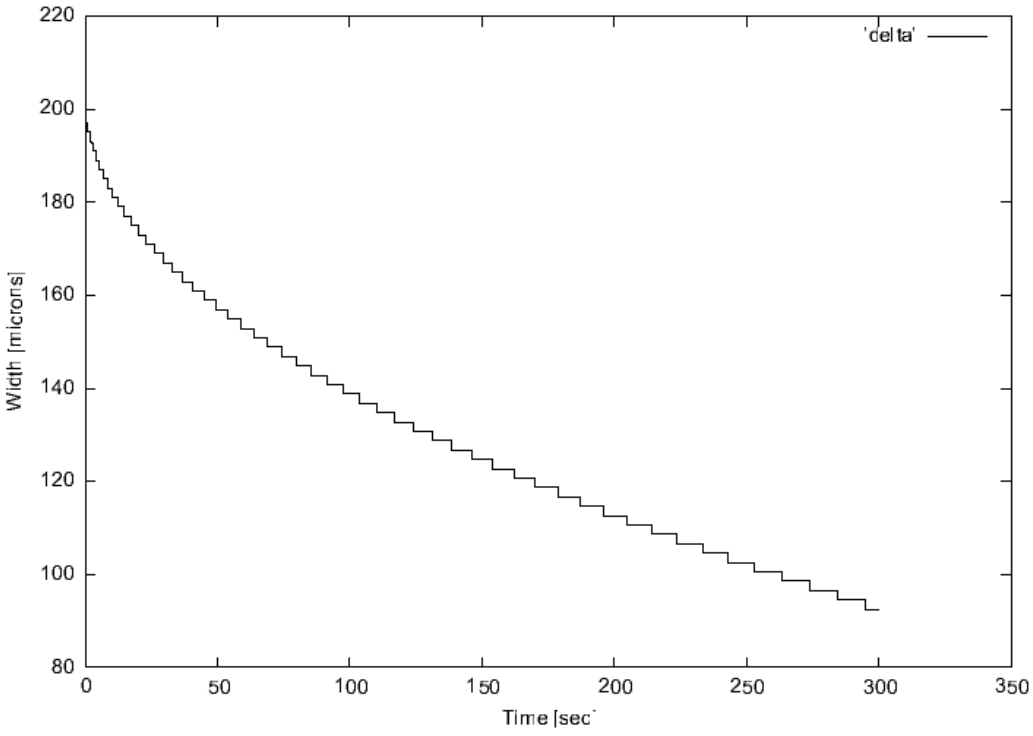

Figure B-17. Nitride Dissolution at 1750°C

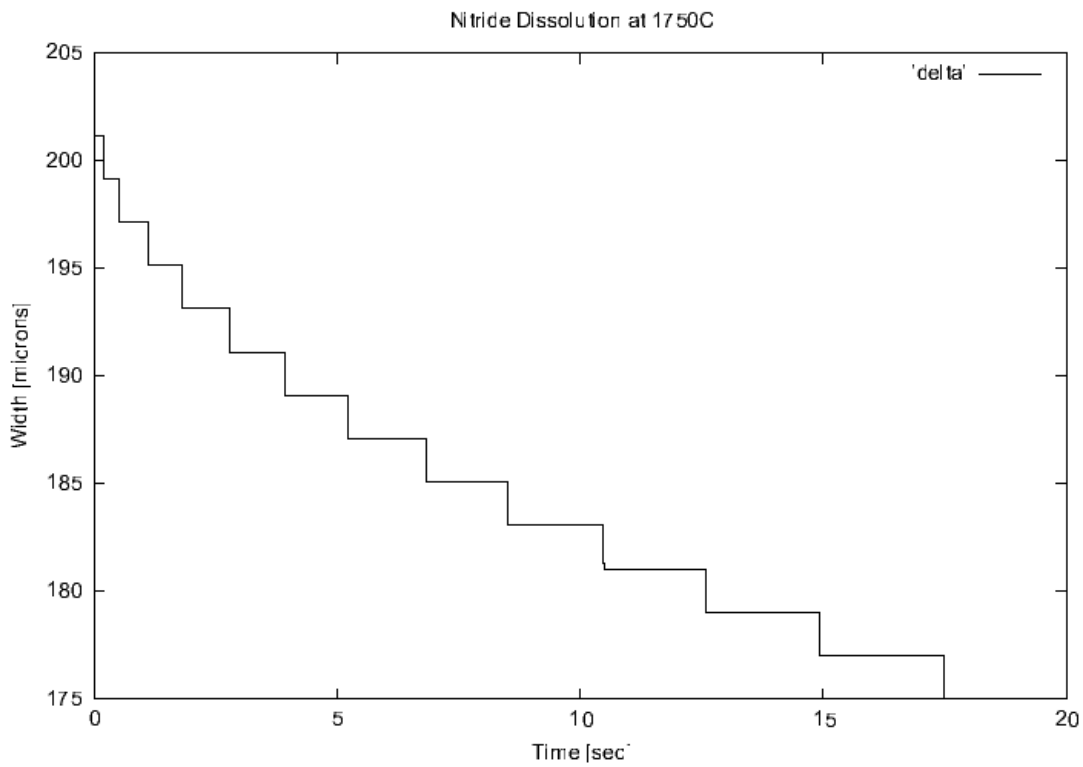

Figure B-18. Nitride Dissolution at 1750°C (Initial 20 Seconds of Simulation)

Table B-1. Comparison of Grow Predictions to Experimental Data

Temperature (°C)	Starting Delta Phase Thickness From Centerline (microns)	Final Delta Phase Thickness From Centerline (microns)	Time (seconds)	Predicted Dissolution Rate (microns/minute)	Measured Dissolution Rate (microns/minute)
1650	203	191	6	120	100
1750	203	187	6	160	180
1850	203	183	6	200	250

The experimental data show slightly more temperature dependence, but the values are of the right order. The greater temperature dependence for the experiments is likely due to the fact that the convection becomes even more significant as the temperature is increased. However, without any specific knowledge about the convective velocity (or the boundary layer thickness), there is no reason to speculate quantitatively on this second-order effect.

It should be noted that without determining the initial dissolution rate and projecting that value forward, the dissolution rate for the entire exposure time may be taken as a worst-case scenario;

i.e., any convection in the real world will accelerate the overall calculated rate. The other interesting point is that the rates for CP Ti, Ti-64, and Ti-6242 were not significantly different. There was, however, a significant scatter band, probably due to the chaotic nature of convection and the presence of some cracks in the consolidated nitride inserts.

B.3 GROW CODE PARAMETRIC STUDIES.

During the GROW code development, enhancements were added to better deal with parametric studies of the evolution of a diffusion zone (DZ) around defects in Ti alloys during melt processing. Several improvements were made to the code in terms of allowing more flexibility with the input files, acquiring intermediate output and redesigning the keep script to deal with stacks of cases. The suite of codes was intended to allow for the study of a distribution of defects with various sizes and central concentrations. Random distributions of point pairs can be generated with the stand-alone codes: rvun.f (uniform, random), rvwn.f (Weibull) or rvln.f (lognormal), or a setup code. The code setup.f is used to set up a complete input file (job) for the runall script for the purpose of studying distributions of starting inclusions. The number of cases is limited to 999. This setup.f code calls upon one of four subroutines as determined by the first letter in the dist file in the working directory. These are:

- sys2d_un.f creates a systematic uniformly distributed array of point pairs (size and concentration)
- rvg2d_un.f creates a square or rectangular array of randomly selected point pairs with a uniform distribution
- rvg2d_wn.f creates a group of point pairs with a Weibull distribution
- rvg2d_ln.f creates a group of point pairs with a lognormal distribution

The lognormal and Weibull distributions do not allow for negative values of size or concentration. (That would not be the case for a normal distribution function.) Negative values are not allowed by sys2d_un.f, and the range is summarized for the user by the rvg2d_un.f routine. (The rvg handle refers to Random Variable Generation.)

When the GROW code is launched for these cases, the core size and DZ size are given in a Figure of Merit output file. The user has discretion as to the critical concentrations above which a core is evident and at which the DZ terminates. An index is given to indicate how the remaining defect is classified, e.g., detectable or stealth. The analyst can then postprocess the results according to adjusted values for the critical compositions for core and DZ limits. A size limit has also been added, below which a defect cannot be found by NDE regardless of the concentration of nitrogen or oxygen.

A series of 41 parametric studies were run with the GROW code to assess the data identified in the literature search and to assess input sensitivities. Several improvements were made to the code as a result of these studies in terms of allowing more flexibility with the input files, acquiring intermediate output, and redesigning the keep script to deal with stacks of cases.

The parameters covered in the study were:

- Particle size: from 2 to 32 mil [0.005 to 0.081 cm]; ultimately extended down to 0.5 mil
- Initial nitrogen concentration in particle: 12 wt.% to 23 wt.%
- Exposure temperature: 1650° to 1850°C, isothermal or continuous cooling
- Melt cycles: single or triple VAR
- Exposure times: 60 to 900 seconds
- Diffusion coefficients: standard or enhanced, up to 100 times
- Mesh spacing: 0.25 to 5 microns

To accommodate large parametric studies, two levels of output detail are available. High-level output summary is provided in level 1 and more detailed output is available in level 2. For detail level = 1 or 2, the output includes: itype (classifies remnant inclusion), final detectable core and undetectable hard alpha sizes, and initial and final nitride dimensions. For detail level = 2, the nitride width versus short exposure time can be used to compute the initial dissolution rate.

A summary of the results of the parametric study is captured in table B-2, which includes input size, inclusion concentration [oxygen or N], far-field concentration, itype (defect type), ktype (severity), and resulting core width and hard alpha width (core + DZ). The baseline case took 22 seconds to run on a Dell Dimension 4550 with a Pentium 4 processor, 2.66-GHz clock speed, 256K of RAM, and a cygwin-bash shell. On the other hand, the smallest particle case (finest mesh) took 7 hours and 10 minutes to complete for the 300-second case. Graphics from some typical outputs are shown in figures B-19 through B-23.

Based on the parametric studies, it has been found that the initial dissolution rates of 50 to 600 microns correlate best with experimental measurements. This is an indication that convection is playing a significant role in the real world. The single and triple VAR cycles used in these studies were unofficially confirmed by an industry casting technology laboratory and one ingot producer. The values in the studies may be somewhat higher in temperature and shorter in time than reality, but these differences tend to offset each other and minimize computer time as well.

Conclusions from the parametric studies are:

- Initial dissolution rates were comparable for thick or medium sized particles.

- Initial dissolution rates were higher for continuous cooling due to the higher initial temperature than the baseline cases.

- Very large increases in dissolution rates were observed for enhanced liquid diffusivities. This confirms that convection is a key player in the real world. Also, there is a lot of scatter in actual dissolution rate data. That would be expected for convection, as flows are complex and depend on particle size, shape, and placement in the liquid pool.

- Dissolution rates decrease at lower concentrations and lower temperatures, as expected.

- Stealth defects are generated for small initial inclusion particle size and enough exposure time at sufficiently elevated temperature; however, if the time or temperature is very high, the stealth defect can be dissolved to the point where it would be expected to be innocuous.

- Shorter exposure times (for medium to thick particles) give the same initial dissolution rates, as expected.

- Overall dissolution progresses systematically as exposure time increases.

- Triple VAR gives more overall dissolution than single VAR.

Table B-2. Grow Code Parametric Study Results

case	Incl Size [mils]	CMAX [wt%]	CMAT [wt%]	itype index	ktype index	Core size [mils]	Hard Alpha [mils]	spacing [microns]	Temperature [C]	Time [s]	Special Items
t1	32.0	23.0	0.002	1	92	66.37	124.84	5.0	1850	300	
t2	32.0	23.0	0.002	1	92	55.70	118.52	5.0	1750	300	
t3	32.0	23.0	0.002	3	88	47.01	96.79	5.0	1650	300	
t4	32.0	18.0	0.002	1	92	65.58	124.84	5.0	1850	300	
t5	32.0	18.0	0.002	1	92	54.91	118.52	5.0	1750	300	
t6	32.0	18.0	0.002	3	88	46.62	96.39	5.0	1650	300	
t7	32.0	12.0	0.002	1	92	64.00	124.84	5.0	1850	300	
t8	32.0	12.0	0.002	1	92	53.73	118.52	5.0	1750	300	
t9	32.0	12.0	0.002	3	88	45.43	95.60	5.0	1650	300	
m1	16.0	23.0	0.002	1	92	50.40	108.80	5.0	1850	300	
m2	16.0	23.0	0.002	1	92	39.60	102.40	5.0	1750	300	
m3	16.0	23.0	0.002	3	88	31.20	80.80	5.0	1650	300	
m4	16.0	18.0	0.002	1	92	49.60	108.80	5.0	1850	300	
m5	16.0	18.0	0.002	1	92	39.20	102.40	5.0	1750	300	
m6	16.0	18.0	0.002	3	88	30.40	80.40	5.0	1650	300	
m7	16.0	12.0	0.002	1	92	48.00	108.80	5.0	1850	300	
m8	16.0	12.0	0.002	1	92	37.60	102.40	5.0	1750	300	
m9	16.0	12.0	0.002	3	88	29.60	80.00	5.0	1650	300	
s1	8.0	23.0	0.002	1	92	42.24	100.80	2.0	1850	300	
s2	8.0	23.0	0.002	1	92	31.52	94.40	2.0	1750	300	
s3	8.0	23.0	0.002	3	88	22.88	72.48	2.0	1650	300	
s4	8.0	18.0	0.002	1	92	41.44	100.80	2.0	1850	300	
s5	8.0	18.0	0.002	1	92	30.88	94.40	2.0	1750	300	
s6	8.0	18.0	0.002	3	88	22.40	72.16	2.0	1650	300	
s7	8.0	12.0	0.002	1	92	37.76	100.80	2.0	1850	300	
s8	8.0	12.0	0.002	1	92	29.28	94.40	2.0	1750	300	
s9	8.0	12.0	0.002	3	88	21.28	71.52	2.0	1650	300	
e1	4.0	18.0	0.002	5	75	0.00	90.32	1.0	1750	300	
e2	2.0	18.0	0.002	6	70	0.00	66.79	1.0	1750	300	
e3	16.0	18.0	0.002	1	92	26.40	54.80	5.0	1750	60	
e4	16.0	18.0	0.002	1	92	55.60	165.60	5.0	1750	900	
e5	32.0	18.0	0.002	1	92	42.40	70.62	2.0	1750	60	10X DD
e6	32.0	18.0	0.002	3	88	38.94	84.18	2.0	1750	60	10X DL
e7	32.0	18.0	0.002	1	92	52.49	417.88	2.0	1850	60	100X DL
e8	32.0	18.0	0.002	3	88	53.60	195.47	2.0	1750	60	100X DL
e9	32.0	18.0	0.002	3	88	52.18	120.12	2.0	1650	60	100X DL
e3a	32.0	18.0	0.002	1	92	42.67	70.72	5.0	1750	60	
c1	16.0	18.0	0.002	3	88	40.00	104.00	5.0	Single VAR	360	
c2	16.0	18.0	0.002	3	88	60.40	176.80	5.0	Triple VAR	1200	
c3	8.0	18.0	0.002	3	88	31.68	95.68	2.0	Single VAR	360	
c4	8.0	18.0	0.002	6	70	0.00	166.08	2.0	Triple VAR	1200	

Notes:
Case m5 is "the baseline"
10X DD: 10X normal Delta Diffusivity (simulation of effect of defect structure)
10X DL: 10X normal Liquid Diffusivity (simulation of effect of convection)
100X DL: 100X normal Liquid Diffusivity (simulation of effect of convection)
used in combination with 10X enhancement on all solid diffusivities
ktype scale was changed on 3/31/04 to run from 1 to 999

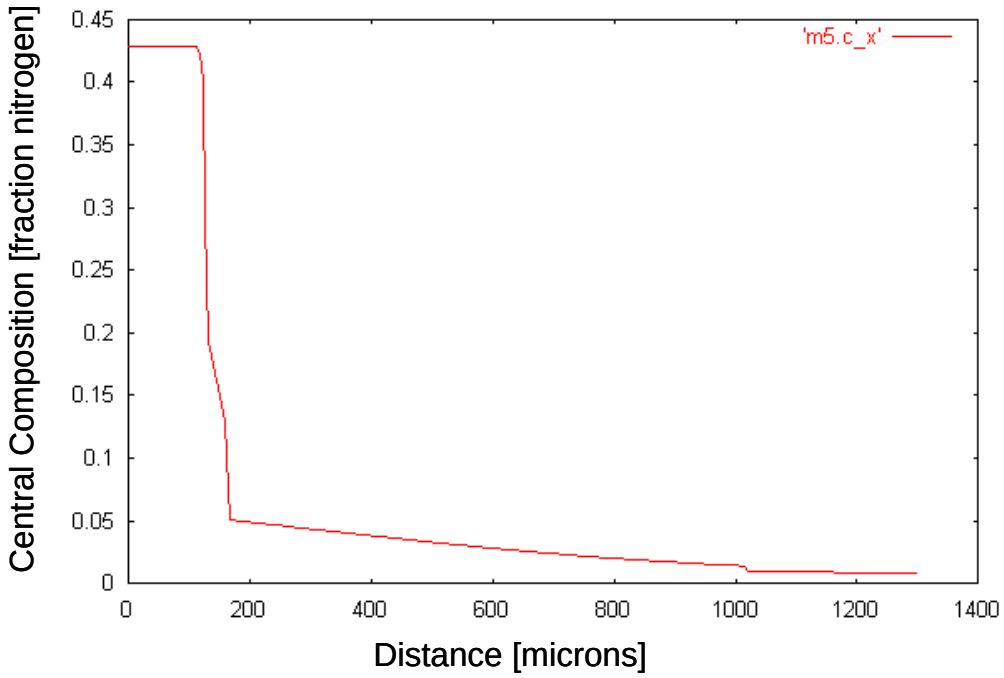

Figure B-19. Baseline Case (M5), Nitrogen Fraction vs Distance

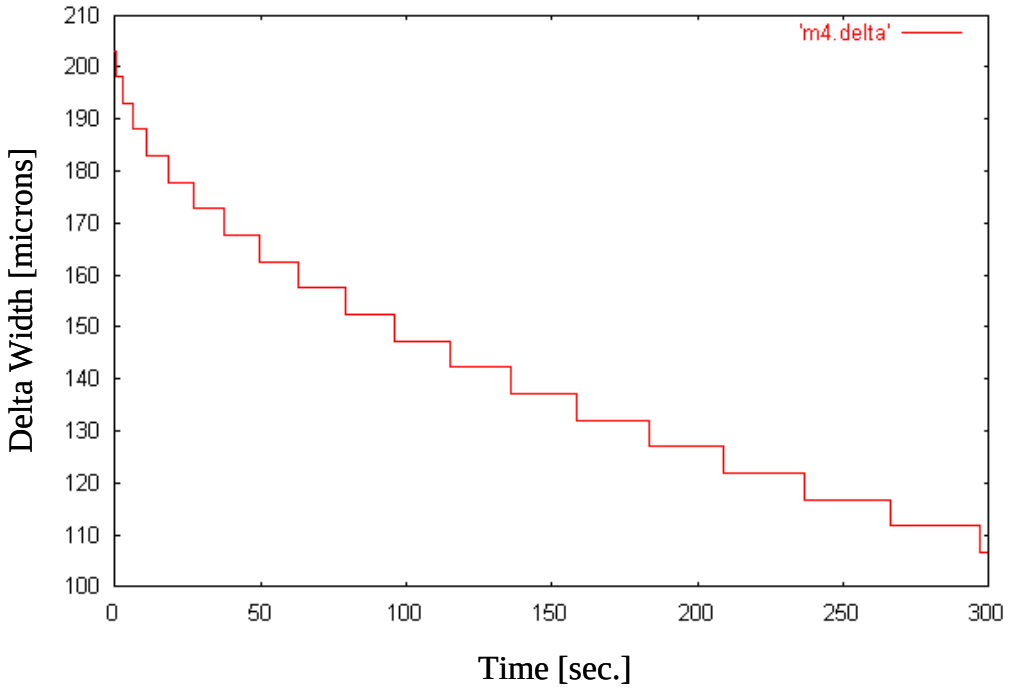

Figure B-20. Case M4, Delta Width vs Time

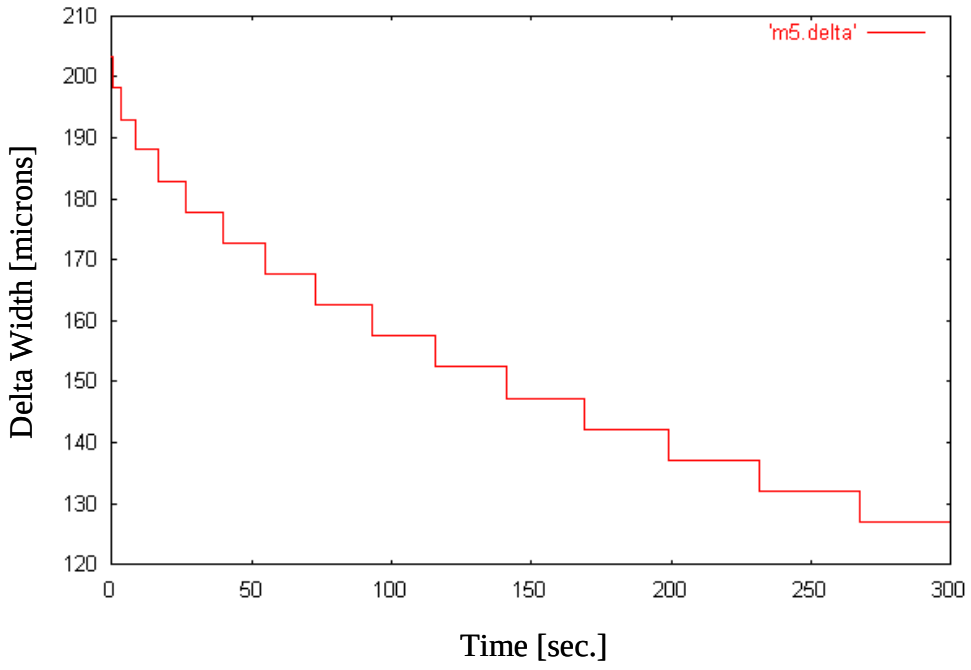

Figure B-21. Baseline Case M5, Delta Width vs Time

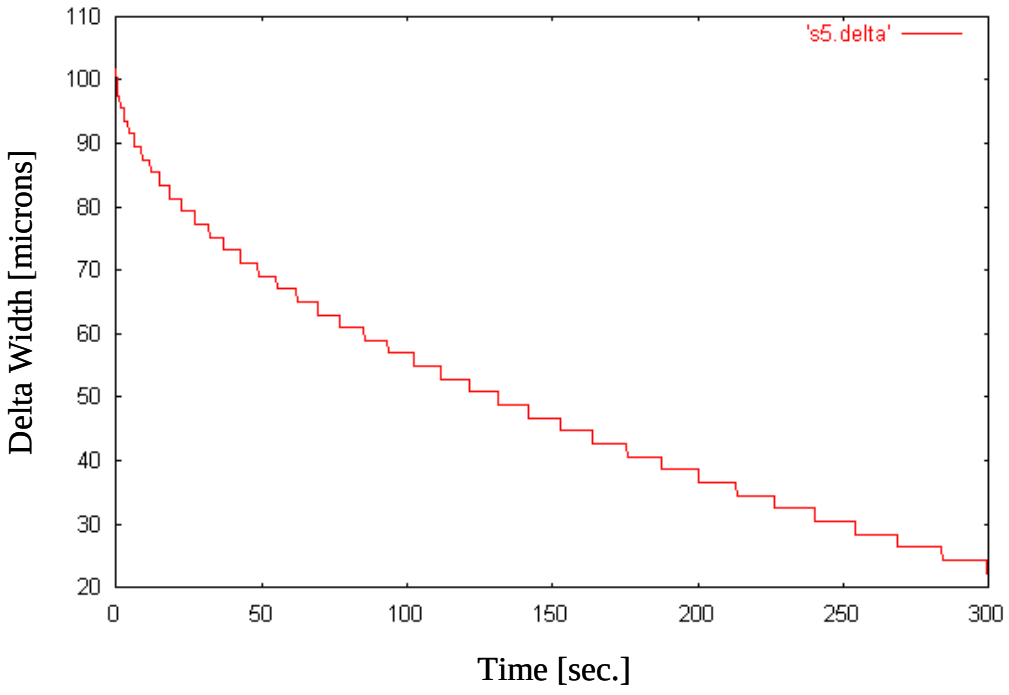

Figure B-22. Case S5, Delta Width vs Time

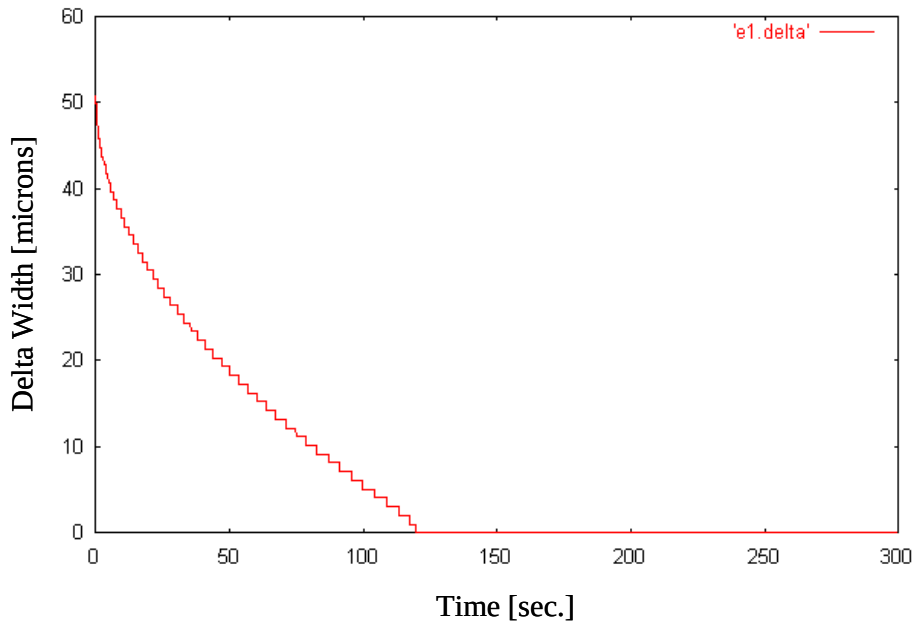

Figure B-23. Case E1, Delta Width vs Time

B.4 STUDIES ON STEALTH ANOMALY REGION AND ON TRIPLE MELT PROCESSING.

A study was also carried out to determine the shape of the stealth anomaly region in size and concentration space at fixed temperature and exposure time. This was visualized using Microsoft® Excel® (figure B-24) and can also be visualized using a gnuplot procedure that was reasonably automated. The stealth region is hyperbolic in shape. The branch at small size and high concentration is bounded, but the branch at large size and low concentration is unbounded (for fixed exposure temperature and time.) At lower temperatures, the stealth anomaly is not created; the original inclusion is preserved due to low diffusivity. At higher temperatures, more dissolution occurs. Whether the stealth anomaly disappears depends on the exact combination of temperature and time selected.

A systematic suite of 70 cases was built with setup.f, run in 40 minutes on a Dell personal computer (without significant mass conservation error), and some of the output (at detail level 1) was edited (to remove alpha headers), grouped, and fed into gnuplot for a surface plot. The result is shown in figure B-25, plotting residual core width in the vertical axis versus initial particle size and nitrogen concentration. As the core widths approach zero (due to smaller initial core sizes or lower nitrogen concentrations), the anomalies can reach a point where the residual core widths are small enough that they may not be detectable and are classified as stealth anomalies. It is interesting to note that for larger initial core sizes at higher concentrations, the resulting core size will increase as nitrogen diffuses into the surrounding material.

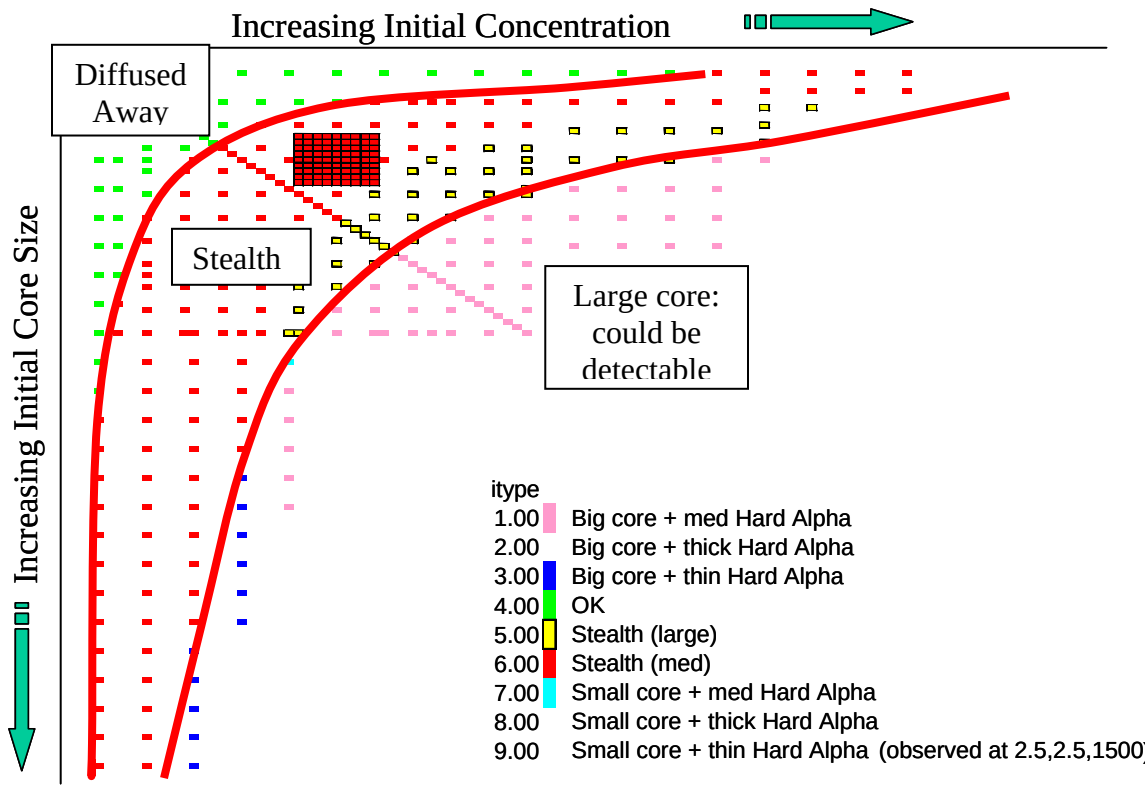

Figure B-24. Stealth Region Predicted for Given Exposure Temperature and Time

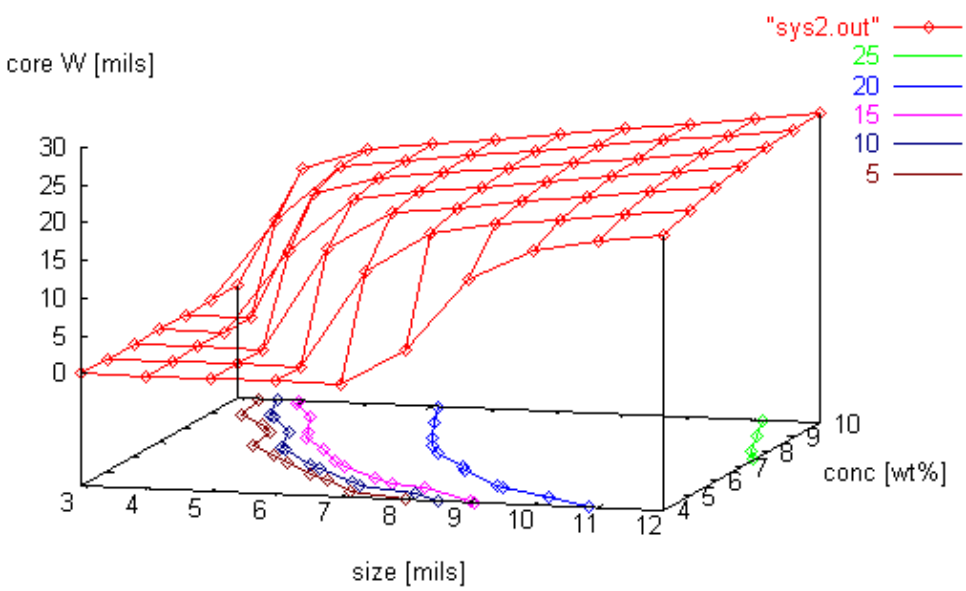

Figure B-25. Core Width as a Function of Initial Particle Size and Concentration for a Representative Exposure History

Further parametric and sensitivity studies were performed, using the one-dimensional version of the code, with the primary objectives to study the effect of the 3 times vacuum arc remelting (3XVAR) process, hard alpha size distribution, and nitrogen concentration in the ingot, on the resulting DZ sizes.

The first study addressed the effect of hold time. A 10-mil hard alpha with uniform 12 wt.% N concentration is placed in Ti base metal, which is held at 2000°C, and subsequently cooled down to 1000°C. Figure B-26 shows different hold times of 0, 2, and 4 minutes. Figures B-27 through B-29 include the resulting nitrogen profiles.

Effect of the cooling rate was studied by holding a 10-mil, 12 wt.% hard alpha at 2000°C and cooling down to 1000°C at different rates. Figure B-30 shows six different rates of cooling. One of the cooling schemes includes a 1-minute dwell at 1800°C. Figure B-31 illustrates the resulting core sizes and core plus DZ sizes. For purposes of this analysis, the DZ was considered the beta and the alpha plus beta material.

The next set of studies simulated a representative 3XVAR process. Figure B-32 illustrates the 12-minute melting process repeated three times. The effect of this melting process on a 10-mil, 12 wt.% N hard alpha was studied. Figures B-33 through B-35 show the nitrogen profile after each melting cycle, and figures B-36 and B-37 show the change in the nitrogen concentration and the size of the delta, alpha, and beta layers as a function of time. Note that the 10-mil core diffuses out completely during the second melting process.

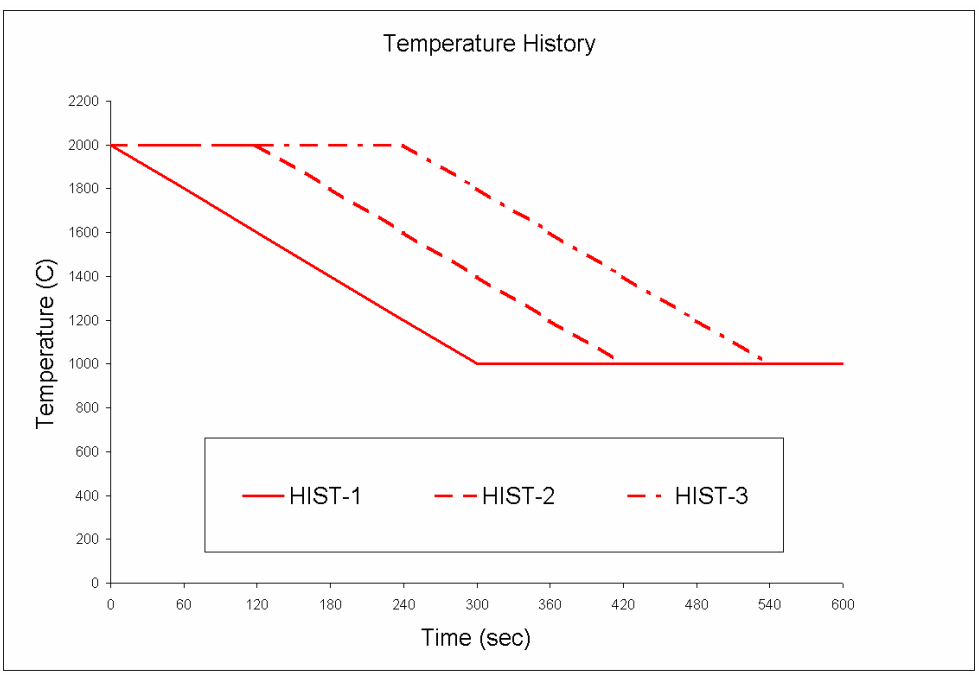

Figure B-26. Time Histories Run to Assess Hold Time Effects

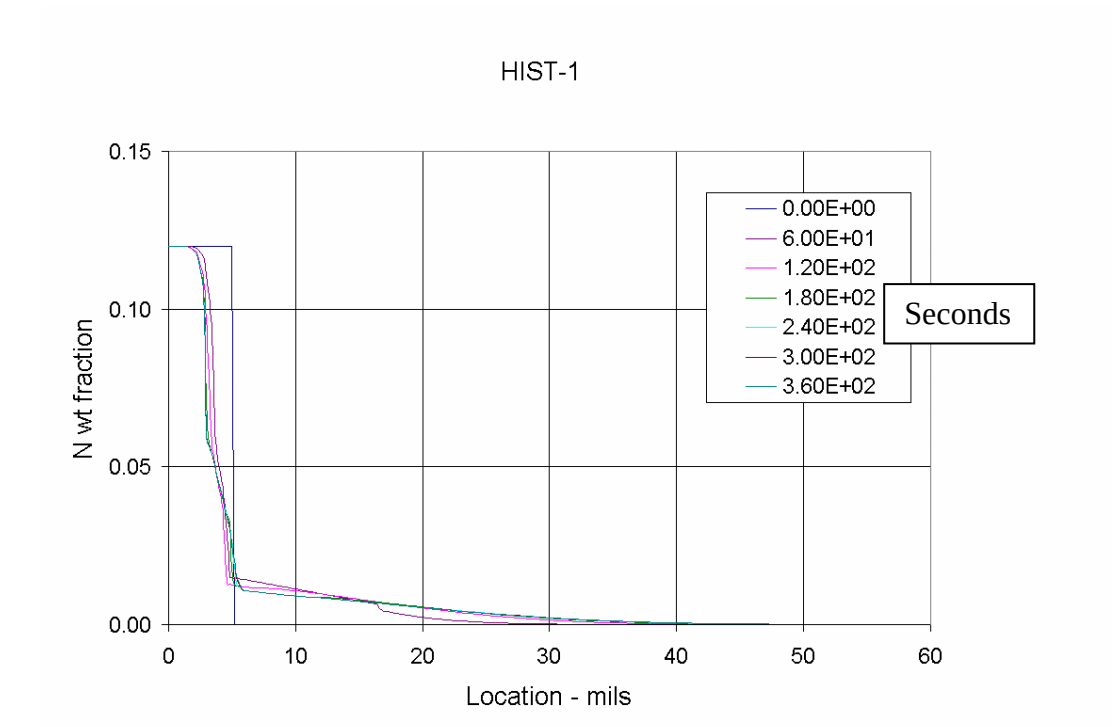

Figure B-27. Nitrogen Profile With no Hold Time at 2000°C

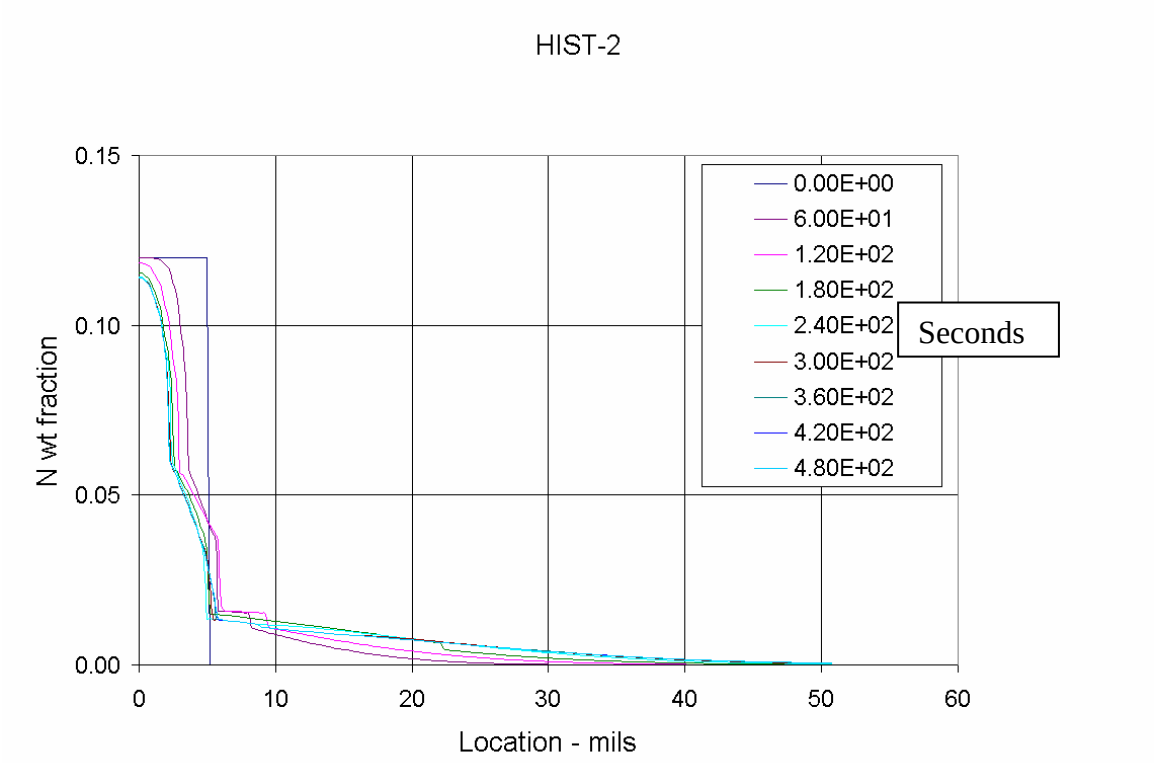

Figure B-28. Nitrogen Profile With 2-Minute Hold at 2000°C

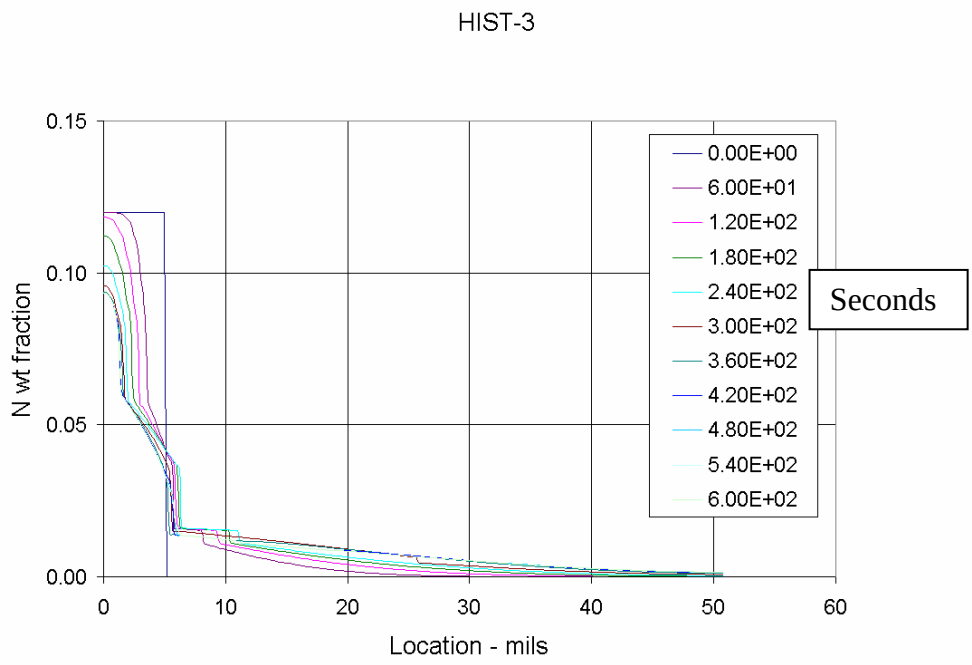

Figure B-29. Nitrogen Profile With 4-Minute Hold at 2000°C

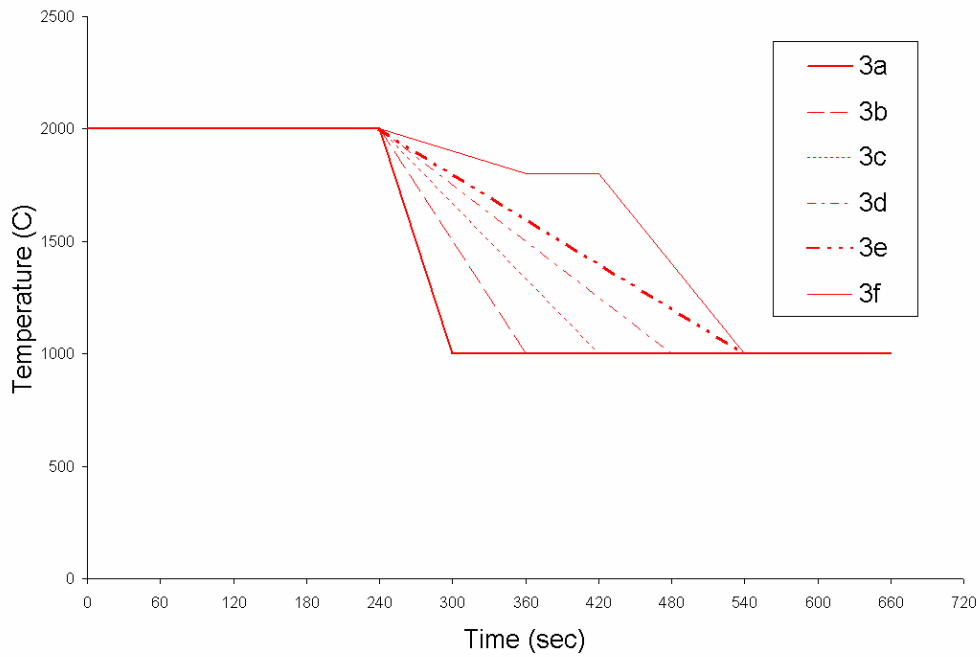

Figure B-30. Time Histories Run to Assess Cooling Rate Effects

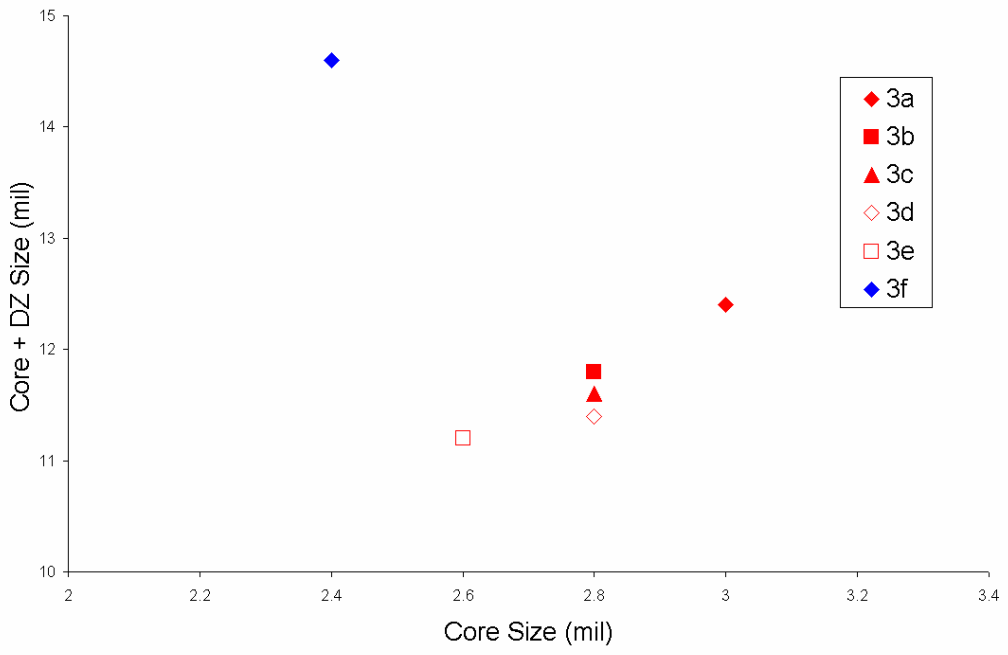

Figure B-31. Resulting Core vs Core Plus Diffusion Zone Size for Varying Cooling Rates

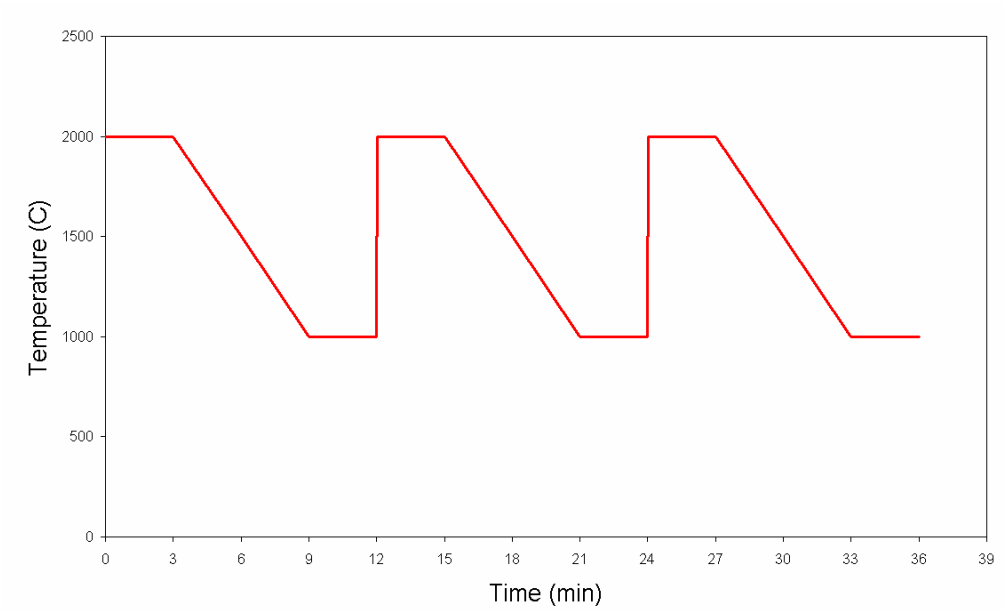

Figure B-32. Representative Temperature History Used to Assess 3XVAR Melt Process

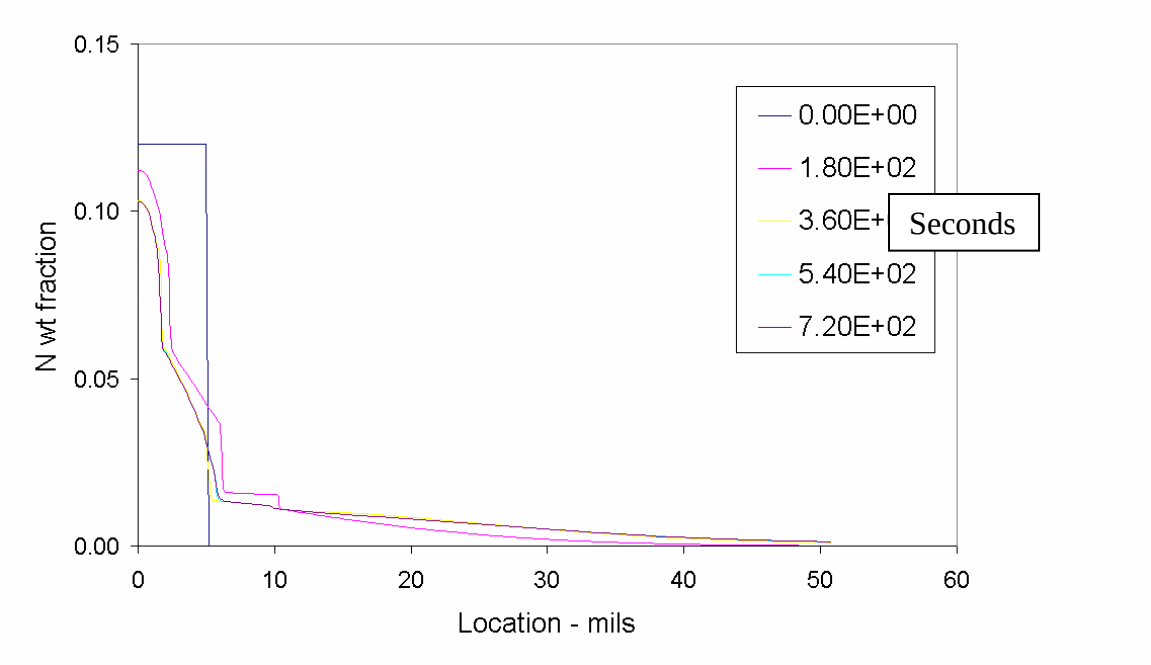

Figure B-33. Nitrogen Profile During 1st Melt

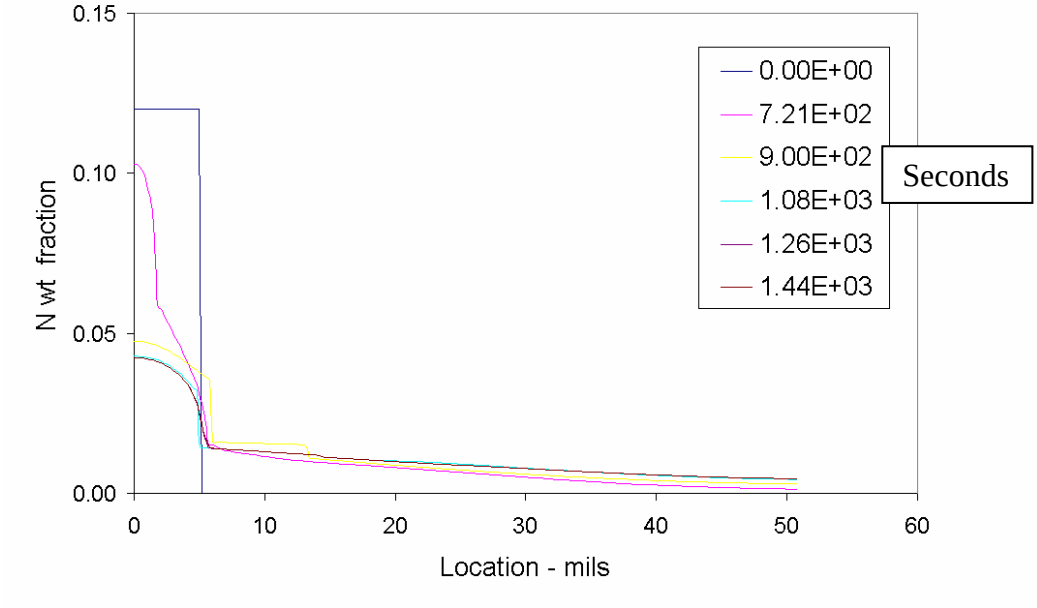

Figure B-34. Nitrogen Profile During 2nd Melt

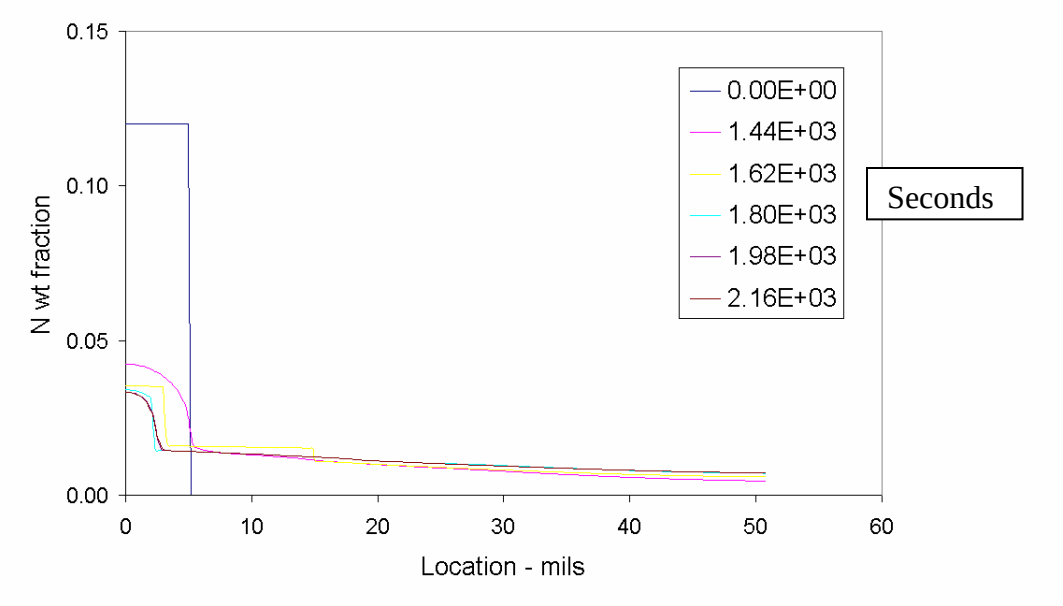

Figure B-35. Nitrogen Profile During 3rd Melt

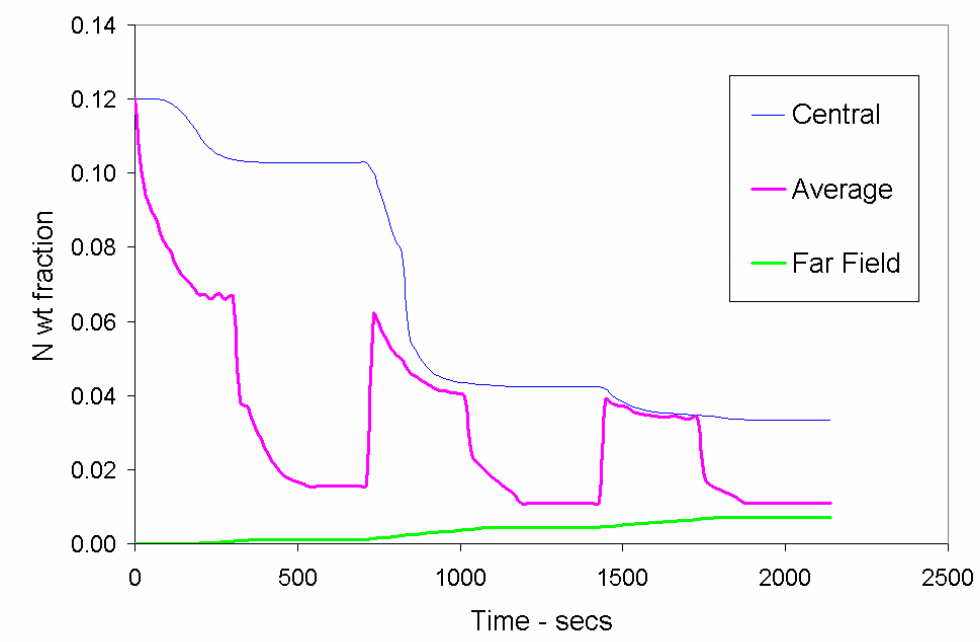

Figure B-36. Change in Nitrogen Concentration as a Function of Time and Location

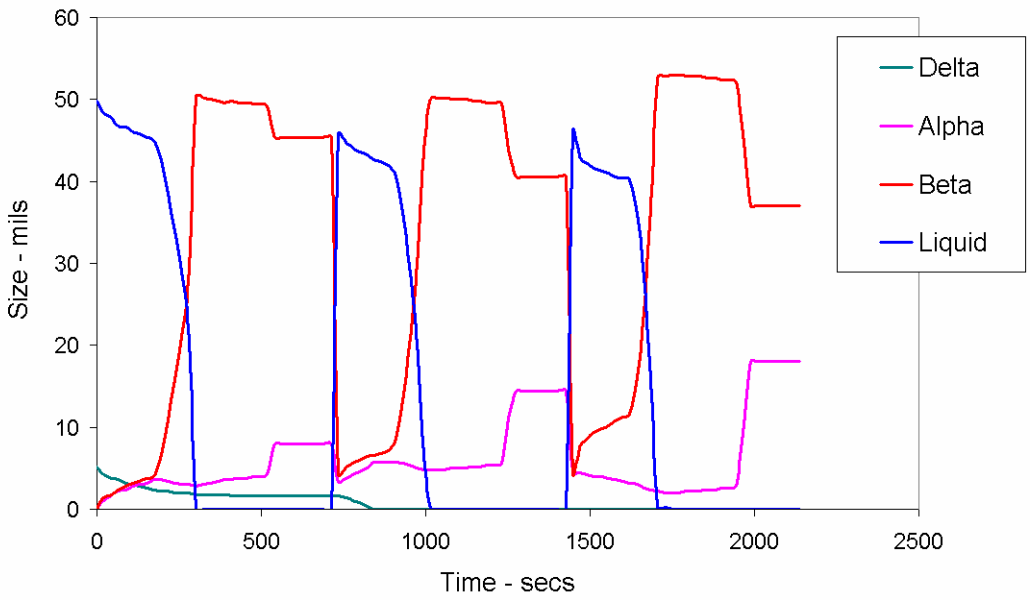

Figure B-37. Change in Size of the Delta, Alpha, and Beta Layers as a Function of Time

Jet Engine Titanium Quality Committee's (JETQC) original data for the core and the core plus DZ sizes are based on 3XVAR billet and bar finds, assumed to be a sample representative of hard alpha anomalies for any titanium alloy. The data were used to derive the hard alpha relative size distribution in the ingot, which includes the core and the DZ sizes. Correlations of the effective core size and the core plus DZ size are approximately linear. Figure B-38 contains the exceedance curve for the effective core size and the core plus DZ size. Figure B-39 illustrates the approximate linearity between the core size and the core plus DZ size. In the present study, the hard alpha size distribution in the ingot is assumed random (exponential distribution). Using a Monte Carlo simulation, 40 core sizes were randomly generated. The generated hard alpha size distribution in the ingot is included in figure B-40. After applying the 3XVAR process shown in figure B-41, the resulting core size and the core plus DZ sizes were computed by the GROW code, with the results shown in figure B-42. The DZ size includes the nitrided beta phase and the alpha plus beta phase. The core versus core plus DZ size correlation is compared with the trend line from the JETQC data in figure B-43. They are approximately parallel for core sizes greater than 20 mils. If the pure beta phase is neglected, which is less than 1wt.% of nitrogen at 1400°C, the GROW code prediction is much closer to the JETQC data, as shown in figures B-44 and B-45.

Nitrogen concentration effect was studied for several hard alpha sizes in the ingot, by changing the core nitrogen concentration from 10% to 20%. After applying the same 3XVAR process as figure B-41, the GROW code predicted little effect on the resulting core plus DZ sizes. This is illustrated in figure B-46.

These studies have demonstrated that the GROW code can provide very useful information about the effect of melting process on the resulting core and the DZ sizes.

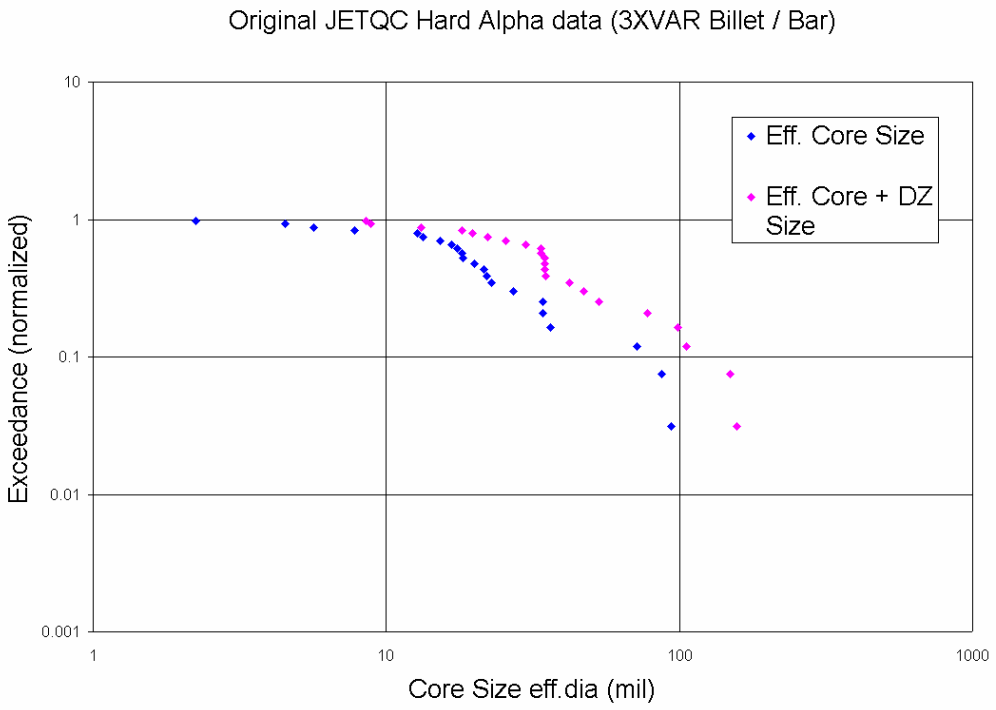

Figure B-38. Exceedance Curve for the Effective Core and Core Plus Diffusion Zone Size

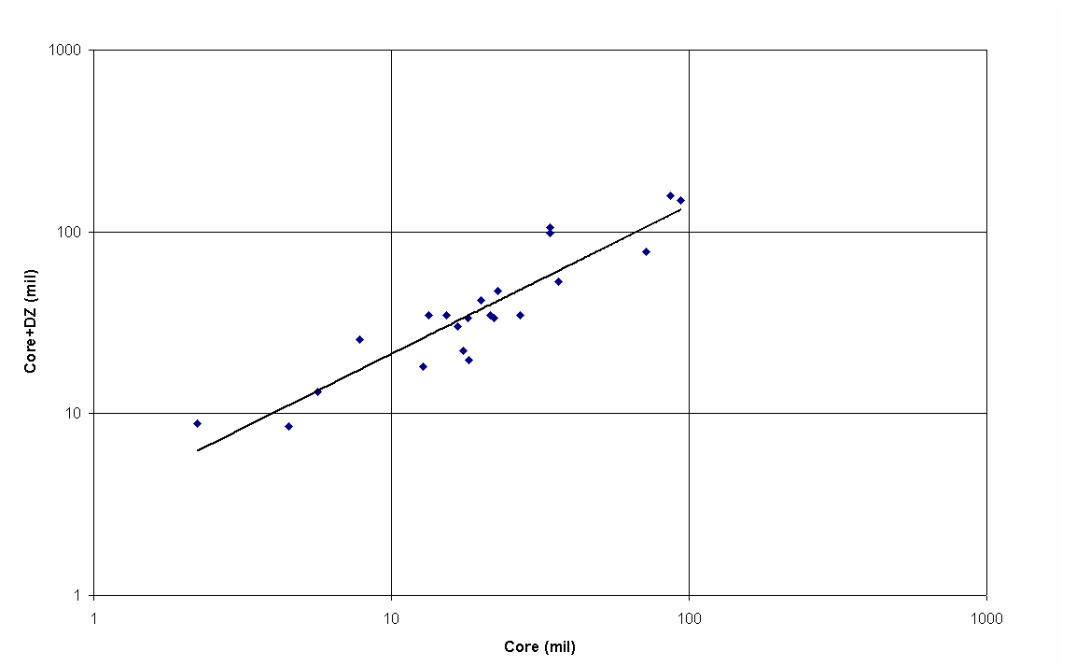

Figure B-39. Relationship of Core to Core Plus Diffusion Zone Size for JETQC Data

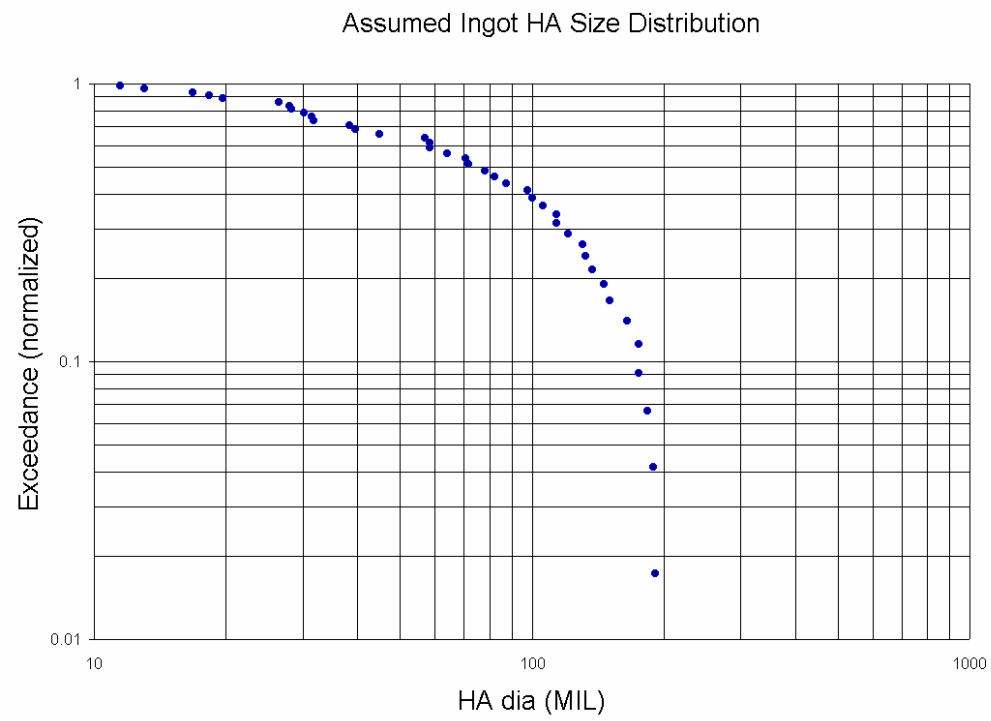

Figure B-40. Assumed Ingot Exceedance Curve for Assessment of 3XVAR Process

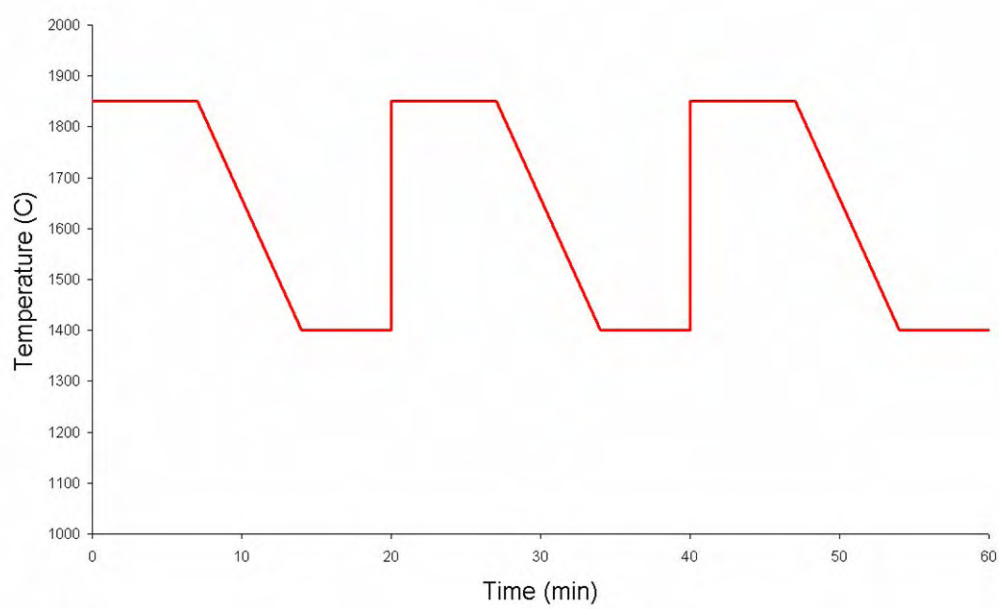

Figure B-41. Representative 3XVAR Process Assumed in Study

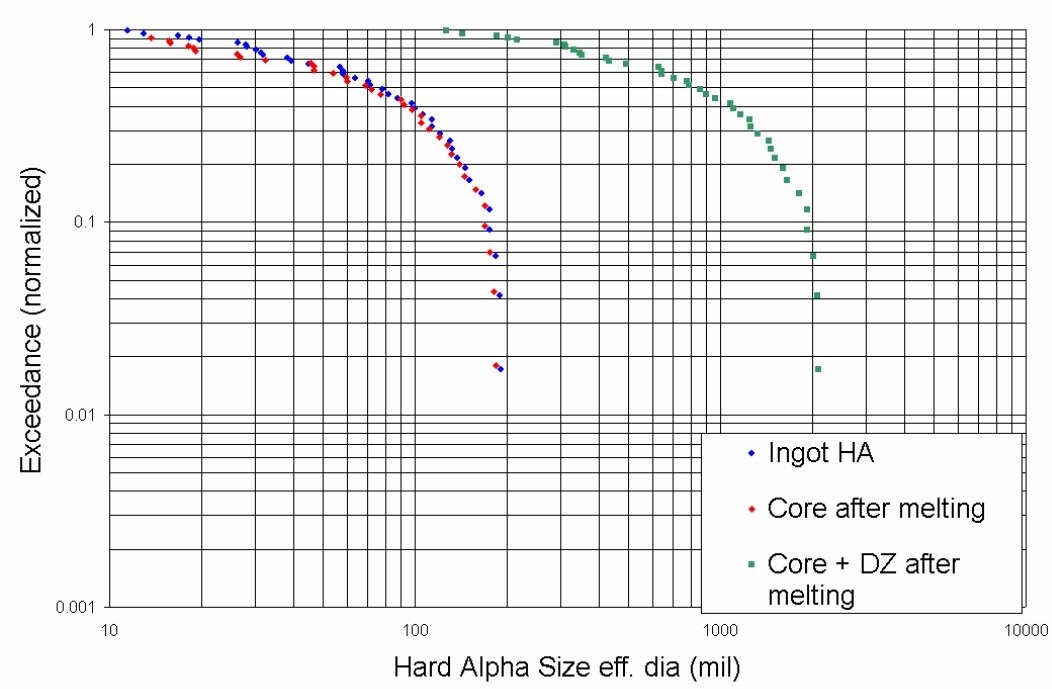

Figure B-42. Hard Alpha Size Distribution Computed by the Grow Code

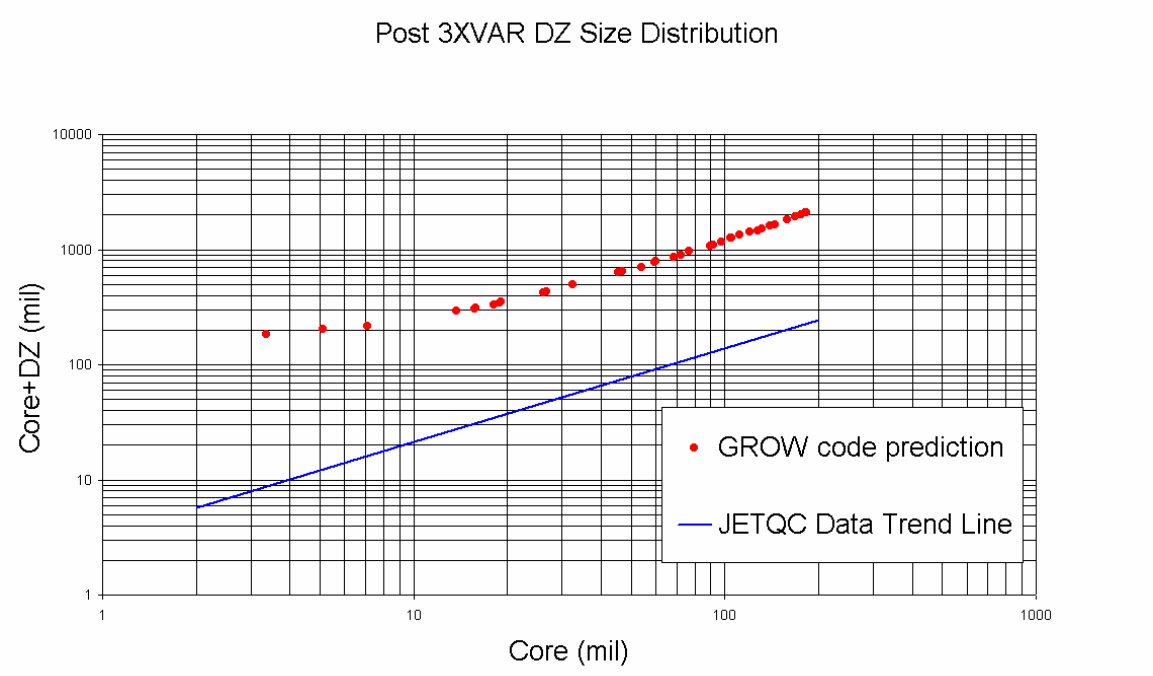

Figure B-43. Predicted Core vs Core Plus Diffusion Zone Size Compared to JETQC

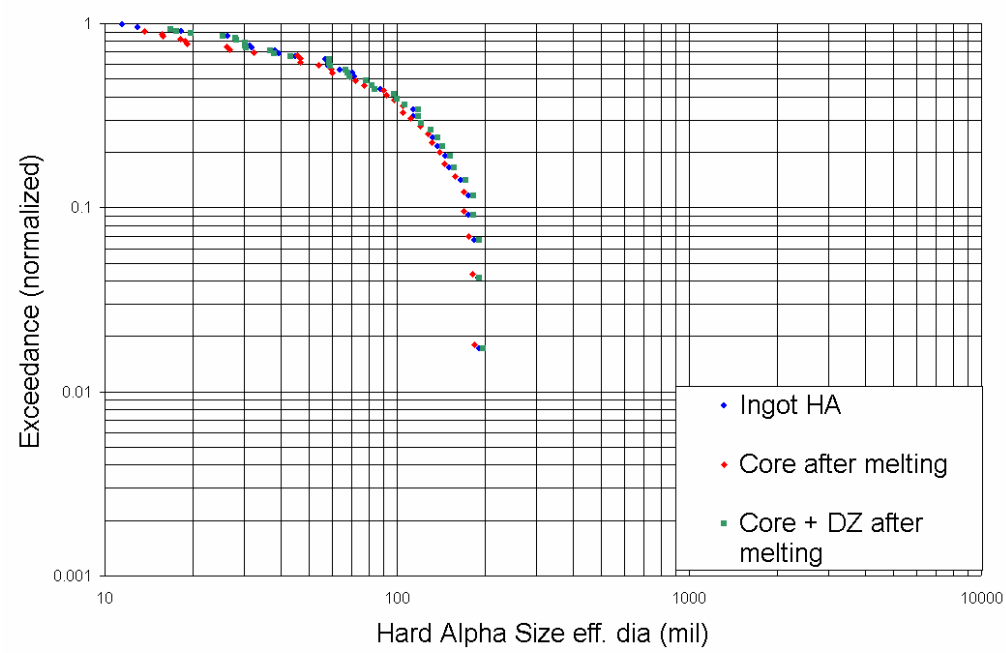

Figure B-44. Hard Alpha Size Distribution Computed by the Grow Code Neglecting Pure Beta Phase

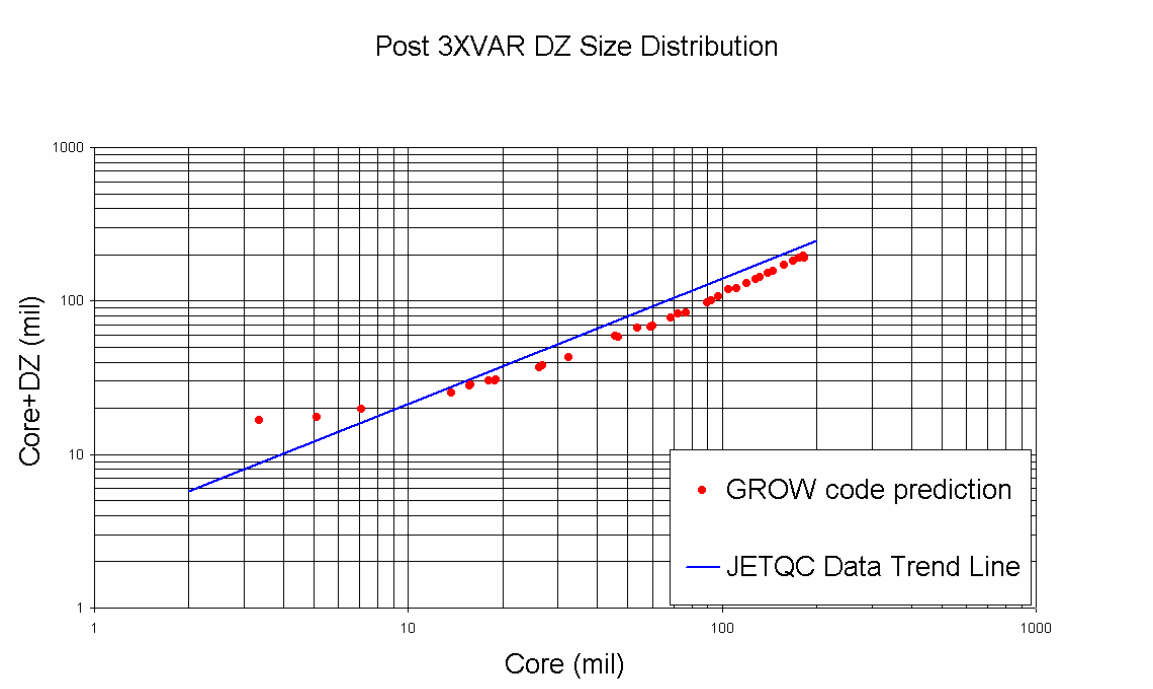

Figure B-45. Comparison of JETQC Data to Predicted Core vs Core Plus DZ Size Neglecting Pure Beta Phase

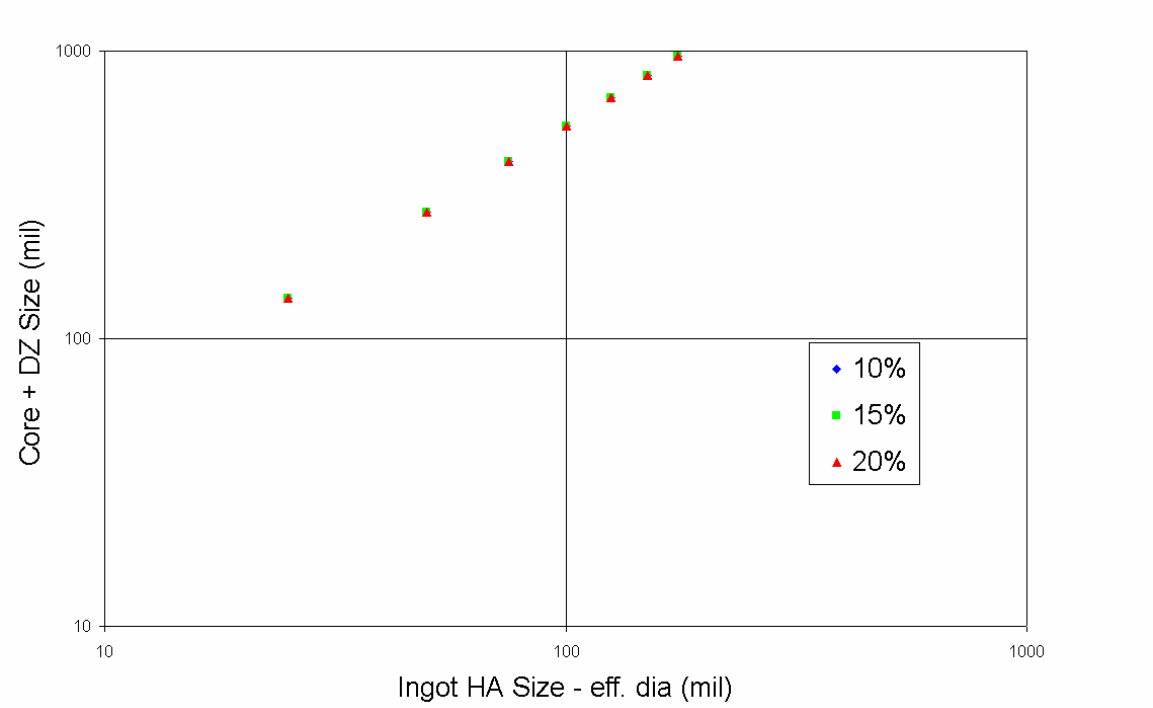

Figure B-46. Effect of Ingot Nitrogen Concentration on Resulting Core Plus DZ Size

B.5 REFERENCES.

B-1. Kirchoff, G., "Vorlesungen uber die Theorie der Warme," Barth, Leipzig, 1894.

B-2. Courant, R., Friedrichs, K.O., and Lewy, H., "Uber die Partiellen Differenzengleichungen der Mathematisches Physik," *Mathematische Annalen*, Vol. 100 1928, pp. 32-74.

B-3. Bellot, J.B., et al., "Dissolution of Hard Alpha Inclusions in Liquid Titanium Alloys," *Metallurgical and Materials Tranactions B*, Vol. 28B, 1997, pp. 1001-1010.

B-4. Bewley, B.P. and Gigliotti, M.F.X., "Dissolution Rate Measurements of TiN in Ti-6242," *Acta Metallurgica*, Vol. 45, 1997, pp. 357-370.

B-5. Buttrill, W.H. and Shamblen, C.E., "Hearth Melt Plus Vacuum Arc Remelt: Production Status," *Titanium'95: Science and Technology*, 1995, pp. 1446-1453, Figure 2.

APPENDIX C—VALIDATION OF DEFORM™ MICROCODE

C.1 INTRODUCTION.

The hard alpha (HA) anomaly distribution developed by the Aerospace Industries Association Rotor Integrity Subcommittee was based on certain assumptions regarding the geometrical changes experienced by a HA anomaly when an ingot is converted to a billet and subsequently to an aircraft engine rotating disk forging. To test the validity of these assumptions, a finite element method-based deformation microcode was developed to predict the change in shape and orientation of HA anomalies during the metal forming processes. The microcode predicts the anomaly behavior more accurately than the empirical methods. The information from the microcode could be used to establish the nature of the anomalies that would be interrogated by ultrasonic nondestructive evaluation methods during the billet and disk forging inspections and to assess the assumptions made with respect to the flaw size used in fracture mechanics analyses. To develop the deformation microcode, the deformation and fracture constitutive properties of HA with various nitrogen (N) contents were required. The testing results and constitutive model development for HA and diffusion zone (DZ) were described in the Turbine Rotor Material Design (TRMD) Phase I final report. That appendix summarizes:

- The development of the deformation microcode.
- Forging experiments that were conducted to validate the microcode.

The objective of this task was to develop a finite element microcode to simulate the deformation of a HA inclusion during forming processes. The code is intended to simulate

- the interaction and deformation among the HA inclusion, nitrogen DZ, and parent material during the forming process.

- degradation of strength of the HA particle due to fracture by using a continuum damage mechanics constitutive model.

C.2 SUMMARY OF ACCOMPLISHMENTS.

The TRMD-II work is a continuation of that started in TRMD-I. Therefore, for the sake of completeness, the TRMD-I accomplishments are listed below.

- Developed and tested microcode to predict shape and orientation of HA anomalies.
    - Microcode is an add-on to the commercial macrodeformation code DEFORM™.
    - DEFORM was developed by Scientific Forming Technologies Corporation.
    - Microcode is available at no extra cost to all licensees of DEFORM.
    - Kept microcode updated with current DEFORM releases.

- Generated constitutive property data for HA and DZ.

- Completed preliminary validation using:

  - First contaminated billet study forging, B1BW3.
  - Data from constitutive property tests.

- Applied microcode to typical Rolls-Royce disk geometries.
- Made preliminary attempts to model anomaly cracking/voiding:

  - Investigated element deletion and remeshing techniques.

  - Steering Committee decided not to pursue development due to resource and technical limitations.

The Phase II accomplishments are listed below, and details are provided in the following sections.

- Developed relationships between anomaly deformation and forging macrostrain:

  - Predicted anomaly deformation quickly and accurately via regression equations.
  - Modified the anomaly distribution used in lifing analysis.

- Completed detailed macro- and microvalidation:

  - Total of 44 synthetic seeds in four forgings.

  - Twenty-eight synthetic seeds cut up for detailed analysis and microcode validation.

  - Sixteen seeds and one forging used for fatigue specimens and other work.

- Microcode development and validation work is complete.

C.3 SEED EVALUATION.

Seeds from pancake forgings seeded billet (SB) SB-1, SB-3, and SB-4 were located using ultrasonic C-scan and time of flight measurements to approximate the depth of the seed from the surface. Once located, wire electro discharge machining was used to remove a cube of material about 0.75″ x 0.75″ x 0.75″ around the seed(s) while maintaining the original orientation from the forging. Several interim machining steps were sometimes used to position the seed in the cube in preparation for ultrasonic characterization.

After the seeds were removed, high-resolution 25-MHz ultrasonic inspections were made from each side of the cubed blocks (figure C-1). In addition, a B-scan was taken from the direction in which the seed was to be polished. This is also the direction from which the indication was located in the forging. The depth and location of the seeds in each cube were then used to quickly polish to the seed and to estimate equal distance for the selected number of polish steps (typically ten) through the seed.

"Cube" as cut from forging

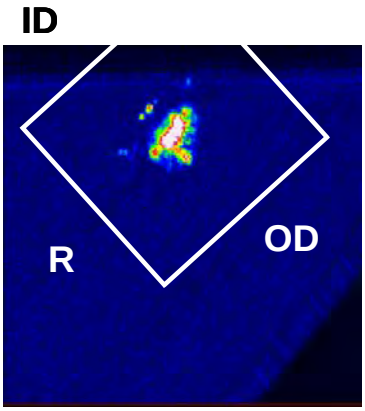

A side up

25 MHz u/t scan prior to cube

Ultrasonic Inspection at 25 MHz

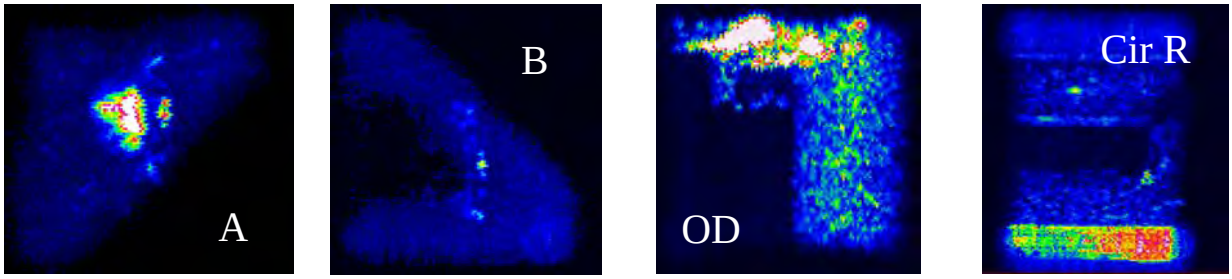

Note: ID and Cir L side not scanned

Figure C-1. Typical Ultrasonic Inspection Data for one Seed SB-1, Seed 1, 0.20″ Diameter, 0.20″ Long, 1.5% N

The steps in the grinding and polishing procedure are listed below and shown in figure C-2:

1. Initial Grind Depth:

   - 120-200 mil (40 mil steps) based on scanning electron microscope (SEM) and Blue Etch results

2. Rough polish and etch—DZ and core revealed?

   - Yes: Go to step 4
   - No: Grind ~40 mil

3. Repeat Step 2 until DZ and core revealed or reach depth of 200 mils
4. Finish polish and etch for examination

5. Photograph (25X- 50X) and analyze nitrogen content (Microprobe)

6. Upon completion of examination (SEM and Microprobe):

- Grind/polish another ~30 mil (~8 sections based on Blue Etch results)
- Final polish
- Etch for examination

7. Repeat step 5 until completely through seed.

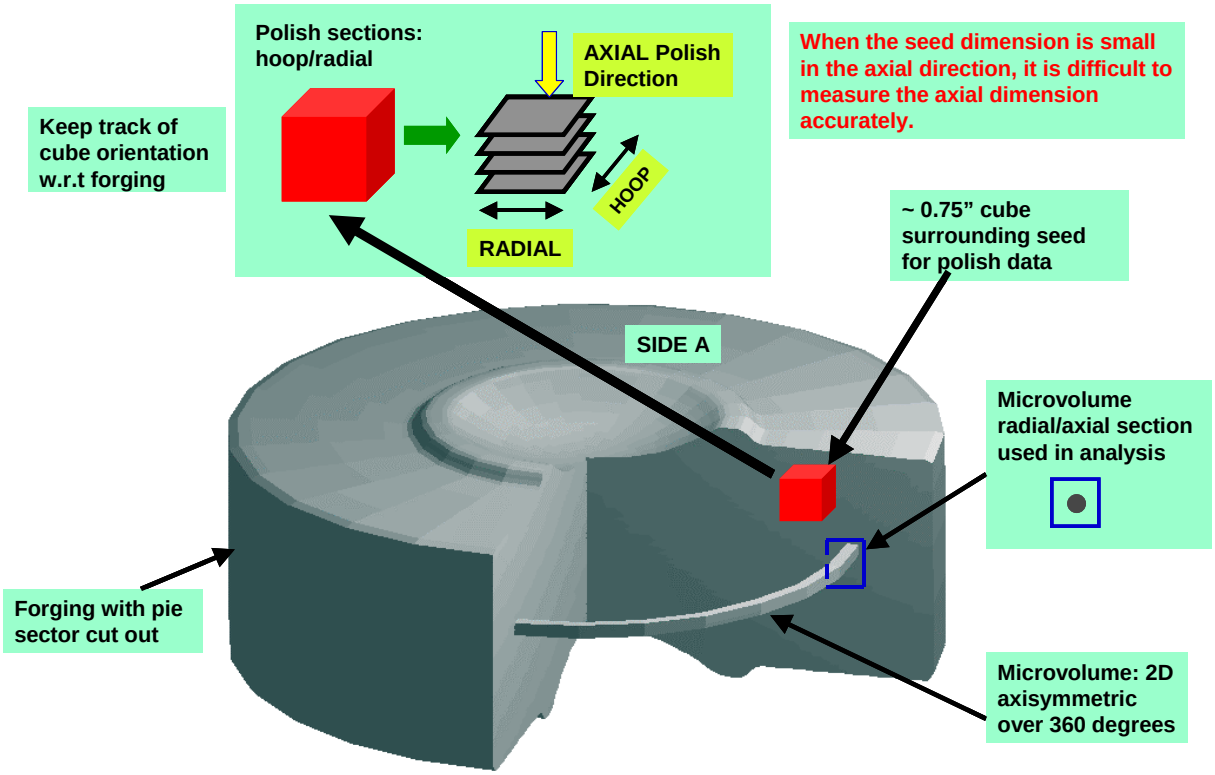

Figure C-2. Seed Polishing Procedure

The overall dimensions of HA seeds and DZ in axial, radial, and hoop directions were measured from the seed polish images as shown in figure C-3. The measured values were recorded for the largest dimensions of the HA and the DZ in the three directions. All the metallographic data have been supplied to Southwest Research Institute® on a CD ROM since it is too large to be included in this report.

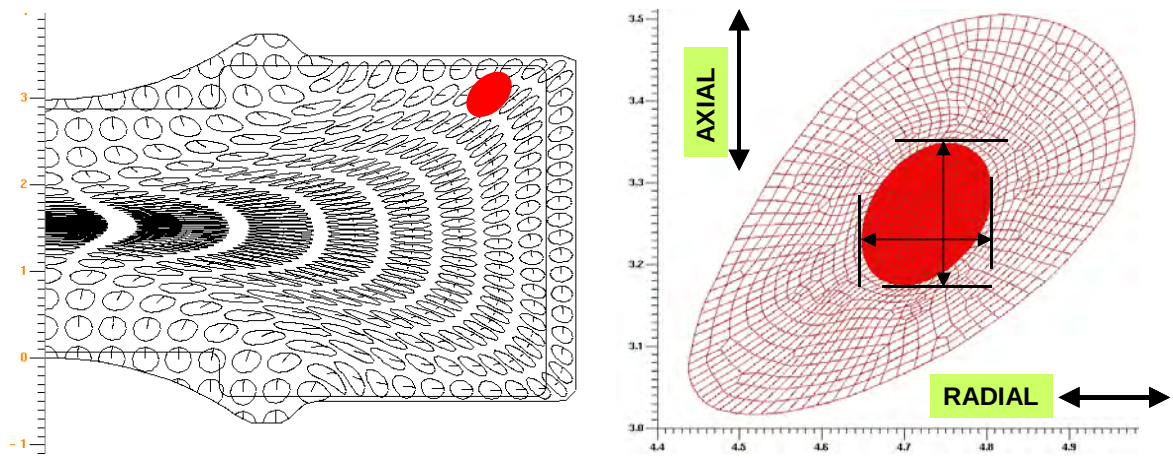

(a) (b)

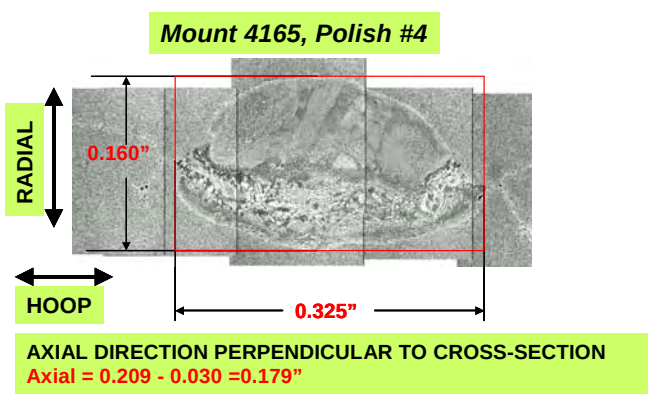

(c)

Figure C-3. Typical Data for One Seed SB-1, Seed 1, DZ Only 1.5% N2, Circumferential Orientation (a) Microvolume Location in the Forging (b) Predicted Microvolume Shape and Seed Deformation and (c) Polished Section With the Largest Dimensions of the Seed

C.4 MICROCODE VALIDATION.

The predicted deformed seed shapes were compared with the measured shapes from the sectioning of the seeds. The validation of microcode predictions consisted of comparing the overall deformed shapes of the seeds and the DZ with the corresponding measured shapes. Since the microcode cannot predict cracking and voiding, it was not possible to validate all the details of inclusion deformation.

Detailed microcode validation was completed with data from 28 seeds. Microcode validation was done in two ways:

a. Direct application of microcode:

- SB-1: Individual seeds

- SB-2: Seeds used for fatigue and other tests and not modeled
- SB-3/SB-4: Seed clusters not modeled: microcode formulated for single seeds

b. Application of microcode-based regression equations (described in sections C.7 and C.8).

- DZ and HA strain as a function of:

  - Nitrogen content of DZ and HA
  - Forging temperature
  - Forging strain rate
  - Forging macrostrain

Results of the direct application of the microcode to the six seeds in forging SB-1 are shown in figures C-4 and C-5. Figure C-4 shows a comparison of measured deformed DZ size with that predicted by the direct application of the microcode. Data are in all three directions: hoop, axial, and radial. The agreement between measurements and predictions is good for the radial and axial deformations. The hoop deformation is overpredicted due to the two-dimensional (2D) axisymmetric assumption. Some outlying points are identified.

Figure C-5 shows a comparison of measured deformed HA size with that predicted by the direct application of the microcode. Data are in all three directions: hoop, axial, and radial. The agreement between measurements and predictions is good for the radial and axial deformations. The hoop deformation is overpredicted due to the 2D axisymmetric assumption. Some outlying points are identified.

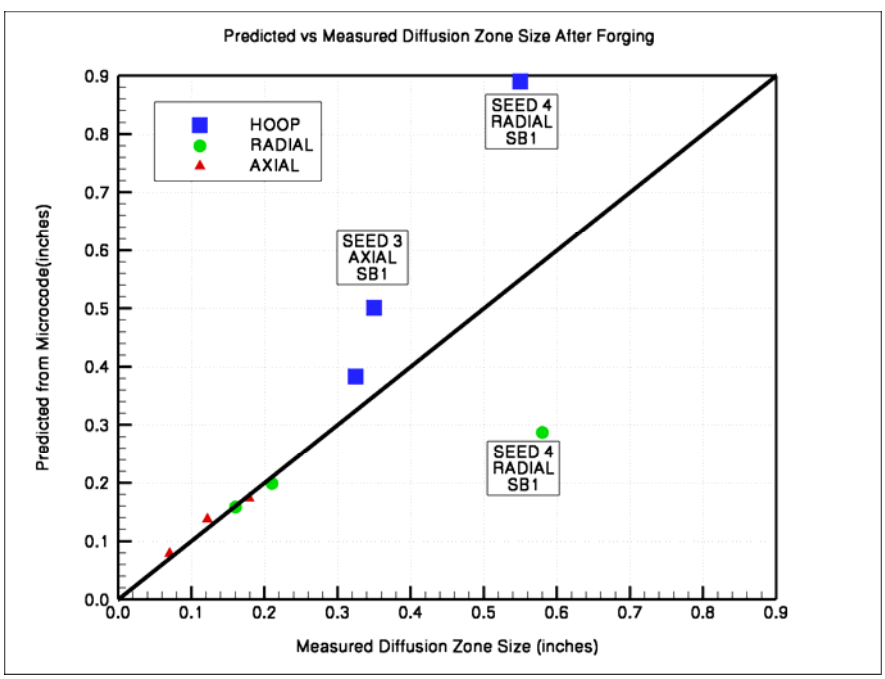

Figure C-4. Comparison of Measured Deformed DZ Size With Predictions From the Direct Application of the Microcode

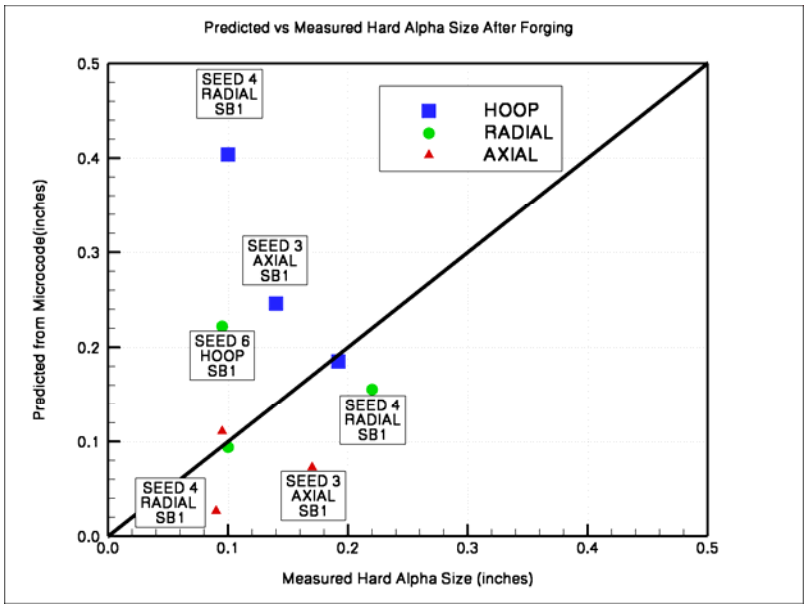

Figure C-5. Comparison of Measured Deformed HA Size With Predictions From the Direct Application of the Microcode

C.5 APPLICATION OF MICROSIMULATION OUTPUT TO ANOMALY DISTRIBUTION.

The deformation microcode is based on a 2D axisymmetric or plane strain model. To more accurately establish the shape of the HA anomaly and the DZ, relationships were generated between the anomaly and DZ deformation and the forging macrostrain, and then these relationships were used to approximate three-dimensional (3D) anomaly deformation in a forging, as shown in figure C-6.

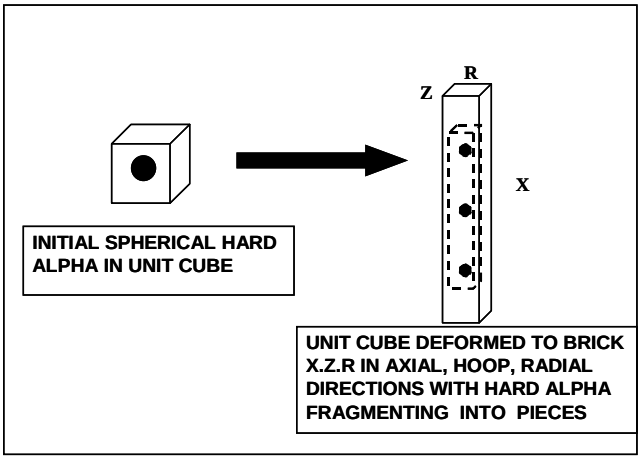

INGOT DIAMETER D1
BILLET DIAMETER D2
X = AXIAL DIMENSION = (D1/D2)**2
R = RADIAL DIMENSION = (D2/D1)
Z = HOOP DIMENSION = (D2/D1)
PRODUCT OF X,R,Z DIMENSIONS = 1
AXIAL STRAIN = ln (D2/D1)**2
RADIAL STRAIN = ln (D1/D2)
HOOP STRAIN = ln (D1/D2)
SUM OF STRAIN COMPONENTS = 0
STRAIN >0 --- TENSION
STRAIN <0 --- COMPRESSION

- Deformation of inclusion is less than base material deformation
- Brick shape surrounding inclusion (dashed lines) is a scaled version of *X, Z, R* (solid lines)
- Regression equations provide these scaling factors
- Regression equations can quickly and accurately predict deformations

Figure C-6. Development of Relationships Between Forging Macrostrain and Inclusion Deformation

Parametric studies with the microcode were performed to evaluate the influence of the following variables on anomaly deformation. All the major variables that influence the deformation of the inclusion were included and are listed in table C-1.

A set of microcode runs was performed with various values of table C-1 variables. The definition of the microvolume used is shown in figure C-7. The runs were defined based on Design of Experiment (DOE) principles to obtain the most information from the fewest number of runs. A full factorial matrix of runs with the end points and with center points was made. A UNIX®-based script file was developed, which automatically set up each run, submitted the simulation, extracted the strain information from the output database, and stored the results in a file compatible for statistical analysis using the software package MINITAB. The finite element mesh consisted of approximately 100 elements in the inclusion, 400 in the DZ and 700 in the base material. Each simulation was completed in 300 time steps with a macrostrain of 0.005 per time step to reach a final macrostrain of 1.5. Each run took about 10 minutes on average on an HP3600 workstation.

Table C-1. Variables Used in Parametric Study

Variable	Variable Name	Two Level and Center Point	
hn	Inclusion N2 content (%)	4, 8	Significant variables
dn	Diffusion zone N2 content (%)	1, 3	
sr	Strain rate (1/sec)	0.1, 1.0	
te	Temperature (°F)	1550, 1750	
sm	Macro forging strain	0.0 - 1.5	
dzh	Diffusion: Inclusion size ratio	2, 4	Insignificant variables
as	Aspect ratio of inclusion	1, 3	
pr	Hydrostatic pressure (ksi)	10, 100	

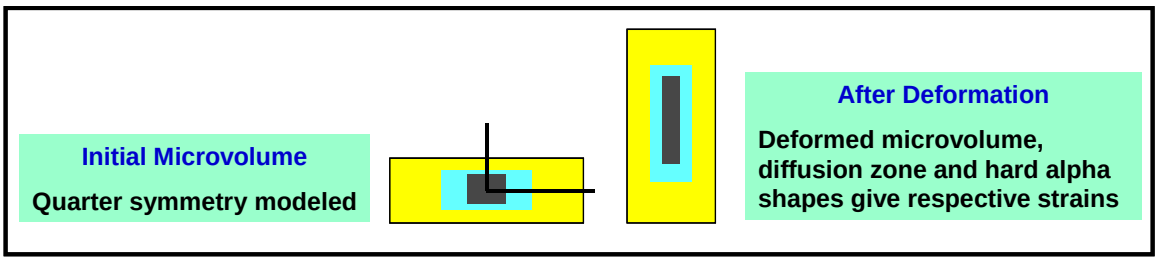

Figure C-7. Definition of Microvolume Used in Parametric Runs

A low value and a high value for each variable were selected to represent the extremes in the variation for that variable, as shown in table C-1. The microcode was run up to a total macrostrain of 1.5, and the inclusion strain was extracted from the output at a total of six intermediate and final values of the macrostrain. A total effective strain of 1.5 corresponds to (a) a diameter reduction of about 47% during ingot conversion (i.e., 20″ diameter reduced to about 10″ diameter) or (b) a height reduction of about 78% during upsetting of a billet (i.e., 10″ high mult reduced to 2.2″ high).

C.6 RESULTS OF PARAMETRIC STUDY.

The influence of the various independent variables on the deformation of the DZ and HA is summarized in table C-2. Based on these results, HA and DZ nitrogen content, forging temperature, strain rate, and macrostrain are the significant variables.

Table C-2. Results of Parametric Study Summarizing the Influence of Various Independent Variables on the Deformation of the DZ and HA

Independent Variables (X's)	Effect of Increasing X	Effect of Increasing X on Deformation of	
		HA	DZ
HA nitrogen content	• Dependence on HA nitrogen content is moderate • HA flow stress is about 25% higher at 8% than at 4% N2 • N2 dependence of the flow stress of failed HA: (55.44 + 4.558n) ksi • Lower HA strain with increasing nitrogen content	Decrease	Increase
DZ nitrogen content	• Dependence on DZ nitrogen content is moderate • DZ flow stress increases with its nitrogen content • Lower DZ strain with increasing nitrogen content • Higher strain imparted to HA with a stronger DZ	Increase	Decrease
Forging strain rate	• Dependence on forging strain rate is significant • Flow stress of the base material is more sensitive to strain rate • As strain rate increases, flow stress of base material increases relative to that of the inclusion and the DZ • Flow stress differential between base material and inclusion decreases with increasing strain rate • Larger HA and DZ strains at higher strain rates	Increase	Increase
Forging temperature	• Dependence on temperature is significant • Flow stress of the base material is more sensitive to temperature • As temperature decreases, flow stress of base material increases relative to that of the inclusion and the DZ • Flow stress differential between base material and inclusion decreases with decreasing temperature • Larger HA and DZ strains at lower temperatures	Decrease	Decrease
DZ to inclusion size ratio	• Inclusion strain increases with size of DZ relative to the inclusion • The larger the DZ, the larger the volume of higher flow stress material • Causes the inclusion to undergo more deformation	Not a significant variable	
Aspect ratio	• No particular trend observed	Not a significant variable	
Hydrostatic pressure	• Very weak pressure dependence • HA flow stress = f(log(pressure)) and has a small influence • Flow stress of HA has a very weak pressure dependence	Not a significant variable	

C.7 REGRESSION ANALYSIS.

As reported previously in TRMD-I, parametric studies with the microcode were performed to evaluate the influence of various processing variables on anomaly deformation. A regression analysis was conducted to obtain the inclusion strain and the DZ strain as a simple linear function of the variables investigated. R^2, which indicated the goodness of fit of the regression equations, was 60.5% for the inclusion strain and 90% for the DZ strain. R^2 values of 90% or greater indicate a good fit.

During TRMD-II, attempts were made to improve the goodness of fit in order to get more accurate predictions. In TRMD-I, only the extreme points were included in the DOE matrix (2**7 = 128 runs with seven variables). Since the TRMD-I results showed little sensitivity with the hydrostatic pressure, this variable was dropped. The regression equations were updated by performing additional DOE runs, including the center points of the independent variables (3**6 = 729 runs with three levels of six variables). The additional runs were included in the DOE matrix with the expectation of improving the goodness of fit R^2. This was, however, not achieved. Considering the nonsmoothness in the inclusion flow behavior with accumulated damage, especially at the higher nitrogen contents, it would be difficult to obtain better accuracy from a simple linear regression equation covering a wide range of the various independent variables.

Therefore, a better regression fit was achieved by including the products of the various independent variables in the regression equations instead of just using the variables themselves. This improved the fit considerably resulting in R^2 values of 97.2% for the inclusion strain and 99.9% for the DZ strain.

Figures C-8 and C-9 show a comparison of the values calculated from the regression equations with the microcode predictions used to generate the regression equations. These figures show that the regression equations provide an accurate representation of the data generated by the microcode. A perfect fit would result in all points lying on the 45-degree line. Here, all the points are clustered around this line with a standard deviation of 0.03116 for the HA strain and 0.01070 for the DZ strain. At low values of strain, the HA flow behavior changes dramatically with accumulated damage, and the goodness of fit is not as good in this region.

The regression coefficients are listed in table C-3. Note here that temperature is normalized by 1000 to keep the values about the same order of magnitude as the other variables.

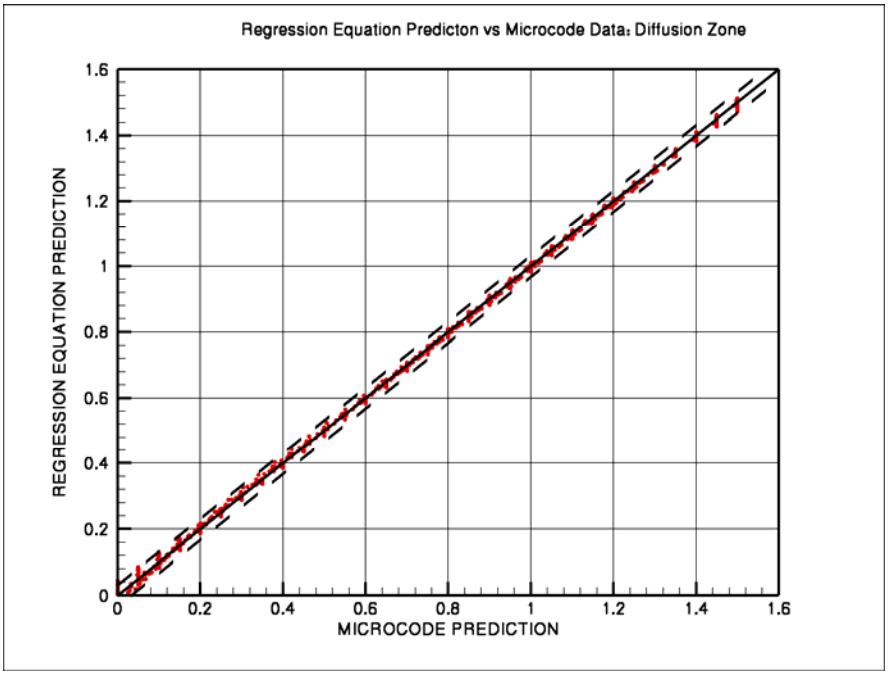

Figure C-8. Comparison of Regression Equation Prediction With Microcode Prediction for the Deformation Strain in the DZ

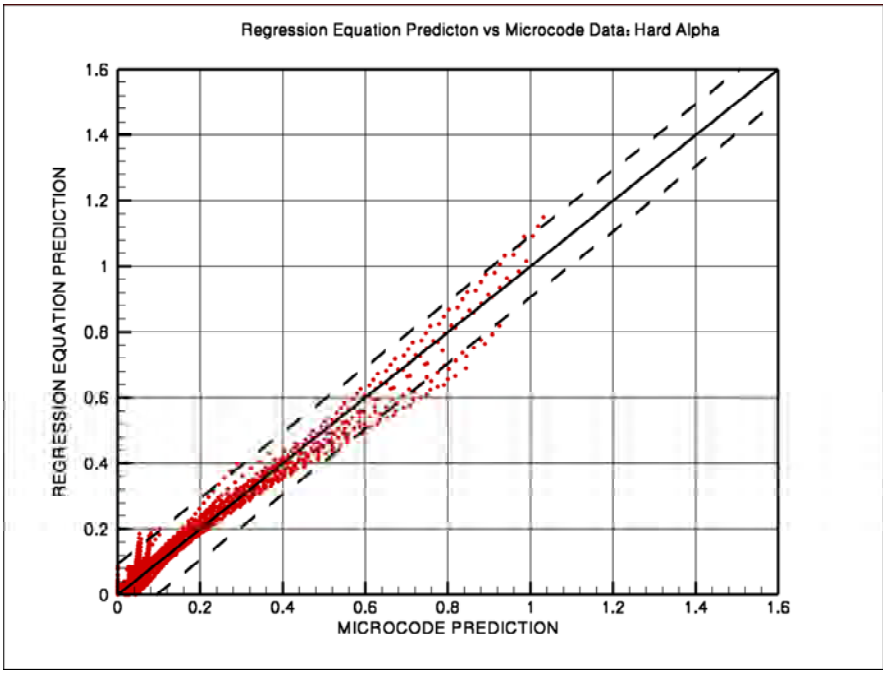

Figure C-9. Comparison of Regression Equation Prediction With Microcode Prediction for the Deformation Strain in the HA

Table C-3. Coefficients in the Regression Equations for the Deformation Strain in the DZ and HA

Diffusion Zone			Hard Alpha			Diffusion Zone			Hard Alpha	
Constant	-9.2672		Constant	-1.622		sr x dn x hn	0.0000003		sr x dn x hn	0.002759
hn	0.01255		hn	0.1546		te x dn x hn	-0.00069		te x dn x hn	-0.002339
dn	-2.9684		dn	0.1874		sm x dn x hn	-0.0001179		sm x dn x hn	0.000218
sr	7.8461		sr	4.8972		sr x sr x hn	-0.000532		sr x sr x hn	0.00421
te	11.1576		te	1.929		te x sr x hn	0.000191		te x sr x hn	0.01228
sm	-13.3307		sm	6.2478		sm x sr x hn	0.0000296		sm x sr x hn	-0.004605
hn x hn	-0.000114		hn x hn	-0.00405		te x te x hn	0.00389		te x te x hn	0.0351
dn x hn	0.000977		dn x hn	0.01013		sm x te x hn	0.002774		sm x te x hn	0.0433
sr x hn	-0.000222		sr x hn	-0.03448		sm x sm x hn	0.0001014		sm x sm x hn	-0.002185
te x hn	-0.01382		te x hn	-0.1539		sr x dn x dn	-0.0001		sr x dn x dn	-0.037244
sm x hn	-0.004442		sm x hn	-0.07066		te x dn x dn	0.02038		te x dn x dn	0.1811
dn x dn	-0.034317		dn x dn	-0.26131		sm x dn x dn	0.001494		sm x dn x dn	-0.029752
sr x dn	-0.05801		sr x dn	0.86273		sr x sr x dn	-0.004898		sr x sr x dn	-0.153171
te x dn	3.7744		te x dn	0.0258		te x sr x dn	0.038535		te x sr x dn	-0.34648
sm x dn	0.10387		sm x dn	0.99355		sm x sr x dn	0.003763		sm x sr x dn	0.069597
sr x sr	0.85969		sr x sr	-2.6345		te x te x dn	-1.19414		te x te x dn	-0.1483
te x sr	-10.0757		te x sr	-5.497		sm x te x dn	-0.078391		sm x te x dn	-0.54659
sm x sr	-0.55024		sm x sr	5.02452		sm x sm x dn	0.00853		sm x sm x dn	0.032648
te x te	-3.3498		te x te	-0.5037		te x sr x sr	-0.51784		te x sr x sr	1.78044
sm x te	19.2221		sm x te	-9.4302		sm x sr x sr	-0.038516		sm x sr x sr	-0.18736
sm x sm	-1.13442		sm x sm	0.98604		te x te x sr	3.215		te x te x sr	1.3852
dn x hn x hn	0.0000045		dn x hn x hn	-0.0001091		sm x te x sr	0.3805		sm x te x sr	-2.92856
sr x hn x hn	0.00004		sr x hn x hn	0.0004235		sm x sm x sr	-0.011002		sm x sm x sr	0.147277
te x hn x hn	0.000049		te x hn x hn	0.00247		sm x te x te	-6.42492		sm x te x te	3.4075
sm x hn x hn	0.0000012		sm x hn x hn	-0.0000102		sm x sm x te	0.75523		sm x sm x te	-0.69242
dn x dn x hn	0.0000376		dn x dn x hn	-0.0015213		sm x sm x sm	-0.034927		sm x sm x sm	0.043631

Variable	Variable Name
hn	Inclusion N2 content (%)
dn	Diffusion zone N2 content (%)
sr	Strain rate (1/sec)
te	Temperature (°F)/1000
sm	Macro forging strain

C.8 VALIDATION OF THE REGRESSION EQUATIONS.

The overall dimensions of the HA seeds and the DZ in the axial, radial, and hoop directions were predicted by application of the regression equations. These values were compared with the measured dimensions. The measured values were recorded for the largest dimensions of the HA and the DZ in these three directions. This was done by evaluating the photographs of the various polished sections. Since the microcode cannot predict cracking and voiding, it was not possible to validate all the details of anomaly deformation. Metallographic data were available for the seeds 1, 3, 4, 6, 13-16, 17-20, 21-24, 29-32, 33-36, and 41-44. The rest of the seeds 2, 5, 7-12, 25-28, and 37-40 were either used for fatigue specimens or other studies.

The regression equations were applied to all the seeds in the synthetically seeded forgings SB-1 to SB-4. Temperature, strain, and strain-rate histories at each of the seed locations were obtained from the model of the forging process using the point-tracking feature in DEFORM. Average values of strain, strain-rate, and temperature over the process were used in the regression equations. Contours of the components of strain in the axial, radial, and hoop directions are shown in figure C-10. Here, negative values indicate compression and positive values indicate tension. The deformation pattern during forging is shown in figure C-11. The figure on the left shows the initial circular pattern in the starting billet. The middle figure shows the deformed pattern in the dogbone forgings SB-1 to SB-3. The figure on the right shows the deformed pattern in the backflow forging SB-4. In all the three figures, the right half of forging shown and the symmetry centerline are on the left edge. The three figures are to different scales.

Figure C-12 shows a comparison of the measured deformed DZ size with that predicted by the regression equations. Data are from all seeds that were cut up. Data are in all three directions: hoop, axial, and radial. Figure C-13 shows the same data as figure C-12, but expressed as the ratio of predictions to measurements on the y axis. Overall, the agreement between measurements and predictions is good. There are some outlying points. The DZ flows smoothly like the base material, but with a higher flow stress, and therefore, the predictions match the measurements well.

Figure C-14 shows a comparison of the measured deformed HA size with that predicted by the regression equations. Data are from all seeds that were cut up. Data are in all three directions: hoop, axial, and radial. Figure C-15 is a zoomed-in view of figure C-14. Figure C-16 shows the same data as figure C-14, but expressed as the ratio of predictions to measurements on the y axis. Overall, the agreement between measurements and predictions is good. There are some outlying points. The flow of HA is discontinuous (depending on when failure occurs with accumulated damage/strain) and therefore, the agreement between the measurements and predictions is not as good as that for the DZ deformation.

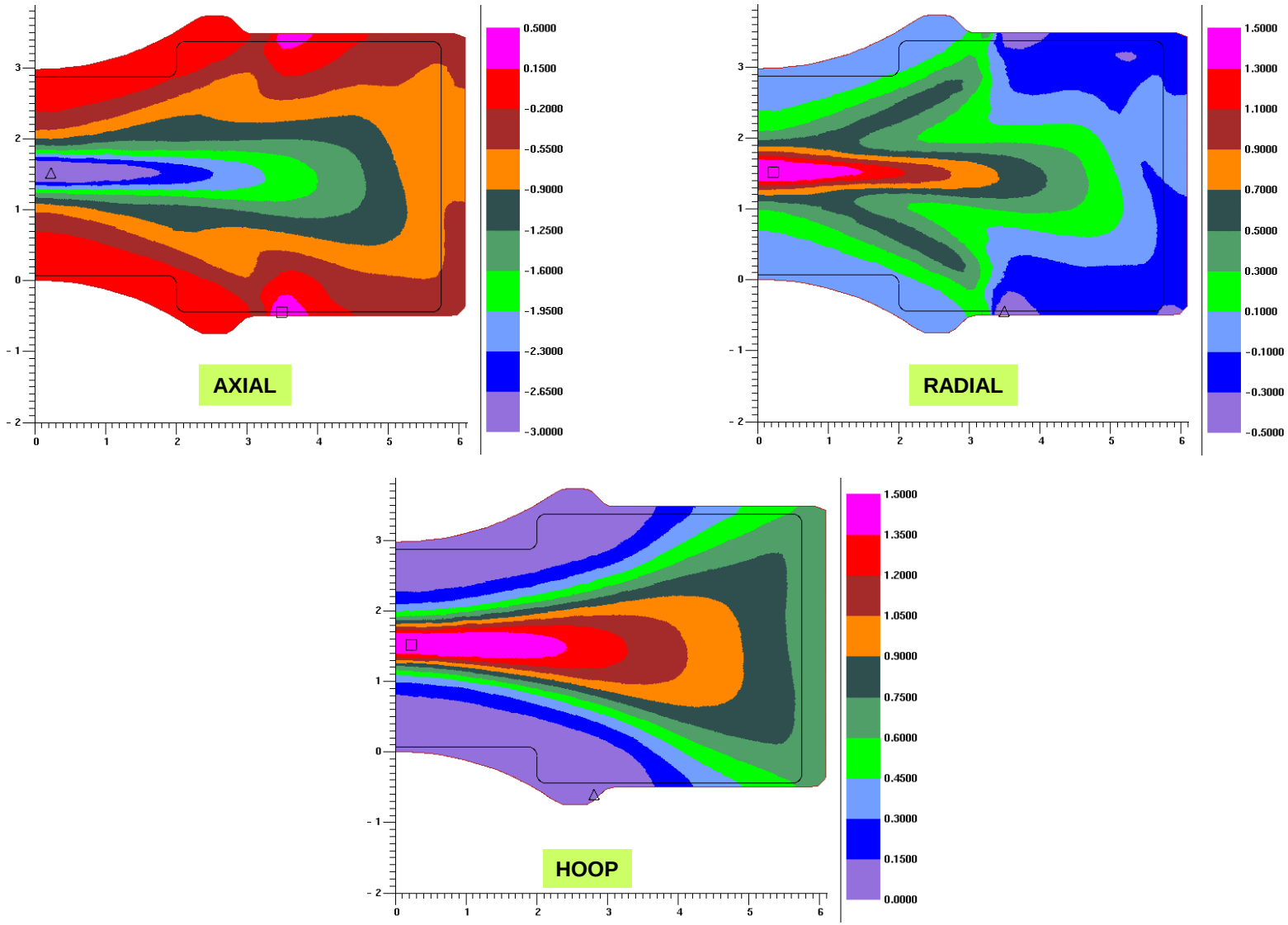

Figure C-10. Axial, Radial, and Hoop Strain Components in Forgings SB-1 to SB-3

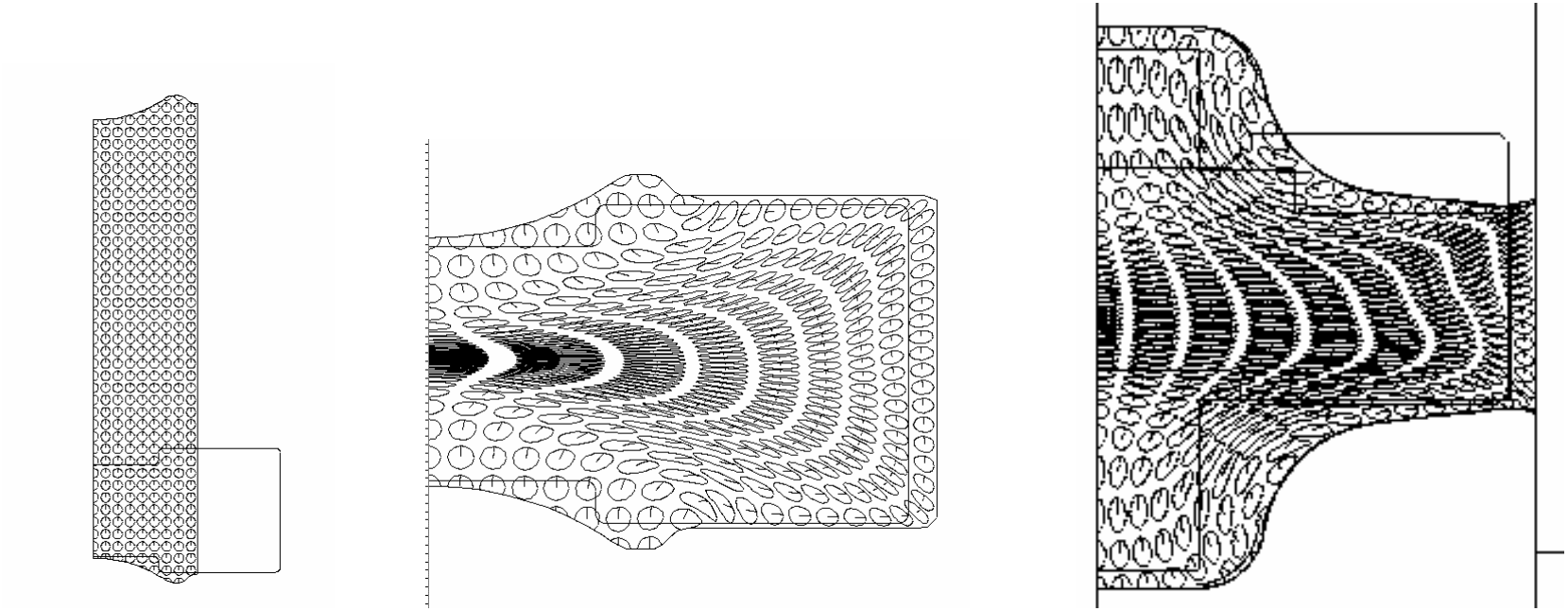

Figure C-11. Graphical Display of Overall Deformation and Orientation

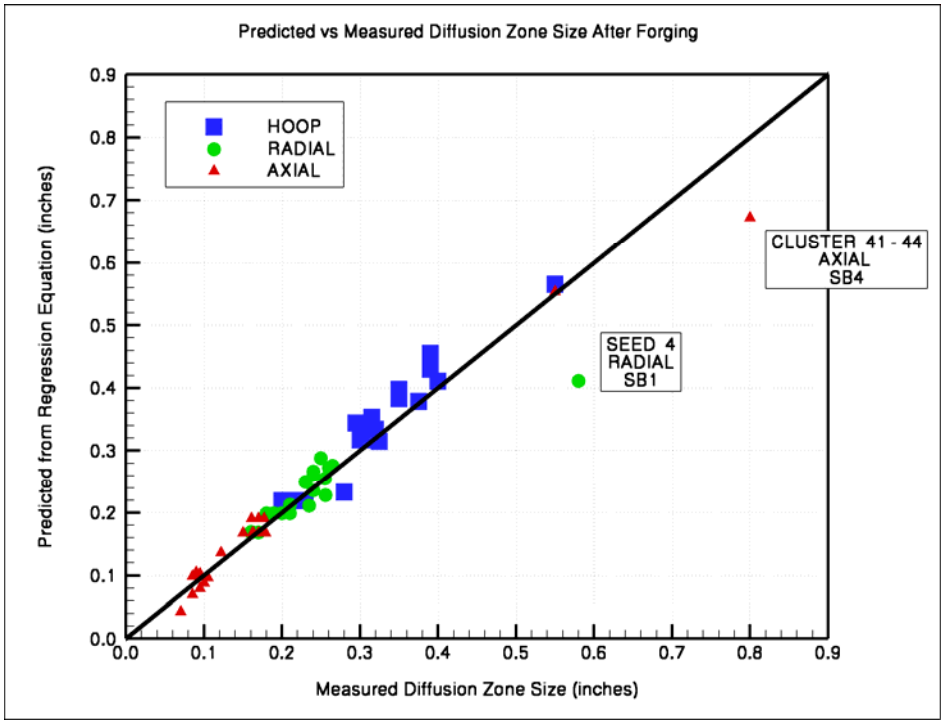

Figure C-12. Comparison of Measured Deformed DZ Size With That Predicted by the Regression Equations

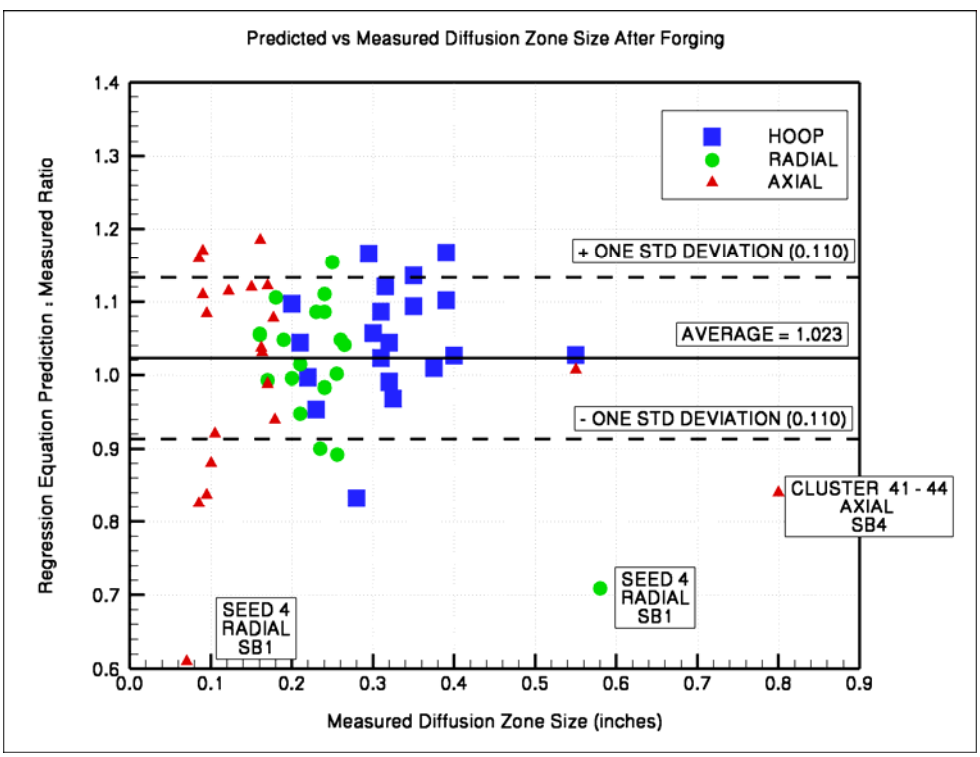

Figure C-13. Comparison of Measured Deformed DZ Size With That Predicted by the Regression Equations (Normalized)

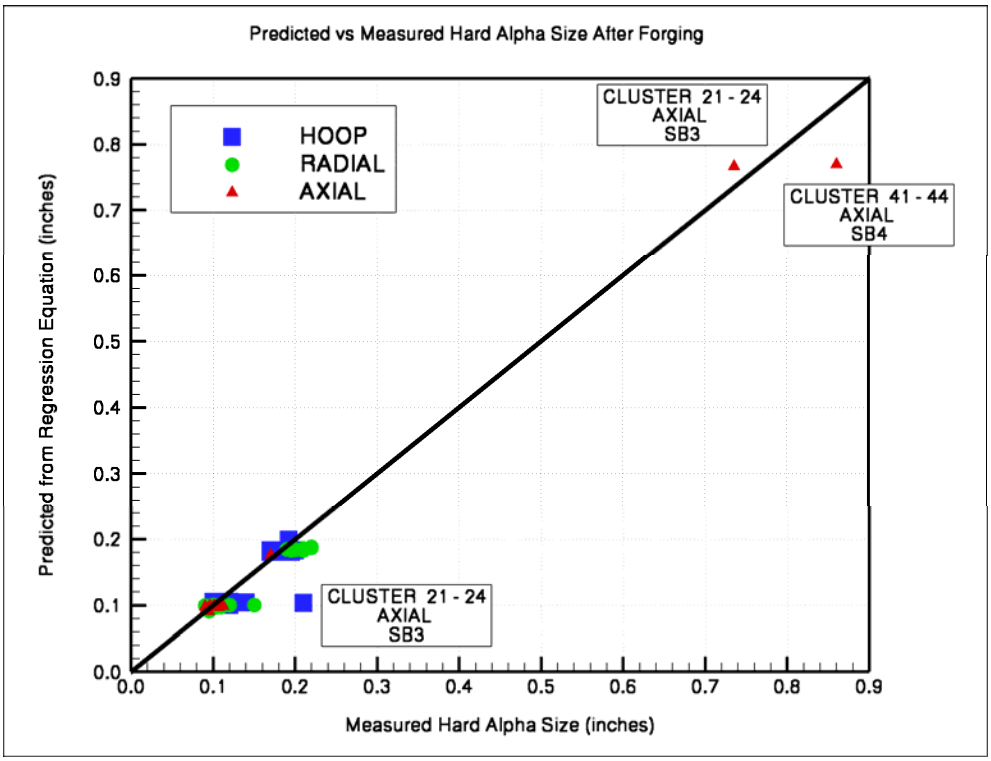

Figure C-14. Comparison of Measured Deformed HA Size With That Predicted by the Regression Equations

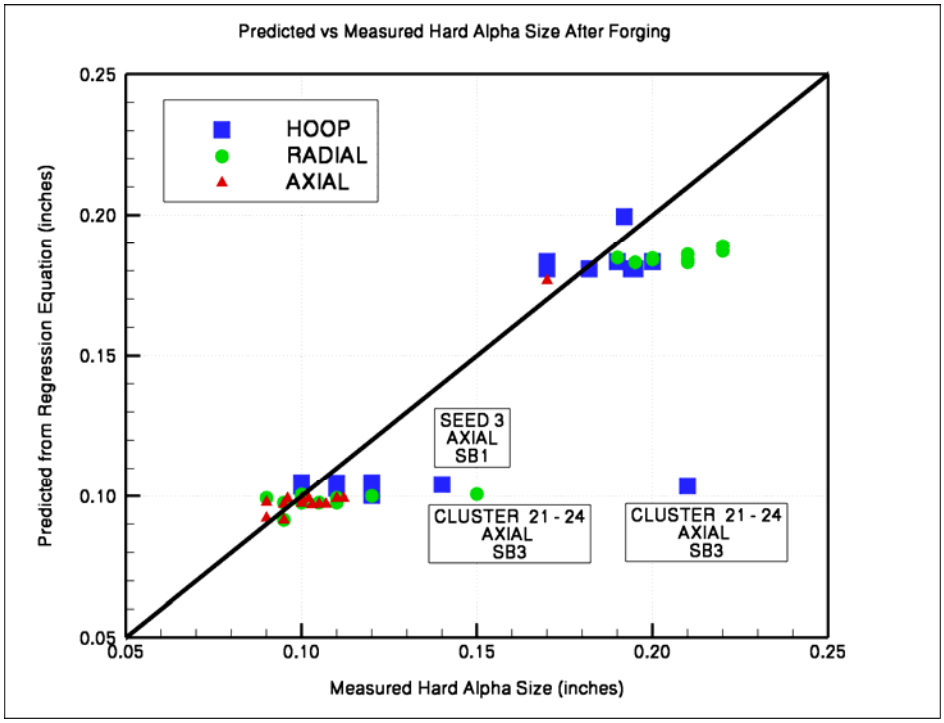

Figure C-15. Zoomed-In View of Figure C-14—Comparison of Measured Deformed HA Size With That Predicted by Regression Equations

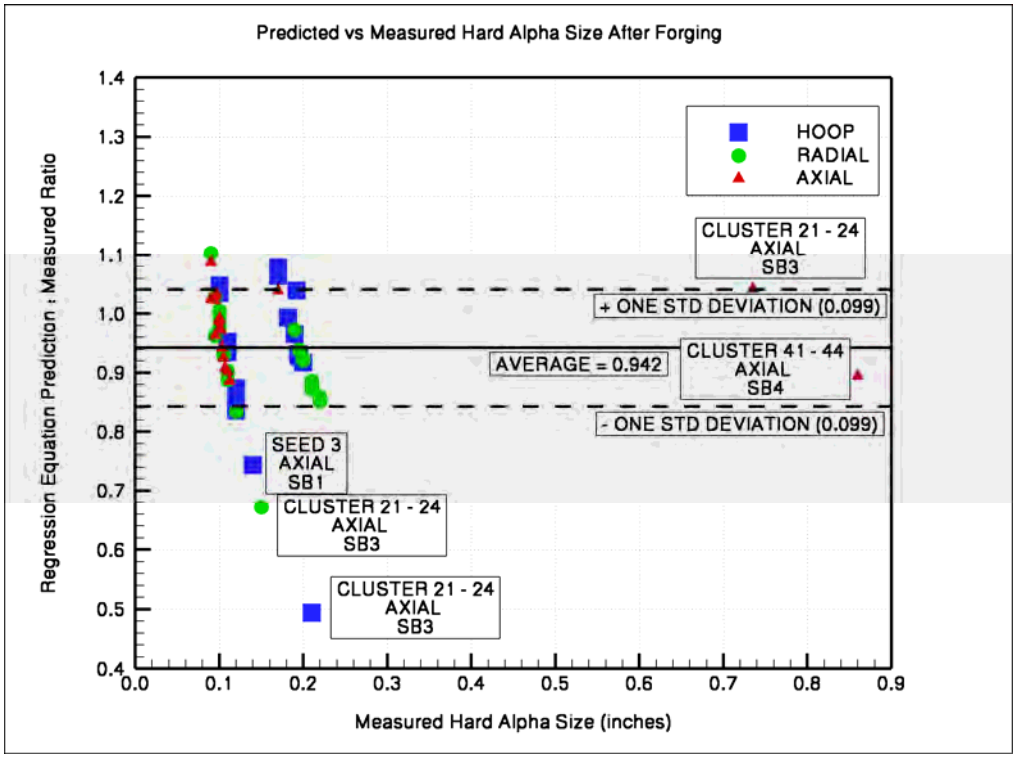

Figure C-16. Comparison of Measured Deformed HA Size With That Predicted by the Regression Equations (Normalized)

C.9 ASSESSMENT OF PREDICTIONS.

The overall predicted deformed shapes have been compared with measurements without looking at the details of fragmentation and voiding. In some cases, the predictions from a direct application of the microcode are in better agreement with the measurements. In other cases, the regression equations are better. The differences between the two can be summarized as:

a. Microcode:

- Treats seed as 2D axisymmetric: ring anomaly over 360 degrees.
- Overpredicts hoop deformation; underpredicts radial/axial deformation.
- Deformation is 3D, which cannot be accurately predicted by 2D methods.

b. Regression equations:

- Use the individual strain components scaled appropriately.
- Do not force the anomaly to be a full 360 degrees.
- Capture the 3D behavior more accurately than the microcode itself.

- Cracked versus noncracked like a step function that is difficult to fit with regression.

- Except for some isolated points, predictions agree reasonably well with measurements.

The reasons for the discrepancies between the predictions and the measurements are:

- Nonsmooth HA flow behavior with accumulated damage, especially at high N2 content.
- A wide range of the various independent variables fitted into a regression equation.
- Inaccuracies in the constitutive property data obtained from a small number of tests.
- Data smoothened and fitted into constitutive equation.
- Cracking and voiding in HA not captured.
- Seeds may be precracked.

The application of the microcode to each individual seed is more involved, and the use of the regression equations is the preferred way of predicting seed behavior. Overall, the results from the regression equations are satisfactory. To further assess the accuracy of the regression equation predictions and obtain error bounds, a sensitivity analysis was performed.

C.10 SENSITIVITY ANALYSIS.

A sensitivity analysis was performed to assess the error bounds in the predictions due to uncertainties in the input variables in the regression equations. The estimated errors in inputs, based on typical forging practices are:

1. HA nitrogen content: $\pm$1%
2. DZ nitrogen content: $\pm$0.25%
3. Deformation strain rate: $\pm$0.05/sec
4. Forging temperature: $\pm$25°F
5. Forging macrostrain: $\pm$0.05

The regression equations were applied to each seed for the nominal conditions and for the above variations in the five input variables for a full factorial DOE of $2^5 = 32$ cases. The error bounds in the predicted deformed dimensions are shown in figures C-17 through C-22 for both the DZ and the HA for deformation in the three directions, hoop, radial, and axial. The average and standard deviation were calculated for the ratio of predicted to measured deformed dimensions and are summarized in table C-4. These values were calculated in two ways: (a) considering all the 32 runs and (b) ignoring the runs with scatter points (ratio <0.8 or >1.2).

The DZ deformation is overpredicted on average by ~ 3% with a standard deviation of ~10%. The HA deformation is underpredicted on average by ~ 5% with a standard deviation of ~ 8%.

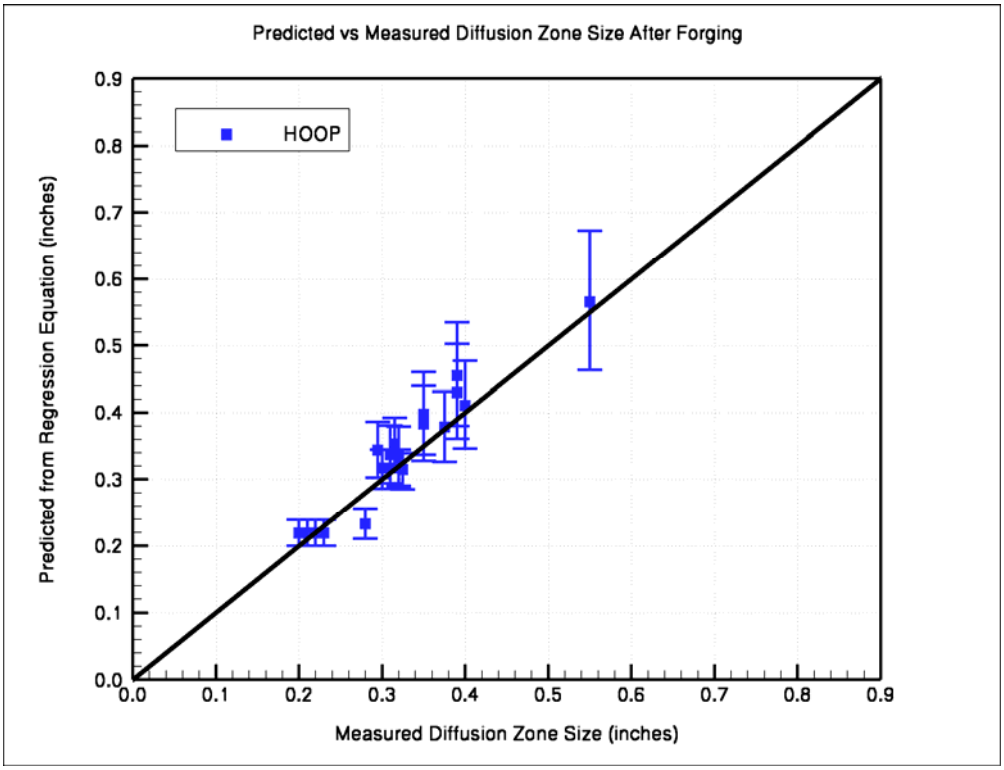

Figure C-17. Results of Sensitivity Analysis for Deformed DZ Size in the Hoop Direction

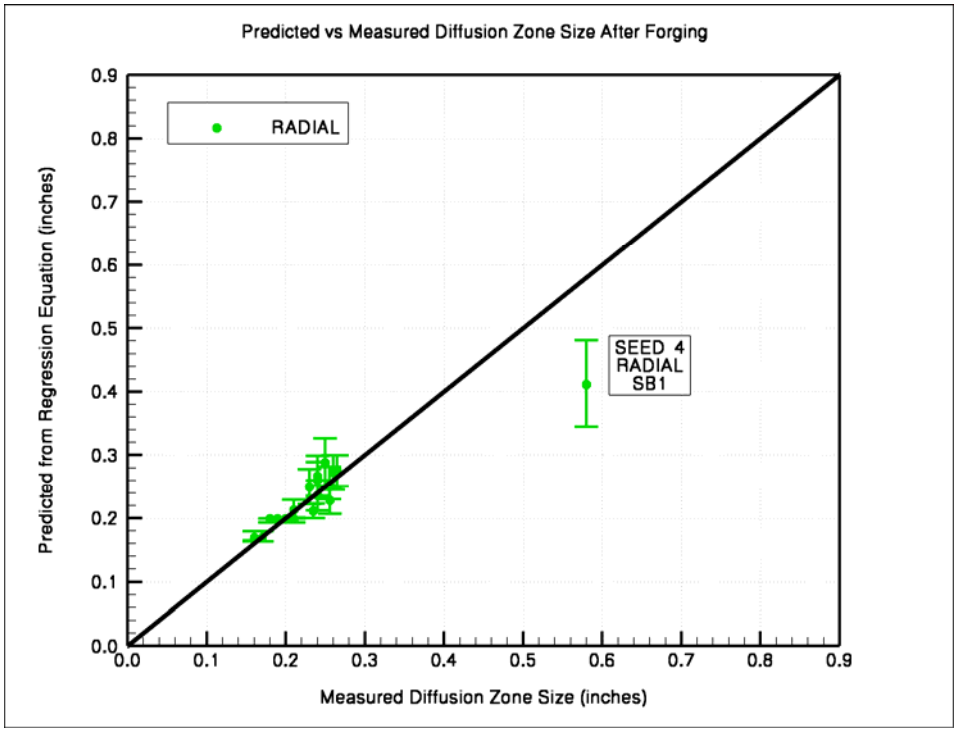

Figure C-18. Results of Sensitivity Analysis for Deformed DZ Size in the Radial Direction

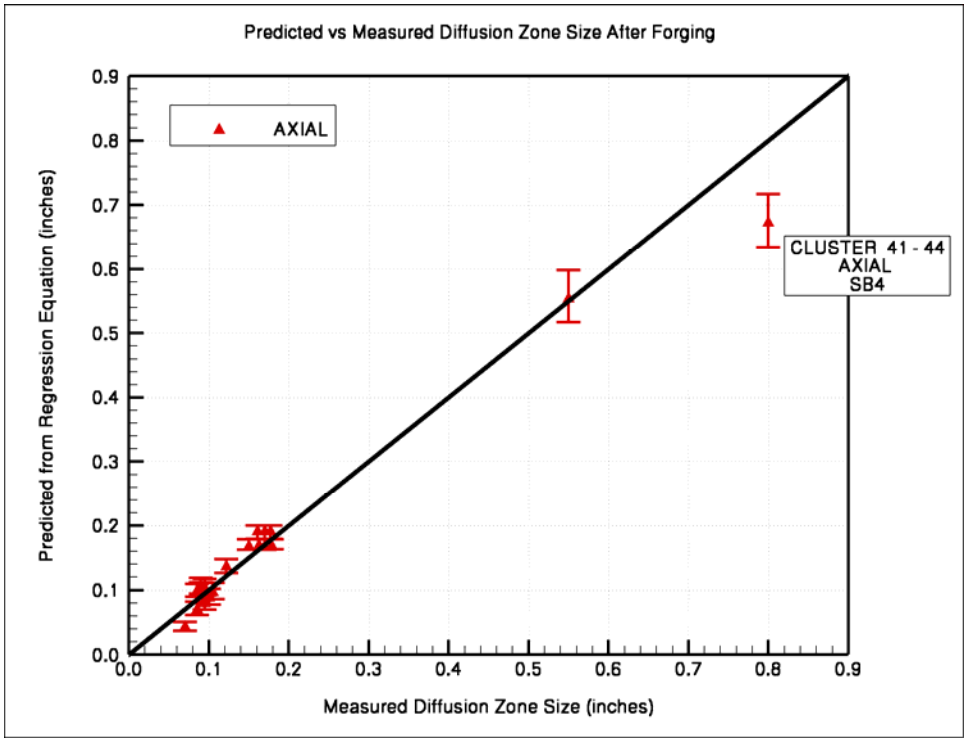

Figure C-19. Results of Sensitivity Analysis for Deformed DZ Size in the Axial Direction

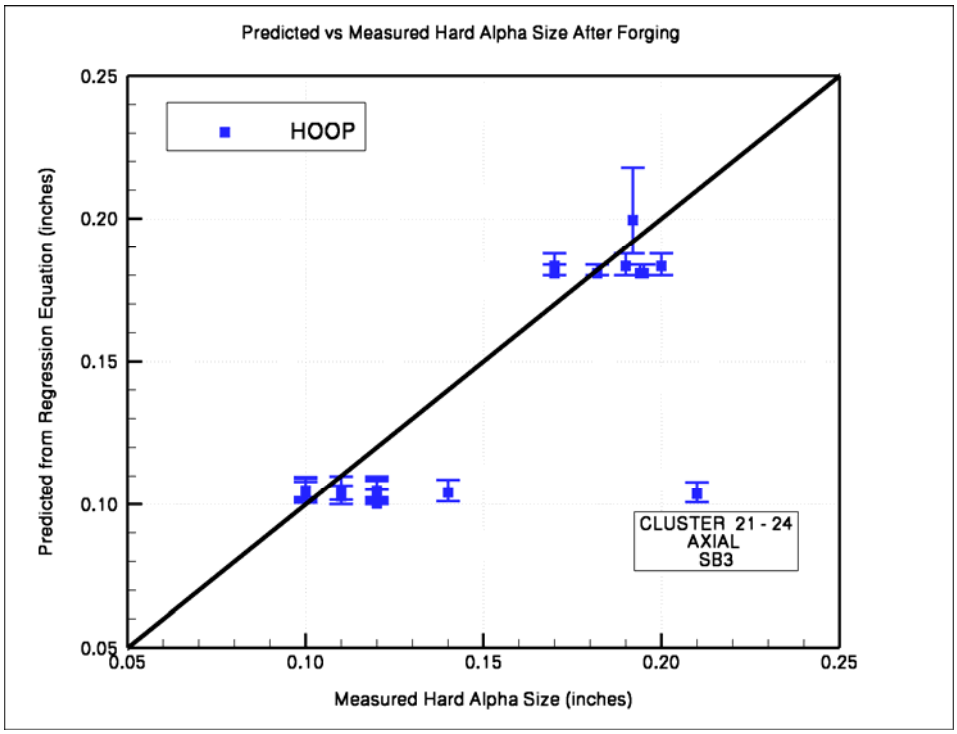

Figure C-20. Results of Sensitivity Analysis for Deformed HA Size in the Hoop Direction

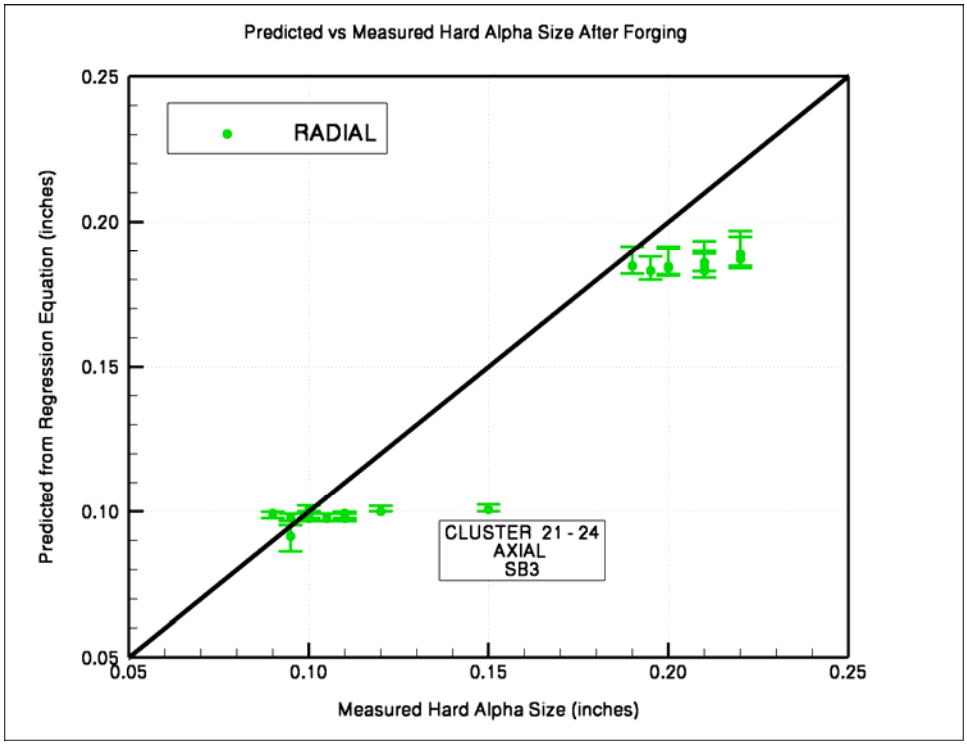

Figure C-21. Results of Sensitivity Analysis for Deformed HA Size in the Radial Direction

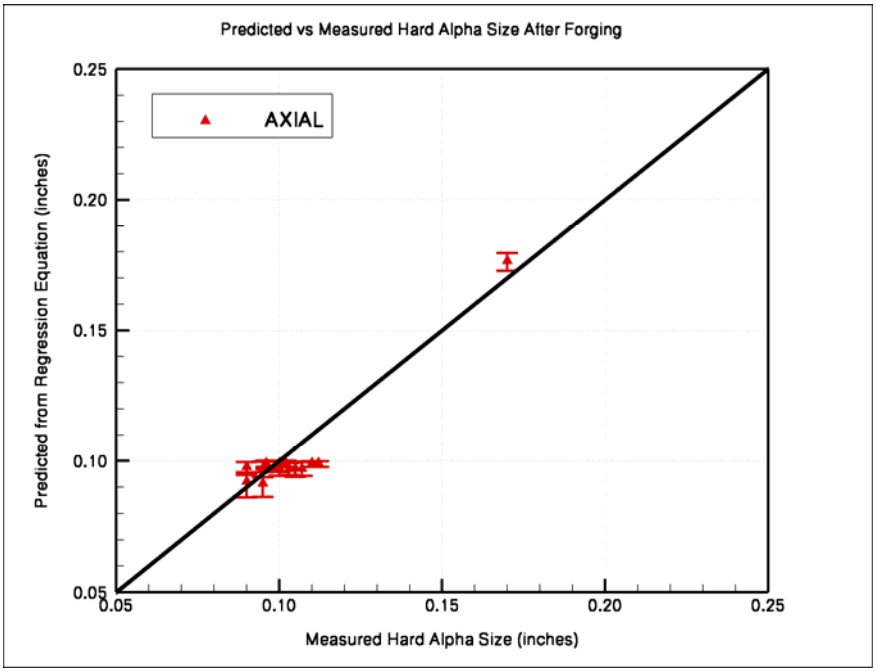

Figure C-22. Results of Sensitivity Analysis for Deformed HA Size in the Axial Direction

Table C-4. Results of Sensitivity Analysis

Deformation	Data From All 32 Runs for Each Seed		Ignoring Scatter Point (<0.8 and >1.2)	
	Average	Standard Deviation	Average	Standard Deviation
Diffusion Zone	1.023	0.110	1.035	0.089
Hard Alpha	0.942	0.099	0.958	0.070

C.11 SYNTHETIC VS NATURAL HA.

The microcode has been validated successfully for synthetic seeds. Validation still needs to be done for naturally occurring HA seeds. The main differences between natural and synthetic HA are shown in table 5.

Table C-5. Natural vs Synthetic HA Characteristics

Natural HA	Synthetic HA
Random size	Controlled size
May be prevoided	Not prevoided
Random nitrogen content	Known nitrogen content
Random Was Beta ratio	Controlled Was Beta ratio
Unknown fragmentation	Documented fragmentation
Unknown reconstitution	Known reconstitution
Uncertain ultrasonic signal response	Known seed physical parameter

Based on the formulation of the microcode, it can be surmised that:

- If the initial location and orientation in the billet can be ascertained by ultrasonic inspection, the final location and orientation can be predicted with reasonable confidence.

- If the initial size can be ascertained by ultrasonic inspection, the final size can be predicted with reasonable confidence for the DZ, but less accurately for the HA.

- Unknowns like prevoiding, fragmentation, and reconstitution will influence the deformation of the HA nugget.

- Because all inputs are not known, a probabilistic Monte Carlo analysis is needed.

The characterization of the following three anomalies, two of which are natural, has also been completed:

- B1BW3B Naturally Seeded Specimen
- B3W2E Naturally Seeded Specimen

- SB-6 Artificially Seeded Specimen

These anomalies are from Pratt & Whitney (P&W) forgings, and the forging conditions are proprietary information. The detailed deformation characteristics of these three seeds have been provided to P&W for their independent assessment of the accuracy of the microcode predictions.

C.12 CONCLUSION.

A microcode was developed and validated to predict the overall size and orientation of hard alpha (HA) anomalies without voiding/cracking. The Design of Experiment (DOE)-based runs were used to develop a correlation between the forging induced macrostrain and the inclusion deformation. The agreement between the measurements and predictions was reasonably good; it was better for the diffusion zone than for the HA deformation.

Performing several microsimulations to evaluate inclusion behavior in various zones of a forging for lifing calculations is time-consuming. The relationships developed here provide a simplified procedure that can translate microcode output as input to Design Assessment of Reliability With INspection (DARWIN®). The simplified procedure keeps the computational effort manageable without sacrificing accuracy.

After the forge modeling of the component forging is completed, the forging macrostrain components in the three directions are available throughout the forging. These strain components can be converted to equivalent inclusion strain components using the relationships developed here. The inclusion strains can then be used to modify the anomaly distribution to be used in lifing analysis. This results in an approximation of the three-dimensional (3D) anomaly deformation in a forging from a two-dimensional (2D) micromodel and enables the microcode output to be input into DARWIN in a simplified but accurate manner. This provides zone dependent scaling factors to the anomaly distribution based on macrodeformation modeling of the component forging process. With this procedure, the need for running the micromodel for each individual point in the forging with different strain components is avoided, and this significantly reduces the required effort. The regression equations developed here can be used with DEFORM™ 2D or 3D output for billet conversion and for component forging.

The microcode methodology developed here is applicable to other anomalies in other alloys provided appropriate constitutive property data are generated.

APPENDIX D—SUMMARY OF ENGINE COMPANY INSPECTION RESULTS FOR SEEDED AND CBS MULTS, PANCAKES, AND DISK FORGINGS FROM TRMD PHASE I PROGRAM

During the Turbine Rotor Material Design (TRMD) Phase I program, forging experiments were conducted to evaluate the relative detectability of hard alpha inclusions in billets versus forgings. These forgings included dogbone and backflow parts that were forged at Schlosser Forge Company using hot-die techniques and pancake and engine disks that were forged at Pratt & Whitney (P&W) Georgia using isothermal press forging.

The Engine Titanium Consortium (ETC) provided inspection results for the RMI Titanium Co. for the contaminated billet study (CBS). Initial TRMD-I program plans only called for GE Aviation inspections of the seeded billets (SB), pancakes, and disks and the CBS pancakes and disks and those inspection results were included in the TRMD-I final report. However, Honeywell, P&W Florida, P&W Georgia, and Rolls-Royce Corporation also voluntarily performed additional inspections of the pancake and disk forgings as program enhancements using company funding. The full compilation of inspection results from the different companies includes a combination of production and laboratory inspections, as well as standard ultrasonic, multizone, and shear wave inspections.

Since these supplementary inspections were not in the initial program plan and conclusions from the ETC had not been received at the time, it was agreed to include only the planned GE inspections in the TRMD-I final report. After further consideration, the TRMD Steering Committee had agreed to document all of the inspection results under the TRMD-II program to preserve these additional results for future reference by the industry team. Conclusions regarding this data are being deferred to the ETC.

Tables D-1 through D-4 include a complete set of inspection results for the seeded and CBS mults, pancakes, and disk forgings from the TRMD-I program. To place the focus on the data and not on the individual companies contributing inspections, the company names have been removed from the tables. Forgings SB6, B1BW3B, and B3W2E were spin tested during the TRMD-II program and received additional interim ultrasonic inspections during the course of the spin testing. Figure D-1 illustrates the inspection surfaces for the disk forgings, and the results of the interim inspections during spin testing have been added as well.

Table D-1. Billet Inspection Results for Mults Targeted for Pancake and Disk Forgings

			Billet Conventional					Billet Phased Array					Billet Multizone				
Sample ID	Ind. #	Company	Depth	Axial Position	% of #3 FBH	% of #2 FBH	S/N	Zone	Axial Position	Radial Depth	% of #2 FBH	S/N	Zone	Axial Position	Radial Depth	% of #2 FBH	S/N
SB-5	45	A	N/I					N/I					2	1.6	1	130	7.4
		C	N/I					3		1.2	95	5.8	N/I				
	46	A	N/I					N/I					1	1	0.7	84	8.1
		C	N/I					2		0.8	80	4.8	N/I				
	47	A	N/I					N/I					3	4	1.8	72	6.4
		C	N/I					4		2	92	5.3	N/I				
	48	A	N/I					N/I					2	4	1	110	6.8
		C	N/I					3		1.3	87	5.2	N/I				
SB-6	49	A	N/I					N/I					2	1	1	109	5.5
		C	N/I					3		1.2	96	7.3	N/I				
B1BW3-B	1	A			N/D			N/I					2	1.695	1	200	7.6
		E		N/D, FBH size not reported				N/I						160%, FBH size not reported			
B3W2-E	1	A	1	2.2	92	*207*	4.5	N/I					2	2.2	1.3	266	12.5
		E		74%, FBH size not reported				N/I						213%, FBH size not reported			
B3W2-G	1	A	1.5	2.2	100	*225*	?	N/I					2	2.2	1.3	177	5.9
		E		N/D, FBH size not reported				N/I						142%, FBH size not reported			

Axial locations for B1BW3B, B3W2E, and B3W2G are locations identified for cutting after inspections were completed.
N/I = Not Inspected
N/D = Not Detected
Inspection amplitudes in underlined italics were calculated, not measured.

Table D-2. Pancake Forging Inspection Results From the TRMD-I Program

PANCAKE				Forging Conventional										Forging Multizone			
Sample ID	Ind. #	Side	Company	10 MHz - Zone	Depth	% of #2 FBH	% of #1 FBH	S/N	5 MHz - Zone	Depth	% of #2 FBH	% of #1 FBH	S/N	10 MHz- Zone	Depth	% of #1 FBH	S/N
SB-5	45	A	A	1	0.3	57	*228*	6.1	2	0.5	240	*960*	6.5	1	0.4	177	16.2
			B		0.35	*56*	224		N/I					N/I			
		B	A	N/D					2	2.9	200	*800*	5	6	3	490	71.7
		OD	B		1.6				N/I					N/I			
	46	A	A	1	0.3	87	*348*	8.2	N/D					2	0.4	151	18.5
			B		0.25	*62.75*	251		N/I					N/I			
		B	A	N/D					2	3	331	*1324*	14.1	6	3	467	18.6
		OD	B		1				N/I					N/I			
	47	A	A	1	1.2	60	*240*	6.2	2	1.2	223	*892*	7.4	3	1.4	229	17.7
			B		1.25	*70.5*	282		N/I					N/I			
		B	A	N/D					2	2.1	240	*960*	9	6	2.1	741	15.8
		OD	B		2				N/I					N/I			
	48	A	A	1	1.1	147	*588*	11.5	2	1	275	*1100*	6.2	3	1	301	25.4
			B		1.1	*140.5*	562		N/I					N/I			
		B	A	N/D					2	2.3	129	*516*	3.9	5	2.3	446	125
		OD	B		0.85				N/I					N/I			
SB-6	49	A	A	1	0.4	40	*160*	5.2	2	0.5	122	*488*	1.7	2	0.5	122	17.5
			B		0.4				N/I					N/I			
		B	A	N/D					2	2.9	121	*484*	2.6	6	2.9	416	29.3
		OD	B		1.65	*31.25*	125		N/I					N/I			
B1BW3-B	1	A	A	1	0.4	40	*160*	2.2	N/D					1	0.4	87	12.8
			B		0.4	*28*	112		N/I					N/I			
			C	1	0.37	*25*	100		N/R					N/I			
		B	A	N/D					2	3	64	*256*	2	6	3	72	6.5
			B			*12.5*	50		N/I					N/I			
			C	N/R					2	3	*25*	100		N/I			
		OD	B		1.5	*88.75*	355		N/I					N/I			
B3W2-E	1	A	A	1	0.6	15	*60*	2.4	2	0.6	64	*256*	1.8	2	0.6	51	7.6
			B		0.6	*17.5*	70		N/I					N/I			
			C	1	0.58	*14.75*	59		N/R					N/I			
		B	A	N/D					2	2.9	41	*164*	1.3	6	2.8	65	11.4
			B			*25*	100		N/I					N/I			
			C	N/R					2	2.88	*25*	100		N/I			
		OD	B		1.5	*28*	112							N/I			
B3W2-G	1	A	A	1	0.6	31	*124*	4.4	2	0.6	49	*196*	8	2	0.6	177	11.6
			B		0.6	*25*	100		N/I					N/I			
			C	1	0.6	*25*	100		N/R					N/I			
			D	N/I					0.6588		*64**	*256**	11	N/I			
		B	A	N/D					2	2.8	28	*112*	2.5	6	2.8	56	7.3
			B			*62.75*	251		N/I					N/I			
			C	N/R					2	2.84	*62.5*	250		N/I			
			D	N/I						2.9	*57**	*228**	7	N/I			
		OD	B		1.75	*70.5*	282		N/I					N/I			

N/D = Not detected.
N/I = Not inspected
N/R = Not reported (don't know if this inspection was completed).
Inspection amplitudes in underlined italics are calculated values, not measured.
*** Company D inspection amplitudes were reported on the basis of a 0.025" FBH. Calculated equivalents are shown.**

Table D-3. SB-5 Disk Forging Inspection Results From the TRMD-I Program

DISK				Forging Conventional - 10 MHz				Forging Conventional - 5 MHz				Forging Multizone		
Sample ID	Ind. #	Side	Company	Depth	% of #1 FBH	% of #2 FBH	SNR	Depth	% of #1 FBH	% of #2 FBH	SNR	Depth	% of #1 FBH	S/N
SB-5	45	A	A	0.18	*172.4*	43.1	7.54		N/I	outside range		0.18	169.8	39.06
				0.18	173.75	*43.4375*	13.95		N/I	N/I			N/I	
			B	0.2	224	*56*	N/R		N/I	N/I			N/I	
			C	0.184	224	*56*	N/R		N/I	N/I			N/I	
		B	A	0.401	*188*	47	11.25		N/I	outside range		0.401	223.8	61.86
				0.401	245	*61.25*	13.46		N/I	N/I			N/I	
			B	0.4	355	*88.75*	N/R		N/I	N/I			N/I	
			C	0.23	N/I				N/I	N/I			N/I	
		C	B	1	501	*125.25*	N/R		N/I	N/I			N/I	
	46	A	A	0.08	*388*	97	24.25	0.08	N/I	outside range		0.08	257	48.75
				0.08	275	*68.75*	41.84		N/I	N/I			N/I	
			B	0.15	251	*62.75*	N/R		N/I	N/I			N/I	
			C	0.078	316	*79*	N/R		N/I	N/I			N/I	
		B	A	1.123	*62.4*	15.6	2.6	1.123	*35*	8.75	2.6	outside range		
				1.123	131.25	*32.8125*	7.15		N/I	N/I			N/I	
			B	1	141	*35.25*	N/R		N/I	N/I			N/I	
			C	1.01	N/I		N/R		N/I	N/I			N/I	
		C	B	0.8	224	*56*	N/R		N/I	N/I			N/I	
	47	A	A	1.475	*451.2*	112.8	20.45	1.475	*350*	87.5	9.55	1.475	388.8	60.59
					N/D				N/I	N/I			N/I	
			B	1.5	501	*125.25*	N/R		N/I	N/I			N/I	
			C	1.5	350	*87.5*	N/R		N/I	N/I			N/I	
		B	A	0.263	*223.2*	55.8	13.5		N/I	outside range		0.263	190.5	28.74
				0.263	162.5	*40.625*	26.59		N/I	N/I			N/I	
			B	0.25	251	*62.75*	N/R		N/I	N/I			N/I	
			C	0.19	N/I		N/R		N/I	N/I			N/I	
		C	B	0.5	355	*88.75*	N/R		N/I	N/I			N/I	
	48	A	A	0.375	*188*	47	5.75		N/I	outside range		0.375	141.3	23.72
				0.375	131.75	*32.9375*	28.65		N/I	N/I			N/I	
			B	0.4	355	*88.75*	N/R		N/I	N/I			N/I	
			C	0.383	178	*44.5*	N/R		N/I	N/I			N/I	
		B	A	1.8	*316*	79	15.6	1.8	*294*	73.5	15.9	1..8	23.5*	4.4*
					outside range				N/I	N/I			N/I	
			C	1.76	N/I		N/R		N/I	N/I			N/I	
		D	B	1.1	316		N/R		N/I	N/I			N/I	

N/I = Not Inspected
N/R = Not Recorded
N/D = Not Detected
Company A completed multiple inspections for each side. Only 1 depth was reported for all Company A inspections.
* Zone 3 transducer used instead of Zone 4 for indication 48 bore multizone inspection
Inspection amplitudes in underlined italics are calculated values, not measured.

Table D-4. Disk Forging Inspection Results From the TRMD-I Program

DISK				Forging Conventional - 10 MHz				Forging Conventional - 5 MHz				Forging Multizone		
Sample ID	Ind. #	Side	Company	Depth	% of #1 FBH	% of #2 FBH	SNR	Depth	% of #1 FBH	% of #2 FBH	SNR	Depth	% of #1 FBH	S/N
SB-6	49	A	A	0.45	*152.4*	38.1	8.11		N/I	outside range		0.45	137.5	31.45
				0.45	195	*48.75*	14.45		N/I	N/I			N/I	
			B	0.5	251	*62.75*	N/R		N/I	N/I			N/I	
			C	N/R	141	*35.25*	N/R		N/I	N/I			N/I	
		B	A	0.32	*188*	47	15		N/I	outside range		0.32	173.8	82
				0.32	190.5	*47.625*	11.88		N/I	N/I			N/I	
			B	0.25	251	*62.75*	N/R		N/I	N/I			N/I	
			C	N/R	224	*56*	N/R		N/I	N/I			N/I	
		C	B	0.9	355	*88.75*	N/R		N/I	N/I			N/I	
			C	N/R	140	*35*	N/R		N/I	N/I			N/I	
B1BW3-B	1	A	A			N/D			N/I	outside range		0.24	66.6	10.8
				0.24	47	*11.75*	1.9		N/I	N/I			N/I	
			B	0.25	63	*15.75*	N/R		N/I	N/I			N/I	
			C	N/R	50	*12.5*	N/R		N/I	N/I			N/I	
		B	A			N/D		0.58	*266.4*	66.6	14.3	0.58	107.8	12.37
				0.58	82.25	*20.5625*	2.88		N/I	N/I			N/I	
			B	0.5	100	*25*	N/R		N/I	N/I			N/I	
			C	N/R	94	*23.5*	N/R		N/I	N/I			N/I	
		C	B	1	224	*56*	N/R		N/I	N/I			N/I	
			C	N/R	94	*23.5*	N/R		N/I	N/I			N/I	
B3W2-E	1	A	A		N/D	N/D			N/I	outside range		0.44	29	2.11
			B	0.5	40	*10*	N/R		N/I	N/I			N/I	
			C	N/R	27	*6.75*	N/R		N/I	N/I			N/I	
		B	A	0.54	*82*	20.5	6		*286*	71.5	15.4	0.54	120.5	32.4
				0.54	155	*38.75*	6.09		N/I	N/I			N/I	
			B	0.5	224	*56*	N/R		N/I	N/I			N/I	
			C	N/R	126	*31.5*	N/R		N/I	N/I			N/I	
		C	B	0.75	25	*6.25*	N/R		N/I	N/I			N/I	
			C	N/R	20	*5*	N/R		N/I	N/I			N/I	

N/I = Not Inspected
N/R = Not Recorded
N/D = Not Detected
Company A completed multiple inspections for each side. Only 1 depth was reported for all Company A inspections.
Inspection amplitudes in underlined italics are calculated values, not measured.

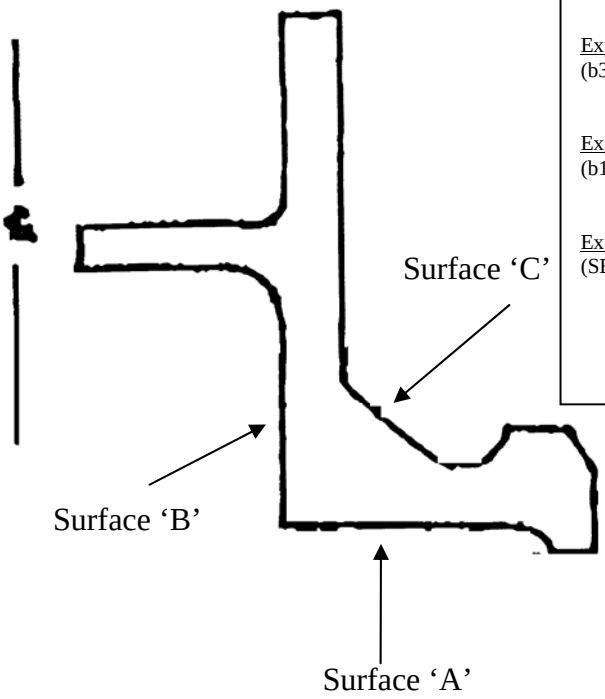

		Surface A	Surface B	Surface C
Expr0002	Before Spin	27% of #1	126% of #1	20% of #1
(b3w2e)	After 5K Spin	41% of #1	98% of #1	51% of #1
	After 10K Spin	41% of #1	51% of #1	63% of #1
Expr0003	Before Spin	50% of #1	94% of #1	94% of #1
(b1bw3b)	After 5K Spin	208% of #1	104% of #1	73% of #1
	After 10K Spin	72% 0f #1	99% of #1	87% of #1
Expr0004	Before Spin	141% of #1	224% of #1	140% of #1
(SB6)	After 5K Spin	171% of #1	184% of #1	90% of #1
	After 10K Spin	134% of #1	199% of #1	120% of #1

Figure D-1. Disk Forging Inspection Surfaces and Spin Testing Interim Inspection Results

APPENDIX E—ULTRASONIC INSPECTION OF FORGINGS

E.1 INTRODUCTION.

Turbine Rotor Material Design (TRMD) Phase II ultrasonic nondestructive evaluation efforts examined both conventional and multizone inspection techniques on natural and seeded anomalies in the final forging shapes. Inspection in the billet and intermediate forging shapes was conducted in TRMD-I. The purpose of this study was to examine the effects of material processing on the location in the forging and ultrasonic response of synthetic and natural hard alpha (HA) anomalies and to compare the inspection sensitivity of conventional and multizone procedures. Forgings identified as seeded billet (SB) SB-1, SB-2, SB-3, SB-4, SB-5, and SB-6 contained synthetic HA seeds that were placed in the billet. Forgings B1BW3B and B3W2E were prepared using Contaminated Billet Study material obtained from the Engine Titanium Consortium and had natural HA indications, which were detected and rejected by multizone billet inspection at a production titanium supplier RMI.

E.2 FORGINGS.

The dogbone forgings (SB-1, SB-2, and SB-3) were about 12 inches in diameter and 4 inches in height, while the backflow forging (SB-4) was about 12 inches in diameter and 7 inches in height at its largest dimension. Figures E-1 and E-2 illustrate the cross-sectional views of these two forgings. The forgings were inspected from both faces, denoted Side A and Side B.

Inspection of the dogbone shapes involved two separate scans from each side, one of the material outside the center machined depression outer dimension (OD) and another of the material beneath the machined depression inner dimension (ID). The backflow forging also required two separate scans from each side, one of the thick center regions (ID) and another of the material surrounding the center region (OD). These regions are identified in figures E-1 and E-2.

The spin disk forgings were about 12 inches in diameter and 5.5 inches in height. Figure E-3 shows the cross-sectional view of the spin disk forging. The forgings were inspected from two surfaces, the bore face and the bore.

A summary of the synthetic seeds placed in the forgings is presented in table E-1. Forgings B1BW3B and B3W2E contained natural indications as found in the billet.

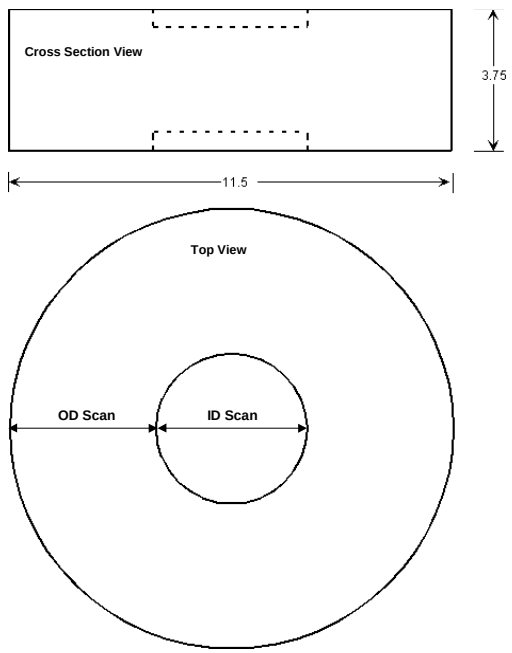

All dimensions are in inches

Figure E-1. Dogbone Forging Configuration

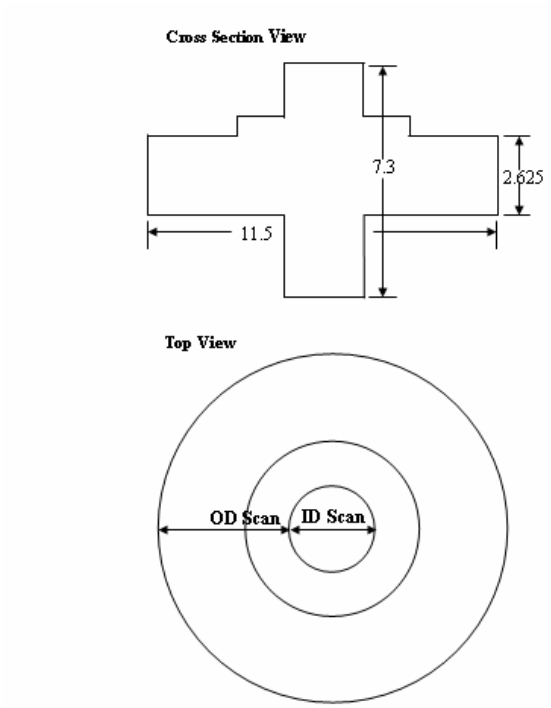

Figure E-2. Backflow Forging Configuration

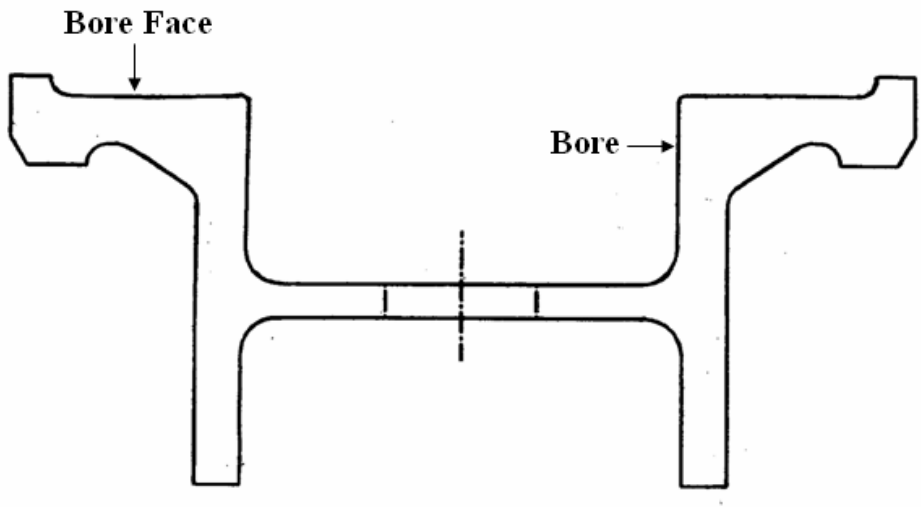

Figure E-3. Spin Disk Forging Configuration

Table E-1. Summary of Synthetic Seeds in Forgings

Forging	Seed No.	% N	Diffusion Zone	Length (inches)	Diameter (inches)
SB-1	1	1.5	Yes	0.200	0.200
	2	1.5	Yes	0.200	0.200
	3	12	Yes	0.200	0.200
	4	12	Yes	0.200	0.200
	5	12	No	0.200	0.100
	6	12	No	0.200	0.100
SB-2	7	1.5	Yes	0.200	0.200
	8	1.5	Yes	0.200	0.200
	9	12	Yes	0.200	0.200
	10	12	Yes	0.200	0.200
	11	12	No	0.200	0.100
	12	12	No	0.200	0.100
SB-3	13-16	12	Yes	0.800	0.200
	17-20	12	Yes	0.800	0.200
	21-24	12	Yes	0.800	0.200
	25-28	12	Yes	0.800	0.200
SB-4	29-32	12	Yes	0.800	0.200
	33-36	12	Yes	0.800	0.200
	37-40	12	Yes	0.800	0.200
	41-44	12	Yes	0.800	0.200
SB-5	45	12	Yes	0.200	0.100
	46	12	Yes	0.200	0.100
	47	12	Yes	0.200	0.100
	48	12	Yes	0.200	0.100
SB-6	49	12	Yes	0.200	0.100

E.3 ULTRASONIC INSPECTION METHODS.

Ultrasonic inspection took place at the GE Aviation Quality Technology Center in Evendale, Ohio. Laboratory equipment and instrumentation meeting all standard production inspection requirements were used for all inspections. Figure E-4 shows an ultrasonic specialist preparing for a disk inspection, and figure E-5 shows one of the dogbone forgings on the turntable of the ultrasonic inspection tank. Figure E-6 shows a closer view of a bore face inspection in progress.

Figure E-4. Ultrasonic Specialist Prepares for Disk Inspection

Figure E-5. Dogbone Forging in Ultrasonic Tank

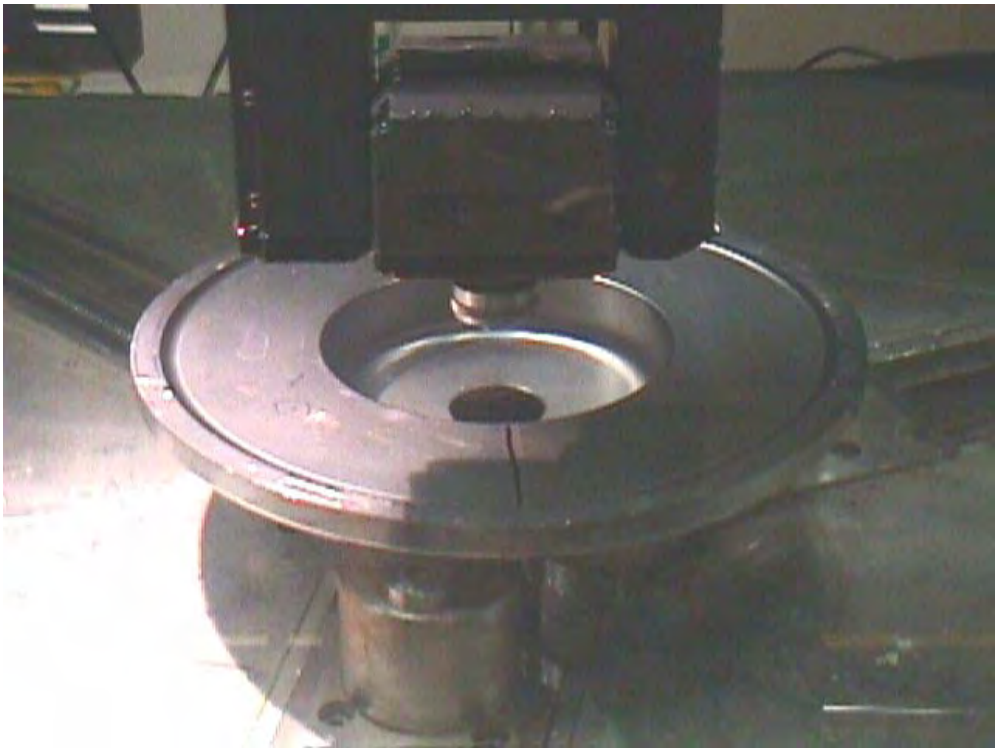

Figure E-6. Close-Up of the Bore Face Inspection

GE conducted three different calibrated inspections on the forgings. Following is a brief description of each inspection and the associated calibration procedure.

E.3.1 CONVENTIONAL #2 FLAT-BOTTOM HOLE INSPECTION.

Conventional inspection as conducted by GE incorporates the use of two overlapping sonic zones to cover the inspection volume in a titanium forging. The near-zone ensonifies material from 0.06 to 1.5 inches in depth using a 10-MHz, 0.375-inch element transducer focused at the surface. The far-zone evaluates material from 0.5 to 3 inches (or to the backwall) deep using a 5-MHz, 0.75-inch element transducer focused at the surface. Both the near- and far-zone transducers were calibrated on a neutral material calibration standard, then adjusted to the equivalent of a #2 flat-bottom hole (FBH) in Ti-64 using correction factors developed by GE. Distance amplitude correction (DAC) was used to adjust the amplitude of all target holes to 80% full screen height. DAC FBH targets in the calibration block were at 0.06-, 0.125-, 0.25-, 0.5-, 1.0-, and 1.5-inch depths.

E.3.2 CONVENTIONAL #1 FBH INSPECTION.

The Conventional #1 FBH inspection is essentially identical to the Conventional #2 FBH inspection except that the calibration was accomplished using #1 FBHs in Ti-64 material. (See description of Conventional #2 FBH inspection.) The far-zone inspection was not completed because most indications were within the near-zone detection depth.

A significant difference between production conventional inspection and the conventional inspections conducted for this study is that ultrasonic C-scans were made of the inspections completed in this study using the multizone software to analyze the digital data. Production conventional inspections use only the signal amplitude to characterize a reflector. Generation of C-scans in this study permitted calculations of signal-to-noise ratio (S/N) for all indications detected by the conventional inspections.

E.3.3 MULTIZONE #1 FBH INSPECTION.

Multizone inspection breaks up the inspection volume into 0.5-inch depth increments. Several different 10-MHz transducers are used, each one focusing in the middle of a different zone. The transducers are designed to maintain uniform beam profiles for each zone. This is in an effort to keep material noise levels at a minimum. Each zone is calibrated on three #1 FBHs placed at the near, middle, and deep side of each 0.5-inch zone. DAC is applied across the three targets to maintain equal inspection sensitivity throughout each zone. Ultrasonic C-scans are generated for all multizone inspections using software specifically designed to permit calculation of S/N for all indications detected. Accept/reject criteria for multizone inspections include an amplitude and S/N value. Exceeding either criterion is grounds for rejection of the indication.

S/N values were calculated using the digital C-scan information and the following formula:

$$S/N = (\text{Peak Signal} - \text{Mean Noise}) / (\text{Peak Noise} - \text{Mean Noise})$$

The peak and mean signals were identified by windowing a region on the C-scan image and calculating the amplitudes using the system software.

E.4 ULTRASONIC RESULTS.

Ultrasonic inspection results for both conventional and multizone inspections are summarized in table E-2 for forgings SB-1, SB-2, SB-3, and SB-4. S/N ratios are presented for the conventional inspections using calculations performed by the multizone software. In these inspections, amplitudes greater than 100% were calculated by correcting for the amount of gain needed to bring the signal back to 100% of the full screen height (FSH). The black areas in table E-2 represent inspections for which the seed location was outside the transducer inspection range. The red areas represent inspections where no indication exceeding the accept/reject criteria was detected.

Table E-2. Ultrasonic Inspection Results for Seeded Billets SB1, SB2, SB3, and SB4

Disk ID	Ind. #	Side	Depth	Conventional -#2 FBH				Conventional -#1 FBH				Multizone - #1 FBH	
				AMP	SNR	AMP	SNR	AMP	SNR	AMP	SNR	AMP	SNR
				10MHz Near Zone		5 MHz Far Zone		10MHz Near Zone		5 MHz Far Zone		10 MHz	
SB-1	1	A	0.1	173.8	70.5			758.6	32.3			708	48.8
	3	A	1.35	48	9.4	66.6	4	106.8	4.8	371.5	13.6	174	21.7
	2	A	1.5	49	3.9			195	9.1			125	10.4
	4	A	1.8			39.1	3.4			182	3.8	45	3.2
	5	A	1.8			60.8	6.4					35	2.5
	6	A	3.5			131.8	23.6			416.9	17	339	14.9
	6	B	0.08	99	21			436.5	22.9			478.6	66.3
	5	B	1	56.8	8.2	101.9	18	275.4	16	371.5	14.3	125.9	13.1
	2	B	1.25	47	7			251.2	16	166	18.9	131.8	13.8
	4	B	2			40	3			190.5	4.7	46.3	3.7
	3	B	2.2			131.8	9.1			588.8	10.6	108.8	8.1
	1	B	3.5									65	4
SB-2	7	A	0.16	70.5	16.3			162.2	7.3			234.4	13.9
	9	A	1.35	65.6	17.3	208.9	44.1	218.8	10.1	851.1	47.7	363.5	29.6
	10	A	1.4					65.6	3				
	8	A	1.7			122.5	8.9			631	20.2	213.8	26.8
	11	A	1.75			50.9	8.7			169.8	11.1	97.5	2.6
	12	A	3.4			154.9	48.1			407.4	18	269.2	8.9
	12	B	0.12	239.9	116.6			812.8	91.4			490	60
	11	B	1	52.9	8.2	89.1	22.3	116.6	5.8	190.5	6.9	95	11
	10	B	1.35					75.4	3.4				
	8	B	2			147.9	16.4			575.4	30	269.2	19.2
	9	B	2.4			134.9	11.1			537	18.8	691.8	43.5
	7	B	3.3			134.9	12.2			467.7	9.7	208.9	10.5
SB-3	13-16	A	0.25	93	22.3			229	21.9			281.8	17.3
	25-28	A	1.5			63.8	20.8	88	4.2	324	16	177.8	22.2
	17-20	A	1.65			138	11.2			631	18.2	158.5	13.8
	21-24	A	2			162	13.9			813	31.5	281.8	31.3
	25-28	B	1			64.6	20.6	100	7.3	257	24	95	9.7
	21-24	B	1.3	66	13.9	72.5	2.8	331	12.8	380	12.6	239.9	20.8
	17-20	B	2			82.3	3.4			282	9.1	417	30
	13-16	B	3.5			141	7			778	22.5	354.8	12.6
SB-4	33-36	A	1.1	60	16.7	104	15.8	295	29.3	407	18.8	316	35.6
	37-40	A	1.5	141	31.7	209	47	113	8.7	776	61.7	759.6	73.5
	29-32	A	2.5			174	15.3			741	62.1	282	93.3
	41-44	A	4.6									363	32.7
	37-40	B	0.8	75	17.5	141	47.8	398	23	525	25.6	407	58.4
	41-44	B	1.25			78.4	8.1	135	43.2	363	30.2	116	38.7
	33-36	B	1.4	67.5	24.6	110	14.5	347	42.7	468	17.6	132	17.1
	29-32	B	4.4			129	19.2			398	16.7	339	26.9

(black) means indication outside transducer inspection range
(red) means indication not detected

05/02/2000

Table E-3 contains a summary of the ultrasonic inspection data for the four spin disk forging inspections. In these inspections, if the signal amplitude from an indication was saturated (i.e., exceeded 100% of the FSH), the gain required to adjust the amplitude to 80% FSH was recorded, and the actual amplitude was calculated. In several of the conventional inspections, the forging geometry did not allow ensonification to the full transducer calibration depth. To permit completion of the inspection, the ultrasonic gate had to be continually adjusted to keep the gate just short of the backwall echo. This procedure caused the sharp changes in noise level seen in several of the conventional C-scans.

E.4.1 FORGING SB-1.

The location of all seeds in SB-1 is shown in figure E-7. All near surface seeds (<1.5″ deep) were detected from both faces by the conventional #2 and #1 inspection near-zone, 10-MHz transducers. Some of the deeper seeds (>1.5″ deep) were not detected by Conventional #2 far-zone, 5-MHz transducer, including seed #2 from either side or seed #1 from Side B. The conventional #1 far-zone, 5-MHz transducer could not detect seeds #2 and #5 from Side A or seed #1 from Side B. A few of the seeds detected by conventional inspections had very high amplitudes, especially seed #1 from Side A and seed #3 from Side B. No trends in the S/N attained by the conventional #1 and #2 inspections were noted.

A substantial increase in background noise level was noted when the conventional inspection sensitivity was increased by 12 dB from #2 FBH calibration to #1 FBH calibration. This increase was especially noticeable in the 5-MHz, far-zone transducer, as shown by comparing the C-scans in figures E-8 and E-9. The increase in noise level for the 10-MHz, near-zone transducer, shown in figures E-10 and E-11, was not as significant. In production, these high-noise levels would make inspection to a #1 FBH sensitivity impractical, since they would require a large number of indications to be evaluated. In forging SB-1, as well as the other three forgings, the synthetic seeds were large enough to produce high-amplitude reflections, most of which could still be easily detected in spite of the high-noise spikes in the conventional #1 far-zone, 5-MHz transducer inspection (figure E-9). However, reflections from somewhat smaller anomalies would likely be undetectable through this high-noise background.

All seeds produced rejectable reflections by the Multizone #1 FBH inspection from both sides. Seeds #4 and #5 from Side A and seeds #1 and #4 from Side B were most difficult to detect, with S/N just over the reject level of 2.5. The noise levels encountered at the various inspection zones were substantially lower than those produced by the conventional #1 inspection and did not exhibit a large amount of variation. This can be seen by comparing the multizone C-scans from zones 3, 4, and 6, shown in figures E-12, E-13, and E-14, with the conventional #1 C-scans, shown in figures E-9 and E-11.

Table E-3. Ultrasonic Inspection Results for Spin Disk Forgings

Sample	Ind. #	Insp. Surface	Depth from Surface	Conventional #2*				Conventional #1**		Multizone #1***		
				Amp	S/N	Amp	S/N	Amp	SNR	Zone	Amp	S/N
				10-MHz Near-Zone Transducer		5-MHz Far-Zone Transducer		10-MHz Near-Zone Transducer		10-MHz Transducer		
SB-5	47	Bore Face	1.475	112.8	20.45	87.5	9.55	n/d	n/d	3	388.8	60.59
		Bore	0.263	55.8	13.5	outside	range	162.5	26.59	1	190.5	28.74
	46	Bore Face	0.08	97	24.25	outside	range	275	41.84	1	257	48.75
		Bore	1.123	15.6	2.6	8.75	2.6	131.25	7.15	outside range		
	45	Bore Face	0.18	43.1	7.54	outside	range	173.75	13.95	1	169.8	39.06
		Bore	0.401	47	11.25	outside	range	245	13.46	1	223.8	61.86
	48	Bore Face	0.375	47	5.75	outside	range	131.75	28.65	1	141.3	23.72
		Bore	1.8	79	15.6	73.5	15.9	outside range		3	23.5	4.4#
SB-6	49	Bore Face	0.45	38.1	8.11	outside	range	195	14.45	1	137.5	31.45
		Bore	.32	47	15	outside	range	190.5	11.88	1	173.8	82
B1BW3B	1	Bore Face	0.24	n/d	n/d	outside	range	47	1.9	1	66.6	10.8
		Bore	0.58	n/d	n/d	66.6	14.3	82.25	2.88	1	107.8	12.37
B3W2E	1	Bore Face	0.44	n/d	n/d	outside	range	n/d	n/d	1	29	2.11
		Bore	0.54	20.5	6	71.5	15.4	155	6.09	1	120.5	32.4

*Calibrate #1 R95 convert to # 2 in Ti-64 with DAC
**Calibrate #1 Ti-64 with DAC
***Calibrate #1 R95 convert to #1 in Ti-64 with DAC
Zone 3 transducer used instead of Zone 4 transducer
Amplitudes expressed as a percentage of calibration FBH
n/d = not detected

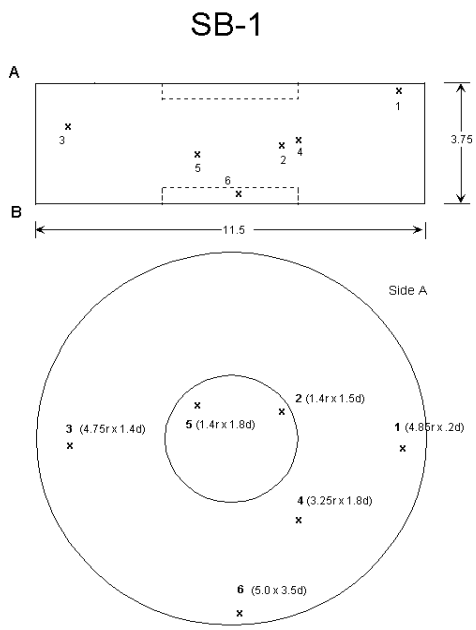

All in dimensions are in inches

Figure E-7. Location of Seeds in Forging SB-1

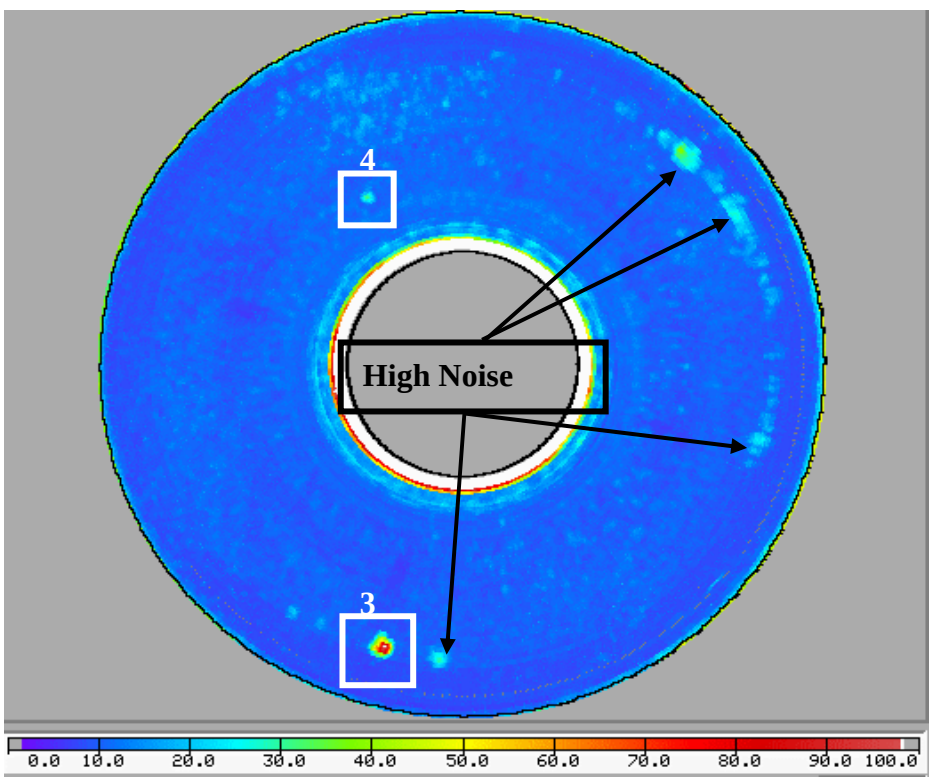

Figure E-8. Forging SB-1 Conventional #2 FBH Far-Zone, 5-MHz Transducer OD Inspection From Side B

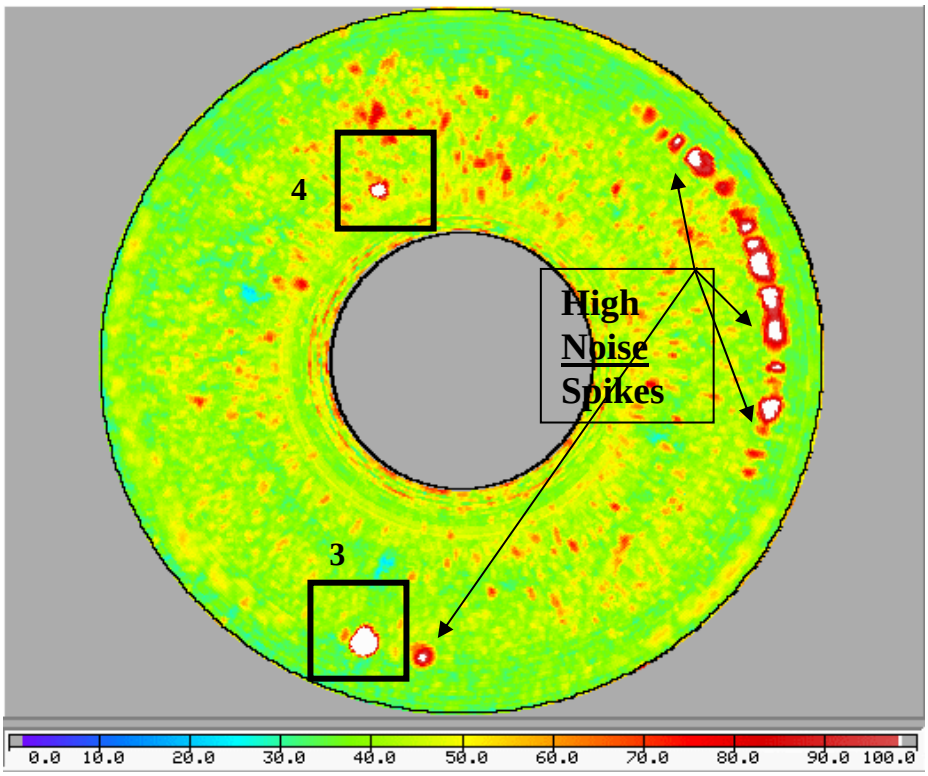

Figure E-9. Forging SB-1 Conventional #1 FBH Far-Zone, 5-MHz Transducer OD Inspection From Side B

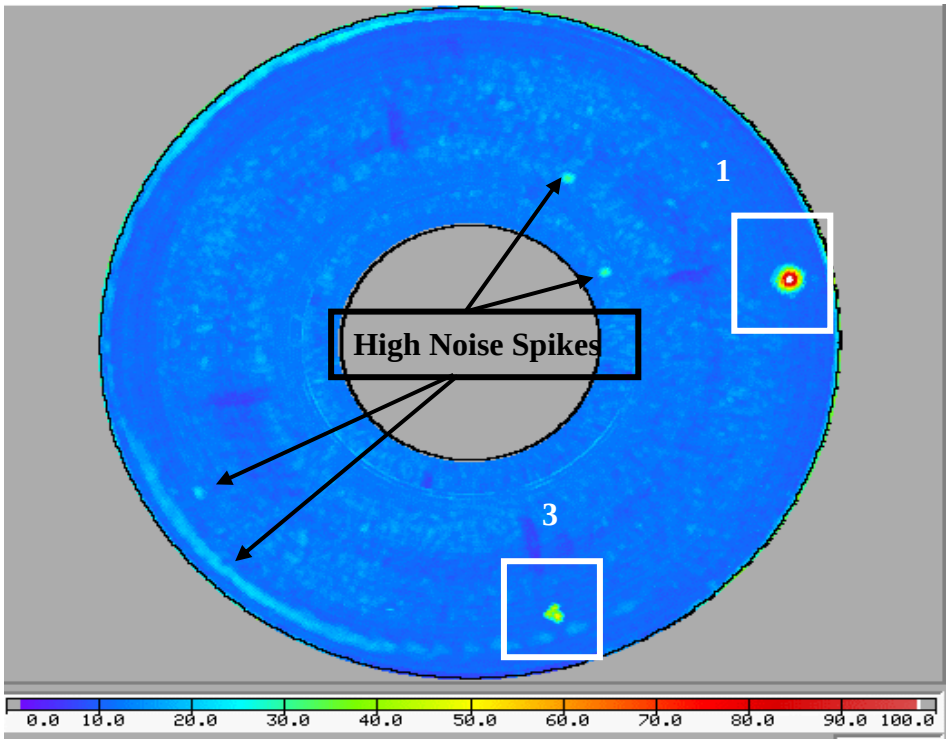

Figure E-10. Forging SB-1 Conventional #2 FBH Near-Zone, 10-MHz Transducer OD Inspection From Side B

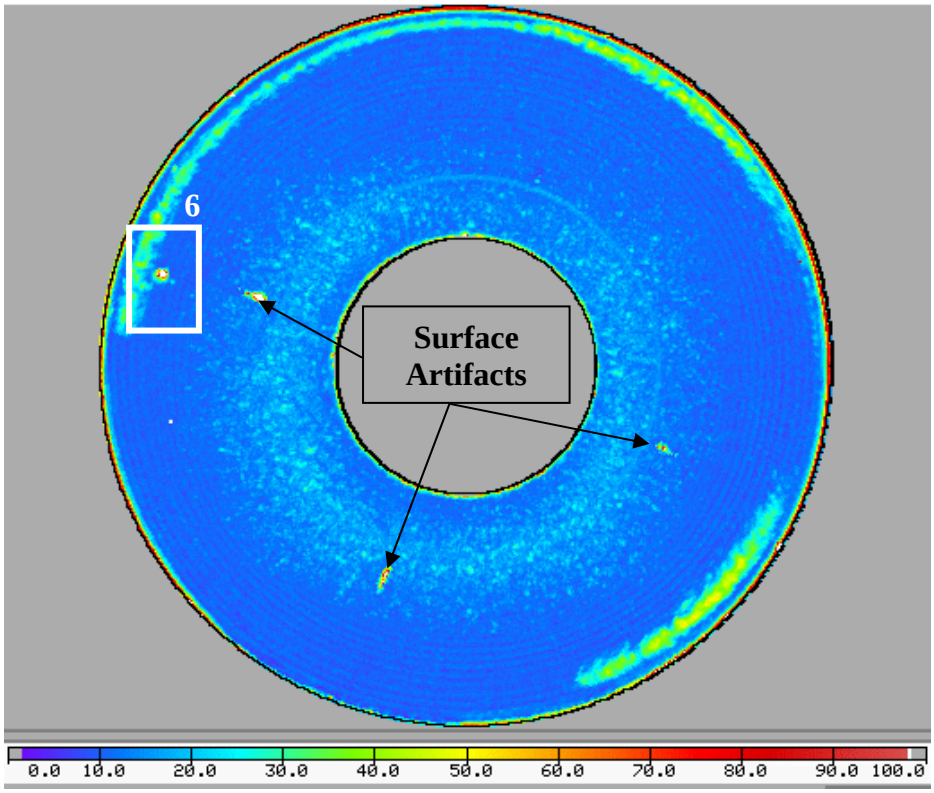

Figure E-11. Forging SB-1 Conventional #1 FBH Near-Zone, 10-MHz Transducer OD Inspection From Side B

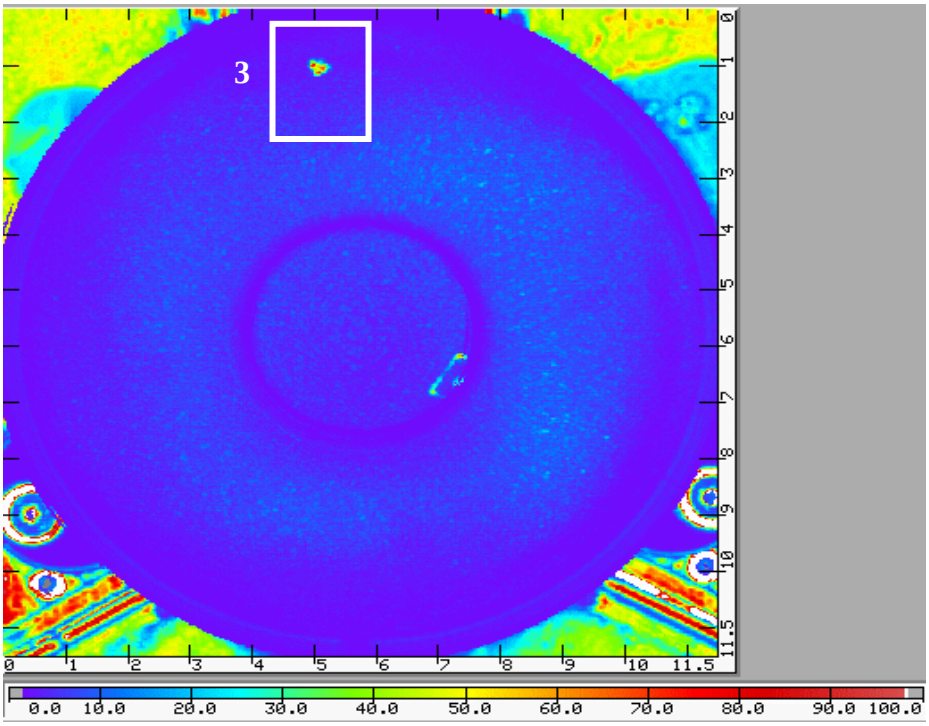

Figure E-12. Forging SB-1 Multizone #1 FBH Zone 3 OD Inspection From Side A

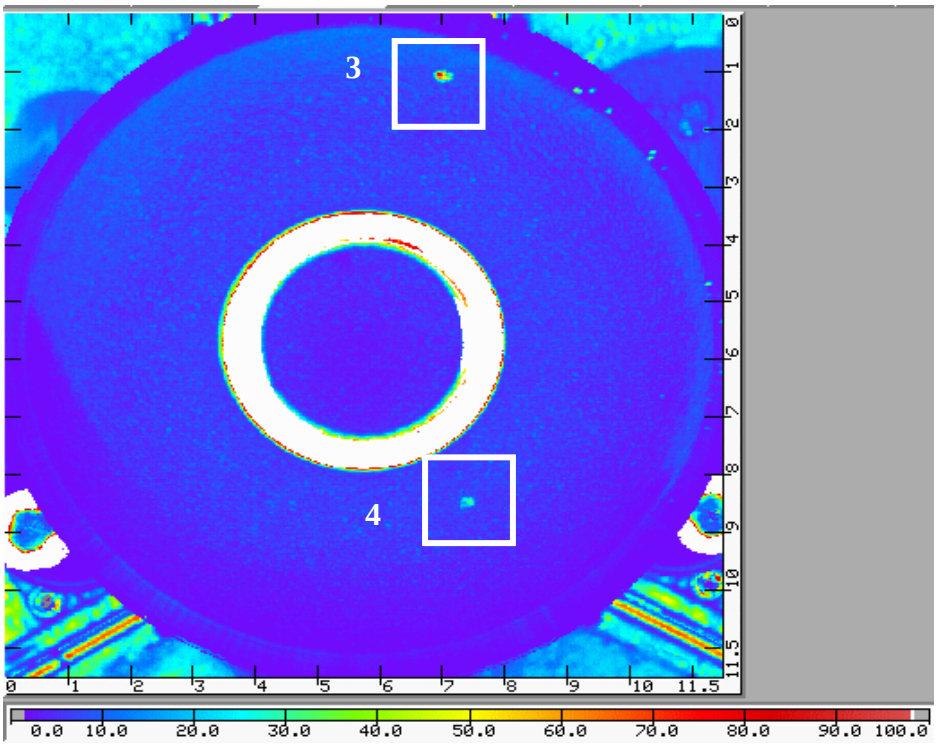

Figure E-13. Forging SB-1 Multizone #1 FBH Zone 4 OD Inspection From Side B

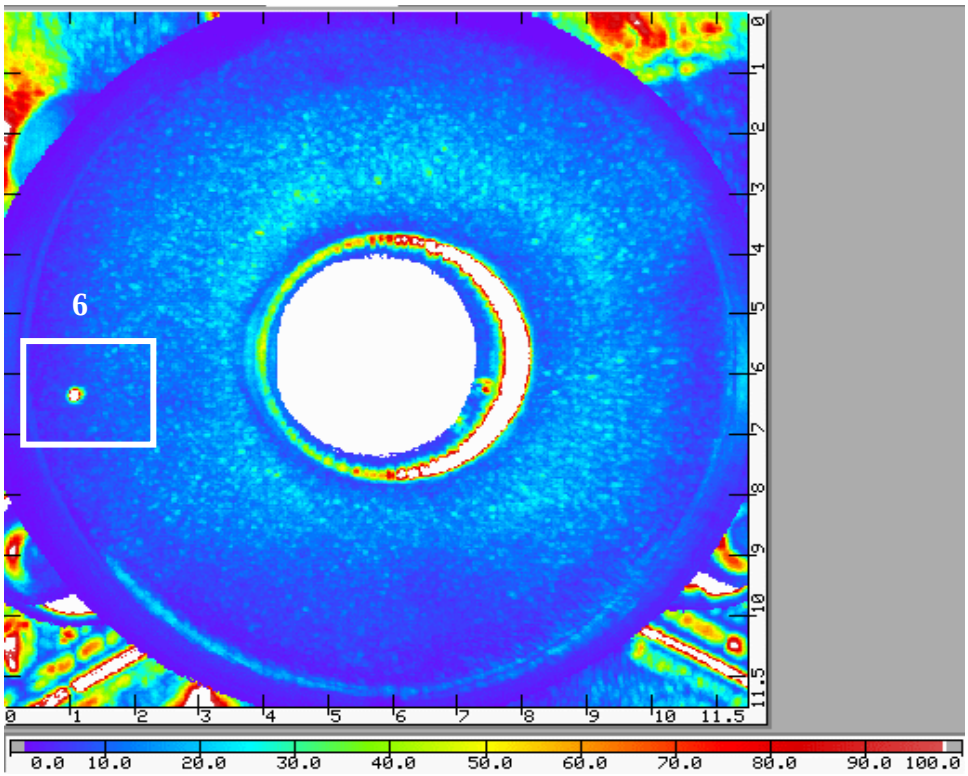

Figure E-14. Forging SB-1 Multizone #1 FBH Zone 6 OD Inspection From Side A

E.4.2 FORGING SB-2.

The locations of all seeds in forging SB-2 are shown in figure E-15. Results of the Conventional #2 and #1 FBH inspections indicated these seeds were somewhat easier to detect than those in forging SB-1. The only exception was seed #10, which was very difficult to detect on the ID scan due to its position directly below the outer edge of the center depression. This vertical edge makes it difficult for the longitudinal sound beam originating from either Side A or Side B to interact with the seed. The result is a loss of signal strength to a level below the reject amplitude for all inspections except the Conventional #1 FBH near-zone, 10-MHz transducer from Side B, which produced a weak but discernable signal (figure E-16).

The same trend in background noise level between the Conventional #1 and #2 FBH inspections seen in the SB-1 results was noted for SB-2 results. The OD C-scans from the Conventional #1 FBH near-zone, 10-MHz transducer and far-zone, 5-MHz transducer inspections, shown in figures E-17 and E-18, have noise levels very similar to those for forging SB-1 (figures E-11 and E-9). These high-noise levels would preclude production inspection to a #1 FBH sensitivity.

All seeds except #10 were detected by the Multizone #1 FBH inspections from both sides. The effect of the outer edge of the center depression was more pronounced on the multizone sound beam due to the larger diameter of the multizone transducer used to inspect zone 3 relative to the diameter of the conventional transducers. As with forging SB-1, the background noise levels of the multizone inspections were significantly lower than those of the Conventional #1 FBH inspection and did not exhibit a large amount of variation from zone to zone, as illustrated by figures E-19 and E-20.

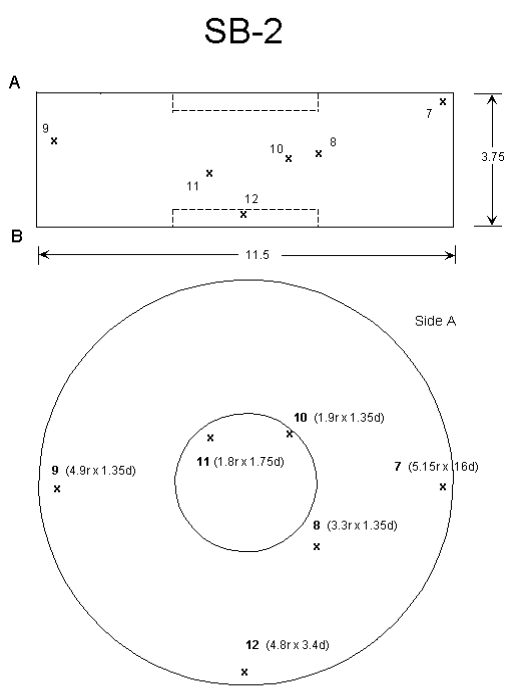

All dimensions are in inches

Figure E-15. Location of Seeds in Forging SB-2

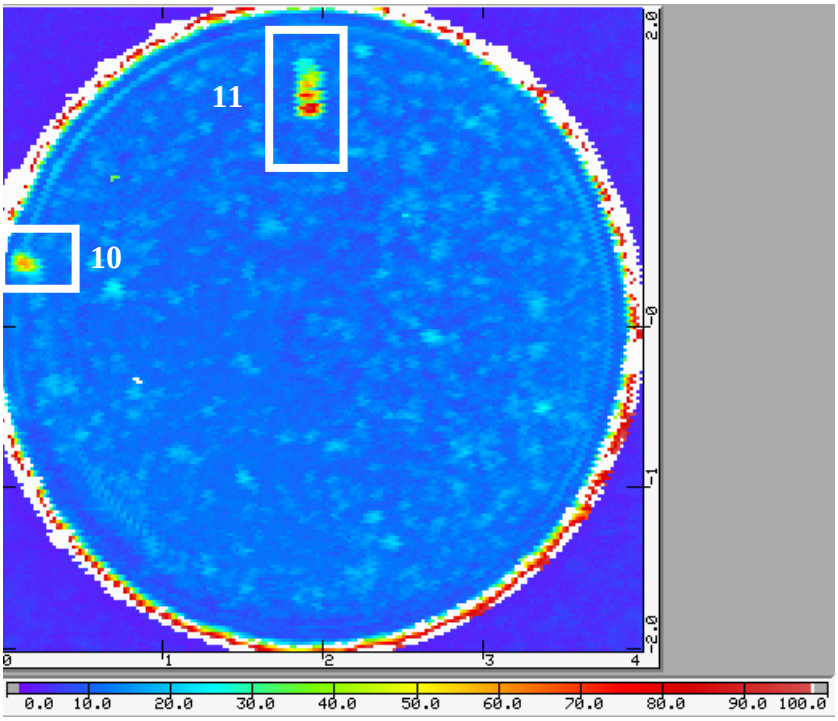

Figure E-16. Forging SB-2 Conventional #1 FBH Near-Zone, 10-MHz Transducer ID Inspection From Side B

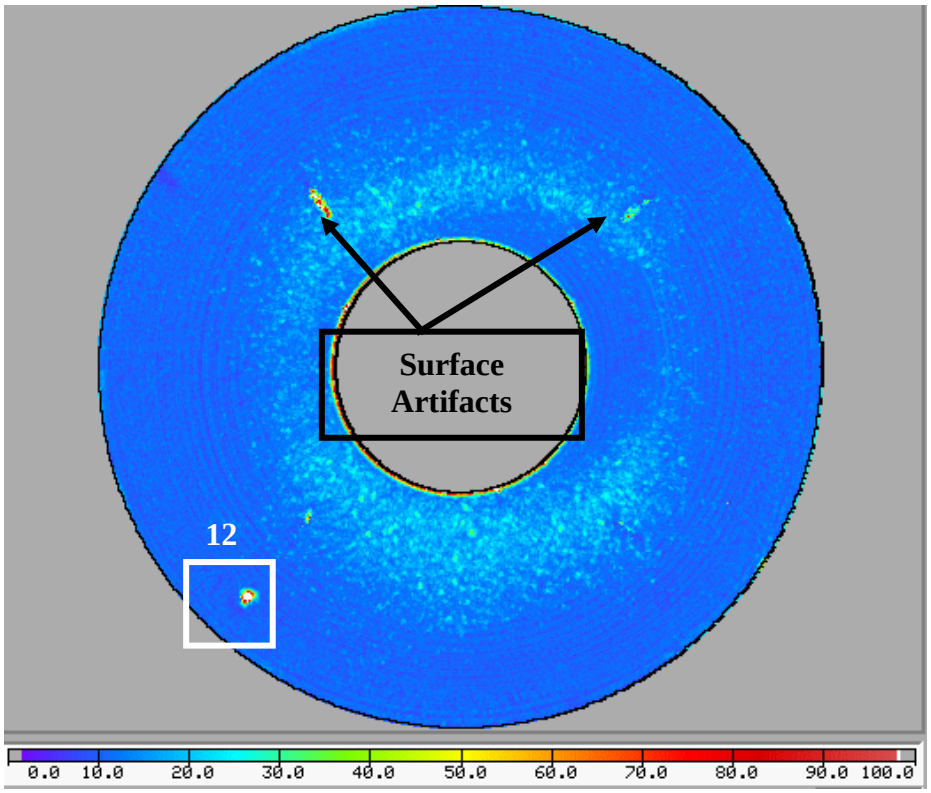

Figure E-17. Forging SB-2 Conventional #1 FBH Near-Zone, 10-MHz Transducer OD Inspection From Side B

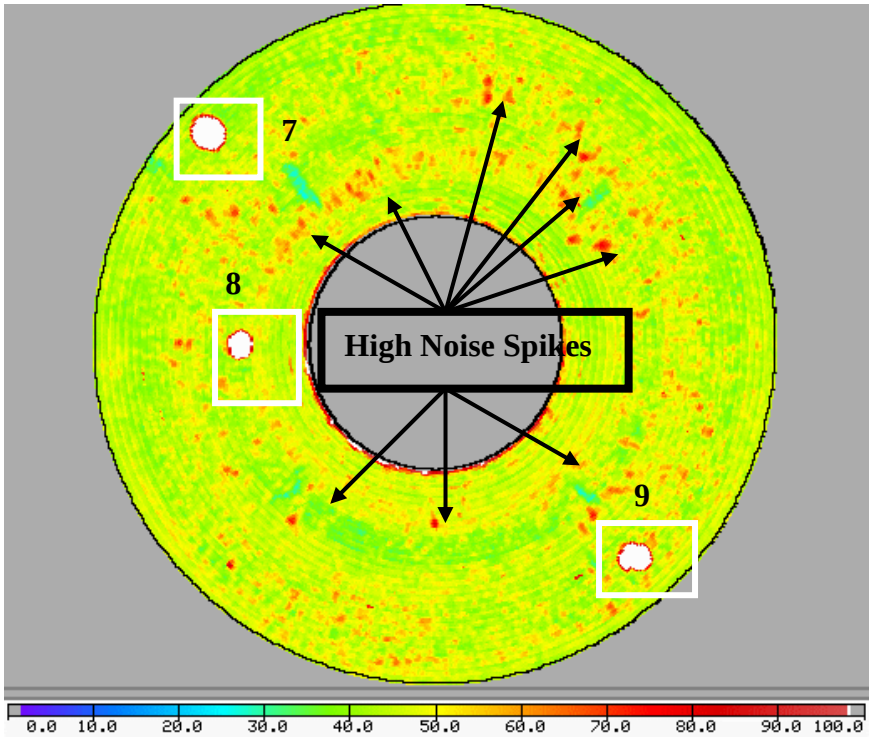

Figure E-18. Forging SB-2 Conventional #1 FBH Far-Zone, 5-MHz Transducer OD Inspection From Side B

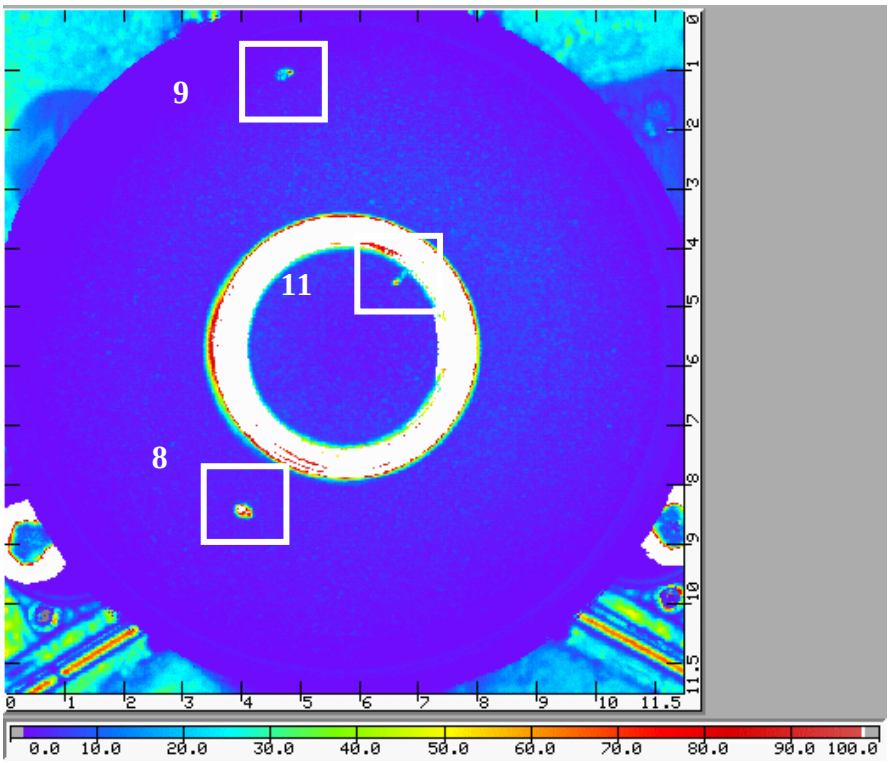

Figure E-19. Forging SB-2 Multizone #1 FBH Zone 4 Inspection From Side A

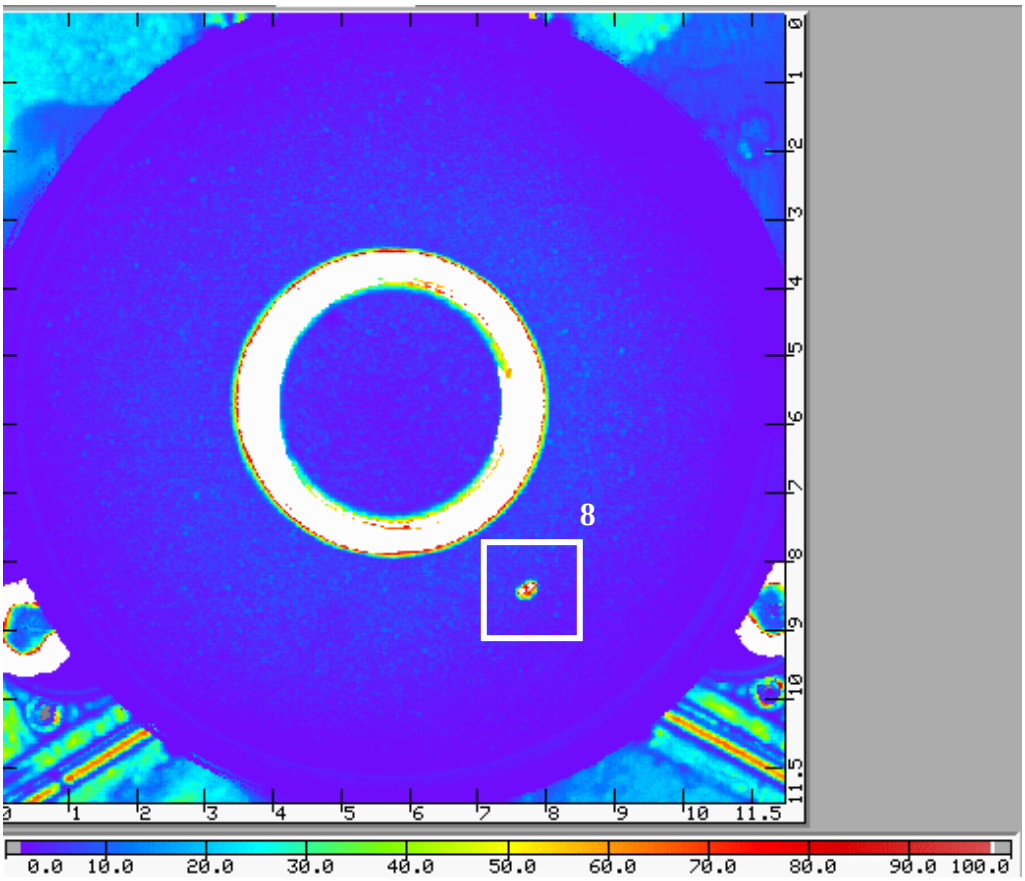

Figure E-20. Forging SB-2 Multizone #1 FBH Zone 4 OD Inspection From Side B

E.4.3 FORGING SB-3.

The locations of the 0.200″ diameter x 0.800″ long multiple HA seeds in forging SB-3 are shown in figure E-21. All these large multiple seeds were detected by all the inspection methods with one exception. The Conventional #2 FBH near-zone, 10-MHz transducer inspection could not detect seeds 25-28 from either side of the forging. As could be expected, most of the amplitudes and S/Ns were relatively high from all multiples and all inspections. The high-noise levels seen in the Conventional #1 FBH scans (i.e., figure E-22) would again make production inspection at that sensitivity level impractical.

Examination of the C-scans indicated that several of the multiples tended to separate during forging. This is most easily seen for seeds #13-16 and seeds #17-20 due to their orientation relative to the longitudinal scans from Sides A and B. This separation is illustrated in the Conventional #1 FBH far-zone, 5-MHz C-scan (figure E-22) and Multizone #1 FBH inspections of zone 4 from Side A and zone 6 from Side B (figures E-23 and E-24). Seeds #25-28 and #21-24 were also detected in the multizone inspection zone 4 scan, since they were at about the same depth as seeds #17-20.

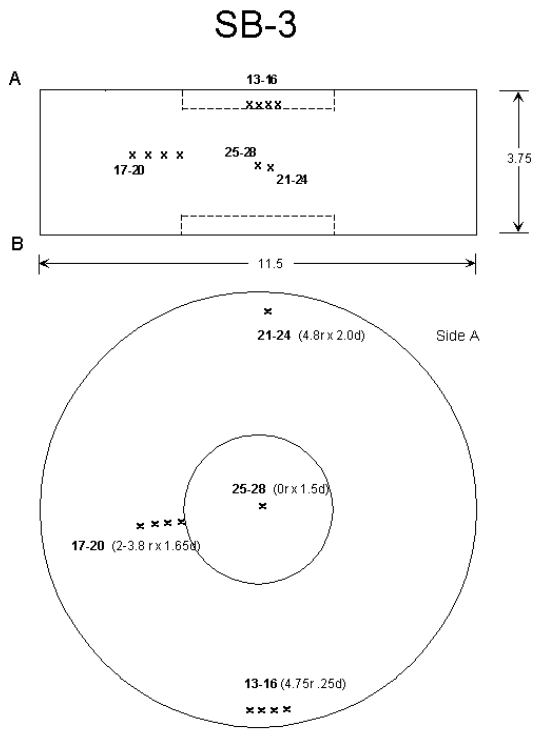

All dimensions are in inches

Figure E-21. Location of Seeds in Forging SB-3

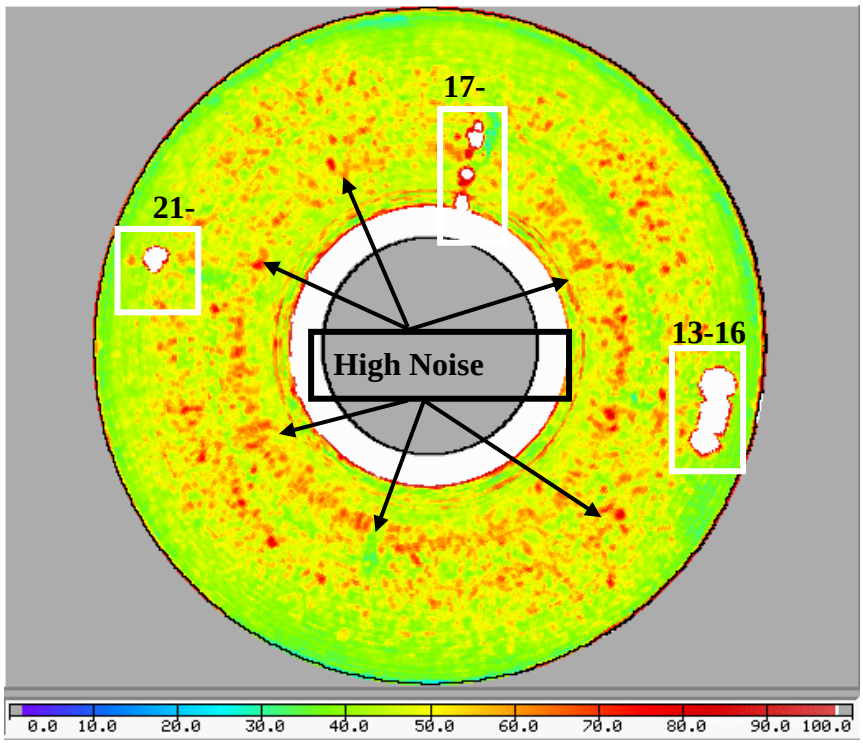

Figure E-22. Forging SB-3 Conventional #1 FBH Far-Zone, 5-MHz Transducer OD Inspection From Side B

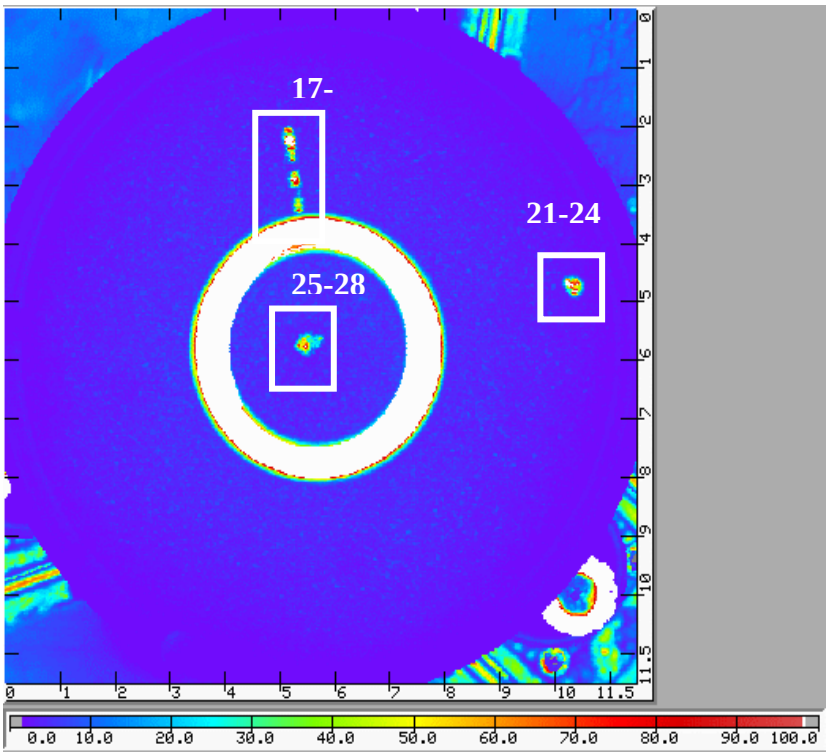

Figure E-23. Forging SB-3 Multizone #1 FBH Zone 4 Inspection From Side A

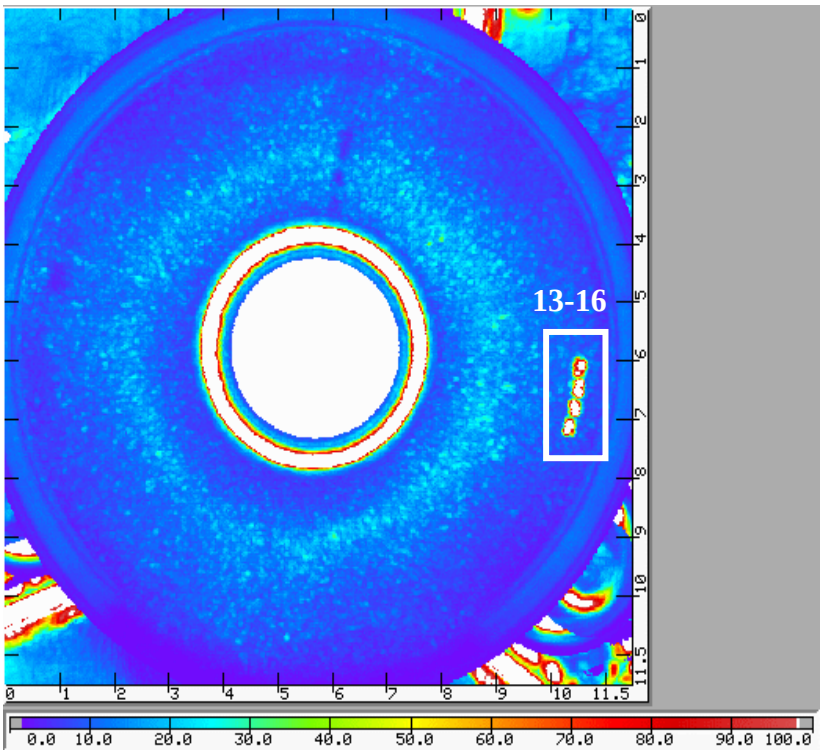

Figure E-24. Forging SB-3 Multizone #1 FBH Zone 6 OD Inspection From Side B

E.4.4 FORGING SB-4.

The locations of the multiple HA seeds in forging SB-4 are shown in figure E-25. The unusual shape and large thickness of this forging presented some interesting inspection challenges. As with forging SB-3, the very large size and high nitrogen content of the multiples made them all relatively easy to detect by all inspections with one exception. Again, the Conventional #2 FBH near-zone, 10-MHz inspection could not detect seeds #41-44 from Side B. This may be due in part to the fact that this multiple separated down the axis of the forging, so only one of the individual seeds may have been inside the inspection range of the 10-MHz transducer.

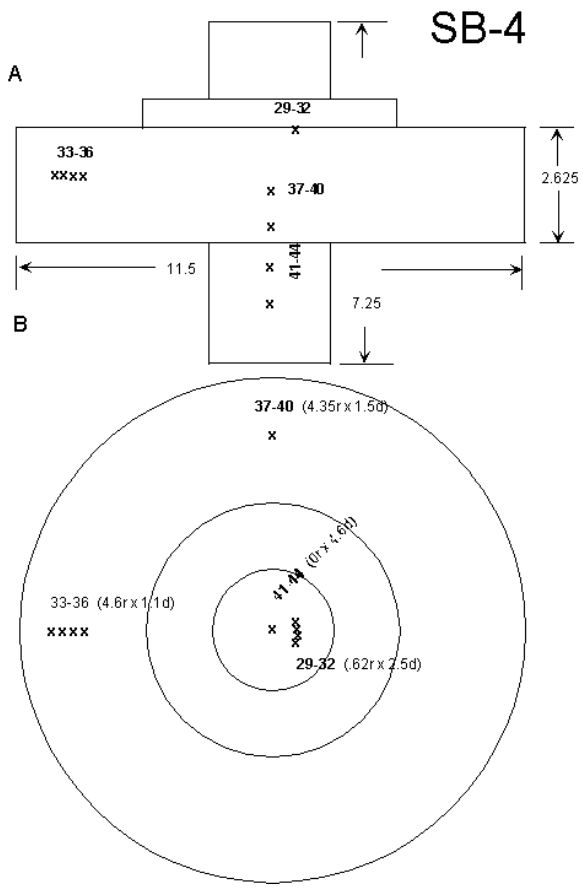

All dimensions are in inches

Figure E-25. Location of Seeds in Forging SB-4

Examination of the C-scans indicated that the multiple seeds #29-32 and #33-36 both separated upon forging. The Conventional #2 and #1 FBH inspections using the far-zone, 5-MHz transducer from Side B, shown in figures E-26 and E-27, both show the separation of #33-36, as well as the Multizone #1 FBH zone 3 inspection from Side B shown in figure E-28. Note again the significant increase in background noise level in figure E-27 when the gain level is increased from Conventional #2 to Conventional #1 FBH sensitivity. Both indications are clearly evident because they produced such large reflected signals. The Multizone #1 FBH noise level is relatively low and uniform.

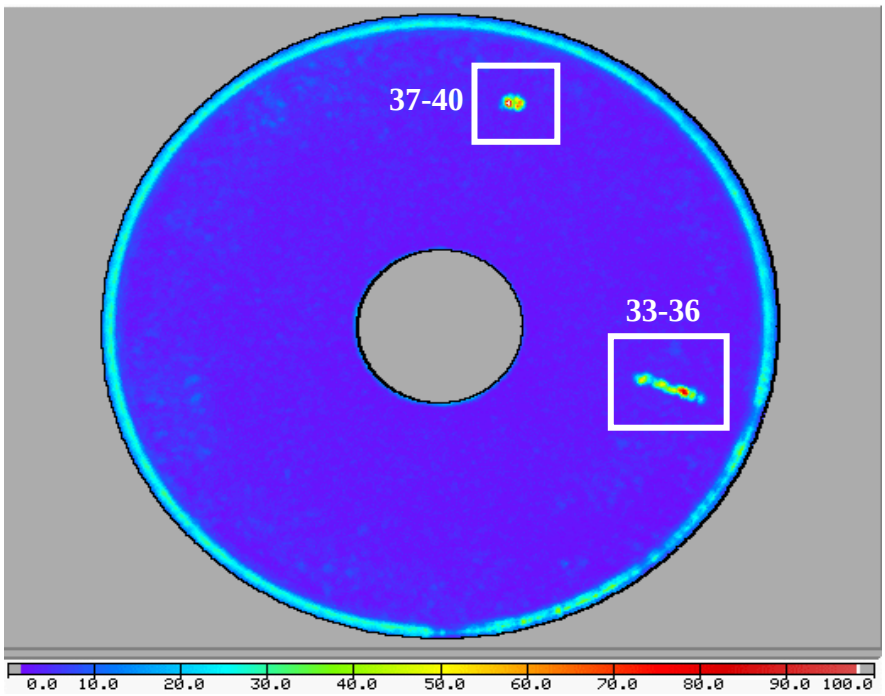

Figure E-26. Forging SB-4 Conventional #2 FBH Far-Zone, 5-MHz Transducer OD Inspection From Side B

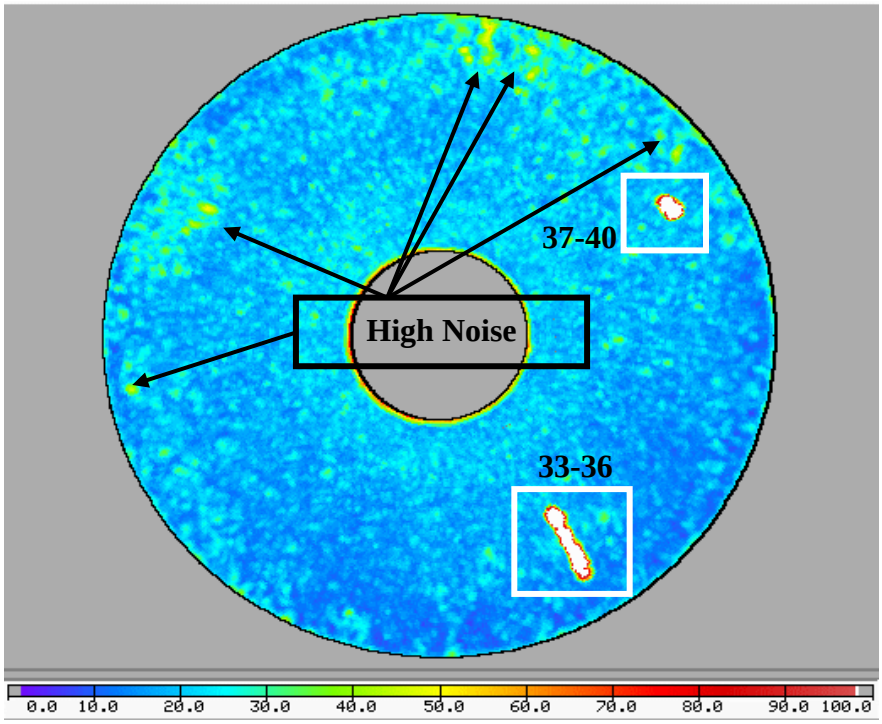

Figure E-27. Forging SB-4 Conventional #1 FBH Far-Zone, 5-MHz Transducer OD Inspection From Side B

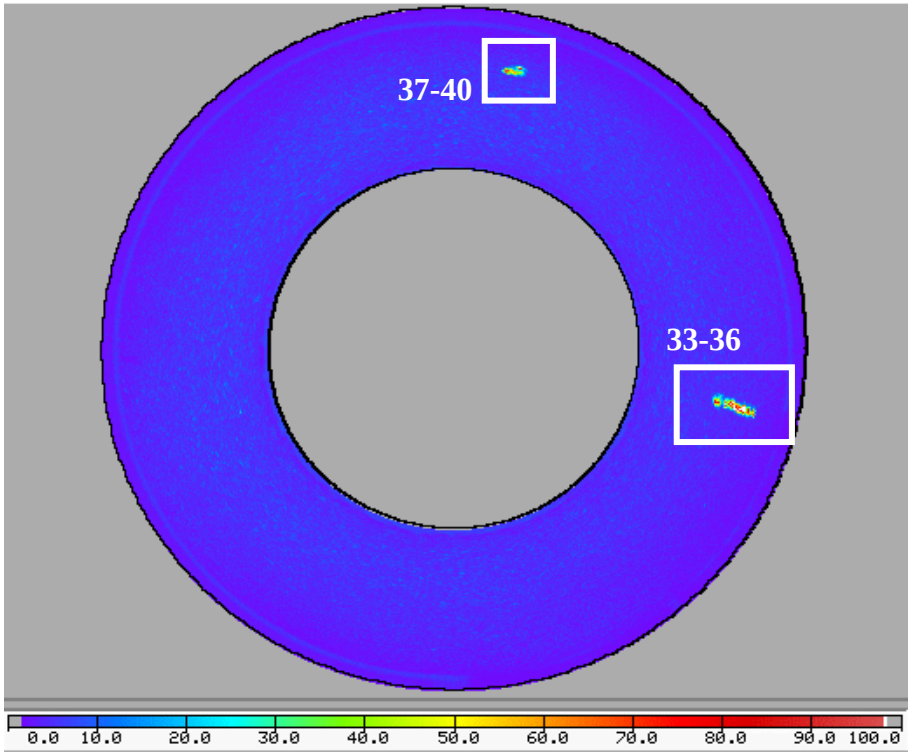

Figure E-28. Forging SB-4 Multizone #1 FBH Zone 3 OD Inspection From Side B

Detection of seeds #29-32 and #41-44 required separate conventional and multizone ID scans due to the geometry of the forging. The 7.3-inch-thick central axial region was more difficult to inspect, although seeds #29-32 were detected by Conventional #1 FBH far-zone, 5-MHz ID inspections from both Side A and Side B, as shown in figures E-29 and E-30. Seeds #41-44 could only be detected from Side B. The multizone inspection detected seeds #41-44 from both Side A using zone 7 (figure E-31) and Side B using zone 3 (figure E-32). Seeds #29-32 were also detected from both sides of the central region using zone 6 from Side A and zone 7 from Side B, as shown in figures E-33 and E-34.

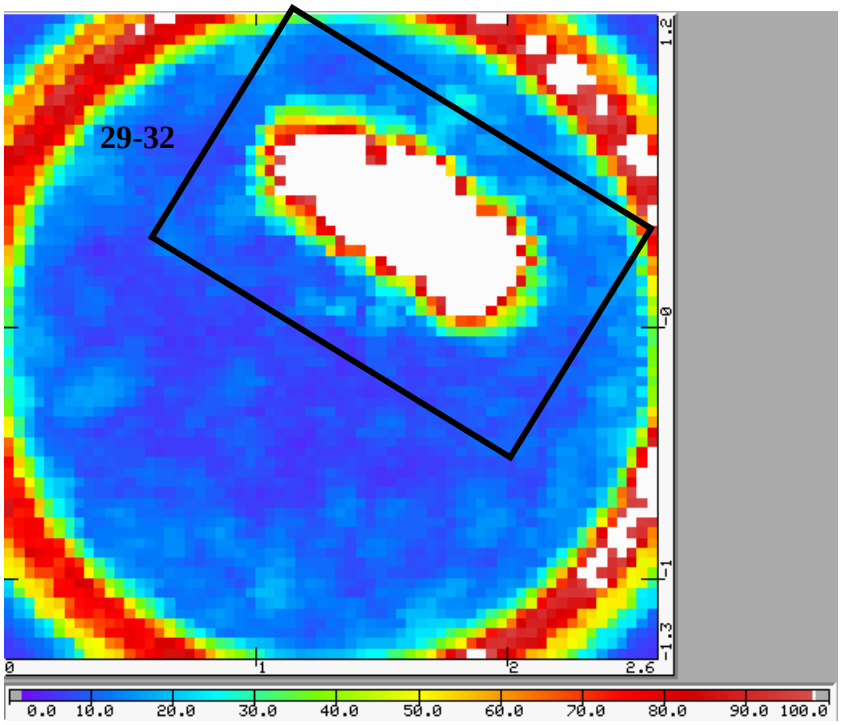

Figure E-29. Forging SB-4 Conventional #1 FBH Far-Zone, 5-MHz Transducer Inspection (ID Scan) From Side A

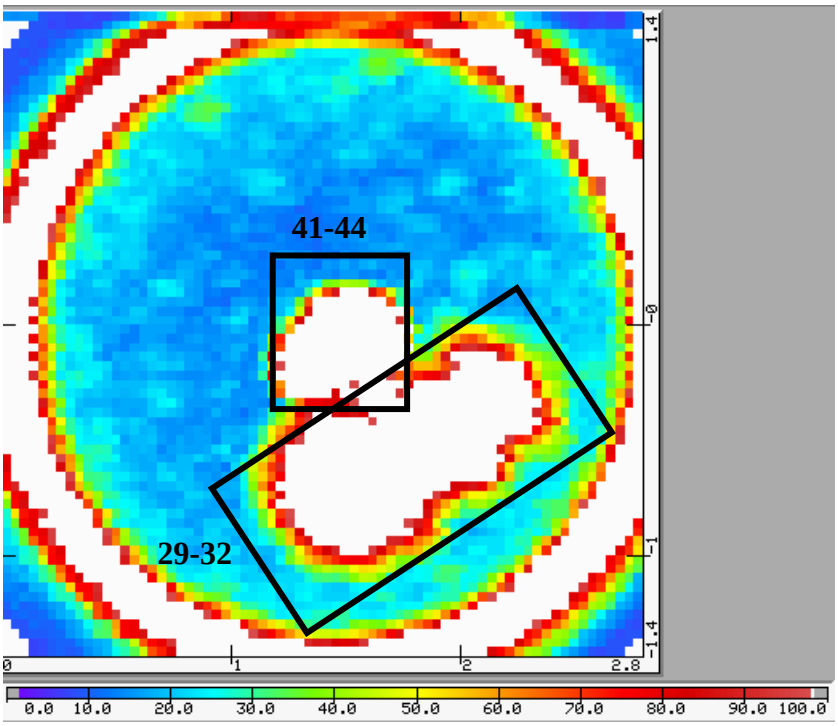

Figure E-30. Forging SB-4 Conventional #1 FBH Far-Zone, 5-MHz Transducer Inspection (ID Scan) From Side B

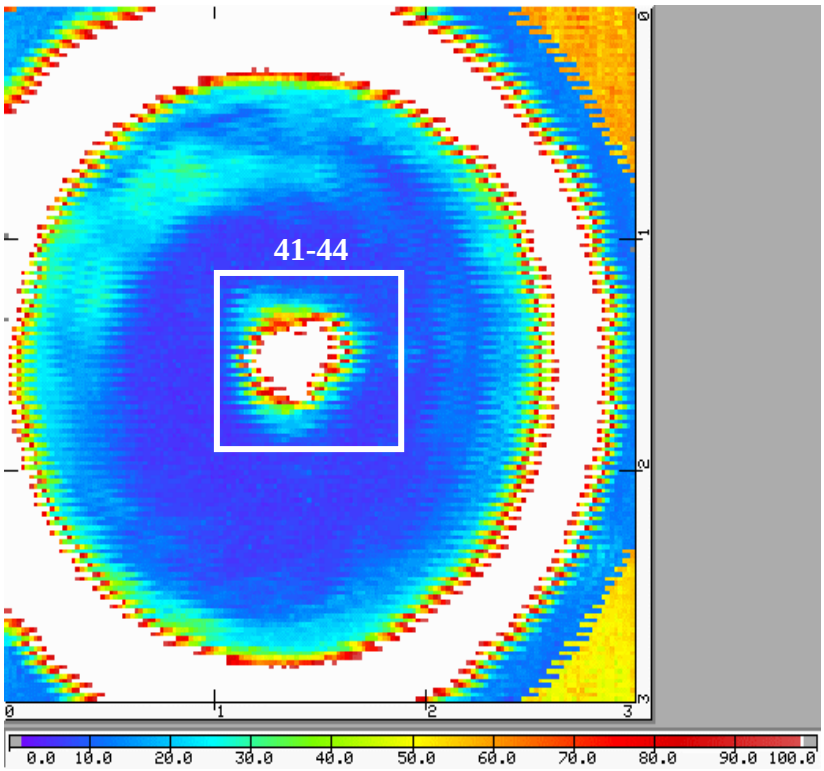

Figure E-31. Forging SB-4 Multizone #1 FBH Zone 7 Inspection (ID Scan) From Side A

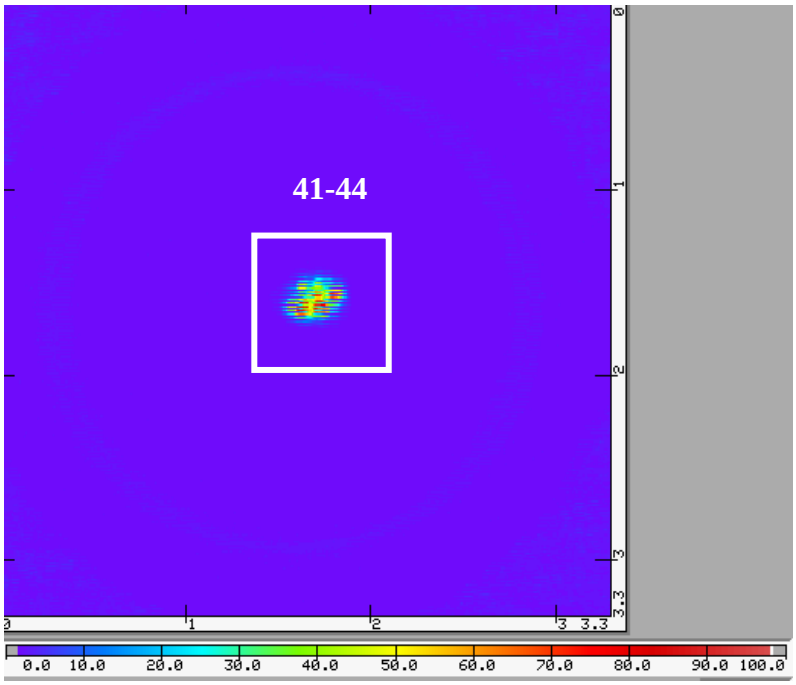

Figure E-32. Forging SB-4 Multizone #1 FBH Zone 3 Inspection (ID Scan) From Side B

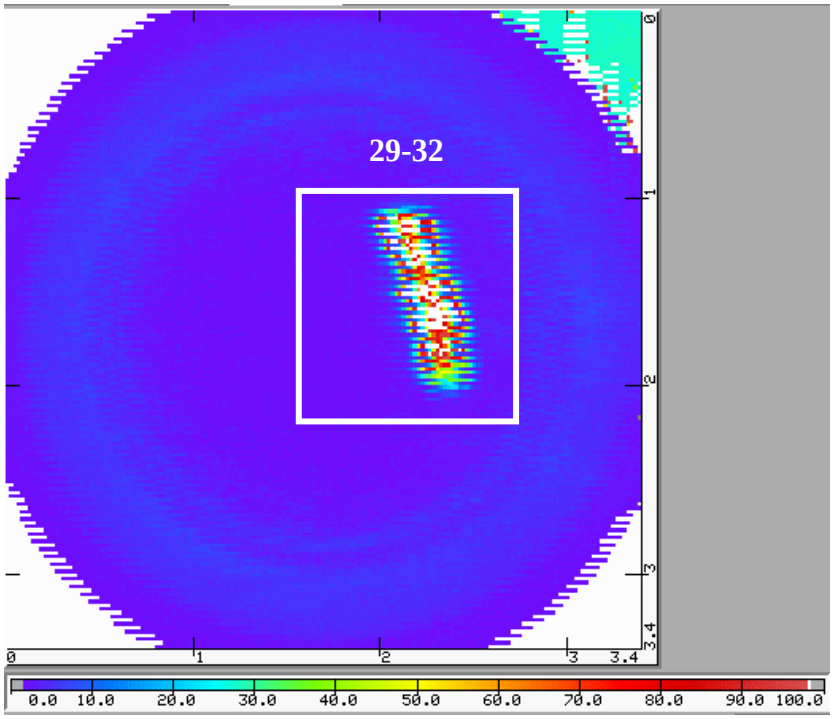

Figure E-33. Forging SB-4 Multizone #1 FBH Zone 6 Inspection (ID Scan) From Side A

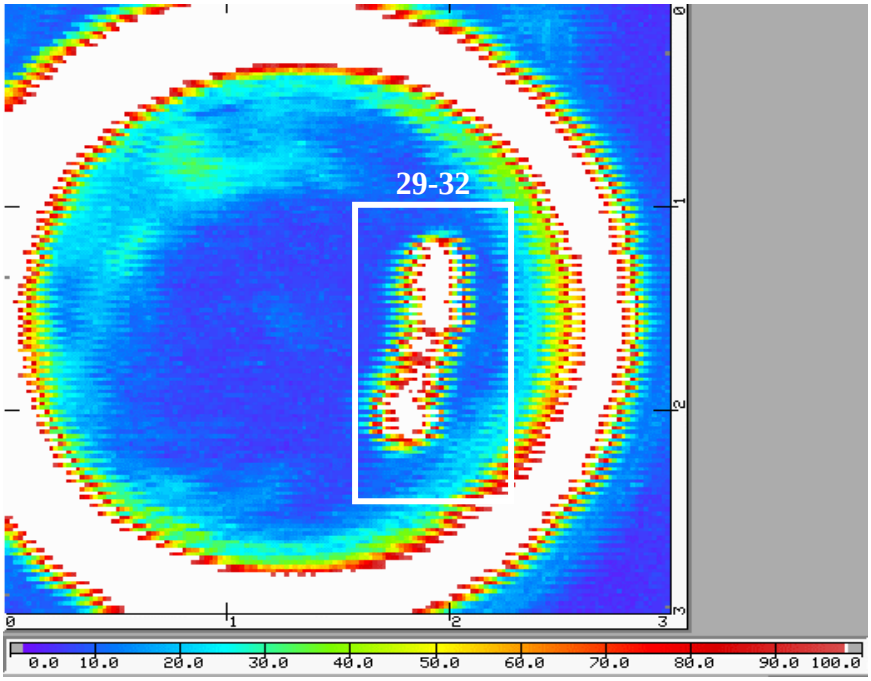

Figure E-34. Forging SB-4 Multizone #1 FBH Zone 7 Inspection (ID Scan) From Side B

E.4.5 FORGING SB-5.

All four seeds, whose locations are identified in figure E-35, were detected from the bore face by the Conventional #2 FBH inspection near-zone, 10-MHz transducer (figure E-36). The deeper seed was also detected by the far-zone, 5-MHz transducer (figure E-37). The near-zone of the Conventional #1 FBH inspection from the bore face detected all seeds except #47, as shown in figure E-38, which could not be distinguished from the noise. The S/Ns were significantly higher for the Conventional #1 FBH bore-face inspection than the Conventional #2 FBH inspection. All seeds were also detected by the multizone inspection from both the bore face (figures E-39 and E-40) and bore (figures E-41 and E-42) except #46 from the bore, which was too close to the bore face to distinguish.

E.4.6 FORGING SB-6.

Seed #49, whose location is shown in figure E-43, was detected by all three inspections from both the bore face and bore. The S/N values were considerably greater for the multizone inspection than either of the conventional inspections.

E.4.7 FORGING B1BW3B.

The HA anomaly location in B1BW3B is shown in figure E-44. The conventional #2 near-zone, 10-MHz inspection could not detect the HA anomaly from either the bore face (figure E-45) or bore (figure E-46), although the anomaly was detected by the far-zone, 5-MHz inspection from the bore only. The conventional #1 inspection was able to detect the anomaly from both the bore face (figure E-47) and bore (figure E-48), although both the amplitude and S/N from the bore face were weak. The multizone inspection detected the HA from both the bore face (figure E-49) and bore (figure E-50) with relatively high S/N.

E.4.8 FORGING B3W2E.

The HA anomaly (location shown in figure E-51) could not be detected from the bore face by either the Conventional #2 or Conventional #1 FBH inspections, as shown in figures E-52 and E-53. Both conventional and near-zone, 10-MHz inspections detected the anomaly from the bore (figures E-55 and E-57), although the signal from the Conventional #2 FBH inspection was very weak (20% amplitude). The Conventional #2 FBH far-zone, 5-MHz (figure E-56) inspection surprisingly produced a much higher amplitude and S/N, even though the HA was just inside the inspection range of the transducer. The multizone inspection detected the HA anomaly from both the bore face (figure E-54) and bore (figure E-58), although the bore-face reflection was relatively weak (29% amplitude and 2.1 S/N).

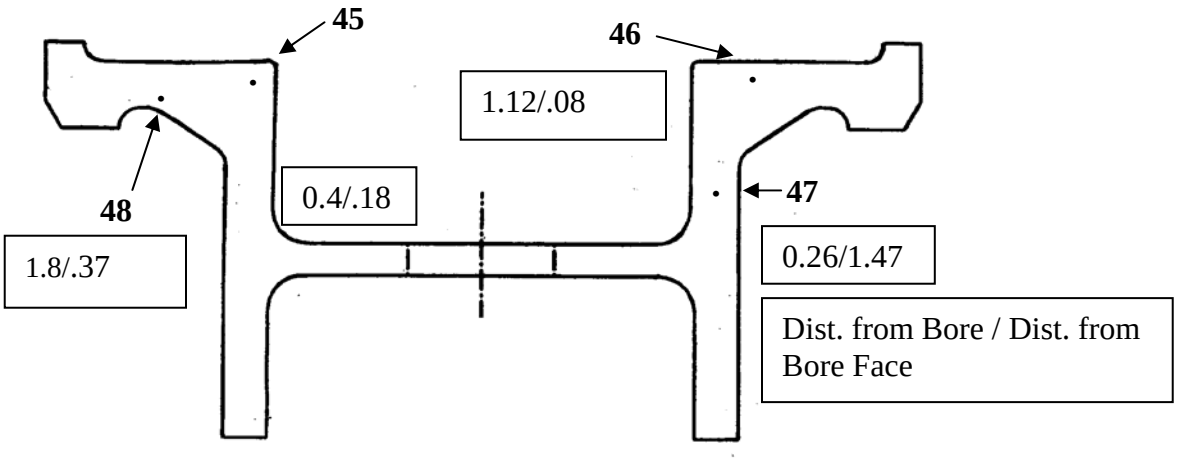

Figure E-35. Forging SB-5 and Seed Locations

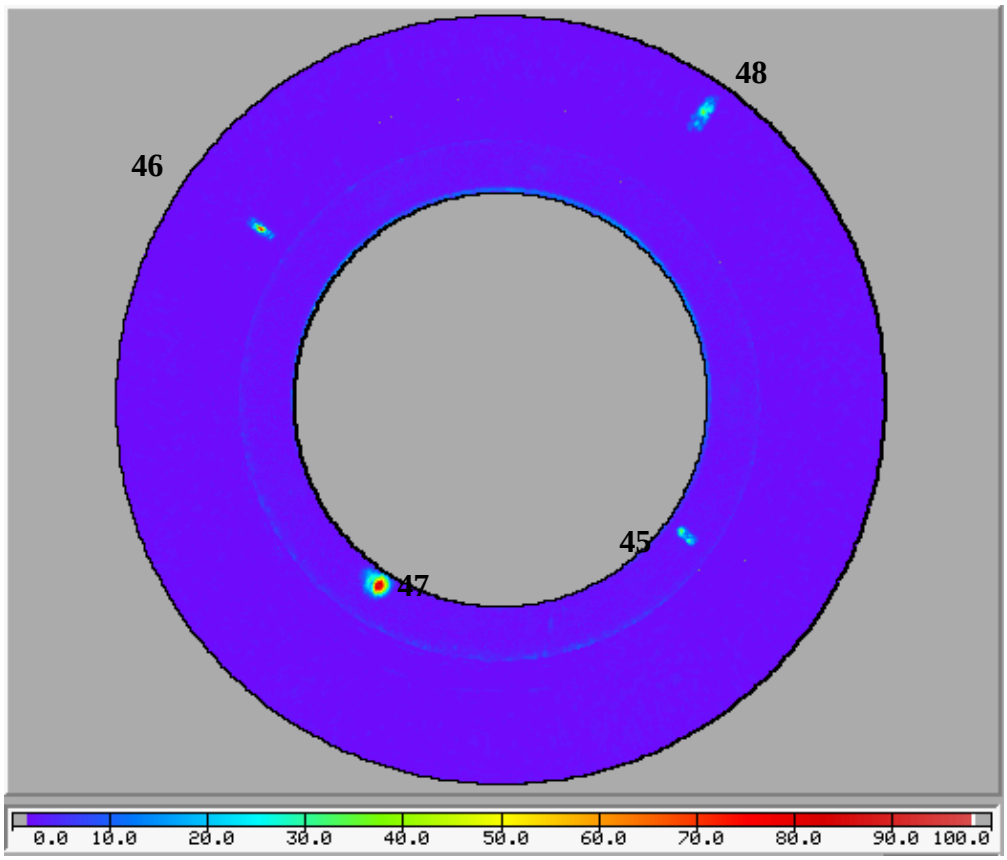

Figure E-36. SB-5 Conventional #2 FBH Bore Face (Near Zone)

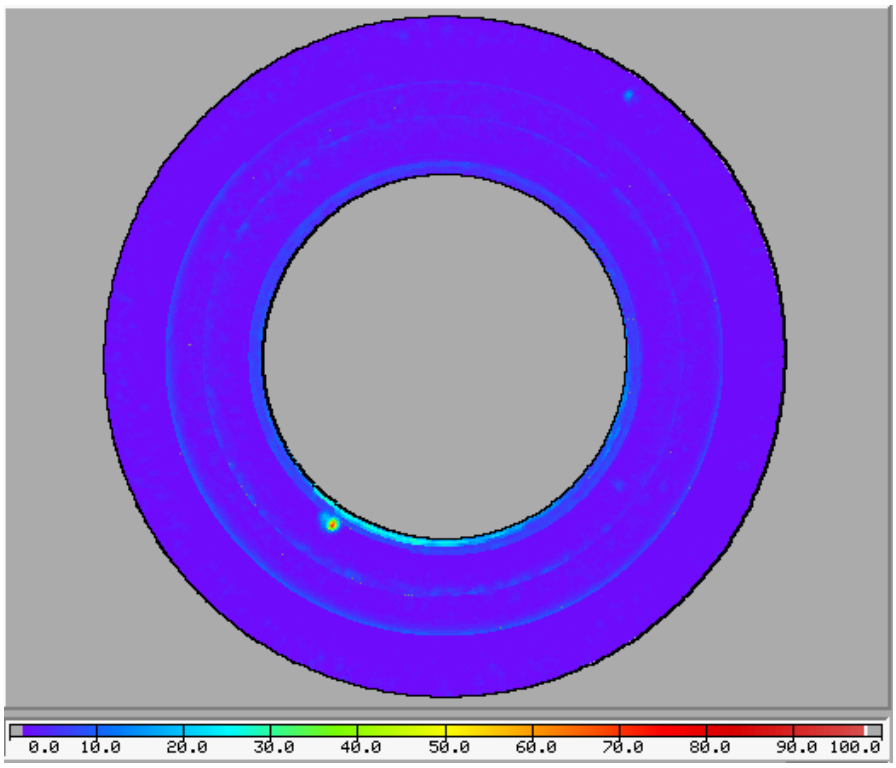

Figure E-37. SB-5 Conventional #2 FBH Bore Face (Far Zone)

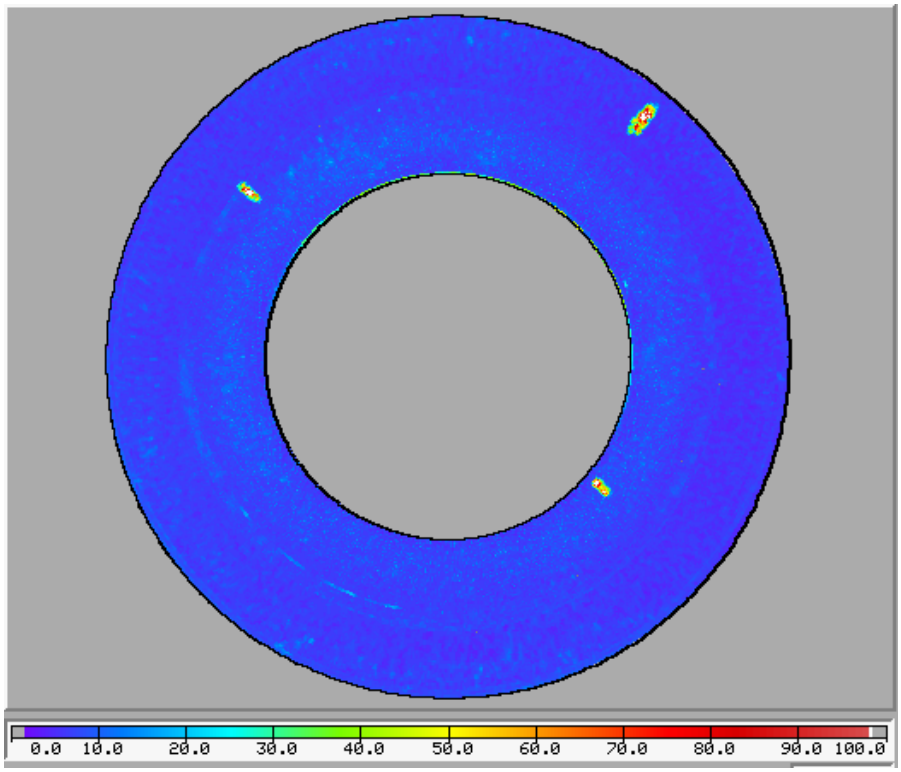

Figure E-38. SB-5 Conventional #1 FBH Bore Face (Near Zone)

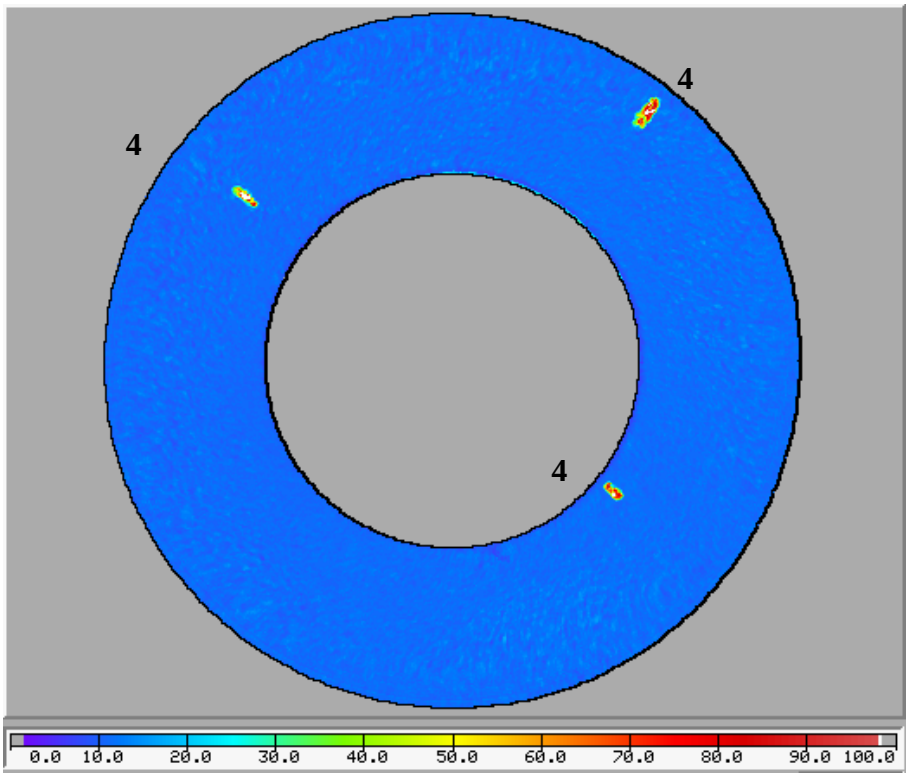

Figure E-39. SB-5 Multizone #1 FBH Bore Face (Zone 1)

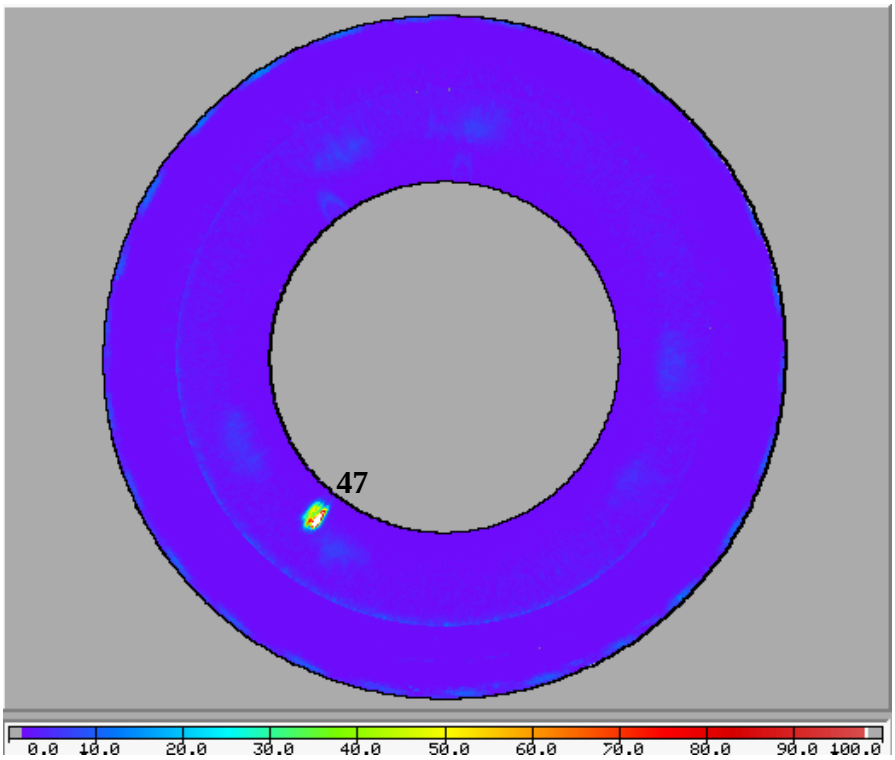

Figure E-40. SB-5 Multizone #1 FBH Bore Face (Zone 3)

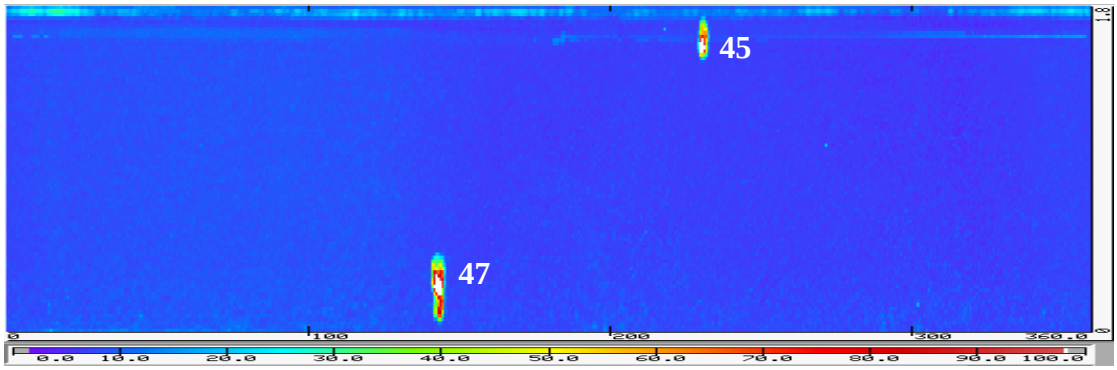

Figure E-41. SB-5 Multizone #1 FBH Bore (Zone 1)

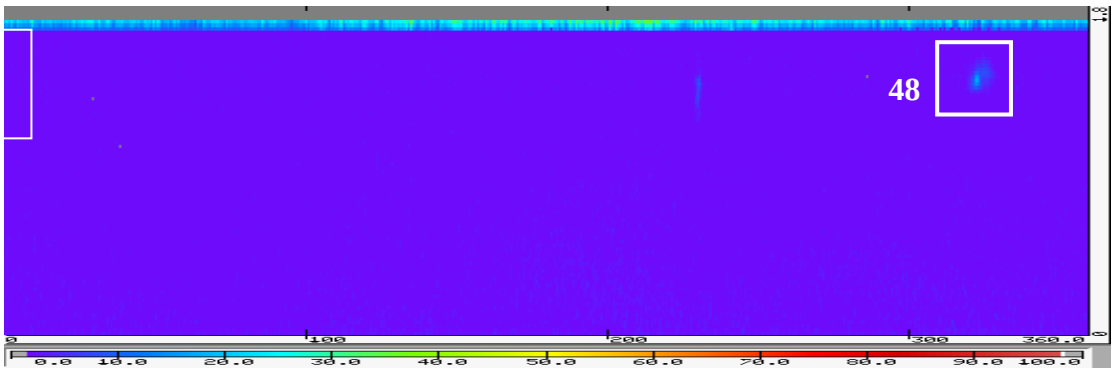

Figure E-42. SB-5 Multizone #1 F Bore (Zone 3)

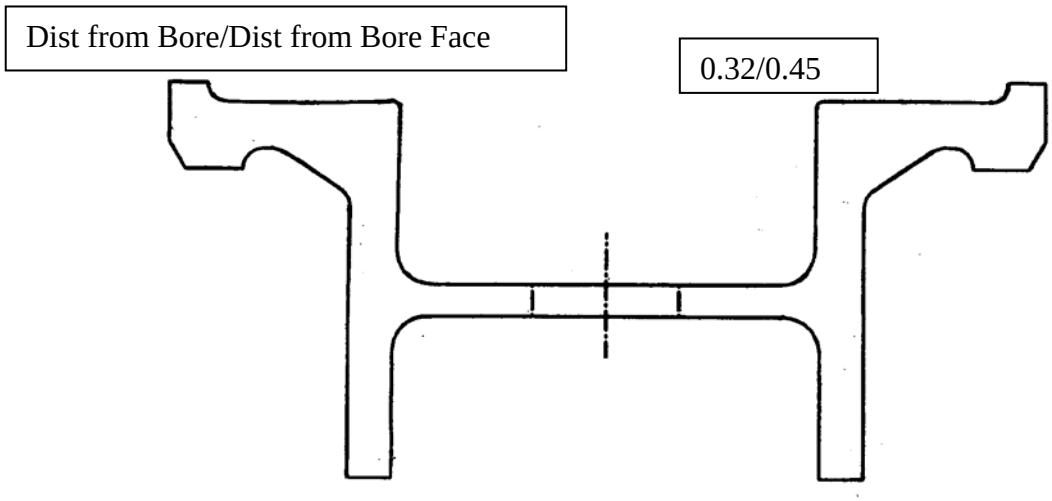

Figure E-43. Forging SB-6 and Indication Location

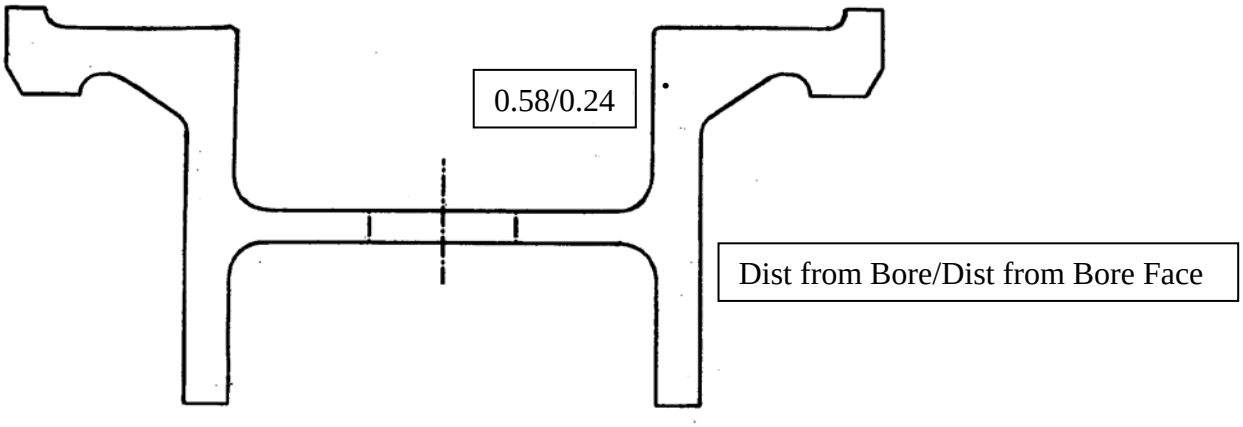

Figure E-44. Forging B1BW3B and Indication Location

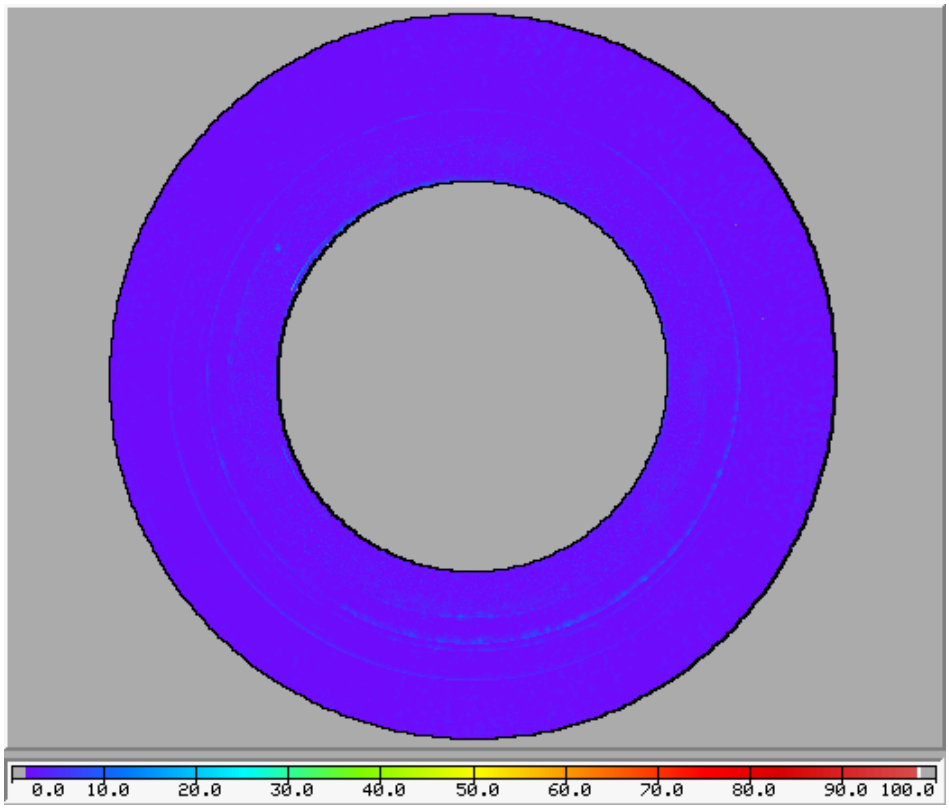

Figure E-45. B1BW3B Conventional #2 FBH Bore Face (Near Zone)

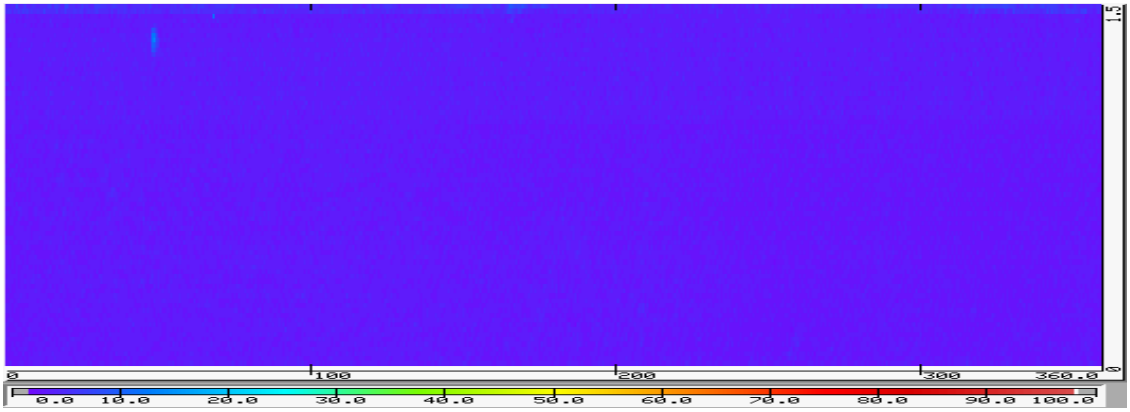

Figure E-46. B1BW3B Conventional #2 FBH Bore (Near Zone)

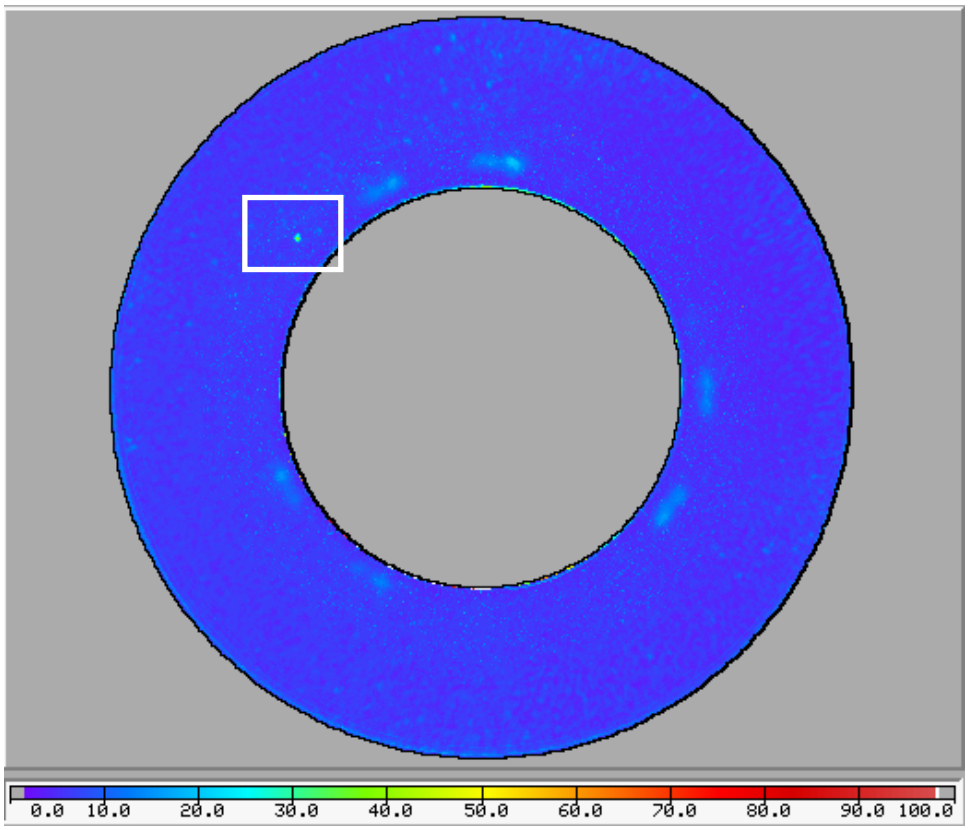

Figure E-47. B1BW3B Conventional #1 FBH Bore Face (Near Zone)

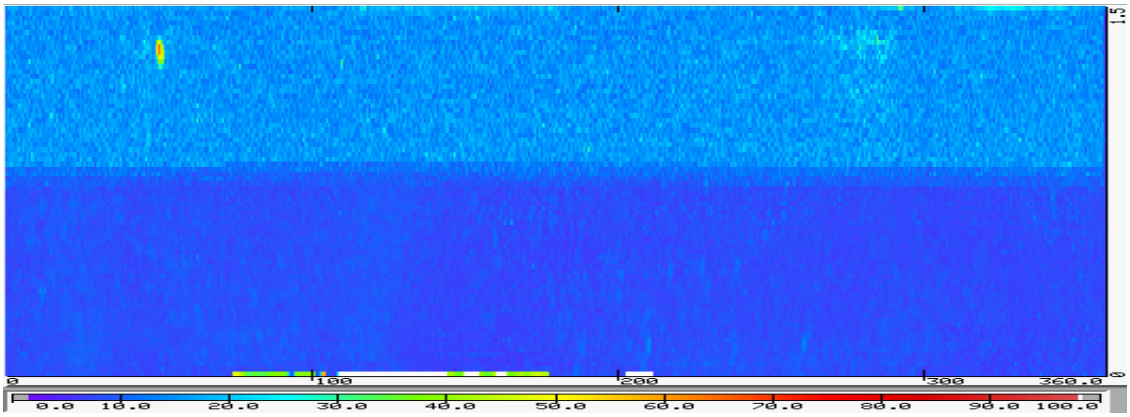

Figure E-48. B1BW3B Conventional #1 FBH Bore (Near Zone)

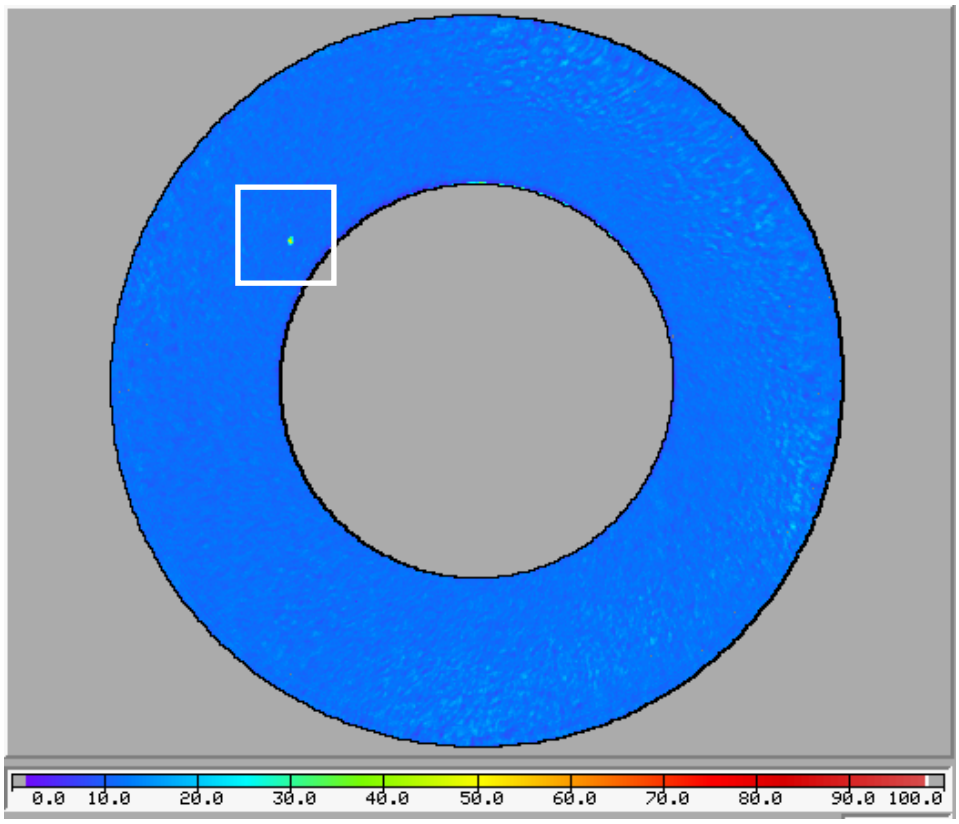

Figure E-49. B1BW3B Multizone #1 FBH Bore Face (Zone 1)

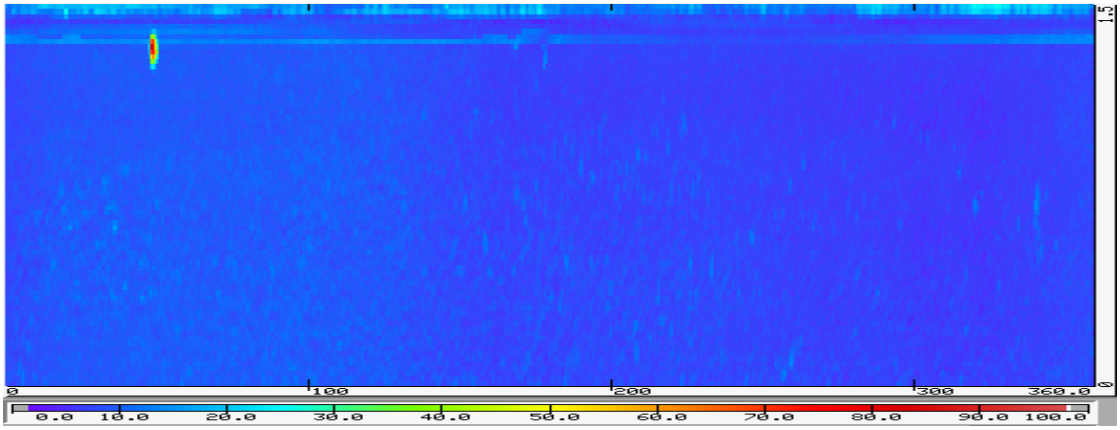

Figure E-50. B1BW3B Multizone #1 FBH Bore (Zone 1)

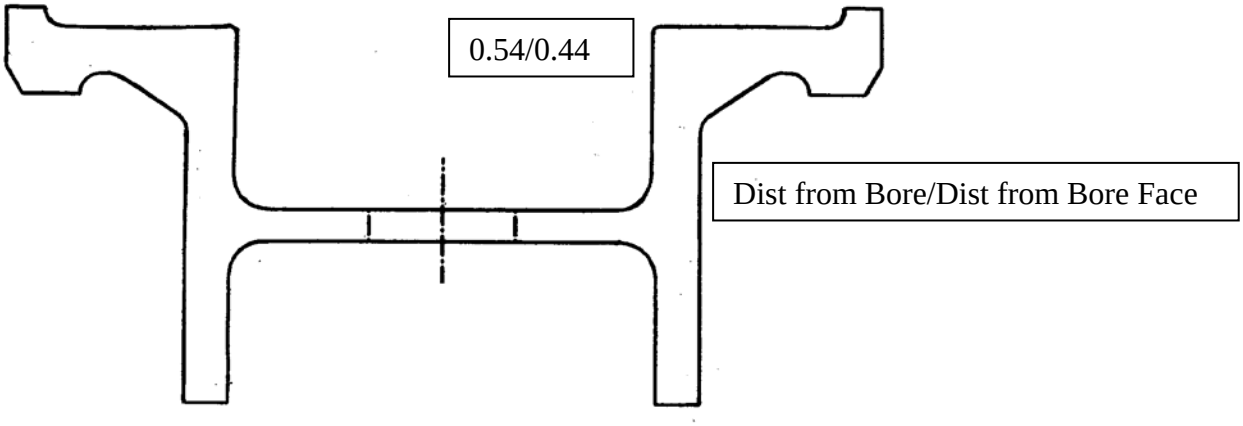

Figure E-51. Forging B3W2E and Indication Location

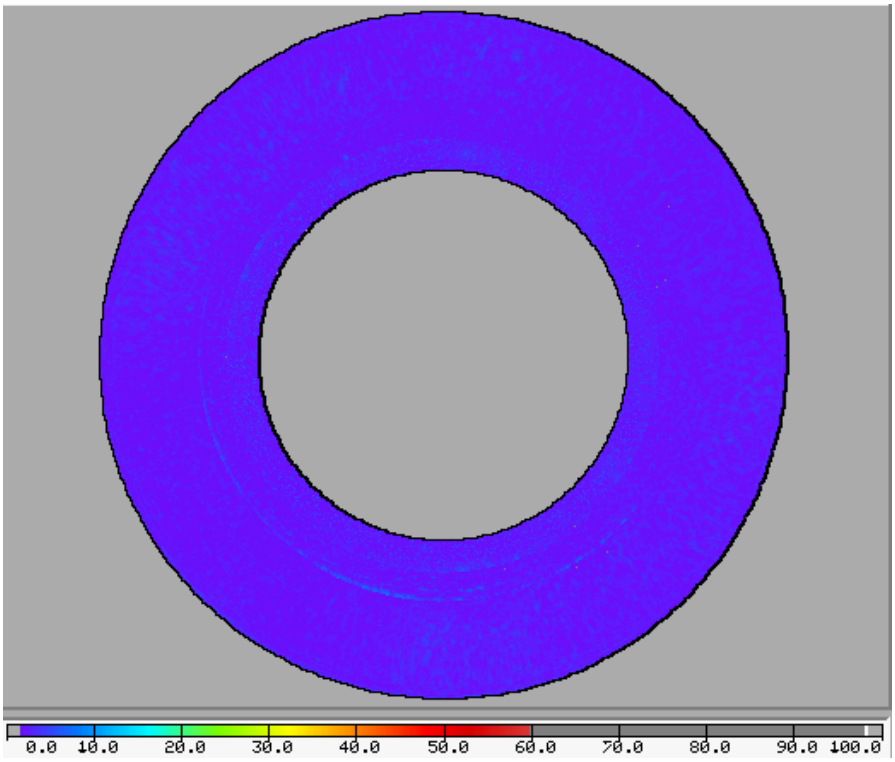

Figure E-52. B3W2E Conventional #2 FBH Bore Face (Near Zone)

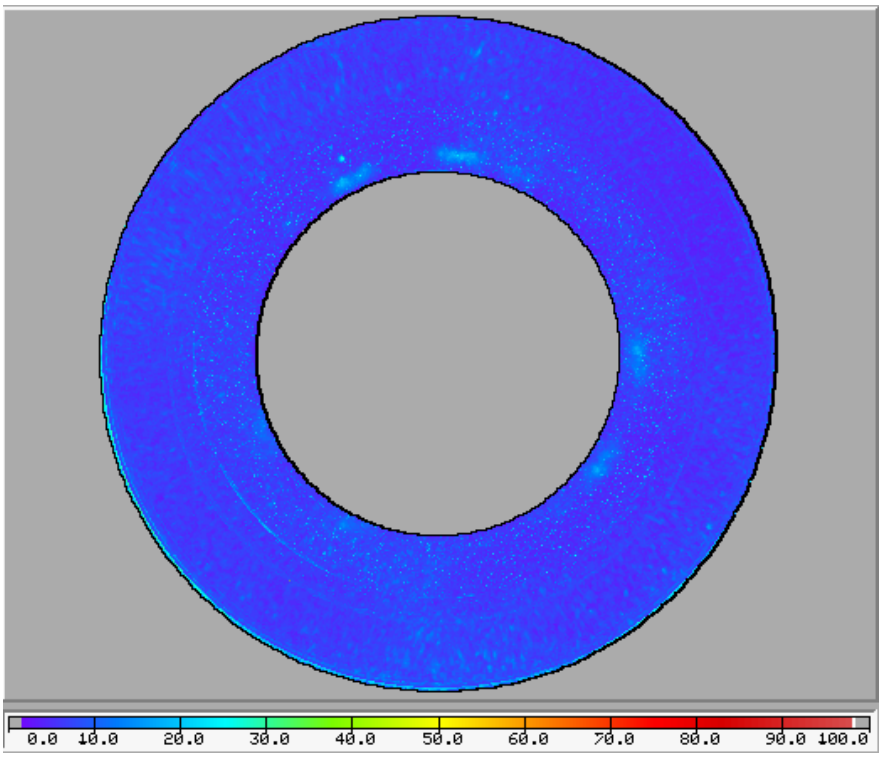

Figure E-53. B3W2E Conventional #1 FBH Bore Face (Near Zone)

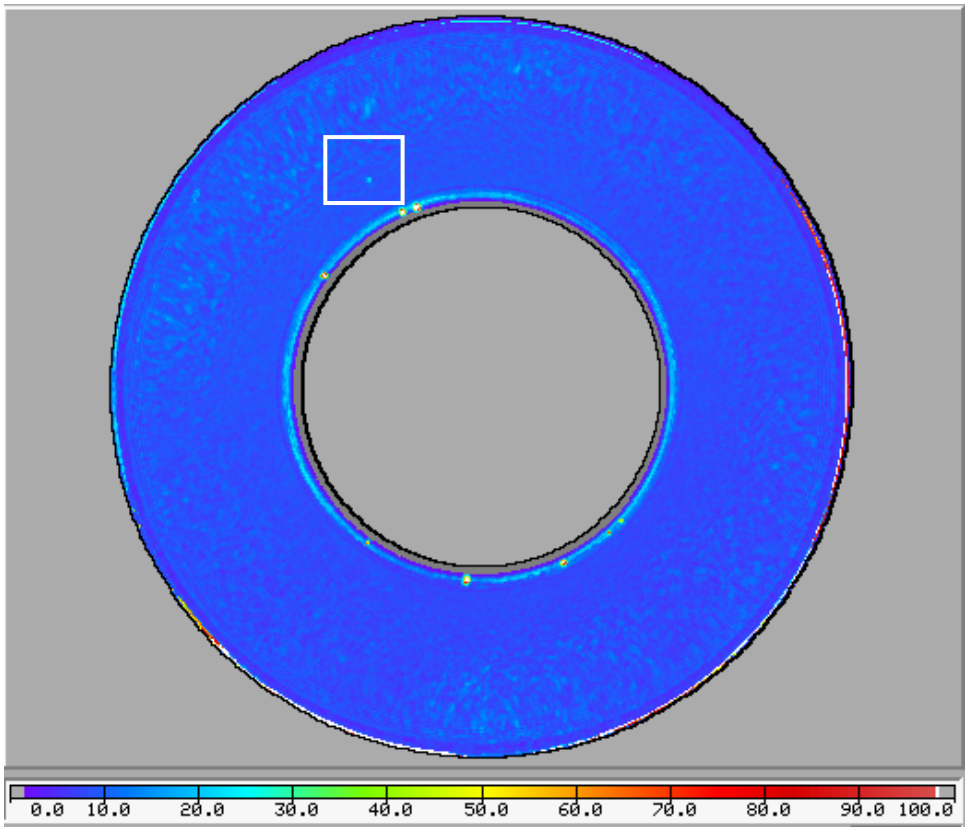

Figure E-54. B3W2E Multizone #1 FBH Bore Face (Zone 1)

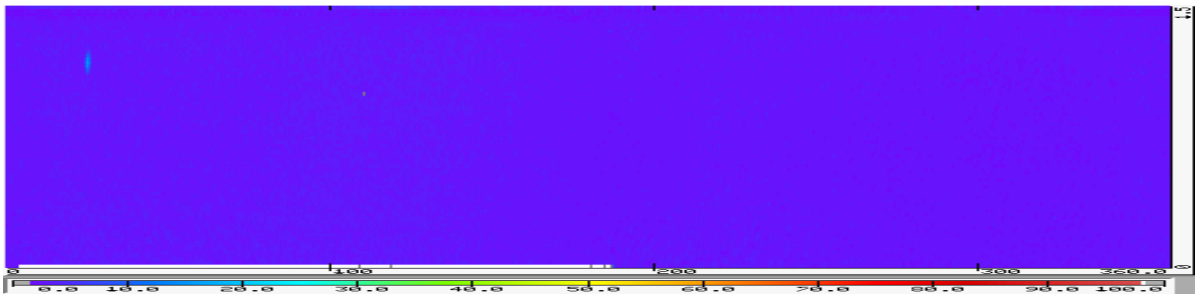

Figure E-55. B3W2E Conventional #2 FBH Bore (Near Zone)

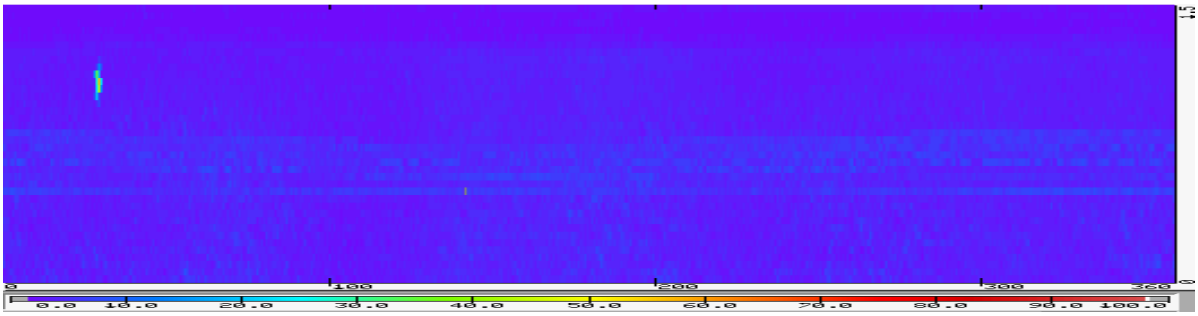

Figure E-56. B3W2E Conventional #2 FBH Bore (Far Zone)

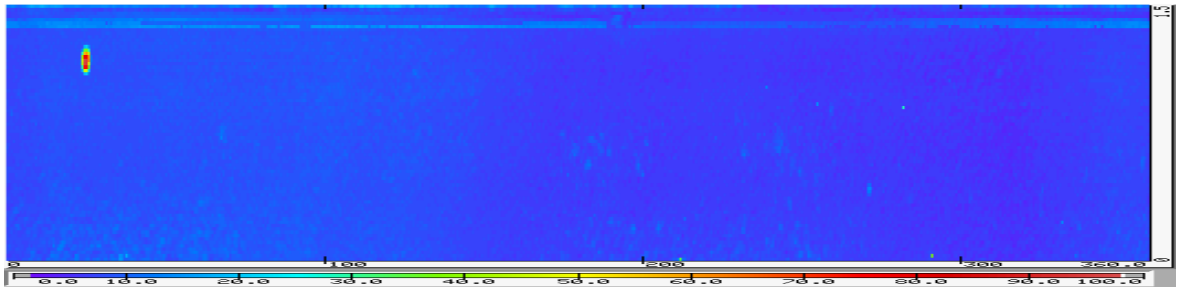

Figure E-57. B3W2E Conventional #1 FBH Bore (Near Zone)

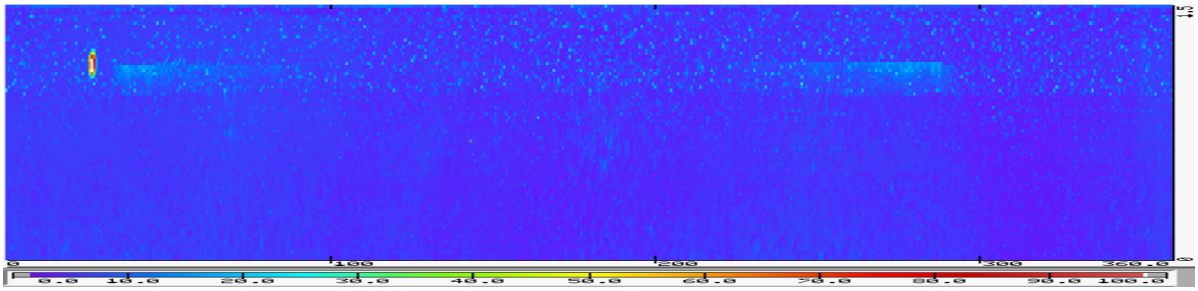

Figure E-58. B3W2E Multizone #1 FBH Bore (Zone 1)

E.5 SUMMARY AND DISCUSSION OF ULTRASONIC RESULTS ON DOGBONE AND BACKFLOW FORGINGS.

E.5.1 EFFECT OF SEED COMPOSITION ON DETECTABILITY.

Evaluation of the detectability of the various seed compositions leads to some interesting comparisons. In forging SB-1, the low nitrogen (N) diffusion zone shell seeds, #1 and #2, were both rather easily detected by all inspections, although the far-zone, 5-MHz transducer could not detect seed #1 from Side B, which was 3.5″ deep, at either #2 or #1 FBH sensitivities. Comparison of the Multizone #1 FBH results on seeds #2 and #3 suggests the presence of the 12% N core had little effect on detectability. Comparison of seeds #4 and #5 implies that the

presence of a diffusion zone around the 12% N core had a negligible effect on detectability, which appears to conflict with the detectability of the diffusion zone noted from seeds #1 and #2.

Since the seed compositions in forging SB-2 were identical to those in forging SB-1, similar results were expected. In fact, the results for similar comparisons in forging SB-2 are essentially analogous. The diffusion zone shells (seeds #7 and #8) were relatively easily detected. Seeds #8 and #9 were both easily detected, suggesting a minor effect of the 12% N core on detectability. Comparison of seeds #10 and #11 were limited by the proximity of seed #10 to the vertical edge of the center depression.

Forgings SB-3 and SB-4 provided no information relative to HA compositional effects on ultrasonic detectability, since all were the same composition (12% N) and all had diffusion zones.

E.5.1.1 Multizone #1 FBH Inspection Detects (Rejects) Essentially All HA Seeds.

All but one of the synthetic HA seeds were detected in the four forgings by the Multizone #1 FBH inspection. All inspections from both sides of the forgings produced rejectable amplitudes and/or S/N. One seed, #10 in forging SB-2, could not be detected by multizone inspection due to its close proximity to the vertical outer edge of the machined center depression.

E.5.1.2 Conventional #2 and #1 FBH Inspection Detects (Rejects) Most HA Seeds.

Both conventional inspections detected most of the seeds in forgings SB-1 and SB-2 with reasonably high amplitudes and S/N. Most of the missed seeds occurred with the far-zone, 5-MHz transducer, probably due to the higher background noise level associated with the deeper scans. The large multiples in forgings SB-3 and SB-4 were generally easily detected by both conventional inspections.

E.5.1.3 High-Background Noise Level Makes Conventional #1 FBH Impractical as a Production Inspection for Forgings SB-1, SB-2, and SB-3.

One of the most noteworthy observations was the substantial increase in background noise level of the Conventional #1 FBH inspection relative to the Conventional #2 FBH and Multizone #1 FBH inspections in forgings SB-1, SB-2, and SB-3. The high background noise produced by the Convention #1 FBH far-zone, 5-MHz transducer would make it impractical to inspect these three forgings to a Conventional #1 FBH high sensitivity in production. It would be anticipated that signals from smaller or lower N seeds probably would have been hidden by the high background noise level of the Conventional #1 FBH inspection and also would not have been detected by the conventional lower sensitivity #2 inspection. The capability of the Multizone inspection to enhance indication S/N of difficult to detect HA inclusions would have been even more evident in this situation.

E.5.1.4 Background Noise Levels of Forging SB-4 Conventional #2 and #1 Inspections are Substantially Lower Than Dogbone Forgings.

The background noise levels in the Conventional #1 FBH OD and ID scans of forging SB-4 were significantly lower than observed in the three dogbone forgings in spite of the increased thickness of the ID scan area. This may be due to a higher degree of recrystallization and enhanced grain flow produced by the more severe backflow forging process, making the grains smaller and more uniform than those produced by the dogbone forging process.

E.5.1.5 Effects of HA Composition and Diffusion Zone on Ultrasonic Response are Inconclusive.

Results from forgings SB-1 and SB-2 were inconclusive relative to the effect of HA composition on ultrasonic detectability. The large reflections provided by the 1.5% N seeds were unexpected, in spite of their large size. Reducing the seed size may have provided more definitive data. The effect of diffusion zones on reflectivity was not clear from the data. These results suggest additional information, perhaps to be provided by the metallographic evaluation, is needed to better understand the ultrasonic behavior of the synthetic seeds.

E.5.1.6 Results Support Earlier Data Suggesting Multizone #1 FBH Inspection is More Effective Than Conventional #2 or #1 FBH Inspection for Detection of HA Seeds in Forgings.

Evaluation of the data from forgings SB-1 through SB-4 provides further evidence that the Multizone #1 FBH inspection can more effectively detect HA anomalies than either Conventional #2 or #1 FBH inspections. This conclusion supports the results from forgings SB-5, SB-6, B1BW3, and B3W2, along with several other studies performed outside this contract. This advantage in detectability becomes more evident as the reflectivity of the HA anomalies diminishes due to smaller size or lower nitrogen content.

E.5.1.7 Hard Alpha (Natural and Synthetic) is Easier to Detect in ihe Billet Than the Subsequent Forging.

Another comparison of interest is the relationship between the capability to ultrasonically detect HA anomalies in billets and forgings. This comparison was done on the first contaminated billet sample (B1BW3A), which was forged into a pancake shape, as well as on the semifinished forging (spin disk) results. All the ultrasonic inspection results to date have suggested that both synthetic and natural HA inclusions are easier to detect in the billet than in the forgings. The data obtained from forgings SB-1 through SB-4 has been combined with the data from the other forgings in figure E-59. The Multizone #1 FBH data from the forgings was numerically converted to the same calibration level (gain level) as the Multizone #2 FBH data from the billet inspections conducted previously. The 45-degree line in figure E-59 represents equivalent response from the billet and forging inspections. Data falling above the 45-degree line indicate a larger response from the billet inspection, while data below the line indicate the corresponding forging provided a larger ultrasonic response. It is apparent that the dogbone and backflow data (Series 1) support the conclusion drawn earlier from the pancake (Series 2) and semifinished forging (Series 3) results; i.e., most HA inclusions, both natural and synthetic, are more reflective in the billet than in the forging.

This detection advantage in billets can be ameliorated somewhat if the forging can be inspected at a higher calibration level (gain level) than the billet. This would appear to be possible in most cases if a multizone inspection is used on the forging. However, the increase in background noise level associated with increasing conventional inspection sensitivity from a #2 FBH to a #1 FBH will undoubtedly result in some forgings (or parts of forgings) being uninspectable at the high-sensitivity Conventional #1 FBH level. Again, these data tend to corroborate the Jet Engine Titanium Quality Committee production anomaly information, which indicates more HA anomalies have been ultrasonically detected in billets than in the subsequent forgings.

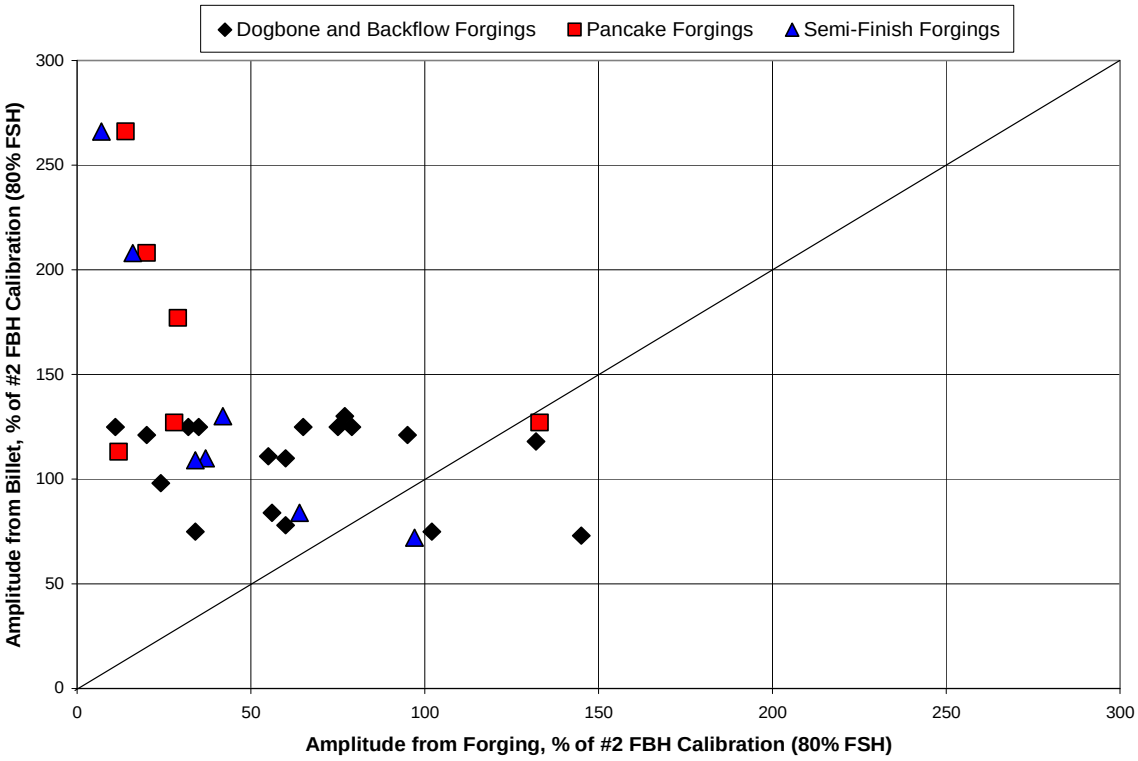

Figure E-59. Hard Alpha Ultrasonic Response in Billets vs Subsequent Forgings

APPENDIX F—DEFORMATION STRAIN NEEDED TO CRACK HARD ALPHA ANOMALIES

F.1 INTRODUCTION.

F.1.1 HARD ALPHA ANOMALY MICROMODELING.

Realistic modeling of hard alpha (HA) anomalies is difficult due to the complex mechanical behavior of the material, as well as the large deformations they can encounter during thermo-mechanical processing, such as ingot to billet conversion, extrusion, or component forging. Furthermore, the large disparity in length scales between the anomaly and the component forging makes it impractical to model the anomaly and the component simultaneously.

Typical aircraft engine disk forging sizes are in the range of 6″ to 30″ (15 cm to 75 cm) in diameter, and typical HA anomaly sizes of concern are about 0.10” (2.5 mm) in size or smaller. Due to this extreme size ratio between the full-scale part and the anomaly, a two-step macro- and microlevel simulation is possible. First, the entire forging process can be simulated (macrolevel) using material properties for the titanium alloy and assuming that the presence of the anomaly has no effect on the bulk flow behavior of the material. Second, a small region around the anomaly can be identified, the geometry and key material properties of the anomaly defined, and a small volume of the matrix material with the nitrogen (N) diffusion zone (DZ) and HA anomaly can be forced through the same deformation pattern as the original material (microlevel simulation).

In the micromodel, the deformation of a volume, referred to as a microvolume, is simulated. The microvolume (figure F-1) consists of the anomaly surrounded by a DZ and then by the parent material. The boundaries of the microvolume extend well beyond that of the anomaly. Beyond the boundaries of the microvolume, the presence of the anomaly is assumed to have a negligible effect on the deformation in the parent material. This is true unless the anomaly size is comparable to the local forging size. The advantage of this approach is that it decouples the deformation of the anomaly and the parent material, allowing each calculation to be performed independently by an appropriate method. In effect, the macro- and micromodels are coupled with a one-way interaction. The one-way micro- and macrocode interaction keeps the computational effort manageable without sacrificing accuracy. This strategy permits realistic and accurate assessments of the effects of forging on anomaly behavior, without increasing the complexity significantly.

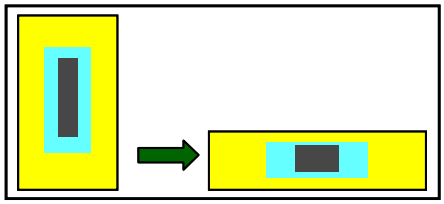

Figure F-1. Definition of Microvolume Consisting of the Anomaly Surrounded by a DZ, and Then by the Parent Material-Initial and Deformed Shapes of the Microvolume are Schematically Shown Here

F.1.2 SUMMARY OF PREVIOUS WORK.

In previous work documented in the Turbine Rotor Material Design (TRMD) Phase I final report [F-1] and in appendix C of the present final report, a deformation microcode implementing this type of micromodel was developed and validated to predict the overall size and orientation of HA anomalies ignoring voiding/cracking. Seeded billet forging experiments were conducted to obtain data to validate the macro- and microcodes, and 28 of the 44 seeds from the seeded forgings were cut up for microcode validation. Good agreement was observed between the measured and predicted anomaly deformation, better for the DZ than for the HA. Regression equations were developed to describe the relationships between anomaly deformation and forging macrostrain. These regression equations provide a means to predict anomaly deformation quickly and accurately for both billet conversion and component forging, and they can be used with both DEFORM™ two-dimensional and three-dimensional.

As part of this previous work, the influence of the various independent variables on the deformation of the DZ and HA was determined. The results are summarized in table F-1. Based on these results, HA and DZ nitrogen content, forging temperature, strain rate, and macrostrain are the significant variables. These results will be useful in understanding the strain-to-cracking study reported here.

Table F-1. Results of Parametric Study Summarizing the Influence of Various Independent Variables on the Deformation of the DZ and the HA

Variable	Effect	Comment
HA N2 content	HA deformation decreases with increasing HA N2	• Dependence on HA nitrogen content is moderate to low • HA flow stress is about 25% higher at 8% than at 4% N2
DZ N2 Content	HA deformation increases with increasing DZ N2	• Dependence on DZ nitrogen content is moderate • DZ flow stress increases with its nitrogen content
Forging strain rate	HA deformation increases with increasing strain rate	• HA more brittle at higher strain rate
Forging temperature	HA deformation decreases with increasing temperature	• HA more brittle at lower temperature
• DZ to HA size ratio • Inclusion aspect ratio • Hydrostatic pressure	Not significant	

F.1.3 OBJECTIVE AND APPROACH.

The objective of this study was to determine the deformation macrostrain required to crack HA anomalies using the deformation microcode developed previously. The study was designed to provide insight into the likelihood of noncracked HA under typical billet conversion and forging

conditions, to provide insight into typical orientations of HA in forgings, and potentially to direct the future development of inspection procedures to enhance detectability of HA anomalies.

The study was comprised of four major activities. The first activity was to determine HA cracking strain and damage (extent of cracking) as a function of nitrogen content and deformation parameters, based on the regression equations. The second activity was to link these relationships with DEFORM™ to predict damage (extent of cracking) in representative forging shapes and to validate the predictions by comparisons with observed cracking in the seeded billet (SB) studies. The third activity was to use this capability to determine the extent of HA cracking under typical production conditions, including a representative ingot-to-billet conversion and two specific production forging shapes. The fourth activity was to predict the forging flow lines along which melt-related anomalies tend to orient, using the same generic forging shapes. The results of each of these four activities are described in turn.

F.2 STRAIN-TO-CRACK HA.

The objective of the first activity was to determine the relationship between HA nitrogen content and strain-to-cracking in the HA using the micro- and macrocodes. The strain to HA cracking was determined as a function of five variables: HA nitrogen content, DZ nitrogen content, deformation temperature, deformation strain rate, and damage. The results are presented as contours of strain to HA cracking as a function of two variables, with the other three variables held constant.

The microcode developed in TRMD-I was based on the UNIX® version of DEFORM. With the move towards personal computer (PC)-based platforms, the microcode was transitioned from UNIX to Windows® 2000-based computers using the PC version of DEFORM. The user interface with this version is totally different from the Unix version. Tests were conducted to ensure that the microcode features worked properly and that the PC version reproduced the Unix results for standard runs. Some minor inconsistencies associated with Fortran 90 versus Fortran 77 were fixed.

A web-based Fortran compilation procedure was created at Scientific Forming Technologies Corporation (licensors of DEFORM) to compile user subroutines. This permits users to compile their user subroutines on the Internet. Two procedures were set up: one for the compilation of subroutines associated with the finite element simulation and the other for subroutines associated with postprocessing. Both procedures were tested, and they worked satisfactorily.

The microcode developed earlier in TRMD-I does not explicitly predict HA cracking. The microcode uses a damage variable to simulate the effects of HA cracking and the value of damage indicates the extent of cracking: 0 = no cracking; 1 = fully cracked. Therefore, the cracking strain and the extent of cracking were based on the accumulated HA damage.

F.2.1 CONSTITUTIVE EQUATIONS FOR HA.

Experimental measurements of the constitutive properties of HA were performed in TRMD-I, and HA constitutive equations were developed from the data. These equations were used here to

obtain the strain to HA cracking and damage. Complete details of the constitutive equations and the experimental testing are provided elsewhere [F-1 and F-2]. A brief summary is provided below.

The flow and fracture behavior of HA was determined experimentally as a function of nitrogen content, stress state, strain, strain rate, and temperature. HA specimens with nitrogen contents ranging from 2 to 11.6 weight percent were fabricated. Stress-strain curves were obtained under various states of stress by performing uniaxial compression, indirect tension, indentation, and plane-strain compression tests at two strain rates. The yield strength was found to increase with increasing nitrogen content and with increasing strain rate, but to decrease with increasing temperature. HA was observed to undergo substantial plastic deformation for nitrogen contents less than 4%, but exhibited brittle fracture with little plastic flow for nitrogen contents 5.5% and higher.

The constitutive equations developed describe the fracture of HA (intact material) and the failure stress of damaged HA as a function of damage using a continuum damage mechanics formulation.

For intact material, the flow or fracture stress, Y_i, of HA is given by:

$$Y_i = Y_n \left[X + Z \ log \left(\frac{P}{Y_n} \right) \right] \tag{F-1}$$

where X = 1.4, Z = 0.94, and P = Pressure (compression is positive).

The fracture stress Y_n of HA is given by:

$$Y_n = \gamma_0 + \gamma_1 N \tag{F-2}$$

Where γ_0 = 55.44 ksi and γ_1 = 0.558 ksi/wt.% N.

For failed HA, the flow stress Y_f is given by

$$Y_f = 0.1\ Y_i \tag{F-3}$$

The onset of fracture is given by Y_f. After the initiation of fracture, the failure stress, Y_D , is considered to decrease with increasing damage according to:

$$Y_D = (1 - D) Y_i + D Y_f \tag{F-4}$$

where D is an internal variable representing the state of damage. The value of D is D = 0 for intact material and D = 1 when the material fails completely.

The damage rate is given by:

$$\dot{D} = c_3 \ \dot{\varepsilon} \tag{F-5}$$

where $\dot{\varepsilon}$ is the strain rate, $c_3 = 18.75\ \dot{\varepsilon}^{0.1516}\left(1 - e^{c_4 N}\right)\ for\ N \geq 4\ wt.\%\ N$,
c_4 = -0.0964 (wt.% N^{-1}) and N is nitrogen content in wt.%.

The accumulated damage at any time is obtained by integrating the damage rate equation:

$$D = \int \dot{D} dt = \int c_3 \ \dot{\varepsilon} dt \tag{F-6}$$

F.2.2 DEFINITIONS OF HARD ALPHA AND DZ.

The constitutive property data generated experimentally in TRMD-I indicate that HA deforms plastically when the nitrogen content is less than 4 wt.%, but fractures when the nitrogen content is 4 wt.% or greater. Guided by these experimental observations, constitutive equations were developed to describe the fracture behavior of HA with high nitrogen contents (>4% N) and the plastic flow behavior of HA with low nitrogen contents (<4% N).

Henceforth, the region with nitrogen content greater than 4% is called a HA and the region with nitrogen content less than 4% is called a DZ. Each is described by its own constitutive equations. The damage/cracking formulation is applied only to HA.

An anomaly will, in general, consist of a HA core surrounded by a DZ. The DZ results from partially dissolved HA cores during melting or conversion steps. In reality, there is no sharp transition between a DZ and a HA at 4% N. The transition from ductile to brittle behavior occurs over a range of nitrogen contents depending on the deformation conditions (strain, strain rate, and temperature) and the beta to (beta + alpha) transition temperature. More work is needed to accurately characterize the transition zone.

F.2.3 STRAIN-TO-CRACKING AND DAMAGE RESULTS.

The HA constitutive and damage equations described above were used to determine the strain to HA cracking and damage. Table F-2 lists the values of the variables used. Calculations were done only up to 8% HA nitrogen content, since there is little difference for higher nitrogen contents.

The calculation steps are summarized below:

1. The HA strain and strain rate were calculated using the regression equations (appendix C), for given HA N2 content, DZ N2 content, strain rate, temperature, and macroforging strain (as listed in table F-2).

Table F-2. Variables Used in Strain-to-Cracking Study

Variable	Min-Max Levels
HA N2 content (wt.%)	4-8
DZ N2 content (wt.%)	1-3
Strain rate (1/sec)	0.1-1.0
Temperature (°F)	1550-1750
Macroforging strain	0.1-2.1
Damage	0-1

2. The HA damage rate was calculated from equation F-5. The damage rate, as a function of HA N2 content, DZ N2 content, strain rate, temperature, and macroforging strain, was saved for use in the DEFORM user subroutine. This table of damage rate values was used when computing the damage for a component forging with the user subroutine. The forging strain rate, temperature, and macrostrain were available at each element in the component forging from DEFORM. Using a table lookup function, the damage rate at each element in the component forging was obtained for the HA and DZ nitrogen contents listed in table F-2. The damage rate was integrated through the forging process using equation F-6 to obtain the total accumulated damage. The damage contours in the component forging are indicative of the extent of cracking for the HA and DZ nitrogen contents listed in table F-2.

3. The forging macrostrains to reach several values of damage in the range of 0 to 1 were calculated. HA cracking starts when the damage exceeds zero. For a damage value of unity, the HA is fully cracked. Cracking occurs over a range of damage and macrostrain. Therefore, cracking was defined to have occurred if the HA damage (from equation F-6) reached a predefined damage value. If the damage calculated in this step exceeded the predefined critical damage, cracking was deemed to have occurred. The corresponding forging strain to reach the extent of cracking defined by this value of damage was calculated. This strain, as a function of HA N2 content, DZ N2 content, strain rate, temperature, and critical damage, was saved for use in the DEFORM user subroutine. The use in the subroutine was again through a table lookup function similar to that described for damage in step 2.

Strain to HA cracking was obtained as a function of five variables:

- HA nitrogen content
- DZ nitrogen content
- Deformation temperature
- Deformation strain rate
- Critical damage indicating the extent of cracking

HA damage was obtained as a function of five variables:

- HA nitrogen content
- DZ nitrogen content
- Deformation temperature
- Deformation strain rate
- Macro strain

Since the microcode does not explicitly predict cracking, damage was used to indicate the extent of cracking. Strain-to-cracking, strain rate, and temperature all refer to macroforging values.

The results were graphed in various ways for ease of use and interpretation. There are a total of five variables. The results are shown as contours in two of the five variables, for given values of the other three (listed in the title of each contour plot). The remaining two variables form the two axes of the contour plots. Typical results and general trends are shown in figures F-2 through F-7. A complete set of all the graphs is included elsewhere [F-3].

The use of the damage and the strain-to-cracking graphs is described below and illustrated in figures F-6 and F-7. Find the plot with the appropriate contour axes; e.g., if strain rate and temperature are known and the results are desired for several HA N2 and DZ N2, a plot with the latter two as the contour axes should be selected. The deformation conditions of macrostrain, strain rate, and temperature are located at the given HA N2 % and DZ N2%, and this gives the damage value. Damage equal to zero indicates an intact HA anomaly. Damage equal to 1 indicates a fully failed HA anomaly. The larger the damage value, the more extensive the cracking of the HA anomaly.

The strain-to-cracking graphs should be used in the same way. Select the graph with the appropriate contour axes. The point at the given values of the five variables is located to obtain the cracking strain contour value. The cracking strain is compared with the macrostrain from a forging model of the deformation process. This determines if a HA anomaly at the location will crack, and the corresponding damage value indicates the extent of cracking.

At low damage values, there is some noise in the results, and they may not appear to follow the general trend. This is because of the inaccuracies in the flow stress data and the damage functions at very low damage and/or macrostrain.

The dependence of damage on strain rate and DZ N2 shows a minimum or a maximum under some conditions. This is because the accumulated damage is a very nonlinear function. It depends not just on the primary variables, but also on the interactions between the primary variables.

HA flow stress depends on damage, strain, strain rate, and temperature. For example, at low macrostrains, the flow stress of HA decreases with decreasing temperature, whereas normal thermal softening would indicate that the flow stress should increase with decreasing temperature. This is because at low macrostrains, more damage occurs at lower temperatures, and the associated reduction in flow stress dominates thermal softening. At higher macrostrains, when damage has occurred at all temperatures, the flow stress shows the normal decrease with increasing temperature.

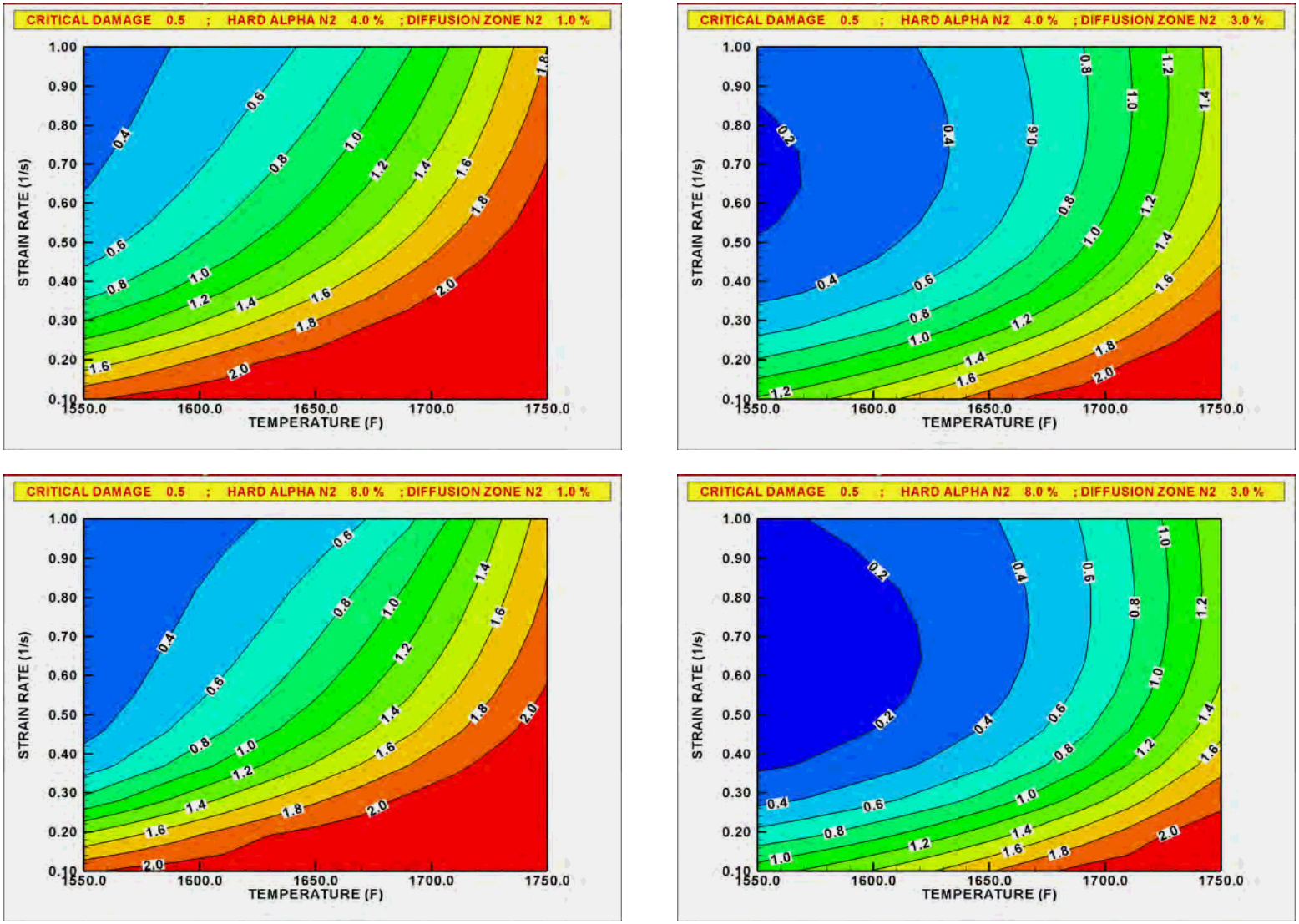

Figure F-2. Contours of Strain-to-Cracking as a Function of Strain Rate and Temperature, Strain-to-Cracking Decreases With Increasing DZ N2% (Compare Left and Right Figures), Strain-to-Cracking Decreases With Increasing HA N2% (Compare Top and Bottom Figures), and Strain-to-Cracking Decreases With Increasing Strain Rate and With Decreasing Temperature

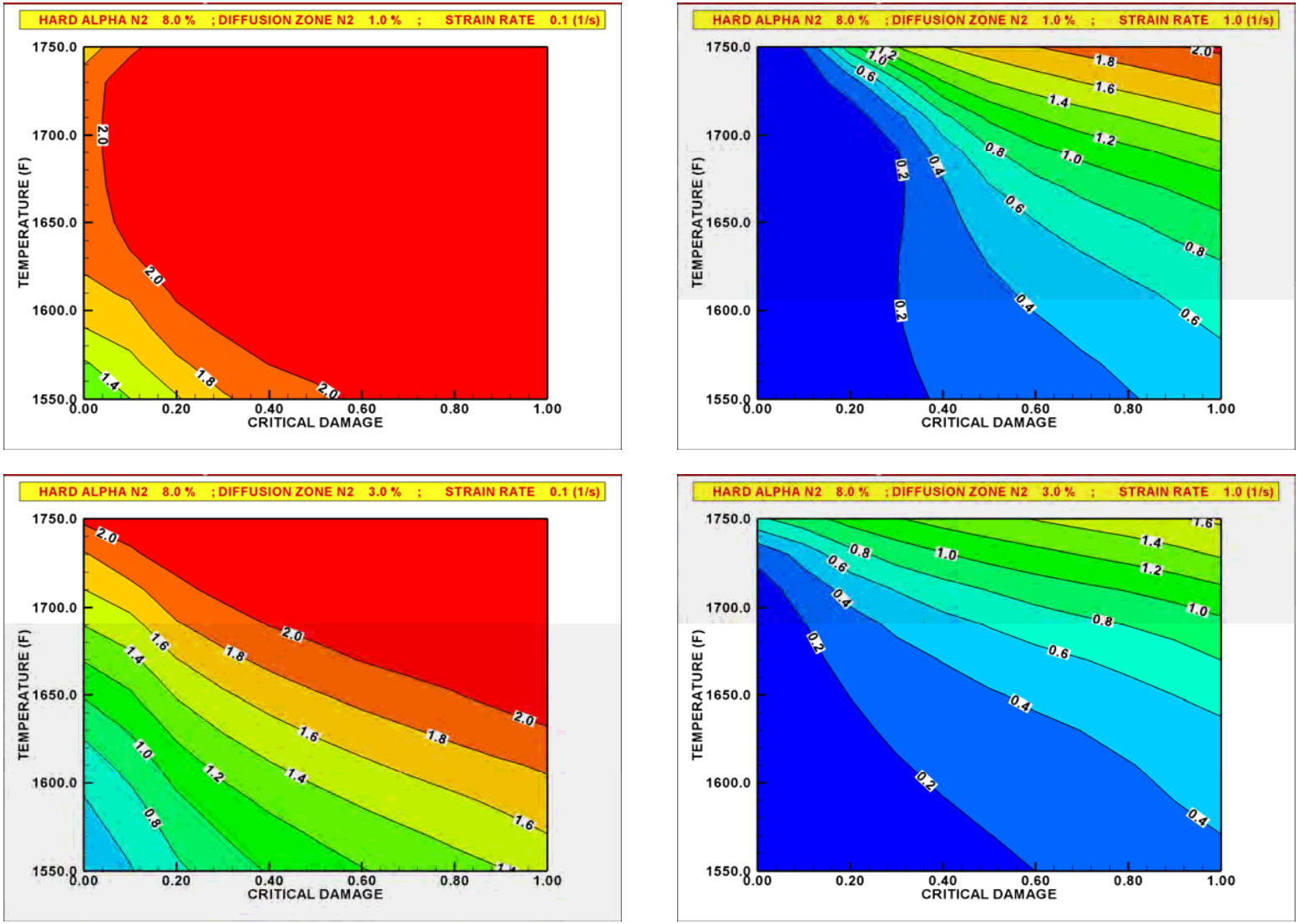

Figure F-3. Contours of Strain-to-Cracking as a Function of Temperature and Damage, Strain-to-Cracking Decreases With Increasing Strain Rate (Compare Left and Right Figures), Strain-to-Cracking Decreases With Increasing DZ N2% (Compare Top and Bottom Figures), and Strain-to-Cracking Decreases With Decreasing Temperature and With Decreasing Critical Damage

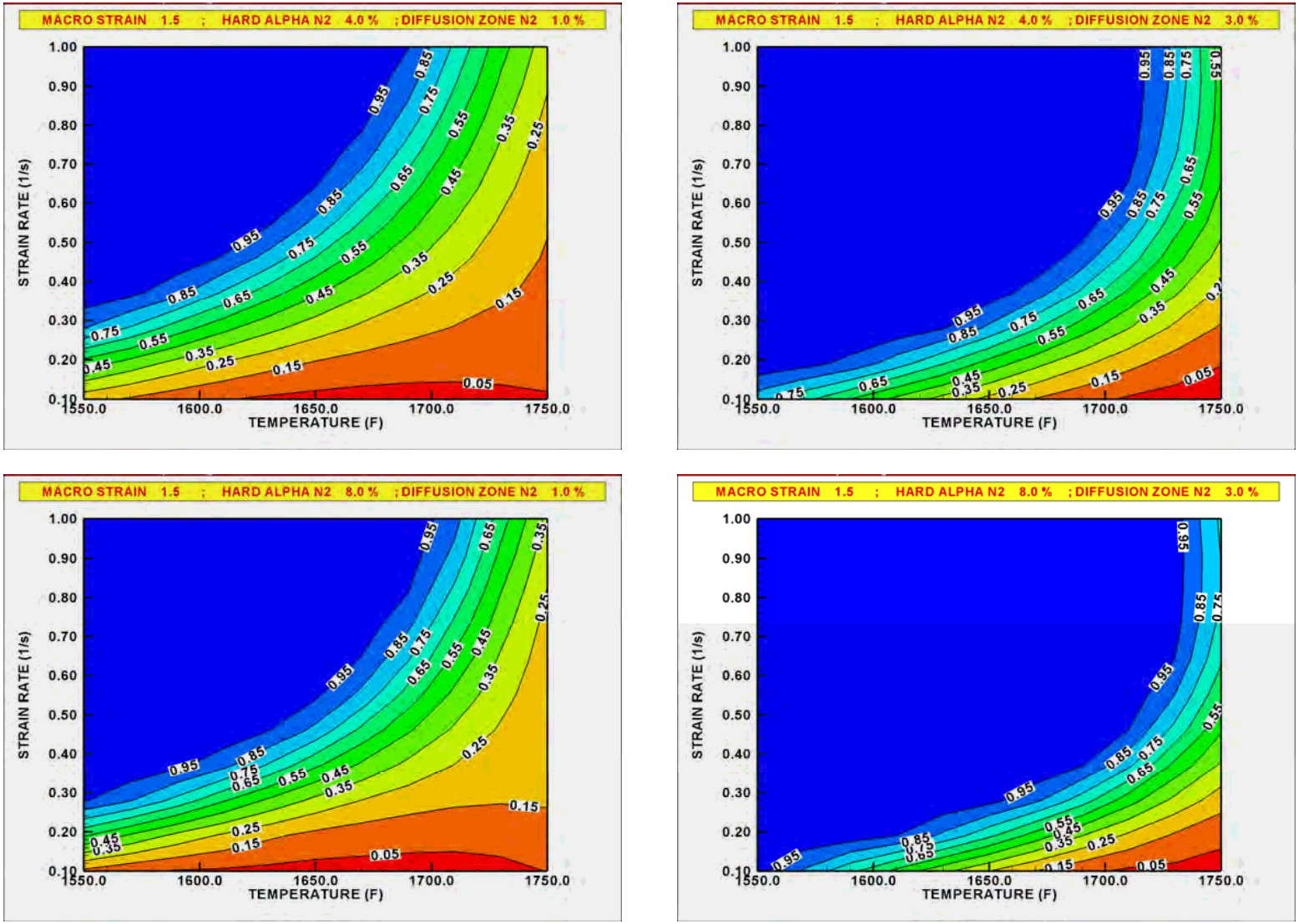

Figure F-4. Contours of HA Damage as a Function of Strain Rate and Temperature, Damage Increases With Increasing DZ N2% (Compare Left and Right Figures), Damage Increases With Increasing HA N2% (Compare Top and Bottom Figures), and Damage Increases With Increasing Strain Rate and With Decreasing Temperature

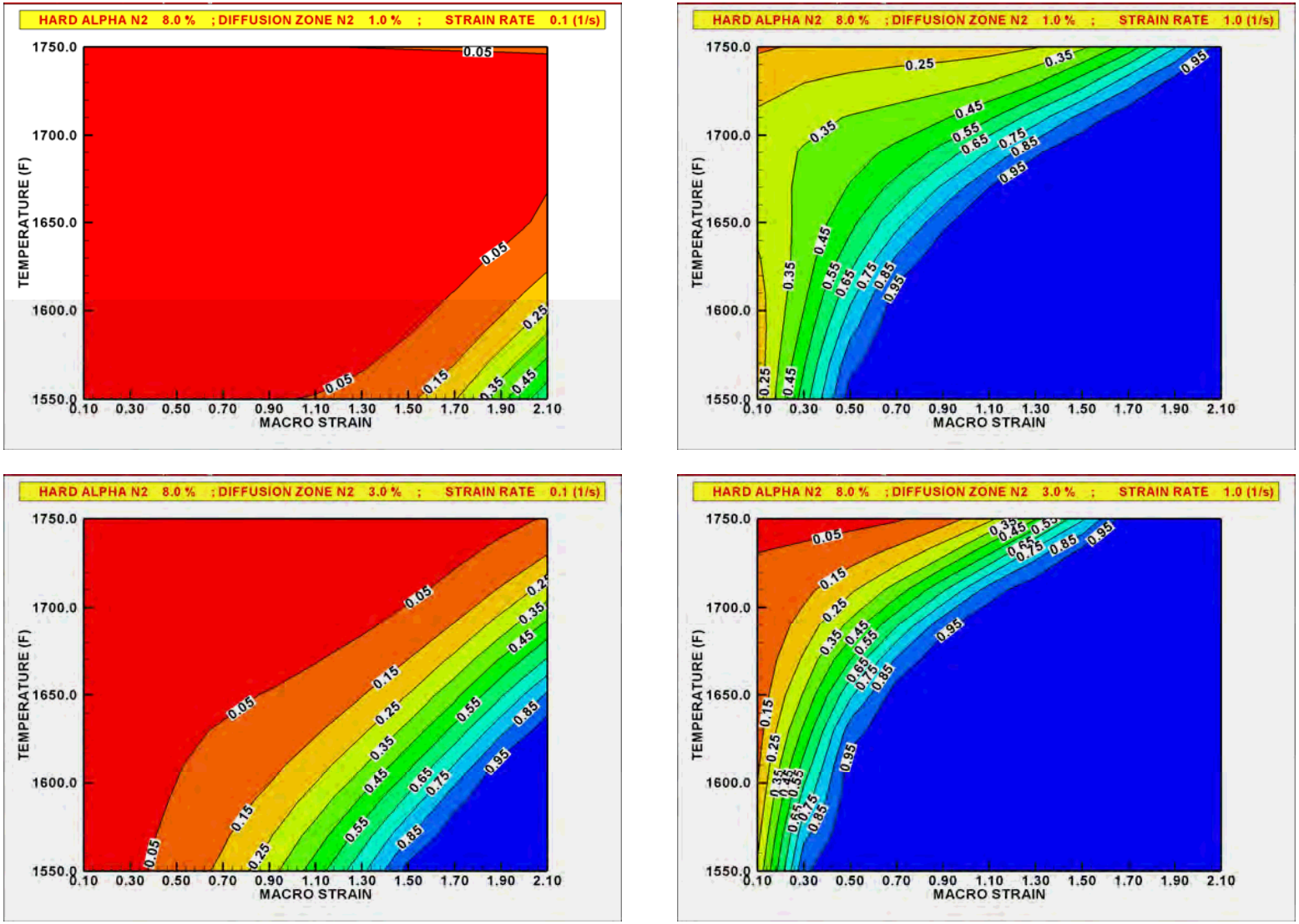

Figure F-5. Contours of HA Damage as a Function of Temperature and Macrostrain, Damage Increases With Increasing Strain Rate (Compare Left and Right Figures), Damage Increases With Increasing DZ N2% (Compare Top and Bottom Figures), and Damage Increases With Decreasing Temperature and With Increasing Macrostrain

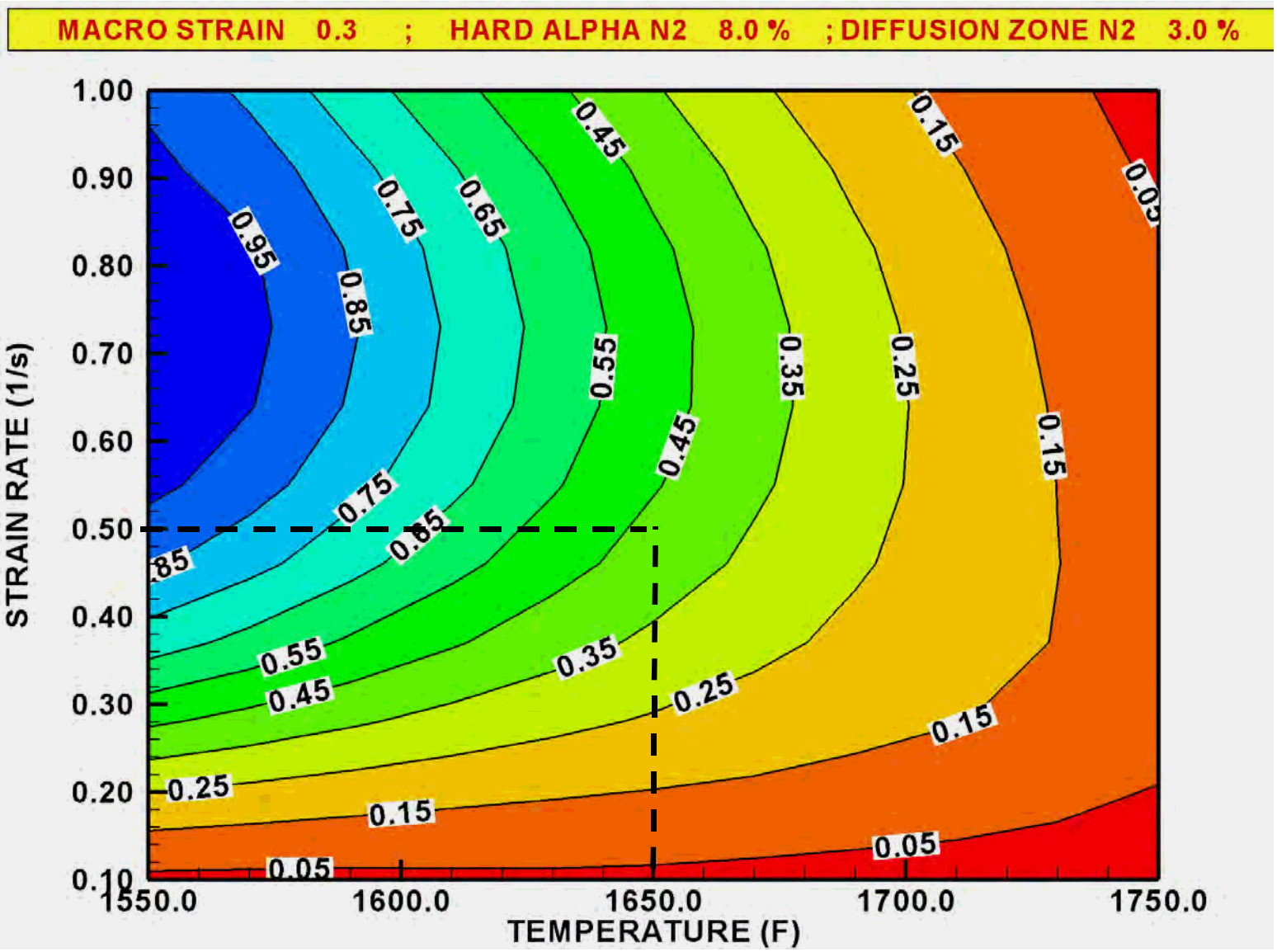

Figure F-6. Example of How to Interpret Damage Graphs With HA N2 at 8%, DZ N2 at 3%, Strain Rate at 0.5/Sec, Temperature at 1650°F, a Macrostrain of 0.3 Would Result in a Damage of 0.42 (Damage = 0 = No Cracking, Damage = 1 = Fully Cracked)

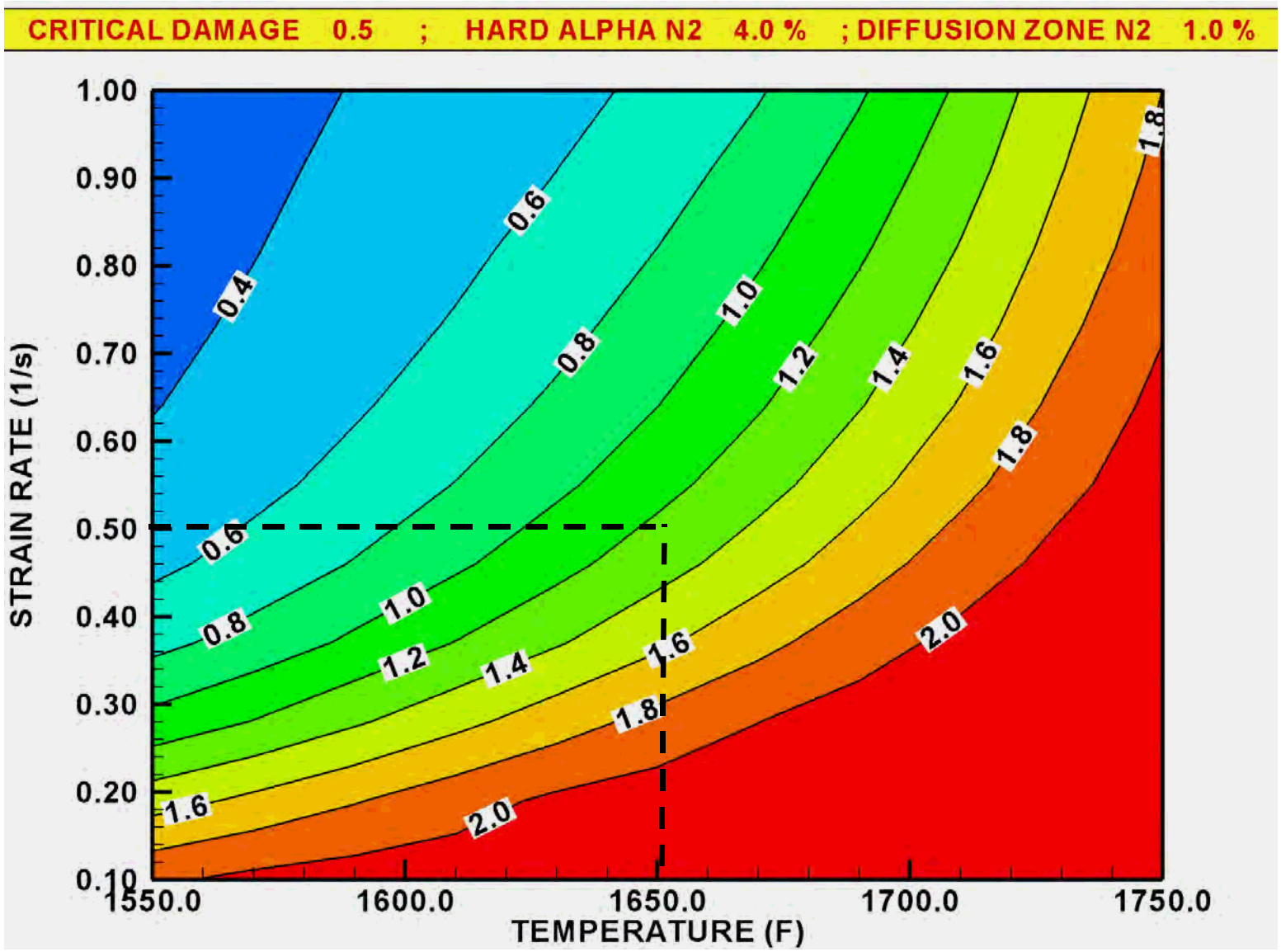

Figure F-7. Example of How to Interpret Strain-to-Cracking Graphs With HA N2 at 4%, DZ N2 at 1%, Strain Rate at 0.5/Sec, Temperature at 1650°F, a Macrostrain of 1.25 Would Result in a Damage of 0.5 (Damage = 0 = No Cracking, Damage = 1 = Fully Cracked)

At higher strain rate, HA deforms more since the ratio of the flow stress of HA to base Ti-64 decreases with strain rate. This is due to two reasons.

First, the flow stress of the base Ti-64 increases more rapidly with strain rate due to its higher ductility and higher strain rate sensitivity as compared to the more brittle HA. Second, at higher strain rates, the HA accumulates more damage, which reduces its flow stress. This reduction in flow stress with accumulated damage is absent in the base Ti-64. Damage is proportional to both strain rate and to strain.

This shows that depending on the deformation region (strain, strain rate, and temperature), the trends in flow stress can be quite different. For this reason, the strain-to-cracking and damage do not vary monotonically with some of the deformation parameters.

To summarize, the strain to HA cracking increases and damage decreases with

- decreasing HA nitrogen content,
- decreasing DZ nitrogen content,
- increasing temperature, and
- decreasing strain rate.

In other words, more forging macrostrain is needed to crack an anomaly with a lower HA nitrogen content, a lower DZ nitrogen content, at a higher temperature, or at a lower strain rate.

F.2.4 HARD ALPHA VS TI-64 FLOW STRESS.

The flow stress of intact and damaged HA (at 8% HA N2 and 3% DZ N2) and Ti-64 were compared at macrostrains equal to 0.05, 0.25, 0.50, 1.00, 1.50, and 2.00 over a range of strain rate and temperature. This was done to show how the relative strengths of HA and Ti-64 change depending on the deformation region (strain, strain rate, and temperature). The flow stress was calculated with equations F-1 through F-6.

Figures F-8 and F-9 show the typical results as contour plots of flow stress in temperature-strain rate space for two contrasting values of macrostrain. Additional results for other macrostrains are available elsewhere [F-3]. The strain and strain rate in these plots refer to macrovalues.

The following conclusions were drawn:

- With increasing macrostrain, HA flow stress decreases due to increased damage and cracking.

- Damage and cracking initiate at high-strain rate and/or low temperature and spread to lower strain rates and higher temperatures with increasing macrostrain.

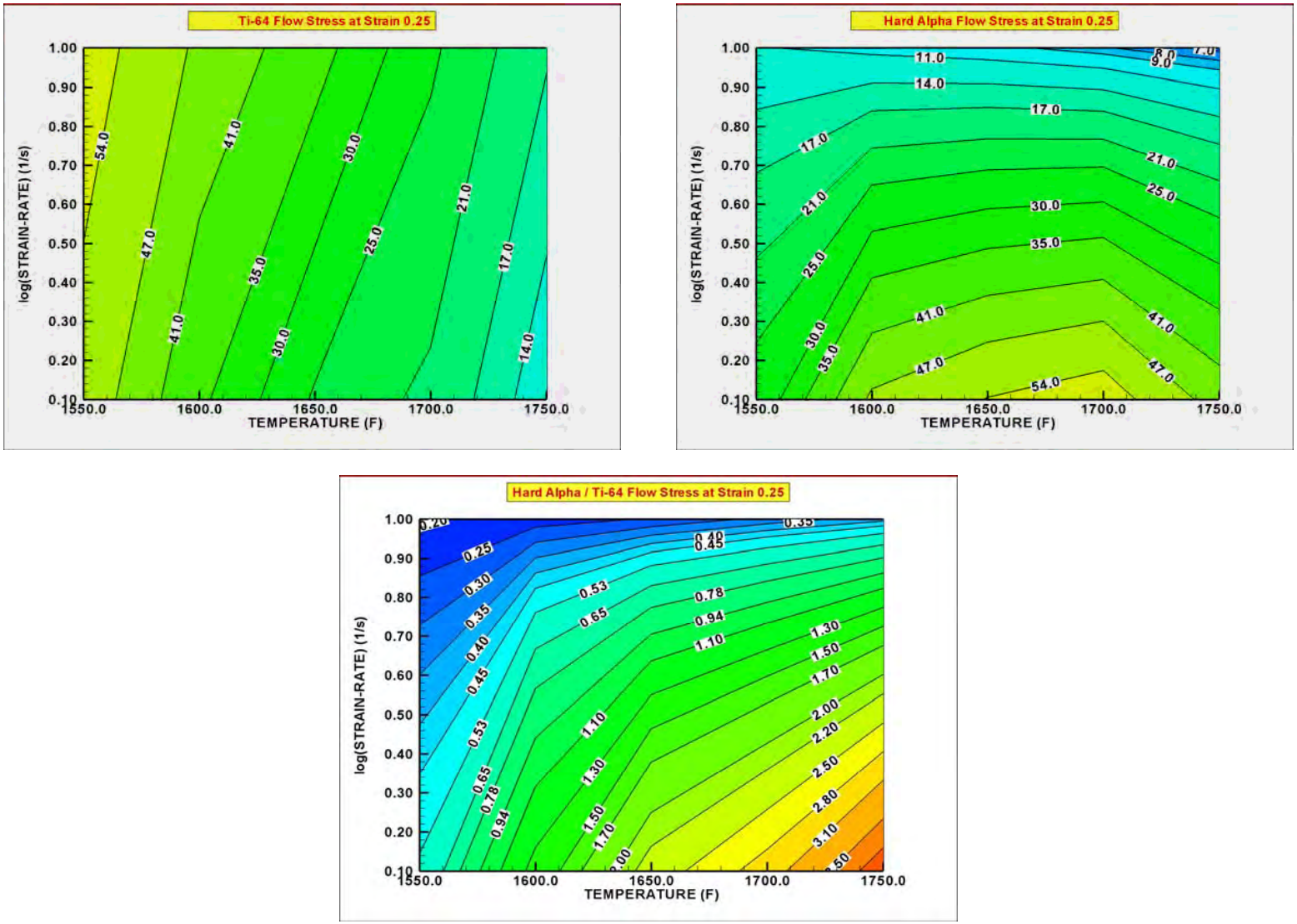

Figure F-8. Hard Alpha vs Ti-64 Flow Stress at Macrostrain 0.25

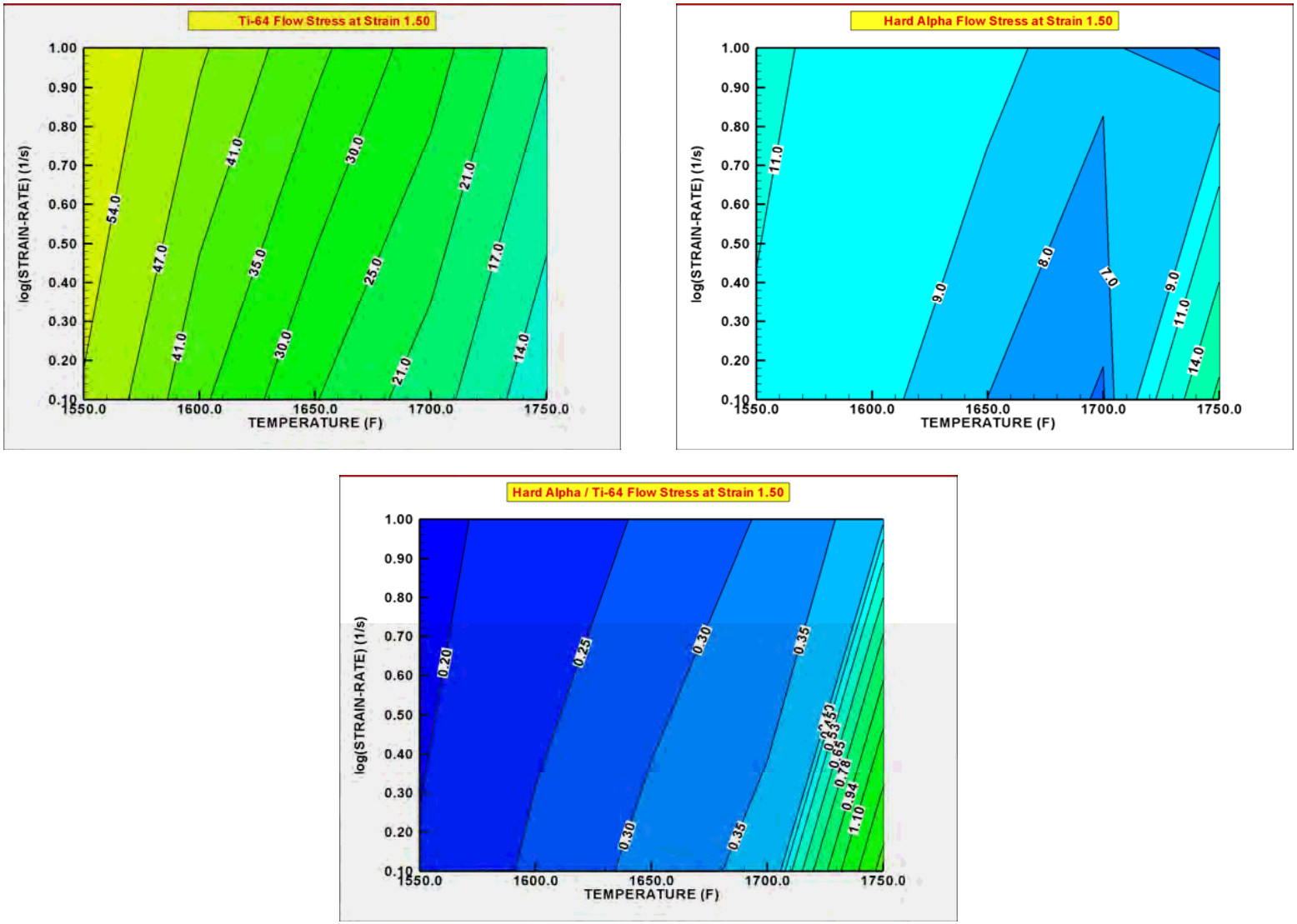

Figure F-9. Hard Alpha vs Ti-64 Flow Stress at Macrostrain 1.50

F.3 CRACKING STRAIN VS FORGING STRAIN.

The objective of the second activity was to evaluate the strain-to-cracking for HA relative to the strain produced during billet conversion and during forging. Contours of strain during the forging of three generic nonproprietary shapes were obtained for one material (Ti-64).

A user subroutine was written to process the damage and strain-to-cracking HA data in DEFORM. The subroutine creates contour plots of the HA damage based on the local forging temperature, strain, and strain rate for given HA and DZ nitrogen contents. The damage values indicate the extent of cracking for the given HA and DZ nitrogen contents. High damage values (approaching 1) indicate severe cracking, whereas low damage values (close to zero) indicate only the onset of cracking.

The model was validated using the data from the seeded dogbone and backflow forgings from TRMD-I.

F.3.1 DEFORM USER SUBROUTINE.

The logic of the user subroutine is summarized below. A complete listing of the subroutine is provided elsewhere [F-3].

Damage rate and strain-to-cracking data are read on the first pass through this subroutine. Since a remeshing triggers a new run, this data must be read after every remesh. The specific format of the file and a comprehensive listed of the file contents are available elsewhere [F-3].

At each element of the finite element mesh in the forging shape, the macroeffective strain, strain rate, and temperature are obtained. These are standard DEFORM variables. The element temperature is obtained as the average of the four nodal temperatures at the corners of the element.

The damage rate and strain-to-cracking data read previously are interpolated to the elemental strain, strain rate, and temperature. The interpolated damage is saved in four user-defined variables at each element:

- Damage at HA N2 = 4% and DZ N2 = 1%
- Damage at HA N2 = 8% and DZ N2 = 1%
- Damage at HA N2 = 4% and DZ N2 = 3%
- Damage at HA N2 = 8% and DZ N2 = 3%

Four contour plots of damage at the extremes of HA N2 and DZ N2 are obtained as output. These graphs show the extent of cracking for anomalies with these nitrogen contents.

F.3.2 MODEL VALIDATION.

Macroforge models of the seeded mults SB-1 to SB-4 (dogbone and reverse flow) were completed. These models were created in TRMD-I and were rerun using the strain-to-cracking DEFORM user subroutine described above. The damage contours at the extremes of HA N2 and DZ N2 are shown in figures F-10 and figure F-11.

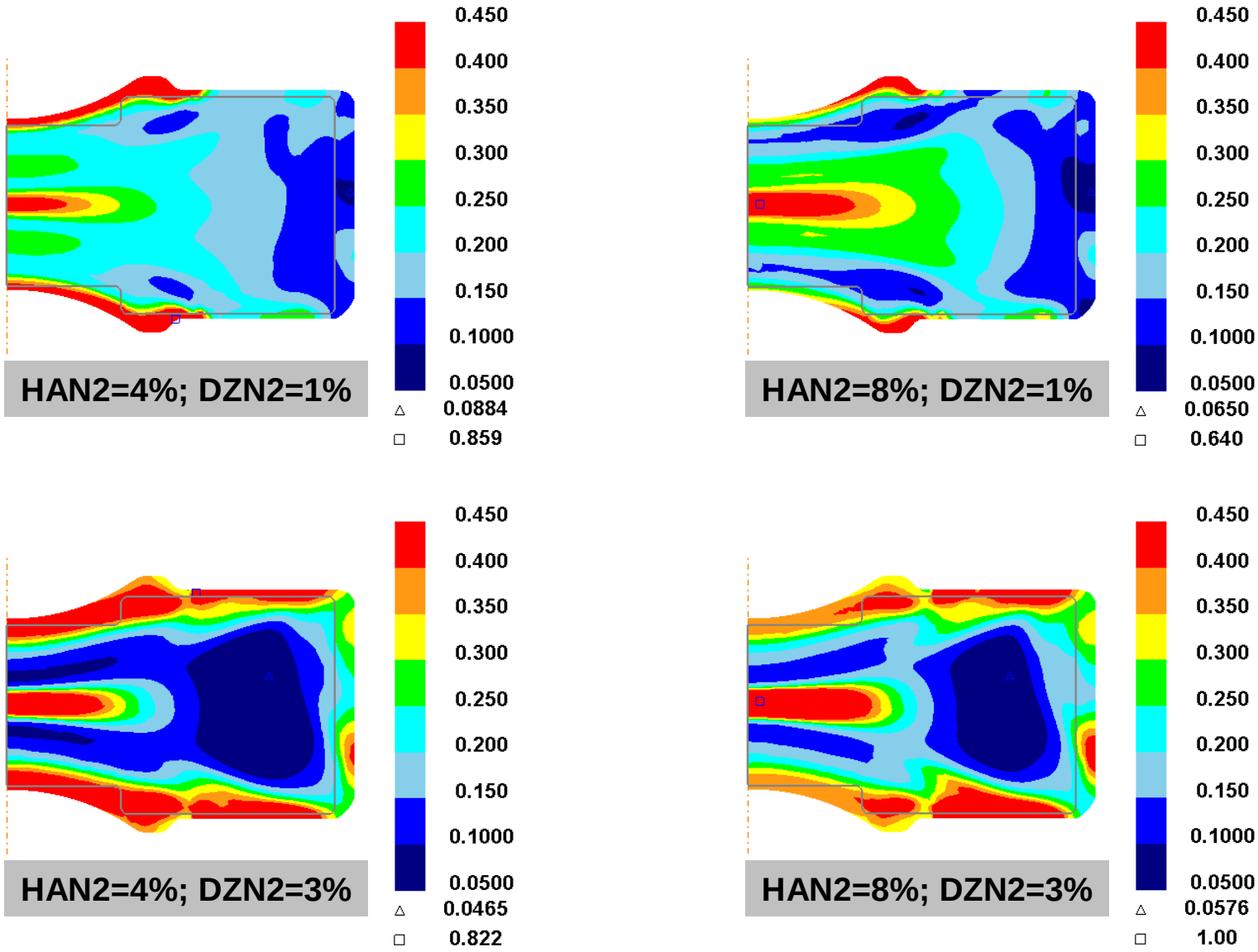

Figure F-10. Damage in SB-1 to SB-3 Damage Increases With DZ N2% and With HA N2%

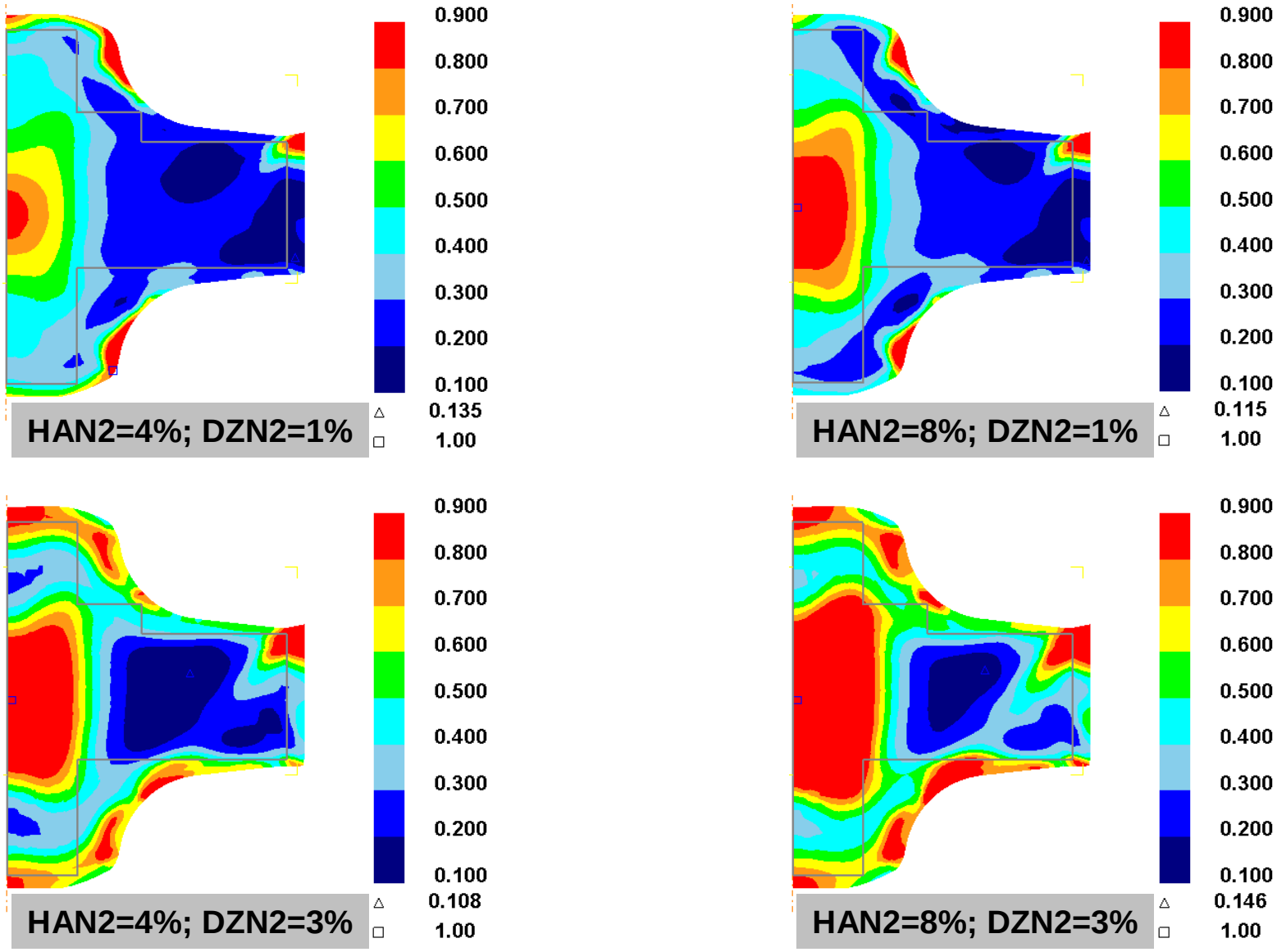

Figure F-11. Damage in SB-4 Damage Increases With DZ N2% and With HA N2%

A total of 44 seeds were fabricated (some with and some without DZs, some individual and some clustered), and these seeds were inserted into billets SB-1 to SB-4 for subsequent forging (see table F-3). Twenty-eight of the 44 seeds were cut up following forging for detailed investigation of deformation and cracking:

- SB-1 (4 seeds cut up): seed numbers 1, 3, 4, 6
- SB-3 (12 seeds cut up): seed numbers 13-16, 17-20, 21-24
- SB-4 (12 seeds cut up): seed numbers 29-32, 33-36, 41-44

Table F-3. Details of Seeds in Forgings SB-1 to SB-4

Forging	Seed No.	%N	DZ	Length (inch)	Diameter (inch)
SB-1	1	1.5	Yes	0.200	0.200
	2	1.5	Yes	0.200	0.200
	3	12	Yes	0.200	0.200
	4	12	Yes	0.200	0.200
	5	12	No	0.200	0.100
	6	12	No	0.200	0.100
SB-2	7	1.5	Yes	0.200	0.200
	8	1.5	Yes	0.200	0.200
	9	12	Yes	0.200	0.200
	10	12	Yes	0.200	0.200
	11	12	No	0.200	0.100
	12	12	No	0.200	0.100
SB-3	13-16	12	Yes	0.800	0.200
	17-20	12	Yes	0.800	0.200
	21-24	12	Yes	0.800	0.200
	25-28	12	Yes	0.800	0.200
SB-4	29-32	12	Yes	0.800	0.200
	33-36	12	Yes	0.800	0.200
	37-40	12	Yes	0.800	0.200
	41-44	12	Yes	0.800	0.200

The left-hand sides of figures F-12, F-14, and F-16 show the initial seed locations, orientation, and nitrogen content in forgings SB-1, SB-3, and SB-4 respectively. Initial seed locations were measured by sonic inspection from the OD and are within $\pm$0.125″ in the scan direction. The right-hand sides of the same figures show a comparison of the final measured (indicated by an x and the letter m) and predicted (indicated by the deformed rectangular shape and the letter p) seed locations. Final seed locations were measured by sonic inspection from the top face and are within $\pm$0.125″ in the scan direction. The measured and predicted locations agree well.

Figures F-13, F-15, and F-17 show a comparison of predicted damage with the extent of cracking in forgings SB-1, SB-3, and SB-4 respectively. The predicted damage is reported at the actual HA and DZ N2 contents in the respective seeds. The extent of cracking correlates approximately with HA damage.

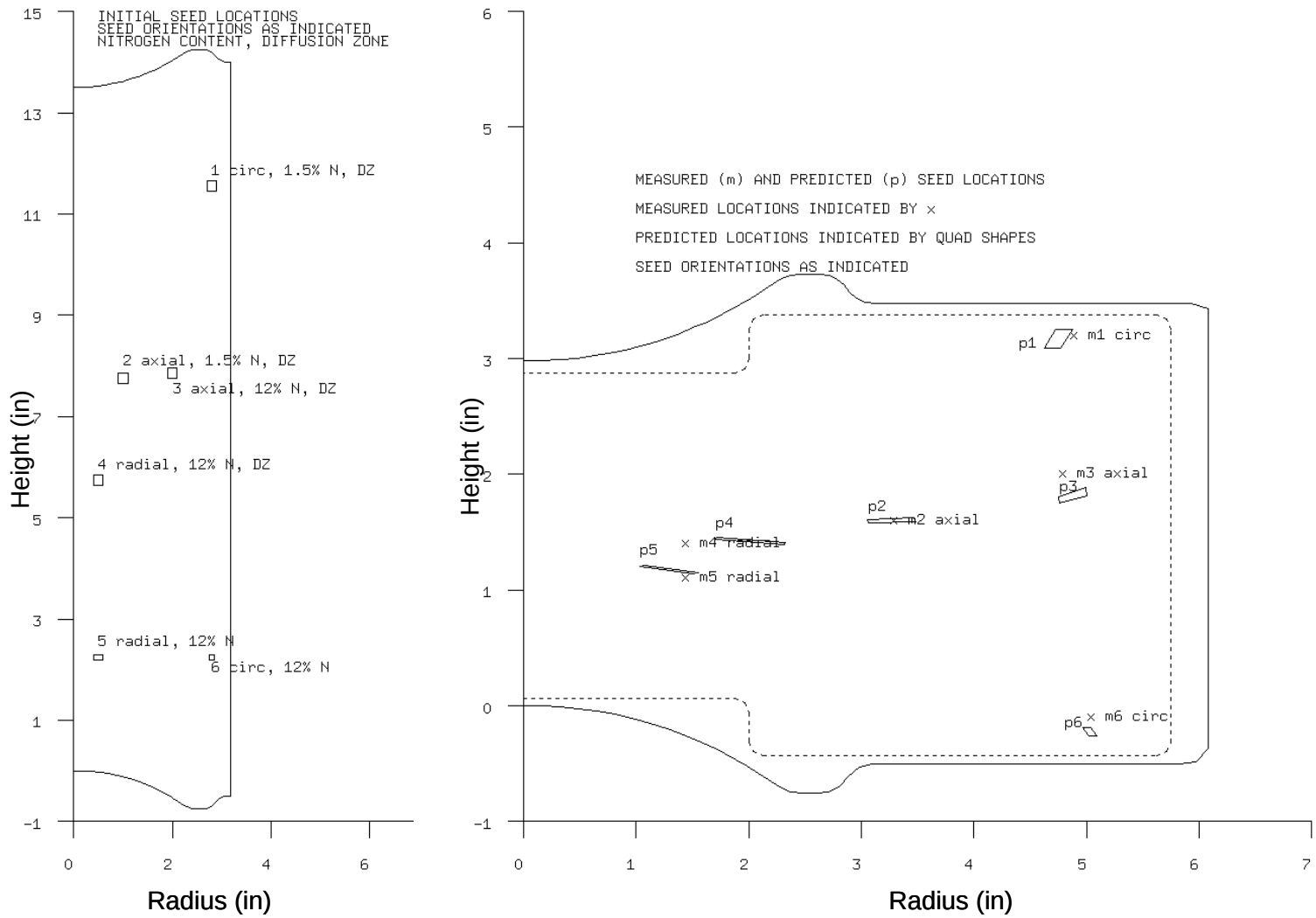

Figure F-12. Measured and Predicted Seed Locations in Forging SB-1

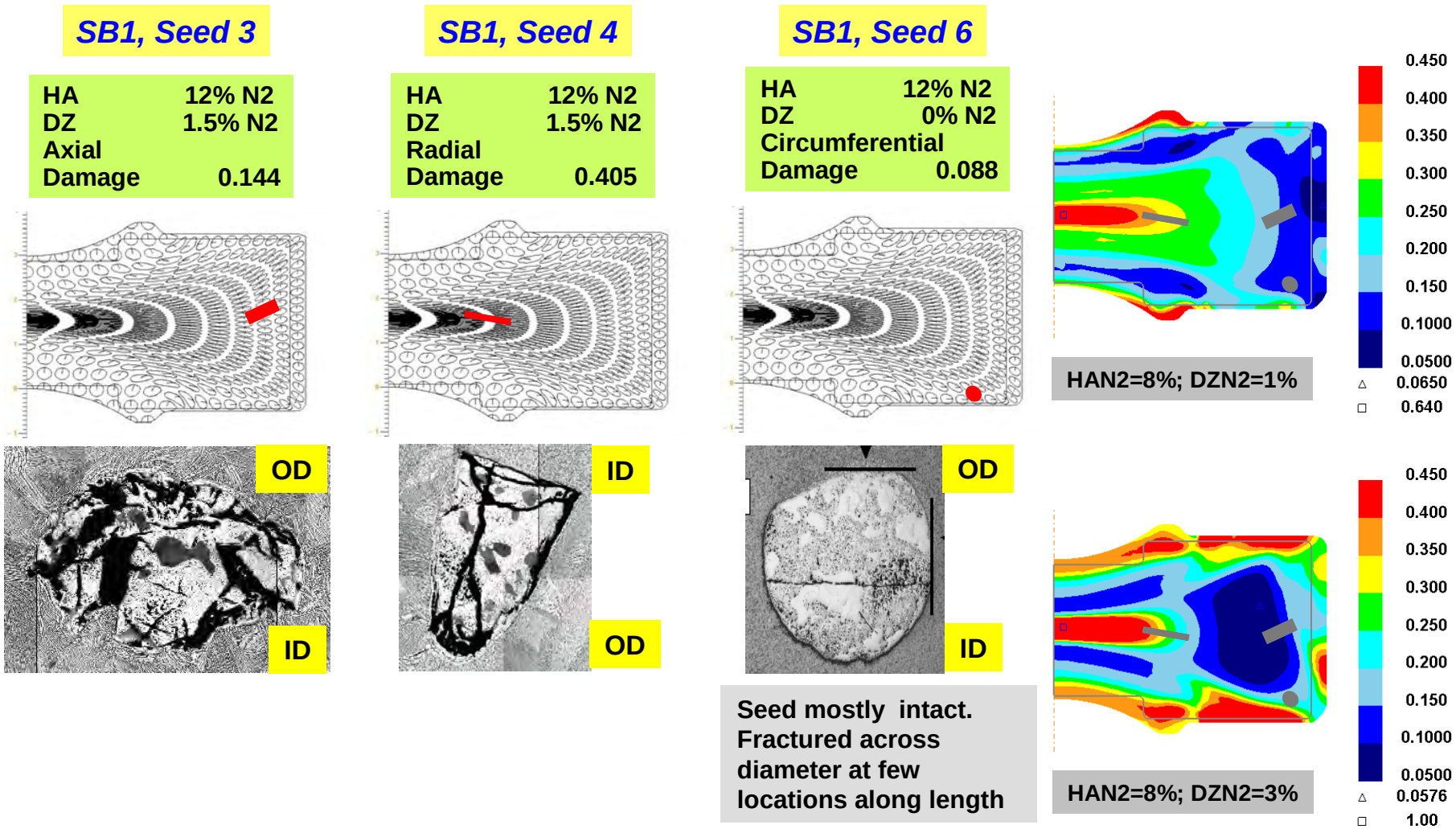

Figure F-13. SB-1 Seeds: Comparison of Predicted Damage With Extent of Cracking

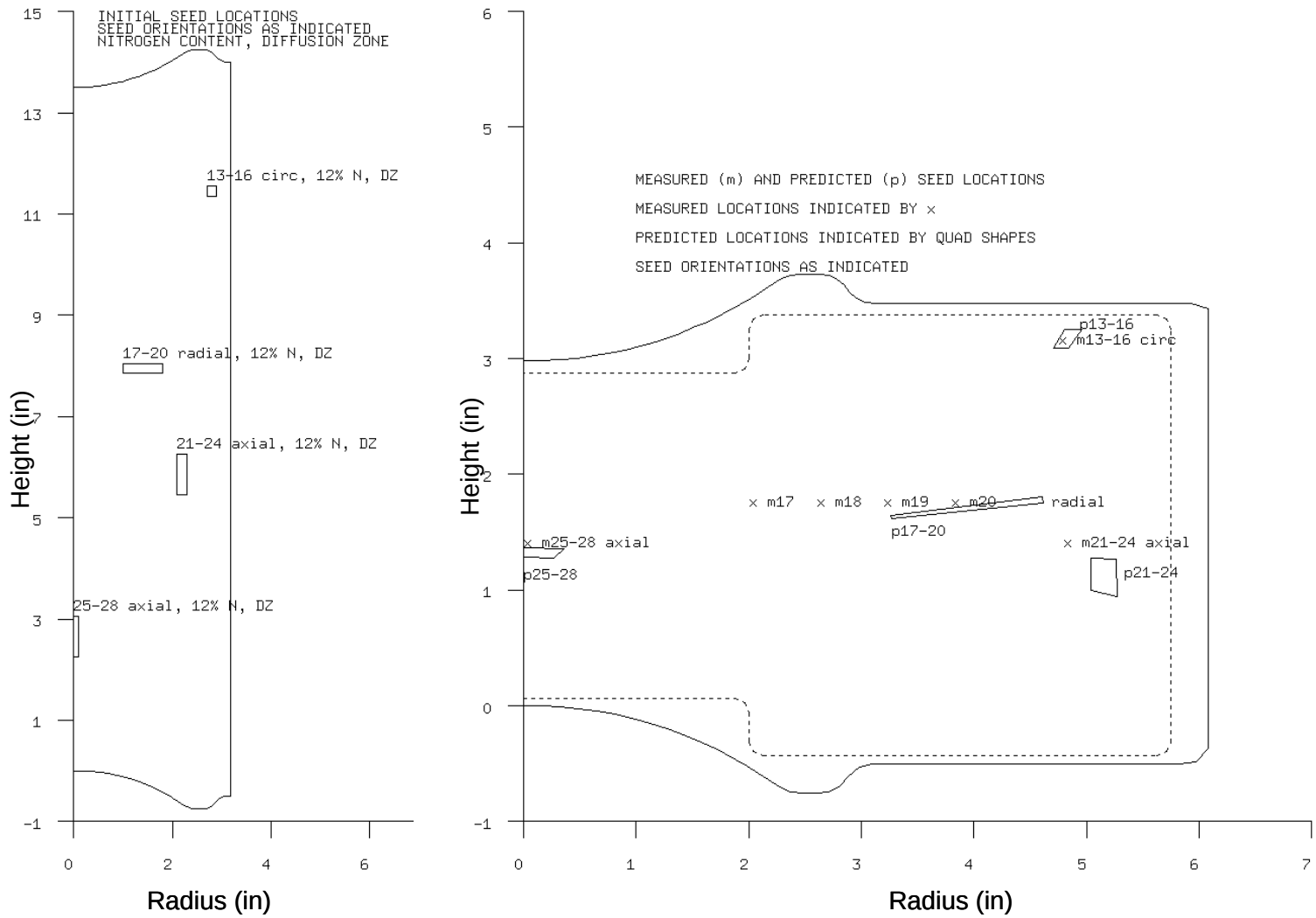

Figure F-14. Measured and Predicted Seed Locations in Forging SB-3

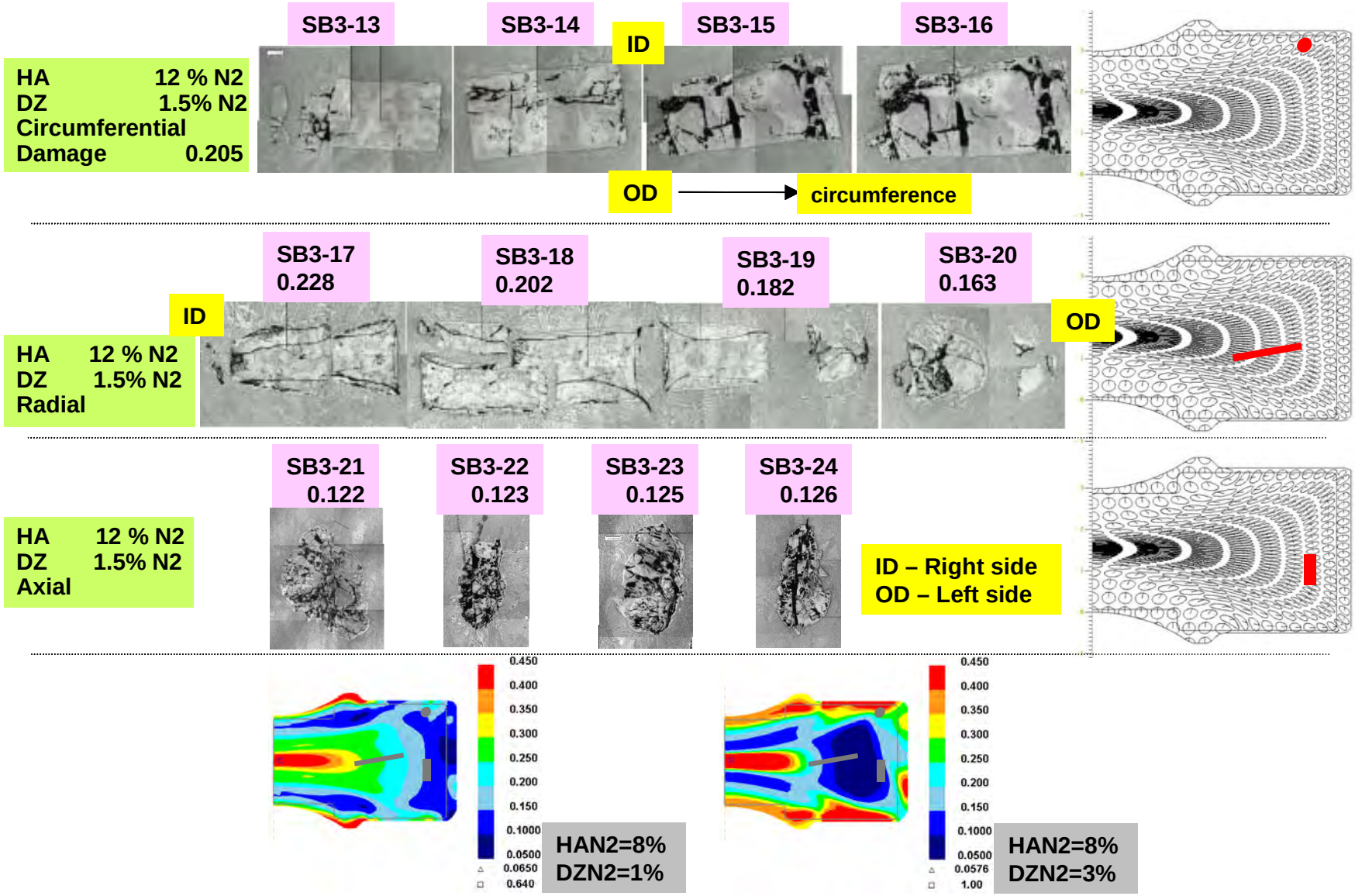

Figure F-15. SB-3 Seeds: Comparison of Predicted Damage With Extent of Cracking

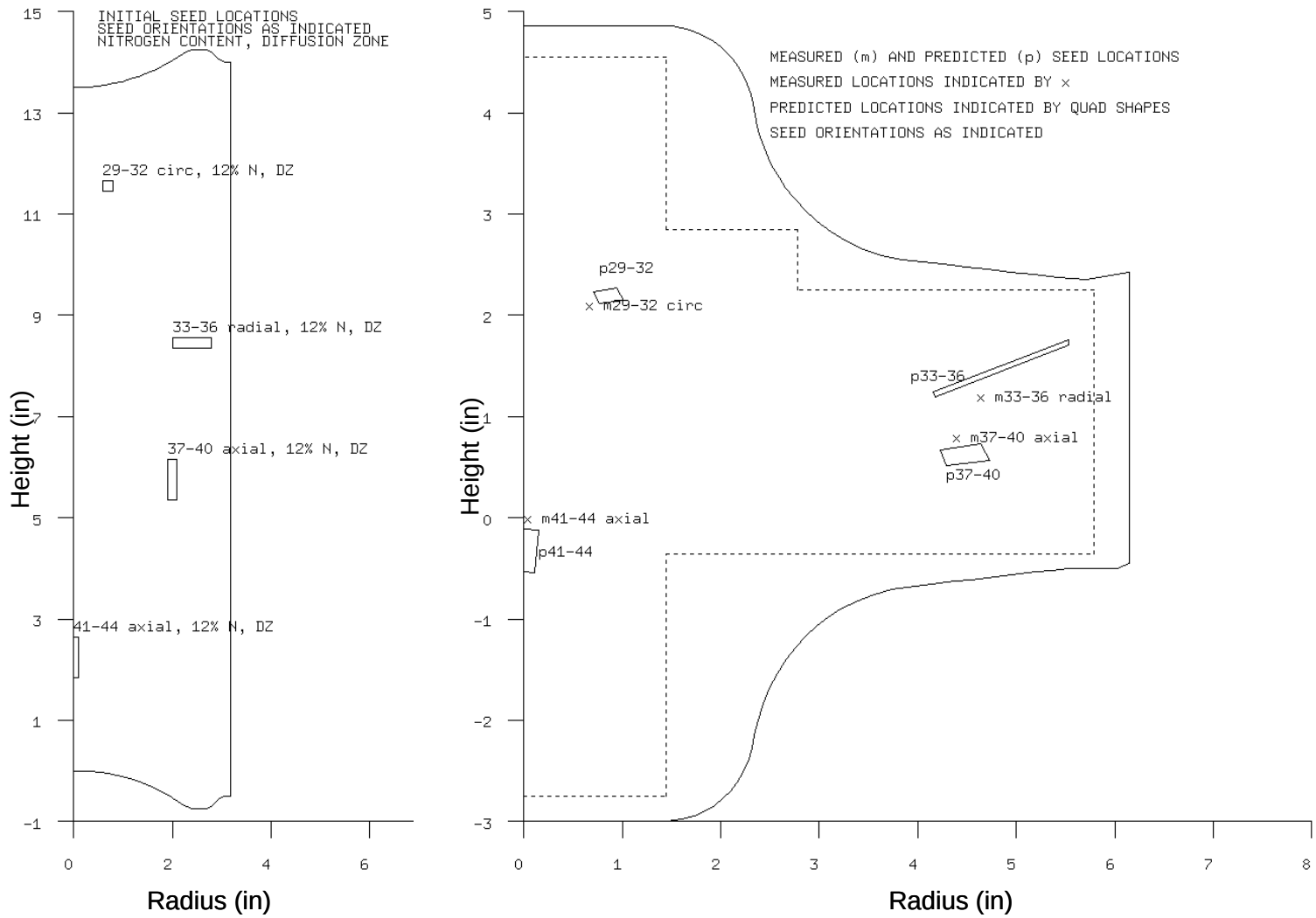

Figure F-16. Measured and Predicted Seed Locations in Forging SB-4

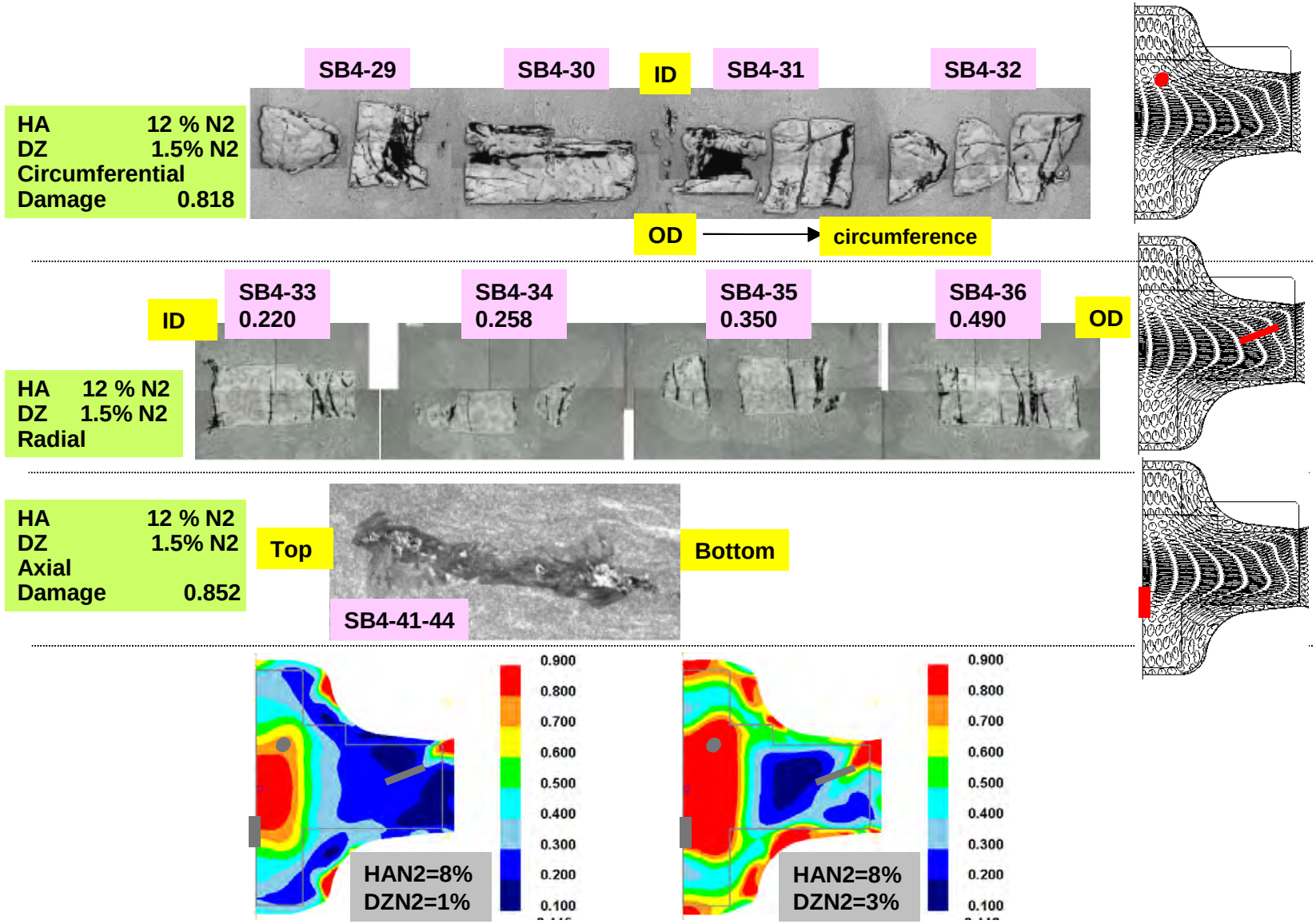

Figure F-17. SB-4 Seeds: Comparison of Predicted Damage With Extent of Cracking

In figure F-18, a summary of the predicted damage and the extent of cracking for all the seeds is shown. The seeds are arranged in order of increasing predicted damage. The predicted damage is qualitatively compared with the photographs of the extent of cracking for all seeds. There is no quantitative measure of the extent of cracking from the photographs. The extent of cracking is estimated qualitatively by a visual inspection of the photographs. The extent of cracking (as observed visually from the photographs) correlates approximately with HA damage. At low (<0.2) and high damage (>0.5), the correlation between damage and the extent of cracking is good. At intermediate damage values (0.2-0.4), there is some scatter in the data.

F.4 CRACKING DURING BILLET CONVERSION AND COMPONENT FORGING.

The objective of this third activity was to determine HA nitrogen content that would not crack during typical production billet and forging conversions of Ti-6Al-4V, using generic shapes. A combination of the strain-to-cracking data and the forging macrostrain data was used to determine the HA nitrogen contents at which cracking occurs.

F.4.1 INGOT-TO-BILLET CONVERSION DAMAGE.

Damage was computed for the ingot-to-billet conversion process assuming a 36″ initial diameter. For other diameters, these results apply for the same initial to final diameter ratio. The analysis assumed uniform strain set equal to ln(square of initial to final diameter ratio). The damage results were tabulated as a function of diameter reduction, HA N2, DZ N2, strain rate, and temperature. The results are summarized in table F-4. Low damage (highlighted in yellow in the table) was observed at high temperature and low strain rate where HA ductility is high. In general, however, typical conversion temperatures and strain rates (highlighted in blue in the table) were observed to result in damage ~1.

F.4.2 APPLICATION OF DAMAGE AND CRACKING STRAIN TO FORGED DISKS.

Three generic forging shapes were used to illustrate the strain-to-cracking capability. Results for any forging should be evaluated on a case-by-case basis. Strains during conversion of ingot-to-billet should be considered in addition to the component forging strains when assessing the cracking of HA anomalies.

The first generic shape used was the seeded billet forgings SB-1 to SB-4 from TRMD-I. The other two shapes were Rolls-Royce forgings.

The two Rolls-Royce forgings that were modeled in TRMD-I (part number (P/N) 68696, acoustic emission (AE) 3007 fan disk and P/N 68014, AE 2100/3007 Stage 14 compressor disk) were used as examples to illustrate the use of the strain-to-cracking subroutines. The forgings are shown in figure F-19. Components selected for this demonstration had to be in commercial service, had to be manufactured from a titanium alloy, and had to be produced by press forging. The fan disk was produced by Wyman-Gordon in Ti-64 alloy, and the compressor disk was produced by SIFCO in Ti-6242 alloy. The fan disk was produced by press-forging in a highly contoured closed die. The compressor disk, being a relatively simple, flat shape, is press-forged as a pancake in open dies.

Figure F-18. Summary of Predicted Damage Compared With Photographs of Extent of Cracking for all Seeds

Table F-4. Damage During Ingot-to-Billet Conversion

Final Diameter (inches)	Strain	HA N2 %	DZ N2 %	Strain Rate (1/sec)	Temperature (°F)	Damage
18	1.39	4	1	0.10	1550	0.158
12	2.20	4	1	0.10	1550	0.691
10	2.56	4	1	0.10	1550	0.997
8	3.01	4	1	0.10	1550	1.000
18	1.39	4	1	0.10	1650	0.020
12	2.20	4	1	0.10	1650	0.148
10	2.56	4	1	0.10	1650	0.248
8	3.01	4	1	0.10	1650	0.370
18	1.39	4	1	0.10	1750	0.040
12	2.20	4	1	0.10	1750	0.045
10	2.56	4	1	0.10	1750	0.049
8	3.01	4	1	0.10	1750	0.053
18	1.39	4	1	0.55	1550	1.000
12	2.20	4	1	0.55	1550	1.000
10	2.56	4	1	0.55	1550	1.000
8	3.01	4	1	0.55	1550	1.000
18	1.39	4	1	0.55	1650	0.718
12	2.20	4	1	0.55	1650	1.000
10	2.56	4	1	0.55	1650	1.000
8	3.01	4	1	0.55	1650	1.000
18	1.39	4	1	0.55	1750	0.137
12	2.20	4	1	0.55	1750	0.488
10	2.56	4	1	0.55	1750	0.706
8	3.01	4	1	0.55	1750	0.973
18	1.39	4	1	1.00	1550	1.000
12	2.20	4	1	1.00	1550	1.000
10	2.56	4	1	1.00	1550	1.000
8	3.01	4	1	1.00	1550	1.000
18	1.39	4	1	1.00	1650	1.000
12	2.20	4	1	1.00	1650	1.000
10	2.56	4	1	1.00	1650	1.000
8	3.01	4	1	1.00	1650	1.000
18	1.39	4	1	1.00	1750	0.253
12	2.20	4	1	1.00	1750	0.925
10	2.56	4	1	1.00	1750	1.000
8	3.01	4	1	1.00	1750	1.000

Final Diameter (inches)	Strain	HA N2 %	DZ N2 %	Strain Rate (1/sec)	Temperature (°F)	Damage
18	1.39	4	3	0.10	1550	0.678
12	2.20	4	3	0.10	1550	1.000
10	2.56	4	3	0.10	1550	1.000
8	3.01	4	3	0.10	1550	1.000
18	1.39	4	3	0.10	1650	0.178
12	2.20	4	3	0.10	1650	0.781
10	2.56	4	3	0.10	1650	1.000
8	3.01	4	3	0.10	1650	1.000
18	1.39	4	3	0.10	1750	0.010
12	2.20	4	3	0.10	1750	0.067
10	2.56	4	3	0.10	1750	0.121
8	3.01	4	3	0.10	1750	0.186
18	1.39	4	3	0.55	1550	1.000
12	2.20	4	3	0.55	1550	1.000
10	2.56	4	3	0.55	1550	1.000
8	3.01	4	3	0.55	1550	1.000
18	1.39	4	3	0.55	1650	1.000
12	2.20	4	3	0.55	1650	1.000
10	2.56	4	3	0.55	1650	1.000
8	3.01	4	3	0.55	1650	1.000
18	1.39	4	3	0.55	1750	0.317
12	2.20	4	3	0.55	1750	1.000
10	2.56	4	3	0.55	1750	1.000
8	3.01	4	3	0.55	1750	1.000
18	1.39	4	3	1.00	1550	1.000
12	2.20	4	3	1.00	1550	1.000
10	2.56	4	3	1.00	1550	1.000
8	3.01	4	3	1.00	1550	1.000
18	1.39	4	3	1.00	1650	1.000
12	2.20	4	3	1.00	1650	1.000
10	2.56	4	3	1.00	1650	1.000
8	3.01	4	3	1.00	1650	1.000
18	1.39	4	3	1.00	1750	0.381
12	2.20	4	3	1.00	1750	1.000
10	2.56	4	3	1.00	1750	1.000
8	3.01	4	3	1.00	1750	1.000

Table F-4. Damage During Ingot-to-Billet Conversion (Continued)

Final Diameter (inches)	Strain	HA N2 %	DZ N2 %	Strain Rate (1/sec)	Temperature (°F)	Damage
18	1.39	8	1	0.10	1550	0.097
12	2.20	8	1	0.10	1550	0.716
10	2.56	8	1	0.10	1550	1.000
8	3.01	8	1	0.10	1550	1.000
18	1.39	8	1	0.10	1650	0.014
12	2.20	8	1	0.10	1650	0.073
10	2.56	8	1	0.10	1650	0.123
8	3.01	8	1	0.10	1650	0.183
18	1.39	8	1	0.10	1750	0.052
12	2.20	8	1	0.10	1750	0.057
10	2.56	8	1	0.10	1750	0.059
8	3.01	8	1	0.10	1750	0.061
18	1.39	8	1	0.55	1550	1.000
12	2.20	8	1	0.55	1550	1.000
10	2.56	8	1	0.55	1550	1.000
8	3.01	8	1	0.55	1550	1.000
18	1.39	8	1	0.55	1650	0.882
12	2.20	8	1	0.55	1650	1.000
10	2.56	8	1	0.55	1650	1.000
8	3.01	8	1	0.55	1650	1.000
18	1.39	8	1	0.55	1750	0.158
12	2.20	8	1	0.55	1750	0.628
10	2.56	8	1	0.55	1750	0.929
8	3.01	8	1	0.55	1750	1.000
18	1.39	8	1	1.00	1550	1.000
12	2.20	8	1	1.00	1550	1.000
10	2.56	8	1	1.00	1550	1.000
8	3.01	8	1	1.00	1550	1.000
18	1.39	8	1	1.00	1650	1.000
12	2.20	8	1	1.00	1650	1.000
10	2.56	8	1	1.00	1650	1.000
8	3.01	8	1	1.00	1650	1.000
18	1.39	8	1	1.00	1750	0.279
12	2.20	8	1	1.00	1750	1.000
10	2.56	8	1	1.00	1750	1.000
8	3.01	8	1	1.00	1750	1.000

Final Diameter (inches)	Strain	HA N2 %	DZ N2 %	Strain Rate (1/sec)	Temperature (°F)	Damage
18	1.39	8	3	0.10	1550	0.839
12	2.20	8	3	0.10	1550	1.000
10	2.56	8	3	0.10	1550	1.000
8	3.01	8	3	0.10	1550	1.000
18	1.39	8	3	0.10	1650	0.191
12	2.20	8	3	0.10	1650	0.979
10	2.56	8	3	0.10	1650	1.000
8	3.01	8	3	0.10	1650	1.000
18	1.39	8	3	0.10	1750	0.016
12	2.20	8	3	0.10	1750	0.069
10	2.56	8	3	0.10	1750	0.119
8	3.01	8	3	0.10	1750	0.180
18	1.39	8	3	0.55	1550	1.000
12	2.20	8	3	0.55	1550	1.000
10	2.56	8	3	0.55	1550	1.000
8	3.01	8	3	0.55	1550	1.000
18	1.39	8	3	0.55	1650	1.000
12	2.20	8	3	0.55	1650	1.000
10	2.56	8	3	0.55	1650	1.000
8	3.01	8	3	0.55	1650	1.000
18	1.39	8	3	0.55	1750	0.473
12	2.20	8	3	0.55	1750	1.000
10	2.56	8	3	0.55	1750	1.000
8	3.01	8	3	0.55	1750	1.000
18	1.39	8	3	1.00	1550	1.000
12	2.20	8	3	1.00	1550	1.000
10	2.56	8	3	1.00	1550	1.000
8	3.01	8	3	1.00	1550	1.000
18	1.39	8	3	1.00	1650	1.000
12	2.20	8	3	1.00	1650	1.000
10	2.56	8	3	1.00	1650	1.000
8	3.01	8	3	1.00	1650	1.000
18	1.39	8	3	1.00	1750	0.564
12	2.20	8	3	1.00	1750	1.000
10	2.56	8	3	1.00	1750	1.000
8	3.01	8	3	1.00	1750	1.000

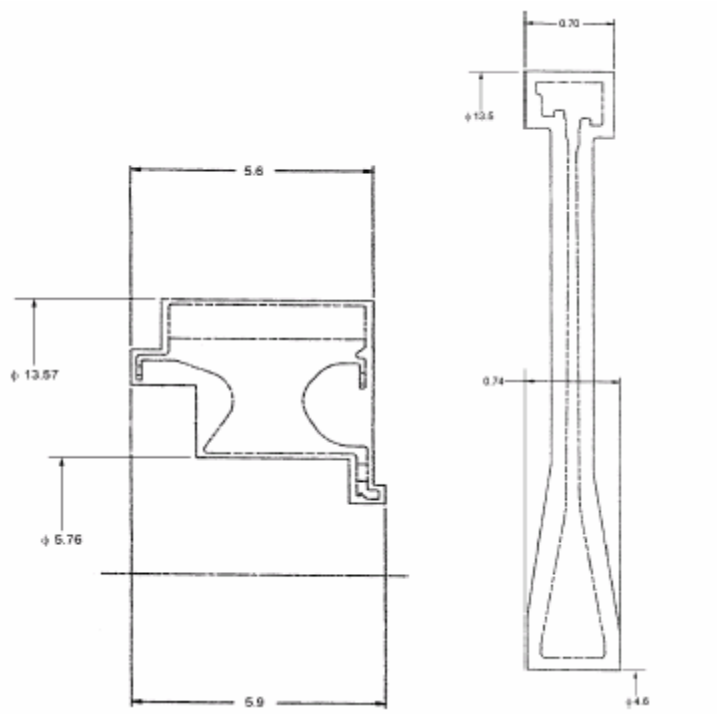

(a) (b)

Figure F-19. (a) Fan Disk Forging and (b) Compressor Disk Forging

Roll-Royce worked with Wyman-Gordon and SIFCO to establish DEFORM forging models for each part. Both forgers use DEFORM in their forging die design operations and agreed to share key word files with Rolls-Royce to run the models in-house. This was successfully accomplished and both models were run at Rolls-Royce. For the fan disk, Rolls-Royce used proprietary Wyman-Gordon flow stress data for Ti-64 to run the macromodel. The data were retained at Rolls-Royce when the key word files were sent to GE Aviation to run the microcode.

Existing forge models of these two parts were used to illustrate the strain-to-cracking capability. The input files of these two were modified to be compatible with the latest PC-based version of DEFORM. Since the strain-to-cracking data were generated for Ti-64, the compressor disk was also modeled as Ti-64 (the actual material was Ti-6242).

Damage for forgings SB-1 to SB-4 for different nitrogen contents was shown earlier in figures F-10 and F-11. Damage, effective strain, effective-strain rate, and temperature contour plots for the seeded forgings SB-1 to SB-4 are available in reference F-3. The plots are shown at different time instants during forging and show the evolution of damage as deformation during forging progresses. Temperatures greater than 1700°F and strain rates less than 0.5/sec cause low rates of HA damage accumulation.

Similar plots for the two Rolls-Royce forgings are shown in figures F-20 and F-21. Note that these figures show only the damage from the forging process. Damage from the conversion process should be added to assess the total extent of HA cracking.

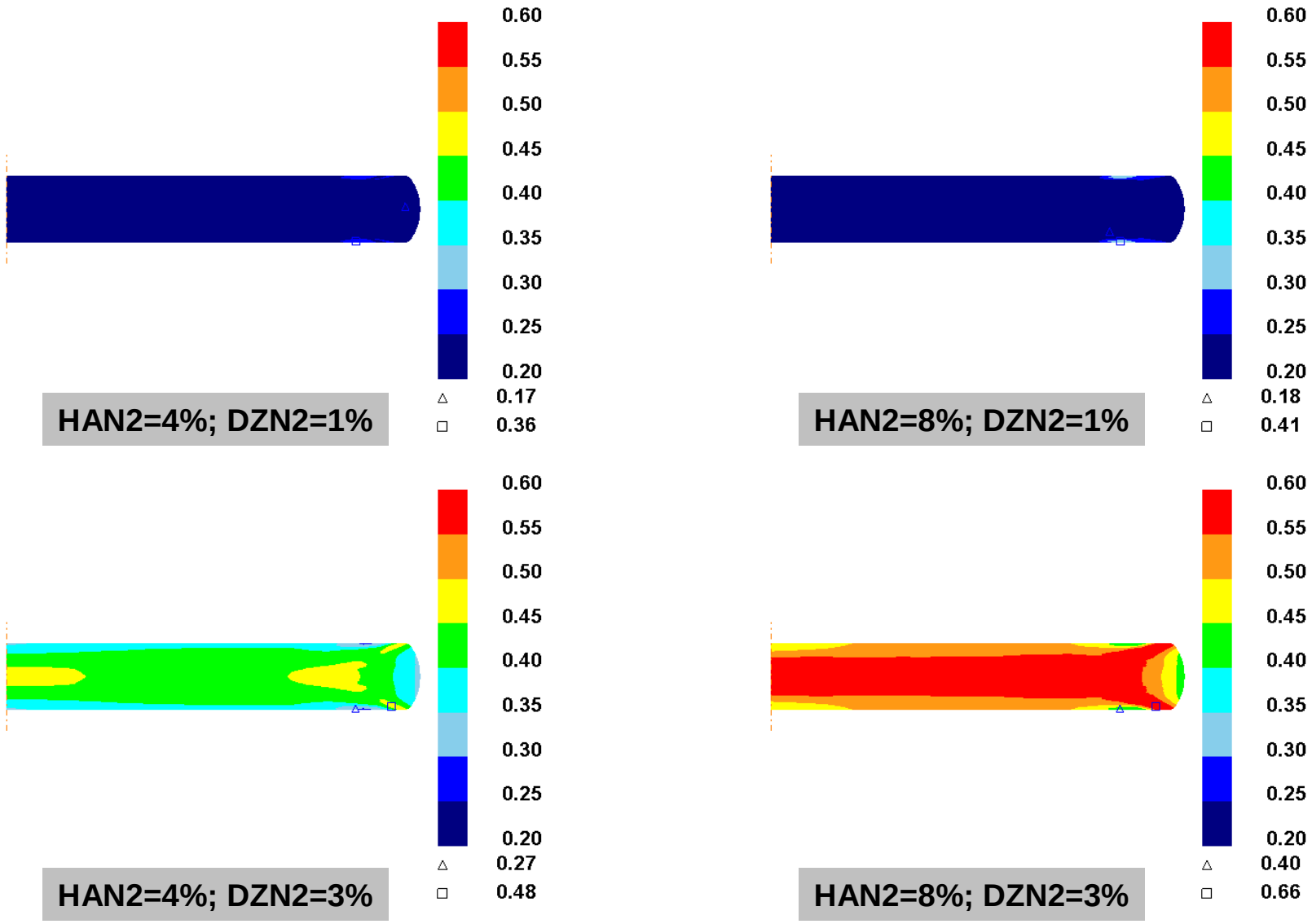

Figure F-20. Damage—AE 2100/3007 Stage 14 Compressor Disk Damage Increases With DZ N2% and With HA N2%

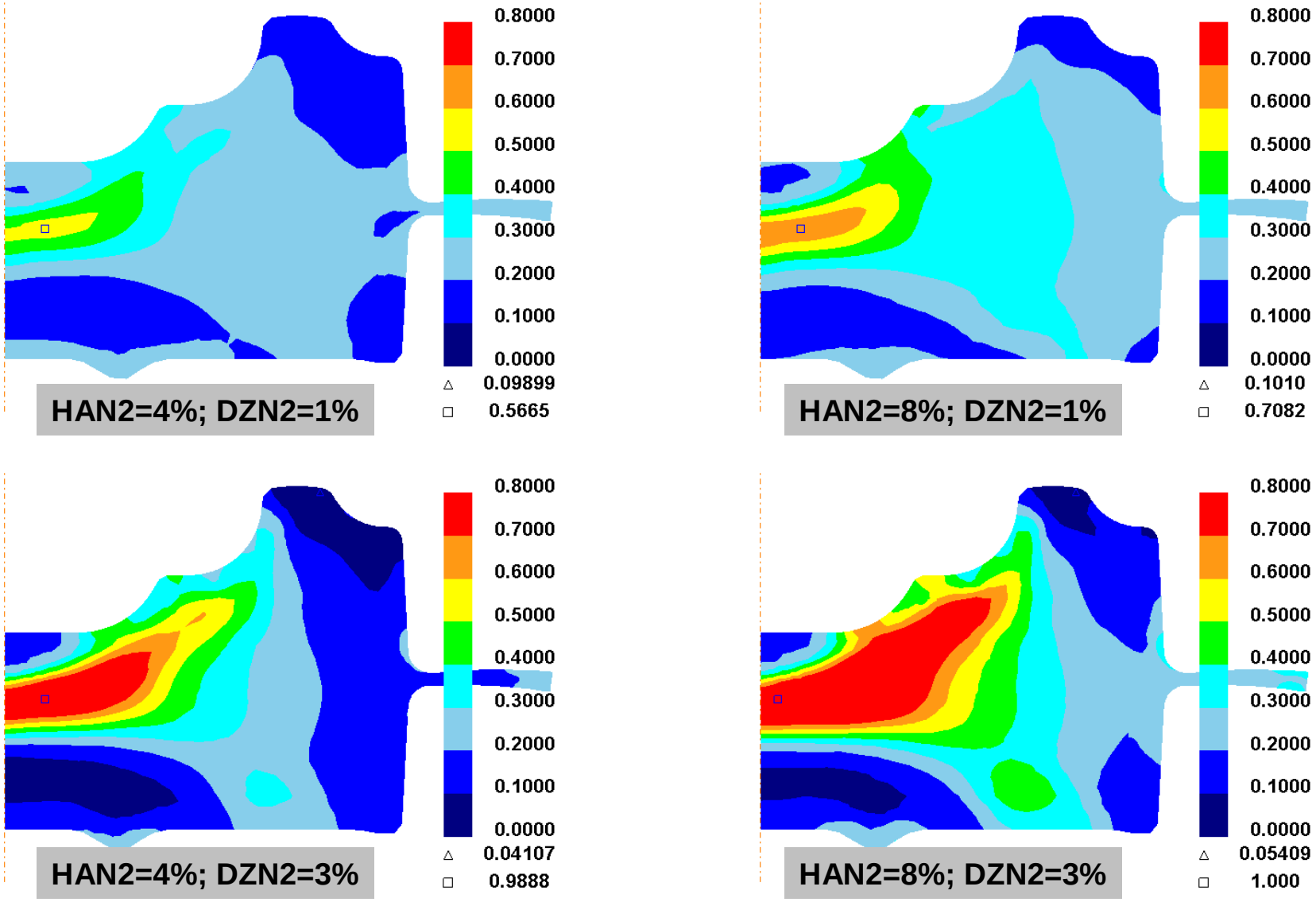

Figure F-21. Damage—AE 3007 Fan Disk Damage Increases With DZ N2% and With HA N2%

F.4.3 STRAIN-TO-CRACKING CONCLUSIONS.

The results of the present study have shown that ingot-to-billet conversion will, under commonly used processing conditions, crack all HA with nitrogen contents greater than 4%, which is the lowest HA nitrogen content evaluated here. The extent of cracking will be less if the conversion is carried out at high temperatures (~1750°F) or low strain rates (~ 0.1/sec). For nitrogen content less than 4%, the anomaly is treated as a DZ. The DZ results from partially dissolved HA cores during melting or conversion steps. If the anomaly is a DZ only (without a HA core), then the TRMD-I flow stress tests indicate that it has good ductility (sections F.2.1 and F.2.2). The DZs only anomaly is unlikely to crack after billet conversion and forging; it would only deform along with the base material, but to a lesser extent depending on its nitrogen content. In reality, there is no sharp transition between a DZ and a HA at 4% N. The transition from ductile to brittle behavior occurs over a range of nitrogen contents depending on the deformation conditions (strain, strain rate, and temperature) and the beta to (beta + alpha) transition temperature. More work is needed to accurately characterize the transition zone.

Figure F-22 shows conceptually the dependence of cracking on nitrogen content in the DZ and HA and the in-between transition zone. This graph was generated using random numbers subject to cracking tendency increasing with N2 content. The plot should not be used to extract any numerical information. The plot shows general trends and no sharp transition in behavior at 4% N. The anomaly is most unlikely to crack in the low-nitrogen content DZ (red dots). The anomaly is most likely to crack in the high-nitrogen content HA region (green dots). In the transition zone of nitrogen content, cracking may or may not occur (blue dots). Some outlying points that did not follow the general trend are noted.

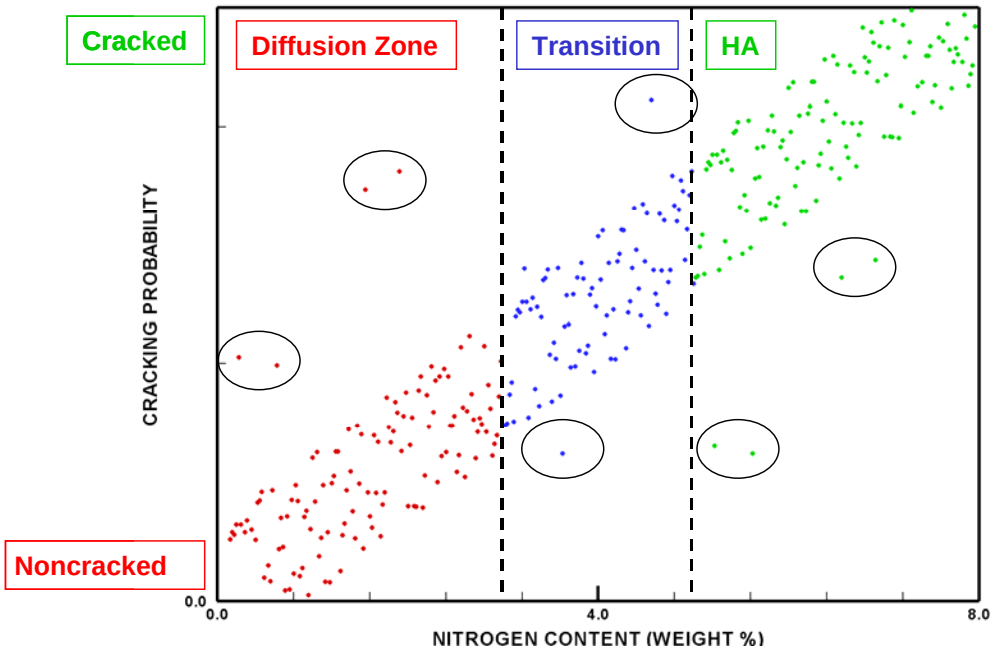

Figure F-22. Conceptual Schematic Illustrating Qualitatively the Dependence of Cracking on Nitrogen Content

In general, ingot-to-billet conversion results in more HA cracking. Component forging results in less cracking but orients anomalies along flow lines.

F.5 ANOMALY ORIENTATION.

The objective of this study was to determine the orientations of melt-related anomalies in the conversion from ingot-to-billet and also the conversion from billet-to-forging. In particular, the important determination was whether melt-related anomalies would likely end up oriented normal to forging surfaces. Forging flow lines along which melt-related anomalies tend to get oriented were predicted for the same three generic shapes defined in section F.4.2. Again, other specific forgings should be modeled and the results evaluated on a case-by-case basis, but the results obtained here should be representative.

The results for the seeded billet forgings SB-1 to SB-4 are shown in figures F-23 and F-24. Figure F-23 shows the flow line deformation. The bottom diagram shows the initial parallel lines in the billet that take on the deformed patterns in the forgings in the upper diagrams. The sonic shape is shown by the inside solid lines. Figure F-24 shows the overall deformation patterns. The bottom diagram shows the initial circular pattern in the starting billet. The middle diagram shows the deformed pattern in the dogbone forgings SB-1 to SB-3. The top diagram shows the deformed pattern in the backflow forging SB-4. In all three diagrams, the right half of forging is shown, and the symmetry centerline is on the left edge. The three diagrams have different scales. Note that these are matrix material deformations, not the HA deformations. The deformed patterns correlate with grain deformation from macroslices.

Similar results for the two Rolls-Royce forgings are shown in figures F-25 through F-28. Figures F-25 and F-27 show how the flow lines change with forging deformation, while figures F-26 and F-28 show the overall deformation patterns.

In some regions of these forgings, the flow lines are normal to forging surfaces. Melt-related anomalies that tend to orient along the flow lines might not be detectable if scanned from the face to which the flow lines are normal. When flow lines are normal to a face, a scan from another face or a shear scan should be used.

High friction (poor lubrication) and/or excessive die chill impede deformation and cause flow lines initially normal to a forging face to stay normal after forging. Geometrical features and metal flow pattern also influence the orientation of forging flow lines.

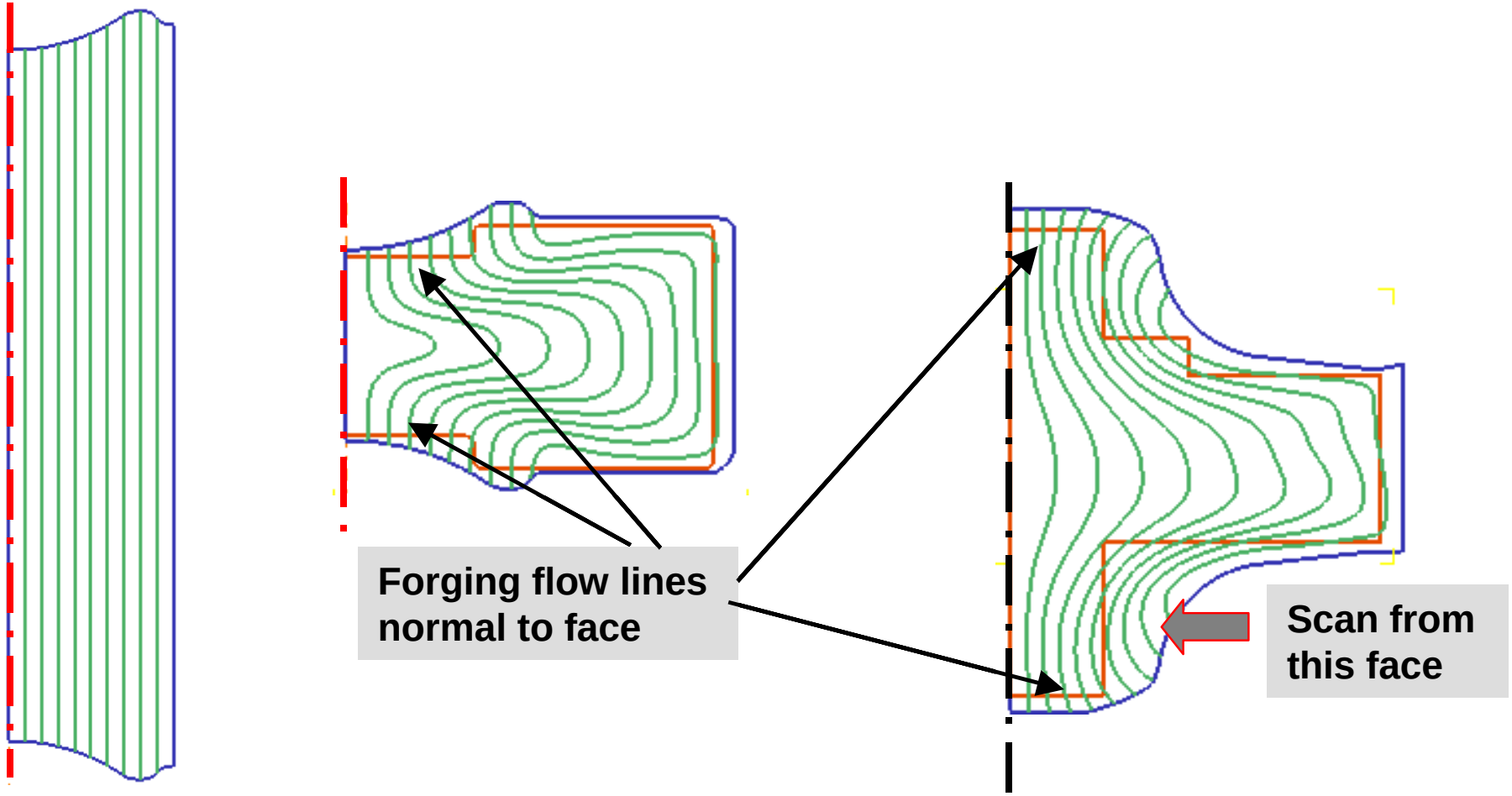

Figure F-23. Flow Lines in Forgings SB-1 to SB-4

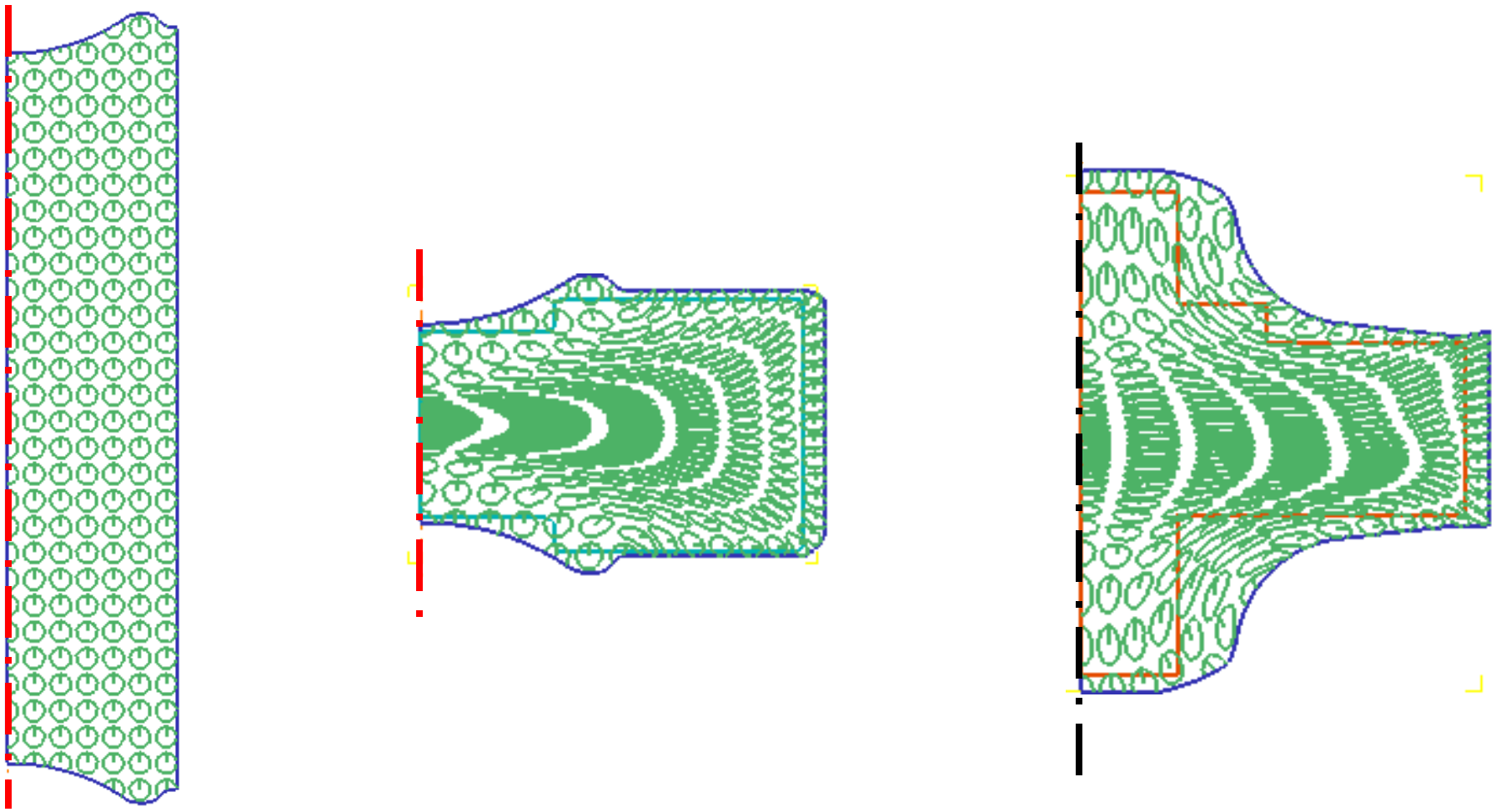

Figure F-24. Graphical Display of Overall Deformation and Orientation in Forgings SB-1 to SB-4

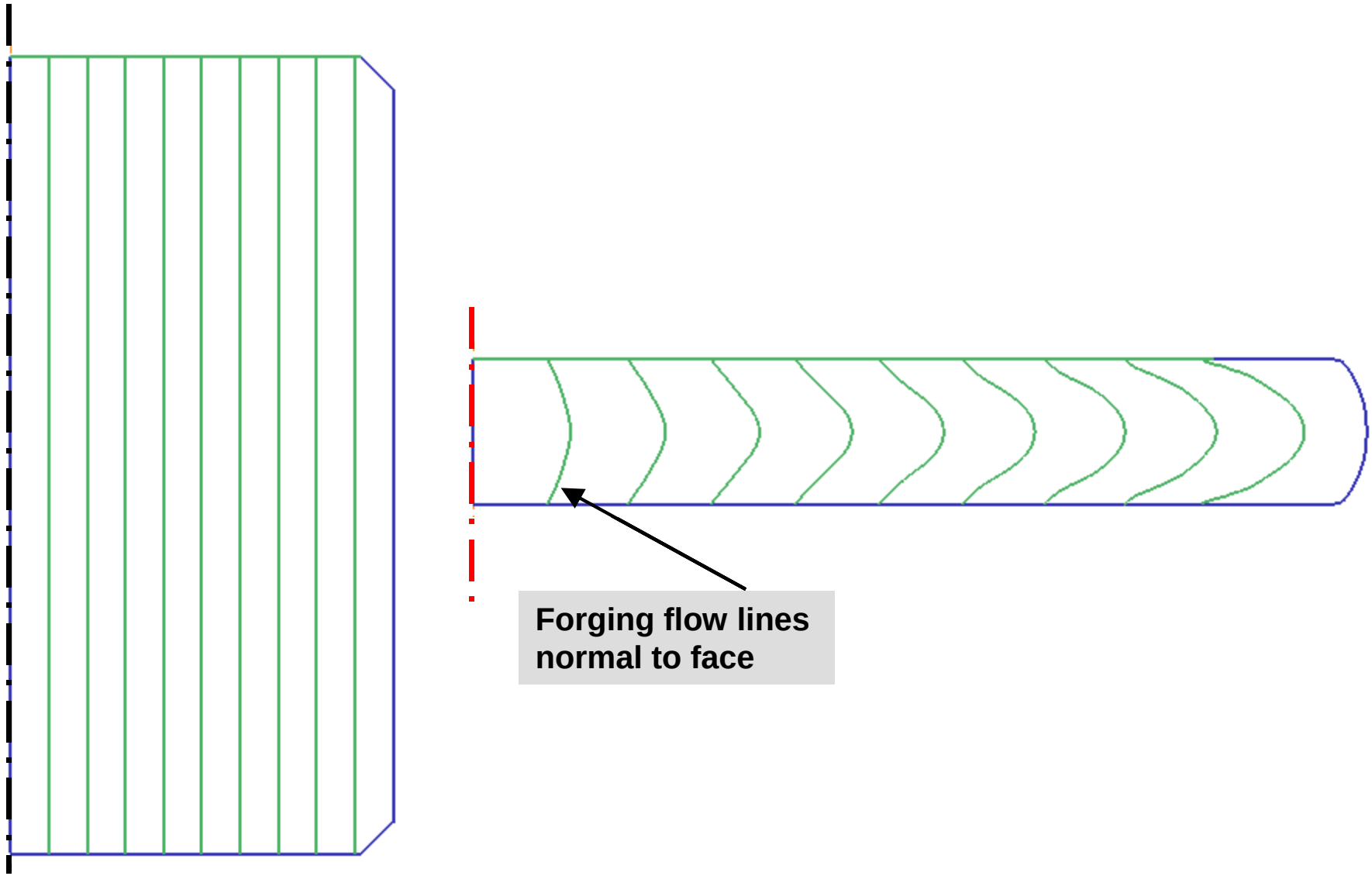

Figure F-25. Flow Lines for AE 2100/3007 Stage 14 Compressor Disk

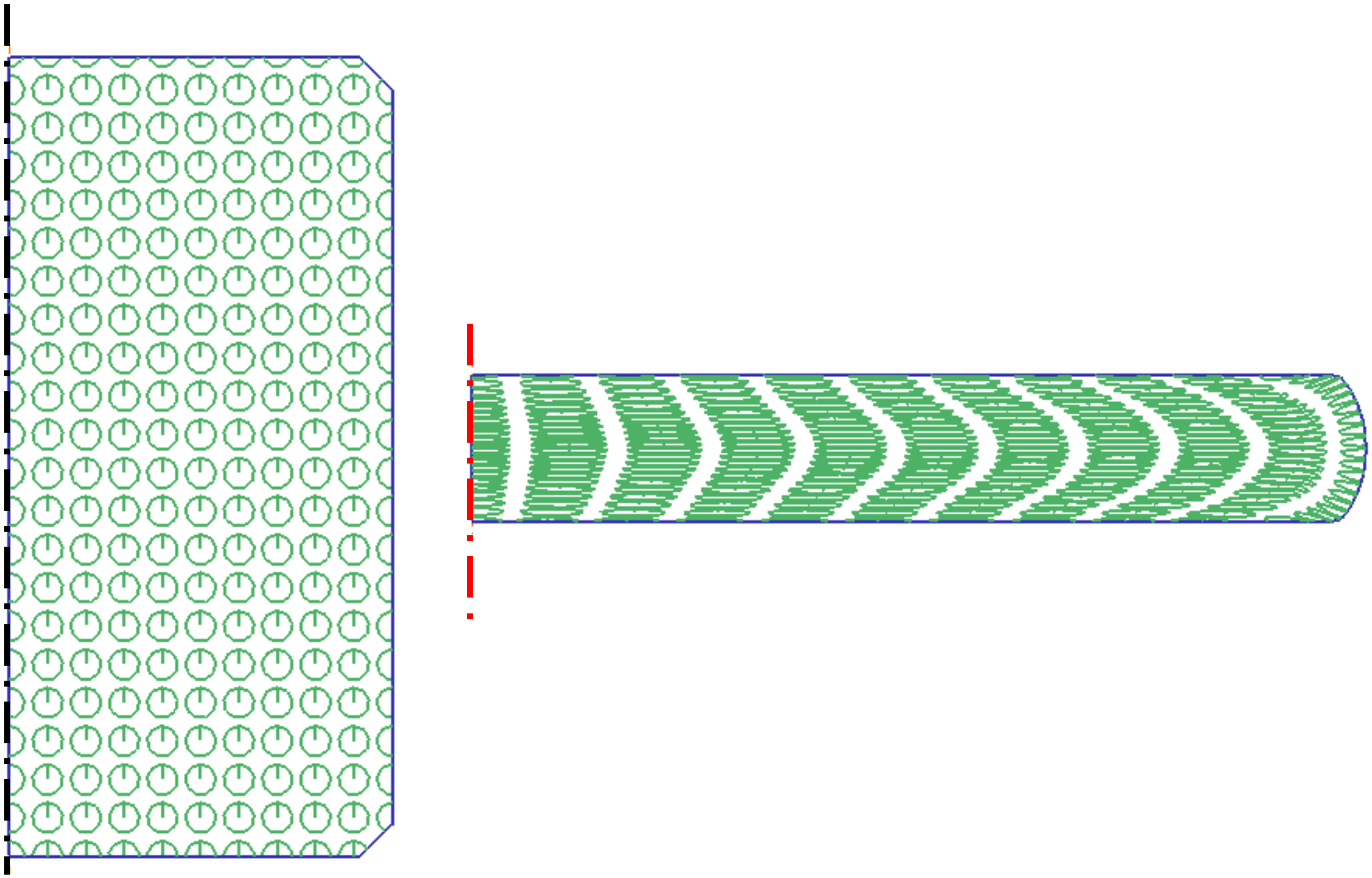

Figure F-26. Graphical Display of Overall Deformation and Orientation in AE 2100/3007 Stage 14 Compressor Disk

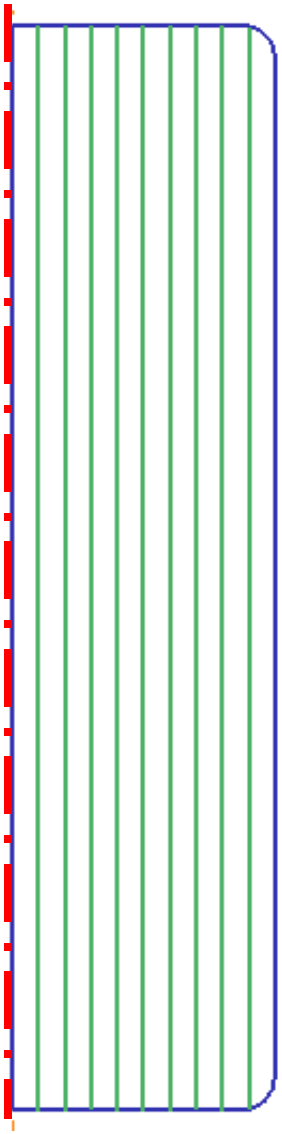

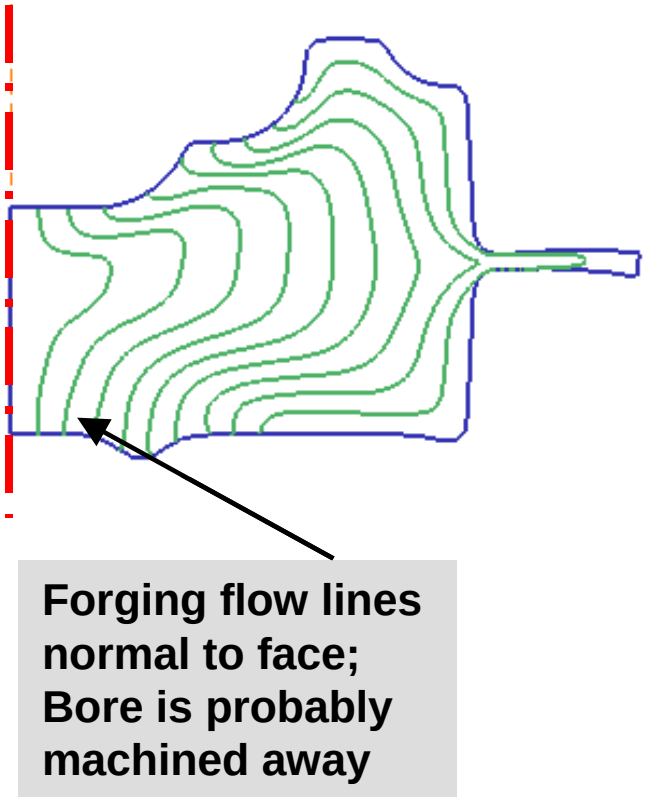

Figure F-27. Flow Lines for AE 3007 Fan Disk

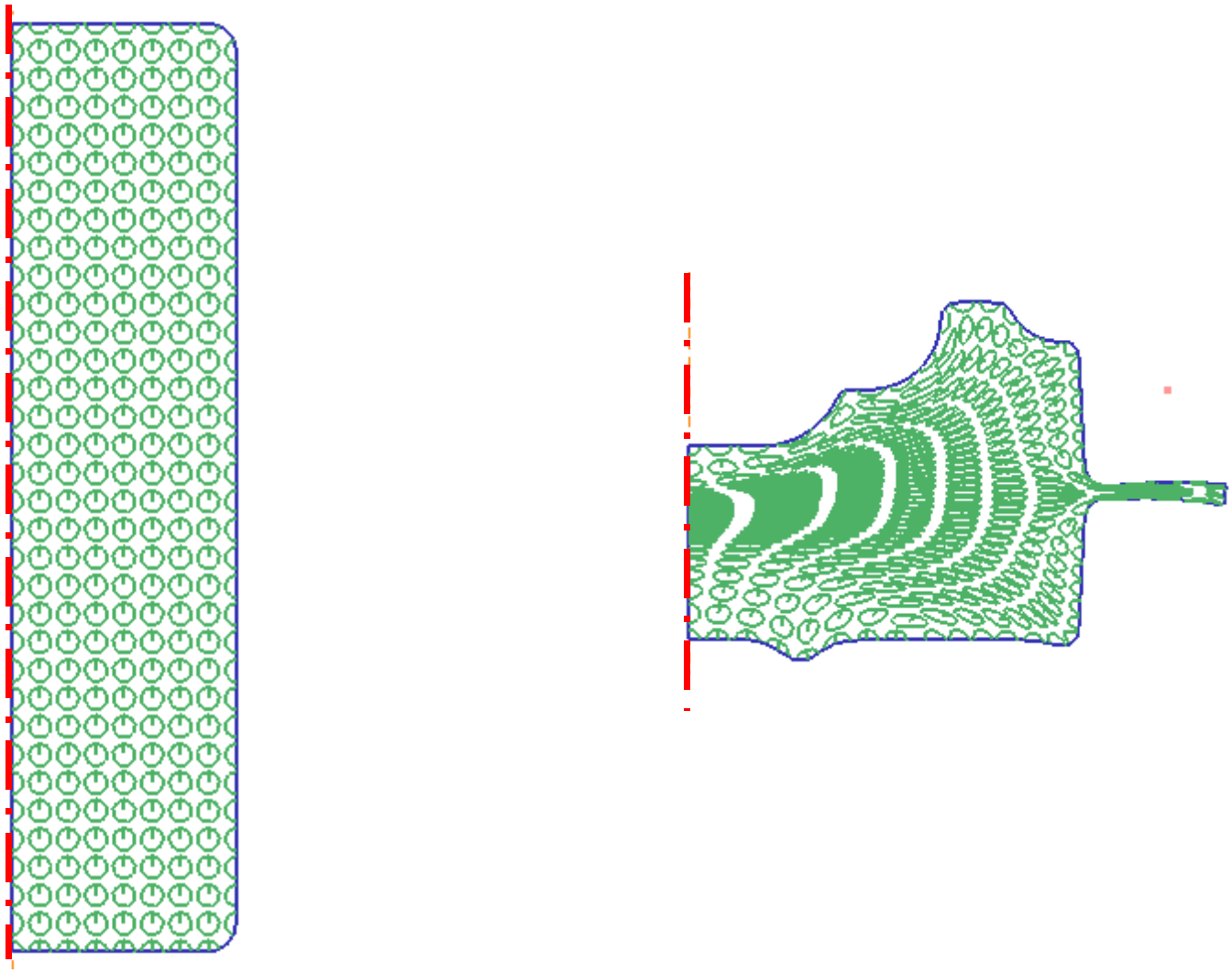

Figure F-28. Graphical Display of Overall Deformation and Orientation in AE 3007 Fan Disk

F.6 SUMMARY AND CONCLUSIONS.

In Phase I and earlier in Phase II of the Turbine Rotor Material Design (TRMD) program, a microcode was developed and validated to predict the shape and orientation of HA anomalies. Design of Experiments-based models were used to correlate anomaly deformation and forging macrostrain. This correlation predicts anomaly deformation quickly and accurately for both billet conversion and component forging and can be used to modify the anomaly distribution used in lifing analyses.

As a follow-on, another activity was defined with the objective of determining the deformation macrostrain required to crack HA anomalies in order to determine the likelihood of noncracked HA under typical forming conditions. The results of this study are reported here. These results may direct the future development of nondestructive evaluation ultrasonic (UT) methods and/or changes to current inspection procedures to enhance anomaly detectability.

HA cracking strain and damage (extent of cracking) were determined as functions of nitrogen content and deformation parameters. The model was validated with the limited seeded billet experimental data from TRMD-II. Extent of cracking correlates approximately with HA damage. The results are shown in a number of ways for ease of use and interpretation.

Strain to HA cracking increases and HA damage decreases with

- decreasing HA N2 and decreasing diffusion zone N2 content,
- increasing temperature, and
- decreasing strain rate.

For Ti-64, temperatures higher than 1700°F and strain rates less than 0.5/second cause low damage and cracking.

Damage and forging flow lines along which anomalies tend to orient were computed for three generic Ti-64 forging shapes as examples. When flow lines are normal to a face, a scan from another face, or a shear scan, should be used to enhance anomaly detectability. These three cases are examples, and in general, the results for any forging should be evaluated on a case-by-case basis.

The following general conclusions can be drawn about the accuracy of the modeling predictions based on the preliminary results reported here. If the initial location and orientation in the billet can be ascertained by UT inspection, the final location and orientation can be predicted with reasonable confidence. If the initial anomaly size/shape can be ascertained by UT inspection, the deformed size/shape can be predicted with reasonable confidence for the diffusion zone, but less accurately for HA. Forging flow lines can be predicted accurately based on the data from many production parts.

The results of the present study show that ingot-to-billet conversion will, under commonly used processing conditions, crack all HA with nitrogen contents greater than 4%, which is the lowest HA nitrogen content evaluated here. The extent of cracking will be less if the conversion is

carried out at high temperatures (~1750°F) or low strain rates (~ 0.1/sec). For nitrogen content less than 4%, the anomaly is treated as a diffusion zone. The diffusion zone results from partially dissolved HA cores during melting or conversion steps. If the anomaly is a diffusion zone only (without a HA core), then the TRMD-I flow stress tests indicate that it has good ductility. The diffusion zones only anomaly is unlikely to crack after billet conversion and forging; it would only deform along with the base material, but to a lesser extent depending on its nitrogen content. In reality, there is no sharp transition between a diffusion zone and a HA at 4% nitrogen. The transition from ductile to brittle behavior occurs over a range of nitrogen contents depending on the deformation conditions (strain, strain rate, and temperature) and the beta to (beta + alpha) transition temperature. More work is needed to accurately characterize the transition zone.

The reasons for the discrepancies between the predictions and the measurements are:

- Nonsmooth HA flow behavior with accumulated damage, especially at high N2 content.
- A wide range of the various independent variables fitted into a regression equation.
- Inaccuracies in the constitutive property data obtained from a rather small number of tests.
- Data smoothed and fitted into constitutive equation.
- Cracking and voiding in HA not captured.
- Unknowns like prevoiding, precracking, fragmentation, and reconstitution will influence the deformation of the HA core.

More validation is needed to verify the accuracy of the predictions. Future work should address the generation of more accurate constitutive behavior data for the HA and the diffusion zone, especially in the ductile-to-brittle transition region at around 4% nitrogen; model enhancement to include cracking, voiding, fragmentation and reconstitution; and the generation of appropriate constitutive property data for anomalies in other Ti-alloys (e.g., Ti-6242 and Ti-17).

F.7 REFERENCES.

F-1. Leverant, G.R., et al., “Turbine Rotor Material Design,” FAA report DOT/FAA/AR-00/64, December 2000.

F-2. Chan, K.S., Perocchi, L., and Leverant, G.R., “Constitutive Properties of Hard Alpha Titanium,” *Metallurgical and Materials Transactions A*, Vol. 31A, 2000, pp. 3029-3040.

F-3. Srivatsa, S., “Deformation Strain Needed to Crack Hard Alpha Anomalies,” Turbine Rotor Material Design Program, Task 2, Effect of Forging on Hard Alpha Morphology, July 2005 (available at DARWIN web site, www.darwin.swri.org).

APPENDIX G—SENSITIVITY OF Ti-17 TO AN OXYGEN-STABILIZED HARD ALPHA

G.1 BACKGROUND.

A recent Ti-6242 compressor disk failure from an uncracked, nonvoided, oxygen (O)-rich stabilized hard alpha raised questions about the sensitivity of other titanium alloys, such as Ti-64 and Ti-17, to similar anomalies. Internal GE Aviation studies demonstrated that at room temperature (RT), elevated oxygen caused Ti-6242 to lose ductility, while dwell low-cycle fatigue(LCF) tests on base-oxygen material containing high-oxygen seeds showed a significant reduction in dwell-fatigue life and formation of internal, flat facets at the high-oxygen seed crack initiation sites. The fracture morphology of these bars was similar to that observed in the compressor disk failure. Similar research and development work was conducted on Ti-64, and showed no degradation in ductility at low temperature. Based on the studies on Ti-6242 and Ti-64, it was determined that beta processed Ti-17 should be assessed to evaluate whether oxygen impacted low-temperature ductility, and if so, whether low-temperature, dwell-fatigue properties were affected.

G.2 EXPERIMENTAL APPROACH.

Two Ti-17 ingots were double vacuum are remelted and converted to a 4″ diameter bar at TIMET, NV. The ingot chemistries are shown in table G-1. Extrusion mults were prepared by TIMET Henderson, and shipped to GE-Corporate Research and Development (CRD) where the mults were extruded from approximately 3.5″ diameter to 2″ diameter. The extrusion temperature for both alloys was selected as 1665°F. In addition to the base- and high-oxygen (0.5% O) materials described above, a seeded extrusion billet was fabricated with high-oxygen (0.5% O) seeds sealed inside base material. Each extrusion was solution heat-treated at 1475°F for 4 hours, water quenched, and aged at 1190°F for 8 hours. Tensile and fatigue specimen blanks were machined from the base- and high-oxygen extrusions. Fatigue specimen blanks were machined from the seeded extrusion, taking care to ensure that the seeds were located inside the final specimen gage length. Figure G-1 shows the seeded test specimen geometry.

Table G-1. Chemistries From Base- and High-Oxygen Ti-17 Ingot

	Al	Mo	Cr	Sn	Zr	Fe	C	O	N	H (ppm)
V8028 - T	4.84	4.00	4.05	1.99	2.00	0.033	0.009	0.115	0.003	32
V8028 - B	4.93	4.09	4.13	2.10	2.11	0.035	0.010	0.128	0.004	40
V8027 - T	4.98	4.09	4.13	1.99	2.09	0.035	0.006	0.475	0.005	18
V8027 - B	4.73	3.94	3.93	1.89	2.00	0.031	0.010	0.505	0.006	15

ppm = parts per minute

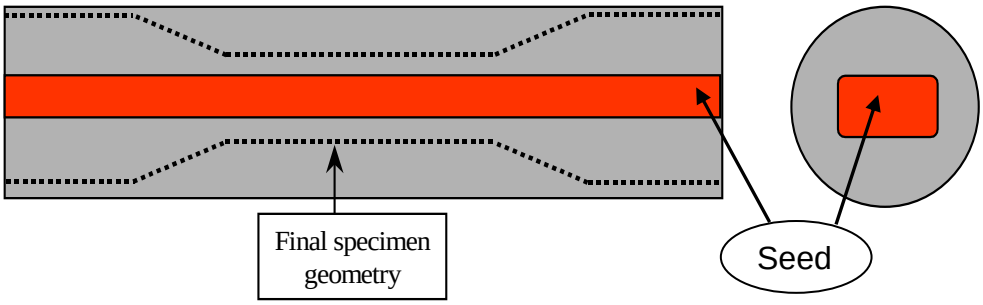

Figure G-1. Seeded Test Bar Geometry

Tensile testing of the base- and high-oxygen alloys was conducted at RT, 250°F, and 500°F. Subsequently, LCF testing was conducted on both alloys at RT and 250°F. LCF tests were conducted at 30 cycles per minute (cpm) and with a 2-minute dwell-cycle. The 2-minute dwell-cycle tests were conducted at different stresses in order to determine the stress to give a 2000 dwell-cycle life. Triplicate 30-cpm LCF tests were then conducted at this stress. After the LCF testing on the base- and high-oxygen specimens was completed, seeded LCF specimens were tested in 30 cpm and 2-minute dwell following similar test procedures.

G.3 RESULTS.

The results are presented in the following sections on microstructure, tensile data, LCF data from base- and high-oxygen Ti-17, and LCF data from base-oxygen material containing high-oxygen seeds.

G.3.1 MICROSTRUCTURE DATA FROM BASE- AND HIGH-OXYGEN Ti-17 EXTRUSIONS.

The extruded and heat-treated microstructures for the base- and high-oxygen alloys are shown in figure G-2. The base-oxygen structure consists of elongated prior beta grains containing a fine transformed beta structure, figure G-2(a). The high-oxygen structure consists of a small volume fraction of spheroidized primary alpha in a transformed beta matrix, figure G-2(b). The microstructures in both extrusions were consistent from front to back and from edge to center.

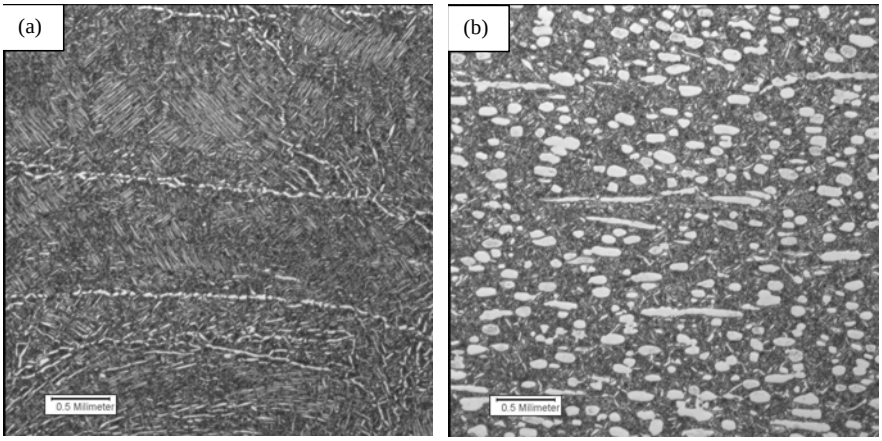

Figure G.2. Microstructures From Ti-17 Extrusions (a) Base Oxygen and (b) High Oxygen

G.3.2 TENSILE DATA FROM BASE- AND HIGH-OXYGEN Ti-17 EXTRUSIONS.

The tensile data are shown in table G-2. The tensile data show excellent repeatability for a given alloy/test temperature, indicating uniformity of material along the length of each extrusion. The data also show that the higher-oxygen material has increased strength of approximately 25 ksi at RT and approximately 15 ksi at 500°F. RT plastic elongation for the high-oxygen material is reduced by one-half to 5%, but at higher temperatures, plastic elongation in the higher-oxygen material is equivalent to, or higher than, the baseline material.

Table G-2. Tensile Properties From Base and High-Oxygen Ti-17

Alloy	Specimen ID	Temperature (°F)	Ultimate Tensize Strength (ksi)	0.2% Yield Strength (ksi)	Elongation (%)	Reduction in Area (%)
Ti-17	1-1	75	167	155	10	22
Ti-17	2-1	75	168	155	10	22
Ti-17	1-2	250	154	137	11	27
Ti-17	2-2	250	155	137	11	26
Ti-17	1-3	500	141	118	8.0	24
Ti-17	2-3	500	143	120	8.0	24
Ti-17+0.5% O	1-1A	75	191	183	5.5	7.0
Ti-17+0.5% O	2-1A	75	193	184	4.5	6.0
Ti-17+0.5% O	1-2A	250	175	160	11	17
Ti-17+0.5% O	2-2A	250	176	161	11	19
Ti-17+0.5% O	1-3A	500	156	136	13	40
Ti-17+0.5% O	2-3A	500	156	136	13	40

G.3.3 LOW-CYCLE FATIGUE DATA FROM BASE AND HIGH-OXYGEN TI-17 EXTRUSIONS.

The LCF data for base-oxygen Ti-17 and high-oxygen Ti-17 are shown in tables G-3 and G-4, respectively. There were a number of issues encountered with the actual LCF testing, resulting in several tests being voided or run at different stress levels than selected due to equipment problems. In addition, the Ti-17 material behaved differently than the Ti-6242 and Ti-64 materials tested previously, resulting in some tests failing on loading, while others unexpectedly ran out. In spite of these issues, there were clear trends arising from the tests. At RT, it was found that the stress for 2000 dwell cycles was 14 ksi higher for high-oxygen Ti-17 material. At 250°F, there was almost no difference in stress for 2000 dwell cycles between the base- and high-oxygen Ti-17. The 30-cpm LCF lives were longer for oxygen-containing material and higher at RT.

Table G-3. Low-Cycle Fatigue Properties From Base-Oxygen Ti-17

Specimen ID	Alloy	Temperature (°F)	Test Type	Stress (ksi)	Cycles	Comments
8028-3-3	Base O	RT	30 cpm	158.5	14,033	Gage
8028-4-1	Base O	RT	30 cpm	158.5	123,535	Runout
8028-5-4	Base O	RT	30 cpm	158.5	8,566	Gage
8028-3-1	Base O	RT	Dwell	155.0	5,016	Runout
8028-5-3	Base O	RT	Dwell	157.0	5,020	Runout
8028-4-2	Base O	RT	Dwell	158.0	1,947	Gage
8028-6-1	Base O	RT	Dwell	159.0	2,078	Gage
8028-6-2	Base O	250	30 cpm	157.0	762	Gage
8028-4-3	Base O	250	30 cpm	158.5	479	Gage
8028-5-1	Base O	250	30 cpm	159.0	5,535	Gage (spike to 159.0 ksi on test start-up)
8028-3-4	Base O	250	Dwell	154.7	Failed on load	Gage
8028-3-2	Base O	250	Dwell	155.0	5,011	Runout
8028-4-4	Base O	250	Dwell	155.0	5,458	Runout
8028-5-2	Base O	250	Dwell	157.0	5,251	Gage

Table G-4. Low-Cycle Fatigue Properties From High-Oxygen Ti-17

Specimen ID	Alloy	Temperature (°F)	Test Type	Stress (ksi)	Cycles	Comments
8027-3-3	High O	RT	30 cpm	172.5	31,764	Gage
8027-4-1	High O	RT	30 cpm	172.5	1,759	Void test due to drift in stress—stress at 1759 cycles was 185 ksi
8027-5-4	High O	RT	30 cpm	172.5	33,023	Gage
8027-3-2	High O	RT	Dwell	168.0	5,008	Runout
8027-6-1	High O	RT	Dwell	171.0	235	Void due to power failure causing sample to fail
8027-5-3	High O	RT	Dwell	173.0	1,662	Gage
8027-4-2	High O	RT	Dwell	178.0	950	Gage
8027-3-1	High O	RT	Dwell	183.0	186	Gage
8027-4-3	High O	250	30 cpm	157.0	8,441	Gage

Table G-4. Low-Cycle Fatigue Properties From High-Oxygen Ti-17 (Continued)

Specimen ID	Alloy	Temperature (°F)	Test Type	Stress (ksi)	Cycles	Comments
8027-5-1	High O	250	30 cpm	157.0	9,414	Gage
8027-6-2	High O	250	30 cpm	157.0	7,462	Gage
8027-3-4	High O	250	Dwell	155.0	5,030	Runout
8027-5-2	High O	250	Dwell	170.0	38	Gage
8027-4-4	High O	250	Dwell	173.3	Failed on load	Gage

G.3.4 LOW-CYCLE FATIGUE DATA FROM BASE-OXYGEN Ti-17 EXTRUSION CONTAINING HIGH-OXYGEN SEEDS.

The LCF data from base-oxygen material containing high-oxygen seeds are shown in table G-5. It was estimated that the stress for 2,000 dwell cycles was 153 ksi at both RT and 250°F, with the 30-cpm life being approximately 20,000 cycles at RT and approximately 4,000 cycles at 250°F.

Table G-5. Low-Cycle Fatigue Properties From Base-Oxygen Ti-17 Containing High-Oxygen (0.5% O) Seeds

Specimen ID	Temperature (°F)	Test Type	Stress (ksi)	Cycles	Comments
8028/7-1-1	RT	30 cpm	153.0	26,914	Gage
8028/7-1-3	RT	30 cpm	153.0	21,495	Gage
8028/7-4-1	RT	30 cpm	153.0	12,116	Radius
8028/7-1-2	RT	Dwell	158.0	294	Gage
8028/7-3-1	RT	Dwell	150.0	5,087	Runout
8028/7-4-3	RT	Dwell	155.0	601	Gage
8028/7-5-2	RT	Dwell	153.0	3,230	Gage
8028/7-2-2	250	30 cpm	153.0	5,710	Radius
8028/7-3-2	250	30 cpm	153.0	3,083	Radius
8028/7-5-1	250	30 cpm	153.0	4,745	Gage
8028/7-2-1	250	Dwell	154.0	Failed on load	Gage
8028/7-2-3	250	Dwell	155.0	4,464	Radius
8028/7-3-3	250	Dwell	153.0	1,357	Gage

G.4 DISCUSSION.

The tensile data for base- and high-oxygen Ti-17 are compared with Ti-64 and Ti-6242 with base- and high-oxygen levels in figures G-3 through G-6. The data are plotted in terms of the delta between base- and high-oxygen tensile strength, 0.2 percent yield strength, percent plastic elongation, and percent reduction in area in figures G-3 through G-6, respectively. The strength

data in figures G-3 and G-4 show that oxygen results in a significantly higher strength increase in Ti-6242 compared with Ti-64 from RT through 500°F. The impact of oxygen on Ti-17 strength lies between Ti-6242 and Ti-64. The ductility data in figures G-5 and G-6 show that oxygen significantly degrades Ti-6242 at RT, whereas Ti-64 remains relatively unaffected. The impact of oxygen on Ti-17 ductility is between Ti-6242 and Ti-64.

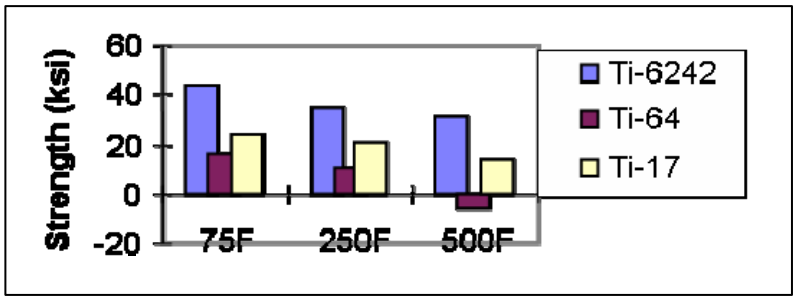

Figure G-3. Impact of Oxygen Addition on Ultimate Tensile Strength

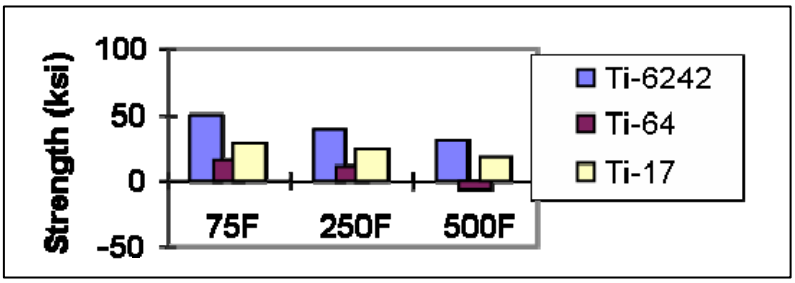

Figure G-4. Impact of Oxygen Addition on 0.2% Yield Strength

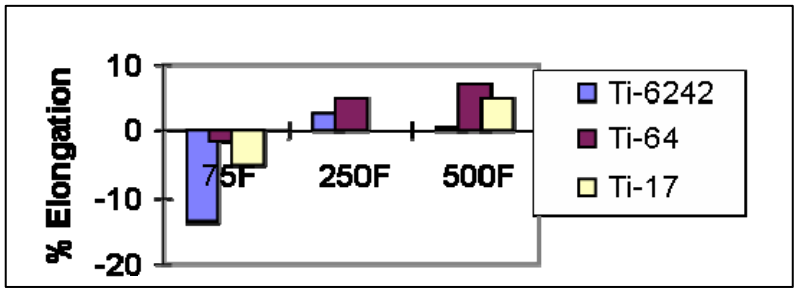

Figure G-5. Impact of Oxygen Addition on Plastic Elongation

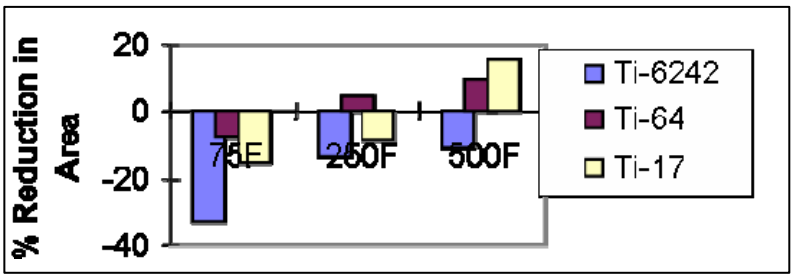

Figure G-6. Impact of Oxygen Addition on Reduction in Area

Table G-6 shows a comparison of the stress for 2000 dwell-cycle failure and the 30-cpm life at that stress for the base- and high-oxygen Ti-17, and the base-oxygen Ti-17 containing high-oxygen seeds. Also shown in table G-6 are the available comparable data for Ti-6242 and Ti-64. The stress data for 2000 dwell cycles versus temperature are shown in figure G-7. Several differences were noted in behavior between Ti-17, Ti-6242, and Ti-64 in relation to the impact of oxygen on fatigue properties:

- RT dwell-fatigue behavior of Ti-17 lay between Ti-6242 and Ti-64.
- RT Ti-17 seeded dwell debit for Ti-17 was ~10× versus ~32× for Ti-6242, and an estimated no impact for Ti-64.
- Crack initiation sites for seeded Ti-17 bars were relatively rough (see figure G-8) compared with the flat, faceted crack initiations in seeded Ti-6242 bars.

Table G-6. Low-Cycle Fatigue Summary for Base- and High-Oxygen Ti-17, Ti-6242, and Ti-64

Alloy	Temperature (°F)	UTS (ksi)	0.2% YS (ksi)	Stress for 2000 Dwell Cycles (ksi)	30-cpm Life at Stress for 2000 Dwell Cycles
Ti-17	RT	167.5	155.0	158.5	~11,000
Ti-17	250	154.5	137	158.0	~600
Ti-17+O	RT	192.0	183.5	172.5	~32,000
Ti-17+O	250	175.5	160.5	157.0	~8,000
Ti-17+Seed	RT	N/A	N/A	153.0	~20,000
Ti-17+Seed	250	N/A	N/A	153.0	~4,000
Ti-6242	RT	137.0	122.5	128.6	~12,000
Ti-6242	250	126.5	106.0	112.2	~19,000
Ti-6242+O	RT	181.0	172.0	151.2	~22,000
Ti-6242+O	250	161.5	145.5	132.9	~9,000
Ti-6242+Seed	RT	N/A	N/A	126 (~1500 cycles)	~47,000 (at 126 ksi)
Ti-64	RT	144.5	132.0	134.9	~13,000
Ti-64	250	131.5	114.0	125.1	~11,000
Ti-64+O	RT	160.5	147.0	137.5	~19,000
Ti-64+O	250	141.5	124.0	117.3	~16,000

UTS = Ultimate tensile strength
YS = Yield strength

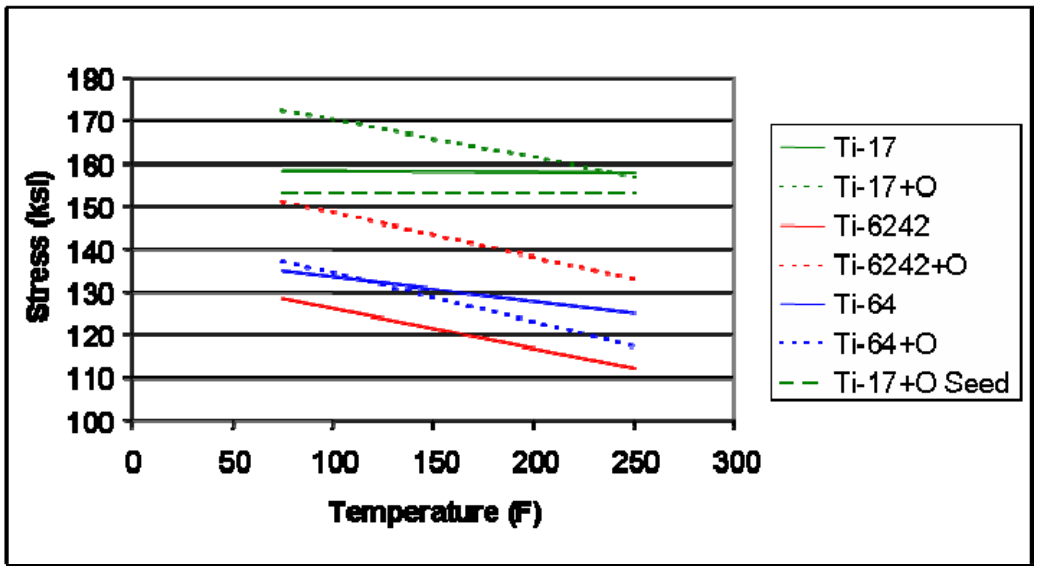

Figure G-7. Stress for 2000 Dwell Cycles vs Temperature

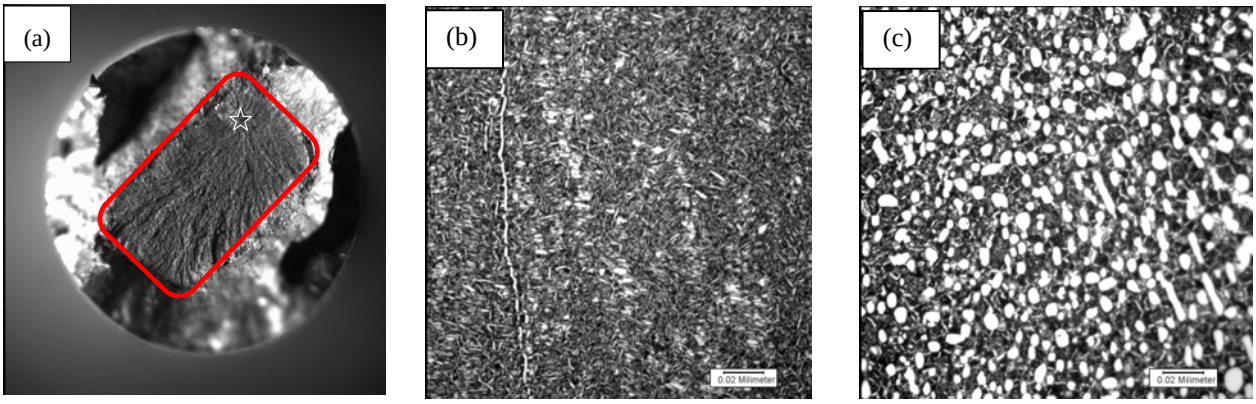

Figure G-8. Crack Initiation Site (a) For Seeded Ti-17 Dwell LCF Bar 4-3 Run at RT and 155 ksi; Approximate Outline of Seed is Indicated by Red Border, and Crack Initiation Location is Indicated by the Star, (b) Microstructure of Base Material, and (c) Surrounding High-Oxygen Seed Material

The Ti-6242 high-oxygen compressor disk failure described in the introduction initiated from a high-oxygen anomaly with a high primary alpha content. Based on the operating stress and temperature profile at the failure location, it is likely that dwell fatigue played a role in cracking the HA. Based on the tensile and fatigue observations above, it is believed that Ti-17 is less sensitive to high-oxygen anomalies than Ti-6242. There are several reasons to account for the reduced sensitivity to dwell fatigue of high-oxygen anomalies in Ti-17, and these are discussed in the sections below.

G.4.1 LOWER PRIMARY ALPHA CONTENT IN A Ti-17 HARD ALPHA ANOMALY.

Literature dwell-fatigue data indicate that primary alpha content is a significant factor, with a higher primary alpha content leading to increased sensitivity to dwell fatigue. In the case of the Ti-6242 compressor disk failure, the hard alpha contained a high-volume fraction of primary alpha, approaching 80%. For an anomaly with similar oxygen content in a Ti-17 part, the primary alpha content would be significantly lower as a result of the bulk of the part being processed above the beta transus. This is seen in comparing the primary alpha content of a Ti-17 high-oxygen anomaly, figure G-2(b) to the approximately 80% primary alpha content anomaly in the failed Ti-6242 disk. The low primary alpha content in the Ti-17 high-oxygen anomaly is at least partly responsible for the absence of a faceted initiation in the seeded Ti-17 bars, figure G-8.

G.4.2 REDUCED COLONY STRUCTURE IN A Ti-17 HARD ALPHA ANOMALY.

An important in assessing the sensitivity of a material to dwell fatigue is the presence of colony structure. Literature data indicate that as an alpha/beta alloy is processed closer to its beta transus, the presence of colony structure is reduced. As described above, a high-oxygen anomaly in Ti-17 is processed closer to its beta transus than an equivalent anomaly in alpha/beta processed Ti-6242, leading to a reduced probability of colonies in the Ti-17 primary alpha-containing anomaly.

G.4.3 REDUCED COLONY STRUCTURE SURROUNDING A Ti-17 HARD ALPHA ANOMALY.

A factor that affects the sensitivity of a material to dwell fatigue is the presence of large colony structure in the surrounding material. In the case of Ti-17, the material surrounding a high-oxygen anomaly will have been beta processed, and subsequently transformed to a basket weave structure, with little evidence of colony structure. The basket weave structure forms readily in Ti-17 due to its increased beta stabilizer content relative to Ti-6242. Material surrounding a high-oxygen anomaly in Ti-6242 may contain extensive colonies of primary alpha grains, depending on the billet conversion and forging conditions.

G.4.4 REDUCED ALPHA STABILIZER AND INCREASED BETA STABILIZER CONTENT IN Ti-17.

A factor affecting the sensitivity of a material to dwell fatigue is the balance of alpha and beta stabilizers in the alloy. In Ti-17, the alpha stabilizer content is lower than Ti-6242 (aluminum, zirconium, and tin). It is known that increased alpha stabilizer content promotes planar slip and increases the potential for sensitivity to dwell fatigue. The beta stabilizer content of Ti-17 (molybdenum and chromium) is higher than Ti-6242 and promotes a higher volume fraction of beta phase, thereby reducing the risk of extended planar slip bands leading to increased sensitivity to dwell fatigue. The lower alpha stabilizer content and higher beta stabilizer content in Ti-17 is also likely to be partly responsible for the absence of a faceted initiation in the seeded Ti-17 bars, see figure G-8.

Based on the tensile and fatigue data presented previously, it is believed that Ti-17 is more sensitive to oxygen anomalies than Ti-64. There are at least two reasons to account for the increased sensitivity to dwell fatigue of high-oxygen anomalies in Ti-17 relative to Ti-64, and these are discussed below.

G.4.5 LOWER DUCTILITY IN A Ti-17 HIGH-OXYGEN ANOMALY.

The absolute ductility of high-oxygen Ti-17 at RT is significantly lower than high-oxygen Ti-64. During a load-controlled dwell-fatigue test in Ti-17 containing a high-oxygen seed, the load will be shed from the weaker base material onto the stronger high-oxygen seed material. Since the high-oxygen seed has a relatively low strain capability, approximately 5% plastic strain to failure in tension, the seed will crack relatively easily, leading to a low-fatigue life. In contrast, a Ti-64 high-oxygen seed in Ti-64 has a much greater strain capability over a Ti-17 high-oxygen seed in Ti-17, resulting in a smaller reduction in dwell-fatigue life for a high-oxygen seed in Ti-64 compared to a high-oxygen seed in Ti-17.

G.4.6 SIMILAR DWELL-FATIGUE BEHAVIOR OF LOW- AND HIGH-OXYGEN Ti-64.

As discussed above, load shedding occurs during a dwell-fatigue test from a lower strength region (base material) to a higher strength region (high-oxygen seed). In the case of Ti-17, there is a larger strength delta between high-oxygen and base material than Ti-64, see figures G-3 and G-4. The result is that more load will be shed onto the high-oxygen seed in Ti-17, and in conjunction with the lower ductility in Ti-17 high-oxygen material, it will lead to a lower dwell-fatigue life.

Aside from the above assessment that the sensitivity of high-oxygen anomalies in Ti-17 to dwell fatigue lies between Ti-6242 and Ti-64, there is a significant difference between the processing of Ti-17, and Ti-6242, and Ti-64 that reduces the probability that a high-oxygen anomaly will be present in Ti-17. This difference in processing is discussed below.

G.4.7 REDUCED OXYGEN CONTENT IN A Ti-17 HARD ALPHA ANOMALY.

The Ti-17 alloy contains 4% chromium, which tends to segregate during ingot solidification. Consequently, Ti-17 ingots are homogenized at high temperatures for long periods of time to reduce the level of chromium segregation. Internal studies have shown that this homogenization treatment results in a large reduction in oxygen content of any high-oxygen anomaly in Ti-17. This type of homogenization treatment is typically not applied to Ti-64 or Ti-6242. There is, therefore, a much lower probability that a high-oxygen anomaly exists in Ti-17 billet than either Ti-6242 or Ti-64 billets. It is likely that had the anomaly responsible for the Ti-6242 disk failure occurred in Ti-17, the Ti-17 homogenization treatment would have completely dispersed the oxygen.

In summary, it has been demonstrated that Ti-17 is less sensitive to high-oxygen anomalies in dwell fatigue than Ti-6242, while it is believed that Ti-17 is likely more sensitive to high-oxygen anomalies in dwell fatigue than Ti-64. The probability of occurrence of high-oxygen anomalies in Ti-17 is substantially lower than in either Ti-6242 or Ti-64, and for this reason, it is argued that had the anomaly responsible for the Ti-6242 disk failure occurred in Ti-17, the Ti-17 homogenization treatment would have completely dispersed the oxygen.

G.5 SUMMARY.

Prior testing of high-oxygen seeded Ti-6242, dwell-LCF bars showed a reduction in dwell-fatigue life and a faceted crack initiation morphology, similar to that observed in a compressor disk failure associated with an oxygen-stabilized hard alpha. Prior testing also revealed that high-oxygen Ti-6242 had low ductility and high strength at RT. Similar testing on Ti-64 with and without elevated oxygen showed a modest increase in low-temperature strength, but little impact on dwell-fatigue properties. In the current work, oxygen impacted Ti-17 tensile properties in a similar manner to Ti-6242, but to a smaller extent; i.e., the strength increase and ductility decrease at RT was smaller than observed in Ti-6242. The same trend was observed in RT dwell-fatigue testing of high-oxygen Ti-17 which was found to be somewhat higher than the base Ti-17; however, the increase was not as significant as was observed in Ti-6242. The dwell-fatigue properties of base-oxygen Ti-17 containing high-oxygen seeds were slightly lower than the base-oxygen material. However, there was no evidence of flat, faceted, internal crack initiation, and the dwell-fatigue debit was significantly lower than Ti-6242. These data indicate that Ti-17 is less sensitive to the presence of oxygen-rich anomalies than Ti-6242, while it was argued that high-oxygen seeds will likely impact Ti-17 RT dwell fatigue more than Ti-64. At 250°F, there was little impact of oxygen on Ti-17 dwell-fatigue properties.

In summary, based on the lower impact of oxygen on Ti-17 dwell-fatigue properties, the smaller dwell debit associated with an embedded high-oxygen seed and the absence of a faceted crack initiation, it is believed that Ti-17 is less sensitive to high-oxygen anomalies than Ti-6242. The Ti-17 ingot homogenization and beta forge practice also increases the probability that any high-oxygen anomaly initially present in a Ti-17 ingot will either be completely dispersed or rendered benign under conditions of low-temperature dwell fatigue.

APPENDIX H—FATIGUE TESTING OF FORGED COUPONS WITH EMBEDDED HARD ALPHA ANOMALIES

Hard alpha (HA) anomalies are often extensively voided and cracked in the final forged rotor configuration. Current life-prediction methodologies commonly assume that an initial fatigue crack size equal to the size of the HA region (high-nitrogen core plus surrounding diffusion zone (DZ)) is present at the beginning of life. This assumption could be overly conservative, however, for smaller HA anomalies and zones with lower nitrogen content, which may be less likely to be extensively cracked and voided after the forging process and, hence, more difficult to detect using nondestructive evaluation. Consequently, these anomalies may play a significant role in the probabilistic risk assessment, especially considering that these smaller anomalies are more likely to remain in the rotor upon entry into service. Therefore, it is useful to assess the cracking tendencies of the HA anomalies under static and fatigue loading in order to evaluate the possibility that some nonzero crack nucleation life could be included in the fatigue life-prediction methodology.

An experimental program was conducted in Turbine Rotor Material Design (TRMD) Phase I [H-1 and H-2] to characterize the damage evolution that occurs in and around HA anomalies. Mechanical tests were conducted on reduced gage section specimens of Ti-6Al-4V containing either synthetic or naturally occurring HA material. In that earlier work, HA anomalies were observed to crack at low static stress levels when the anomalies were located at the surface, although crack extension into the matrix was problematic under static loading. Embedded HA anomalies exhibited substantially higher resistance to cracking under static load, but still cracked substantially at applied stresses around 80 to 120 ksi. Fatigue crack growth into the matrix from surface anomalies occurred relatively quickly. Low stress ratio fatigue tests on embedded anomalies at applied maximum stresses ranging from 75 ksi to 100 ksi did exhibit crack growth into the matrix and eventual specimen failure. However, comparisons of observed cracking with Flight_Life predictions suggested that some significant number of fatigue cycles could be required to form a dominant, growing fatigue crack in the matrix, for both synthetic and natural HA anomalies.

However, the very small number of tests performed in TRMD-I represented a very limited parameter range, and the tests may not have been fully representative of actual hardware under actual service conditions. For example, actual hardware would have experienced a complete forging operation after anomaly formation, and it is possible that this forging operation would have either nucleated more severe initial cracks in the HA anomaly or even grown cracks into the matrix itself.

Additional testing was performed in TRMD-II to continue these investigations. The coupon specimens in TRMD-II were extracted from forgings that had been seeded with synthetic HA anomalies prior to forging for the purpose of validating the DEFORM™ microcode (see appendix C). A selection of different anomaly compositions was tested, including high-nitrogen core plus DZ, high-nitrogen core only, and low-nitrogen DZ only (also called was-beta).

The work performed herein and documented in this appendix consisted of machining rectangular blanks from forged components, fabricating specimens, instrumenting specimens with an

acoustic emission sensor, and fatigue testing the specimens at low load ratio until failure. The primary results obtained include the fracture surfaces (and description of anomaly), total observed cyclic life (including both crack nucleation and growth), and acoustic emission data. The Flight_Life fracture mechanics computer code was used to predict the fatigue crack growth lifetime of each test, and the analytical and experimental results were compared.

H.1 MATERIAL AND PROCEDURES.

The seeded forgings from which the specimens were extracted had been produced during TRMD-I. The artificial HA seeds for the forging mults were manufactured by GE Corporate Research and Development Center (GE-CRD) using a proprietary process outlined in Appendix H of the TRMD-I Final Report [H-1]. GE-CRD also placed the seeds into the forging mults. The mults were then forged into one of two different shapes at Schlosser Forge Company using hot-die techniques. A more complete description of the manufacturing process, along with a detailed tabulation of seed compositions and locations, is contained in the TRMD-I final report [H-1]. All the synthetic cores had a nominal nitrogen content of 12%, and the DZ were nominally 2% nitrogen.

Maps of the anomalies in the forgings were provided from ultrasonic inspections performed by GE Aviation. These maps consisted of dimensional descriptions of anomaly positions in the forgings. The forged disks used herein included a subset of the disks originally produced and included two anomalies from forging seeded billet (SB) SB-1 (a was-beta and a core only), one anomaly with DZ from SB-2, and anomaly clusters with DZs from SB-3 and SB-4, as described more fully in table H-1. Each of the indications in the forgings was labeled with master numbers as tracked and identified in table H-1. The resulting specimen/test identification tracked both disk forging as well as anomaly identification (for instance, specimen/test SB2-9 was extracted from forged billet SB-2 and the anomaly was no. 9). This numbering scheme is consistent with the tables in the TRMD-I final report. In addition to these five synthetic anomalies, one additional specimen (SHI-2) remaining from TRMD-I was tested. This specimen contained a small, embedded anomaly with a core nitrogen content nominally 6% and a surrounding DZ.

Based on the map of anomalies in a given forging, a cut plan was developed to excise blanks suitable for fabricating a fatigue test specimen. The size of the blanks excised from the forgings is described in table H-1 and illustrated in figures H-1 through H-5. Note that figures H-2 and H-3 illustrate cutting performed on the same SB-1 forging. An examination of figures H-1 through H-5 also shows that two forging shapes were used: so-called dogbone (figures H-1 through H-4) and backflow geometries (figure H-5).

Table H-1. Description of the Embedded Anomaly Specimens Subjected to Fatigue Testing

Blank Variables			Disk ID	Indication ID	Anomaly Description
ID	Orientation	Size (inch)			
SB2-9	circumferential	6 × 2.5 × 0.5 (large chordal segment)	SB-2	#9	core + DZ
SB1-2	circumferential	6.5 × 3 × 1	SB-1	#2	was-beta
SB1-5	radial/circum	6.5 × 3 × 1	SB-1	#5	core only
SB3-25c	radial	8 × 3.5 × 1	SB-3	#25-28	cluster + DZ
SB4-37c	circumferential	6.5 × 1.925 × 1.5	SB-4	#37-40	cluster + DZ
SHI-2	axial	premachined (Phase I specimen)	n/a	n/a	core only (6% N)

GE Aviation used the schematics shown in figures H-1 through H-5 to cut up the forgings and produce blanks suitable for machining specimens. These blanks were carefully excised using the electro-discharge machining (EDM) technique. Once the blanks were supplied to Southwest Research Institute®, additional marking similar to the typical examples shown for three of the blanks in figure H-6 was performed to guide the machine shop used to extract fatigue test specimens (Metal Samples, Munford, AL). Metal Samples then electro-discharge machined the sample from the blanks, paying particular attention to keep the anomaly in the center of the gage section of the specimen. Surface grinding was then employed on all faces to eliminate the recast zone associated with the electro-discharge machining of the specimen.

The general fatigue test specimen geometry used is shown in figure H-7. To mitigate premature fatigue failure, the edges of the specimens were carefully broken with a deburring tool. Note that in all cases (despite what the print indicates), all anomalies were internal and were nominally centered in the specimen gage section. In some cases, the length of the two grip ends of the specimen was extended, although the gage section was typically fixed at 1 by 0.5 inch. Since the anomaly clusters were larger in size, the gage section in those two cases was twice as large (1.5- by 0.7-inch section).

The strength levels of the forged Ti-6Al-4V were determined by extracting tensile specimens from cutoff sections of the forgings. A map of the tensile specimens, along with ID number, is indicated in figure H-8. The tensile properties are summarized in table H-2, indicating an overall ultimate strength in the range of 142-150 ksi, yield strength of 136 to 143 ksi, and percent elongation at failure of 16% to 18%. Slight differences between the two forgings (SB-1 and SB-2) are evident, although on balance, given the replicate variability, these differences are not notable.

Blank ID: SB2-9
Forging: SB-2
Defect: #9 indication
Blank: 6.0 long x 2.5 wide x 0.5 thick *(defect in center)*

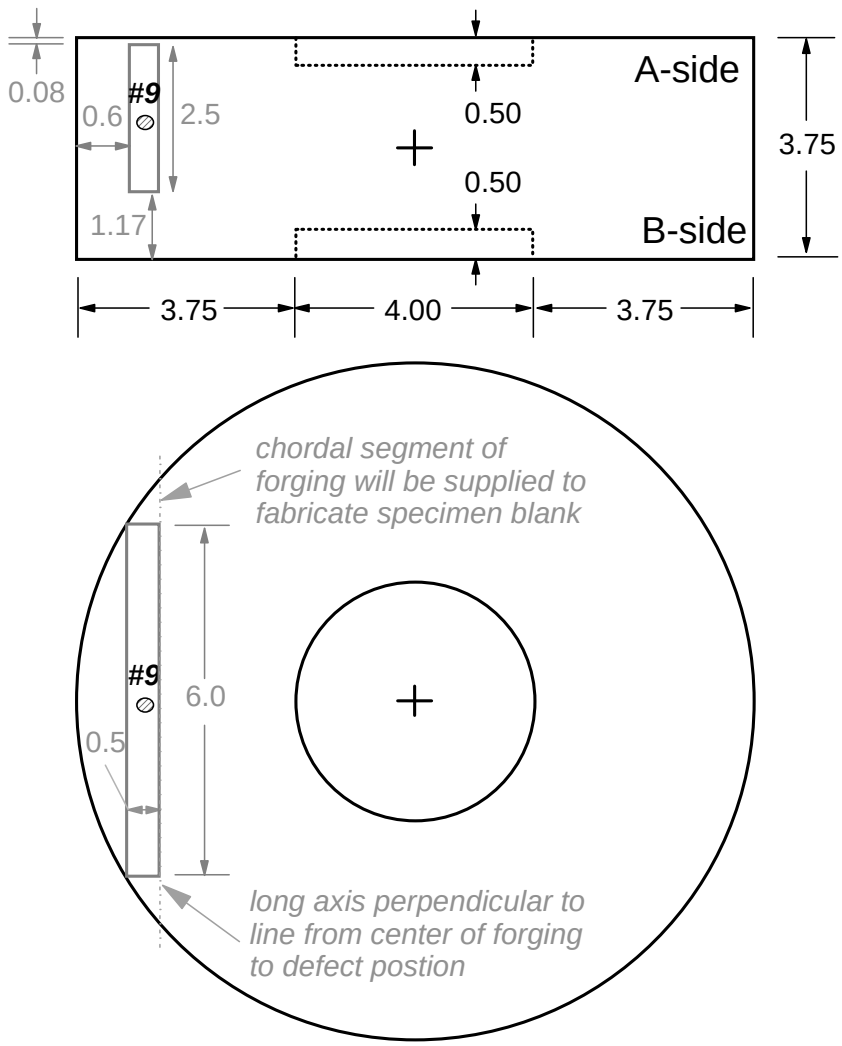

All dimensions are in inches

Figure H-1. Blank Extraction in the Original Forging Used to Create Specimen SB2-9

Blank ID: SB1-2
Forging: SB-1
Defect: #2 indication
Blank: 6.5 long x 3 wide x 1 thick *(defect in center)*

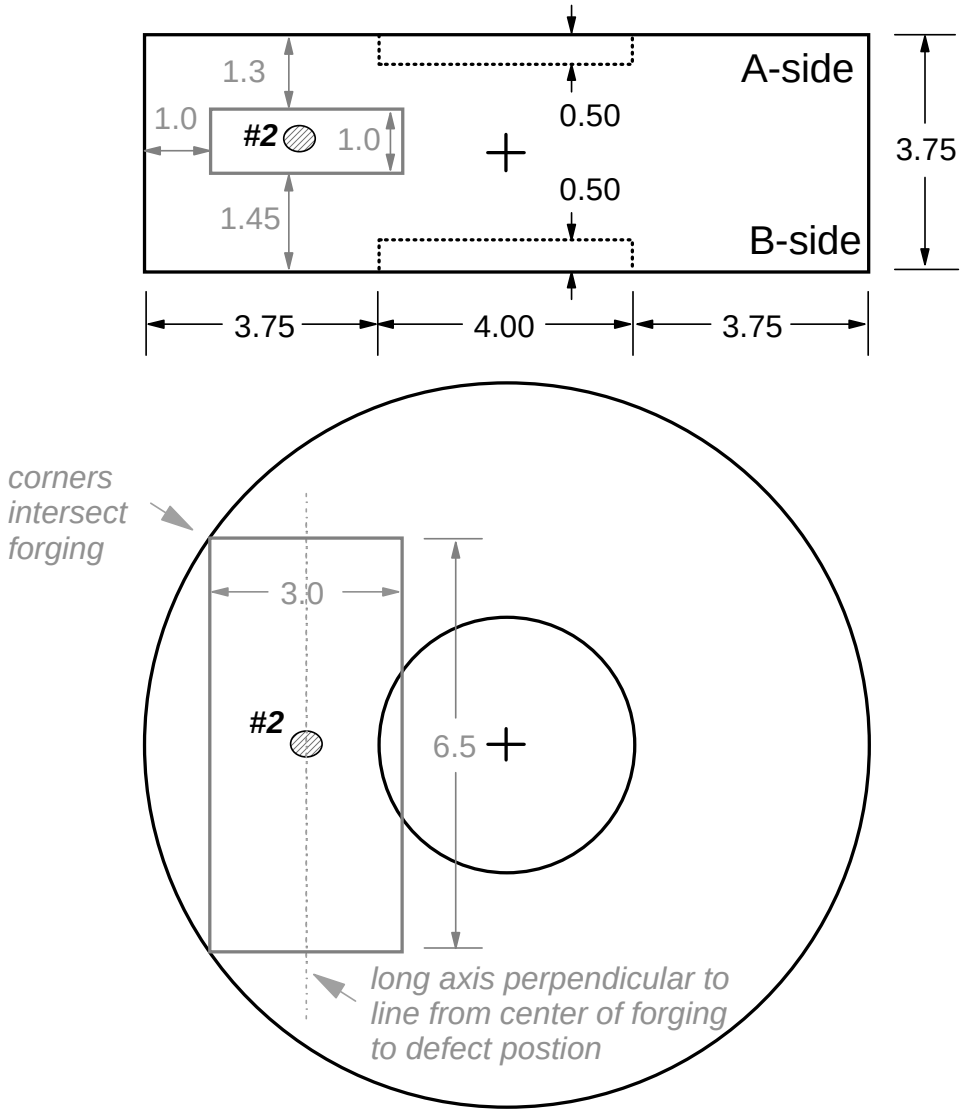

All dimensions are in inches

Figure H-2. Blank Extraction in the Original Forging Used to Create Specimen SB1-2

Blank ID: SB1-5
Forging: SB-1
Defect: #5 indication
Blank: 6.5 long x 3 wide x 1 thick *(defect in center)*

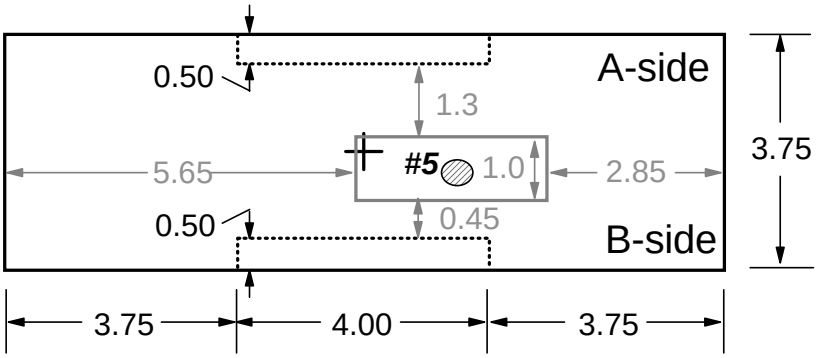

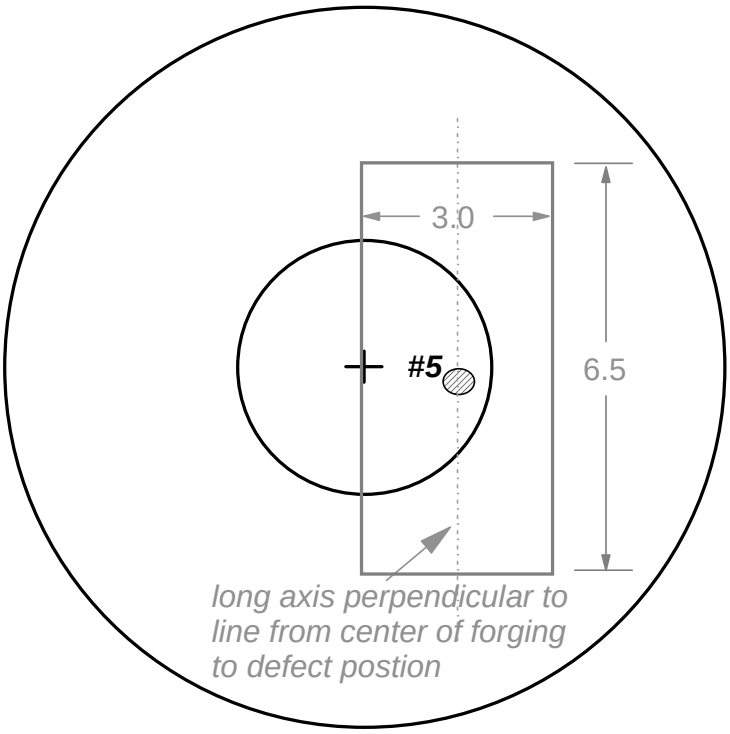

All dimensions are in inches

Figure H-3. Blank Extraction in the Original Forging Used to Create Specimen SB1-5

Blank ID: SB3-25c
Forging: SB-3
Defect: #25-28 cluster
Blank: 8 long x 3.5 wide x 1 thick *(cluster in center)*

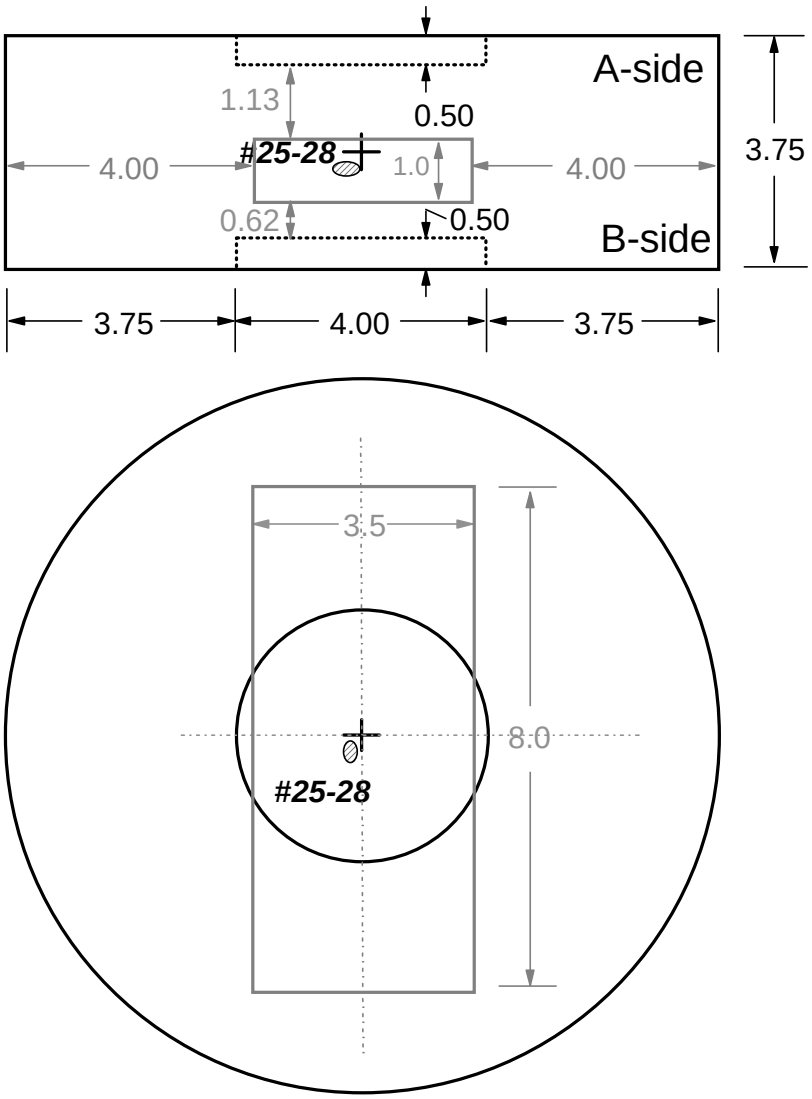

All dimensions are in inches

Figure H-4. Blank Extraction in the Original Forging Used to Create Specimen SB3-25C

Blank ID: SB4-37c
Forging: SB-4
Defect: #37-40 cluster
Blank: 6.5 long x 1.925 wide x 1 thick *(cluster in center)*

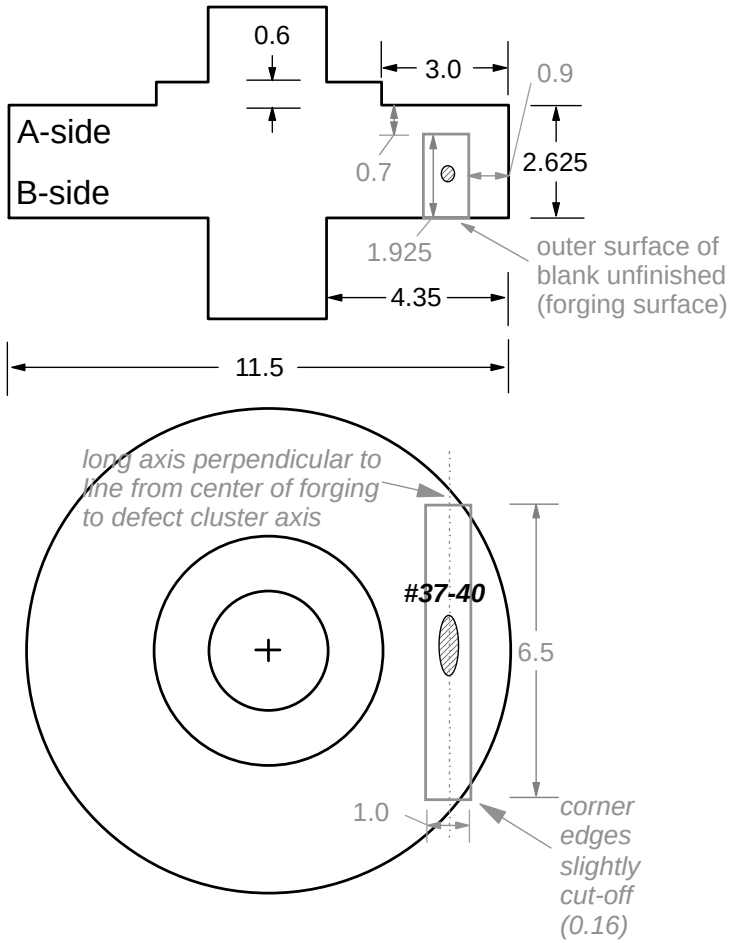

All dimensions are in inches

Figure H-5. Blank Extraction in the Original Forging Used to Create Specimen SB4-37C

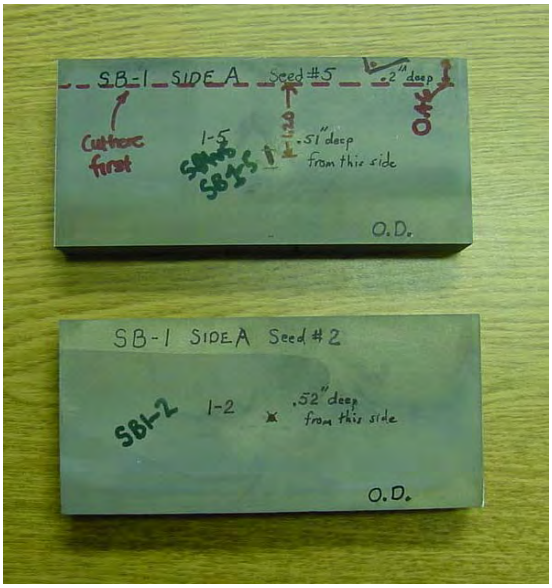

SB1-2 (side A)

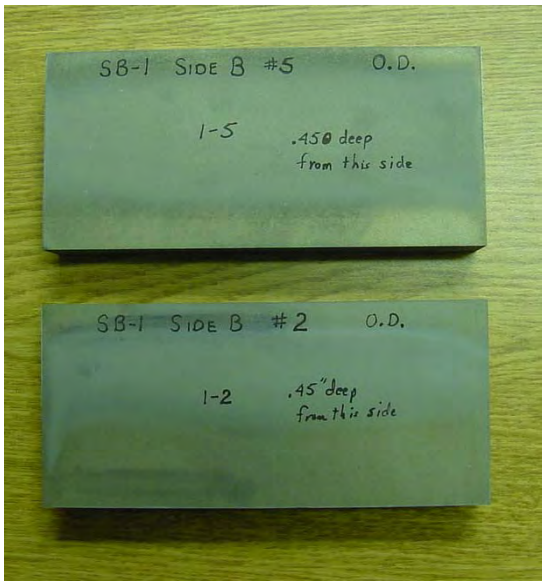

SB1-2 (side B)

SB2-9 (side)

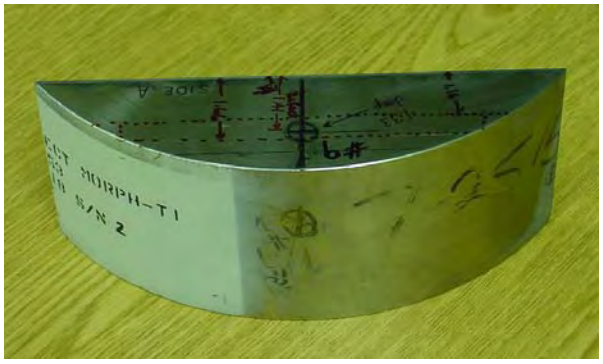

SB2-9 (top)

Figure H-6. Typical Blanks Excised From Forging and Prior to Machining Fatigue Test Specimen

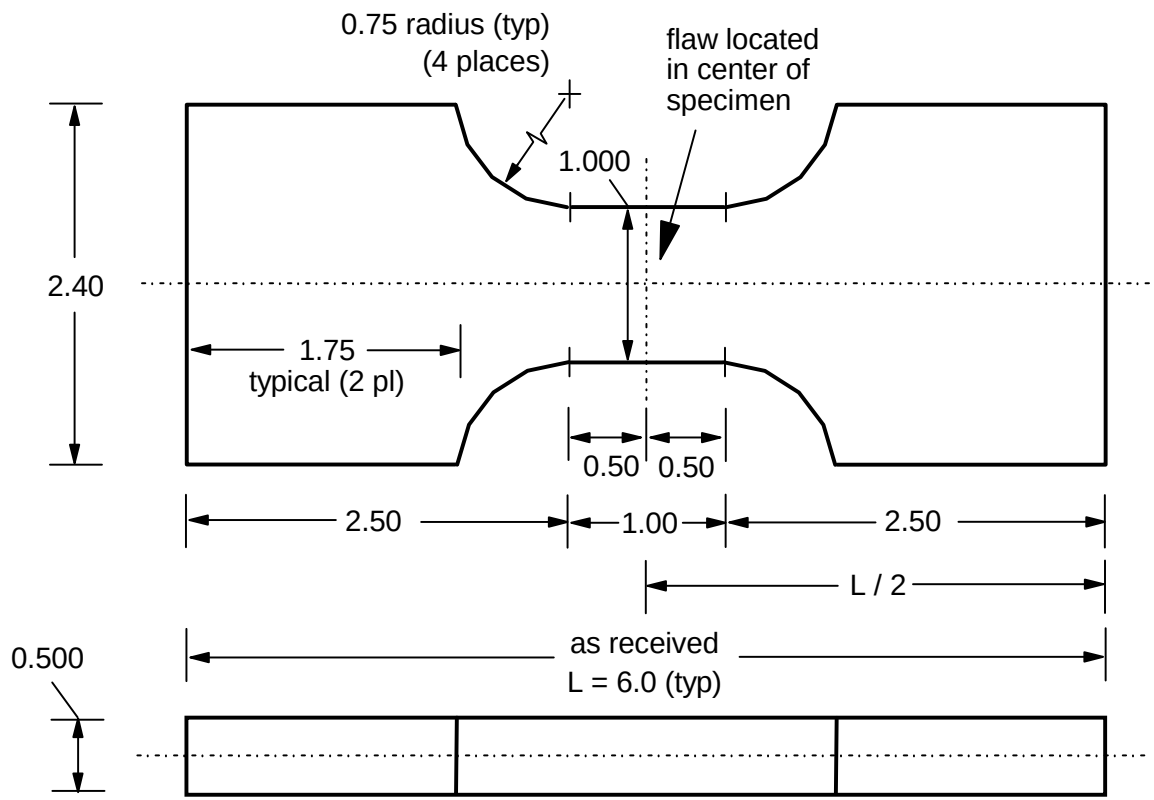

Note: All dimensions in inches

Flaw is either located on the surface or below the surface in the center of the specimen.

Drawn: P. C. McKeighan				Southwest Research Institute San Antonio, Texas	
Date: December 1996					
Matl: Ti-6-4	Tolerances (inches) Basic Dimension	Decimals 2 place	Decimals 3 place	Fractions	Title: Specimen to Determine Hard-Alpha Cracking Behavior
Finish: 32 rms	under 6	±0.01	±0.005	±1/32	Drawing Number: 06-7445-330_a; Scale: -- none --
	6-24 incl	±0.03	±0.010	±1/16	
Qty Reqd: N/A	over 24	±0.06	±0.015	±1/6	Filename: c:\pcm\drawings\misc\faa_4; Sheet 1 of 3
	angles	±0° 30'		±1° 0'	

Figure H-7. Basic Geometric Dimensions of the Fatigue Test Specimen

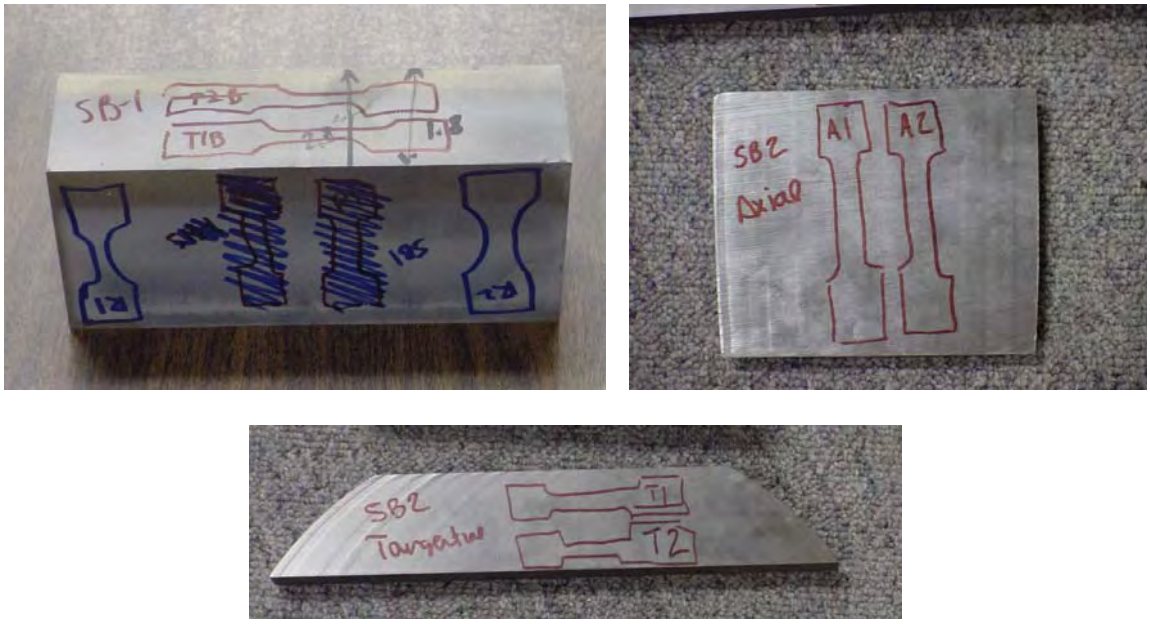

Figure H-8. Blanks Used to Machine Tensile Test Specimen to Measure Strength of Forged Material

Table H-2. Tensile Properties in Three Directions From Two Forged Billets

Ti-6Al-4V Bulk Material	Specimen Orientation	Specimen ID No.	Yield Strength (ksi)	Ultimate Strength (ksi)	Percent Elongation
SB-1	radial	R1 R2	136.5 135.8	142.4 141.5	17 17
		average:	136.2	142.0	17
	tangential	T1B T2B	138.2 140.3	143.9 147.0	18 18
		average:	139.3	145.5	18
SB-2	axial	A1 A2	140.1 140.6	148.0 148.8	16 16
		average:	140.4	148.4	16
	tangential	T1 T2	142.4 142.7	149.6 150.5	17 17
		average:	142.6	150.1	17

Fatigue testing was performed in a servohydraulic test machine outfitted with hydraulic grips. A typical fatigue test setup is shown in figure H-9 illustrating one set of hydraulic grips, the test specimen, and instrumentation. All fatigue testing was performed at a load ratio of R = 0.1. Four different stress levels were used, as detailed in table H-3. Cyclic loading was performed in a closed-loop computer control to ensure accurate applied loads. Cyclic frequencies were in the

range of 1 to 10 Hz with the actual sinusoidal frequency, depending upon what was controllable without excessive overdriving of the command signal.

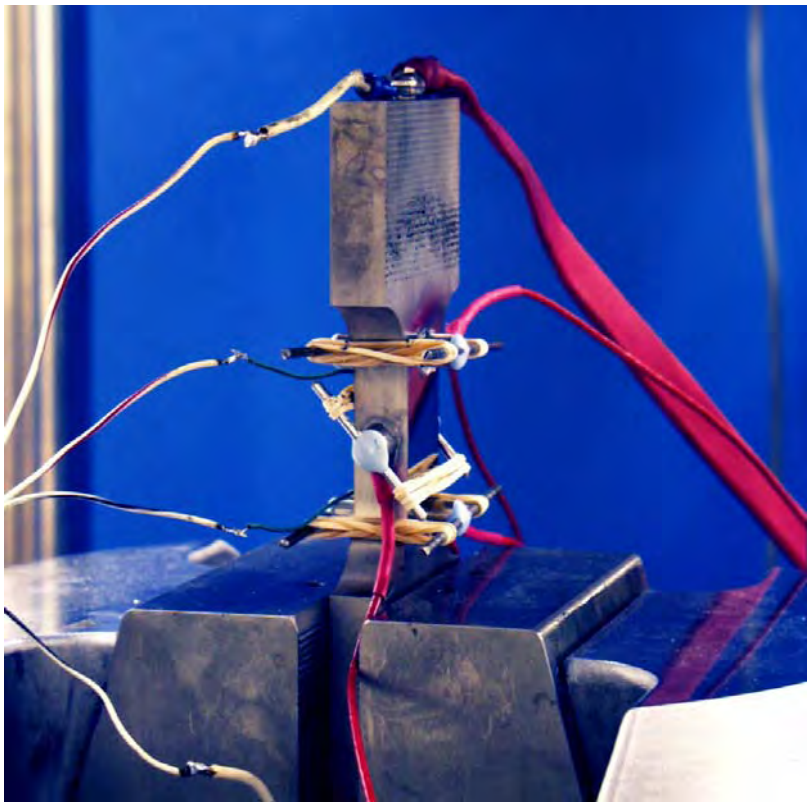

Figure H-9. Fatigue Test Setup Showing Hydraulic Grip (One End) and Acoustic Emission Hardware

Table H-3. Applied Stresses and Cyclic Life of the Six Fatigue Test Specimens

Specimen ID No.	Anomaly Type	σ_{max}, ksi	Load Ratio, *R*	Cycles to Failure
SB4-37C	cluster + DZ	40	0.1	76,483
SB2-9	core + DZ	40	0.1	253,199
SB1-5	core only	75	0.1	22,203
SB3-25C	cluster + DZ	75	0.1	3,759
SB1-2	was-beta	85	0.1	39,868
SHI-2	core (Phase I)	95	0.1	10,000

During fatigue testing on five of the six specimens, marker bands were periodically injected into the loading sequence to create features on the fracture surface to track crack morphology. This marker band strategy, obtained by cycling at $R = 0.7$ (low amplitude, high frequency) for a short period of time, was shown during TRMD-I testing to mark the fracture surface. The

number of marker bands applied during cycling ranged from 1 to 24. The total cycle count applied to the specimen did not include these marker bands.

When damage occurs in a material, the process results in a release of energy in a variety of forms including acoustic energy. The acoustic emission (AE) technique measures the acoustic activity in a specimen so as to infer damage and/or crack progression. This method is exceptionally difficult to calibrate and, as such, the data are most effectively used as a qualitative indicator of damage; further interpretation must be based on empirical methods linking AE to physically observed damage. During testing, a Physical Acoustics Corporation MISTRAS 2001 system was used with two NANO-30 AE transducers (0.3 inch diameter) mounted on the gage section of the specimen. The microphones chosen optimized both size and frequency response characteristics. The frequency range for the microphone was 750 kHz and below, well above the maximum required.

H.2 RESULTS AND DISCUSSION.

H.2.1 CYCLIC LIFE AND FRACTURE SURFACES.

The test conditions and cyclic life for each of the six fatigue tests are included in table H-3 and graphed in figure H-10. Not surprisingly, the two anomaly cluster specimens exhibited considerably shorter lives (3 to 6 times shorter) than the single anomaly specimens for the two replicate stress levels, since the total anomaly size in the cluster specimens was greater than in the single anomaly specimens.

Photographs of the fracture surfaces created during fatigue testing, along with a summary of test condition, are provided in figures H-11 through H-16. The approximate dimensions of the core and DZ are indicated for each test in these figures (an explanation of the method by which dimensions were assigned is provided in section 3). This measurement, performed posttest and based on the fracture surface features, is a rough, first order engineering approximation of the size of the internal microstructural feature nominally identified as core and DZ. However, as noted by a close examination of the fracture surfaces, these anomalies tended to be irregular in shape. The exception is the SHI-2 specimen remaining from TRMD-I, shown in figure H-15, where the shape is rectangular (a cross section of a uniform cylinder). This anomaly is more regularly shaped because this blank did not undergo the forging process to which the other anomalies were subjected.

Marker bands were most evident for the SB4-37C cluster depicted in figure H-11. A close examination of the fracture surface clearly illustrates that the crack initiated on several planes, nucleating later in the process as the cracks grew into the base metal of the specimen. Multiple-site nucleation was also apparent to some degree in SB1-5, shown in figure H-13.

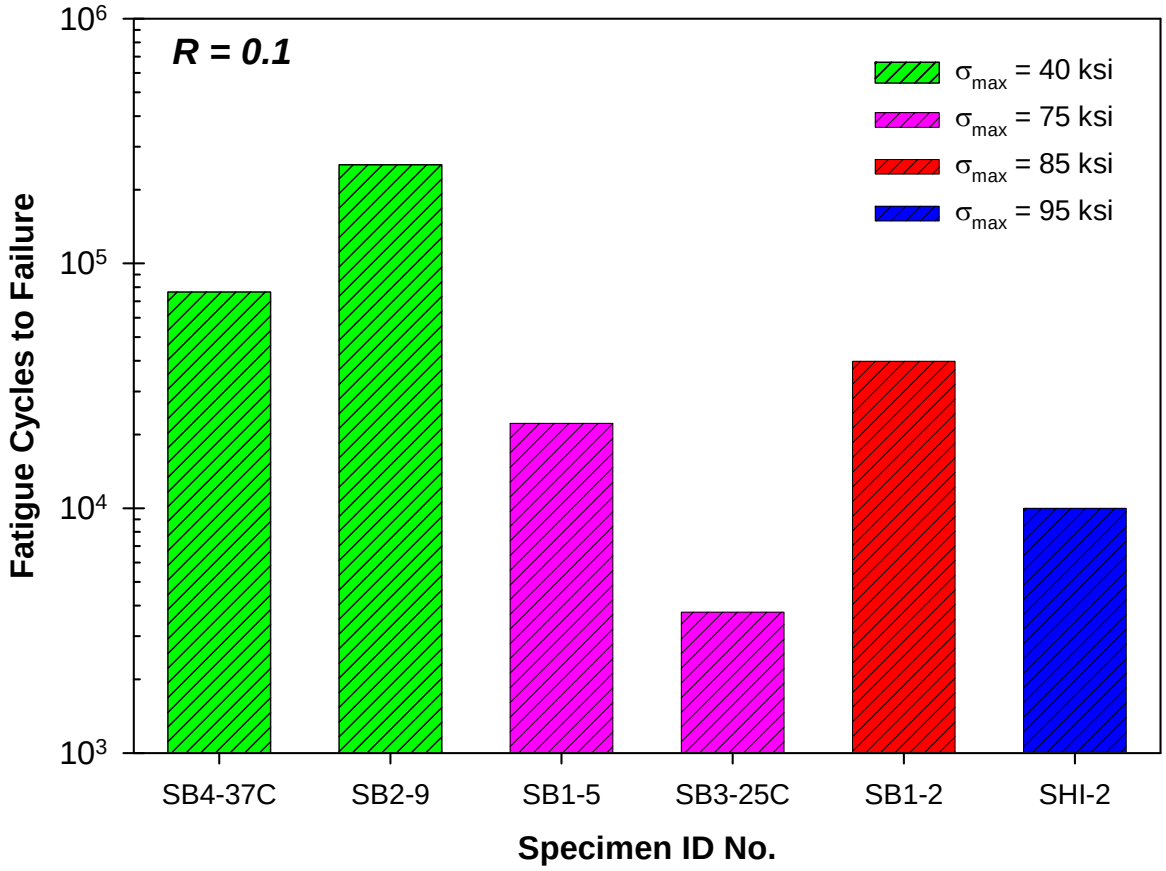

Figure H-10. Fatigue Life Results Indicating Applied Stress Level

Defect ID =	**SB4-37C**
Defect Type =	**Cluster + DZ**
Spec. Dimensions =	**1.5 x 0.7**
Stress Level =	**40 ksi, R=0.1**
Cycles to Failure =	**76,483**
No. of Marker Bands =	**7**
Defect 2c =	**0.40**
Defect 2a =	**0.36**
Defect Polygonal Area =	**0.096**
Est Aspect Ratio (a/c) =	**0.9**
Areal 2c =	**0.37**
Areal 2a =	**0.33**

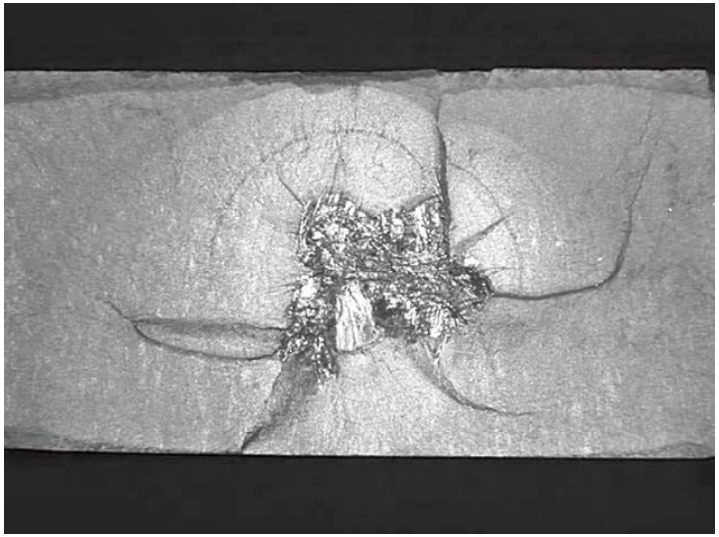

Figure H-11. Test Parameters for SB4-37C Including Defect Type, Stresses, and Posttest Measurements of Initial Flaw Size

Defect ID =	**SB2-9**
Defect Type =	**defect + DZ**
Spec. Dimensions =	**1.0 x 0.5**
Stress Level =	**40 ksi, R=0.1**
Cycles to Failure =	**253,199**
No. of Marker Bands =	**24**
Defect 2c =	**0.20**
Defect 2a =	**0.23**
Defect Polygonal Area =	**0.035**
Est Aspect Ratio (a/c) =	**1.14**
Areal 2c =	**0.20**
Areal 2a =	**0.23**

Figure H-12. Test Parameters for SB2-9 Including Defect Type, Stresses, and Posttest Measurements of Initial Flaw Size

Defect ID =	**SB1-5**
Defect Type =	**Defect core only**
Spec. Dimensions =	**1.0 x 0.5**
Stress Level =	**75 ksi, R=0.1**
Cycles to Failure =	**22,203**
No. of Marker Bands =	**5**
Defect 2c =	**0.23**
Defect 2a =	**0.16**
Defect Polygonal Area =	**0.031**
Est Aspect Ratio (a/c) =	**0.68**
Areal 2c =	**0.24**
Areal 2a =	**0.16**

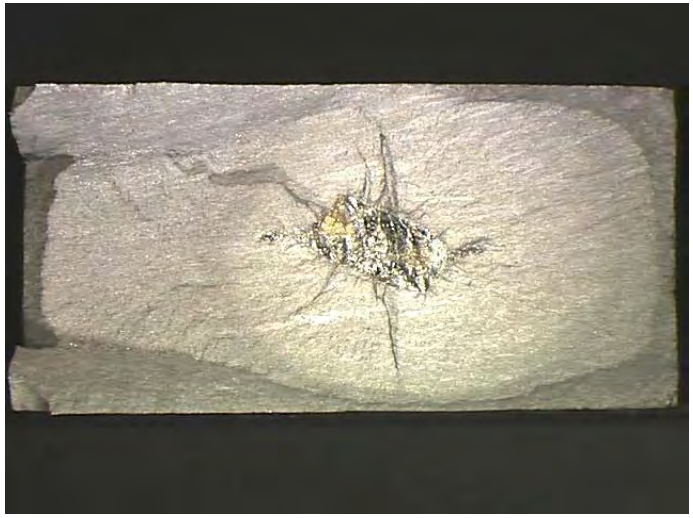

Figure H-13. Test Parameters for SB1-5 Including Anomaly Type, Stresses, and Posttest Measurements of Initial Flaw Size

Defect ID =	**SB3-25C**
Defect Type =	**Cluster + DZ**
Spec. Dimensions =	**1.5 x 0.7**
Stress Level =	**75 ksi, R=0.1**
Cycles to Failure =	**3,759**
Marker Band Applied =	**3,000 N_{mark}=15K**
Marker Stress =	**75 ksi, R=0.7**
Marker Width =	**0.030**
Marker 2c =	**0.60**
Marker 2a =	**0.42**
Defect 2c =	**0.34**
Defect 2a =	**0.40**
Defect Polygonal Area =	**0.105**
Est Aspect Ratio (a/c) =	**1.2**
Areal 2c =	**0.33**
Areal 2a =	**0.40**

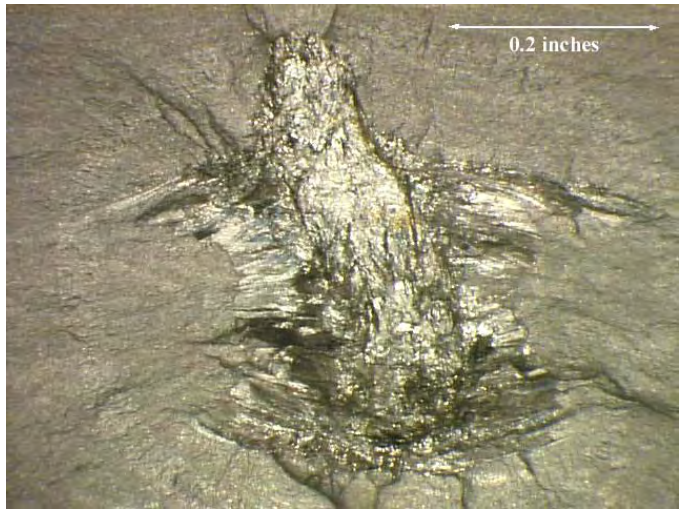

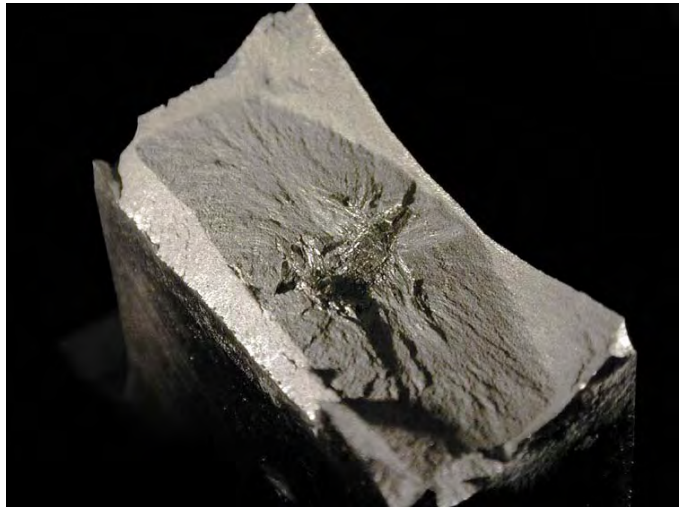

Figure H-14. Test Parameters for SB3-25C Including Anomaly Type, Stresses, and Posttest Measurements of Initial Flaw Size

Defect ID =	**SHI-2**
Defect Type =	**Synthetic + DZ (Ph. I)**
Spec. Dimensions =	**1.0 x 0.5**
Stress Level =	**95 ksi. R=0.1**
Cycles to Failure =	**10,000**
No. of Marker Bands =	**none**
Defect 2c =	**0.05**
Defect 2a =	**0.11**
Defect Polygonal Area =	**0.005**
Est Aspect Ratio (a/c) =	**2.2**
Areal 2c =	**0.05**
Areal 2a =	**0.12**

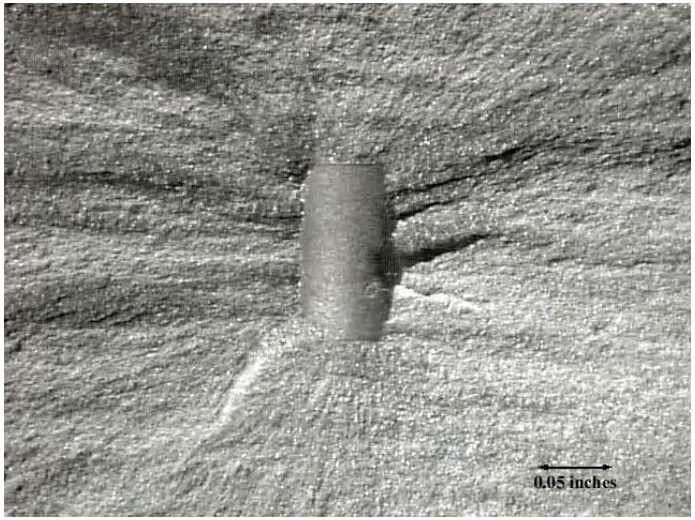

Figure H-15. Test Parameters for SHI-2 Including Anomaly Type, Stresses, and Posttest Measurements of Initial Flaw Size

Defect ID =	**SB1-2**
Defect Type =	**was-beta**
Spec. Dimensions =	**1.0 x 0.5**
Stress Level =	**85 ksi, R=0.1**
Cycles to Failure =	**39,868**
No. of Marker Bands =	**4**
Defect 2c =	**0.27**
Defect 2a =	**0.05**
Defect Polygonal Area =	**0.013**
Est Aspect Ratio (a/c) =	**0.2**
Areal 2c =	**0.29**
Areal 2a =	**0.06**

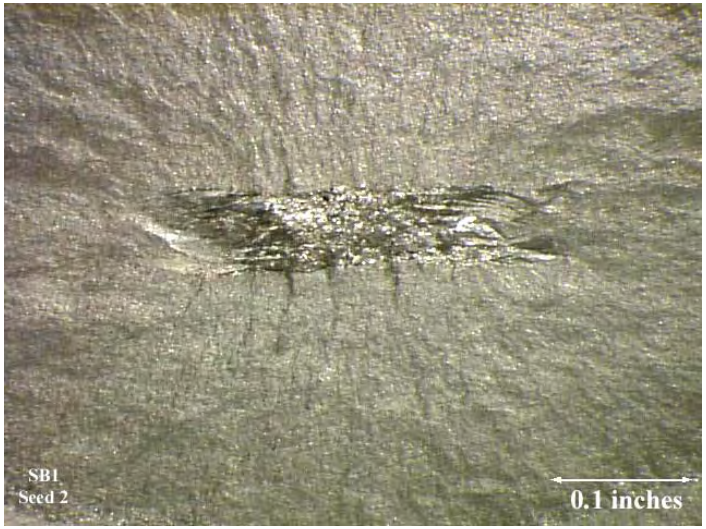

Figure H-16. Test Parameters for SB1-2 Including Anomaly Type, Stresses, and Posttest Measurements of Initial Flaw Size

H.2.2 ACOUSTIC EMISSION DATA.

AE data are available in two forms: (1) a cumulative count is provided summing all the acoustic events recorded during a test and (2) a further acoustic measure is provided with the so-called acoustic energy, or more appropriately, the measured area under the rectified signal envelope. This empirically based measure provides a unitless cumulative count of acoustic energy as the fatigue test progresses.

Acoustic data are shown for all tests in figures H-17 and H-18. Due to the empirical nature of AE, interpreting these data are problematic. Nevertheless several observations are notable. In general, beginning from the first applied fatigue cycle, acoustic events and energy gradually increase as fatigue cycling progresses. This is likely the most important finding from the AE data. Although the observation is empirical, it suggests that damage progression occurred immediately and increased during fatigue cycling. This suggests that the crack nucleation process initiated early in life. Furthermore, step changes especially in acoustic events are notable in several instances where marker bands were applied. It is also interesting to note that the highest levels of acoustic energy were noted for the two anomaly cluster specimens, SB4-37C and SB3-25C. In these cases, measured energy levels were 10 to 100 times higher than in the single anomaly specimens. Presumably this increase in acoustic energy is indicative of the larger size of the anomaly clusters in comparison to the single anomaly cases.

H.3 FATIGUE LIFE ANALYSIS OF THE TESTS.

The experimental record provides information on the total number of fatigue cycles required to cause specimen separation. Some portion of these cycles were required to nucleate a fatigue crack, and the remaining portion of the cycles were required to propagate the fatigue crack to failure. However, the experimental record itself provides no explicit information about the numbers of fatigue cycles associated with nucleation versus propagation. As was noted in the introduction, the conventional analysis assumption is that the nucleation life is zero, and that the total fatigue lifetime is equivalent to the fatigue crack growth (FCG) lifetime.

To evaluate the accuracy of this assumption for the six coupon tests conducted in TRMD-II, the FCG life for each specimen was calculated using the Flight_Life fatigue crack growth analysis module contained in the DARWIN® computer code. The standard EC02 stress-intensity factor solution for an elliptical embedded crack in a rectangular plate was employed. The first-order analytical correction to the physical crack size based on the crack tip reversed plastic zone size (a correction employed for conservatism in service analyses) was turned off to avoid any possible over-conservatism in the FCG calculations. FCG properties were based on the Ti-6Al-4V vacuum FCG testing performed in TRMD-I (a summary of these properties is contained in appendix A of the TRMD-II final report).

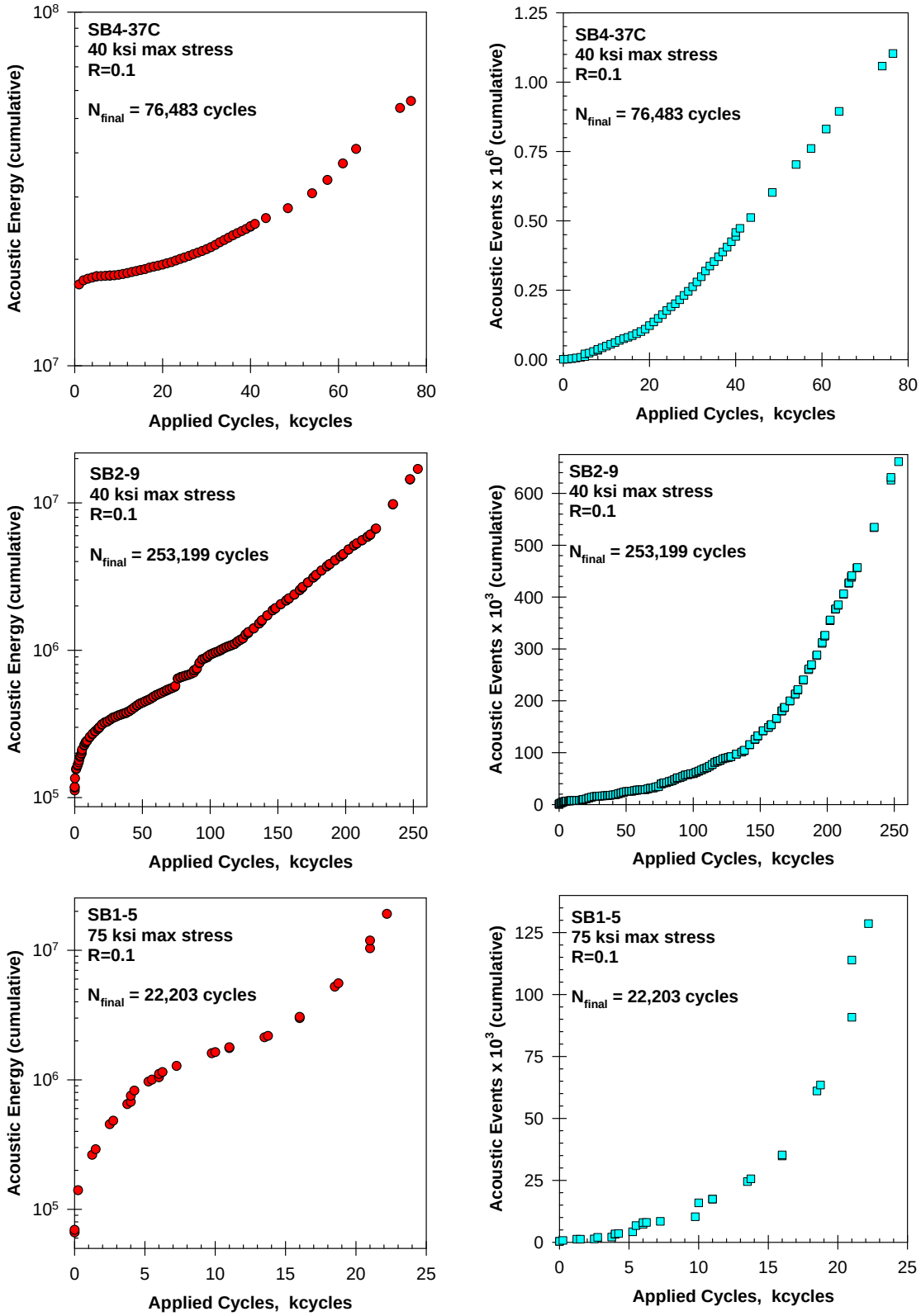

Figure H-17. Acoustic Energy and Acoustic Event Count for Tests SB4-37C, SB2-9, and SB1-5

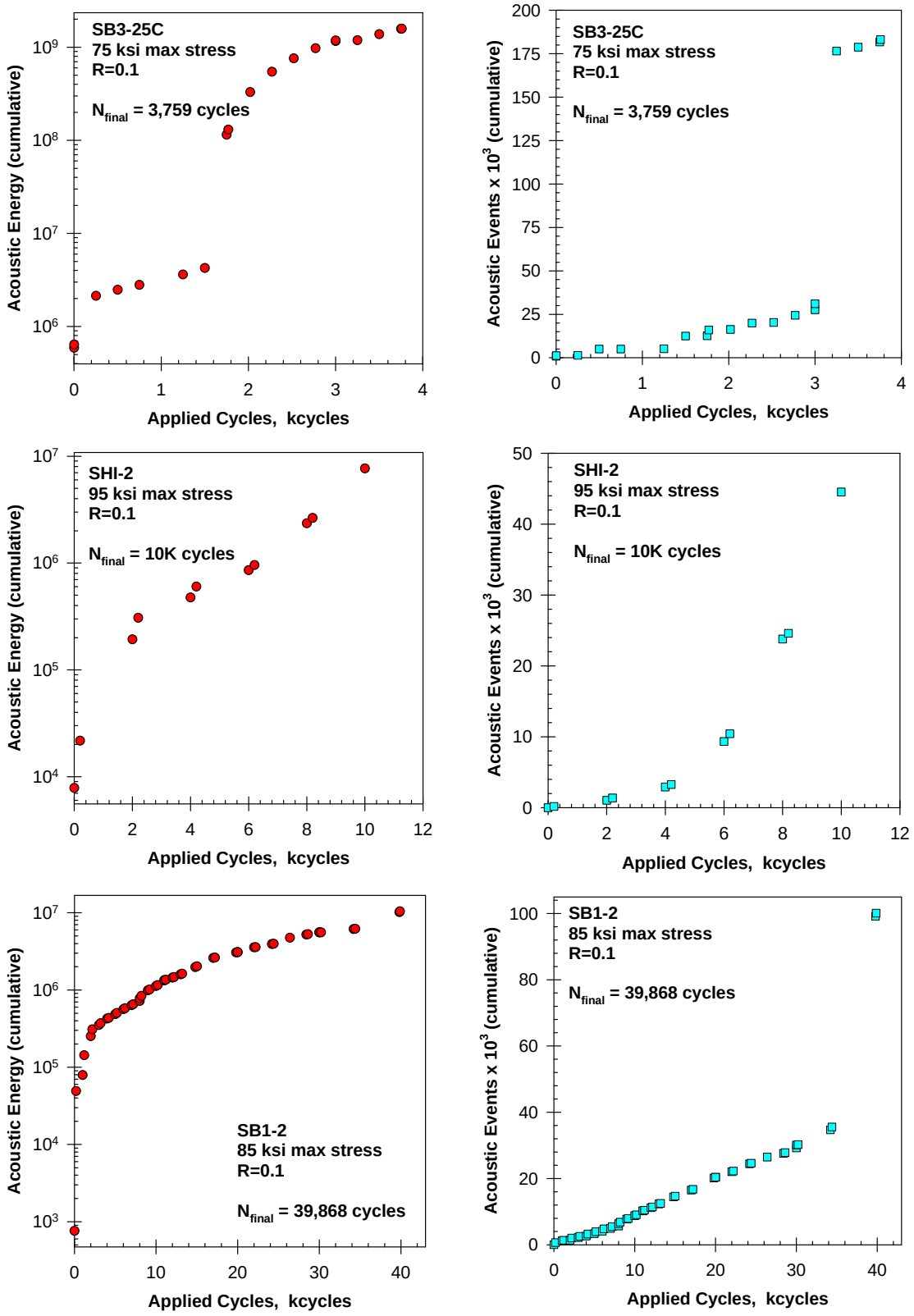

Figure H-18. Acoustic Energy and Acoustic Event Count for Tests SB3-25C, SHI-2, and SB1-2

One of the most critical decisions to make in performing the FCG analysis is the selection of the initial crack size. The size and shape of the initial HA anomaly was obvious from the posttest fractography (see figures H-11 through H-16). What was not obvious was the best way to assign an initial elliptical size and shape to the often irregular shape of the actual anomaly. The first approach investigated was to identify the approximate maximum dimensions of the anomaly in the cross-sectional plane in both the length and width directions. However, this circumscribed ellipse also encloses some titanium matrix material that would not be expected to crack nearly as quickly as the high-nitrogen anomaly. Exploratory FCG analyses using these numbers gave FCG lives that were extremely short. Therefore, a second approach was investigated and ultimately adopted in which an idealized ellipse is inscribed fully within the anomaly (in other words, this is the largest ellipse that does not circumscribe titanium matrix material). The two ellipses created by these two different definitions for specimen SB4-37C are shown in figure H-19. The initial defect (crack) dimensions provided in figures H-11 through H-16 are based on this inscribed definition. Note that the dimensions were assigned without differentiating between core and DZ.

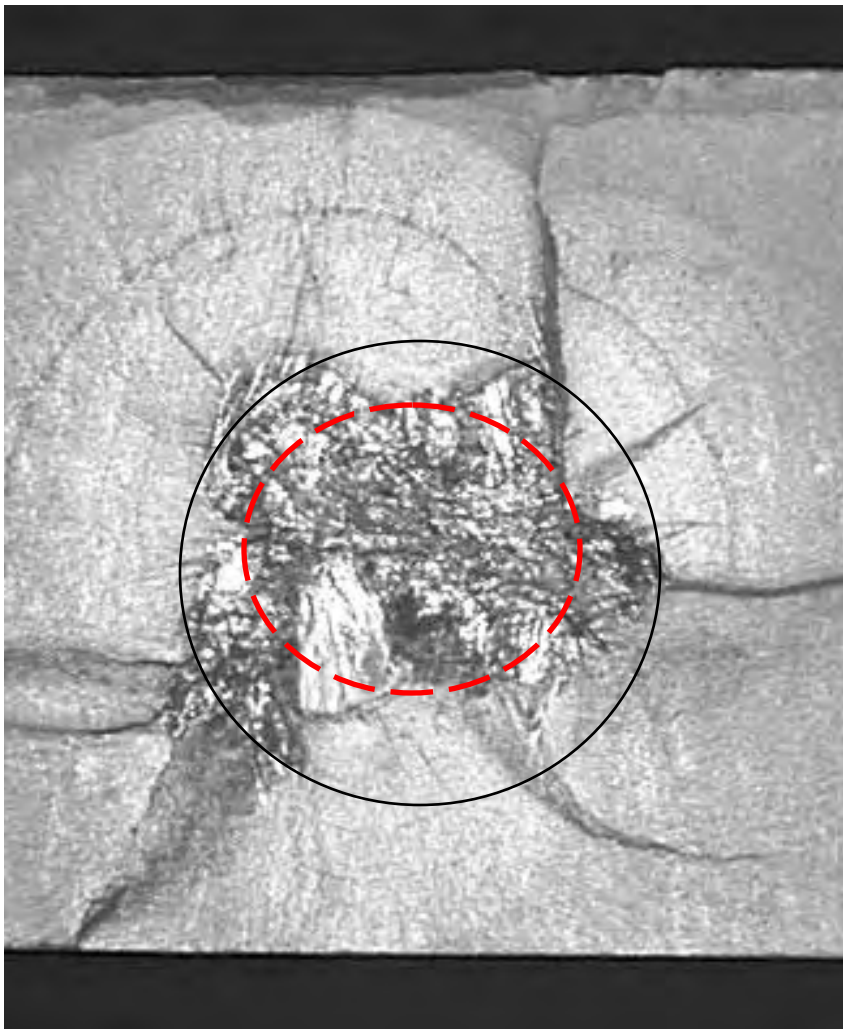

Figure H-19. Illustration of Circumscribed and Inscribed Definitions of Initial Crack Size for Specimen SB4-37C

Table H-4 summarizes the inputs for the fracture mechanics life calculations, the resulting calculated FCG life, the observed test life, and the *A/P* ratio of the actual experimental life to the predicted analysis life for the six tests. Here, 2*c* and 2*a* are the total length and width of the central embedded defect in a rectangular plate of stated length and width, and the initial ΔK is the calculated stress-intensity factor range for the initial defect dimensions. The actual and predicted lifetimes are also shown in figure H-20.

Table H-4. Summary of FCG Calculations

Specimen	Type	Plate		Defect		σ_{max}	$\Delta\sigma$	Test Life	Analysis Life	Initial ΔK	*A/P*
		length	width	2*c*	2*a*						
		(in.)	(in.)	(in.)	(in.)	(ksi)	(ksi)	(cycles)	(cycles)	(ksi-in$^{1/2}$)	
SB4-37C	cluster	1.5	0.7	0.27	0.25	40	36	76,483	41,906	15.1	1.8
SB2-9	core+DZ	1.0	0.5	0.126	0.225	40	36	253,199	78,812	12.9	3.2
SB1-5	core only	1.0	0.5	0.19	0.096	75	67.5	22,203	5,609	21.7	4.0
SB3-25C	cluster	1.5	0.7	0.22	0.4	75	67.5	3,759	1,275	32.3	2.9
SHI-2	Ph I: core+DZ	1.0	0.5	0.05	0.11	95	85.5	10,000	5,093	22.7	2.0
SB1-2	DZ only	1.0	0.5	0.169	0.05	85	76.5	39,868	5,737	19.7	6.9

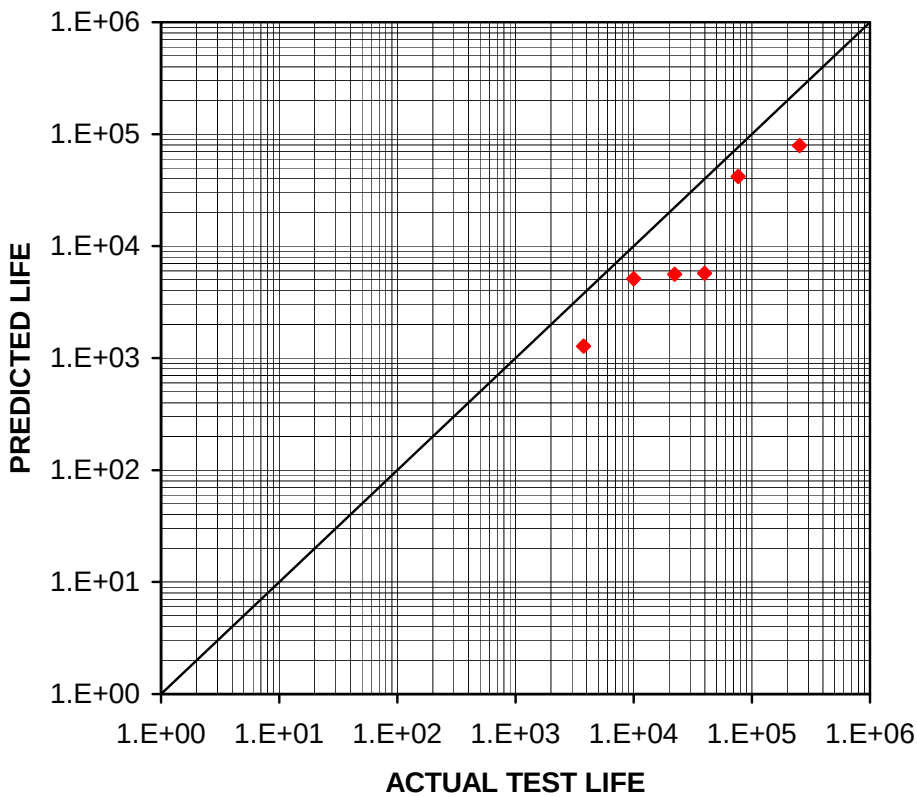

Figure H-20. Comparison of Predicted Fatigue Crack Growth Lifetime and Actual Total Fatigue Test Lifetime

It is clear that the actual total fatigue life was significantly larger than the calculated FCG life for all six tests. The actual total life was nearly always at least twice as long as the calculated FCG life, and the average A/P ratio was about 3.5. The difference between the two numbers was greatest for the was-beta specimen (SB1-2) in which the anomaly was completely low nitrogen DZ material without any high-nitrogen core; in this case, the A/P ratio was 6.9.

There are several possible explanations for the difference between observed total life and calculated FCG life.

- It is possible that some significant number of cycles was required for the crack to form (or nucleate) and begin growing.

- It is possible that the formation and interaction of multiple cracks on multiple planes caused some retardation of crack growth.

- It is possible that some residual stresses may have remained around the HA anomaly that reduced the crack driving force and therefore reduced the FCG rate. This hypothesis is explored further in appendix I. However, it should be noted that the applied stresses in several of these tests were sufficiently large, and the analytical studies in appendix I suggest that the residual stress effects would be minor. Those residual stress effects appear to be greatest when the crack driving force is near threshold, but the initial (smallest) crack driving force (represented by ΔK) in these six tests was generally well above threshold (see again table H-4).

- It is possible that some of the differences can be attributed to the difference between high-nitrogen core material and low-nitrogen DZ material, since the initial crack sizes treated both anomaly compositions as being the same. It was not possible to distinguish between different levels of nitrogen content with simple visual observation of the fracture surfaces, and so this hypothesis could not easily be evaluated further. This line of thinking is generally supported by the long life observed for the DZ-only anomaly. However, a simple paradigm in which the initial crack size is set equal to the core size would fail to define any initial crack size for this particular specimen.

H.4 REFERENCES.

H-1. Leverant, G.R., et al., “Turbine Rotor Material Design,” FAA report DOT/FAA/AR-00/64, December 2000.

H-2. McKeighan, P.C., Nicholls, A.E., Perocchi, L.C., and McClung, R.C., “Sensing Crack Nucleation and Growth in Hard Alpha Defects Embedded in Ti-6Al-4V Alloy,” *Nontraditional Methods of Sensing Stress, Strain and Damage in Materials and Structures: Second Volume, ASTM STP 1323*, G.F. Lucas, P.C. McKeighan and J.S. Ransom, Editors, American Society for Testing and Materials, West Conshohocken, PA., 2001.

APPENDIX I—EFFECTS OF RESIDUAL STRESSES CAUSED BY DIFFERENTIAL THERMAL EXPANSION IN AND AROUND HARD ALPHA PARTICLES IN TITANIUM ALLOYS

I.1 INTRODUCTION.

Coupon tests on specimens containing seeded hard alpha (HA) defects were conducted in the Turbine Rotor Material Design (TRMD) Phase I project [I-1]. The results of the coupon testing indicated that the fracture and fatigue strengths of the embedded HA were higher than anticipated. The presence of residual stresses caused by differential thermal expansion was postulated as a potential explanation for the observed behavior. The primary objective of this work is to quantify the magnitude of the residual stresses and to determine the impact of the residual stresses on fracture and fatigue strength. Specifically, the focus is to determine if the TRMD-I experimental results can be explained by including residual stress effects.

With respect to fracture strength, this work addresses the applied stress required to first crack the HA particle during monotonic loading. From a fatigue perspective, this work investigates the effect of residual stresses on the stress-intensity factor, K, of a crack spanning the HA particle and its impact on fatigue crack growth life. A brief review of the experimental fracture and fatigue testing from TRMD-I [I-1] has been included as a foundation for the present work. Descriptions of the experimental methods used to measure the coefficient of thermal expansion for HA and the analytical methods used to approximate the residual stress fields are included. The subsequent sections on fracture and fatigue include descriptions of the analytical models and comparisons of the experimental and analytical results.

I.2 SUMMARY REVIEW OF EXPERIMENTAL RESULTS.

I.2.1 PROCEDURE.

The experimental results summarized in this section were carried out in TRMD-I, which are described in appendix H of reference I-1 and discussed in reference I-2. The preparation of artificially seeded defects and the complex procedure used to implant the seeded defects and their diffusion zones (DZ) into Ti-64 material blanks were developed and carried out by GE Corporate Research and Development (GE-CR&D). The seeded blanks were machined into dogbone geometry specimens for static (fracture) and fatigue testing. The gage length and width of the specimens were each 1″ with a thickness of 0.5″.

Both surface and subsurface geometries as well as two HA defect sizes were tested. A typical test specimen and the geometry of the HA defects are presented in figure I-1. The small defects had HA cores with average diameters (in inches) of 0.031″ and lengths of 0.078″ and DZs with diameters of 0.059″. For the large defects, the core dimensions were a diameter of 0.078″ and length of 0.195″ with a DZ diameter of 0.125″. The nitrogen (N) content of the seeded HA defects was determined to be approximately 5.5% (referred to as HA-6N).

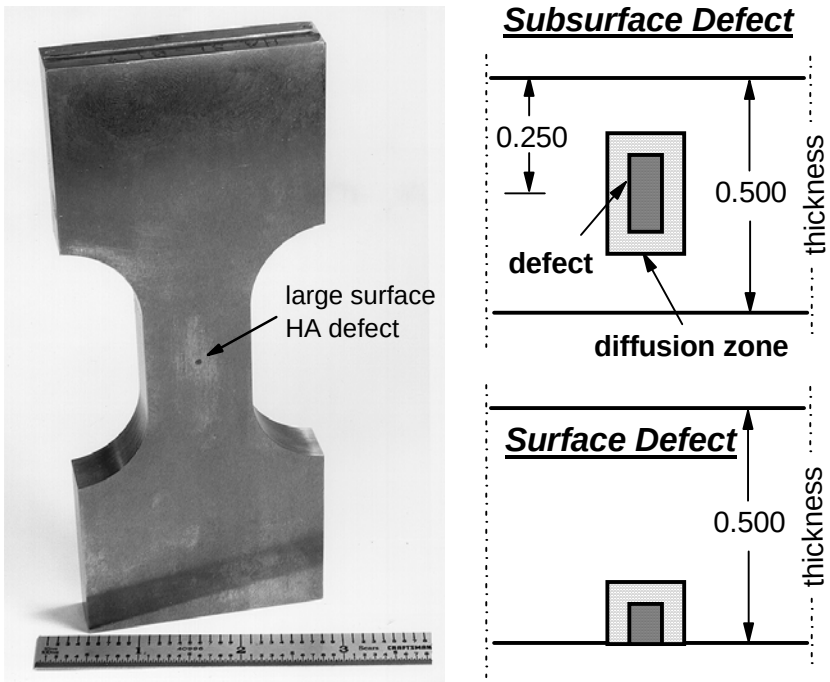

Dimensions are in inches

Figure I-1. Typical Test Specimen Containing a Seeded HA Defect

Testing was carried out with hydraulic wedge grips in a 200-kip servohydraulic test machine. All specimens were monitored with acoustic emission (AE) and potential drop (PD) during testing to detect crack formation and growth. In addition, frequent visual inspections were performed on specimens with surface defects.

A complete description of the techniques used in preparation and testing of the specimens can be found in references I-1 and I-2.

I.2.2 FRACTURE TEST RESULTS.

Static tests were performed on both surface and subsurface defects to determine the applied stress at which cracking of the HA particle and DZ occurred. The specimens were loaded to a specified stress level while monitored by the described techniques. Upon unloading, the subsurface specimens were examined by metallographic sectioning.

In the surface specimens, crack initiation in the core was observed in all cases at stresses less than 20 ksi, and in many cases less than 10 ksi. In the embedded specimens, significant cracking of the subsurface cores first occurred at applied tensile stresses on the order of 80 to 110 ksi, according to the PD and AE results.

With respect to cracking of the HA particles, the experimental data indicate that the interior HA were able to withstand applied remote stresses four times larger than the surface HA.

I.2.3 FATIGUE TEST RESULTS.

The fatigue tests were carried out with an R ratio ($R = S_{min}/S_{max}$) of 0.1 at a variety of stress levels as specified in table I-1. In the surface HA specimens, cracking of the defect and growth in the matrix was observed at stress levels S_{max} of 40 and 50 ksi. Although the subsurface HA particles cracked, the cracking was predominately confined to the DZ, and no cracking into the matrix was observed in the specimens tested at 50 ksi. Significant crack growth into the matrix was observed in both of the embedded HA specimens tested at 75 ksi. In the cases where crack growth occurred, the final crack sizes are included in table I-1 (when available).

Table I-1. Summary Table of Fatigue Testing Results From Reference I-1

Specimen Number	Defect Size	Nitrogen Content	Defect Type	Max Stress [ksi]	Number of Cycles	Final Crack Size
HA-SL-C1[1]	L	H	S	40	24,000	Growth
LHS-B	L	H	S	50	10,000	Growth
RMI-E1	R	M	S	50	23,000	Growth to breakthrough
HA-IS-E1	S	H	I	50	10,000	No growth
LHI-2	L	H	I	50	25,000	No growth
LLI-2	L	L	I	75	20,000	0.174″ x 0.214″
LMI	L	M	I	75	10,000	0.376″ x 0.419″
HA-IS-D1[2]	S	H	I	80	20,000	Growth in DZ
RMI-F1	R	M	I	50 62 75 100	42,000 15,000 24,000 13,300	No growth ? ? Failure

Notes:
Defect Size (diameter): S = small (0.031″), R = natural (0.04″), L = large (0.078″)
Nitrogen Content: L = low (1.6%), M = medium (2.7%), H = high (6%)
Defect Type: S = surface, I = interior (subsurface)
[1] Static/Fatigue Test—fatigue cycling carried out at R = 0.05 after 40 ksi static test
[2] Static/Fatigue Test—fatigue cycling carried out after 100 ksi static test

In addition, a pair of fatigue tests (one surface defect and one subsurface defect) were carried out on specimens with naturally occurring HA defects from the Engine Titanium Consortium contaminated billet study. In the specimen with the surface HA, cracking to breakthrough occurred after almost 23,000 cycles at a maximum stress of 50 ksi. In the fatigue test on the subsurface defect, four loading steps were used with maximum stresses of 50, 62.5, 75, and 100 ksi. The specimen failed after 13,300 cycles at the 100 ksi stress level, but sustained over 90,000 cycles at the various stress levels (all ≥50 ksi).

The experimental data again demonstrated that the embedded HA specimens were more resistant to fatigue than the surface defect specimens. Life predictions made using the Flight_Life model [I-1] (neglecting any potential residual stress effects) consistently underpredicted the experimental behavior.

I.3 METHODS.

This section describes the measurement of the coefficient of thermal expansion (CTE) and the model used to determine the residual stress profile in and around the HA particle.

I.3.1 COEFFICIENT OF THERMAL EXPANSION.

Fabrication and testing of the specimens to determine the CTE of synthetic HA samples were performed by GE-CR&D. Specimens with five nitrogen contents (nominally 2%, 4%, 6%, 9%, and 12%) were tested along with two baseline Ti-64 specimens. Measurements of the percent expansion were made using a pushrod dilatometer. By making high accuracy measurement of changes in length for a specific temperature profile, the dilatometer is used to determine CTE. The measurements were taken between room temperature and the post-HIP (hot isostatically pressed) temperature of 1650ºF (900ºC). Plots of the percent expansion results as a function of temperature for the different specimens are presented in figure I-2.

The CTE is determined from the slope of the percent expansion versus temperature plots. Table I-2 contains the CTE values based predominately on least squares regressions to the experimental data.

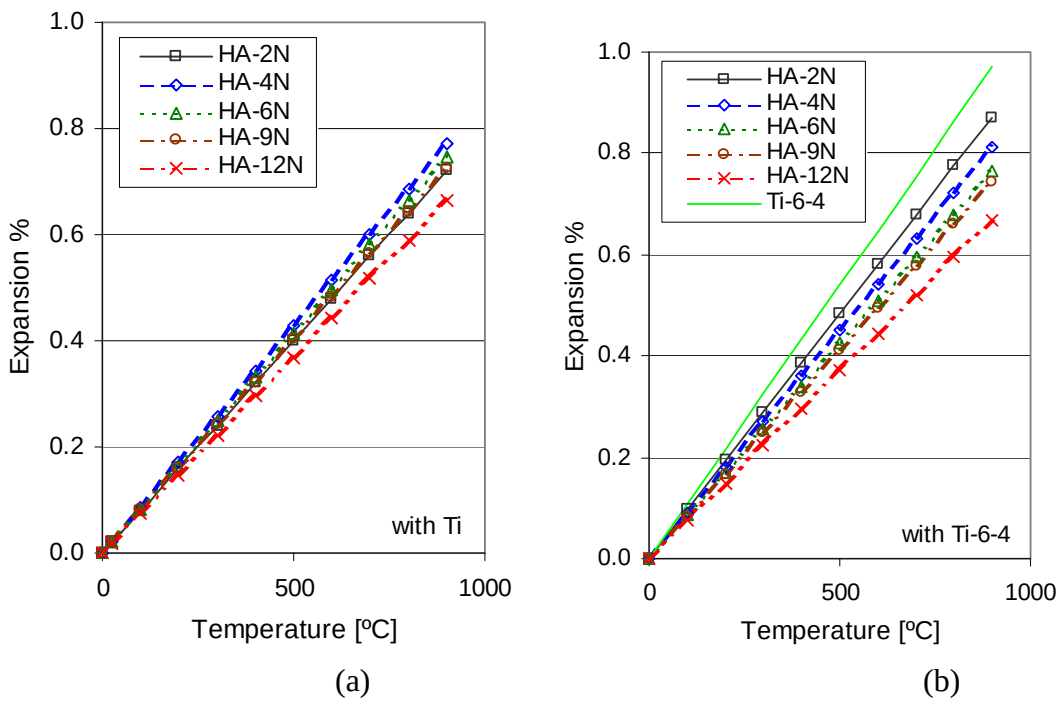

Figure I-2. Coefficient of Thermal Expansion Data for HA Particles With Varying Nitrogen Content Made From Either (a) Pure Titanium or (b) Ti-64

Table I-2. Property Data for HA Particles With Varying Nitrogen Content

% Nitrogen	With Ti CTE [1/ºF]	With Ti-64 CTE [1/ºF]	*E* [I-3 and I-6]	ν [I-3]
Ti-64 Matrix		5.998 E-6	1.65 E7 [I-6]	0.342
HA-2N	4.445 E-6	5.381 E-6		
HA-4N	4.753 E-6	5.022 E-6		
HA-6N	4.607 E-6	4.719 E-6		
HA-9N	4.470 E-6	4.587 E-6		
HA-12N	4.099 E-6	4.128 E-6		
TiN		5.22 E-6	4.60 E+7 [I-3]	0.192

I.3.2 QUANTIFICATION OF THE RESIDUAL STRESSES IN AND AROUND HA DEFECTS.

Residual stresses in the HA defect and surrounding matrix arise from differences in CTE, stiffness (*E*) and Poisson's ratio (ν) between the HA and the Ti-64 matrix. At the post-HIP temperature of 1650ºF (900ºC), the material is assumed to be residual stress free. As the material cools to the room temperature of 77ºF (25ºC), the differences between the HA and the matrix introduce residual stresses. The residual stress profile is calculated based on an elastic solution developed by Brooksbank and Andrews [I-3 through I-5] for thermal expansion differences between cylindrical or spherical inclusions and the surrounding matrix.

The cylindrical and spherical particle geometries are shown in figure I-3. The parameters used in the residual stress characterization came from a variety of sources. The CTE coefficients were determined from the GE CR&D experimental data described above. The (*E*), as well as the Poisson's ratio, for TiN reported by Brooksbank and Andrews [I-3] were assumed for HA. The stiffness and Poisson's ratio for the Ti-64 matrix were taken from the ASM Metals Handbook [I-6]. Sensitivity studies found that potential errors in these assumptions would have only a minor impact on the results and conclusions.

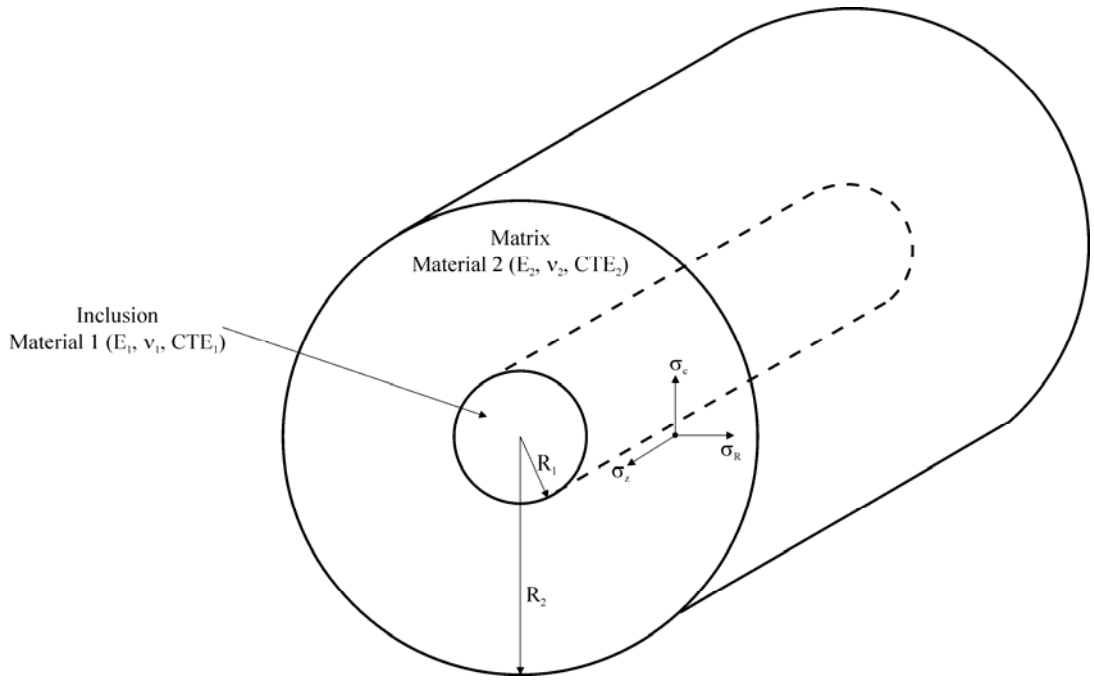

(a)

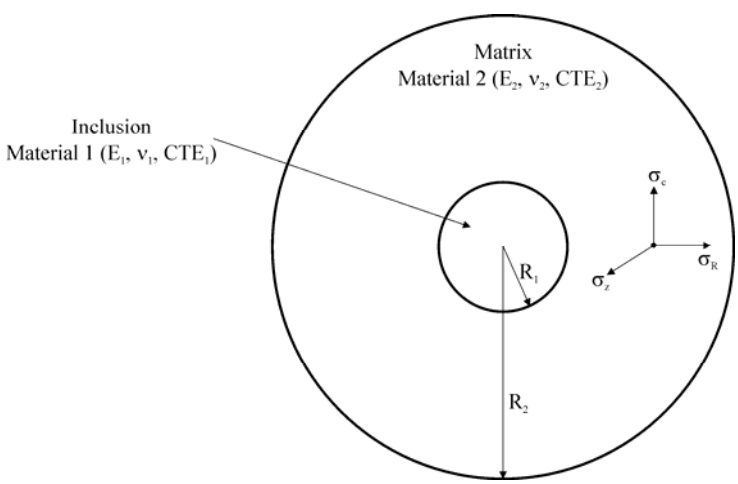

(b)

Figure I-3. Schematics of the Geometry of the (a) Cylindrical and (b) Spherical Shaped Particles and the Associated Matrix

The stress profile for all of the cases had a characteristic shape (figure I-4). The HA particle was subjected to uniform compression. The maximum stress in the matrix occurred at the particle-matrix interface and the magnitude of the stress decreased dramatically as distance from the particle increased. The effect of the particle becomes practically negligible at a distance of one particle radius away from the interface.

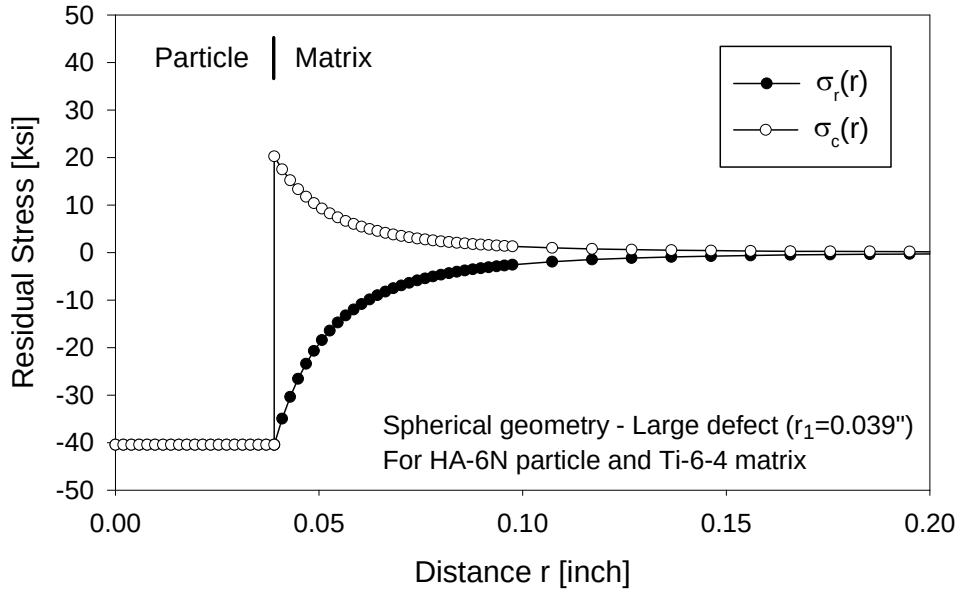

Figure I-4. Residual Stress Profile as a Function of Distance for a Spherically Shaped 6% N HA Particle in a Ti-64 Matrix

The residual stress profile for the case representing the experimental tests—large HA-6N particle in a Ti-64 matrix cooling from a temperature of 1650º to 77ºC—is presented in figure I-4. According to the analysis, the stress in the HA particle for this case is -40.46 ksi (compression). Depending on the nitrogen content, the residual stresses in the particles ranged from -17.94 to -55.23 ksi for the bounding minimum and maximum values in table I-2 corresponding to HA-2N and HA-12N.

I.4 FRACTURE STRENGTH MODELING.

The objective of the modeling in this section is to determine the nominal stress required to cause cracking of the HA core. With the residual stresses in the HA particle quantified, the magnitude of the nominal stress required to fracture the particle can be determined. After cooling, the embedded HA particles are in a state of triaxial compression. A fracture model, based on previous modeling work by Chan from TRMD-I in appendix C of references I-1 and I-7, has been implemented here. The local pressure (based on the principal stresses) varies as a function of the nominal tensile stress, as the stress state becomes less triaxial. This loading path can be compared with the fracture criterion developed in references I-1 and I-7 to determine the nominal tensile stress when particle cracking occurs.

The fracture strength for HA under uniaxial compression at 1750°F (954°C) as a function of nitrogen content was determined in Chan, et al. [I-7] to be equal to

$$Y_n \text{ [ksi]} = 55.44 + 4.558\, N \qquad \text{(I-1)}$$

where N is the percent nitrogen content. A general expression for fracture strength (Y_i) for a given stress state was then normalized by the fracture strength (Y_n) for uniaxial compression to obtain

$$Y_i = Y_n\,[1.4+0.94*\log(P/Y_n)]. \qquad \text{(I-2)}$$

where P is the local pressure. Equation I-2 describes the fracture strength curve (Y_i versus P) for HA.

Pressure experienced by the particle was also expressed in terms of the principal stresses as

$$P = (\sigma_{11}+\sigma_{22}+\sigma_{33})/3 \qquad \text{(I-3)}$$

When an applied nominal tensile stress (σ_∞) was included, the principal stresses became

$$\begin{aligned} \sigma_{11} &= \sigma_r \\ \sigma_{22} &= \sigma_c + \sigma_\infty \\ \sigma_{33} &= \sigma_z \end{aligned} \qquad \text{(I-4)}$$

where σ_r, σ_c, and σ_z are the stresses determined from Brooksbank and Andrews [I-3] and illustrated in figure I-3.

By substituting equation I-4 into equation I-3, the pressure P was expressed as

$$P = (\sigma_r+\sigma_c+\sigma_z)/3 + \sigma_\infty/3 \qquad \text{(I-5)}$$

With the stresses (σ_r, σ_c, σ_z) from the thermal expansion calculations fixed, the applied stress σ_∞ is varied and plotted against pressure on the same axis as the fracture strength/pressure plot. In the case of a surface defect, the free surface cannot support a normal stress and, therefore, σ_z was set equal to zero.

It is important to note that in this formulation, compression is positive (+) and tension is negative (-). This unusual sign convention was necessary in order to fit the data to the logarithmic equation form [I-7].

I.5 FRACTURE STRENGTH RESULTS.

The results for the experimental case—a large cylindrical HA-6N particle in a Ti-64 matrix—are shown in figure I-5 for the surface and subsurface HA particles.

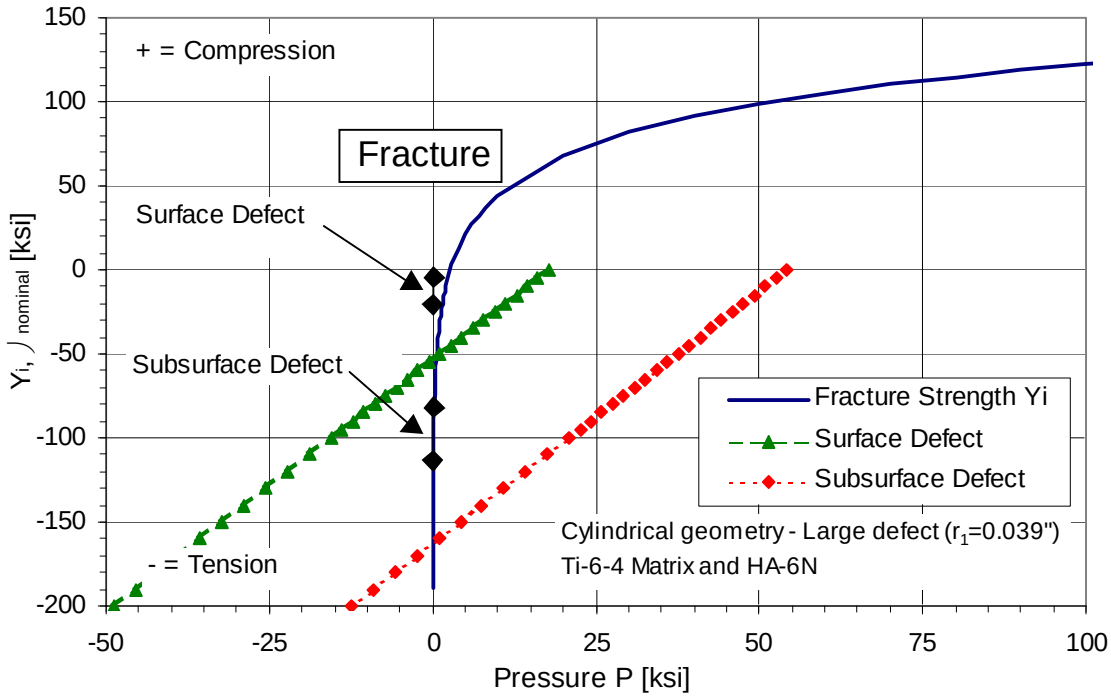

Figure I-5. Comparison of Fracture Strength and Applied Pressure (As a Function of Applied Stress) for HA-6N Surface and Subsurface Defects

The intersection of the fracture strength (Y_i versus P) and applied stress (σ_∞ versus P) curves mark the nominal applied stress where cracking in the HA was expected to occur. For a HA with a nitrogen content of nominally 6%, the calculated applied stresses were 53 ksi for the surface case and 162 ksi for the subsurface case. These values can be compared with the experimentally measured values of 5-20 ksi for the fracture of HA particles located at the surface and 80-115 ksi for embedded HA from the TRMD-I testing [I-1].

The magnitudes of the stresses at which fracture of the HA particle is predicted to occur are consistently larger than that observed experimentally. The relative increases in fracture strength between surface and subsurface defects appear to be quite similar in figure I-5 for both the experimental and predicted cases. Specifically, the ratio of the predicted to experimental (average) results was 4.3 times for the surface case and 1.66 times for the subsurface case. The results, both the general trends and the relative magnitudes, imply that the triaxial residual stresses caused by the thermal expansion differences delay the onset of fracture in the subsurface HA particles during the static load tests.

An analysis of the fracture stresses for a thick specimen under typical plane-strain conditions and excluding the residual stresses was also conducted in order to verify that the effect was correctly attributed to the residual stresses, and not caused by constraint alone. The findings indicated that the triaxiality of the constraint induced by the residual stresses dominates the plane-strain conditions.

The discrepancies between the experimental and predicted results are attributed in part to several assumptions made in the modeling. One of the primary sources of error is that the Brooksbank and Andrews model assumes that the cylinder extends completely through the thickness. In actuality, the seeded HA cylinder makes up roughly the middle 50% of the thickness. The resulting calculation of σ_z is thereby too high, and as a result of the higher residual stress, the applied stress to fracture is overpredicted by the load line being shifted too far to the right. An additional assumption is that the residual stresses (σ_r, σ_c) calculated using the assumed geometry also apply to the surface defect. The validity of both of these assumptions could be quantified with a detailed finite element model.

The results presented in this section are for a cylindrical geometry. This analysis could not be applied to a spherical geometry, which assumes axisymmetry and does not allow for proper consideration of the different surface/subsurface constraints.

I.6 FATIGUE MODELING.

The approach taken in the case of fatigue modeling is to examine the effect of the particle and matrix differences on the stress-intensity factor, K. When determining the stress-intensity factor of a crack at the HA particle, the following factors can be significant:

- The effect of the residual stresses caused predominately by thermal expansion differences during the cooling process.

- The effect of the differences in elastic constants (E, ν) between particle and matrix.

The impact of each of these factors was investigated initially. The effect of the residual stresses on K was determined to be more significant than the elastic constant differences caused by the presence of the particle. The relatively small effect of the particle was coincidentally due to the particular values of stiffness and Poisson's ratio. Specifically, the stress-intensity factor for a cracked circular inclusion under uniform tension developed by Erdogan and Gupta [I-8] reduced to the penny crack solutions for the E and ν values in this case. As a result of this finding, the subsequent analyses only include the residual stress field effects of the HA particle.

A variety of geometric cases were considered, including stress-intensity factor solutions for a crack embedded within a particle, a crack spanning a particle, and a crack spanning a particle and growing in the surrounding matrix. As a result of the experimental findings that HA particles (with their high nitrogen content) often crack quickly under loading, the case of a crack spanning a particle and growing into the surrounding matrix was selected for investigation. This is essentially a damage tolerance type of approach where the initial crack size is assumed equal to the HA particle and where any type of crack nucleation/formation is neglected.

The residual stresses were implemented with a superposition of stress-intensity factor solutions for the nominal stress applied away from the crack and the residual stresses from the cooling process.

$$K_{\text{total}} = K_{\text{nominal}} + K_{\text{residual}} \qquad \text{(I-6)}$$

The stress-intensity factor for residual stresses was determined by using a weight function approach where the K solution for an annular ring of load at a specific distance from a circular penny crack (developed originally by Sneddon and found in reference I-9) was integrated over the residual stress profile described previously.

The weight function integrals for the cylindrical and spherical geometries have the following forms:

$$K = \int_0^a 2\sqrt{\frac{a}{\pi}} \frac{\sigma_{\text{residual}}(r)}{\sqrt{a^2 - r^2}} dr \quad \text{for cylindrical} \tag{I-7a}$$

$$K = \int_0^a \frac{2}{\sqrt{\pi a}} \frac{\sigma_{\text{residual}}(r) \cdot r}{\sqrt{a^2 - r^2}} dr \quad \text{for spherical} \tag{I-7b}$$

where the residual stress profile determined earlier as a function of r is used.

In the case when the stress profile is constant, the integrals in 7 (a and b) reduce to the more familiar forms:

$$K = \sigma\sqrt{\pi a} \quad \text{for a through crack (cylindrical)} \tag{I-8a}$$

$$K = 2\sigma\sqrt{\frac{a}{\pi}} \quad \text{for a penny shaped crack (spherical)} \tag{I-8b}$$

I.7 FATIGUE RESULTS.

The total stress-intensity factor K_{total} and the relative contributions to K from residual stress and the nominal applied stress are shown in figure I-6 for HA-6N and Ti-64 matrix and assuming a large defect with a spherical geometry. The results in figure I-6 are for a specific applied stress of 75 ksi, although the characteristic shapes and observed trends apply to a complete range of applied stresses. The compressive residual stresses in the HA particle result in a negative stress-intensity factor when the crack is within the particle. When the crack completely spans the particle, and even when it has grown into the matrix, the compressive residual stresses in the HA particle act to keep the crack closed and substantially reduce K_{total}. The region between K_{nominal} and K_{total} when the crack spans the particle and begins to grow into the matrix represents the significant contribution of the residual stresses. It is interesting to note how quickly the K_{nominal} and K_{total} curves converge as the crack grows (figure I-6). This convergence usually occurs within growth of the crack a distance of one particle radius into the matrix.

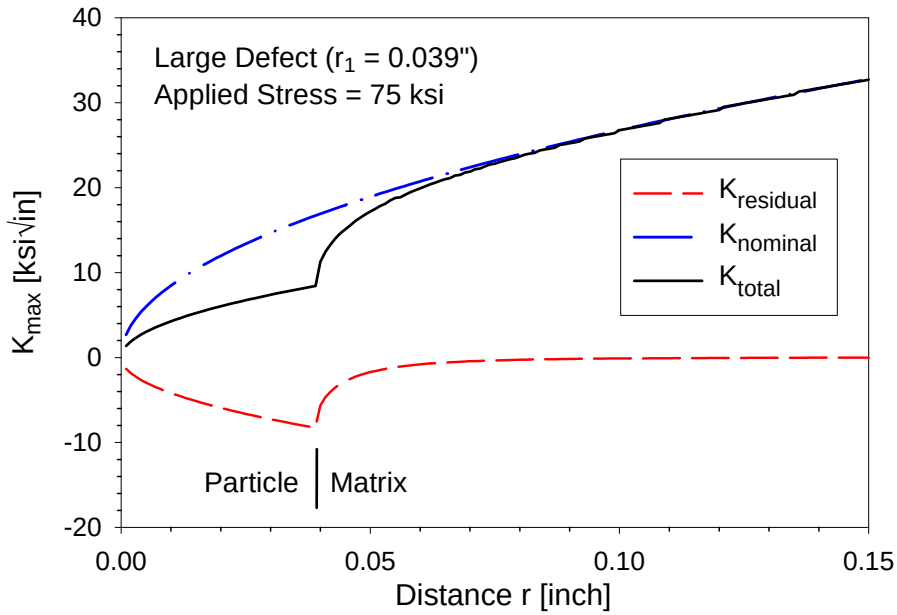

Figure I-6. Composition of the Stress-Intensity Factor Demonstrating the Relative Contributions of the Nominal Applied Stress and Residual Stresses for a Range of Crack Sizes

The reduction in K due to the residual stresses can impact the onset of fatigue crack growth as well as the fatigue life of a component. The following sections detail comparisons with the material's fatigue threshold and with experimentally measured fatigue lives.

I.7.1 COMPARISONS OF K AND THRESHOLD.

Two methods for comparing the stress-intensity factor with the material threshold have been investigated.

- The solution for K_{max} resulting from superposition of the maximum applied stress can be compared directly to the threshold ΔK_{th}. The threshold value is dependent on R ratio, as shown in the experimental data from TRMD-I [I-1] in figure I-7 and table I-3. The experimental threshold ΔK_{th} data (figure I-7 and table I-3) were fit to a Walker type equation resulting in the relation

$$\Delta K_{th}\ [\text{ksi}\sqrt{\text{in}}] = 8.8865*(1-R)^{0.417} \qquad \text{(I-9)}$$

- For the nominal applied R ratio of 0.1, the K_{max} values are compared to the corresponding threshold value of 8.50 ksi √in. The plot of applied stress versus K (figure I-8) shows the impact of the residual stresses on K_{max} for the large defect. No growth was observed in the experimental testing at the 50 ksi stress level; however, crack growth was observed at 75 ksi. The residual stress corrected curve (K_{total}) correctly predicts the observed growth/no growth behavior, whereas the analysis without residual stresses ($K_{nominal}$) would have falsely predicted growth at the 50 ksi level.

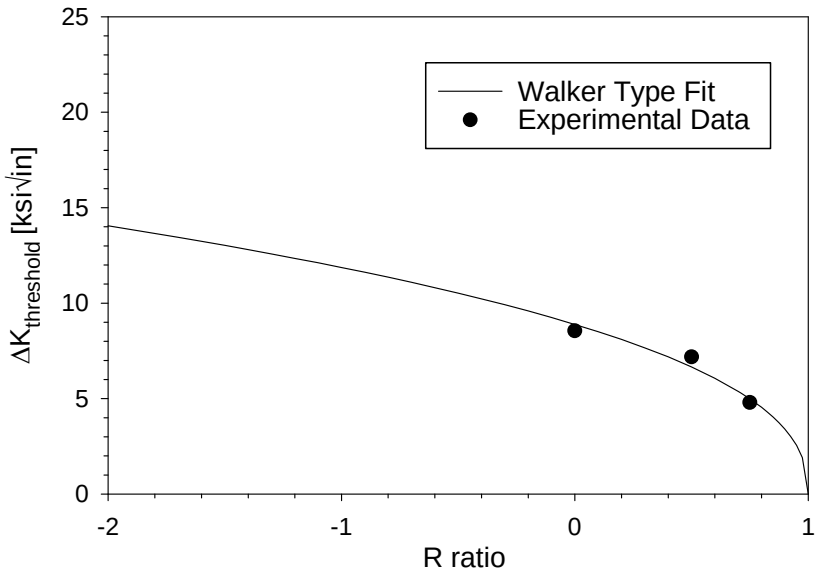

Figure I-7. Plot of Experimental Threshold (ΔK_{th}) Data [I-1] as a Function of R Ratio and Resulting Walker Type Equation Fit

Table I-3. Threshold Stress-Intensity Factors (ΔK_{th}) for Ti-64 at Several R Ratios [I-1]

R ratio (S_{min}/S_{max})	Threshold ΔK_{th} [ksi√in]
0	8.553
0.5	7.185
0.75	4.798

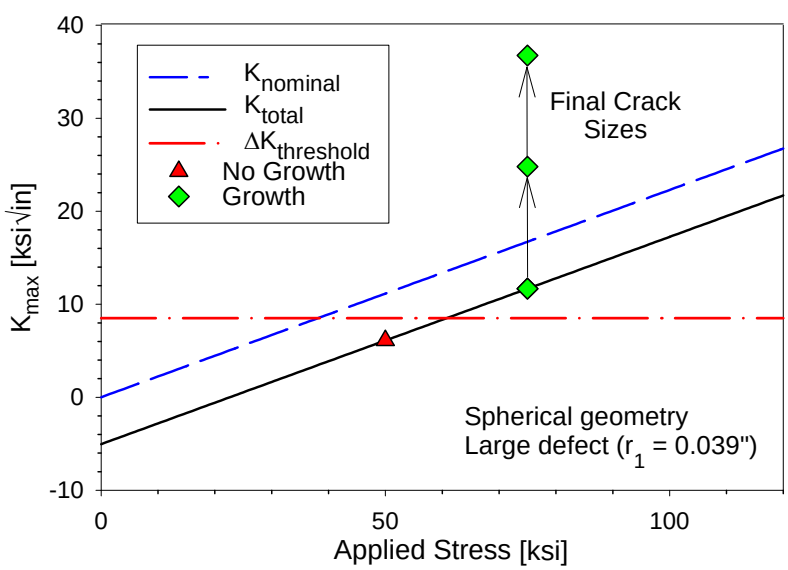

Figure I-8. Comparison of K_{max} With the Threshold Corresponding to the Applied R = 0.1

This analysis compares K_{max} and ΔK_{th} and thereby assumes that any stresses below zero will not contribute to fatigue crack growth. Even though the residual stress corrected K_{min} may be below zero, the effective stress range ΔK is assumed to range from 0 to K_{max}, instead of from K_{min} to K_{max}. While this is a reasonable assumption, a more rigorous treatment of R ratio has been carried out in the second analysis.

The presence of the compressive residual stresses from the particle does not affect the magnitude of the stress range (ΔS), but rather causes a shift in the R ratio. The resulting ΔK can be compared to the ΔK_{th} resulting from the appropriately shifted R ratio. Based on the relation in equation I-9, the comparison of ΔK with ΔK_{th} as functions of the applied stress is shown in figure I-9 for the large defect geometry. The stress-intensity factor range ΔK increases proportionately to the applied stress. At high stress levels (>90 ksi), the applied stress dominates the residual stress and the effective R ratio approaches the nominal applied R of 0.1. At midrange stress levels (50-90 ksi), the residual stresses significantly reduce the R ratio—resulting in higher ΔK_{th} values. For the applied stress level of 75 ksi, the R ratio is reduced from 0.1 to -0.954 by the residual stresses (for a large HA-6N defect). As the applied stress approaches the magnitude of the residual stress, the R ratio approaches negative infinity and ΔK_{th} increases toward positive infinity. The results in this region are not meaningful, since the relationship between ΔK_{th} and R is being extrapolated well beyond the available data.

The region of crack growth is represented by the area above the ΔK_{th} curve in figure I-9. The region of significance, however, lies between the threshold curve for the nominal R ratio and the R ratio affected threshold curve including the residual stresses. Cracks with ΔK values in this region would have been falsely predicted to grow using the standard analysis.

The potential impact of several parameters has been investigated and is illustrated in figure I-10. The results are presented for spherical HA-12N defects, where the 12% N case represents the largest difference in CTE and results in the largest residual stresses, as well as for a TiN particle, where this case represents one of the smallest differences in CTE. The nitrogen percentage influences the magnitude of the residual stresses, which then affects the R ratio and the resulting ΔK_{th} curve. In this manner, the effect of the residual stresses has essentially been bounded by the pair of TiN and HA-12N ΔK_{th} curves. It is important to note that while K_{max} and K_{min} vary, the ΔK associated with the initial crack size is independent of the composition of the HA. The general shape of the ΔK_{th} curves remains the same—approaching the nominal $R = 0.1$ value at high stresses and approaching positive infinity as the applied stress approaches the residual stress. Variations in the HA nitrogen content result in the demonstrated shifts in the threshold curve. Sensitivity studies were performed with the other parameters (E, ν) and demonstrated that the nitrogen content is the most significant factor. Additionally, comparisons were performed using a cylindrical geometry and resulted in findings and trends that were very similar to the above for the spherical case.

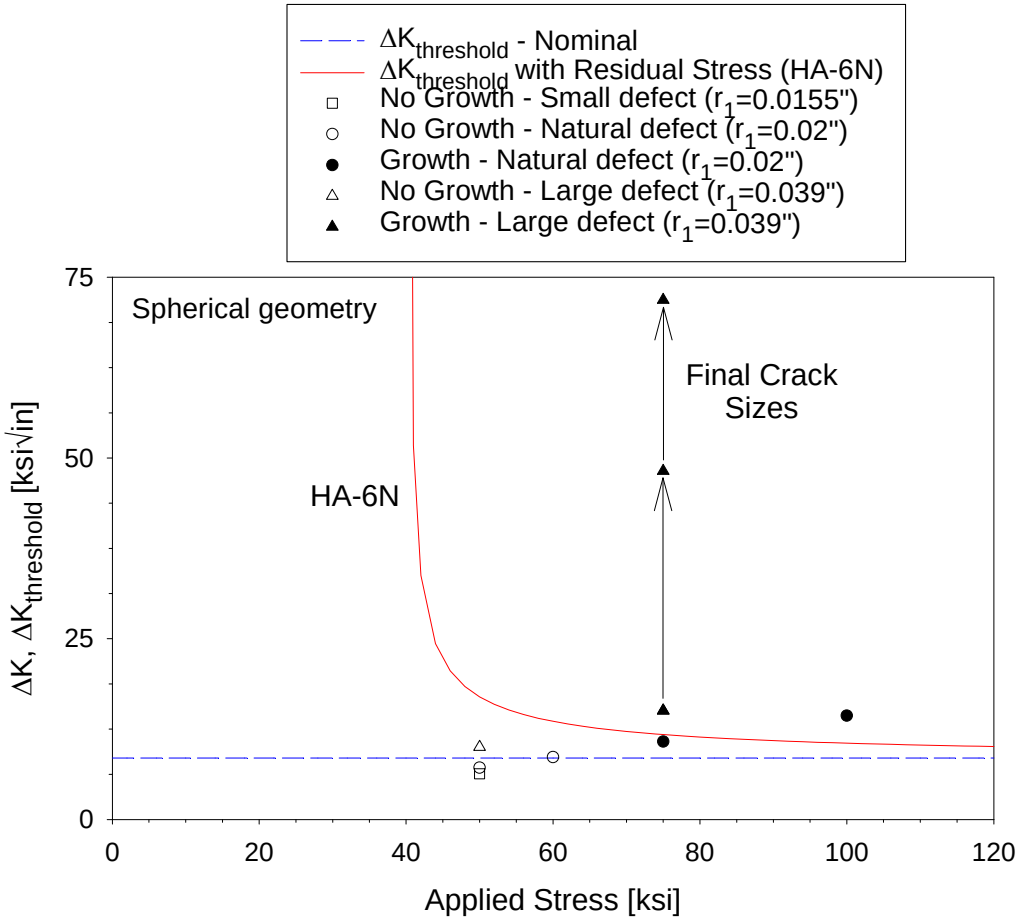

Figure I-9. Comparison of ΔK Versus Applied Stress Showing the Resulting ΔK_{th} Curve and Experimental Data Where Crack Growth/No Growth was Observed

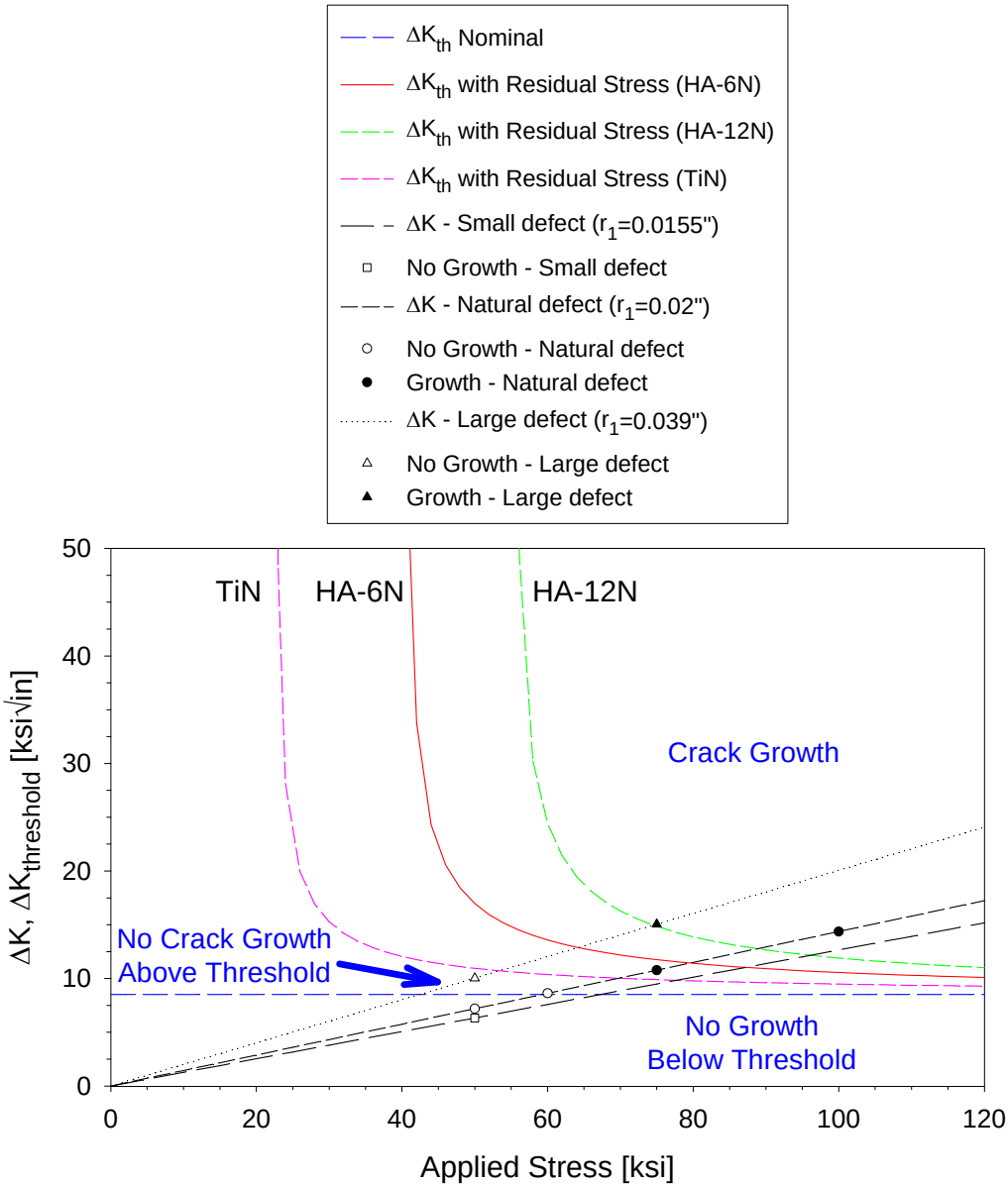

Figure I-10. Sensitivity of ΔK and ΔK_{th} as a Function of Applied Stress for HA Particles With Differing Nitrogen Contents

I.7.2 IMPACT OF THE RESIDUAL STRESSES ON FATIGUE LIFE.

After characterizing the impact of residual stresses on the stress-intensity factor and the growth/no growth threshold criteria, the natural extension is to assess the influence of the residual stresses on the fatigue life of propagating cracks.

Fatigue life predictions were performed by integrating the Paris relation for crack growth rate (CGR) from an initial crack size to a final crack size. The CGR relation developed in TRMD-I [I-1] for Ti-64 in vacuum was used. Because of variations in the stress ratio during crack

growth, a Paris relation based on $\Delta K_{\text{effective}}$ from the Newman crack closure model was used.

$$\frac{da}{dN} = A \cdot \left(\Delta K_{\text{effective}}\right)^n \tag{I-10}$$

This relation was selected as a means of representing CGR data for multiple R ratios as a single relation. The effective stress-intensity factor $\Delta K_{\text{effective}}$ is based on closure and represents the portion of the cycles when the crack is fully open and contributing to crack growth;

$$\Delta K_{\text{effective}} = \left(\frac{1 - S_{\text{open}} / S_{\max}}{1 - R} \right) \Delta K \tag{I-11}$$

where the opening stress is a function of the R ratio, the constraint parameter α, and the ratio of the maximum stress to the flow stress S_o;

$$\frac{S_{\text{open}}}{S_{\max}} = fcn\left(R, \alpha, \frac{S_{\max}}{S_o} \right) \tag{I-12}$$

Detailed relations for the opening stress S_{open} can be found in reference I-10. CGR data were available for Ti-64 under vacuum conditions in reference I-1. The resulting parameters for the crack growth relations from reference I-1 used in the life-prediction analyses are presented in table I-4. A constant value of $S_{\max}/S_o$ of 0.6 was assumed in the development of the CGR fit [I-1] and has also been used in the life predictions. The constraint parameter α has physical meaning and usually ranges from 1 for plane-stress conditions to 3 for plane-strain conditions. The optimal value of α = 2.027 was determined in reference I-1 by collapsing the experimental CGR data from R ratios of 0, 0.5, and 0.75.

Table I-4. Coefficients for the Newman Crack Closure CGR Model for Ti-64 Under Vacuum Conditions at 75ºF Determined in Reference I-1

Parameter	Value
Alpha α	2.027
$S_{\max}/S_o$	0.6
Coefficient A	8.093e-12
Exponent n	5.105

The life-prediction analyses are based on crack growth from a crack equal to the initial defect (large defect, 0.039″) to a final crack size of 0.1. The actual ratio of $S_{\max}/S_o$ varies for the individual stress levels examined (table I-5). However, since a fixed ratio of 0.6 was used in the development of the CGR equation, the fixed value of $S_{\max}/S_o$ of 0.6 was also used in conjunction with the CGR parameters (table I-4) for the life predictions. This assumption has only a minor effect on these particular calculations.

The life-prediction results are presented in table I-5 for both the spherical and cylindrical geometries. The analyses were carried out for cases with no residual stresses, with a HA-6N particle in Ti-64 (representing the experimental specimens) and with a HA-12N particle in Ti-64 (representing the largest residual stresses). The compressive residual stresses, as anticipated, result in decreases in ΔK and thereby longer fatigue lives. The magnitude of the effect on life, shown as the ratio of life with residual stress to life with no residual stresses (table I-5), generally ranges from 1.3 to 4, but is heavily dependent on the applied stress level.

Table I-5. Impact of the Residual Stresses on Fatigue Life Predictions

For S_{max}/S_o = 0.6			S_{max} = 50 ksi		S_{max} = 75 ksi		S_{max} = 100 ksi	
Particle	Matrix	p [ksi]	Life [Cycles]	Ratio	Life [Cycles]	Ratio	Life [Cycles]	Ratio
Spherical Geometry								
No Residual Stresses		0	60830	1.00	7677	1.00	1768	1.00
HA-6N	Ti-64	-40.46	270900	4.45	15030	1.96	2711	1.53
HA-12N	Ti-64	-55.23	1721000	28.29	25630	3.34	3557	2.01
Cylindrical Geometry								
No Residual Stresses		0	6067	1.00	765.6	1.00	176.3	1.00
HA-6N	Ti-64	-26.87	13450	2.22	1184	1.55	236.9	1.34
HA-12N	Ti-64	-36.42	23960	3.95	1519	1.98	276.4	1.57
Actual S_{max}/S_o			0.385		0.577		0.769	

p = residual stress in the HA particle

A direct comparison of the experimental and predicted fatigue lives is not possible because of the variety of data available (no crack, some growth, or growth to failure). However, some meaningful observations and comparisons can be made by examining specific cases. The experimental and predicted data for the subsurface defect cases are presented in table I-6. The predicted results are based on an initial crack size equal to the specific defect size, but are based on HA with the high 6% N content. In the 50 ksi cases, no crack growth was observed in the applied cycles (ranging from 10,000 to 42,000); however, this result is somewhat expected when one considers the large number of cycles predicted for growth to the selected final crack size (0.1″). At the 75 ksi stress level, substantial crack growth was observed in both specimens after 10,000 and 20,000 cycles and compares reasonably well with the predicted 15,000 cycles. The life predictions correctly predicted the observed experimental behavior in all of the cases to this point.

After being subjected to prior loading at stress levels of 50, 62, and 75 ksi, the specimen containing the natural defect failed after 13,300 cycles at 100 ksi, which exceeded the predicted life of 8,600 ksi. At the lower stress levels for this specimen, the life predictions exceeded the number of applied experimental cycles, and it was unclear when crack formation occurred. At the 100 ksi level, the model underpredicted the experimental failure life, which implies that a portion of the cycles may have gone toward formation of the crack.

Table I-6. Direct Comparison of Experimental and Predicted Fatigue Lives for Individual Specimens With Subsurface Defects

Max Stress (ksi)	Specimen Number	Defect			Experimental (k cycles)	Growth?		Predicted (no $\sigma_{\rho\varepsilon\sigma}$) (k cycles)	Predicted (with σ_{res}) (k cycles)	Predicted correctly?	
		Size	Content	Type		Yes	No			Yes	No
50	HA-IS-E1	S	H	I	10		✓	313.4	1194.0	✓	
50	LHI-2	L	H	I	25		✓	60.8	270.9	✓	
75	LLI-2	L	L	I	20	✓		7.7	15.0	✓	
75	LMI	L	M	I	10	✓		7.7	15.0	✓	
50	RMI-F1	N	M	I	42		✓	205.0	798.3	✓	
62					15	?	?	65.6	149.8		
75					24	?	?	25.9	46.6		
100					13.3	✓		6.0	8.6		✓

Defect Size (diameter): S = small (0.031″), R = natural (0.04″), L = large (0.078″)
Nitrogen Content: L = low (1.6%), M = medium (2.7%), H = high (6%)
Defect Type: S = surface, I = interior (subsurface)

It is important to note that significant numbers of cycles may be required for the crack to form initially, to develop a stable shape, and to grow through particle/DZ interfaces. Evidence of these cycles are observed in the two specimens tested at 75 ksi. Specimen LLI-2 has a smaller final crack size after 20,000 cycles than specimen LMI has after 10,000 cycles. These observed differences can be attributed to variabilities associated with fatigue and the phenomenon described. The life predictions assume that the particle is initially cracked and the crack growth is a continuous process.

I.8 DISCUSSION.

The original motivation for this work was to quantify the residual stresses and to address their ability to explain the experimental behavior in fracture and fatigue tests. To this end, this work has made several simplifications and assumptions with regard to geometry and composition.

The HA particle geometry was modeled as a perfect cylinder or sphere in this work. Some of the strengths, weaknesses, and issues related to geometry have been explored in the individual analyses. The reality, however, is that the HA geometry is most commonly irregular-shaped, and there is evidence that cracking does not occur uniformly with only portions of the HA particle cracking. The geometry assumptions are reasonable approximations that have provided valuable findings. More complicated geometries have not been further explored in this work because of the natural variabilities associated with them and the relatively small gains to be obtained by such modeling.

A secondary geometry issue is the DZ. The nitrogen content of the DZ transitions between the HA particle and the matrix. The varying nitrogen content is expected to reduce the magnitude of the residual stresses because of the more gradual CTE differences.

The presence of the DZ has been neglected in the modeling performed here. The influence of DZ could be modeled using a finite element analysis to determine the resulting residual stresses. Since the objective of this work was to characterize the potential effects, the particle/matrix cases (neglecting DZ) were selected as they provide an upper bound for the potential effects. This decision can be rationalized by the fact that the particle/DZ/matrix case is bounded between the no residual stress and the particle/matrix cases.

The residual stresses introduced by thermal expansion differences in the HA particles are by their nature compressive. The compressive residual stresses result in apparently high fracture and fatigue strengths. In fatigue specifically, the residual stresses result in a decrease in stress-intensity factor and longer than expected life. For these reasons, exclusion of the compressive residual stresses from component life prediction is conservative from a design standpoint. Knowledge of the potential effects of residual stresses, however, is useful when selecting stress levels and expected lives during laboratory (e.g., spin pit tests) and/or field certification tests.

I.9 CONCLUSIONS.

In this work, the coefficient of thermal expansion values for hard alpha (HA) particles containing varying nitrogen contents were quantified and used in the determination of a residual stress

profile for the region in and around the HA defect. The effects of the compressive residual stresses have been investigated with regard to the onset of crack formation and the growth of fatigue cracks and resulting lives when the HA particles are subjected to cyclic loads. Based on this study, the following conclusions can be drawn:

- Inclusion of residual stresses in the analytical models can be used to explain the apparent high strengths of the specimens with embedded HA particles tested in the Turbine Rotor Material Design Phase I program.

- The fracture strength model explains the qualitative observations related to the experimental fracture strength. The fracture strength of the embedded (subsurface) particle is nominally 3-5 times the strength of the surface particles.

- The stress-intensity factor evaluation, including residual stresses, was able to quantitatively explain the threshold-related fatigue behavior—growth versus no growth, including cases where the traditional analysis (no residual stresses) incorrectly predicted growth when no growth occurred. A range of ΔK threshold curves incorporating the residual stresses has been presented for HA particles with different nitrogen contents. At high applied stresses, the effect of the residual stresses is relatively small, with its significance increasing as stress level decreases.

- Lastly, because the residual stresses present are compressive, their effect only reduces the impact of the applied stresses and thereby results in lower stress-intensity factors and longer lives. Designs and life predictions made using the traditional analysis methods neglecting residual stresses will be conservative.

I.10 REFERENCES.

I-1. Leverant, G.R., et al., "Turbine Rotor Material Design," FAA report DOT/FAA/AR-00/64, December 2000.

I-2. McKeighan, P.C., Perocchi, L.C., Nicholls, A.E., and McClung, R.C., "Characterizing the Cracking Behavior of Hard Alpha Defects in Rotor Grade Ti-6-4 Alloy," *Fatigue Behavior of Titanium Alloys*, R. R. Boyer, D. Eylon and G. Lütjering, eds., The Minerals, Metals & Materials Society, Rosemont, IL, 1999, pp. 349-356.

I-3. Brooksbank, D. and Andrews, K.W., "Stress Fields Around Inclusions and Their Relation to Mechanical Properties," *Journal of the Iron and Steel Institute*, Vol. 210, 1972, pp. 246-255.

I-4. Brooksbank, D. and Andrews, K.W., "Tessellated Stresses Associated With Some Inclusions in Steel," *Journal of the Iron and Steel Institute*, Vol. 207, 1969, pp. 474-483.

I-5. Brooksbank, D. and Andrews, K.W., "Thermal Expansion of Some Inclusions Found in Steels and Relation to Tessellated Stresses," *Journal of the Iron and Steel Institute*, Vol. 206, 1968, pp. 595-599.

I-6. *ASM Handbook*, American Society of Metals, Vol. 2, 1991.

I-7. Chan, K.S., Perocchi, L., and Leverant, G.R., "Constitutive Properties of Hard Alpha Titanium," *Metallurgical and Material Transactions A*, Vol. 31A, 2000, pp. 3029-3040.

I-8. Erdogan, F. and Gupta, G.D., "The Inclusion Problem With a Crack Crossing the Boundary," *International Journal of Fracture*, Vol. 11, 1975, pp. 13-27.

I-9. Murakami, Y., *Stress Intensity Factors Handbook*, Pergamon Press, 1988.

I-10. Newman, J.C., Jr., "A Crack Opening Stress Equation for Fatigue Crack Growth," *International Journal of Fracture*, Vol. 24, 1984, pp. R131-R135.

APPENDIX J—SPIN PIT TESTS OF TITANIUM ROTORS CONTAINING NATURAL AND SEEDED HARD ALPHA ANOMALIES

J.1 INTRODUCTION.

Spin pit tests of Ti-6Al-4V disks containing natural and seeded hard alpha (HA) inclusions were completed during the Turbine Rotor Material Design (TRMD) Phase II program to validate the Flight_Life fracture mechanics code in DARWIN® and the assumptions used to develop the HA anomaly distributions in the Federal Aviation Administration Advisory Circular 33.14. The spin pit tests were conducted with three disks forged during the TRMD-I program [J-1]. Disks B1BW3B and B3W2E contained natural anomalies identified during production billet inspections. Disk seed billet (SB) SB-6 contained a seed introduced into the billet during the TRMD-I program. This report summarizes the accomplishments under this spin test program. Additional details regarding the material processing through disk forging are included in the TRMD-I final report [J-1].

J.2 PRETEST ANALYSIS.

Multiple original equipment manfacturers performed either production or laboratory ultrasonic (UT) inspections of each of these disks in the billet form, the interim pancake shape, and the final disk forging during TRMD-I. These inspections were performed to track the movement of the inclusions through the forging process for validation of DEFORM™ analytical predictions, to assess the impact of forging on inspectability, and to assess expected variability from laboratory to laboratory. Appendix D contains the results of these inspections with measured indication locations and signal amplitude. Two additional mults, SB-5 (seeded), and B3W2-G (natural HA), also received multiple billet and forging inspections during the TRMD program and are included in that appendix as well. These inspection data were delivered to the Engine Titanium Consortium (ETC) program, and conclusions regarding inspectability of the billets relative to forgings are deferred to the ETC.

DEFORM analyses were run during TRMD-I to select the candidate forging, to identify the seed placement location for the seeded mults, and to identify which of the mults containing naturally occurring anomalies were acceptable for spin testing. The inclusions were backtracked through the forging process from the desired location in the forged disk to identify where the inclusions needed to be in the mults. To maximize the crack growth from these inclusions, it was desired to have the seeds as close to the corner of the disk bore as possible without intersecting the surface, since this location was predicted to have the highest stress in the part during the spin tests. Plots illustrating comparisons of the DEFORM predictions to the inclusion locations identified by inspection are included in the TRMD-I final report. For all forgings, the DEFORM predictions agreed well with the measured inclusion locations. Figure J-1 shows a quick-look summary of the pretest estimates of the inclusion locations in the disk forgings.

Disk	Surface	Depth
SB-6	A	0.5 in.
	B	0.25 in.
B3W2E	A	0.5 in.
	B	0.5 in.
B1BW3B	A	0.25 in.
	B	0.5 in.

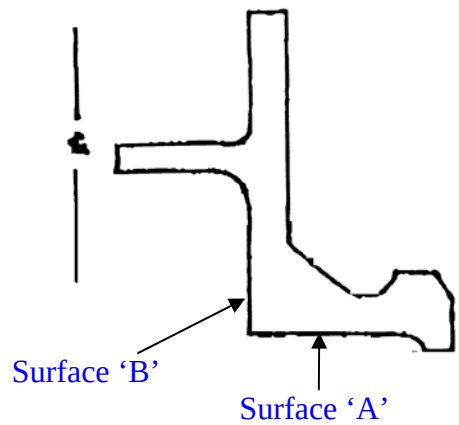

Figure J-1. Locations of HA as Determined by UT Inspections

A simple disk-forging sonic inspection shape was selected as the configuration for spin testing. Finished machining to a flight-weight design with blade slots was not required since this would have added cost, time, and complexity and would not have further improved the ability to grow a crack from the inclusions. Prior to spin testing, ANSYS 2D axisymmetric stress analyses were performed to predict the stresses at the inclusions for multiple candidate forgings. Figure J-2 shows a representative hoop stress prediction contour plot for the selected disk forging spinning at 18,000 revolutions per minute (rpm). The finite element model contains the disk forging and an additional block of material used to represent the arbor for studies to assess the desired interference fit between the disk and arbor. Since the bore stresses remain elastic and the interference fit with the arbor remains tight, scaling of the stresses for other speeds can be accomplished by multiplying the stresses by the ratio of the speeds squared.

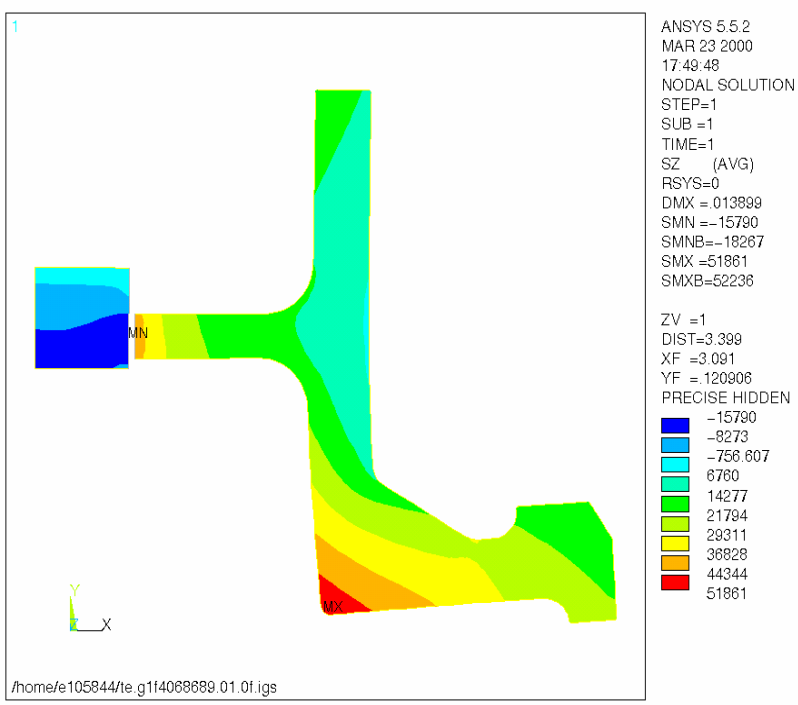

Figure J-2. Predicted Hoop Stress at 18,000 rpm

The ANSYS stress analysis results were subsequently input into a standalone version of Flight_Life to predict the crack growth life from the inclusions and select the desired test speeds. It was desired to select a speed that would result in approximately 15,000 cycles of crack growth life assuming a 0.2″ crack (the size of the diffusion zone (DZ) of the seed placed in disk SB-6). The actual size of the natural anomalies in disks B1BW3B and B3W2E was unknown at the start of testing, but it was assumed that they were approximately the same size as the SB-6 seed. In the pretest analysis, it was assumed that there was no incubation and crack growth would initiate at the start of testing. This resulted in desired speeds of 17,800 rpm for disk SB-6, 17,400 rpm for disk B1BW3B, and 19,500 rpm for disk B3W2E. Since disk SB-6 was tested first, the initial growth assumptions and selected speeds could be adjusted for the remaining two disks based on the test observations.

J.3 TEST SETUP AND TEST PLAN.

The rig hardware was designed and the spin testing was performed at Test Devices, Inc., in Hudson, MA. Each disk had its own dedicated spindle and arbor. The selected forging configuration with its extension toward the inner diameter was well suited for an interference fit assembly with the spindle and arbor. The spindle and arbor interference fit assembly minimized cost to the program using standard rig hardware already familiar to Test Devices. The interference fit between the arbor and the disk was analyzed in ANSYS to verify that the radial growth of the disk would not result in the fit opening up. Based on this analysis and a maximum target speed of 19,500 rpm, it was initially determined that an interference of 0.008″ on the diameter would be sufficient (figure J-3).

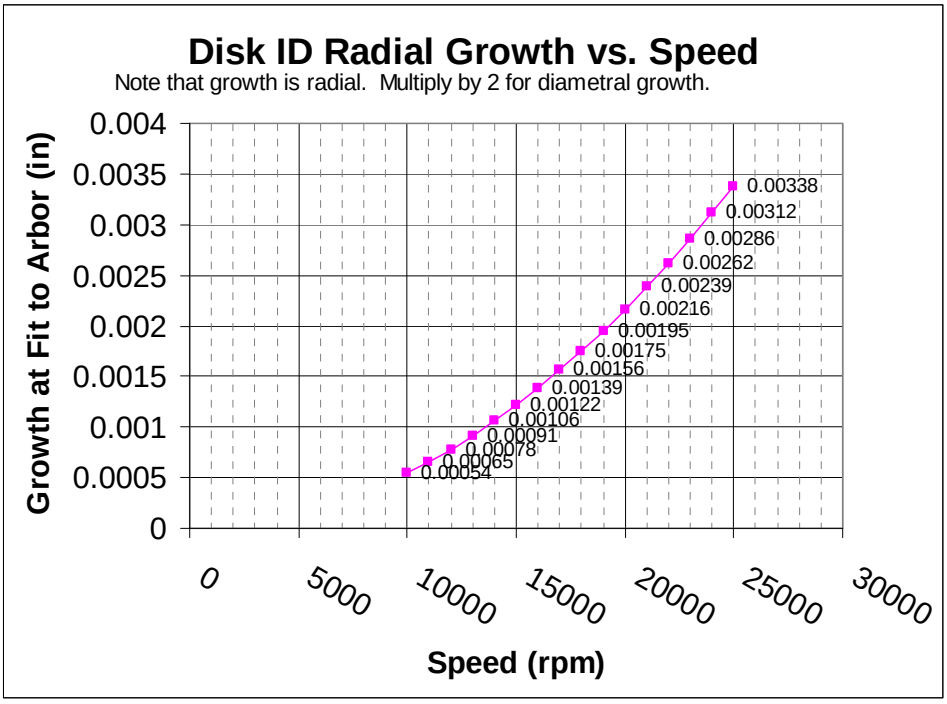

Figure J-3. ANSYS Prediction of Radial Growth of Disks vs Speed at Interference Fit to Arbor

Since the objective of this testing was to assess the crack growth from internal HA inclusions, and surface-initiated cracks were not desired, the surfaces of the disks were shot peened to 6A intensity to reduce any concerns regarding premature surface-initiated failure. Based on the depths of inclusions, the cracks were not predicted to grow close enough to the surface in the first 10,000 cycles of testing for peening to have an effect on the crack growth. If the cracks did approach the surface into the peened residual stress layer, the cracks would have been large enough and growing fast enough by then that the peening would not likely have a significant impact on the total crack growth life.

Strain gages were installed on disk SB-6 to validate the analytical stress predictions. The strain gage locations and orientations are identified in table J-1, with reference to the surfaces identified in figure J-1. Strain measurements were recorded during an initial three cycles of testing prior to the low-cycle fatigue cyclic testing. Figure J-4 shows the results of the strain survey, and figure J-5 shows a comparison of the measured strains to analytical model predictions. In all cases, the model agreed well with the test measurements.

Table J-1. Strain Gage Installation on Disk SB-6

Gage ID	Surface Location	Gage Type	Gage Orientation	Angular Location	Estimated Max Strain
TRMD1	Surface B at 0.5″ from surface A	UNIAXIAL	HOOP	0	0.003 in./in.
TRMD2	Surface B at 0.5″ from surface A	UNIAXIAL	HOOP	225	0.003 in./in.
TRMD3A	Surface A at 0.5″ from surface B	BIAXIAL	HOOP/RADIAL	0	0.003 in./in.

With spin testing of known defects (of unknown DZ size), there is a concern of premature failure of the disk. During the testing, the disks' vibration amplitude and phase were monitored in an attempt to identify the onset of crack growth and to halt the testing before the cracks grew to rupture and risk damaging the fracture surface. A progressive increase in vibration amplitude or a shift in the vibration phase was expected to indicate a growing crack.

The initial disk spin test plan called for spinning in 5000 cycle increments with removals from the rig for interim fluorescent penetrant inspection (FPI) and sonic inspections. The sonic inspections were intended to further assist with monitoring the growth of the inclusions. After the inspections were completed, the disks were to be returned for an additional 5000 cycles to maximize the growth of the defect while attempting to avoid failing the disks. After the completion of the second set of 5,000 spin cycles (10,000 total), the disks would again receive FPI and sonic inspections. If the sonic inspections indicated that the defects were not growing, adjustments to the test speeds would be made prior to continuing testing.

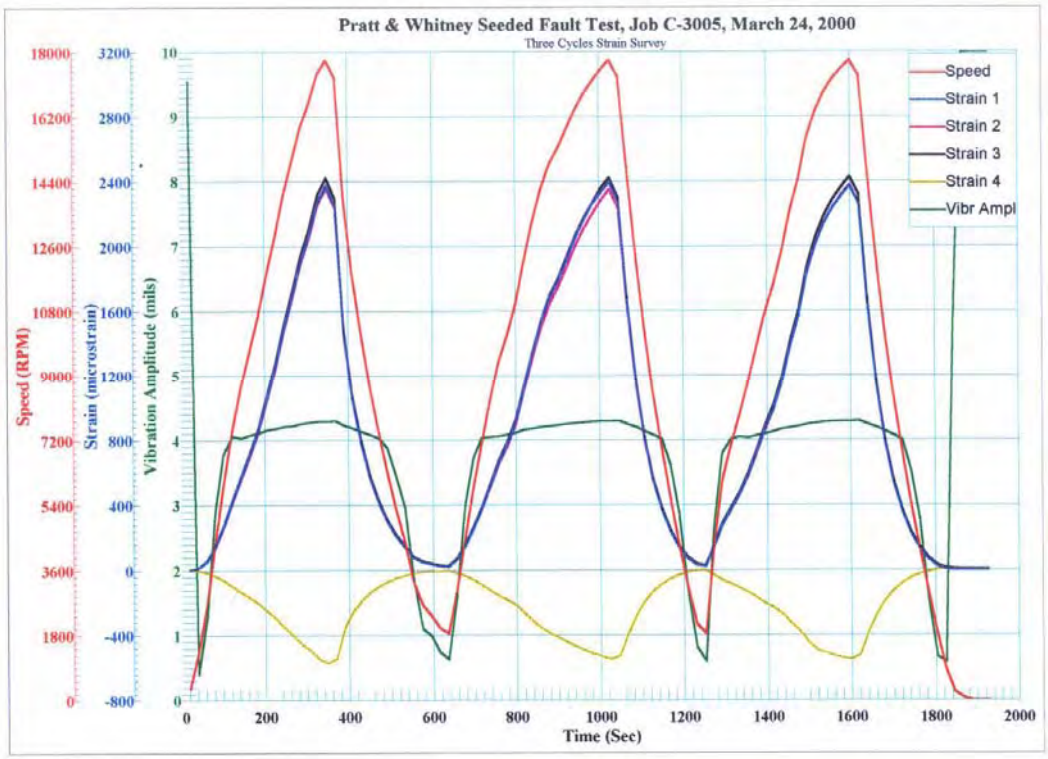

Figure J-4. Strain Survey Results for Disk SB-6

Radial

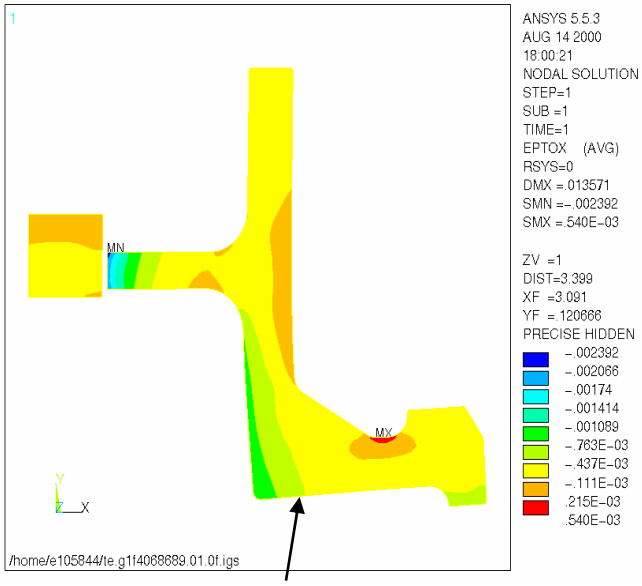

Measured Strain = -0.000560

Hoop

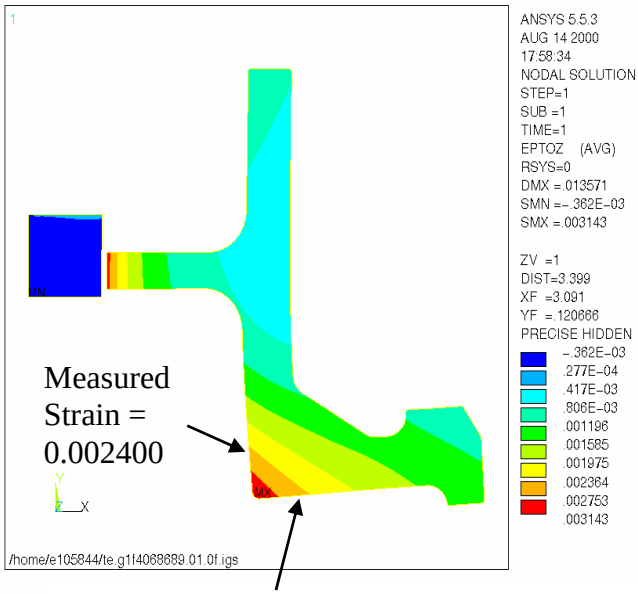

Measured Strain = 0.002430

Figure J-5. Disk SB-6 Measured Strains Agree Well With Analytical Predictions

J.4 TEST RESULTS.

All three disks completed their initially planned 10,000 cycles of testing without a rupture and without strong conclusive evidence of crack propagation. The vibration monitoring system at Test Devices had not shown any indication of crack growth on any of the disks. Since disk SB-6, which was tested first, did not indicate any growth, the speed of disk B1BW3B was increased to 18,000 rpm, and disk B3W2E was increased to 22,000 rpm for the initial 10,000 cycles of testing.

In addition to the normal incidence UT inspections initially planned, angled UT scans were added to the test program. The angled scans provided the only indication of possible internal crack growth out from HA core. These angled scans were added at each inspection interval starting at 5000 cycles of testing. No angled scans were completed prior to the start of the test program (0 cycles). All of the angled scans were completed from the disk axial face in the vicinity of the inclusion (figure J-1 surface A). Figures J-6 through J-8 include B-scan images for the angled scans on each of the three disks at 5,000 and 10,000 cycles. In the B-scan images, the response signal will separate as a crack or cracks extend out from the core. Signal separation was observed with disks SB-6 and B3W2E at 5,000 and 10,000 cycles. Reflections are observed from each of the crack fronts extending out from the core as well as a reflection in between, from the core itself. Meanwhile, disk B1BW3B did not indicate any signal separation at 5,000 or 10,000 cycles. FPI inspections of all three disks did not indicate any surface connected cracks.

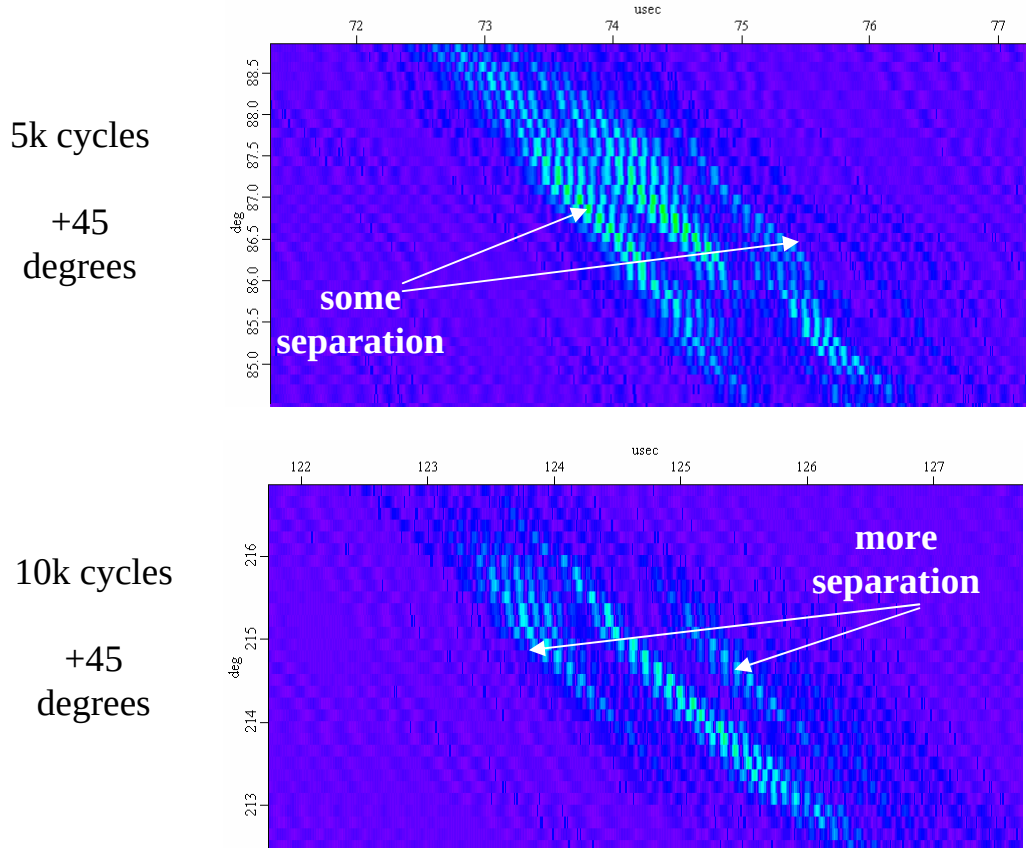

Figure J-6. Angled B-Scans of Disk SB-6 at 5,000 and 10,000 Cycles

5k cycles

+45 degrees

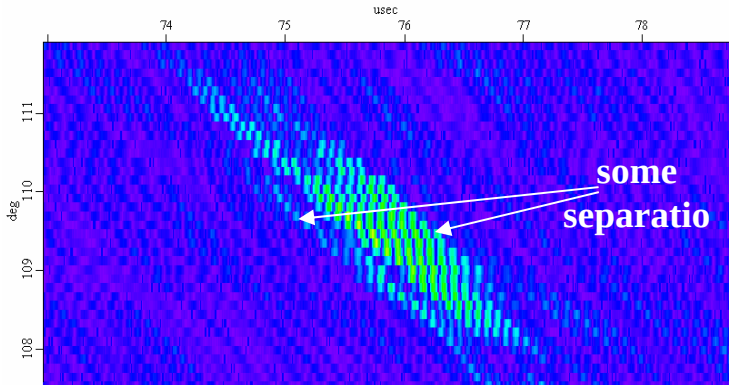

10k cycles

+45 degrees

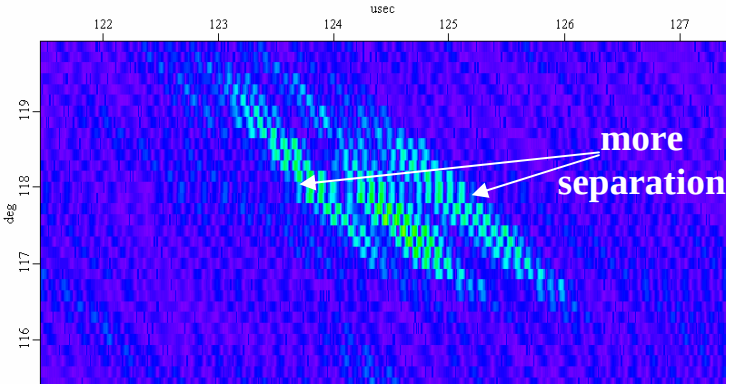

Figure J-7. Angled B-Scans of Disk B3W2E at 5,000 and 10,000 Cycles

5k cycles

-45 degrees

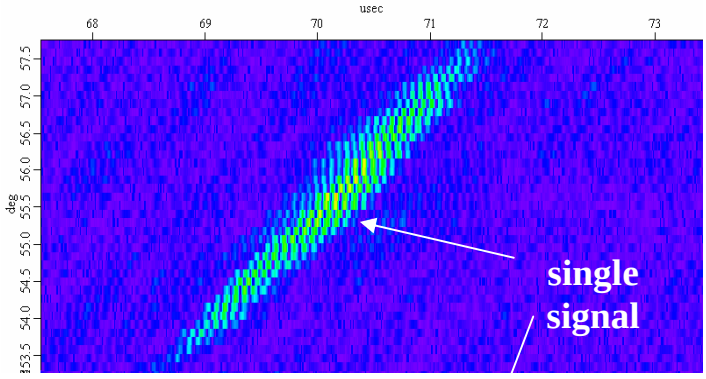

10k cycles

-45 degrees

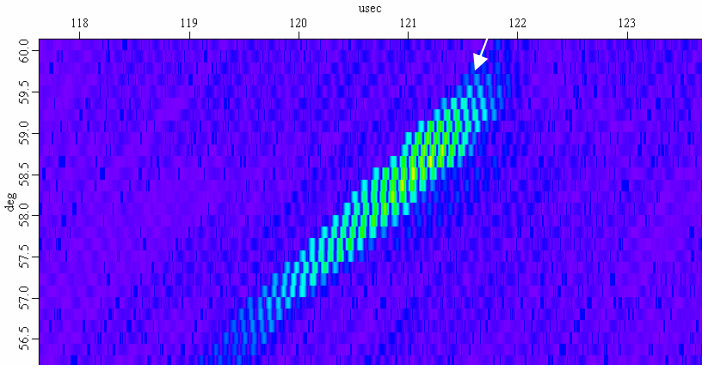

Figure J-8. Angled B-Scans of Disk B1BW3B at 5,000 and 10,000 Cycles

After completion of the inspections at 10,000 cycles, the Steering Committee agreed to return the disks to Test Devices, Inc. for additional testing. While the angled scans did indicate some possible crack growth, the normal incidence inspections were inconclusive at the time. Meanwhile, the crack monitoring system at Test Devices, Inc. had not indicated any crack growth. In addition, prior specimen testing at Southwest Research Institute® during TRMD-I had indicated that stresses between 75 and 100 ksi were required to get cracks to grow from embedded HA inclusions [J-1]. During the first 10,000 cycles of testing, predicted stresses at the inclusions ranged from 40 to 55 ksi. Based on the available data, the Steering Committee agreed to increase the speeds during the remaining testing to generate stresses of 75 ksi at the locations of the inclusions and to spin each of the disks for an additional 7500 cycles.

Table J-2 summarizes the test speeds, predicted disk stresses, and predicted crack growth lives for assumed crack sizes of 0.1″ and 0.2″ diameter. These assumptions were based on the seed placed in the SB-6 mult, which had a 0.1″ diameter core, 0.2″ diameter DZ, and was 0.2″ long. Typical sizes of prior cutups from the same billet indicated that the natural inclusions could likely be similar in size to the seed in SB-6.

Table J-2. Test Speed, Stress, and Life Predictions for Spin Disks

Initial 10,000 Cycles of Testing						
Disk	Maximum Speed (rpm)	Minimum Speed (rpm)	Stress at Flaw (ksi)	Disk Max Stress (ksi)	Predicted Life for 0.2″ Flaw	Predicted Life for 0.1″ Flaw
SB-6	17,800	1780	39.6	50.7	14,900	81,200
B1BW3B	18,000	1800	41.9	51.9	11,900	55,700
B3W2E	22,000	2200	54.9	77.5	6600	14,100
Increased Speed Spin Testing						
Disk	Maximum Speed (rpm)	Minimum Speed (rpm)	Stress at Flaw (ksi)	Disk Max Stress (ksi)	Predicted Life for 0.1" Flaw*	Total Cycles Tested**
SB-6	24,500	2450	75	96	3234	15,145
B1BW3B	24,100	2410	75	93	4437	17,500
B3W2E	25,700	2570	75	106	4796	16,038

*Predicted life at increased speed does not include crack growth at lower speed
**Total cycles include 10,000 cycles at low speed and balance at higher speed

All three disks containing embedded HA inclusions completed spin testing and successfully grew cracks from the inclusions. Disks SB-6 and B3W2E both burst prior to completion of the planned 7500 additional test cycles at increased speeds but tested beyond the initial life predictions. Disk SB-6 burst at 15,145 total cycles (10,000 cycles at 17,800 rpm followed by 5,145 cycles at 24,500 maximum rpm). Disk B3W2E burst at 16,038 total cycles (10,000 cycles

at 22,000 rpm followed by 6,038 cycles at 25,700 maximum rpm). The crack monitoring system did not indicate any crack growth in either of these tests prior to a vibration amplitude spike during the final cycle when the disks burst, as illustrated in figure J-9, tracking from right to left. Analyses had predicted that burst would occur at the same cycle as when the cracks reached the surface, so it is possible to conclude that the crack monitoring system was not sensitive enough to detect propagation while the crack remained subsurface.

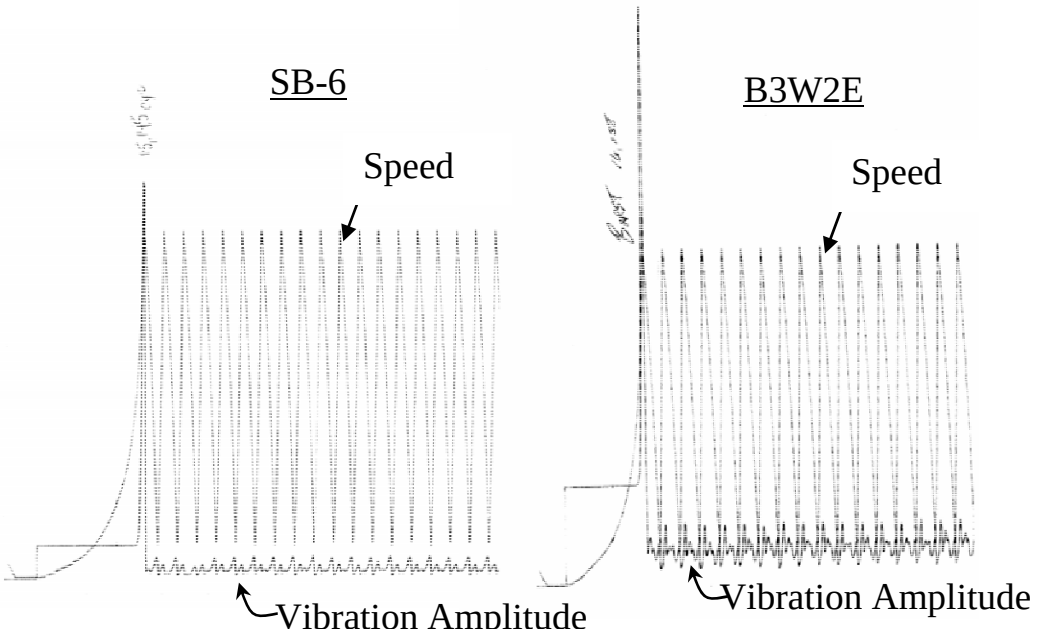

Figure J-9. Vibration Amplitude and Speed Recorded at End of Test of Burst Disks

Disk B1BW3B completed, without a burst, 17,500 total cycles of spin testing (10,000 cycles at 18,000 max rpm and 7,500 cycles at 24,100 max rpm). This disk was returned to Pratt & Whitney for additional inspections. FPI inspections did not indicate any surface connected cracks. The amplitudes from the normal incidence UT inspections (figure J-10) were within typical inspection-to-inspection variations with some increases and some decreases. However, when looking at the data as a whole, the amplitudes did follow a general downward trend. Since the crack was growing in a plane aligned with the inspection (normal to the surface), the crack tip itself had a weaker reflection than the core, and as it grew, it was likely disrupting the stronger reflection from the HA core. Meanwhile, the angled UT inspection amplitudes at 17,500 cycles increased with increasing test cycles, as had all of the prior amplitudes. Figure J-11 illustrates the change in amplitude for the angled scans relative to the normal scans. The angled inspections were all scanned from the disk axial face (Surface A), while the normal scans were from a combination of three surfaces. The same inspector completed all inspections.

In addition to the changes in amplitude, the scanned images indicated a measurable change in size of the inclusions in B1BW3B between 10,000 and 17,500 cycles. The normal incidence C-scans (figure J-12) indicated an apparent increase in radial length between 10,000 and 17,500 cycles. Normal incidence time-of-flight scans (figure J-13) also indicated an apparent increase

in length. There were multiple indications (figure J-14) associated with the fatigue crack (or cracks), possibly due to a faceted crack surface or crack branching. Consistent with the normal scans, the apparent radial length of the indication from the angled scans (figure J-15) increased by approximately a factor of 3 from 10,000 cycles to 17,500 cycles. Unlike the prior inspections of disk B1BW3B at 10,000 cycles, a separation of signals had developed at 17,500 cycles, indicating growth relative to the depth direction (figure J-16). While these inspections are not typically used to determine an actual size of a crack, a best estimate was that the resulting fatigue crack (or cracks) covered about 0.4″ radially and 0.2″ axially.

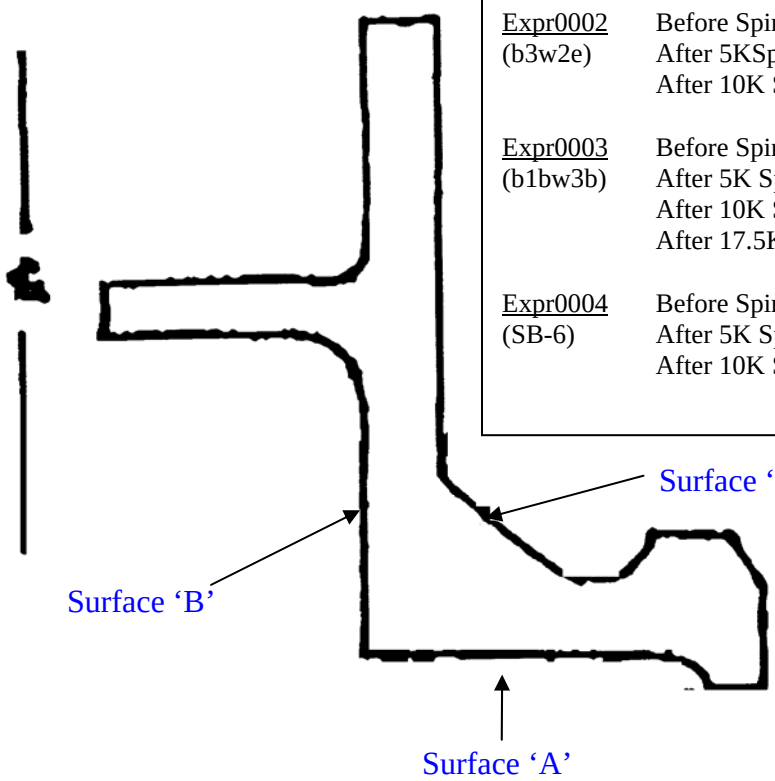

NORMAL INSPECTIONS		Surface A	Surface B	Surface C
Expr0002 (b3w2e)	Before Spin	27% of #1	126% of #1	20% of #1
	After 5KSpin	41% of #1	98% of #1	51% of #1
	After 10K Spin	41% of #1	51% of #1	63% of #1
Expr0003 (b1bw3b)	Before Spin	50% of #1	94% of #1	94% of #1
	After 5K Spin	208% of #1	104% of #1	73% of #1
	After 10K Spin	72% of #1	99% of #1	87% of #1
	After 17.5K Spin	41% of #1	61% of #1	81% of #1
Expr0004 (SB-6)	Before Spin	141% of #1	224% of #1	140% of #1
	After 5K Spin	171% of #1	184% of #1	90% of #1
	After 10K Spin	134% of #1	199% of #1	120% of #1

ANGLED INSPECTIONS		Surface A
Expr0002 (b3w2e)	After 5KSpin	36% of #1
	After 10K Spin	96% of #1
Expr0003 (b1bw3b)	After 5K Spin	42% of #1
	After 10K Spin	64% of #1
	After 17.5K Spin	112% of #1
Expr0004 (SB-6)	After 5K Spin	186% of #1
	After 10K Spin	343% of #1

Figure J-10. Summary of Normal Incidence and Angled UT Inspection Amplitudes

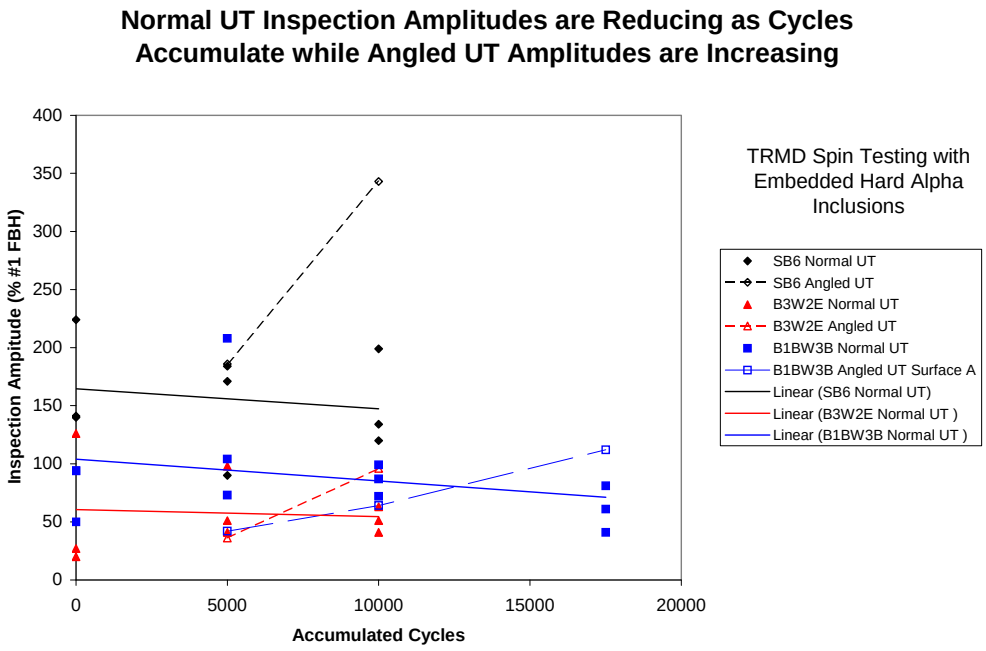

Figure J-11. Comparison of Changes in UT Inspection Amplitude vs Test Cycles

10k cycles

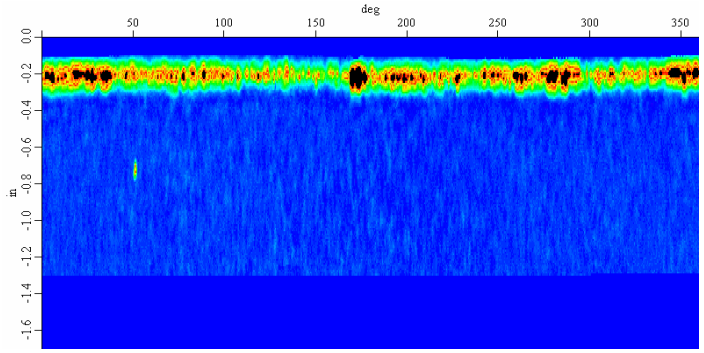

17.5k cycles

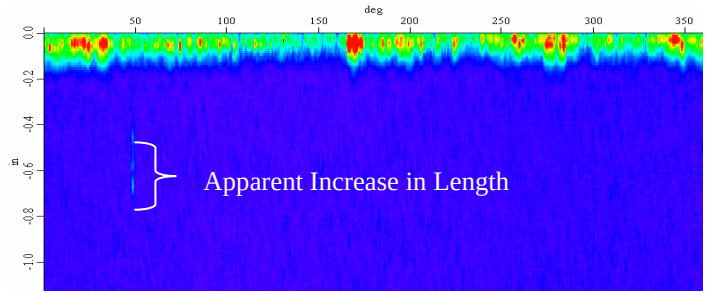

10 MHz normal incidence C-scan

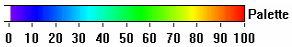

Figure J-12. Disk B1BW3B Normal Incidence C-Scans at 10,000 and 17,500 Cycles

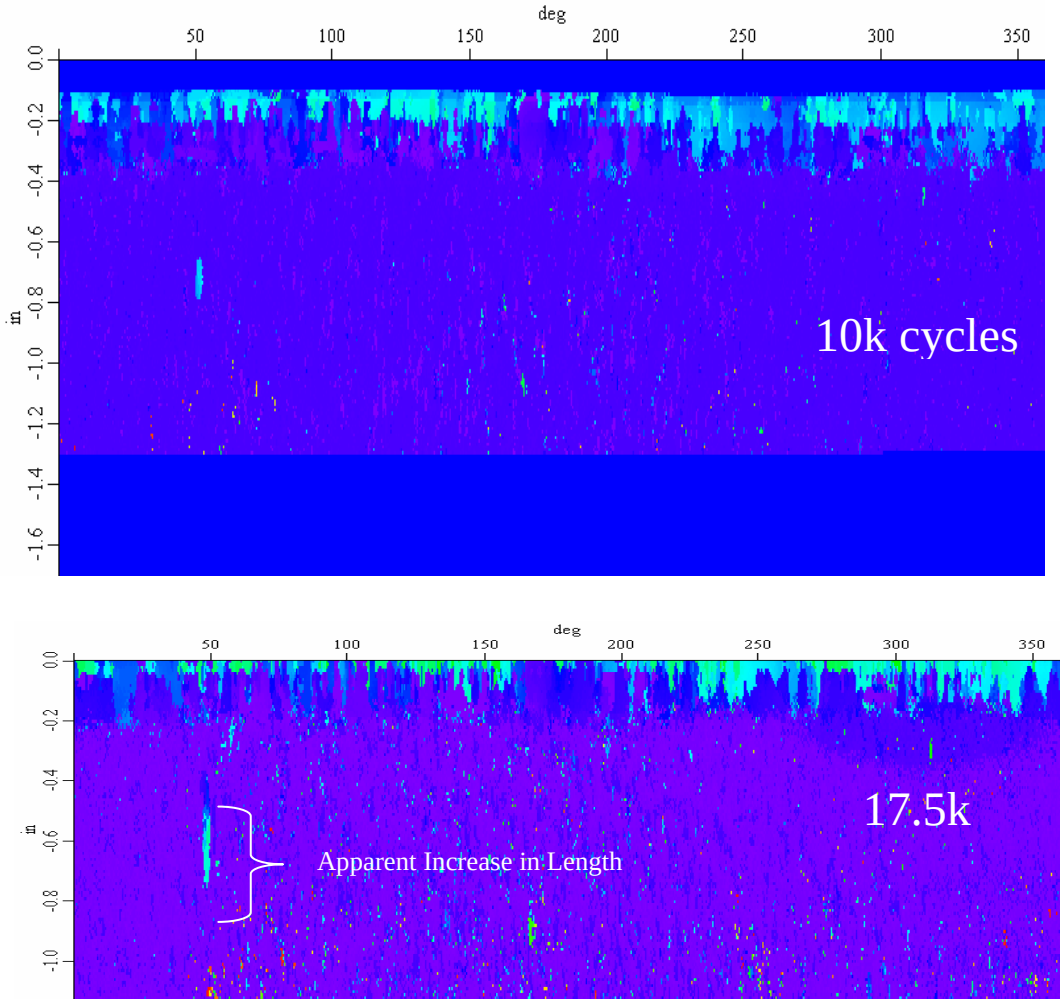

Figure J-13. Disk B1BW3B 10-MHz Normal Incidence Time-of-Flight Scans

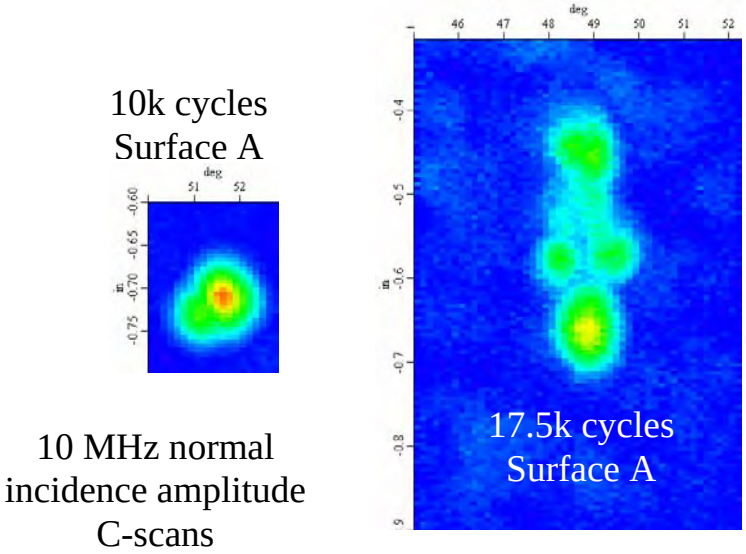

Figure J-14. Normal Incidence C-Scans Indicate 3 Times Growth at 17,500 Cycles

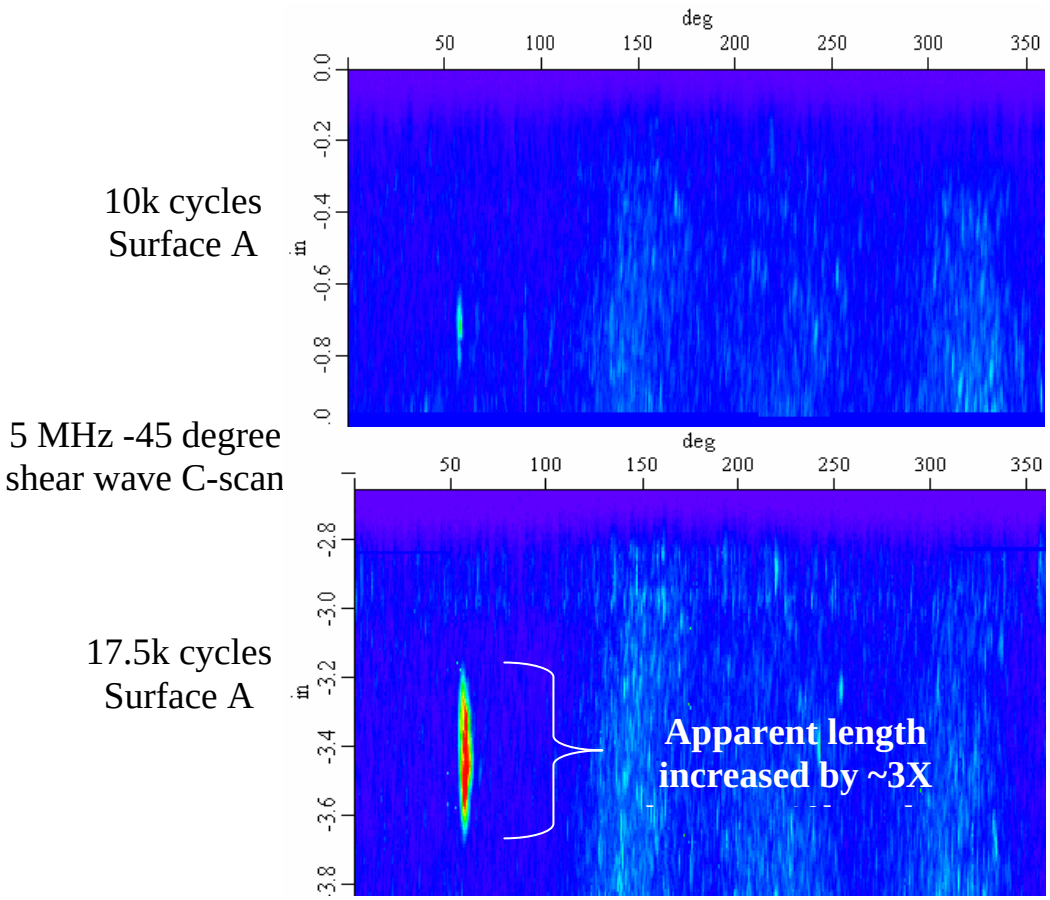

Figure J-15. Disk B1BW3B Angled C-Scans Indicate Growth at 17,500 Cycles

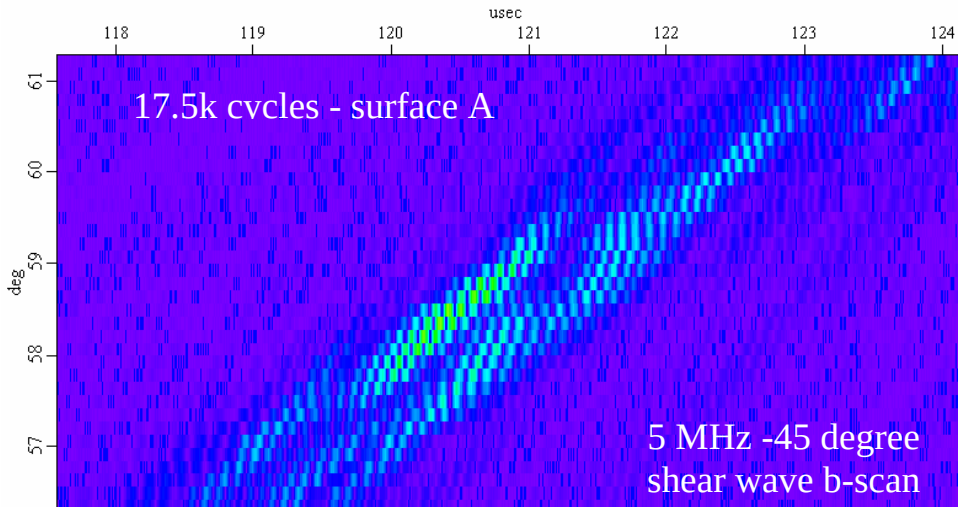

Figure J-16. Signal Separation was Observed in Disk B1BW3B at 17,500 Cycles

Upon completion of the conventional normal incidence UT inspections and the angled scans, disk B1BW3B was shipped to GE Aviation for an added multizone inspection. The disk was multizone inspected (#1 FBH calibration) from the bore face and bore directions. Comparison of the C-scans (figures J-17 and J-18) from before and after spin pit testing indicated a decrease in the reflected amplitude of the anomaly from both inspection directions, consistent with the trends observed from the conventional normal incidence inspections. To try and better understand this phenomenon, additional UT shear scans from the bore face (figure J-19) and bore (figure J-20) were also conducted at GE Aviation. The high-angle shear wave inspections produced a sizable indication, suggesting crack growth had initiated from the original HA indication and was propagating in the radial axial plane, consistent with the conclusions from the Pratt & Whitney angled scans.

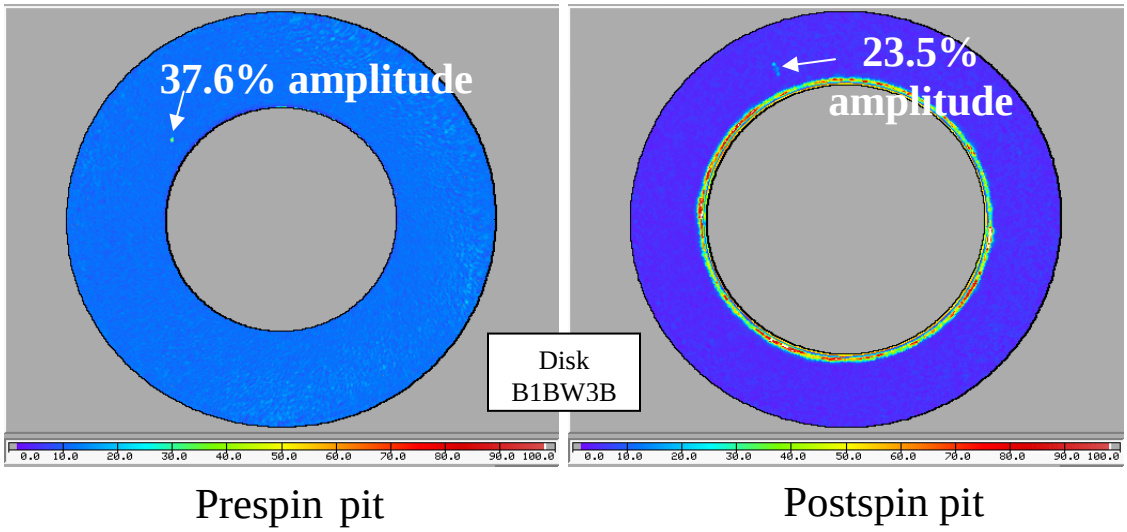

Figure J-17. Multizone UT Inspection of Bore Face Decreased Relative to Pretest Inspection

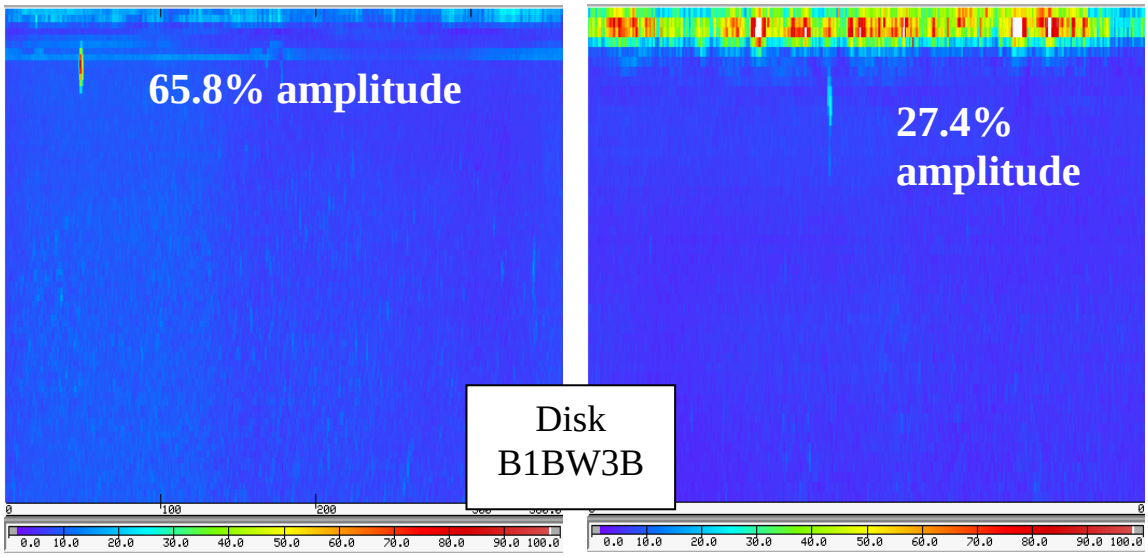

Prespin pit Postspin pit

Figure J-18. Multizone UT Inspection of Bore Decreased Relative to Pretest Inspection

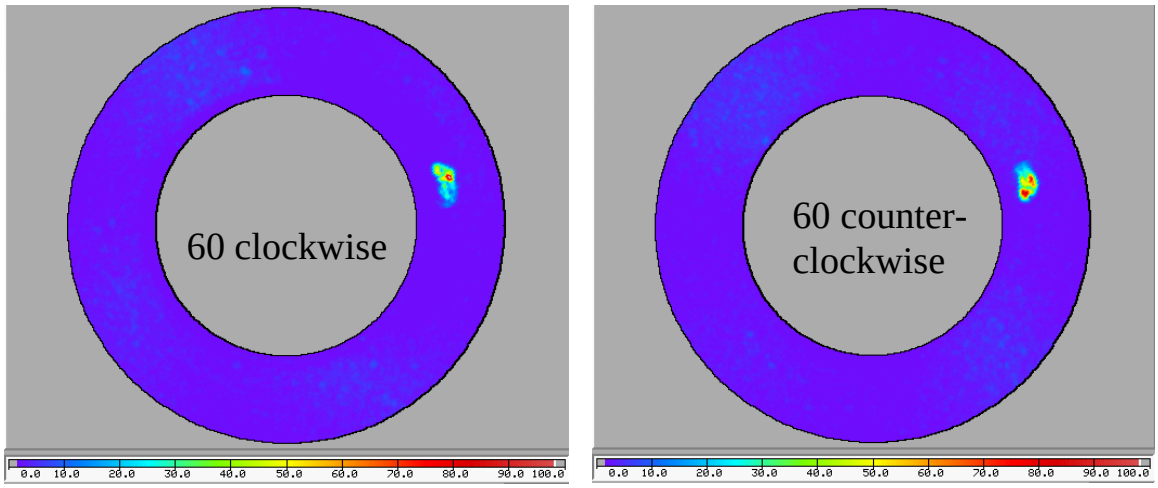

Postspin pit

Figure J-19. Disk B1BW3B 60-Degree Shear UT Inspection From Bore Face

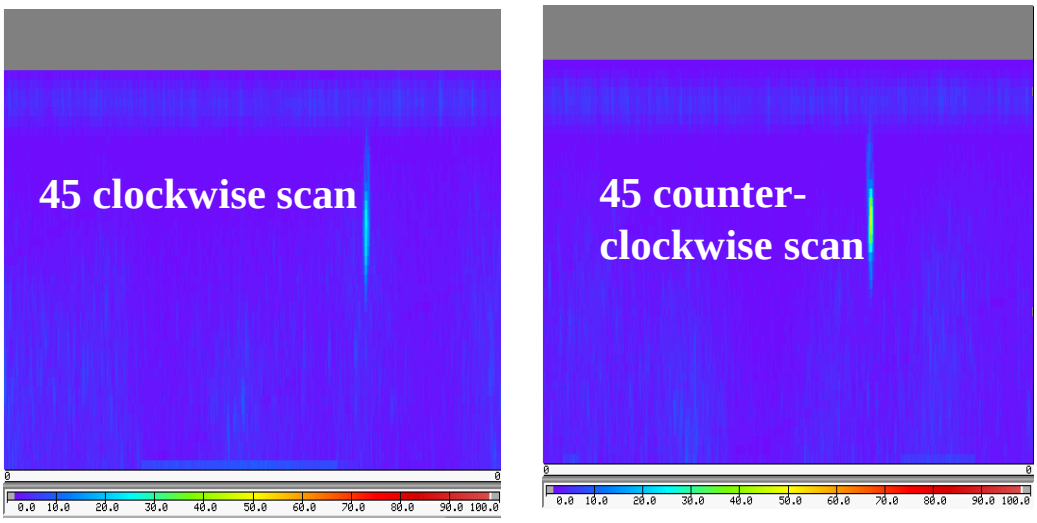

Postspin pit

Figure J-20. Disk B1BW3B 45-Degree Shear UT Inspection From Bore

J.4.1 POSTTEST FRACTOGRAPHIC INSPECTIONS.

Disks SB-6 and B3W2E were shipped to Pratt & Whitney for fractography after bursting in the spin rig. One side of the fracture surface was preserved on each of the disks. The mating surface on each disk, however, was covered with lead after becoming embedded in the lead bricks surrounding the spin rig. The goals of the fractography were to evaluate the crack growth from the embedded HA inclusions to identify the origin location of the fracture, map the size and shape of the inclusions, and determine the number of striations on the fracture surface. The fractography was performed by visual inspection with the assistance of a scanning electron microscope (SEM). Backscattered electrons were used in an attempt to enhance the images but had little effect.

Prior to completing the fractography on the spin disks, two coupon specimens previously fatigue tested at Southwest Research Institute were assessed to provide a baseline reference. Specimens LMI, a seeded specimen with 6% nitrogen core measuring 0.18″ x 0.06″ surrounded by a DZ measuring 0.25″ x 135″, and RMI F1, a natural embedded HA from the Contaminated Billet Study billet (same source as the natural HA in disks B1BW3B and B3W2E), were evaluated. The RMI F1 core measured 0.055″ long by 0.0204″ wide on average with an average DZ size of 0.17″ long and 0.039″ wide. Core fractures were brittle intergranular fractures with secondary cracks, in particular on the boundaries between the core and DZ. In the DZs, the fracture surfaces generally exhibited a brittle fracture mode of platelet alpha along with cleavage and secondary cracks. Beyond the DZ, the fractography was showing a cleavage fracture mode with secondary cracks in areas closest to the DZ. Further out, in addition to cleavage, there was striation formation with microvoids and secondary tearing cracks.

Fractography of the spin disks was initially completed on disk SB-6. The fatigue fracture initiated from the embedded HA seed. The HA was located approximately 0.18″ from the inside

dimension surface. The core measured approximately 0.198″ long and 0.1″ wide, approximately equal to the size and shape of the original seed core inserted into the mult. The shapes of the core and DZ are shown in figure J-21. Higher-magnification SEM fractography was completed in seven directions surrounding the inclusion. Figure J-22 illustrates the differences in topography in the core area, the DZ, and the crack progression area. Fracture features were similar to those observed in the seeded specimen with the exception that no striations were observed in the disk.

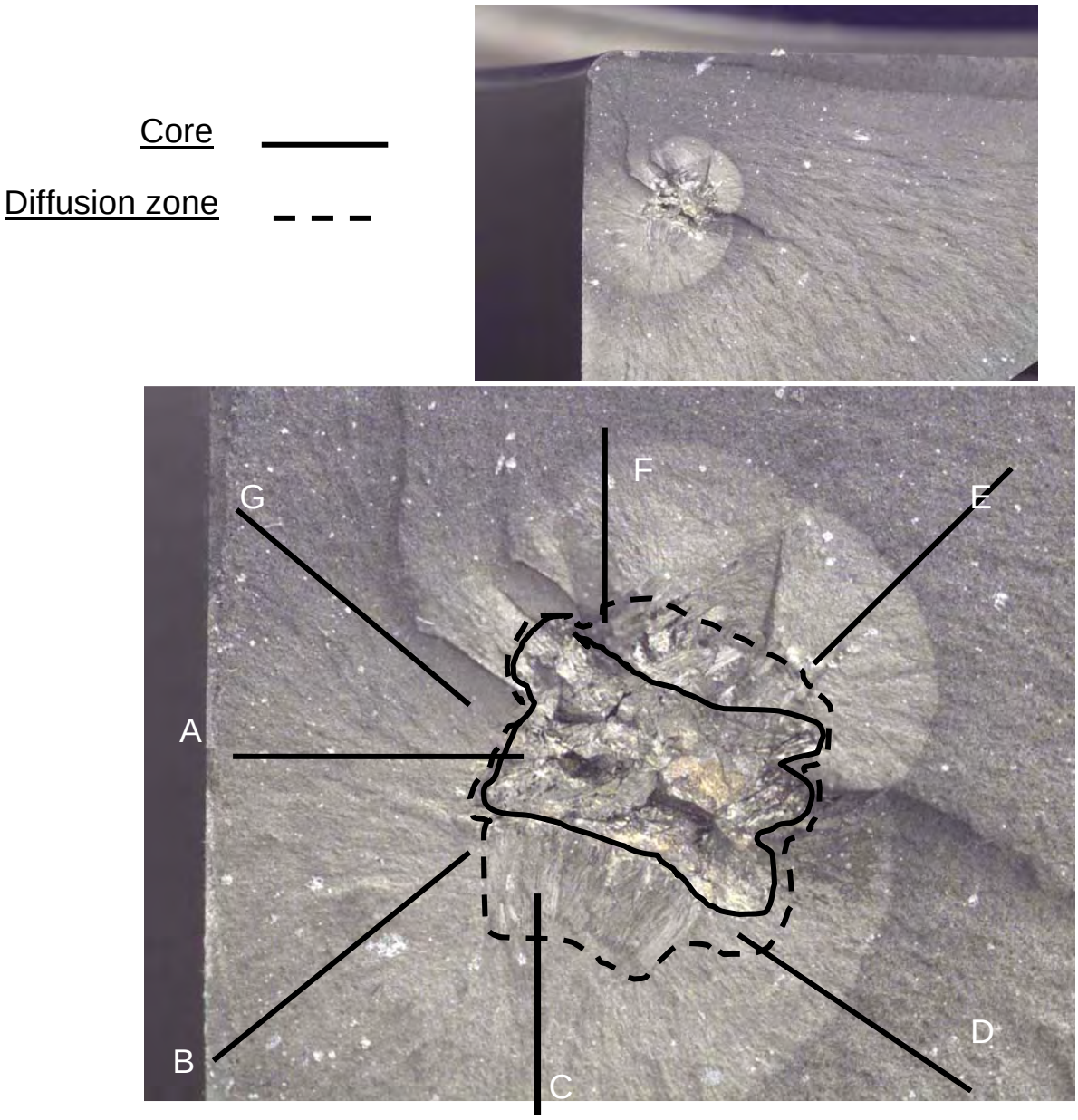

Figure J-21. Disk SB-6 Fracture Surface at Inclusion With Scanning Directions Identified

Disk SB-6

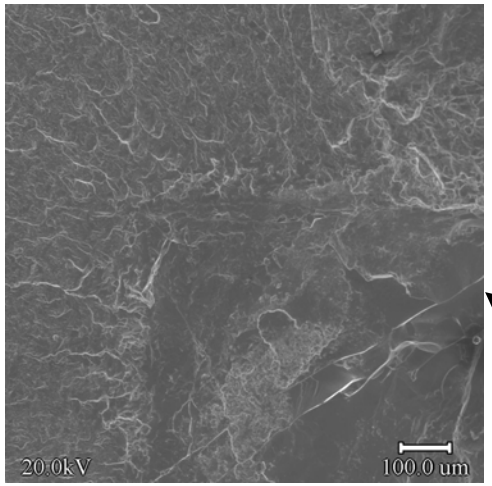

100x

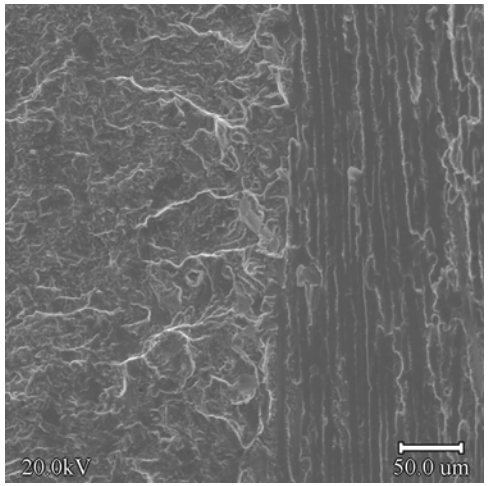

250x

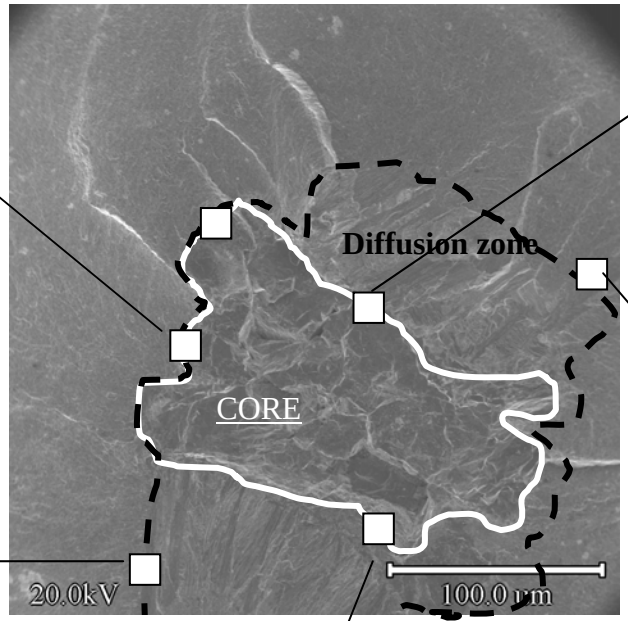

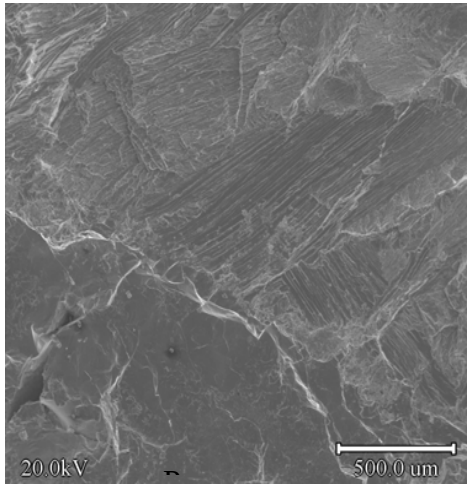

50x

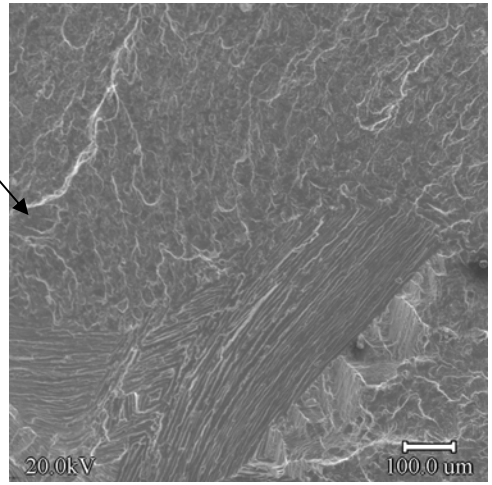

100x

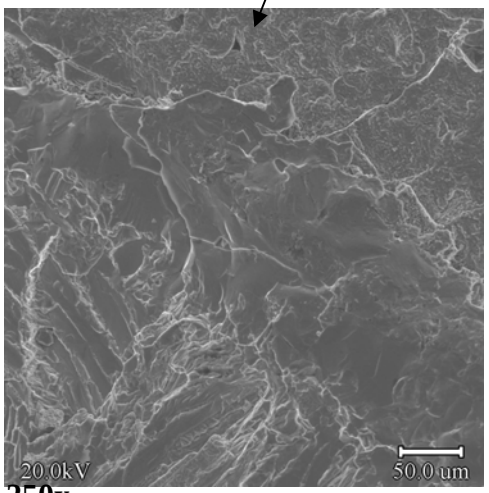

250x

Figure J-22. Fractography Features on the Borders of Core, DZ, and Crack Progressive Area

An examination of the fracture surface on disk B3W2E also indicated a fatigue fracture initiated from the interior HA inclusion (figure J-23). Fractographic features were examined in the core and DZ as well as in eight directions around the inclusion. The HA consisted of a smaller core within a larger elongated DZ (figure J-24). The core was segregated into two primary areas connected by a smaller narrow band of core. The location of the core was approximately 0.416″ from the axial face and 0.557″ radially outward from the edge of the bore. The DZ consisted of a narrow band measuring approximately 0.8″ long and 0.06″ wide on average. The boundaries of the DZ were defined based on differences in fractography features between the DZ and the base material. Table J-3 contains a summary of the fractography features observed from the DZ outward in the eight directions. No striations were observed on the fracture surface.

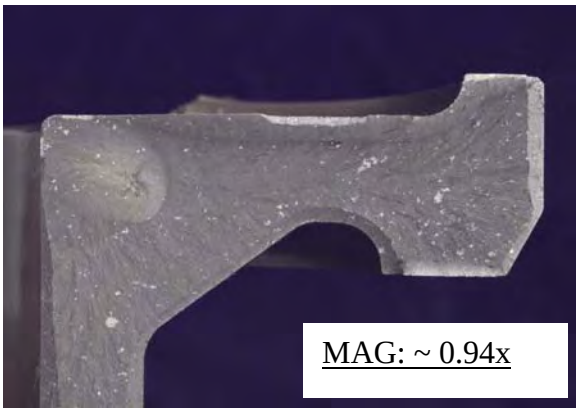

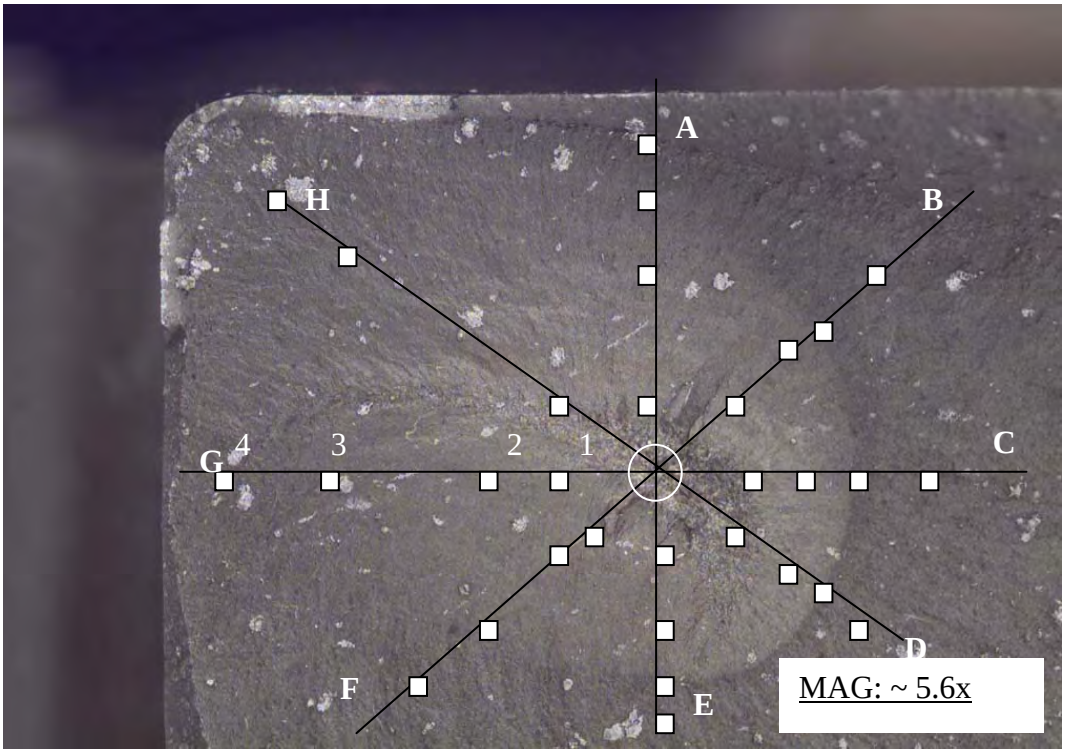

Figure J-23. Disk B3W2E Fracture Surface at Inclusion With Scan Directions Identified

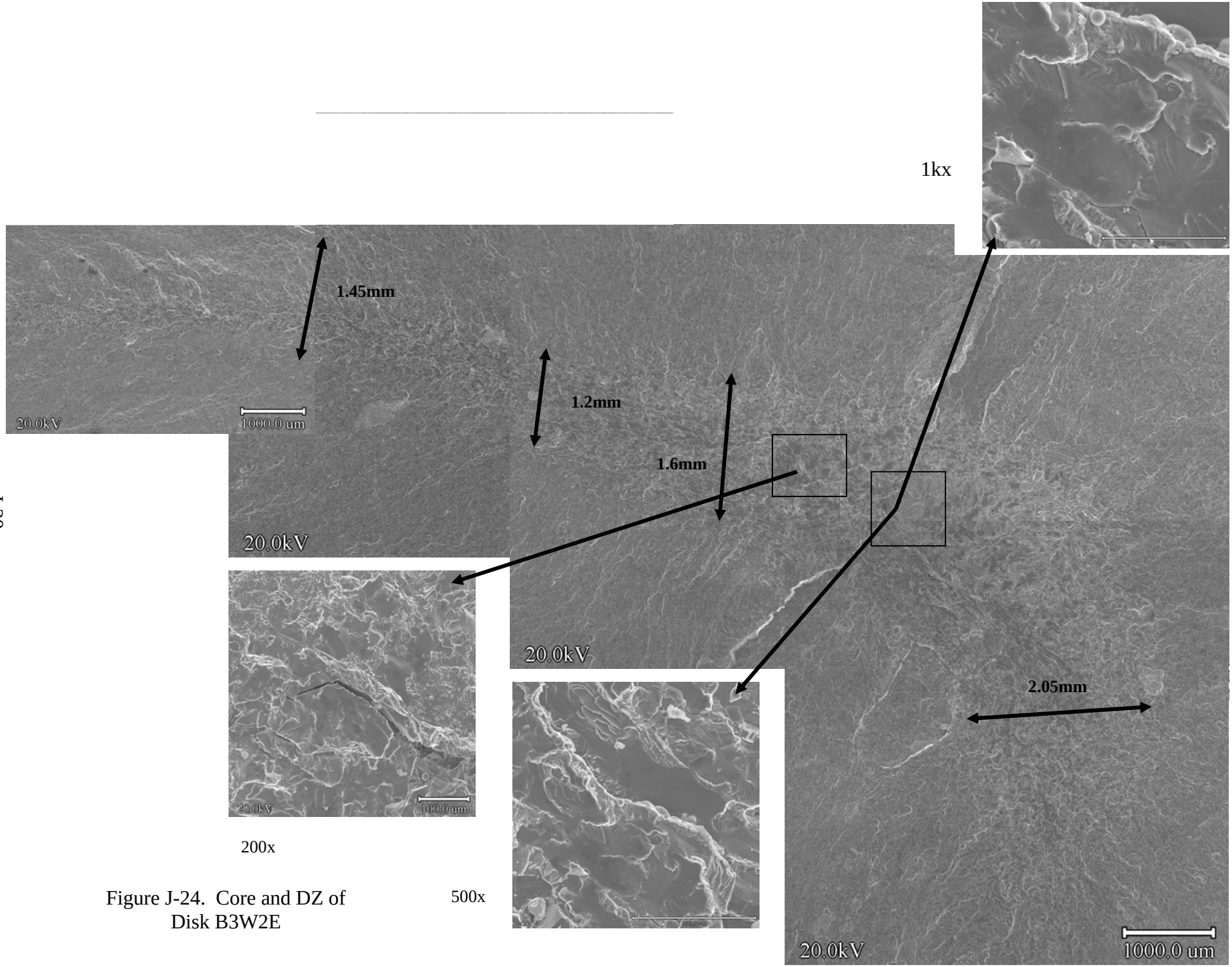

Figure J-24. Core and DZ of Disk B3W2E

Table J-3. Summary of Disk B3W2E Fracture Features vs Location

Direction	Point 1	Point 2	Point 3	Point 4
A	Feathery cleavage with secondary cracks	Feathery cleavage with secondary cracks	Feathery cleavage with secondary cracks	Feathery cleavage with secondary cracks
B	Cleavage with secondary cracks	Mix cleavage, tearing cracks, and voids	Mix voids, dimples, and secondary cracks	Dimples
C	Feathery cleavage with secondary cracks	Feathery cleavage with secondary cracks	Mix voids, dimples, and secondary cracks	Dimples, voids
D	Brittle platelet alpha and secondary cracks	Cleavage with secondary cracks	Mix voids, dimples, and secondary cracks	Dimples
E	Feathery cleavage with secondary cracks	Feathery cleavage with secondary cracks	Mix voids, dimples, and secondary cracks	Dimples
F	Feathery cleavage with secondary cracks	Feathery cleavage with secondary cracks, perhaps, striation formation	Mix cleavage, tearing cracks, and dimples	Dimples and tearing cracks
G	Feathery cleavage with secondary cracks	Cleavage with secondary cracks, voids	Cleavage with secondary cracks, voids	Dimples and tearing cracks
H	Brittle, platelet alpha and secondary cracks	Cleavage with secondary cracks	Cleavage with secondary cracks	Dimples and tearing cracks

Based on the lack of striations observed in disks SB-6 and B3W2E and the apparent crack growth in B1BW3B observed from the UT inspections, the TRMD Steering Committee agreed to discontinue testing of disk B1BW3B. The disk was scheduled to be cut open for fractography rather than risk damaging the fracture surface with continued testing. The UT inspections were used to identify the location of the crack on the disk (figure J-25) and define initial cutting planes beyond the boundaries of the crack. After the section was removed from the disk, the axial and radial faces were progressively polished until the edge of the crack was reached and the crack was then pulled open to observe the fracture surface. Unlike the fractographic assessments of burst disks, SB-6 and B3W2E, some limited striations were identified at a single location on disk B1BW3B. However, there was not a significant amount of striations to conclusively estimate the crack growth life.

The crack in disk B1BW3B was elliptical shaped with the longer axis following the orientation of the HA DZ, which was also oriented in the direction of the stress gradient, normal to the corner of the bore. The crack front measured approximately 0.345″ in the axial direction and 0.283″ in the radial direction (figure J-26). The fracture surface was examined using a field emission electron microscope. Boundaries of the HA core, DZ, and base material were identified

based on the fracture surface topography (figures J-27 and J-28). The core measured 0.073 inches long by 0.036″ wide and was centered 0.518″ from the bore and 0.275″ from the disk axial face. The DZ surrounded the core and measured approximately 0.06″ wide on average by 0.37″ long.

Figure J-25. Location of Crack Identified on Disk B1BW3B by UT Inspections

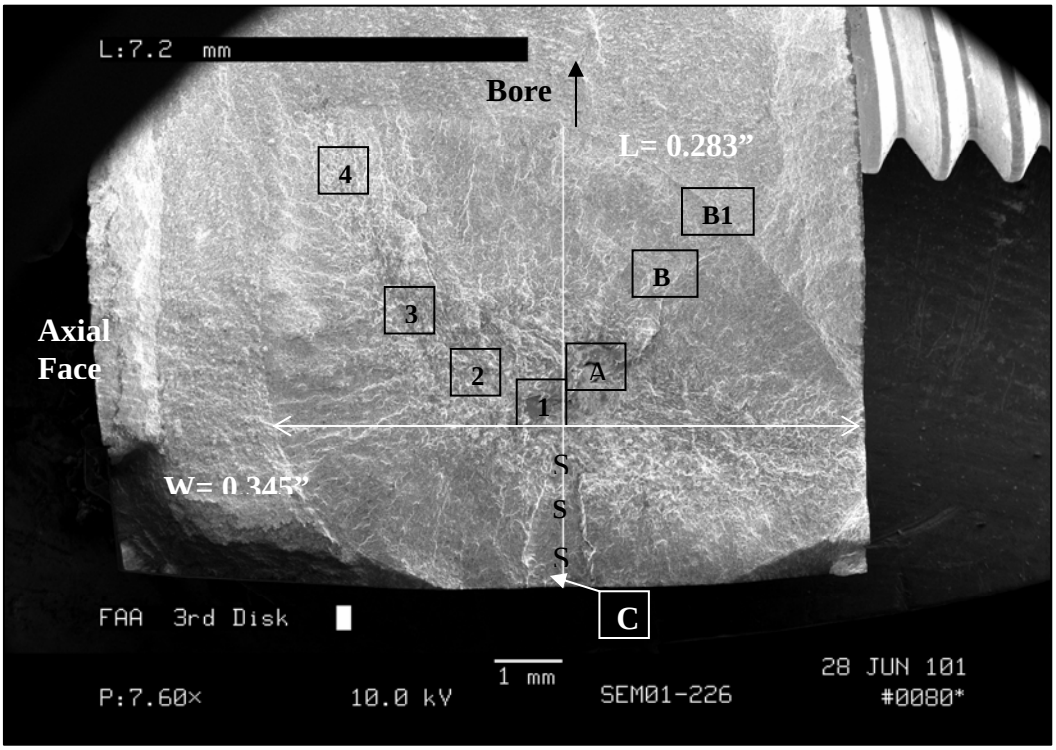

Figure J-26. Dimensions of Fatigue Progression Area

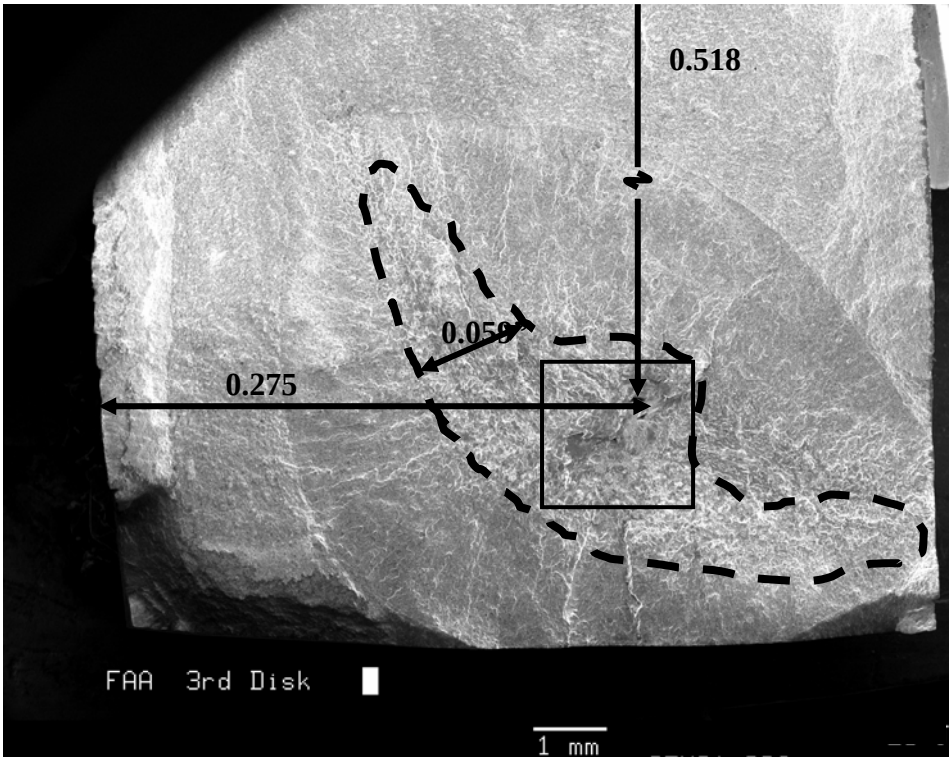

Figure J-27. Outline of HA DZ and Location of Core

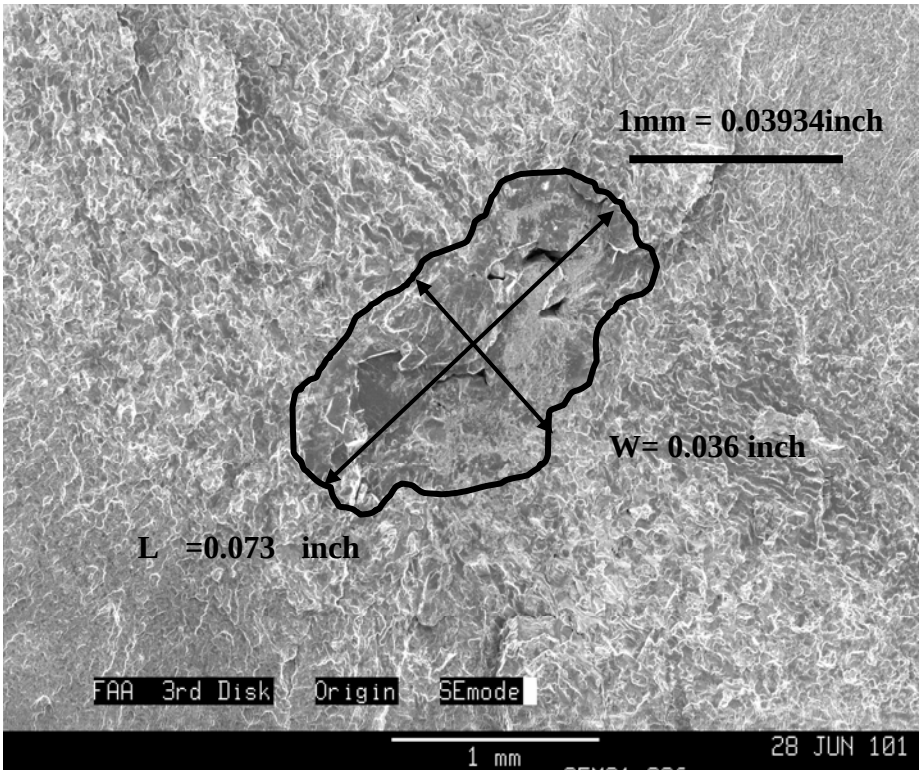

Figure J-28. Dimensions of HA Core

Table J-4 and figures J-29 through J-31 summarize the features observed on the fracture surface. A fractographic assessment of the core area identified brittle transgranular fractures with secondary cracks. In the DZs, the fracture surfaces generally exhibited a brittle fracture mode of platelet alpha along with cleavage and secondary cracks. Beyond the DZ, the fractography showed a mixed mode with cleavage with secondary cracks, dimples, and (in one location) striation formation.

Table J-4. Disk B1BW3B Fractography Features

Direction	Point 1	Point 2	Point 3	Point 4
Bore corner	Brittle platelet alpha and secondary cracks	Brittle platelet alpha and secondary cracks	Brittle platelet alpha, secondary cracks, and voids	Mix cleavage, striation formation, secondary cracks, and dimples
Rim	Feathery cleavage with secondary cracks	Feathery cleavage with secondary cracks and voids	Mix cleavage with, secondary cracks and voids	Mix cleavage, with secondary cracks, voids, and dimples
Bore away from corner	Brittle transgranular alpha and secondary cracks (Point A)	Cleavage with secondary cracks (Point B)	Cleavage with secondary cracks (Point B1)	

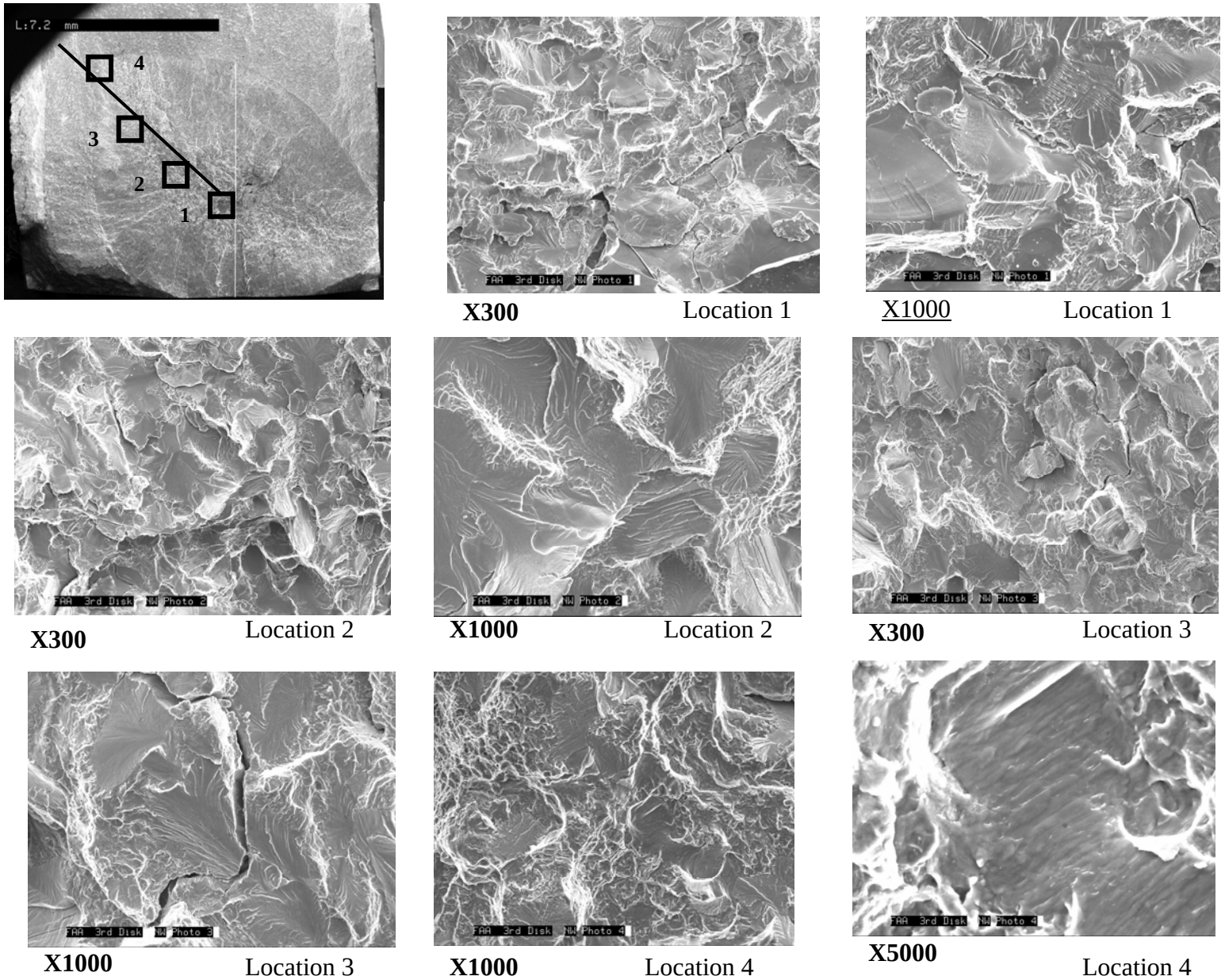

Figure J-29. Diffusion Zone and Crack Progression Fractography in Direction Toward Corner of the Bore

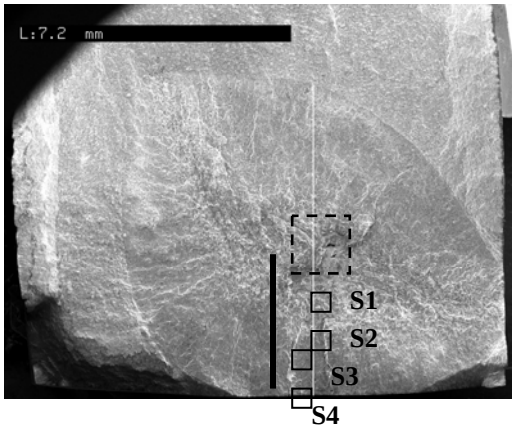

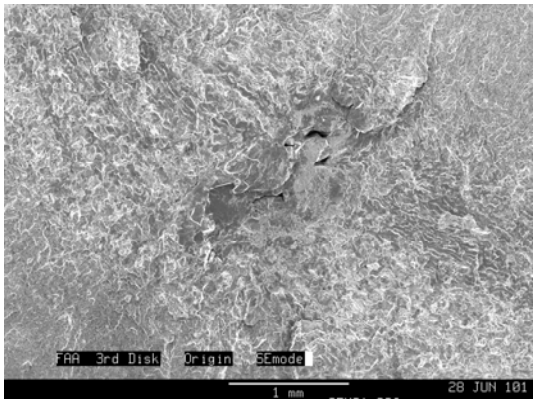

X1000 Hard Alpha Core

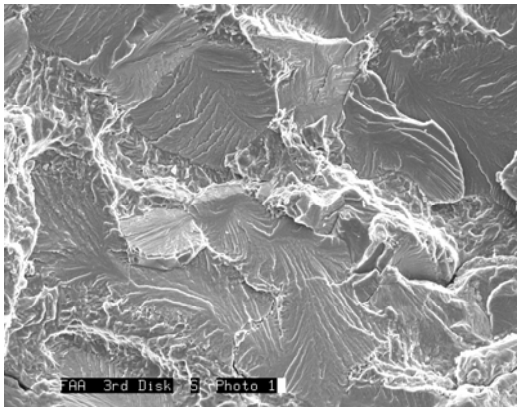

X1000 Location S1

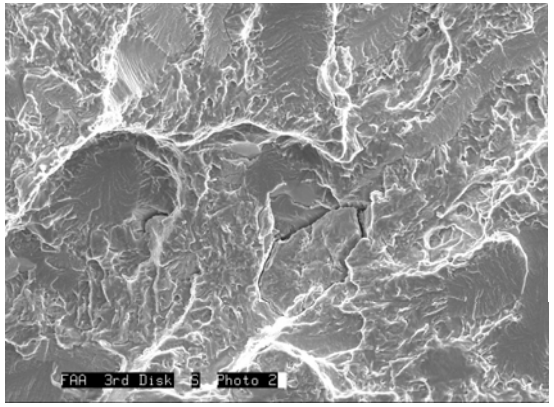

X1000 Location S2

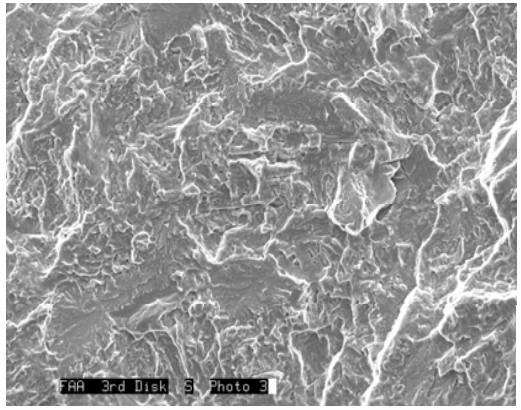

X1000 Location S3

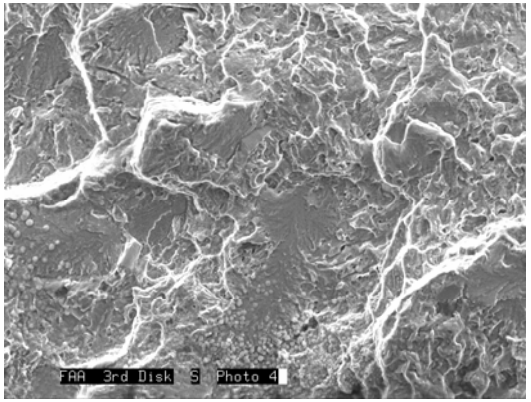

X1000 Location S4

Figure J-30. DZ and Crack Progression Fractography in Direction Toward Rim

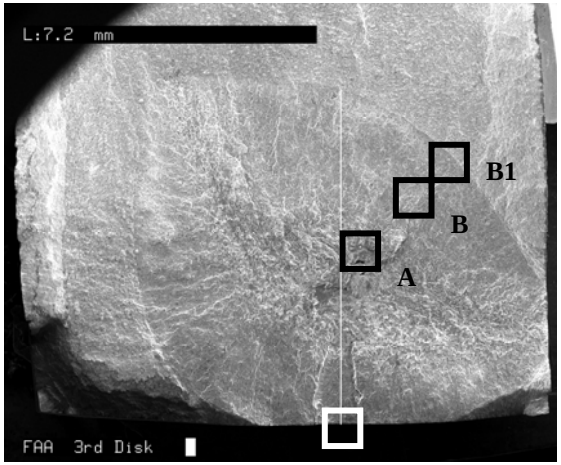

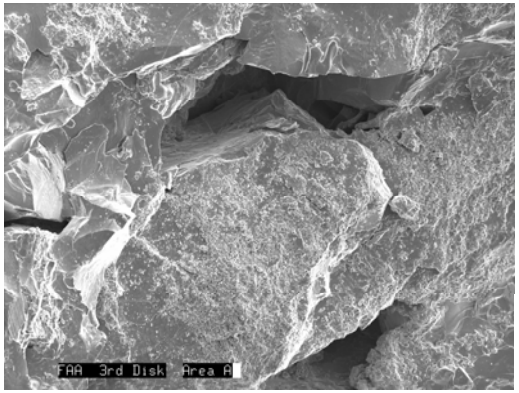

X250 **Area A**

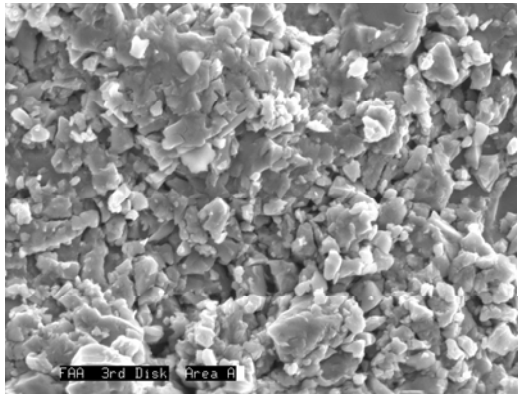

X5000 **Area A**

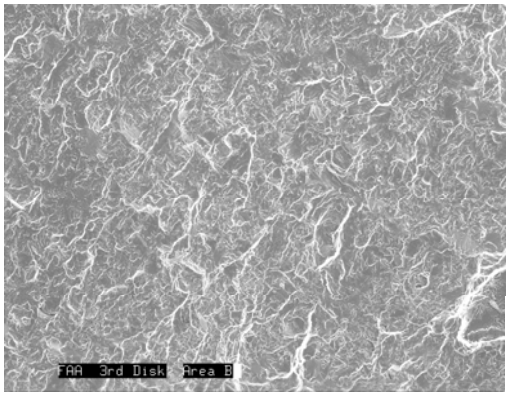

X300 **Area B**

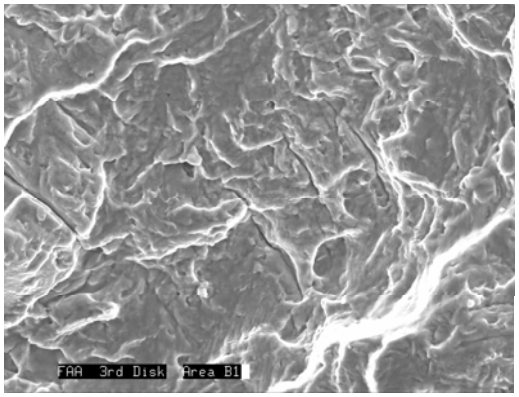

X2500 **Area B1**

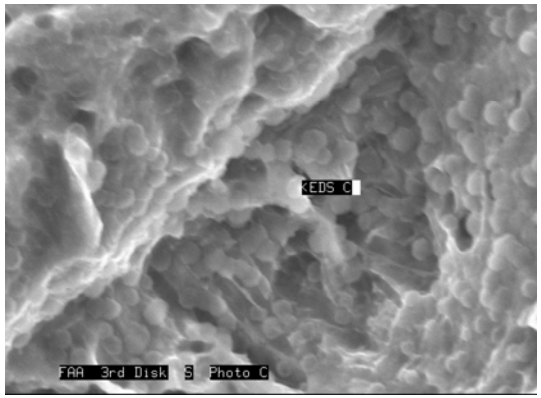

X5000 **Area C**

Figure J-31. DZ and Crack Progression Fractography in Direction Toward Bore Away From Corner and in a Single Location in the Direction Toward the Rim

J.4.2 FLIGHT_LIFE COMPARISONS TO TEST DATA.

Results from the fractographic assessments of the three spin disks were used to evaluate the crack growth predictions from Flight_Life. Pretest crack growth predictions were updated to include the measured HA core sizes and locations. Figure J-32 identifies the locations of the HA core centers. Table J-5 summarizes the test speeds, disk stresses, test durations, and predicted crack growth lives for each of the three disks. No incubation was assumed in the analyses. For disk SB-6, the analysis assumed the initial crack was circular with a diameter equal to the diameter of the core. For disks B3W2E and B1BW3B, the analyses assumed the initial crack was circular with a diameter equal to the maximum length of the core in the plane of the crack. The crack growth predictions for SB-6 and B3W2E, which had both run to rupture, matched the test results within a few hundred cycles. For disk B1BW3B, the final crack size was assumed equal to 0.345″, the axial width of the actual crack. The predictions for disk B1BW3B exceeded the actual test results by approximately 1000 cycles, still acceptable agreement. Scatter in material crack growth rates (figure J-33) could account for the variability in actual to predicted crack growth lives.

Disk	Surface	Depth (in.)
SB-6	A	0.410
	B	0.230
B3W2E	A	0.410
	B	0.550
B1BW3B	A	0.275
	B	0.518

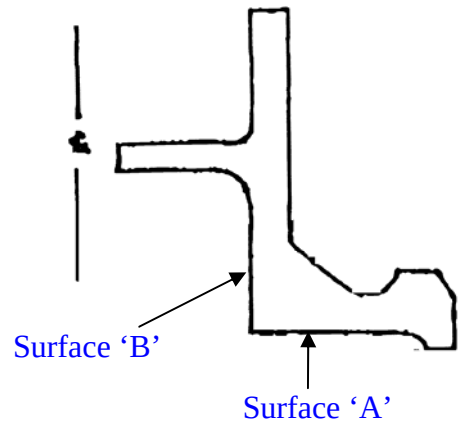

Figure J-32. Locations of HA Core Centers

Table J-5. Test Speed, Stress, and Life Predictions for Spin Disks

Initial 10,000 Cycles of Testing						
Disk	Maximum Speed (rpm)	Minimum Speed (rpm)	Stress at Flaw (ksi)	Disk Max Stress (ksi)	Initial Crack Diameter (inch)	10,000 Cycle Diameter (inch)
SB-6	17,800	1780	40.1	50.7	0.100	0.107
B3W2E	22,000	2200	54.4	77.5	0.074	0.108
B1BW3B	18,000	1800	39.4	51.9	0.073	0.074
Increased Speed Spin Testing						
Disk	Maximum Speed (rpm)	Minimum Speed (rpm)	Stress at Flaw (ksi)	Disk Max Stress (ksi)	Predicted Total Life (cycles)	Total Cycles Tested (cycles)
SB-6	24,500	2450	75.9	96	15,335	15,145
B3W2E	25,700	2570	74.3	106	16,035	16,038
B1BW3B	24,100	2410	70.6	93	18,699	17,500

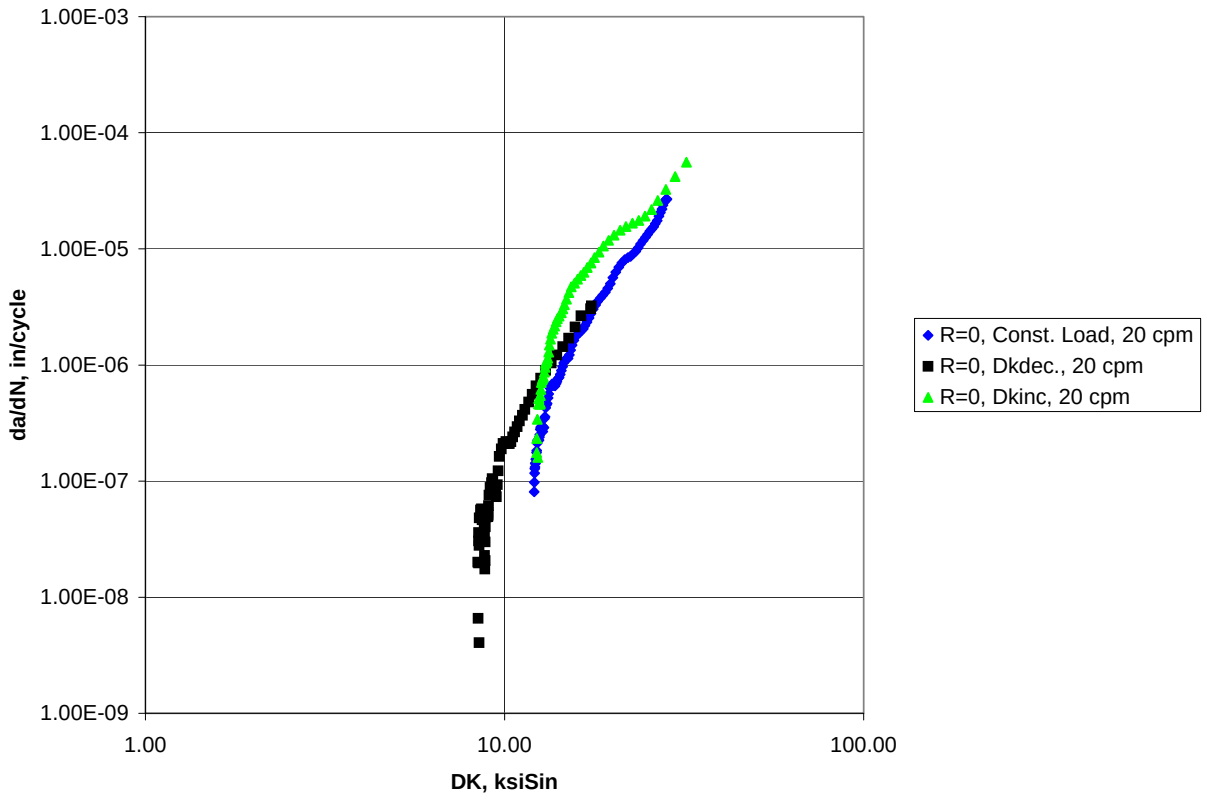

Figure J-33. Ti-6Al-4V Vacuum Crack Growth Rates at Room Temperature

The predictions for the spin test disks based on starting crack sizes equal to the core diameter agreed very well with the spin pit test results better than expected, considering the potential variability in initial crack formation. However, for disk SB-6, this assumption resulted in an assumed initial crack size smaller than the full size of the HA seed core (figure J-34). There were expectations that, for the crack growth portion of the disk life, an analysis based on HA core area would have been more representative. A follow-on sensitivity study, using core area rather than diameter for disk SB-6, reduced the predicted life from 15,335 to 12,718 cycles (figure J-35). The predictions are still acceptably close to the test results. Contrary to the assumptions used by the Rotor Integrity Sub-committee to set up the initial HA anomaly size distributions, for both the seeded HA as well as the natural HA, the test experience indicates a closer correlation of initial crack size to the core size than to the total core plus DZ size.

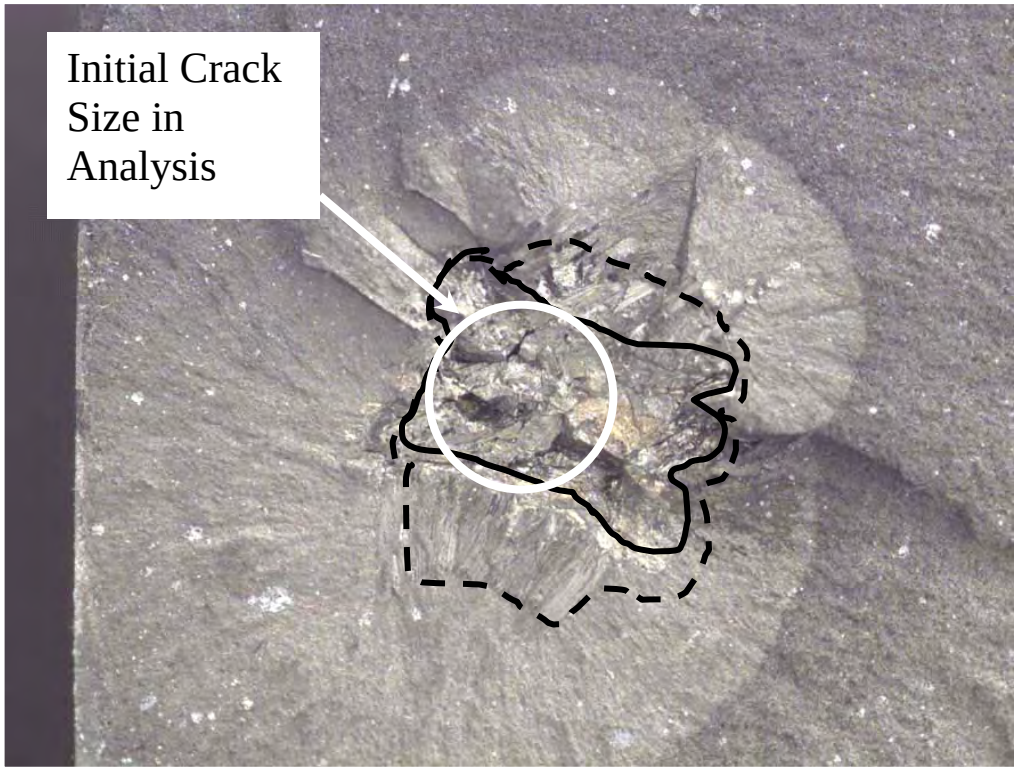

Figure J-34. Disk SB-6: Initial Analysis Based on Core Diameter

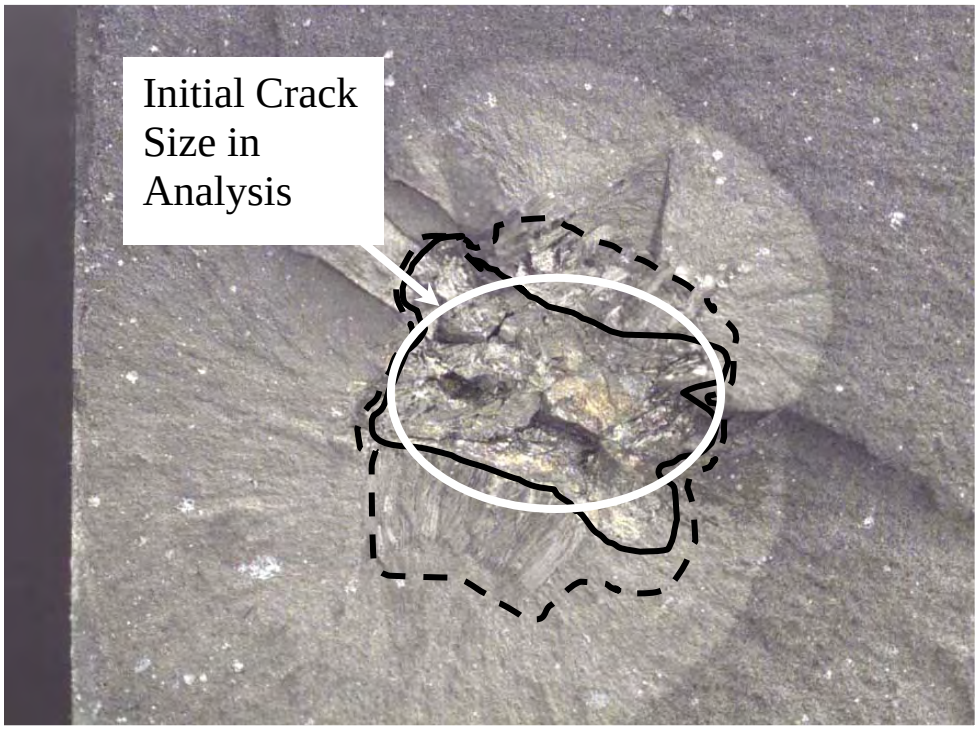

Figure J-35. Disk SB-6: Follow-Up Analysis Based on Core Area

J.4.3 VACUUM CRACK GROWTH SPECIMEN TESTING.

To verify that the fatigue crack growth (FCG) properties for the spin test disks were comparable to the assumptions in the analysis, vacuum FCG tests were performed with 2″ compact tension (C(T)) specimens machined from the spin disks. The specimens were machined from locations in the disk circumferentially away from the HA inclusions. Specimen thickness was 0.5″. The crack growth plane in the specimens was aligned with the crack growth plane (the axial/radial plane) in the spin disks (figure J-36). All tests were conducted at room temperature at a stress ratio of $R = 0.1$.

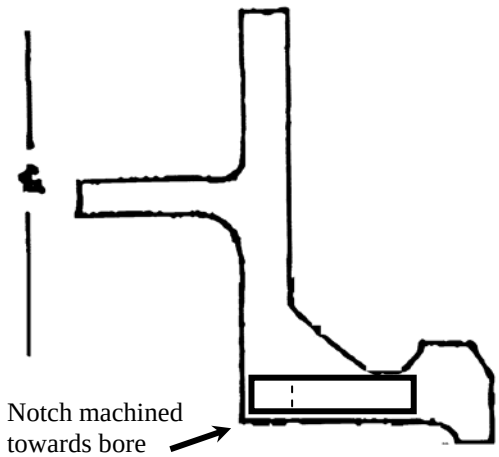

Figure J-36. Crack Growth Specimen Orientation in Spin Disks

Precracking in a vacuum was attempted because of concerns about introducing moisture into the crack if it was precracked in air. Attempts to precrack the first C(T) specimen from disk B3W2E in the vacuum chamber failed to initiate a crack after 3 million cycles at progressively higher stress intensities up to $\Delta K = 38$ ksi√in. The specimen ultimately cracked at the fixturing pinhole. The remaining specimens were successfully precracked in air, consistent with the TRMD-I vacuum FCG tests.

A total of seven vacuum FCG tests on three specimens from two disks were completed. The region II (Paris regime) tests were all conducted at about 20 cpm, consistent with the TRMD-I testing, while the region I (near-threshold regime) tests were conducted at 10 Hz. No significant sensitivity to testing frequency was observed. The test results were very repeatable and agreed well with most of the data from the tests completed at GE during TRMD-I (figure J-37). Note that TRMD-I tests were conducted with either a surface crack specimen (401-4) or a single-edge notch button head specimen (407-4A and 407-4B). All region I tests were run with decreasing ΔK except for the constant load amplitude test 401-4 (TRMD-I), which exhibited a higher threshold (lower FCG rate) than the decreasing-ΔK tests. All region II tests were run with constant load amplitude except for the increasing-ΔK test 407-4B (TRMD-I), which exhibited a higher FCG rate than the constant load amplitude tests. Additional specimens tested under TRMD-II had uneven crack growth or failed from the grips. Those results are not recommended for use in life-prediction models, and hence were not included in the summary.

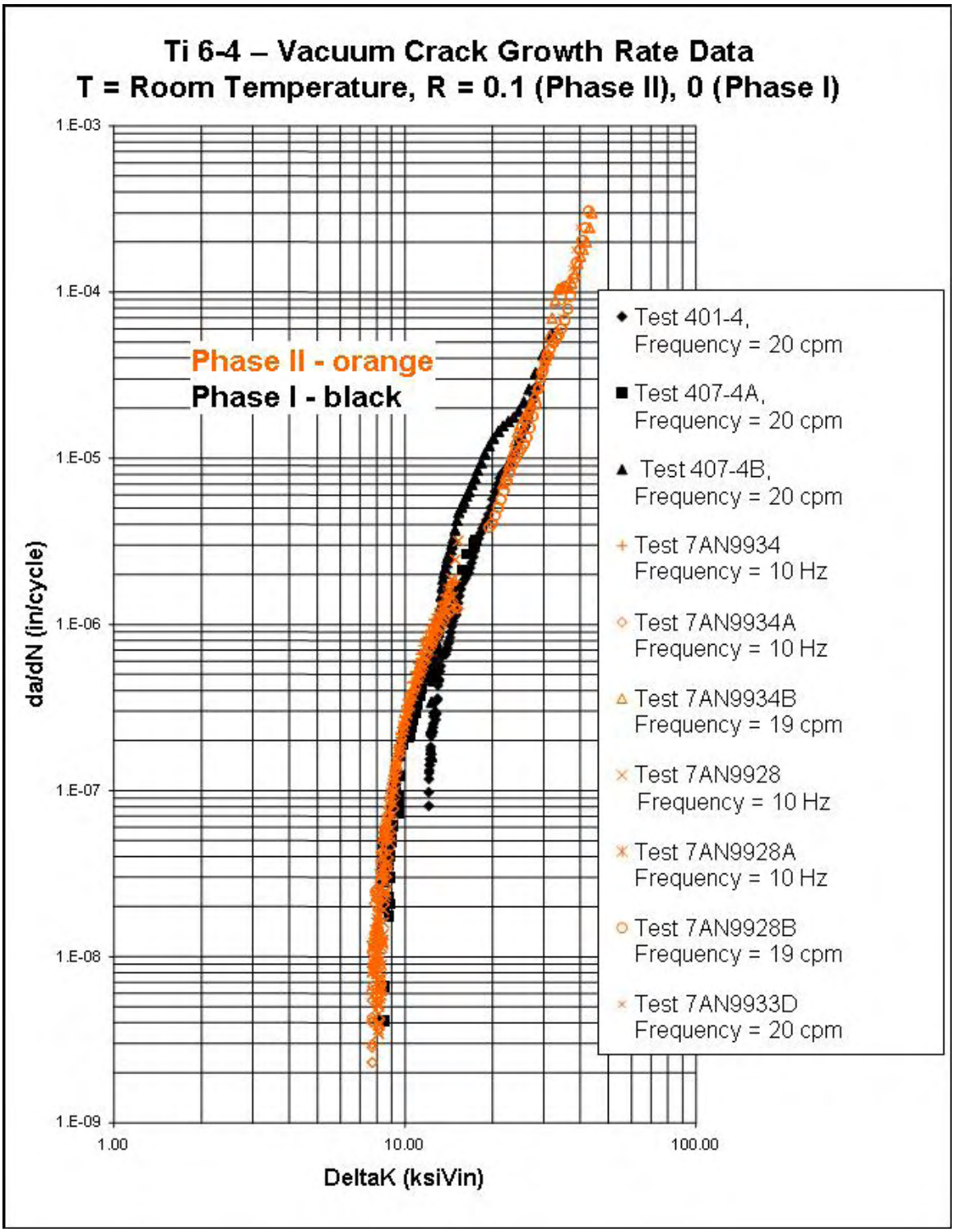

Figure J-37. Comparison of TRMD-I and II Vacuum Fatigue Crack Growth Test Results

J.5 SUMMARY.

The spin test program for the three disks containing embedded HA anomalies provided valuable lessons learned in areas of material deformation modeling, nondestructive testing inspections of HA anomalies, real-time crack detection, characteristics of fatigue crack progression from HA anomalies, and analytical modeling for FCG of embedded anomalies. The following are some of the more significant specific lessons learned under this test program:

1. The DEFORM predictions completed under TRMD-I for tracking the location of the HA anomalies through the forging process agreed well with UT inspection and posttest fractography results.

2. Angled UT inspections amplitudes and C-scan imaging provided more consistent indications of crack growth than did normal incidence UT inspections. Additional development is needed to reliably detect embedded crack growth in rotating disks.

3. Fatigue striations could not be consistently observed with sufficient clarity on the fracture surfaces of these titanium forgings to estimate fatigue crack growth rates.

4. Predictions of initial crack sizes for crack growth analyses of embedded HA anomalies agree more closely with the HA core size than core plus DZ size.

5. Precracking tests in vacuum indicated far greater resistance to crack initiation than testing in air.

J.5 REFERENCE.

J-1. Leverant, G.R., et al., “Turbine Rotor Material Design,” FAA report DOT/FAA/AR-00/64, December 2000.

APPENDIX K—VACUUM FATIGUE CRACK GROWTH TESTING

K.1 INTRODUCTION.

Vacuum fatigue crack growth (FCG) tests were performed at Honeywell and GE Aviation during Phase II of the Turbine Rotor Material Design (TRMD) program on four different materials: Ti-6242, Waspaloy, IN-718 (test matrix divided between GE Aviation and Honeywell), and U720. This appendix contains brief descriptions of the testing system, specimens, test procedures, material pedigree, test matrices, and test results.

K.2 TEST EQUIPMENT.

All FCG testing at Honeywell was performed on a 20-kip MTS servohydraulic test system. The closed-loop feedback for this test frame was Fracture Technology Associates' direct current electric potential drop system interfaced to a MTS 458 analog controller. The test frame was aligned in accordance with American Society for Testing and Materials (ASTM) E 1012-93a for a thick rectangular specimen using four strain gauges.

The vacuum system was a Centorr model S-60-Ind-Cyo8-A-10 with a Cryogenics model CT8 cryopump. The pressure in the vacuum chamber was monitored by two ion gages and the environment by a Hiden Analytical 201:60-R 3.11 R Quadrupole. This system is capable of achieving pressure levels in the upper to mid 1×10^{-8} torr range in approximately 24 hours.

Specimen heating was done by a 3-kW Ameritherm induction system.

K.3 SPECIMEN DESCRIPTIONS.

Two types of specimen geometries were employed in this testing. Most tests were conducted using a surface-crack tension (SC[T]) specimen, also known as a Kb bar specimen. A specimen drawing for the GE Aviation Kb bar specimen is provided in figure K-1, and a specimen drawing for the Honeywell SC(T) specimen is provided in figure K-2. These specimens have a rectangular cross section in the gage section of nominal dimensions 0.168 by 0.400 inch (GE Aviation) or 0.226 by 0.450 inch (Honeywell). A semielliptical crack is centered on one of the wide faces. This crack is initiated from an electro-discharge machining (EDM) notch with initial dimensions 0.007 inch deep by 0.014 inch long (GE Aviation) or 0.010 inch deep by 0.020 inch long (Honeywell). The GE Aviation specimen has buttonhead ends, and the Honeywell specimen is threaded.

GE used a single-edge notch button head (SENBH) specimen to obtain near-threshold data. A specimen drawing is provided in figure K-3. This geometry has a nominal gage section of 0.100 by 0.400 inch with a 0.010-inch-deep EDM notch on one narrow face of the specimen.

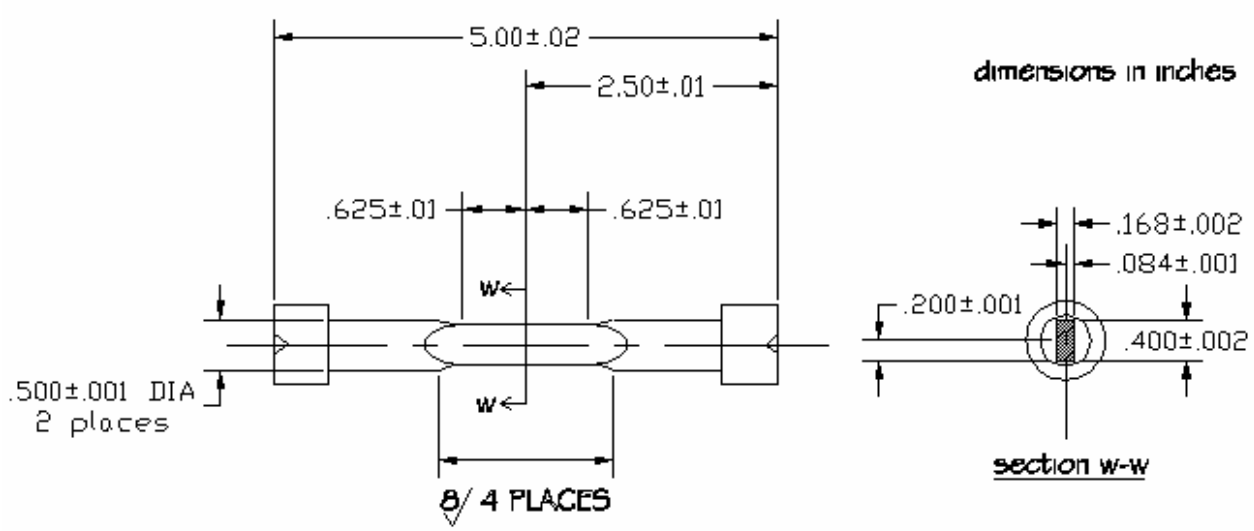

Figure K-1. GE Aviation Kb Bar Specimen Drawing

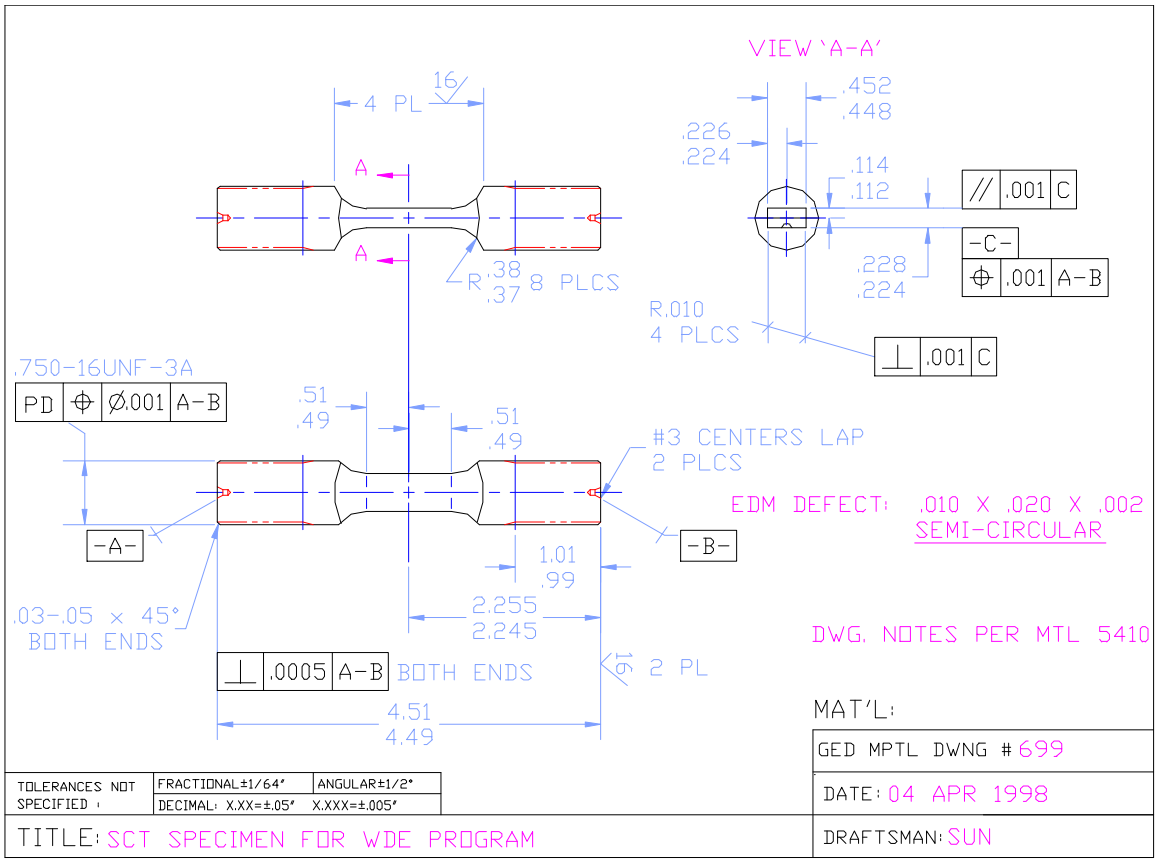

Figure K-2. Honeywell SC(T) Specimen Drawing

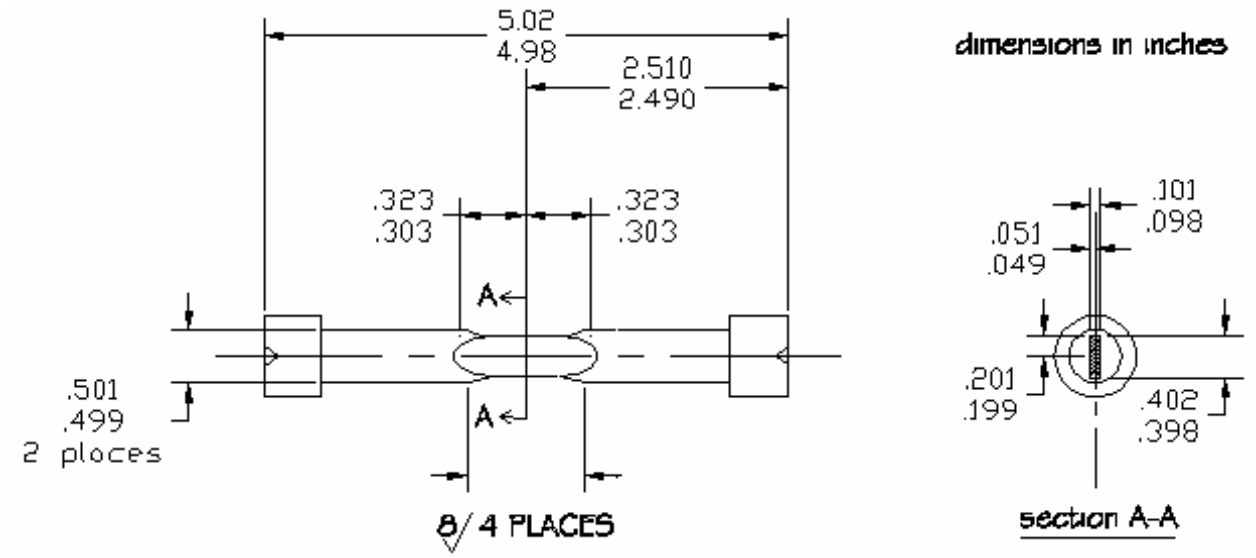

Figure K-3. GE Aviation SENBH Specimen Drawing

K.4 TEST PROCEDURES.

Precracking of the SC(T) and Kb bar specimens was conducted in laboratory air at room temperature under constant load conditions. Precracking of the SENBH specimen was conducted in vacuum under contant load conditions. Precrack loading frequencies were 10 Hz (GE Aviation) or 3.33 Hz (Honeywell). Semicircular precracks in SC(T) or Kb specimens were grown to a nominal size of 0.015 by 0.030 inch, except for higher stress ratio tests at GE Aviation, where precracks were grown to approximately 0.030 inch deep by 0.060 inch long. Precracks in SENBH specimens at GE Aviation were grown to lengths between 0.030 and 0.060 inch; lengths were closer to 0.060 for higher stress ratios.

Following precracking, all crack growth tests were conducted under high-vacuum conditions. Vacuum levels generally ranged between 10^{-7} and 10^{-8} torr.

Crack lengths were monitored using the direct current electric potential drop method, with crack sizes posttest corrected from visual measurements of marked initial and final crack dimensions on the fracture surfaces. Stress-intensity factors were calculated from the Newman-Raju [K-1] solution for SC(T) and the Harris [K-2] solution for SENBH. Tests were conducted under either constant load or constant ΔK-gradient (increasing or decreasing) at constant stress ratio, where the ΔK-gradient was as high as ±20/inch (Honeywell) or ±30/inch (GE Aviation). Research at the engine companies [K-3] indicated that these gradients, which are more severe than the recommendations of ASTM E 647, do not significantly influence the measured growth rates and are necessary to obtain adequate data on small specimens. Crack growth rates were calculated with incremental polynomial methods. Test frequency was 0.33 Hz (20 cpm) for all tests.

K.5 MATERIAL PEDIGREE.

K.5.1 Ti-6242.

The Ti-6242 was alpha + beta forged, solution heat-treated below the beta transus, rapid air cooled, and aged. This material was supplied by Pratt & Whitney (P&W), and only two tests were conducted on this material. Note that the vacuum FCG tests on Ti-6242 in TRMD-I were performed on different material supplied by Honeywell. Details of those tests and the associated pedigree information are contained in the final report of TRMD-I [K-4]. The purpose of these two tests was to compare the vacuum FCG behavior of the coarse-grained P&W material with the fine-grained Honeywell material tested during TRMD-I.

K.5.2 WASPALOY.

The Waspaloy material was supplied by P&W from turbine disk forgings. It was double melt, hot-die forged, solutioned, stabilized, and precipitation hardened. Material for specimens was extracted from forgings of either a low-pressure turbine (LPT) disk (figure K-4) or a high-pressure turbine disk (HPT) (figure K-5). Specimens 1-11 were extracted from the LPT forging, whereas specimens 206-1 through 206-5 were extracted from the HPT forging.

K.5.3 IN-718.

The IN-718 material was provided by GE. The material is a fine-grained nickel alloy with average grain size of ASTM 9.4, as shown below in figure K-6. The material was forged at Wyman Gordon with the serial no. 1346 and heat code A25326. The IN-718 was solutionized between 1725° and 1875°F for 1 hour. Following the solutionizing, the material was aged at 1325°F for 8 hours, followed by another age at 1150°F for 8 hours. The 1200°F 0.2% yield strength is 141.0 ksi.

K.5.4 PM U720.

The powder metallurgy (PM) U720 material was provided by NASA-Glenn Research Center in pancake form. Due to export control considerations, details on the PM U720 material are not provided in this report.

Waspaloy Section #1 For Vacuum Crack Growth Testing

Forging H/C:	AACET-1
Forging Type:	LPT Disk Forging
Forge Processing:	Hot Die Forged, Solution, Stabilized and Precipitation Heat Treated
Mill:	Special Metals
Heat No.:	9-18133
Melt Date:	1/6/98
Melt Process:	Multiple Melt VIM, VAR
Conversion Source:	Special Metals
Billet No.:	A1

Mill Chemistry

	C	Mn	Si	P	S	Cr	Fe	Co	Mo	Al	Ti	Zr	B	Cu	Pb	Bi	Ni
Top	0.032	0.01	0.07	0.003	0.0002	19.32	0.92	13.25	4.04	1.33	3.06	0.064	0.0064	0.02	<3 ppm	<0.3 ppm	Balance
Bot	0.035	0.01	0.08	0.001	0.0003	19.28	0.91	13.17	4.07	1.34	3.15	0.071	0.0073	0.03	<3 ppm	<0.3 ppm	Balance

1000F - Tensile Properties:

0.2% Yield Strength	**135 KSI**
Ultimate Tensile Strength	**185 KSI**
Elongation	**19 %**
Reduction of Area	**29 %**

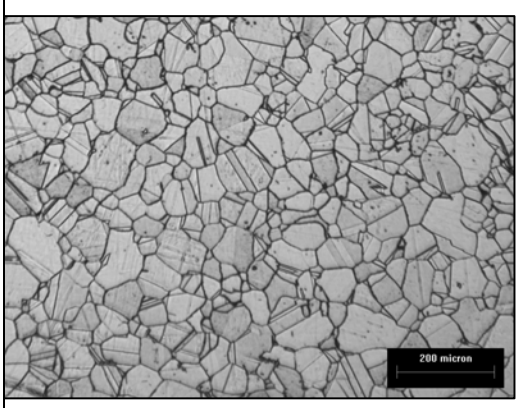

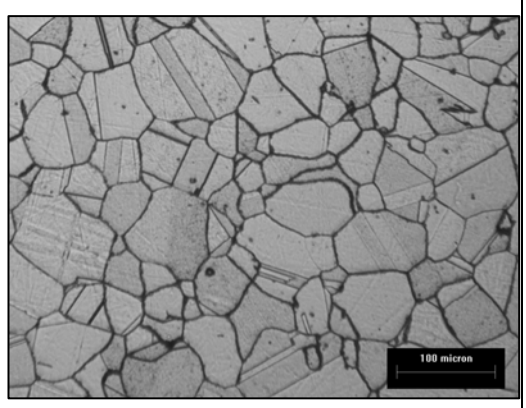

Average Grain size for entire cross section, ASTM 6-7

VIM = Vacuum induction melting
VAR = Vacuum arc remelting

Figure K-4. Pedigree Information of Waspaloy LPT Disk Material

Waspaloy Section #2 For Vacuum Crack Growth Testing

Forging H/C:	AADKH-3
Forging Type:	HPT Disk Forging
Forge Processing:	Hot Die Forged, Solution, Stabilized and Precipitation Heat Treated
Mill:	Special Metals
Heat No.:	9-19072
Melt Date:	3/10/99
Melt Process:	Multiple Melt VIM, VAR
Conversion Source:	Special Metals
Billet No.:	B2

Mill Chemistry

	C	Mn	Si	P	S	Cr	Fe	Co	Mo	Al	Ti	Zr	B	Cu	Pb	Bi	Ni
Top	0.031	0.01	0.05	0.001	0.0003	19.33	1.09	13.23	4.06	1.33	3.08	0.063	0.0066	0.01	<3 ppm	<0.3 ppm	Balance
Bot	0.031	0.01	0.05	0.001	0.0003	19.29	1.09	13.18	4.09	1.33	3.17	0.067	0.0072	0.02	<3 ppm	<0.3 ppm	Balance

1000F - Tensile Properties:

0.2% Yield Strength	**120 KSI**
Ultimate Tensile Strength	**174 KSI**
Elongation	**20 %**
Reduction of Area	**23 %**

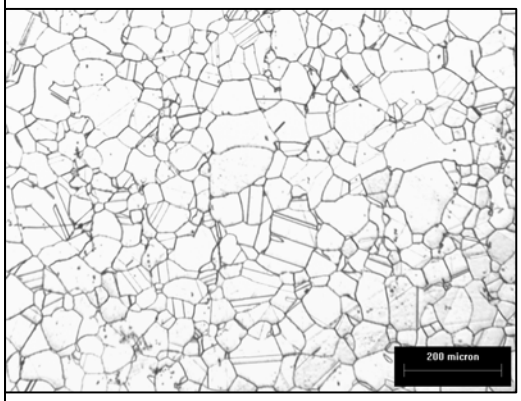

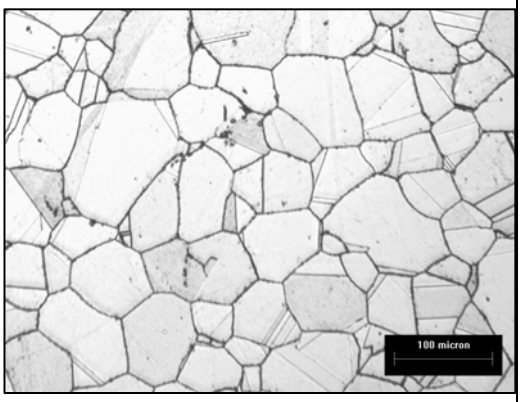

Average Grain size for entire cross section, ASTM 5-7

Figure K-5. Pedigree Information of Waspaloy HPT Disk Material

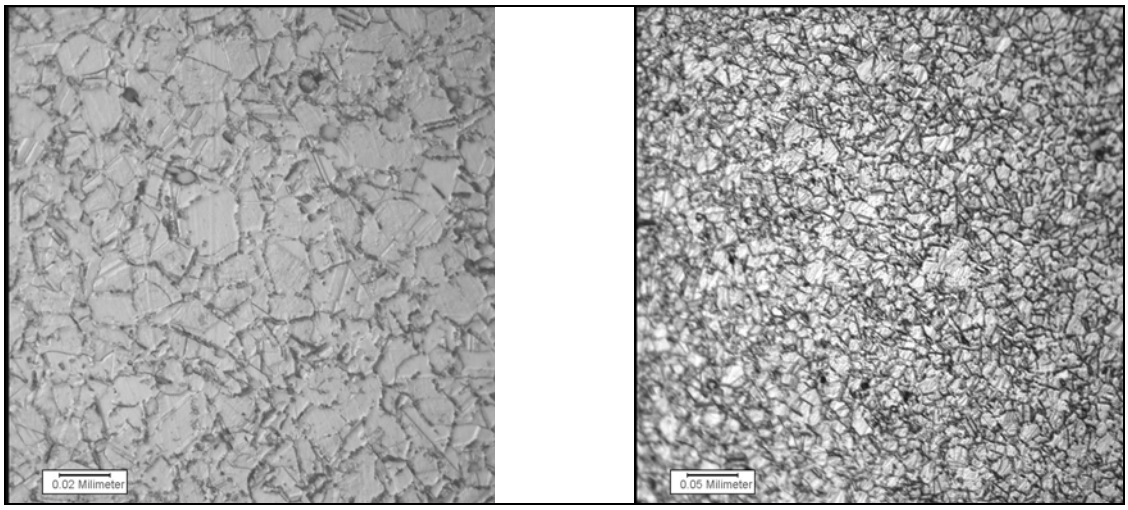

Figure K-6. Microstructure of IN-718 Forging Material

K.6 TEST MATRICES.

Detailed test matrices are provided for each material in tables K-1 through K-4.

Table K-1. Ti-6242 Vacuum FCG Test Matrix

Specimen ID	T (°F)	Frequency (cpm)	*R*-Ratio
1425	600	20	0.05
1426	600	20	0.05

cpm = Cycles per minute

Table K-2. Waspaloy Vacuum FCG Test Matrix

Test ID	Specimen ID	Temperature (°F)	*R*-Ratio	ΔK Region
1	1	500	0.05	I (Threshold)
2	2	500	0.5	I (Threshold)
3	7	500	0.05	II (Paris)
4	5	500	0.5	II (Paris)
5	8	800	0.05	I (Threshold)
6	8	800	0.05	II (Paris)
7	3	800	0.5	I (Threshold)
8	6	800	0.5	II (Paris)
9	9	1200	0.05	I (Threshold)
10	9	1200	0.05	II (Paris)

Table K-3. Waspaloy Vacuum FCG Test Matrix (Continued)

Test ID	Specimen ID	Temperature (°F)	*R*-Ratio	Δ*K* Region
11	10	1200	0.5	I (Threshold)
12	11	1200	0.5	II (Paris)
13	206-1	500	0.05	I & II
14	206-2	500	0.5	II (Paris)
15	206-3	800	-0.5	I (Threshold)
16	206-3	800	-0.5	II (Paris)
17	206-5	1200	-0.5	I (Threshold)
18	206-5	1200	-0.5	II (Paris)
Air4	4	500	0.05	Air

Table K-4. IN-718 Vacuum FCG Test Matrix

Specimen Test ID	Specimen Type	T (°F)	*R*-Ratio	FCG Regime	Test Site
4470-407-1	SENBH	75	0	I (Threshold); II (Paris)	GE
4470-401-1	Kb	75	0	I (Threshold); II (Paris)	GE
4470-401-2	Kb	75	0.5	I (Threshold); II (Paris)	GE
4470-401-4	Kb	75	0.7	II (Paris)	HON
4470-401-5	Kb	600	0.05	II (Paris)	HON
4470-401-8	Kb	1000	0	I (Threshold); II (Paris)	GE
4470-407-2	SENBH	1000	0	I (Threshold)	GE
4470-401-6	Kb	1000	0.5	II (Paris)	HON
4470-407-5	SENBH	1000	0.7	I (Threshold)	GE
4470-401-7	Kb	1000	0.7	II (Paris)	HON
4470-401-9	Kb	1200	0	II (Paris)	GE
4470-407-7	SENBH	1200	0	I (Threshold)	GE
4470-407-6	SENBH	1200	0.7	II (Paris)	GE

Table K-5. PM U720 Vacuum FCG Test Matrix

ID	Temperature (^{o}F)	*R*-Ratio	Regime	Status
E2-11	800	0.05	Paris Region II	Complete
E2-2	800	0.05	Near Threshold	Complete
E2-3	800	0.50	Paris Region II	Complete
E2-4	800	0.50	Near Threshold	Complete
E2-5	1200	0.05	Paris Region II	Complete
E2-6	1200	0.05	Near Threshold	Postponed

K.7 RESULTS.

K.7.1 Ti-6242.

The vacuum FCG test results for 600ºF, *R* = 0.05, obtained in the present study (coarse-grained P&W material) are presented in figure K-7. In figure K-8, these results are compared with the TRMD-I results for the (Honeywell) fine-grained Ti-6242. The data sets shown in figure K-8 are in reasonable agreement with each other. However, the data for specimen #1426 should be used with caution as this specimen experienced highly asymmetric crack growth (see fractograph in figure K-9).

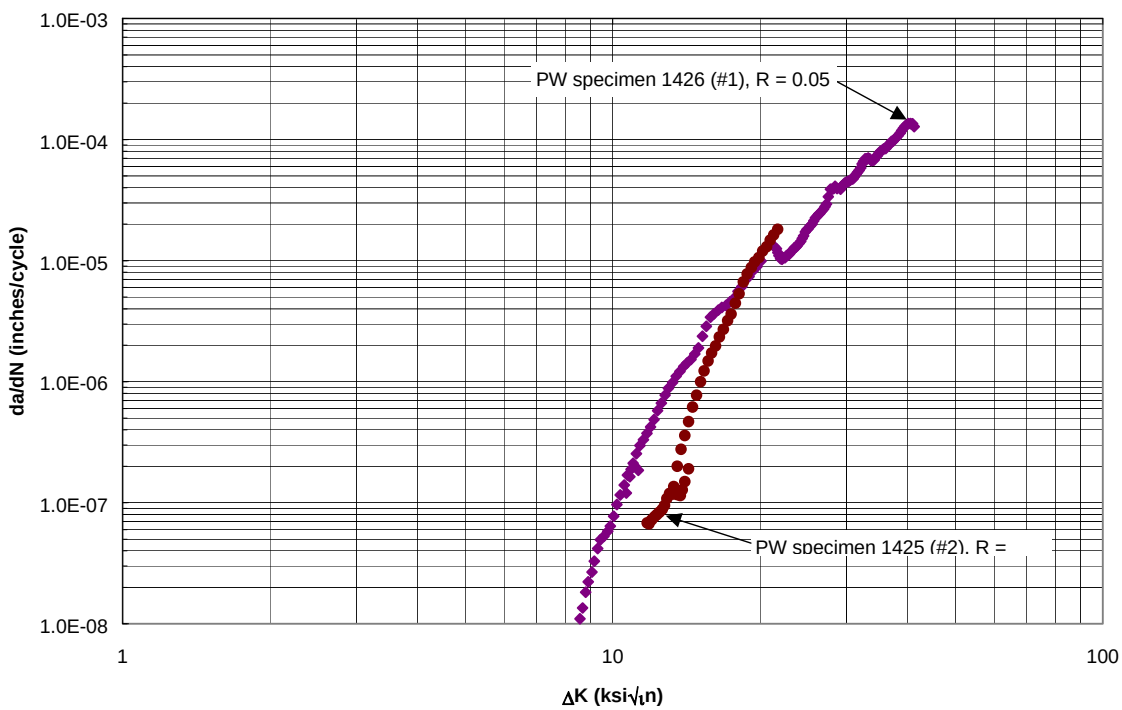

Figure K-7. Ti-6242 Vacuum FCG Test Results for P&W Material

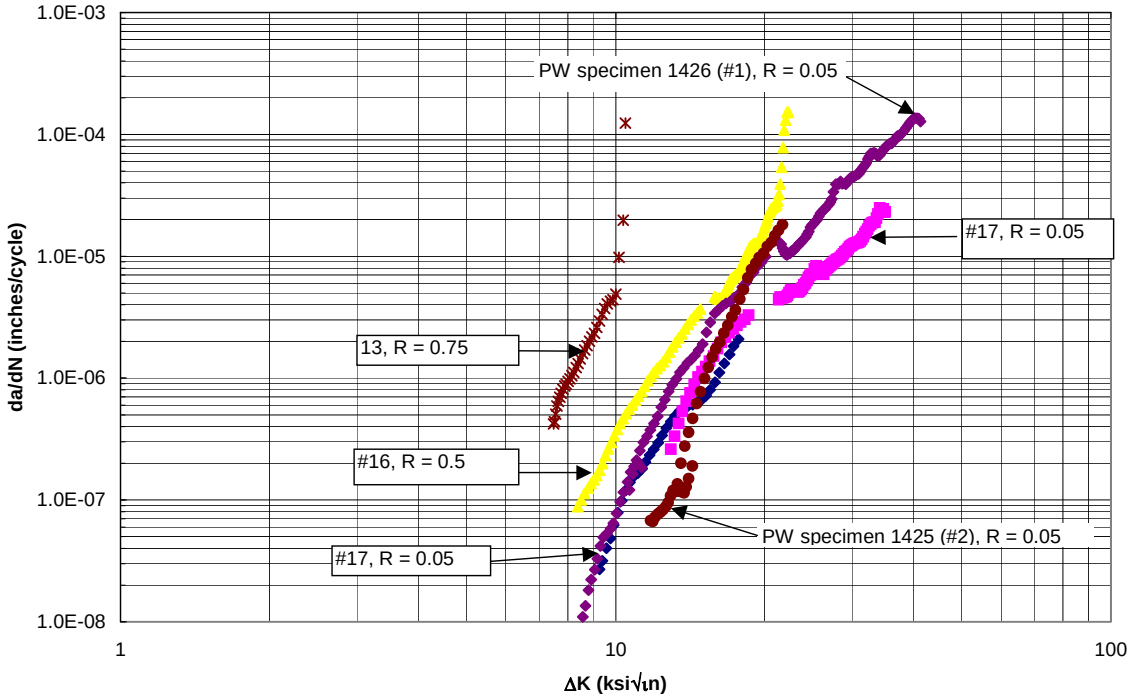

Figure K-8. Ti-6242 Vacuum FCG Test Results for P&W and Honeywell Materials

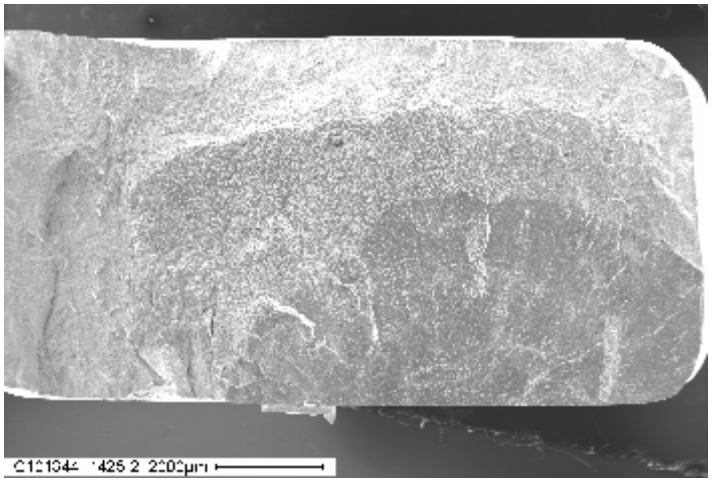

Figure K-9. Fracture Surface for P&W Specimen #1426

K.7.2 WASPALOY.

A total of 18 vacuum FCG tests and one air FCG test were conducted on Waspaloy. Figures K-10 through K-12 show the effect of temperature on FCG rate at various stress ratios. Figures K-13 through K-15 show the effect of stress ratio on FCG rates at various temperatures. Figure K-16 shows the effect of environment (air versus vacuum) on FCG rates at R = 0.05, 500°F.

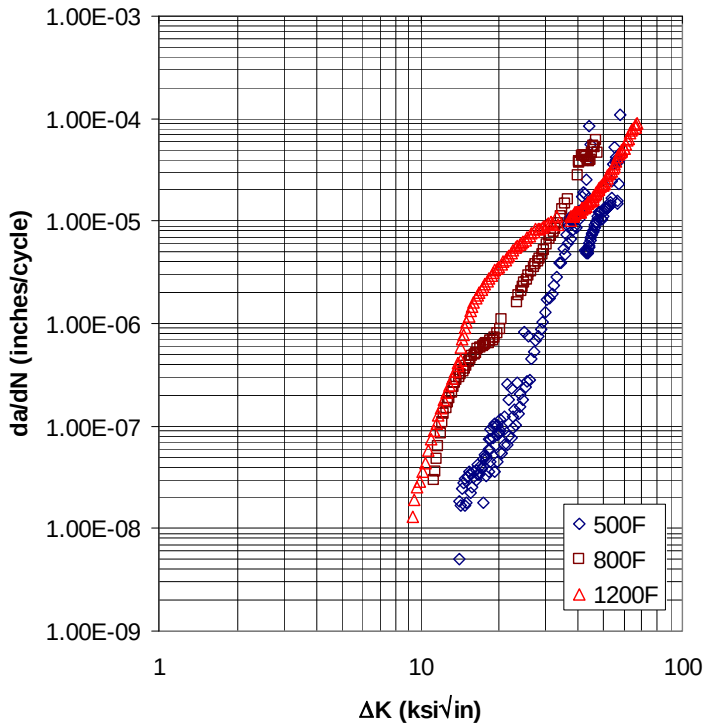

Figure K-10. Waspaloy Vacuum FCG Test Results Showing Effect of Temperature at R = 0.05

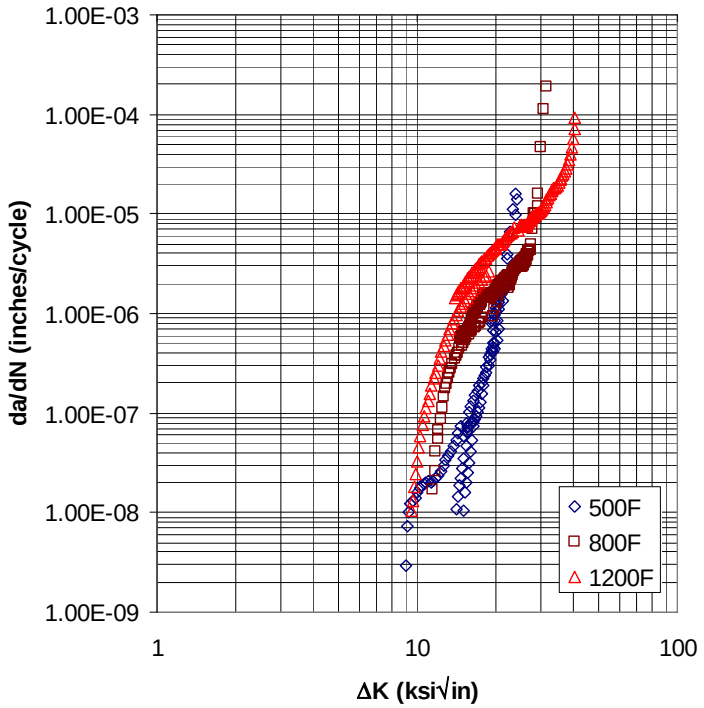

Figure K-11. Waspaloy Vacuum FCG Test Results Showing Effect of Temperature at R = 0.5

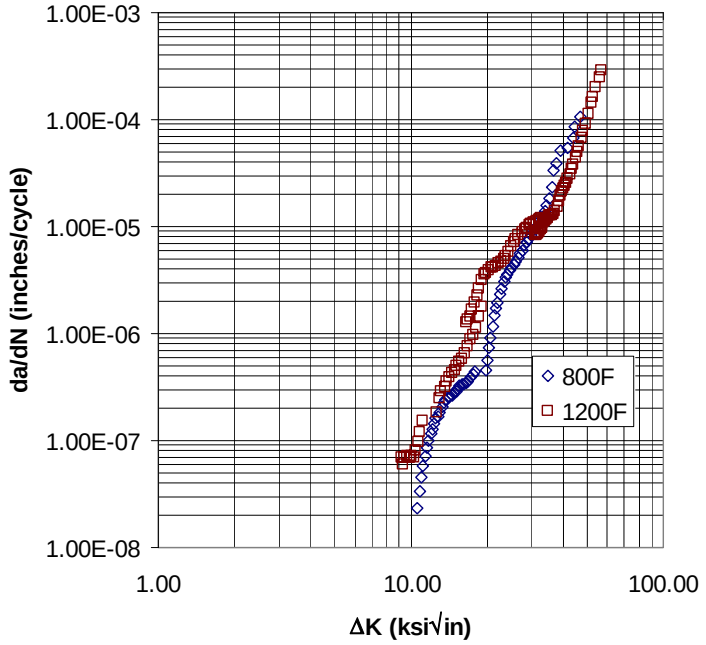

Figure K-12. Waspaloy Vacuum FCG Test Results Showing Effect of Temperature at *R* = -0.5

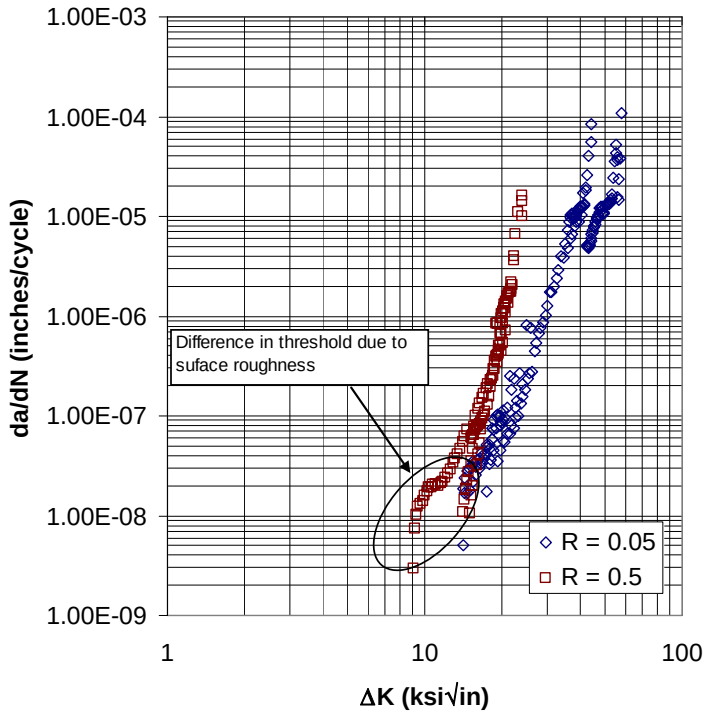

Figure K-13. Waspaloy Vacuum FCG Test Results Showing Effect of Stress Ratio at 500°F

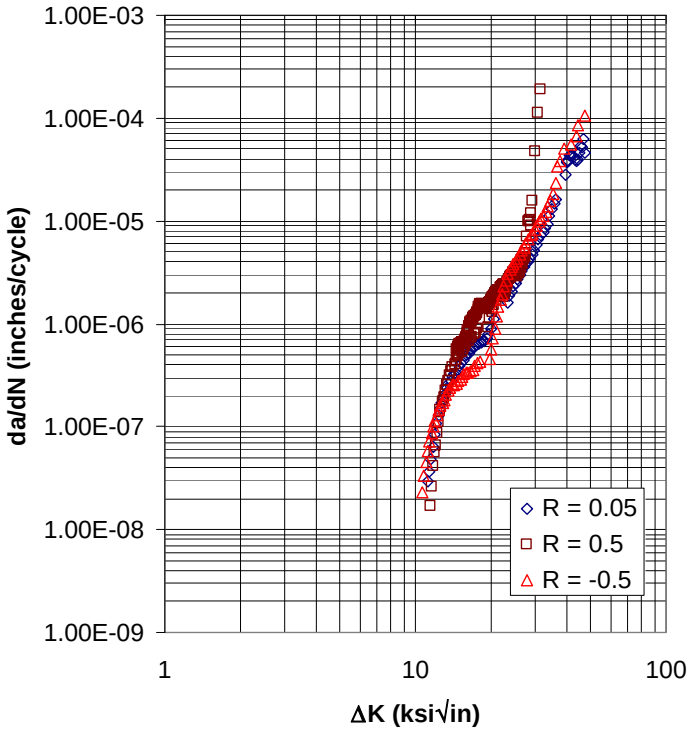

Figure K-14. Waspaloy Vacuum FCG Test Results Showing Effect of Stress Ratio at 800°F

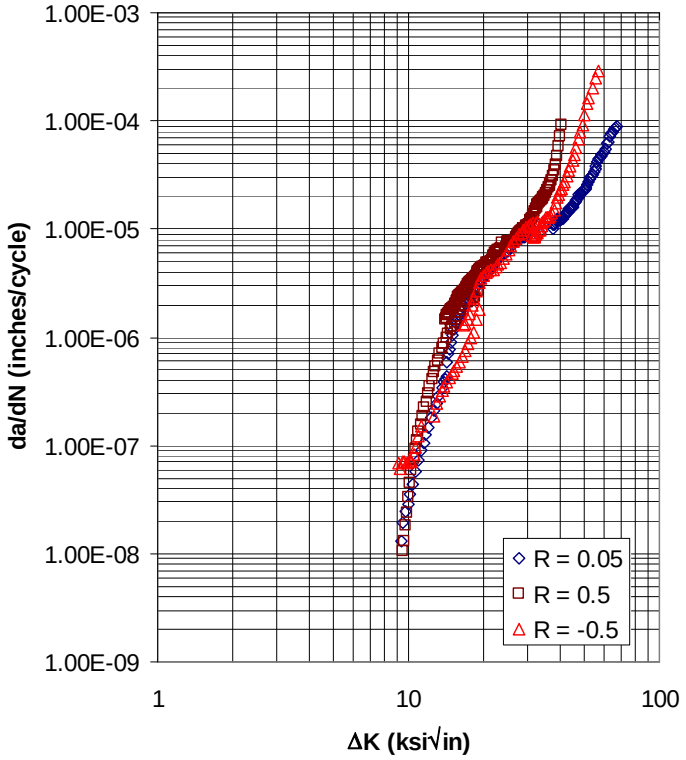

Figure K-15. Waspaloy Vacuum FCG Test Results Showing Effects of Stress Ratio at 1200°F

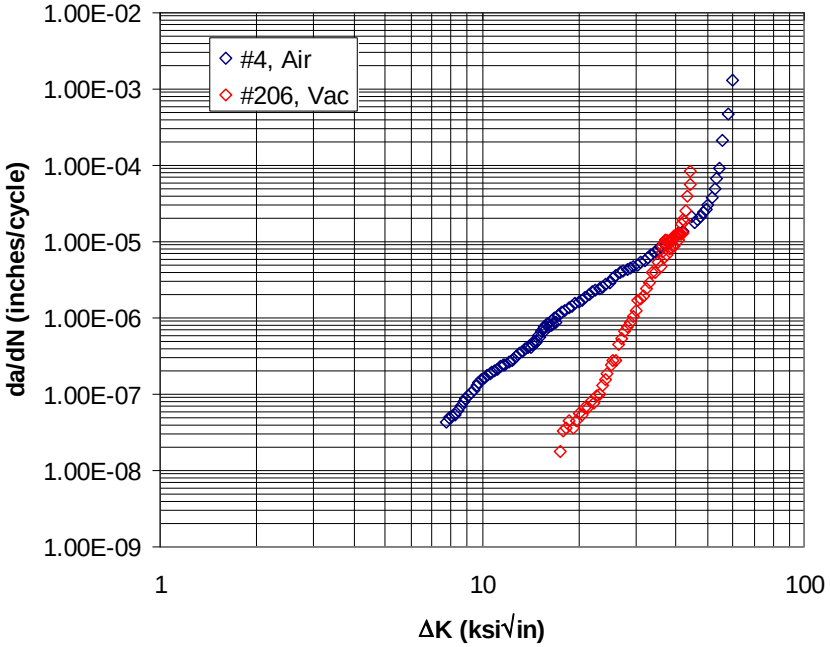

Figure K-16. Effect of Environment (Air vs Vacuum) on FCG Rates in Waspaloy at R = 0.05, 600°F

K.7.3 IN-718.

A total of 13 successful vacuum FCG tests on IN-718 were completed. Two different specimen types (SENBH and SC[T]) were used, but the results show no appreciable difference between these geometries, and the resulting data can be combined for regression purposes.

Figures K-17 through K-19 show the effect of temperature on crack growth rates at various stress ratios. Figures K-20 and K-21 show the effect of change in stress ratio on the crack growth rate at 1000° and 1200°F.

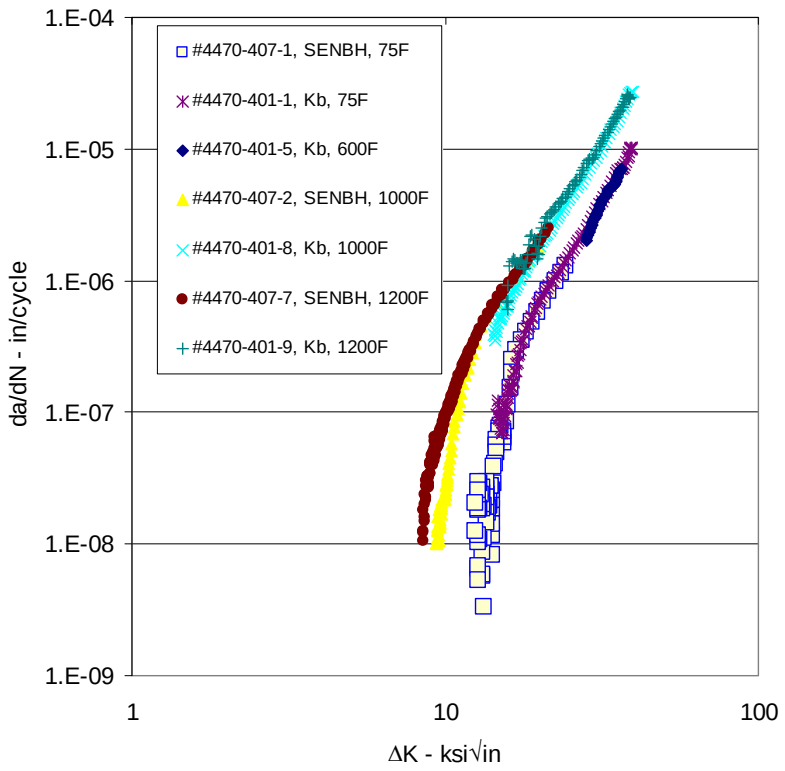

Figure K-17. IN-718 Vacuum FCG Test Results Showing Effect of Temperature at $R = 0$

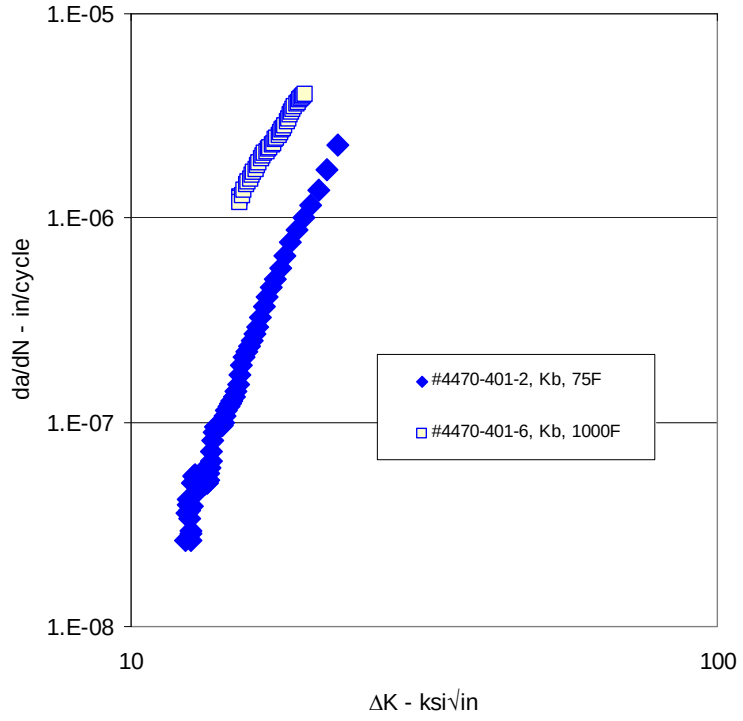

Figure K-18. IN-718 Vacuum FCG Test Results Showing Effect of Temperature at $R = 0.5$

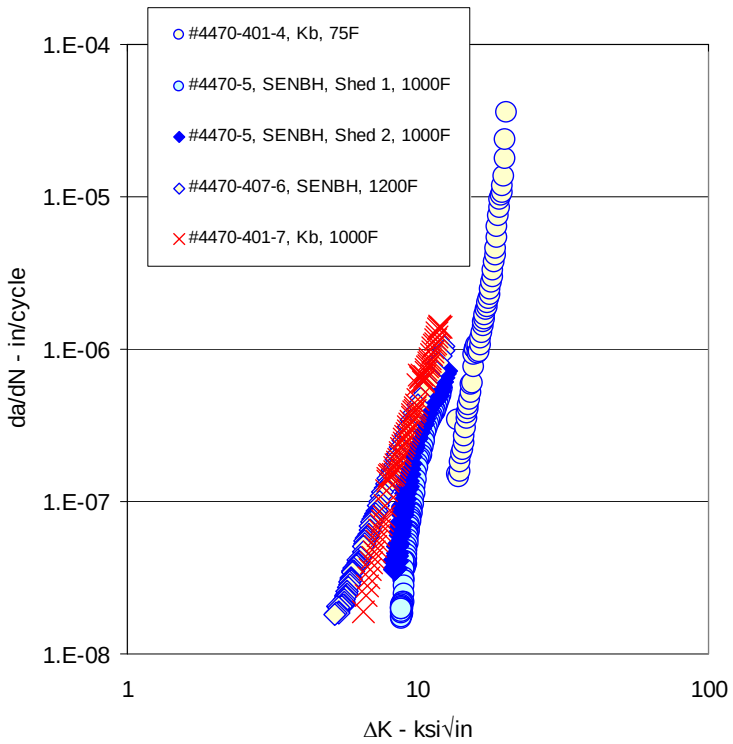

Figure K-19. IN-718 Vacuum FCG Test Results Showing Effect of Temperature at R = 0.7

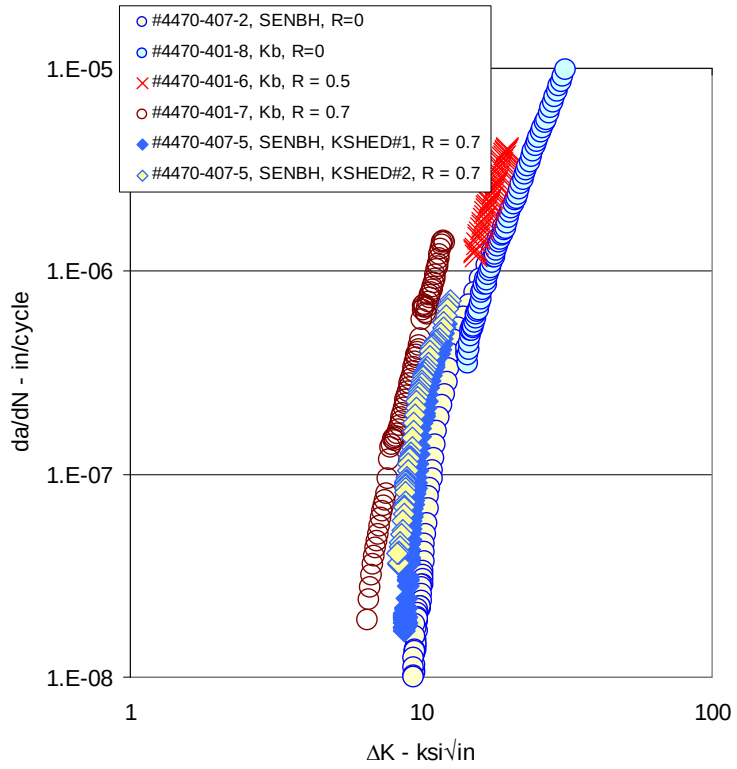

Figure K-20. IN-718 Vacuum FCG Test Results Showing Effect of Stress Ratio at 1000°F

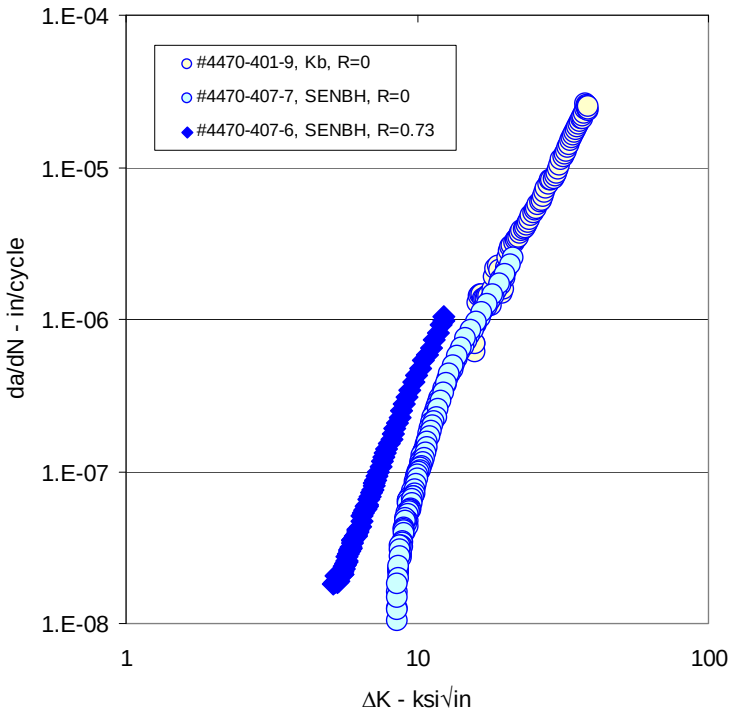

Figure K-21. IN-718 Vacuum FCG Test Results Showing Effect of Stress Ratio at 1200°F

K.8 TABULATED TEST RESULTS.

K.8.1 Ti-6242.

P&W1426, T = 600°F, *R* - 0.05	
ΔK	*da/dN*
11.28	1.85E-07
11.11	2.00E-07
10.89	1.89E-07
10.72	1.69E-07
10.56	1.40E-07
10.36	1.16E-07
10.21	9.67E-08
10.04	7.75E-08
9.88	6.42E-08
9.77	5.82E-08
9.60	5.29E-08
9.44	4.95E-08
9.31	4.19E-08
9.17	3.29E-08
9.07	2.68E-08
8.92	2.22E-08
8.81	1.82E-08
8.68	1.35E-08
8.58	1.10E-08
10.66	1.20E-07
10.83	1.64E-07
11.01	2.12E-07
11.18	2.55E-07
11.37	2.97E-07
11.56	3.32E-07
11.75	3.75E-07
11.94	4.22E-07
12.15	4.85E-07
12.35	5.78E-07
12.57	6.65E-07
12.79	7.77E-07
13.00	8.83E-07
13.25	9.83E-07
13.47	1.11E-06
13.71	1.22E-06
13.96	1.33E-06
14.18	1.42E-06
14.45	1.53E-06
14.71	1.69E-06
14.97	1.90E-06
15.25	2.37E-06
15.52	2.87E-06
15.84	3.41E-06
16.11	3.64E-06
16.42	3.90E-06
16.70	4.11E-06
17.04	4.25E-06
17.35	4.56E-06
17.71	4.91E-06
18.01	5.58E-06
18.34	6.08E-06
18.67	6.96E-06
18.98	7.40E-06
19.37	8.32E-06
19.69	8.91E-06
20.07	9.96E-06
21.40	1.30E-05
21.57	1.25E-05
21.72	1.17E-05
21.85	1.10E-05
22.01	1.04E-05
22.17	1.03E-05
22.33	1.05E-05
22.49	1.06E-05
22.65	1.10E-05
22.82	1.12E-05
22.96	1.14E-05
23.16	1.19E-05
23.33	1.23E-05
23.49	1.28E-05
23.66	1.29E-05
23.81	1.33E-05
24.03	1.39E-05
24.21	1.44E-05
24.36	1.52E-05
24.53	1.60E-05
24.73	1.73E-05
24.92	1.81E-05
25.08	1.84E-05
25.29	1.93E-05
25.53	2.01E-05
25.72	2.14E-05
25.93	2.26E-05
26.14	2.34E-05
26.32	2.42E-05
26.46	2.45E-05
26.70	2.57E-05
26.93	2.67E-05
27.11	2.79E-05
27.32	2.93E-05
27.53	3.37E-05
27.82	3.89E-05
28.06	3.91E-05
28.25	3.94E-05
28.45	4.10E-05
28.70	3.94E-05
29.16	3.89E-05
29.35	4.10E-05
29.53	4.23E-05
29.75	4.38E-05
29.96	4.43E-05
30.13	4.48E-05
30.31	4.52E-05
30.52	4.61E-05
30.78	4.71E-05
30.98	4.77E-05
31.15	4.93E-05
31.37	5.17E-05
31.60	5.36E-05
31.85	5.58E-05
32.06	5.82E-05
32.29	6.28E-05
32.52	6.61E-05
32.75	6.95E-05
33.00	6.96E-05
33.22	7.05E-05
33.45	6.96E-05
33.72	6.69E-05
33.97	6.75E-05
34.16	6.80E-05
34.40	7.12E-05
34.65	7.36E-05
34.91	7.67E-05
35.20	8.02E-05
35.44	8.13E-05
35.70	8.36E-05
36.06	8.42E-05
36.31	8.77E-05
36.51	8.99E-05
36.77	9.19E-05
37.06	9.68E-05
37.38	9.73E-05
37.67	1.01E-04
37.92	1.03E-04
38.24	1.08E-04
38.61	1.13E-04
38.89	1.18E-04
39.18	1.24E-04
39.49	1.29E-04
39.82	1.33E-04
40.17	1.36E-04
40.55	1.35E-04
40.91	1.35E-04
41.25	1.28E-04

P&W1425, T = 600°F, *R* - 0.05	
Δ*K*	*da/dN*
14.28	1.90E-07
14.03	1.49E-07
13.87	1.28E-07
13.74	1.15E-07
13.56	1.17E-07
13.41	1.20E-07
13.25	1.18E-07
13.06	1.19E-07
12.91	1.08E-07
12.77	9.49E-08
12.62	8.78E-08
12.46	8.31E-08
12.31	7.97E-08
12.17	7.64E-08
12.01	7.22E-08
11.87	6.67E-08
11.76	6.80E-08
13.33	1.36E-07
13.55	2.00E-07
13.79	2.77E-07
14.03	3.59E-07
14.29	4.67E-07
14.57	6.17E-07
14.84	7.73E-07
15.11	9.95E-07
15.38	1.23E-06
15.66	1.48E-06
15.93	1.73E-06
16.22	1.97E-06
16.52	2.34E-06
16.84	2.70E-06
17.16	3.19E-06
17.45	3.61E-06
17.80	4.44E-06
18.11	5.32E-06
18.48	6.66E-06
18.81	7.77E-06
19.20	8.78E-06
19.50	9.74E-06
19.88	1.06E-05
20.23	1.20E-05
20.61	1.30E-05
20.97	1.48E-05
21.32	1.63E-05
21.71	1.81E-05

K.8.2. Waspaloy.

1, T = 500°F, *R* = 0.05	
Δ*K*	*da/dN*
16.58	4.21E-08
16.28	2.99E-08
15.78	2.56E-08
15.46	2.20E-08
15.05	1.78E-08
14.70	1.67E-08
20.87	1.23E-07
20.37	9.74E-08
19.94	8.57E-08
19.63	8.11E-08
18.98	7.62E-08
18.30	7.49E-08
18.27	5.87E-08
17.50	5.21E-08
20.18	1.15E-07
20.26	9.08E-08
19.80	8.75E-08
19.67	1.01E-07
19.42	9.96E-08
19.09	1.04E-07
19.00	9.91E-08
18.50	9.18E-08
18.46	7.38E-08
18.21	5.80E-08
17.91	5.13E-08
17.84	4.72E-08
17.41	4.84E-08
17.44	4.05E-08
17.08	3.77E-08
16.96	4.10E-08
16.72	3.37E-08
16.63	3.34E-08
16.31	3.75E-08
16.01	3.63E-08
15.84	3.13E-08
15.61	3.43E-08
15.39	3.56E-08
15.17	3.12E-08
14.87	3.02E-08
14.66	2.83E-08
14.34	2.43E-08
14.23	1.67E-08
14.08	1.85E-08
14.03	5.08E-09

1, T = 500°F, *R* = 0.05	
Δ*K*	*da/dN*
21.47	2.53E-07
21.84	1.80E-07
22.29	2.33E-07
22.62	1.22E-07
22.93	1.43E-07
23.33	2.66E-07
23.93	2.06E-07
24.91	8.19E-07
25.82	7.63E-07

7, T = 500°F, *R* = 0.05	
Δ*K*	*da/dN*
15.54	3.92E-07
15.66	3.81E-07
15.79	3.83E-07
15.96	3.88E-07
16.10	4.05E-07
16.25	4.31E-07
16.44	4.42E-07
16.61	4.59E-07
16.80	4.77E-07
17.02	5.06E-07
17.20	5.28E-07
17.41	5.65E-07
17.63	6.30E-07
17.86	6.57E-07
18.09	7.24E-07
18.32	7.44E-07
18.57	8.08E-07
18.79	8.72E-07
19.04	9.66E-07
19.32	1.11E-06
19.58	1.17E-06
19.80	1.21E-06
20.08	1.23E-06
20.38	1.28E-06
20.68	1.26E-06
20.95	1.33E-06
21.22	1.41E-06
21.53	1.51E-06
21.82	1.60E-06
22.14	1.67E-06
22.47	1.79E-06
22.75	1.86E-06
23.09	1.94E-06
23.43	2.04E-06
23.74	2.11E-06
24.04	2.21E-06
24.42	2.27E-06
24.81	2.29E-06
25.11	2.44E-06
25.43	2.67E-06
25.83	3.12E-06
26.26	3.40E-06
26.63	3.33E-06
27.00	3.48E-06
27.35	3.39E-06
27.75	3.29E-06
28.15	3.40E-06
28.61	3.57E-06
29.08	3.68E-06
29.44	3.79E-06
29.83	3.84E-06
30.30	3.94E-06
30.70	4.17E-06
31.12	4.40E-06
31.55	4.60E-06
31.98	4.93E-06
32.55	4.84E-06

7, T = 500°F, R = 0.05	
ΔK	*da/dN*
42.65	5.20E-06
42.83	5.16E-06
43.00	4.96E-06
43.13	4.94E-06
43.32	4.90E-06
43.47	4.88E-06
43.68	5.19E-06
43.88	5.46E-06
44.11	5.70E-06
44.34	6.06E-06
44.57	6.54E-06
44.77	6.94E-06
44.99	7.35E-06
45.25	7.65E-06
45.51	7.92E-06
45.75	7.98E-06
46.00	8.22E-06
46.24	8.68E-06
46.47	9.30E-06
46.73	9.74E-06
46.99	9.63E-06
47.21	1.04E-05
47.50	1.11E-05
47.80	1.20E-05
48.11	1.21E-05
48.34	1.23E-05
48.69	1.23E-05
49.02	1.05E-05
49.27	1.05E-05
49.49	1.05E-05
49.73	1.10E-05
50.31	1.25E-05
50.56	1.27E-05
50.83	1.33E-05
51.18	1.34E-05
51.52	1.33E-05
51.87	1.34E-05
52.23	1.38E-05
52.61	1.37E-05
52.90	1.44E-05
53.18	1.53E-05
53.52	1.66E-05
53.94	2.44E-05
54.45	3.57E-05

206-1, T = 500°F, R = 0.05	
ΔK	*da/dN*
17.45	1.77E-08
17.82	3.28E-08
18.17	3.60E-08
18.53	4.53E-08
19.29	3.55E-08
19.68	4.53E-08
20.08	5.68E-08
20.47	5.39E-08
20.92	6.61E-08
21.35	6.62E-08
21.76	7.92E-08
22.18	7.63E-08
22.64	9.60E-08
23.11	1.01E-07
23.56	1.32E-07
24.07	1.55E-07
24.54	1.82E-07
25.07	2.38E-07
25.54	2.71E-07
26.07	2.79E-07
26.62	4.46E-07
27.13	5.33E-07
27.66	6.73E-07
28.24	7.62E-07
28.87	8.69E-07
29.42	1.03E-06
30.04	1.27E-06
30.55	1.72E-06
31.16	1.75E-06
31.87	1.95E-06
32.45	2.38E-06
33.15	2.89E-06
33.76	3.95E-06
34.55	3.90E-06
35.25	5.36E-06
35.84	4.79E-06
36.68	6.02E-06
37.33	6.59E-06
38.09	8.03E-06
38.88	8.89E-06
39.66	8.74E-06
40.53	1.04E-05
41.38	1.72E-05
42.08	1.93E-05

206-1, T = 500°F, R = 0.05	
ΔK	*da/dN*
36.18	7.31E-06
36.40	8.86E-06
36.67	9.63E-06
36.91	1.03E-05
37.16	1.06E-05
37.43	1.04E-05
37.70	1.01E-05
37.95	9.79E-06
38.29	9.73E-06
38.58	9.92E-06
38.82	1.04E-05
39.15	1.12E-05
39.52	1.18E-05
39.84	1.20E-05
40.13	1.23E-05
40.43	1.25E-05
40.81	1.24E-05
41.20	1.24E-05
41.53	1.27E-05
41.91	1.33E-05
42.27	1.84E-05
42.74	2.56E-05
43.46	3.98E-05
44.29	8.44E-05
44.45	5.64E-05

2, T = 500°F, R = 0.5	
ΔK	*da/dN*
15.64	6.46E-08
15.37	4.60E-08
15.13	3.52E-08
14.91	2.75E-08
14.69	2.22E-08
14.47	1.86E-08
14.28	1.45E-08
14.10	1.07E-08
16.55	7.29E-08
16.33	5.35E-08
16.07	4.15E-08
15.89	3.16E-08
15.67	2.51E-08
15.48	1.98E-08
15.28	1.58E-08
15.10	1.05E-08
15.17	5.93E-08

2, T = 500°F, R = 0.5	
ΔK	*da/dN*
15.38	6.47E-08
15.57	7.07E-08
15.75	7.37E-08
15.96	7.81E-08
16.18	8.05E-08
16.40	8.23E-08
16.61	8.73E-08
16.84	9.41E-08
17.07	1.01E-07
17.29	1.11E-07
17.53	1.30E-07
17.77	1.58E-07
18.02	1.93E-07
18.24	2.37E-07
18.47	2.90E-07
18.76	3.60E-07
19.02	3.94E-07
19.23	4.08E-07
19.48	4.53E-07
19.74	5.10E-07
20.02	6.59E-07
20.28	8.48E-07
20.56	1.10E-06

5, T = 500°F, R = 0.5	
ΔK	*da/dN*
9.03	2.90E-09
9.12	7.38E-09
9.28	1.01E-08
9.45	1.23E-08
9.62	1.32E-08
9.82	1.42E-08
9.99	1.58E-08
10.20	1.76E-08
10.44	1.89E-08
10.62	1.92E-08
10.83	2.04E-08
11.06	2.06E-08
11.29	2.01E-08
11.52	2.09E-08
11.78	2.20E-08
12.05	2.36E-08
12.31	2.60E-08
12.60	2.94E-08
12.89	3.35E-08
13.18	3.73E-08
13.47	4.16E-08
13.81	4.66E-08
14.08	5.40E-08
14.36	6.19E-08
14.64	7.33E-08
15.53	7.83E-08
15.79	1.01E-07
16.09	1.17E-07
16.39	1.32E-07
16.69	1.50E-07
17.02	1.68E-07
17.36	1.87E-07
17.69	2.05E-07
18.05	2.27E-07
18.41	2.55E-07
18.75	2.95E-07
19.12	3.47E-07
19.51	4.19E-07
19.89	4.50E-07
20.27	5.45E-07
20.69	7.06E-07
21.26	1.35E-06
21.60	2.17E-06
22.24	3.60E-06

206-2, T = 500°F, R = 0.5	
ΔK	*da/dN*
18.99	8.33E-07
19.27	8.46E-07
19.42	4.49E-07
19.49	4.98E-07
19.58	6.67E-07
19.75	8.45E-07
19.89	9.58E-07
20.03	1.05E-06
20.18	1.13E-06
20.34	1.20E-06
20.49	1.29E-06
20.68	1.40E-06
20.86	1.51E-06
21.04	1.59E-06
21.23	1.67E-06
21.44	1.72E-06
21.65	1.74E-06
21.84	1.83E-06
22.05	2.03E-06
22.28	3.95E-06
22.64	6.59E-06
23.19	1.10E-05
23.91	1.60E-05
23.98	9.87E-06
24.11	1.42E-05

8, T = 800°F, R = 0.05	
ΔK	*da/dN*
20.42	1.72E-06
19.95	1.41E-06
19.52	1.27E-06
19.15	1.16E-06
18.76	1.13E-06
18.31	1.11E-06
17.99	1.08E-06
17.59	1.07E-06
17.17	1.05E-06
16.90	1.00E-06
16.51	9.83E-07
16.14	9.50E-07
15.86	8.99E-07
15.50	8.77E-07
15.15	8.48E-07
14.86	7.96E-07
14.55	7.53E-07
14.23	7.08E-07
13.95	6.58E-07
13.65	6.25E-07
13.33	6.06E-07
13.05	5.76E-07
12.76	5.41E-07
12.48	5.15E-07
12.21	4.73E-07
11.92	4.23E-07
11.65	3.81E-07
11.39	3.46E-07
11.14	3.13E-07
10.88	2.76E-07
10.63	2.31E-07
10.36	1.82E-07
10.11	1.41E-07
9.84	1.09E-07
9.59	8.40E-08
9.33	6.99E-08
18.71	1.14E-06
19.14	1.30E-06
19.56	1.44E-06
20.01	1.59E-06
20.47	1.71E-06
20.95	1.84E-06
21.45	2.00E-06
21.98	2.20E-06
22.52	2.40E-06

23.04	2.51E-06
23.58	2.68E-06
24.15	2.85E-06
24.76	3.06E-06
25.33	3.40E-06
25.97	3.79E-06
26.63	4.21E-06
27.27	4.55E-06
27.95	4.91E-06
28.64	5.28E-06
29.34	5.87E-06
30.08	6.85E-06
30.88	7.95E-06
31.65	8.98E-06
32.47	9.84E-06
36.04	1.73E-05
36.31	2.28E-05
36.50	2.17E-05
36.70	2.26E-05
37.12	2.49E-05
37.63	2.51E-05
38.16	2.49E-05
38.77	2.43E-05
39.40	2.25E-05
40.03	2.16E-05
40.68	2.25E-05
41.38	2.56E-05
42.26	2.98E-05
43.02	2.87E-05
43.67	3.40E-05
44.37	2.53E-05

8, T = 800°F, R = 0.05	
ΔK	*da/dN*
18.71	1.14E-06
19.14	1.30E-06
19.56	1.44E-06
20.01	1.59E-06
20.47	1.71E-06
20.95	1.84E-06
21.45	2.00E-06
21.98	2.20E-06
22.52	2.40E-06
23.04	2.51E-06
23.58	2.68E-06
24.15	2.85E-06
24.76	3.06E-06
25.33	3.40E-06
25.97	3.79E-06
26.63	4.21E-06
27.27	4.55E-06
27.95	4.91E-06
28.64	5.28E-06
29.34	5.87E-06
30.08	6.85E-06
30.88	7.95E-06
31.65	8.98E-06
32.47	9.84E-06
36.04	1.73E-05
36.31	2.28E-05
36.50	2.17E-05
36.70	2.26E-05
37.12	2.49E-05
37.63	2.51E-05
38.16	2.49E-05
38.77	2.43E-05
39.40	2.25E-05
40.03	2.16E-05
40.68	2.25E-05
41.38	2.56E-05
42.26	2.98E-05
43.02	2.87E-05
43.67	3.40E-05
44.37	2.53E-05

3, T = 800°F, R = 0.5	
ΔK	*da/dN*
17.78	8.92E-07
17.46	8.21E-07
17.21	7.94E-07
16.88	7.54E-07
16.59	7.27E-07
16.33	6.77E-07
16.06	6.49E-07
15.76	6.08E-07
15.54	5.66E-07
15.33	5.33E-07
15.05	5.12E-07
14.82	4.80E-07
14.60	4.42E-07
14.38	4.07E-07
14.13	3.81E-07
13.96	3.49E-07
13.73	3.12E-07
13.54	2.81E-07
13.35	2.54E-07
13.16	2.22E-07
12.98	1.96E-07
12.81	1.76E-07
12.62	1.47E-07

3, T = 800°F, R = 0.5	
ΔK	*da/dN*
19.47	9.37E-07
19.84	1.12E-06
20.23	1.32E-06
20.62	1.51E-06
21.01	1.68E-06
21.40	1.85E-06
22.30	2.04E-06
22.41	2.00E-06
22.53	1.91E-06
22.66	1.94E-06
22.80	2.03E-06
22.95	2.15E-06
23.10	2.27E-06
23.27	2.42E-06
23.45	2.59E-06
23.65	2.74E-06
23.85	2.84E-06
24.06	2.89E-06
24.26	2.97E-06
24.48	3.03E-06
24.71	3.13E-06
24.94	3.23E-06
25.20	3.39E-06

6, T = 800°F, R = 0.5	
ΔK	*da/dN*
14.69	5.62E-07
14.78	5.82E-07
14.86	5.95E-07
14.95	6.11E-07
15.03	6.33E-07
15.10	6.44E-07
15.20	6.41E-07
15.30	6.51E-07
15.37	6.51E-07
15.46	6.50E-07
15.55	6.52E-07
15.64	6.64E-07
15.74	6.72E-07
15.84	6.97E-07
15.94	7.29E-07
16.03	7.56E-07
16.14	8.09E-07
16.23	8.67E-07
16.32	9.11E-07
16.43	9.63E-07
16.54	1.01E-06
16.64	1.04E-06
16.73	1.05E-06

206-3, T = 800°F, *R* = -0.5	
Δ*K*	*da/dN*
18.01	4.36E-07
17.61	4.18E-07
17.27	3.91E-07
16.92	3.60E-07
16.62	3.42E-07
16.26	3.32E-07
15.97	3.33E-07
15.65	3.23E-07
15.35	3.10E-07
15.10	2.90E-07
14.78	2.76E-07
14.56	2.62E-07
14.30	2.57E-07
14.01	2.53E-07
13.78	2.41E-07
13.52	2.27E-07
13.27	2.08E-07
13.05	1.84E-07
12.85	1.70E-07
12.59	1.60E-07
12.40	1.45E-07
12.20	1.27E-07
11.99	1.15E-07
11.79	1.01E-07
11.59	8.55E-08
11.40	7.16E-08
11.19	5.86E-08
11.00	4.55E-08
10.82	3.31E-08
10.65	2.33E-08

206-3, T = 800°F, *R* = -0.5	
Δ*K*	*da/dN*
19.79	4.52E-07
20.06	5.66E-07
20.40	7.32E-07
20.74	9.11E-07
21.10	1.17E-06
21.45	1.48E-06
21.78	1.72E-06
22.14	1.97E-06
22.54	2.31E-06
22.98	2.66E-06
23.40	3.05E-06
23.79	3.35E-06
24.20	3.59E-06
24.61	3.86E-06
25.08	4.09E-06
25.56	4.36E-06
26.03	4.66E-06
26.55	5.12E-06
27.07	5.60E-06
27.62	6.02E-06
28.18	6.69E-06
28.76	7.18E-06
29.35	7.60E-06
29.90	8.29E-06
30.51	9.04E-06
31.18	9.83E-06
31.75	1.04E-05
32.40	1.12E-05
33.13	1.22E-05
33.87	1.38E-05
34.56	1.59E-05
35.33	1.86E-05
36.15	2.31E-05
36.91	3.38E-05
37.76	3.89E-05
39.30	5.07E-05
41.69	5.49E-05
44.00	6.70E-05
44.69	8.55E-05
47.12	1.07E-04

9, T = 1200°F, *R* = 0.05	
Δ*K*	*da/dN*
14.24	4.39E-07
13.84	3.89E-07
13.58	3.40E-07
13.15	2.89E-07
12.94	2.46E-07
12.57	2.09E-07
12.29	1.83E-07
12.02	1.49E-07
11.73	1.27E-07
11.47	1.06E-07
11.21	8.91E-08
10.91	7.32E-08
10.67	5.75E-08
10.41	4.40E-08
10.18	3.54E-08
9.95	2.91E-08
9.73	2.50E-08
9.51	1.93E-08
9.32	1.32E-08

9, T = 1200°F, *R* = 0.05	
Δ*K*	d*a*/d*N*
13.94	4.11E-07
14.17	5.83E-07
14.39	7.05E-07
14.57	7.77E-07
14.81	9.02E-07
14.99	1.04E-06
15.26	1.17E-06
15.49	1.34E-06
15.75	1.45E-06
16.00	1.60E-06
16.25	1.76E-06
16.53	1.90E-06
16.80	2.04E-06
17.09	2.17E-06
17.38	2.29E-06
17.66	2.40E-06
17.96	2.56E-06
18.27	2.73E-06
18.61	2.92E-06
18.94	3.10E-06
19.27	3.28E-06
19.58	3.45E-06
19.92	3.59E-06
20.30	3.82E-06
20.70	4.00E-06
21.08	4.19E-06
21.44	4.37E-06
21.81	4.60E-06
22.19	4.89E-06
22.58	5.20E-06
23.00	5.51E-06
23.42	5.73E-06
23.85	5.88E-06
24.28	6.10E-06
24.72	6.25E-06
25.18	6.52E-06
25.63	6.85E-06
26.11	7.24E-06
26.59	7.61E-06
27.10	7.94E-06
27.59	8.25E-06
28.11	8.27E-06
28.59	8.48E-06
29.09	8.54E-06
29.65	8.88E-06
30.19	9.18E-06
30.82	9.51E-06
31.35	9.77E-06
31.90	9.56E-06
33.27	1.09E-05
33.74	9.26E-06
37.52	1.00E-05
37.72	1.12E-05
37.89	1.10E-05
38.08	1.11E-05
38.34	1.10E-05
38.59	1.13E-05
38.87	1.19E-05
39.03	1.20E-05
39.39	1.24E-05
39.82	1.22E-05
40.06	1.23E-05
40.33	1.22E-05
40.61	1.23E-05
40.86	1.23E-05
41.04	1.23E-05
41.27	1.30E-05
41.62	1.33E-05
42.07	1.35E-05
42.35	1.36E-05
42.58	1.39E-05
42.96	1.39E-05
43.36	1.46E-05
43.72	1.54E-05
44.03	1.54E-05
44.36	1.57E-05
44.70	1.57E-05
45.02	1.59E-05
45.47	1.64E-05
45.90	1.72E-05
46.31	1.79E-05
46.68	1.85E-05
47.12	1.93E-05
47.53	1.99E-05
47.91	2.06E-05
48.29	2.13E-05
48.75	2.17E-05
49.22	2.22E-05
49.66	2.23E-05
50.06	2.28E-05
50.55	2.34E-05
51.06	2.45E-05
51.64	2.61E-05
52.09	2.74E-05
52.59	2.90E-05
53.14	3.01E-05
53.74	3.11E-05
54.30	3.21E-05
54.84	3.40E-05
55.37	3.59E-05
56.00	3.78E-05
56.67	4.22E-05
57.21	4.45E-05
57.80	4.60E-05
58.35	4.72E-05
59.00	4.90E-05
59.79	5.07E-05
60.33	5.13E-05
60.99	5.55E-05
61.74	6.11E-05
62.47	6.44E-05
63.30	7.18E-05
64.07	7.61E-05
64.98	7.99E-05
66.04	8.30E-05
66.59	8.75E-05
67.49	9.00E-05

10, T = 1200°F, R = 0.5	
ΔK	*da/dN*
18.90	2.68E-06
18.50	2.40E-06
18.10	2.30E-06
17.68	2.18E-06
17.29	2.07E-06
16.90	1.95E-06
16.56	1.81E-06
16.21	1.67E-06
15.89	1.56E-06
15.58	1.45E-06
15.27	1.36E-06
14.96	1.26E-06
14.69	1.17E-06
14.40	1.07E-06
14.12	9.80E-07
13.85	8.85E-07
13.59	7.92E-07
13.33	6.98E-07
13.09	6.14E-07
12.87	5.39E-07
12.61	4.74E-07
12.43	4.13E-07
12.17	3.56E-07
11.98	3.02E-07
11.78	2.54E-07
11.55	2.21E-07
11.37	1.88E-07
11.18	1.57E-07
11.00	1.32E-07
10.82	1.11E-07
10.65	9.30E-08
10.49	7.58E-08
10.31	5.91E-08
10.17	4.55E-08
9.98	3.30E-08
9.88	2.42E-08
9.71	1.82E-08
9.58	1.29E-08
9.46	1.06E-08

10, T = 1200°F, R = 0.5	
ΔK	*da/dN*
14.01	1.45E-06
14.14	1.51E-06
14.29	1.58E-06
14.42	1.65E-06
14.56	1.71E-06
14.71	1.78E-06
14.87	1.80E-06
15.02	1.86E-06
15.16	1.92E-06
15.32	2.02E-06
15.49	2.13E-06
15.67	2.24E-06
15.84	2.34E-06
16.02	2.44E-06
16.21	2.54E-06
16.39	2.60E-06
16.57	2.70E-06
16.75	2.79E-06
16.94	2.87E-06
17.12	2.97E-06
17.32	3.09E-06
17.54	3.20E-06
17.75	3.29E-06
17.94	3.38E-06
18.15	3.51E-06
18.35	3.62E-06
18.58	3.76E-06
18.81	3.92E-06
19.02	4.04E-06
19.24	4.19E-06
19.48	4.30E-06
19.71	4.43E-06
19.95	4.52E-06
20.19	4.64E-06
20.43	4.87E-06
20.67	4.86E-06
20.92	4.91E-06
21.17	5.00E-06
21.45	5.24E-06
21.70	5.49E-06
21.96	5.73E-06
22.22	6.05E-06
22.49	6.20E-06
22.77	6.43E-06
23.05	6.44E-06

23.33	6.61E-06
23.60	7.36E-06
24.60	6.79E-06
24.72	7.44E-06
24.86	7.54E-06
25.00	7.64E-06
25.12	7.68E-06
25.28	7.56E-06
25.44	7.57E-06
25.61	7.67E-06
25.76	7.64E-06
25.92	7.62E-06
26.10	7.62E-06
26.27	7.65E-06
26.46	7.76E-06
26.66	8.00E-06
26.86	8.32E-06
27.07	8.56E-06
27.27	8.72E-06
27.46	8.95E-06
27.68	9.20E-06
27.92	9.43E-06
28.14	9.63E-06
28.38	9.91E-06
28.63	1.00E-05
28.86	1.01E-05
29.10	1.02E-05
29.36	1.04E-05
29.63	1.06E-05
29.87	1.08E-05
30.16	1.12E-05
30.44	1.15E-05
30.72	1.20E-05
31.02	1.25E-05
31.31	1.30E-05
31.61	1.38E-05
31.91	1.45E-05
32.20	1.53E-05
32.54	1.61E-05
32.85	1.69E-05
33.18	1.76E-05
33.53	1.81E-05
33.89	1.84E-05
34.24	1.89E-05
34.60	1.94E-05

34.96	2.04E-05
35.38	2.18E-05
35.74	2.31E-05
36.11	2.41E-05
36.49	2.52E-05
36.91	2.65E-05
37.35	2.86E-05
37.78	3.13E-05
38.20	3.47E-05
38.65	3.95E-05
39.10	4.65E-05
39.58	5.75E-05
40.06	7.11E-05
40.56	9.16E-05

206-5, T = 1200°F, *R* = -0.5	
Δ*K*	*da/dN*
19.12	1.80E-06
18.66	1.44E-06
18.15	1.13E-06
17.71	9.82E-07
17.27	8.73E-07
16.81	7.61E-07
16.41	6.60E-07
16.02	5.83E-07
15.65	5.39E-07
15.26	4.96E-07
14.91	4.60E-07
14.55	4.24E-07
14.22	3.89E-07
13.88	3.54E-07
13.61	3.21E-07
13.26	2.86E-07
13.01	2.48E-07
12.65	1.86E-07
11.20	1.52E-07
10.94	1.21E-07
10.71	9.62E-08
10.48	8.20E-08
10.27	7.06E-08
10.10	7.22E-08
9.88	6.87E-08
9.64	7.15E-08
9.45	7.01E-08
9.27	6.06E-08
9.15	6.97E-08

206-5, T = 1200°F, *R* = -0.5			
Δ*K*	*da/dN*		
16.51	1.29E-06	35.99	1.29E-05
16.85	1.35E-06	36.46	1.28E-05
17.18	1.46E-06	36.92	1.31E-05
17.54	1.67E-06	37.44	1.40E-05
17.94	1.96E-06	37.97	1.51E-05
18.30	2.27E-06	38.49	1.74E-05
18.70	2.64E-06	39.12	1.96E-05
19.10	3.18E-06	39.61	2.11E-05
19.50	3.52E-06	40.28	2.26E-05
19.91	3.70E-06	40.95	2.39E-05
20.32	3.94E-06	41.45	2.59E-05
20.83	4.12E-06	42.01	2.77E-05
21.30	4.21E-06	42.76	3.09E-05
21.77	4.26E-06	43.54	3.50E-05
22.29	4.51E-06	44.24	3.85E-05
22.79	4.74E-06	45.00	4.35E-05
23.32	4.94E-06	45.72	4.92E-05
23.87	5.30E-06	46.51	5.65E-05
24.44	5.79E-06	47.52	6.71E-05
25.02	6.47E-06	48.44	7.92E-05
25.60	7.12E-06	49.34	9.23E-05
26.16	7.64E-06	50.46	1.13E-04
26.79	8.27E-06	51.66	1.44E-04
27.66	8.87E-06	52.52	1.61E-04
28.27	9.34E-06	53.94	2.03E-04
28.83	9.84E-06	55.80	2.50E-04
29.39	1.03E-05	56.93	2.88E-04
30.02	1.07E-05		
30.70	1.10E-05		
31.44	1.13E-05		
32.17	1.15E-05		
32.86	1.19E-05		
30.97	8.58E-06		
31.28	8.44E-06		
31.67	8.37E-06		
31.99	8.69E-06		
32.26	8.91E-06		
32.64	9.31E-06		
32.98	9.72E-06		
33.34	9.94E-06		
33.78	1.08E-05		
34.17	1.13E-05		
34.60	1.17E-05		
35.04	1.21E-05		
35.47	1.27E-05		

K.8.3 IN-718.

4470-407-1, SENBH, T = 75°F, *R* = 0	
Δ*K*	*da/dN*
24.21	1.29E-06
23.45	1.15E-06
22.44	9.92E-07
21.39	8.36E-07
20.44	7.01E-07
19.71	5.81E-07
18.85	4.82E-07
18.22	4.09E-07
17.56	3.49E-07
16.88	2.96E-07
16.41	2.51E-07
16.36	2.02E-07
16.14	1.55E-07
15.86	1.14E-07
15.69	8.60E-08
15.40	6.28E-08
15.34	5.90E-08
15.40	6.42E-08
15.33	7.16E-08
15.11	7.83E-08
14.86	7.43E-08
14.84	7.20E-08
14.66	6.24E-08
14.57	5.66E-08
14.52	4.98E-08
14.44	4.11E-08
14.34	3.89E-08
14.26	2.91E-08
14.21	2.19E-08
14.21	1.87E-08
14.11	1.44E-08
14.08	1.15E-08
14.10	8.22E-09
14.08	1.41E-08
14.07	1.88E-08
14.11	2.14E-08
14.12	2.58E-08
14.02	2.77E-08
13.96	2.77E-08
13.83	2.12E-08
13.78	1.73E-08
13.79	1.97E-08
13.73	1.91E-08
13.72	1.85E-08
13.59	2.35E-08
13.59	2.63E-08
13.64	1.89E-08
13.60	1.45E-08
13.54	2.37E-08
13.59	2.98E-08
13.61	2.28E-08
13.33	1.94E-08
13.20	1.87E-08
13.21	8.76E-09
13.16	5.65E-09
13.22	5.85E-09
13.23	3.35E-09
13.25	1.10E-08
13.21	2.41E-08
13.20	2.67E-08
13.20	1.99E-08
12.97	2.40E-08
12.95	2.90E-08
12.91	1.88E-08
12.95	1.09E-08
12.79	1.79E-08
12.76	1.88E-08
12.79	1.03E-08
12.81	6.51E-09
12.78	1.18E-08
12.79	6.83E-09
12.78	5.26E-09
12.79	2.36E-08
12.79	2.96E-08
12.78	2.56E-08
12.54	2.03E-08
12.45	1.26E-08

4470-401-1, Kb, T = 75°F, *R* = 0	
Δ*K*	*da/dN*
14.62	9.67E-08
14.70	1.14E-07
14.79	1.23E-07
14.83	1.05E-07
14.88	9.45E-08
14.92	8.97E-08
14.97	9.26E-08
15.02	9.45E-08
15.07	8.82E-08
15.11	7.58E-08
15.15	6.95E-08
15.18	6.93E-08
15.20	6.93E-08
15.24	7.30E-08
15.29	7.38E-08
15.33	8.21E-08
15.36	8.90E-08
15.41	8.74E-08
15.45	9.46E-08
15.50	1.08E-07
15.56	1.17E-07
15.62	1.11E-07
15.68	1.07E-07
15.73	1.13E-07
15.77	1.28E-07
15.83	1.38E-07
15.91	1.51E-07
16.01	1.47E-07
16.07	1.60E-07
16.14	1.51E-07
16.21	1.45E-07
16.28	1.57E-07
16.36	1.54E-07
16.44	1.75E-07
16.50	1.71E-07
16.59	1.90E-07
16.67	2.07E-07
16.78	2.06E-07
16.87	2.31E-07
16.96	2.38E-07
17.07	2.71E-07
17.20	2.79E-07
17.33	2.99E-07
17.46	3.36E-07
17.60	3.46E-07
17.75	3.53E-07
17.90	3.88E-07
18.08	4.27E-07
18.24	4.47E-07
18.42	4.52E-07
18.61	4.89E-07
18.81	5.25E-07
18.99	5.42E-07
19.20	5.86E-07
19.44	6.27E-07
19.68	6.73E-07
19.92	6.86E-07
20.16	7.17E-07
20.41	7.56E-07
20.66	7.91E-07
20.92	8.31E-07
21.19	8.78E-07
21.48	9.25E-07
21.76	9.61E-07
22.05	1.00E-06
22.36	1.06E-06
22.68	1.10E-06
22.98	1.15E-06
23.31	1.21E-06
23.64	1.28E-06
23.98	1.35E-06
24.33	1.43E-06
24.68	1.51E-06
25.05	1.60E-06
25.41	1.70E-06
25.79	1.80E-06
26.20	1.91E-06
26.61	2.01E-06
27.01	2.11E-06
27.43	2.19E-06
27.83	2.28E-06
28.24	2.45E-06
28.65	2.64E-06
29.11	2.86E-06
29.57	3.06E-06
30.08	3.32E-06
30.56	3.58E-06
31.04	3.82E-06
31.57	4.06E-06
32.08	4.35E-06
32.58	4.67E-06
33.11	4.94E-06
33.62	5.28E-06
34.11	5.71E-06
34.64	6.15E-06
35.13	6.59E-06
35.60	6.95E-06
36.10	7.11E-06
36.53	7.09E-06
36.86	7.19E-06
37.20	7.32E-06
37.53	7.53E-06
37.80	8.05E-06
38.10	8.51E-06
38.41	8.86E-06
38.63	9.41E-06
38.86	9.85E-06
39.11	1.02E-05
39.22	1.03E-05
39.37	1.01E-05
39.51	1.00E-05

4470-401-2, Kb, T = 75°F, *R* = 0.5											
Δ*K*	*da/dN*		11.71	1.49E-08		12.86	5.54E-08		17.10	4.11E-07
10.87	2.94E-08		11.72	1.12E-08		12.92	5.30E-08		17.37	4.56E-07
10.90	2.64E-08		11.73	1.35E-08		12.97	4.93E-08		17.66	5.02E-07
10.93	2.51E-08		11.73	1.58E-08		12.99	4.60E-08		17.97	5.64E-07
10.95	2.36E-08		11.74	1.90E-08		13.03	4.98E-08		18.31	6.53E-07
10.94	2.21E-08		11.77	2.32E-08		13.09	5.35E-08		18.69	7.56E-07
10.95	2.12E-08		11.81	2.81E-08		13.14	5.63E-08		19.15	8.75E-07
10.96	1.63E-08		11.84	2.67E-08		13.19	5.66E-08		19.67	1.01E-06
10.98	1.63E-08		11.86	2.33E-08		13.24	5.49E-08		20.27	1.16E-06
11.00	1.58E-08		11.89	2.35E-08		13.29	5.17E-08		20.90	1.37E-06
11.02	1.16E-08		11.92	2.20E-08		13.34	5.00E-08		21.62	1.72E-06
11.03	1.29E-08		11.94	2.16E-08		13.37	4.94E-08		22.54	2.27E-06
11.05	1.35E-08		11.96	2.13E-08		13.41	5.03E-08			
11.06	1.45E-08		11.98	2.14E-08		13.46	5.06E-08			
11.08	1.53E-08		12.00	2.14E-08		13.50	5.03E-08			
11.11	1.73E-08		12.02	2.17E-08		13.55	5.20E-08			
11.13	1.89E-08		12.05	2.07E-08		13.59	5.60E-08			
11.19	1.44E-08		12.07	1.87E-08		13.64	6.01E-08			
11.22	1.39E-08		12.09	1.77E-08		13.69	6.42E-08			
11.24	9.40E-09		12.10	1.72E-08		13.74	7.24E-08			
11.25	6.27E-09		12.12	1.60E-08		13.80	8.11E-08			
11.25	8.22E-09		12.13	1.67E-08		13.87	8.93E-08			
11.26	1.24E-08		12.15	1.83E-08		13.96	9.47E-08			
11.27	1.81E-08		12.17	2.07E-08		14.04	9.71E-08			
11.30	2.32E-08		12.19	2.33E-08		14.13	9.75E-08			
11.34	2.77E-08		12.21	2.66E-08		14.20	9.66E-08			
11.37	2.54E-08		12.24	2.96E-08		14.27	9.67E-08			
11.39	2.06E-08		12.27	3.06E-08		14.35	1.00E-07			
11.41	1.80E-08		12.31	3.09E-08		14.47	1.08E-07			
11.43	1.61E-08		12.34	2.54E-08		14.57	1.15E-07			
11.45	1.12E-08		12.36	2.13E-08		14.67	1.20E-07			
11.46	1.14E-08		12.37	1.75E-08		14.77	1.24E-07			
11.46	1.22E-08		12.38	1.87E-08		14.87	1.28E-07			
11.48	1.21E-08		12.39	2.16E-08		14.97	1.34E-07			
11.49	1.34E-08		12.42	2.63E-08		15.10	1.42E-07			
11.51	1.48E-08		12.45	3.59E-08		15.21	1.54E-07			
11.53	1.72E-08		12.49	3.96E-08		15.33	1.70E-07			
11.54	1.42E-08		12.53	4.19E-08		15.45	1.89E-07			
11.56	1.50E-08		12.58	3.69E-08		15.59	2.09E-07			
11.58	1.54E-08		12.61	3.37E-08		15.75	2.23E-07			
11.59	1.51E-08		12.64	2.95E-08		15.92	2.36E-07			
11.61	1.55E-08		12.66	2.63E-08		16.08	2.50E-07			
11.62	1.57E-08		12.68	2.85E-08		16.24	2.70E-07			
11.64	1.66E-08		12.70	3.87E-08		16.42	2.95E-07			
11.66	1.80E-08		12.74	5.01E-08		16.62	3.25E-07			
11.68	1.90E-08		12.80	5.47E-08		16.85	3.69E-07			

4470-401-4, Kb, T = 75°F, *R* = 0.7	
Δ*K*	*da/dN*
13.62	3.45E-07
13.76	1.52E-07
13.87	1.43E-07
13.96	1.58E-07
14.05	1.82E-07
14.17	2.05E-07
14.28	2.19E-07
14.37	2.42E-07
14.47	2.70E-07
14.58	3.05E-07
14.68	3.50E-07
14.80	3.81E-07
14.89	4.07E-07
14.98	4.33E-07
15.10	4.69E-07
15.21	5.23E-07
15.31	5.84E-07
15.42	5.99E-07
15.53	7.62E-07
15.63	9.29E-07
15.71	1.01E-06
15.82	1.01E-06
15.93	1.06E-06
16.07	1.07E-06
16.18	9.34E-07
16.28	9.65E-07
16.40	1.07E-06
16.52	1.19E-06
16.62	1.29E-06
16.74	1.41E-06
16.86	1.51E-06
16.97	1.58E-06
17.07	1.68E-06
17.20	1.82E-06
17.33	1.90E-06
17.43	2.02E-06
17.54	2.15E-06
17.66	2.29E-06
17.79	2.48E-06
17.91	2.73E-06
18.03	2.97E-06
18.15	3.29E-06
18.30	3.71E-06
18.42	4.12E-06
18.53	4.55E-06
18.66	5.39E-06
18.81	6.42E-06
18.94	7.44E-06
19.06	8.45E-06
19.18	9.53E-06
19.33	1.01E-05
19.44	1.07E-05
19.57	1.17E-05
19.71	1.36E-05
19.89	1.78E-05
20.03	2.37E-05
20.20	3.60E-05

4470-401-5, Kb, T = 600°F, *R* = 0	
Δ*K*	*da/dN*
28.197	2.01117E-06
28.389	2.11797E-06
28.582	2.2224E-06
28.768	2.32209E-06
28.958	2.42172E-06
29.174	2.54087E-06
29.375	2.66324E-06
29.574	2.77994E-06
29.771	2.88189E-06
29.972	2.97102E-06
30.160	3.0465E-06
30.369	3.1251E-06
30.563	3.24922E-06
30.755	3.39189E-06
30.973	3.55506E-06
31.155	3.71653E-06
31.361	3.86303E-06
31.552	4.00073E-06
31.754	4.09059E-06
31.958	4.17837E-06
32.146	4.23645E-06
32.347	4.28916E-06
32.568	4.39843E-06
32.731	4.54025E-06
32.948	4.70993E-06
33.155	4.85818E-06
33.331	4.98263E-06
33.518	5.05337E-06
33.733	5.06937E-06
33.914	5.10976E-06
34.119	5.17765E-06
34.308	5.25611E-06
34.496	5.31606E-06
34.705	5.3938E-06
34.901	5.5035E-06
35.063	5.64315E-06
35.269	5.83332E-06
35.443	6.06635E-06
35.618	6.2821E-06
35.825	6.47944E-06
35.980	6.66116E-06
36.202	6.81654E-06
36.368	6.96543E-06
36.518	7.09487E-06

4470-407-2, SENBH, T = 1000°F, *R* = 0	
Δ*K*	*da/dN*
19.83	1.84E-06
19.16	1.65E-06
18.42	1.43E-06
17.61	1.24E-06
16.78	1.07E-06
16.00	9.20E-07
15.33	7.91E-07
14.65	6.84E-07
14.05	5.99E-07
13.49	5.26E-07
12.97	4.55E-07
12.53	3.90E-07
12.50	3.33E-07
12.30	2.85E-07
12.04	2.49E-07
11.82	2.17E-07
11.57	1.90E-07
11.36	1.63E-07
11.22	1.39E-07
11.11	1.20E-07
10.98	1.05E-07
10.90	9.52E-08
10.73	8.58E-08
10.66	7.71E-08
10.62	6.75E-08
10.48	5.75E-08
10.44	5.02E-08
10.32	4.52E-08
10.30	4.10E-08
10.30	3.70E-08
10.19	3.34E-08
10.19	3.20E-08
10.18	3.04E-08
10.14	2.85E-08
10.05	2.83E-08
10.08	2.75E-08
10.06	2.58E-08
10.01	2.36E-08
9.94	2.24E-08
9.94	2.19E-08
9.92	2.17E-08
9.94	2.19E-08
9.92	2.23E-08
9.78	2.17E-08
9.75	2.05E-08
9.76	1.97E-08
9.76	1.87E-08
9.78	1.70E-08
9.68	1.52E-08
9.64	1.42E-08
9.64	1.36E-08
9.64	1.46E-08
9.68	1.74E-08
9.70	1.95E-08
9.69	1.96E-08
9.52	1.83E-08
9.48	1.58E-08
9.48	1.30E-08
9.50	1.07E-08
9.52	1.05E-08
9.52	1.16E-08
9.51	1.34E-08
9.52	1.36E-08
9.48	1.34E-08
9.40	1.24E-08
9.42	1.12E-08
9.42	1.01E-08
9.40	1.01E-08

4470-401-8, Kb, T = 1000°F, *R* = 0	
Δ*K*	*da/dN*
14.28	3.93E-07
14.37	4.16E-07
14.43	3.51E-07
14.49	3.84E-07
14.57	4.12E-07
14.64	4.44E-07
14.73	4.76E-07
14.83	5.11E-07
14.93	5.32E-07
15.02	5.07E-07
15.10	5.29E-07
15.20	5.37E-07
15.29	5.60E-07
15.39	5.87E-07
15.50	6.12E-07
15.61	6.29E-07
15.71	6.57E-07
15.83	6.44E-07
15.94	6.93E-07
16.05	7.32E-07
16.18	7.80E-07
16.31	8.10E-07
16.45	8.55E-07
16.60	9.15E-07
16.75	8.55E-07
16.88	9.05E-07
17.02	9.54E-07
17.18	1.01E-06
17.34	1.04E-06
17.51	1.11E-06
17.70	1.17E-06
17.87	1.17E-06
18.03	1.21E-06
18.21	1.27E-06
18.38	1.32E-06
18.57	1.38E-06
18.76	1.44E-06
18.96	1.49E-06
19.16	1.53E-06
19.37	1.59E-06
19.58	1.61E-06
19.79	1.72E-06
20.01	1.84E-06
20.25	1.96E-06
20.51	2.05E-06
20.76	2.15E-06
21.01	2.24E-06
21.26	2.27E-06
21.52	2.38E-06
21.79	2.52E-06
22.07	2.68E-06
22.37	2.83E-06
22.69	3.00E-06
22.99	3.16E-06
23.30	3.31E-06
23.63	3.46E-06
23.96	3.67E-06
24.31	3.90E-06
24.69	4.14E-06
25.05	4.34E-06
25.42	4.56E-06
25.80	4.82E-06
26.21	5.07E-06
26.63	5.36E-06
27.03	5.57E-06
27.44	5.99E-06
27.88	6.39E-06
28.35	6.83E-06
28.79	7.24E-06
29.26	7.72E-06
29.76	8.18E-06
30.27	8.56E-06
30.74	9.17E-06
31.24	9.82E-06
31.79	1.04E-05
32.26	1.12E-05
32.79	1.21E-05
33.36	1.30E-05
33.84	1.39E-05
34.38	1.48E-05
34.97	1.55E-05
35.39	1.62E-05
35.86	1.76E-05
36.38	1.89E-05
36.93	2.04E-05
37.37	2.13E-05
37.80	2.29E-05
38.27	2.43E-05
38.76	2.62E-05
39.03	2.67E-05
39.32	2.70E-05
39.62	2.74E-05

4470-401-6, Kb, T = 1000°F, *R* = 0.5	
Δ*K*	*da/dN*
15.30	1.26793E-06
15.29	1.24272E-06
15.37	1.19896E-06
15.49	1.27965E-06
15.61	1.37627E-06
15.73	1.4519E-06
15.85	1.50574E-06
15.97	1.55161E-06
16.09	1.61292E-06
16.21	1.67629E-06
16.33	1.73713E-06
16.44	1.8038E-06
16.56	1.87243E-06
16.68	1.93754E-06
16.80	1.99775E-06
16.92	2.06079E-06
17.03	2.118E-06
17.15	2.16575E-06
17.27	2.21729E-06
17.39	2.2588E-06
17.51	2.3259E-06
17.63	2.40314E-06
17.73	2.4721E-06
17.85	2.54423E-06
17.97	2.62121E-06
18.08	2.69358E-06
18.21	2.75188E-06
18.33	2.8341E-06
18.44	2.93614E-06
18.55	3.05869E-06
18.68	3.17397E-06
18.79	3.28391E-06
18.91	3.39883E-06
19.02	3.48873E-06
19.14	3.58825E-06
19.27	3.6807E-06
19.38	3.77696E-06
19.50	3.82279E-06
19.61	3.89725E-06
19.74	3.94066E-06
19.84	4.02381E-06

4470-5, SENBH, Shed 1, T = 1000°F, *R* = 0.7	
Δ*K*	*da/dN*
12.16	5.50E-07
12.07	5.23E-07
11.96	4.93E-07
11.86	4.63E-07
11.75	4.37E-07
11.66	4.12E-07
11.57	3.95E-07
11.47	3.86E-07
11.35	3.77E-07
11.24	3.67E-07
11.13	3.59E-07
11.13	3.48E-07
11.04	3.35E-07
10.92	3.21E-07
10.82	3.06E-07
10.71	2.86E-07
10.61	2.65E-07
10.52	2.46E-07
10.44	2.28E-07
10.36	2.12E-07
10.29	2.00E-07
10.22	1.93E-07
10.13	1.87E-07
10.05	1.79E-07
9.98	1.67E-07
9.90	1.53E-07
9.85	1.38E-07
9.80	1.25E-07
9.75	1.13E-07
9.71	1.05E-07
9.67	9.69E-08
9.62	9.09E-08
9.58	8.49E-08
9.54	8.25E-08
9.50	8.01E-08
9.47	7.70E-08
9.43	7.39E-08
9.40	7.08E-08
9.36	6.78E-08
9.33	6.36E-08
9.31	6.35E-08
9.29	6.16E-08
9.27	5.92E-08
9.24	5.66E-08
9.23	5.34E-08
9.21	5.12E-08
9.18	4.77E-08
9.17	4.73E-08
9.15	4.50E-08
9.15	4.23E-08
9.13	3.88E-08
9.11	3.66E-08
9.09	3.81E-08
9.08	3.94E-08
9.04	4.07E-08
9.02	4.08E-08
9.00	4.04E-08
8.99	3.58E-08
8.99	3.15E-08
9.00	3.04E-08
9.00	3.01E-08
9.01	2.79E-08
8.95	2.46E-08
8.94	2.21E-08
8.89	1.97E-08
8.89	1.84E-08
8.89	1.80E-08
8.87	2.00E-08
8.85	2.18E-08
8.84	2.15E-08
8.83	2.03E-08
8.82	2.01E-08
8.81	2.08E-08
8.81	1.96E-08
8.80	1.91E-08
8.78	2.02E-08
8.78	2.06E-08
8.78	1.98E-08
8.77	1.85E-08
8.76	1.78E-08
8.76	1.73E-08
8.76	1.70E-08
8.76	1.74E-08
8.77	1.86E-08
8.76	1.91E-08
8.76	2.00E-08
8.76	2.01E-08
8.78	1.95E-08
8.77	1.97E-08

4470-5, SENBH, Shed 2, T = 1000°F, *R* = 0.7	
Δ*K*	*da/dN*
12.53	7.14E-07
12.44	6.85E-07
12.28	6.51E-07
12.17	6.05E-07
12.00	5.60E-07
11.90	5.28E-07
11.72	4.95E-07
11.55	4.68E-07
11.35	4.57E-07
11.20	4.49E-07
11.04	4.35E-07
10.96	4.29E-07
10.94	4.30E-07
10.91	4.30E-07
10.90	4.23E-07
10.78	4.07E-07
10.74	3.79E-07
10.58	3.53E-07
10.48	3.34E-07
10.42	3.25E-07
10.29	3.14E-07
10.19	3.04E-07
10.13	3.01E-07
10.07	2.87E-07
10.02	2.78E-07
9.94	2.68E-07
9.87	2.58E-07
9.79	2.52E-07
9.72	2.38E-07
9.66	2.30E-07
9.59	2.13E-07
9.50	1.96E-07
9.45	1.80E-07
9.42	1.64E-07
9.37	1.50E-07
9.32	1.36E-07
9.22	1.27E-07
9.19	1.22E-07
9.16	1.21E-07
9.10	1.21E-07
9.09	1.21E-07
9.12	1.19E-07
9.07	1.13E-07
9.03	1.04E-07
8.96	9.60E-08
8.92	9.41E-08
8.93	9.29E-08
8.91	9.14E-08
8.90	9.12E-08
8.86	9.12E-08
8.85	9.20E-08
8.83	8.99E-08
8.88	8.84E-08
8.85	8.49E-08
8.83	8.12E-08
8.80	7.28E-08
8.78	6.99E-08
8.72	6.83E-08
8.73	6.39E-08
8.69	5.93E-08
8.61	5.25E-08
8.53	5.07E-08
8.51	4.60E-08
8.51	4.37E-08
8.47	4.09E-08
8.37	3.66E-08
8.35	3.61E-08
8.35	3.58E-08
8.35	3.65E-08
8.36	4.12E-08
8.36	4.04E-08
8.37	4.14E-08
8.28	4.04E-08

4470-401-7, Kb, T = 1000°F, *R* = 0.7	
Δ*K*	*da/dN*
6.5	1.90E-08
6.6	2.41E-08
6.7	2.79E-08
6.8	3.18E-08
6.8	3.57E-08
6.9	3.95E-08
7.0	4.32E-08
7.1	4.68E-08
7.2	5.08E-08
7.2	5.56E-08
7.3	6.03E-08
7.4	6.52E-08
7.5	6.99E-08
7.5	7.46E-08
7.6	8.00E-08
7.7	9.48E-08
7.8	1.18E-07
7.9	1.36E-07
7.9	1.41E-07
8.0	1.48E-07
8.1	1.51E-07
8.1	1.47E-07
8.2	1.52E-07
8.3	1.58E-07
8.4	1.66E-07
8.4	1.75E-07
8.5	1.82E-07
8.6	1.90E-07
8.7	2.00E-07
8.7	2.10E-07
8.8	2.21E-07
8.9	2.32E-07
8.9	2.44E-07
9.0	2.56E-07
9.1	2.67E-07
9.2	2.79E-07
9.2	2.93E-07
9.3	3.07E-07
9.4	3.22E-07
9.5	3.38E-07
9.5	3.55E-07
9.6	3.72E-07
9.7	3.86E-07
9.7	3.99E-07
9.8	4.14E-07
9.9	4.32E-07
10.0	4.64E-07
10.0	5.81E-07
10.1	6.76E-07
10.2	6.47E-07
10.2	6.66E-07
10.3	6.81E-07
10.4	6.19E-07
10.5	6.14E-07
10.5	6.62E-07
10.6	7.08E-07
10.7	7.36E-07
10.8	7.59E-07
10.9	7.85E-07
10.9	8.11E-07
11.0	8.39E-07
11.1	8.70E-07
11.2	9.12E-07
11.2	9.66E-07
11.3	1.02E-06
11.4	1.06E-06
11.5	1.09E-06
11.5	1.15E-06
11.6	1.21E-06
11.7	1.28E-06
11.8	1.35E-06
11.8	1.38E-06
11.9	1.41E-06
12.0	1.38E-06

4470-407-7, SENBH, T = 1200°F, *R* = 0	
Δ*K*	*da/dN*
20.29	2.07E-06
19.80	1.89E-06
19.33	1.69E-06
18.85	1.53E-06
18.35	1.41E-06
17.89	1.31E-06
17.38	1.22E-06
16.91	1.12E-06
16.44	1.03E-06
16.00	9.32E-07
15.56	8.54E-07
15.18	7.83E-07
14.79	7.18E-07
14.43	6.59E-07
14.09	6.03E-07
13.80	5.52E-07
13.51	5.07E-07
13.27	4.69E-07
13.01	4.35E-07
12.78	4.03E-07
12.57	3.74E-07
12.37	3.46E-07
12.19	3.19E-07
12.01	3.00E-07
11.87	2.81E-07
11.73	2.66E-07
11.58	2.50E-07
11.45	2.37E-07
11.32	2.24E-07
11.21	2.07E-07
11.06	1.92E-07
10.92	1.75E-07
10.81	1.61E-07
10.74	1.50E-07
10.72	1.43E-07
10.65	1.39E-07
10.58	1.37E-07
10.52	1.32E-07
10.43	1.26E-07
10.35	1.19E-07
10.30	1.15E-07
10.25	1.09E-07
10.16	1.03E-07
10.12	9.89E-08
10.08	9.90E-08
10.04	9.61E-08
10.00	9.28E-08
9.94	8.94E-08
9.89	8.61E-08
9.84	8.23E-08
9.82	7.78E-08
9.77	7.62E-08
9.73	7.35E-08
9.68	7.37E-08
9.64	7.03E-08
9.60	6.38E-08
9.56	6.18E-08
9.53	6.17E-08
9.53	5.91E-08
9.49	6.15E-08
9.43	6.55E-08
9.42	6.68E-08
9.37	6.22E-08
9.34	6.36E-08
9.29	6.42E-08
9.29	6.10E-08
9.22	5.33E-08
9.20	4.74E-08
9.17	4.00E-08
21.31	2.51E-06
20.86	2.30E-06
20.00	2.00E-06
19.12	1.70E-06
18.28	1.46E-06
17.40	1.27E-06
16.65	1.10E-06
15.94	9.68E-07
15.27	8.49E-07
14.70	7.48E-07
14.15	6.51E-07
13.71	5.68E-07
13.27	4.96E-07
12.91	4.34E-07
12.60	3.79E-07
12.30	3.29E-07
12.08	2.89E-07
11.87	2.55E-07
11.68	2.28E-07
11.50	2.11E-07
11.36	1.98E-07
11.20	1.83E-07
11.05	1.71E-07
10.90	1.56E-07
10.80	1.43E-07
10.69	1.31E-07
10.59	1.21E-07
10.51	1.14E-07
10.40	1.08E-07
10.32	1.05E-07
10.24	1.01E-07
10.17	9.84E-08
10.09	9.45E-08
10.02	8.92E-08
9.94	8.19E-08
9.87	7.62E-08
9.82	7.13E-08
9.77	6.87E-08
9.74	6.78E-08
9.67	6.49E-08
9.62	6.11E-08
9.57	5.65E-08
9.51	5.56E-08
9.46	5.57E-08
9.43	5.38E-08
9.36	5.20E-08
9.33	4.73E-08
9.27	4.49E-08
9.29	4.30E-08
9.26	4.51E-08
9.19	4.76E-08
9.13	4.90E-08
9.08	4.69E-08
9.06	4.29E-08
9.01	4.17E-08
8.99	4.08E-08
9.00	3.94E-08
8.97	3.44E-08
8.93	3.40E-08
8.89	3.17E-08
8.87	2.86E-08
8.84	2.75E-08
8.84	2.70E-08
8.83	2.89E-08
8.81	3.00E-08
8.79	3.24E-08
8.76	3.26E-08
8.72	3.05E-08
8.71	2.73E-08
8.67	2.24E-08
8.67	2.17E-08
8.67	2.28E-08
8.63	2.38E-08
8.62	1.98E-08
8.58	1.59E-08
8.54	1.25E-08
8.52	1.05E-08
8.56	1.22E-08
8.58	1.48E-08
8.52	1.81E-08

4470-401-9, Kb, T = 1200°F, *R* = 0	
Δ*K*	*da/dN*
15.73	6.93E-07
15.78	6.09E-07
15.81	6.94E-07
15.91	9.22E-07
16.09	1.29E-06
16.29	1.41E-06
16.50	1.45E-06
16.69	1.44E-06
16.86	1.36E-06
17.03	1.36E-06
17.19	1.37E-06
17.36	1.42E-06
17.55	1.41E-06
17.72	1.25E-06
17.86	1.22E-06
17.96	1.24E-06
18.08	1.37E-06
18.24	1.57E-06
18.44	1.89E-06
18.68	2.16E-06
18.93	2.22E-06
19.19	2.09E-06
19.44	1.82E-06
19.60	1.61E-06
19.72	1.48E-06
19.82	1.58E-06
19.96	1.85E-06
20.19	2.19E-06
20.42	2.54E-06
20.67	2.81E-06
20.95	2.98E-06
21.23	3.08E-06
21.51	3.18E-06
21.79	3.31E-06
22.05	3.35E-06
22.33	3.46E-06
22.63	3.67E-06
22.92	3.81E-06
23.22	3.92E-06
23.51	4.01E-06
23.81	4.17E-06
24.12	4.37E-06
24.42	4.52E-06
24.73	4.76E-06
25.06	5.03E-06
25.41	5.25E-06
25.73	5.38E-06
26.06	5.62E-06
26.41	5.87E-06
26.76	6.09E-06
27.09	6.40E-06
27.44	6.87E-06
27.82	7.30E-06
28.22	7.76E-06
28.61	8.15E-06
29.03	8.28E-06
29.44	8.39E-06
29.79	8.66E-06
30.15	9.10E-06
30.54	9.61E-06
30.91	1.04E-05
31.32	1.11E-05
31.76	1.16E-05
32.14	1.21E-05
32.54	1.27E-05
32.97	1.34E-05
33.32	1.41E-05
33.73	1.49E-05
34.15	1.56E-05
34.52	1.61E-05
34.87	1.69E-05
35.25	1.76E-05
35.66	1.84E-05
35.99	1.93E-05
36.33	2.00E-05
36.69	2.07E-05
36.94	2.09E-05
37.18	2.16E-05
37.43	2.28E-05
37.70	2.43E-05
38.00	2.59E-05
38.17	2.54E-05
38.33	2.51E-05
38.49	2.47E-05
38.63	2.38E-05
38.78	2.42E-05
38.90	2.49E-05

4470-407-6, SENBH, T = 1200°F, *R* = 0.7	
Δ*K*	*da/dN*
12.31	1.03E-06
12.31	9.83E-07
12.08	9.12E-07
11.77	8.16E-07
11.46	7.26E-07
11.16	6.53E-07
10.84	5.89E-07
10.53	5.34E-07
10.24	4.80E-07
9.96	4.28E-07
9.72	3.83E-07
9.47	3.43E-07
9.26	3.07E-07
9.06	2.76E-07
8.87	2.50E-07
8.71	2.27E-07
8.53	2.07E-07
8.39	1.90E-07
8.29	1.75E-07
8.17	1.62E-07
8.02	1.51E-07
7.89	1.41E-07
7.78	1.31E-07
7.69	1.24E-07
7.58	1.16E-07
7.50	1.08E-07
7.36	9.96E-08
7.28	9.31E-08
7.20	8.72E-08
7.14	8.31E-08
7.08	8.02E-08
7.02	7.64E-08
6.94	7.28E-08
6.88	6.88E-08
6.83	6.53E-08
6.78	6.08E-08
6.73	5.90E-08
6.70	5.87E-08
6.64	5.70E-08
6.58	5.53E-08
6.53	5.33E-08
6.49	5.09E-08
6.47	4.67E-08
6.38	4.30E-08
6.24	4.17E-08
6.25	4.06E-08
6.24	3.99E-08
6.22	3.86E-08
6.16	3.76E-08
6.14	3.77E-08
6.04	3.62E-08
5.99	3.53E-08
5.98	3.50E-08
5.97	3.41E-08
5.91	3.19E-08
5.90	3.12E-08
5.91	3.11E-08
5.88	3.05E-08
5.84	2.96E-08
5.79	2.85E-08
5.77	2.75E-08
5.72	2.57E-08
5.73	2.55E-08
5.68	2.47E-08
5.65	2.45E-08
5.63	2.39E-08
5.60	2.27E-08
5.58	2.18E-08
5.57	2.12E-08
5.54	2.11E-08
5.46	2.07E-08
5.43	2.06E-08
5.27	2.06E-08
5.36	2.03E-08
5.36	1.90E-08
5.31	1.87E-08
5.22	1.85E-08
5.15	1.82E-08

K.8.1 REFERENCES.

K-1. Newman, J.C., Jr. and Raju, I.S., "Stress Intensity Factor Equations for Cracks in Three-Dimensional Finite Bodies," *Fracture Mechanics: Fourteenth Symposium—Volume 1, ASTM STP 791*, 1983, pp. I-238-I-265.

K-2. Harris, D.O., "Stress Intensity Factors for Hollow Circumferentially Notched Round Bars," *Journal of Basic Engineering*, Vol. 89, 1967, pp. 49-54.

K-3. Sheldon, J.W., Bain, K.R., and Donald, J.K., "Investigation of the Effects of Shed-Rate, Initial K_{max}, and Geometric Constraint on ΔK_{th} in Ti-6Al-4V at Room Temperature," *International Journal of Fatigue*, Vol. 21, 1999, pp. 733-741.

K-4. Leverant, G.R., et al., "Turbine Rotor Material Design," FAA report DOT/FAA/AR-00/64, December 2000.

APPENDIX L—INSPECTION OF NICKEL ANOMALIES

L.1 ULTRASONIC INSPECTION OF IN-718 MULTS.

Eight double melt IN-718 billet sections (mults) of approximately 8″ diameter and identified by a supplier as having internal sonic indications were delivered to Pratt & Whitney (P&W) for further ultrasonic (UT) scanning. C-scans were made for each mult using a 5-MHz transducer with 5″ focal length and 0.68″ diameter. The calibration setup was performed using flat entry samples with #1 flat-bottom holes (FBH). Calculations were made using the flaw response model developed at Iowa State University to account for the difference in the response between a flat entry surface and the curved entry surface of the mults. Also, the setup was made so that #2 FBH response corresponded with 80% full screen height (FSH). Distance amplitude correction (DAC) was applied so that sensitivity was equivalent through the depth of the inspection. Each indication was identified and compared to #2 FBH signal response, and the spatial extent of the indications was recorded where possible.

Figure L-1 shows the C-scan for mult 804085-1A. The indication appears to extend over a long circumferential distance because it is near the center at a depth of 3.7″. The 60° length of the indication corresponds to 0.31″, and the position of highest amplitude corresponds to approximately 60% of a #2 FBH. It cannot be determined from the UT data whether the apparent anomaly contains voids, foreign material, or an aberrant grain structure. It appears, however, that there is a noisy grain structure, since there is weak UT response spread throughout the C-scan. Since the indication is near the centerline, and other regions in the C-scan correspond to the appearance of large grain structure, it is likely that the apparent anomaly is actually due to large grains. The colorbar that is shown in figure L-1 applies to all the C-scan images of the mults and the pancakes.

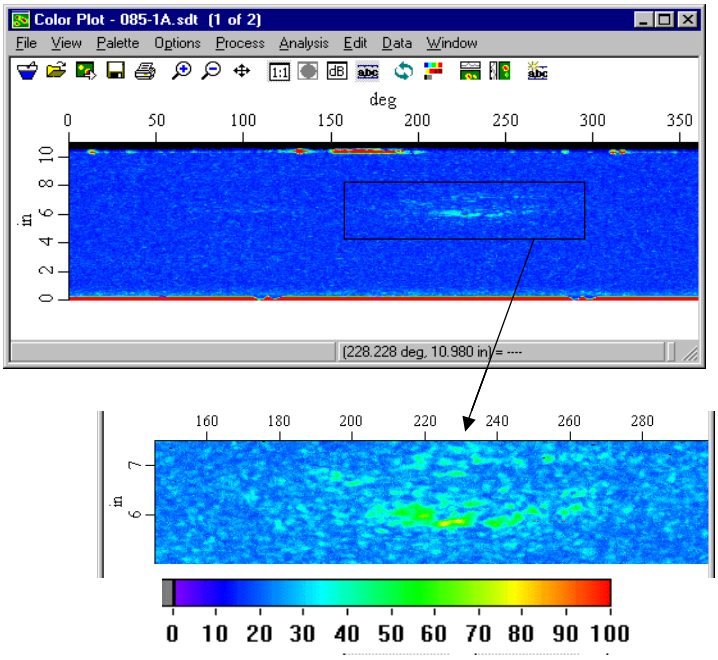

Figure L-1. C-Scan Images for Mult 804085-1A

Figure L-2 shows the C-scan for mult 804085-2X. Again, there is a fairly noisy appearance to the C-scan image that may be caused by grain structure. Two distinct UT response signals can be seen at the circumferential region of 0° to 20°; the largest response corresponds to approximately 130% of a #2 FBH. The depth of the indications is approximately 2.5″ below the surface.

(a)

(b)

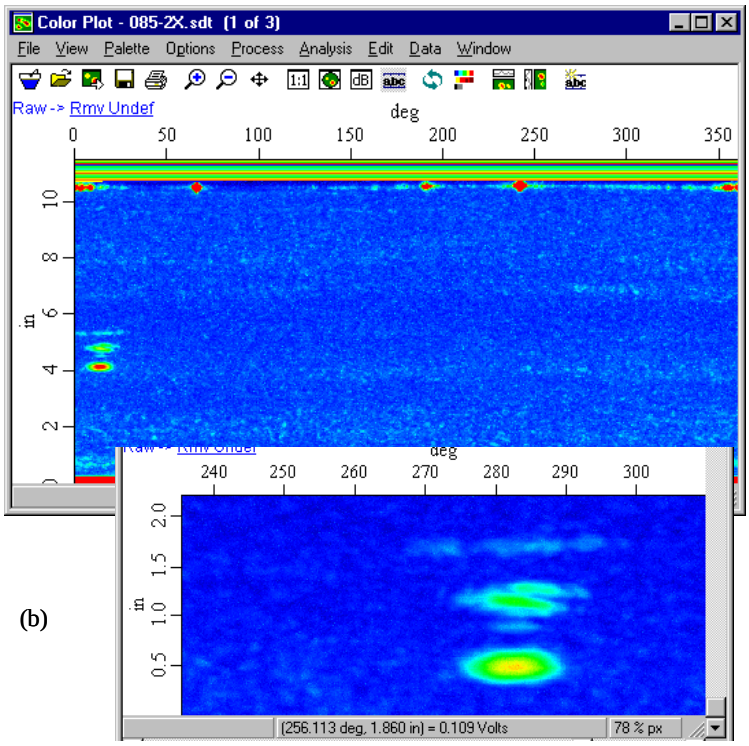

Figure L-2. C-Scan Images for Mult 804085-2X (a) Full C-Scan and (b) Concentrated Rescan in Region of Largest Reflectors

The C-scan image for mult 804085-3A is shown in figure L-3, and the noisy structure is apparent. What appears to be an inclusion at 90% of #2 FBH sensitivity may be a higher concentration of large grains. The grain noise is most apparent nearer the center of the billet, since the noise is amplified by the application of DAC, and the values plotted in the C-scan are primarily from near the billet center.

Figure L-4 shows the C-scan image for mult 804085-3X. It is apparent that six distinct features are present. All of the features are at depths between 2.25″ and 2.5″, and the largest reflector has an amplitude that is 190% of a #2 FBH. The calculated beam width at a depth of 2.5″ is 0.3″ in the circumferential direction and 0.23″ in the axial direction, and those are the approximate dimensions of the features identified in the C-scan. Therefore, the features have spatial extent that is less than the dimensions of the beam and can be considered point reflectors.

Figure L-5 shows the C-scan image for mult 804618-5A1 with a distinct feature that is near the center of the billet. The feature has an amplitude of 200% of a #2 FBH and is at a depth of approximately 3.7″.

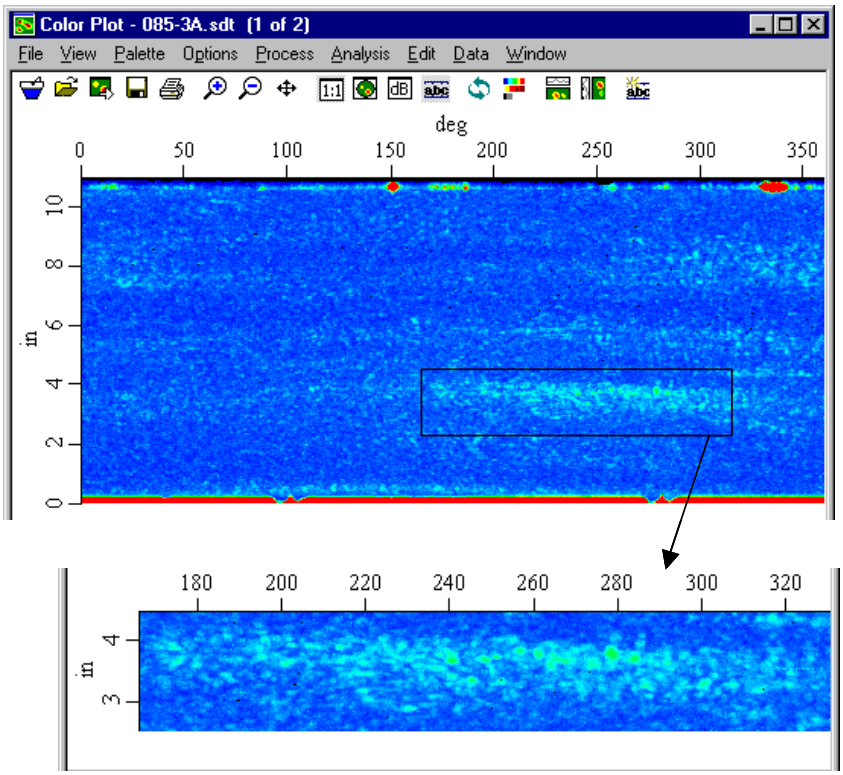

Figure L-3. C-Scan Image for 804085-3A

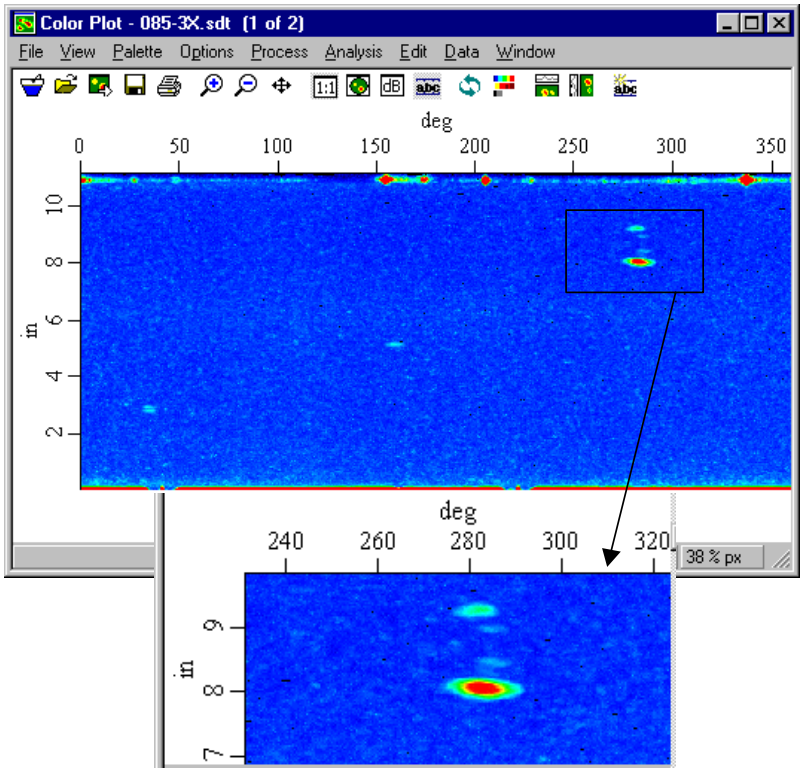

Figure L-4. C-Scan Image of Mult 804085-3X

(a)

(b)

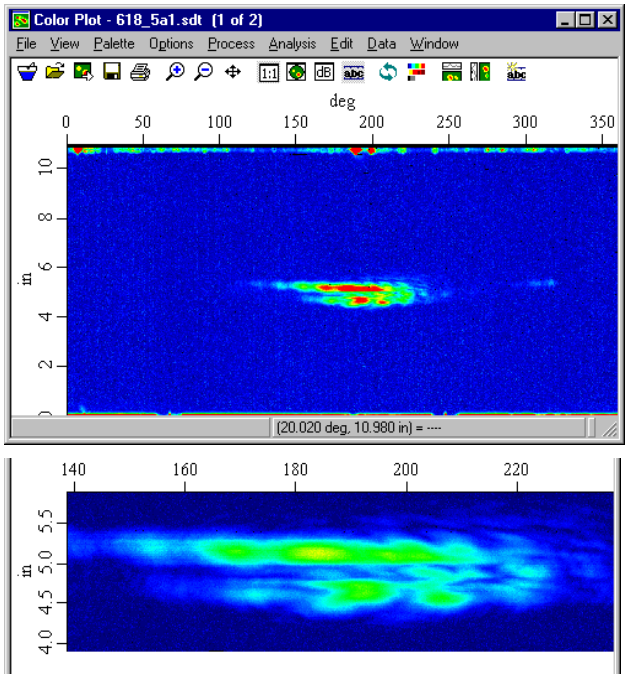

Figure L-5. C-Scan Image for 804618-5A1 (a) Full C-Scan and (b) Concentrated Rescan Without Signal Saturation

Mult 804618-5A2 is a separate billet section from the mult labeled 5A1. The C-scan image for 5A2 is shown in figure L-6. The indication is at a depth of 3.3″ and is likely smaller than the beam dimensions. The reflected amplitude for this indication is approximately 40% of a #2 FBH.

(a)

(b)

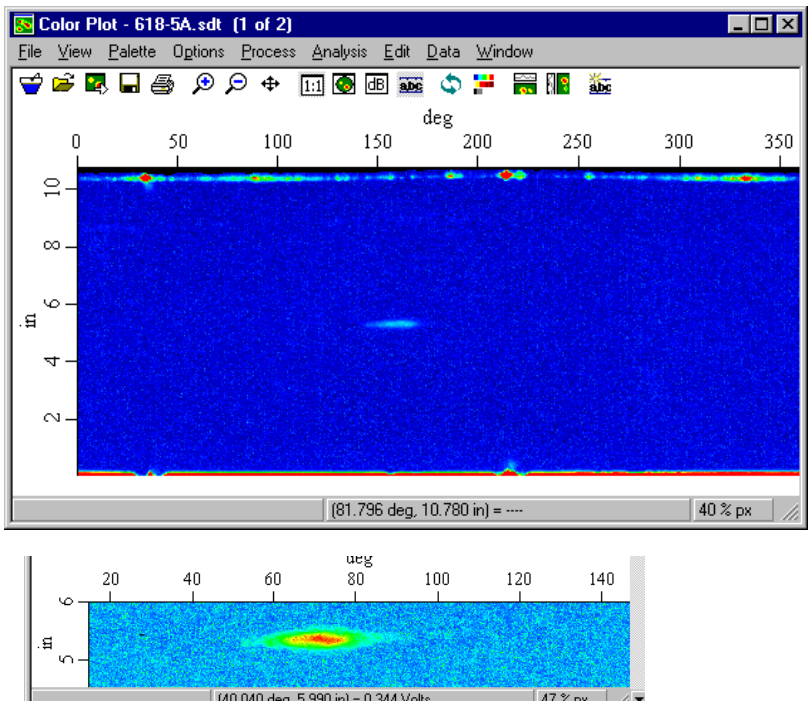

Figure L-6. C-Scan Image for 804618-5A2

Figure L-7 shows the C-scan image for 804539-5A that has its strongest indication signal, 60% of a #2 FBH, at a depth of 2.25″. Two weaker reflections can be seen at axial positions that are offset on either side from the larger signal by approximately 0.45″. The weaker reflectors were noted when rescanning to improve the resolution in the region of the larger indication.

(a)

(b)

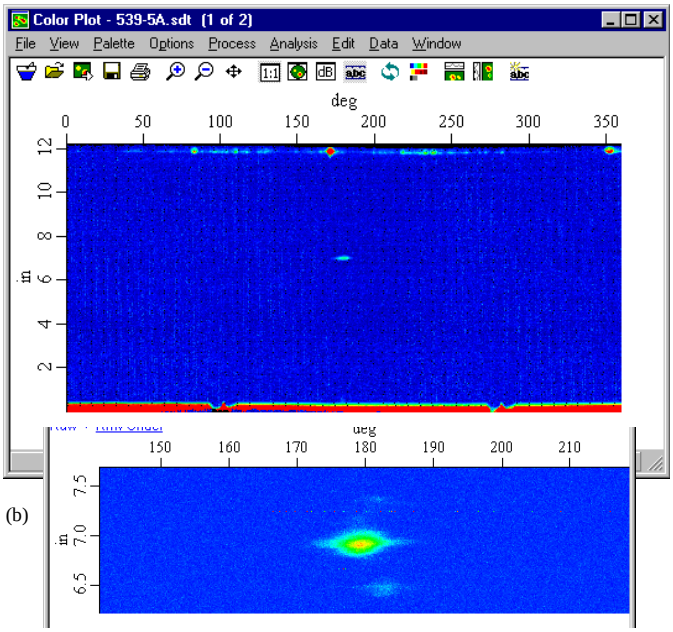

Figure L-7. C-Scan Images for 804539-5A, (a) Full Scan and (b) Rescan of Indication Area With Higher Resolution

The C-scan image for mult 804539-5X is shown in figure L-8. The indication is 2.5″ below the surface and has an amplitude of 55% of a #2 FBH.

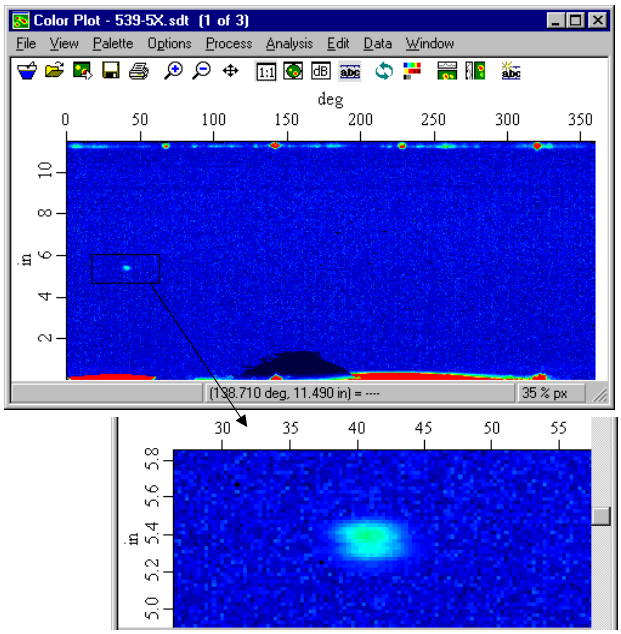

Figure L-8. C-Scan Image of 804539-5X

L.2 ULTRASONIC INSPECTION OF IN-718 FORGED PANCAKES.

After the 8″ diameter mults were forged to the pancake shape of 16″ diameter and 2.9″ thick, UT inspections were performed to determine the positions of the indications. The pancakes, as-received at P&W, had a surface finish with significant machining grooves that caused a high amplitude ringdown signal in some of the pancakes. An example of the ringdown is shown in figure L-9. This ringdown was thought to be masking the indication signals in some of the pancakes. Indications were seen in only three of the eight pancakes. Efforts within the laboratory to reduce the effects of the machining grooves with a hand-held grinding wheel were not sufficient, and the pancakes were sent to a supplier that was able to apply a ground surface to the pancakes.

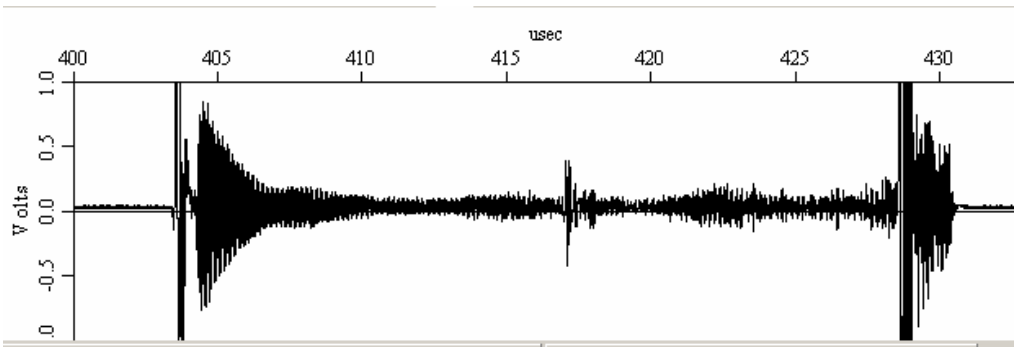

(a)

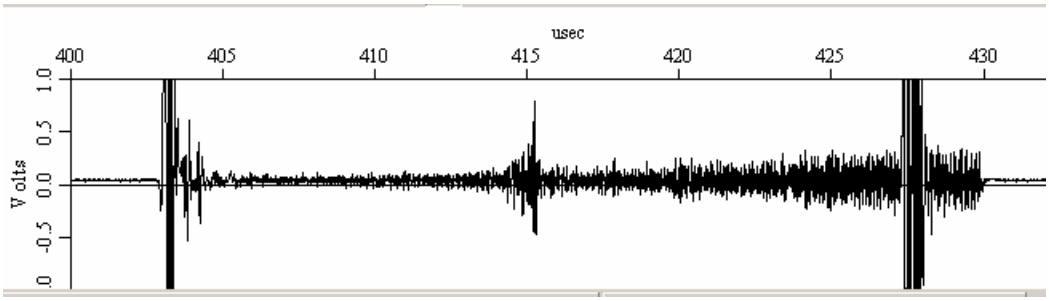

(b)

Figure L-9. (a) Example of Front Surface Ringdown Caused by Machining Grooves and (b) Signal Response With a Smooth Surface

The pancakes were rescanned, and again only the same three pancakes produced signals for suspected inclusions. Several attempts were made to use zoned and angle scanning to try to identify the positions of the previous indications in the other five pancakes. It appears that the indications in those five mults may have been either voids that closed during the forging operation, or the ultrasonic indications in the mults were caused by large grains that were refined during recrystallization at the pancake forging step. For the three pancakes with identified indications, blanks with dimensions of approximately 2″ x 3″ (thickness) x 6″ with the

indications centered were cut from the pancakes to make large volume, round low-cycle fatigue (LCF) samples. The blanks were rescanned and the positions of the indications verified for production of the LCF samples. Results of the UT evaluations of the pancakes are presented below.

UT scans were produced for the pancakes with a 10-MHz probe having a nominal focal length of 3″ and a diameter of 3/8″. Calibration was performed so that #1 FBH sensitivity was achieved at 80% FSH using IN-718 calibration standards. DAC was applied. The setup procedure was typical of IN-718 forging inspections.

The C-scan for pancake 804539-5X is shown in figure L-10 with the outline drawn for cutting the blank from which to make the LCF sample. The prediction for the position of the indication using DEFORM™ was 5.7″ radially and 1.5″ deep. The position of the indication was very close to the predicted position with a radial position of 5.8″ and depth from one side of the pancake of 1.5″ and from the other side of 1.3″. Figure L-11 shows a higher resolution scan at a shorter water path with a box drawn around the indication of dimension 0.4″ x 0.4″. The largest UT response from the features within the box corresponds to ~100% of #1 FBH, but the extent of the indication is obviously larger than the 0.016″ diameter of a #1 FBH.

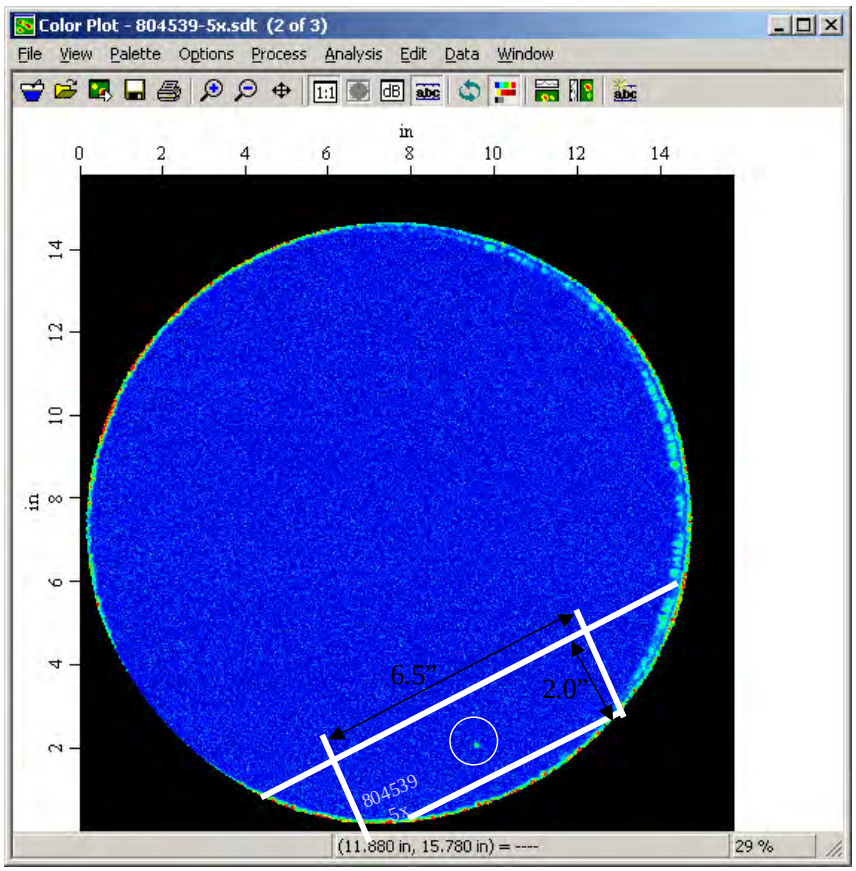

Figure L-10. C-Scan of Pancake 804539-5X With Setup of #1 FBH Sensitivity

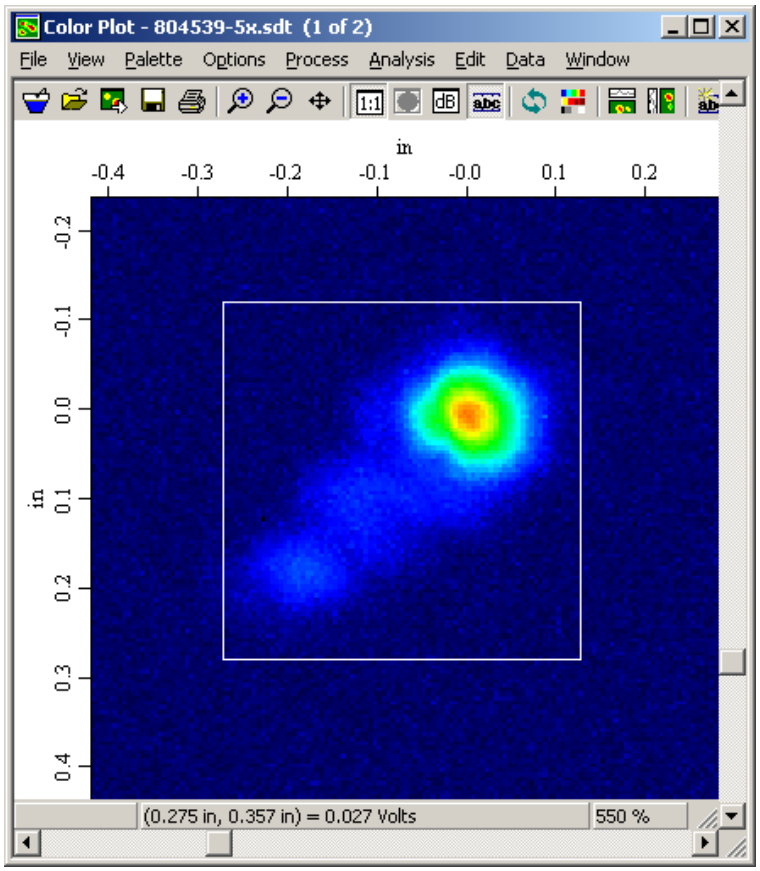

Figure L-11. C-Scan of Indication in Pancake 804539-5X with Focus Closer to the Indication to Provide More Resolution

The C-scan for pancake 804539-5A is shown in figure L-12 with the outline drawn on the C-scan image for cutting the blank from which to make the LCF sample. The position of the indication is very close to the position predicted by DEFORM. DEFORM predicted a radial position of 4.8″ and a depth of 1.5″, and the indication was actually at 5.0″ radially and 1.3″ to 1.5″ deep. Figure L-13 shows a higher resolution scan at a shorter water path with a box drawn around the indication of dimension 0.6″ x 0.4″. The largest UT response from the features within the box corresponds to ~50% of #1 FBH, but the extent of the indication is obviously larger than the 0.016″ diameter of a #1 FBH.

The C-scan for pancake 804618-5A is shown in figure L-14 with the outline drawn on the C-scan image for cutting the blank from which to make the LCF sample. The position of the indication is very close to the position predicted by DEFORM. DEFORM predicted a radial position of 1.2″ and a depth of 1.5″, and the actual radial position was 1.4″ and depth was 1.5″. Figure L-15 shows a higher resolution scan at a shorter water path with a box drawn around the indication of dimension 0.6″ x 0.8″. The largest UT response from the features within the box corresponds to ~125% of #1 FBH, but the extent of the indication is seen to nearly fill the 0.6″ x 0.8″ box and is significantly larger than the 0.016″ diameter of a #1 FBH.

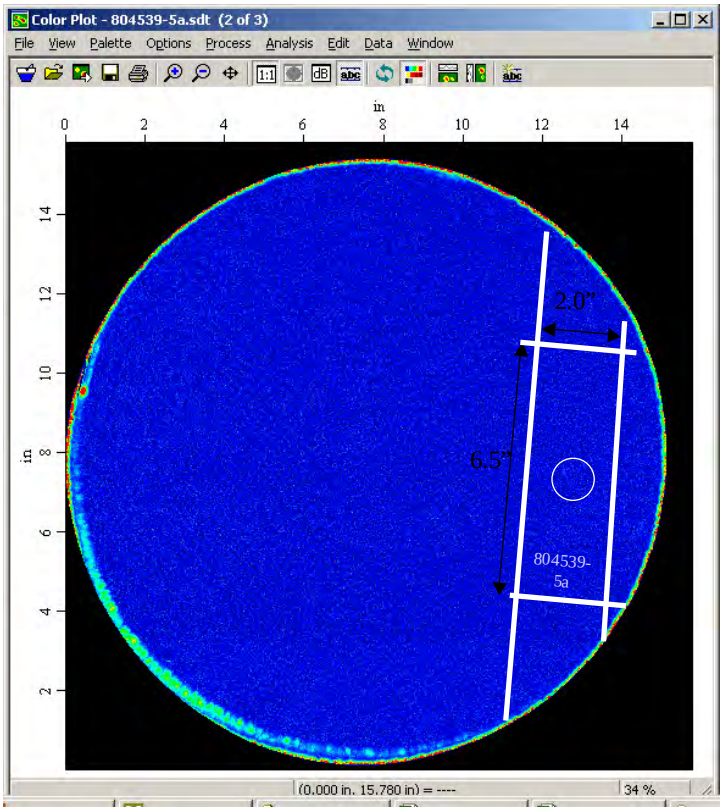

Figure L-12. C-Scan of Pancake 804539-5A With Setup of #1 FBH Sensitivity

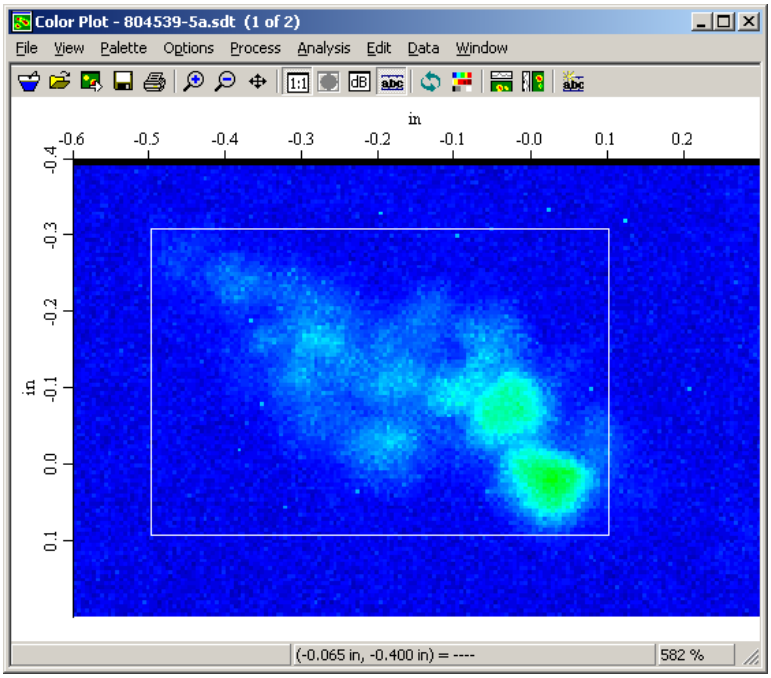

Figure L-13. C-Scan of Indication in Pancake 804539-5A With Focus Closer to the Indication to Provide More Resolution

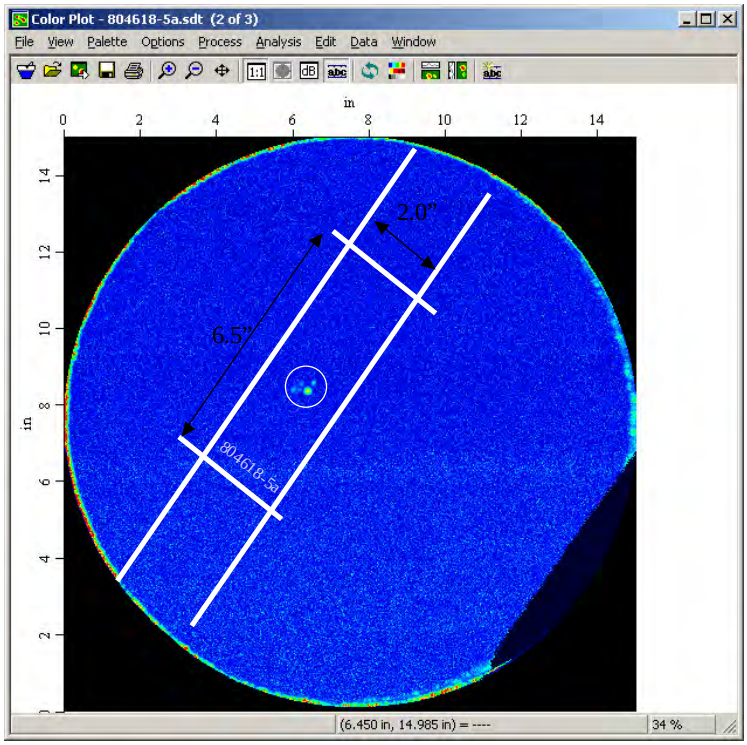

Figure L-14. C-Scan of Pancake 804618-5A With Setup of #1 FBH Sensitivity

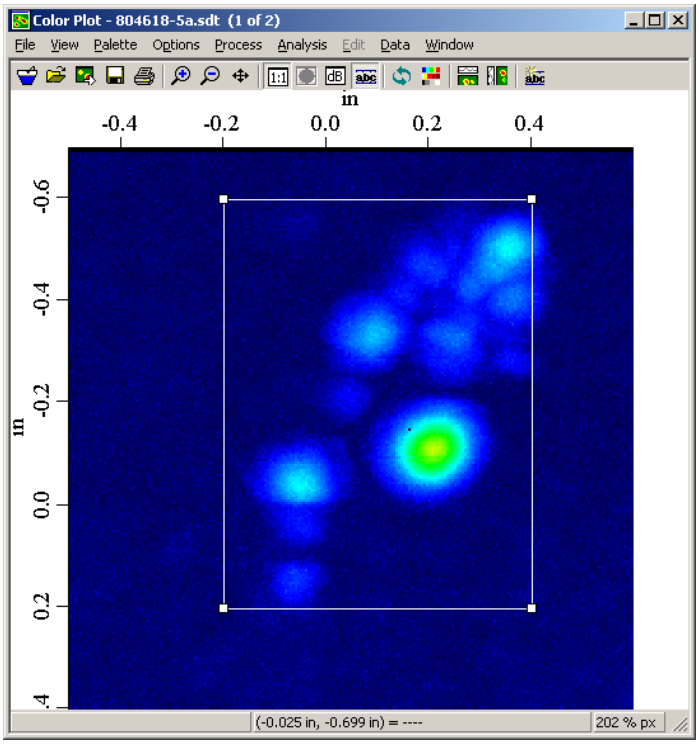

Figure L-15. C-Scan of Indication in Pancake 804618-5A With Focus Closer to the Indication to Provide More Resolution

After removing the blanks from the three pancakes, scans were made to ensure that the features were centered in the blanks. Measurements were made to define the positions of the indications with respect to the edges of the blanks, and the edges of the blanks were determined by scanning the top of the blank with the UT beam focused on the surface. The region of the indication was then rescanned with the same coordinates system. Based on the resulting measurements, detailed fatigue specimen machining drawings have been developed in an attempt to center the inclusions in the gage section. The fatigue testing of these specimens is planned in a separate program that follows Turbine Rotor Material Design-Phase II.

APPENDIX M—THERMOMECHANICAL FATIGUE CRACK GROWTH TESTING

M.1 INTRODUCTION.

Aircraft turbine engines operate in a complex thermal environment, and frequently the stress and thermal cycles are not totally in phase. The so-called stress rain flow method is often used to define cycles for fatigue crack growth (FCG) analysis. In this method, the major cycle is defined in terms of the maximum stress in the cycle and the temperature at the maximum stress time point. There is often a time point later in the mission with a higher temperature but a lower stress, and this characteristic of the history may be ignored by the stress rain flow method. It is possible, however, that this higher temperature may have some impact on the FCG rate.

To investigate this issue further, the program team conducted an exploratory study of thermo-mechanical fatigue (TMF) crack growth. The common high-temperature, nickel-based superalloy IN-718 was chosen for investigation. A simple matrix of isothermal and TMF experiments was designed for the specific purpose of determining if the out-of-phase thermal history had a significant influence on FCG rates, and if the stress rain flow method was a adequate means of characterizing the damage in TMF cycles. All crack growth tests and analysis were performed at GE Aviation.

M.2 MATERIALS AND PROCESSING.

Crack growth specimens were obtained from two compressor rotor spool production forgings provided by GE Aviation. The forging pedigree is summarized below:

- Supplier serial no.: 800 207
- Heat number: C32734 A30856

The forging was solutionized between 1725° and 1875°F for 1 hour. Following the solutionizing, the material was aged at 1325°F for 8 hours, followed by another age at 1150°F for 8 hours. Figures M-1 and M-2 document the microstructures from the two forgings. The grain size was estimated to be American Society for Testing and Materials (ASTM) GS 10. The 1200°F 0.2% yield strength was 141.0 ksi.

M.3 SPECIMEN GEOMETRY AND TEST TECHNIQUE.

Crack growth testing was performed using a Kb bar specimen geometry (see specimen drawing in appendix K). The nominal gage section thickness and width were 0.168″ and 0.400″. Specimen orientations are summarized in table M-1.

All of the data were acquired using the direct current electrical potential drop technique. This technique is a modification of the method described by Gangloff [M-1]. The adaptation of the potential drop method to the Kb bar geometry is described by VanStone and Richardson [M-2]. The *da/dN* and *dc/dN* values were calculated using the seven-point incremental polynomial method. The Newman-Raju [M-3] solution was used to calculate the stress-intensity factor values. Most tests employed an initial crack size, nominally, of 0.015″ x 0.030″.

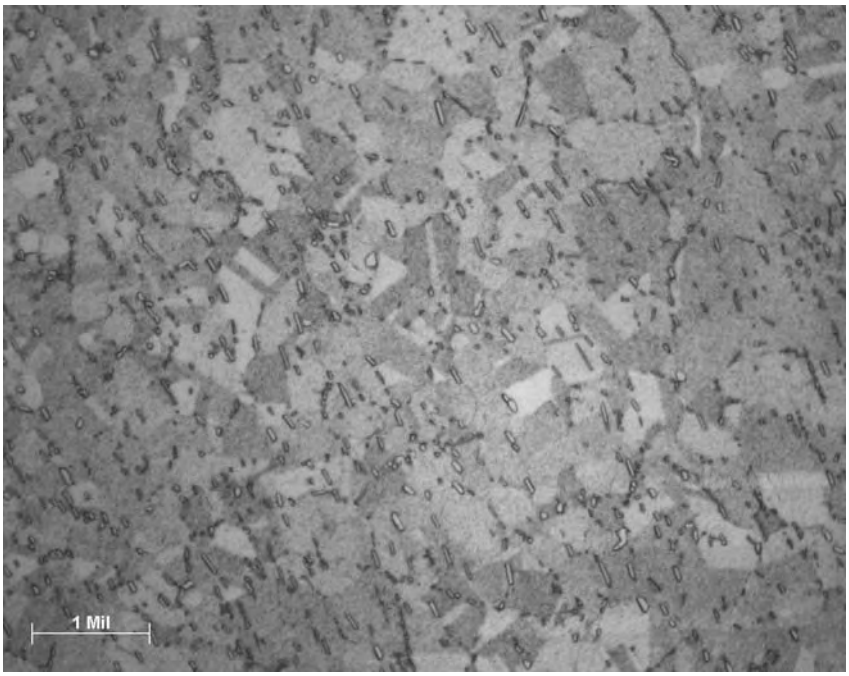

Figure M-1. Microstructure of Specimen A30856-14 (Grain size approximately ASTM GS 10)

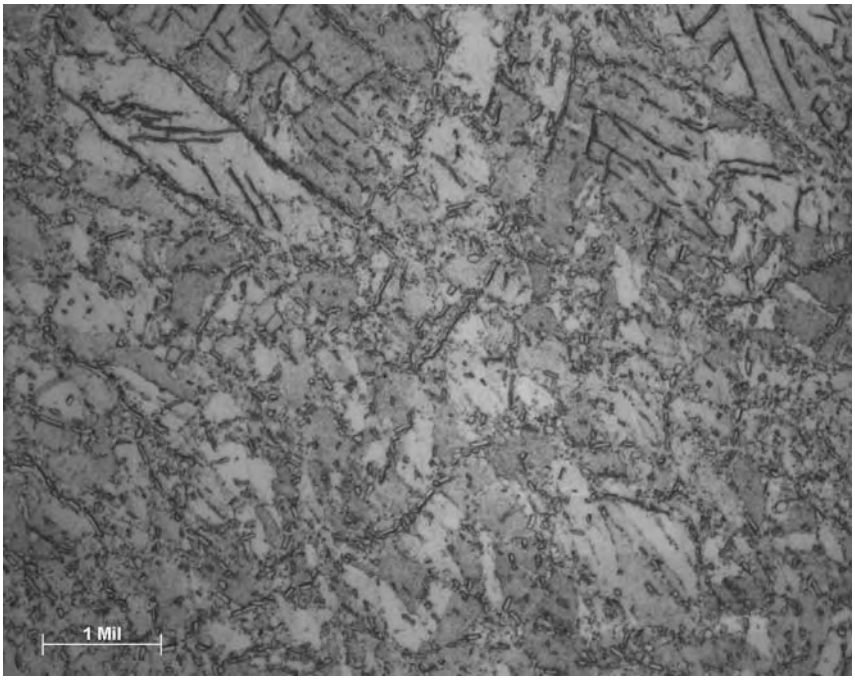

Figure M-2. Microstructure of Specimen C32734-1 (Grain size approximately ASTM GS 10)

Table M-1. TMF Specimen Orientations

Specimen Number	Region of Forging	Orientation	
		Specimen Axis	Fatigue Crack Plane (a x $2c$)
C32734-1	Bore	Radial	Tangential x axial
C32734-2	Bore	Radial	Tangential x axial
C32734-3	Bore	Radial	Tangential x axial
C32734-5	Bore	Radial	Tangential x axial
C32734-7	Bore	Tangential	Radial x axial
C32734-8	Bore	Tangential	Radial x axial
C32734-9	Bore	Tangential	Radial x axial
C32734-10	Bore	Tangential	Radial x axial
C32734-11	Bore	Tangential	Radial x axial
A30856-13	Bore	Radial	Tangential x axial
A30856-14	Bore	Radial	Tangential x axial
A30856-15	Bore	Radial	Tangential x axial
A30856-16	Bore	Radial	Tangential x axial
A30856-17	Bore	Radial	Tangential x axial
A30856-19	Bore	Tangential	Radial x axial
A30856-20	Bore	Tangential	Radial x axial
A30856-21	Bore	Tangential	Radial x axial
A30856-22	Bore	Tangential	Radial x axial
A30856-23	Bore	Tangential	Radial x axial

M.4 DEFINITION OF TMF CYCLES.

Four different TMF cycle types were employed. TMF cycles were designed to balance several difference considerations. They should be representative of actual engine cycles, and they should have significantly different lives than comparable isothermal cycles. Temperature cycling should be slow enough to avoid excessively high transient thermal stresses, but fast enough that total test times (and therefore test costs) would not exceed program budgets. The typical duration of a single TMF cycle (all types) was approximately 210 seconds. The maximum variation in temperature within the specimen (less than 15°F) occurred during specimen heating and resulted in less than 3-ksi thermal stress.

For each type of waveform, the total time of the waveform was dependent on the characteristic heating and cooling rates between the minimum and maximum temperatures. Once these rates were established for a given waveform, the loads were appropriately mapped to the temperature profile using a dual channel TMF simulator. An Ameritherm induction heater was used for all tests. The induction coil design was a 4-0-4 wrap design. The nominal inside diameter of the wrapping was 1 inch. Both a control thermocouple and a monitoring thermocouple were applied to the specimen and straddled the crack plane. During the experiment, the specimen was shielded from any laboratory air currents by enclosing the volume between the specimen grips with plastic sheathing.

M.4.1 TEST TYPE I.

As shown in figure M-3, the 450°F leg from 0 to 120 ksi remains constant. The magnitude of the stress cycle at 1100°F varies, as shown below for each TMF cycle type I(a) through I(d).

TMF Cycle Type	1100°F Stress Cycle
I(a)	70 ksi to 120 ksi to 0 ksi
I(b)	50 ksi to 100 ksi to 0 ksi
I(c)	30 ksi to 80 ksi to 0 ksi
I(d)	10 ksi to 60 ksi to 0 ksi

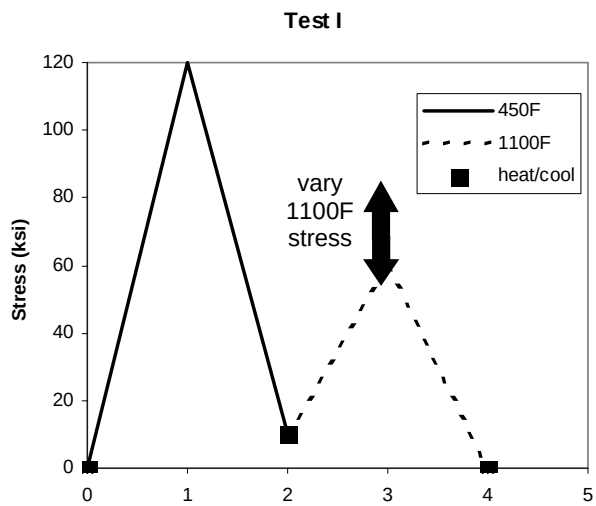

Figure M-3. Schematic of TMF Test Type I

M.4.2 TEST TYPE II.

An R = 0 stress cycle at 450°F is followed by a thermal cycle at zero stress. The thermal cycle consists of heating from 450° to 1100°F and then cooling back to 450°F (see figure M-4).

M.4.3 TEST TYPE III.

An R = 0, 120-ksi cycle is performed at 450°F. The specimen is then heated to 1100°F and a cycle to -60 ksi is performed. At zero stress, the specimen is cooled to 450°F (see figure M-5).

M.4.4 TEST TYPE IV.

As shown in figure M-6, a 0 ksi to 120 ksi to 60 ksi stress cycle is performed at 450°F. The specimen is held at 60 ksi and heated to 1100°F. At 1100°F, the specimen is unloaded to 0 ksi.

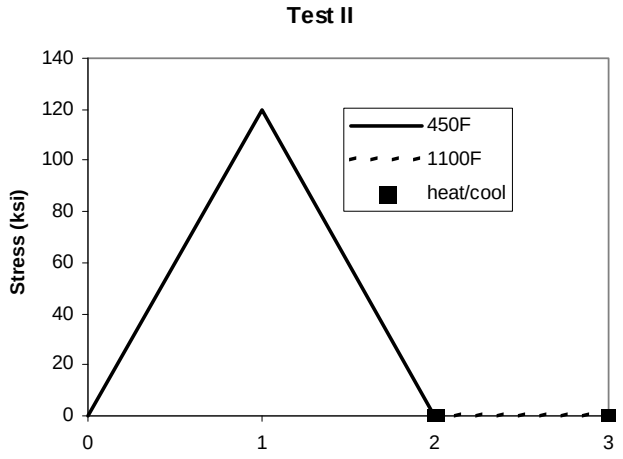

Figure M-4. Schematic of TMF Test Type II

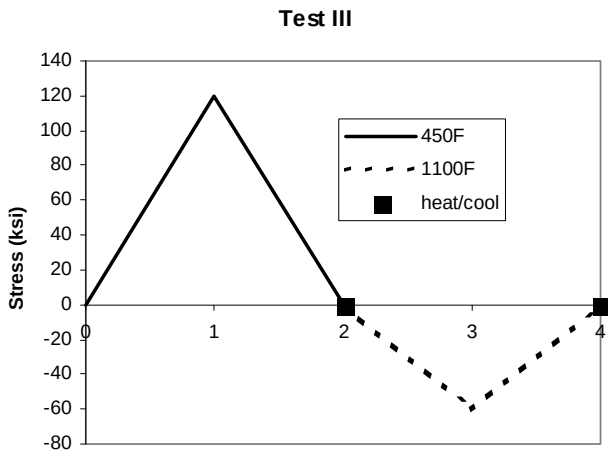

Figure M-5. Schematic of TMF Test Type III

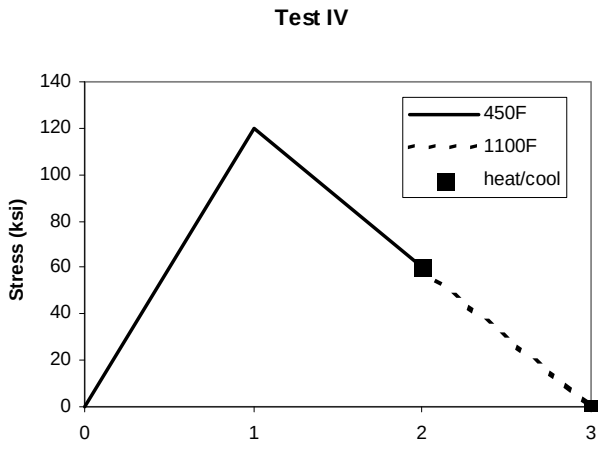

Figure M-6. Schematic of TMF Test Type IV

M.5 TEST MATRIX.

The test matrix is given in table M-2. Two experiments were planned for each of the ten test conditions listed in the table. Isothermal tests were performed at 450º, 800º, and 1100ºF.

Nineteen of 20 experiments were performed successfully. A successful result was obtained for only one of the two TMF Type I (b) experiments.

Table M-2. Test Matrix for TMF Crack Growth Experiments

Test Type	Temp. (°F)	Max Stress (ksi)	Temp. (°F)	Max Stress (ksi)	Specimen Number	
450°F Isothermal	450	120			C32734-1	A30856-14
800°F Isothermal	800	120			C32734-7	A30856-13
1100°F Isothermal	1100	120			C32734-8	A30856-16
TMF Type I (a)	450	120	1100	120	C32734-9	A30856-22
TMF Type I (b)	450	120	1100	100		A30856-17
TMF Type I (c)	450	120	1100	80	C32734-5	A30856-23
TMF Type I (d)	450	120	1100	60	C32734-2	A30856-19
TMF Type II	450	120	1100	0	C32734-3	A30856-15
TMF Type III	450	120	1100	-60	C32734-10	A30856-21
TMF Type IV	450	120	1100	60	C32734-11	A30856-20

M.6. RESULTS.

The results of the six pedigree crack growth rate tests are shown in figure M-7. This figure indicates that cyclic crack growth rate increases with increasing temperature. The 800ºF crack growth rates are slightly higher than the 450ºF results. The 1100ºF crack growth rates are much larger than those at 450ºF. At low to intermediate ΔK, the 1100ºF crack growth is approximately 10 times faster than the 450ºF results.

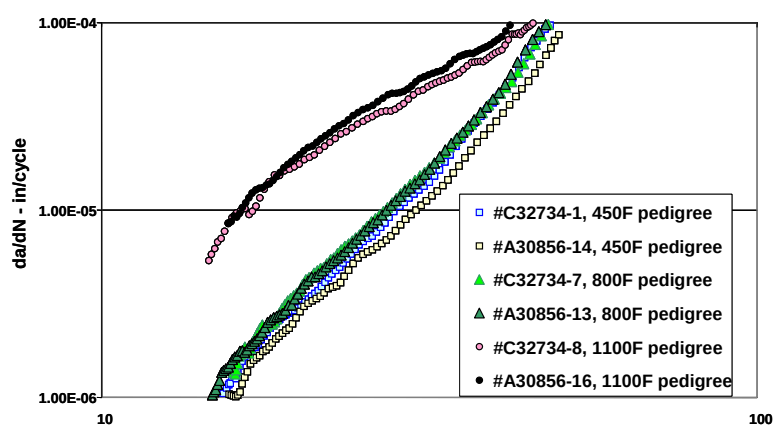

Figure M-7. Results of the Isothermal IN-718 Crack Growth Tests

The results of the Type II TMF tests clearly show the influence of the thermal cycle on the crack growth rate response. Figures M-8 through M-10 compare the measured crack growth in TMF Type II tests with the isothermal pedigree tests at 450°, 1100°, and 800ºF, respectively. Figure M-8 shows that the crack growth rates measured in the Type II TMF tests are slightly more rapid than the crack growth rates in the 450°F pedigree test even though the only fatigue cycle occurred at 450ºF. Figure M-9 shows that the Type II TMF crack growth rates are significantly lower than the isothermal crack growth rates measured at 1100ºF, the highest temperature in the Type II TMF test. Figure M-10 shows that crack growth rates in the Type II TMF test are similar to those measured in 800ºF isothermal pedigree tests.

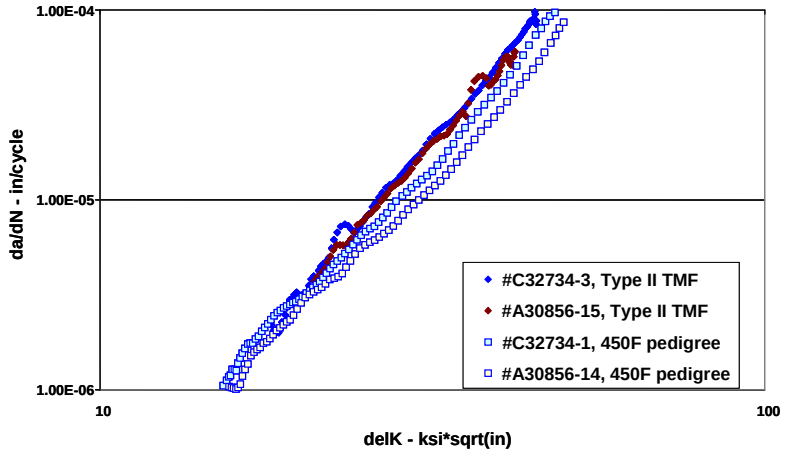

Figure M-8. Comparison of Crack Growth Rates Measured in Type II TMF Tests and 450°F Isothermal Tests

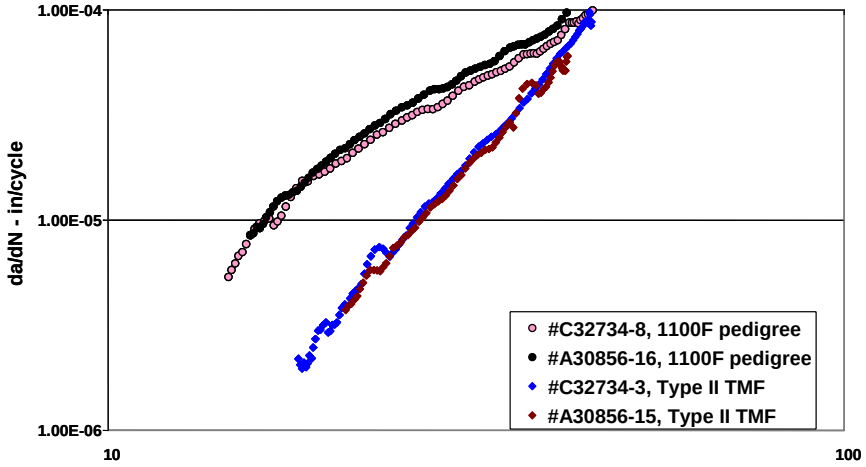

Figure M-9. Comparison of Crack Growth Rates Measured in Type II TMF Tests and 1100°F Isothermal Tests

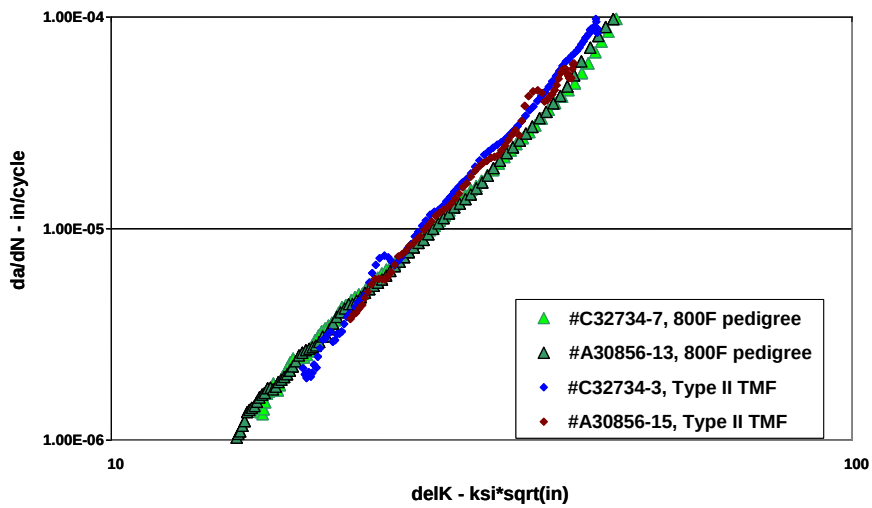

Figure M-10. Comparison of Crack Growth Rates Measured in Type II TMF Tests and 800°F Isothermal Tests

The lifetimes of all TMF tests were predicted by the conventional stress rain flow method, and these predictions are compared with the actual test lives in figure M-11. Also shown on this figure are predictions and test results for additional TMF tests on René 95 and René 88DT conducted independently by GE Aviation (not under Turbine Rotor Material Design-II). The figure shows that the stress rain flow predictions exhibit a nonconservative bias in the predictions. In other words, TMF cycles produce faster crack growth rates, on average, than are predicted by the stress rain flow method. The bias is less severe for IN-718 than for the René alloys.

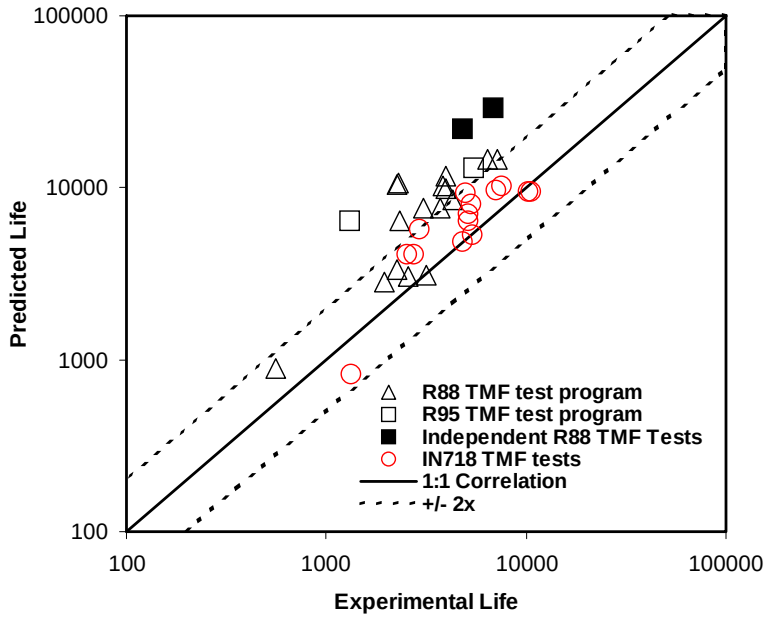

Figure M-11. Comparison of Experimental Lifetimes With Predictions Based on the Conventional Stress Rain Flow Method for IN-718, René 95, and René 88DT Subjected to TMF Histories

M.7 REFERENCES.

M-1. Gangloff, R.P., "Electrical Potential Monitoring of Crack Formation and Subcritical Growth from Small Defects," *Fatigue of Engineering Materials and Structures*, Vol. 4, 1981, pp. 15-33.

M-2. VanStone, R.H. and Richardson, T.L., "Potential Drop Monitoring of Cracks in Surface-Flawed Specimens," *ASTM STP 877*, 1985, pp. 148-166.

M-3. Newman, Jr., J.C. and Raju, I.S., "Analysis of Surface Cracks in Finite Plates Under Tension or Bending Loads," NASA TP 1578, 1979.

APPENDIX N—DEVELOPMENT OF NEW WEIGHT FUNCTION STRESS-INTENSITY FACTOR SOLUTIONS

N.1 INTRODUCTION.

Early versions of Design Assessment of Reliability With Inspection (DARWIN®), which were focused on inherent material anomalies, contained stress-intensity factor (SIF) (also denoted as *K*) solutions for cracks in simple rectangular plates. However, as surface damage began to be addressed, more complex SIF solutions for cracks emanating from the surface were required.

The initial treatment of the surface damage problem was focused on boltholes, and so additional SIF solutions for cracks emanating from holes were required. It is common to assume for cracks at holes that the stress gradient on the crack plane varies only in one direction, away from the hole. The SIF solutions for cracks subjected to this type of stressing are called univariant SIF solutions. Numerous SIF solutions for cracks at holes are available in the literature, but these solutions are generally for simple loads applied remotely in the form of uniform tension, bend, or pin loading. Although the resulting stress variations on the crack plane are nonlinear, they follow specific distributions associated with these specific remote loads. However, in actual components, the stresses on the crack plane may take an arbitrary nonlinear form, the gradient cannot be described by simple curve-fitting, and modal superposition of simple solutions is not feasible. To address these problems, new SIF solutions were derived for DARWIN based on the weight function (WF) formulation. The first generation of these new WF solutions was univariant in nature.

More advanced treatments of surface damage problems can require that the stress variation on the crack plane be specified in two dimensions instead of the one single direction constrained by the univariant WF formulation. In this case, a more general bivariant WF formulation is required. The formulation, implementation, and validation of univariant and bivariant WF methods for DARWIN are summarized in this appendix.

N.2 UNIVARIANT WEIGHT FUNCTION STRESS-INTENSITY FACTOR SOLUTIONS FOR PART-THROUGH CRACKS AT HOLES.

N.2.1 WEIGHT FUNCTION FORMULATION.

A WF (also known as influence function or Green's function) formulation enables the evaluation of SIFs by integrating over the crack surface a product of the applied stress in the uncracked body with the WF for the cracked structure. The analytical forms for WFs can be derived for some simple geometries, but approximate WF forms are used for complex configurations, especially with free surfaces. In DARWIN, one-dimensional WFs are available to determine the SIFs resulting from a stress gradient varying in only the crack depth direction (away from the hole).

The univariant fracture mechanics modules in DARWIN for a surface crack (SC) at a hole and a corner crack (CC) at a hole use the approximate WF method proposed by Glinka [N-1-N-3]. The corresponding crack types are SC18 and CC08, respectively. The approximate solutions are

based on a three-term expansion around the crack tip singularity. The WF for the *c*-tip (the maximum depth position for the surface crack, or the tip at the plate surface for a corner crack) is

$$W_c = \frac{2}{\sqrt{2\pi(c-x)}}\left[1 + M_{1c}\sqrt{\frac{c-x}{c}} + M_{2c}\frac{c-x}{c} + M_{3c}\left(\frac{c-x}{c}\right)^{\frac{3}{2}}\right] \tag{N-1}$$

The WF for the *a*-tip (the crack tip in the bore of the hole for either a surface or corner crack) is:

$$W_a = \frac{2}{\sqrt{\pi x}}\left[1 + M_{1a}\sqrt{\frac{x}{c}} + M_{2a}\cdot\frac{x}{c} + M_{3a}\left(\frac{x}{c}\right)^{\frac{3}{2}}\right] \tag{N-2}$$

The variable x is normal to the axis of the hole and is the distance measured from the location where the crack emanates; i.e., the root of the hole. The parameters M_{1c}, M_{2c},…, etc. depend on the geometrical parameters and are defined by reference solutions. At the *c*-tip, M_{1c}, M_{2c}, and M_{3c} are defined by reference N-2

$$\begin{aligned} M_{1c} &= \frac{\pi}{\sqrt{2Q}}\left(4Y_0 - 6Y_1\right) - \frac{24}{5} \\ M_{2c} &= 3 \\ M_{3c} &= 2\left(\frac{\pi}{\sqrt{2Q}}Y_0 - M_{1c} - 4\right) \end{aligned} \tag{N-3}$$

and at the *a*-tip, M_{1a}, M_{2a}, and M_{3a} are given by:

$$\begin{aligned} M_{1a} &= \frac{\pi}{\sqrt{4Q}}\left(30F_1 - 18F_0\right) - 8 \\ M_{2a} &= \frac{\pi}{\sqrt{4Q}}\left(60F_0 - 90F_1\right) + 15 \\ M_{3a} &= -\left(1 + M_{1a} + M_{2a}\right) \end{aligned} \tag{N-4}$$

In these equations, Q is the shape factor for an elliptical crack and can be approximated by:

$$Q = \begin{cases} 1 + 1.464(a/c)^{1.65}, & a/c \le 1 \\ 1 + 1.464(a/c)^{-1.65}, & a/c > 1 \end{cases} \tag{N-5}$$

F_0, F_1, Y_0, and Y_1 are normalized SIFs or the reference solutions. F_0 and F_1 are obtained at the *a*-tip, and Y_0 and Y_1 are at the *c*-tip. The subscripts identify the two associated reference loads on

the crack surfaces: 0 denotes uniform tension, and 1 denotes a linearly decreasing bending stress $\sigma_r(x) = -x/c+1$ where x shares the same definition in the WFs.

The SIFs at the a- and c-tips, $K_{a,c}$, can be determined by directly integrating the product of the WF and the stress variation over the crack depth c as

$$K_{a,c} = \int_0^c W_{a,c}\sigma(x)dx \tag{N-6}$$

where $\sigma(x)$ is the univariant stress applied on the crack surface, and the integration is carried out from $x = 0$ to $x = c$. Note that the univariant stress variation is derived from the stress variation based on an uncracked body along the crack plane in the corresponding cracked body, and the stress is the component normal to the crack plane.

The formulation remains the same whether the hole is centered or off-center in the width of the plate, and whether the surface crack is centered or off-center through the thickness of the plate. The off-center effect of the surface crack from the mid-plane of the plate in the crack type SC18, and any offset of the hole from the center of the plate in both crack types SC18 and CC08, are accounted for in the reference solutions used inside the WFs.

N.2.2 REFERENCE SOLUTIONS.

Numerical methods were used to generate highly accurate reference solutions for the approximate WF formulation. The reference solutions for two-dimensional cracks at holes were derived using the FADD3D fracture mechanics software, a general boundary element (BE) code for three-dimensional linear elastic fracture analysis [N-4]. FADD3D includes a novel cracktip element that allows the computation of SIFs directly from the nodal information along the crack front. The BE approach uses fewer elements than finite element (FE) approaches, substantially reducing the modeling effort while maintaining exceptional accuracy [N-5 and N-6]. To facilitate the use of FADD3D, Southwest Research Institute® developed supplemental procedures for pre- and postprocessing.

Reference solutions were generated at a wide range of combinations of geometrical aspect ratios. For the crack type SC18 (surface crack at a hole), the geometrical aspect ratios in the reference solution matrix were:

R/t=0.25, 1.0, 2.0
c/a=0.001, 0.2, 0.4, 1.0, 2.0
B/b=0.0, 0.8
$a/(t-T)$=0.1, 0.8
$c/[b-(B+R)]$=0.0, 0.05, 0.1, 0.2, 0.5, 0.8
T/t=0.0, 0.5, 0.8

where T is the offset of the surface crack from the mid-plane of the plane, $2t$ is the plate thickness, R is the radius of the hole, B is the offset of the hole from the plate center, b is

one-half the plate width, a is the crack depth along the bore direction, and c is the crack depth along the plate width.

For the crack type CC08 (corner crack at a hole), the geometrical aspect ratios were

R/t=0.25, 1.0, 2.0
c/a=0.001, 0.2, 0.4, 1.0, 2.0
B/b=0.0, 0.8
a/t=0.1, 0.8
$c/[b-(B+R)]$=0.0, 0.05, 0.1, 0.2, 0.5, 0.8

In this case, t is designated as the plate thickness instead of one-half the plate thickness denoted in SC18. In both crack types, the reference solutions for cracks with small crack depth and high aspect ratio (such as the geometrical aspect ratios at $c/[b-(B+R)]$ = 0.0 and c/a = 0.001) were derived from the analytical WF solutions for through-thickness cracks at holes described in section N.2.3.

Figure N-1 shows an example model for a corner crack at a hole (here the detailed mesh is shown only for the crack surface). Nine-node double curved patch elements were used. The number of elements depends on the proximity of the bolthole and crack to the free surfaces. For an off-center hole with a deep crack with high aspect ratio, the number of elements may increase quickly. Typically, the number of elements is around 1000.

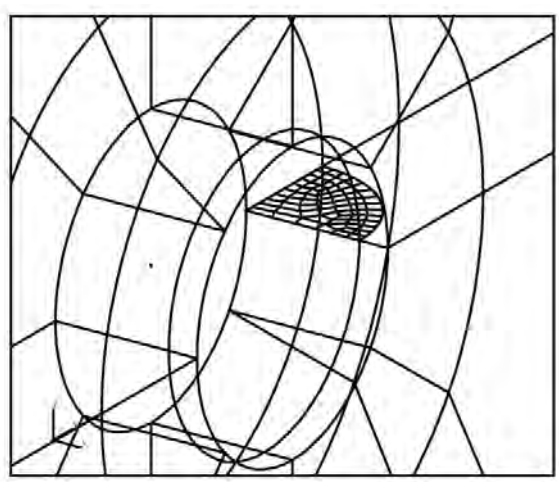

Figure N-1. FADD3D Model (a/c = 1, a/t = 0.8, R/t = 1)

Some reference solutions with extreme geometry values were difficult to generate with FADD3D due to convergence problems. In this case, a new hybrid finite element method (FEM)-boundary element method (BEM) computer program, FADD3D-FEM, was used to generate the required reference solutions. FADD3D-FEM capitalizes on the advantages of both FE and BEMs while at the same time resolving the compatibility between these two methods. It enables using a smaller number of BEs by modeling the region away from the crack by FEs and detailing only the region around the crack with BEs. Figure N-2 illustrates this coupling between a local BE

model and a global FE model. The local BE surface meshes are modeled around the crack, and the FE volumetric meshes are placed away from the crack (in this case, for a corner crack at an off-center hole in a plate). As a result, a much more numerically stable and computationally efficient solution can be achieved.

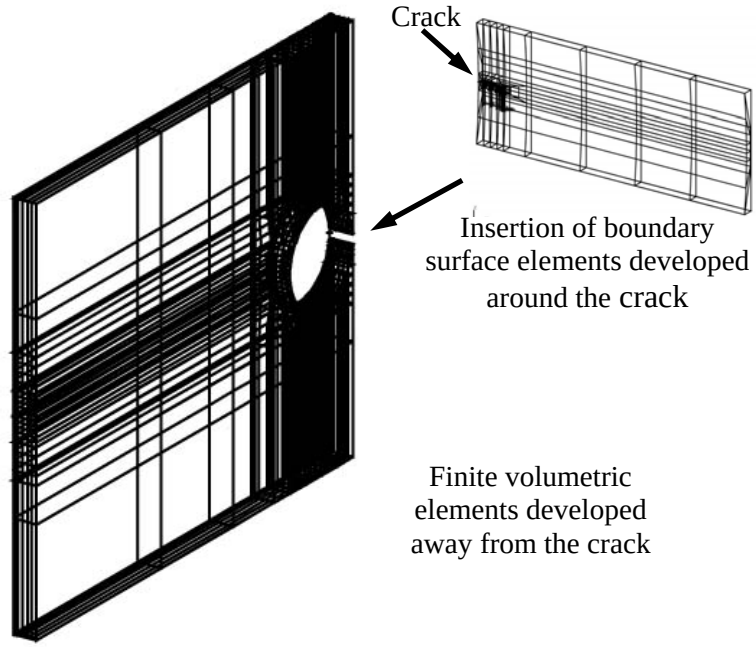

Figure N-2. Hybrid FEM/BEM Model

Figure N-3 shows an example of the improvement and convergence in solutions for the variation of SIFs along the crack perimeter for a corner crack at an off-center hole subjected to uniform tension applied on crack surface. In this example, the geometry configuration is $R/t = 2$, $c/a = 0.2$, $a/t = 0.1$, $B/b = 0.8$, and $c/[b-(B+R)] = 0.8$, where R is the radius of the hole, B is the offset of the hole from the plate center, t is the plate thickness, $2b$ is the plate width, and both c and a define the crack dimensions where c is the crack depth in the plate width direction and a is the crack depth along the bore.

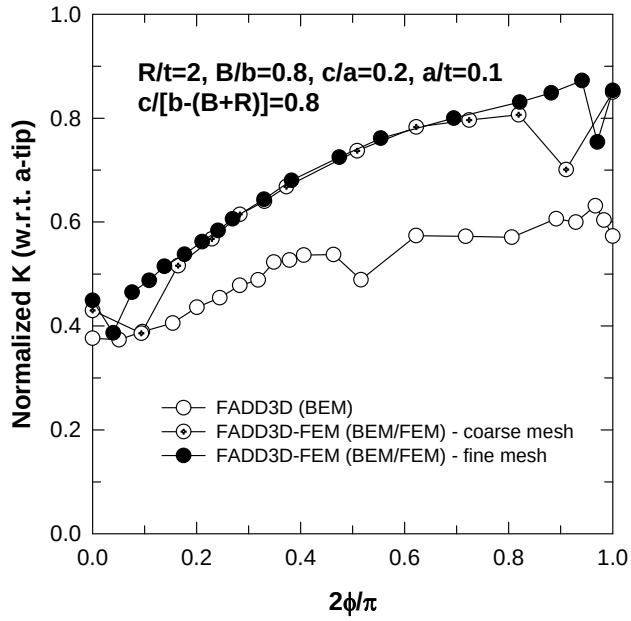

Figure N-3. Improvement in SIF Solutions Using the Hybrid FADD3D-FEM Code

N.2.3 COMPARISONS AND VALIDATION.

To verify the WF formulation, the SIFs evaluated at the *a*- and *c*-tips by the WF method using the univariant stress gradient around a hole in a plate subjected to remote tension were compared with independent FADD3D results using the same meshes and the same nonlinear stress field. The comparisons were performed for all aspect ratio combinations considered. The differences were less than 1%.

These FADD3D results for uniform remote tension were further evaluated by comparison with the widely used Newman-Raju solutions for cracks at holes under uniform remote tension [N-7 and N-8]. Sample comparisons with the FE solution [N-8] are shown in figure N-4. Here, $F(\phi)$ is the normalized SIF, $K/(\sqrt{\pi a}/\phi)$, and $2\phi/\pi$ denotes the angular position around the crack perimeter, where $2\phi/\pi = 0$, or 2 is the *a*-tip in the bore, and $2\phi/\pi = 1$ is the *c*-tip. FADD3D and Newman-Raju results compared favorably in many cases. In those cases where significant inconsistencies were observed, FE computations using the commercial code finite element analysis (FEA) crack were performed as an independent check. To achieve similar resolution to FADD3D, FEA crack computations used at least 6000 elements. The FADD3D results were confirmed by the FEA crack results. Note that the older Newman-Raju FE solutions, which employed fewer degrees of freedom, are less accurate at free surfaces due to the relatively coarse meshes used.

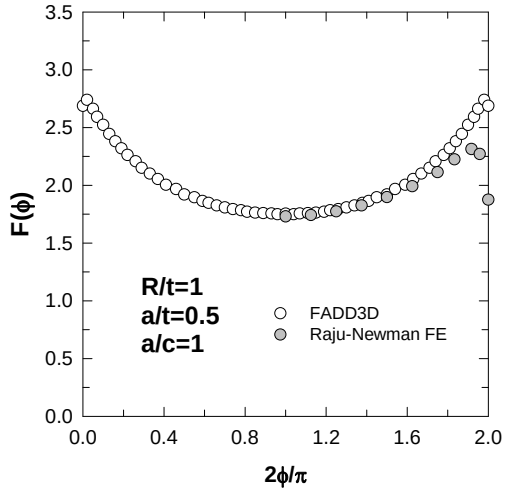

(a)

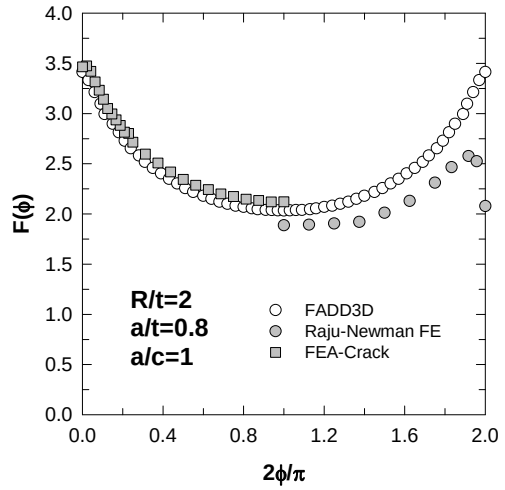

(b)

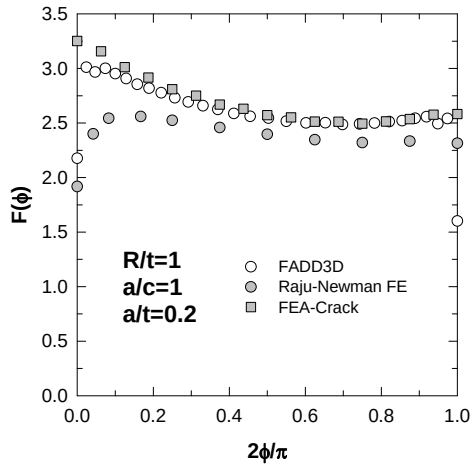

(c)

Figure N-4. Selected Normalized SIF Results From FADD3D, Newman-Raju, and FEA Crack for (a-b) Center Surface Crack and (c) Corner Crack at a Hole in a Plate Under Remote Tension

N.3 WEIGHT FUNCTION STRESS-INTENSITY FACTOR SOLUTIONS FOR THROUGH-THICKNESS CRACKS AT HOLES.

N.3.1 REFERENCE STRESS.

The WF SIF solution for through-thickness cracks at holes in DARWIN (denoted TC13) was analytically derived. The formulation assumes a two-dimensional plate configuration with an off-center hole. The derivation was based on the tabulated SIF solutions for through-thickness cracks at off-center holes subjected to remote tension given in the NASGRO® TC03 module [N-9]. The SIF solutions were evaluated at the combinations of geometrical aspect ratios of $(b–B)/b$ = 0.1, 0.2, 0.5, 0.7, 1.0, and $R/(b–B)$ = 0.05, 0.1, 0.3, 0.5, 0.7, 0.8, and 0.9, where b is one-half the plate width, R is the radius of the hole, and B is the offset of the hole from the plate center. To facilitate the derivation, the stress variation normal to the net section was required. The variation was determined numerically using two-dimensional FEA for these geometric combinations. It was found that, if normalized by the average net section stress and plotted against the normalized net section coordinate, the stress variation is independent of the offset of the hole for a fixed $R/(b–B)$ ratio. Figure N-5 supports such a conclusion, indicating that the normalized stress variations for a variety of offsets are nearly coincident for any given fixed $R/(b–B)$ ratio.

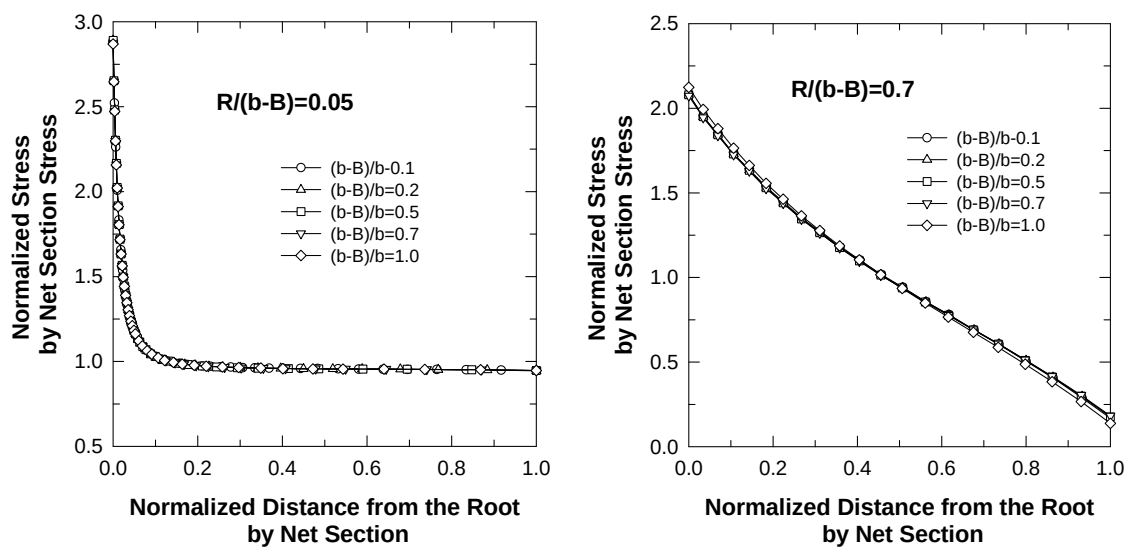

(a) (b)

Figure N-5. Variations of Normalized Stress Across the Net Section by the Average Net Section Stress for a Variety of Hole Offsets: (a) $R/(b–B)$ = 0.05 and (b) $R/(b–B)$ = 0.7

Such a conclusion greatly reduces the number of FEA computations for stress variations and facilitates the interpolation of stress gradients when deriving the WFs. The net section stress is designated as the reference stress and can be simplified as a two-term product: the average net section stress as a function of $(b–B)/b$ and $R/(b–B)$, and the normalized stress variation as a function of $R/(b–B)$ and the normalized coordinate $x/(b–B–R)$, or;

$$\sigma_r(x) = \sigma_{net}\left(\frac{b-B}{b}, \frac{R}{b-B}\right) \cdot \bar{\sigma}\left(\frac{R}{b-B}, \frac{x}{b-B-R}\right) \tag{N-7}$$

where σ_{net} is the average net section stress and $\bar{\sigma}$ the normalized stress variation along the normalized net section coordinate whose profile is dictated by the $R/(b-B)$ ratio only.

N.3.2 WEIGHT FUNCTIONS.

The WF for a through-thickness crack at an off-center hole in a finite plate is given by

$$W_c\left(\tilde{x}, \xi; \frac{b-B}{b}, \frac{R}{b-B}\right) = \frac{1}{\sqrt{2\pi\xi}} \sum_{i=1}^{5} \beta_i\left(\xi; \frac{b-B}{b}, \frac{R}{b-B}\right) \cdot \left(1 - \frac{\tilde{x}}{\xi}\right)^{i-\frac{3}{2}} \tag{N-8}$$

where the subscript i varies from 1 to 5, ξ symbolizes the normalized crack length by the net section $a/(b-B-R)$, and $\tilde{x}$ represents the normalized coordinate varying from 0 to ξ. The coefficients β_i's are tabulated as a function of normalized crack depth ξ and normalized plate dimensions $(b-B)/b$ and $R/(b-B)$. For a general stress variation $\sigma(x)$, the SIF can be expressed in terms of an integral over the whole crack depth [N-10]:

$$K\left(\xi; \frac{b-B}{b}, \frac{R}{b-B}\right) = \sqrt{R}\int_0^{\xi} \sigma(\tilde{x}) \cdot W_c\left(\tilde{x}, \xi; \frac{b-B}{b}, \frac{R}{b-B}\right) d\tilde{x} \tag{N-9}$$

The integration is carried out numerically using Gauss-Chebyshev quadrature with convergence check.

N.3.3 VERIFICATION.

Consistency checks of the predicted results using the crack type TC13 against the reference solutions were performed to confirm the same results as the reference solutions were obtained when the stress variations corresponding to the reference stress were used. The verification consists of a variety of combination of geometrical aspect ratios as the tabulated SIF solutions for the NASGRO TC03 module. Respectively, they are $(b-B)/b$ = 0.1, 0.2, 0.5, 0.7, 1.0; $R/(b-B)$ = 0.05, 0.1, 0.3, 0.5, 0.7, 0.8, 0.9; and $a/(b-B-R)$ = 0.0, 0.02, 0.05, 0.1, 0.2, 0.3, 0.5, 0.7, 0.9, 0.95, and 0.98. Selective comparisons are given in figure N-6 for $(b-B)/b$ = 0.1 and 1.0. In the graphs, the normalization factor for the SIF is $\sqrt{\pi a}$, where a denotes the crack depth. The comparisons indicate the predicted solutions are in good agreement with the reference solutions.

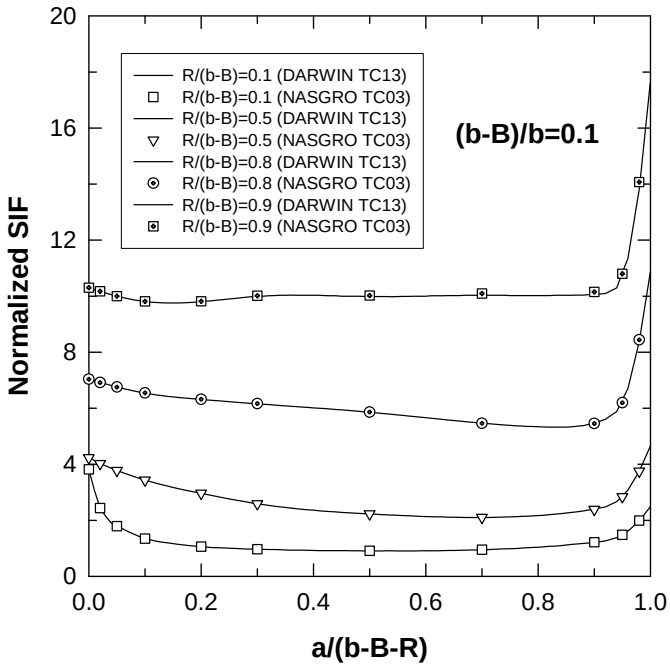

(a)

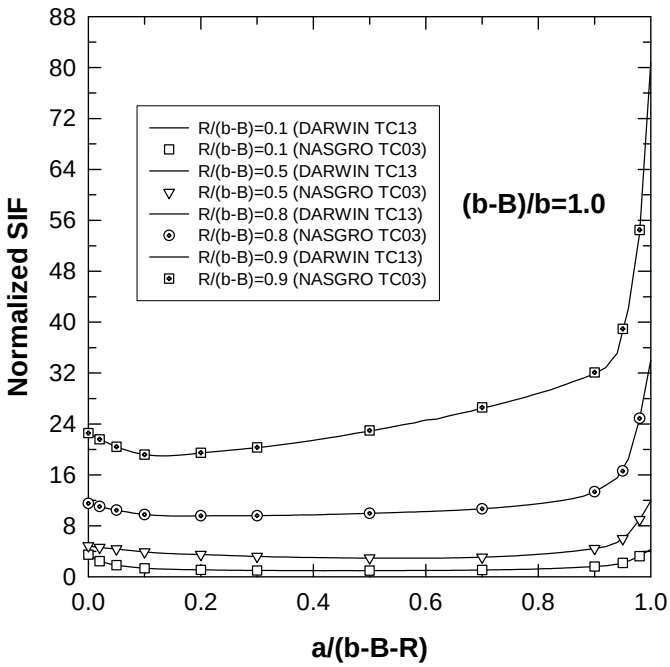

(b)

Figure N-6. Consistency Check of the Predicted TC13 Results Using the Reference Stress Against the Tabulated TC03 Solutions in NASGRO for (a) $(b–B)/b$ = 0.1 and (b) $(b–B)/b$ = 1.0 (The normalization factor for SIF is $\sqrt{\pi a}$, where a is the crack depth.)

N.4 A NEW WEIGHT FUNCTION STRESS-INTENSITY FACTOR SOLUTION FOR THE CORNER CRACK IN A PLATE UNDER GENERAL BIVARIANT STRESSING.

N.4.1 BACKGROUND.

Nearly all existing WF SIF solutions (including the solutions described in the two previous sections) are limited to stresses that vary in one dimension only (so-called univariant gradients). However, the actual variation of stresses in a cracked part can be considerably more complex, varying arbitrarily in all directions on the crack plane. In this case, it may be necessary to employ a SIF solution that admits this general bivariant stress field.

Bivariant SIF solutions for embedded cracks in infinite bodies can be analytically derived [N-11 and N-12]. However, the analytical procedure becomes much more complex when free surfaces are introduced, and few solutions are available. As a consequence, numerical solutions derived from FE and BE methods are often used.

The CC01 solution in NASGRO [N-13], based on the Raju-Newman FE solutions [N-14] through interpolation, is a commonly used bivariant solution. However, the application is limited by the assumed linear stress variation across the plate thickness and width.

The NASCRAC software [N-15] permits the calculation of K for general bivariant stress fields using a root mean square (rms)-averaged effective SIF for the entire crack boundary along the direction associated with the corresponding degree of freedom. However, this method does not provide information on the specific local variation in K, and it exhibits accuracy limitations, especially at deeper crack lengths [N-16].

Zhao, et al. [N-17] developed an approach based on the slice synthesis method in which SIFs obtained from two perpendicular cross-sectional slices in a three-dimensional body that intersect at the crack front are synthesized to determine the SIF corresponding to that specific elliptical angle. However, accuracy is again an issue for this approximate method, and the computational speed of the algorithm can become impractical for some fatigue crack growth (FCG) applications.

Highly accurate SIF solutions for cracked structural components with general stress distributions are possible with a point WF (PWF) formulation. Several PWFs have been proposed that can be used as the integrand in the surface integral for SIFs. The PWF for a circular crack in an infinite body has long been available [N-12 and N-18]. Oore and Burns [N-19] and Orynyak [N-20 and N-21] have developed PWFs for elliptical cracks. The formulation proposed by Oore and Burns represents the PWF in terms of a contour integral. In contrast, Orynyak's approximate PWF is a much simpler functional form constructed similar to the PWF for circular cracks.

A recent version of NASGRO [N-13] includes a bivariant SIF solution for the corner crack in a plate based on a hybrid approach developed by Fujimoto [N-22], using the PWF of Orynyak while extending the Petroski-Achenbach method [N-23] to three-dimensional cracks. The hybrid method uses a WF formulation capable of correctly spatially weighting loads applied at any point on the crack surface while permitting existing solutions for elliptical or part-elliptical flaws to be

used as reference solutions. However, some inconsistencies have been discovered for deep cracks when using different sets of reference solutions.

Glinka [N-24] has further extended the work done by Oore and Burns, and his new formulation is, in principle, applicable to cracks of arbitrary shape. However, some accuracy issues remain unresolved, and the integration scheme employed introduces substantial computation speed issues.

N.4.2 WEIGHT FUNCTION FORMULATION.

A new bivariant WF formulation is illustrated here for a corner crack in a rectangular plate of finite width and thickness (figure N-7). The corner crack is assumed to have a quarter-elliptical shape that can be characterized by two degrees of freedom, the crack dimensions *c* and *a* in the width and thickness directions, respectively.

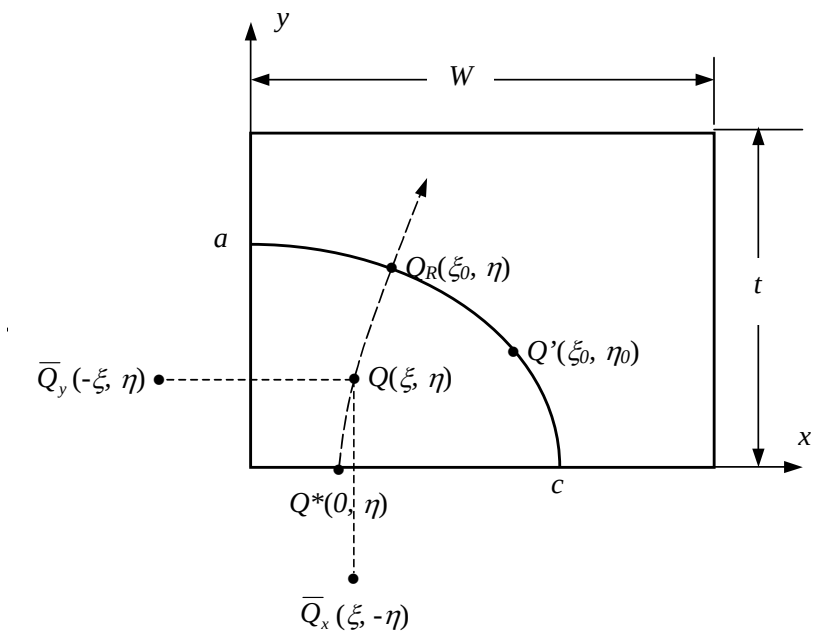

Figure N-7. Geometry Configuration and Nomenclature for Corner Crack in Plate

Due to its simplicity and accuracy, the PWF proposed by Onynyak for an elliptical crack in an infinite body was used as the basic WF. This form can be written as

$$W_{QQ'} = \frac{\sqrt{R^2 - r^2}}{\pi \ell_{QQ'}^2 \sqrt{\pi R}} \tag{N-10}$$

The equation represents the weighting effects on any point *Q'* along the crack front contributed by a point unit load applied at *Q* on the elliptical crack surface. Here, *R* is the distance between Q^* and Q_R, *r* the distance between *Q* and Q^*, and $\ell_{QQ'}$ the distance between *Q* and Q'.

The definitions for Q, Q', Q_R, and Q^* are more concise using elliptical coordinate notation. Respectively, they are given by $Q=(\xi,\eta)$, $Q'=(\xi_0,\eta_0)$, $Q_R=(\xi_0,\eta)$, and $Q^*=(0,\eta)$ where ξ and η are the parameters in the elliptical coordinate system to identify a point along the crack plane with its origin at the center of the crack. It can be seen that Q, Q_R, and Q^* are defined along the same elliptical angle η. ξ_0 is the elliptical radius defining the elliptical crack front. This PWF equation is similar to the one for circular cracks derived by Kassir and Sih [N-12] as well as Shah and Kobayashi [N-11] except for different definitions for the length parameters. The validity of this PWF is demonstrated by a comparison with Shah and Kobayashi's analytical derivation [N-11] for embedded cracks subjected to crack-opening stresses applied on the crack plane (figure N-8). Here $2\phi/\pi$ is the normalized elliptical angular position along the perimeter of the embedded crack.

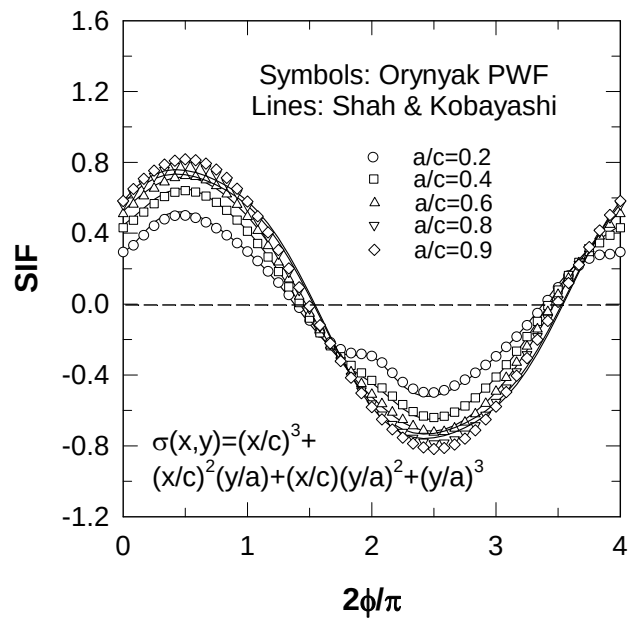

Figure N-8. Comparison of Orynyak PWF Method With Shah-Kobayashi Analytical Results

To account for the free boundary correction for a quarter-elliptical corner crack in a quarter-infinite body, equation N-10 was modified to include two additional length parameters. Now the basic PWF applicable at Q' for a point unit load applied at Q is given by

$$W_{QQ'}=\frac{\sqrt{R^2-r^2}}{\pi\ell_{QQ'}^2\sqrt{\pi R}}\left(1+\frac{\ell_{QQ'}^2}{\ell_{\overline{Q}_xQ'}^2}+\frac{\ell_{QQ'}^2}{\ell_{\overline{Q}_yQ'}^2}\right) \tag{N-11}$$

The additional length parameters $\ell_{\overline{Q}_xQ'}$ and $\ell_{\overline{Q}_yQ'}$ correct the free surface effects for a corner crack by assuming a symmetrical stress distribution for an imaginary prolonged crack extending into the other three quadrants. In reference to figure N-7, $\ell_{\overline{Q}_xQ'}$ is the distance between $\overline{Q}_x$ and Q', and $\ell_{\overline{Q}_yQ'}$ the distance between $\overline{Q}_y$ and Q'. The locations, $\overline{Q}_x$ and $\overline{Q}_y$, are points symmetrical to the location of point load Q with respect to the x and y axes.

Additional correction terms are required to account for finite width and thickness effects. Following several exploratory investigations, a formulation was identified with reasonable numerical accuracy and stable convergent approach. The PWF at Q' for a point unit load applied at Q for a quarter-elliptical crack in a finite plate is thus provided by

$$W_{QQ'} = \frac{\sqrt{R^2 - r^2}}{\pi \ell_{QQ'}^2 \sqrt{\pi R}} \left(1 + \frac{\ell_{QQ'}^2}{\ell_{\bar{Q}_x Q'}^2} + \frac{\ell_{QQ'}^2}{\ell_{\bar{Q}_y Q'}^2} \right) \left[1 + \Pi_1 \sqrt{1 - \frac{r}{R}} + \Pi_2 \left(1 - \frac{y}{y'} \right) + \Pi_3 \left(1 - \frac{x}{x'} \right) \right] \tag{N-12}$$

where x and y define the Cartesian coordinates of Q, and $x' = c\sqrt{1 - x^2/a^2}$ and $y' = a\sqrt{1 - x^2/c^2}$. The SIF can therefore be evaluated by performing surface integration across the crack area. For a given stress distribution $\sigma(x,y)$ applied on the crack plane obtained from an uncracked body subjected to remote loadings, the SIF is written as

$$K = \int_0^a \int_0^{c\sqrt{1-\frac{y^2}{a^2}}} \sigma(x, y) \cdot W_{QQ'} dxdy \tag{N-13}$$

The parameters Π_1, Π_2, and Π_3 are calibrated by reference solutions at both a- and c-tips to characterize the finite boundary effects. Accordingly, in this approach, three reference stress solutions are required at each tip, and the SIF at a- and c-tips can be determined by

$$K^{a,c} = \int_0^a \int_0^{c\sqrt{1-\frac{y^2}{a^2}}} \sigma(x, y) \frac{\sqrt{R^2 - r^2}}{\pi \ell_{QQ^{a,c}}^2 \sqrt{\pi R}} \left(1 + \frac{\ell_{QQ^{a,c}}^2}{\ell_{\bar{Q}_x Q^{a,c}}^2} + \frac{\ell_{QQ^{a,c}}^2}{\ell_{\bar{Q}_y Q^{a,c}}^2} \right) \left[1 + \Pi_1^{a,c} \sqrt{1 - \frac{r}{R}} + \Pi_2^{a,c} \left(1 - \frac{y}{y'} \right) + \Pi_3^{a,c} \left(1 - \frac{x}{x'} \right) \right] dxdy \tag{N-14}$$

where the superscripts a and c denote parameters associated with a- and c-tips, respectively.

To facilitate the computation, equation N-14 is preferably written in terms of elliptical coordinate parameters instead of Cartesian. For $\alpha = a/c \le 1$, the relationships between Cartesian and elliptical coordinates (ξ, η) are as follows:

$$x = b \cosh \xi \cos \eta, \; y = b \sinh \xi \sin \eta, \; b = \sqrt{c^2 - a^2} \tag{N-15}$$

For any point along the crack front, the elliptical radius in elliptical coordinate system is the same and is given by

$$\xi_0 = \frac{1}{2}\ln\left(\frac{1+\alpha}{1-\alpha}\right) \tag{N-16}$$

The above equation is derived by eliminating the dependency on the elliptical angle η among coordinate transformation equations. The Cartesian coordinates for Q, Q_R, Q^*, Q', $\overline{Q}_x$, and $\overline{Q}_y$ in terms of elliptical coordinate parameters are as follows:

$$Q = \left(b\cosh\xi\cos\eta, b\sinh\xi\sin\eta\right) \tag{N-17}$$

$$Q_R = \left(b\cosh\xi_0\cos\eta, b\sinh\xi_0\sin\eta\right) \tag{N-18}$$

$$Q^* = \left(b\cos\eta, 0\right) \tag{N-19}$$

$$Q' = \left(b\cosh\xi_0\cos\eta, b\sinh\xi_0\sin\eta\right) \tag{N-20}$$

$$\overline{Q}_x = \left(-b\cosh\xi\cos\eta, b\sinh\xi\sin\eta\right) \tag{N-21}$$

$$\overline{Q}_y = \left(b\cosh\xi\cos\eta, -b\sinh\xi\sin\eta\right) \tag{N-22}$$

and the infinitesimal area becomes

$$dxdy = b^2\left(\sinh^2\xi + \sin^2\eta\right)d\eta d\xi \tag{N-23}$$

Furthermore, the integration limits are converted from $y: 0 \to a\sqrt{1-x^2/c^2}$ and $x: 0 \to c$ to $\xi: 0 \to \xi_0$ and $\eta: 0 \to \pi/2$. The integration sequence is now interchangeable.

To accelerate the evaluation of surface integral described in equation N-14, DARWIN provides two separate modules for crack-opening stresses that can be simplified by polynomials in addition to modules for general stressing. These modules contain preintegrated terms derived based on prescribed polynomial forms in one-dimensional and two-dimensional variations. The applicable polynomial for stress variation in one dimension is

$$\sigma(x,y) = \sigma(x) = \sum_{i=0}^{6} p_i\left(\frac{x}{W}\right)^i \tag{N-24}$$

for stress variations along the x direction only, or

$$\sigma(x,y) = \sigma(y) = \sum_{i=0}^{6} q_i\left(\frac{y}{t}\right)^i \tag{N-25}$$

for stress variations along the y axis only, where t and W represent the plate thickness and width (ref. figure N-7). The polynomial for stress variation in two dimensions contains cross product terms and is given by

$$
\begin{aligned}
\sigma(x,y) = g_{00} + g_{10}\frac{x}{W} + g_{01}\frac{y}{t} + \\
g_{20}\left(\frac{x}{W}\right)^2 + g_{11}\frac{x}{W}\frac{y}{t} + g_{02}\left(\frac{y}{t}\right)^2 + \\
g_{30}\left(\frac{x}{W}\right)^3 + g_{21}\left(\frac{x}{W}\right)^2\frac{y}{t} + g_{12}\frac{x}{W}\left(\frac{y}{t}\right)^2 + g_{03}\left(\frac{y}{t}\right)^3 + \\
g_{31}\left(\frac{x}{W}\right)^3\frac{y}{t} + g_{22}\left(\frac{x}{W}\right)^2\left(\frac{y}{t}\right)^2 + g_{13}\frac{x}{W}\left(\frac{y}{t}\right)^3 + \\
g_{32}\left(\frac{x}{W}\right)^3\left(\frac{y}{t}\right)^2 + g_{23}\left(\frac{x}{W}\right)^2\left(\frac{y}{t}\right)^3 + g_{33}\left(\frac{x}{W}\right)^3\left(\frac{y}{t}\right)^3
\end{aligned}
\tag{N-26}
$$

The coefficients for the polynomials p_i, q_i, and g_i are determined by regressions to the actual stress variations in the component of interest.

N.4.3 REFERENCE SOLUTIONS.

The WF method requires an accurate set of reference solutions for a matrix of crack geometries. These reference solutions were numerically generated using the FADD3D fracture mechanics software, a general boundary element code for three-dimensional linear elastic fracture analysis [N-4]. Development of BE models is much less labor-intensive than FE models, since only surfaces must be meshed. This was especially important for the large number of crack models required in the current effort. FADD3D has been shown to maintain exceptional accuracy even with relatively coarse meshes [N-5 and N-6].

Reference solutions were generated for the corner crack in a plate at 150 different combinations of geometrical aspect ratios: *a/c* = 0.1, 0.2, 0.4, 0.6, 0.8, 1.0; *c/W* = 0.1, 0.2, 0.5, 0.8, 0.9; and *a/t* = 0.1, 0.2, 0.5, 0.8, 0.9. For *a/c* and *a/t* less than 0.1 and approaching zero, reference stress solutions for edge cracks were generated and used. For *a/c* larger than 1, the reference solutions were obtained from the corresponding *c/a* ratios by reversing the stress field and the associated geometry dimensions. As a result, the expanded reference solution matrix constitutes a discrete database covering a complete range of aspect ratio combinations; i.e., *a/c* from 0 to ∞, *a/t* from 0 to 0.9, and *c/W* from 0 to 0.9. For any arbitrary combination of aspect ratios, the reference solutions are determined from the matrix of specific solutions through Hermite interpolation.

Three sets of reference solutions were determined for each crack geometry. These are denoted as solutions for unit tension, unit bending along the *x* axis, and unit bending along the *y* axis. The solutions were generated by applying the reference stresses on the crack plane in the corresponding uncracked body. The three reference stresses are given by $\sigma_0 = 1$, $\sigma_1 = -y/a + 1$, and $\sigma_2 = -x/c + 1$.

Figure N-9 depicts a sample boundary element mesh pattern used to simulate the crack surface for *c/a* = 1, *a/t* = 0.5, and *c/W* = 0.5. To describe this crack surface, 64 nine-node boundary surface elements were specified. Each element had four corners, one embedded, and four intermediate nodes, and four doubly curved sides.

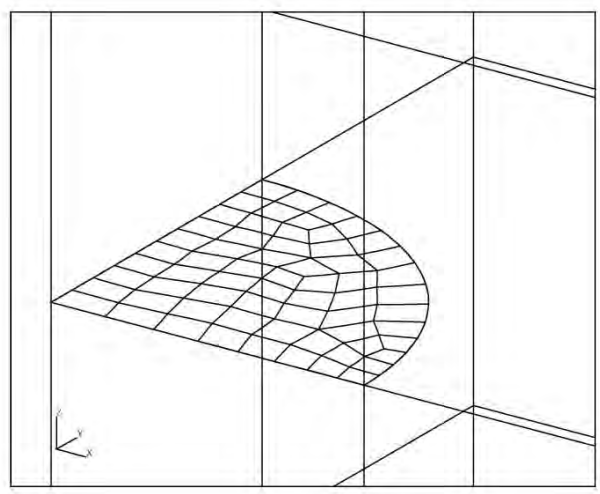

Figure N-9. Boundary Element Mesh Pattern Used to Simulate Crack Surface for FADD3D Computation; *c/a* = 1, *a/t* = 0.5, and *c/W* = 0.5

Figure N-10 shows selected reference solutions numerically determined by FADD3D for various *a/t* ratios at *c/a* = 1 and *c/W* = 0.5. The variations were plotted against the parametric elliptical angle ϕ measured along the crack front from the *c*-tip, the surface tip along the plate width direction. Here $2\phi/\pi = 0$ corresponds to the *c*-tip and $2\phi/\pi = 1$ to the *a*-tip. $F(\phi)$ is the normalized SIF, given by $K\big/\sqrt{\pi a/Q}$, where Q is the shape factor associated with the *a/c* ratio. Q is defined by

$$Q = \begin{cases} 1 + 1.464\left(a/c\right)^{1.65}, & \text{for } a/c \le 1 \\ 1 + 1.464\left(c/a\right)^{1.65}, & \text{for } a/c > 1 \end{cases} \tag{N-27}$$

The FADD3D results, like many numerical solutions, often exhibit sharp changes at the intersection of the crack perimeter with a free surface ($2\phi/\pi = 0$ and 1) because of the complex nature of the singularity at that point. To minimize the effect of this numerical artifact, the reference solution values for the *a*- and *c*-tip are generally taken at the first node inside the free surface, between 2° and 3° from the free surface.

The same bivariant WF formulation was employed to derive bivariant SIF solutions for a quarter-elliptical corner crack at a hole, denoted CC10 in DARWIN. The same FADD3D models used to generate reference solutions for the univariant WF SIF solution CC08 were used to generate reference solutions for CC10, except that an additional reference solution for a linear stress gradient along the *y* direction was obtained for each geometry model.

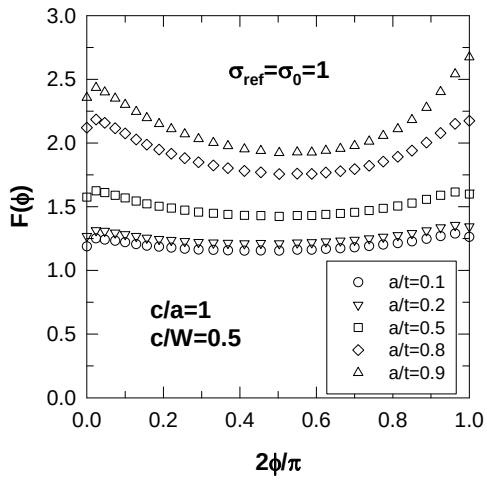

(a)

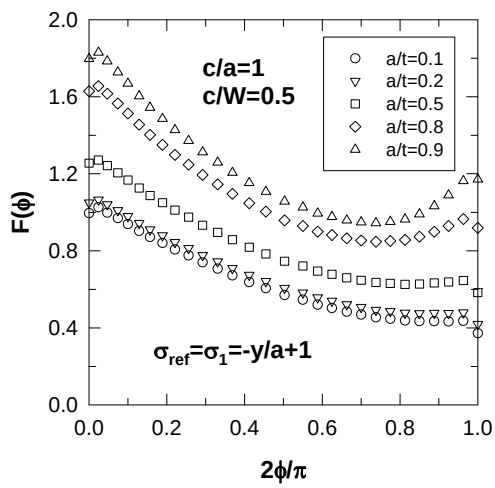

(b)

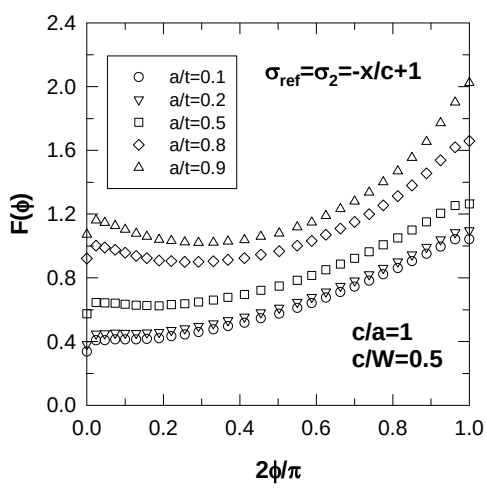

(c)

Figure N-10. Selected Normalized SIF Results From FADD3D Graphs Correspond to Three Reference Stresses: (a) Unit Tension, (b) Bending Along *x* Axis, and (c) Bending Along *y* Axis

N.4.4 VALIDATION.

Independent numerical results using FADD3D have been used to validate the bivariant WF solutions. Selected comparisons are presented here to demonstrate the numerical accuracy achieved by the formulation.

For validation, two types of stress variation—one univariant and one bivariant—were applied on the crack plane. The univariant stress distribution was specified as:

$$\sigma_{uni} = \left(-\frac{y}{a} + 1 \right)^3 \tag{N-28}$$

which varies from 1.0 at the plate surface to zero at the *a*-tip, the surface tip in the plate thickness direction. The bivariant stress distribution contains cross-product terms and is given by

$$\sigma_{bi} = \left(-\frac{x}{c} + 1 \right)^3 \left(-\frac{y}{a} + 1 \right)^3 \tag{N-29}$$

This stress distribution varies from 1.0 at the center of the crack and bivariantly approaches zero at both surface tips. The distribution functions contain a third-order dependency to represent a steep stress gradient. These two stress fields are illustrated in figure N-11. The specified stress functions can be transformed into expanded polynomials, as described in equations N-25 and N-26.

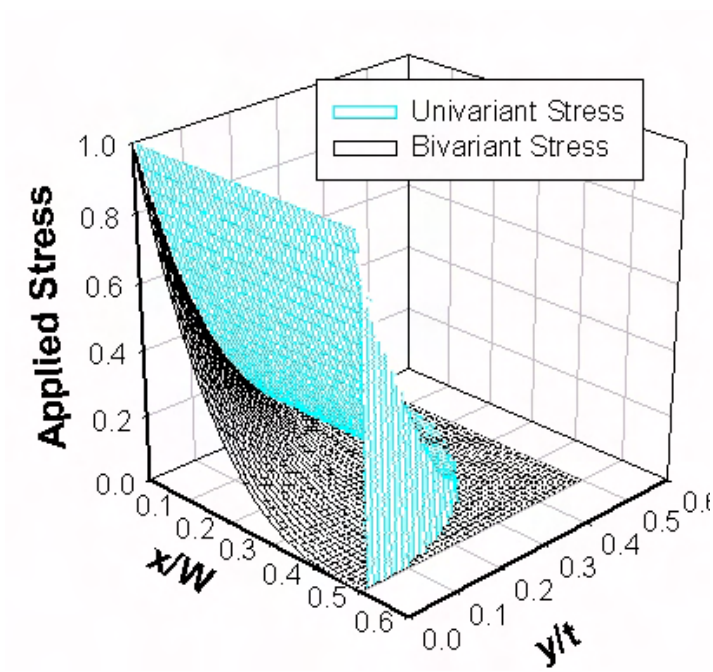

Figure N-11. Surface Plots Showing Stress Distributions Specified by Univariant and Bivariant Stress Functions

Two aspect ratios were used for demonstration; *a/c* = 0.4 and 1.0. The normalized SIF variations as a function of parametric elliptical angle along the crack front for two stress distributions are shown in figures N-12 and N-13 for *a/c* = 1.0 and *a/c* = 0.4, respectively. The normalization factor is the same as previously defined, $\sqrt{\pi a/Q}$.

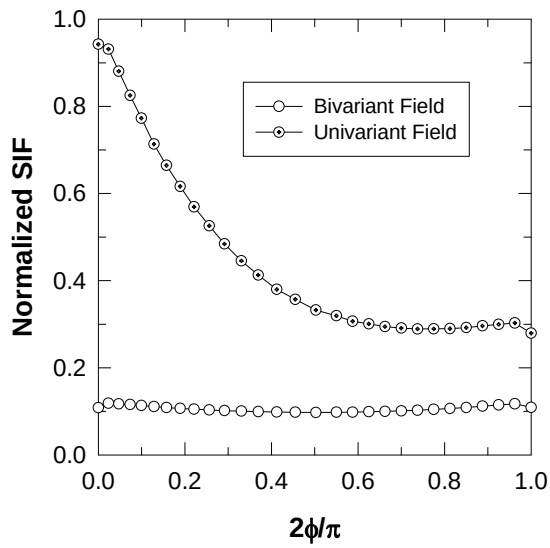

Figure N-12. Normalized SIF From FADD3D for *a/c* = 1.0

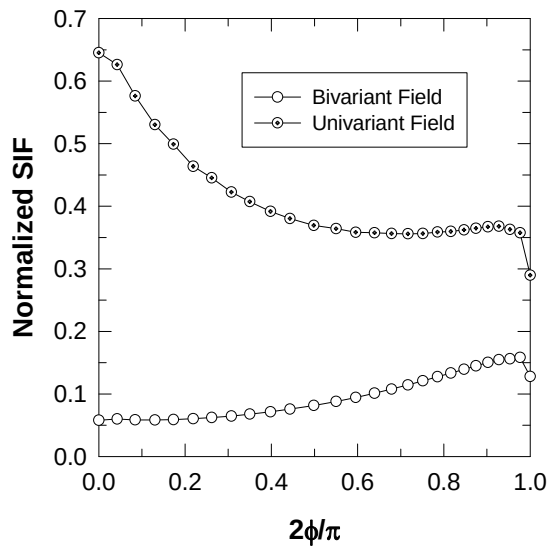

Figure N-13. Normalized SIF From FADD3D for *a/c* = 0.4

The predicted results at both *a*- and *c*-tips using the new bivariant *K* solutions for corner crack in plate were plotted against these two sets of numerical results obtained from FADD3D. The predicted results were taken at 3 degrees below free surface, while the computed results were based on the next available data points below the free surface. The comparison, depicted in figure N-14, indicates very good agreement.

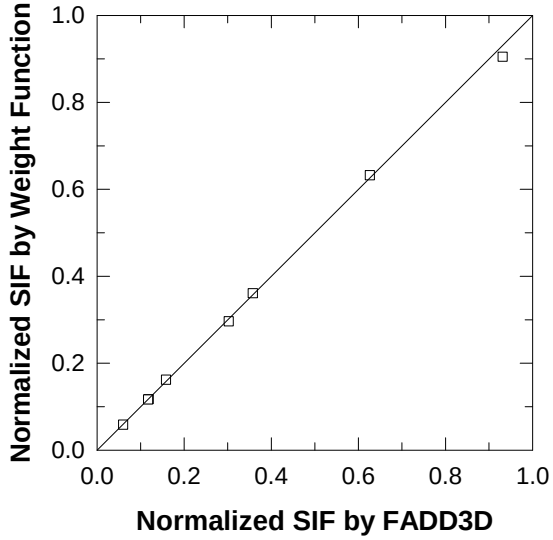

Figure N-14. Comparison of FADD3D and WF SIF Solutions for Corner Crack in Plate

N.4.5 UNIVARIANT SOLUTIONS VS BIVARIANT SOLUTIONS.

Are bivariant solutions really needed? Are conventional univariant solutions adequate? The answers to these questions certainly depend on the specific stress fields involved, but the errors introduced by using a univariant solution for a highly bivariant stress field can be substantial. This is illustrated by the selected results for univariant and bivariant stress distributions shown in figure N-11. In this example, a univariant solution to the bivariant stress field would be identical to the solution for the univariant stress field, since the univariant stress field is identical to the bivariant stress field along one primary axis of the crack. However, the bivariant stress distribution decreases to zero at both surface tips, while the univariant stress distribution is uniform in the *y* direction and applies a much larger resultant force on the crack plane than the bivariant stress field. The resulting univariant SIF solution dramatically overestimates the actual SIF by a factor of three at the *a*-tip ($2\phi/\pi = 1$) and nearly a factor of ten at the *c*-tip ($2\phi/\pi = 0$), as shown in figure N-12.

N.4.6 DYNAMIC TABULAR INTERPOLATION.

As described in the previous section on the formulation of bivariant SIF solutions, the solutions make use of integration of WFs over the crack surface. For bivariant solutions, this integration procedure is extremely time-consuming, especially with convergence checks. Several steps such as tabulating parts of the integration for interpolation have been incorporated to reduce the total computation time. However, although the execution time for one single FCG computation is acceptable, this scheme still needs improvement for probability analysis where thousands of FCG analyses are performed.

To achieve a reasonable computation time without the loss of numerical accuracy, an approach using an SIF table interpolation scheme is generally used. This approach generates a table of SIF

solutions at the very beginning with the given stressing at specific incremental geometric combinations. Subsequently, during the FCG computation, the SIF values for any given crack dimensions can be determined through interpolation among those tabulated data. While this approach has been used successfully for other SIF solutions in NASGRO, the computing effort for filling up the SIF tables for a bivariant solution can still be quite demanding, especially for extreme geometrical combinations.

Denoting this previous tabular approach as the static approach, a new algorithm was derived that makes use of a more dynamic approach. Instead of filling up the entire SIF table for the full range of possible geometry parameters at the very beginning, the generation of SIF solutions to support interpolation at specific geometric combinations is performed only if it is necessary. For the purpose of illustration, see the schematic in figure N-15. A geometric combination is specified by two geometric ratios $(c/a)_i$ and $(a/t)_j$ as indicated at the grid points in figure N-15, where the subscript i varies from 1 to m, and the subscript j from 1 to n. The static SIF table interpolation approach requires generating $(m \times n)$ SIF solutions corresponding to all grid points. However, the dynamic approach starts with identifying a geometric square (as indicated by *SQR1* in figure N-15) enclosing the *a/t* and *c/a* ratios defined by the given initial crack dimensions (as P_1 in figure N-15). Within this geometric square, the number of required SIF solutions is 16 (4 by 4). Once the *K* solutions within the geometric square *SQR1* are filled, the SIF solutions at the given geometric ratios of *c/a* and *a/t* can be determined by interpolation. For a new crack configuration, the same procedure is repeated. For instance, if the geometrical aspect ratios of the new crack dimensions correspond to P_2 in figure N-15, then the grid points within the geometric square *SQR2* will be designated for new *K* generation. However, since the scan over this square reveals there are pre-existing solutions at nine of the intersected grid points, only seven additional solutions are required.

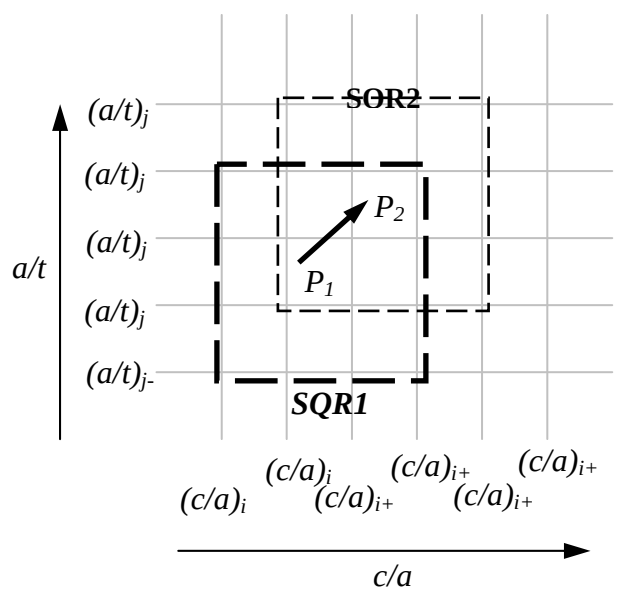

Figure N-15. Dynamic SIF Table Interpolation Scheme

Besides reducing the overall computation time, the dynamic SIF table interpolation approach has two key features: an adjustable resolution and a nearly constant computation time for a given resolution. The resolution corresponding to the grid size depicted in figure N-15 governs the overall computation time. To achieve a faster computation time, the resolution can be relaxed slightly, with a possibility of losing some numerical accuracy caused by interpolation. However, once the resolution is fixed, the computation time for a life calculation remains almost constant regardless of the number of crack increments, since the time spent for interpolating the SIF solution for any given geometric ratio is minimal in comparison to the time required to generate the SIF solutions for the table.

N.5 REFERENCES.

N-1. Glinka, G. and Shen, G., "Universal Features of Weight Functions for Cracks in Mode I," *Engineering Fracture Mechanics*, Vol. 40, 1991, pp. 1135-1146.

N-2. Shen, G. and Glinka, G., "Weight Functions for a Surface Semi-Elliptical Crack in a Finite Thickness Plate," *Journal of Theoretical and Applied Fracture Mechanics*, Vol. 15, 1991, pp. 247-255.

N-3. Kiciak, A., Glinka, G., and Eman, M., "Weight Functions and Stress-Intensity Factors for Corner Quarter-Elliptical Crack in Finite Thickness Plate Subjected to In-Plane Loading," *Engineering Fracture Mechanics*, Vol. 60, 1998, pp. 221-238.

N-4. Xiao, L. and Mear, M.E., *FADD3D User's Manual*, Dept. of Engineering Mechanics, University of Texas at Austin, 1998.

N-5. Li, S., Mear, M.E., and Xiao, L., "Symmetric Weak-Form Integral Equation Method for Three Dimensional Fracture Analysis," *Computer Methods in Applied Mechanics and Engineering*, Vol. 151, 1998, pp. 435-539.

N-6. Li, S. and Mear, M.E., "Singularity-Reduced Integral Equations for Discontinuities in Linear Elastic Media," *International Journal of Fracture*, Vol. 93, 1998, pp. 87-114.

N-7. Newman, J.C., Jr. and Raju, I.S., "Stress-Intensity Factor Equations for Cracks in Three-Dimensional Finite Bodies," *Fracture Mechanics: 14th Symposium – Volume 1: Theory and Analysis, ASTM STP 791*, American Society for Testing and Materials, 1983, pp. I-238-I-265.

N-8. Raju, I.S. and Newman, J.C., Jr., "Stress-Intensity Factors for Two Symmetric Corner Cracks," *Fracture Mechanics, ASTM STP 677*, American Society of Testing and Materials, 1979, pp. 411-430.

N-9. Yeh, F. and Mettu, S.R., "Stress-Intensity Factors for a Through Crack From an Offset Hole in a Finite Plate by Boundary Element Method," JSC 28935, 2000.

N-10. Wu, X.-R. and Carlsson, A.J., *Weight Functions and Stress Intensity Factor Solutions*, Pergamon Press, New York, 1991.

N-11. Shah, R.C. and Kobayashi, A.S., "Stress-Intensity Factor for an Elliptical Crack Under Arbitrary Normal Loading," *Engineering Fracture Mechanics*, Vol. 3, 1971, pp. 71-96.

N-12. Kassir, M.K. and Sih, G.C., "Three-Dimensional Crack Problems," *Mechanics of Fracture*, Vol. II, G.C. Sih ed., Noordhoff, Holland, 1975.

N-13. *NASGRO Reference Manual*, Version 4.1, NASA Johnson Space Center and Southwest Research Institute®, 2003.

N-14. Raju, I.S. and Newman, J.C., Jr., "Stress-Intensity Factors for Corner Cracks in Rectangular Bars," in *Fracture Mechanics: 19th Symposium, ASTM STP 969*, T.A. Cruse, ed., American Society for Testing and Materials, Philadelphia, PA, 1988, pp. 43-55.

N-15. Harris, D.O., Bianca, C.J., Eason, E.D., Salter, L.D., and Thomas, J.M., "NASCRAC: A Computer Code for Fracture Mechanics Analysis of Fatigue Crack Growth," *Proc. 28th Structures, Structural Dynamics, and Materials Conference*, Monterey, California, Part 1, 1987, pp. 662-667.

N-16. Favanesi, J.A., Clemmons, T.G., and Lambert, T.J., "Fracture Mechanics Life Analytical Methods Verification Testing," *NASA CR 4602*, 1994.

N-17. Zhao, W., Newman J.C., Jr., Sutton, M.A., Wu X.R., and Shivakumar, K.N., "Analysis of Corner Cracks at Hole by a 3-D Weight Function Method With Stresses From Finite Element Method," *NASA TM 110144*, 1995.

N-18. Smith, F.W., Kobayashi, A.S., and Emery, A.F., "Stress-intensity factors for Penny-Shaped Cracks, Part I – Infinite Solid," *ASME Journal of Applied Mechanics*, Vol. 34, 1967, pp. 947-952.

N-19. Oore, M. and Burns, D.J., "Estimation of Stress-Intensity Factors for Embedded Irregular Crack Subjected to Arbitrary Normal Stress Fields," *Journal of Pressure Vessel Technology*, Vol. 102, 1980, pp. 202-211.

N-20. Orynyak, I.V., Borodii, M.V., and Torop, V.M., "Approximate Construction of a Weight Function for Quarter-Elliptical, Semi-Elliptical, and Elliptical Cracks Subjected to Normal Stresses," *Engineering Fracture Mechanics*, Vol. 40, 1994, pp. 143-151.

N-21. Orynyak, I.V. and Borodii, M.V., "Point Weight Function Method Application for Semi-Elliptical Mode I Cracks," *International Journal of Fracture*, Vol. 70, 1995, pp. 117-124.

N-22. Fujimoto, W.T., "A Weight Function Approach for Tracking the Growth of Surface and Radial Cracks Through Residual Stress Fields or Bi-Variant Stress Fields," *Proc. 2000 USAF Aircraft Structural Integrity Program Conference*, San Antonio, Texas, 2000.

N-23. Petroski, H.J. and Achenbach, J.D., "Computation of the Weight Function From a Stress-Intensity Factor," *Engineering Fracture Mechanics*, Vol. 10, 1978, pp. 257-266.

N-24. Glinka, G. and Reinhardt, W., "Calculation of Stress Intensity Factors for Cracks of Complex Geometry and Subjected to Arbitrary Nonlinear Stress Fields," *Fatigue and Fracture Mechanics*, *ASTM STP 1389*, G.R. Halford and J.P. Gallagher, eds., American Society for Testing and Materials, West Conshohocken, PA, 2000, pp. 348-370.

APPENDIX O—LITERATURE SURVEY ON THE STABILITY AND SIGNIFICANCE OF RESIDUAL STRESSES DURING FATIGUE

O.1 INTRODUCTION.

O.1.1 BACKGROUND.

The fatigue behavior of a mechanical or structural component is a strong function of the load history that it experiences. The amplitude of the applied load cycles is a primary variable influencing the fatigue lifetime, and the mean (or maximum) value of the load in each cycle is a secondary variable that can also have a major influence on fatigue.

However, the stresses resulting from applied service loading are not the only stresses of significance for fatigue. Many components also contain residual stresses that were established prior to placing the component into service and which remain in place during the service life. These residual stresses do not cycle as the applied loads cycle—they are effectively static—and so they do not directly influence the amplitudes of the in-service cyclic loading. They do influence the mean or maximum value of the load in each cycle, and, therefore, they can have a major influence on fatigue. It should also be noted that these residual stresses are generally self-equilibrating. They do not induce a net external force on the component, so any regions of compressive residual stress are counterbalanced by other regions of tensile residual stress.

Residual stresses can arise from many sources. Some residual stresses are an inherent byproduct of the manufacturing process. Welding, machining, forming, hardening, casting, and forging can all cause residual stresses to remain in the finished product (see, for example, the many review articles in the ASM "Handbook of Residual Stress and Deformation of Steel," Totten, et al., 2002). In some cases, additional steps are added to the manufacturing process for the specific purpose of inducing beneficial compressive residual stresses (which reduce the mean stress and increase the fatigue life) at fatigue critical locations. Shot peening (SP) and related surface treatments such as laser peening, low plasticity burnishing, and deep rolling are the most common examples of this approach. Cold expansion of holes and autofrettage of thick cylinders are also widely employed. Finally, other residual stresses can result from pre-service and in-service loading. A proof test (typically to some specified load or pressure above the normal maximum service conditions) or a maximum load in-service can cause local yielding at stress concentrations that causes residual stresses to form and remain.

The conventional wisdom is that the fatigue nucleation life (the number of cycles required to form fatigue microcracks) is a function of the alternating stress amplitude but not the mean stress, whereas the growth rates of fatigue cracks are a function of both the stress amplitude and mean stress. This paradigm implies that residual stresses have relatively little influence on fatigue crack nucleation, but potentially a significant influence on fatigue crack growth (FCG). The influence on FCG may be especially pronounced when the fatigue cracks are relatively small and the driving force for FCG is near the grow/no-grow threshold; in this case, a residual stress may be the critical difference between a fatigue microcrack growing or arresting. It follows, then, that the effect of residual stresses on stress-life (S-N) behavior (commonly characterized as the number of fatigue cycles required to fracture a smooth laboratory specimen at different

constant applied stress amplitudes and mean stresses) is complex. To the extent that the S-N curve is driven by crack nucleation behavior, the effects may be small, but to the extent that the S-N curve is driven by crack growth, including the growth of microcracks, the effects of residual stresses may be large. Manufacturing processes that induce residual stresses may also induce other material changes—for example, changes in surface roughness or microstructural deformation—that have independent effects (beneficial or deleterious) on fatigue crack nucleation and growth, and so the true effects of residual stress may not always be obvious.

However, one of the biggest complications is that the initial residual-stress field inherent in, or induced by, the manufacturing process may not remain stable throughout the service life. The residual stresses can relax and redistribute due to a variety of mechanisms. A single applied load that causes yielding in a region of residual stress (due to the superposition of residual and applied loads of the same sign) will result in changes in the residual stresses upon removal of the applied load. Repeated cyclic loading can also cause gradual changes in the residual stresses over time, even if no single fatigue cycle induces local yielding. Exposure to elevated temperatures can also relax residual stresses. Finally, extension of a fatigue crack through an initial residual-stress field can cause significant changes in the residual-stress field under some conditions.

Residual stresses can create a dilemma for customers and regulators of mechanical and structural components, especially in safety-critical applications. On the one hand, compressive residual stresses are often beneficial and can result in substantial improvements in fatigue life. However, it can be challenging to consistently impose the same initial residual-stress state from part to part during the manufacturing process; more challenging still is to ensure through process control and measurement that the assumed or designed residual-stress state is, in fact, actually present in each as-manufactured component. The potential for changes in the residual-stress state in service can raise further questions, including the continuing challenge of measuring or monitoring the evolving residual-stress state.

As a result, it is the official policy of some customers and regulators that official credit will not be granted for beneficial residual stresses. In other words, the designed component must meet all required life and reliability goals without considering the beneficial effect of the residual stress, effectively assuming that it is not present. For example, the United States Air Force (USAF) "Damage Tolerant Design Handbook" provides the following guidance for the specific case of fastener holes:

> "In practice, the growth of flaws from fastener holes can be retarded by the use of interference fit fasteners, special hole preparation such as cold work, and to some degree, by joint assembly procedures like friction due to joint clamp-up. Because these procedures delay flaw growth, the slow crack growth lives (or intervals) can be significantly longer than those obtained from structure containing conventional low torque clearance fasteners.
>
> Experience has shown that to achieve the beneficial effects of these techniques consistently, exceptionally high quality process control is required during manufacture. However, this is not always obtained. As a result, it is thought

> unwise to consider all interference or hole preparation systems effective in retarding crack growth.
>
> As stated in JSSG-2006 [*DOD Joint Service Specification Guide-Aircraft Structures*] paragraph A3.12.1.g, to maximize safety of flight and to minimize the impact of manufacturing errors, the damage tolerance guidelines should be met without considering the beneficial effects of specific joint design and assembly procedures such as interference fit fasteners, cold expanded holes, and joint clamp-up."

The actual existence of the residual stress is regarded as an additional safety factor, and the manufacturer will generally continue to impose the residual stress—even without official credit—because experience has shown that it makes their parts last longer and their end-use customers safer and happier. In practice, some customers and regulators do give some official credit for beneficial residual stresses—as the USAF "Damage Tolerant Design Handbook" acknowledges in the paragraph following the quotation cited above, "Exceptions to this policy can be considered"—and such credits have become standard in certain applications. Some rule-of-thumb methods have been developed to guide these credits, but such rules of thumb are not always based on rigorous engineering analysis.

Existing production design paradigms and tools often do not address residual stresses explicitly, or do not address them through rigorous analytical methods, and (as noted earlier) neither do some certification regulations. However, there are a number of current motivations to change this situation. First of all, as aging systems (in which beneficial residual-stress treatments were routinely applied) approach the end of their certified design lifetimes (such original design lifetimes not including residual-stress effects), residual-stress effects offer a potential sound engineering rationale for life extension. Second, several new life enhancement methods—including laser shock peening and low plasticity burnishing—may provide deeper and more stable compressive residual stresses, and so the potential benefit for fatigue lifetime assurance may become too prominent and too promising to dismiss. Third, an increased awareness of inherent residual stresses—perhaps beneficial, perhaps detrimental—in some manufactured components is evolving. If these inherent residual stresses are present in the components, but not present in the same measure in the baseline tests used to generate the material design properties, and not considered explicitly in the design scheme, then the resulting designs may sometimes be nonconservative relative to calculated life limits.

O.1.2 PURPOSE AND SCOPE OF THIS DOCUMENT.

The purpose of this document is to provide a broad literature survey of the current understandings of significant residual-stress issues for fatigue lifetime. The survey focuses explicitly on the stability of the residual-stress fields under fatigue conditions, including redistribution and relaxation due to static mechanical load, repeated cyclic loads, thermal exposure, and crack extension. The implications of the initial and evolving residual-stress state for fatigue behavior are addressed, with special attention to FCG. The bias towards FCG rather than S-N or strain-life behavior is consistent with the damage tolerance focus of the research grant funding this survey. This bias also concedes the significant complications (cited earlier)

associated with the complex effects of some life enhancement methods on fatigue crack formation and early growth. Brief attention is given, where appropriate, to the major approaches to FCG life analysis proposed and practiced in the literature. Relatively little attention is paid to the detailed analysis of initial residual-stress states (especially for life enhancement methods that involve substantial changes to the material state) and to the experimental methods used to measure residual stresses. Both of these topics are large and complex and were judged to be beyond the scope of the present investigations. There is a strong focus on surface and near-surface residual stresses (as opposed to bulk residual stresses, such as might be formed in the interior of a thick component due to thermal or mechanical deformation mechanisms during manufacturing). This focus is consistent with the observation that critical fatigue damage and fatigue cracking typically initiates and progresses at or very near the component surface, and these surface and near-surface issues have received the vast majority of the attention in the scientific literature.

The literature survey is based on a comprehensive (but not exhaustive) bibliography assembled over a period of several years and currently containing well over 300 citations. Computer searches of the major technical journals and other significant publication databases were employed widely, in addition to the usual tracing of cited references in each new article as it was catalogued. The bibliography has been limited to English-language journal articles and conference papers that are available to the general public. Foreign language articles, academic theses and dissertations, and technical reports with limited circulation were not included. In most cases, the significant results first reported in these other media (or at least the highlights thereof) were eventually published in the traditional English-language technical literature. The bibliography itself contains the complete text of the abstract (or equivalent) of each article, and is available upon request from the author of this document. A majority of the articles in the bibliography are cited in this survey.

This literature survey is not a definitive critical review. No attempt was made to evaluate the relative merits of the different explanations and models proposed, and no attempt was made to provide clear answers on important issues, beyond reporting the preponderance of the published opinions. These are worthy and needed goals, but the technical scope of the present effort was too broad and the available resources too limited to go into critical depth in any or all topics. That effort is left for future work. A short discussion at the end of the survey document summarizes some of the major trends and repeated observations from the survey. There is also an intent to continue updating the bibliography itself, and perhaps this review document, as new articles are identified or published.

The scope of the survey is generally very broad. Primary attention is given to the residual stresses resulting from four major classes of manufacturing operations: peening and related surface treatments, cold expansion of holes, welding, and machining (and in that order of dramatically descending breadth). Within those four major areas, a wide variety of metallic materials are considered. Special attention is given to materials and applications specifically related to aircraft gas turbine engines. However, materials and applications related to other products such as aircraft structures, welded steel structures, automotive components, and machinery have also been included without hesitation, because the technical insights and quantitative models are often relevant (either directly or indirectly) to gas turbine engines.

Most cited articles focus exclusively on one of the four major residual stress-inducing manufacturing processes (peening, cold expansion, welding, and machining). However, a few review articles address issues that cut across multiple processes. Notable among these are an early review by Rosenthal (1959); a classic treatment by Vöhringer (1983, 1987a) updated more recently in Löhe and Vöhringer (2002); two additional articles by Löhe, et al. (2002) and Lu (2002) in the same ASM Handbook (Totten, et al. 2002), and recent articles by Fitzpatrick and Edwards (1998) and Webster and Ezeilo (2001). Schulze (2005) has very recently published an extensive volume addressing mechanical surface treatments (different peening methods and deep rolling) and associated residual stresses.

Slightly less than half of the articles in the bibliography directly address the stability of residual stresses. The remaining articles provide supporting information on initial residual-stress fields or the impact of the residual stresses on fatigue or FCG behavior.

Note that this report deliberately employs an alternative citation format (alphabetically and chronologically bibliographic) rather than the traditional numerical sequence due to the very large number of citations and the need to keep the document simple to update in the future.

O.2 PEENING AND RELATED SURFACE TREATMENTS.

Shot peening is perhaps the most widely used mechanical treatment to modify the surface state of metallic materials, and it is often used for the specific purpose of improving the fatigue strength and the fatigue life. SP causes inhomogeneous plastic deformation of the near-surface layers that induces numerous changes in the material state, including not only residual stresses but also microhardness, dislocation density, surface roughness, surface defects, and phase composition. Vöhringer (1987b) has reviewed these changes, their characterization, and their relationship to various peening parameters.

For convenience, this survey will simultaneously consider a number of related mechanical surface treatments including glass bead peening (GBP), water peening, and laser shock peening (LSP), along with deep rolling (DR) and low-plasticity burnishing (LPB). Although the specific mechanics and mechanisms of these techniques vary, they share the common characteristic that localized plastic deformation of arbitrary engineering surfaces is used to induce compressive residual stresses near the surface. Some of the salient differences in the results of the various techniques will be highlighted in later discussions.

Applications of peening are common in the gas turbine industry, and these engine applications are well-represented in the residual-stress literature. For example, König (2002) from MTU has provided a survey of life enhancement issues associated with SP of aeroengines. Reed and Viens (1960), Burck, et al. (1970), and Leverant, et al. (1979), all from Pratt & Whitney, published groundbreaking papers on the effects of peening on fatigue, as well as the effects of fatigue on peening residual stresses, for engine alloys, including Ti-6Al-4V and Udimet 700. Happ, et al. (1987) from GE Aviation investigated residual stress and low-cycle fatigue (LCF) effects due to SP of bolthole and dovetail configurations, and Tufft (2002), also from GE, explored different approaches to modeling the effects of SP on fatigue life. Cao, et al. (1994) and Khadhraoui, et al. (1997), including technical staff from SNECMA, published experimental data and

numerical models to characterize the relaxation of SP residual stresses in Astroloy and IN-718 due to fatigue cycling and thermal exposure. Lautridou and DuQuenne (1996), also from SNECMA, investigated the effects of SP on the fatigue behavior of a nickel-based powder metallurgy alloy. Ezeilo, et al. (1993) compared the SP residual-stress distributions in a selection of engine alloys in collaboration with Rolls-Royce UK, while Lindermann, et al. (2002) studied the influence of SP and DR on high-temperature fatigue of Udimet 720 in collaboration with Rolls-Royce Deutschland. Zhuang and Wicks (2003) surveyed mechanical surface treatment technologies, including SP, LSP, and LPB, for gas turbine engine components. Recently published research at the U.S. Air Force Research Laboratory focused on turbine engine applications includes studies of SP effects in fretting fatigue (Lee and Mall, 2004 and 2005), SP residual-stress effects on FCG life (John, et al., 2001 and 2002), LSP residual-stress effects on FCG life (Ruschau, et al., 1999), and thermal exposure effects on SP residual-stress relaxation (Buchanan, et al., 2006). The USAF has also funded several investigations into the measurement of surface residual stresses in new and used turbine discs (Vukelich, et al., 2002; Berkley, et al., 1997 and 1999). Prevéy and colleagues have published extensively on residual-stress stability and fatigue effects in laboratory coupons of IN-718 and Ti-6Al-4V (Prevéy, et al., 1997; Prevéy, 2000; Prevéy, et al., 2000; Prevéy, et al., 2001) as well as actual Ti-6Al-4V fan blades and vanes (Prevéy, et al., 2003a and 2003b) and Ti-6246 compressor blades (Prevéy, et al., 2004).

Peening and related techniques have been applied to a very wide range of metallic materials. In addition to the engine alloys cited above, many other materials have also been considered in studies of residual-stress stability, including many different steels, stainless steels, and aluminum alloys. Over 90 articles have been identified to date that provide data and/or models specifically addressing the stability of residual stresses induced by peening and related mechanical treatments in all materials.

O.2.1 INITIAL RESIDUAL-STRESS FIELDS.

Many investigations have characterized the initial residual-stress fields resulting from peening and related treatments. A comprehensive treatment of these investigations is outside the scope of the current survey. Nearly all of the articles cited later on various stability issues also provide some quantitative data on the initial residual-stress state prior to mechanical or thermal loading.

Representative experimental data on initial residual-stress fields due to SP, LSP, and LPB of IN-718 were published by Zhuang and Wicks (2003), as shown in figure O-1. Several general trends can be noted. The peak compressive residual stress occurs slightly beneath the surface, decreasing slightly immediately at the surface. The compressive stresses then decay deeper beneath the surface, eventually becoming slightly tensile due to self-equilibration. Residual stresses due to SP are shallower than the corresponding profiles due to LSP or LPB, although the magnitudes of the peak compressive stresses are often comparable.

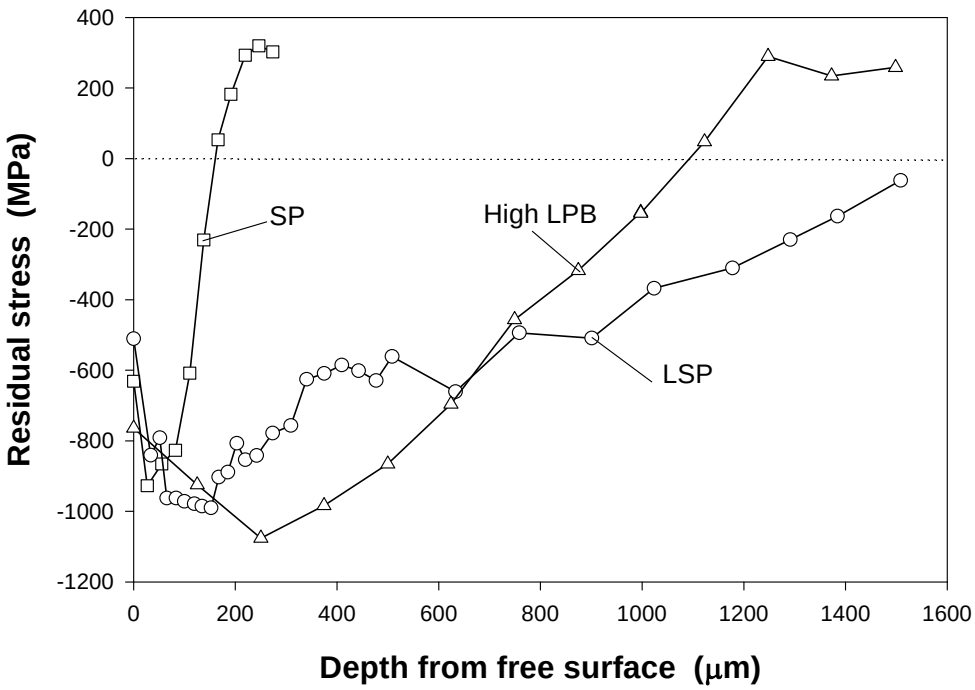

Figure O-1. Representative Initial Residual-Stress Profiles in IN-718 due to SP, LSP, and LPB (Zhuang and Wicks, 2003)

Representative experimental data on initial residual-stress fields due to SP in several different engine alloys were provided by Ezeilo, et al. (1993), as shown in figure O-2. Again, several common trends may be noted. The peak compressive residual stresses near the surface (the residual stresses at the surface itself are not shown in this figure) are often on the order of the yield strength of undeformed material. The tensile residual stresses deeper beneath the surface are generally of much smaller magnitude and decay towards zero slowly with increasing depth. The pair of curves for Udimet 720 are due to different SP conditions, and they serve as a reminder that the initial residual-stress profile is a strong function of various SP parameters, including the type, density, shape, diameter, and size distribution of the shot; the velocity or pressure; the exposure time or coverage; the impact angle, mass flow, and nozzle diameter; and the distance from the nozzle to the workpiece (Vöhringer, 1987b).

Numerical models to predict these initial residual-stress profiles have been developed (Meister, 1996 and Cao, et al., 1994) but are much less common than experimental measurements. Tufft (2002) has proposed a simple functional form that she claims can empirically describe the initial profile of SP residual stresses for many materials, if experimental data are available to which the equation can be fitted. Robertson (1971) has proposed a different functional form for the same purpose.

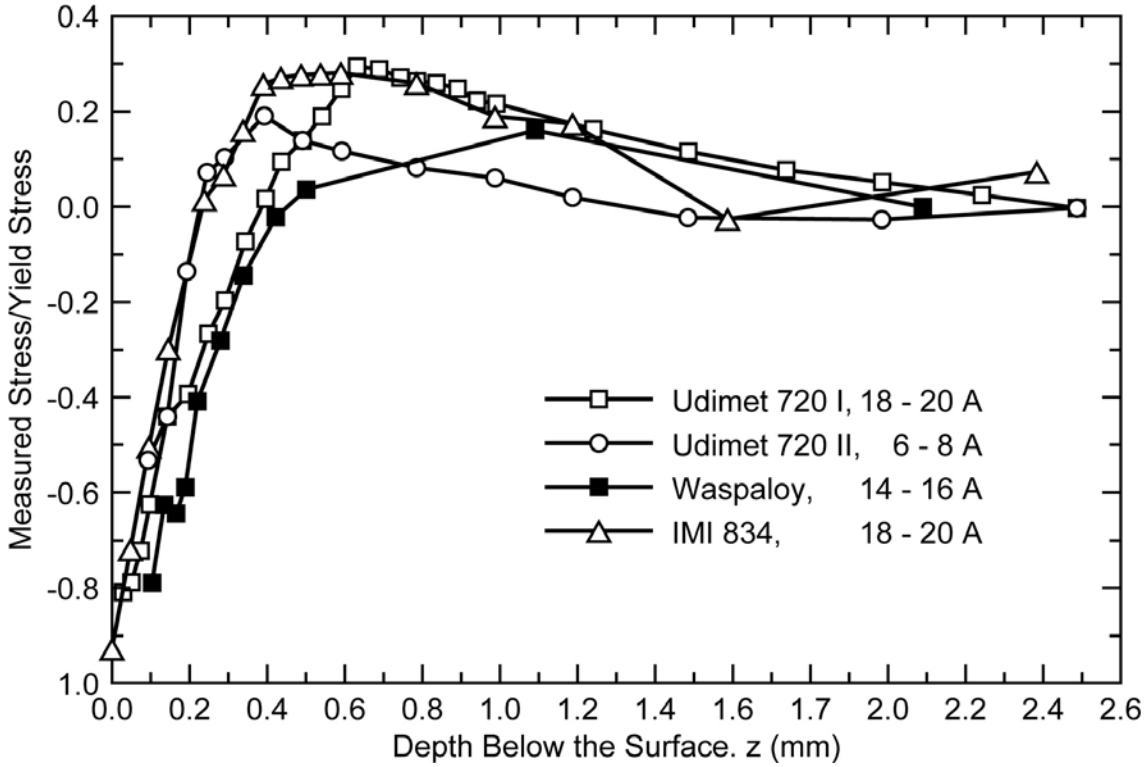

Figure O-2. Representative Initial Residual-Stress Profiles in Various Gas Turbine Alloys Due to SP (Ezeilo, et al., 1993)

O.2.2 FATIGUE LIFE EFFECTS.

O.2.2.1 Stress-Life Behavior.

The most common reason for peening is to improve the fatigue life, and there is extensive evidence of this effect in the literature. For example, early research by Reed and Viens (1960) found a 25% improvement in the endurance limit due to GBP of Ti-6Al-4V. Dorr and Wagner (1999) showed life improvements ranging from 5 times to 100 times in various specialty titanium alloys. Lautridou and DuQuenne (1996) found 2 times to 5 times improvements for a nickel-based powder metallurgy alloy. Happ, et al. (1987) published early data for elevated temperature LCF of peened René 95 bolthole specimens showing 10 times life improvements compared to unpeened specimens at lower stress levels (see figure O-3). Lee and Mall (2004 and 2005) studied the effect of SP on fretting fatigue of Ti-6Al-4V. Everett, et al. (2000) documented the beneficial effects of SP and LSP on the fatigue life behavior of Al 2024 and 4340 steel. Nikitin, et al. (2004) compared the effects of DR and LSP on fatigue for as-received and electropolished specimens of 304SS at two temperatures. Nalla, et al. (2003) compared the effects of DR and LSP on the fatigue life of Ti-6Al-4V at two temperatures. Prevéy, et al. (2003a, 2003b, and 2004) evaluated the effects of several different surface treatments on the fatigue life of Ti-6Al-4V first-stage blades and vanes and Ti-6246 compressor blades. Many of the papers cited later in discussions of thermal and cyclic stability also provide data for the effects of peening and related surface treatments on fatigue life.

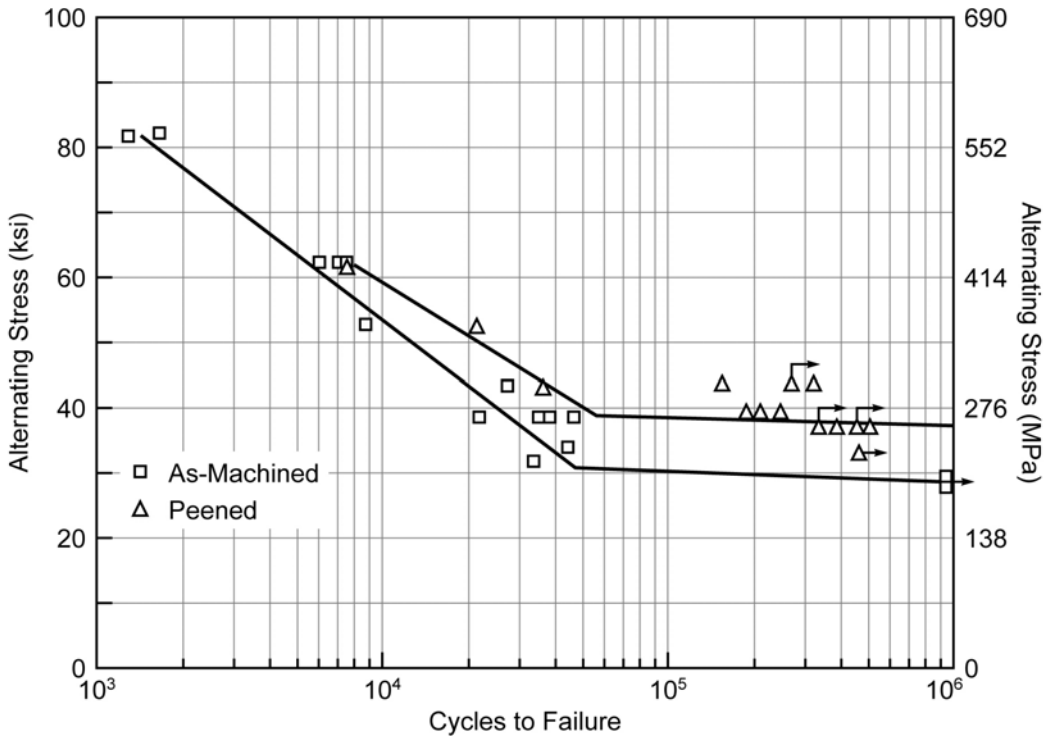

Figure O-3. Effect of SP on Fatigue Behavior of René 95 Disk Bolthole Specimens (Happ, et al., 1987)

Wagner (1999) has demonstrated that the effects of SP on fatigue life are actually much more complex than just residual stresses. He systematically shot peened, stress-relieved (SR), and electropolished (EP) rotating beam fatigue specimens of an equiaxed Ti-6Al-4V alloy. Selected results are summarized in figure O-4. He found that SP alone significantly increased the fatigue strength and fatigue life compared to EP without SP. However, SP followed by SR to remove the residual stresses resulted in a significant decrease in fatigue strength, attributed to increases in surface roughness. A subsequent EP step (now SP+SR+EP) resulted in a net increase in fatigue strength compared to the original EP condition, even though no residual stresses remained, and this benefit was attributed to cold work of the surface layers. However, SP+SR+EP was not as beneficial as SP alone (residual stresses remaining), and SP+EP to remove surface roughness without changing residual stresses gave similar results to SP alone.

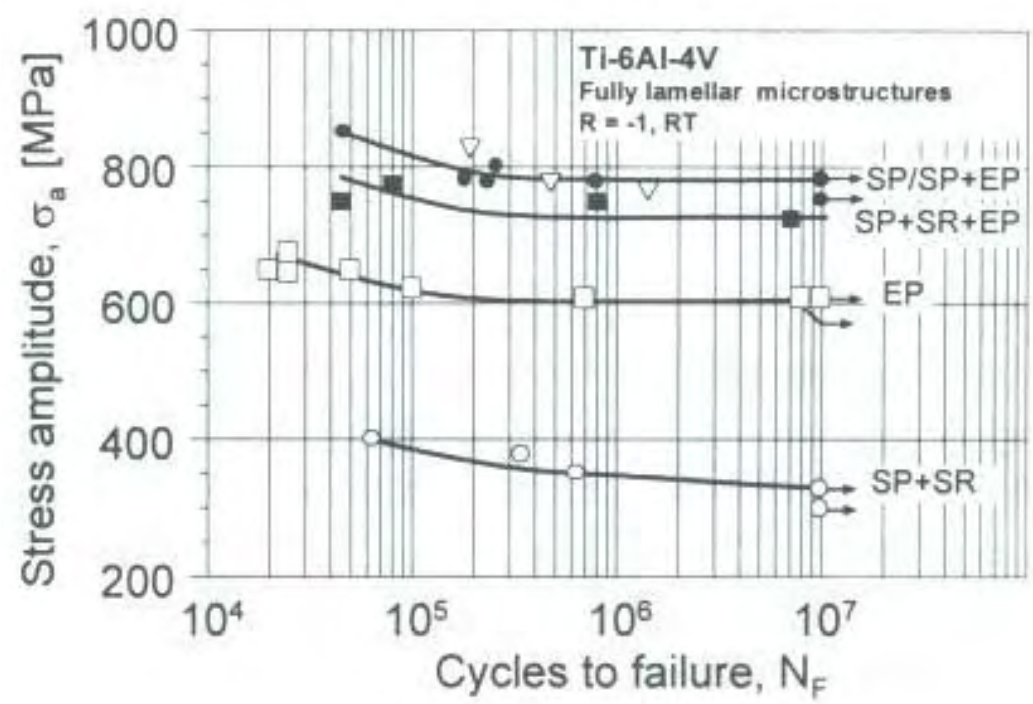

Figure O-4. Effect of Various Surface Conditions on Fatigue Life in Ti-6Al-4V (Wagner, 1999)

Sridhar, et al. (1996) published results showing a decrease in fatigue life for the titanium alloys IMI685 and IMI318 (Ti-6Al-4V) at both ambient and elevated temperatures due to GBP, attributing the differences to residual-stress relaxation and increased surface roughness.

It must be emphasized that most of the studies cited above were academic investigations in which peening and testing conditions were chosen to illustrate various effects. Surface treatments were generally not optimized for maximum fatigue benefit, and testing conditions were generally not optimized for maximum fidelity to service conditions. Therefore, the specific quantitative conclusions should not be regarded as being entirely general, but qualitative observations about various issues and effects are nevertheless instructive.

O.2.2.2 Fatigue Crack Growth Behavior.

SP can also have a beneficial effect on the growth rates of fatigue cracks emanating from the treated surface, although less attention has been given to the FCG problem compared to S-N fatigue approaches. Burck, et al. (1970) apparently published one of the earliest such studies, evaluating glass bead blasting effects in the wrought nickel-based superalloy Udimet 700, and finding dramatic decreases in FCG rates. Elber (1974) studied SP effects on FCG and fracture in D6AC steel, deriving a simple superposition model to rationalize FCG rates with and without SP residual stresses. Hack and Leverant (1982) performed a detailed investigation of the substantial effects of SP compressive residual stresses on the crack-opening and growth rate behaviors of surface fatigue cracks, pointing out that such effects are more pronounced than the effects of SP on fatigue crack nucleation. The effects of SP on small fatigue cracks have been addressed

directly by Misumi and Ohkubo (1987), De Los Rios, et al. (1996), and Natkaniec-Kocanda, et al. (1996). Turnbull, et al. (1998) investigated SP effects on FCG rates in Waspaloy, and Ruschau, et al. (1999) studied LSP effects on FCG in Ti-6Al-4V. Other data for SP effects on FCG have been published by Mutoh, et al. (1987), De Los Rios, et al. (1995), and Honda, et al. (2005) for aluminum alloys; Everett, et al. (2000) for Al 2024 and 4340 steel; Berns and Weber (1986) for a medium carbon steel; and De Los Rios, et al. (2000) for 316 SS. Everett, et al. (2000) also studied LSP effects. Nalla, et al. (2003) published limited data for DR effects on FCG rates. Continuing the theme first introduced by Hack and Leverant (1982), Zhu and Shaw (1995) and Ruschau, et al. (1999) employed closure models to correlate FCG rate data with and without SP residual stresses.

The analysis of FCG behavior in complex residual-stress fields induced by SP and related techniques is not necessarily as simple as invoking superposition or closure arguments to modify traditional FCG analysis methods. The residual-stress fields also distort the shapes of the resulting fatigue cracks so that conventional semielliptical shapes are no longer representative. Prevéy, Telesman, et al. (2000) have published a particularly striking example of a fatigue crack growing in a residual-stress field induced by LPB (see figure O-5). Wilks, et al. (1994) commented on the same phenomenon in their review article.

O.2.3 RESIDUAL-STRESS STABILITY.

O.2.3.1 Thermal Relaxation.

The stability of peening residual stresses during thermal exposure is especially important for gas turbine engine applications. Numerous researchers have investigated thermal stability in both common titanium and nickel alloys. This survey will first focus on residual-stress stability at elevated temperature without simultaneous mechanical loading or cycling, and then consider those synergisms in section) O.2.3.3.

Leverant, et al. (1979) were the first to report on residual-stress stability in Ti-6Al-4V. They found that 600°F (316°C) thermal exposure alone caused only a small (perhaps 20%) relaxation in surface and near-surface residual stresses from SP. Vöhringer, et al. (1984) found no relaxation of SP residual stresses at the surface in Ti-6Al-4V at temperatures up to 572°F (300°C) for annealing times up to 60,000 minutes. At higher temperatures, ranging from 752°F (400°C) up to 1112°F (600°C), they found progressively greater relaxation—from 50% after 10,000 minutes at 752°F (400°C) up to nearly complete relaxation at 932°F (500°C) and above. Gray, et al. (1987) published limited data later reprinted by Wagner (1997 and 1999), showing some relaxation at 662°F (350°C) after only 30 hours and much greater relaxation at 932°F (500°C) and 1112F (600°C). Lee and Mall (2004) found only about 10% relaxation of SP residual stress at the specimen surface after 24 hours at 212°F (100°C), about 30% relaxation at 500°F (260°C), and 95% relaxation at 698°F (370°C).

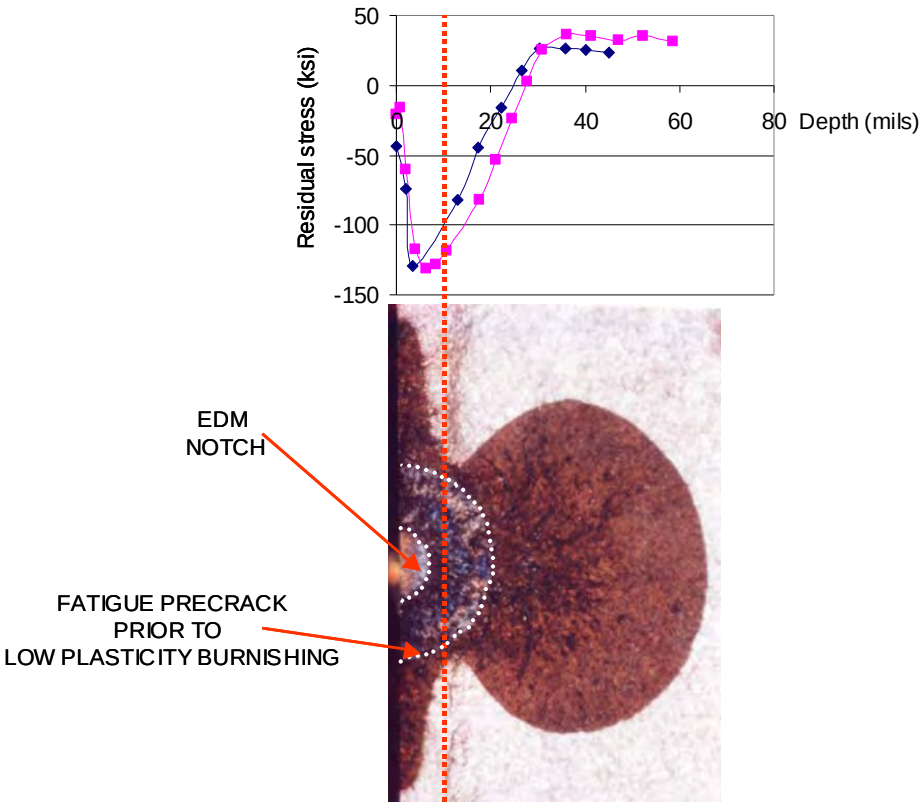

Figure O.5. Effect of LPB on Residual Stresses and Fatigue Crack Shape Development in IN-718 (Prevéy, et al., 2000)

Prevéy, et al. (1997) compared thermal relaxation in Ti-6Al-4V for residual stresses produced by SP, gravity peening (GP), and LSP. SP parameters were deliberately chosen to produce a high level of cold work (75% at the surface), while GP and LSP processes yielded much lower levels of cold work (5% to 10%). Residual stresses from SP relaxed somewhat at 615°F (325°C) and extensively at 890°F (475°C) after 600 minutes. GP residual stresses were stable at 615°F (325°C) but relaxed significantly at 890°F (475°C). LSP residual stresses were relatively stable at both 615°F (325°C) and 795°F (425°C). Data at 615°F (325°C) for all three peening processes are shown in figure O-6.

Nalla, et al. (2003) compared thermal relaxation at 842°F (450°C) in Ti-6Al-4V for residual stresses produced by DR and LSP. Exposure of only 45 minutes caused significant reductions—50% or more—in residual stress for both DR and LSP.

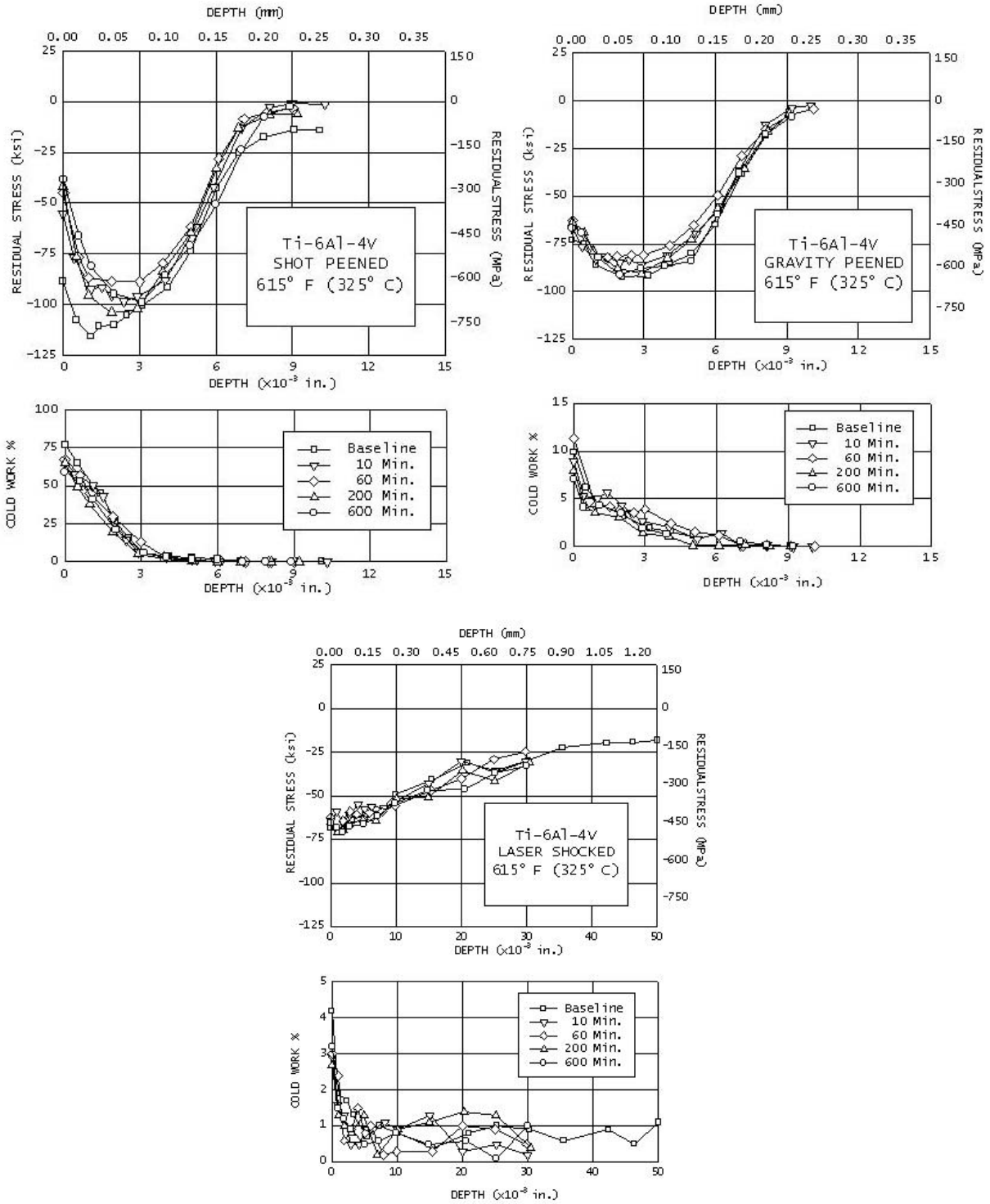

Figure O-6. Thermal Relaxation at 615°F (325°C) of Residual Stress in Ti-6Al-4V Induced by SP (Top Left), GP (Top Right), and LSP (Bottom), Along With the Corresponding Changes in Cold-Work Percentage (Prevéy, et al., 1997)

Prevéy, et al. (2004) compared thermal relaxation of Ti-6246 after 100 hours at 700°F (371°C) for SP and LPB. The SP residual stresses relaxed about 50% at the surface but were stable at all depths below about 0.002 in., and the LPB residual stresses (which were initially 50% lower at the surface than for the corresponding SP treatment) were stable everywhere.

Berger and Gregory (1999) studied thermal relaxation of SP residual stresses in the β-titanium alloy Timetal 21s at 662°F (350°C) and 842°F (450°C). Relaxation of surface residual stresses was significant at both temperatures and increased with increasing aging time through 1000 minutes.

Nickel-based superalloys are designed for higher temperature applications. Khadhraoui, et al. (1997) studied thermal relaxation in IN-718 after 10 and 100 hours at 1112°F (600°C) and 1202°F (650°C) for two different SP conditions. Residual stresses relaxed substantially (50% to 75%) at the surface but were more stable with increasing distance beneath the surface. Prevéy, et al. (1997) (see also Prevéy, 2000) compared the thermal stability of residual stresses from SP, GP, and LSP in IN-718 at 980°F (525°C) and 1240°F (670°C) at times up to 2000 minutes. Residual stresses from SP relaxed roughly 50% at the surface but were again more stable with increasing distance from the surface. GP residual stresses were slightly more stable—decreasing only 30% or less—and LSP residual stresses were relatively unchanged (see figure O-7). As in their previously cited study of Ti-6Al-4V, Prevéy, et al. (1997) noted that peening with higher percentages of cold work was less stable. Prevéy, et al. (2000) compared the thermal stability of peening residual stresses in IN-718 at 1112°F (600°C) after 1 hour and 10 hours for SP and three LPB conditions. Residual stresses relaxed substantially at and near the surface for SP but were somewhat stable for LPB, again attributed to differences in cold-work percentage. Cammett, et al. (2005) directly addressed the effects of different SP coverages on residual stress, cold work, and thermal stability in IN-718 after 10 hours at 977°F (525°C). Although heavier coverage induced somewhat higher initial residual stresses, the resulting relaxed residual-stress fields after thermal exposure were relatively insensitive to coverage, although heavier coverage tended to be associated with slightly lower relaxed residual stresses. Relaxed stresses were generally 30% to 50% lower than initial residual stresses at the surface, and more stable with increasing distance from the surface.

Isolated thermal stability results are available for other nickel-based superalloys. Cao, et al. (1994) reported residual-stress measurements for Astroloy. At 1022°F (550°C), slight relaxation occurred in the near-surface layer only during the first hour, remaining stable thereafter through 100 hours. More relaxation (50% to 70% at the surface) occurred during the first hour at 1202°F (650°C) with only slight changes at longer times. Tufft (2002) showed thermal exposure results for René 88DT after 5 hours or 100 hours at 1000°F (538°C), 1150°F (621°C), and 1300°F (704°C). Surface and near-surface residual stresses relaxed from 40% to 60%. Masmoudi and Castex (1988) published limited measurements of surface residual stresses in IN-100 at exposure temperatures ranging from 932°F (500°C) to 1292°F (750°C). Relaxation varied from 50% at the lower temperatures to almost 100% at the higher temperatures, and nearly all changes occurred within the first 10 hours. Buchanan, et al. (2006) presented additional studies on IN-100 at temperatures of 1202°F (650°C) and 1300°F (704°C) with exposure times ranging up to 300 hours. Surface residual stresses relaxed by roughly 50% but stabilized quickly (after about 1 hour), while interior residual stresses continued to relax slowly with increased exposure time, as

shown in figure O-8. Gabb, et al. (2004) examined residual stresses in production René 95 turbine disks removed from T700 helicopters after serving full lives, and then subjected the disks to additional thermal exposure at 593°C, 650°C, and 704°C (1100°F, 1200°F, and 1300°F). Residual-stress relaxation increased with greater exposure temperature, time, initial compressive stress, and initial cold work.

Thermal stability of SP residual stresses in selected steels was also investigated. Hoffmann, et al. (1987) considered three different heat treatments of a .45% plain carbon steel at exposure temperatures ranging from 392°F (200°C) to 1022°F (550°C) and exposure times up to 1000 minutes. Relaxation of surface stresses was a strong function of temperature, and only limited information was shown for subsurface stresses. Schulze, et al. (1993) published similar results for 4140 steel at temperatures ranging from 482°F (250°C) through 842°F (450°C) and exposure times up to 6000 minutes. Surface stresses relaxed from 15% to 85% with increasing temperature, but again only limited information was shown for subsurface stresses. Menig, et al. (2002c) later added a comparison with thermal relaxation of LSP surface stresses at 572°F (300°C) and 842°F (450°C). Prevéy and Cammett (2002) studied thermal relaxation for different SP coverages in 4340 steel at 475°F (246°C) after 24 hours. Surface and near-surface relaxation was minor (10% to 30%) and residual stresses were generally stable below a depth of about 0.004 in. Tufft (2002) found only minor changes in SP residual stresses for Marage 250 steel after 16 hours at 250°F (121°C), 400°F (204°C), and 600°F (316°C). Krull, et al. (1999) studied thermal stability of SP and water peening residual stresses in austenitic and martensitic phases of 316SS at 392°F (200°C), 572°F (300°C), and 752°F (400°C). Childs (1988) observed substantial decreases in SP residual stresses in 403 stainless steel in times as short as one hour at temperatures as low as 300°F (150°C), with comparable or larger decreases at longer times and temperatures up to 1100°F (595°C).

Roth and Wortman (2002) found that exposure temperatures of 250°F (121°C) associated with adhesive bonding heat cycles of 1-hour duration induced a relaxation of SP residual stresses in the aluminum alloy 7050-T7451 that was maximum at the surface and about 30%. Exposures up to 12 hours at 185°F (85°C) caused no noticeable relaxation. Potter and Millard (1976) found no thermal relaxation in 7075-T6 after about 20 hours at 200°F (93°C), but significant relaxation for similar time scales at 225°F (107°C) and 250°F (121°C).

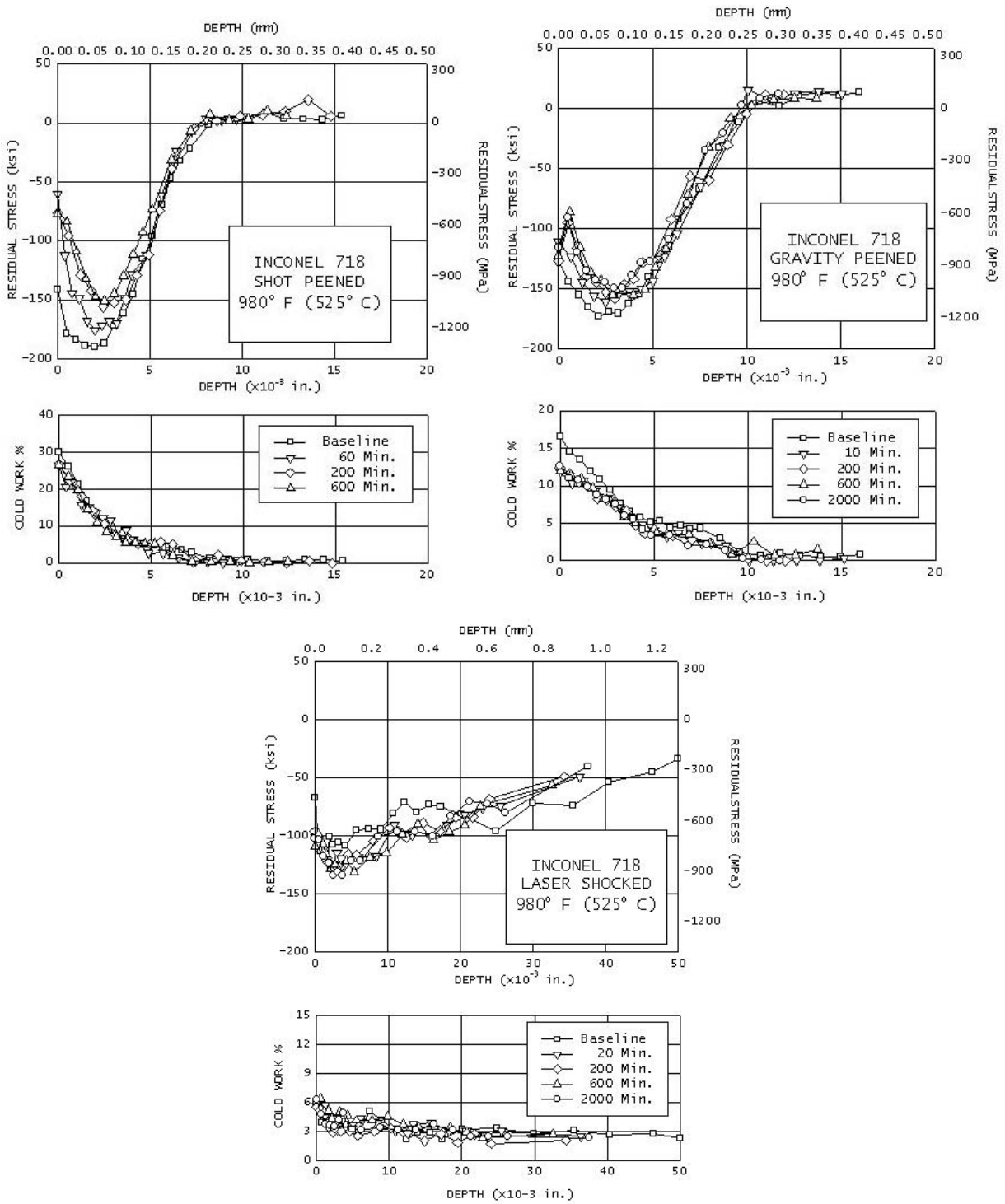

Figure O-7. Thermal Relaxation at 980°F (525°C) of Residual Stress in IN-718 Induced by SP (Top left), GP (Top right), and LSP (Bottom), Along With the Corresponding Changes in Cold-Work Percentage (Prevéy, et al., 1997)

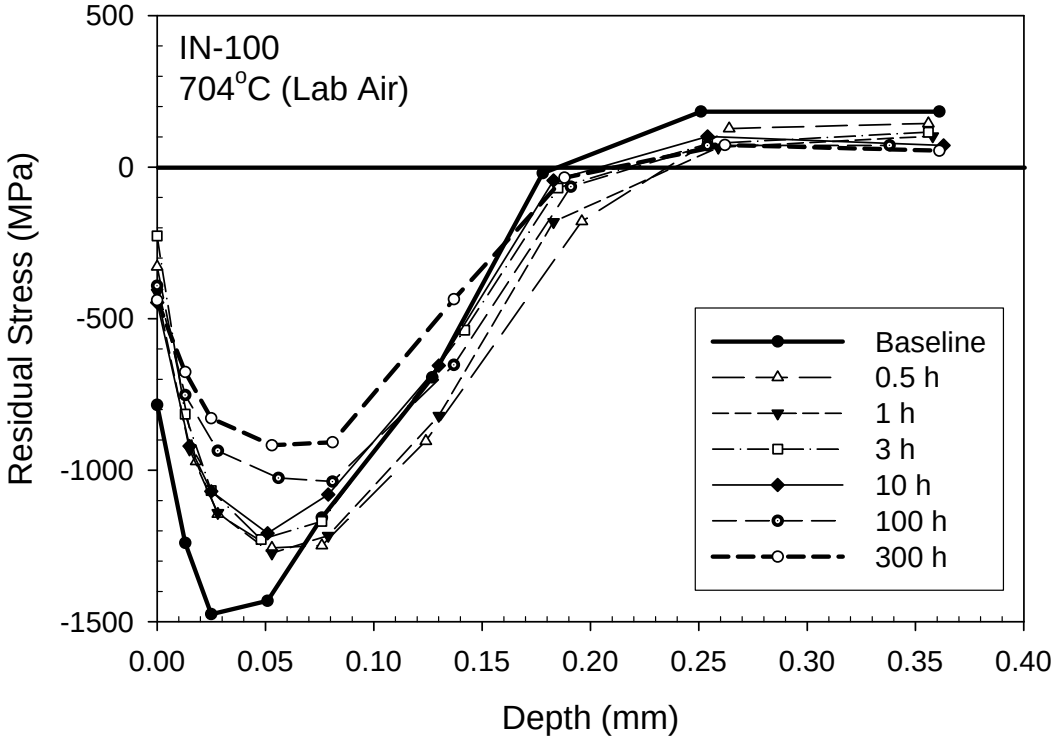

Figure O-8. Residual-Stress Distribution in IN-100 Versus Exposure Time at 1300°F (704°C) (Buchanan, et al., 2006)

Two primary approaches were proposed for modeling the thermal stability of peening residual stresses. Vöhringer, et al. (1984) and his colleagues (for example, Hoffmann, et al., 1987; Schulze, et al., 1993; Eigenmann, et al., 1994; Berger and Gregory, 1999; Menig, et al., 2002c) at the Institut für Werkstoffkunde, University of Karlsruhe, Germany, have widely used a so-called Zener-Wert-Avrami function (Vöhringer, 1983) of the general form:

$$\frac{\sigma^{RS}(T,t)}{\sigma_0^{RS}} = \exp\left[-(At)^m\right] \tag{O-1}$$

where A is a function of material and temperature according to

$$A = C\exp(-Q/kT) \tag{O-2}$$

to fit experimental data for surface residual stresses. This is still something of an empirical rather than predictive approach, and the parameter m has been found to change with aging temperature. This approach does not appear to have been extended to subsurface changes in residual stresses.

Khadhraoui, et al. (1997) and Cao, et al. (1994) published some details of a more sophisticated numerical approach to modeling thermal stability, while also treating initial residual-stress formation and cyclic stability. Their method, which has been implemented in the "Shotpeen"

software, includes an Avrami-type formulation to describe the kinetics of recovery. Published results include predictions of the entire residual-stress profile in agreement with experimental measurements. Exercising the model requires information about the limiting state of recovery and the integrated width of x-ray diffraction peaks, so additional predictive capability appears to be required for the model to be practical in an engineering context.

It must be emphasized strongly, as was noted earlier in passing, that the thermal stability of peening residual stresses is dependent on several critical peening parameters, including coverage, intensity, and the resulting cold work. Therefore, the individual experimental results cited above cannot be regarded as being entirely general. In fact, in several cases, the researchers noted that peening parameters were selected to highlight relaxation phenomena, and some of these conditions may not be representative of common peening practice in production environments.

O.2.3.2 Static Relaxation.

Relaxation and redistribution of residual stress occurs when the summation of the residual stress and applied stress due to subsequent mechanical loading exceeds the yield condition of the material. Simple mechanics models for this phenomenon have been outlined in classic review papers by Vöhringer (1983 and 1987a). Several specific studies of the effects of quasi-static mechanical loading on peening residual stresses in 4140 steel have been published by Vöhringer and his colleagues at Karlsruhe, including Hanagarth, et al. (1990), Eigenmann, et al. (1994), Eigenmann (1995), and Holzapfel, et al. (1996a, 1996b, 1998). Kirk (1987) reported similar studies in a variety of materials and Cammett, et al. (1993) did the same for 301 stainless steel. More recently, Prevéy, et al. (2001) briefly investigated overload relaxation of SP and LPB residual stresses in Ti-6Al-4V. Smith, et al. (2001) compared experimental measurements and finite element analyses of the changes in peening residual stresses following simple tensile loading and a single fatigue cycle for an En15R steel. Static effects are also included in numerous studies of cyclic relaxation cited below, and will be discussed further in that context.

O.2.3.3 Cyclic Relaxation.

The more significant issue for gas turbine engines and many other mechanical components is the potential effect of repeated fatigue cycling on residual-stress relaxation and redistribution, even when the individual mechanical load cycles do not cause macroscopic plastic deformation. This topic has received extensive attention in the literature. To date, over 65 articles have been identified that address the cyclic stability of peening residual stresses, including numerous investigations focused on titanium alloys, nickel-based superalloys, aluminum alloys, and a wide range of steels. Synergisms with other relaxation mechanisms, such as thermal activation, are also considered.

The landmark Leverant, et al. (1979) paper was again the first investigation of this phenomenon in titanium alloys. They experimentally observed additional relaxation of residual stresses in Ti-6Al-4V with fatigue cycling at 600°F (316°C) compared to thermal exposure alone (which caused only mild relaxation), and the extent of relaxation increased with increasing cyclic strain amplitude (±0.3% versus ±0.6%, both with positive mean strains). Vöhringer, et al. (1984) found only limited residual-stress relaxation during continued fatigue after the first cycle (on

which more substantial relaxation occurred, due to static effects) for cyclic bending of Ti-6Al-4V sheet. Recent studies of Ti-6Al-4V (Altenberger, et al., 2002a and 2002b; Noster, et al., 2002) found extensive relaxation of surface residual stresses from DR at the fatigue half-life for high-temperature fatigue (460 MPa stress amplitude, R = -1, 842°F [450°C]). More detailed Ti-6Al-4V data published by Nalla, et al. (2003) showed relaxed residual-stress profiles following fatigue cycling at several different temperatures for both DR and LSP. As shown in figure O-9, room temperature cyclic relaxation was minimal for LSP and moderate for DR, but extensive for both processes at 842°F (450°C) and for DR at 482°F (250°C). Since all cycling was at R = -1, these data likely include both static and cyclic effects, because the superposition of compressive residual stresses and compressive applied stresses will induce further yielding, especially at elevated temperatures. Prevéy, et al. (2003b) found mild (perhaps 10% to 30%) relaxation of LPB residual stresses following room temperature fatigue cycling of Ti-6Al-4V single-edge vane feature specimens at two fully reversed stress amplitudes. Cheong, et al. (2004) performed LCF tests at R = 0.05 on disk bore feature specimens of Ti-6Al-4V, finding about a 20% reduction in surface residual stress from SP and little or no change in LPB residual stresses, which were initially about 3 times smaller than SP residual stresses. Lee and Mall (2004 and 2005) observed significant relaxation of SP residual stresses under fretting fatigue at elevated temperature.

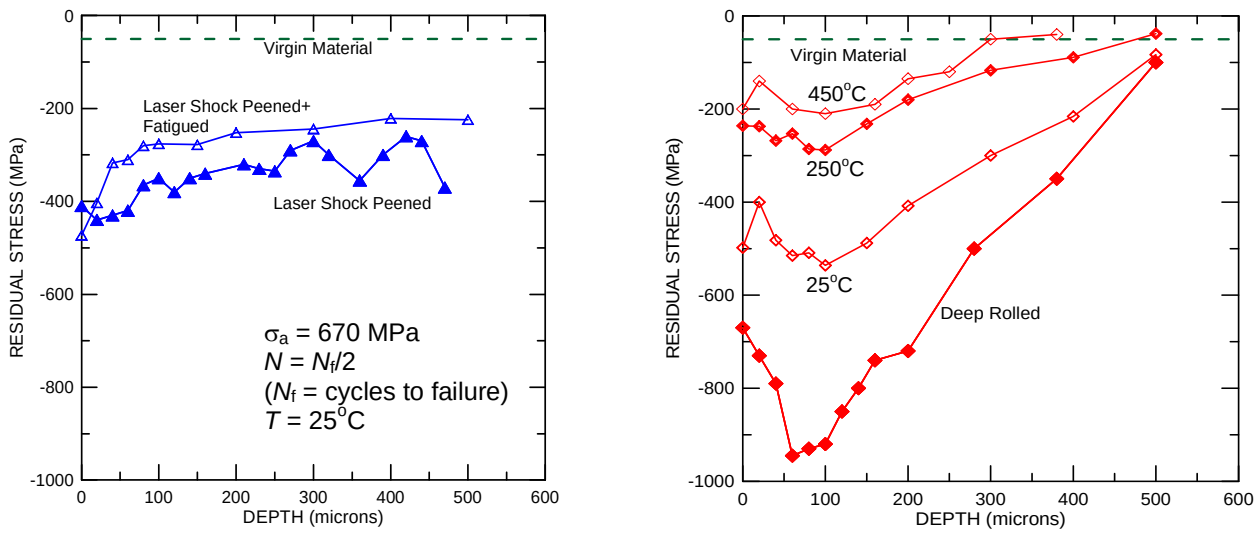

Figure O-9. Residual-Stress Profiles Before and After Fatigue Cycling in Ti-6Al-4V for LSP (Left) and DR (Right) at Various Temperatures (Nalla, et al., 2003)

Relatively few studies of cyclic stability are available for nickel-based superalloys. Cao, et al. (1994) studied SP residual stresses in Astroloy and found that elevated temperature fatigue cycling at R = 0 caused only small amounts of additional relaxation compared to thermal exposure alone for 1202°F (650°C). Tufft (2002) found progressive relaxation with elevated temperature fatigue cycling in René 88DT, although the effects of cycling did not appear to be much more severe than the effects of temperature alone. Zhuang and Halford (2001) have published models of SP residual-stress stability in IN-718 without validating experimental measurements. Boggs and Byrne (1973) performed some early work on cyclic stability of SP stresses in two nickel-cobalt alloys, noting moderate relaxation in one alloy and little relaxation in the other, but providing few details.

Berkley, et al. (1997 and 1999) measured surface residual stresses on 305 Waspaloy superalloy disks (both compressor and turbine) from the F100 and T56 engines, varying in life from zero to greater than 8000 engine cycles. Data scatter was considerable, but most disks with 4000-8000 cycles generally exhibited 30% to 60% relaxation of surface residual stresses. Further discussion on the scope and significance of this work is available in Vukelich, et al. (2002). Belassel, et al. (2000 and 2002) performed a limited number of laboratory coupon tests in a companion study.

Limited information is available on cyclic relaxation of peening residual stresses in aluminum alloys, but the available data suggest minimal to moderate relaxation. Seppi (1975) published one of the very earliest investigations in a short paper where he noted a 20% reduction in residual stresses following tension fatigue cycling of 7075-T6. Potter and Millard (1976) found no significant cyclic relaxation of SP stresses at either R = -1 or R = 0.5 in 7075-T6, and Hammond and Meguid (1990) (see also Meguid and Hammond, 1989) observed no significant relaxation following rotating bending in 7075-T6. Rasouli Yazdi and Lu (1999) reported moderate relaxation of SP residual stresses in 7075 at different fatigue stress amplitudes, but most changes occurred on the first cycle. Bonnafé, et al. (1987) found little SP relaxation in 7075-T7351 at two different stress amplitudes (R = 0.1), but more substantial relaxation in 2024-T351. Fontanari, et al. (2001) reported only mild (5% to 20%) relaxation of SP surface stresses and less relaxation of subsurface stresses following R = 0.1 bending fatigue in 6082-T5. Zinn and Scholtes (1999) studied SP residual-stress stability in several aluminum alloys (including 2017, 5083, 5754, 6082, and 7020) with reversed bending and found that surface stresses typically relaxed 30% to 40% by the end of the fatigue life, but that stress relaxation was the most pronounced during the first cycle (again, likely a static effect). Bathias, et al. (1988) observed moderate (10% to 40%) relaxation of peening residual stress in both 2024 and 7075 during the first 20 cycles for both high-cycle fatigue and low-cycle fatigue, and mostly stable behavior thereafter, until late in life when additional relaxation occurred due to microcrack formation. Relaxation was slightly greater at the higher applied stresses.

Extensive information is available on the stability of peening residual stresses in steels. The relevant literature is summarized in table O-1, which indicates the authorship, date, specific grade of steel(s) considered, and any special issues in the investigation. Unless otherwise specified, researchers performed axial fatigue tests on smooth shot-peened specimens. A detailed analysis and discussion of these collective data is beyond the scope of the current effort, but some selected observations are in order. Notable work includes the early research of Taira and Murakami (1960), Esquivel and Evans (1968), and Kodama (1972), and the extensive investigations on 4140 by the group at the University of Karlsruhe (Eigenmann, Schulze, Holzapfel, Wick, Menig, Vöhringer, and their colleagues).

Table O-1. Summary of Published Research on Cyclic Relaxation of Peening Residual Stress in Steels

Authors	Date	Steel Grade	Special Notes
Taira and Murakami	1960	S40C medium C	Reversed bending
Esquivel and Evans	1968	4130	
Kodama	1972	JIS SS41	Reversed bending
Neff	1981	cast 0.28C	Four-point bending, $R = 0$
McClinton and Cohen	1982	1040	
Bergström and Ericsson	1984	4140	Smooth and notched, $R = 0$ and -1
Bergström and Ericsson	1986	4140	Smooth and notched, $R = 0$ and -1
Berns and Weber	1986	50CrV4	Bending
Bergström and Ericsson	1987	4140	Smooth and notched, $R = 0$ and -1
Bignonnet, et al.	1987	E460 and E550	Welded T-joints
Bignonnet	1987	35 NCD 16	Four different loading types
Misumi, et al.	1987	S45C	Reversed bending with small hole
Qiu and Wang	1987	GC-4 superhigh strength	
Cao and Castex	1988	4135	Plane bending
Meguid and Hammond	1989	080M40 (medium C)	
Hammond and Meguid	1990	080M40 (medium C)	
Cammett, et al.	1993	301 SS	
Zeller	1993	Ck 45, X5 CrNiMo 18 10	Rotating bending
Eigenmann, et al.	1994	4140	
Farrahi, et al.	1995	60SC7 spring steel	Torsion, $R = -1$
Iida and Taniguchi	1996	S45C	Reversed bending
Schulze, et al.	1996	4140	Stress control vs. strain control
Holzapfel, et al.	1996b	4140	Bending, elevated temperature
Holzapfel, et al.	1998	4140	Bending, elevated temperature
Iida and Hirose	1999	0.45% C carburized	Reversed bending
Wick, et al.	1999a	4140	Warm peening, cyclic bending
Wick, et al.	1999b	4140	Warm peening, cyclic bending
Wick, et al.	2000	4140	Warm peening, cyclic bending
Batista, et al.	2000	Carbo-nitrided 4130	Contact fatigue (gears)
Smith, et al.	2001	En15R	Tension-compression cycling
Menig, et al.	2002a	4140	Warm peening, torsion
Menig, et al.	2002b	4140	Warm peening, different heat treats
Torres, et al.	2002	4340	Rotating bending, different hardnesses
Torres and Voorwald	2002	4340	Rotating bending, different SP intensities
Teodosio, et al.	2003	API 5L X70, 31803 SS	Complex changes in weldments
Capello, et al.	2004	C45, 39NiCrMo3	$R = -1$
Nikitin, et al.	2004	304SS	LSP, DR at elevated T, $R = -1$

A general theme of many papers is that residual-stress relaxation is more pronounced for larger cyclic stress or strain amplitudes (for example, Bergström and Ericsson, 1986; Eigenmann, et al., 1994; and Wick, et al., 2000). Under some conditions, little or no relaxation of peening residual stresses occurs, especially for small fatigue stress amplitudes (see Esquivel and Evans, 1968; Iida and Hirose, 1999). Complete or nearly complete relaxation of residual stresses is rare and occurs only for severe cycling, sometimes with an additional influence from elevated temperature (for example, Zeller, 1993; Holzapfel, et al., 1998). McClinton and Cohen (1982) reported unique results for $R = 0$ (zero-tension) fatigue cycling with the maximum stress on the order of the yield strength, resulting in the originally compressive surface residual stress changing to tensile (this did not occur for their fatigue cycling at lower stress amplitudes). Teodosio, et al. (2003) observed complex fluctuations in residual stresses during fatigue cycling of a peened weldment.

Several studies that employed reversed bending found significant relaxation of the compressive surface residual stress on the first fatigue cycle, followed by a much more gradual relaxation with continuing cycling (for example, Taira and Murakami, 1960; Kodama, 1972; Qui and Wang, 1987; and Wick, et al., 2000). The large change on the first cycle is apparently due to the static effect, when the superposition of residual stress and applied stress of the same sign exceed the yield condition. Subsequent changes are attributable to true cyclic effects. The remaining residual stress as a fraction of the original residual stress often decreased linearly with the logarithm of the cycles during this second stage of relaxation.

The rate and extent of cyclic residual-stress relaxation was observed to depend on many parameters, including the shot-peening intensity and coverage (Torres and Voorwald, 2002), peening temperature (Wick, et al., 2000; Menig, et al., 2002a), the original hardness of the material (Torres, et al., 2002), and the loading type (Bignonnet, 1987).

Representative results of Wick, et al. (2000) for room temperature peening of 4140 are shown in figure O-10. Here, the measured surface residual stress is shown after 1 cycle and after 10^4 cycles of fatigue loading at different stress amplitudes, compared to an initial as-peened value of about 600 N/mm^2 (compressive). Note the systematic decrease in residual stress with stress amplitude on the first cycle above a critical stress amplitude, and the additional systematic decrease with further cycling above a second (higher) critical stress amplitude. Relaxation is negligible at the lowest fatigue stress amplitude and extensive at the highest fatigue stress amplitude.

Several researchers have developed models to characterize or predict cyclic relaxation of peening residual stresses in various materials. The most common model is an empirical form based on the observation (cited earlier) that residual stress often decreases linearly with the logarithm of the fatigue cycles after initial static relaxation (Kodama, 1972; Neff, 1981; Bergström and Ericsson, 1986; Eigenmann, et al., 1994; and Holzapfel, et al., 1996b and 1998). The two constants in this power-law equation are typically determined by fitting the available experimental data, and are themselves functions of other variables such as the stress amplitude.

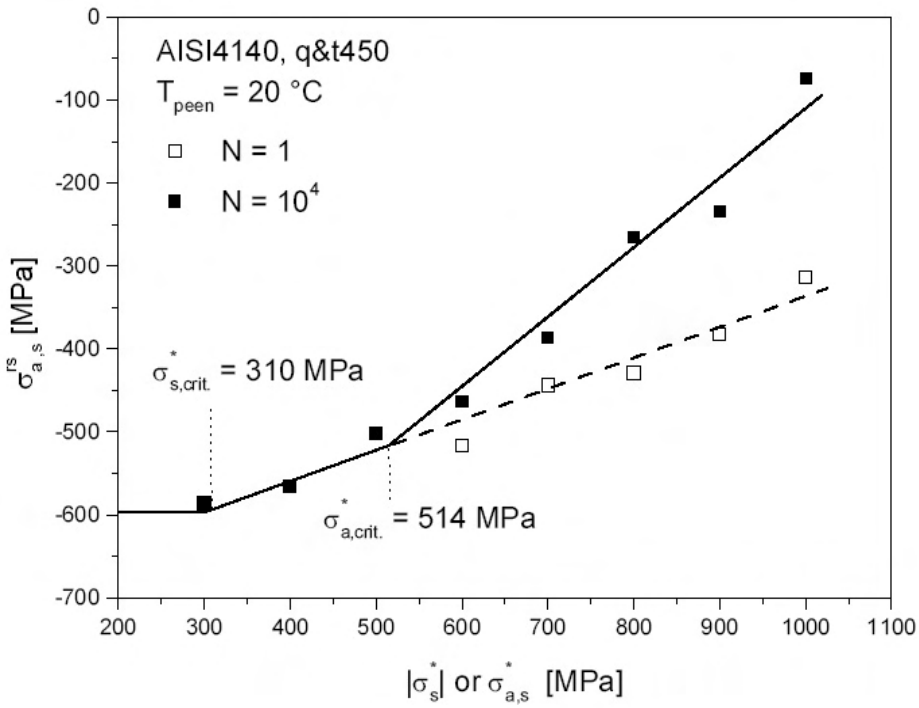

Figure O-10. Surface Residual Stress as a Function of Fatigue Stress Amplitude After 1 Cycle and 10^4 Cycles (Wick, et al., 2000)

The other common approach is a sophisticated numerical model, generally based on finite elements. Lu, Flavenot, and their colleagues (Lu and Flavenot, 1987 and 1988; Lu, et al., 1988; Rasouli Yazdi and Lu, 1999) apparently developed the first such model, a simplified inelastic analysis based on finite elements and employing a group of internal parameters that characterize local inelastic mechanisms. They applied the model to predict cyclic relaxation of peening and machining stresses in various steels and an aluminum alloy. Cao and colleagues developed another early numerical model for residual-stress relaxation with particular attention to material cyclic softening and applied it to steels (Cao and Castex, 1988) and nickel-based superalloys (Cao, et al., 1994), also incorporating thermal relaxation effects (see also Khadhraoui, et al., 1997). Batista, et al. (2000), Zhuang and Halford (2001), and more recently Meguid, et al. (2005) have each published numerical models implemented in finite element contexts. Detailed discussion of these numerical models is beyond the scope of the present survey. All have shown some apparent success in predicting experimentally observed relaxation, but all require the determination of multiple material parameters, complicating their practical use in a production engineering environment.

O.3 COLD EXPANSION OF HOLES.

Holes in structural members create local stress concentrations that can become preferred sites for fatigue crack initiation and growth. To mitigate this tendency, methods for cold expansion (CX) of the hole have been developed as a means of inducing compressive residual stresses around the edge of the hole.

While a number of CX processes have been developed, the split-sleeve process (Phillips, 1974) has been the most widely used. This process involves placing a longitudinally split sleeve within the hole and then drawing an oversized tapered mandrel through the assembly. The hole is expanded enough to cause permanent plastic deformation. Upon removal of the mandrel, the surrounding elastic material attempts to return to its undeformed state, producing a self-equilibrating residual-stress field. This residual stress is compressive (and therefore beneficial) in an annular region adjacent to the hole, and slightly tensile farther away from the hole. The growth of fatigue cracks may be significantly delayed, if not arrested altogether, by these compressive residual stresses. This split-sleeve method has been successfully commercialized by Fatigue Technology, Inc. (FTI), including derivatives of the split-sleeve approach, and many CX researchers cite FTI methodologies explicitly in their published studies.

The CX process was widely applied to aircraft structures, and so it should not be surprising that the great majority of the scientific literature on CX residual stresses addresses high-strength aluminum alloys. However, Rufin (1993) from FTI published an overview of CX technology for aircraft engine applications. Sha, et al. (1980) published selected results from an early USAF-funded study at Pratt & Whitney of the fatigue behavior of cold-expanded holes in Ti-6246, and Ezeilo, et al. (1994) reported work (with Rolls-Royce connections) on IN-718. Rich and Impellizzeri (1977) included a mill-annealed Ti-6Al-4V in their aircraft-motivated study. A limited number of papers have addressed CX behavior in steels (Almer, et al., 1998 and 2000; Prawoto and Winholz, 2001; Su, et al., 1986; and Toparli, et al., 1997). The literature also includes attention to nonaerospace applications such as rails (Cannon, et al., 1985). The autofrettage method employed to induce compressive residual stresses in the bores of cannons and thick-section gun barrels (Clark, 1984; Underwood, et al., 2001; Stacey and Webster, 1988a and 1988b) can also be regarded as an alternative form of CX.

O.3.1 INITIAL RESIDUAL-STRESS FIELDS.

The CX process is much simpler from a mechanics perspective than peening, welding, or machining, and so it is amenable to simpler analytical approaches. Hsu and Forman (1975) and Rich and Impellizzeri (1977) were among the first to propose simple radial expansion models for the CX process, and Chang, 1977; Wang, 1988; Clark, 1991; Guo, 1993; and Ball, 1995 developed models of increasing complexity and accuracy. Ball (1995) provides a thorough review of these various models.

Numerical approaches such as the finite element (FE) method were also employed to characterize the initial residual stresses resulting from CX. Sha, et al. (1980) reported on an early MARC analysis, and Armen, et al. (1984) published one of the first detailed FE investigations. Heller, et al. (1991) included the effects of a pre-existing crack in their FE study. These earlier efforts and some later ones (Ball and Lowry, 1998; Moreira, et al., 2004) employed two-dimensional (2D) plane stress or plane-strain models that neglected through-thickness variations in the resulting residual-stress fields.

Poussard, et al. (1995) also performed plane stress and plane-strain FE analyses, but further developed axisymmetric models in a first attempt to explore variations through the thickness. Pavier, et al. (1997) went on to simulate the actual process of pulling the mandrel through the

hole in his axisymmetric FE models and added a fully three-dimensional (3D) model of the same process shortly thereafter (Pavier, et al., 1998). His axisymmetric and fully 3D models gave very similar results. Figure O-11 (Pavier, et al., 1998) shows this agreement and also the substantial differences in residual stresses between the entrance face, mid-thickness, and the exit face. Papanikos and Meguid (1998) and Chakherlou and Vogwell (2003) published 3D models with lower resolution, and Kang, et al. (2002) added finish reaming to his 3D FE simulation. Zhang, Edwards, and Fitzpatrick (2002) wrote a brief yet thorough comparison of various 2D and 3D FE models, including selected comparisons with x-ray measurements.

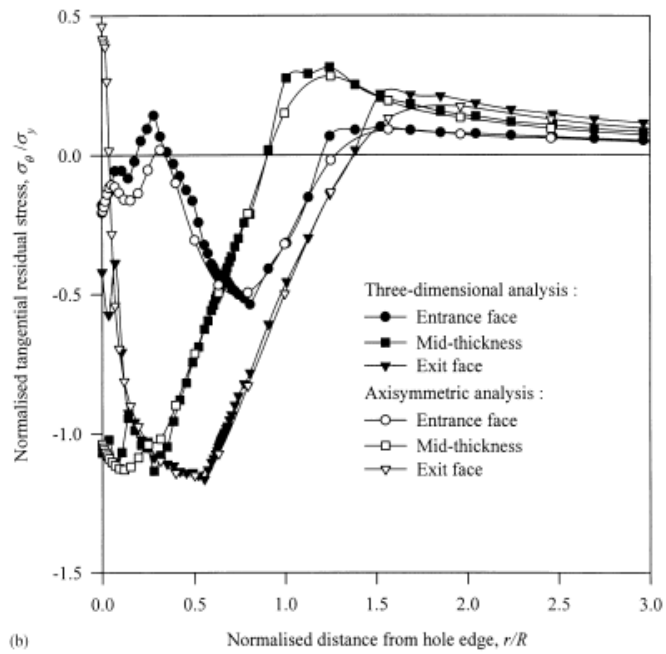

Figure O-11. Residual Tangential Stress Fields Following Cold Expansion as Predicted By 3D and Axisymmetric FE Analyses (Pavier, et al., 1998)

Özdemir and Edwards (1996) and Wang and Edwards (1998) used the modified Sachs method and neutron diffraction methods, respectively, in attempts to measure experimentally the actual variations in residual stress, both through the thickness and around the perimeter of the hole, resulting from the split-sleeve CX method. They confirmed that the actual distributions of residual stress are quite complex, and they qualitatively confirmed the trends from the numerical modeling. Stefanescu, et al. (2002) later showed relatively good agreement between neutron and x-ray diffraction measurement methods. Zhang, Fitzpatrick, and Edwards (2002) employed the contour method to investigate 3D effects on the crack plane.

O.3.2 FATIGUE LIFE EFFECTS AND MODELS.

The conventional wisdom is that CX of holes has a relatively small effect on the number of cycles required to initiate a fatigue crack at an open hole (e.g., Ball and Lowry, 1998; Chandawanich and Sharpe, 1979). The primary fatigue benefit accrues during the crack growth phase of life. For this reason, and because of the historical emphasis on damage tolerance

methods for aircraft structures, most of the studies and models for CX effects have focused on the FCG problem.

The classical approach to FCG life prediction for cold-expanded holes is to combine an analytical estimate of the residual stresses normal to the crack plane with a weight function method to calculate the stress-intensity factor, in which the weight function is directly integrated with the residual stresses along the length of the crack. The effects of (remote) applied loading are linearly superimposed with the (local) static residual stresses to determine the total stress intensity factor range. Grandt and his colleagues performed some of the ground-breaking studies following this paradigm (Grandt, 1975 and 1978; Cathey and Grandt, 1980). Similar approaches were followed later by Chandawanich and Sharpe (1979), Clark (1991), and Ball and Lowry (1998). Sample results from Ball and Lowry (1998) are shown in figure O-12. In the top figure, experimental measurements of residual stresses are compared with various analytical and numerical models, and in the bottom figure, the resulting predictions of crack growth are compared with fatigue test data. Note that the residual stresses in this paradigm are typically taken to be the initial residual stresses, prior to any loading, crack growth, or thermal exposure.

Pavier, et al. (1999) developed a sophisticated FE analysis of the fracture mechanics problem to compute effective stress-intensity factors for cracks emanating from the edge of a cold-worked hole. This work was a response to various concerns about the applicability of the classical superposition—weight function method, including stress relaxation and redistribution effects due to crack growth. They concluded that the traditional weight function method generally underestimated the effective stress-intensity factor and therefore could lead to non-conservative life predictions.

The 3D variations in CX residual stresses (especially through-thickness variations) cited earlier have a significant implication for the practical FCG analysis problem. Traditional FCG life analysis assumes that the fatigue cracks have idealized, regular shapes such as quarter-elliptical corner cracks and straight through cracks. Common stress-intensity factor solutions for cracks at holes are based on these geometric simplifications. However, real fatigue cracks at CX holes have been shown to have complex shapes. This was shown clearly by the early work of Pell, et al. (1989), who published photographs of cracks with distinct “P” shapes indicative of highly nonuniform growth rates across the thickness. More recently Kokaly, et al. (2005a) has published numerous fractographs of fatigue cracks growing from CX and non-CX holes in plates of different thicknesses, demonstrating a variety of complex shapes. Others such as Saunder and Grandt (2000) have documented only the significant differences in surface crack lengths on the entry and exit sides.

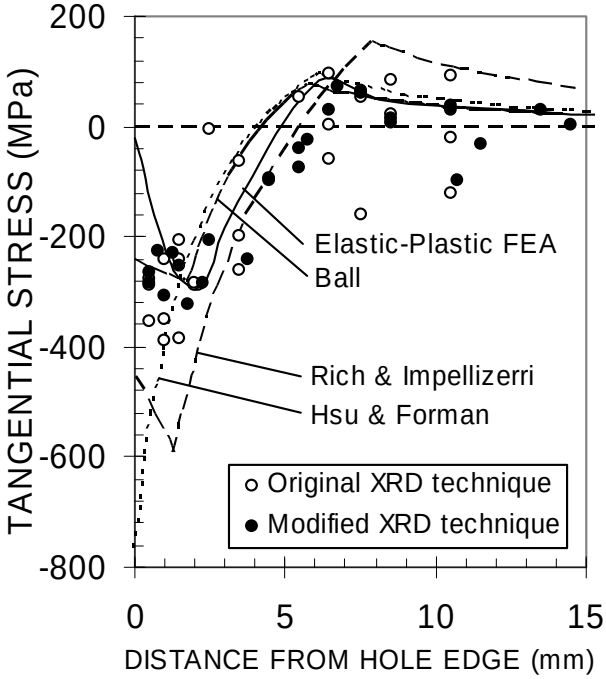

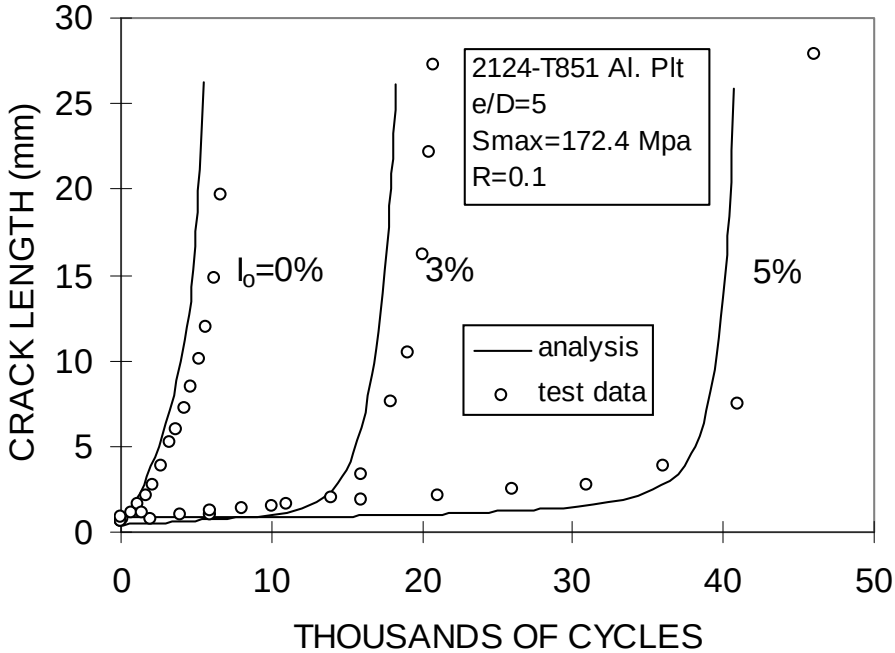

Figure O-12. Comparisons of Analytically Predicted vs Experimentally Measured Values for Residual Stress Normal to the Crack Plane (Top) and Crack Length as a Function of Fatigue Cycles (Bottom) (Ball and Lowry, 1998)

O.3.3 RESIDUAL-STRESS STABILITY.

It is noteworthy that all of the residual-stress models and fatigue crack growth predictions cited above are based exclusively on the initial residual-stress field for a cold-expanded hole, with no adjustments for any residual-stress relaxation or redistribution. Several early researchers speculated about the possibility of changes in the residual-stress field (e.g., Sha, et al., 1980; Mann and Jost, 1983) but had no data to evaluate their suspicions. Only a handful of more recent researchers have directly addressed the stability of CX residual stresses.

O.3.3.1 Static Relaxation.

One of the simplest and most significant effects on CX residual stresses is the effect of significant applied mechanical loads, especially in compression. These compressive excursions, which can occur frequently in spectrum loading of aircraft structures, can substantially decrease the compressive residual-stress field at the edge of the hole. The change occurs because the sum of residual and applied compressive stresses exceeds the yield strength of the material, but the total stress is limited by the yield surface of the material. When the applied compressive stress is removed, the local elastic unloading results in a decreased compressive residual stress. This effect was cited by Ball and Lowry (1998) as an interpretation of unpublished life results. The same effect was investigated more directly, albeit with limited scope, by Stefanescu, et al. (2003), who measured residual-stress fields at CX holes before and after single compressive loads. The applied compressive loads were relatively small—only a fraction of the material yield strength—but the changes in the residual-stress field were substantial, as shown in figure O-13.

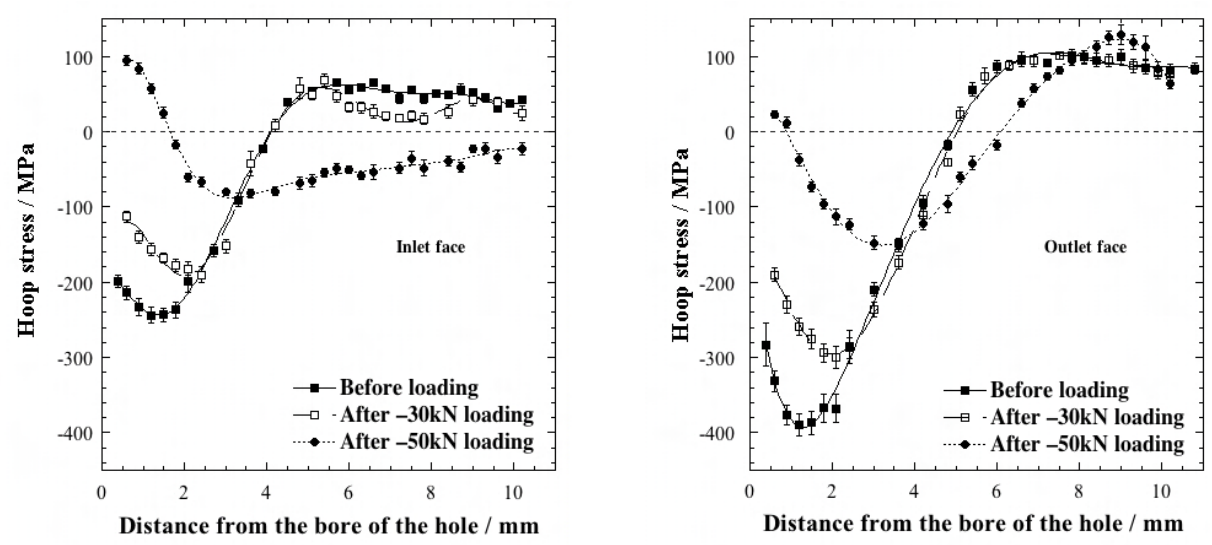

(a) (b)

Figure O-13. Residual Stresses Measured by X-Ray Diffraction Along the Transverse Direction of a Cold-Expanded Hole Specimen on the (a) Inlet Face and (b) Outlet Face Before and After Compressive Loading (Stefanescu, et al., 2003)

O.3.3.2 Cyclic Relaxation.

Three studies were found to date that investigated cyclic relaxation of CX residual stresses. Hermann and Moffatt (1991) performed R = 0.05 fatigue tests on the aluminum-lithium alloy 2091 following FTI CX. They measured significant relaxation after 10^6 fatigue cycles at an applied maximum stress of 70 MPa (nominally 210 MPa at the edge of the hole, in comparison to a material yield strength of 350 MPa), but only minimal further relaxation with additional cycling. Ezeilo, et al. (1994) reported noticeable reductions in residual stress with fatigue cycling in IN-718, but provided relatively few quantitative details in their short paper. Özdemir and Edwards (1997) studied cyclic relaxation effects at R = 0.1 in reamed 4% FTI expanded holes in 7050-T76. They found no discernable relaxation when applied cyclic stresses were below the fatigue limit (150 MPa), but a clear effect at higher loads. Selected results are shown in figure O-14. When cycled at the fatigue limit, residual stresses continued to relax with additional numbers of cycles.

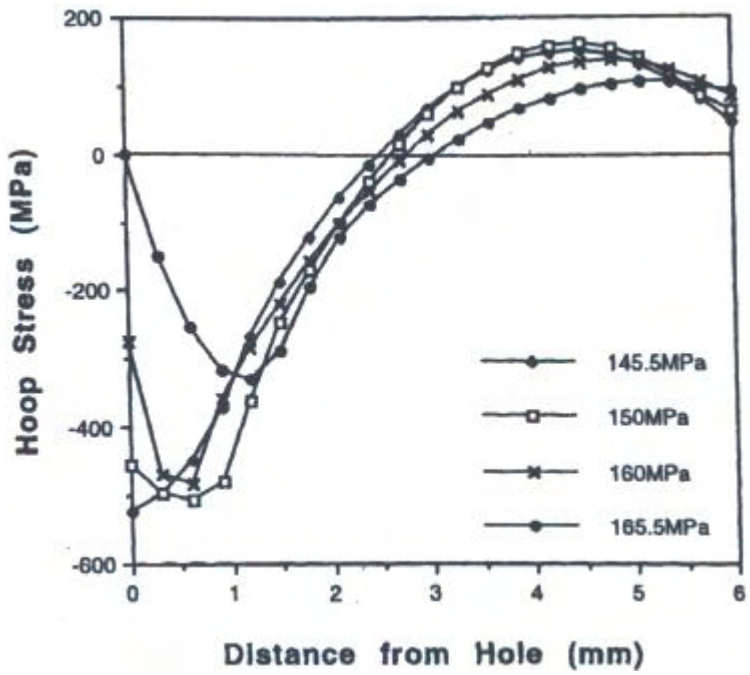

Figure O-14. Residual Hoop Stress Distributions at Reamed 4% FTI-Expanded Holes Fatigued for 50,000 Cycles at Different Applied Stresses (Ozdemir and Edwards, 1997)

O.3.3.3 Thermal Relaxation.

Since the preponderance of published research on CX residual stresses has focused on aluminum alloys and aircraft structural applications, little work has been done on the thermal relaxation issue. Clark and Johnson (2003) investigated stress relaxation in 7050-T7451 at temperatures ranging from 71°C to 104°C (approximately one-half of the melting temperature of the alloy). They found little relaxation (5% to 15%) after 250 hours, and relatively small changes in fatigue lives, although their experiments were complicated by several other issues.

Lacarac, et al. (2001) and Garcia-Granada, et al. (2001) investigated a new high-temperature aluminum alloy 2650 developed for advanced supersonic transport applications. Studies were conducted at 150°C with 1000 hour exposures. As shown in figure O-15, the creep exposure resulted in significant residual stress changes at the exit face (where the CX residual stresses were the highest) but only minimal changes at the entrance face. Since fatigue cracks typically initiate and grow most quickly at the entrance face (where the compressive residual stresses are the lowest), it appears that the creep exposure would have relatively little effect on the growth of these small corner cracks. Once the cracks grow and transition to become through cracks, the residual-stress relaxation would have more of an effect, and this was confirmed by subsequent FCG testing (Lacarac, et al., 2001). The relaxation effects appeared to be slightly more pronounced when the elevated temperature exposure was accompanied by tensile loading, and substantially more pronounced when high temperatures were superimposed with compressive loading. The latter effect is presumably linked to the effect of static compressive loads discussed in Section O.3.3.1.

No studies of thermal relaxation effects on cold-expanded holes in gas turbine engine alloys at operating temperatures were found in the open literature. Sha, et al. (1980) speculated that these effects could be significant for Ti-6246 applications, but their limited LCF testing of bolthole specimens with a superimposed dwell period demonstrated increased lives, perhaps attributable to other factors. Work cited earlier on cold-expanded holes in IN-718 (Ezeilo, et al., 1994) considered only room temperature conditions.

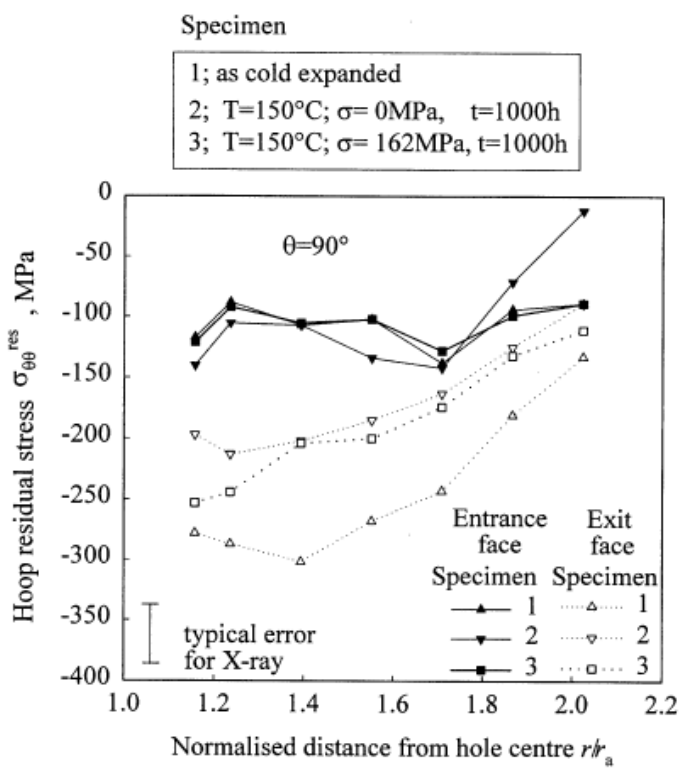

Figure O-15. Hoop Residual Stresses Measured Using X-Ray Diffraction After Cold Expansion and 150°C Exposure (Lacarac, et al., 2001)

The thermal relaxation models developed to address elevated temperature exposure of SP and related surface enhancement residual stresses (as discussed in section O.2.3.1) should be applicable to elevated temperature exposure of cold-expanded holes, but this does not appear to have been investigated and reported in the open literature.

O.3.3.4 Relaxation Due to Crack Growth.

Stefanescu (2004a) recently reported some interesting work on the apparent effects of FCG on CX residual stresses. His data suggested systematic changes in residual-stress fields with crack extension, as shown in figure O-16. Companion tests with electro-discharge machining slots simulating crack extension found more pronounced changes in residual-stress fields. Subsequent predictions of FCG rates based on classical weight function techniques agreed more closely with experimental measurements when the evolving residual-stress field was used rather than the initial residual-stress field (Stefanescu, 2004b), as illustrated in figure O-17. As Stefanescu noted, this result stands in apparent contradiction to the numerous successful predictions by earlier researchers using only the initial residual-stress field. The mechanisms by which the residual-stress change occurs with crack extension are not clear. When residual stresses are tensile, the mechanism for relaxation with crack growth is obvious (see section O.4.2.2), but this argument does not appear to be immediately applicable to crack growth in compressive residual-stress fields. Stefanescu suggested the changes were related to the localized plastic deformation around the crack during fatigue cycling but proposed no working model.

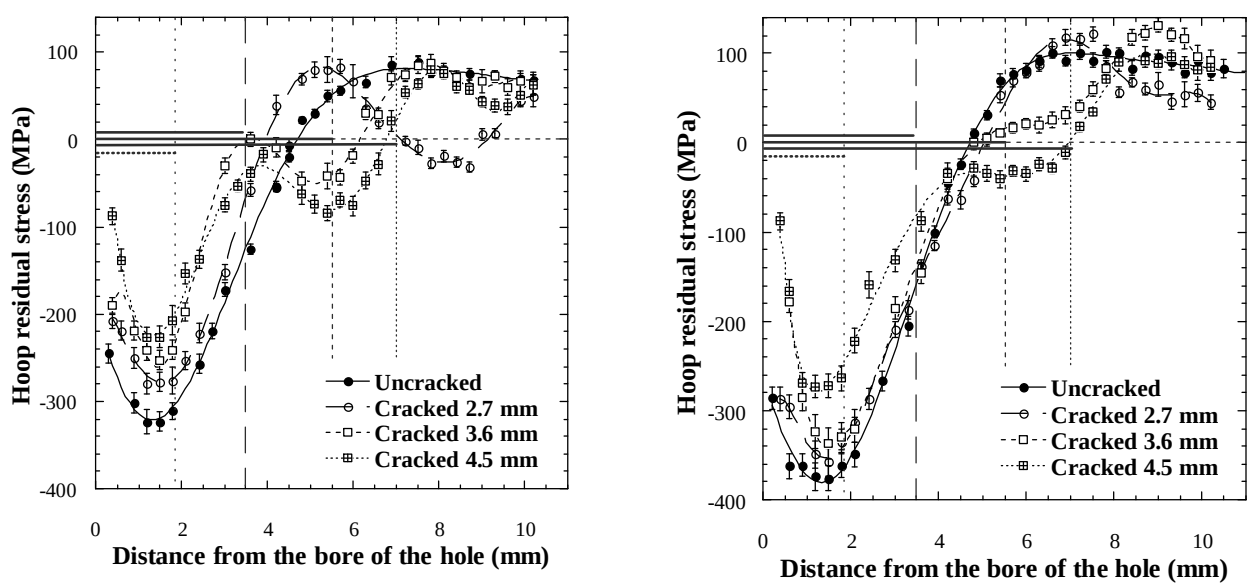

Figure O-16. Residual Stresses Measured Using X-Ray Diffraction for Different Average Fatigue Crack Lengths at the (a) Inlet Face and (b) Outlet Face (Stefanescu, 2004a)

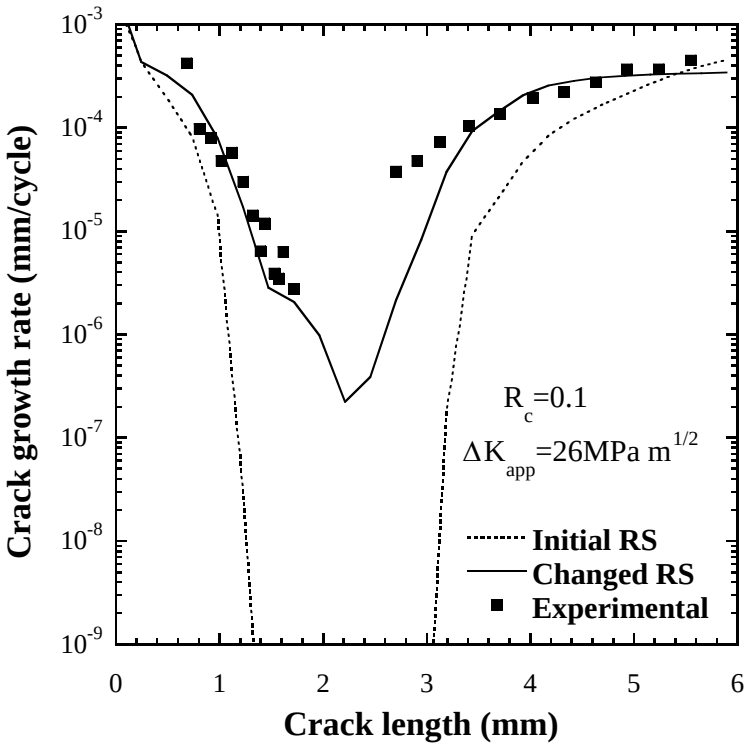

Figure O-17. Comparisons of Measured FCG Rates for Thickness-Averaged Crack Lengths With Predictions Based On Initial or Evolving Residual-Stress Fields (Stefanescu, 2004b)

O.4 WELDING.

In peening and cold expansion, beneficial compressive residual stresses are deliberately induced into the final manufactured part for the specific purpose of enhancing fatigue performance. In contrast, welding residual stresses are an inherent and largely unavoidable byproduct of the manufacturing process itself, and they are largely deleterious to fatigue performance. After solidification of the weld bead, the bead is prevented from contracting during cooling by the surrounding parent material. The parent material thus undergoes compression due to contraction forces in the weld, and the correspondingly the weld bead and heat-affected zone are put into tension. The maximum tensile residual stresses in the welded joint itself may approach the yield strength of the parent material.

The majority of the scientific literature addressing residual-stress effects on weldment fatigue has focused on steels, although some limited attention has been given to alloys of titanium (Adams, 1973) and aluminum (Berkovits, et al., 1998; Dalle Donne and Raimbeaux, 2001; James, et al., 2004). Most researchers have emphasized fatigue crack growth behavior rather than crack formation or S-N behavior.

O.4.1 FATIGUE LIFE EFFECTS AND MODELS.

Calculation of the initial residual-stress field via numerical analysis of the welding process is a challenging effort beyond the scope of the current survey. Terada (1976) developed a simple functional form for the residual-stress field at a weld bead in a wide plate as a first step in deriving stress-intensity factors for cracks perpendicular to the weld bead. Tada and Paris (1983) and later Smith (1985) proposed alternative functional forms and, in turn, derived alternative expressions for the stress-intensity factor. Terada and Nakajima (1985) used the same residual-stress fields to develop *K* solutions for a crack approaching the weld bead. Rybicki, et al. (1981) proposed another simple functional form and corresponding *K* solutions for girth-welded pipes.

Adams (1973) was apparently among the first to propose a simple superposition approach using weight function methods to determine the net effect of residual stresses and applied loads on fatigue crack growth in welded joints. Similar approaches were employed with general success by Glinka (1979 and 1987), Parker (1982), and Nelson (1982). Parker (1982) noted that special attention is needed when weight function superposition methods infer physically inadmissible interpenetration of opposing crack faces. Miyazaki, et al. (2002) reported successful applications of the superposition approach but also proposed an inherent strain method for more complex problems.

Numerous other researchers have proposed that a crack closure approach is a superior means of addressing residual-stress effects on crack growth in weldments. This approach assumes that the residual-stress field influences the crack-opening stress (the stress at which the fatigue crack tip first becomes fully open during the loading cycle), and that the resulting changes in the effective stress-intensity factor range correlate with changes in the fatigue crack growth rate. The crack-opening levels are determined using either experiment or analysis. Miyamoto, et al. (1973) focused his pioneering work on FE analysis of fatigue crack closure on the welding problem, and Fukuda and Sugino (1980) employed a similar numerical approach to predict how welding residual stresses influenced crack-opening behavior. Nelson (1982) applied a simpler closure analysis method and critically compared the results with the superposition approach for some of the Glinka (1979) data, suggesting that the closure approach was sometimes superior. Glinka (1987) himself later suggested that the two approaches should give similar results under many conditions. Fukuda, et al. (1979) and later Itoh, et al. (1989) and Kang, et al. (1989 and 1990) measured crack-opening levels experimentally and then used these values to correlate crack growth rate data. Kang, et al. (1990) pointed out that closure approaches must address the complex partial opening that can occur when fatigue cracks grow from compressive to tensile residual-stress regimes. Itoh, et al. (1989) as well as Ohta, et al. (1988 and 1993) observed that cracks growing in tensile residual-stress fields under tensile applied stress ratios exhibit no effect of the tensile residual-stress field on crack growth rates, because the crack tip is already fully open during the entire fatigue cycle. Beghini and Bertini (1990) and Beghini, et al. (1994) suggested a simple approach to modify the traditional superposition method to account for certain closure effects. Wang (1996 and 1999) extended a strip-yield fatigue crack growth model for plasticity-induced crack closure to address residual stresses in weldments.

O.4.2 RESIDUAL-STRESS STABILITY.

Most of the fatigue crack growth analyses cited above did not address changes in the residual-stress field in their formulation, although some researchers (e.g., Nelson, 1982; and Glinka, 1987) speculated on the potential effect of these changes. However, numerous other researchers have directly addressed changes in residual-stress distributions due to a variety of mechanisms, including static loading, cyclic loading, and crack extension. Thermal relaxation of welding residual stresses has not been addressed explicitly in this survey, although it should be noted that postweld heat treatment is often performed for the explicit purpose of relieving deleterious tensile residual stresses in the weldment.

O.4.2.1 Static and Cyclic Relaxation.

Numerous researchers have reported significant relaxation and redistribution of residual stresses on the first loading cycle, followed by minimal further relaxation on subsequent cycles. Iida, et al. (1997) and Iida and Takanashi (1998) reported this result for both R= 0 and R = -1 cycling on notched specimens, and then Takanashi, et al. (2000) found a similar result for smooth butt welds, proposing a simple mechanics model as explanation. Typical results for the change in the residual stress at a single point near the weld center line with cycling are shown in figure O-18 (Iida and Takanashi, 1998). Note that the magnitude of the decrease in the residual stress on the first cycle corresponds with the magnitude of the applied static stress, indicating a simple shakedown behavior. Typical changes in the residual-stress profile after fatigue cycling at two different stress amplitudes are shown in figure O-19 (Takanashi, et al., 2000). Note that both the tensile and compressive residual stresses are relaxed towards zero, although the changes are more pronounced for the tensile stresses.

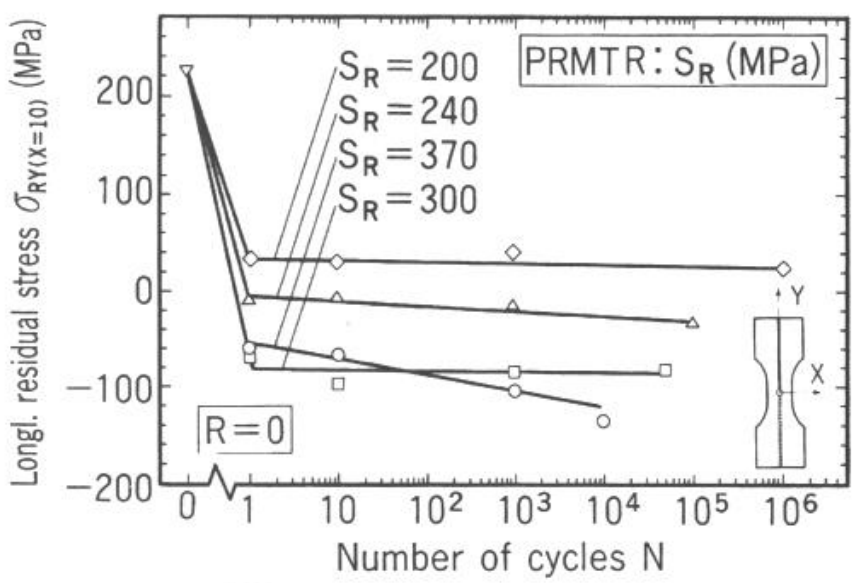

Figure O-18. Change in Longitudinal Residual Stress at a Distance 10 mm From the Weld Center Line With Application of Static or Fatigue Loads (Iida and Takanashi, 1998)

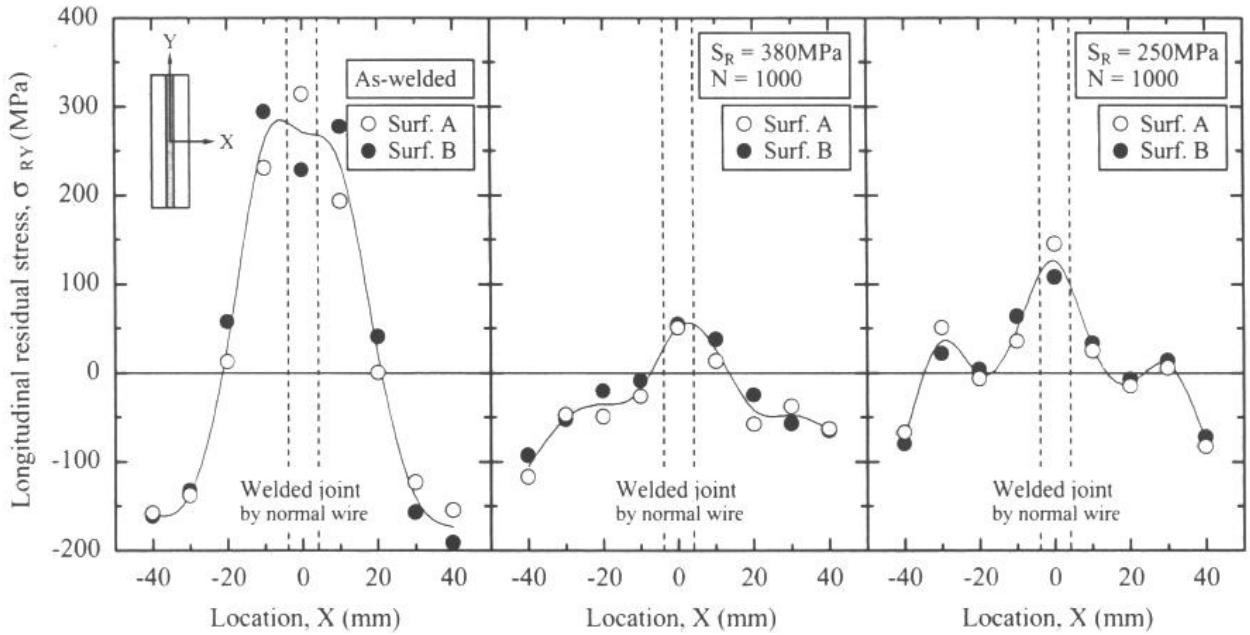

Figure O-19. Transverse Distributions of Longitudinal Residual Stresses in Smooth Butt-Welded Joint Before and After Fatigue Cycling (Takanashi, et al., 2000)

Nitschke-Pagel and Wohlfahrt (2000) experimentally measured a relaxation of residual stresses in welded high-strength steel in proportion to the magnitude of a single applied static tensile load, but minimal changes with further cycling, and minimal changes with static compressive loads. Lachmann, Nitschke-Pagel, and Wohlfahrt (2000) confirmed the same general trends with corresponding Barkhausen Noise measurements of residual stress. Han, et al. (2002) found a large change in residual stresses on the first load cycle for low-strength steel, but very small changes with further cycling. Dattoma, et al. (2004) developed a FE model of residual-stress relaxation in weldments that predicted significant changes on the first cycle but no further changes after 10 cycles. Blom (1995) reported experiments in which residual-stress measurements were performed before cycling and at two different numbers of fatigue cycles, neither of which was a single cycle. He found some appreciable relaxation between the two cycle counts in some tests, although the largest relaxation (50% to 80% of the initial value) was recorded at the first cycle count. Lopez Martinez, et al. (1997) published maps of residual-stress distributions measured by neutron diffraction for as-welded and TIG-dressed specimens with and without static loading or spectrum fatigue cycling. They concluded that the static load caused appreciable relaxation and that the variable amplitude fatigue showed the same degree of relaxation as the static load case, suggesting that the fatigue relaxation occurred early during the fatigue loading and was correlated to the occurrence of maximum load in the spectrum. Khanna, et al. (2001) studied residual stresses in spot welds using Moiré interferometry methods and reported that residual stress decreased at weld center but increased at the weld edge after 1000 to 10000 cycles; no data were reported after only one cycle. James, et al. (2004) recently reported an interesting result based on detailed synchrotron diffraction measurements of the full residual-stress distribution; they claimed significant increases in tensile residual stress with fatigue cycling, but offered no potential explanations.

O.4.2.2 Relaxation Due to Crack Growth.

Fukuda and Tsuruta (1979) were apparently the first to study the effect of fatigue crack extension on the tensile residual-stress fields resulting from the welding process. They experimentally measured a progressive decrease in the residual stresses as a through-thickness fatigue crack extended under $R = 0$ cycling, as shown in figure O-20. The amplitude of the applied stress cycle was small enough that relaxation of the residual-stress field due to purely static or cyclic load mechanisms was not significant, as confirmed by measurements performed before and after substantial fatigue cycling (without cracking).

Fukuda (1989) later developed a simple analytical method to predict the redistribution of tensile residual stress with crack extension, and showed good agreement with experimental measurements. Park, et al. (2004) developed a numerical model for a similar purpose. Terada (2005) recently published another equation for tensile residual-stress redistribution with crack extension, which showed favorable agreement with limited experimental data.

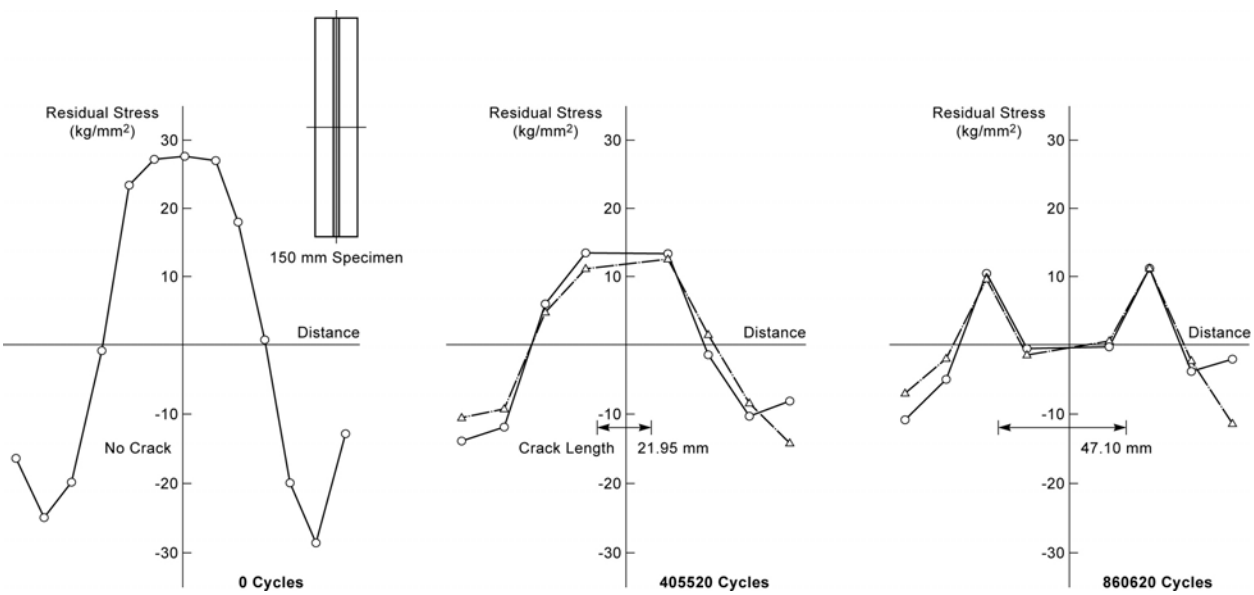

Figure O-20. Changes in Welding Residual-Stress Profile With Crack Extension
(Fukuda and Tsuruta, 1979)

O.5 MACHINING.

Machining techniques for metallic materials such as cutting, grinding, and turning typically induce residual stresses at the part surface as a byproduct of the thermal cycling, microstructural transformations, and deformation associated with material separation. Although these residual stresses are typically of much smaller magnitude (at least for good machining practice) than the residual stresses resulting from peening, cold expansion, or welding, they are sometimes large enough to become significant for fatigue behavior. These machining-induced residual stresses are also subject to potential relaxation and redistribution.

The available information in the scientific literature about the stability of machining residual stresses is very limited, although this may be indicative of the limited significance of the issue. There is a broader literature on the formation and measurement of the initial residual-stress state due to machining, but this survey did not attempt to address that literature comprehensively. Some limited information is also available on fatigue life effects, mostly focused on S-N behavior, because the depth of the machining residual-stress fields is generally too shallow to affect fatigue crack growth behavior except for the smallest crack sizes. However, it should be noted that machining effects on S-N behavior also involve surface roughness and other factors, not simply residual-stress effects.

The most extensive work on the stability of residual stresses induced by machining was performed by James (1982); see also James and Morris (1981). James studied surface milling as part of a broader study of residual-stress formation and stability in Al 2219-T851, and characterized the changes in the surface residual stress with R = -1 fatigue cycling at different stress amplitudes (all significant fractions of the yield strength). A simple model was proposed to predict the results.

Bathias, et al. (1988) investigated the relaxation of tensile residual stresses due to milling of Al 2024 and 7075, finding a rapid and nearly total relaxation during the first few cycles of fatigue loading.

Flavenot and Skalli (1988) performed experimental measurements of the initial and cyclically relaxed residual-stress profiles in 42CD4 grade steel due to different grinding conditions. Lu, Flavenot, and Turbat (1988) used their FE model (cited earlier in the treatment of peening residual stresses) to predict this relaxation behavior.

Kuhn, et al. (1991) published data on relaxation of residual stresses due to milling of 1045 steel in various heat-treat conditions and with various stress concentrations. Residual stresses relaxed substantially, especially in softer conditions and at larger fatigue stress amplitudes.

Alam, et al. (2000) reported only limited information about relaxation of residual stresses due to turning of XC80 steel.

O.6 OTHER PROCESSES.

It is useful to cite, for completeness, a few published studies on residual-stress relaxation under other conditions. One set of these studies focuses on the relaxation of mean stress during strain-controlled fatigue, while another set addresses the relaxation of residual stresses induced by different mechanical deformation processes. Some of the studies were published many years ago and were particularly significant in the historical development of the topic.

O.6.1 MEAN STRESS RELAXATION.

Morrow performed the landmark early research on cyclic relaxation of mean stresses (Morrow and Sinclair, 1958; Ross and Morrow, 1960; Morrow, et al., 1960) in careful experimental studies of 4340 (in three different heat-treat conditions) and A286 steels. He performed

displacement-controlled fatigue tests on axial specimens with an imposed mean stress and measured the change in the mean stress with continued cycling for different values of constant applied stress amplitude. Morrow then developed an empirical equation in the general form of a power law on the logarithm of applied cycles to describe the observed behavior. Martin, et al. (1971) and Jhansale and Topper (1973) later continued this line of research by applying their more general inelastic deformation models to treat mean stress relaxation in steels. Taira, et al. (1964) independently performed some early investigations of mean stress relaxation during torsional fatigue of a plain carbon steel. More recent work on mean stress relaxation in steels has been reported by Gong and Norton (1999) and Lindgren and Lepistö (2002).

O.6.2 MECHANICAL DEFORMATION.

One of the earliest studies of the cyclic stability of mechanically induced residual stresses was documented in a classic paper by Pattinson and Dugdale (1962). They bent beams of mild steel or hard aluminum alloy to a known curvature and then straightened them to introduce a controlled residual stress. Following various amounts of flexural cycling, the remaining residual stress in the beam was measured. Residual stress faded rapidly in the mild steel at low numbers of cycles, but fading was pronounced in the aluminum alloy only after about 10^7 cycles.

Gould and Pittella (1972) imposed a residual stress in 1100 Al by cold working and then measured the decay of this residual stress during double-bending fatigue tests. Applied loads were relatively severe, and observed decreases in residual stress were substantial

Radhakrishnan and Prasad (1976) applied a tensile prestrain to axial specimens of 0.23% C steel to generate a residual stress due to differences in deformation between surface and core. Relaxation of this residual stress during subsequent $R = 0$ fatigue cycling was observed to follow a power-law relationship with respect to the logarithm of the elapsed cycles.

Underwood, et al. (1977) induced residual stresses in bend specimens of a nickel-chromium-molybdenum steel by localized plastic indentation, and then performed fatigue crack growth tests. Considerations of residual-stress redistribution due to the effects of notching and crack extension were required to obtain perform accurate analyses.

Almer, et al. (1998 and 2000) studied the effects of residual stresses induced by prestrain on fatigue crack initiation and growth in 1080 steel. Microscopic (localized) residual stresses faded rapidly and had little impact on fatigue behavior. Macroscopic residual stresses were more significant for fatigue, especially as their fading and/or redistribution interacted with fatigue crack growth.

O.7 DISCUSSION.

It is clear from the sheer volume of this survey that a great deal has been observed, measured, modeled, and learned during the past 50 years about the stability of residual stresses. Many engineering metals have been considered, including significant attention to materials commonly employed in aircraft gas turbine engines. The major sources of induced and inherent residual stress—peening and related surface treatments, CX of holes, welding, and machining—have all

received appropriate levels of attention, although a few specialized combinations of factors (e.g., cyclic relaxation of residual stresses from CX of holes in engine materials at elevated temperature) have not been investigated in any depth.

The body of knowledge, while extensive, has not yet provided definitive observations, explanations, and models for all relaxation phenomena. Nevertheless, a critical reading of the literature incorporated in this survey leads naturally to a series of general observations and conclusions that should provide a solid foundation for further study, model development, and practical implementation.

First of all, it is clearly important to discern and separate the different relaxation phenomena. Residual-stress relaxation can occur due to thermal effects, static mechanical load effects, cyclic load effects, and crack extension effects. The specific mechanisms are different for each of these different effects, and the various effects often superimpose. For example, the first cycle of fatigue loading often induces static relaxation effects, while subsequent load reversals can induce cyclic relaxation effects. Fatigue cycling at elevated temperature can invoke both thermal and cyclic phenomena. A failure to discern and separate these different effects can lead to some confusion, and some researchers appear to have fallen victim to such confusion. From a more positive perspective, discernment and separation of the different phenomena facilitates simpler and more accurate modeling of each individual effect, and these simple models can be superimposed in some situations.

The available literature provides some general insight into the significance of the various relaxation phenomena. For example, thermal relaxation effects do not appear to be extremely large for most practical application temperatures for common engineering metals. Some academic studies subjected materials to temperatures greater than their normal operating envelope and observed substantial relaxation, but relaxation at normal operating temperatures tended to be moderate.

Static relaxation effects appear to be relatively easy to identify and characterize based on knowledge of the initial residual-stress field and the applied service loading. In general, compressive loading tends to relax beneficial compressive residual-stress fields in proportion to the magnitude of the applied loading. Tensile loading typically has no effect on compressive residual stresses unless the applied loads are so large as to cause yielding when superimposed with the self-equilibrated tensile residual-stress fields.

Many of the pronounced cyclic relaxation effects identified in the literature appear to be static effects on the first loading cycle (compressive loads relaxing compressive peening residual stresses, or tensile loads relaxing tensile welding residuals, for example). Once these static effects are set aside, the remaining true cyclic relaxation tends to be gradual and moderate unless the applied fatigue stress amplitudes are large. However, no generalized quantitative criteria appears to be available to characterize “moderate” and “large” in this last statement.

The effects of crack extension on tensile residual-stress fields are relatively easy to identify and understand. The effects of crack extension on compressive fields are not so clear and require further study. Only limited data are available to suggest that such an effect even exists.

No effort was made in this survey to perform a quantitative evaluation of the various models that have been proposed to characterize or predict thermal, static, cyclic, or crack extension effects on residual stress. However, some general observations are in order. Simple thermal activation models were developed to treat thermal relaxation effects, although their generality and truly predictive nature has not yet been established. It should not be difficult to formulate a general treatment of static relaxation based on simple mechanics arguments (superposition of two known stress fields and comparison with an established cyclic yield criterion). This does not appear to have been done yet outside of simple, idealized profiles or a general FE treatment. Empirical models may be useful for focused, well-characterized cyclic relaxation problems. The more general numerical models proposed for cyclic relaxation are encouraging but require some further detailed study to evaluate their practicality. Tractable models were proposed for relaxation of tensile residual stresses due to crack extension, but no well-established theory has yet been laid out for crack extension effects on compressive fields.

The available evidence suggests that, in practical engineering applications, induced residual stresses due to CX, peening, or related manufacturing techniques rarely relax fully to zero. Although some relaxation commonly occurs due to one or more mechanisms, and so final residual-stress fields are rarely the same as the initial stress fields, some significant fraction of the initial residual-stress field often remains at the end of the relevant fatigue exposure. Static effects appear to be the most deleterious, and these should be easily predictable in most cases. Most of the severe degradation of residual stresses reported in the literature appears to be attributable to unrealistically severe thermal or mechanical loading conditions.

Having said that, characterizing and employing the correct residual-stress field is essential for accurate life modeling. It is clear that residual-stress effects on S-N lifetimes and fatigue crack growth lives can be very substantial. A life prediction based on an incorrect assumption about residual stress may be seriously in error. In view of the uncertainties associated with residual stresses, appropriately conservative assumptions are in order. Some further investigation of the probabilistic aspects of residual-stress analysis appears to be warranted.

Established methods for modeling the growth of fatigue cracks in residual-stress fields using weight function stress-intensity factors and superposition techniques appear to provide satisfactory accuracy in many cases. Special attention must be given to the effects of stress ratio on crack growth, and appropriate crack closure methods may also be satisfactory for this purpose. Several issues can complicate the analysis and may require further attention, including the multidimensionality of stress fields, nonelliptical crack shapes, and crack face contact.

Finally, it is important to remember that the effects of peening and related techniques, CX, welding, and machining on fatigue behavior are not limited to residual-stress effects, and this is especially true for S-N behavior. The same manufacturing processes that induce residual stresses can also influence the surface quality, microstructure, and material condition, all of which may independently influence fatigue life. Residual-stress effects appear to be dominant for many fatigue crack growth problems, but this may require experimental confirmation. The most significant complication in fatigue crack growth is perhaps the possibility of substantial changes in the stable fatigue crack shape, which can greatly complicate the accurate characterization of the stress-intensity factor and hence the accurate prediction of FCG rate.

O.8 ACKNOWLEDGEMENTS.

Figure 1 is reprinted with the permission of ASME International. Figure 4 is © TMS (The Minerals, Metals, and Materials Society), Warrendale, PA, and is reprinted with the permission of TMS. Figures 6 and 7 are reprinted with permission of ASM International®, all rights reserved (www.asminternational.org). Figures 9, 10, and 15 are reprinted with permission from Elsevier. Permission to reproduce figures 11, 13, 16, and 17 is granted by the Council of the Institution of Mechanical Engineers. Figures 12 and 14 are reprinted with permission from Blackwell Publishing. Figures 18 and 19 are reprinted with the kind authorization of the International Institute of Welding.

O.9 BIBLIOGRAPHY.

Adams, N.J.I., 1973, "Crack Growth in the Vicinity of Welds," *Welding Research Supplement*, pp. 508-s-513-s.

Alam, A.M., Chieragatti, R., and Lavelle, B., 2000, "A New Device for In Situ Residual Stress Measurement During Fatigue Testing," *Materials Science Forum*, Aedermannsdorf, Switzerland, Trans Tech Publications, Vol. 347/349, pp. 358-362.

Almer, J.D., Cohen, J.B., and Winholtz, R.A., 1998, "The Effects of Residual Macrostresses and Mircostresses on Fatigue Crack Propagation," *Metallurgical and Materials Transactions A*, Vol. 29A, pp. 2127-2136.

Almer, J.D., Cohen, J.B., and Moran, B., 2000, "The Effects of Residual Macrostresses and Microstresses on Fatigue Crack Initiation," *Materials Science and Engineering A*, Vol. A284, pp. 268-279.

Altenberger, I., Noster, U., Boyce, B.L., Peters, J.O., Scholtes, B., and Ritchie, R.O., 2002a, "Effects of Mechanical Surface Treatment on Fatigue Failure in Ti-6Al-4V: Role of Residual Stresses and Foreign-Object Damage," ECRS 6, Proc. of the 6th European Conference on Residual Stresses Materials Science Forum, Coimbra, Portugal, *Materials Science Forum*, Vol. 404, No. 4, pp. 457-462.

Altenberger, I., Noster, U., Scholtes, B., and Ritchie, R., 2002b, "High Temperature Fatigue of Mechanically Surface Treated Materials," *Proc. 8th International Conference on Shot Peening (ICSP-8)*, Garmisch-Partenkirchen, Germany, L. Wagner, editor, Wiley-VCH GmbH & Co. KGaA, pp. 483-489.

Armen, H., Levy, A., and Eidinoff, H.L., 1984, "Elastic-Plastic Behavior of Coldworked Holes," *Journal of Aircraft*, Vol. 21, No. 3, pp. 193-201.

Ball, D.L., 1995, "Elastic-Plastic Stress Analysis of Cold Expanded Fastener Holes," *Fatigue and Fracture of Engineering Materials and Structures*, Vol. 18, No. 1, pp. 47-63.

Ball, D.L. and Lowry, D.R., 1998, "Experimental Investigation on the Effects of Cold Expansion of Fastener Holes," *Fatigue and Fracture of Engineering Materials and Structures*, Vol. 21, pp. 17-34.

Bathias, C., Bonnafe, J.P., Lebrun, J.L., and Maeder, G., 1988, "X-Ray Diffraction and Acoustic Emission Study of Fatigue Damage in Aluminum Alloys," *Analytical and Experimental Methods for Residual Stress Effects in Fatigue, ASTM STP 1004*, Champoux, Underwood, and Kapp, editors, American Society for Testing and Materials, pp. 25-36.

Batista, A.C., Dias, A.M., Lebrun, J.L., LeFlour, J.C., and Inglebert, G., 2000, "Contact Fatigue of Automotive Gears: Evolution and Effects of Residual Stresses Introduced by Surface Treatments," *Fatigue and Fracture of Engineering Materials and Structures*, Vol. 23, pp. 217-228.

Beghini, M. and Bertini, L., 1990, "Fatigue Crack Propagation Through Residual Stress Fields With Closure Phenomena," *Engineering Fracture Mechanics*, Vol. 36, No. 3, pp. 379-387.

Beghini, M., Bertini, L., and Vitale, E., 1994, "Fatigue Crack Growth in Residual Stress Fields: Experimental Results and Modelling," *Fatigue and Fracture of Engineering Materials and Structures*, Vol. 17, No. 12, pp. 1433-1444.

Belassel, M., Brauss, M., and Berkley, S.G., 2000, "Residual Stress Relaxation in Nickel Base Alloys Subjected to Low Cycle Fatigue," *Proc. 6th International Conference on Residual Stresses: ICRS-6*, Oxford, UK, pp. 144-151.

Belassel, M., Brauss, M., Pineault, J., and Berkley, S.G., 2002, "Fatigue Damage Mechanism and Stress Relaxation in Shot Peened and Polished Nickel Base Materials," ECRS 6, Proc. of the 6th European Conference on Residual Stresses Materials Science Forum, Coimbra, Portugal, *Materials Science Forum*, Vol. 404, No. 4, pp. 451-455.

Berger, M.-C. and Gregory, J.K., 1999, "Residual Stress Relaxation in Shot Peened Timetal 21s," *Materials Science & Engineering A*, Vol. A263, pp. 200-204.

Bergström, J. and Ericsson, T., 1984, "Relaxation of Shot Peening Induced Compressive Stress During Fatigue of Notched Steel Samples," *Proc. Second International Conference on Shot Peening, ICSP-2*, Chicago, Illinois, pp. 241-248.

Bergström, J. and Ericsson, T., 1986, "Relaxation of Shot Peening Induced Compressive Stress During Fatigue of Notched Steel Samples," *Surface Engineering*, Vol. 2, No. 2, pp. 115-120.

Bergström, J. and Ericsson, T., 1987, "X-ray Microstructure and Residual Stress Analysis of Shot Peened Surface Layers During Fatigue Loading," *Proc. 3rd International Conference on Shot Peening (ICSP3)*, Garmisch-Partenkirchen, Germany, H. Wohlfahrt, R. Kopp, and O. Vöhringer, editors, DGM Informationsgesellschaft Verlag, Oberursel, pp. 221-230.

Berkley, S.G., Bradley, E.F., and Thomas, M.C., 1997, "A New Approach to Tracking Turbine Engine Low Cycle Fatigue Disk Life (Phase IIB)," 41st Annual Air Transport Association Non-Destructive Testing Forum.

Berkley, S.G., Bradley, E.F., and Thomas, M.C., 1999, "Residual Stress in New, In-Service and Retired Disks," 1999 ASIP Conference, San Antonio, Texas.

Berkovits, A., Kelly, D.W., and Di, S., 1998, "Considerations of the Effect of Residual Stresses on Fatigue of Welded Aluminium Alloy Structures," *Fatigue and Fracture of Engineering Materials and Structures*, Vol. 21, pp. 159-170.

Berns, H. and Weber, L., 1986, "Influence of Residual Stresses on Crack Growth," *Impact Surface Treatment*, S.A. Megrid, editor, Elsevier, pp. 31-44.

Bignonnet, A., 1987, "Fatigue Strength of Shot-Peened Grade 35 NCD 16 Steel—Variation of Residual Stresses Introduced by Shot Peening According to Type of Loading," *Proc. 3rd International Conference on Shot Peening (ICSP3)*, Garmisch-Partenkirchen, Germany, H. Wohlfahrt, R. Kopp and O. Vöhringer, editors, DGM Informations-gesellschaft Verlag, Oberursel, pp. 659-666.

Bignonnet, A., Lieurade, H.P., Picouet, L., and Castex, L., 1987, "Shot Peening of Welded Joints and Residual Stress Relaxation During Fatigue," *Proc. 3rd International Conference on Shot Peening (ICSP3)*, Garmisch-Partenkirchen, Germany, H. Wohlfahrt, R. Kopp, and O. Vöhringer, editors, DGM Informationsgesellschaft Verlag, Oberursel, pp. 585-593.

Blom, A.F., 1995, "Spectrum Fatigue Behaviour of Welded Joints," *International Journal of Fatigue*, Vol. 17, No. 7, pp. 485-491.

Boggs, B.D. and Byrne, J.G., 1973, "Fatigue Stability of Residual Stress in Shot Peened Alloys," *Metallurgical Transactions*, Vol. 4, pp. 2153-2157.

Bonnafé, J.P., Maeder, G., and Bathias, C., 1987, "Study of Fatigue Damage in Shot Peened Aluminium Alloys Using Acoustic Emission and Macro/Microscopic X-Ray Diffraction Investigations," *Proc. 3rd International Conference on Shot Peening (ICSP3)*, Garmisch-Partenkirchen, Germany, H. Wohlfahrt, R. Kopp, and O. Vöhringer, editors, DGM Informationsgesellschaft Verlag, Oberursel, pp. 485-497.

Buchanan, D.J., John, R., and Ashbaugh, N.E., 2006, "Thermal Residual Stress Relaxation in Powder Metal IN100 Superalloy," *Journal of ASTM International*, Vol. 3, Paper ID JAI12552.

Burck, L.H., Sullivan, C.P., and Wells, C.H., 1970, "Fatigue of a Glass Bead Blasted Nickel-Base Superalloy," *Metallurgical Transactions*, Vol. 1, pp. 1595-1600.

Cammett, J.T., Sauer, C.A., and Arnold, T.E., 1993, "Observations on Shot Peening Residual Stresses in 17Cr-7Ni Austenitic Stainless Steel and Their Redistribution via Mechanical Loading," *Proc. 5th International Conference on Shot Peening (ICSP5)*, Oxford, UK, D. Kirk, editor, pp. 283-290.

Cammett, J.T., Prevéy, P.S., and Jayaraman, N., 2005, "The Effect of Shot Peening Coverage on Residual Stress, Cold Work, and Fatigue in a Nickel-Based Superalloy," *Proc. 9th International Conference on Shot Peening (ICSP-9)*, Paris, Marne la Vallée, France, Paper 261.

Cannon, D.F., Sinclair, J., and Sharpe, K.A., 1985, "Improving the Fatigue Performance of Bolt Holes in Railway Rails by Cold Expansion," *Proc., International Conference and Exposition on Fatigue, Corrosion Cracking, Fracture Mechanics, and Failure Analysis*, Salt Lake City, Utah, pp. 353-369.

Cao, W. and Castex, L., 1988, "Modelling of the Shot Peening Residual Stress Relaxation in Steel Structure Under Cyclic Loading," International Conference on Residual Stresses, Nancy, France, G. Beck, S. Denis, and A. Simon, editors, pp. 631-637.

Cao, W., Khadhraoui, M., Brenier, B., Guedou, J.Y., and Castex, L., 1994, "Thermomechanical Relaxation of Residual Stress in Shot Peened Nickel Base Superalloy," *Materials Science and Technology*, Vol. 10, pp. 947-954.

Capello, E., Davoli, P., Filippini, M., and Foletti, S., 2004, "Relaxation of Residual Stresses Induced by Turning and Shot Peening on Steels," *Journal of Strain Analysis*, Vol. 39, No. 3, pp. 285-290.

Cathey, W.H. and Grandt, A.F., Jr., 1980, "Fracture Mechanics Consideration of Residual Stresses Introduced by Coldworking Fastener Holes," *Journal of Engineering Materials and Technology*, Vol. 102, pp. 85-91.

Chakherlou, T.N. and Vogwell, J., 2003, "The Effect of Cold Expansion on Improving the Fatigue Life of Fastener Holes," *Engineering Failure Analysis*, Vol. 10, pp. 13-24.

Chandawanich, N. and Sharpe, W.N., Jr., 1979, "An Experimental Study of Fatigue Crack Initiation and Growth From Coldworked Holes," *Engineering Fracture Mechanics*, Vol. 11, pp. 609-620.

Chang, J.B., 1977, "Prediction of Fatigue Crack Growth at Cold-Worked Fastener Holes," *Journal of Aircraft*, Vol. 14, No. 9, pp. 903-908.

Cheong, W., Zhuang, W., and Zhang, L., 2004, "Study of Residual Stress Relaxation Using X-Ray Diffraction," *Key Engineering Materials*, Vols. 274-276, pp. 871-876.

Childs, W.H., 1988, "The Effect of Elevated Temperature on Shot Peened 403 Stainless Steel," *Analytical and Experimental Methods for Residual Stress Effects in Fatigue, ASTM STP 1004*, Champoux, Underwood, and Kapp, editors, American Society for Testing and Materials, pp. 21-24.

Clark, D.A. and Johnson, W.S., 2003, "Temperature Effects on Fatigue Performance of Cold Expanded Holes in 7050-T7451 Aluminum Alloy," *International Journal of Fatigue*, Vol. 25, pp. 159-165.

Clark, G., 1984, "Fatigue Crack Growth Through Residual Stress Fields – Theoretical and Experimental Studies on Thick-Walled Cylinders," *Theoretical and Applied Fracture Mechanics*, Vol. 2, pp. 111-125.

Clark, G., 1991, "Modelling Residual Stresses and Fatigue Crack Growth at Cold-Expanded Fastener Holes," *Fatigue and Fracture of Engineering Materials and Structures*, Vol. 14, No. 5, pp. 579-589.

Dalle Donne, C. and Raimbeaux, G., December 2001, "Residual Stress Effects on Fatigue Crack Propagation in Friction Stir Welds," *Advances in Fracture Research, ICF10*, Proc. 10th International Conference on Fracture, Honolulu, Hawaii, Paper 125.

Dattoma, V., DeGiorgi, M., and Nobile, R., 2004, "Numerical Evaluation of Residual Stress Relaxation by Cyclic Load," 2004, *Journal of Strain Analysis*, Vol. 39, No. 6, pp. 663-672.

De Los Rios, E.R., Walley, A., Milan, M.T., and Hammersley, G., 1995, "Fatigue Crack Initiation and Propagation on Shot-Peened Surfaces in A316 Stainless Steel," *International Journal of Fatigue*, Vol. 17, pp. 493-499.

De Los Rios, E.R., Mercier, P., and El-Sehily, B.M., 1996, "Short Crack Growth Behaviour Under Variable Amplitude Loading of Shot Peened Surfaces," *Fatigue and Fracture of Engineering Materials and Structures*, Vol. 19, No. 2/3, pp. 175-184.

De Los Rios, E.R., Trull, M., and Levers, A., 2000, "Modelling Fatigue Crack Growth in Shot-Peened Components of Al 2024-T351," *Fatigue and Fracture of Engineering Materials and Structures*, Vol. 23, pp. 709-716.

Dorr, T. and Wagner, L., 1999, "Fatigue Response of Various Titanium Alloys to Shot Peening," *Surface Treatment IV: Computer Methods and Experimental Measurements*, Proc. 4th International Conference on Computer Methods and Experimental Measurements for Surface Treatment Effects, Assisi, Italy, pp. 349-357.

Eigenmann, B., Schulze, V., and Vöhringer, O., 1994, "Surface Residual Stress Relaxation in Steels by Thermal or Mechanical Treatment," *Proc. 4th International Conference on Residual Stresses*, Baltimore, Maryland, pp. 598-607.

Eigenmann, B., 1995, "Residual Stresses Due to Thermal, Thermo-Chemical, and Mechanical Surface Treatments: Generation, Determination, Evaluation," *Computer Methods and Experimental Measurements for Surface Treatment Effects II*, Proc. International Conference on Computer Methods and Experimental Measurements for Surface Treat, pp. 17-25.

Elber, W., 1974, "Effects of Shot-Peening Residual Stresses on the Fracture and Crack-Growth Properties of D6AC Steel," *Fracture Toughness and Slow-Stable Cracking, ASTM STP 559*, American Society for Testing and Materials, pp. 45-58.

Esquivel, A.L. and Evans, K.R., 1968, "X-ray Diffraction Study of Residual Macrostresses in Shot-Peened and Fatigued 4130 Steel," *Experimental Mechanics*, pp. 496-503.

Everett, R.A., Jr., Matthews, W.T., Prabhakaran, R., Newman, J.C., Jr., and Dubberly, M.J., December 2000, "The Effects of Shot and Laser Peening on Crack Growth and Fatigue Life in 2024 Aluminum Alloy and 4340 Steel," USAF Structural Integrity Program Conference, San Antonio, Texas.

Ezeilo, A., Webster, G., Webster, P.J., and Webster, P.S., 1993, "Comparison of Shot Peening Residual Stress Distributions in a Selection of Materials," *Proc. 5th International Conference on Shot Peening (ICSP5)*, Oxford, UK, D. Kirk, editor, pp. 275-282.

Ezelio, A.N., Webster, P.S., Webster, G.A, and Webster, P.J., 1994, "Influence of Cyclic Loading on Residual Stress Distribution Caused by Cold Hole Expansion, *Proc. 4th International Conference on Residual Stresses*, Baltimore, Maryland, pp. 1275-1284.

Farrahi, G.H., LeBrun, J.L., and Couratin, D., 1995, "Effect of Shot Peening on Residual Stress and Fatigue Life of a Spring Steel," *Fatigue and Fracture of Engineering Materials and Structures*, Vol. 18, No. 2, pp. 211-220.

Fitzpatrick, M.E. and Edwards, L., 1998, "Fatigue Crack/Residual Stress Field Interactions and Their Implications for Damage-Tolerant Design," *Journal of Materials Engineering and Performance*, Vol. 7, No. 2, pp. 190-198.

Flavenot, J.F. and Skalli, N., 1988, "Effects of Grinding Conditions on Fatigue Behavior of 42CD4 Grade Steel; Comparison of Different Fatigue Criteria Incorporating Residual Stresses," *Mechanical Relaxation of Residual Stresses, ASTM STP 993*, L. Mordfin, ed., American Society for Testing and Materials, pp. 91-111.

Fontanari, V., Frendo, F., Rosellini, W., and Scardi, P., 2001, "Analysis of Residual Stress Distribution in Shot Peened Al 6082 T5 Alloy Subjected to Fatigue Loading," *Surface Treatment V*, Proc. 5th Int. Conf. on Computer Methods and Experimental Measurements for Surface Treatment Effects, pp. 333-342.

Fukuda, S., Watari, S., and Horikawa, K., 1979, "An Experimental Study of Effect of Welding Residual Stress Upon Fatigue Crack Propagation Based on Observation of Crack Opening and Closure," *Transactions of Japan Welding Research Institute*, Vol. 8, No. 2, pp. 265-271.

Fukuda, S. and Tsuruta,Y., 1979, "A Preliminary Study of the Influence of Welding Residual Stress Upon Fatigue Crack Propagation," *Recent Research on Mechanical Behavior of Solids*, University of Tokyo Press, pp. 401-419.

Fukuda, S. and Sugino, M., 1980, "A Numerical Study of the Effect of Welding Residual Stress Upon Fatigue Crack Propagation With Attention Paid to the Phenomenon of Crack Opening and Closure," *Numerical Methods in Fracture Mechanics*, pp. 615-629.

Fukuda, S., 1989, "Analysis of Crack Propagation in Residual Stress Field Using Computer Algebra," *Nuclear Engineering and Design 111*, pp. 21-15.

Gabb, T.P., Telesman, J., Kantzos, P.T., Bonacuse, P.J., Barrie, R.L., and Hornbach, D.J., 2004, "Stress Relaxation in Powder Metallurgy Superalloy Disks," *TMS Letters*, Vol. 1, No. 5, pp. 115-116.

Garcia-Granada, A.A., Lacarac, V.D., Holdway, P., Smith, D.J., and Pavier, M.J., 2001, "Creep Relaxation of Residual Stresses Around Cold Expanded Holes," *Journal of Engineering Materials and Technology*, Vol. 123, pp. 125-131.

Glinka, G., 1979, "Effect of Residual Stresses on Fatigue Crack Growth in Steel Weldments Under Constant and Variable Amplitude Loads," *Fracture Mechanics, ASTM STP 677*, C.W. Smith, editor, American Society for Testing and Materials, pp. 198-214.

Glinka, G., 1987, "Residual Stresses in Fatigue and Fracture: Theoretical Analyses and Experiments," Advances in Surface Treatment and Residual Stresses, A. Niku-Lari, ed., Pergamon Press, pp. 413-454.

Gong, Y. and Norton, M., 1999, "Cyclic Response and Fatigue of Steels Subjected to Strain Control With Non-Zero Means," *Journal of Testing and Evaluation*, Vol. 27, pp. 15-30.

Gould, R. W. and Pittella, C.F., 1972, "An X-Ray Investigation of Fatigue Behavior of Cold Worked Aluminum," Proc., 21st Annual Conference on Applications of X-Ray Analysis, Denver, Colorado, L.S. Birks, C.S. Barrett, J.B. Newkirk, and C.O. Ruud, editors, Plenum Press, *Advances in X-Ray Analysis*, Vol. 16, pp. 354-366.

Grandt, A.F., Jr., 1975, "Stress Intensity Factors for Some Through-Cracked Fastener Holes," *International Journal of Fracture*, Vol. 11, No. 2, pp. 283-294.

Grandt, A.F., Jr., 1978, "Stress Intensity Factors for Cracked Holes and Rings Loaded With Polynomial Crack Face Pressure Distributions," *International Journal of Fracture*, Vol. 14, pp. R221-R229.

Gray, H., Wagner, L., and Lutjering, G., 1987, "Influence of Shot Peening Induced Surface Roughness, Residual Macrostresses and Dislocation Density on the Elevated Temperature HCF-Properties of Ti Alloys," *Proc. 3rd International Conference on Shot Peening (ICSP3)*, Garmisch-Partenkirchen, Germany, H. Wohlfahrt, R. Kopp, and O. Vöhringer, editors, DGM Informationsgesellschaft Verlag, Oberursel, pp. 447-457.

Guo, W., 1993, "Elastic-Plastic Analysis of a Finite Sheet With a Cold-Worked Hole," *Engineering Fracture Mechanics*, Vol. 46, No. 3, pp. 465-472.

Hack, J.E. and Leverant, G.R., 1982, "Influence of Compressive Residual Stress on the Crack-Opening Behavior of Part-Through Fatigue Cracks," *Residual Stress Effects in Fatigue, ASTM STP 776*, American Society for Testing and Materials, pp. 204-223.

Hammond, D.W. and Meguid, S.A., 1990, "Crack Propagation in the Presence of Shot-Peening Residual Stresses," *Engineering Fracture Mechanics*, Vol. 37, No. 2, pp. 373-387.

Han, Lee, S.T., and Shin, B., 2002, "Residual Stress Relaxation of Welded Steel Components Under Cyclic Load," *Materials Technology*, Vol. 73, No. 9, pp. 414-420.

Hanagarth, H., Vöhringer, O., and Macherauch, E., 1990, "Relaxation of Shot Peening Residual Stresses of the Steel 42 CrMo 4 by Tensile or Compressive Deformation," *Proc. 4th International Conference on Shot Peening (ICSP4)*, Tokyo, K. Iida, editor, Japan Society of Precision Engineering, pp. 337-345.

Happ, M.B., Mourer, D.P., and Schmidt, R.L., 1987, "Residual Stress Analysis and LCF Test Results for Peened Bolt Hole and Dovetail Configureurations," *Proc. ASM Conference on Residual Stress in Design, Process and Materials Selection*, Cincinnati, Ohio, ASM International, pp. 127-136.

Heller, M., Jones, R., and Williams, J.F., 1991, "Analysis of Cold-Expansion for Cracked and Uncracked Fastener Holes," *Engineering Fracture Mechanics*, Vol. 39, No. 2, pp. 195-212.

Hermann, R. and Moffatt, J., 1991, "Experiments and Analysis of the Fatigue Life Improvements in Fastener Holes of Aluminium-Lithium Alloy 2091," *Proc., International Aluminum-Lithium Conference*, Garmisch-Partenkirchen, Germany, pp. 621-626.

Hoffmann, J., Scholtes, B., Vöhringer, O., and Macherauch, E., 1987, "Thermal Relaxation of Shot Peening Residual Stresses in the Differently Heat Treated Plain Carbon Steel Ck 45," *Proc. 3rd International Conference on Shot Peening (ICSP3)*, Garmisch-Partenkirchen, Germany, H. Wohlfahrt, R. Kopp, and O. Vöhringer, editors, DGM Informationsgesellschaft Verlag, Oberursel, pp. 239-246.

Holzapfel, H., Schulze, V., Vöhringer, O., and Macherauch, E., 1996a, "Relaxation Behaviour of Shot Peening Induced Residual Stresses in AISI 4140 due to Quasistatic Uniaxial Loading at Elevated Temperatures," *Proc. 6th International Conference on Shot Peening (ICSP6)*, San Francisco, J. Champaigne, editor, pp. 385-396.

Holzapfel, H., Schulze, V., Vöhringer, O., and Macherauch, E., 1996b, "Stability and Relaxation Behaviour of Shot Peening Induced Residual Stresses in AISI 4140 During Bending Fatigue," *Proc. 6th International Conference on Shot Peening (ICSP6)*, San Francisco, J. Champaigne, editor, pp. 413-423.

Holzapfel, H., Schulze, V., Vöhringer, O., and Macherauch, E., 1998, "Residual Stress Relaxation in an AISI 4140 Steel Due to Quasistatic and Cyclic Loading at Higher Temperatures," *Materials Science & Engineering A*, Vol. A248, pp. 9-18.

Honda, T., Ramulu, M., and Kobayashi, A., 2005, "Effect of Shot Peening on Fatigue Crack Growth in 7075-T7351," *Journal of ASTM International*, Vol. 2, Issue 6, Paper ID JAI12569.

Hsu, Y.C. and Forman, R.G., 1975, "Elastic-Plastic Analysis of an Infinite Sheet Having a Circular Hole Under Pressure," *Journal of Applied Mechanics, Trans. ASME*, Vol. 42, No. 2, pp. 347-352.

Iida, K. and Taniguchi, K., 1996, "Relaxation of Residual Stress Distribution Produced by Shot Peening Under Fatigue Test," *Proc. 6th International Conference on Shot Peening (ICSP6)*, San Francisco, J. Champaigne, editor, pp. 397-402.

Iida, K., Yamamoto, S., and Takanashi, M., 1997, "Residual Stress Relaxation by Reversed Loading," *Welding in the World/Le Soudage dans le Monde*, Vol. 39, No. 3, pp. 138-144.

Iida, K. and Takanashi, M., 1998, "Relaxation of Welding Residual Stresses by Reversed and Repeated Loadings, *Welding in the World*, Vol. 41, pp. 314-327.

Iida, K. and Hirose, Y., 1999, "The Residual Stress Distribution in Shot Peened Carburized Steel Under Fatigue," *Proc. 7th International Conference on Shot Peening*, Warsaw, Poland, pp. 96-101.

Itoh, Y.Z., Suruga, S., and Kashiwaya, H., 1989, "Prediction of Fatigue Crack Growth Rate in Welding Residual Stress Field," *Engineering Fracture Mechanics*, Vol. 33, No. 3, pp. 397-407.

James, M.R. and Morris, W.L., 1981, "The Relaxation of Machining Stresses in Aluminum Alloys During Fatigue," *Residual Stress for Designers and Metallurgists*, ASM, pp. 169-188.

James, M.R., 1982, "The Relaxation of Residual Stresses During Fatigue," *Residual Stress and Stress Relaxation*, Proc. 28th Sagamore Army Materials Research Conference, Lake Placid, New York, pp. 297-314.

James, M.N., Hattingh, D.G., Hughes, D.J., Wei, L.-W., Patterson, E.A., and Quintana Da Fonseca, J., 2004, "Synchrotron Diffraction Investigation of the Distribution and Influence of Residual Stresses in Fatigue," *Fatigue and Fracture of Engineering Materials and Structures*, Vol. 27, pp. 609-622.

Jhansale, H.R. and Topper, T.H., 1973, "Engineering Analysis of the Inelastic Stress Response of a Structural Metal Under Variable Cyclic Strains," *Cyclic Stress-Strain Behavior—Analysis, Experimentation, and Failure Prediction, ASTM STP 519*, American Society for Testing and Materials, pp. 246-270.

John, R., Larsen, J.M., Buchanan, D.J., and Ashbaugh, N.E., Oct. 8-11, 2001, "Incorporating Residual Stresses in Life Prediction of Turbine Engine Disks," NATO RTO (AVT) Symp. on Monitoring and Management of Gas Turbine Fleets for Extended Life and Reduced Costs.

John, R., Larsen, J.M., Buchanan, D.J., and Ashbaugh, N.E., 2002, "Incorporating Residual Stresses in Life Prediction of Turbine Engine Components," *Fatigue 2002, Proc. 8th International Fatigue Congress, Stockholm*, EMAS, Vol. 2, pp. 1063-1070.

Kang, K.J., Song, J.H., and Earmme, Y.Y., 1989, "Fatigue Crack Growth and Closure Through a Tensile Residual Stress Field Under Compressive Applied Loading," *Fatigue and Fracture of Engineering Materials and Structures*, Vol. 12, No. 5, pp. 363-376.

Kang, K.J., Song, J.H., and Earmme, Y.Y., 1990, "Fatigue Crack Growth and Closure Behaviour Through a Compressive Residual Stress Field," *Fatigue and Fracture of Engineering Materials and Structures*, Vol. 13, No. 1, pp. 1-13.

Kang, J., Johnson, W.S., and Clark, D.A., 2002, "Three-Dimensional Finite Element Analysis of the Cold Expansion of Fastener Holes in Two Aluminum Alloys," *Journal of Engineering Materials and Technology, Transactions of the ASME*, Vol. 124, pp. 140-145.

Khadhraoui, M., Cao, W., Castex, L., and Guedou, J.Y., 1997, "Experimental Investigations and Modelling of Relaxation Behaviour of Shot Peening Residual Stresses at High Temperature for Nickel Base Superalloys," *Materials Science and Technology*, Vol. 13, pp. 360-367.

Khanna, S.K., He, C., and Agrawal, H.N., 2001, "Residual Stress Measurement in Spot Welds and the Effect of Fatigue Loading on Redistribution of Stresses Using High Sensitivity Moire Interferometry," *Journal of Engineering Materials and Technology, Transactions of the ASME*, Vol. 123, pp. 132-138.

Kirk, D., 1987, "Effects of Plastic Straining on Residual Stresses Induced by Shot Peening," *Proc. 3rd International Conference on Shot Peening (ICSP3)*, Garmisch-Partenkirchen, Germany, H. Wohlfahrt, R. Kopp, and O. Vöhringer, editors, DGM Informationsgesellschaft Verlag, Oberursel, pp. 213-220.

Kodama, S., 1972, "The Behaviour of Residual Stress During Fatigue Stress Cycles," *Proc. International Conference of Mechanical Behavior of Materials*, Vol. II, pp. 111-118.

Kokaly, M.T., Ransom, J.S., Restis, J.H., and Reid, L., 2005a, "Observations and Analysis of Fatigue Crack Growth From Cold Expanded Holes," *Proc. 8th Joint NASA/FAA/DoD Conference on Aging Aircraft*, Palm Springs, California.

König, G., 2002, "Life Enhancement of Aero Engine Components by Shot Peening: Opportunities and Risks," *Proc. 8th International Conference on Shot Peening (ICSP-8)*, Garmisch-Partenkirchen, Germany, L. Wagner, editor, Wiley-VCH GmbH & Co. KGaA, pp. 13-22.

Krull, P., Nitschke-Pagel, Th., and Wohlfahrt, H., 1999, "Stability of Residual Stresses in Shot Peened and High Pressure Water Peened Stainless Steels at Elevated Temperatures," *Proc. 7th International Conference on Shot Peening (ICSP7)*, Warsaw, Poland, A. Nakonieczny, editor, Institute of Precision Mechanics.

Kuhn, G., Hoffmann, J.E., Eifler, D., Scholtes, B., and Macherauch, E., 1991, "Instability of Machining Residual Stresses in Differently Heat Treated Notched Parts of SAE 1045 During Cyclic Deformation," *Residual Stresses—III: Science and Technology*, Proc. International Conference on Residual Stresses, Elsevier Applied Science, Vol. 2, pp. 1294-1301.

Lacarac, V.D., Smith, D.J., and Pavier, M.J., 2001, "The Effect of Cold Expansion on Fatigue Crack Growth From Open Holes at Room and High Temperature," *International Journal of Fatigue*, Vol. 23, pp. S161-S170.

Lachmann, C., Nitschke-Pagel, Th., and Wohlfahrt, H., 2000, "Characterisation of Residual Stress Relaxation in Fatigue Loaded Welded Joints by X-Ray Diffraction and Barkhausen Noise Method," ECRS 5, *Proc of the 5th European Conference on Residual Stresses*, Delft-Noordwijkerhout, the Netherlands, *Materials Science Forum*, Vol. 347, No. 3, pp. 374-379.

Lautridou, J.C. and DuQuenne, C., 1996, "Effect of Shot-Peening on the Fatigue Strength of Nickel-Based Super-Alloys Produced by Powder Metallurgy," *Bulletin du Cercle d'âetudes des mâetaux*, Vol. 16, No. 12, pp. 21.1-21.10.

Lee, H. and Mall, S., 2004, "Stress Relaxation Behavior of Shot-Peened Ti-6Al-4V Under Fretting Fatigue at Elevated Temperature," *Materials Science and Engineering*, Vol. A366, pp. 412-420.

Lee, H. and Mall, S., 2005, "Fretting Fatigue and Stress Relaxation Behaviors of Shot-Peened Ti-6Al-4V," *Journal of ASTM International*, Vol. 2, Issue 5, Paper ID JAI12031.

Leverant, G.R., Langer, B.S., Yuen, A., and Hopkins, S.W., 1979, "Surface Residual Stresses, Surface Topography and the Fatigue Behavior of Ti-6Al-4V," *Metallurgical Transactions A*, Vol. 10A, pp. 251-257.

Lindermann, J., Grossmann, K., Raczek, T., and Wagner, L., 2002, "Influence of Shot Peening and Deep Rolling on High Temperature Fatigue of the Ni-Superalloy Udimet 720 LI," *Proc. 8th International Conference on Shot Peening (ICSP-8)*, Garmisch-Partenkirchen, Germany, L. Wagner, editor, Wiley-VCH GmbH & Co. KGaA, pp. 454-460.

Lindgren, M. and Lepistö, T., 2002, "Effect of Mean Stress on Residual Stress Relaxation in Steel Specimens," *Materials Science and Technology*, Vol. 18, pp. 845-849.

Löhe, D., Lang, K.-H., and Vöhringer, O., 2002, "Residual Stress and Fatigue Behavior," *Handbook of Residual Stress and Deformation of Steel*, G. Totten, M. Howes, T. Inoue, editors, ASM International, Materials Park, Ohio, pp. 27-53.

Löhe, D. and Vöhringer, O., 2002, "Stability of Residual Stresses," *Handbook of Residual Stress and Deformation of Steel*, G. Totten, M. Howes, T. Inoue, editors, ASM International, Materials Park, Ohio, pp. 54-69.

Lopez Martinez, L., Lin, R., Want, D., and Blom, A.F., 1997, "Investigation of Residual Stresses in As-Welded and TIG-Dressed Specimens Subjected to Static/Spectrum Loading," *Proc. of the North European Engineering and Science Conference (NESC)*): "Welded High-Strength Steel Structures," Stockholm, Sweden, A.F. Blom, editor, EMAS Publishing, London, England,.

Lu, J. and Flavenot, J.F., 1987, "Use of a Finite Element Method for the Prediction of the Shot-Peened Residual Stress Relaxation during Fatigue," *Proc. 3rd International Conference on Shot Peening (ICSP3)*, Garmisch-Partenkirchen, Germany, H. Wohlfahrt, R. Kopp, and O. Vöhringer, editors, DGM Informationsgesellschaft Verlag, Oberursel, pp. 391-398.

Lu, J. and Flavenot, J.F., 1988, "Prediction of Residual Stress Relaxation During Fatigue Loading and Taking Residual Stresses in a Multiaxial Fatigue Criteria Into Account," International Conference on Residual Stresses, Nancy, France, G. Beck, S. Denis, and A. Simon, editors, pp. 784-790.

Lu, J., Flavenot, J.F., and Turbat, A., 1988, "Prediction of Residual Stress Relaxation During Fatigue," *Mechanical Relaxation of Residual Stresses*, *ASTM STP 993*, L. Mordfin, editor, American Society for Testing and Materials, pp. 75-90.

Lu, J., 2002, "Prestress Engineering of Structural Material: A Global Design Approach to the Residual Stress Problem," *Handbook of Residual Stress and Deformation of Steel*, G. Totten, M. Howes, T. Inoue, editors, ASM International, Materials Park, Ohio, pp. 11-26.

Mann, J.Y. and Jost, G.S., 1983, "Stress Fields Associated With Interference Fitted and Cold-Expanded Holes," *Metals Forum*, Vol. 6, No. 1, pp. 43-53.

Martin, J.F., Topper, T.H., and Sinclair, G.M., 1971, "Computer Based Simulation of Cyclic Stress-Strain Behavior With Applications to Fatigue," *Materials Research and Standards*, Vol. 11, No. 2, pp. 23-28.

Masmoudi, N. and Castex, L., 1988, "The Effect of Temperature and Time on the Stress Relaxation of Shot Peened Nickel Based Superalloy IN100," International Conference on Residual Stresses, Nancy, France, G. Beck, S. Denis, and A. Simon, editors, pp. 710-715.

McClinton, M. and Cohen, J.B., 1982, "Changes in Residual Stress During the Tension Fatigue of Normalized and Peened SAE 1040 Steel," *Materials Science and Engineering*, Vol. 56, pp. 259-263.

Meguid, S.A. and Hammond, D.W., 1989, "Fatigue Fracture and Residual Stress Relaxation in Shot-Peened Components," *Proc. 2nd International Conference on Residual Stresses, ICRS 2*, Nancy, France, pp. 797-802.

Meguid, S., Shagal, G., Stranart, J., Liew, K., and Ong, L., 2005, "Relaxation of Peening Residual Stresses Due to Cyclic Thermo-Mechanical Overload," *ASME Journal of Engineering Materials and Technology*, Vol. 127, pp. 170-178.

Meister, T.J., 1996, "Overcoming Detrimental Residual Stress in Titanium by the Shot Peening Process," *Surface Performance of Titanium*: *Proc. Symp. on Surface Performance of Titanium*, Cincinnati, Ohio, TMS, pp. 253-263.

Menig, R., Schulze, V., and Vöhringer, O., 2002a, "Residual Stress Relaxation and Fatigue Strength of AISI 4140 Under Torsional Loading After Conventional Shot Peening, Stress Peening, and Warm Peening," *Proc. 8th International Conference on Shot Peening (ICSP-8)*, Garmisch-Partenkirchen, Germany, L. Wagner, editor, Wiley-VCH GmbH & Co. KGaA, pp. 311-316.

Menig, R, Schulze, V., and Vöhringer, O., 2002b, "Influence of Optimized Warm Peening on Residual Stress Stability and Fatigue Strength of AISI 4140 in Different Material States," *Proc. 8th International Conference on Shot Peening (ICSP-8)*, Garmisch-Partenkirchen, Germany, L. Wagner, editor, Wiley-VCH GmbH & Co. KGaA, pp. 317-323.

Menig, R., Schulze, V., and Vöhringer, O., 2002c, "Comparison of Surface Characteristics and Thermal Residual Stress Relaxation of Laser Peened and Shot Peened AISI 4140," *Proc. 8th International Conference on Shot Peening (ICSP-8)*, Garmisch-Partenkirchen, Germany, L. Wagner, editor, Wiley-VCH GmbH & Co. KGaA, pp. 498-504.

Misumi, M. and Ohkubo, M., 1987, "Deceleration of Small Crack Growth by Shot-Peening," *International Journal of Materials and Product Technology*, Vol. 2, No. 1, pp. 36-47.

Miyamoto, H., Miyoshi, T., and Fukuda, S., 1973, "An Analysis of Crack Propagation in Welded Structures," *Significance of Defects in Welded Structures*, Proceedings of the Japan-U.S. Seminar, Tokyo, pp. 189-202.

Miyazaki, K., Mochizuki, M., Kanno, S., Hayashi, M., Shiratori, M., and Yu, Q., 2002, "Analysis of Stress Intensity Factor Due to Surface Crack Propagation in Residual Stress Fields Caused by Welding," *Japan Society of Mechanical Engineers International Journal*, Series A, Vol. 45, No. 2, pp. 199-207.

Moreira, P., De Matos, P., Pinho, S., Pastramă, S., and Camanho, P., 2004, "The Residual Stress Intensity Factors for Cold-Worked Crack Holes: A Technical Note," *Fatigue and Fracture of Engineering Materials and Structures*, Vol. 27, pp. 879-886.

Morrow, J. and Sinclair, G.M., 1958, "Cycle-Dependent Stress Relaxation," *Symposium on Basic Mechanisms of Fatigue, ASTM STP 237*, pp. 83-99.

Morrow, J., Ross, A.S., and Sinclair, G.M., 1960, "Relaxation of Residual Stresses Due to Fatigue Loading," *SAE Transactions*, Vol. 68, pp. 40-48.

Mutoh, Y., Fair, G.H., Noble, B., and Waterhouse, R.B., 1987, "The Effect of Residual Stresses Induced by Shot-Peening on Fatigue Crack Propagation in Two High Strength Aluminium Alloys," *Fatigue and Fracture of Engineering Materials and Structures*, Vol. 10, No. 4, pp. 261-272.

Nalla, R.K., Altenberger, I., Noster, U., Liu, G.Y., Scholtes, B., and Ritchie, R.O., 2003, "On the Influence of Mechanical Surface Treatments—Deep Rolling and Laser Shock Peening—on the Fatigue Behavior of TI-6AL-4V at Ambient and Elevated Temperatures," *Materials Science and Engineering*, Vol. A355, pp. 216-230.

Natkaniec-Kocanda, D., Kocanda, S., and Miller, K.J., 1996, "Influence of Shot-Peening on Short Crack Behavior in a Medium Carbon Steel," *Fatigue and Fracture of Engineering Materials and Structures*, Vol. 19, No. 7, pp. 911-917.

Neff, P.J., 1981, "A Quantitative Evaluation of Surface Residual Stress and its Relation to Fatigue Performance," *Residual Stress for Designers and Metallurgists*, L.J. VandeWalle, editor, ASM, pp. 119-135.

Nelson, D.V., 1982, "Effects of Residual Stress on Fatigue Crack Propagation," *Residual Stress Effects in Fatigue, ASTM STP 776*, American Society for Testing and Materials, pp. 172-194.

Nikitin, I., B. Scholtes, H. Maier, and I. Altenberger, 2004, "High Temperature Fatigue Behavior and Residual Stress Stability of Laser-Shock Peened and Deep Rolled Austenitic Steel AISI 304," *Scripta Materialia*, Vol. 50, pp. 1345-1350.

Nitschke-Pagel, Th. and Wohlfahrt, H., 2000, "Residual Stress Relaxation in Welded High Strength Steels Under Different Loading Conditions," *Proc. 6th International Conference on Residual Stresses: ICRS-6*, Oxford, UK, pp. 1495-1502.

Noster, U., Altenberger, I., Ritchie, R., and Scholtes, B., 2002, "Isothermal Fatigue Behavior and Residual Stress States of Mechanically Surface Treated Ti-6Al-4V: Laser Shock Peening vs. Deep Rolling," *Proc. 8th International Conference on Shot Peening (ICSP-8)*, Garmisch-Partenkirchen, Germany, L. Wagner, editor, Wiley-VCH GmbH & Co. KGaA, pp. 447-453.

Ohta, A., Kosuge, M., Mawari, T., and Nishijima, S., 1988, "Fatigue Crack Propagation in Tensile Residual Stress Fields of Welded Joints Under Fully Compressive Cycling," *International Journal of Fatigue*, Vol. 10, No. 4, pp. 237-242.

Ohta, A., McEvily, A.J., and Suzuki, N., 1993, "Fatigue Crack Propagation in a Tensile Residual Stress Field Under a Two-Step Programmed Test," *International Journal of Fatigue*, Vol. 15, No. 1, pp. 9-12.

Özdemir, A.T. and Edwards, L., 1996, "Measurement of the Three-Dimensional Residual Stress Distribution Around Split-Sleeve Cold-Expanded Holes," *Journal of Strain Analysis*, Vol. 31, No. 6, pp. 413-421.

Özdemir, A.T. and Edwards, L., 1997, "Relaxation of Residual Stresses at Cold-Worked Fastener Holes Due to Fatigue Loading," *Fatigue and Fracture of Engineering Materials and Structures*, Vol. 20, No. 10, pp. 1443-1451.

Papanikos, P. and Meguid, S.A., 1998, "Three-Dimensional Finite Element Analysis of Cold Expansion of Adjacent Holes," *International Journal of Mechanical Science*, Vol. 40, No. 10, pp. 1019-1028.

Park, E.J., Kim, E.J. and Yoo, S.H., 2004, "Prediction of the Crack Opening Behaviour for the Fatigue Crack Propagating in Welding Residual Stress Field," *Key Engineering Materials*, Vols. 270-273, No. Pt. 1-3, pp. 96-101.

Parker, A.P., 1982, "Stress Intensity Factors, Crack Profiles, and Fatigue Crack Growth Rates in Residual Stress Fields," *Residual Stress Effects in Fatigue, ASTM STP 776*, American Society for Testing and Materials, pp. 13-31.

Pattinson, E.J. and Dugdale, D.S., 1962, "Fading of Residual Stresses Due to Repeated Loading," *Metallurgia*, Vol. 66, pp. 228-230.

Pavier, M J., Poussard, C.G.C., and Smith, D.J., 1997, "A Finite Element Simulation of the Cold Working Process for Fastener Holes," *Journal of Strain Analysis*, Vol. 32, No. 4, pp. 287-300.

Pavier, M.J., Poussard, C.G.C. and Smith, D.J., 1998, "Finite Element Modelling of the Interaction of Residual Stress With Mechanical Load for a Crack Emanating from a Cold Worked Fastener Hole," *Journal of Strain Analysis*, Vol. 33, No. 4, pp. 275-289.

Pavier, M.J., Poussard, C.G.C., and Smith, D.J., 1999, "Effect of Residual Stress Around Cold Worked Holes on Fracture Under Superimposed Mechanical Load," *Engineering Fracture Mechanics*, Vol. 63, No. 6, pp. 751-773.

Pell, R.A., Beaver, P.W., Mann, J.Y., and Sparrow, J.G., 1989, "Fatigue of Thick-Section Cold-Expanded Holes With and Without Cracks," *Fatigue and Fracture of Engineering Materials and Structures*, Vol. 12, No. 6, pp. 553-567.

Phillips, J. L., 1974, "Sleeve Coldworking Fastener Holes," Vol. 1, AFML-TR-74-10, Air Force Materials Laboratory, Wright-Patterson AFB, Ohio.

Potter, J.M. and Millard, R.A., 1976, "The Effect of Temperature and Load Cycling on the Relaxation of Residual Stresses," *Proc. 25th Conference on Application of X-Ray Analysis*, H.F. McMurdie, C.S. Barrett, J.B. Newkirk, and C.O. Ruud, editors, pp. 309-319.

Poussard, C., Pavier, M.J., and Smith, D.J., 1995, "Analytical and Finite Element Predictions of Residual Stresses in Cold Worked Fastener Holes," *Journal of Strain Analysis*, Vol. 30, No. 4, pp. 291-304.

Prawoto, Y. and Winholtz, R.A., December 2001, "Fatigue Crack Growth With Tensile Residual Stresses," *Advances in Fracture Research, ICF10, Proc. 10th International Conference on Fracture*, Honolulu, Hawaii, Paper 983, 2001,.

Prevéy, P.S., Hornbach, D.J., and Mason, P.W., 1997, "Thermal Residual Stress Relaxation and Distortion in Surface Enhanced Gas Turbine Engine Components," *Proc. 17th Heat Treating Society Conference and Exposition and the 1st International Induction Heat Treating Symposium*, Indianapolis, Indiana, ASM, pp. 3-12.

Prevéy, P.S., 2000, "The Effect of Cold Work on the Thermal Stability of Residual Compression in Surface Enhanced IN718," *Proc. 20th ASM Materials Solutions Conference & Exposition*, St. Louis, Missouri, pp. 426-434.

Prevéy, P.S., Telesman, J., Gabb, T., and Kantzos, P., 2000, "FOD Resistance and Fatigue Crack Arrest in Low Plasticity Burnished IN718," *Proc. 5th National Turbine Engine High Cycle Fatigue Conference*, Chandler, Arizona.

Prevéy, P.S., Shepard, M.J., and Smith, P.R., 2001, "The Effect of Low Plasticity Burnishing on the HCF Performance and FOD Resistance of Ti-6Al-4V," *Proc. 6th National Turbine Engine High Cycle Fatigue (HCF) Conference*, Jacksonville, Florida.

Prevéy, P. and Cammett, J., 2002, "The Effect of Shot Peening Coverage on Residual Stress, Cold Work and Fatigue in a Ni-Cr-Mo Low Alloy Steel," *Proc. 8th International Conference on Shot Peening (ICSP-8)*, Garmisch-Partenkirchen, Germany, L. Wagner, ditor, Wiley-VCH GmbH & Co. KGaA, pp. 293-304.

Prevéy, P.S., Hornbach, D., Ravindranath, R., and Cammett, J.T., 2003a, "Application of Low Plasticity Burnishing to Improve Damage Tolerance of a Ti-6Al-4V First Stage Fan Blade," *Proc. 44th AIAA/ASME/ASCE/AHS Structures*, Structural Dynamics & Materials Conference, Norfolk, Virginia.

Prevéy, P.S., Jayaraman, N., and Ravindranath, R.A., 2003b, Effect of Surface Treatments on HCF Performance and FOD Tolerance of a Ti-6Al-4V Vane," *Proc. 8th National Turbine Engine High Cycle Fatigue (HCF) Conference*, Monterey, California.

Prevéy, P.S., Jayaraman, N., and Shepard, M.J., 2004, "Improved HCF Performance and FOD Tolerance of Surface Treated Ti-6-2-4-6 Compressor Blades," *Proc. 9th National Turbine Engine High Cycle Fatigue Conference*, Pinehurst, North Carolina.

Qui, Q., and Wang, R., 1987, "Changes in the State of the Material by Shot Peening," *Proc. 3rd International Conference on Shot Peening (ICSP3)*, Garmisch-Partenkirchen, Germany, H Wohlfahrt, R. Kopp, and O. Vöhringer, editors, DGM Informationsgesellschaft Verlag, Oberursel, pp. 231-238.

Radhakrishnan, V.M. and Prasad, C.R., 1976, "Relaxation of Residual Stress With Fatigue Loading," *Engineering Fracture Mechanics*, Vol. 8, pp. 593-597.

Rasouli Yazdi, S. and Lu, J., 1999, "Prediction of Relaxation of Residual Stress Induced by Shot Peening in Aluminum Alloys," *Proc. SEM Annual Conference on Theoretical, Experimental, and Computational Mechanics*, pp. 880-883.

Reed, E.C. and Viens, J.A., 1960, "The Influence of Surface Residual Stress on Fatigue Limit of Titanium," *Journal of Engineering for Industry, Transactions of the ASME*, pp. 76-78.

Rich, D.L. and Impellizzeri, L.F., 1977, "Fatigue Analysis of Cold-Worked and Interference Fit Fastener Holes," *Cyclic Stress-Strain and Plastic Deformation Aspects of Fatigue Crack Growth, ASTM STP 637*, pp. 153-175.

Robertson, G.T., 1971, "The Effects of Shot Size on the Residual Stresses Resulting from Shot Peening," SAE Technical Paper 710284, Reported in *The Shot Peener*, Vol. 11, No. 3, 1987, pp. 46-48.

Rosenthal, D., 1959, "Influence of Residual Stress on Fatigue," *Metal Fatigue*, G. Sines and J. L. Waisman, editors, McGraw-Hill, pp. 170-196.

Ross, A.S. and Morrow, J., 1960, "Cycle-Dependent Stress Relaxation of A-286 Alloy," *Journal of Basic Engineering, Transactions of the ASME*, pp. 654-660.

Roth, M. and Wortman, C., 2002, "Relaxation of Shot Peening Residual Stresses in the 7050-T7451 Aluminium Alloy After Heat Cycles for Adhesive Bonding," *Proc. 8th International Conference on Shot Peening (ICSP-8)*, Garmisch-Partenkirchen, Germany, L. Wagner, editor, Wiley-VCH GmbH & Co. KGaA, pp. 208-214.

Rufin, A.C., 1993, "Extending the Fatigue Life of Aircraft Engine Components by Hole Cold Expansion Technology," *Journal of Engineering for Gas Turbines and Power, Transactions of the ASME*, Vol. 115, pp. 165-171.

Ruschau, J.J., John, R., Thompson, S.R., and Nicholas, T., 1999, "Fatigue Crack Growth Rate Characteristics of Laser Shock Peened Ti-6Al-4V," *Journal of Engineering Materials and Technology, ASME*, Vol. 121, pp. 321-329.

Rybicki, E.F., Stonesifer, R.B., and Olson, R.J., 1981, "Stress Intensity Factors Due to Residual Stresses in Thin-Walled Girth-Welded Pipes," *Journal of Pressure Vessel Technology, Transactions of the ASME*, Vol. 103, pp. 66-75.

Saunder, T.J. and Grandt, A.F., Jr., 2000, "The Effect of Edge Distance on Coldworking Fastener Holes," *Proc. 4th Joint DoD/FAA/NASA Conference on Aging Aircraft*, St. Louis, Missouri.

Schulze, V., Vöhringer, O., and Macherauch, E., 1993, "Thermal Relaxation of Shot Peening Induced Residual Stresses in a Quenched and Tempered Steel 42 Cr Mo 4," *Proc. 5th International Conference on Shot Peening (ICSP5)*, Oxford, UK, D. Kirk, editor, pp. 265-274.

Schulze, V., Lang, K.-H., Vöhringer, O., and Macherauch, E., 1996, "Relaxation of Shot Peening Induced Residual Stresses in Quenched and Tempered Steel AISI 4140 Due to Uniaxial Cyclic Deformation," *Proc. 6th International Conference on Shot Peening (ICSP6)*, San Francisco, J. Champaigne, editor, pp. 403-412.

Schulze, V., 2005, Modern Mechanical Surface Treatment: States, Stability, Effects, Wiley-VCH, Weinheim, Germany, ISBN 3-527-31371-0, 400 pps.

Seppi, F.L., 1975, "Relief of Shot-Peened Compressive Layer by Fatigue Loading," *Proc. of a Workshop on Nondestructive Evaluation of Residual Stress*, San Antonio, Texas, NTIAC-76-2, pp. 73-74.

Sha, G.T., 1980, Cowles, B.A., and Fowler, R.L., "Fatigue Life of a Coldworked Hole," *Emerging Technologies in Aerospace Structures, Design, Structural Dynamics and Materials Proc*. The Aerospace Conference—Century 2—Emerging Technology Conferences, San Francisco, California, pp. 125-140.

Smith, D.J., Farrahi, G.H., Zhu, W.X, and McMahon, C.A., 2001, "Experimental Measurement and Finite Element Simulation of the Interaction Between Residual Stresses and Mechanical Loading," *International Journal of Fatigue*, Vol. 23, pp. 293-302.

Smith, E., 1985, "The Stress Intensity Factor for a Crack Perpendicular to a Longitudinal Weld in a Large Plate," *International Journal of Fracture*, Vol. 27, pp. 75-79.

Sridhar, B.R., Ramachandra, K., and Padmanabhan, K.A., 1996, "Effect of Shot Peening on the Fatigue and Fracture Behaviour of Two Titanium Alloys," *Journal of Materials Science*, Vol. 31, pp. 5953-5960.

Stacey, A. and Webster, G.A., 1988a, "Stress Intensity Factors Caused by Residual Stress Fields in Autofrettaged Tubing," *Analytical and Experimental Methods for Residual Stress Effects in Fatigue, ASTM STP 1004*, pp. 37-53.

Stacey, A. and Webster, G.A., 1988b, "Influence of Residual Stress on Fatigue Crack Growth in Thick-Walled Cylinders," *Analytical and Experimental Methods for Residual Stress Effects in Fatigue, ASTM STP 1004*, American Society for Testing and Materials, pp. 107-121.

Stefanescu, D., Bouzina, A., Dutta, M., Wang, D.Q., Fitzpatrick, M.E., and Edwards, L., 2002, "Comparison of Residual Stress Measurements Using Neutron and X-Ray Diffraction Around Cold Expanded Hole," *Journal of Neutron Research*, Vol. 9, pp. 399-405.

Stefanescu, D., Dutta, M., Wang, D.Q., Edwards, L., and Fitzpatrick, M.E., 2003, "The Effect of High Compressive Loading on Residual Stresses and Fatigue Crack Growth at Cold Expanded Holes," *Journal of Strain Analysis*, Vol. 38, No. 5, pp. 419-427.

Stefanescu, D., 2004a, "Measurement and Prediction of Fatigue Crack Growth From Cold Expanded Holes Part 1: The Effect of Fatigue Crack Growth on Cold Expansion Residual Stresses," *Journal of Strain Analysis*, Vol. 39, No. 1, pp. 25-39.

Stefanescu, D., 2004b, "Measurement and Prediction of Fatigue Crack Growth From Cold Expanded Holes Part 2: Prediction of Fatigue Crack Growth From Cold Expanded Holes," *Journal of Strain Analysis*, Vol. 39, No. 1, pp. 41-53.

Su, X., Gu, M., and Yan, M., 1986, "A Simplified Residual Stress Model for Predicting Fatigue Crack Growth Behavior at Coldworked Fastener Holes," *Fatigue and Fracture of Engineering Materials and Structures*, Vol. 9, No. 1, pp. 57-64.

Tada, H. and Paris, P.C., 1983, "The Stress Intensity Factor for a Crack Perpendicular to the Welding Bead," *International Journal of Fracture*, Vol. 21, pp. 279-284.

Taira, S. and Murakami, Y., 1960, "On the Changes in Residual Stresses Due to Repeated Stressing," *Proc. 3rd Japan Congress on Testing Materials*, Kyoto, Japan, pp. 52-55.

Taira, S., Honda, K., and Abe, T., 1964, "X-Ray Investigation on Fatigue Damage of Metals (on the Changes in Half-Value Breadth of X-Ray Diffraction Line and Macro-residual Stress in Torsional Fatigue With Mean Stress)," *Proc. 7th Japan Congress on Testing Materials*, Kyoto, Society of Materials Science, pp. 26-30.

Takanashi, M., Kamata, K., and Kunihiro, I., 2000, "Relaxation Behavior of Welding Residual Stresses by Fatigue Loading in Smooth Longitudinal Butt Welded Joints," *Welding in the World*, Vol. 44, pp. 28-34.

Teodosio, J.R., Cindra, F.M., and Pedrosa, P.D., 2003, "Relaxation of Residual Stresses During Fatigue Cycles in Steels," THERMEC'2003, Parts 1-5, International Conference on Processing & Manufacturing of Advanced Materials, Madrid, Spain, *Materials Science Forum*, Vol. 426, No. 4, pp. 3981-3986.

Terada, H., 1976, "An Analysis of the Stress Intensity Factor of a Crack Perpendicular to the Welding Bead," *Engineering Fracture Mechanics*, Vol. 8, pp. 441-444.

Terada, H., and Nakajima, T., 1985, "Analysis of Stress Intensity Factor of a Crack Approaching Welding Bead," *International Journal of Fracture*, Vol. 27, pp. 83-90.

Terada, H., 2005, "Stress Intensity Factor Analysis and Fatigue Behavior of a Crack in the Residual Stress Field of Welding," *Journal of ASTM International*, Vol. 2, Issue 5, Paper ID JAI12558.

Toparli, M., Ozel A., and Aksoy, T., 1997, "Effect of the Residual Stresses on the Fatigue Crack Growth Behavior at Fastener Holes," *Materials Science and Engineering A225*, pp. 196-203.

Torres, M., Pereira do Nascimento, M., and Voorwald, H., 2002, "Consideration of Shot Peening Treatment Applied to a High Strength Aeronautical Steel With Different Hardnesses," *Proc. 8th International Conference on Shot Peening (ICSP-8)*, Garmisch-Partenkirchen, Germany, L. Wagner, editor, Wiley-VCH GmbH & Co. KGaA, pp. 37-43.

Torres, M.A.S. and Voorwald, H.J.C., 2002, "An Evaluation of Shot Peening, Residual Stress and Stress Relaxation on the Fatigue Life of AISI 4340 Steel," *International Journal of Fatigue*, Vol. 24, pp. 877-886.

Totten, G., Howes, M., and Inoue, T., 2002, editors, *Handbook of Residual Stress and Deformation of Steel*, ASM International, Materials Park, Ohio.

Tufft, M., 2002, "Modeling of Fatigue Behavior Due to Shot Peening Conditions," *Proc. 8th International Conference on Shot Peening (ICSP-8)*, Garmisch-Partenkirchen, Germany, L. Wagner, editor, Wiley-VCH GmbH & Co. KGaA, pp. 530-539.

Turnbull, A., De Los Rios, E.R., Tait, R.B., Laurant, C., and Boabaid, J.S., 1998, "Improving the Fatigue Crack Resistance of Waspaloy by Shot Peening," *Fatigue and Fracture of Engineering Materials and Structures*, Vol. 21, pp. 1513-1524.

Underwood, J.H., Pook, L.P., and Sharples, J.K., 1977, "Fatigue-Crack Propagation Through a Measured Residual Stress Field in Alloy Steel," *Flaw Growth and Fracture, ASTM STP 631*, American Society for Testing and Materials, pp. 402-415.

Underwood, J.H., Parker, A.P., Troiano, E., Vigilante, G.N., and Whitherell, M.D., December 2001, "Fatigue and Hydrogen Cracking in Cannons With Mechanical and Thermal Residual Stresses," *Advances in Fracture Research, ICF10, Proc. 10th International Conference on Fracture*, Honolulu, Hawaii, Paper 986.

Vöhringer, O., 1983, "Relaxation of Residual Stresses," *Proc. European Conference on Residual Stresses*, Karlsruhe, E. Macherauch and V. Hauk, editors, DGM Informationsgesellschaft, pp. 47-80.

Vöhringer, O., Hirsch, Th., and Macherauch, E., 1984, "Relaxation of Shot Peening Induced Residual Stresses of TiAl6V4 by Annealing or Mechanical Treatment," *Proc. 5th International Conference on Titanium*, Munich, FRG, Vol. 4, pp. 2203-2210.

Vöhringer, O., 1987a, "Relaxation of Residual Stresses by Annealing or Mechanical Treatment," *Advances in Surface Treatments, Technology – Applications – Effects: Residual Stresses, Vol. 4, Pergamon Press*, pp. 367-396.

Vöhringer, O., 1987b, "Changes in the State of the Material by Shot Peening," *Proc. 3rd International Conference on Shot Peening (ICSP3)*, Garmisch-Partenkirchen, Germany, H. Wohlfahrt, R. Kopp, and O. Vöhringer, editors, DGM Informationsgesellschaft Verlag, Oberursel, pp. 185-204.

Vukelich, S., Russ, S., Berkley, S., and Bradley, E.F., 2002, "Residual Stress Measurement and its Application to Achieve Predicted Full Life Potential of Low Cycle Fatigue (LCF) Limited Engine Disks," *Proc. 9th International Symposium on Transport Phenomena and Dynamics of Rotating Machinery*, Honolulu, Hawaii.

Wagner, L., 1997, "Mechanical Surface Treatments on Titanium Alloys: Fundamental Mechanisms," *Surface Performance of Titanium*, TMS, pp. 199-215.

Wagner, L., 1999, "Effect of Mechanical Surface Treatments on Fatigue Performance of Titanium Alloys," *Fatigue Behavior of Titanium Alloys*, TMS, pp. 253-265.

Wang, D.Q. and Edwards, L., 1998, "Neutron Diffraction Determination of the Complete 3D Residual Stress Distribution Surrounding a Cold Expanded Hole," *Proc. 4th European Conference on Residual Stresses*, pp. 619-626.

Wang, G.S., 1988, "An Elastic-Plastic Solution for a Normally Loaded Center Hole in a Finite Circular Body," *International Journal of Pressure Vessels and Piping*, Vol. 33, pp. 269-284.

Wang, G.S., 1996, "To Analyse Fatigue Crack Growth in Residual Stress Field at Welded Joints," *Proc. of the 6th International Fatigue Congress – Fatigue '96*, Berlin Germany, G. Lütjering and H. Nowack, editors, Pergamon, Vol. II, pp. 1219-1224.

Wang, G.S., 1999, "A Strip Yield Analysis of Fatigue Crack Growth in the Residual Stress Field," *International Journal of Fracture*, Vol. 96, pp. 247-277.

Webster, G.A. and Ezeilo, A.N., 2001, "Residual Stress Distribution and Their Influence on Fatigue Lifetimes," *International Journal of Fatigue*, Vol. 23, pp. S375-S383.

Wick, A., Schulze, V., and Vöhringer, O., 1999a, "Influence of the Shot Peening Temperature on the Relaxation Behaviour of Residual Stresses During Cyclic Bending," *Proc. 7th International Conference on Shot Peening*, Warsaw, Poland, pp. 102-109.

Wick, A., Schulze, V., and Vöhringer, O., 1999b, "Shot Peening and Stress Peening of AISI 4140 at Increased Temperatures," *Proc. 7th International Conference on Shot Peening*, Warsaw, Poland, pp. 110-116.

Wick, A., Schulze, V., and Vöhringer, O., 2000, "Effects of Warm Peening on Fatigue Life and Relaxation Behaviour of Residual Stresses in AISI 4140 Steel," *Materials Science and Engineering A*, Vol. A293, pp. 191-197.

Wilks, M.D.B., Nowell, D., and Hills, D.A., 1994, "The Influence of Residual Stress on Crack Growth Rate," *Proc. 4th International Conference on Residual Stresses*, Baltimore, Maryland, pp. 1238-1245.

Zeller, R., 1993, "Influence of Stress Peening on Residual Stresses and Fatigue Limit," *Residual Stresses*, DGM Informationsgesesellschaft Verlag, pp. 907-917.

Zhang, Y., Edwards, L., and Fitzpatrick, M.E., November 2002, "Finite Element Simulation of Hole Cold Expansion Process in EN8 Steel Plates," UK ABAQUS User Group Conference.

Zhang, Y., Fitzpatrick, M.E., and Edwards, L., 2002, "Measurement of the Residual Stresses Around a Cold Expanded Hole in an EN8 Steel Plate Using the Contour Method," *Materials Science Forum, Vols*. 404-407, pp. 527-532.

Zhu, X.Y. and. Shaw, W.J.D., 1995, "Correlation of Fatigue Crack Growth Behaviour With Crack Closure in Peened Specimens," *Fatigue Fract. Engng Mater. Struct.*, Vol. 18, No. 7/8, pp. 811-820.

Zhuang, W.Z. and Halford, G.R., 2001, "Investigation of Residual Stress Relaxation Under Cyclic Load," *International Journal of Fatigue*, Vol. 23, pp. S31-S37.

Zhuang, W. and Wicks, B., 2003, "Mechanical Surface Treatment Technologies for Gas Turbine Engine Components," *Journal of Engineering for Gas Turbine and Power*, Vol. 125, pp. 1021-1025.

Zinn, W. and Scholtes, B., 1999, "Mechanical Surface Treatments of Lightweight Materials—Effects on Fatigue Strength and Near-Surface Microstructures," *Journal of Materials Engineering and Performance*, Vol. 8(2), pp. 145-151.

APPENDIX P—RISK ASSESSMENT FOR LARGE NUMBERS OF INHERENT MATERIAL ANOMALIES

P.1 INTRODUCTION.

Inherent metallurgical anomalies are extremely rare in most gas turbine materials. For example, the titanium alloys commonly used in commercial gas turbine engine rotors and disks have an occurrence rate of less than one anomaly per million pounds of material for a median anomaly size of 20 mil [P-1]. However, some materials may exhibit relatively higher anomaly occurrence rates compared to those found in premium grade titanium alloys. Components constructed from these materials may have several significant anomalies that form into growing cracks that can ultimately lead to failure. Additional probabilistic considerations are required for the proper treatment of materials with multiple anomalies, which is the focus of this appendix.

P.2 RISK ASSESSMENT ASSOCIATED WITH RARE ANOMALIES.

P.2.1 INHERENT MATERIAL ANOMALIES.

The probability of fracture associated with a rare material anomaly is dependent on both the size and the location of the anomaly within a component. For inherent material anomalies, the uncertainty associated with location can be addressed by subdividing the component into a number of subregions or zones of approximately equal risk. With a zone, the probability of fracture p_i is given by

$$p_i = P\left(F_{i|A} \bigcap A\right) \tag{P-1}$$

where event $F_{i|A}$ is fracture failure in zone i given an anomaly in zone i, and event A is the occurrence of an anomaly in zone i.

Since these two events can be considered statistically independent, equation P-1 can be expressed as

$$p_i = p_{i|A} \bullet p_A \tag{P-2}$$

where $p_{i|A}$ and p_A are the probabilities associated with events $F_{i|A}$ and A, respectively. p_A is modeled as a Poisson process with a mean occurrence rate λ_i that is proportional to the volume of material in the zone:

$$\lambda_i = \frac{V_i}{V} \lambda_V \tag{P-3}$$

where V_i = volume of zone i, V = volume of the component, and λ_V = mean occurrence rate associated with the component volume. The probability of fracture for a component is modeled as a series system of the m zones [P-2 and P-3]:

$$p_F = P[F_1 \cup F_2 \cup \ldots \cup F_m] = 1 - P\left[\bigcap_{i=1}^{m} \overline{F_i}\right] \tag{P-4}$$

If the mean anomaly occurrence rate is relatively small, the probability of more than one significant anomaly in the component is negligible. In this situation, equation P-4 reduces to [P-4]

$$p_F \cong \sum_{i=1}^{m} p_i \tag{P-5}$$

P.2.2 INDUCED MATERIAL ANOMALIES.

Induced anomalies are generally located on surface features such as boltholes and slots. In contrast with inherent anomalies, the mean anomaly occurrence rate associated with induced anomalies λ_i is proportional to the surface area A_i of the feature:

$$\lambda_i = \frac{A_i}{A}\lambda_S \tag{P-6}$$

where λ_S = anomaly occurrence rate on a per unit surface area basis, and A = reference surface area.

If the component is modeled as a series system consisting of the features that may contain induced anomalies, then equations P-4 and P-5 can be used to estimate the probability of fracture.

P.2.3 LIFE LIMITING LOCATION.

Since crack growth life is dependent on the applied stresses and the geometry of the crack (and associated boundary conditions), it is necessarily dependent on the anomaly location. Cracks usually experience the highest growth rate da/dN in regions of relatively high stress and low constraint, leading to relatively lower crack growth life N:

$$N = \int_{a_o}^{a_f} \left[\frac{da}{dN}\right]^{-1} da \tag{P-7}$$

where a_o and a_f are the initial and final crack sizes.

The life-limiting location is defined as the position of an anomaly within a zone that results in the lowest deterministic crack growth life value for a specified anomaly size. Within a zone, the conditional probability of fracture is bounded by the probability of fracture at the life-limiting location:

$$P\left(F_{i|A}\right) \le P\left(F_{i|A,L}\right) \tag{P-8}$$

or:

$$p_{i|A} \le p_{i|A,L} \tag{P-9}$$

where event $F_{i|A,L}$ is the fracture of a component given that an anomaly is placed at the life-limiting location in the zone, and $p_{i|A,L}$ is the probability associated with this event. Equation P-9 provides a conservative (upper bound) estimate for the conditional probability of fracture associated with a zone. As the number of zones is increased, the value of $p_{i|A}$ approaches $p_{i|A,L}$.

P.3 RISK ASSESSMENT ASSOCIATED WITH LARGE NUMBERS OF ANOMALIES.

Consider a zone that has multiple anomalies. The probability of fracture within the zone can be expressed as

$$\begin{aligned} p_i &= P\left[\begin{array}{l}\left(F_{i|A_1}\bigcap A_1\right)\bigcup\left(F_{i|A_2}\bigcap A_2\right)\\ \cdots\bigcup\left(F_{i|A_{n-1}}\bigcap A_{n-1}\right)\bigcup\left(F_{i|A_n}\bigcap A_n\right)\end{array}\right] \\ &= P\left[1-\bigcap_{j=1}^{n}\left(\bar{F}_{i|A_j}\bigcap A_j\right)\right] \end{aligned} \tag{P-10}$$

or:

$$\bar{p}_i = P\left(\bar{F}_i\right) = P\left[\bigcap_{j=1}^{n}\left(\bar{F}_{i|A_j}\bigcap A_j\right)\right] \tag{P-11}$$

where event $F_{i|A_j}$ is the fracture failure associated with zone *i* given that *j* anomalies are present, and A_j is the occurrence of *j* anomalies in a zone.

Noting that the events A_j are mutually exclusive and collectively exhaustive, if events $F_{i|A_j}$ and are A_j independent, then equation P-10 can also be expressed as

$$p_i = \sum_{j=1}^{n} P\left(F_{i|A_j}\right) \bullet P\left(A_j\right) \tag{P-12}$$

The probability of fracture of a component is equal to the probability union of the zones. If equation P-11 is substituted into equation P-4, the following expression is obtained:

$$p_F = 1 - P\left\{\bigcap_{i=1}^{m}\left[\bigcap_{j=1}^{n} \overline{F}_{i|A_j} \bigcap A_j\right]\right\} \tag{P-13}$$

If zone failures are treated as independent events, equation P-13 becomes

$$p_F = 1 - \prod_{i=1}^{m}\left(1 - p_i\right) \tag{P-14}$$

In general, zone failures are at least partially correlated, primarily due to the stress values associated with inertia loading. Equation P-14 provides a conservative estimate of the component failure probability, provided that correlation among zone failures is nonnegative. Note that if the number of anomalies is relatively small, equation P-14 reduces to equation P-5.

P.3.1 MULTIPLE ANOMALIES AT LIFE-LIMITING LOCATION.

When multiple anomalies are present, the conditional probability of fracture of a zone can be modeled as a series system consisting of the failure associated with each anomaly:

$$P\left(F_{i|A_j}\right) = 1 - P\left(\bigcap_{j=1}^{n} \overline{F}_{i|A_j}\right) \tag{P-15}$$

As previously noted, $F_{i|A_j}$ has an upper bound value associated with the life-limiting location as specified in equation P-9. If this bound is applied (i.e., assume all anomalies are at the life-limiting location), equation P-14 becomes:

$$P\left(F_{i|A_j}\right) \le 1 - \left[P\left(\overline{F}_{i|A_j,L}\right)\right]^j \tag{P-16}$$

P.3.2 POISSON DISTRIBUTED ANOMALIES.

Suppose that the occurrence of anomalies can be modeled as a Poisson distribution [P-5]:

$$P\left(A_j\right) = \frac{\left(\lambda_i\right)^j}{j!} \exp\left(-\lambda_i\right) \tag{P-17}$$

where λ_i is the mean anomaly occurrence rate for the zone.

Substituting the expressions in equations P-16 and P-17 into equation P-12, the probability of fracture for a zone becomes

$$p_i = \sum_{j=1}^{n} \left[\left\{ 1 - \left[P\left(\bar{F}_{i|A_j,L} \right) \right]^j \right\} \bullet \frac{\left(\lambda_i\right)^j}{j!} \exp\left(-\lambda_i\right) \right] \tag{P-18}$$

Which can also be expressed as [P-6]

$$p_i = 1 - \exp\left[-\lambda_i \cdot p_{i|A,L} \right] \tag{P-19}$$

Substituting this expression for p_i in equation P-14, the component probability of fracture becomes

$$p_F = 1 - \prod_{i=1}^{m} \exp\left[-\lambda_i \cdot p_{i|A,L} \right] \tag{P-20}$$

P.4 APPLICATION TO COMPRESSOR DISK OF COMMERCIAL AIRCRAFT GAS TURBINE ENGINE.

Figure P-1 shows the probabilistic fracture mechanics methodology for the aircraft gas turbine engine compressor disk. Internal stresses and temperatures are determined using finite element analysis results, and the disk has a design life of 20,000 flight cycles. Deterministic crack growth life is computed using stress-intensity factor solutions for cracks in rectangular plates. For probabilistic computations, the component is subdivided into 31 zones (figure P-1). Surface and subsurface anomalies are placed at the life-limiting locations of the interior and exterior zones, respectively.

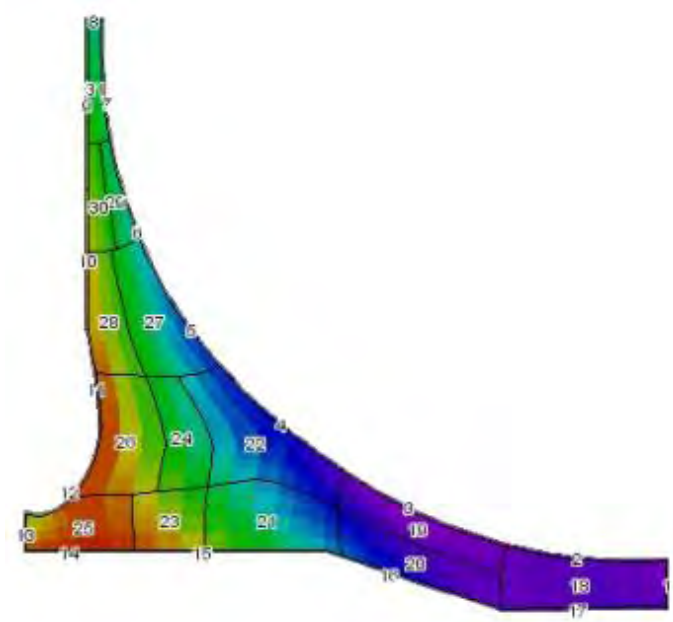

Figure P-1. Axisymmetric Finite Element Model of a Gas Turbine Compressor Disk Subdivided Into Zones

P.4.1 LIMIT STATE.

Failure within a zone occurs when the maximum stress-intensity factor K exceeds the fracture toughness K_C:

$$g(X,\ Y, N) = K_C - K(X,\ Y, N)\ <\ 0 \tag{P-21}$$

where $g(X, Y, N)$ is dependent on the number of flight cycles N, a vector of input variables unrelated to inspections X; and a vector of input variables related to inspections Y.

P.4.2 RANDOM VARIABLES.

Three X random variables are considered for use in crack growth life computations, including initial anomaly size, applied stress, and material properties. The initial anomaly size random variable X_1 is typically a dominant random variable, often characterized as an exceedance curve (e.g., hard alpha anomalies, figure P-2). It can be expressed as a cumulative distribution function [P-3] as follows:

$$F_{X_1}(a) = \begin{cases} 0 & a < a_{\min} \\ 1 - \dfrac{D(a) - D(a_{max})}{D(a_{min}) - D(a_{max})} & a_{\min} \le a \le a_{\max} \\ 1 & a > a_{\max} \end{cases} \tag{P-22}$$

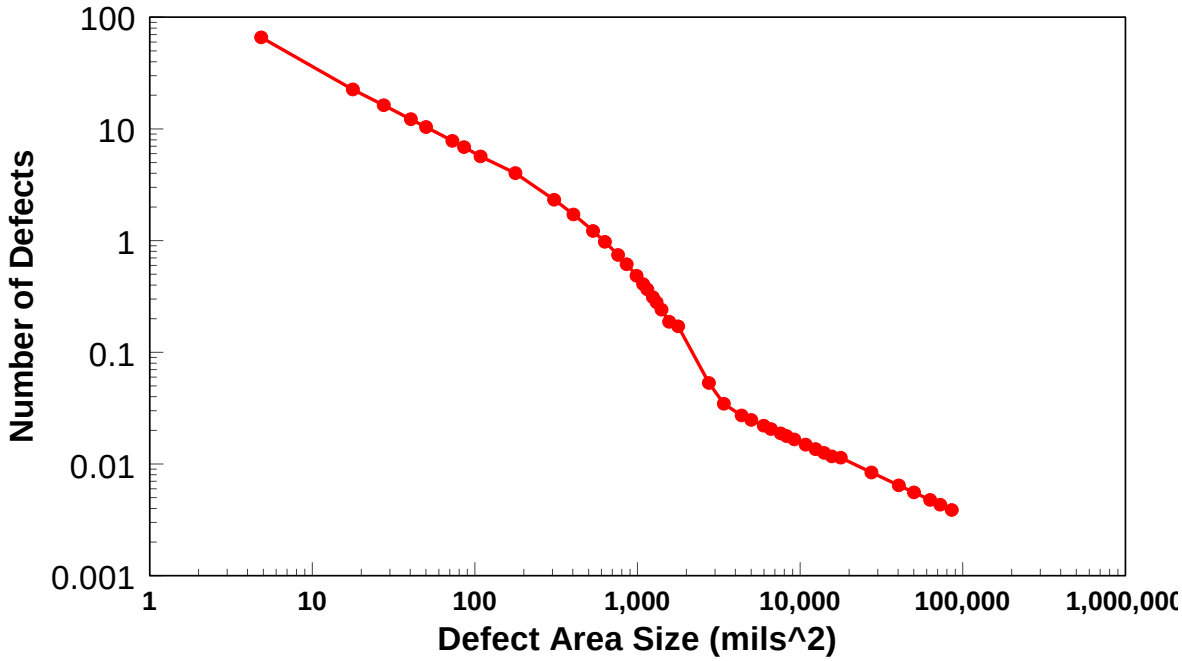

Figure P-2. Distribution Function of Titanium Rare Inherent Material Anomalies Expressed in Exceedance Curve Format

Applied stress is modeled as the product of deterministic stress S_{FEM} (often obtained from finite element analysis) and a stress scatter variable X_2:

$$S = X_2 \, S_{FEM} \tag{P-23}$$

The crack growth life is expressed in terms of the deterministic life N_{NOM} and a life scatter factor X_3 that accounts for material variability:

$$N = X_3 \, N_{NOM} \tag{P-24}$$

The Y random variables are the inspection (shop visit) times and the probability of detection (PoD). The probability of detecting an anomaly from a population of anomalies (P_{det}) is

$$P_{det} = \int_0^{\infty} POD(a) \cdot f(a) \, da \tag{P-25}$$

where *PoD(a)* is the probability of detecting an anomaly with a size (area) greater than *a* (figure P-3) and *f(a)* is the probability density function associated with an anomaly of size *a*.

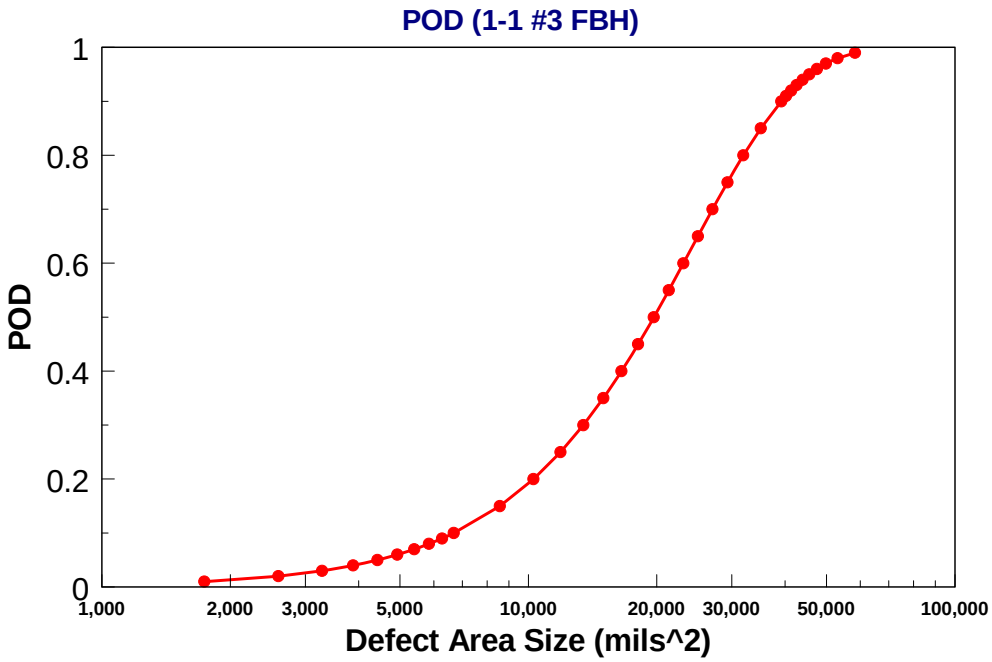

Figure P-3. Probability of Detection Random Variable

P.4.3 COMPONENT RISK RESULTS ASSOCIATED WITH RARE ANOMALIES.

Probability of fracture values associated with the gas turbine engine compressor disk (figure P-1) were computed using a combined technique of numerical integration and importance sampling [P-7]. Numerical results associated with rare inherent material anomalies (figure P-2) are indicated in table P-1. For the risk critical zone, the range of values for the mean anomaly occurrence rate is on the order of 10^{-7} to 10^{-5}, and the range of values for the conditional probability of fracture is on the order of 10^{-4} to 10^{-2}. It can be observed that the majority of the risk is concentrated in 3 to 4 zones of the 31 zones.

Table P-1. Probability of Fracture Results Associated With Rare Inherent Material Anomalies for Risk Critical Zones of Gas Turbine Engine Compressor Disk

Zone	$p_{i\|A}$	λ_i	p_i	p_i / p_F (%)
6	2.00E-04	4.19E-06	8.39E-10	0.2
8	4.00E-04	9.59E-07	3.84E-10	0.1
9	2.00E-04	8.73E-06	1.75E-09	0.4
10	3.29E-03	5.31E-06	1.75E-08	4.3
11	2.19E-02	3.05E-06	6.67E-08	16.3
12	1.95E-02	1.94E-06	3.79E-08	9.3
13	5.41E-03	5.64E-07	3.05E-09	0.7
14	2.37E-02	1.17E-06	2.77E-08	6.8
15	9.98E-04	2.39E-06	2.39E-09	0.6
21	1.00E-04	5.32E-05	5.32E-09	1.3
23	4.02E-04	2.76E-05	1.11E-08	2.7
25	3.51E-03	3.16E-05	1.11E-07	27.2
26	1.40E-03	6.92E-05	9.69E-08	23.8
28	2.00E-04	5.80E-05	1.16E-08	2.8
30	2.99E-04	3.58E-05	1.07E-08	2.6
31	1.00E-04	3.84E-05	3.84E-09	0.9

P.4.4 INFLUENCE OF MULTIPLE ANOMALIES ON PROBABILITY OF FRACTURE.

The results indicated in table P-1 are based on anomaly occurrence rates associated with hard alpha titanium anomalies. For these rare anomalies, component risk can be computed using equation P-5, where it is assumed that there is no more than one significant anomaly in the component. However, as anomalies become more plentiful, it becomes increasingly likely that more than one significant anomaly will be present in the disk, and equation P-5 is no longer valid. In this situation, component risk could be computed using equations P-14 and P-18 for a finite number of anomalies or equation P-20 for an infinite number of anomalies. Normalized risk values based on use of these equations are shown in figure P-4. In figure P-4(a), it can be observed for this example that the component risk results are nearly identical for all three approaches when the mean zone anomaly occurrence rate is less than about 10^{-3}. Since the zone anomaly occurrence rate for titanium ranges from10^{-7} to 10^{-5}, all of these approaches are valid for this anomaly type. As shown in figures P-4(a) and P-4(b), the results do not differ substantially unless the anomaly rate is in the range of 10^{-1} to 10^{2}, an increase of roughly six to seven orders of magnitude.

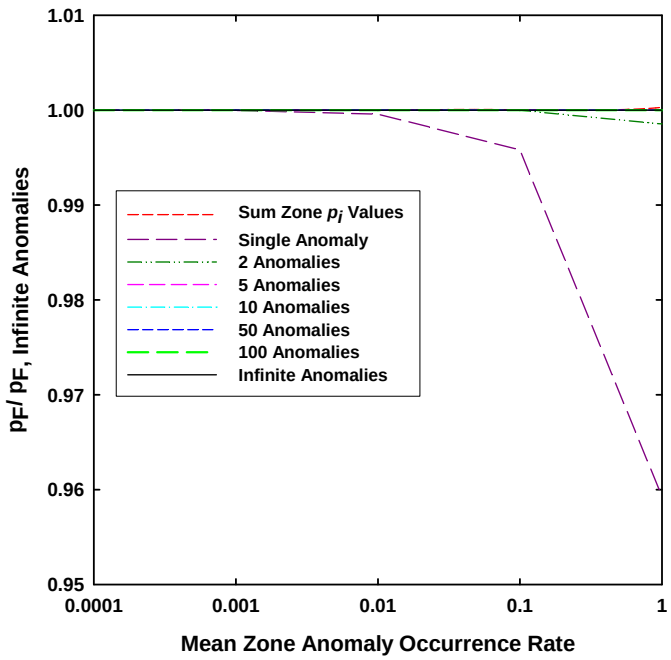

(a)

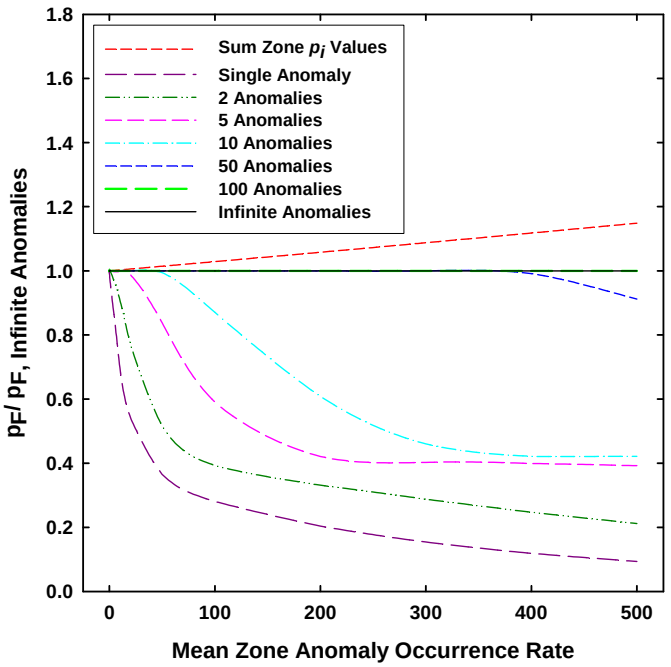

(b)

Figure P-4. Influence of Number of Anomalies on Normalized Component Risk Values (a) Relatively Rare Anomalies and (b) Relatively Frequent Anomalies

The results shown in figure P-4 are limited to the compressor disk example for a specific range of values for the conditional probability of fracture. To generalize the results, consider a fictitious component consisting of 100 zones that have identical values for the anomaly occurrence rate and conditional probability of fracture. For this component, the ratio of the component risk computed using equations P-5 and P-20 can be expressed as

$$\frac{\sum_{i=1}^{m} p_{i|A,L} \bullet p_A}{1-\prod_{i=1}^{m} \exp\left[-\lambda_i \bullet p_{i|A,L}\right]} \cong \frac{m\lambda_i p_{i|A,L}}{1-\exp\left[-\lambda_i \bullet p_{i|A,L}\right]^m} \tag{P-26}$$

The influences of anomaly occurrence rate and conditional probability of fracture on component risk evaluated using equation P-26 is illustrated in figure P-5. In figure P-5(a), it can be observed that when the conditional probability of fracture is relatively large, an anomaly occurrence rate of 10^{-2} or greater will have an influence on the results. As shown in figure P-5(b), if the conditional probability of fracture is reduced, the anomaly occurrence rate must be on the order of 1 or greater to influence the results.

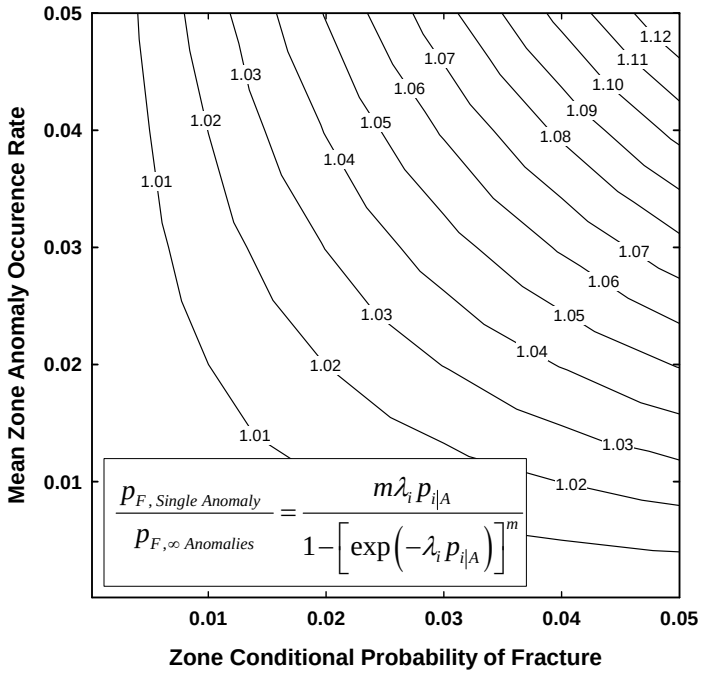

(a)

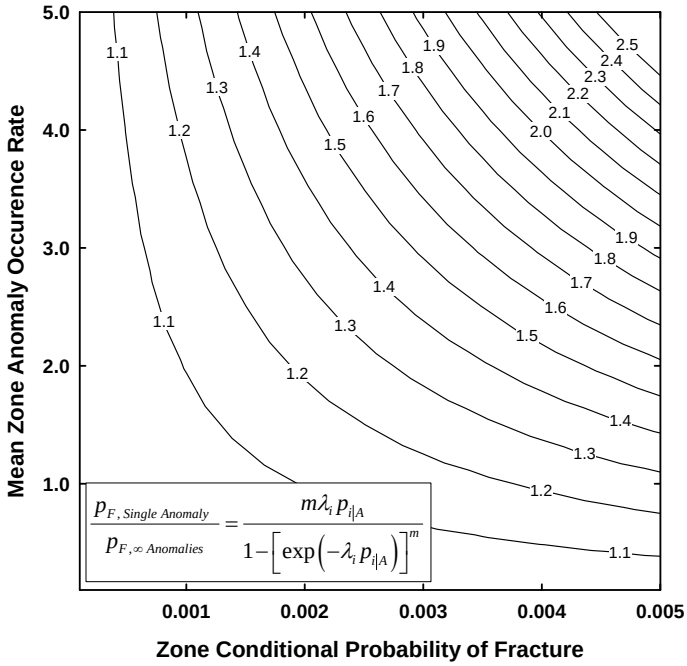

(b)

Figure P-5. Influence of Zone Anomaly Occurrence Rate λ_i and Conditional Probability of Fracture $p_{i|A}$ on Normalized Component Risk Associated for $p_{i|A}$ Values With Relative Magnitudes (a) 10^{-2} and (b) 10^{-3}

P.5 REFERENCES.

P-1. Aerospace Industries Association Rotor Integrity Subcommittee, "The Development of Anomaly Distributions for Aircraft Engine Titanium Disk Alloys," *Proceedings 38th Structures, Structural Dynamics, and Materials Conference*, Kissimmee, FL, 1997, pp. 2543-2553.

P-2. Leverant, G.R., et al., "Turbine Rotor Material Design," FAA report DOT/FAA/AR-00/64, December 2000.

P-3. Wu, Y.T., Enright, M.P., and Millwater H.R., "Probabilistic Methods for Design Assessment of Reliability With Inspection," *AIAA Journal*, Vol. 40, No. 5, 2002, pp. 937-946.

P-4. Freudenthal, A.M., Garrelts, J.M, and Shinozuka, M., "The Analysis of Structural Safety," *Journal of the Structural Division*, ASCE, Vol. 92, No. ST1, 1966, pp. 267-325.

P-5. Haldar, A. and Mahadevan, S., "Probability, Reliability, and Statistical Methods in Engineering Design," Wiley, 2000.

P-6. Roth, P.G., "Probabilistic Rotor Design System—Final Report," AFRL-PR-WP-TR-1999-2122, Air Force Research Laboratory, Cincinnati, OH, 1998.

P-7. Huyse, L. and Enright, M.P., "Efficient Statistical Analysis of Failure Risk in Engine Rotor Disks Using Importance Sampling Techniques," *Proceedings 44th Structures, Structural Dynamics, and Materials Conference*, Norfolk, VA, AIAA Paper 2003-1838, 2003.

APPENDIX Q—ADAPTIVE OPTIMAL SAMPLING METHODOLOGY FOR MULTIPLE ANOMALIES

A recent Federal Aviation Administration (FAA) Advisory Circular 33.14-1 describes a probabilistic damage tolerance process that can be used to predict the probability of fracture associated with titanium rotors. This document was developed for titanium materials with hard alpha anomalies. Since the anomaly occurrence rate associated with titanium is extremely small, component failure probability can be approximated as the sum of the failure probabilities of subregions (zones) of approximately equal risk.

Some materials may exhibit relatively higher anomaly occurrence rates compared to those found in premium grade titanium alloys. For these materials, a single disk could contain a number of significant anomalies that occur simultaneously in several zones. In this situation, the disk probability of fracture is defined as a series system consisting of a number of zones of approximately equal risk.

Reliability prediction of general systems may require significant computations, particularly if correlation among members and postfailure material behavior are considered [Q-1 and Q-2]. Over the past several decades, a number of approaches were used to improve the efficiency of computations associated with system reliability predictions, such as bounding methods [Q-3 and Q-4] and various variance reduction techniques [Q-5, Q-6, and Q-7]. Over the past several years, a number of methods have been developed to improve the efficiency of zone-based system reliability predictions, such as tailored response surface [Q-8], zone refinement [Q-9], importance sampling [Q-8 and Q-10], and parallel processing [Q-11], and other improvements.

In this appendix, a methodology is presented for variance reduction of sampling-based series system reliability predictions based on optimal allocation of Monte Carlo samples to the individual failure modes. It is an extension of a technique developed previously for titanium materials (appendix U). An algorithm is presented for adaptively allocating samples to member failure modes based on initial estimates of the individual member failure probabilities. The methodology is demonstrated for a simple series system and a gas turbine engine disk modeled using the zone-based series system approach.

Q.1 OPTIMAL SAMPLING METHOD FOR SERIES SYSTEMS.

Consider the series system shown in figure Q-1, which consists of five members with an applied load. Illustrative values of the bivariant probability densities for the individual member failure modes are shown in figure Q-2. Also shown is the member limit state:

$$g(R_i, S_i) = R_i - S_i \tag{Q-1}$$

where R_i and S_i are resistance and applied stress for member i, respectively. From figure Q-2, it can be observed that members 1, 4, and 5 have a significant probability of occurrence in the failure region ($R_i \leq S_i$) and should have a larger contribution to system failure compared to members 2 and 3. An importance sampling strategy would place the samples near the limit state (i.e., near members 1, 4, and 5). However, some samples should be provided for members 2 and

3 to quantify their contribution to system failure. The optimal allocation of samples is identified by minimizing the variance of the system failure probability, described in the equations below.

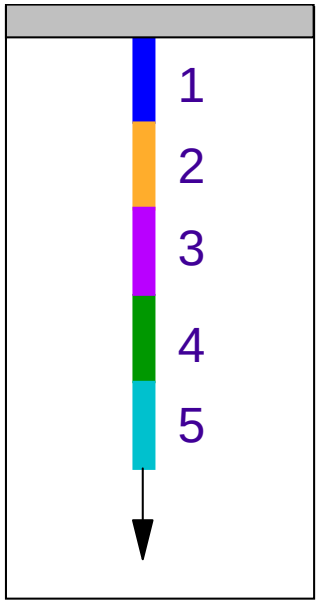

Figure Q-1. General Five-Member Structural System Under Applied Load

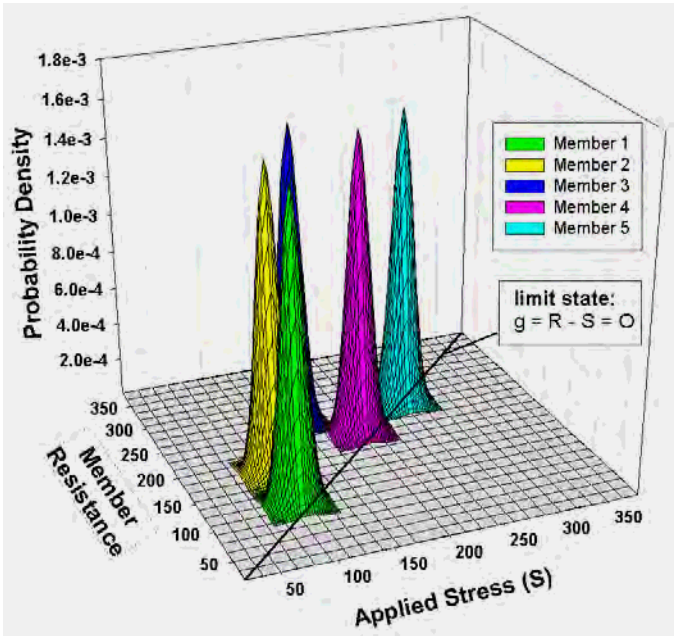

Figure Q-2. Illustrative Bivariant Probability Densities Reveal the Relative Values of Member Failure Probabilities in a System

The failure probability P_f of a series system of *m* independent members can be expressed as

$$P_f = 1 - \prod_{i=1}^{m} [1 - P_i] \tag{Q-2}$$

where $(1 - P_i)$ is the survival probability associated with member i. The variance of P_f is

$$Var(P_f) = \prod_{i=1}^{m} E\left([1 - P_i]^2\right) - \left\{\prod_{i=1}^{m} E[1 - P_i]\right\}^2 \tag{Q-3}$$

For a large number of samples n_i, the member survival probability can be approximated as a normal distribution with the following mean and variance:

$$E(1 - P_i) = 1 - p_i \tag{Q-4}$$

$$Var(1 - P_i) \cong p_i (1 - p_i) / n_i \tag{Q-5}$$

Noting that

$$E\left([1 - P_i]^2\right) = \left(E[1 - P_i]\right)^2 + Var(1 - P_i) \tag{Q-6}$$

equation Q-3 becomes

$$Var(P_f) = \prod_{i=1}^{m} \left[(1 - p_i)^2 + \frac{p_i(1 - p_i)}{n_i}\right] - \prod_{i=1}^{m} (1 - p_i)^2 \tag{Q-7}$$

To identify values of n_i that minimize $Var(P_f)$, the following optimization formulation is used:

$$\min \quad Z(n) = \prod_{i=1}^{m} \left[(1 - p_i)^2 + \frac{p_i(1 - p_i)}{n_i}\right] - \prod_{i=1}^{m} (1 - p_i)^2 \tag{Q-8}$$

subject to:

$$N = \sum_{i=1}^{m} n_i \tag{Q-9}$$

where n_i is the number of Monte Carlo samples used to estimate the survival probability of member *i* and *N* is the total number of samples for the system.

Equations Q-8 and Q-9 are solved using the Lagrange-multiplier method.

$$\phi\{\boldsymbol{n},\lambda\} = \prod_{i=1}^{m}\left[\left(1-p_i\right)^2 + \frac{p_i\left(1-p_i\right)}{n_i}\right] - \prod_{i=1}^{m}\left(1-p_i\right)^2 + \lambda\left(N - \sum_{i=1}^{m} n_i\right) \tag{Q-10}$$

subject to the following conditions at the optimum:

$$\frac{\partial\phi}{\partial n_i} = 0 \qquad i = 1, 2, \ldots m \tag{Q-11}$$

$$\frac{\partial\phi}{\partial\lambda} = 0 \tag{Q-12}$$

Applying these conditions to equation Q-10:

$$\frac{\partial\phi}{\partial n_i} = \frac{-p_i\left(1-p_i\right)\prod_{i=1}^{m}\left[\left(1-p_i\right)^2 + \frac{p_i\left(1-p_i\right)}{n_i}\right]}{n_i^2\left[\left(1-p_i\right)^2 + \frac{p_i\left(1-p_i\right)}{n_i}\right]} - \lambda = 0 \tag{Q-13}$$

$$\frac{\partial\phi}{\partial\lambda} = N - \sum_{i=1}^{m} n_i = 0 \tag{Q-14}$$

Combining equations Q-13 and Q-14:

$$n_i = \sqrt{\frac{p_i\left(1-p_i\right)\prod_{\substack{j=1\\ j\neq i}}^{m}\left[\left(1-p_j\right)^2 + \frac{p_j\left(1-p_j\right)}{n_j}\right]}{-\lambda}} \tag{Q-15}$$

Substituting equation Q-15 into Q-14:

$$N = \sum_{i=1}^{m}\sqrt{\frac{p_i\left(1-p_i\right)\prod_{\substack{j=1\\ j\neq i}}^{m}\left[\left(1-p_j\right)^2 + \frac{p_j\left(1-p_j\right)}{n_j}\right]}{-\lambda}} \tag{Q-16}$$

Combining equations Q-15 and Q-16, the optimal number of samples for each member failure mode is given by

$$n_i = N \frac{\sqrt{p_i\left(1-p_i\right)\prod_{\substack{j=1\\ j\neq i}}^{m}\left[\left(1-p_j\right)^2+\frac{p_j\left(1-p_j\right)}{n_j}\right]}}{\sum_{i=1}^{m}\sqrt{p_i\left(1-p_i\right)\prod_{\substack{j=1\\ j\neq i}}^{m}\left[\left(1-p_j\right)^2+\frac{p_j\left(1-p_j\right)}{n_j}\right]}} \qquad \text{(Q-17)}$$

Q.2 OPTIMAL SAMPLING APPLICATION: FIVE-MEMBER SERIES SYSTEM.

To illustrate the methodology, equation Q-17 is used to identify the optimal number of samples for the five-member series system shown in figure Q-1. Member resistances R_i are modeled as independent lognormal random variables each subjected to a deterministic stress S_i. The main descriptors for these variables are indicated in table Q-1, and associated probability densities are shown in figure Q-3. The limit state is given by equation Q-1 and can be solved analytically for each member failure mode. Analytical member failure probability results P_i are indicated in table Q-2.

Table Q-1. Applied and Ultimate Stress Values Associated With the Five-Member Series System Example

Variable	Units	Name	Mean	Standard Deviation	Distribution
S	MPa	Applied Stress	100.0	0.0	Deterministic
R_1	MPa	Ultimate Stress, Member 1	190.0	38.0	Lognormal
R_2	MPa	Ultimate Stress, Member 2	200.0	40.0	Lognormal
R_3	MPa	Ultimate Stress, Member 3	215.0	43.0	Lognormal
R_4	MPa	Ultimate Stress, Member 4	225.0	45.0	Lognormal
R_5	MPa	Ultimate Stress, Member 5	240.0	48.0	Lognormal

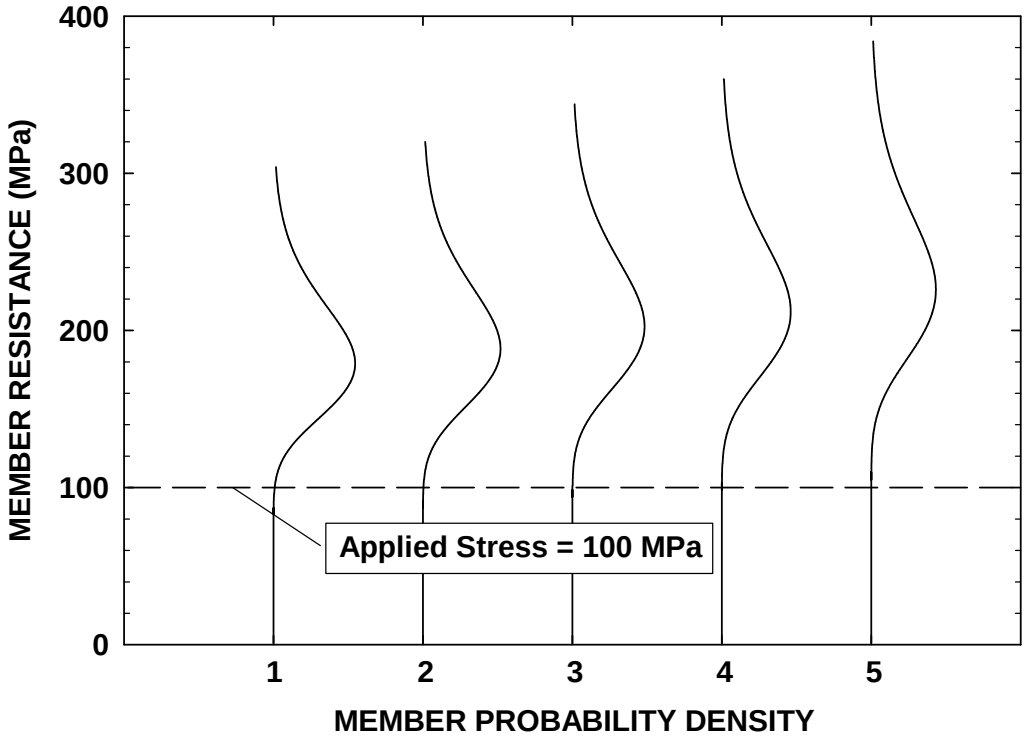

Figure Q-3. Probability Densities Associated With Member Resistances for the Five-Member Structural System Shown in Figure Q-1

Table Q-2. Allocation of Samples to Members for Uniform and Optimal Sampling Strategies

Member	P_i	Uniform Sampling			Optimal Sampling		
		n_i	σ_i	COV_i	n_i	σ_i	COV_i
1	9.38E-04	200000	6.84E-05	0.07	442192	4.60E-05	0.05
2	3.82E-04	200000	4.37E-05	0.11	282047	3.68E-05	0.10
3	9.68E-05	200000	2.20E-05	0.23	141994	2.61E-05	0.27
4	3.83E-05	200000	1.38E-05	0.36	89368	2.07E-05	0.54
5	9.46E-06	200000	6.88E-06	0.73	44399	1.46E-05	1.54
System	1.46E-03	1000000	8.55E-05	0.06	1000000	6.92E-05	0.05

COV = Coefficient of variation

Equation Q-1 can also be solved using numerical simulation with the variance of the member and system failure probabilities given by equations Q-5 and Q-7, respectively. Suppose that one million Monte Carlo samples are used to predict the failure of the system. For uniform sampling, the same number of samples is allocated to the failure prediction of each member (i.e., n_i = 200,000 for each member, see table Q-2. For optimal sampling, equation Q-17 is used to specify the number of samples for each member based on the analytical solution for p_i, indicated in

equation Q-2. The standard deviation and coefficient of variation (COV) of the sampling-based member failure probability estimates, σ_i and COV_i, respectively, are given by

$$\sigma_i = \sqrt{\frac{p_i(1-p_i)}{n_i}} \tag{Q-18}$$

$$COV_i = \frac{\sigma_i}{p_i} \tag{Q-19}$$

Values for these variables are indicated in table Q-2. The variance of the system failure probability is also indicated in table Q-2. Comparing the values of the system failure probability P_f to the individual member failure probabilities P_i, it can be observed that members 1 and 2 contribute significantly to system failure (over 90% of system failure can be attributed to these two members). When optimal sampling is used, the failure probability COV values of members 1 and 2 are smaller compared to the values for uniform sampling, leading to an overall reduction in the variance of the system failure probability. On the other hand, the failure probability COV is larger for the remaining members in the system when optimal sampling is used (the member 5 failure probability COV value associated with optimal sampling is more then double the value associated with uniform sampling). Probability densities for the P_i estimates associated with the uniform and optimal sampling methods are shown in figure Q-4. The influence of optimal sampling on the probability density function of P_i is significant for all of the members considered, particularly for the strongest and weakest members (5 and 1, respectively).

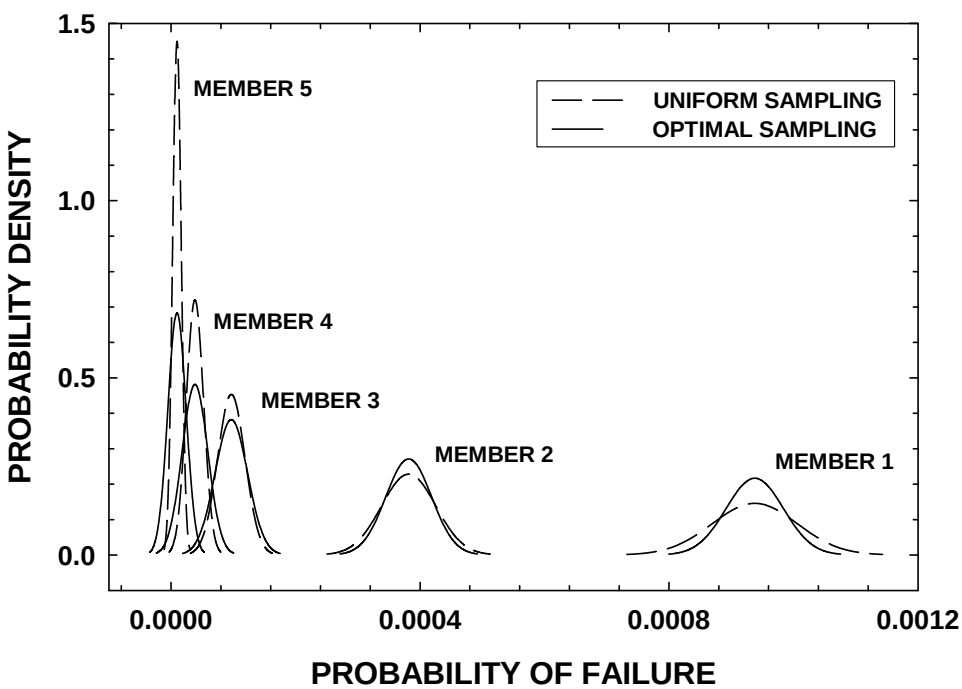

Figure Q-4. Probability Densities Associated With P_i Estimates for the Uniform and Optimal Sampling Strategies

Q.3 ADAPTIVE OPTIMAL SAMPLING.

Equation Q-17 indicates that the optimum number of samples for an individual member failure mode is dependent on knowledge of the failure probability P_i for all of the member failure modes. However, since p_i values are unknown prior to sampling, initial estimates of these values are required to make an estimate of the optimal number of samples in each zone. The efficiency and accuracy of the optimal sampling method is highly dependent on the number of samples n_i used for the initial estimate of p_i. If n_i is too large, the method is inefficient (i.e., provides no benefit over uniform sampling). On the other hand, if n_i is too small, the method may be inaccurate. For example, if the number of samples for a member is so small that the limit state is not violated for any of the samples, then p_i is estimated as equal to zero and n_i is also zero. Accuracy of the initial estimate can be improved by setting a minimum value for p_i when no samples violate the limit state (i.e., $p_i = 1/ n_i$). Depending on the limit state for a member, p_i can sometimes be estimated using a non-sampling-based method (e.g., numerical integration of dominant random variable(s), among others).

The optimal number of samples for each failure mode can be computed adaptively using the following procedure:

1. Estimate p_i using a small number of Monte Carlo samples or other efficient strategy.

2. Compute optimal number of samples n_i for each member failure mode using equation Q-17.

3. Compute p_i and P_f using Monte Carlo sampling with estimated optimal n_i.

4. Repeat steps 2-3 until $\Delta\sum n_i \le \varepsilon$.

If the individual p_i values are relatively small, the optimal number of samples for the system can be estimated as [Q-12 and Q-13]

$$N = \frac{k_{\alpha/2}^{\;2}}{\gamma^2 P_f^{\;2}} \left[\sum_{i=1}^{m} \sqrt{p_i} \right]^2 \qquad \text{(Q-20)}$$

where $k_{\alpha/2}$ = standard normal variate for a $(1-\alpha)$ confidence level, and $\gamma = (p_f - P_f)/P_f$ = sampling error [Q-8].

Q.4 APPLICATION OF ADAPTIVE OPTIMAL SAMPLING TO ZONE-BASED SYSTEM.

Figure Q-5 shows the adaptive optimal sampling method for the aircraft rotor disk. The disk is discretized into 64 zones (i.e., it is modeled as a series system consisting of 64 members). A fracture mechanics-based limit state is applied to each zone, and three primary random variables are used to model the uncertainties associated with material properties, applied stress, and initial anomaly size. Individual p_i values are relatively small, so equation Q-20 can be used to estimate the optimal number of samples for the system with $k_{\alpha/2}$ = 95% and γ = 10%. Complete details

regarding the disk and values of the associated deterministic and random variables are provided in reference Q-10.

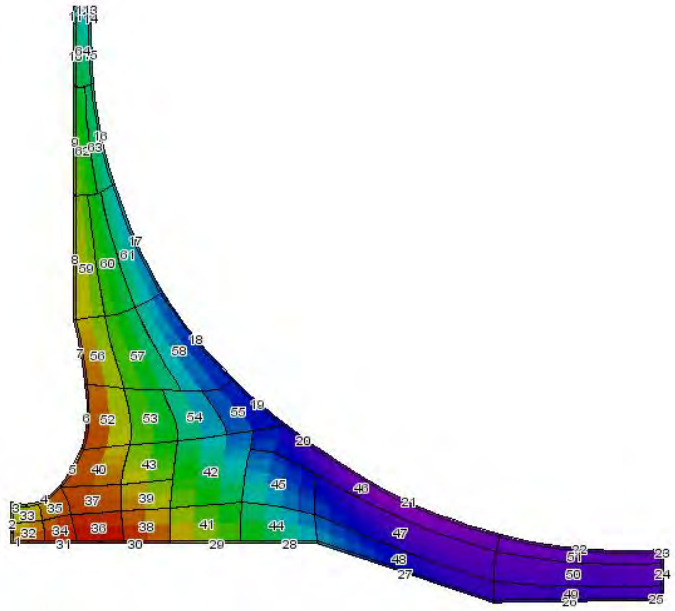

Figure Q-5. The Adaptive Optimal Sampling Methodology is Illustrated for an Aircraft Rotor Disk [Q-10]

The following methods are used to estimate initial p_i values prior to sampling: (1) uniform sampling—same number of samples in each zone (i.e., 100, 1000, and 10000 samples per zone), (2) first failure—sampling is performed in a zone until either the limit state is violated or a specified number of samples (100 or 1000 samples per zone) have been applied (p_i is estimated as one divided by the number of samples to first failure), and (3) critical defect—p_i is estimated directly assuming that the dominant variable (initial anomaly size) is random and the remaining variables are deterministic [Q-14]. For methods (1) and (2), p_i is set equal to $1/n_i$ if no limit state violations occur within n_i for a given zone.

The influence of the initial p_i estimate on the predicted probability of failure is shown in figures Q-6, Q-7, and Q-8 for a relatively weak zone, a strong zone, and the disk, respectively. In figure Q-6, the error in the initial p_i estimate for a weak zone is between 1% and 29% depending on the method used, but is within 8% for the converged solution (i.e., after the adaptive optimal sampling algorithm is applied). In figure Q-7, it is shown that the sampling error for a strong zone is 1%-67% for the initial estimate and 5%-65% for the converged solution. Since the strong zone has a small influence on P_f, the relatively large postconvergence sampling error associated with some of the methods has a relatively small impact on the error associated with P_f. Sampling error for the system is shown in figure Q-8, with values of 0.5%-660% and 2%-8% for the initial and converged estimates, respectively. As shown in figure Q-8, all converged P_f values fall within the 10% error bounds at 95% confidence, regardless of the method used for the initial prediction of p_i values. This result suggests that sampling accuracy is somewhat independent of the method used to estimate initial p_i values, provided that converged values are used to compute P_f.

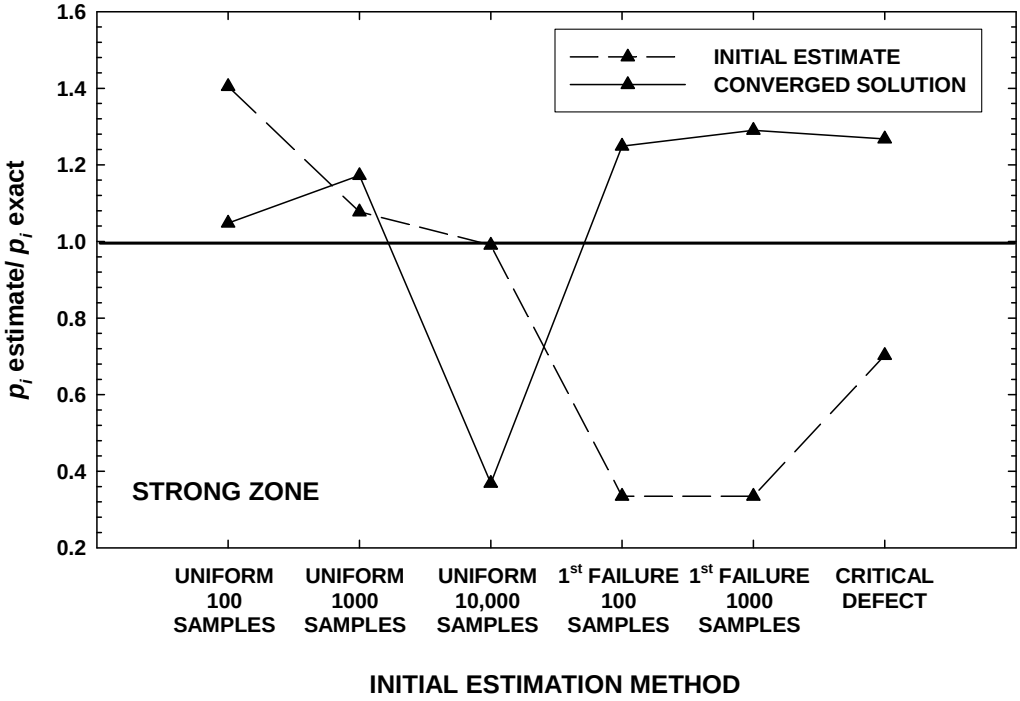

Figure Q-6. Influence of Initial p_i Estimates on Failure Probability Predictions for a Relatively Weak Zone

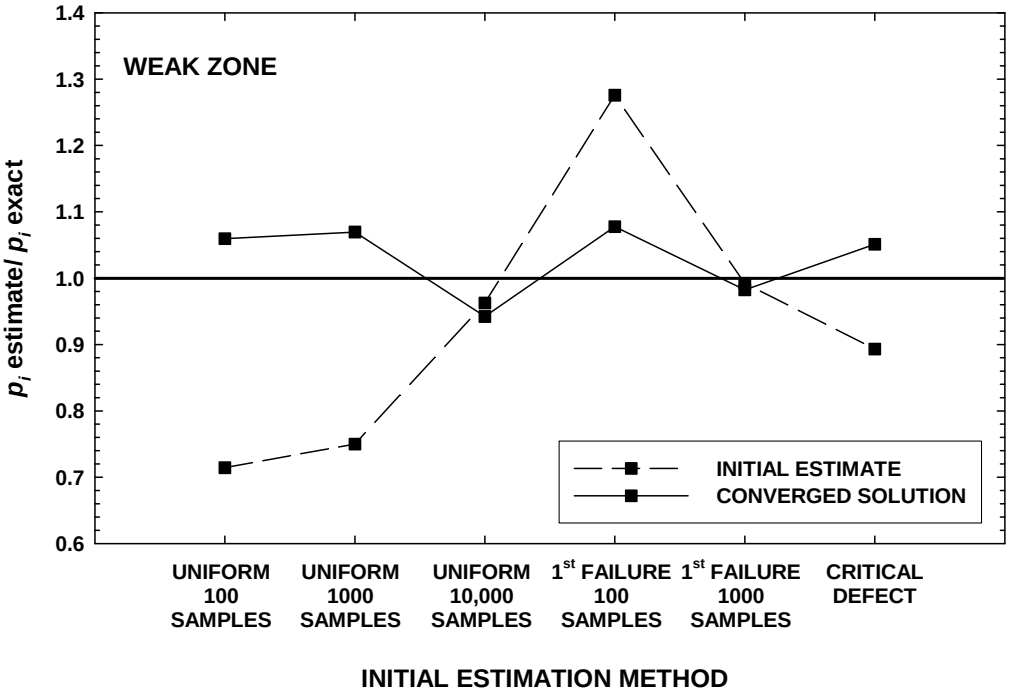

Figure Q-7. Influence of Initial p_i Estimates on Failure Probability Predictions for a Relatively Strong Zone

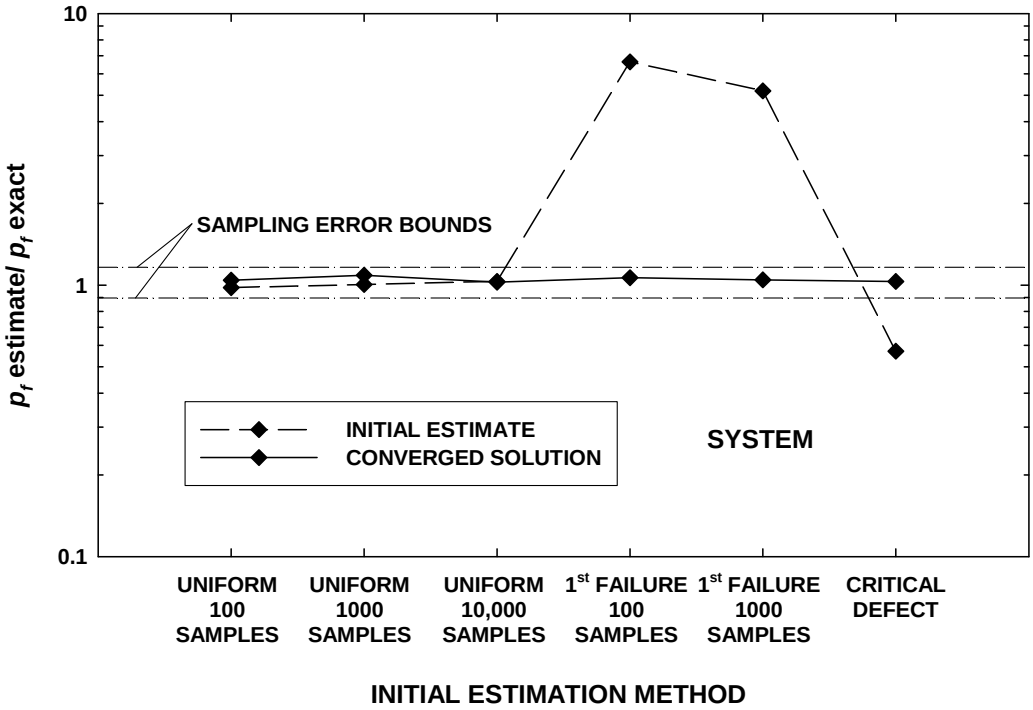

Figure Q-8. Influence of Initial p_i Estimates on Failure Probability Prediction of Disk P_f (System)

The influence of the method used to estimate p_i on computational efficiency is shown in figures Q-9, Q-10, and Q-11 for a weak zone, a strong zone, and the system, respectively. For the weak zone (figure Q-9), a wide range of values for the number of samples (i.e., limit state evaluations) is required to estimate p_i for the various methods considered. However, converged solutions require a similar number of samples ranging from 3774 (uniform sampling with 1,000 samples) to 10,600 (uniform sampling with 100 samples per zone). For the strong zone (figure Q-10), the range of samples for converged solutions ranges from 591 (critical defect) to 10,000 (uniform sampling with 10,000 samples per zone). The initial estimate appears to have a significant influence on the sampling efficiency of strong zones, with the most efficient methods requiring the fewest number of samples for the initial estimate. The number of samples associated with the system is shown in figure Q-11. For the converged solution, the number of samples ranges from about 1.0E5 (critical defect) to over 2.0E6 (uniform sampling with 100 samples per zone). These results indicate that sampling efficiency is highly dependent on the method used to estimate initial p_i values.

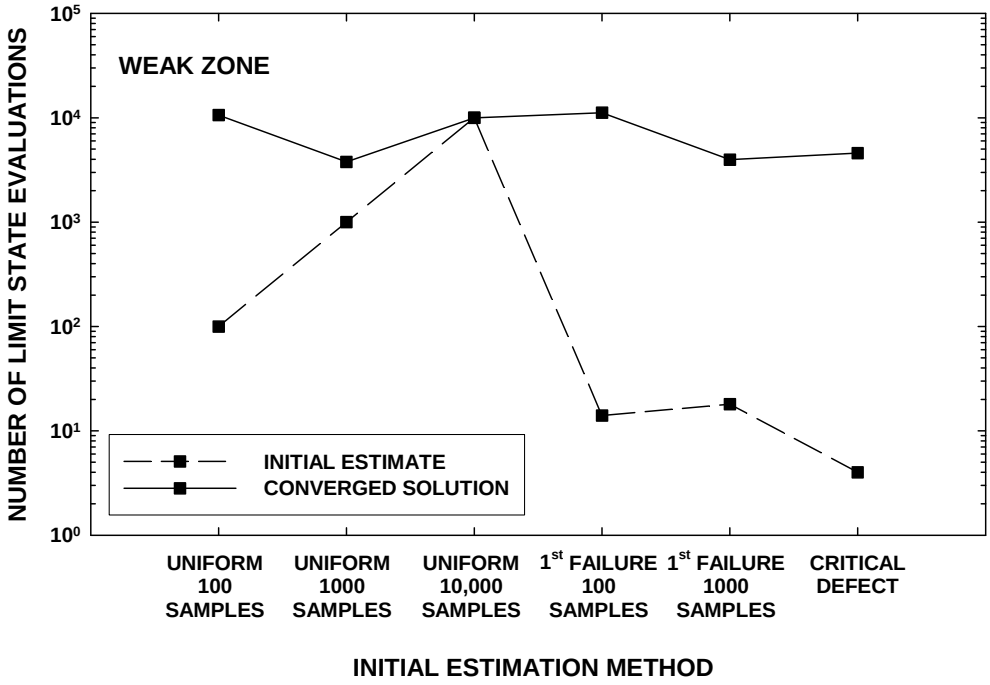

Figure Q-9. Influence of Initial p_i Estimates on Number of Limit State Evaluations Required to Accurately Predict Failure Probability for a Relatively Weak Zone

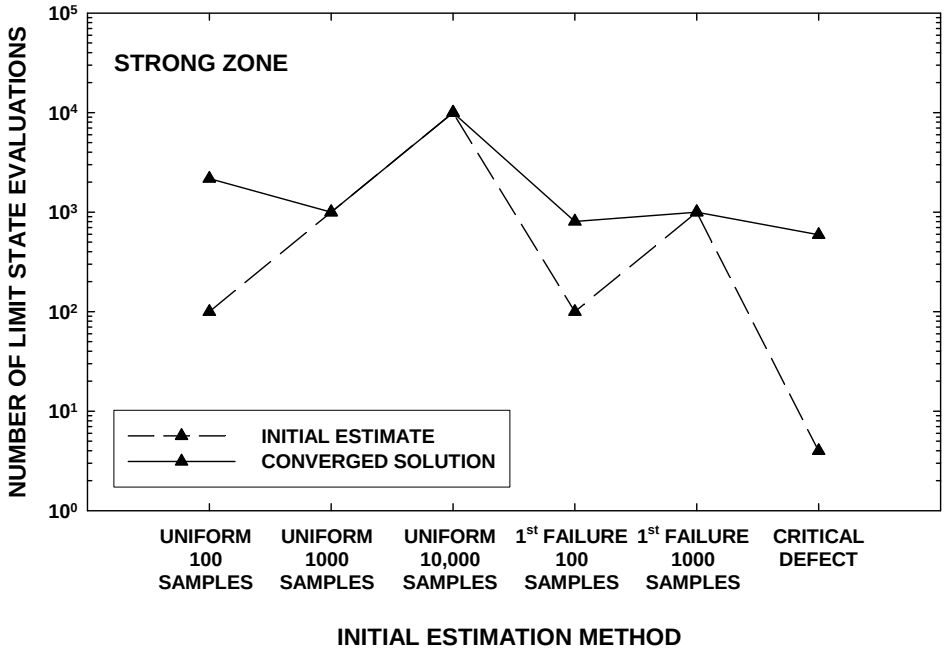

Figure Q-10. Influence of Initial p_i Estimates on Number of Limit State Evaluations Required to Accurately Predict Failure Probability for a Relatively Strong Zone

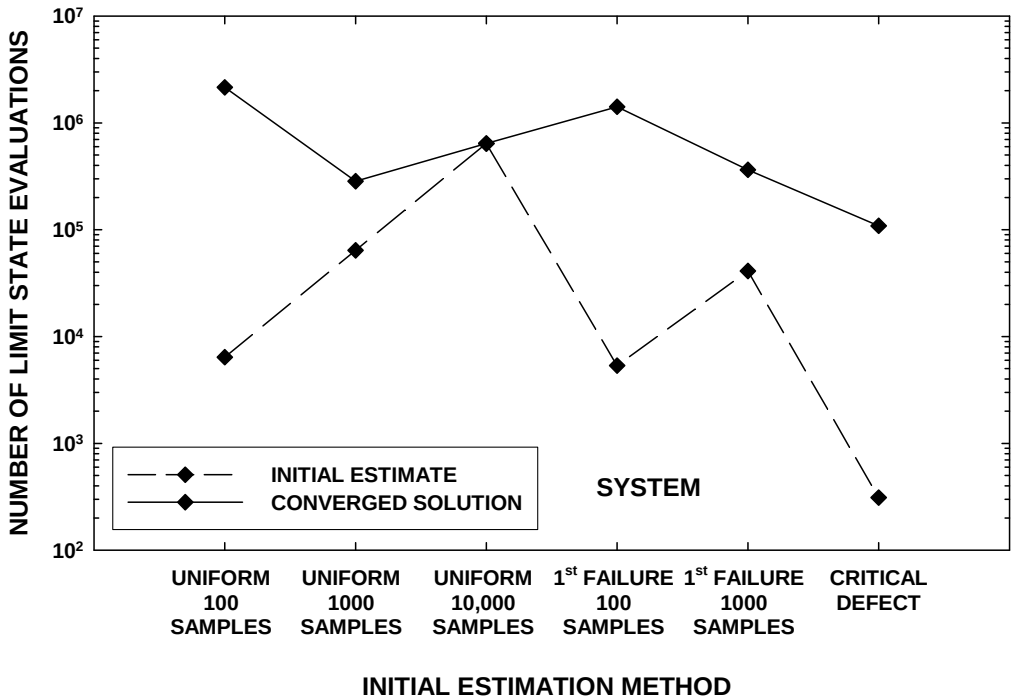

Figure Q-11. Influence of Initial p_i Estimates on Number of Limit State Evaluations Required to Accurately Predict Disk (System) Failure Probability

Q.5 SUMMARY.

A methodology was presented for variance reduction of sampling-based series system reliability predictions based on optimal allocation of Monte Carlo samples to individual failure modes. An algorithm was presented for adaptively allocating samples to member failure modes based on initial estimates of the individual member failure probabilities. The optimal sampling methodology was demonstrated for a simple series system in which it was shown that the variance of the system failure probability is reduced compared to a uniform sampling approach, due to the reduced variances in the failure probabilities associated with the weakest members. The adaptive optimal sampling methodology was illustrated for a gas turbine engine disk modeled using several methods to estimate the failure probability p_i in each zone prior to optimal sampling. For the example problem considered, it was shown that the computational accuracy of the method does not appear to depend on the initial p_i estimate, whereas the computational efficiency is highly dependent on the initial p_i estimate. The results can be applied to improve the efficiency of sampling-based series system reliability predictions.

Q.6 REFERENCES.

Q-1. Hendawi, S. and Frangopol, D.M., "System Reliability and Redundancy in Structural Design and Evaluation," *Structural Safety*, Vol. 16, 1994, pp. 47-71.

Q-2. Enright, M.P. and Frangopol, D.M., "Failure Time Prediction of Deteriorating Fail-Safe Structures," *Journal of Structural Engineering*, Vol. 124, 1998, pp. 1448-1457.

Q-3. Ditlevsen, O., "Narrow Reliability Bounds for Structural Systems," *Journal of Structural Mechanics*, Vol. 7, 1979, pp. 453-472.

Q-4. Melchers, R.E., *Structural Reliability Analysis and Prediction*, John Wiley, New York, 1987.

Q-5. Mahadevan, S. and Raghothamachar, P., "Adaptive Simulation for System Reliability Analysis of Large Structures," *Computers and Structures*, Vol. 77, 2000, pp. 725-734.

Q-6. Au, S.K. and Beck, J.L., "First Excursion Probabilities for Linear Systems by Very Efficient Importance Sampling," *Probabilistic Engineering Mechanics*, Vol. 16, 2001, pp. 193-207.

Q-7. Mori, Y. and Kato, T., "Multinormal Integrals by Importance Sampling for Series System Reliability," *Structural Safety*, Vol. 25, 2003, pp. 363-378.

Q-8. Wu, Y.T., Enright, M.P., and Millwater, H.R., "Probabilistic Methods for Design Assessment of Reliability With Inspection," *AIAA Journal*, Vol. 40, 2002, pp. 937-946.

Q-9. Millwater, H.R., Enright, M.P., and Fitch, S.K., "A Convergent Probabilistic Techniques for Risk Assessment of Gas Turbine Disks Subject to Metallurgical Defects," AIAA Paper 2002-1382, *Proc. 43rd AIAA/ASME/ASCE/AHS/ASC Structures, Structural Dynamics, and Materials Conference*, Denver, Colorado, 2002.

Q-10. Huyse, L. and Enright, M.P., "Efficient Statistical Analysis of Failure Risk in Engine Rotor Disks Using Importance Sampling Techniques," AIAA Paper 2003-1838, *Proc. 44th AIAA/ASME/ASCE/AHS/ASC Structures, Structural Dynamics, and Materials Conference*, Norfolk, Virginia, 2003.

Q-11. Millwater, H.R., Shook, B.D., Guduru, S., and Constantinides, G., "Application of Parallel Processing Methods to Probabilistic Fracture Mechanics Analysis of Gas Turbine Disks," Paper AIAA-2004-1745, *Proc. 45th AIAA/ASME/ASCE/AHS/ASC Structures, Structural Dynamics, and Materials Conference*, Palm Springs, California, 2004.

Q-12. Wu, Y.-T., Enright, M.P., and Millwater, H.R., "Efficient and Accurate Methods for Probabilistic Analysis of Titanium Rotors," Paper PMC2000-221, *Proc. 8th ASCE Joint Specialty Conference on Probabilistic Mechanics and Structural Reliability*, Notre Dame, Indiana, 2000.

Q-13. Enright, M.P. and Millwater, H.R., "Optimal Sampling Techniques for Zone-Based Probabilistic Fatigue Life Prediction," AIAA Paper 2002-1383, *Proc. 43rd AIAA/ASME/ASCE/AHS/ASC Structures, Structural Dynamics, and Materials Conference*, Denver, CO, 2002.

Q-14. Leverant, G.R., et al., "Turbine Rotor Material Design—Final Report," FAA report DOT/FAA/AR-00/64, December 2000.

APPENDIX R—CONFIDENCE BOUNDS

The probability of failure is a random variable, and the variability associated with it is dependent on the number of samples that are generated to estimate it. Numerical simulation methods can be used to develop a statistical estimate of the probability of failure. The estimate is developed using an algorithm known as a pseudo-random number generator that simulates sequences of input values that are based on a specified initial or seed value. When the seed value is altered, the simulator generates a different sequence of random numbers, which results in a slightly different estimate for the failure probability (figure R-1). The range of values associated with a specified seed value can be quantified using established statistical methods that relate the boundary values to a specified confidence interval.

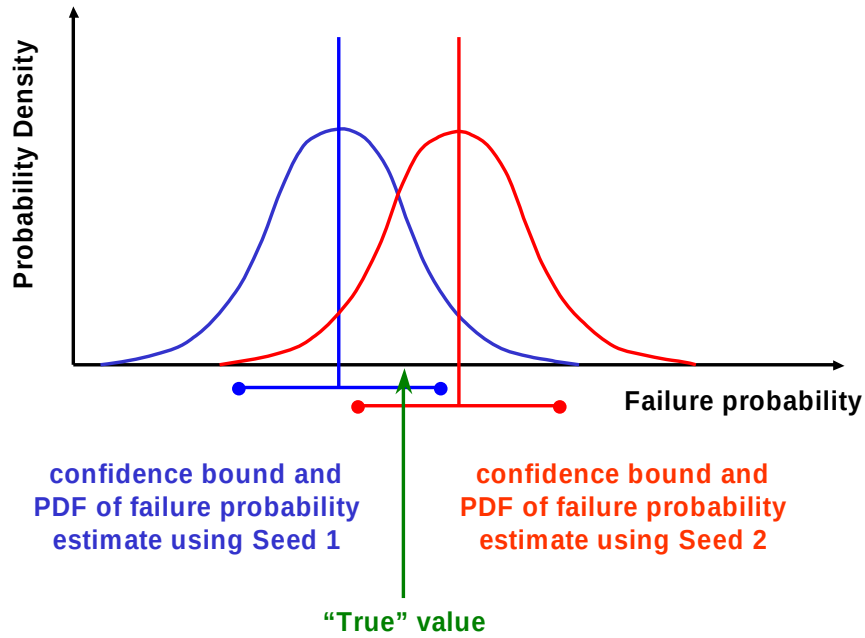

PDF = Probability density function

Figure R-1. Uncertainty Associated With Failure Probability Estimates for Two Different Seed Values

R.1 MONTE CARLO CONFIDENCE BOUNDS.

Failure probability predictions based on Monte Carlo simulation have an associated sampling error that can be approximated as a normal distribution (figure R-2).

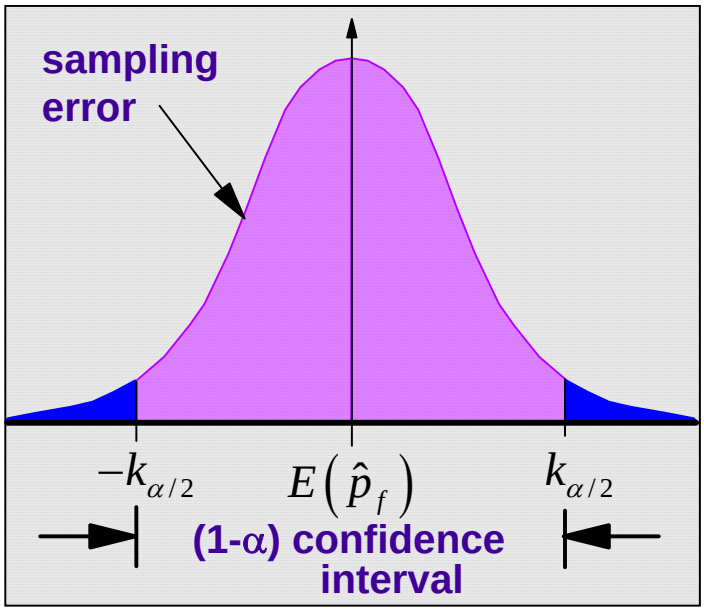

Figure R-2. Confidence Bounds Associated With Monte Carlo Simulation

The conditional probability of fracture of a zone $\hat{p}_{i|d}$ can be estimated using Monte Carlo simulation. The standard deviation $\sigma_{\hat{p}_{i|d}}$ associated with the estimate can be expressed as [R-1]

$$\sigma_{\hat{p}_{i|d}} = \sqrt{\frac{\hat{p}_{i|d}\left(1-\hat{p}_{i|d}\right)}{n_i}} \tag{R-1}$$

where n_i = number of Monte Carlo samples in zone i.

Since the failure probability associated with a zone is typically much smaller than 1, the Coefficient of Variation (COV) of the Monte Carlo estimate can be expressed as

$$COV = \frac{\sigma_{\hat{p}_{i|d}}}{\hat{p}_{i|d}} = \sqrt{\frac{\hat{p}_{i|d}\left(1-\hat{p}_{i|d}\right)}{\hat{p}_{i|d}^2}} \cong \frac{1}{\sqrt{\hat{p}_{i|d}\, n_i}} \tag{R-2}$$

Upper and lower confidence bounds for zone unconditional failure probability are as follows [R-1]:

$$\text{lower limit: } \alpha_i \hat{p}_{i|d} - \alpha_i k_{\alpha/2} \sigma_{\hat{p}_{i|d}} \tag{R-3}$$

$$\text{upper limit: } \alpha_i \hat{p}_{i|d} + \alpha_i k_{\alpha/2} \sigma_{\hat{p}_{i|d}} \tag{R-4}$$

where α_i = defect occurrence rate, $k_{a/2}$ = standard normal variate, the number of standard deviations from the mean value for the (1-a_i) confidence interval (e.g., $k_{\alpha/2}$ = 1.96 for a 95% confidence interval).

For conservative disk failure probability predictions, it is also assumed that zone fracture failure events are uncorrelated. The disk failure probability mean $\mu_{\hat{p}_f}$ and standard deviation $\sigma_{\hat{p}_f}$ are therefore:

$$\sigma^2_{\hat{p}_f} = \sum_{i=1}^{m} \alpha_i^2 \cdot \sigma^2_{\hat{p}_{i|d}} \tag{R-5}$$

$$\mu_{\hat{p}_f} = \sum_{i=1}^{m} \alpha_i \cdot \hat{p}_{i|d} \tag{R-6}$$

where m = number of zones

The upper and lower confidence bounds for disk unconditional failure probability (with and without inspection) are

$$\text{lower limit: } \mu_{\hat{p}_f} - k_{\alpha/2}\sigma_{\hat{p}_f} \tag{R-7}$$

$$\text{upper limit: } \mu_{\hat{p}_f} + k_{\alpha/2}\sigma_{\hat{p}_f} \tag{R-8}$$

Examples of Monte Carlo confidence bounds are shown in figure R-3 for a zone associated with a typical rotor disk (impeller). In figure R-3, the mean conditional and unconditional probability of failure results are shown along with upper and lower bounds associated with 10,000 samples and 95% confidence levels. These bounds can be used to assess the uncertainty associated with Monte Carlo sampling.

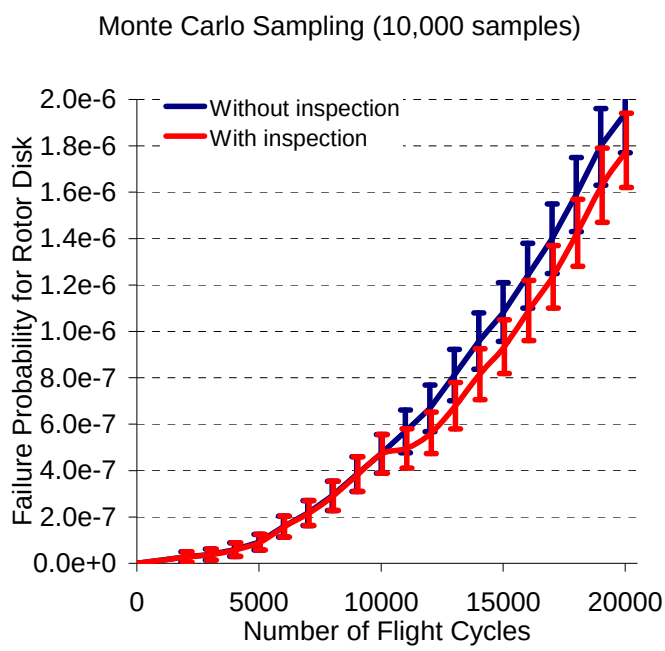

Figure R-3. Example—Monte Carlo Confidence Bounds

R.2 IMPORTANCE SAMPLING CONFIDENCE BOUNDS.

When the DARWIN® importance sampling (IS) method is used, the conditional probability of failure without inspection $\hat{p}_{i|d,\,no\,insp}$ is estimated using numerical integration, and the associated uncertainty is negligible. However, numerical sampling is used to estimate the probability of failure with inspection $\hat{p}_{i|d,\,insp}$, and the uncertainty associated with it can be quantified using the following equation:

$$COV \cong \frac{1}{\sqrt{\hat{p}_{i|d}\, n_i}} \cong \frac{1}{\sqrt{\dfrac{\hat{p}_{i|d,\,insp}}{\hat{p}_{i|d,\,no\,insp}}\, n_i}} = \sqrt{\frac{\hat{p}_{i|d,\,no\,insp}}{\hat{p}_{i|d,\,insp}\, n_i}} \qquad \text{(R-9)}$$

If $\hat{p}_{i|d,\,no\,insp}$ is roughly the same order of magnitude as $\hat{p}_{i|d,\,insp}$, the COV of the IS estimate will be substantially smaller than the COV of a Monte Carlo estimate for an equal number of samples. Typically, 100 times fewer samples are required to achieve the confidence bound values that are similar to the Monte Carlo method.

Examples of IS confidence bounds are shown in figure R-4 for a zone associated with a typical rotor disk (100 samples, 95% confidence). Monte Carlo confidence bound results are shown in figure R-3 for the same zone. Comparing these figures, it can be observed that the IS confidence bounds are slightly narrower than those associated with the Monte Carlo simulation. Since the IS bounds were achieved using 100 times fewer samples, this illustrates the computational efficiency associated with IS.

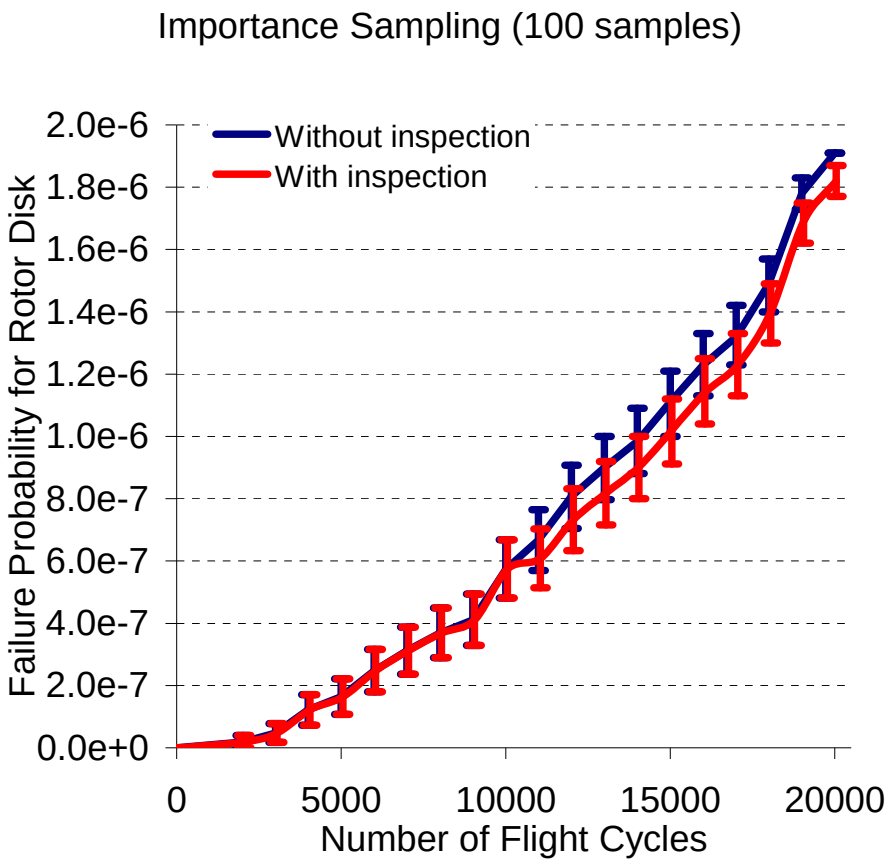

Figure R-4. Example—IS Confidence Bounds

R.3 REFERENCE.

R-1. Ang, H.-S. and Tang, W.H., *Probability Concepts in Engineering Planning and Design*, John Wiley, New York, 1975.

APPENDIX S—IMPORTANCE SAMPLING TECHNIQUES

S.1 INTRODUCTION.

Several sampling-based probabilistic analysis methods can be used to predict the life of disks subjected to periodic inspection. Monte Carlo simulation provides accurate results (the accuracy is dependent on the failure probability, confidence interval, and number of random samples) but is relatively inefficient because the failure limit state must be evaluated for each random sample using a fatigue crack growth algorithm.

The importance sampling (IS) method focuses analysis on the initial conditions (anomaly size and other random variables) that would result in lives shorter than the specified design life. This approach reduces the size of the analysis region and is significantly more efficient than Monte Carlo simulation. This appendix describes the IS algorithm as implemented in Design Assessment of Reliability INspection (DARWIN®).

DARWIN considers the following random variables related to the occurrence or detection of anomalies: initial anomaly size, location, inspection time, and probability of anomaly detection during inspection. The uncertainty associated with the finite element stress results is modeled by means of a lognormally distributed stress scatter factor *B*. The actual stress is

$$\sigma_{actual} = B \times \sigma_{FE} \tag{S-1}$$

Considerable uncertainty may be associated with the crack growth model. Because DARWIN is intended as a practical design tool, a simple random variable model is used to represent the uncertainty associated with the crack growth law [S-1]. The random variable model essentially adds an error band to the regression curve of the d*d*/d*N* data. For instance, for a Paris growth equation, the equation becomes

$$\frac{\mathrm{d}d}{\mathrm{d}N} = S \times C\left(\Delta K\right)^m \tag{S-2}$$

where ΔK denotes the change in stress-intensity factor K over the interval dN, and C and m are material coefficients associated with the Paris equation.

S.2 MONTE CARLO SAMPLING.

The conditional failure probabilities in each zone can be estimated using Monte Carlo simulation. Sample values of the initial anomaly size *d*, the stress scatter factor *B*, and the life scatter factor *S* can be generated to compute the service life *N* while accounting for potential in-service inspections. DARWIN has the capability to schedule inspections at random intervals. For each of these samples, a limit state function is evaluated, and the failure probability is estimated as the fraction of failed samples. Although easily implemented, the failure probability estimates obtained with Monte Carlo simulation are subject to random sampling error and converge slowly to the exact failure probability. In addition, when the failure probability is

small—as is typically the case in structural applications—most of the samples do not result in failures. This is illustrated in figure S-1.

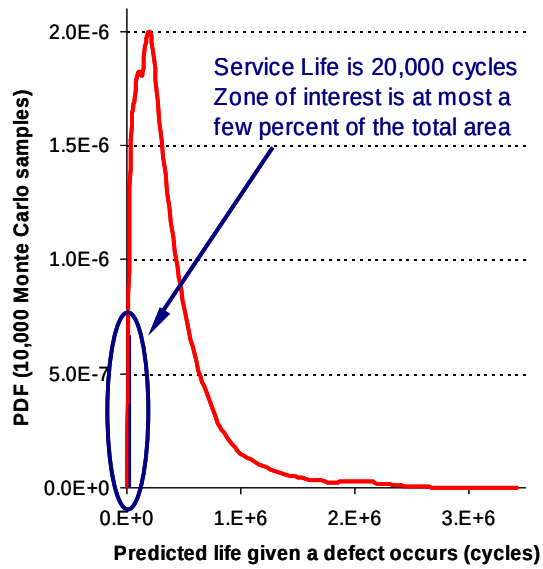

Figure S-1. Sample Histogram of Life

S.3 IMPORTANCE SAMPLING METHOD.

As shown in figure S-1, significant computational gains could be achieved by generating only the samples that fail. The IS implementation in DARWIN achieves these gains. It is a hybrid method that combines numerical integration with random sampling. The method [S-2] consists of two steps:

1. Compute the failure probability when no in-service inspections are performed by numerical integration of the conditional failure probability p_{cond} over all random variables for each zone:

$$p_{cond} = \iiint_{failure} f_d(d)\, f_B(B)\, f_S(S)\, \mathrm{d}d\,\mathrm{d}B\,\mathrm{d}S \qquad \text{(S-3)}$$

   where d is the initial anomaly size, B the stress scatter factor, and S the life scatter factor, f represents the probability density functions (pdf). The critical anomaly size d^* is defined as the smallest anomaly, which will cause the disk to fail within the specified service life.

2. To assess the effectiveness of the inspection schedule, use the results of Step 1 to generate only those samples that will result in a life smaller than the target service life, i.e., fail, if not inspected. Limit the simulation to these conditional samples to estimate the effectiveness of the inspection.

By definition, the failure domain in the probability integral in equation S-3 is limited to the anomalies that exceed the critical anomaly size. Equivalently, this can be rewritten as

$$p_{cond} = \iint \Pr(d \geq d^*) f_B(B) f_S(S) \mathrm{d}B\mathrm{d}S \tag{S-4}$$

The first step of the numerical integration procedure of the conditional failure probability consists of computing the predicted life as a function of the initial anomaly size and the stress and life scatter factors. Because the life scales linearly with the life scatter factor, this response surface can be reduced to a function of only two variables (see figure S-2).

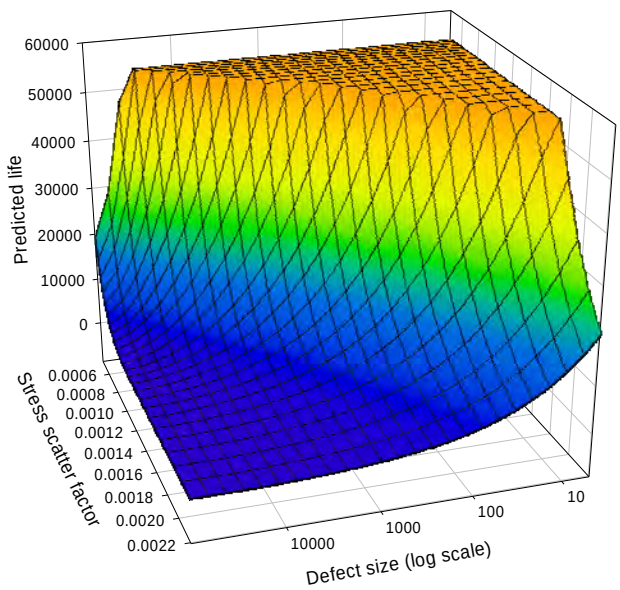

Figure S-2. Predicted Life Response Surface

The critical anomaly size d^*, associated with each value of the life and stress scatter factors, can subsequently be computed from this response surface. The critical anomaly size is then plugged into the cumulative distribution function of the initial defect size to determine the exceedance probability of the critical anomaly size as a function of the life and stress scatter factors (figure S-3).

According to equation S-4, the conditional failure probability p_{cond} in a zone is equal to the integral of the exceedance probability in figure S-3 over the stress and life scatter factors (see figures S-4 and S-5). To ensure an accurate integration of the total probability, the integration domain for the life and stress scatter factors in DARWIN is [-5σ, 3σ] and [-3σ, 5σ], respectively, where σ is the standard deviation.

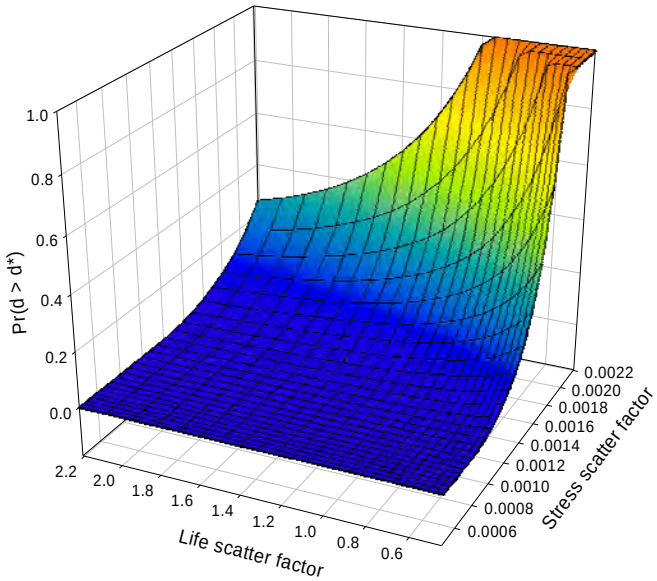

Figure S-3. Exceedance Probability of the Critical Defect Size

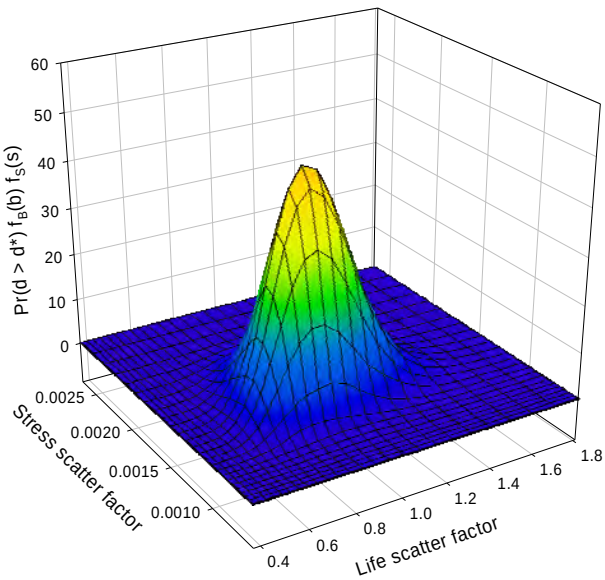

Figure S-4. Three-Dimensional Plot of the Integrand in Equation S-4, Used for the Computation of the Failure Probability Without Inspection

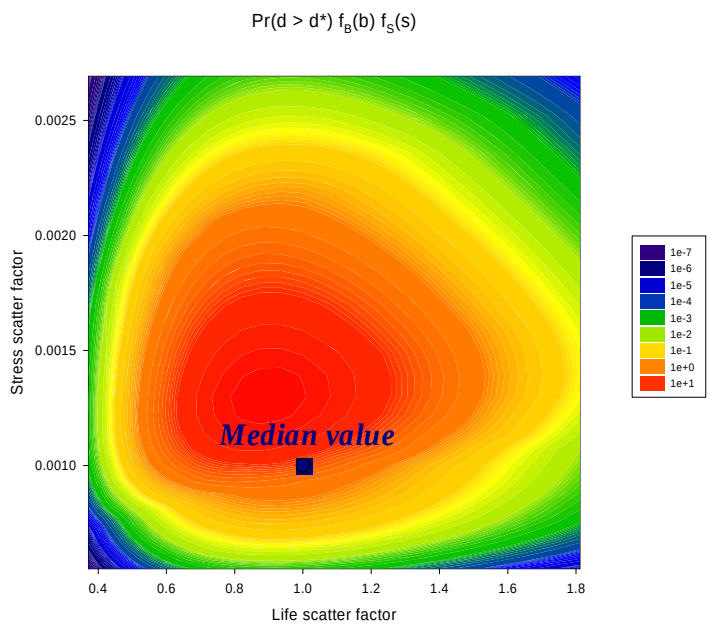

Figure S-5. Contour Plot of Integrand in Equation S-4

The ranges of values of the random variables that fall within the failure domain are identified during integration of equation S-4. Monte Carlo samples generated from the failure domain are used to assess the influence of inspection on risk. These samples are often referred to as conditional samples (i.e., samples given that a failure has occurred).

The efficient generation of conditional samples in a general-purpose IS tool is by no means a trivial task [S-3]. However, due to the nature of the numerical integration scheme for the failure probability without inspection, the conditional probability density functions, required for the cases with inspection, are readily obtained in DARWIN:

- Integration of figure S-4 over the stress scatter factor B results in a conditional likelihood curve for the life scatter factor S from which, upon appropriate scaling, a conditional life scatter factor S_i is sampled using the inverse cumulative distribution function method.

- This value S_i is plugged into equation S-4 and a sample stress scatter factor B_i can be obtained from the following likelihood curve:

$$\Pr(d \geq d^* | S_i) f_B(B) f_B(S_i) \tag{S-5}$$

  This conditional likelihood curve for the stress scatter factor B is obtained by setting S = S_i in figure S-4.

- The exceedance probability $\Pr(d > d^* \mid B_i, S_i)$ corresponding to the sample values S_i and B_i is shown in figure S-3. This exceedance probability value determines the critical anomaly size d* through the initial anomaly distribution. A sample initial anomaly size d_i is subsequently generated from the pdf $f_d(d)$, which is truncated and rescaled to include only anomaly values $d > d^*$.

The conditional sample values d_i, B_i, and S_i are subsequently used to assess the life when in-service inspections are performed. Figure S-6 illustrates that each of these samples results in a failure if no inspection is performed (the target service life is 20,000 cycles in this example).

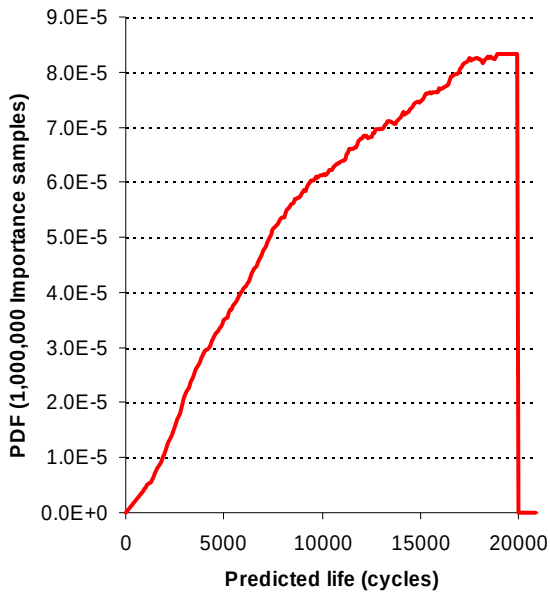

Figure S-6. The pdf of the Service Life for the Conditional Samples Used in IS

S.3.1 VERIFICATION OF THE IMPORTANCE SAMPLING RESULTS.

The Monte Carlo results are an unbiased estimator for the true failure probability. Unfortunately, the estimator converges rather slowly to the true failure probability and requires a lot of samples when the probability is small. Provided that the IS density covers the entire failure domain (which is the case in DARWIN), the IS results are also unbiased [S-4].

Figure S-7 shows the conditional failure probability p_{cond} (equation S-4) for a surface zone of an impeller. It demonstrates the improved accuracy of the IS algorithm compared to Monte Carlo. Sufficient samples were used to remove sampling uncertainty from the failure probability estimates.

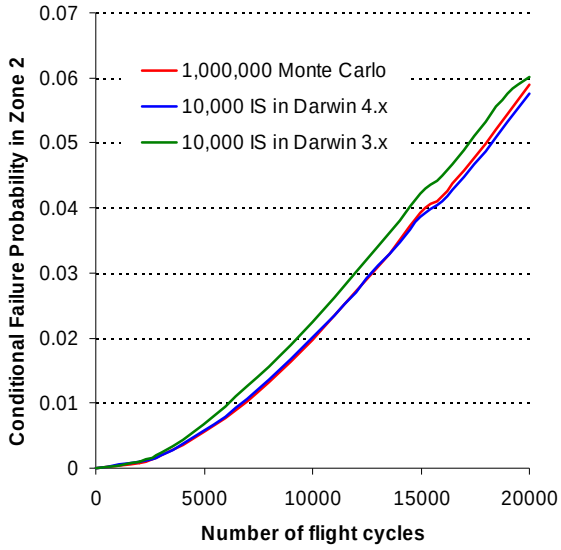

Figure S-7. Verification of the Importance Sampling Algorithm in DARWIN

S.4 REFERENCES.

S-1. Yang, J.N., Salivar, G.C., and Annis, C.G. Jr., "Statistical Modeling of Fatigue-Crack Growth in a Nickel-Base Super-Alloy," *Engineering Fracture Mechanics*, Vol. 18, 1983, pp. 257-270.

S-2. Wu, Y.-T. (Justin), Enright, M.P., and Millwater, H.R., "Probabilistic Methods for Design Assessment of Reliability with Inspection," *AIAA Journal*, Vol. 40, No. 5, 2002, pp. 937-946.

S-3. Au, S.K. and Beck, J.L., "Estimation of Small Failure Probabilities in High Dimensions by Subset Simulation," *Probabilistic Engineering Mechanics*, Vol. 16, 2001, pp. 263-277.

S-4. Madsen, H.O., Krenk, S., and Lind, N.C., *Methods of Structural Safety*, Prentice-Hall, Englewood Cliffs, NJ, 1986.

APPENDIX T—PROBABILISTIC SENSITIVITIES

T.1 INTRODUCTION.

The ability to quantify the sensitivity of the probability of fracture (POF) to changes in the distribution parameters that characterize the random variables is very valuable for design and analysis. This information can be used to identify the relative importance of the input random variables to ensure that a complete and accurate analysis has been accomplished.

Probabilistically based sensitivity methods in probabilistic analysis are well established, particularly for first- and second-order reliability methods. For these methods, the sensitivity factors (derivatives of the safety index with respect to the random variables [T-1]), derivatives of the POF with respect to the random variable parameters (e.g., $\partial P / \partial \mu$ and $\partial P / \partial \sigma$), and omission factors [T-2] are included in the probabilistic computations computed. This information is an essential component of a probabilistic analysis and often critical towards understanding the physical mechanisms underlying failure and modifying the design to mitigate and manage risk.

Variance-based methods [T-3 and T-4] were applied to design under uncertainty problems [T-5 and T-6]. Variance-based methods are capable of identifying the contributions of the main and interaction effects and the total sensitivity index (the sum of all the sensitivity indices, including all the interaction effects) for any parameter upon the model output. Groups of variables can also be considered. The method requires multiple multidimensional integrals computed by Monte Carlo sampling.

Sampling-based sensitivities, however, have received much less attention. Karamchandani [T-7] presented the fundamental concept by directly differentiating the POF integral with respect to the parameters of the random variables (e.g., mean and standard deviation), then reformulating the modified integral as an expected value operator such that sampling methods could be used to compute the sensitivities. The modified integral can be computed using common numerical techniques such as Monte Carlo sampling or importance sampling. However, the method was only valid for normally distributed random variables. Wu [T-8] generalized the concept to other probability distributions and extended it to system reliability problems using importance sampling for the probability calculations. He also suggested a nondimensionalizing approach to compare probabilistic sensitivities across random variables.

In this appendix, the sensitivity methods developed by Karamchandani [T-7] and Wu [T-8] are extended for application to additional parameters of random variables (upper and lower bounds of an initial crack size distribution). Variance estimates and associated confidence bounds are introduced for the probabilistic sensitivity estimates. A significant feature of the computation is that sampling-based sensitivities can be computed directly from the Monte Carlo results associated with failure probability computations without additional limit state calculations, and are therefore very inexpensive to compute.

This appendix is organized as follows. The essential mathematics for computing the POF of a gas turbine disk subject to (potentially) a rate of high-frequency anomalies is outlined in section T.2. Section T.3 outlines the probabilistic sensitivities in a hierarchical fashion; with respect to

the disk, unconditional POF of a zone, and conditional (assumes an anomaly is present) POF of a zone. Variance estimates for the probabilistic sensitivities are next derived, again in a hierarchical fashion. Finally, a numerical example is presented of a hypothetical titanium compressor disk and the sensitivities are verified against finite difference (FD) estimates.

T.2 PROBABILISTIC FATIGUE METHODOLOGY.

The probabilistic methodology employs a zone-based system reliability approach to compute the POF of a turbine disk as a function of flight cycles. For inherent anomalies, i.e., anomalies contained in the material before manufacturing (for example, hard alpha), a zone represents a volume of material in which each subregion of a zone generally has a uniform stress state, the same properties, and anomaly distribution. In other words, the risk computed for each subregion of material in the zone will be the same; or nearly so, thus, the material is grouped into a zone and the POF of the disk for an anomaly originating anywhere in the zone is computed. In practice, a single life-limiting location is chosen to locate the cracks originating from anomalies in a zone. For induced anomalies, i.e., anomalies introduced during manufacturing or maintenance, a zone represents a feature such as a bolthole surface. Again, a life-limiting location of the feature is chosen as the location at which to locate initial cracks caused by anomalies.

The methodology was initially developed for inherent hard alpha particles contained in titanium materials. These particles are usually precracked and very brittle compared to the base material. As such, an initiation life near zero is often seen and is assumed in the following methodology; however, extension to other forms of damage such as maintenance induced and other anomalies in materials other than titanium may have a nonnegligible crack formation time. The methodology can be enhanced to include nonnegligible crack formation time but is not addressed here.

Hard alpha anomalies in rotor-grade titanium are a very rare occurrence such that the probability of a disk containing more than one anomaly is negligible. Other gas turbine materials may have a relatively higher probability of occurrence. As such, the methodology presented herein accounts for either a relatively low or high rate of anomaly occurrence.

A concise outline of the governing mathematics is given below to serve as an outline for the subsequent differentiation of the equations in order to compute the sensitivities. More details regarding the methodology can be found in references T-9 and T-10.

T.2.1 PROBABILISTIC TREATMENT OF MULTIPLE ANOMALIES.

The POF within an individual zone, $P_{F,zone}$, can be computed as

$$P_{F,zone} = \sum_{i=1}^{\infty} P[i\ anomalies] \cdot P[\ fracture \mid i\ anomalies] \qquad \text{(T-1)}$$

where $P[i\ anomalies]$ is the probability of containing i anomalies in the zone, and $P[\ fracture \mid i\ anomalies]$ is the POF given i anomalies in the zone.

The probability of having i anomalies is given by a Poisson distribution as

$$P[i\ anomalies] = \frac{\exp(-\lambda)\cdot\lambda^i}{i!} \tag{T-2}$$

where λ is the mean anomaly occurrence rate for the material. The POF given that i anomalies are present is

$$P[\ fracture\,|\,i\ anomalies] = 1 - P[no\ \ fracture\,|\,i\ anomalies] \tag{T-3}$$

$$= 1 - \prod_{j=1}^{i} P[no\ \ fracture\,|\,anomaly\ \ j] \tag{T-4}$$

The conditional POF for a given number of cycles, N_o, is defined as

$$P[g(\tilde{x}) \le 0] = P[N_f \le N_o] \tag{T-5}$$

where $g(\tilde{x})$ denotes the limit state for the zone of interest, N_f the estimated cycles to failure, and N_o the user-specified number of cycles, and the analysis is conditioned on an anomaly being present. Therefore,

$$P[no\ \ fracture\,|\,anomaly\ \ j] = P[g_j > 0] \tag{T-6}$$

equation T-4 can be expressed as

$$P[\ fracture\,|\,i\ anomalies] = 1 - (P[g > 0])^i \tag{T-7}$$

Inserting equations T-2 and T-7 into equation T-1:

$$P_{F,zone} = \sum_{i=1}^{\infty}\left\{\frac{\exp(-\lambda)\cdot\lambda^i}{i!}\cdot(1 - P[g > 0])^i\right\} \tag{T-8}$$

or

$$P_{F,zone} = 1 - \exp\left[-\lambda\left(1 - P[g > 0]\right)\right] \tag{T-9}$$

or

$$P_{F,zone} = 1 - \exp\left[-\lambda\left(P[g \le 0]\right)\right] \tag{T-10}$$

where λ and the limit state $g(\tilde{x})$ are specific for each zone. For a rare anomaly occurrence rate, λ is small and $P_{F,zone} \approx \lambda\cdot P[g \le 0]$.

In the context of this appendix, $P[g \le 0]$ is calculated using Monte Carlo sampling; therefore, to simplify the proceeding notation, $P[g \le 0]$ is written as P_{MC}, which represents the conditional POF computed using Monte Carlo sampling. Therefore, equation T-10 becomes

$$P_{F,zone} = 1 - \exp\left[-\lambda \cdot P_{MC}\right] \tag{T-11}$$

T.2.2 DISK RISK.

The POF of the disk can be modeled as a series system of the zones:

$$P_F = 1 - \prod_{k=1}^{m} P(no\ \ failure\ in\ zone\ k) = 1 - \prod_{k=1}^{m} \left[1 - P_{F,k}\right] \tag{T-12}$$

where m equals the number of zones. For small zone failure probabilities, $P_{F,k}$, the disk failure probability reduces to $P_F \approx \sum_{k=1}^{m} P_{F,k}$.

T.2.3 RANDOM VARIABLES CONSIDERED.

Three random variables are considered in the analysis: propagation scatter (uncertainty in the fracture mechanics calculations and material crack growth rate variability), stress scatter (uncertainty in the magnitude of the applied stresses), and the initial crack size.

T.2.3.1 Propagation Scatter.

Propagation scatter is a collection of uncertainties related to prediction of fatigue life, e.g., cycles to failure, such as scatter in fatigue crack growth rate or uncertainty in the numerical prediction of cycles to failure. As such, propagation scatter is modeled as a random variable that multiples the numerically predicted cycles to fracture:

$$N_f = B \cdot N'_f \tag{T-13}$$

where N_f is the cycles to fracture used to estimate the POF, N'_f is the numerically predicted cycles to failure from a fracture mechanics algorithm, and B is modeled using a two parameter lognormal distribution described by a median and coefficient of variation (COV). Therefore, the sensitivity of the POF with respect to the median and COV of propagation scatter is computed.

Propagation scatter is modeled as an independent random variable for each zone since the error in fracture mechanics modeling may be feature, and therefore, location dependent. As a result, sensitivities with respect to median and COV are developed for each zone. In certain circumstances, the median and COV values used will be the same for each zone. In that instance, a “cumulative” effect of the sensitivities can be developed that determines the sensitivity of the disk POF with respect to a single propagation scatter median and COV.

T.2.3.2 Stress Scatter.

Variations in applied stresses are simulated using a multiplier that can be considered random, i.e.:

$$\sigma = S \cdot \sigma' \tag{T-14}$$

where σ represents the stresses used in the calculation of the POF, σ' are the stresses input (from an arbitrary source, e.g., finite element analysis), and S is modeled using a two-parameter lognormal distribution described by a median and coefficient of variation. Therefore, the sensitivity of the POF with respect to the median and COV of stress scatter is computed. Stress scatter is modeled as a fully dependent random variable across zones to simulate variability in inertia-based loading that affects all zones, e.g., revolutions per minute (rpm). Therefore, a single sensitivity of the POF of the disk with respect to the median and COV of stress scatter is determined for the entire disk.

T.2.3.3 Initial Crack Size—Anomaly Distribution.

The initial crack size is a critical element of predicting the POF. An anomaly distribution for hard alpha particles in titanium has been developed and calibrated by industry [T-11]. An industry-developed distribution for surface anomalies is in process.

The format for the anomaly distribution is an exceedance curve that presents the cumulative number of anomalies equal to or greater than a specific size, referenced to a weight, volume, or area of material. An example of an exceedance curve is shown in figure T-1. The cumulative distribution function (CDF) of anomalies as a function of anomaly size can be calculated from the exceedance curve as

$$F_A(a) = 1 - \frac{N[a] - N[a_{\max}]}{N[a_{\min}] - N[a_{\max}]} = \frac{N[a_{\min}] - N[a]}{N[a_{\min}] - N[a_{\max}]} \tag{T-15}$$

where F_A denotes the CDF of initial crack size, $a_{\min}$ is the minimum crack size specified, $a_{\max}$ is the maximum crack size specified, $N[a]$ is the number of anomalies greater than or equal to size a, $N[a_{\max}]$ is the number of anomalies associated with the largest anomaly size, and $N[a_{\min}]$ is the total number of anomalies greater than or equal to the minimum anomaly size. The corresponding probability density function (pdf) is given as

$$f_A(a) = -\frac{dN[a]}{da} \cdot \frac{1}{N[a_{\min}] - N[a_{\max}]} \tag{T-16}$$

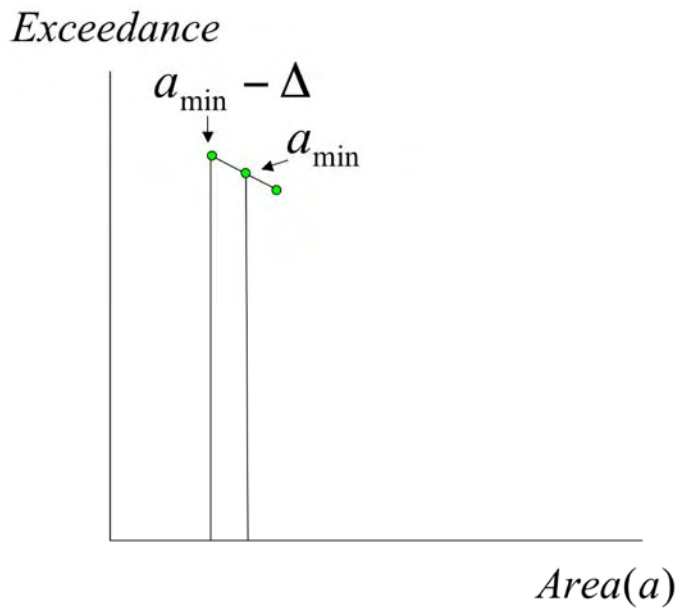

Figure T-1. Illustration: Perturbation of $a_{\min}$

The initial anomaly size exceedance curve is specified numerically in tabular form. Therefore, the pdf becomes

$$f_A(a) = -\frac{N[a_i] - N[a_{i+1}]}{a_i - a_{i+1}} \cdot \frac{1}{N[a_{\min}] - N[a_{\max}]} \tag{T-17}$$

where a_i and a_{i+1} are the tabular values of crack size that bound crack size a. The units for describing the initial crack size can be given in terms of crack area, length or depth.

The exceedance curve also defines the probability of occurrence of an anomaly in that it is a function of a reference amount of material; either weight, volume, or area. For example, if the reference volume used to develop the exceedance curve is Ψ, then the mean occurrence rate of an anomaly of any size in a zone of volume Ψ_i is $\lambda_i = N(a_{\min}) \cdot \frac{\Psi_i}{\Psi}$.

Critical components of modeling an exceedance curve are the specification of the bounds $a_{\min}$ and $a_{\max}$. These bounds define the range of crack sizes that will be considered in the analysis. For example, if $a_{\max}$ is increased, this will introduce an increment of large potentially dangerous anomalies, but the probability of having such anomalies may be very small, and the combined effect may or may not be significant. Thus, the implication of increasing $a_{\max}$ is unclear. A similar situation holds for $a_{\min}$. In other words, the judicious values to use for $a_{\max}$ and $a_{\min}$ are not obvious, and, in effect, the ideal case is to develop an exceedance curve such that the POF is not sensitive to the bounds, and, therefore, an adequate range of the exceedance curve was developed. As a result, probabilistic sensitivities with respect to the bounds of the exceedance curve, $a_{\min}$ and $a_{\max}$, are computed.

T.3 PROBABILISTIC SENSITIVITIES FOR RANDOM VARIABLE STATISTICAL PARAMETERS.

Probabilistic sensitivities are defined as the partial derivative of the POF with respect to the parameters of the random variables. In the proceeding sections, the mathematics for computing probabilistic sensitivities will be given initially in general terms using the parameter θ, where θ represents a parameter of a random variable, and then described in detail for the specific random variable parameters considered in this implementation.

T.3.1 SENSITIVITY OF THE POF WITH RESPECT TO A GENERAL PARAMETER.

The POF of the disk is given by equation T-12. The partial derivative of this equation with respect to any parameter θ is defined as

$$\frac{\partial P_F}{\partial \theta} = \sum_{i=1}^{\hat{n}} \left[\prod_{k=1}^{n} \frac{\partial P_{F,i}}{\partial \theta} \frac{(1-P_{F,k})}{(1-P_{F,i})} \right] \tag{T-18}$$

where $\hat{n}$ is defined as the number of zones affected by the random variable, which pertains to θ. For stress scatter $\hat{n} = n$, for life propagation scatter $\hat{n} = 1$, and for the exceedance curve $\hat{n}$ equals number of zones that use a particular exceedance curve. Typically, only one exceedance curve is used per disk, and therefore, $\hat{n} = n$ for the exceedance curve. In situations where the same values of propagation scatter median and COV are used for all zones, it is possible to develop a cumulative sensitivity for propagation scatter by setting $\hat{n} = n$.

In equation T-18, $\prod_{k=1}^{n}(1-P_{F,k}) = 1-P_F$ and $\frac{\partial P_{F,i}}{\partial \theta} \cdot \frac{1}{(1-P_{F,i})}$ are constant within the product operator. As a result, this equation can be simplified to the following equation:

$$\frac{\partial P_F}{\partial \theta} = \sum_{i=1}^{\hat{n}} (1-P_F) \cdot \left(\frac{\partial P_{F,i}}{\partial \theta} \cdot \frac{1}{(1-P_{F,i})} \right) \tag{T-19}$$

Also, P_F is independent of *i*, therefore, the sensitivity of the disk POF with respect to a statistical parameter θ can written:

$$\frac{\partial P_F}{\partial \theta} = (1-P_F) \cdot \sum_{i=1}^{\hat{n}} \left(\frac{\partial P_{F,i}}{\partial \theta} \cdot \frac{1}{(1-P_{F,i})} \right) \tag{T-20}$$

T.3.2 SENSITIVITY OF THE POF PER ZONE WITH RESPECT TO θ.

From inspection of equation T-20, it can be seen that the term $\frac{\partial P_{F,i}}{\partial \theta}$ is needed to compute the sensitivity of the disk; therefore, we compute the partial derivative of equation T-11 was computed with respect to θ:

$$\frac{\partial P_{F,i}}{\partial \theta} = \left(\frac{\partial \lambda_i}{\partial \theta} \cdot P_{MC_i} + \lambda_i \cdot \frac{\partial P_{MC_i}}{\partial \theta} \right) \cdot \exp\left[-\lambda_i \left(P_{MC_i} \right) \right] \tag{T-21}$$

or

$$\frac{\partial P_{F,i}}{\partial \theta} = \left(1 - P_{F,i}\right) \cdot \left(\frac{\partial \lambda_i}{\partial \theta} \cdot P_{MC_i} + \lambda_i \cdot \frac{\partial P_{MC_i}}{\partial \theta} \right) \tag{T-22}$$

In equation T-22, the term $\frac{\partial \lambda_i}{\partial \theta}$ is only nonzero when formulating the sensitivity with respect to $a_{\min}$ of the exceedance curve, which is a function of λ_i, and for all other sensitivities, this term is zero. This term defines the change in the probability of having an anomaly as a function of $a_{\min}$ and is negative, i.e., increasing $a_{\min}$ will reduce the probability of having an anomaly. λ_i is defined as $\lambda_i = N(a_{\min}) \cdot \frac{\Psi_i}{\Psi}$, and the resulting partial derivative is

$$\begin{aligned} &\frac{\partial(\lambda_i)}{\partial a_{\min}} = \frac{\partial N(a_{\min})}{\partial a_{\min}} \cdot \frac{\Psi_i}{\Psi} = \\ &-f_A(a_{\min}) \cdot \left[N(a_{\min}) - N(a_{\max}) \right] \cdot \frac{\Psi_i}{\Psi} = \\ &-f_A(a_{\min}) \cdot \left[N(a_{\min}) - N(a_{\max}) \right] \cdot \frac{\lambda_i}{N(a_{\min})} \end{aligned} \tag{T-23}$$

T.3.3 SENSITIVITY OF THE CONDITIONAL POF PER ZONE WITH RESPECT TO θ.

In this research, P_{MC} is the conditional POF computed using Monte Carlo sampling. The probability is conditional in that a crack is assumed present in a zone. In integral form, P_{MC} is written:

$$P_{MC} = \int_{g(\tilde{x}) \le 0} f_x(\tilde{x}) \cdot d\tilde{x} \tag{T-24}$$

where $\tilde{x}$ is a vector of random variables, $f_{\tilde{x}}(\tilde{x})$ is the joint pdf of $\tilde{x}$, and g is the limit state function defined such that $g(\tilde{x}) \le 0$ defines fracture.

Inserting the indicator function $I(\tilde{x})$, which is defined as equal to one if $g(\tilde{x}) \le 0$ and zero otherwise

$$P_{MC} = \int_{-\infty}^{\infty} I(\tilde{x}) f_{\tilde{x}}(\tilde{x}) d\tilde{x} \tag{T-25}$$

Take the derivative of this equation to compute the partial derivative of P_{MC} with respect to a parameter of the random variable j, denoted θ_j,

$$\frac{\partial P_{MC}}{\partial \theta_j} = \frac{\partial}{\partial \theta_j} \cdot \int_{-\infty}^{\infty} I(\tilde{x}) f_{\tilde{x}}(\tilde{x}) \cdot d\tilde{x} = \int_{-\infty}^{\infty} I(\tilde{x}) \cdot \frac{\partial f_{\tilde{x}}(\tilde{x})}{\partial \theta_j} \cdot d\tilde{x} + \text{Boundary Term} \tag{T-26}$$

where the boundary term arises if a perturbation in parameter θ_j affects the failure domain. This term is discussed in more detail below.

If the random variables are independent, the joint pdf can be written as a product of the individual random variable pdfs as:

$$f_{\tilde{X}}(\tilde{x}) = \prod_{i=1}^{nrv} f_{X_i}(x_i) \tag{T-27}$$

where *nrv* denotes the number of random variables.

The parameter θ_j is a parameter of only one of the pdfs comprising the joint density for the independent random variables, therefore $\frac{\partial f_{\tilde{X}}(\tilde{x})}{\partial \theta_j} = \frac{\partial f_{X_j}(x_j)}{\partial \theta_j}$ and equation T-26 becomes:

$$\frac{\partial P_{MC}}{\partial \theta_j} = \int_{-\infty}^{\infty} I(\tilde{x}) \cdot \frac{\partial f_{x_j}(x_j)}{\partial \theta_j} \cdot \frac{1}{f_{x_j}(x_j)} \cdot f_{\tilde{x}}(\tilde{x}) \cdot d\tilde{x} + \text{Boundary Term} \tag{T-28}$$

$$= E\left[I(\tilde{x}) \cdot \frac{\partial f_{x_j}(x_j)}{\partial \theta_j} \cdot \frac{1}{f_{x_j}(x_j)} \right] + \text{Boundary Term} \tag{T-29}$$

Based on equation T-29, the sensitivity of the conditional POF with respect to a statistical parameter of a random variable probability distribution can be computed using the expected value operator and a boundary term (if needed). The expected value can be approximated using Monte Carlo sampling such that

$$\frac{\partial P_{MC}}{\partial \theta_j} \cong \frac{1}{N} \sum_{n=1}^{N} \left[I(\tilde{x}) \cdot \kappa(x_j, f_x, \theta_j) \right] + \text{Boundary Term} \tag{T-30}$$

where N is the number of samples and κ is a kernel function defined generically as

$$\kappa(x, f_x, \theta) = \frac{df_x(x)}{d\theta} \cdot \frac{1}{f_x(x)} \tag{T-31}$$

k is distribution and parameter specific and is derived analytically for each distribution type and parameter of interest.

A boundary term will be needed if the derivative is being taken with respect to a parameter that explicitly affects the failure domain. Many situations do not need the boundary term. For example, derivatives of a normal distribution with respect to the mean or standard deviation or derivatives of a lognormal distribution with respect to the median or COV do not require a boundary term. Examples of distributions that do require a boundary term are derivatives with respect to the bounds of any truncated distribution such as a uniform, truncated normal, or a tabular exceedance curve.

For problems with one random variable, Leibnitz's rule is used to determine the boundary term:

$$\frac{\partial P}{\partial \theta} = \frac{\partial}{\partial \theta} \int_{a(\theta)}^{b(\theta)} f_x(x)dx = \int_{a(\theta)}^{b(\theta)} \frac{\partial f_x(x)}{\partial \theta_j} dx + f(b(\theta), x) \cdot \frac{\partial b(\theta)}{\partial \theta} - f(a(\theta), x) \cdot \frac{\partial a(\theta)}{\partial \theta} \qquad \text{(T-32)}$$

The boundary term will be needed for any sensitivities with respect to the bounds of a truncated distribution, such as the exceedance curve, but may be small or zero in particular cases.

T.3.4 SENSITIVITY OF SAMPLING-BASED CONDITIONAL POF WITH RESPECT TO MEDIAN OF STRESS AND PROPAGATION SCATTER.

The following derivation applies equally to the stress scatter and propagation scatter random variables because both variables are modeled with a lognormal distribution. The kernel function for a lognormal distribution with respect to the median is

$$\kappa(x, \log\text{normal}, \tilde{X}) = \frac{\ln(x) - \ln(\tilde{X})}{\tilde{X} \cdot \ln(1 + \text{cov}^2)} \qquad \text{(T-33)}$$

The sensitivity of the POF can be determined from equation T-30 using the kernel given in equation T-33, not including the boundary term. A boundary term is not needed because perturbations in the median of a lognormal distribution do not affect the integration domain. Therefore, the sensitivity is given by

$$\frac{\partial P_{MC}}{\partial \tilde{X}} = E\left[I(\tilde{x}) \cdot \kappa(x, \log\text{normal}, \tilde{X}) \right] \qquad \text{(T-34)}$$

which is approximated as

$$\frac{\partial P_{MC}}{\partial \tilde{X}} \cong \frac{1}{M} \sum_{i=1}^{M} I(\tilde{x}) \cdot \kappa(x, \log\text{normal}, \tilde{X}) \qquad \text{(T-35)}$$

T.3.5 SENSITIVITY OF SAMPLING-BASED CONDITIONAL POF WITH RESPECT TO COV OF PROPAGATION AND STRESS SCATTER.

The following derivation applies equally to the stress scatter and propagation scatter random variables because both variables are modeled using the lognormal distribution. The kernel function for a lognormal distribution with respect to the COV is

$$\kappa(x, \log\text{normal}, \text{cov}) = \frac{\text{cov}\cdot\left(-\ln\left(1+\text{cov}^2\right)+\left(\ln(\tilde{X})-\ln(x)\right)^2\right)}{\left(1+\text{cov}^2\right)\cdot\ln\left(1+\text{cov}^2\right)^2} \tag{T-36}$$

The sensitivity of the POF can be determined from equation T-30 using the kernel given in equation T-36.

$$\frac{\partial P_{MC}}{\partial\,\text{cov}} = E\left[I(\tilde{x})\cdot\kappa(x, \log\text{normal}, \text{cov})\right] \tag{T-37}$$

which is approximated as:

$$\frac{\partial P_{MC}}{\partial\,\text{cov}} \cong \frac{1}{M}\sum_{i=1}^{M} I(\tilde{x})\cdot\kappa(x, \log\text{normal}, \text{cov}) \tag{T-38}$$

A boundary term is not needed because perturbations in the COV of a lognormal distribution do not affect the integration domain.

T.3.6 SENSITIVITY OF SAMPLING-BASED CONDITIONAL POF WITH RESPECT TO MINIMUM ANOMALY SIZE.

The sensitivity with respect to $a_{\min}$ is defined such that the slope of the exceedance curve at $a_{\min}$ is unchanged, as shown in figure T-2.

The kernel function with respect to $a_{\max}$ for a tabular exceedance curve is derived as

$$\kappa(a, f_A, a_{\min}) = \frac{df_A(a)}{da_{\min}}\cdot\frac{1}{f_A(a)} = f_A(a_{\min}) \tag{T-39}$$

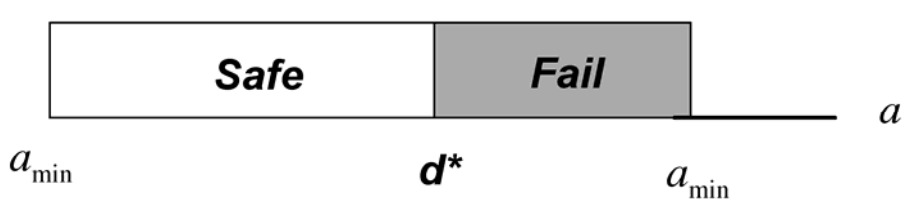

Figure T-2. Failure Domain for Defect Distribution as the Only Random Variable

where $f_A(a_{\min})$ is the pdf of the anomaly distribution evaluated at $a_{\min}$ given by equation T-17, and the sensitivity, per equation T-29, is

$$\frac{\partial P_{MC}}{\partial a_{\min}} = E[I(\tilde{x})] \cdot f_A(a_{\min}) = P_{MC} \cdot f_A(a_{\min}) + \text{Boundary Term} \tag{T-40}$$

The boundary term is zero if the anomaly distribution is the only random variable because perturbations in $a_{\min}$ will not affect the failure domain. For example, if we determine a critical crack size, d^*, with $a_{\min} \le d^* \le a_{\max}$, such that $g(d^*) = 0$, then failure occurs for any cracks larger than d^*. Hence, the failure domain is the region from $x = d^*$ until $x = a_{\max}$, and perturbations in $a_{\min}$ will not affect the failure domain. This situation is shown in figure T-3.

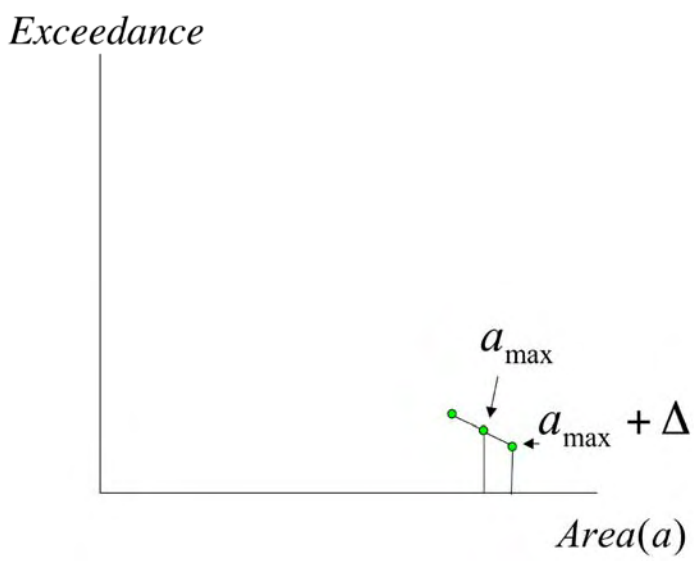

Figure T-3. Illustration: Perturbation of $a_{\max}$

Mathematically, from Leibnitz's rule

$$\frac{\partial P_{MC}}{\partial a_{\max}} = \frac{\partial}{\partial a_{\max}} \int_{d^*}^{a_{\max}} f_a(a)da = \int_{d^*}^{a_{\max}} \frac{\partial f_a(a)}{\partial a_{\max}} da + f(a_{\max}, a) \cdot \frac{\partial a_{\max}}{\partial a_{\max}} - f(d^*, a) \cdot \frac{\partial d^*}{\partial a_{\max}} \tag{T-41}$$

However, $\frac{\partial a_{\max}}{\partial a_{\min}} = 0$ and $\frac{\partial d^*}{\partial a_{\min}} = 0$ and equation T-41 reduces to

$$\frac{\partial P_{MC}}{\partial a_{\max}} = \frac{\partial}{\partial a_{\max}} \int_{d^*}^{a_{\max}} f_a(a)da = \int_{d^*}^{a_{\max}} \frac{\partial f_a(a)}{\partial a_{\max}} da \tag{T-42}$$

Hence, the boundary term is zero.

However, for higher dimensional problems, i.e., more random variables, a portion of the failure domain could intersect the situation where $x_1 = a_{\min}$ and a boundary term would be nonzero. In this situation, calculation of the boundary term cannot be obtained without additional sampling. It can be shown that the boundary term is related to $f_A(a_{\min})P[g(\tilde{x}) \le 0 \mid x_1 = a_{\min}]$. That is, a probability problem is solved with the initial crack size set to $a_{\min}$. Thus, the estimate $f_A(a_{\min})$ is an upper bound to the true boundary term for problems with additional random variables. Therefore, in general, the sensitivity is bounded by

$$P_{MC} \cdot f_A(a_{\min}) - f_A(a_{\min}) \le \frac{\partial P_{MC}}{\partial a_{\min}} \le P_{MC} \cdot f_A(a_{\min}) \tag{T-43}$$

However, for most problems, the boundary term will be close to zero because $P[g(\tilde{x}) \le 0 \mid x_1 = a_{\min}]$ will likely be small and the sensitivity will be close to the lower bound. That is, the conditional POF given that all cracks initiate at the smallest size of the exceedance curve will be small if not zero, Therefore, by default, the boundary term for sensitivities with respect to $a_{\min}$ is neglected and use equation T-40. This value is an upper bound to the true sensitivity.

The unconditional sensitivity of the zone to $a_{\min}$ can be simplified using the above results. Inserting equations T-40 and T-23 into equation T-22 and simplified, obtains

$$\frac{\partial P_{F,i}}{\partial a_{\min}} = (1 - P_{F,i}) \cdot \lambda_i \cdot f_A(a_{\min}) \cdot \frac{N[a_{\max}]}{N[a_{\min}]} \cdot P_{MC} \tag{T-44}$$

T.3.7 SENSITIVITY OF SAMPLING-BASED CONDITIONAL POF WITH RESPECT TO MAXIMUM ANOMALY SIZE.

The sensitivity with respect to $a_{\max}$ is defined such that the slope of the exceedance curve at $a_{\max}$ is unchanged, as shown in figure T-3.

The kernel function with respect to $a_{\max}$ for a tabular exceedance curve is derived as

$$\kappa(a, f_A, a_{\max}) = \frac{df_A(a)}{da_{\max}} \cdot \frac{1}{f_A(a)} = -f_A(a_{\max}) \tag{T-45}$$

where $f_A(a_{\max})$ is the pdf of the anomaly distribution evaluated at $a_{\max}$ and the sensitivity is

$$\begin{aligned} \frac{\partial P_{MC}}{\partial a_{\max}} &= -E[I(\tilde{x})] \cdot f_A(a_{\max}) + \text{Boundary Term} = \\ &-P_{MC} \cdot f_A(a_{\max}) + \text{Boundary Term} \end{aligned} \tag{T-46}$$

The boundary term can be estimated from the one random variable problem. A boundary term will be needed if the anomaly distribution is the only random variable because perturbations in $a_{\max}$ will affect the failure domain. From Leibnitz's rule:

$$\frac{\partial P_{MC}}{\partial a_{\max}} = \frac{\partial}{\partial a_{\max}} \int_{d^*}^{a_{\max}} f_a(a)da = \int_{d^*}^{a_{\max}} \frac{\partial f_a(a)}{\partial a_{\max}} da + f(a_{\max}, a) \cdot \frac{\partial a_{\max}}{\partial a_{\max}} - f(d^*, a) \cdot \frac{\partial d^*}{\partial a_{\max}} \tag{T-47}$$

However, $\frac{\partial a_{\max}}{\partial a_{\max}} = 1$ and $\frac{\partial d^*}{\partial a_{\max}} = 0$ and $\frac{\partial P_{MC}}{\partial a_{\max}}$ reduces to

$$\frac{\partial P_{MC}}{\partial a_{\max}} = \frac{\partial}{\partial a_{\max}} \int_{d^*}^{a_{\max}} f_a(a)da = \int_{d^*}^{a_{\max}} \frac{\partial f_a(a)}{\partial a_{\max}} da + f(a_{\max}) \tag{T-48}$$

Hence, the boundary term for a one-dimensional problem is $f_A(a_{\max})$.

For higher dimensional problems, however, a portion of the failure domain may not intersect the condition where $x_1 = a_{\max}$ and the boundary term may not be equal to $f_A(a_{\max})$. In this situation, calculation of the boundary term cannot be obtained without additional computation. It can be shown that boundary term is related to $f_A(a_{\max})P[g(\tilde{x}) \le 0 \mid x_1 = a_{\max}]$. Thus, the estimate $f_A(a_{\min})$ is an upper bound to the true boundary term for problems with additional random variables. Therefore, in general, the sensitivity is bounded by

$$-P_{MC} \cdot f_A(a_{\max}) \le \frac{\partial P_{MC}}{\partial a_{\max}} \le -P_{MC} \cdot f_A(a_{\max}) + f_A(a_{\max}) \tag{T-49}$$

However, for most problems the boundary term will be close to $f_A(a_{\max})$ because $P[g(\tilde{x}) \le 0 \mid x_1 = a_{\max}]$ will likely be close to one and, therefore, the sensitivity will be close to the upper bound. That is, the conditional POF given that all cracks initiate at the largest size of the exceedance curve will be close to, if not one. Therefore, by default, the boundary term for sensitivities with respect to $a_{\max}$ is included and a value equal to $f_A(a_{\max})$ is used. The sensitivity with respect to $a_{\max}$ becomes

$$\frac{\partial P_{MC}}{\partial a_{\max}} = -P_{MC} \cdot f_A(a_{\max}) + f_A(a_{\max}) = f_A(a_{\max})(1 - P_{MC}) \tag{T-50}$$

This value is an upper bound to the true sensitivity.

The mathematical equations for computing sensitivities of the disk and zone POF were derived for specific random variables and probability distributions. Extension of the sensitivities to other random variables or other distribution types is straightforward unless a boundary term is required. Equation T-30 is used to determine the sensitivity with a new kernel evaluated as shown in equation T-31. Estimates of the boundary term require additional computations or a bounding approximation.

T.4 VARIANCE ESTIMATES.

The sensitivity values are estimated using Monte Carlo sampling, therefore the sensitivities themselves are random variables. As such, variance estimates and confidence bounds are useful.

T.4.1 VARIANCE ESTIMATE OF SENSITIVITY-EQUATION—ZONE-BASED CONDITIONAL POF.

The conditional POF for a zone is determined using Monte Carlo sampling. The variance estimate of the sensitivity can be determined as shown below. Different equations are used for $a_{\min}$ and $a_{\max}$ than for propagation and stress scatter since simpler equations can be developed for the variance of $a_{\min}$ and $a_{\max}$.

T.4.2 STRESS AND PROPAGATION SCATTER.

The variance associated with the stress and crack propagation life scatter random variables can be identified by applying the variance operator to an expanded definition of the probabilistic sensitivity obtained from Monte Carlo sampling:

$$\begin{aligned}
&V[\frac{\partial P_{MC_i}}{\partial \theta}] = V[E[I(x)\frac{\partial f}{\partial \theta}\cdot\frac{1}{f}]] = V[\frac{1}{M}\sum_{k=1}^{M} I(x)\frac{\partial f}{\partial \theta}\cdot\frac{1}{f}\ ] = \frac{1}{M}V[\ I(x)\frac{\partial f}{\partial \theta}\cdot\frac{1}{f}] = \\
&\frac{1}{M}\{E[(I(x)\frac{\partial f}{\partial \theta}\cdot\frac{1}{f})^2] - E[(I(x)\frac{\partial f}{\partial \theta}\cdot\frac{1}{f})]^2\} = \frac{1}{M}\{E[(I(x)\frac{\partial f}{\partial \theta}\cdot\frac{1}{f})^2] - S_\theta{}^2\} = \\
&\frac{1}{M}\{\frac{1}{M}\sum_{k=1}^{N}(I(x)\frac{\partial f}{\partial \theta}\cdot\frac{1}{f})^2 - S_\theta{}^2\} = \frac{1}{M^2}\sum_{k=1}^{M}(I(x)\frac{\partial f}{\partial \theta}\cdot\frac{1}{f})^2 - \frac{S_\theta{}^2}{M}
\end{aligned} \tag{T-51}$$

T.4.3 MINIMUM AND MAXIMUM ANOMALY SIZES.

The equation for $\frac{\partial P_{MC}}{\partial \theta}$ simplifies for θ equal to $a_{\min}$ or $a_{\max}$. This information can be used to develop a simplified variance equation as follows:

$$V[\frac{\partial P_{MC}}{\partial a_{\min}}] = V[\ f_A(a_{\min})\cdot P_{MC}] = f_A^2(a_{\min})V[P_{MC}]$$

$V[P_{MC}]$ is obtained from standard sampling estimates as [T-12]

$$V[P_{MC}] = \frac{1}{M}(1-P_{MC})P_{MC} \tag{T-52}$$

Therefore

$$V[\frac{\partial P_{MC}}{\partial a_{\min}}] = f_A^2(a_{\min})\frac{P_{MC}(1-P_{MC})}{M} \tag{T-53}$$

Similarly

$$V[\frac{\partial P_{MC}}{\partial a_{\max}}] = f_A^2(a_{\max})\frac{P_{MC}(1-P_{MC})}{M} \tag{T-54}$$

The 95% confidence bounds are then computed assuming the variation follows a normal distribution and as:

$$S_\theta - 1.96\sqrt{V} \le S_\theta \le S_\theta + 1.96\sqrt{V} \tag{T-55}$$

T.4.4 VARIANCE ESTIMATE—ZONE-BASED UNCONDITIONAL POF.

The zone-based unconditional POF can be derived from the conditional POF based on equation T-22:

$$\begin{aligned} &V[\frac{\partial P_{F,i}}{\partial \theta}] = \\ &V[\left(1-P_{F,i}\right)\cdot\left(\frac{\partial \lambda_i}{\partial \theta}\cdot P_{MC_i} + \lambda_i \cdot \frac{\partial P_{MC_i}}{\partial \theta}\right)] = \\ &(1-P_{F,i})^2\left(\left(\frac{\partial \lambda_i}{\partial \theta}\right)^2 V[P_{MC_i}] + \lambda_i^2 V[\frac{\partial P_{MC,i}}{\partial \theta}]\right) \end{aligned} \tag{T-56}$$

where the term $\frac{\partial \lambda_i}{\partial \theta}$ is only nonzero when formulating the sensitivity with respect to $a_{\min}$ of the exceedance curve, and $V[P_{MC}]$ is obtained from equation T-52.

For $a_{\min}$, one can use equation T-56 or alternatively use equation T-44 and obtain

$$\begin{aligned} &V[\frac{\partial P_{F,i}}{\partial a_{\min}}] = \\ &V\left[(1-P_{F,i})\cdot \lambda_i \cdot f_A(a_{\min})\cdot \frac{N[a_{\max}]}{N[a_{\min}]}\cdot P_{MC}\right] = \\ &\left((1-P_{F,i})\cdot \lambda_i \cdot f_A(a_{\min})\frac{N[a_{\max}]}{N[a_{\min}]}\right)^2 \cdot V[P_{MC}] \end{aligned} \tag{T-57}$$

Using equation T-52 for $V[P_{MC}]$, the variance for $a_{\min}$ becomes

$$V[\frac{\partial P_{F,i}}{\partial a_{\min}}] = \left((1-P_{F,i})\cdot \lambda_i \cdot f_A(a_{\min})\frac{N[a_{\max}]}{N[a_{\min}]}\right)^2 \cdot \frac{P_{MC_i}\cdot(1-P_{MC_i})}{M_i} \tag{T-58}$$

where M_i indicates the number of samples used for zone *i*.

T.4.5 VARIANCE ESTIMATES—DISK POF.

The variance estimates for the disk can be derived from equation T-20 as

$$
\begin{aligned}
&V[\frac{\partial P_F}{\partial \theta}] = V[(1-P_F)\sum_{i=1}^{\hat{n}} \frac{\partial P_{F,i}}{\partial \theta} \cdot \frac{1}{(1-P_{F,i})}] = \\
&V[(1-P_F)\sum_{i=1}^{\hat{n}} \left(\frac{\partial \lambda_i}{\partial \theta} \cdot P_{MC_i} + \lambda_i \frac{\partial P_{MC_i}}{\partial \theta} \right)] = (1-P_F)^2 V[\sum_{i=1}^{\hat{n}} \left(\frac{\partial \lambda_i}{\partial \theta} \cdot P_{MC_i} + \lambda_i \frac{\partial P_{MC_i}}{\partial \theta} \right)] = \\
&(1-P_F)^2 \sum_{i=1}^{\hat{n}} V[\frac{\partial \lambda_i}{\partial \theta} \cdot P_{MC_i} + \lambda_i \frac{\partial P_{MC_i}}{\partial \theta}] = (1-P_F)^2 \sum_{i=1}^{\hat{n}} \left(\left(\frac{\partial \lambda_i}{\partial \theta} \right)^2 \cdot V[P_{MC_i}] + \lambda_i^2 \cdot V[\frac{\partial P_{MC_i}}{\partial \theta}] \right)
\end{aligned}
\tag{T-59}
$$

where the term $\frac{\partial \lambda_i}{\partial \theta}$ is only nonzero for sensitivities with respect to $a_{\min}$.

T.5 COMPUTATIONAL PROCEDURE.

The sequence of analysis (1) determines the conditional POF (P_{MC}) using equation T-5 and the sensitivity of the conditional POF ($\frac{\partial P_{MC}}{\partial \theta}$) using, generically, equation T-30, and more specifically equations T-35 and T-38 for stress scatter and propagation scatter, and equations T-44 and T-50 for the bounds of the exceedance curve. The summation term contained in these equations is evaluated during each Monte Carlo sample as done for determining the POF; (2) determines the unconditional POF for a zone from equation T-11 and the sensitivity of the unconditional POF using equation T-22; (3) determine the POF for the disk using equation T-12 and the sensitivity of the disk POF using equation T-20; and (4) determines variance estimates and confidence bounds for the sensitivities of the conditional POF using equations T-51, T-53, and T-54, the sensitivities of the unconditional POF using equations T-56 or T-58, and the sensitivities of the disk using equation T-59.

T.6 NUMERICAL EXAMPLES.

The model consists of a square cross section titanium ring as outlined by Advisory Circular 33.14-1 [T-13]. The titanium ring is axisymmetric, has a rectangular cross section, is under rotation, and has an external load applied at the rim to simulate blade loading. The maximum principal stress is in the circumferential direction. The crack grows under constant amplitude, e.g., start-up/shutdown, cyclical loading until fracture, defined as when the stress-intensity factor exceeds the fracture toughness. The POF of the disk before twenty thousand cycles is computed using Monte Carlo sampling.

The titanium ring cross section was divided into 24 zones as shown in figure T-4. Only half the cross section were modeled due to symmetry. The stresses are determined from finite element analysis. An enlarged view of Zone 2 is shown in the inset. The initiation site of the crack is located at the life-limiting location of the zone. In practice, a zone-refinement convergence algorithm [T-14] would ordinarily be exercised to ensure accuracy but is not germane for the

purpose of verifying the sensitivity equations. The exceedance curve used to represent the initial crack size distribution is obtained from industry-defined data [T-11] and represents rotor-grade titanium, vintage 1995, that was nondestructively inspected in the billet and forging stages by an ultrasonic inspection method calibrated to a #3 flat-bottom hole. The aspect ratio (a/c) of the initial crack is one; the crack may become elliptical in shape during crack growth depending upon the stress gradient and proximity to a free surface. The input data summarizing the problem are given in table T-1. The median value for stress scatter is 0.001 in order to convert the input stresses from psi to the required units of ksi.

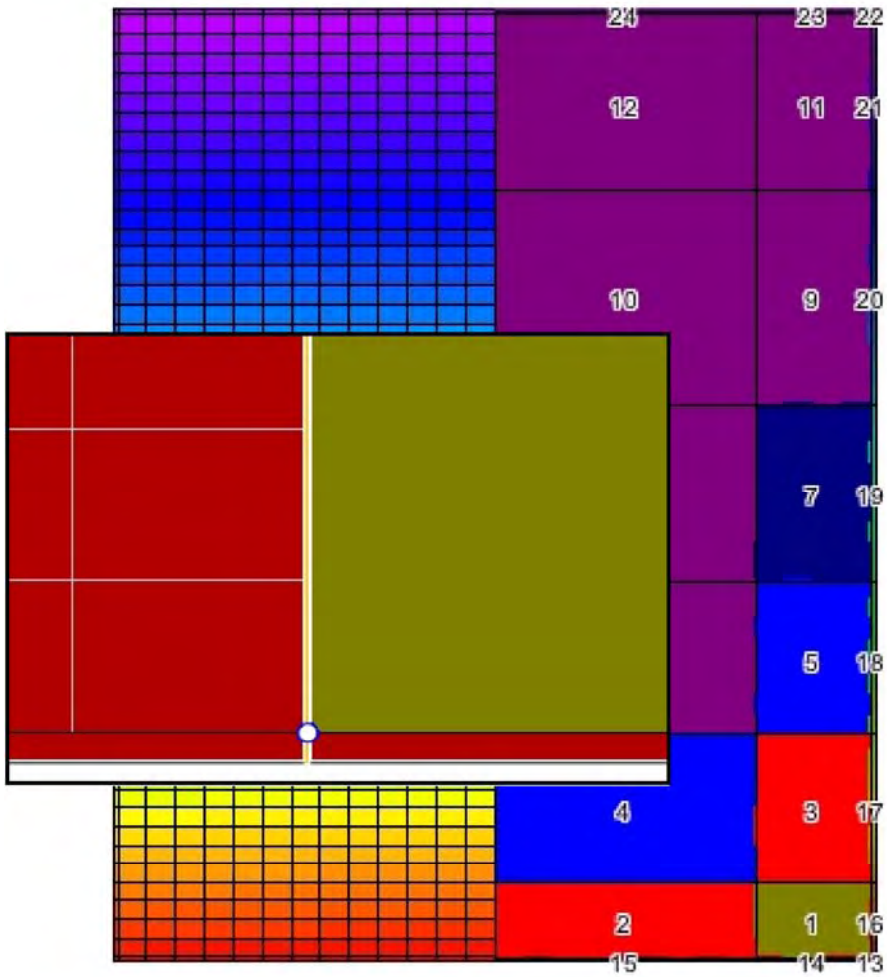

Figure T-4. Zone Discretization of Rectangular Cross Section With Close-Up View of Zone 2

Table T-1. Example Problem Input Data

Property	Description	Comment
Loading	Constant amplitude, 0-81-0 ksi (558 MPa)	Max speed = 6800 rpm
da/dN-Δ*K*	C = 5.248E-11 (9.25E-13 SI), m = 3.87, Kc = 58.7 ksi-in^-1/2 (64.6 MPa-m^-1/2)	Paris law with no threshold (C—constant, m—exponent, Kc—fracture toughness) U.S. units: *da/dN* (in/cycle), Δ*K* (ksi-in^-1/2) SI units: *da/dN* (m/cycle), Δ*K* (MPa-m^-1/2)
Initial crack size	aia.post95.3fbh.3fbh.dist	Post 95 material, inspected in billet and forging with a #3 flat-bottom hole ultrasonic inspection
Propagation scatter	Median = 1, COV = 0.1	lognormal distribution—for all zones
Stress scatter	Median = 1, COV = 0.1	lognormal distribution

The numerical results from the sensitivity equations are compared with FD estimates. The FD estimates are obtained by perturbing the parameter of interest, rerunning the analysis, and approximating the sensitivity as

$$\frac{\partial P}{\partial \theta} \approx \frac{\Delta P}{\Delta \theta} = \frac{P(\theta + \Delta\theta) - P(\theta)}{\Delta \theta} \tag{T-60}$$

where P represents the POF (either zone (conditional or unconditional) or the disk) for the baseline (unperturbed) analysis, P' represents the POF for the perturbed analysis, and $\Delta\theta$ represents the perturbed parameter. The perturbation size is chosen arbitrarily as a few percent of nominal. The perturbation size must be large enough to evoke a significant enough change in the computed POF relative to the unperturbed analysis.

Note that it is exceedingly laborious to obtain FD estimates in that a very large number of Monte Carlo samples must be used to prevent the difference in the POF from being masked by sampling variance, or a very refined importance sampling method must be used [T-15 and T-16]. In addition, a separate analysis must be performed for each sensitivity estimate. In the examples below, six additional analyses are required to obtain the FD estimates, whereas the sensitivity equations provide all sensitivities in a single analysis.

T.6.1 SINGLE-ZONE VERIFICATION—CONDITIONAL POF

In this example, only Zone 2 (see inset figure T-4) is considered. Zone 2 is a principal zone in that a large portion of the disk risk originates from the probability of a anomaly being contained in the zone and the ensuing crack growing to fracture; primarily due to the high stress state and the near surface effect.

Table T-2 shows the comparison of the sensitivity $\frac{\partial P_{MC}}{\partial \theta}$ with respect to FD approximations. Two million samples were used for all Monte Carlo analyses in order to minimize sampling variance. The perturbations sizes used were 1 percent for propagation scatter median and COV, and stress scatter median. Five percent perturbations were used for the stress scatter COV and the bounds of the exceedance curve. The perturbations sizes were chosen to be of size such that the change in the POF was sufficient to calculate FD estimates.

Table T-2. Comparison of Sensitivity Equations and FD Estimates

Random Variable Parameter	Sensitivity Method	FD[a]
Propagation scatter median	-5.148E-2	-5.195E-2
Propagation scatter COV	4.765E-3	5.500E-3
Stress scatter median	2.037E+2	2.093E+2
Stress Scatter COV	9.042E-2	9.860E-2
Exceedance curve $a_{\min}$	6.497E-3	6.416E-3
Exceedance curve $a_{\max}$	3.260E-10	3.602E-10

[a] 2E6 samples used for all analyses

The comparisons between the equations and FD estimates are very close. A positive sensitivity indicates that an increase in the parameter will increase the POF, and conversely, a negative sensitivity indicates that an increase in the parameter will decrease the POF. The propagation scatter median sensitivity is negative because this variable multiplies the computed cycles to failure estimated from fracture mechanics algorithms. Thus, a larger value increases the cycles to failure and, therefore, reduces the POF.

T.6.2 SINGLE-ZONE VERIFICATION—UNCONDITIONAL POF.

The sensitivities of the unconditional POF with respect to the statistical parameters can be derived from the sensitivities of the conditional POF per equation T-22 with the caveat that the term $\frac{\partial \lambda_i}{\partial \theta}$ is only nonzero when formulating the sensitivity with respect to $a_{\min}$. For all other parameters the sensitivity can be written:

$$\frac{\partial P_{F,i}}{\partial \theta} = \left(1 - P_{F,i}\right) \cdot \lambda_i \cdot \frac{\partial P_{MC_i}}{\partial \theta} \tag{T-61}$$

and the sensitivity with respect to $a_{\min}$ can be determined from equation T-44.

T.6.3 NONDIMENSIONALIZED SENSITIVITY.

Wu [T-8] proposed a nondimensionalized coefficient $\frac{\partial P}{\partial \theta_j} \cdot \frac{\sigma_j}{P}$, where σ_j denotes the standard deviation of the random variable X_j and P denotes the probability of failure in order to remove the dimensions associated with the sensitivities such that comparisons can be made across random variables. The equation can be modified by nondimensionalizing by the parameter in question instead of σ in order to generalize the approach, i.e.:

$$S_{\theta_j} = \frac{\partial P}{\partial \theta_j} \cdot \frac{\theta_j}{P} \tag{T-62}$$

The nondimensionalized sensitivities are identical for conditional and unconditional analyses with the exception of the sensitivity with respect to $a_{\min}$ due to the $\frac{\partial \lambda_i}{\partial a_{\min}}$ term included in the unconditional sensitivity. The results in table T-3 indicate that the most important variable in the model is the stress scatter median. For example, increasing the median value for the stress scatter by 1 percent would increase the conditional and unconditional POF of Zone 2 by 5 percent. Increasing the propagation scatter median by 1 percent will lower the POF by approximately 1 percent. Increasing the COV of stress scatter by 5 percent will increase the POF by approximately 1 percent. Clearly, the sensitivities are local, and large changes in a parameter would require rerunning the analysis to determine updated sensitivities.

Table T-3. Nondimensionalized Sensitivities (Conditional and Unconditional)

Random Variable Parameter	Nondimensionalized Sensitivity $S_\theta = \frac{\partial P}{\partial \theta_j} \cdot \frac{\theta}{P}$
Propagation scatter median	-1.35E+0
Propagation scatter COV	1.25E-2
Stress scatter median	5.32E+0
Stress scatter COV	2.36E-1
Exceedance curve $a_{\min}$	5.99E-1(C) / 3.97E-4(U)[c]
Exceedance curve $a_{\max}$	9.46E-4

C = Conditional
U = Unconditional

T.6.4 MULTIZONE, 24 ZONES TOTAL.

A comprehensive analysis considering all 24 zones is considered next. The problem parameters are given in table T-1. The FD results were obtained as before, except importance sampling [T-15 and T-16] was used to compute the analyses instead of Monte Carlo sampling in order to reduce runtime.

These results are shown in table T-4. The equations and the FD results are in good agreement. A cumulative sensitivity for the disk is computed by summing over all zones as in equation T-20. The sensitivity with respect to $a_{\min}$ shows some disparity due to the extremely small sensitivity.

Table T-4. Comparison of Disk POF Sensitivity Equations With FD Estimates

Random Variable Parameter	Sensitivity Method	FD*
Stress scatter median	1.035E+0	1.066E+0
Stress scatter COV	7.409E-4	7.796E-4
Exceedance curve $a_{\min}$	8.883E-9	6.58E-8
Exceedance curve $a_{\max}$	5.989E-12	5.258E-12
Propagation scatter median-cumulative	-2.369E-4	-2.553E-4
Propagation Scatter COV-cumulative	5.891E-5	4.938E-5

* Importance sampling [T-15 and T-16]

T.7 SUMMARY

A methodology was developed and demonstrated to predict the sensitivities of the POF of a zone-based probabilistic fatigue analysis with respect to the parameters of the probability distributions of the input random variables without additional limit state calculations. The elements of the methodology include:

- Sensitivities are computed at the zone level (both conditional and unconditional) and for the entire disk.
- Sensitivities are computed with respect to the median and COV of the propagation scatter and stress scatter random variables and with respect to the bounds of the initial crack size exceedance curve.
- The necessity for the boundary term was discussed, and limiting solutions were obtained for the bounds of the initial crack size exceedance curve.
- Variance estimates are developed and used to determine upper and lower 95% confidence bounds on the sensitivity estimates.

- The formulas use the existing failure samples, and no further fatigue calculations are required.

- The methodology can be extended straightforwardly to consider other random variables and distribution functions.

The FD estimates of the POF, although theoretically possible, are extremely laborious and involve multiple analyses with very high precision requirements on the probability calculations. Therefore, a mathematical development and corresponding software implementation is necessary to make such sensitivity calculations practical.

T.8 NOMENCLATURE.

$a_{\min}$	=	Minimum anomaly size of the initial crack size exceedance curve
$a_{\max}$	=	Maximum anomaly size of the initial crack size exceedance curve
B	=	Random variable representing uncertainty in fatigue crack propagation scatter
$E[\cdot]$	=	Expected value operator
$f_A(a)$	=	pdf of the initial crack size exceedance curve
$f_A(a_{\min})$	=	pdf of the initial crack size exceedance curve evaluated at $a_{\min}$
$f_A(a_{\max})$	=	pdf of the initial crack size exceedance curve evaluated at $a_{\max}$
λ	=	Mean anomaly occurrence rate
$\hat{n}$	=	Number of zones affected by a particular random variable
$N(a)$	=	Exceedance value associated with initial crack size
P	=	Probability of fracture
$P_{F,k}$	=	POF for an anomaly within zone k
P_F	=	POF of a disk
S	=	Random variable representing uncertainty in applied loading
$V[\cdot]$	=	Variance operator
κ	=	Kernel function for determining sampling-based sensitivities
σ	=	Applied stress used to calculate POF

σ' = Applied stress input from external source

Ψ = Reference volume or surface area of component per initial crack size exceedance curve

Ψ_i = Volume or surface area of zone

θ_j = Statistical parameter of pdf associated with variable x_j

$\tilde{x}$ = Vector of random variables, $\tilde{x} = (x_1, x_2, \ldots, x_{nrv})$

$\tilde{X}$ = Median value of random variable X

T.9 REFERENCES.

T-1. Madsen, H.O., Krenk L., and Lind N.C., *Methods of Structural Safety*, Dover Publications, 2006.

T-2. Madsen, H.O., "Omission Sensitivity Factors," *Structural Safety*, Vol. 5, No. 1, 1988, pp. 35-45.

T-3. Sobol, I.M., "Sensitivity Analysis of Nonlinear Mathematical Models," *Mat. Model. Comput. Exp.*, Vol. 1, pp. 407-414, 1993, [translation of Sobol, I.M., "Sensitivity Estimates for Nonlinear Mathematical Models," *Matematicheskoe Modelirovanie*, Vol. 2, 1990, pp. 112-118 (in Russian)].

T-4. Sobol, I.M., "Global Sensitivity Indices for Nonlinear Mathematical Models and Their Monte Carlo Estimates," *Mathematics and Computers in Simulation*, Vol. 55, Nos. 1-3, 2001, pp. 271-280.

T-5. Chan, K., Saltelli, A., and Tarantola, S., "Sensitivity Analysis of Model Output: Variance-Based Methods Make the Difference," *Proc. of the 1997 Winter Simulation Conference*, S. Andradottir, K.J. Healy, D.H. Withers, and B.L. Nelson, editors, 1997.

T-6. Chen, W., Jin, R., and Sudjianto, A., "Analytical Variance-Based Global Sensitivity Analysis in Simulation-Based Design Under Uncertainty," *ASME Journal of Mechanical Design*, Vol. 127, No. 5, 2005, pp. 875-886.

T-7. Karamchandani., A.K., "New Approaches to Structural System Reliability," Ph.D. Thesis, Department of Civil Engineering, Stanford University, 1990.

T-8. Wu, Y.-T., "Computational Methods for Efficient Structural Reliability and Reliability Sensitivity Analysis," *AIAA Journal*, Vol. 32, No. 8, 1994, pp. 1717-1723.

T-9. Enright, M.P. and Huyse, L., "Methodology for Probabilistic Life Prediction of Multiple Anomaly Materials," AIAA Paper-2005-2213, *46th AIAA/ASME/ASCE/AHS/ASC Structures, Structural Dynamics and Materials Conference*, Austin, Texas, 2005.

T-10. Enright, M.P., Huyse, L., and McClung, R.C., "Fracture Mechanics-Based Probabilistic Life Prediction of Components with Large Numbers of Inherent Material Anomalies," *Proc. 9th International Conference on Structural Safety and Reliability (ICOSSAR)*, Rome, Italy, 2005, pp. 601-607.

T-11. Aerospace Industries Association Rotor Integrity Sub-Committee, "The Development of Anomaly Distributions for Aircraft Engine Titanium Disk Alloys," *38th AIAA Structures, Dynamics and Materials Conference*, 1997, pp. 2543-2553.

T-12. Ang, A.H.-S. and Tang, W.H., *Probability Concepts in Engineering Planning and Design*, Basic Principles, Vol. 1, J.Wiley & Sons, 1975.

T-13. Federal Aviation Administration, "Damage Tolerance for High Energy Turbine Engine Rotors," U.S. Department of Transportation, Advisory Circular AC 33.14-1, 2001.

T-14. Millwater, H.R., Enright, M.P., and Fitch, S.H.K., "A Convergent Probabilistic Technique for Risk Assessment of Gas Turbine Disks Subject to Metallurgical Defects," AIAA Paper 2002-1383, *43rd AIAA/ASME/ASCE/AHS/ASC Structures, Structural Dynamics, and Materials Conference*, Non-Deterministic Approaches Forum, Denver, CO, 2002.

T-15. Wu, Y.-T., Enright, M.P., and Millwater, H.R., "Probabilistic Methods for Design Assessment of Reliability with Inspection," *AIAA Journal*, Vol. 40, No. 5, 2002, pp. 937-946.

T-16. Huyse, L. and Enright, M.P., "Efficient Statistical Analysis of Failure Risk in Engine Rotor Disks Using Importance Sampling Techniques," AIAA Paper 2003-1838, *44th AIAA/ASME/ASCE/AHS/ASC Structures, Structural Dynamics and Materials Conference*, Norfolk, VA, 2003.

APPENDIX U—OPTIMAL SAMPLING FOR ZONES

U.1 INTRODUCTION.

When computational accuracy must be assured, the effort associated with simulation-based probabilistic life prediction can be significant. Since fatigue failure probabilities are typically very small for gas turbine engine disks associated with commercial aircraft (i.e., on the order of 10^{-9} per flight cycle), a large number of Monte Carlo samples may be required to satisfy computational accuracy requirements. In this appendix, techniques for reducing the total variance associated with probabilistic life prediction are compared for a disk with a fixed number of zones. It is shown that reallocation of samples based on risk contribution factors or an optimal approach can significantly reduce the total number of samples required for a specified accuracy. In addition, a hybrid approach is presented in which optimal sampling is combined with a semiautomated zone refinement procedure. This approach is illustrated for an aircraft rotor disk in which it is shown that zone refinement influences mean disk risk, whereas optimal sampling influences disk risk variance. These strategies can be used to improve the efficiency of zone-based probabilistic fatigue life predictions where computational accuracy must be assured.

U.2 DISK-BASED VARIANCE REDUCTION.

The variance of the failure probability in each zone $\sigma_{\hat{p}_i}$ is dependent on the number of samples [U-1]:

$$\sigma_{\hat{p}_i} = \sqrt{\frac{\hat{p}_i(1-\hat{p}_i)}{n_i}} \tag{U-1}$$

where $\hat{p}_i =$ probability of fracture estimate in zone i given an initial anomaly, and n_i = number of samples in zone i.

The mean and variance of the disk failure probability are as follows:

$$\mu_{\hat{P}_f} = \sum_{i=1}^{m} \delta_i \hat{p}_i \tag{U-2}$$

$$\sigma^2_{\hat{P}_f} = \sum_{i=1}^{m} \delta_i^{\,2} \sigma^2_{\hat{p}_i} \tag{U-3}$$

where $\hat{p}_f$ is the failure probability estimate for the disk.

The confidence bounds for the disk (figure U-1) are

$$\text{lower bound} = \mu_{\hat{P}_f} - k_{\alpha/2}\sigma_{\hat{P}_f} \tag{U-4}$$

$$\text{upper bound} = \mu_{\hat{P}_f} + k_{\alpha/2}\sigma_{\hat{P}_f} \tag{U-5}$$

where $k_{\alpha/2}$ = standard normal variate for a $(1-\alpha)$ confidence interval.

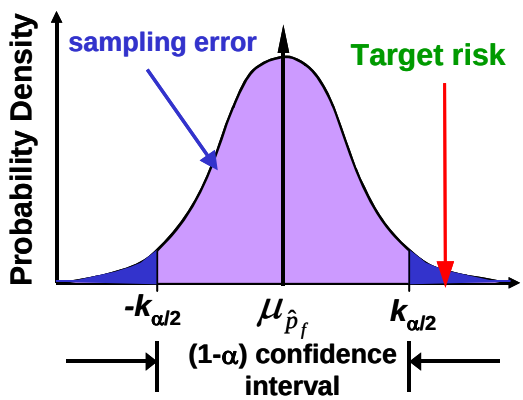

Figure U-1. Confidence Intervals Associated With Simulation-Based Probabilistic Fatigue Life Prediction

Disk-based variance reduction focuses on decreasing the overall disk variance by reallocating samples to zones that have the most significant contribution to risk. Disk risk confidence bounds can be used to ensure that the failure probability of a disk does not exceed the target value for a given confidence (e.g., 95%). As shown in figure U-2, if disk variance can be reduced, then the mean disk risk can be increased yet satisfy the risk target for a given confidence.

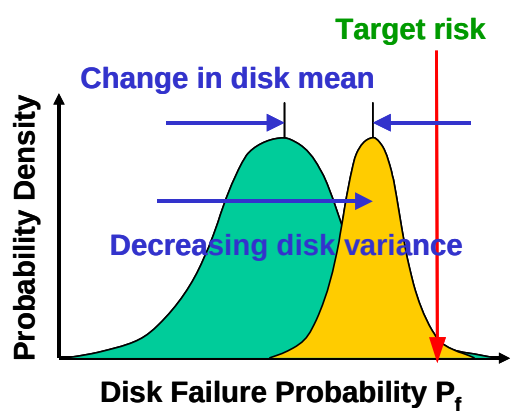

Figure U-2. Disk Variance Reduction Allows Higher Mean Disk Failure Probability for a Given Target Risk

Two approaches for reallocating samples are considered for reducing disk variance: Risk contribution factor (RCF) approach and an optimal approach. For the RCF approach, the number of samples, n_i, in each zone is based on an estimate of the zone RCF_i:

$$n_i = RCF_i \cdot N \tag{U-6}$$

$$\text{where } RCF_i = \frac{\delta_i \hat{p}_i}{\hat{P}_f} \tag{U-7}$$

$$N = \frac{k_{\alpha/2}{}^2}{\gamma^2} \frac{(1-P_f)}{P_f} \tag{U-8}$$

= total number of samples in disk

$$\text{and } \gamma = \left(\frac{\hat{P}_f - P_f}{P_f} \right) = \text{ relative sampling error}$$

For the optimal approach [U-2], the number of samples is

$$n_i = \frac{\delta_i \sqrt{p_i(1-p_i)}}{\sum_{i=1}^{m} \delta_i \sqrt{p_i(1-p_i)}} N \tag{U-9}$$

where

$$N = \frac{k_{\alpha/2}{}^2}{\gamma^2 P_f{}^2} \left[\sum_{i=1}^{m} \delta_i \sqrt{p_i(1-p_i)} \right]^2 \tag{U-10}$$

Further details regarding the development of these relationships can be found in reference U-3.

U.3 APPLICATION OF DISK-BASED VARIANCE REDUCTION FOR A TITANIUM ROTOR DISK WITH A FIXED NUMBER OF ZONES.

Consider the aircraft rotor geometry shown in figures U-3 and U-4. The design life of the disk is 20,000 flight cycles. Internal stresses and temperatures are identified using finite element analysis based on operational loading conditions. Five primary random variables are considered for probabilistic analysis. The main descriptors for three of these variables (stress scatter, life scatter, and inspection time) are indicated in table U-1. For the remaining two variables

(anomaly area and probability of detection [PoD]), empirical distributions (AIA POST95-3 flat-bottom hole (FBH)-3FBH anomaly distribution, #3 FBH 1:1 Reject Calibration PoD Curve) found in Advisory Circular 33.14-1 were used for probabilistic fatigue life predictions. Forty-four zones were used to model the disk.

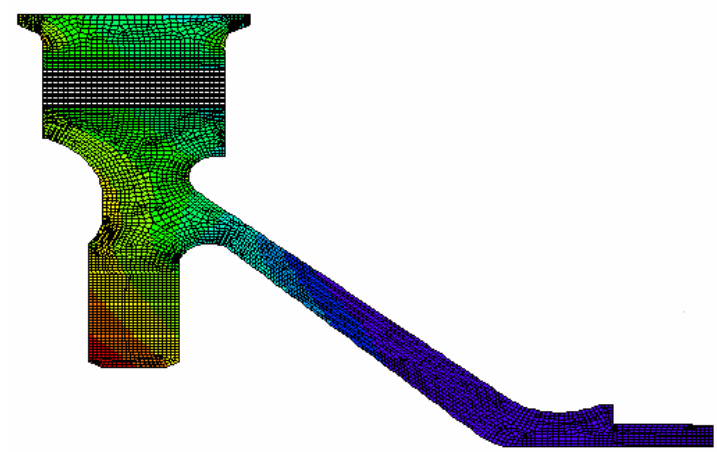

Figure U-3. Aircraft Rotor Disk Application—Cross Section

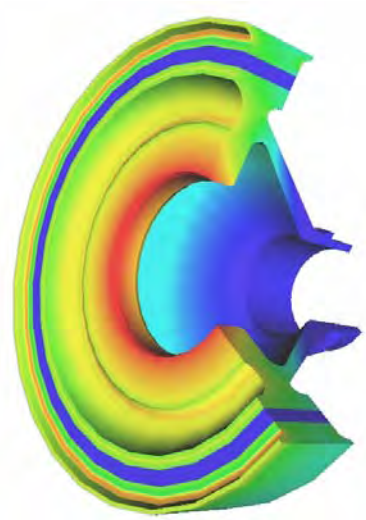

Figure U-4. Aircraft Rotor Disk Application—Three-Dimensional View

Table U-1. Titanium Aircraft Rotor Application Example—Random Variables

Random Variable	Median	COV (%)	Distribution
Stress scatter	1.0	20	Lognormal
Life scatter	1.0	40	Lognormal
Inspection time	10,000 cycles	20	Normal

COV = Coefficient of variation

Failure probability results are shown in figure U-5 (100 samples per zone). It can be observed that the mean disk failure probability is below the target risk value (1.0 E-9). However, the upper confidence bound result (no inspection) is well above the target risk, so variance reduction is needed. As shown in figure U-6, the desired variance reduction can be achieved by increasing the number of samples in each zone to 100,000. However, this requires a total of over 4 million samples for the disk.

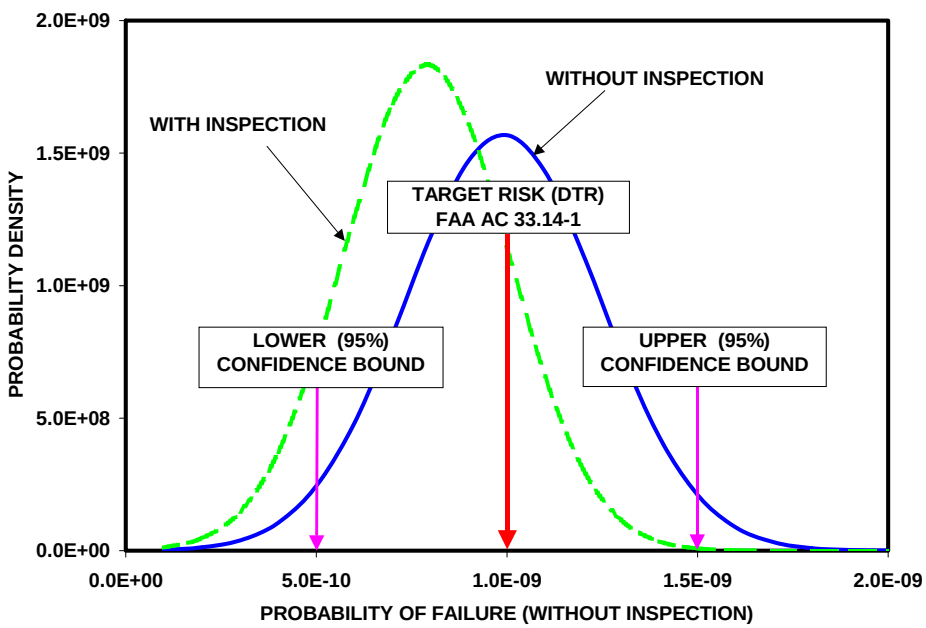

Figure U-5. Upper Confidence Bounds on Disk Risk Results for Fixed Number of Zones Initially do not Satisfy Federal Aviation Administration Target Risk

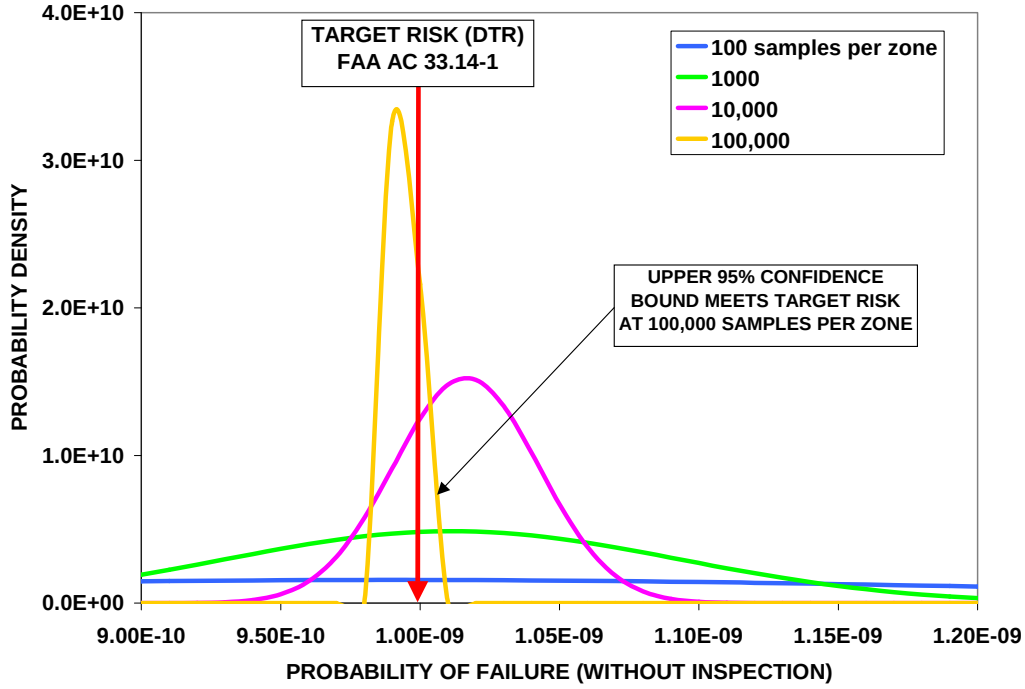

Figure U-6. Increasing the Number of Zone Samples Reduces Variance but is Computationally Expensive

In figure U-7, a comparison of the confidence bounds versus number of disk samples is shown for three sample allocation approaches: uniform (i.e., same number of samples in all zones), RCF, and optimal. For a specified number of samples, it can be observed that, compared to the uniform approach, the confidence bounds are narrower for the RCF and optimal approaches. The target risk can be achieved with the RCF and optimal approaches with approximately 40,000 disk samples (over 4 million disk samples are required for the uniform approach). It is interesting to note that the optimal method converges only slightly faster than the RCF approach.

U.4 HYBRID APPROACH: ZONE REFINEMENT COMBINED WITH OPTIMAL SAMPLING.

As stated previously, the disk failure probability decreases with increasing zone discretization. As shown in figure U-8, if the total number of samples within a disk remains fixed, then the primary effect of zone refinement is a decrease in mean disk failure probability. On the other hand, disk variance reduction primarily influences the disk risk coefficient of variation (COV) (figure U-9). A hybrid approach is proposed in which zone refinement is used with relatively few samples per zone to establish a mean disk failure probability value that is below the target risk. Disk variance reduction methods are then applied to ensure that the disk risk upper confidence bound satisfies the target failure probability constraint.

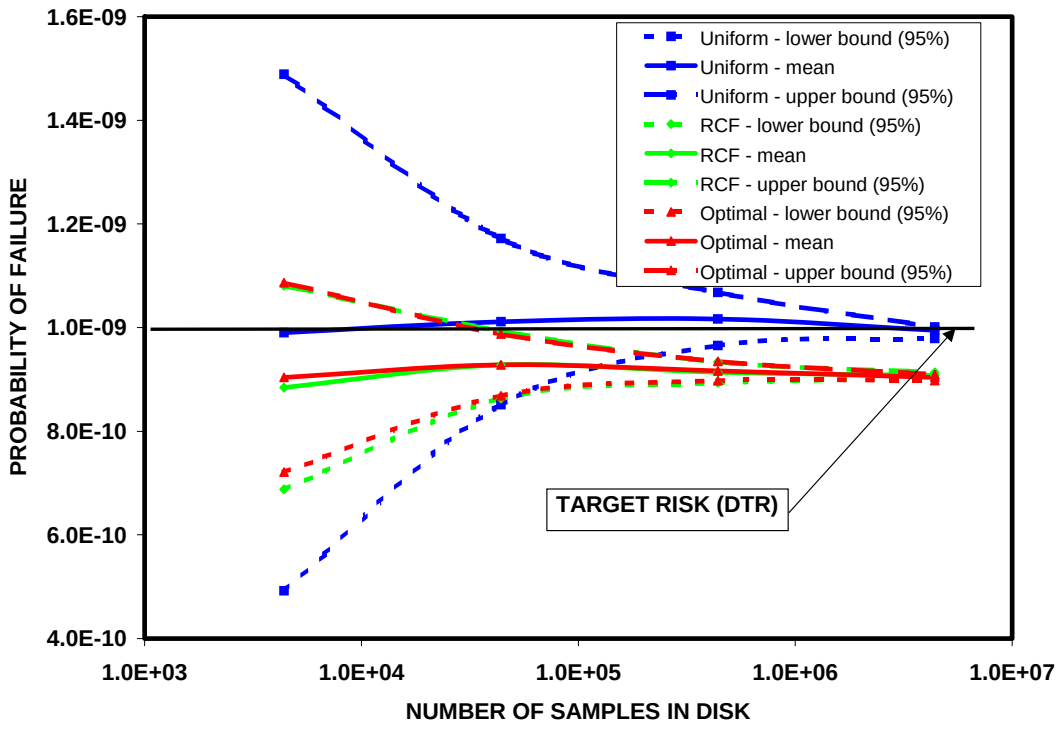

Figure U-7. Comparison of Three Disk Variance Reduction Techniques (Uniform, RCF, and Optimal)

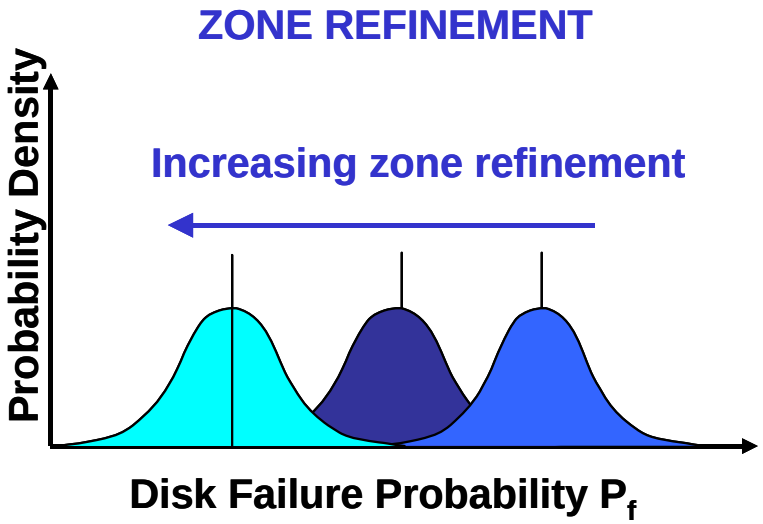

Figure U-8. For a Fixed Number of Disk Samples, Zone Refinement Primarily Influences Mean Disk Risk

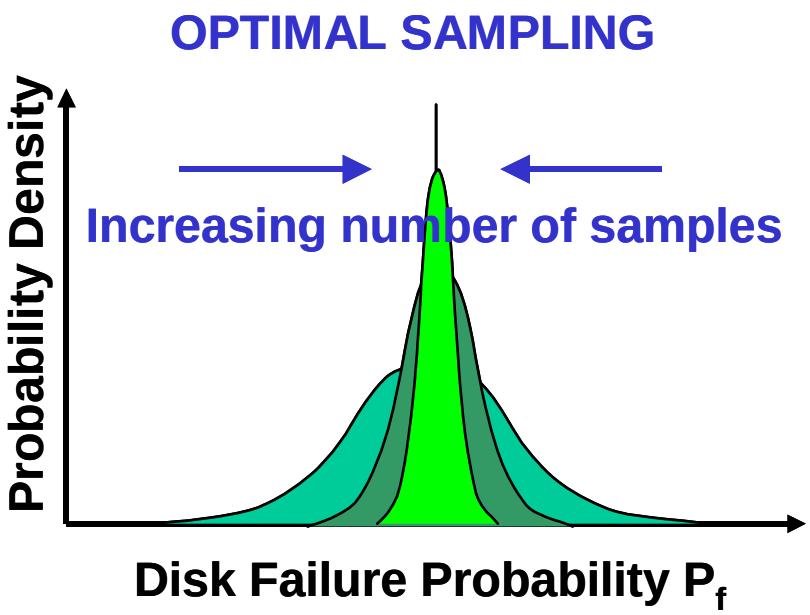

Figure U-9. Optimal Sampling Primarily Influences Disk Risk COV

U.4.1 APPLICATION EXAMPLE: HYBRID APPROACH.

This example illustrates the hybrid approach which combines zone refinement with optimal sampling discussed in the previous section. Consider again the aircraft rotor disk shown in figures U-3 and U-4. The disk is subjected to five successive zone refinements using the semiautomated algorithm in DARWIN® 3.5 [U-4], see figure U-10. The number of disk samples is held constant during zone refinement (3800 total disk samples). A final iteration is performed in which the samples are reallocated to risk critical zones using the optimal sampling approach.

Normalized disk risk mean and COV values are shown in figure U-11 for each iteration. It can be observed that during iterations 1-5 (zone refinement only), the disk risk mean decreases significantly, but disk risk COV remains relatively high. During iteration 6 (optimal sampling only) the disk risk COV decreases significantly (note: the total number of samples is increased to 4700 for the final iteration).

In figure U-12, the 95% confidence bounds are shown for zone refinement iterations 1-5 (uniform indicates equal number of samples in each zone with a constant number of disk samples). For comparison purposes, the confidence bounds associated with the optimal approach are also shown (note: in figure U-12, the optimal approach is applied at each zone refinement iteration). For this example, the target risk could have been achieved by applying optimal sampling after zone refinement iteration number 2. On the other hand, the target could also be achieved using zone refinement only (target satisfied at zone refinement 3). However, since the human time associated with zone refinement is generally significantly greater than for disk variance reduction, optimal sampling should be applied as soon as it is practical to do so (i.e., apply as soon as mean disk failure probability is sufficiently lower than target risk).

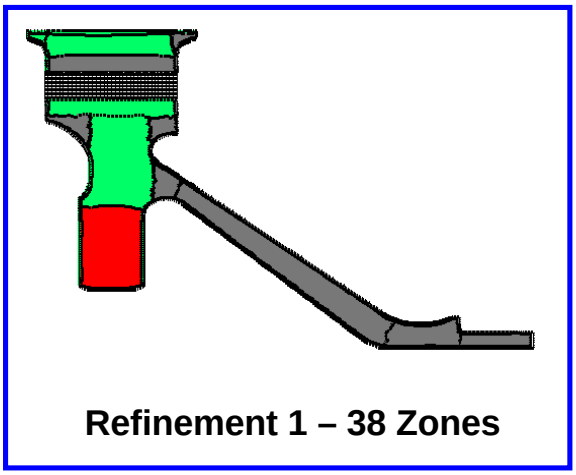

(a)

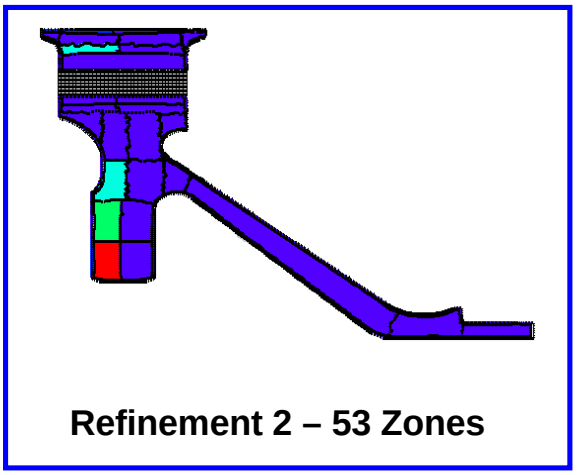

(b)

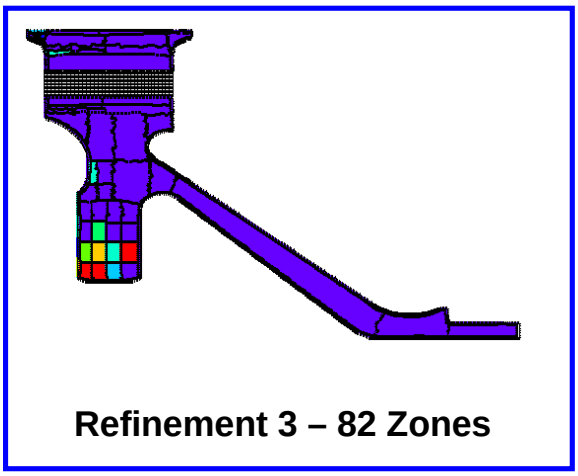

(c)

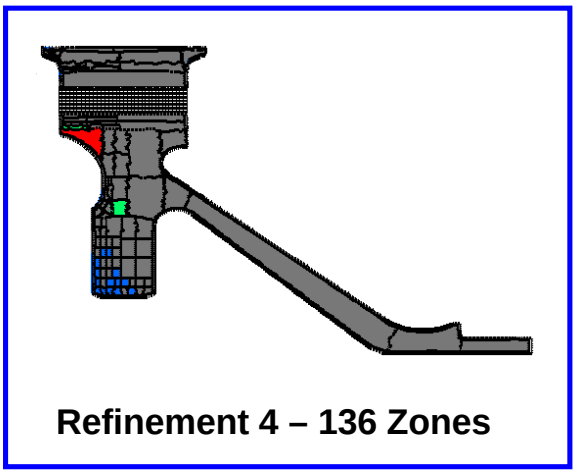

(d)

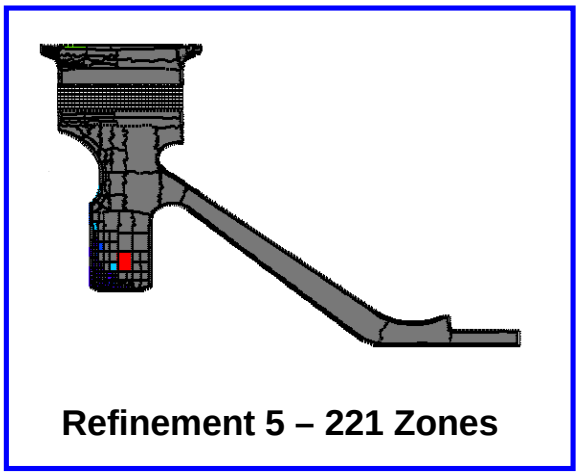

(e)

Figure U-10. Hybrid Approach Application—Zone Refinement Sequence

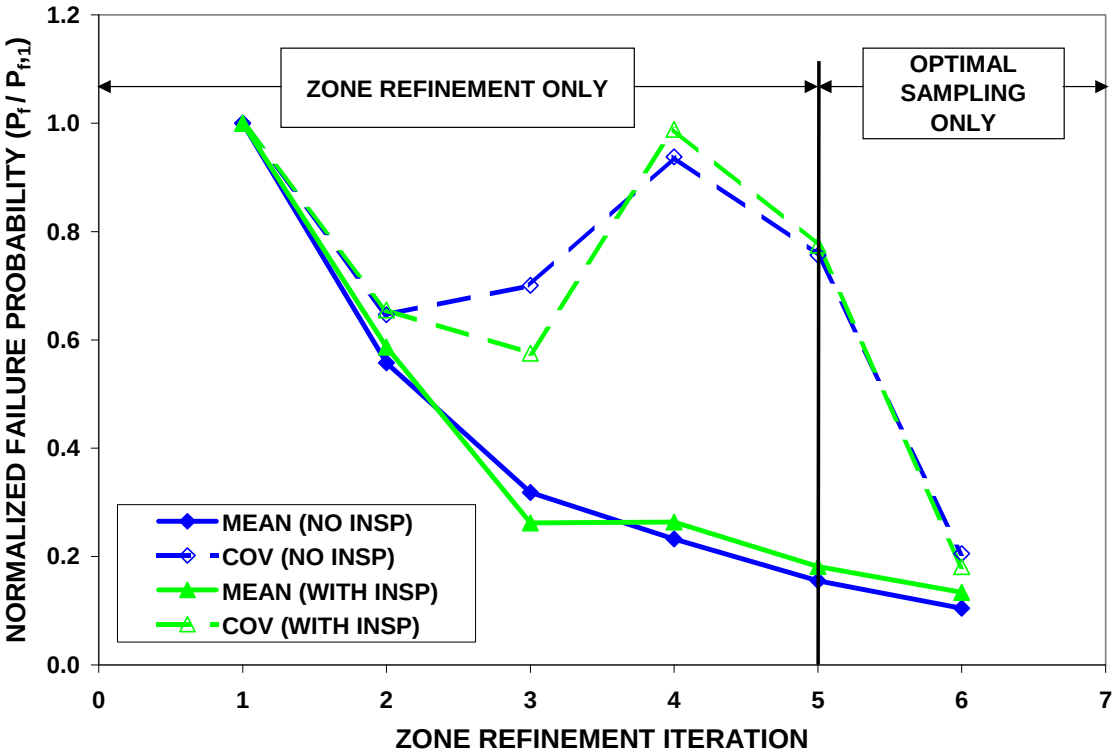

Figure U-11. Hybrid Approach Results: Iterations 1-5 Zone Refinement, Iteration 6—Optimal Sampling

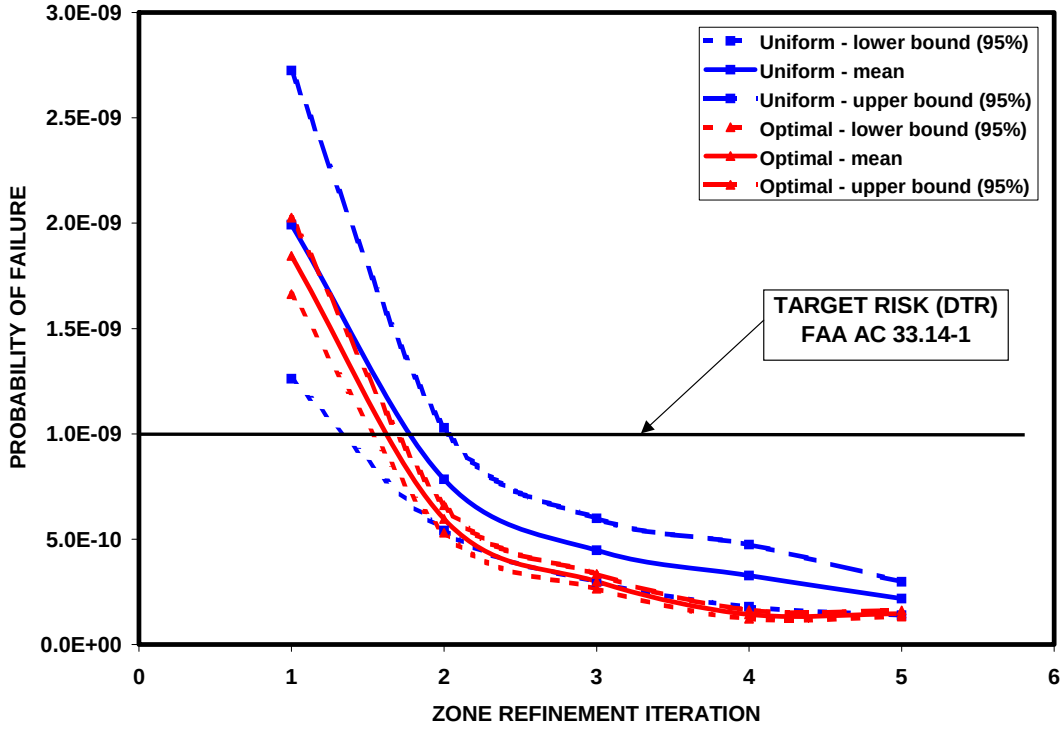

Figure U-12. Comparison of 95% Confidence Bounds for Uniform Sampling and Optimal Sampling Versus Refinement Iteration

U.5 REFERENCES.

U-1. Ang, A. H-S. and Tang, W.H., *Probability Concepts in Engineering Planning and Design*, Wiley, New York, 1975, pp. 252-253.

U-2. Wu, Y.T., Enright, M.P., and Millwater, H.R. "Probabilistic Methods for Design Assessment of Reliability With INspection," *AIAA Journal*, Vol. 40, No. 5, 2002, pp. 937-976.

U-3. Wu, Y-T., Millwater, H.R., and Enright, M.P., "Efficient and Accurate Methods for Probabilistic Analysis of Titanium Rotors," *Proceedings, 8th ASCE Specialty Conference on Probabilistic Mechanics and Structural Reliability*, South Bend, IN, July 24-26, 2000.

U-4. Millwater, H.R., Enright, M.P., and Fitch, S., "A Convergent Probabilistic Technique for Risk Assessment of Gas Turbine Disks Subject to Metallurgical Defects," *Proceedings, 43rd Structures, Structural Dynamics, and Materials Conference*, Denver, CO, April 22-25, 2002.

APPENDIX V—EFFICIENT CONDITIONAL FAILURE ANALYSIS

V.1 INTRODUCTION.

Although many engineering systems and components have a very low probability of failure, the consequences of some failures can be catastrophic. The low failure probability precludes the safety certification of such systems or components on the basis of repeated experiments. Therefore, the certification must necessarily be done on the basis of adequately validated computational models. Conditional failure analysis (CFA) can be used to provide insight into the failure of a component and the most likely range of values of the input random variables associated with failure. It not only provides valuable information to the engineer for improvement of component design, but also helps to validate the mathematical models and probabilistic input distributions associated with reliability computations. The CFA technique outlined in this appendix is based on a generation of conditional failure samples obtained during computation of component reliability. It provides a graphical description of the failure region that can be used for failure analysis. The technique is illustrated for a practical design problem involving the fatigue crack growth limit state of a gas turbine engine component. The results can be applied to failure analysis and model validation of general aerospace components.

V.2 NOMENCLATURE.

d_{min}	Minimum anomaly size
d_{max}	Maximum anomaly size
$exc(d)$	Number of anomalies of size greater than or equal to d
$E(x \mid F)$	Conditional expectation (mean value) of x given failure
$f_X(x)$	pdf of random variable X
$f_{X \mid F}(x \mid F)$	Conditional PDF of x given failure
$F_X(x)$	Cumulative distribution function (CDF) of random variable X
$F_{X \mid F}(x \mid F)$	Conditional CDF of random variable X given failure
$h(x)$	Importance sampling density
K_{Ic}	Fracture toughness
n	Number of random variables
$N_{service}$	Service life (in flight cycles)
N_{target}	Target number of flight cycles
N_{fail}	Number of flight cycles to failure
$\mathrm{Var}(X)$	Variance of the random variable X
$\boldsymbol{X}$	Random variables (vector if bold)
x	Sample value of random variable X
$\boldsymbol{x}^*$	Value of $\boldsymbol{X}$ at MPP
$\sigma_{applied}$	Actual, applied stress level
σ_{FE}	Stress level predicted by FE model

V.3 NEED FOR CONDITIONAL FAILURE ANALYSIS.

The design of engineering systems and components is affected by uncertainties (e.g., incomplete understanding of the physics, lack of information, inherently variable operating conditions, among many others). When a probabilistic evaluation is performed, the effects of uncertainty

must be accounted regardless of the source of the uncertainties. If the random variables $\boldsymbol{x}$ are characterized by a probability density function (pdf), the failure probability p_F can be computed as an integral over the failure domain:

$$p_F = \int_{failure}^{n-fold} \cdots \int f_X(\mathbf{x}) d\mathbf{x} = \int_{g(\mathbf{x})<0}^{n-fold} \cdots \int f_X(\mathbf{x}) d\mathbf{x} \tag{V-1}$$

where $g(\boldsymbol{x}) < 0$ is the failure domain.

From a design perspective, it is important to identify the range of values of the individual random variables that lead to failure (referred to as CFA) so that they can be avoided where possible. In CFA the original pdf of the random variables is redefined in terms of failure F, where F describes the failure domain $\{\boldsymbol{x} \mid (g(\boldsymbol{x}) < 0)\}$. In this context, the conditional failure density $f_{\boldsymbol{X}}(\boldsymbol{x} \mid F)$ of a random variable $\boldsymbol{X}$ (i.e., pdf of $\boldsymbol{x}$ given that F has occurred) can be written as

$$f_X(x \mid F) = f_X\left[x \mid g(x) < 0\right] \tag{V-2}$$

A typical reliability assessment identifies the risk associated with a specific limit state or set of limit states with a focus on the most likely combination of variables that lead to failure. CFA provides additional insight regarding the physics of the problem. For example, computational models typically involve approximations that are valid only for a particular range of input parameters. The high-density region of a joint conditional failure density $f_{\boldsymbol{X}}(\boldsymbol{x} \mid F)$ represents the combinations of input parameters $\boldsymbol{X}$ for which the computational model must adequately predict the physical behavior. It can be compared to the densities of the input variables to ensure that none of the model assumptions are violated. This helps to validate that the physics are adequately represented in the computational model.

CFA also provides information useful for selecting the pdfs that best fit the experimental data. Typically, an explicit pdf is selected based on a goodness-of-fit test, such as Kolmogorov-Smirnov [V-1] or its tail-improved Anderson-Darling version [V-2], the Shapiro-Wilks test [V-3], or the Chi-square test [V-4], among others. A good fit often cannot be achieved over the entire range, and the fit results may be influenced by data values that do not contribute to failure. Since the pdf is used for failure probability computations, the accuracy of the fit is most critical in the neighborhood of the most probable failure point (MPP). The MPP may or may not be located in the tail of the fitted distribution. The conditional density provides more detail regarding the range of values over which a good fit must be achieved.

In this appendix, several approaches for generating conditional densities are discussed. A CFA technique is presented, in which the conditional densities are generated during the computation of component reliability using a hybrid approach [V-5] consisting of numerical integration combined with the response surface method [V-6]. The technique is illustrated for a practical design problem involving the fatigue crack growth limit state of an aircraft gas turbine engine component. It provides the additional information needed for statistical analysis of the failure region associated with each random variable. The results can be applied to failure analysis and model validation of general aerospace components.

V.4 APPROACHES FOR GENERATING CONDITIONAL PROBABILITY DISTRIBUTIONS.

Typical quantities of interest for CFA include the conditional mean $E(\mathbf{x}|F)$, conditional variance $\mathrm{Var}(\mathbf{x}|F)$, and $\mathbf{x}^*$, the values of the input variables $\mathbf{x}$ at the MPP:

$$E(\mathbf{x}\,|\,F) = \int f_{\mathbf{X}}(\mathbf{x}\,|\,F)\,\mathbf{x}\,d\mathbf{x} = \int_{g(x)<0} \mathbf{x}\; f_{\mathbf{X}}(\mathbf{x})\,d\mathbf{x} \tag{V-3}$$

$$\mathrm{Var}(\mathbf{x}\,|\,F) = \int \left[\mathbf{x} - E(\mathbf{x}\,|\,F)\right]^2 f_{\mathbf{X}}(\mathbf{x}\,|\,F)\,d\mathbf{x} \tag{V-4}$$

$$\mathbf{x}^* = \arg\left\{\max\left[\,f_{\mathbf{X}}(\mathbf{x}\,|\,F)\right]\right\} = \arg\left\{\max_{g(\mathbf{x})<0}\left[\,f_{\mathbf{X}}(\mathbf{x})\right]\right\} \tag{V-5}$$

A number of techniques can be used to generate conditional densities. For example, direct Monte Carlo simulation can be used using the following procedure: (1) generate a sample from the original (unconditional) density function $f(\mathbf{x})$, (2) evaluate the limit state $g(\mathbf{x})$, and (3) if $g(\mathbf{x}) < 0$, accept the sample (i.e., use in evaluation of the conditional metric of interest), otherwise, reject the sample. However, this method is very inefficient because approximately $1/p_F$ of the samples are required to generate a single sample from the conditional density function. Since additional samples are required for a statistical analysis of failure (e.g., estimation of second or higher order moments, correlations, etc.), this approach requires many more samples than are ordinarily required for Monte Carlo-based failure probability computations.

Second moment methods can be used to identify the MPP. The MPP (or, equivalently, the Point of Maximum Likelihood) identifies the most likely combination of random variables associated with failure. However, no expressions are available to easily compute the conditional statistics:

$$E(h(x)\,|\,F) = \int f_X(x\,|\,F)\,h(x)\,dx = \int_{g(x)<0} f_X(x)\,h(x)\,dx \tag{V-6}$$

The location of the MPP can, however, be used as a starting point to construct approximations to the conditional density $f(\mathbf{x}\,|\,F)$. For example, the asymptotic importance sampling density (ISD) [V-7] is fairly straightforward to construct from the MPP location and main curvature direction of the limit state function at the MPP. The AIS estimator typically has a small variance, which makes it a good candidate to evaluate the conditional expectations in equation V-6 typically required for failure analysis.

Importance sampling (IS) can also be used to characterize conditional densities. The efficiency of IS depends on the selection of an ISD. The IS method leads to an unbiased estimate provided that the ISD is nonzero over the entire failure domain [V-8]:

$$p_F = \int f_X(x\,|\,F)\,dx = \int_{g(x)<0} f(x)\,dx = \int_{g(x)<0} w(x)\,h(x)\,dx \tag{V-7}$$

where $w(\mathbf{x}) = f(\mathbf{x})/h(\mathbf{x})$ is the location dependent scaling factor associated with the ISD. The variance of the IS-based failure probability estimate is given by [V-9]:

$$\mathrm{Var}(p_F) = \int_{g(x)<0} \left(w(x) - p_F \right)^2 h(x)\, dx \tag{V-8}$$

Equation V-8 shows that that the optimal choice for the ISD is given by the conditional density $f(\boldsymbol{x} \mid F)$ when $w(\boldsymbol{x}) = p_F$ for all $\boldsymbol{x}$, and the variance $Var(p_F)$ is zero. The conditional density is obtained by adjusting $w(\boldsymbol{x})$ to reduce $Var(p_F)$ to a small value. Au and Beck [V-9] recently demonstrated that the conditional failure density is obtained as the asymptotically density resulting of iterative Markov Chain Monte Carlo simulations, based on an arbitrary ISD. This removes the need to perform the potentially computationally expensive limit state analysis.

An approach is presented where the ISD is given by the exact conditional density. The failure probability is computed using numerical integration, and the conditional densities are generated as a byproduct of the integration. If the random variables are independent, equation V-1 can be expressed as

$$p_F = \int_{failure}^{n-fold} \cdots \int f_{x_1}(x_1) \cdot f_{x_2}(x_2) \cdots f_{x_n}(x_n)\, dx_1 \cdot dx_2 \cdots dx_n \tag{V-9}$$

It is possible to solve the limit state function $g(\boldsymbol{x})$ for one of the random variables, say X_1. In most applications, this cannot be done in closed form. However, if an accurate response surface can be generated for the problem, X_1 can be solved numerically. If the failure domain can be described in terms of X_1, equation V-9 can be rewritten as

$$p_F = \int^{(n-1)-fold} \cdots \int F_{x_1}\left[x_1(x_2, x_3, \cdots, x_n) \mid F \right] \cdot f_{x_2}(x_2) \cdots f_{x_n}(x_n)\, dx_2 \cdots dx_n \tag{V-10}$$

This process can be repeated for the remaining random variables, X_2, …, X_n. The cumulative distribution function (CDF) for the n-th random variable $F_{Xn}(x_n \mid F)$ is the conditional CDF of X_n given failure F. Conditional samples for X_n, say $x_{n,i}$, can be generated directly from $F_{Xn}(x_n \mid F)$. Conditional samples for the (n-1)-th random variable are generated using $F_{Xn-1}(x_{n-1} \mid F)$ for the range of values $x_n|F$. This process of back-substitution is repeated for all remaining random variables.

The accuracy of the conditional density estimate is dependent on the techniques used for numerical integration and identification of the failure domain. This approach is practically limited to problems with relatively few variables and a well-defined failure domain.

V.5 APPLICATION TO AIRCRAFT GAS TURBINE ENGINE COMPONENT.

This example demonstrates the use of conditional densities (generated as part of the importance sampling method in Design Assessment Reliability With INspection (DARWIN®)) to predict the failure behavior of a gas turbine engine component (figure V-1). The conditional densities of the primary (non-inspection-related) random variables are provided, including a comparison of the statistical descriptors for the original and conditional densities. The use of the conditional densities for failure analysis (i.e., CFA) is illustrated, providing insight for design and maintenance planning decisions.

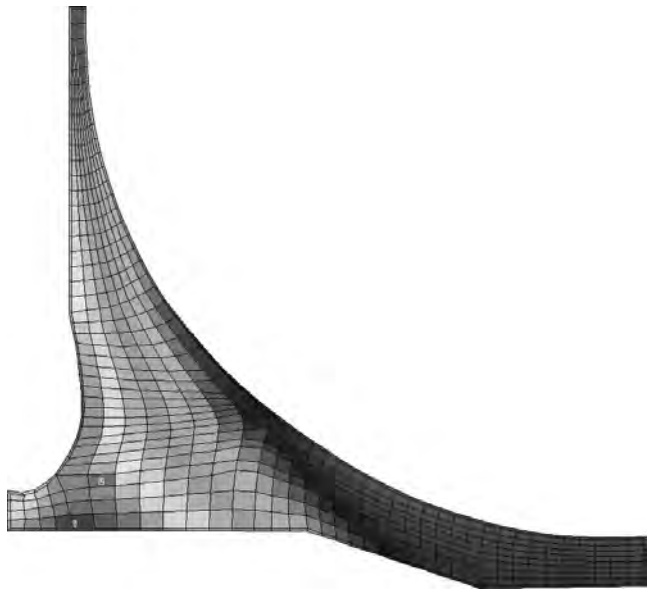

Figure V-1. Application Example: Commercial Aircraft Gas Turbine Engine Component

V.5.1 LIMIT STATE.

A fatigue crack growth failure limit state is considered, in which it is assumed that material failure (i.e., fracture) occurs when the maximum stress-intensity factor K exceeds the fracture toughness K_{I_c} . If an initial anomaly is present, the probability of fracture p_F can be expressed as

$$p_F = \mathrm{P}(K \geq K_{I_c}) = \mathrm{P}(N_{fail} \leq N_{service}) \tag{V-11}$$

V5.2 RANDOM VARIABLES.

The uncertainty associated with fatigue crack growth computations is modeled using three general random variables related to variability in initial anomaly size, applied stress, and material properties [V-10]. In this application, each of the random variables is treated as an independent random variable. The initial anomaly size is based on an exceedance model developed by the Aerospace Industries Association [V-11]. The model is converted to a CDF as follows [V-5]:

$$CDF(d_i) = \frac{exc(d_{\min}) - exc(d)}{exc(d_{\min}) - exc(d_{\max})} \tag{V-12}$$

The exceedance and CDF curves of the initial anomaly size distribution used in this application are shown in figure V-2. In equation V-12, it is assumed that the CDF is bounded at either end of the exceedance curve (the validity of this assumption is addressed later in this appendix).

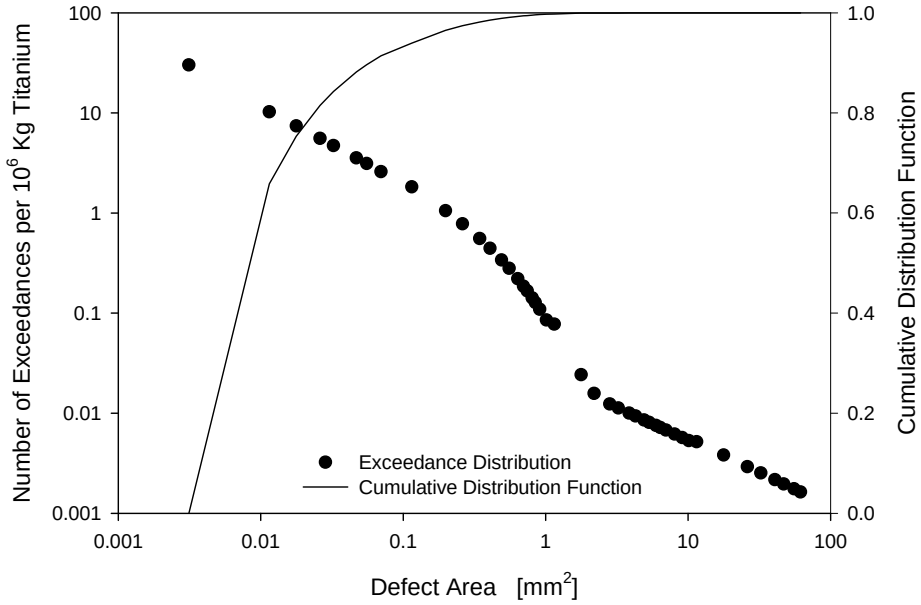

Figure V-2. Exceedance Values and Corresponding Cumulative Distribution Associated With Initial Anomaly Size

The uncertainty associated with applied stress is modeled as a lognormally distributed stress scatter factor *B*. In practice, this uncertainty may be relatively small with a coefficient of variation (COV) of 10% or less. In this application the COV is set to 20% to explore the influence of this variable (the median value is set to 1.0). The applied stress is equal to the product of the stress scatter factor and FE stress results σ_{FE}:

$$\sigma_{applied} = b \times \sigma_{FE} \tag{V-13}$$

The influence of materials-related variability on fatigue crack growth life is modeled using a lognormally distributed life scatter factor *S*. In this application example, it is assumed to have a median value of 1.0 and a 20% COV. The fatigue crack growth life N_{fail} is equal to the product of the life scatter factor and the deterministic fatigue crack growth life N_{FCG}:

$$N_{fail} = s \times N_{FCG} \tag{V-14}$$

For this example, fatigue crack growth is modeled as [V-12]

$$\frac{\mathrm{d}a}{\mathrm{d}N} = C\left(\Delta K\right)^m \tag{V-15}$$

where *a* is the crack size, and *C* and *m* are empirical regression coefficients associated with the Paris Law. For this model, the life scatter can also be considered as an error band applied to the regression curve of the d*a*/d*N* data. If life scatter is included, equation V-15 can be expressed as

$$\frac{\mathrm{d}a}{\mathrm{d}N} = \frac{1}{s} \times C\left(\Delta K\right)^m \tag{V-16}$$

V.5.3 CRACK GROWTH LIFE RESPONSE SURFACE.

Figure V-3 shows how the median predicted life N_{FCG} decreases with increasing initial anomaly size d and stress scatter value b. The computational cost of setting up this response surface can be considerably reduced if it can be truncated in regions that do not influence risk. The computational cost of predicting the fatigue crack growth life N_{FCG} is directly proportional to the median life value itself. The likelihood of failure becomes negligible if the median life $N_{FCG} >> N_{target}$. In DARWIN the response surface is truncated at life values five standard deviations above the median life scatter value. In addition, since the predicted life increases monotonically with decreasing values of the initial anomaly size and stress scatter factor, the response surface can be truncated for relatively small anomaly ($d < d_t$) or stress scatter ($b < b_t$) values. Practical experience has indicated that organizing the computations in this manner reduces the computational cost of response surface preparation by 30% to 60%.

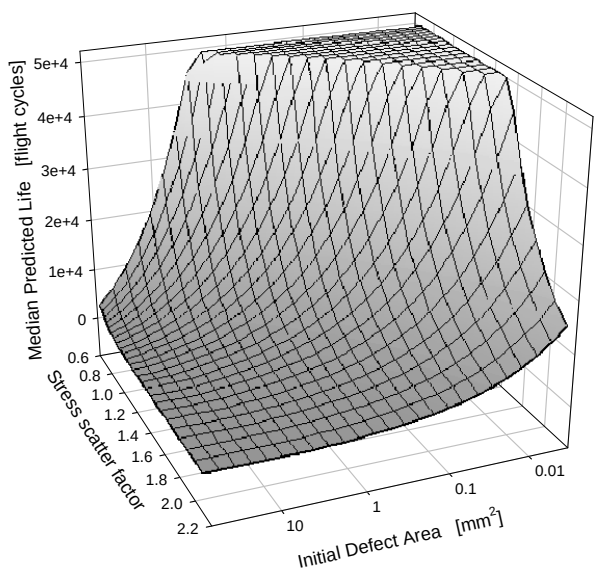

Figure V-3. Response Surface of Predicted Life Associated With Life and Stress Scatter Factor Values

V.5.4 NUMERICAL INTEGRATION OVER ORIGINAL DENSITIES.

The probability of fracture can be expressed as an integral over the failure domain in terms of the three independent random variables described in the previous section:

$$p_F = \iiint_{failure} f_d(d)\, f_B(b)\, f_S(s)\mathrm{d}d\mathrm{d}b\mathrm{d}s \tag{V-17}$$

To solve this integral, the failure domain must be identified. Introduce a critical anomaly size d^* defined as the smallest anomaly that will cause fracture within a specified service life $N_{service}$.

Since the failure domain is limited to the anomalies that exceed the critical anomaly size (i.e., $d > d^*$), equation V-17 can be rewritten as

$$p_F = \iint \left(1 - F_D\left[d^*(b,s)\right]\right) f_B(b)\, f_S(s)\mathrm{d}b\mathrm{d}s \qquad \text{(V-18)}$$

where

$$F_D\left[d^*(b,s)\right] = \Pr\left[d \le d^*(b,s)\right] \qquad \text{(V-19)}$$

and $d^*(b,s)$ is the critical anomaly size d^* associated with specific values of the life and stress scatter factors. The values $d^*(b,s)$ are obtained directly from a response surface of predicted life values (figure V-3) by setting the predicted life equal to N_{target}/s. The corresponding exceedance probability $\Pr(d > d^*(b,s))$ is computed using the initial anomaly CDF, as shown in figure V-4. Introducing the stress scatter and life scatter random variables, the probability density of the integrand of equation V-18 (i.e., $\Pr(d \ge d^*)\, f_B(b)\, f_S(s)$) is obtained, as shown in figure V-5. The failure probability at $N_{service}$ is equal to the integral of the pdf shown in this figure. The conditional densities are obtained based on the failure region identified during evaluation of equation V-19 and are subsequently used for importance sampling to predict the influence of inspection on the probability of fracture (see references V-5 and V-13 for further details on the importance sampling method in DARWIN).

V.5.5 GENERATION OF CONDITIONAL DENSITIES.

The conditional pdfs can be developed during the numerical integration with little additional effort. This is a key advantage over the use of Monte Carlo methods that may require many samples. The process is outlined below.

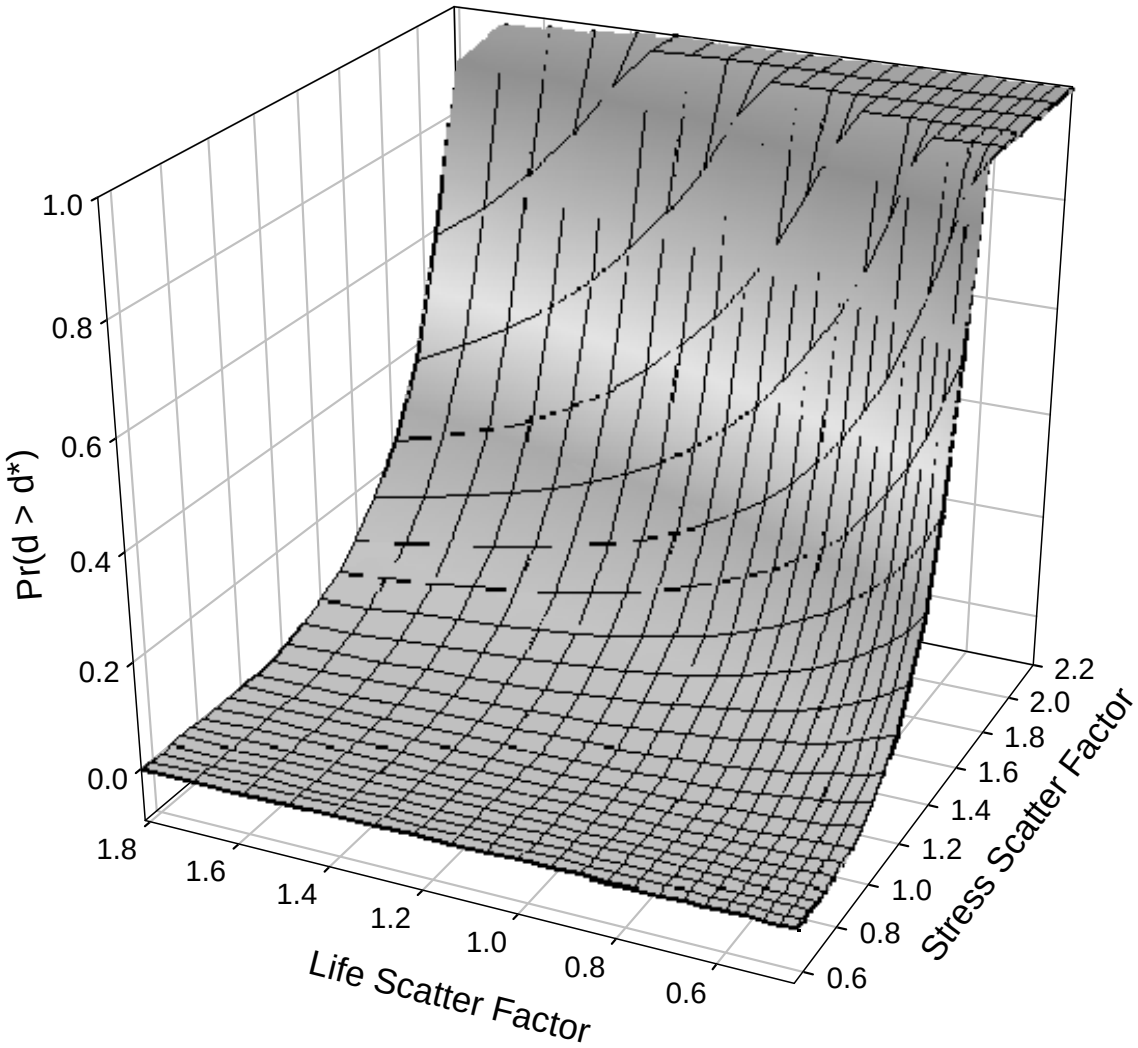

Figure V-4. Exceedance Probability Pr($d > d^*$) Associated With Life and Stress Scatter Factor Values

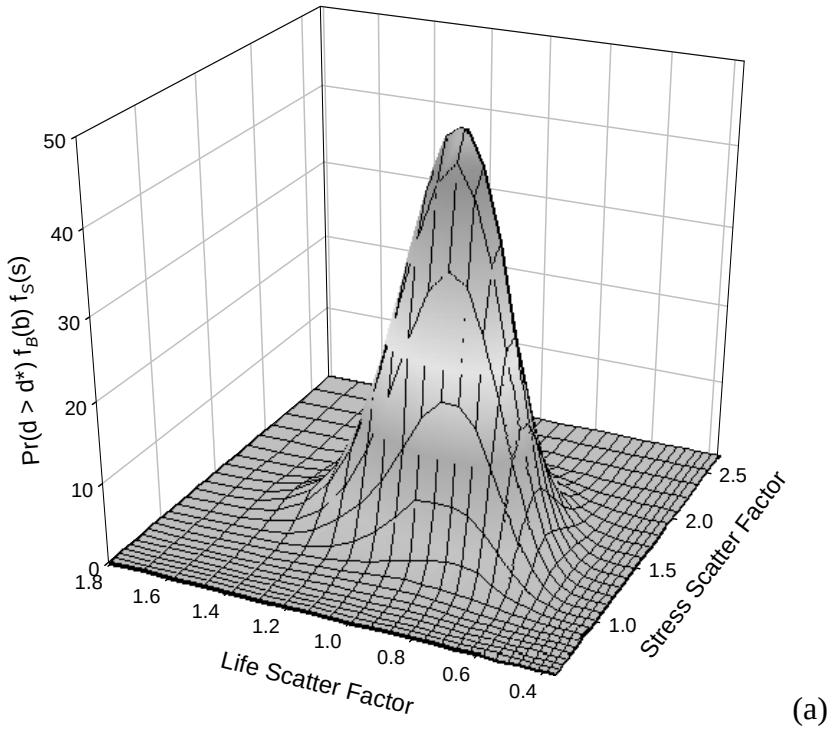

(a)

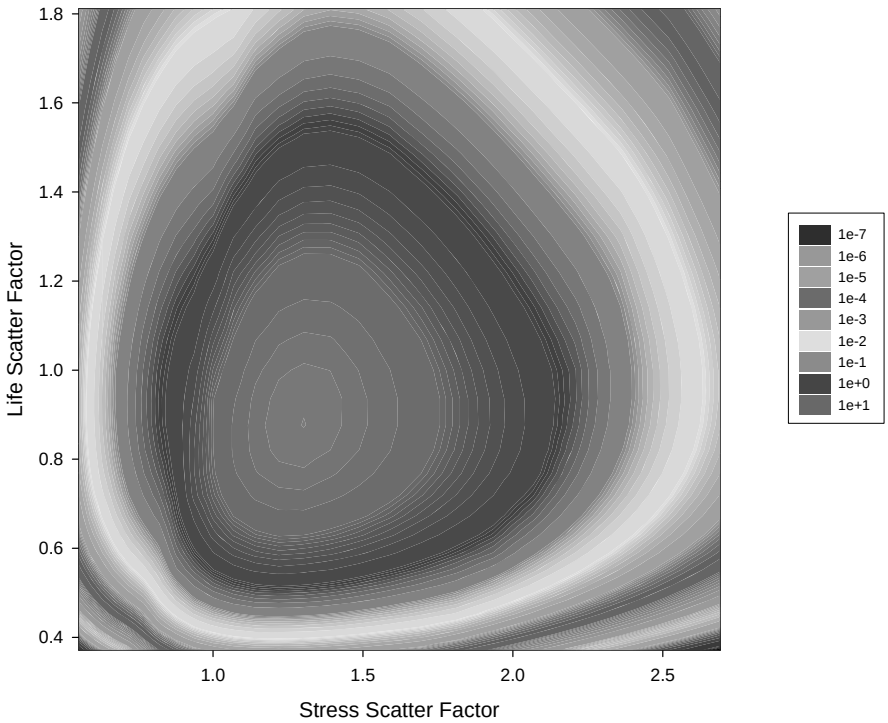

(b)

Figure V-5. Conditional Failure Density Associated With Life and Stress Scatter Factor Values: (a) Three-Dimensional Plot and (b) Contour Plot

Integrate $\Pr(d \geq d^*) f_B(b) f_S(s)$) (see figure V-5) over the stress scatter factor *B*. This results in a conditional likelihood curve for the life scatter factor *S*.

- Obtain a conditional life scatter factor sample value s_i from this conditional density.
- Obtain a sample stress scatter factor b_i from the likelihood curve $\Pr(d \geq d^* | s_i) f_B(b) f_s(s_i)$. In effect, the conditional likelihood curve for the stress scatter factor *B* is obtained by setting S = s_i in figure V-4.

The exceedance probability $\Pr(d > d^* | b_i, s_i)$ corresponding to the sample values s_i and b_i is shown in figure V-4. The critical anomaly size d^* can be derived from the exceedance probability value $\Pr(d > d^* | b_i, s_i)$ through the initial anomaly distribution (figure V-1). A sample initial anomaly size d_i is subsequently generated from the conditional pdf $f_D(d \mid d > d^*)$, which is a truncated and rescaled version of the original initial anomaly size distribution and includes only anomaly values that exceed the critical anomaly (i.e., $d > d^*$).

V5.6 FAILURE ANALYSIS OF CONDITIONAL DENSITIES.

The joint density is dependent on several random variables and is difficult to visualize in two-dimensional space. Original and conditional joint pdfs for each pair of random variables (i.e., stress scatter and initial anomaly size, stress scatter and life scatter factor, and life scatter factor and initial anomaly size) were therefore constructed, as shown in figure V-6. It is important to note that these conditional densities are readily obtained as a byproduct of the numerical integration scheme in DARWIN and do not require sampling. A significant number of samples (about $1{,}000/p_F$ or $100{,}000/p_F$ samples—depending on the desired accuracy of the conditional histograms) would be required if these densities were generated using Monte Carlo sampling.

The conditional densities in figure V-6(d) and (f) indicate that failure is most likely to occur when the initial anomaly area is approximately 0.1 mm^2 (note: the initial anomaly size is plotted on a logarithmic scale). Smaller anomalies are plentiful (see figure V-6(a) and (c)) but do not cause failure before the specified service life of 20,000 cycles. Although failure is virtually guaranteed when large anomalies are present, they do not occur frequently enough to have a significant influence on risk. It is interesting to note that the joint conditional likelihood values are very small near the truncated tails of the anomaly distribution. It can be concluded that, for this example, the tails of the initial anomaly distribution do not have a significant influence on the total risk. Therefore, although the anomaly distribution is truncated, this assumption does not appear to have an influence on the conditional density and associated failure probability predictions.

The high-density regions associated with the life scatter factor are nearly identical for the original (figure V-6(a) and (b)) and conditional (figure V-6(d) and (e)) densities. This indicates that, in this example, the failure risk is not very sensitive to the uncertainty in the fatigue crack growth model.

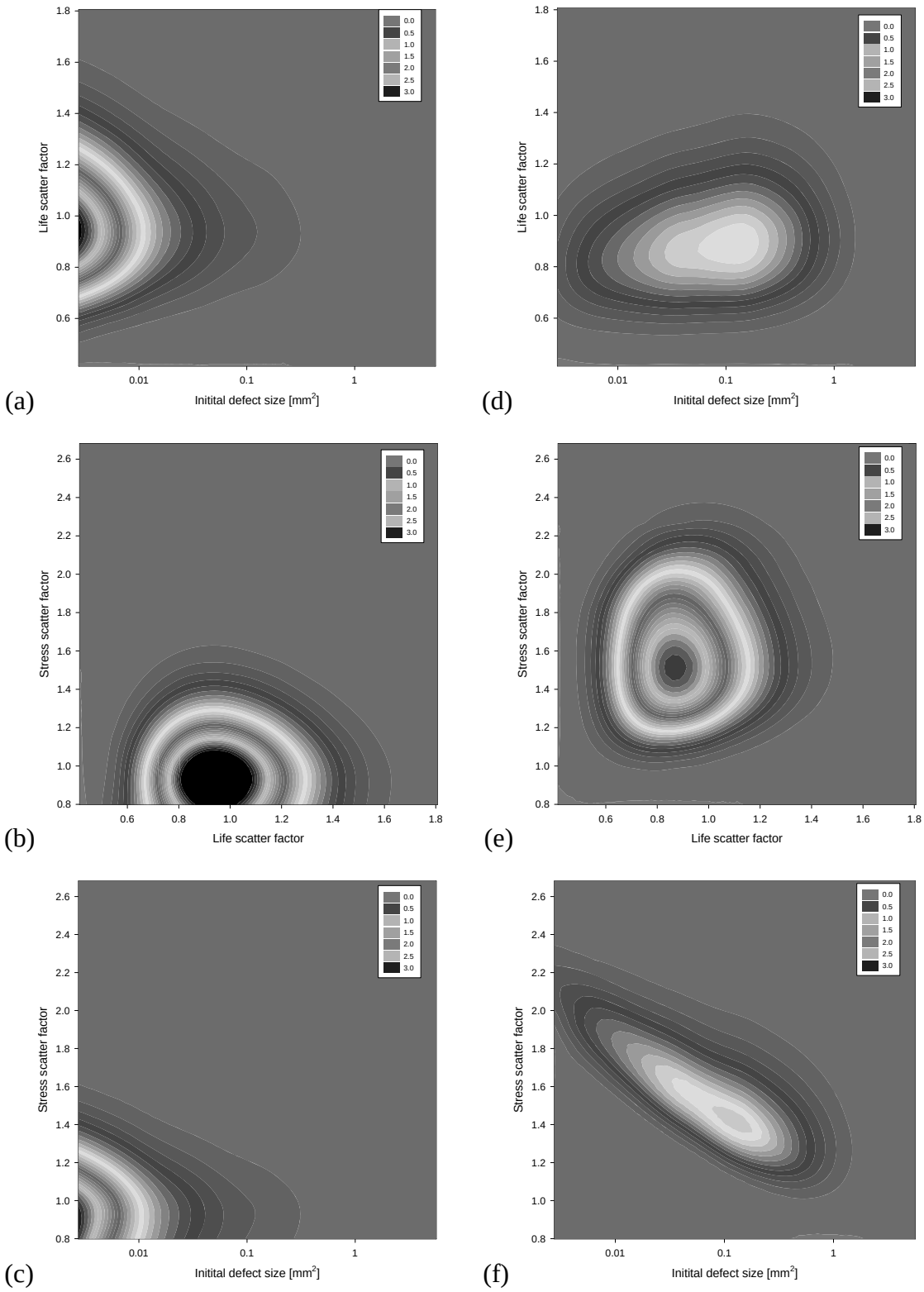

Figure V-6. Joint Original and Conditional Probability Densities: (a,b,c) Original Densities; (d,e,f) Conditional Densities

For the stress scatter factor, the high-density region in the conditional density is located near stress values that are approximately 60% greater than for these associated with the original density (compare figure V-6(b) and (c) with (e) and (f), respectively). This indicates that failure is more likely to occur for large stress scatter values.

Summary statistics for the original and conditional densities associated with the three random variables are indicated in table V-1. The results in table V-1 indicate that failure is more likely to occur if the median stress scatter factor is about 60% larger than average and the geometric mean initial anomaly size is about 8 times larger than average (based on the original densities). The conditional density associated with the life scatter factor is very similar to the original density, suggesting that it may not have as much influence on the failure as the other random variables. It is interesting to note that the COV associated with the logarithm of initial anomaly size conditional density is much smaller than the COV of the original density. This is entirely due to a shift in the mean since the standard deviation has actually increased. This illustrates the overall reduction in variability associated with the conditional initial anomaly density.

Table V-1. Summary Statistics for the Original and Conditional Densities Associated With Gas Turbine Engine Random Variables

Random Variable	Statistical Descriptor	Original Density	Conditional Density
Initial anomaly area *d*	mean (mm^2)	16.0	125.0
Log (*d*)	COV	42.5%	30%
Stress scatter factor *B*	median	1.0	1.63
Stress scatter factor *B*	COV	20.0%	16.0%
Life scatter factor *S*	median	1.0	0.928
Life scatter factor *S*	COV	20.0%	20.0%
S and *B*	correlation	0.0	0.09
d and *S*	correlation	0.0	0.15
d and *B*	correlation	0.0	-0.72

The three random variables are uncorrelated. However, the conditional variables $x|F$ are correlated since they are all related by the failure event F. The strong negative correlation between conditional stress scatter factor and conditional initial anomaly size (table V-1) suggests that failure is not likely to occur for small initial anomalies unless the stress scatter factor is relatively high. However, large initial anomalies can lead to failure even when stress is relatively small. The likelihood of failure due to a combination of large anomaly and small stress scatter is about equal to the likelihood of failure caused by a combination of small anomalies and high-stress scatter values (see figure V-6(f)). Some correlation also exists among the remaining conditional variables.

V.6 APPLICATION OF CFA TO SELECTION OF MANUFACTURING INSPECTION METHOD.

Nondestructive inspection methods can be used to reduce the probability of fracture of engine disks. Assume that five different crack inspection techniques (IT 1-5) with lognormal pdf are available (figure V-7). The median probability of detection (PoD) value decreases by an order of magnitude for each IT, and the amount of scatter is identical for all ITs. These inspections are applied before the component is placed in service. The influence of these inspections on the cumulative probability of fracture of a typical engine disk [V-13] is shown in figure V-8. It can be observed that the largest changes in the probability of fracture occur when the technique is changed from IT-2 to IT-3, and from IT-3 to IT-4. Techniques IT-1 and IT-2 have only a small influence on probability of fracture reduction.

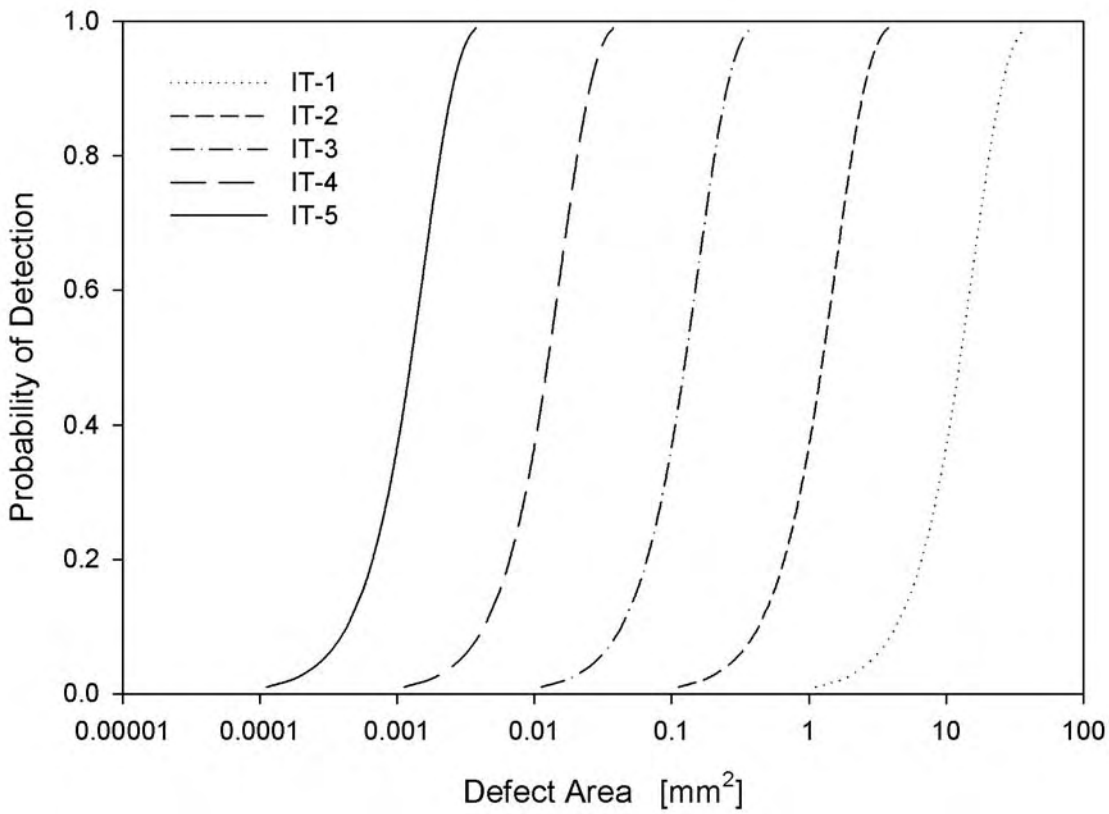

Figure V-7. Probability of Detection Curves Associated With Several Inspection Techniques

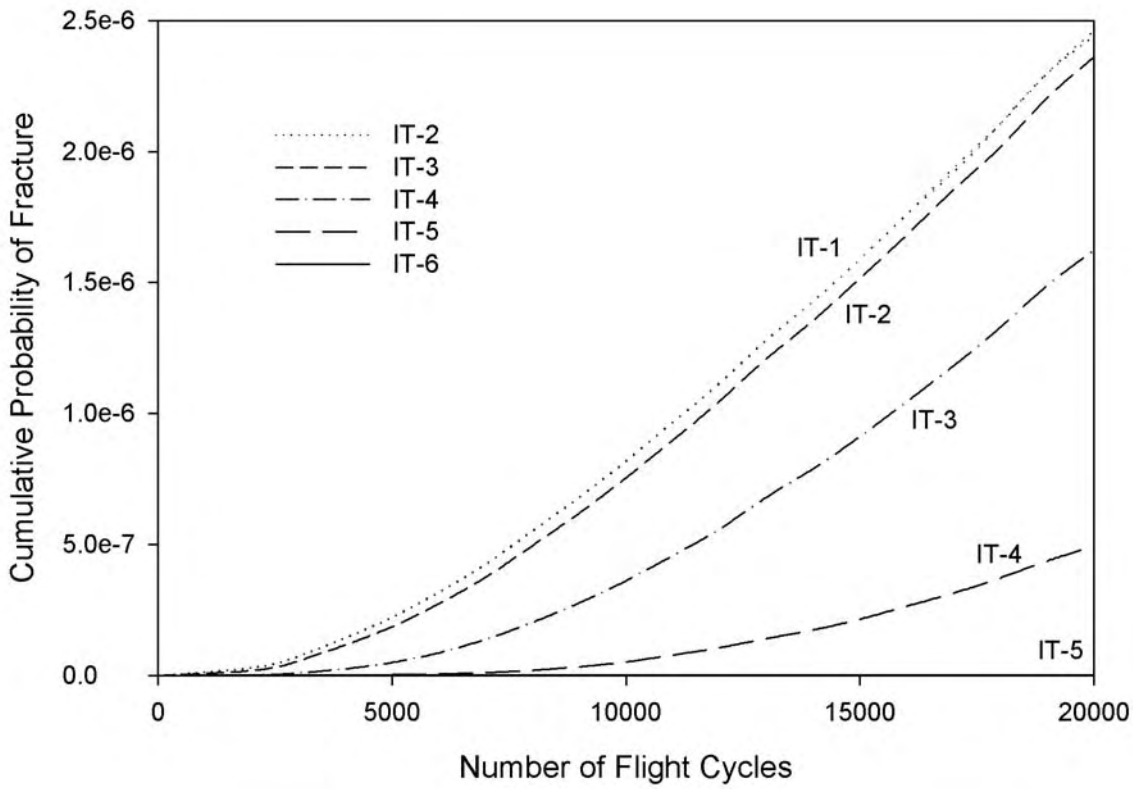

Figure V-8. Failure Probability per Flight Cycle Associated With Several Inspection Techniques

The most effective ITs detect cracks that can lead to fracture during the service life of the component. CFA can be used to identify the techniques that focus on the cracks that can lead to fracture. This is illustrated by superimposing the ITs from figure V-7 on the densities from figure V-6(a) and (d), as shown in figure V-9. When the ranges of detection for the each of the ITs are overlaid on top of the original densities (figure V-9(a)), it appears that only IT-5 and IT-6 significantly influence the probability of fracture results. However, since many of the smaller cracks shown in this figure do not lead to failure within the service life, this result is misleading. Overlaying the ranges of IT-4 and IT-5 with the conditional densities (figure V-9(b)), it can be observed that a significant portion of the cracks that lead to fracture can be detected. This is consistent with the cumulative probability simulation results shown in figure V-8, and demonstrates how the conditional densities can be used for maintenance planning decisions. It is important to note that the results shown in figure V-9 are based on conditional densities only. Since no simulations are required to quantify the influence of the various inspections on the probability of fracture, the results can be achieved much more efficiently.

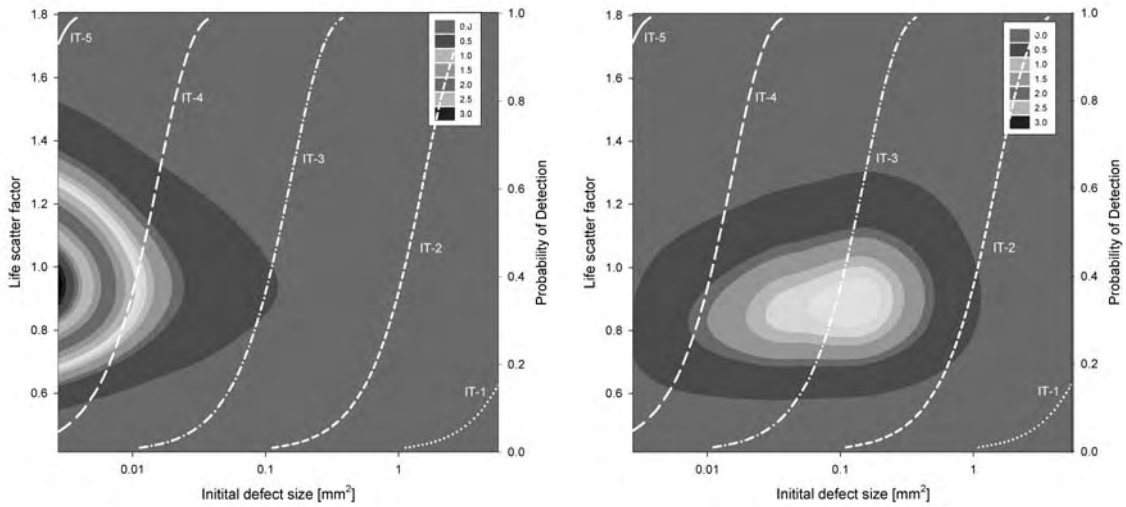

(a) (b)

Figure V-9. Overlay of Inspection PoD Curves and Initial Anomaly Densities: (a) Original Densities and (b) Conditional Densities

V.7 SUMMARY.

This appendix demonstrates a method for generating conditional failure densities when only a small number of random variables are present. The following observations can be made regarding the CFA technique presented in this appendix:

- It provides the engineer with valuable information regarding the most likely combination of input variables associated with failure (similar to the most probable failure point associated with the first-order reliability method).
- It indicates the most important range of values for each of the input random variables can be used to guide modeling and validation experiments for these variables.
- It can be used as a measure of the sensitivity of a random variable to the probability of fracture (i.e., the degree to which these densities differ indicates the relative sensitivity).
- The conditional densities can be used to efficiently gauge the effectiveness of in-service or maintenance inspections. In this case, no simulations are required to select the most effective inspection.

The technique provides the additional information needed for statistical analysis of the failure regions associated with the random variables. The results can be applied to failure analysis and model validation of general aerospace components.

V.8 REFERENCES.

V-1. Chakravarti, I.M., Laha, R.G., and Roy, J., *Handbook of Methods of Applied Statistics, Volume I*, John Wiley and Sons, 1967, pp. 392-394.

V-2. Stephens, M.A., "EDF Statistics for Goodness of Fit and Some Comparisons," *Journal of the American Statistical Association*, 69, 1974, pp. 730-737.

V-3. Shapiro, S.S. and Wilks, M.B., "An Analysis of Variance Test for Normality (Complete Samples)," *Biometrika*, 52 (3/4), pp. 591-611, 1965.

V-4. Snedecor, G.W. and Cochran, W.G., *Statistical Methods, Eighth Edition*, Iowa State University Press, 1989.

V-5. Wu, Y.-T., Enright, M.P., and Millwater, H.R., "Probabilistic Methods for Design Assessment of Reliability with Inspection," *AIAA Journal*, 40(5), 2002, pp. 937-946.

V-6. Myers, R.H. and Montgomery, D.C., *Response Surface Methodology: Process and Product Optimization Using Design of Experiments*, John Wiley, New York, 2002.

V-7. Maes, M.A., Breitung, K., and Dupuis, D.J., "Asymptotic Importance Sampling," *Structural Safety* 12, 1993, pp. 167-186.

V-8. Madsen, H.O., Krenk, S., and Lind, N.C., *Methods of Structural Safety*, Prentice-Hall, Englewood Cliffs, NJ, 1986.

V-9. Au, S.K. and Beck, J.L., "Application of Subset Simulation to Seismic Risk Analysis," *15th ASCE Engineering Mechanics Conference*, Columbia University, New York, NY, CD-ROM, 2002.

V-10. Leverant, G.R. et al., "Turbine Rotor Material Design," FAA report DOT/FAA/AR-00/64, December 2000.

V-11. Aerospace Industries Association Rotor Integrity Subcommittee, "The Development of Anomaly Distributions for Aircraft Engine Titanium Disk Alloys," *Proceedings, 38th Structures, Structural Dynamics, and Materials Conference*, Kissimmee, FL, April 7-10, 1997, pp. 2543-2553.

V-12. Paris, P.C. and Erdogan, F., "A Critical Analysis of Crack Propagation Laws," *Journal of Basic Engineering*, ASME, 85(4), 1963, pp. 528-534.

V-13. Huyse, L. and Enright, M.P., "Efficient Statistical Analysis of Failure Risk in Engine Rotor Disks Using Importance Sampling Techniques," *Proceedings of the 44th AIAA/ASME/ASCE/AHS/ASC Structures, Structural Dynamics, and Materials Conference, Non-Deterministic Approaches Forum*, Norfolk, VA, April 7-10, 2003, AIAA Paper 2003-1838.

APPENDIX W—LIST OF PUBLICATIONS AND PRESENTATIONS DURING "TURBINE ROTOR MATERIAL DESIGN, PHASE II" GRANT

W.1 PUBLICATIONS.

1. "A Convergent Zone-Refinement Method for Risk Assessment of Gas Turbine Disks Subject to Low-Frequency Metallurgical Defects," H. R. Millwater, M. P. Enright, and S. K. Fitch, accepted for publication in *ASME Journal of Engineering for Gas Turbines and Power*.

2. "A Literature Survey on The Stability and Significance of Residual Stresses During Fatigue," R. C. McClung, accepted for publication in *Fatigue and Fracture of Engineering Materials and Structures*.

3. "Efficient Conditional Failure Analysis–Application to an Aircraft Engine Component," Huyse, L. and Enright, M.P., *Structure and Infrastructure Engineering*, Taylor & Francis, Vol. 2, No. 3, 2006, pp. 221-230.

4. "Fracture Mechanics-Based Probabilistic Life Prediction of Components With Large Numbers of Inherent Material Anomalies," M. P. Enright, L. Huyse, and R. C. McClung, *Proceedings, Ninth International Conference on Structural Safety and Reliability* (ICOSSAR), Rome, Italy, June 2005, pp. 601-607.

5. "A Probabilistic Framework for Risk Prediction of Gas Turbine Engine Components With Inherent or Induced Material Anomalies," M. P. Enright, R. C. McClung, and L. Huyse, Paper GT-2005-68982, *Proceedings of the 50th ASME International Gas Turbine & Aeroengine Technical Congress*, Reno, Nevada, June 2005.

6. "Surface Damage Tolerance Analysis of a Gas Turbine Engine Rotor," A. Jameel, Paper GT-2005-68760, *Proceedings of the 50th ASME International Gas Turbine & Aeroengine Technical Congress*, Reno, Nevada, June 2005.

7. "Applications of the Generalized Conditional Expectation Method for Enhancing a Probabilistic Fatigue Design Code, " F. N. Momin, H. R. Millwater, R. W. Osborn, and M. P. Enright, Paper AIAA-2005-2146, *Proceedings of the 46th AIAA/ASME/ASCE/AHS/ ASC Structures, Structural Dynamics, and Materials Conference, Non-Deterministic Approaches Forum*, Austin, Texas, April 2005.

8. "Application of Probabilistic Sensitivities to Probabilistic Fatigue Analysis of Gas Turbine Engine Disks," R. W. Osborn and H. R. Millwater, Paper AIAA-2005-2147, *Proceedings of the 46th AIAA/ASME/ASCE/AHS/ASC Structures, Structural Dynamics, and Materials Conference, Non-Deterministic Approaches Forum*, Austin, Texas, April 2005.

9. "Methodology for Probabilistic Life Prediction of Multiple Anomaly Materials," M. P. Enright and L. Huyse, Paper AIAA-2005-2213, *Proceedings of the 46th*

AIAA/ASME/ASCE/ AHS/ASC Structures, Structural Dynamics, and Materials Conference, Non-Deterministic Approaches Forum, Austin, Texas, April 2005. Also published in *AIAA Journal*, Vol. 44, No. 4, pp. 787-793.

10. "A Software Framework for Probabilistic Fatigue Life Assessment of Gas Turbine Engine Rotors," R. C. McClung, M. P. Enright, H. R. Millwater, G. R. Leverant, and S. J. Hudak, Jr., *Journal of ASTM International*, Vol. 1, September 2004, Paper JAI11563. Also published in *Probabilistic Aspects of Life Prediction, ASTM STP 1450,* W. S. Johnson and B. M. Hillberry, eds., ASTM International, West Conshohocken, PA, 2004, pp. 199-215.

11. "Application of a Conditional Expectation Response Surface Approach to Probabilistic Fatigue," F. N. Momin, H. R. Millwater, R. W. Osborn, and M. P. Enright, *Proceedings of the 9th ASCE Specialty Conference on Probabilistic Mechanics and Structural Reliability*, ASCE Paper PMC2004-204, Albuquerque, New Mexico, July 2004.

12. "Efficient Fracture Design for Complex Turbine Engine Components," R. C. McClung, M. P. Enright, Y.-D. Lee, L. Huyse, and S. Fitch, Paper GT-2004-53323, *Proceedings of the 49th ASME International Gas Turbine & Aeroengine Technical Congress*, Vienna, Austria, June 2004. Accepted for publication in *ASME Journal of Engineering for Gas Turbines and Power*.

13. "Adaptive Optimal Sampling Methodology for Zone-Based Probabilistic Life Prediction," M. P. Enright, H. R. Millwater, and L. Huyse, Paper AIAA-2004-1829, *Proceedings of the 45th AIAA/ASME/ASCE/AHS/ASC Structures, Structural Dynamics, and Materials Conference, Non-Deterministic Approaches Forum*, Palm Springs, California, April 2004. Also published in *AIAA Journal*, Vol. 44, No. 3, pp. 523-528.

14. "Application of Parallel Processing to Probabilistic Fracture Mechanics Analysis of Gas Turbine Disks," H. R. Millwater, B. D. Shook, S. Guduru, and G Constaninides, Paper AIAA-2004-1745, *Proceedings of the 45th AIAA/ASME/ASCE/AHS/ASC Structures, Structural Dynamics, and Materials Conference, Non-Deterministic Approaches Forum*, Palm Springs, California, April 2004.

15. "Methodology for Application of 3-D Stresses to Surface Damage-Based Risk Assessment," C. Waldhart, M. P. Enright, and S. H. K. Fitch, Paper AIAA-2004-1599, *Proceedings of the 45th AIAA/ASME/ASCE/AHS/ASC Structures, Structural Dynamics, and Materials Conference, Non-Deterministic Approaches Forum*, Palm Springs, California, April 2004.

16. "Probabilistic Methodology for Life Prediction of Aircraft Turbine Rotors," M. P. Enright, L. Huyse, R. C. McClung, and H. R. Millwater, *Proceedings of the 9th Biennial ASCE Aerospace Division International Conference on Engineering, Construction and Operations in Challenging Environments (Earth & Space 2004)*, R. B. Malla & A. Maji, eds., ASCE, Houston, TX, March 2004, pp. 453-460.

17. "A New Tool for Design and Certification of Aircraft Turbine Rotors," G. R. Leverant, R. C. McClung, H. R. Millwater, and M. P. Enright, *ASME Journal of Engineering for Gas Turbines and Power*, Vol. 126, January 2004, pp. 155-159.

18. "Effects of CTE-Induced Residual Stresses Around Hard Alpha Particles on Fatigue Crack Growth in Ti-6Al-4V," P. J. Laz, K. S. Chan, R. C. McClung, and G. R. Leverant, *Fatigue and Fracture of Engineering Materials and Structures*, Vol. 26, No. 12, December 2003, pp. 1145-1157.

19. "Probabilistic Surface Damage Tolerance Assessment of Aircraft Turbine Rotors," M. P. Enright, Y-D. Lee, R. C. McClung, L. Huyse, G. R. Leverant, H. R. Millwater, and S. K. Fitch, Paper GT-2003-38731, *Proceedings of the 48th ASME International Gas Turbine & Aeroengine Technical Congress*, Atlanta, Georgia, June 2003.

20. "Efficient Statistical Analysis of Failure Risk in Engine Rotor Disks Using Importance Sampling Techniques," L. Huyse and M. P. Enright, AIAA Paper 2003-1838, *Proceedings of the 44th AIAA/ASME/ASCE/AHS/ASC Structures, Structural Dynamics, and Materials Conference, Non-Deterministic Approaches Forum*, Norfolk, VA, April 2003.

21. "Application of an XML-Based Database for Probabilistic Analysis," H. R. Millwater, S. K. Fitch, M. P. Enright, and L. Huyse, AIAA Paper 2003-1837, *Proceedings of the 44th AIAA/ASME/ASCE/AHS/ASC Structures, Structural Dynamics, and Materials Conference, Non-Deterministic Approaches Forum*, Norfolk, VA, April 2003.

22. "A New Tool for Design and Certification of Aircraft Turbine Rotors," G. R. Leverant, R. C. McClung, H. R. Millwater, and M. P. Enright, Paper GT-2002-30303, *Proceedings of the 47th ASME International Gas Turbine & Aeroengine Technical Congress*, Amsterdam, The Netherlands, June 2002.

23. "Optimal Sampling Techniques for Zone-Based Probabilistic Fatigue Life Prediction," M. P. Enright and H. R. Millwater, AIAA Paper 2002-1383, *Proceedings of the 43rd AIAA/ASME/ASCE/AHS/ASC Structures, Structural Dynamics, and Materials Conference, Non-Deterministic Approaches Forum*, Denver, Colorado, April 2002.

24. "A Convergent Probabilistic Technique for Risk Assessment of Gas Turbine Disks Subject to Metallurgical Defects," H. R. Millwater, M. P. Enright, and S. K. Fitch, AIAA Paper 2002-1382, *Proceedings of the 43rd AIAA/ASME/ASCE/AHS/ASC Structures, Structural Dynamics, and Materials Conference, Non-Deterministic Approaches Forum*, Denver, Colorado, April 2002.

25. "Probabilistic Methods for Design Assessment of Reliability With Inspection," Y.-T. Wu, M. P. Enright, and H. R. Millwater, *AIAA Journal*, Vol. 40, No. 5, 2002, pp. 937-946.

26. "Efficient and Accurate Methods for Probabilistic Analysis of Titanium Rotors," Y.-T. Wu, H. R. Millwater, and M. P. Enright, Paper PMC2000-221, *Proceedings of the*

8th ASCE Specialty Conference on Probabilistic Mechanics and Structural Reliability, South Bend, Indiana, July 2000.

27. "A Probabilistically-Based Damage Tolerance Analysis Computer Program for Hard Alpha Anomalies in Titanium Rotors," H. Millwater, J. Wu, D. Riha, M. Enright, G. Leverant, C. McClung, C. Kuhlman, G. Chell, Y. Lee, S. Fitch, and J. Meyer, Paper 2000-GT-0421, *Proceedings of the 45th ASME International Gas Turbine & Aeroengine Technical Congress*, Munich, Germany, May 2000.

28. "Probabilistic Methods for Design Assessment of Reliability With Inspection (DARWIN)," Y.-T. Wu, M.P. Enright, H.R. Millwater, G. Chell, C. Kuhlman, and G.R Leverant, Paper AIAA-2000-1510, *Proceedings of the 41st AIAA/ASME/ASCE/AHS/ASC Structures, Structural Dynamics, and Materials Conference,* Atlanta, Georgia, April 2000.

29. "Probabilistic Fatigue Life Sensitivity Analysis of Titanium Rotors," M.P. Enright and Y.-T. Wu, Paper AIAA-2000-1647, *Proceedings of the 41st AIAA/ASME/ASCE/ AHS/ASC Structures, Structural Dynamics, and Materials Conference*, Atlanta, Georgia, April 2000.

W.2 PRESENTATIONS (NO PUBLISHED PAPERS).

1. "The DARWIN Computer Program for Probabilistic Damage Tolerance Analysis of Engine Rotors," R. C. McClung and M. P. Enright, *Australian Defence Force Engine Symposium*, Melbourne, Australia, October 2003.

2. "An Executive Update on the Turbine Rotor Material Design (TRMD) Program," R. C. McClung; "Summary of New DARWIN Capabilities for Surface Damage Tolerance Assessment and Related Enhancements," M. Enright, L. Huyse, Y. Lee, G. Chell, C. McClung, G. Leverant, H. Millwater, and S. Fitch; "Recent Probabilistic Computational Efficiency Improvements in DARWIN," L. Huyse, M. Enright, H. Millwater, and S. Fitch; "Application of DARWIN to Evaluate Risk of Fracture Due to Material Anomalies in Gas Turbine Engines," A. Jameel, D. Lehmann, J. Tschopp, and J. Dubke, *6th Annual FAA/Air Force/NASA/Navy Workshop on the Application of Probabilistic Methods to Gas Turbine Engines*, Solomon's Island, Maryland, March 2003.

3. "Update on the FAA Turbine Rotor Material Design Program," G.R. Leverant; "Crack Nucleation and Growth Data and Modeling," R. C. McClung; "DARWIN Enhancements for Probabilistic Risk Assessment," H.R. Millwater and M.P. Enright; "Probabilistic Reliability Validation of an Impeller Using DARWIN," S. Muju, R. Nelson, and J. Lentz, *5th Annual FAA/Air Force/NASA/Navy Workshop on the Application of Probabilistic Methods to Gas Turbine Engines*, Westlake, Ohio, June 2001.

4. "A Probabilistically-Based Damage Tolerance Analysis Computer Program for Engine Rotor Integrity," H. R. Millwater, M. P. Enright, R. C. McClung, and G. R. Leverant, *12th AeroMat Conference and Exhibition (AeroMat 2001)*, TES-4.6, Long Beach, California, June 2001.

5. "A Probabilistic Damage Tolerance Analysis Computer Program for Engine Rotor Integrity," H. R. Millwater, M. P. Enright, R. C. McClung, and G. R. Leverant, *Forum 57, American Helicopter Society, Special Session on Engine Life Management: Addressing Fleet Risk with Innovative Approaches*, Washington, DC, May 2001.

6. "Development of a Probabilistic Damage Tolerant Code (DARWIN) for Turbine Rotor Materials," G. Leverant, C. McClung, H. Millwater, and J. Wu, *4th Annual FAA/Air Force Workshop on the Application of Probabilistic Methods to Gas Turbine Engines*, Jacksonville, Florida, December 1999.

7. "A Probabilistically-Based Damage Tolerance Analysis Computer Program for Hard Alpha Defects in Titanium Rotors," H. Millwater, J. Wu, M. Enright, D. Riha, G. Leverant, C. McClung, G. Chell, C. Kuhlman, S. Fitch, M. Gorelik, D. Hermann, G. Mihlbachler, and D. Lehmann, *USAF Structural Integrity Program Conference*, San Antonio, Texas, November 1999.